Vol. 38 Nos 1–4
May–August 1997

ISSN: 0263–8223

COMPOSITE STRUCTURES

EDITOR: I.H. MARSHALL

Special Issue

Ninth International Conference on Composite Structures

DISTRIBUTION STATEMENT A
Approved for public release;
Distribution Unlimited

DTIC QUALITY INSPECTED 4

ELSEVIER

COMPOSITE STRUCTURES

The past few decades have seen outstanding advances in the use of composite materials in structural applications. There can be little doubt that, within engineering circles, composites have revolutionised traditional design concepts and made possible an unparalleled range of new exciting possibilities as viable materials of construction. *Composite Structures*, an International Journal, disseminates knowledge between users, manufacturers, designers and researchers involved in structures or structural components manufactured using composite materials.

The journal publishes papers which contribute to knowledge in the use of composite materials in engineering structures. Papers may be on design, research and development studies, experimental investigations, theoretical analyses and fabrication techniques relevant to the application of composites in load-bearing components for assemblies. These could range from individual components such as plates and shells to complete composite structures.

Editor

PROFESSOR I. H. MARSHALL
Department of Mechanical and Manufacturing Engineering,
University of Paisley, Paisley PA1 2BE, UK

Editorial Board

S. Adali
University of Natal, Republic of South Africa

W. M. Banks
University of Strathclyde, Glasgow, UK

P. Beardmore
Ford Motor Co., Dearborn, Michigan, USA

C. W. Bert
University of Oklahoma, Norman, USA

H. F. Brinson
University of Houston, Texas, USA

A. R. Bunsell
Ecole Nationale Superieure des Mines de Paris, France

Lien-Wen Chen
National Cheng Kung University, Tainan, Taiwan

R. Byron Pipes
University of Delaware, Newark, USA

A. H. Cardon
Free University of Brussels, Pleinlann, Belgium

T. Hayashi
Research Centre of Computational Mechanics, Inc.,
Tokyo, Japan

R. Jones
Monash University, Clayton, Victoria, Australia

A. W. Leissa
The Ohio State University, Columbus, USA

F. L. Matthews
Imperial College, London, UK

A. Miravete
University of Zaragoza, Spain

K. Moser
Universität Innsbruck, Austria

Y. Narita
Hokkaido Institute of Technology, Sapporo, Japan

A. N. Palazotto
Air Force Institute of Technology, Dayton, Ohio, USA

G. J. Turvey
University of Lancaster, Bailrigg, UK

J. F. M. Wiggenraad
National Aerospace Laboratory, Emmeloord,
The Netherlands

Publishing Office
Elsevier Science Ltd, The Boulevard, Langford Lane, Kidlington, Oxford OX5 1GB, UK
[*Tel:* (+44) (01865) 843730; *Fax:* (+44) (01865) 843969]

Advertising Offices
North America—Elsevier Science Inc., 660 White Plains Road, Tarrytown, NY 10591-5153, USA
Rest of the World—Elsevier Science Ltd, The Boulevard, Langford Lane, Kidlington, Oxford OX5 1GB, UK
[*Tel:* (+44) (01865) 843000; *Fax:* (+44) (01865) 843010]

Subscriptions

1997—Three volumes, four issues per volume, plus one volume, one issue (Volumes 37–40). Annual Institutional Subscription Rates 1997: Europe, The CIS and Japan 3653.00 Dutch Guilders. All other countries US$2255.00. Associated Personal Subscription rates are available on request for those whose institutions are library subscribers. Dutch Guilder prices exclude VAT. Non-VAT registered customers in the European Community will be charged the appropriate VAT in addition to the price listed. Prices include postage and insurance and are subject to change without notice.

For orders, claims, product enquiries (no manuscript enquiries) please contact the Customer Support Department at the Regional Sales Office nearest to you: **The Americas:** Elsevier Science Customer Support Department, PO Box 945, New York, NY 10010, USA (Tel: (+1) 212-633-3730/1-888 4ES-INFO; Fax: (+1) 212-633-3680; Email: usinfo-f@elsevier.com). **Japan:** Elsevier Science Customer Support Department, 9-15 Higashi-Azabu 1-chome, Minato-ku, Tokyo 106, Japan (Tel: (+3) 5561-5033; Fax: (+3) 5561-5047; Email: info@elsevier.co.jp). **Asia Pacific (*excluding Japan*):** Elsevier Science (Singapore) Pte Ltd, No. 1 Temasek Avenue, 17-01 Millenia Tower, Singapore 039192 (Tel: +65) 434-3727; Fax: (+65) 337-2230; Email: asiainfo@elsevier.com.sg). **Rest of the World:** Elsevier Science Customer Service Department, PO Box 211, 1001 AE Amsterdam, The Netherlands (Tel: (+31) 20-485-3757; Fax: (+31) 20-485-3432; Email: nlinfo-f@elsevier.nl).

Back Issues

Back issues of all previously published volumes are available direct from Elsevier Science Offices (Oxford and New York). Complete volumes and single issues can be purchased for 1992–1996. Earlier issues are available in high quality photo-duplicated copies as complete volumes only.

PERIODICALS POSTAGE PAID AT RAHWAY, NEW JERSEY. *Composite Structures* (ISSN 0263-8223) is published monthly as three volumes per year, four issues per volume, plus one volume, one issue, by Elsevier Science Ltd, The Boulevard, Langford Lane, Kidlington, Oxford OX5 1GB, UK. The annual subscription in the USA is $2255. *Composite Structures* is distributed by Mercury Airfreight International Ltd, 2323 Randolph Avenue, Avenel, NJ 07001-2413, USA. POSTMASTER: Please send address changes to *Composite Structures*, c/o Elsevier Science Regional Sales Office, Customer Support Department, 655 Avenue of the Americas, New York, NY 10010, USA. [Tel: (+1) 212-633-3730/1-888 4ES-INFO; Fax: (+1) 212-633-3680; E-mail: usinfo-f@elsevier.com].

© 1997 Elsevier Science Ltd. All rights reserved

COMPOSITE STRUCTURES

VOL. 38 1997

SPECIAL ISSUE

Ninth International Conference
on Composite Structures

EDITOR

I. H. MARSHALL

DTIC QUALITY INSPECTED 8

ELSEVIER

19980414 150

ContentsDirect delivers the table of contents of this journal, by e-mail, approximately two–four weeks prior to each issue's publication. To receive this free service send an e-mail message to cdsubs@elsevier.co.uk.

© 1997 Elsevier Science Ltd. All rights reserved.

Upon acceptance of an article by the journal, the author(s) will be asked to transfer copyright of the article to the publisher. The transfer will ensure the widest possible dissemination of information. This journal and the individual contributions contained in it are protected by the copyright of Elsevier Science Ltd and the following terms and conditions apply to their use:

Photocopying
Single photocopies of single articles may be made for personal use as allowed by national copyright laws. Permission of the publisher and payment of a fee is required for all other photocopying, including multiple or systematic copying, copying for advertising or promotional purposes, resale, and all forms of document delivery. Special rates are available for educational institutions that wish to make photocopies for non-profit educational classroom use.

In the USA, users may clear permissions and make payment through the Copyright Clearance Center, 222 Rosewood Drive, Danvers, MA 01923, USA. In the UK, users may clear permissions and make payment through the Copyright Licensing Agency Rapid Clearance Service (CLARCS), 90 Tottenham Court Road, London W1P 9HE, UK. In other countries where a local copyright clearance centre exists, please contact it for information on required permissions and payments.

Derivative Works
Subscribers may reproduce tables of contents or prepare lists of articles including abstracts for internal circulation within their institutions. Permission of the publisher is required for resale or distribution outside the institution.

Permission of the publisher is required for all other derivative works, including compilations and translations.

Electronic Storage
Permission of the publisher is required to store electronically any material contained in this journal, including any article or part of an article. Contact the publisher at the address indicated.

Except as outlined above, no part of this publication may be reproduced, stored in a retrieval system or transmitted in any form or by any means, electronic, mechanical, photocopying, recording or otherwise, without prior written permission of the publisher.

Notice
No responsibility is assumed by the publisher for any injury and/or damage to persons or property as a matter of products liability, negligence or otherwise, or from any use or operation of any methods, products, instruction or ideas contained in the material herein.

Although all advertising material is expected to conform to ethical (medical) standards, inclusion in this publication does not constitute a guarantee or endorsement of the quality or value of such product or of the claims made of it by its manufacturer.

♾ ™The paper used in this publication meets the minimum requirements of American National Standard for Information Sciences—Permanence of Paper for Printed Library Materials, ANSI Z39.48-1984.

The Item-fee Code for this publication is: 0263-8223/97 $17.00

Typeset in Great Britain by Unicus Graphics Ltd, Horsham
Printed in Great Britain by Galliard (Printers) Ltd, Great Yarmouth

ELSEVIER

Composite Structures **38** (1997) iii–viii
© 1997 Elsevier Science Limited
Printed in Great Britain All rights reserved
0263-8223/97/$17.00

Contents

Special Issue: Ninth International Conference on Composite Structures

vii Preface
I. H. MARSHALL (UK)

1 National Engineering Laboratory Composite Structures Award

3 Analysis of pultruded glass reinforced plastic beams with semi-rigid end connections
G. J. TURVEY (UK)

17 Actuation and sensing of piezolaminated sandwich type structures
H. ABRAMOVICH & B. PLETNER (Israel)

29 Buckling analysis of functionally graded plates subjected to uniaxial loading
E. FELDMAN & J. ABOUDI (Israel)

37 A new laminated triangular finite element assuring interface continuity for displacements and stresses
O. POLIT & M. TOURATIER (France)

45 An investigation into the eigen-nature of cracked composite beams
A. A. EL-HAMID HAMADA (Egypt)

57 Composite wraps for ageing infrastructure: concrete columns
S. HANNA & R. JONES (Australia)

65 First-ply failure strength of laminate composite pressure vessels
T. Y. KAM, Y. W. LIU & F. T. LEE (Republic of China)

71 The role of material nonlinearities in composite structures
W. K. CHIU, S. GALEA & R. JONES (Australia)

83 On the response of MMC laminated plates to non-uniform temperature loading: the effect of temperature-dependent material properties
E. FELDMAN & I. BELOSTOTSKY (Israel)

91 Design, fabrication and testing of a composite bracket for aerospace applications
M. G. S. J. THUIS & C. BIEMANS (The Netherlands)

99 Multiple eigenvalue optimization of composite structures using discrete third order displacement models
C. M. MOTA SOARES, C. A. MOTA SOARES & V. M. FRANCO CORREIA (Portugal)

111 Determination of the load-carrying capacity of steel fibre reinforced concrete beams
J. A. PURKISS, P. J. WILSON (UK) & P. BLAGOJEVIĆ (Serbia)

119 Buckling behaviour of laminated beam structures using a higher-order discrete model
M. A. RAMOS LOJA, J. INFANTE BARBOSA & C. M. MOTA SOARES (Portugal)

133 Study of damage evolution in composites using damage mechanics and micromechanics
Y. W. KWON & C. T. LIU (USA)

141 Fibre-reinforced caissons for offshore applications
P. J. BOOTHBY & C. D. JOHNSTONE (UK)

151 Axisymmetric vibration analysis of laminated hollow cylinders with ring stiffeners
J. YE (UK)

157 Interlaminar stresses in laminated composite plates, cylindrical/spherical shell panels damaged by low-velocity impact
S. GANAPATHY & K. P. RAO (India)

169 The stability of composite material stiffened conical shells under axial compression
L. LI (Canada)

179 Compressible flow analysis of filling and post-filling in injection molding with phase-change effect
K.-H. HAN & Y.-T. IM (South Africa)

191 Local buckling loads of sandwich panels made with laminated faces
M. A. AIELLO & L. OMBRES (Italy)

203 Composite nozzle dam in the steam generator of a nuclear reactor
J. H. OH, D. G. LEE & T. R. KIM (Korea)

215 Adhesively bonded lap-joints for the composite–steel shell structure of high-speed vehicles
K. C. SHIN, Y. G. KIM, D. G. LEE & J. M. CHOI (Korea)

229 Composite side-door impact beams for passenger cars
S. S. CHEON, D. G. LEE & K. S. JEONG (Korea)

241 Flexural–torsional buckling of pultruded fiber reinforced plastic composite I-beams: experimental and analytical evaluations
J. F. DAVALOS, P. QIAO & H. A. SALIM (USA)

251 Improvement of the dynamic properties of a steel–composite hybrid flexspline of a harmonic drive
S. H. OH, S. H. CHANG & D. G. LEE (Korea)

261 A three-dimensional modelling technique for predicting the linear elastic property of opened-packing woven fabric unit cells
P. TAN, L. TONG & G. P. STEVEN (Australia)

273 Stress expressions of single-lap adhesive joints of dissimilar adherends
Z. J. WU (Republic of China), A. ROMEIJN & J. WARDENIER (The Netherlands)

281 Simplified linear and non-linear analysis of stepped and scarfed adhesive-bonded lap-joints between composite laminates
F. MORTENSEN & O. T. THOMSEN (Denmark)

295 Analysis and design of fiber reinforced plastic composite deck-and-stringer bridges
H. A. SALIM, J. F. DAVALOS, P. QIAO & S. A. KIGER (USA)

309 Manufacture of one-piece automotive drive shafts with aluminium and composite materials
D. H. CHO, D. G. LEE & J. H. CHOI (Korea)

321 Development of guide rollers using electroplated carbon fiber–epoxy composite for thin polymer film processing
K. G. BANG, J. K. CHOI, H. S. KIM, D. G. LEE & H. S. JEON (Korea)

329 Optimum bolted joints for hybrid composite materials
J. H. OH, Y. G. KIM & D. G. LEE (Korea)

343 Investigation on cutting mechanism in small diameter drilling for GFRP (thrust force and surface roughness at drilled hole wall)
K. OGAWA, E. AOYAMA, H. INOUE, T. HIROGAKI, H. NOBE, Y. KITAHARA, T. KATAYAMA & M. GUNJIMA (Japan)

351 Optimal design of composite hood with reinforcing ribs through stiffness analysis
D.-Y. KWAK, J.-H. JEONG, J.-S. CHEON & Y.-T. IM (South Korea)

361 Mechanical properties prediction of textile-reinforced composite materials using a multiscale energetic approach
D. BIGAUD & P. HAMELIN (France)

373 The influence of FRP inserts on the energy absorption of a foam-cored sandwich panel
M. S. FOUND, A. M. ROBINSON & J. J. CARRUTHERS (UK)

383 Nonlinear closed-form high-order analysis of curved sandwich panels
E. BOZHEVOLNAYA & Y. FROSTIG (Denmark)

395 The effect of tooling geometry on a new continuous fabrication system for SMC using roll forming
T. HIRAI & M. HIRAI (Japan)

405 Reduction in tensile and flexural strength of unidirectional glass fibre-epoxy with increasing specimen size
M. R. WISNOM & J. W. ATKINSON (UK)

413 Vibration control of an active laminated beam
P. GAUDENZI, R. CARBONARO & R. BARBONI (Italy)

421 Analysis of a glass-fibre sandwich panel for car body constructions
P. GAUDENZI, A. PASCUCCI, R. BARBONI (Italy) & A. HOROSCHENKOFF (Germany)

435 Effects of temperature on the creep behaviour of woven and stitched composites
R. G. BATHGATE, C. H. WANG & F. PANG (Australia)

447 Reliability formulation for composite laminates subjected to first-ply failure
T. Y. KAM & E. S. CHANG (Republic of China)

453 Free and forced vibration analysis of thin, laminated, cylindrically curved panels
N. S. BARDELL, J. M. DUNSDON & R. S. LANGLEY (UK)

463 Free vibration analysis of coplanar sandwich panels
N. S. BARDELL, J. M. DUNSDON & R. S. LANGLEY (UK)

477 Free vibration and flutter of damaged composite panels
R. M. V. PIDAPARTI (USA)

483 Thermogravimetric and binder removal analysis of injection moulded reinforced ceramic composite
R. K. Y. LI, C. M. L. WU & T. L. WONG (Hong Kong)

489 Transverse shear effects in discrete optimization of laminated compressed cylindrical shells
A. MUC (Poland)

499 Two-dimensional modelling of solid–fluid composites
T. KATAYAMA, H. YAMAMOTO & K. NISHITANI (Japan)

509 Damage growth analysis of low velocity impacted composite panels
L. REIS & M. DE FREITAS (Portugal)

517 Application of roll forming to SMC forming
T. KATAYAMA, Y. HAYAKAWA, M. HAKOTANI & M. SHINOHARA (Japan)

525 Effect of cracks on thermal stress and strain of a tape automated bonded package
C. M. L. WU, J. K. L. LAI (Hong Kong) & Y. WU (Republic of China)

531 Development of a composite boring bar
S. NAGANO, T. KOIZUMI, T. FUJII, N. TSUJIUCHI, H. UEDA & K. STEEL (Japan)

541 Buckling and vibration analysis of composite plate and shell structures using the PASSAS software package
D. J. DAWE & S. WANG (UK)

553 Use of woven CFRP for externally pressurized domes
J. BŁACHUT & L. S. DONG (UK)

565 Shape control of non-symmetric piezolaminated composite beams
M. EISENBERGER & H. ABRAMOVICH (Israel)

573 Compressive failure of carbon–foam sandwich composites with holes and/or partial delamination
Y. W. KWON (USA), S. H. YOON (Korea) & P. J. SISTARE (USA)

581 'Good vibrations', the science and application of intrinsically damped composite materials
I. D. GRANT, A. T. LOWE & S. THOMAS (UK)

589 Compressive behaviour of large undamaged and damaged thick laminated panels
G. ZHOU (UK)

599 Size effects in thin CFRP panels subjected to impact
M. S. FOUND, I. C. HOWARD & A. P. PARAN (UK)

609 The influence of reinforcement ring width on the buckling response of carbon fibre composite panels with circular cut-outs
J. EIBLMEIER (Canada) & J. LOUGHLAN (UK)

623 Minimum cost design of hybrid composite cylinders with temperature dependent properties
S. ADALI & V. E. VERIJENKO (South Africa)

631 The behaviour of open and closed section carbon fibre composite beams subjected to constrained torsion
J. LOUGHLAN & M. ATA (UK)

649 Finite element analysis of bonded repairs to edge cracks in panels subjected to acoustic excitation
R. J. CALLINAN, S. C. GALEA & S. SANDERSON (Australia)

661 Matrix crack-induced delamination in composite laminates under transverse loading
J. WANG & B. L. KARIHALOO (Denmark)

667 Adaptive post-buckling response of carbon fibre composite plates employing SMA actuators
S. P. THOMPSON & J. LOUGHLAN (UK)

679 Numerical analysis of a sling support arrangement for GRP composite pressure vessels
D. H. NASH & W. M. BANKS (UK)

ELSEVIER

Composite Structures **38**, No. 1–4, pp. vii–viii
© 1997 Elsevier Science Ltd. All rights reserved
Printed in Great Britain
0263-8223/97/$17.00

PII:S0263-8223(97)00136-0

Preface

Herein are contained the papers presented at the Ninth International Conference on Composite Structures (ICCS/9) held at the University of Paisley, Scotland in September 1997. The Conference was sponsored by the University of Paisley with co-sponsorship kindly provided by Renfrewshire Enterprise, Renfrewshire Council and The Chivas and Glenlivet Group. Additionally, thanks are due to the US Air Force European Office of Aerospace Research and Development (EOARD) and the US Army, Research, Development and Standardisation Group — United Kingdom for their contribution to the success of the conference.

The Conference forms a natural and ongoing progression from the eight previous highly successful ICCS events which have attracted a large international gathering of specialists in composite structures. Twenty-six countries are represented at the present conference.

Although each ICCS conference makes a unique contribution to knowledge and has many memorable highlights in the social programme, this year's event has a special significance in that it coincides with the centenary of its major sponsor. In 1897, Paisley College of Science and Art (now the University of Paisley) was founded with a specific aim to enhance practical engineering knowledge in the west of Scotland. One hundred years later it is fitting that a technical conference which brings together engineers and scientists from virtually every corner of the world should take place. Only by a free exchange of knowledge can some real progress be made.

It is also timely to reflect upon the issues which have been addressed over the years in the ICCS series of biennial conference. Since the first event in 1981 there have been many advances in the field of composite structures. Fibrous forms of reinforcement have been developed which are stronger and stiffer than before. Matrix materials are tougher with enhanced resistance to a wide variety of environmental influences. Analytical models are far more sophisticated, leading to greater understanding of the physical behaviour of load bearing composites. All of these factors, along with tremendous advances in computational power, allows today's designers of composite structures unprecedented flexibility and scope. In particular, finite element modelling techniques have become a formidable tool in the design process with PC-based systems more than adequate for all but the most complicated problems. However, before being carried away on an analytical sea of euphoria it is worth remembering that experimental evidence to corroborate theoretical predictions is still unavailable in many instances. Clearly considerable caution must be exercised if complicated composite structures are being designed using software that has been validated using much simpler benchmarks.

Notwithstanding the aforementioned words of caution it is a fact that composite materials continue to find many and diverse practical applications. Indeed there are few industries which do not recognise the benefits of designing a material to assist a particular function rather than the traditional converse of compromising functionality by accepting the limitations of existing materials.
Conferences such as ICCS are but one means of disseminating knowledge and in so doing enhance understanding. 'Show me and I will understand' is surely an appropriate phrase in this context.

To authors, session chairmen and contributors go our sincere thanks for their effort. They are the essence of any conference.

Particular thanks are due to:

THE INTERNATIONAL ADVISORY PANEL

W. M. Banks — University of Strathclyde, UK
A. M. Brandt — Polish Academy of Sciences, Poland

A. R. Bunsell — Ecole des Mines de Paris, France
T. Hayashi — Japan Plastic Inspection Association, Japan
R. M. Jones — Virginia Polytechnic and State Institute, USA
A. Miravete — University of Zaragoza, Spain
J. Rhodes — University of Strathclyde, UK

THE CONFERENCE SECRETARY

Miss Janet Syme

ably assisted by:

Miss Michelle Martin

Grateful thanks are due to many other individuals who contributed generously to the success of the event. As always a final thanks to Nan, Simon, Louise, and Richard for their support throughout the conference.

I. H. Marshall

ELSEVIER

Composite Structures **38**, No. 1–4, pp. 1–2
© 1997 Elsevier Science Ltd

Ninth International Conference on Composite Structures (ICCS/9), University of Paisley, Scotland, September 1997

National Engineering Laboratory Composite Structures Award

The ICCS/9—NEL Composite Structures Award was bestowed on the paper *Design, Fabrication and Testing of a Composite Bracket for Aerospace Applications* by H. G. S. J. Thuis and C. Biemans (National Aerospace Laboratory, Voorsterweg 31, 8316 PR Marknesse, The Netherlands).

The above picture shows from left to right, Frank Kinghorn, General Manager NEL, Bert Thuis and Ian H. Marshall.

When announcing this award at the Conference Dinner, Frank Kinghorn, Chairman of the Awards Committee, stressed the "severe

difficulties in chosing a particular paper due to the extremely high standards of the papers in many areas". However, as this biennial award has traditionally reflected particular conference themes it was considered appropriate to recognise a paper which considered a composite replacement of a metal forging designed using an optimisation module thereby achieving a weight reduction of 43%. The bracket was subsequently manufactured and successfully tested to well in excess of its design load.

Our congratulations go to the successful authors.

The next in this highly successful series biennial "Paisley" Composite Structures Conference, which commenced in 1981, will be held in September 1999. Those wishing to be put on the mailing list for information should contact:

Janet Syme
Conference Secretary
Dept. of Mechanical & Manufacturing
Engineering & The Quality Centre
University of Paisley
Paisley PA1 2BE

ELSEVIER

Composite Structures Vol. 38, No. 1–4, pp. 3–16
© 1997 Elsevier Science Ltd. All rights reserved
Printed in Great Britain
0263-8223/97/$17.00 + 0.00

PII:S0263-8223(97)00036-6

Analysis of pultruded glass reinforced plastic beams with semi-rigid end connections

G. J. Turvey

Engineering Department, Lancaster University, Bailrigg, Lancaster LA1 4YR, UK

The influence coefficient method of analysis has been used to derive closed-form expressions for the mid-span deflection and end rotations of shear deformable uniform section beams with semi-rigid end connections. The formulae have been recast into performance indices which define the reduction in mid-span deflection, the increase in load carrying capacity and the increase in span relative to an otherwise identical simply supported beam for two practical load distributions: (1) a point load at mid-span and (2) a uniform load over the entire span. Expressions are also presented for the required rotation capacity of the semi-rigid end connections. Initial rotational stiffness data, derived from full-scale tests on web and web and flange cleat connections between two sizes of pultruded glass reinforced plastic (GRP) WF-section are used in the formulae to evaluate the performance indices for the practical range of span-to-depth ratios for load case (1). The values obtained quantify the benefits to be derived from exploiting semi-rigid end connection stiffness in the design of pultruded GRP beams with the current, very limited, range of section sizes. © 1997 Elsevier Science Ltd.

NOTATION

- A Gross cross-sectional area of a WF- or I-section beam
- A_w Web cross-sectional area of a WF- or I-section beam
- E Longitudinal elastic modulus of the beam
- G Shear modulus of the beam
- I Major-axis second moment of area of beam cross-section
- k_i Constants (i=1–4)
- K Rotational stiffness of the beam end connection
- L Beam span
- Q Total load (point or distributed) on the beam
- α Dimensionless shear flexibility of the beam ($=EI/GAL^2$ or EI/GA_wL^2)
- β Dimensionless rotational flexibility of the beam end connection ($=EI/KL$)
- δ Mid-span deflection of the beam
- κ_c Mid-span deflection–span ratio ($=\delta/L$)
- λ_δ Deflection reduction index
- λ_Q Load enhancement index
- λ_L Span enhancement index
- θ Rotation of the beam end connection
- θ_c Required beam end connection rotation for a prescribed mid-span deflection–span ratio

INTRODUCTION

Over the past few years there has been a growing awareness of the potential benefits that may be derived from the appropriate use of fibre reinforced polymer composites in the construction industry. Glass reinforced plastic (GRP) materials are the most widely used in industry at present, but interest in carbon, aramid and hybrid (glass-carbon) fibre reinforced polymer composites is growing, especially in Japan and North America.

It is the uncertainty regarding the long-term corrosion resistance and durability of conventional construction materials, e.g. steel reinforcement and concrete, which has pro-

moted renewed interest in fibre reinforced polymer composites. GRP possesses a number of advantages including low cost, high corrosion resistance and low weight, but it does have the disadvantage of low stiffness. There are situations in the construction industry which require lightweight structures to operate in harsh environments, e.g. offshore platforms and chemical process plant. For these applications fibre reinforced polymer composites are potentially strong candidate materials. Indeed, GRP is frequently used in walkway structures or support frames in both the offshore and process industries. Its use in similar applications in the water industry is growing.

There are, however, a number of other factors (apart from the low modulus of GRP) which are inhibiting the rate at which fibre reinforced polymer composites are being applied in the construction industry. For GRP at least cost does not appear to be an important inhibiting factor. However, toxic emissions produced by some of the matrix materials of pultruded GRP sections in the fire environment are legitimate causes for concern and are being actively addressed by the composites industry. In the future, phenolic resins may eventually supplant the cheaper polyester resins, because of their superior fire-performance characteristics.

Another major inhibiting factor is the lack of knowledge among structural engineers of the load–deformation characteristics of GRP materials and components. Presently, little design guidance is available. For pultruded GRP components the major US manufacturers have recognized this problem and have published design manuals [1,2]. While these documents are useful, they have a number of shortcomings — at least from the standpoint of structural engineers practising within the UK. First, the design manuals use the US system of units. Second, they are based on permissible stress design philosophy. And third, they relate to particular proprietary products. Although recognized structural design standards for fibre reinforced polymer composites are to be hoped for in the future, interim documents are already beginning to emerge [3,4]. Quinn [4] brings up to date an earlier publication which has enjoyed widespread use in the UK for many years, whereas the document by Clarke [3] — the most code-like of all — follows the Eurocode format and is based on limit state design philosophy.

Although the factors mentioned above continue to slow the pace of application of GRP in primary load-bearing situations, perhaps the most important factors are simply the lack of knowledge of the actual behaviour of simple beams, columns and joints and the rather limited range of *standard* structural section sizes. Lack of knowledge of the real behaviour of beams and their end connections has lead to the situation that beams are generally designed as simply supported and that large *knockdown* factors on material strength are often used. The consequence is that such beams only operate at a small fraction of their ultimate strength. It is, of course, recognized that, because of their low modulus, GRP beams are likely to be designed for the deflection limit state and, in consequence, will generally be lightly stressed. Ordinarily this would not matter, but when, for a given load requirement, the deflection limit of a section is just exceeded a large penalty has to be paid in moving to the next larger section, because the range of sections is small. One way of improving the performance of the present range of *standard* structural sections is to make use of the semi-rigid nature of the end connections. This, of course, presupposes that adequate knowledge of connection behaviour exists.

During the past 7 years a number of tests have been carried out on beam-to-column connections between pultruded GRP sections and knowledge of their real behaviour is beginning to accumulate [5–10]. Although insufficient testing has yet taken place to enable semi-rigid design procedures to be developed for these materials, enough test data are available to enable preliminary studies to be made of the potential performance gains to be realized with the current range of beam sections. This is the main objective of the present paper. In order to carry out such a study closed-form expressions for the deformation response of shear deformable beams with semi-rigid end connections have been developed. These formulae have been used with real connection data to quantify the reduction in deflection, the increase in load and the increase in span of a semi-rigid beam relative to an otherwise identical simply supported beam for two basic load configurations and the practical range of span-to-depth ratios. In addition, the rotation capacities required of the semi-rigid connections to achieve these performance gains have been defined.

SHEAR DEFORMABLE SEMI-RIGID BEAM ANALYSIS

It is usual to take account of shear deformation in the analysis and design of pultruded GRP beam sections because the shear modulus of GRP is low. From the practical design standpoint two load cases for the design of pultruded GRP beams are of particular importance. They are: (1) a point load at mid-span and (2) a uniform load extending over the whole span. Figure 1(a) and (b) shows the two load cases and Fig. 1(c) shows the linear moment–rotation characteristic of the semi-rigid beam end connections. In the sequel simple closed-form expressions are presented for the deformations of semi-rigid shear deformable beams subjected to these two types of loading.

First-order shear deformation beam theory in conjunction with the method of influence coefficients has been used to derive the expressions for the mid-span deflections and the joint rotations of single span beams subjected to the two basic load configurations. Other analysis techniques could, of course, have been used to achieve the same results. However, the method of influence coefficients proved to be particularly easy and insightful to use. No details of the method are presented here as it is well known and adequately documented elsewhere [11]. It is convenient to present the results for each of the two load cases together below.

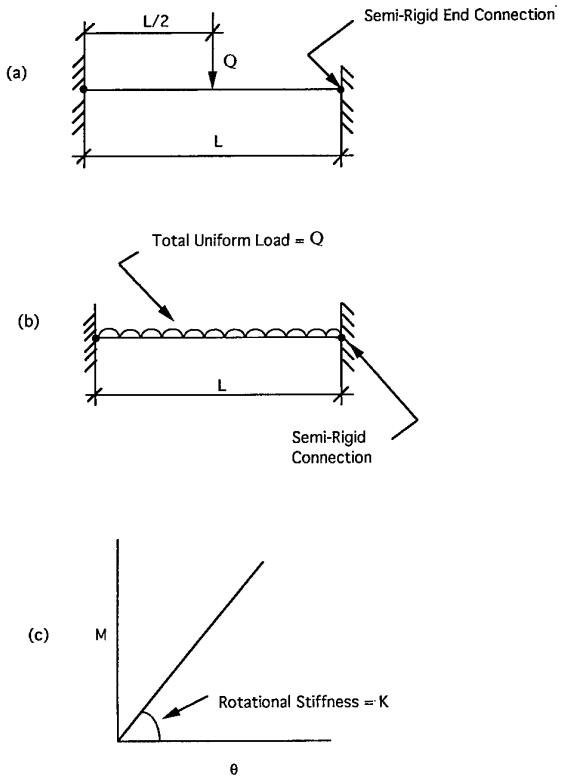

Fig. 1. Geometry and material properties of a single span shear deformable beam with semi-rigid end connections: (a) load case 1 — point load at mid-span, (b) load case 2 — uniform load over the entire span and (c) moment (m)–rotation (θ) characteristic of the end connections.

Point load at mid-span/uniformly loaded beam

The expression for the mid-span deflection is given as

$$\delta = \frac{QL^3}{k_1 EI}\left(\frac{1+48\alpha+k_2\beta+96\alpha\beta}{1+2\beta}\right) \tag{1}$$

in which δ is the deflection, Q is the total load, L is the span, E is the longitudinal elastic modulus, I is the major-axis second moment of area, α is the dimensionless shear flexibility of the beam and β is the dimensionless rotational flexibility of the end connections. The values of the constants, k_1 and k_2 (and k_3 and k_4 arising in formulae presented later) are given in Table 1 for the two load cases. It should also be appreciated that the $\alpha\beta$ term in the numerator of eqn (1) implies that coupling exists between the shear flexibility of the beam and the rotational flexibility of the end connections.

For Euler–Bernoulli (shear-rigid) beams, the shear flexibility parameter, α, is zero and eqn (1) simplifies to

$$\delta = \frac{QL^3}{k_1 EI}\left(\frac{1+k_2\beta}{1+2\beta}\right) \tag{2}$$

It is readily shown that eqn (2) degenerates further to yield the classical mid-span deflection results. Thus, for a beam with simply supported ends $\beta = \infty$ and $\delta = QL^3k_2/2k_1EI$. Likewise, for

Table 1. Values of k_i (i=1–4) for the constants in the deflection, etc. expressions for beams subjected to a point load at mid-span or a uniform load over the entire span

Beam load distribution	k_1	k_2	k_3	k_4
Point load at mid-span	192	8	8	4
Uniform load over entire span	384	10	12	5

a beam with clamped ends $\beta = 0$ and $\delta = QL^3/k_1EI$.

The expression for the rotation of the semi-rigid end connections (which, of course, are equal and opposite) is given by

$$\theta = \frac{QL^2}{k_3EI}\left(\frac{\beta}{1+2\beta}\right) \tag{3}$$

It should be appreciated that eqn (3) implies that the joint rotation is independent of the beam shear flexibility parameter, α.

It is readily shown that eqn (3) degenerates further to yield the classical beam end rotations. Thus, for the case of a beam with clamped ends $\beta = 0$ and $\theta = 0$. Likewise, for a beam with simply supported ends $\beta = \infty$ and $\theta = QL^2/2k_3EI$.

SEMI-RIGID VERSUS SIMPLY SUPPORTED BEAMS

Performance indices

The case for using semi-rigid beam analysis and design with fibre reinforced polymer composites must rest on the performance gains that may be achieved in practice. It is the objective of this paper to quantify these gains. As the design of pultruded GRP beams is currently based on simply supported beam response, it is sensible to measure the performance of a semi-rigid beam relative to an otherwise identical simply supported beam, i.e. in terms of performance indices. These performance indices may be expressed in terms of the reduction in beam deflection, the increase in load-carrying capacity or the increase in span. It is convenient to present these performance indices separately.

Deflection reduction index (λ_δ)
the simply supported and semi-rigid beams have the same span and support the same loads, then the deflection reduction index, λ_δ, may be expressed as

$$\lambda_\delta = \left(\frac{1+48\alpha+k_2\beta+96\alpha\beta}{k_4+48\alpha+k_2\beta+96\alpha\beta}\right) \tag{4}$$

It is beneficial to examine briefly the degenerate forms of eqn (4). First, if the beams are shear-rigid then $\alpha = 0$ and eqn (4) reduces to

$$\lambda_\delta = \left(\frac{1+k_2\beta}{k_4+k_2\beta}\right) \tag{5}$$

Further simplification of eqn (5) depends on the nature of the semi-rigid connection. Thus, if $\beta = \infty$, i.e. the ends are simply supported, then $\lambda_\delta = 1$. On the other hand, if $\beta = 0$, i.e. the ends are clamped, then $\lambda_\delta = 1/k_4$. These two values of the index, λ_δ, represent the practical limits of the deflection reduction index. In other words, by clamping the beam ends it is possible to reduce the mid-span deflection to one $(1/k_4)^{th}$ of the value of a similarly loaded simply supported beam (see Table 1). These results are, of course, well known and serve to verify the degeneracy of eqn (4).

Load enhancement index (λ_Q)
If the simply supported and semi-rigid beams have the same span and are subjected to the same deflection limits at mid-span, then the load enhancement index, λ_Q, for a beam with semi-rigid end connections is given as

$$\lambda_Q = \frac{1}{\lambda_\delta} \tag{6}$$

irrespective of whether the beam is shear-rigid or shear-flexible. For the clamped beam, $\beta = 0$ and, hence, $\lambda_Q = k_4$. Similarly, for the simply supported beam, i.e. $\beta = \infty$, the index $\lambda_Q = 1$. These two values of λ_Q represent the limits of the range of this index. They indicate that clamping the beam ends allows the load supporting capacity to be increased to k_4 times that of an otherwise identical simply supported beam. This fact is, of course, well known and confirms the degeneracy of eqn (6).

Span enhancement index (λ_L)
If the loads and deflection limits are prescribed, then the performance of a beam with semi-rigid end connections may be measured, relative to an otherwise identical simply supported beam, in terms of the increase in the span that it may operate over. The analysis for this index is a little more complex than for the two preceding indices and does not lead directly to a closed-form expression for the span enhancement index. Instead, it is determined as one of the roots of a cubic equation.

For the beam with semi-rigid end connections and carrying a point load at mid-span or a uniform load over the entire span the form of the cubic equation for the span enhancement index is as follows:

$$\lambda_L^3 + k_2\lambda_L^2\beta - k_4\lambda_L - k_2\beta = 0 \quad (7)$$

It turns out that only one of the roots of eqn (7) is positive and it is this which gives the span enhancement index, λ_L. It should also be appreciated that the beam shear flexibility parameter, α, is absent from eqn (7), so that shear flexibility is not a factor in span enhancement.

It is of interest to consider briefly the degenerate forms of eqn (7). For the case of a clamped beam, i.e. $\beta = 0$, eqn (7) simplifies to

$$\lambda_L^3 - k_4\lambda_L = 0 \quad (8)$$

The roots of eqn (8) are: $\lambda_L = \sqrt{k_4}$, 0 and $+\sqrt{k_4}$ and, therefore, the span enhancement index $\lambda_L = \sqrt{k_4}$. Likewise, for the case of a simply supported beam, i.e. $\beta = \infty$, eqn (7) simplifies to

$$\lambda_L^2 - 1 = 0 \quad (9)$$

The roots of eqn (9) are: $\lambda_L = -1$ and $+1$ and, therefore, the span enhancement index $\lambda_L = 1$. These two values of the span enhancement index, λ_L, represent the practical limits. Thus, it is apparent that by clamping the beam ends it is possible to increase the span to $\sqrt{k_4}$ times that of the corresponding simply supported beam.

Rotation requirements of the end connections

In order to take advantage of the semi-rigidity of the end connections, they must exhibit adequate rotation capacity prior to the onset of material damage and a reduction in rotational stiffness. From the design standpoint it is advantageous to express the rotational capacity in terms of the serviceability limit on mid-span deflection, i.e. in terms of the deflection–span ratio, κ_c. End connection rotation capacity expressions have been derived for shear deformable beams with semi-rigid end connections. These are presented below.

Point load at mid-span/uniform load over the entire span

The rotation capacity, θ_c, of the end connection required to achieve a prescribed mid-span deflection–span ratio, κ_c, is obtained by combining eqns (1) and (3) so that

$$\theta_c = \frac{k_1}{k_3}\left(\frac{\kappa_c\beta}{1 + 48\alpha + k_2\beta + 96\alpha\beta}\right) \quad (10)$$

It should, of course, be appreciated that the $\alpha\beta$-term in the denominator of eqn (10) indicates the existence of coupling between the shear flexibility of the beam and the rotational flexibility of the end connections.

It is also of interest to examine, briefly, the degenerate forms of eqn (10). First, if the beam is shear-rigid, i.e. $\alpha = 0$, then eqn (10) reduces to

$$\theta_c = \frac{k_1}{k_3}\left(\frac{\kappa_c\beta}{1 + k_2\beta}\right) \quad (11)$$

Further degeneration of eqn (11) depends, of course, on the value of the rotational flexibility, β, of the end connection. For the case of $\beta = 0$, i.e. clamped ends, the required rotation capacity $\theta_c = 0$. This result conforms with our expectations, namely that for a beam with clamped supports no rotation capacity is required irrespective of the prescribed mid-span deflection–span ratio, κ_c. Likewise, for the case of $\beta = \infty$, i.e. simply supported ends, eqn (11) reduces to $\theta_c = k_1\kappa_c/k_2k_3$. These two results for $\beta = 0$ and ∞ are well known and confirm the degeneracy of eqn (10).

PULTRUDED GRP BEAM PROPERTIES AND SEMI-RIGID JOINT STIFFNESSES

While the foregoing shear deformable semi-rigid beam analysis and performance indices are quite general, it is the present purpose to focus on pultruded GRP beam sections and the types and characteristics of the semi-rigid joints used to connect them. It is convenient to deal with the beam properties first. Because of the dominant role of the US pultrusion industry, *standard* structural sections are produced mainly by US pultruders [1,2]. The most popular pultruded sections for beam applications are WF-(wide flange) and I-sections. It is, therefore, proposed to select two sizes of each section for use in the numerical calculations which are presented later in the paper. The two sizes are the

Table 2. Details of the cross-section geometry of two sizes of pultruded GRP WF- and I-section

Section type	Depth (mm)	Web and flange thickness (mm)	Major axis second moment of area (mm^4)	Gross cross-sectional area (mm^2)	Web cross-sectional area (mm^2)
WF-section	101.6	6.4	3,304,900	1864.5	567.7
I-section	101.6	6.4	1,831,400	1219.4	567.7
WF-section	203.2	9.5	41,282,000	5632.2	1754.8
I-section	203.2	9.5	23,080,000	3696.8	1754.8

101.6 and 203.2 mm deep sections. Details of the cross-section geometry for each section size and shape are given in Table 2. Although the pultruded GRP material is orthotropic, only the longitudinal elastic modulus and the in-plane shear modulus are needed to evaluate the performance indices. These moduli are given for the EXTREN™ series of structural pultrusions in Ref. 2. The longitudinal modulus, E, for the deeper section is 17.24 kN/mm^2, whereas for the shallower section it is slightly larger at 17.93 kN/mm^2. However, the shear modulus is the same for all section sizes at 2.93 kN/mm^2.

In order to provide meaningful performance index values for the pultruded WF- and I-sections, it is necessary to use realistic semi-rigid joint flexibility data. It is, therefore, sensible to use rotational stiffness data derived from tests on semi-rigid connections between pultruded GRP sections. Such data are not very extensive. It appears that most of the published test data relate to joints between the 203.2 mm deep WF-sections [5–8]. Recently, Turvey and Cooper [9,10] have reported on a number of semi-rigid joint tests between the 101.6 and 203.2 mm deep WF-sections. The connections were all bolted and were in two arrangements. In the first arrangement the connection between the column flange and beam web was via a pair of web cleats and in the second arrangement an additional set of cleats was provided between the upper and lower beam flanges and the column flange. Details of the web and flange cleat connections for the small and large size wide flange sections are shown in Fig. 2(a) and (b), respectively. The web cleat connections are similar to the connections shown in Fig. 2 but with the flange cleats absent. The moment–rotation behaviour observed in these tests was broadly in line with comparable test data reported elsewhere [5–8]. In the tests reported by Turvey and Cooper [9,10] care was taken to determine the initial rotational stiffnesses. It is these stiffnesses which are required for the evaluation of the parameters in the performance indices. The initial rotational stiffness typical of each arrangement and for each of the two section depths is given in Table 3.

It should, of course, be appreciated that the initial stiffnesses given in Table 3 were all derived from tests on WF-sections. It has been assumed that the same initial rotational stiffness values apply to the I-section semi-rigid connections.

VARIATION OF THE SHEAR AND ROTATIONAL FLEXIBILITY PARAMETERS

Before evaluating the three performance indices for the pultruded GRP WF- and I-sections it is, perhaps, worthwhile to see how the beam shear flexibility parameter, α, and the rotational flexibility parameter, β, of the semi-rigid end connections vary. In order to be able to show these variations for different section depths and shapes it is convenient to plot the α and β-values as functions of the span-to-depth ratio. The variations of α and β with the span-to-depth ratio are shown in Fig. 3 and Fig. 4, respectively. In Fig. 3 two sets of α-values are presented for each section depth and shape. The reason for calculating two α-values for each case is that the shear deformable beam analysis used to derive the performance indices does not include a shear correction parameter to compensate for inadequate modelling of the shear stress distribution over the beam cross-section. Thus, by evaluating the α parameter on the basis of the gross and the web cross-sectional areas of the beam section, upper and lower bound α-values are determined. It is evident from the shape of the curves shown in Fig. 3 that the shear flexibility parameter, α, is large at small span-to-depth ratios and decays rapidly as the span-to-depth ratio increases. It may, therefore, be inferred that the influence of the α-parameter on the performance indices is most

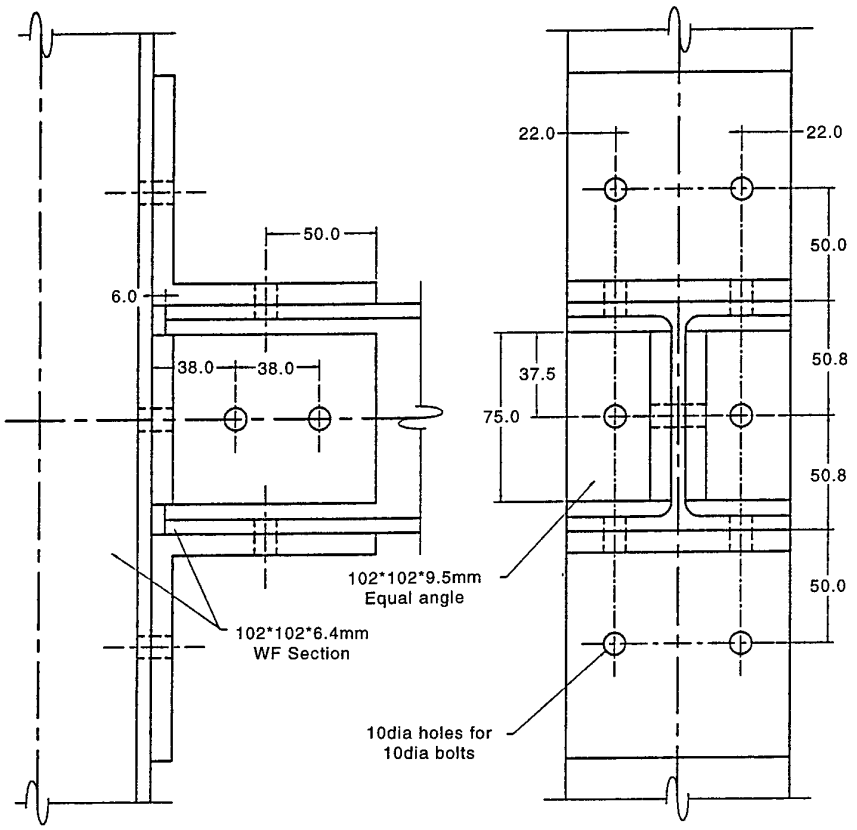

(a)

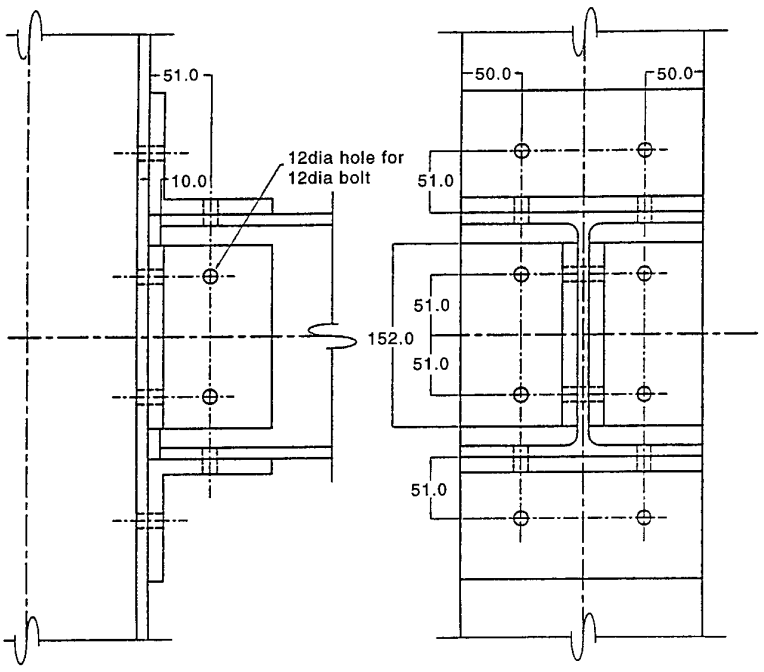

(b)

Fig. 2. Bolted beam-to-column web and flange cleat connections: (a) layout of 101.6 mm WF-section connection and (b) layout of 203.2 mm WF-section connection.

Table 3. Initial rotational stiffnesses for semi-rigid bolted joints between pultruded GRP WF- and I-sections

Type of bolted connection	Section depth (mm)	Initial rotational stiffness (kNm/radian)
Web cleats	101.6	14
Web + flange cleats	101.6	85
Web cleats	203.2	100
Web + flange cleats	203.2	500

significant at small span-to-depth ratios. From Fig. 3 it is also clear that the α-values based on the web area of the cross-section are larger than the α-values based on the gross area of the cross-section. Furthermore, the α-values for the WF-sections are generally larger than the α-values for the I-sections and the difference between corresponding values is greater when the web rather than the gross cross-sectional area is used. For the two depths of section chosen, it appears that the section depth does not have much effect on the α-parameter.

The dimensionless rotational flexibility parameter, β, of the connections is shown plotted against the span-to-depth ratio in Fig. 4. The general shape of the curves in Fig. 4 is similar to the α-parameter curves shown in Fig. 3, though they assume much larger values. As one might expect the β-values for semi-rigid web cleat connections are greater than for web and flange cleat connections. Also the β-values for WF-sections are larger than the β values for the corresponding I-sections.

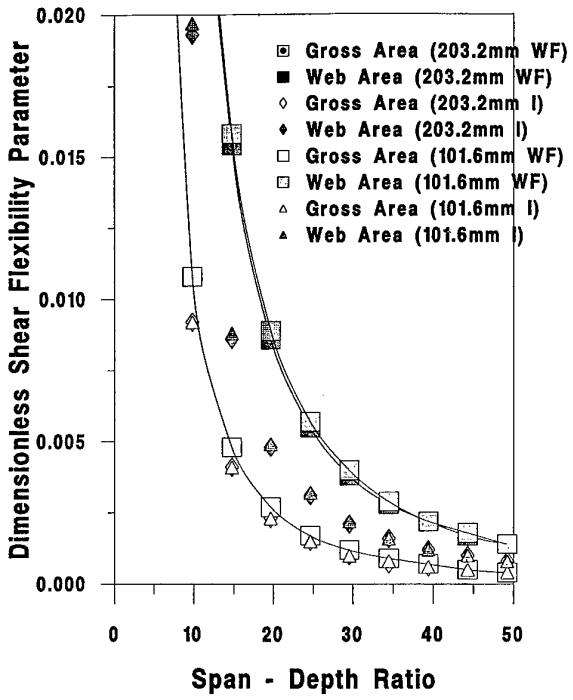

Fig. 3. Beam shear flexibility parameter (gross and web cross-sectional area values) versus span–depth ratio for 101.6 and 203.2 mm deep pultruded GRP WF- and I-sections.

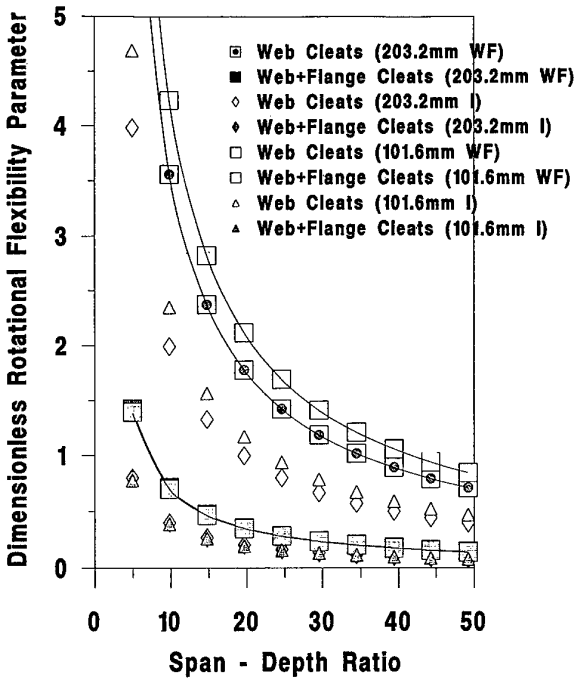

Fig. 4. Semi-rigid end connection rotational flexibility parameter (web and web+flange cleats) versus span–depth ratio for 101.6 and 203.2 mm deep pultruded GRP WF- and I-sections.

EVALUATION OF PERFORMANCE INDICES AND END CONNECTION ROTATION REQUIREMENTS FOR PULTRUDED GRP BEAMS

Having defined general expressions for the performance indices and end connection rotation requirements for the two load cases and also having quantified the α- and β-parameters for two common forms of bolted connection used to join pultruded GRP sections, it is of interest to obtain quantitative information which demonstrates the potential gains to be derived from taking account of the rotational stiffness inherent in the beam end connections. The performance indices will be considered first and then the end connection rotation requirements.

The deflection reduction, load enhancement and span enhancement performance indices are plotted against span-to-depth ratio in Fig. 5, Fig. 6 and Fig. 7, respectively for WF- and I-

section beams subjected to a point load at mid-span. In each figure the data are presented for two section depths and shapes of cross-section. In addition, the effects of shear deformation of the beam based on the gross and web areas of the cross-section are compared with the results for a shear-rigid beam. Furthermore, results are also presented for the

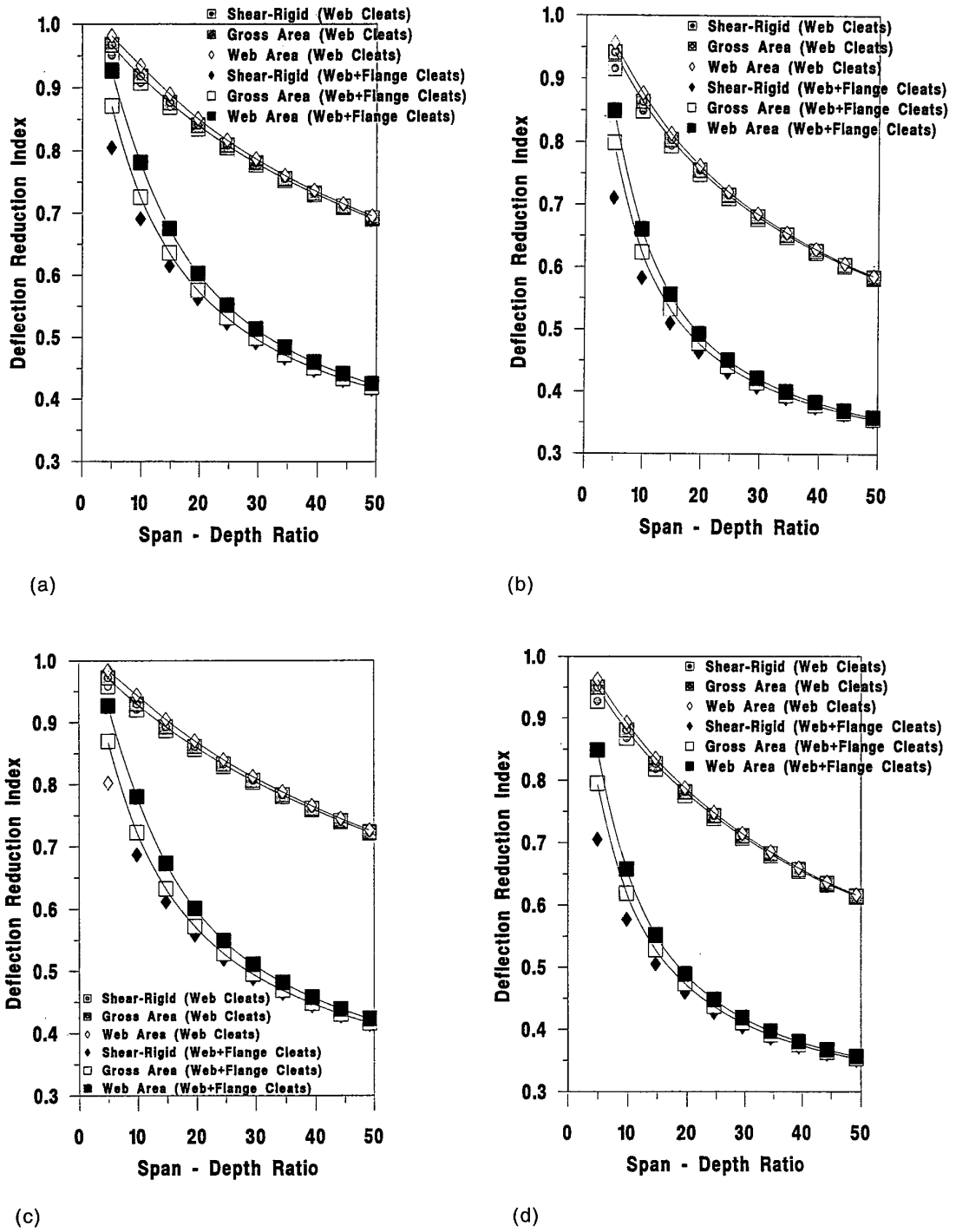

Fig. 5. Deflection reduction index versus span–depth ratio for pultruded GRP beams with semi-rigid end connections (web and web+flange cleats) and subjected to a point load at mid-span: (a) 203.2 mm WF-section, (b) 203.2 mm I-section, (c) 101.6 mm WF-section and (d) 101.6 mm I-section.

two connection arrangements, viz. web cleats and web and flange cleats.

Thus, Fig. 5 shows the deflection reduction index versus span-to-depth ratio. The variations of the index for 203.2 mm deep WF- and I-sections are shown in Fig. 5(a) and (b), respectively. The trends in both figures are similar, but the index values are smaller for the I-section which indicates that the I-section benefits more than the WF-section from the

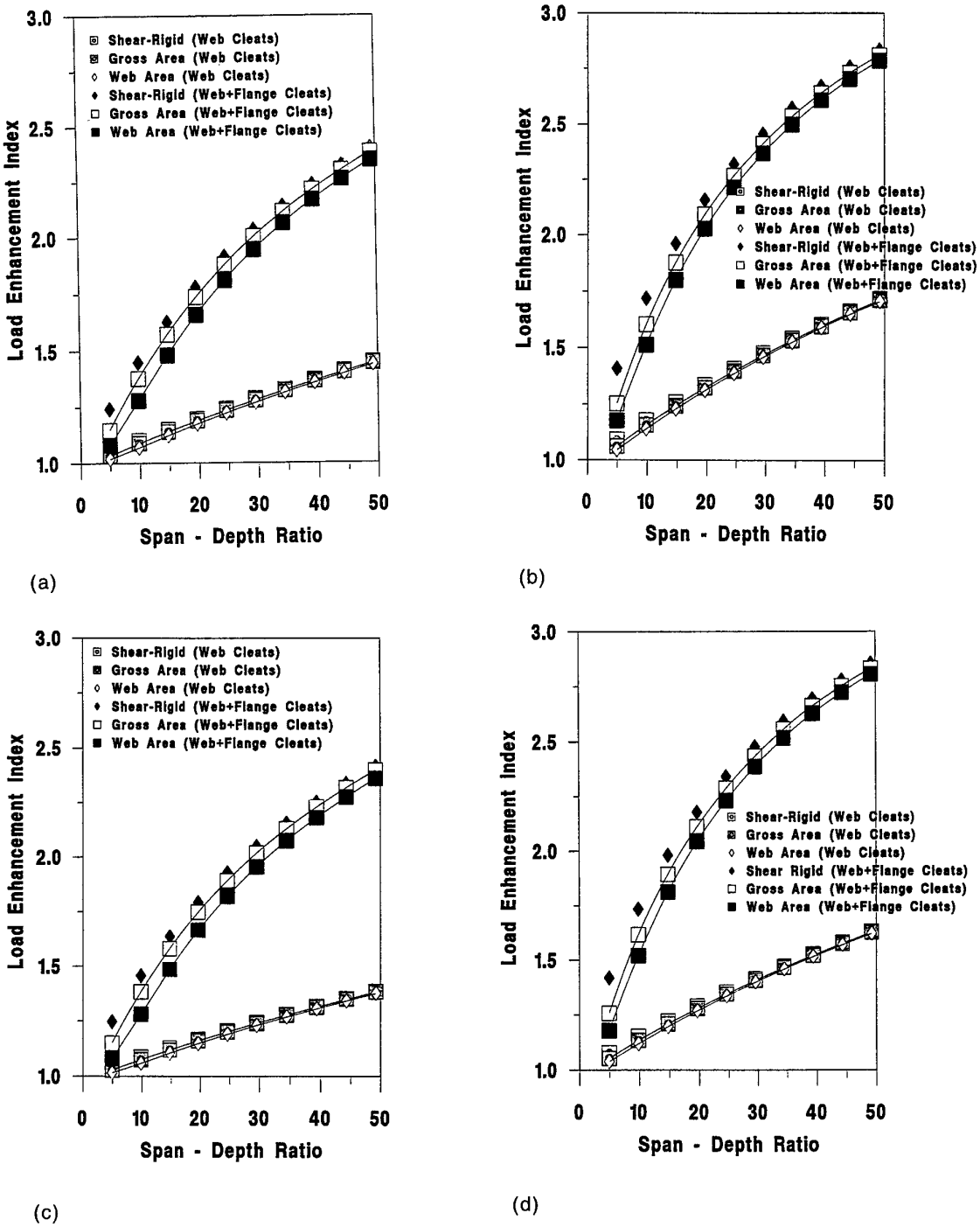

Fig. 6. Load enhancement index versus span–depth ratio for pultruded GRP beams with semi-rigid end connections (web and web+flange cleats) and subjected to a point load at mid-span: (a) 203.2 mm WF-section, (b) 203.2 mm I-section, (c) 101.6 mm WF-section and (d) 101.6 mm I-section.

connection semi-rigidity in reducing the mid-span deflections. This is so regardless of whether web cleats or web and flange cleats are employed in the end connections. Clearly, the deflection reduction indices for web and flange cleats are much smaller than for web cleats alone. For example, for the 203.2 mm WF-section with a span-to-depth ratio of about 10 the deflection reduction index varies from 0.69 to 0.78 (depending on whether the beam is shear-rigid or shear-flexible) when web and flange cleats are used in the connection, whereas for a web cleat connection the index varies from 0.91 to 0.93. In other words, exploiting the inherent rotational stiffness of the beam end connections leads to mid-span reductions in deflection of 22–31% for the web and flange cleat connection and 7–9% for the web connection. The corresponding reductions in mid-span deflection for the 203.2 mm I-section (see Fig. 5b) are 34–42% and 12–15%, respectively. It is also clear from Fig. 5(a) and (b) that shear deformation raises the value of the deflection reduction index and this may be quite significant at short spans. Thus, shear deformation tends to offset the benefits of the rotational stiffness of the end connection. In Fig. 5(c) and (d) the deflection reduction index versus span-to-depth ratio is plotted for the 101.6 mm deep WF- and I-sections, respectively. The results are very similar to the results for the corresponding larger section size and shape.

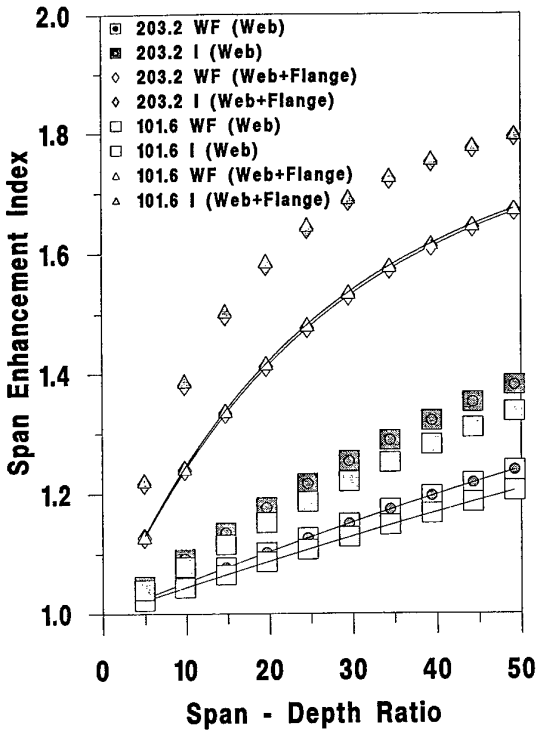

Fig. 7. Span enhancement index versus span–depth ratio for 101.6 and 203.2 mm deep pultruded GRP WF- and I-section beams with semi-rigid end connections (web and web+flange cleats) and subjected to a point load at mid-span.

The load enhancement index versus span-to-depth ratio for shear deformable beams with semi-rigid end connections and subjected to a point load at mid-span are shown in Fig. 6(a) and (b) for the 203.2 mm deep WF- and I-sections, respectively. As expected the benefits of semi-rigid end connections increase as the span of the beam increases. The increase in the load enhancement index is almost linear for the web connection but shows signs of non-linearity for the web and flange connection. Again, it is evident that the increase in load carrying capacity appears to be greater for I-sections than WF-sections for the same semi-rigid end connection arrangement. For example, at a span-to-depth ratio of about 10 (see Fig. 6a), a 203.2 mm WF-section with web cleat end connections is able to support between 7 and 10% more load than a simply supported beam, whereas the same WF-section with web and flange cleats is able to support between 28 and 45% more load depending on the nature of the beam's shear flexibility. The corresponding increases in load carrying capacity for the 203.2 mm deep I-section (see Fig. 6b) are 14–18% and 51–72%. Again, these figures show that the beam's shear flexibility reduces the benefits of enhanced load carrying capacity derived from the semi-rigid end connections. Corresponding load enhancement versus span-to-depth ratio curves for 101.6 mm deep WF- and I-sections are shown in Fig. 6(c) and (d), respectively. The load enhancement indices are very similar to the values for their deeper section counterparts.

The span enhancement index versus span-to-depth ratio plots for the two section depths, shapes and connection arrangements are shown in Fig. 7. It is evident that, regardless of section depth and shape, the span enhancement index increases almost linearly with the span-to-depth ratio when a web cleat connection arrangement is adopted. It also appears that the span enhancement index is significantly larger for I-sections than for WF-sections, especially at large spans and with web and flange cleat end connections. However, when web and flange

cleats are used, the difference between the span enhancement indices for the different section depths of the same shape is negligible. The variation of the span enhancement index with span-to-depth ratio is non-linear for web and flange cleat end connections. In this figure no distinction between results for shear-rigid and shear deformable beams is made as the index is independent of the shear flexibility parameter, α. It is of interest to compare the index values for a span-to-depth ratio of 10. Thus, for a WF-section with web cleats the span increase (compared to a simply supported beam) varies from 4 to 5% depending on the section depth, whereas for an I-section the increase in span varies from 8 to 9%. The corresponding span increases for beams with web and flange cleat connections are 24% for the WF-section and 38–39% for the I-section.

The required rotation capacity of the semi-rigid end connection versus span-to-depth ratio is shown in Fig. 8(a) and (b) for 203.2 mm deep WF- and I-sections, respectively. These figures have been compiled assuming the the mid-span deflection–span ratio, $\kappa_c = 0.005$. Although the curves in both figures show similar trends, it is evident that the required end connection rotations are somewhat smaller for the I-section. In the case of shear-rigid beams the required end rotation capacity of the connection reduces as the span increases. Moreover, as the span increases the affect of the beam's shear flexibility on the end connection rotation diminishes. However, for short spans the shear flexibility of the beam has a significant effect in reducing the required rotation capacity of the end connection. For example, in the case of a 203.2 mm WF-section (see Fig. 8a) for a span-to-depth ratio of 10 a rotation capacity of 15 mrad for a shear-rigid beam reduces to between 10 and 13 mrad depending on the degree of shear flexibility of the beam. The corresponding value for the I-section is 14 mrad reducing to between 11 and 12.5 mrad. The end connection rotation capacity versus span-to-depth ratio plots for the 101.6 mm deep WF- and I-sections are shown in Fig. 8(c) and (d), respectively. These figures are similar to those of their deeper section counterparts and do not merit further discussion.

A set of performance index and end rotation capacity results have also been produced for pultruded WF- and I-section beams uniformly loaded over their entire span, but are not reproduced here for space reasons. The results trends are similar to those for a point load at mid-span though the index values differ somewhat. For example, if the deflection index values for the point load case are compared with the uniform load case, it is evident that the latter deflection reduction index values are smaller. This suggests that the benefits of semi-rigidity of the end connections are greater under uniform loading than under point loading at mid-span, i.e. the mid-span deflection is smaller. Likewise comparing the load enhancement indices for a point load at mid-span with their corresponding indices for a uniformly loaded beam, it is again evident, particularly in the case of web and flange cleat connections, that the values for uniform loading are larger. Hence, the benefit of the semi-rigid connection in enhancing the load supporting capacity is greater under uniform loading. On the other hand, when the the span enhancement indices for the cases of a point load at mid-span and a uniform load over the entire span are compared it appears that the indices are very similar which suggests that the load distribution does not influence the index — it is the flexibility of the end connection which plays the dominant role.

Finally, comparing the end connection rotation requirement for the point load and uniform load cases, it is clear that the rotation requirement is larger for the uniform load case.

CONCLUDING REMARKS

Simple closed-form expressions for the mid-span deflection and end connection rotations have been derived for shear deformable semi-rigidly connected elastic beams. The formulae are based on first-order shear deformation theory and the connections are assumed to have a linear moment–rotation characteristic. The formulae have been converted into performance indices which define the mid-span deflection, the load carrying capacity and the increase in span of a semi-rigidly connected beam relative to an otherwise identically loaded simply supported beam. Moment–rotation data derived from web and web and flange cleat connection tests between 101.6 and 203.2 mm deep WF-sections have been used to calculate the beam shear flexibility and end connection rotation flexibility parameters for both WF- and I-section pultruded GRP beams. These parameters

have been used in the formulae to quantify the performance indices and end rotation requirements as functions of the span-to-depth ratio for mid-span point loaded beams with the two types of conventional semi-rigid connection configurations. The results indicate that substantial reductions in the mid-span deflection, increases in the load carrying capacity and increases in the span are possible especially for the web and flange cleat connections. For pul-

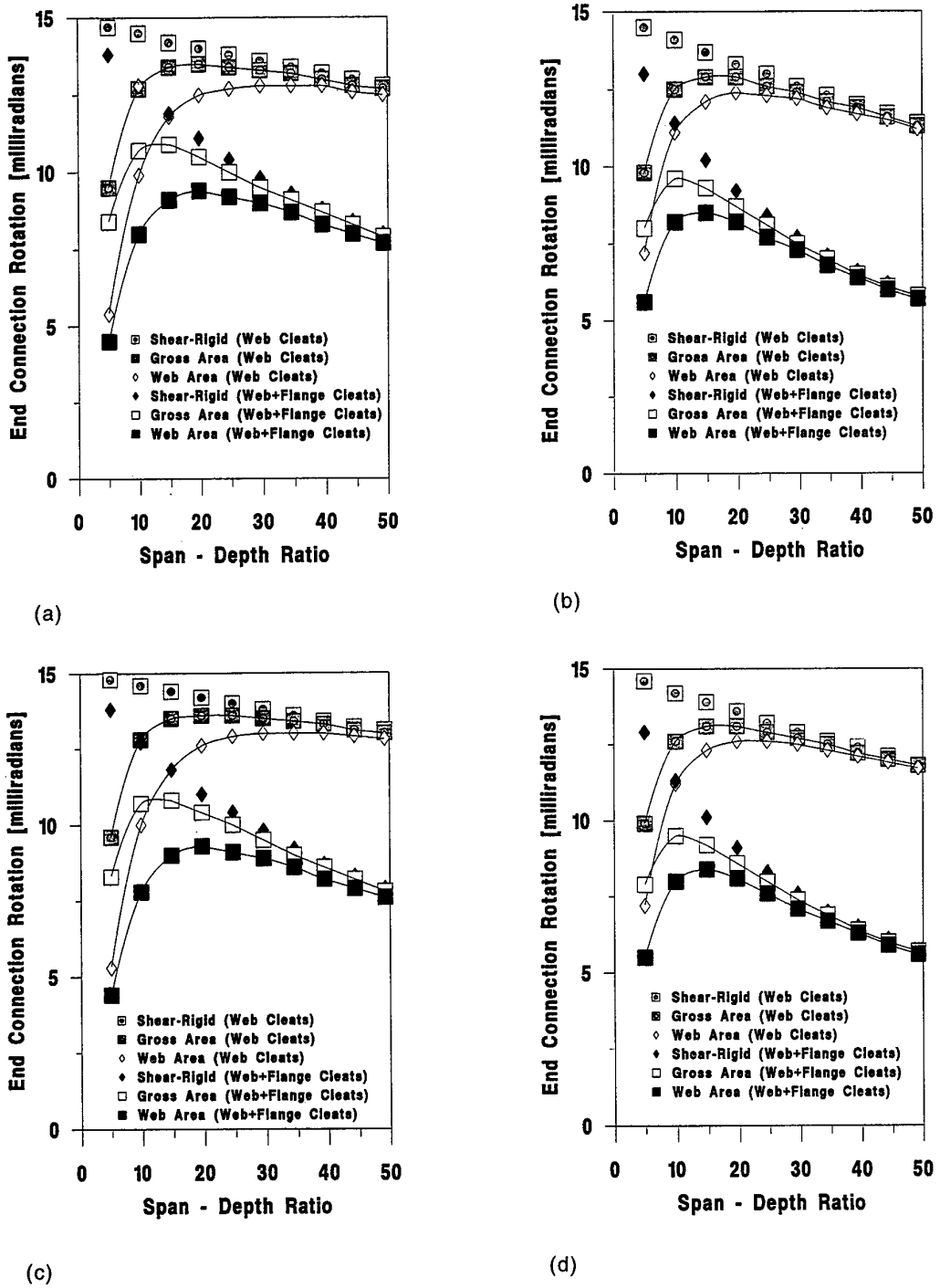

Fig. 8. End connection rotation requirement versus span–depth ratio for pultruded GRP beams with semi-rigid end connections (web and web+flange cleats) and subjected to a point load at mid-span: (a) 203.2 mm WF-section, (b) 203.2 mm I-section, (c) 101.6 mm WF-section and (d) 101.6 mm I-section.

truded GRP sections knowledge of these performance improvements is particularly important as the current practice is to design beams as simply supported and the range of section sizes is very limited. Thus, the information provided in the paper allows the structural engineer to decide for a given span-to-depth ratio whether or not the additional capacity available from the semi-rigid connection is sufficient to allow a beam to be used which is designed as simply supported and is on the limit of its performance.

ACKNOWLEDGEMENTS

The author wishes to acknowledge support from EPSRC (Grant No. GR/J41703) for Mr C. Cooper who prepared Fig. 2 and carried out the tests to determine the initial rotational stiffnesses of the web and web and flange cleat connections between pultruded GRP WF-sections. He also wishes to record his indebtedness to Mr Gordon Elliott for help and advice with the influence coefficient method of analysis. Finally, the author wishes to express his appreciation to the Engineering Department for supporting his research.

REFERENCES

1. Creative Pultrusions Inc., *Creative Pultrusions Design Guide*. Creative Pultrusions, Alum Bank, PA, 1988.
2. Morrison Molded Fiber Glass, *EXTREN Fiberglass Structural Shapes: Design Manual*. Morrison Molded Fiber Glass, Bristol, VA, 1989.
3. Clarke, J. L. (ed.), *Structural Design of Polymer Composites: EUROCOMP Design Code and Handbook*. E. and F. N. Spon, London, 1996.
4. Quinn, J. A., *Composites — Design Manual*. James Quinn Associates, Liverpool, 1995.
5. Bank, L. C. *et al.*, Beam-to-column connections for pultruded FRP shapes. *Proceedings of the ASCE First Materials Engineering Congress*, Denver, CO, 1990, pp. 804–813.
6. Bass, A. J. and Mottram, J. T., Behaviour of connections in frames of fibre reinforced-polymer section. *The Structural Engineer* 1994, **72** (17), 280–285.
7. Mosallam, A. S. *et al.*, Performance of pultruded FRP connections under static and dynamic loads. *J. Reinforced Plastics and Composites* 1994, **13** (5), 386–407.
8. Mottram, J. T., Tests on nominally pinned connections for pultruded frames for the EUROCOMP project. In Clarke, J. L. (ed.). *Structural Design of Polymer Composites: EUROCOMP Design Code and Handbook*. E. and F. N. Spon, London, 1996, pp. 705–718.
9. Turvey, G. J. and Cooper, C., Semi-rigid pultruded GRP frame connections: tests to determine static moment–rotation characteristics. *Proceedings of the 7th European Conference on Composite Materials,* London, Vol. 2, 1996, pp. 295–300.
10. Turvey, G. J. and Cooper, C., Characterization of the short term static moment–rotation response of bolted connections between pultruded GRP beam and column WF-sections. *Proceedings of the 2nd International Conference on Advanced Composite Materials in Bridges and Structures*, Montreal, 1996, pp. 927–934.
11. Morice, P. B., *Linear Structural Analysis: An Introduction to the Influence Coefficient Method Applied to Statically Indeterminate Structures*. Thames and Hudson, London, 1969.

ELSEVIER

Composite Structures Vol. 38, No. 1–4, pp. 17–27
© 1997 Elsevier Science Ltd. All rights reserved
Printed in Great Britain
0263-8223/97/$17.00 + 0.00

PII:S0263-8223(97)00037-8

Actuation and sensing of piezolaminated sandwich type structures

H. Abramovich & B. Pletner

Faculty of Aerospace Engineering, Technion, Israel Institute of Technology, 32000 Haifa, Israel

A new piezolaminated sandwich type structure to be eventually used as a smart wall for active control of sound radiated by harmonically excited thin walled structures is proposed. The present study presents the equations of motion of the new adaptive sandwich structures in a sufficiently accurate model in a form readily for solution either in closed-form or by approximate methods. The theoretical natural frequencies are compared with an approximate evaluation and test results yielding a good correlation. It also yields the axial strains and the curvature of the composite beam leading to the calculation of equivalent mechanical loads produced by the piezoceramic actuator for inclusion in a finite element code. The numerical results are compared with experimental ones obtained during a test series on a cantilever sandwich beam equipped with piezoceramic sensors and actuators and constructed according to the new proposed concept. The influence of the input voltage on the performance of the new sandwich structure is investigated. The beam tip deflection induced by the piezoceramic actuators is measured and compared with numerical and finite element predictions to yield a very good match. Both the numerical and the experimental results show the applicability of the new proposed concept. © 1997 Elsevier Science Ltd.

INTRODUCTION

A common form of an adaptive structure is a thin type structure equipped with piezoelectric laminae. These laminae are made of piezoelectric materials such as Polyvinylidene Fluoride (PVDF) — a piezoelectric copolymer film [1] or Lead Zirconia Titanate (PZT) [2] — a piezoceramic based material available at present in relatively small rectangular patches. The figure of merit of such laminae is their capability of transducing electric fields into mechanical strains, and mechanical strains into electrical charges. These 'active' laminae are used either to actuate the hosting structure by inducing strains in the non-piezoelectric, 'passive' laminae, or to sense deflections of the hosting structure by measuring the local strain fields. The active laminae, the actuators, can be continuous over the entire domain of the structure, as in the PVDF case, or discontinuous as in the case of piezoceramic (PZT) patches. A survey on piezoelectricity and its use can be found in Ref. [3].

A vast number of studies deal with the use of piezoceramic patches to control the vibrations of flexible structures like beams and plates and their deflections. Such are the studies of Cud-

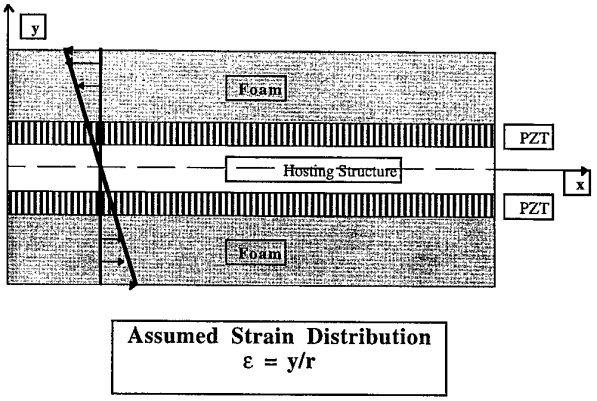

Fig. 1. The assumed strain distribution across the beam (not to scale).

Table 1. Dimensions and material properties

	PZT Patch	Aluminum Beam	Foam Beam
Thickness (mm)	$2a = 0.1905$	$2d = 0.75$	$2\hat{a} = 11.65$
Width (mm)	$w_1 = 50$	$w = 60$	$w = 60$
Density, ρ (kg/m^3)	7700	2700	80
Young's Mod. (Pa)	$E_p = 5\times10^{10}$	$E_s = 7\times10^{10}$	$E_F = 75\times10^6$
Length (mm)	$l = 50$	$L = 300$	$L = 300$
Piezo. Const., d_{31} (m/V)	180×10^{-12}	—	—

ney *et al.* [4], Clark *et al.* [5], Akella *et al.* [6] and Batra and Ghosh [7] to quote only a few. Other researchers, such as Main *et al.* [1], Kim *et al.* [8], Chandra and Chopra [9] and Pletner and Abramovich [10], try to model composite structures, which include PZT actuators, and to evaluate the influence of the actuators induced strains on the overall behavior of the structures.

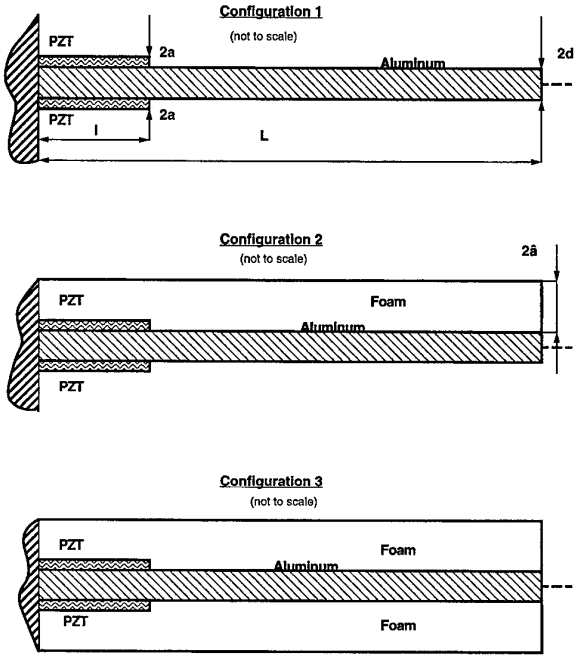

Fig. 2. The various sandwich configurations used in the tests (not to scale).

The subject of noise attenuation using active beside passive means has been presented in numerous studies in the literature. Crane *et al.* [11], Dungan *et al.* [12], Wang [13], Kim *et al.* [14], Bao *et al.* [15], Ko and Tongue [16], Balachandran *et al.* [17] and recently, Pletner *et al.* [18], represent only a few references in which theoretical and experimental efforts were made to apply active acoustical control to reduce noise levels. In some of these works [13–18], use was made of PZT patches acting to induce strains and to control and then attenuate interior noise.

While the control part of the smart-adaptive structures problem is well advanced it seems that the development of accurate models for induced strain actuation and sensing local strains are essential for the correct and efficient design of smart/adaptive structures and their use for vibration suppression, noise attenuation, shape control and vibration steering.

The majority of the smart structures do not involve sandwich structures. A few studies [19,20] do concentrate on sandwich type struc-

Table 2. Formulae for calculating induced curvatures and axial strain ($N = M = 0$) sandwich configuration 1: PZT, host beam, (PZT) k

Configuration	Curvatureκ	Axial Strainχ
Two Sided Active Symmetric PZTs	$\dfrac{2\Lambda\alpha}{d(\rho E + 2\gamma)}$	$\dfrac{2\rho_A\Lambda^*}{(\rho E + 2\rho_A)}$
Two Sided Symmetric PZTs (only 1 Active)	$\dfrac{\Lambda\alpha}{d(\rho_E + 2\gamma)}$	$\dfrac{\rho_A\Lambda}{(\rho + 2\rho_A)}$
One Sided Active PZT		
Approx.	$\dfrac{\Lambda\alpha}{d(\rho_E + \gamma)}$	$\dfrac{\rho_A\Lambda}{(\rho_E + \rho_A)}$
Exact	$\dfrac{3\Lambda\rho_A(1+\rho_A)(1-\beta)}{d[\rho_E + \gamma - 3\beta\rho_A(1+\rho_A)]}$	$\dfrac{\rho_A\Lambda(1-\alpha/\gamma)}{(\rho_E + \rho_A - \alpha\rho_A/\gamma)}$

Table 3. Formulaae for calculating induced curvatures and axial strain embedded PZTs ($N = M = 0$) sandwich configuration 2: [foam beam, PZT, host beam, (PZT)†k, foam beam]

Configuration	Curvature κ	Axial Strain χ
Two Sided Active Symmetric PZTs	$\frac{2\Lambda\alpha}{d(\rho_E + 2\gamma + 2\rho_F\gamma_1)}$	$\frac{2\rho_A\Lambda^*}{(\rho_E + 2\rho_A + 2\rho_F\rho_{\mathring{A}})}$
Two Sided Symmetric PZTs (only 1 Active)	$\frac{\Lambda\alpha}{d(\rho_E + 2\gamma + 2\rho_F\gamma_1)}$	$\frac{\rho_A\Lambda}{(\rho_E + 2\rho_A + 2\rho_F\rho_{\mathring{A}})}$
One Sided Active PZT		
Approx.	$\frac{\Lambda\alpha}{d\gamma_3}$	$\frac{\rho_A\Lambda}{(\rho_E + \gamma_4)}$
Exact	$\frac{3\Lambda\rho_A(1 + \rho_A - \rho_A\alpha_1/\gamma_5)}{d(\gamma_3 - 3\rho_A\alpha_1)}$	$\frac{\rho_A\Lambda(1 - \alpha\alpha_1/\gamma_3)}{(\rho_E + \gamma_4 - 3\rho_A\alpha_1 2/\gamma_3)}$

*For the case where in-phase voltage is supplied to both PZTs. For the out-of-phase voltage case, $\chi = 0$.
†k = 1 — the PZT is available. $k = 0$ — the PZT is not available.

tures, using the PZT actuators either on the outside faces [19] or in the thickness-shear mode [20]. Therefore, the present study is aimed at developing a sufficiently accurate model of a new piezolaminated sandwich type structure to be eventually used as smart walls for active control of sound radiated by harmonically excited thin walled structures. Sandwich structures consisting of stiff facing sheets and a relatively soft lightweight core such as rigid

Table 4. Formulae for calculating induced curvatures and axial strain embedded PZTs ($N = M = 0$) sandwich configuration 3: [foam beam, PZT, host beam, (PZT) k]

Configuration	Curvature κ	Axial Strain χ
Two Sided Active Symmetric PZTs		
Approx.	$\frac{2\Lambda\alpha}{d(\rho_E + 2\gamma + \rho_F\gamma_1)}$	$\frac{2\rho_A\Lambda^*}{(\rho_E 2\rho_A + \rho_F\rho_{\mathring{A}})}$
Exact	$\frac{6\Lambda\rho_A(1 + \rho_A - \alpha_4/\gamma_9)}{d(\gamma_8 - 3\alpha_4 2/\gamma_9)}$	$\frac{2\rho_A\Lambda^*(1 - \alpha_2\alpha_4/\gamma_8)}{(\gamma_9 - 3\alpha_4 2/\gamma_8)}$
Two Sided Symmetric PZTs (only 1 Active)		
Approx.	$\frac{\Lambda\alpha}{d(\rho_E + 2_\gamma + \rho_F\gamma_1)}$	$\frac{\rho_A\Lambda}{(\rho_E + 2\rho_A + \rho_F\rho_{\mathring{A}})}$
Exact	$\frac{3\Lambda\rho_A(1 + \rho_A - \alpha_4/\gamma_9)}{d(\gamma_8 - 3\alpha_4 2/\gamma_9)}$	$\frac{\rho_A\Lambda(1 - \alpha_2\alpha_4/\gamma_8)}{(\gamma_9 - 3\alpha_4 2/\gamma_8)}$
One Sided Active PZT		
Approx.	$\frac{\Lambda\alpha}{d(\rho_E + \gamma + \rho_F\gamma_1)}$	$\frac{\rho_A\Lambda}{(\rho_E + \rho_A + \rho_F\rho_{\mathring{A}})}$
Exact	$\frac{3\Lambda\rho_A(1 + \rho_A - \alpha_3/\gamma_7)}{d(\gamma_6 - 3\alpha_3 2/\gamma_7)}$	$\frac{\rho_A\Lambda(1 - \alpha_2\alpha_3/\gamma_6)}{(\gamma_7 - 3\alpha_3 2/\gamma_6)}$

*For the case where in-phase voltage is supplied to both PZTs. For the out-of-phase voltage case, $\chi = 0$.
†k = 1 — the PZT is available. $K = 0$ — the PZT is not available.
where $\rho_A = a/d$; $\rho_{\mathring{A}} = \mathring{a}/d$; $\rho_E = E_s/E_p$; $\rho_F = E_F/E_p\alpha = 3(1 + \rho_A)\rho_A$; $\alpha_1 = 1 + \rho_A + 2\rho_F\rho_{\mathring{A}}$; $\alpha_2 = \alpha/\rho_A$; $\alpha_3 = (1 + \rho_A)\rho_A + \rho_F[(1 + 2\rho_A)\rho_{\mathring{A}} + \rho_{\mathring{A}}^2]$; $\alpha_4 = \alpha_3 - \alpha/3$; $\beta = \rho_A/(\rho_E + \rho_A)$; $\gamma = 3\rho_A + 6\rho_A^2 + 4\rho_A^3$; $\gamma_1 = 3(1 + 2\rho_A)^2\rho_{\mathring{A}} + 6(1 + 2\rho_A)\rho_{\mathring{A}}^2 + 4\rho_{\mathring{A}}^3$; $\gamma_2 = 3\rho_{\mathring{A}} + 6\rho_{\mathring{A}}^2 + 4\rho_{\mathring{A}}^3$; $\gamma_3 = \rho_E + \gamma + \rho_F(\gamma_1 + \gamma_2)$; $\gamma_4 = \alpha_1 - 1$; $\gamma_5 = \rho_E + \gamma_4$; $\gamma_6 = \rho_E + \gamma + \rho_F\gamma_1$; $\gamma_7 = \rho_E + \rho_A + \rho_F\rho_{\mathring{A}}$; $\gamma_8 = \rho_E + 2\gamma + \rho_F[3(1 + \rho_A)^2\rho_{\mathring{A}} + 6(1 + \rho_A)\rho_{\mathring{A}}^2 + 4\rho_{\mathring{A}}^3]$; $\gamma_9 = \rho_E + 2\rho_A + \rho_F\rho_{\mathring{A}}$.

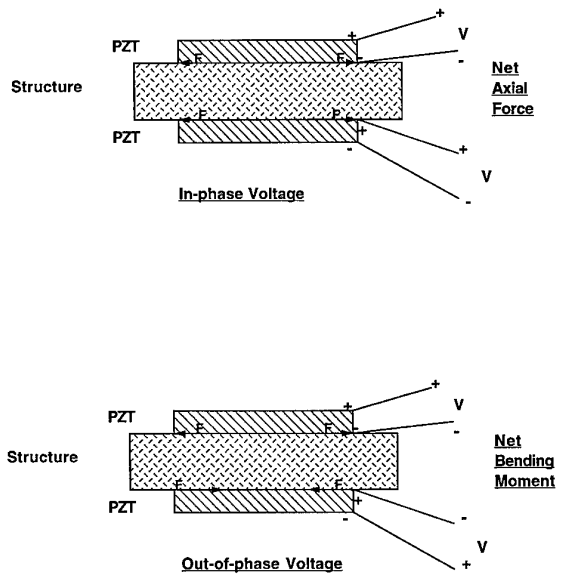

Fig. 3. The wiring configurations of the two PZTs.

foam or honeycomb are highly efficient in bending. An excellent review on computational models of sandwich structures can be found in Ref. [21].

Providing the sandwich structure with means of sensing the vibrational motions induced by external noise and means of actuation to reduce the amplitudes of those motions will yield a new advanced structure having the efficiency of a sandwich one together with an ability of active noise attenuation. This new structure will be constructed from five main layers: a thin metal plate equipped with PZT patches for sensing and actuation sandwiched between the usual faces and foam core. This new emerging sandwich construction offers many advantages over the conventional surface-mounted constructions. For example, far better protection of the piezoceramic patches and its electrical leads and wires is obtained. Moreover, sensing and actuation is done independently without the need to mount and change the host structure, and at relatively low bending stresses which will not be detrimental to the brittle piezoceramic patches.

The present study presents the equations of motion of the new adaptive sandwich structure in a form ready for solution either in closed-form or by approximate methods. It also yields the axial strains and the curvature of the composite beam leading to the calculation of equivalent mechanical loads produced by the piezoceramic actuator for inclusion in a finite element code. The numerical results are compared with experimental ones obtained during a test series on a cantilever sandwich beam equipped with piezoceramic sensors and actuators and constructed according to the new proposed concept. The influence of the input voltage on the performance of the new sandwich structure is investigated. The beam tip deflection induced by the piezoceramic actuators is measured and compared with numerical predictions to yield a very good match. Both the numerical and the experimental results show the applicability of the new proposed concept.

FORMULATION OF THE PROBLEM

The axial strain and curvature of the beam

It is assumed that the unstrained state of the material is defined when the PZT layer (the actuator) is attached to or embedded in the structure with no electrical field applied to the actuator and no external tractions (forces or moments) acting on the structure. Therefore the axial strain distribution along the composite structure has the form (see Fig. 1)

$$\varepsilon_x = y/r + \chi \tag{1}$$

where r is the radius of curvature (the curvature $\kappa = 1/r$), y is the distance from the neutral axis and χ is a constant.

Assuming that all materials are isotropic we get the stresses in each component of the composite structure, as

$$(\sigma_x)_s = E_s\varepsilon_x \tag{2a}$$

$$(\sigma_x)_p = E_p\varepsilon_x \tag{2b}$$

$$(\sigma_x)_F = E_F\varepsilon_x \tag{2c}$$

where σ is the axial stress in the composite beam, E is Young's modulus, $()_s$ the structure

Table 5. Natural frequencies of the beam — various configurations

Configuration	Mode	Freq. (Hz) Approx.	Freq. (Hz) Prog.	Freq. (Hz) Test
Aluminium beam + 2 PZTs	123	6.69, 41.94, 117.48	8.2, 48.53, 128.61	7.25, 42.0, 108.0
Aluminum beam + 2 PZTs + 1 Foam beam	12	24.4, 152.8	24.76, 153.66	22.0, 148.0
Aluminum beam + 2 PZTs + 2 Foam beams	12	29.8, 186.7	30.11, 187.4	26.25, 185.5

to which the PZT patches are bonded, $()_p$ a piezoceramic, PZT, layer and $()_F$ the foam beam.

The piezoceramic layers provide the ability to apply stress and therefore axial forces to the structure (the actuator mode). The piezoelectric effect is characterized by the piezoelectric proportionality constants, d_{31} and d_{32} (see Table 1), that relate the electrical field, Æ, applied across the thickness of the patch (usually denoted as 3-direction) with the strains induced in the longitudinal directions (the so called 1- and 2-directions) when the patch is unconstrained. For a one-dimensional case the free strain in the 1-direction is defined as:

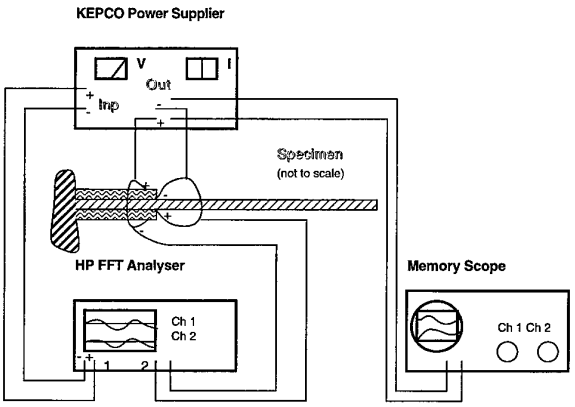

Fig. 4. The schematic test set-up.

$$\Lambda = d_{31}Æ \tag{3}$$

For the present derivation, the 1- and 3-directions correspond to the x and y directions, respectively. Applying Hook's Law to eqn (3) yields

$$\sigma_p = E_p d_{31}Æ \tag{4}$$

Here σ_p is the effective stress applied to the actuator layer due to the piezoelectric effect. It is assumed that all parts of the composite structure are perfectly bonded, with the adhesive layer's thickness being negligible. Now the applied stresses and the beam stress environment are known. Resultant axial forces and moments can now be summed to find the beam axial force–strain and moment–curvature relationships

$$\Sigma F_x = 0 \Rightarrow -N + w\int \sigma_p dy = w\int (\sigma_x) dy \tag{5a}$$

$$\Sigma M_z = 0 \Rightarrow -M + w\int \sigma_p y dy = w\int (\sigma_x) y dy \tag{5b}$$

where N and M are the outside applied axial force and moment, respectively, w the composite beam width, and (σ_x) the stress in the x direction in a given layer. The integral is on the left and right hand of the eqn (5a,b), according to the composite beam configuration (see Fig. 2).

Making the appropriate substitutions yields the formulas presented in Tables 2–4.

Table 6. Experimental results

No Foam Beams			1 Foam Beam (at f_1 = 22 Hz)			2 Foam Beams (at f_1 = 26.25 Hz)	
V_{in} (Volts)	V_{out} (Volts)	W (mm)	V_{in} (Volts)	V_{out} (Volts)	W (mm)	V_{in} (Volts)	W (mm)
1 active PZT, at f_1 = 7.25 Hz			1 active PZT			2 active PZTs	
38	16.7	14.5	36	2.5	1.04	107	2.9
34	15.21	12.25	63	3.25	1.61	125	3.28
30	13.7	12	72	3.51	1.8	98	2.57
26	12.2	10.8	90	4.06	2.05	89	2.33
23	10.8	9.4	99	4.36	2.3	80	2.1
19	9.2	6.95	108	4.74	2.44	72	1.84
15	7.6	6.5	126	5.44	2.75	54	1.38
11	5.7	3.85	144	6.27	3	36	0.91
1 active PZT, at f_2 = 42 Hz			2 active PZT				
71	45.5	7.65	36	–	1.2	–	–
62	41.7	6.83	45	–	1.42	–	–
53	37.2	6.1	54	–	1.65	–	–
44	32.3	5.25	63	–	1.75	–	–
36	27.15	4.4	72	–	1.94	–	–
27	21.5	3.45	81	–	2.1	–	–
18	15.6	2.5	90	–	2.29	–	–
9	9.02	1.43	108	–	2.57	–	–

One should remember that the axial strain for two active PZTs case is possible only when *in-phase* voltage is supplied to both PZTs, while for the *out-of-phase* voltage case, $\chi = 0$ (see Fig. 3). Applying *out-of-phase* voltage to both PZTs results in a pure bending moment. Note that in case the width of the PZT patch, w_1, is not equal to the width of the beam, w (in general $w \geq w_1$), the symbol ρ_A in Tables 2–4, is to be replaced by δ_A, which is defined as:

$$\delta_A = \rho_A w_1 / w \tag{6}$$

Table 7. Experimental results — forced vibrations with two sensing PZTs

V_{out} (Volts)	W (mm) peak-to-peak
No Foam Beams at $f = 34.25$ Hz	
14.9	5.0
22.06	8.0
24	10.0
1 Foam Beam at $f = 30.0$ Hz	
2.12	1.4
2.84	2.4
3.54	3.1
2 Foam Beams at $f = 39.5$ Hz	
1.6	1.59
2.1	2.2
2.6	2.88

The dynamic equations of motion

The equation of motion for an Euler–Bernoulli type beam (which is our case) is given by

$$D_i \partial^4 y_i / \partial x^4 + m_i \partial^2 y / \partial t^2 = 0 \tag{7}$$

where the subscript i denotes the following (see also Fig. 1)

$$\begin{aligned} i &= 1 \; 0 \leq x_1 \leq l \\ i &= 2 \; l \leq x_2 \leq L \end{aligned} \tag{8}$$

The D_i and the m_i represent the flexural rigidity and the mass per unit length of the beam, respectively.

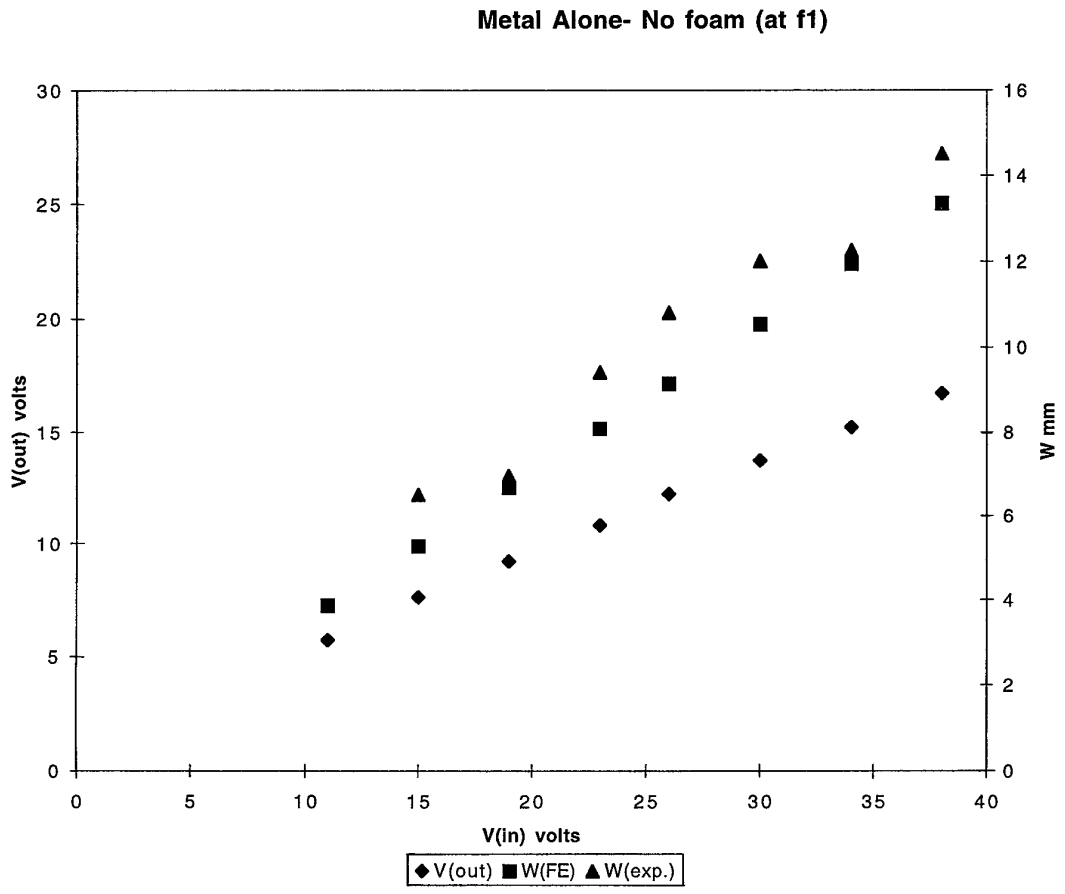

Fig. 5. PZT–Struct.–PZT Config. (at $f_1 = 7.25$ Hz)

The boundary conditions associated with the problem are

$$\begin{aligned} &\text{at } x = 0 \; y_1 = 0; \; \partial y_1/\partial x = 0 \\ &\text{at } x = L \; \partial^2 y_2/\partial x^2 = 0; \; \partial^3 y_2/\partial x^3 = 0 \end{aligned} \tag{9}$$

The other four conditions to solve the problem come from the compatibility of displacements and equilibrium of forces at $x = 1$, namely satisfaction of the following continuity conditions

$$\begin{aligned} &\text{at } x = 1 \; y_1 = y_2 \\ &\partial y_1/\partial x = \partial y_2/\partial x \\ &-D_1 \partial^2 y_1/\partial x^2 = -D_2 \partial^2 y_2/\partial x^2 \\ &-D_1 \partial^3 y_1/\partial x^3 = -D_2 \partial^3 y_2/\partial x^3 + m_p \end{aligned} \tag{10}$$

where m_p represents the induced piezo-bending moment given by

$$m_p = E_p \kappa \tag{11}$$

Substituting the relevant dimensions, material properties and the boundary and continuity conditions yield the natural frequencies of the beam for the various configurations used in the present study (the Prog. results presented in Table 5).

Computer code was written to calculate the natural frequencies of various configurations of the beam. The results are presented in Table 5. The approximated results stem from a straightforward calculation of the natural frequencies for a cantilever beam, and thus neglecting the mass and stiffness of the PZTs.

It can be seen from the comparison presented in Table 5, that neglecting the PZTs can lead to a large error for the PZT–Aluminum–PZT configuration (see Approx. vs. Prog. in Table 5), whereas for the other two configurations, the neglect reasonable.

The theoretical predictions are, as expected, higher than the experimental measured frequencies, with the highest difference being for the first configuration. This might be attributed both to the correct detection of the natural frequency as well as to the beam not being fully clamped. Overall, the theoretical predictions

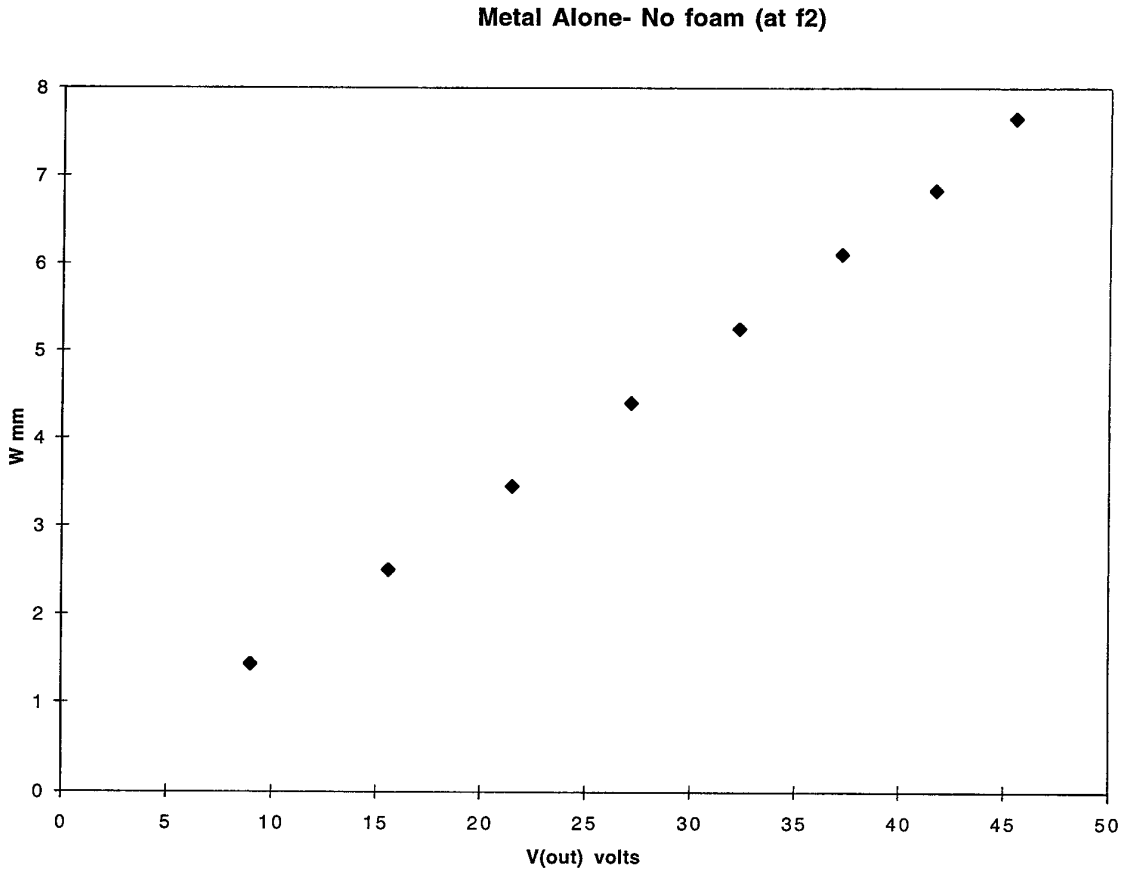

Fig. 6. V_{out} vs. lateral displacement W (PZT–Struct.–PZT Config. at $f_2 = 42$ Hz).

are close to the experimental values derived from above.

THE EXPERIMENTAL TEST SET-UP

The experimental test set-up is presented in a schematic view in Fig. 4. It consists of a .75 mm thickness aluminium beam (the base structure) having a length of 30 cm and width of 6 cm. The beam is clamped at one side and free at the other one. A pair of PZT patches (for dimensions, see Table 1) is glued to the beam, as can be seen from Fig. 4.

Three types of configurations were tested: (1) PZT–Structure–PZT, (2) Foam–PZT–Structure–PZT, and (3) Foam–PZT–Structure–PZT–Foam.

The composite structure was driven by the PZTs acting as actuators. At the beginning only one PZT was driving the structure (by changing the input voltage, V_{in}, supplied via the KEPCO power supply) while the second one served as a sensor (its output, V_{out}, being monitored on an oscilloscope). The natural frequencies were found for each configuration using Lissajous figures. Then AC voltage was supplied to the PZT at the first and/or second natural frequencies of the specific configuration while the tip displacement of the composite beam was measured continuously. Once a correlation was established between the beam tip lateral displacement and the voltage output, V_{out}, the whole structure was also driven by a pair of PZTs *connected out-of-phase*.

The experimental results are presented in Tables 6 and 7 and in Figs 5–9. ANSYS®[22] finite element code was used and its results are presented in Fig. 5. A very good match is exhibited between the experimental results and those predicted by the finite element code. In Figs 5–8, one can see a linear dependence between V_{out} and V_{in}, as well as between the beam tip displacement and V_{in}. This holds true for the three configurations tested. Adding foam beams leads to the need for a higher input

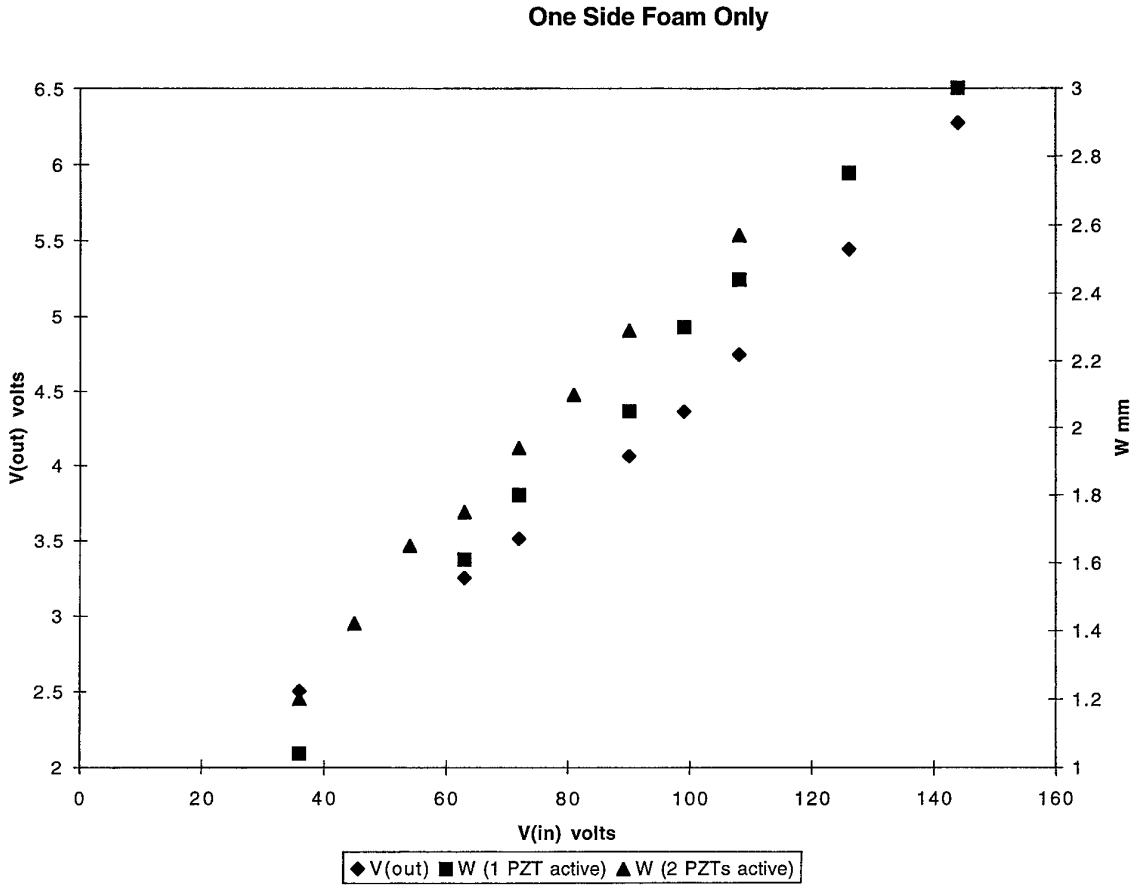

Fig. 7. Foam–PZT–Struct.–PZT Config. (at f_1 = 22 Hz) with 1 and 2 active PZTs.

voltage to overcome the relatively high added damping and to sustain the same beam tip displacement (see Table 6). Activating two *out-of-phase* PZTs does not mean twice beam tip displacement, as compared with only one active PZT. This cannot be said intuitively, as the composite structure is not symmetric (see Table 7) and the results show less than twice. It is also worthwhile to note the different behavior of the three configurations tested, as they appear in Fig. 9. If one defines the static deflection parameter, Δ, as the curvature, χ, per unit half-thickness of the hosting structure, d, and unit free piezo strain, Λ, an optimal ρ_E ratio can be found for other given parameters, such as ρ_p, ρ_F and $\rho_{\hat{a}}$. The static deflection parameter can serve as an index to the matching of the PZT thickness to the other components thickness, not only for the static case, but also for the dynamic one [23]. It is clear that configuration 1 has a different peak as compared to the other two configurations. Considering the value of $\rho_E = 0.254$ (with $\rho_p = 1.4$, $\rho_F = 0.0015$ and $\rho_{\hat{a}} = 15.53$) used in the tests, one can see a good matching for configuration 1 while the other two have a poor matching, yielding a lower performance (less deflections) for configurations 2 and 3 (see also Table 7).

Finally, each configuration was driven also at *of-resonance* frequencies, measuring the beam tip displacement and the generated output voltage. The data are presented in Table 7 and show a linear relationship.

DISCUSSION AND CONCLUSIONS

A new type of smart structure is proposed. It consists of a sandwich structure equipped with PZT actuators glued to an aluminum beam which is placed inside the sandwich.

This structure has the advantages of sandwich structures with an addition of enhanced capability to react to external stimuli, yielding an advanced smart structure. Another important advantage of the proposed configuration is its

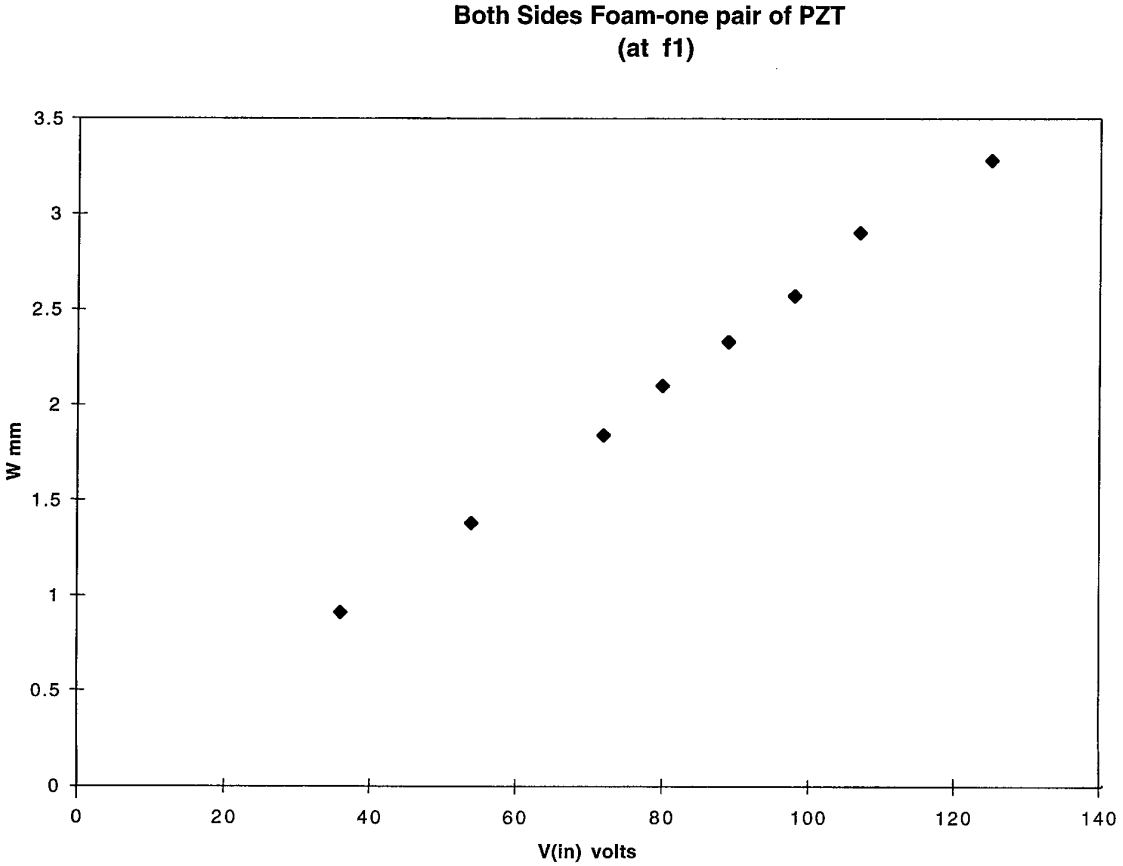

Fig. 8. Foam–PZT–Structure–PZT–Foam Config. (at $f_1 = 26.25$ Hz) with a pair of active PZTs (at first natural frequency).

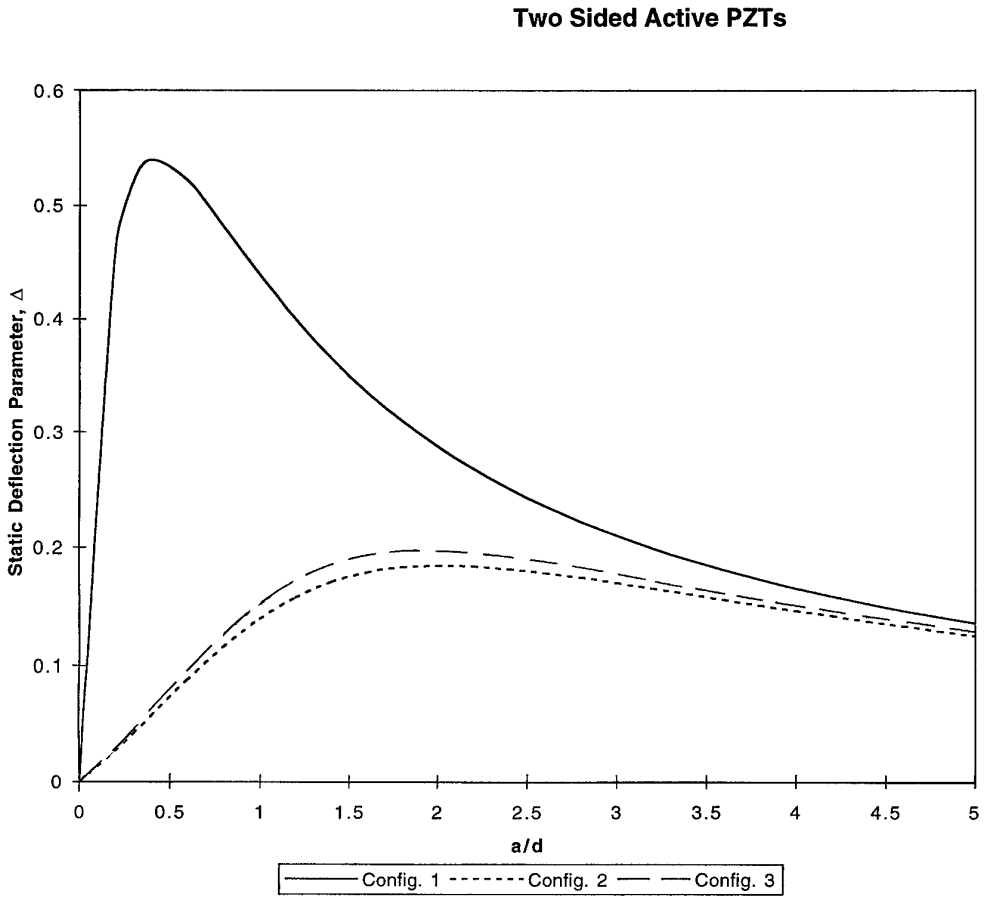

Fig. 9. A comparison between the three beam configurations $\rho_F = 0.0015$, $\rho_E = 1.4$, $\rho_{\hat{a}} = 15.53$.

natural protection of the PZTs and the wires, as they are embedded inside the structure with no exposure to the surroundings.

A theoretical model was developed for the proposed structure. Preliminary test results showed that the new model can be applied to, yielding a good correlation with experimental results. Both the theoretical/numerical and the experimental results show the applicability of the new proposed concept.

REFERENCES

1. Miller, S.E., Abramovich, H. and Oshman, Y., Active distributed vibration control of anisotropic piezoelectric laminated plates. *J. Sound and Vibration* 1995, **183**, 797–817.
2. Main, J.A., Garcia, E. and Howards, D., Optimal placement and sizing of paired piezoactuators in beams and plates. *Smart Mater. Struct.* 1994, **3**, 373–381.
3. Rao, S.S. and Sunar, M., Piezoelectricity and its use in disturbance sensing and control of flexible structures: A survey. *Appl. Mech. Rev.* 1994, **47**, 113–123.
4. Cudney, H. H., Alberts, T. E. and Colvin, J. A., A classical approach to structural control with piezoelectrics. *AIAA-92-2462-CP, 33rdh AIAA/ASME/ASCE/AHS/ASC Structures, Structural Dynamics, and Materials Conference, April 13–15, 1992/Dallas, TX, USA*, pp. 2118–26.
5. Clark, R.L., Flemming, M.R. and Fuller, C.R., Piezoelectric actuators for distributed vibration excitation of thin plates: A comparison between theory and experiment. *J. Vibration and Acoustics, Trans. ASME* 1993, **115**, 332–339.
6. Akella, P., Chen, X., Cheng, W., Hughes, D. and Wen, J.T., Modeling and control of smart structures with bonded piezoelectric sensors and actuators. *Smart Mater. Struct.* 1994, **3**, 344–353.
7. Batra, R.C. and Ghosh, K., Deflection control during dynamics deformations of a rectangular plate using piezoceramic elements. *AIAA J.* 1995, **33**, 1547–1548.
8. Kim, J., Varadan, V.V., Varadan, V.K. and Bao, X.Q., Finite-element modeling of a smart cantilever plate and comparison with experiments. *Smart Mater. Struct.* 1996, **5**, 165–170.
9. Chandra, R. and Chopra, I., Structural modeling of composite beams with induced-strain actuators. *AIAA J.* 1993, **31**, 1692–1701.
10. Pletner, B. and Abramovich, H., Actuation and sensing in piezolaminated anisotropic shells: theoretical, numerical and experimental investigation. *TAE Report No. 779*, Technion, I.I.T., Haifa, Israel, May 1996.

11. Crane, S. P., Cunefare, K. A., Englestad, S. P. and Powell, E. A., A comparison of optimization formulations for design minimization of aircraft interior noise. *AIAA-96-11480-CP, 37th AIAA/ASME/ASCE/AHS/ASC Structures, Structural Dynamics, and Materials Conference*, April 15–17, 1996/Salt Lake City, UT, USA, pp. 1504–1514.
12. Dungan, M. R., Mollo, C., Vlahapoulos, N. and Anderson, W. J., Acoustic vibration model of a composite shell with sound absorption material. *AIAA-96-1348-CP, 37th AIAA/ASME/ASCE/AHS/ASC Structures, Structural Dynamics, and Materials Conference*, April 15–17, 1996/Salt Lake City, UT, USA, pp. 267–273.
13. Wang, B.T., Active control of far-field sound radiation by a beam with piezoelectric control transducers: physical system analysis. *Smart Mater. Struct.* 1994, **3**, 476–484.
14. Kim, J., Varadan, V.V. and Varadan, V.K., Finite element-optimization methods for the active control of radiated sound from a plate structure. *Smart Mater. Struct.* 1995, **4**, 318–326.
15. Bao, X., Varadan, V.V. and Varadan, V.K., Active control of sound transmission through a plate using a piezoelectric actuator and sensor. *Smart Mater. Struct.* 1995, **4**, 231–239.
16. Ko, B. and Tongue, B.H., Acoustic control using a self-sensing actuator. *J. Sound and Vibration* 1995, **187**, 145–165.
17. Balachandran, B., Sampath, A. and Park, J., Active control of interior noise in a three-dimensional enclosure. *Smart Mater. Struct.* 1996, **5**, 89–97.
18. Pletner, B, Abramovich, H. and Idan, M., A new methodology for active control of structure-radiated noise. *Proc. of the 7th Int. Conference on Adaptive Structures*, Sept. 23–5, 1996, Rome, Italy.
19. Birman, V. and Simonyan, A., Theory and applications of cylindrical sandwich shells with piezoelectric sensors and actuators. *Smart Mater. Struct.* 1994, **3**, 391–396.
20. Sun, C.T. and Zhang, X.D., Use of thickness-shear mode in adaptive sandwich structures. *Smart Mater. Struct.* 1995, **4**, 202–206.
21. Noor, A.K., Burton, W.S. and Bert, C.W., Computational models for sandwich panels and shells. *Appl. Mech. Rev.* 1996, **19**, 155–199.
22. Swanson Analysis Systems, *ANSYS® User's Manual — Revision 5.0*, 1992.
23. Kim, S.J. and Jones, J.D., Influence of piezo-actuator thickness on the active vibration control of a cantilever beam. *J. Intelligent Material Systems and Structures* 1995, **6**, 610–623.

ELSEVIER

Composite Structures Vol. 38, No. 1–4, pp. 29–36
© 1997 Elsevier Science Ltd. All rights reserved
Printed in Great Britain
0263-8223/97/$17.00 + 0.00

PII:S0263-8223(97)00038-X

Buckling analysis of functionally graded plates subjected to uniaxial loading

Esther Feldman & Jacob Aboudi

Department of Solid Mechanics, Materials and Structures, Faculty of Engineering, Tel Aviv University, Ramat Aviv 69978, Israel

Elastic bifurcational buckling of functionally graded plates under in-plane compressive loading is studied. It is supposed that the gradients of material properties throughout the structure are produced by a spatial distribution of the local reinforcement volume fraction $v_f = v_f(x, y, z)$. To analyze the problem, a method based on a combination of micromechanical and structural approaches is employed. This establishes the effective constitutive behavior at every point of a nonhomogeneous composite plate and provides a buckling criterion. The derived criterion enables one to calculate the critical buckling load R_x^{cr} for a given distribution $v_f(x, y, z)$.

Furthermore, with the aim to improve the buckling resistance of the functionally graded plate, the functional $R_x^{cr}(v_f)$ is maximized. This yields an optimal spatial distribution $v_f(x, y, z)$ of the reinforcement phase.

Results are presented for both short- and long-fiber SiC/Al plates in which the fibers are nonuniformly distributed in the x-, y-, or z-directions. The effects of length-to-width ratio of the plate, and of different types of boundary conditions are studied. Buckling load improvements of up to 100%, as compared to the corresponding uniformly reinforced structure, are shown. © 1997 Elsevier Science Ltd.

INTRODUCTION

The traditional approach to fabricating composite materials implies that the reinforcement phase is distributed either uniformly or randomly such that the resulting mechanical, thermal, or physical properties do not vary spatially at the macroscopic level. Recently, a new concept involving tailoring or engineering the microstructure of a composite material to specific applications has taken root. This idea has given rise to the term functionally graded materials' (FGM) to describe this newly emerging class of composites. FGMs are a new generation of composite materials in which the microstructural details are spatially varied through nonuniform distribution of the reinforcement phase, by using reinforcements with different properties, sizes and shapes, as well as by interchanging the roles of reinforcement and matrix phases in a continuous manner. The result is a microstructure that produces continuously changing thermal and mechanical properties at the macroscopic or continuum level.

Such an approach offers a number of advantages over the more traditional methods of tailoring the material properties and opens up new horizons for novel applications. Grading or tailoring the internal microstructure of a composite material or a structural component allows the designer to truly integrate both material and structural considerations into the final design and final product. This brings the entire structural design process to the material level in the purest sense, thereby increasing the number of possible material configurations for specific design applications.

The potential benefits that may be derived from functionally graded composites have led to increased activities in the areas of processing and materials science of these materials. However, in order to develop a component made of FGM it is necessary to model such a component and investigate its required properties. Thus, an accurate modeling of the FGM is essential to its

development. There are presently two approaches for the modeling of FGM.

The first is based on a homogenization of the FGM in which the microstructural effects are decoupled from the global response by calculating pointwise effective thermoelastic properties without regard as to whether the actual microstructure admits the presence of a representative volume element (RVE), and subsequently using these properties in the global analysis of the heterogeneous material. In the second approach the coupling between the microstructural and the global macrostructural effects is accounted for.

Recent special issues edited by Pindera *et al.* [1–3], and by Needleman and Suresh [4] have been devoted to various topics dealing with the mechanics and material aspects of multiphased and functionally graded composites. A review paper that summarizes a higher order theory for functionally graded composites which explicitly couples the microstructural details with material's macrostructure has been presented by Pindera *et al.* [5].

The concept of FGM can also be utilized for the management of a material's microstructure so that the buckling behavior of a structure made of this material can be improved. In this investigation the idea of tailoring the microstructure of a composite material for the purpose of improving the buckling behavior of a plate is pursued. It is supposed that the gradients of material properties throughout the structure are produced by changing the local reinforcement volume fraction v_f over the planform and/or through the thickness of the plate.

To determine the buckling load of a plate for a given spatial distribution of reinforcement volume fraction $v_f(x, y, z)$, the proposed micro-to-macro approach [6,7] is further extended to include the buckling analysis of functionally graded plates. The micromechanical analysis performed in the present study relies on the RVE-based version of the method of cells [8]. As a result, a buckling criterion incorporating the effective constitutive behavior at every point of the plate, is obtained. This criterion allows one to calculate the critical buckling load R_x^{cr} for a given function $v_f(x, y, z)$.

Consequently, for a greater buckling resistance of a FGM plate the function $R_x^{cr}(v_f)$ should be maximized. This leads to an optimal spatial distribution $v_f(x,y,z)$ of the reinforcement phase.

To illustrate the proposed approach, results are presented for both short- and long-fiber SiC/Al unidirectional plates, with reinforcements nonuniformly distributed in the x-, y-, or z-directions. The effects of length-to-width and length-to-thickness ratios and different types of boundary conditions are studied. Substantial buckling load improvements, as compared to the corresponding uniformly reinforced plate, are shown.

THEORETICAL FORMULATION

An elastic, midplane symmetric, functionally graded rectangular composite plate, subjected to an in-plane compressive loading, is considered. The structure is reinforced by either long fibers or discontinuous ones, with the reinforcements volume fraction v_f being a function of the spatial coordinates x, y, z. The coordinates x and y define the plane of the plate, and z-axis is oriented in the thickness direction. The nondimensional coordinates $\xi = x/a$, $\eta = y/b$, $\zeta = z/h$, and the aspect ratio of the plate $\lambda = a/b$ are introduced, where a, b and h represent the plate's length, width, and thickness, respectively.

Governing equations to bifurcational buckling of a nonhomogeneous plate

In the present study, the buckling behavior of a nonhomogeneous plate is described in terms of the stress function Φ and the out-of-plane displacement w, in the framework of the classical plate theory. The corresponding system of governing equations may be obtained elsewhere [9]

$$\begin{aligned}&(D_{11}w_{,\xi\xi}+\lambda^2 D_{12}w_{,\eta\eta}+2\lambda D_{16}w_{,\xi\eta})_{,\xi\xi}\\&\quad+\lambda^2(D_{12}w_{,\xi\xi}+\lambda^2 D_{22}w_{,\eta\eta}+2\lambda D_{16}w_{,\xi\eta})_{,\eta\eta}\\&\quad+2\lambda(D_{16}w_{,\xi\xi}+\lambda^2 D_{26}w_{,\eta\eta}+2\lambda D_{66}w_{,\xi\eta})_{,\xi\eta}\\&\quad-\lambda^2(\Phi_{,\eta\eta}w_{,\xi\xi}-2\Phi_{,\xi\eta}w_{,\xi\eta}+\Phi_{,\xi\xi}w_{,\eta\eta})=0\end{aligned}\tag{1}$$

$$\begin{aligned}&\lambda^2(\lambda^2 A_{11}^*\Phi_{,\eta\eta}+A_{12}^*\Phi_{,\xi\xi\eta}-\lambda A_{16}^*\Phi_{,\xi\eta})_{,\eta\eta}\\&\quad+(\lambda^2 A_{12}^*\Phi_{,\eta\eta}+A_{22}^*\Phi_{,\xi\xi}-\lambda A_{26}^*\Phi_{,\xi\eta})_{,\xi\xi}\\&\quad-\lambda(\lambda^2 A_{16}^*\Phi_{,\eta\eta}+A_{26}^*\Phi_{,\xi\xi}-\lambda A_{66}^*\Phi_{,\xi\eta})_{,\xi\eta}=0\end{aligned}\tag{2}$$

Here $\boldsymbol{A}^*$ and $\boldsymbol{D}$ are the stiffness matrices which are given, for example, by Whitney [10].

Further, the behavior of simply supported (SS) and clamped (C) plates subjected to com-

pressive edge displacements $\bar{\Delta}_x$ in the x-direction will be analyzed. Depending on the in-plane boundary conditions at the edges $\eta = 0$, 1, two cases are considered, namely: the edges $\eta = 0$, 1 are immovable in the y-direction (SS1- and C1-cases); the edges $\eta = 0$, 1 are unloaded (SS2- and C2-cases). In all instances, the in-plane displacements at the edges are unrestricted in tangential direction.

Introducing the average edge shortenings in both in-plane directions

$$\bar{\Delta}_x = \int_0^1 [u(1, \eta) - u(0, \eta)]\mathrm{d}\eta;$$

$$\bar{\Delta}_y = \int_0^1 [\mathrm{v}(\xi, 1) - \mathrm{v}(\xi, 0)]\mathrm{d}\xi$$

(where u and v are the in-plane displacements), and using the expressions for $\bar{\Delta}_x$, $\bar{\Delta}_y$ in terms of Φ, w, given in an earlier paper [7], the boundary conditions may be formulated as follows:

SS1 at $\xi = 0$, 1: $\Phi_{,\xi\eta} = w = M_{\xi\xi} = 0$;

$$\frac{1}{a}\int_0^1\int_0^1 (\lambda^2 A_{11}^* \Phi_{,\eta\eta} + A_{12}^* \Phi_{,\xi\xi})\mathrm{d}\xi\mathrm{d}\eta = \bar{\Delta}_x$$

at $\eta = 0$, 1: $\Phi_{,\xi\eta} = w = M_{\eta\eta} = 0$;

$$\int_0^1\int_0^1 (\lambda^2 A_{12}^* \Phi_{,\eta\eta} + A_{22}^* \Phi_{,\xi\xi})\mathrm{d}\xi\mathrm{d}\eta = 0$$

SS2 at $\xi = 0$, 1: $\Phi_{,\xi\eta} = w = M_{\xi\xi} = 0$;

$$\frac{1}{a}\int_0^1\int_0^1 (\lambda^2 A_{11}^* \Phi_{,\eta\eta} + A_{12}^* \Phi_{,\xi\xi})\mathrm{d}\xi\mathrm{d}\eta = \bar{\Delta}_x$$

at $\eta = 0$, 1: $\Phi_{,\xi\xi} = \xi_\eta = w = M_{\eta\eta} = 0$

C1 at $\xi = 0$, 1: $\Phi_{,\xi\eta} = w = w_{,\xi} = 0$;

$$\frac{1}{a}\int_0^1\int_0^1 (\lambda^2 A_{11}^* \Phi_{,\eta\eta} + A_{12}^* \Phi_{,\xi\xi})\mathrm{d}\xi\mathrm{d}\eta = \bar{\Delta}_x$$

at $\eta = 0$, 1: $\Phi_{,\xi\eta} = w = w_{,\eta} = 0$;

$$\int_0^1\int_0^1 (\lambda^2 A_{12}^* \Phi_{,\eta\eta} + A_{22}^* \Phi_{,\xi\xi})\mathrm{d}\xi\mathrm{d}\eta = 0$$

C2 at $\xi = 0$, 1: $\Phi_{,\xi\eta} = w = w_{,\xi} = 0$;

$$\frac{1}{a}\int_0^1\int_0^1 (\lambda^2 A_{11}^* \Phi_{,\eta\eta} + A_{12}^* \Phi_{,\xi\xi})\mathrm{d}\xi\mathrm{d}\eta = \bar{\Delta}_x$$

at $\eta = 0$, 1: $\Phi_{,\xi\xi} = \Phi_{,\xi\eta} = w = w_{,\eta} = 0$ (3)

where $M_{\alpha\beta}$ (α, $\beta = \xi$, η) are the moment resultants.

To fulfill the buckling analysis of a FGM plate, one needs to determine the constitutive behavior at every point of the structure, so that the stiffnesses involved in eqns (1)–(3) can be calculated. The required constitutive law can be obtained by a suitable micromechanical approach. In the present work, the micromechanical analysis performed relies on the RVE-based method of cells [8]. That is, at every point (x, y, z) of the plate this micromechanical method is employed, using the values of material properties of fiber and matrix phases, as well as the reinforcement volume fraction at that point $\mathrm{v}_f(x, y, z)$. This enables one to establish the effective constitutive law of a functionally graded composite in the form

$$\boldsymbol{\sigma}(x, y, z) = \boldsymbol{C}(x, y, z)\boldsymbol{\varepsilon}(x, y, z)$$

where $\boldsymbol{\sigma}$ and $\boldsymbol{\varepsilon}$ are stress and strain tensors, and $\boldsymbol{C}$ represents the effective stiffness tensor.

Determination of the critical buckling load

An approximate solution to the above-formulated problem is sought in the form

$$\Phi(\xi, \eta) = -\frac{a^2}{\lambda^2} R_x \frac{\eta^2}{2} - a^2 R_y \frac{\xi^2}{2} + \sum_{p=1}^{P}\sum_{q=1}^{Q} F_{pq} X_p(\xi) X_q(\eta)$$

$$w(\xi, \eta) = \sum_{m=1}^{M}\sum_{n=1}^{N} W_{mn} \sin \pi m\xi \sin \pi n\eta$$

(for SS-cases)

$$w(\xi, \eta) = \sum_{m=1}^{M}\sum_{n=1}^{N} W_{mn} X_m(\xi) X_n(\eta)$$

(for C-cases) (4)

where $X_i (i = 1, 2, \ldots)$ are beam eigenfunctions satisfying boundary conditions $X_i(0) = X_i(1) = X_i'(0) = X_i'(1) = 0$. It can be readily seen that one needs to determine the coefficients of the series (4), and the values of R_x, R_y (having the meanings of normal in-plane loads at the edges $x = 0, a$ and $y = 0, b$).

To calculate the coefficients F_{pq}, W_{mn}, the series (4) are substituted into the governing eqns (1) and (2), and the Galerkin procedure is employed. The compatibility equation (2) is multiplied by $X_r(\xi)X_s(\eta)$ and integrated over the

plate surface. Equation (1) is multiplied by $\sin \pi i\xi \sin \pi j\eta$ for SS-cases or by $X_i(\xi)X_j(\eta)$ for C-cases and integrated over the plate surface as well. For SS-cases, to account for the boundary conditions on the bending moments, boundary integrals are included in the formulation of the Galerkin equations (see Whitney [10] for details). As a result, the following equations are obtained

$$\sum_p \sum_q S_1^{rspq} F_{pq} = R_x S_{2x}^{rs} + R_y S_{2y}^{rs}$$

$$(r = 1, \ldots, P,\ s = 1, \ldots, Q) \tag{5}$$

$$\sum_m \sum_n S_3^{ijmn} W_{mn} + \sum_m \sum_n \sum_p \sum_q S_4^{ijmnpq} W_{mn} F_{pq}$$

$$+ \sum_m \sum_n (R_x S_{5x}^{ijmn} + R_y S_{5y}^{ijmn}) W_{mn} = 0$$

$$(i = 1, \ldots, M,\ j = 1, \ldots, N) \tag{6}$$

The coefficients $S_1^{rspq}, \ldots, S_{5y}^{ijmn}$, which are analogous to those given in an earlier paper [9] involve surface integrals from different elements of stiffness matrices $\boldsymbol{A}^*$ and $\boldsymbol{D}$, multiplied by the beam or trigonometric functions.

To determine the values of R_x, R_y, the approximation (4) for the stress function is substituted into the boundary conditions (2) for the edge shortenings. This yields

S1, C1

$$R_x \int_0^1 \int_0^1 A_{11}^* \mathrm{d}\xi \mathrm{d}\eta + R_y \int_0^1 \int_0^1 A_{12}^* \mathrm{d}\xi \mathrm{d}\eta$$

$$= -\frac{\bar{\Delta}_x}{a} + \frac{1}{a^4} \sum_p \sum_q F_{pq} S_{2x}^{pq}; \tag{7}$$

$$R_x \int_0^1 \int_0^1 A_{12}^* \mathrm{d}\xi \mathrm{d}\eta + \mathrm{R_y} \int_0^1 \int_0^1 A_{22}^* \mathrm{d}\xi \mathrm{d}\eta$$

$$= \frac{1}{a^4} \sum_p \sum_q F_{pq} S_{2y}^{pq}$$

S2, C2

$$R_x \int_0^1 \int_0^1 A_{11}^* \mathrm{d}\xi \mathrm{d}\eta$$

$$= -\frac{\bar{\Delta}_x}{a} + \frac{1}{a^4} \sum_p \sum_q F_{pq} S_{2x}^{pq};\ R_y = 0$$

For all the boundary conditions considered, the solution to (7) may be written as

$$R_x = e_{1x} \bar{\Delta}_x + \sum_p \sum_q e_{2x}^{pq} F_{pq};$$

$$R_y = e_{1y} \bar{\Delta}_x + \sum_p \sum_q e_{2y}^{pq} F_{pq} \tag{8}$$

From substitution of relationships (8) into eqn (5) it is possible to get F_{pq} in the form

$$F_{pq} = \phi_{pq} \bar{\Delta}_x \tag{9}$$

Finally, substituting (8) and (9) into eqn (6), one obtains

$$\sum_m \sum_n (S_3^{ijmn} - \bar{\Delta}_x Q_x^{\mathrm{ijmn}}) \mathrm{W_{mn}} = 0$$

$$(\mathrm{i} = 1, \ldots, \mathrm{M},\ \mathrm{j} = 1, \ldots, \mathrm{N}) \tag{10}$$

where

$$Q_x^{ijmn} = -\Big[e_{1x} S_{5x}^{ijmn} + e_{1y} S_{5y}^{ijmn} + \sum_p \sum_q \phi_{pq} (S_4^{ijmnpq}$$

$$+ e_{2x}^{pq} S_{5x}^{ijmn} + e_{2y}^{pq} S_{5y}^{ijmn}) \Big]$$

From eqn (10), the buckling criterion is readily obtained

$$\det[\boldsymbol{Q}_x^{-1} \boldsymbol{S}_3 - \bar{\Delta}_x \boldsymbol{I}] = 0 \tag{11}$$

where $\boldsymbol{I}$ is an identity matrix.

The buckling criterion (11) enables one to calculate the critical buckling displacement $\bar{\Delta}_x^{cr}$ (as the minimal eigenvalue of the matrix $\boldsymbol{Q}_x^{-1} \boldsymbol{S}_3$) and, according to (8), to obtain the critical buckling load R_x^{cr} for a given reinforcement volume fraction $\mathrm{v}_f(\xi, \eta, \zeta)$.

Optimal reinforcement distributions

For greater buckling resistance of a FGM plate, the functional $R_x^{cr}(\mathrm{v}_f)$ should be maximized. In the present work, this is achieved as follows. Function v_f is expanded into the Legendre polynomials

$$\mathrm{v}_f(\xi,\eta,\zeta) = \sum_{\mathrm{i}=0}^{\mathrm{I}} \sum_{\mathrm{j}=0}^{\mathrm{J}} \sum_{\mathrm{k}=0}^{\mathrm{K}} \mathrm{V_{ijk}} \mathrm{P_i}(\xi) \mathrm{P_j}(\eta) \mathrm{P_k}(\zeta) \tag{12}$$

with V_{ijk} being unknown coefficients to be determined. This allows one to represent the buckling load as $R_x^{cr} = R_x^{cr}(V_{ijk})$. It is further required that the total amount of reinforcements (namely the plate weight) remains a given constant

$$\int_{\xi=0}^{1} \int_{\eta=0}^{1} \int_{\zeta=-1/2}^{1/2} \mathrm{v}_f \mathrm{d}\xi \mathrm{d}\eta \mathrm{d}\zeta = \mathrm{v}_f^* = \mathrm{const} \tag{13}$$

Thereafter the objective function $R_x^{cr}(V_{ijk})$ is maximized, with V_{ijk} being a set of design variables subject to the above constraint (13). Two additional constraints stem from the following requirements on the volume fraction v_f: $v_f > 0$, $v_f < 1$.

Once an optimal set of design variables has been obtained, the corresponding optimal distribution v_f^{opt} of the reinforcement phase is easily calculated from (14). The described procedure should be repeated for different numbers of terms retained in the series (4) and (14) to ensure the convergence of the proposed procedure.

Considering in more detail the affect of the plate thickness on the buckling behavior, it may be shown that, for symmetrically laminated nonhomogeneous plates with the same aspect ratio λ, the same reinforcement distribution $v_f(\xi, \eta, \zeta)$, and subjected to the same boundary conditions, the following relationship holds

$$R_x^{(1)cr}/R_x^{(2)cr} = h_1^3/h_2^3 \qquad (14)$$

where $R_x^{(1)cr}$ is the critical buckling load for a plate of thickness h_1, and $R_x^{(2)cr}$ is the critical buckling load for a plate of thickness h_2. From (15) follows, in particular, that the above-mentioned plates will possess the same optimal volume fraction distribution $v_f^{opt}(\xi, \eta, \zeta)$.

RESULTS AND DISCUSSION

To illustrate the proposed approach, consider SiC/Al unidirectional plates with reinforcements oriented in the x-direction. Results are presented for the temperature $T = 100°C$, at which the material properties are taken as follows: for SiC fibers, Young's modulus $E = 414$ GPa, and Poisson's ratio $\nu = 0.3$; for the aluminum matrix (2024-T4 alloy), $E = 70.5$ GPa, and $\nu = 0.33$. It is assumed that SiC reinforcements comprise 30% of the plate volume, i.e. $v_f^* = 0.3$. As an initial guess (which is needed to start an optimization procedure) assume that a plate is uniformly reinforced, that is $v_f(\xi, \eta, \zeta) = v_f^* = 0.3$.

For the purpose of estimation the effect of a functionally graded plate, introduce a ratio R_x^{opt}/R_x^{hom}, where R_x^{opt} and R_x^{hom} stand for the critical buckling loads for a functionally graded plate with optimal distribution $v_f^{opt}(\xi, \eta, \zeta)$ and for its homogeneous counterpart, respectively. Furthermore, three examples of tailoring the distribution of reinforcement phase are considered; for each of them one of the coordinate directions is chosen as a functionally graded one.

Short-fiber plate with reinforcements nonuniformly distributed in the x-direction

Consider a SiC/Al plate reinforced by short SiC fibers oriented in the x-direction, with the fibers' aspect ratio equal to 7. The fibers' distribution is nonuniform only in the x-direction, such that $v_f = v_f(x)$.

In Fig. 1(a), optimal distributions of a SiC phase along the x-axis are exhibited for a rectangular plate subjected to different types of boundary conditions. Due to the symmetry of the problem, here and further only a half of a functionally graded coordinate axis is shown. It may be seen that the distributions $v_f^{opt}(x/a)$ are dissimilar for simply supported and clamped

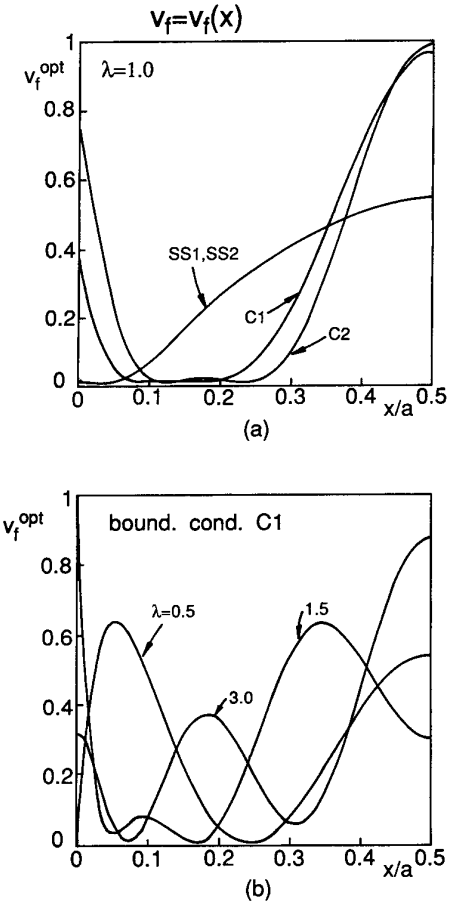

Fig. 1. Optimal reinforcement volume fraction distributions along the x-axis for short-fiber functionally graded plates (the fibers are oriented in the x-direction, fiber aspect ratio = 7), (a) for various types of boundary conditions, (b) for several values of aspect ratio λ.

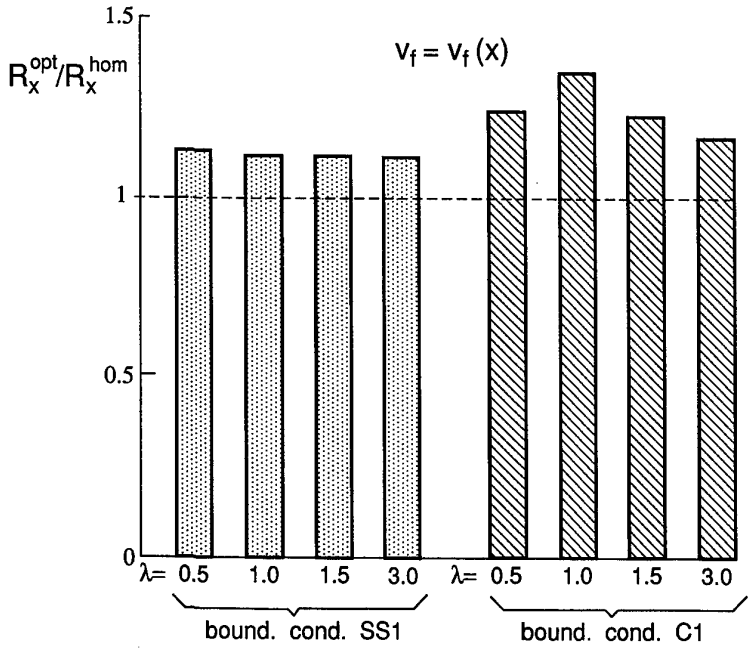

Fig. 2. Buckling load improvements for short-fiber functionally graded plates (the fibers are oriented in the x-direction, fiber aspect ratio = 7); the fibers are non-uniformly distributed in the x-direction.

plates. Moreover, a beneficial effect of a non-homogeneous reinforcement is quite different as well: for the boundary conditions SS1 and SS2 $R_x^{opt}/R_x^{hom} = 1.11$, while for C1- and C2-cases $R_x^{opt}/R_x^{hom} = 1.35$ and 1.42, respectively.

The effect of the plate aspect ratio λ is illustrated in Fig. 1(b) for a clamped structure (boundary condition C1). As is apparent from the graphs, the optimal distribution of a reinforcement phase is strongly affected by the value of the length-to-width ratio. Notice that the improvements in the buckling load also depend essentially on a/b: $R_x^{opt}/R_x^{hom} = 1.24$, 1.35, 1.23, 1.17, and 1.16 for $\lambda = 0.5$, 1.0, 1.5, 2.0, and 3.0, respectively. These results indicate that for the cases considered the maximum advantage over a uniform reinforcement may be achieved for a clamped rectangular plate.

An additional insight into the buckling load improvements that may be attained for the case considered is provided by Fig. 2 where the histograms of R_x^{opt}/R_x^{hom} are presented for two types of the out-of-plane boundary conditions and for several values of λ.

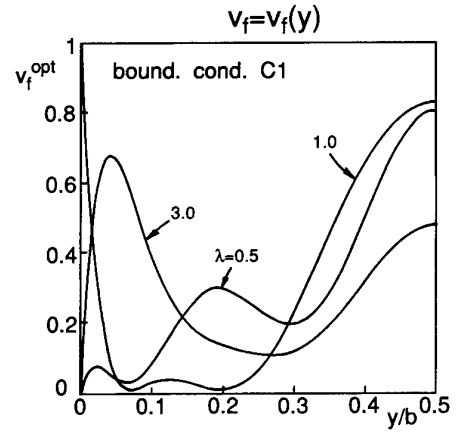

Fig. 3. Optimal reinforcement volume fraction distributions along the y-axis for long-fiber functionally graded plates (the fibers are oriented in the x-direction), for several values of aspect ratio λ.

Long-fiber plate with fibers nonuniformly distributed in the y-direction

Consider a long-fiber SiC/Al plate such that the fibers are oriented along the x-axis and the spacings between them (in the y-direction) are not equal; i.e. $v_f = v_f(y)$.

Regarding the influence of different boundary conditions on the buckling behavior of functionally graded plates, similar trends are observed, as compared to the above considered case of short-fiber plates with $v_f = v_f(x)$. That is, the optimal volume fraction distributions and the corresponding buckling loads for simply supported and clamped plates differ significantly. For rectangular plates, $R_x^{opt}/R_x^{hom} = 1.09$, 1.13, 1.23, and 1.27 for SS1-, SS2-, C1-, and C2-boundary conditions, respectively. Examining

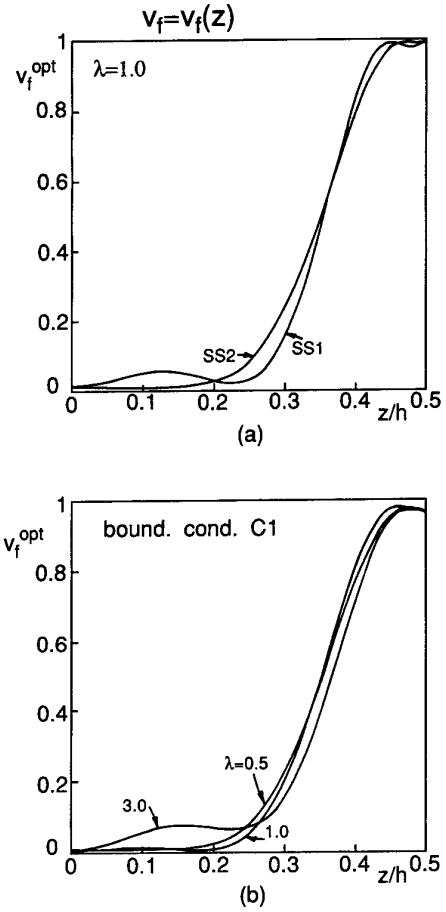

Fig. 4. Optimal reinforcement volume fraction distributions through the thickness for long-fiber functionally graded plates (the fibers are oriented in the x-direction), (a) for two types of simply supported boundary conditions, (b) for a clamped plate and several values of aspect ratio λ.

the effect of plate's aspect ratio, it should be pointed out, that, as indicated in Fig. 3, the optimal distributions $v_f^{opt}(\eta)$ may differ greatly from each other for various values of a/b. The improvements in the buckling loads, corresponding to the graphs shown in the figure, are as follows: $R_x^{opt}/R_x^{hom} = 1.19$, 1.23, 1.12 and 1.09 for $\lambda = 0.5$, 1.0, 1.5 and 3.0, respectively.

Long-fiber plate with fibers nonuniformly distributed through the thickness

Consider a long-fiber SiC/Al plate such that the fibers are oriented along the x-axis and nonuniformly distributed in the direction normal to the midsurface, so that $v_f = v_f(z)$.

It turns out that in this case, for all the boundary conditions and aspect ratios considered, the optimal volume fraction distributions $v_f^{opt}(\zeta)$ are quite similar and, moreover, particularly high values of R_x^{opt}/R_x^{hom} may be obtained. This is illustrated in Fig. 4(a), where the optimal reinforcement distributions through the thickness are shown for a rectangular plate subjected to the two types of simply supported boundary conditions, and in Fig. 4(b), where results are presented for clamped plates with different aspect ratios λ. As viewed in Fig. 4, matrix-rich regions next to the middle-plane are observed, which occupy about 50% of the plate thickness. In the vicinity of the plate surfaces, fiber clustering takes place.

The buckling load improvements corresponding to the graphs presented in Fig. 4(a) are as follows: $R_x^{opt}/R_x^{hom} = 1.95$ and 2.02 for rectangu-

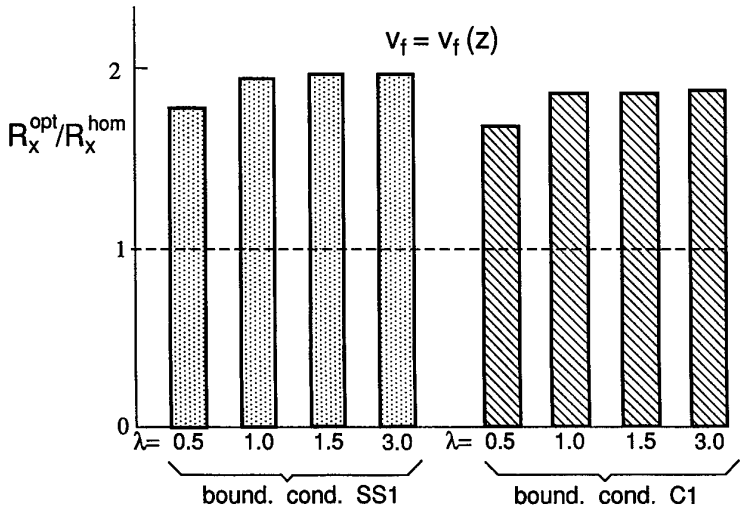

Fig. 5. Buckling load improvements for long-fiber functionally graded plates (the fibers are oriented in the x-direction); the fibers are nonuniformly distributed in the thickness direction.

lar plates subjected to SS1- and SS2-boundary conditions, respectively. The beneficial effect of a nonhomogeneous reinforcement for various values of the aspect ratio λ is shown in Fig. 5, both for simply supported and clamped functionally graded structures.

ACKNOWLEDGEMENTS

The first author is grateful for the support of this research by the Ministry of Absorption of the State of Israel. The second author gratefully acknowledges the support of the Diane and Arthur Belfer Chair of Mechanics and Biomechanics.

REFERENCES

1. Pindera, M.-J., Arnold, S.M., Aboudi, J. and Hui, D., Use of composites in functionally graded materials. *Composites Engng* 1994, **4** (1), 1–145.
2. Pindera, M.-J., Aboudi, J., Arnold, S.M. and Jones, W.F., Use of composites in multi-phased and functionally graded materials. *Composites Engng* 1995, **5** (7), 743–974.
3. Pindera, M.-J., Aboudi, J., Glaeser, A. and Arnold, S. M., Use of composites in multi-phased and functionally graded materials. *Composites (Part B: Engineering)*, March 1997, in press.
4. Needleman, A. and Suresh, S., Mechanics and physics of layered and graded materials. *J. Mech. Phys Solids* 1996, **44** (5), 643–825.
5. Pindera, M.-J., Aboudi, J. and Arnold, S. M., Recent advances in the mechanics of functionally graded composites. In: *Aerospace Thermal Structures and Materials for a New Era (Progress in Astronautics and Aeronautics)*, Vol. 168, pp. 181–203, Thornton, E. A. (ed.). American Institute of Aeronautics and Astronautics, Washington, D.C., 1995.
6. Feldman, E. and Aboudi, J., Postbuckling analysis of metal–matrix laminated plates. *Composites Engng* 1994, **4**, 151–167.
7. Feldman, E., Postbuckling analysis of laminated plates made of discontinuous metal matrix composites. *Composite Struct.* 1995, **32**, 89–96.
8. Aboudi, J., *Mechanics of Composite Materials — A Unified Micromechanical Approach*. Elsevier, Amsterdam, 1991.
9. Feldman, E., Thes effect of temperature-dependent material properties on elasto-viscoplastic buckling behaviour of non-uniformly heated MMC plates. *Composite Struct.* 1996, **35**, 65–74.
10. Whitney, J. M., *Structural Analysis of Laminated Anisotropic Plates*. Technomic, Lancaster, PA, 1987.

ELSEVIER

Composite Structures Vol. 38, No. 1–4, pp. 37–44
© 1997 Elsevier Science Ltd. All rights reserved
Printed in Great Britain
0263-8223/97/$17.00 + 0.00

PII:S0263-8223(97)00039-1

A new laminated triangular finite element assuring interface continuity for displacements and stresses

O. Polit[a,b] & M. Touratier[a]

[a]*LM²S, URA CNRS 1776, ENSAM, 151 Bd de l'Hopital, 75013, Paris, France*
[b]*Université Paris X, IUT, Dépt. GMP, 1 Chemin Desvallières, 92410, Ville d'Avray, France*

The objective of this paper is to present a new 81-degrees-of-freedom finite element for geometrically and materially linear elastic multilayered composite, moderately thick plates. The element is a six nodes C^1 triangular element based on a new kind of kinematics and built from Argyris interpolation for bending, and Ganev interpolation for membrane displacements and transverse shear rotations. The kinematics allow both, the continuity conditions for displacements and transverse shear stresses at the interfaces between layers of a laminated structure, and the boundary conditions at the upper and lower surfaces of the plates, to be exactly ensured. The representation of the transverse shear strains by cosine functions allows one to avoid shear correction factors. The element performances are evaluated on some standard plate tests and also in comparison with an exact three-dimensional solution for multilayered plates both for statics and dynamics. © 1997 Elsevier Science Ltd.

INTRODUCTION

The aim of this work is to analyse the mechanical behaviour of multilayered structures by plate finite elements including transverse shear effects and continuity requirements between layers in order to predict displacements and stresses of such structures for design applications. Many of the existing analysis methods for multilayered anisotropic plates are direct extensions of those developed earlier for homogeneous isotropic and orthotropic plates, see Noor [1]. In fact, many approaches utilize a displacement field which does not account for the contact requirement at the interfaces of multilayered structure. A synthesis is given in Ref. [2]. A finite element of triangular shape has been proposed by Di Sciuva [3] based on a third-order refined shear deformation theory satisfying interlaminar continuity. In this work, piecewise linear functions are introduced using the Heaviside operator.

We present a new C^1 plate finite element based on a refined kinematic model, see Touratier [4], incorporating:

(1) the transverse shear strains with cosine distributions,
(2) the continuity conditions between layers of the laminate for both displacements and transverse shear stresses,
(3) the satisfaction of the boundary conditions at the top and bottom surfaces of the plates, without shear correction factors, using five independent generalized displacements (three translations and two rotations).

The element is of triangular shape and the generalized displacements are approximated by higher-order polynomials based on:

(i) Argyris [5] interpolation for the transverse normal displacement,

(ii) Ganev [6] interpolation for the membrane displacements and for the transverse shear rotations.

Finally, some tests in linear statics and dynamics have been achieved, and show that the element has a good behaviour and gives with only a few elements accurated computations for displacements and stresses compared to the exact three-dimensional solutions for multilayered plates.

THE DISPLACEMENT FIELD FOR LAMINATED PLATES

Let $(x_1, x_2, x_3 = z)$ denote the Cartesian co-ordinates such that x_1 and x_2 are in the midplane ($z = 0$) of the plate, while z is the transverse normal co-ordinate. We denote by $u_i^{(k)}(x_1, x_2, z)$, $i \in \{1, 2, 3\}$ the Cartesian components of the displacement field for the kth layer of a multilayered plate, and we suppose that the transverse normal strain denoted by ε_{33} is negligible, according to the moderately thick plate hypothesis. Since the material behaviour is linearly elastic and that this work is limited to small disturbances (small displacements), strains and stresses are classically denoted by $\varepsilon_{ij}^{(k)}$ and $\sigma_{ij}^{(k)}$.

In order to prescribe:

(1) cosine distribution across the thickness for transverse shear stresses,
(2) boundary conditions on the upper and lower faces of the plates for transverse shear stresses,
(3) interlayer continuity for displacements and transverse shear stresses,

we assume in the kth layer [7]:

$$\sigma_{13}^{(k)}(x_1, x_2, z, t) = \left(\bar{C}_{55}^{(k)}\left(f'(z) - \frac{h}{\pi} b_{55} f''(z)\right) + a_{55}^{(k)}\right)\gamma_1^0(x_1, x_2, t) + \left(\bar{C}_{45}^{(k)}\left(f'(z) - \frac{h}{\pi} b_{44} f''(z)\right) + a_{54}^{(k)}\right)\gamma_2^0(x_1, x_2, t)$$

$$\sigma_{23}^{(k)}(x_1, x_2, z, t) = \left(\bar{C}_{45}^{(k)}\left(f'(z) - \frac{h}{\pi} b_{55} f''(z)\right) + a_{45}^{(k)}\right)\gamma_1^0(x_1, x_2, t) + \left(\bar{C}_{44}^{(k)}\left(f'(z) - \frac{h}{\pi} b_{44} f''(z)\right) + a_{44}^{(k)}\right)\gamma_2^0(x_1, x_2, t) \tag{1}$$

In these equations $f(z) = h/\pi \sin \pi z/h$ and $f'(z) = \mathrm{d}f(z)/\mathrm{d}z$; h is the thickness of the plate; γ_1^0 and γ_2^0 are the transverse shear strains at $z = 0$; $\bar{C}_{ij}^{(k)}$ are the moduli of the material for the kth layer taking into account of the zero transverse normal stress hypothesis. The constitutive law is expressed as

$$[\sigma^{(k)}] = [\bar{C}^{(k)}][\varepsilon^{(k)}] \tag{2}$$

with

$$\{\bar{C}_{ij}^{(k)} = C_{ij}^{(k)} - C_{i3}^{(k)} C_{j3}^{(k)} / C_{33}^{(k)}$$

for $i, j = 1, 2, 6$ $\bar{C}_{ij}^{(k)} = C_{ij}^{(k)}$

for $i, j = 4, 5$

In eqn (2), $C_{ij}^{(k)}$ are the three-dimensional moduli of the material for the kth layer, and eqns (1) and (2) account for layers having orthotropic axes oriented at various angles with respect to the plate axes.

Otherwise, $\varepsilon_{33} = 0$ allows one to put down $u_3^{(k)}(x_1, x_2, z, t) = u_3(x_1, x_2, z, t) = v_3(x_1, x_2, t)$. Then, from strain definitions we have for the transverse shear strains

$$2\varepsilon_{\beta 3}^{(k)}(x_1, x_2, z, t) = v_3(x_1, x_2, t)_{,\varepsilon} + u_\varepsilon^{(k)}(x_1, x_2, z, t)_{,3} \tag{3}$$

From (2), the transverse shear strains may also be written under the following form

$$2\varepsilon_{13}^{(k)} = S_{55}^{(k)} \sigma_{13}^{(k)} + S_{45}^{(k)} \sigma_{23}^{(k)}$$
$$2\varepsilon_{23}^{(k)} = S_{45}^{(k)} \sigma_{13}^{(k)} + S_{44}^{(k)} \sigma_{23}^{(k)} \tag{4}$$

where $[S^{(k)}] = [\bar{C}^{(k)}]^{-1}$ are the material compliances.

Substituting (1) into (4), then equating (3) and (4), and performing an integration with respect to the z co-ordinate, it follows

$$\begin{aligned}\{u_1^{(k)} &= v_1 - zv_{3,1} + (f_1 + g_1^{(k)})(v_{3,1} + \theta_1) \\ &\quad + g_2^{(k)} v_{3,2} + \theta_2) u_2^{(k)} \\ &= v_2 - zv_{3,2} + g_3^{(k)}(v_{3,1} + \theta_1) \\ &\quad + (f_2 + g_4^{(k)})(v_{3,2} + \theta_2) u_3 = v_3 \end{aligned} \quad (5)$$

where in-plane displacements v_α have been introduced and where functions f_1, f_2, $g_1^{(k)}$, ..., $g_4^{(k)}$ are immediately deduced from eqn (1) and the above integration performed with respect to the z co-ordinate. Other coefficients (b_{ij}, $a_{ij}^{(k)}$,...) are determined from the boundary conditions on the top and bottom surfaces of the plate, and from the continuity requirements at the layer interfaces for displacements and stresses, see Béakou and Touratier [7]. Hereafter, the superscript (k) for $u_\alpha^{(k)}$ components is deleted in order to simplify the finite element description of the model.

THE TRIANGULAR SIX NODE FINITE ELEMENT FOR SEMI-THICK LAMINATES

The finite element construction is now briefly described. Based for example on the principle of virtual powers, the discrete formulation of the boundary value problem in linear elasticity is classically deduced from the following function:

$$\begin{aligned} &a(\vec{u}^h, \vec{u}^{*h})_{\cup\Omega_e} \\ &\quad = f(\vec{u}^{*h})_{\cup\Omega_e} + F(\vec{u}^{*h})_{\cup C_e}, \ \forall \vec{u}^{*h} \end{aligned} \quad (6)$$

where $\cup\Omega_e$ is the triangulation of the multilayered structure and $\cup C_e$ is the edge of the meshed structure. In addition, $\vec{u}^h$ is the finite element approximation of the displacement field $\vec{u}$ given above by eqn (5) and $\vec{u}^{*h}$ is the finite element approximation of the corresponding virtual velocity field $\vec{u}^*$. Linear functions f and F represent the body (including inertia terms) and surface external loads, actually surface and line loads respectively due to the integration performed throughout the thickness in eqn (6). The superscript h introduced in eqn (6) indicates the finite element approximation. Then, it is also used for finite element approximation of the generalized displacements in (5), denoted by v_i^h and θ_α^h where $i = 1, 2, 3$ and $\alpha = 1, 2$. Thus, the finite element approximation of functions v_i and θ_α are briefly indicated hereafter.

The elementary stiffness matrix is obtained by computing the bilinear form given in (6) at the elementary level as

$$a(\vec{u}^h, \vec{u}^{*h})_{\Omega_e} = \int_{\Omega_e} [E_e^{*h}]^T [A_e] [E_e^h] \mathrm{d}\Omega_e \quad (7)$$

where $[A_e]$ is the material behaviour matrix for a multilayered finite element resulting of the integration with respect to the thickness co-ordinate, and $[E_e^h]$ is the following vector

$$\begin{aligned}[E_e^h]^T = [&v_{1,1}^h v_{1,2}^h \vdots v_{2,1}^h v_{2,2}^h \vdots v_{3,1}^h v_{3,2}^h v_{3,11}^h v_{3,22}^h v_{3,12}^h \\ &\vdots \theta_1^h \theta_{1,1}^h \theta_{1,2}^h \vdots \theta_2^h \theta_{2,1}^h \theta_{2,2}^h] \end{aligned} \quad (8)$$

The matrix $[E_e^{*h}]$ is defined by an analogous expression introducing the superscript *. The form given by (8) for the vector $[E_e^h]$ may be seen as the vector of generalized strains for the proposed model. So, we must now explicit the interpolation for each approximated generalized displacement and its derivatives appearing in (8). In Fig. 1 (from Bernadou [8]) local degrees of freedom for the interpolation of the v_3^h function are given, and Argyris interpolation for v_3^h obtained from this set of degrees of freedom is P_5. In the same way, Fig. 2 (from Bernadou [8]) gives the set of local degrees of freedom for the other generalized displacements v_α^h and β_α^h. Ganev interpolation constructs from this set is P_4. In this two figures, derivative degrees of freedom are local because they are expressed with respect to the directions associated with the edges of the triangle.

So, the discrete form of the vector $[E_e^h]$ can be written as

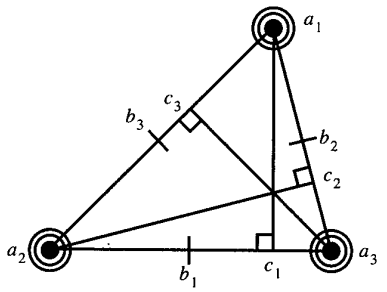

$P_K = P_5(K)$; $dim\ P_K = 21$;
$\Sigma_K = \{p(a_i), Dp(a_i)(a_{i-1} - a_i), Dp(a_i)(a_{i+1} - a_i),\ 1 \le i \le 3;$
$D^2 p(a_i)(a_{j+1} - a_{j-1})^2,\ 1 \le i,j \le 3;\ Dp(b_i)(a_i - c_i),\ 1 \le i \le 3\}$

Fig. 1. Set Σ_K of the local degrees for freedom of a function p for Argyris triangle.

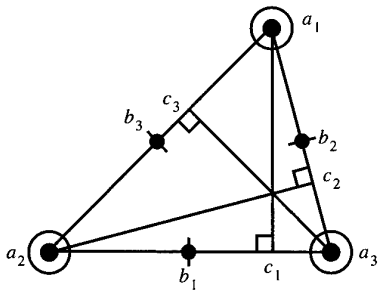

$P_K = P_4(K)$; $dim\ P_K = 15$;
$\Sigma_K = \{p(a_i),\ Dp(a_i)(a_{i-1}-a_i),$
$Dp(a_i)(a_{i+1}-a_i),\ p(b_i),\ Dp(b_i)(a_i-c_i),\ 1 \le i \le 3\}.$

Fig. 2. Set Σ_K of the local degrees for freedom of a function p for Ganev triangle.

$$[E_e^h] = [\Lambda][T_e][D_e][Q_e] \tag{9}$$

where $[Q_e]$ is the vector of degrees of freedom in global co-ordinates, $[D_e]$ is a transformation matrix between local and global co-ordinates taking account of local derivative degrees of freedom. Finally, in eqn (9) the matrix product $[\Lambda]$ $[T_e]$ gives interpolations for each component of the vector $[E_e^h]$ in terms of all barycentric monomial terms for the matrix $[\Lambda]$ and constant coefficients for the matrix $[T_e]$.

Then, it is evident from (7) and (9) that the stiffness matrix is obtained as

$$[K_e] = \int_{\Omega_e}[D_e]^T[T_e]^T[\Lambda]^T[A_e][\Lambda][T_e][D_e]d\Omega_e \tag{10}$$

The elementary mass matrix $[M_e]$ is given after an integration with respect to the thickness as follow

$$\int_{\Omega_e}[U_e^{*h}]^T[I_e][\ddot{U}_e^h]d\Omega_e = [Q_e^*]^T[M_e][\ddot{Q}_e] \tag{11}$$

where $[I_e]$ is the inertia matrix, $(\ddot{}) = \partial^2()/\partial t^2$, t is the time; $[U_e^h]$ is the vector of generalized displacements deduced from eqn (5) and given by

$$[U_e^h]^T = [v_1^h\ v_2^h\ v_3^h\ v_{3,1}^h v_{3,2}^h \theta_1^h \theta_2^h] \tag{12}$$

Finally, $[U_e^{*h}]$ is the vector of generalized virtual velocity consistently associated to (12).

Load vector construction does not need to be presented here as it is classic. The elementary matrices are integrated using a 16 point integration rule which integrates exactly eight order polynomials, see Dunavant [9].

NUMERICAL EVALUATION OF THE ELEMENT

Basic tests

Firstly, standard basic tests for plate elements have been considered:

(1) rank deficiency,
(2) shear locking,
(3) mesh orientation sensitivity,
(4) convergence properties.

For all these classical tests, the new finite element exhibits a very good behaviour:

(1) six zero eigenvalues,
(2) no shear locking when the plate becomes thin and very thin,
(3) no sensitivity to mesh orientation with few elements,
(4) very good convergence properties.

In addition, two kind of models have been tested:

(i) laminated SINUS model including interlayer continuity given by (5), denoted SIN CONT,
(ii) laminated SINUS model without interlayer continuity deduced from (5) with $g_i = 0$, $i \in \{1, 2, 3, 4\}$ and $f_1 = f_2 = f$, denoted SIN.

Static problem

The Srinivas' problem [10] is considered to evaluate the performances of the element to compute deflection and stresses for a thick three-layered plate. The plate is simply supported (B.C: SA-1 on all its edges) and submitted to a transverse normal uniform load ($f_3 = -1$.SI). The material properties of the three-layered (sandwich) square plate are given in Ref. [10] and the skin by core ratio is $\beta = 15$ while geometric characteristics of the plate are:

(1) length of the side $a = 10$ SI,
(2) total thickness $e = 10$ SI,
(3) thickness of the skin (symmetric plate) $e_s = 0.1$ SI,
(4) thickness of the core $e_c = 0.8$ SI.

Table 1 shows results deduced from the proposed triangular finite element associated with the two models denoted SIN CONT and SIN. It is clear for deflection and stresses that the interlayer continuity model SIN CONT is the best model and gives very accurate results in com-

Table 1. Deflections and stresses for an orthotropic sandwich plate under an uniform load

Value for $N = 4$	Ref. value [10]	SIN CONT	SIN
$v_3E_x1,/p_0$	121.72	121.88	115.46
σ_{11}/p_0			
Top skin at top surface	66.787	66.742	66.891
Top skin at interface	48.299	48.215	50.060
Core at upper interface	3.2379	3.2143	3.3373
Core at lower interface	−3.2009	−3.2143	−3.3373
Bottom skin at interface	−48.028	−48.215	−50.060
Bottom skin at bottom surface	−66.513	−66.742	−66.891
σ_{22}/p_0			
Top skin at top surface	46.424	46.581	45.721
Top skin at interface	34.955	35.109	35.148
Core at upper interface	2.4941	2.3406	2.3432
Core at lower interface	−2.3476	−2.3406	−2.3432
Bottom skin at interface	−35.353	−35.109	−35.148
Bottom skin at bottom surface	−46.821	−46.581	−45.721
σ_{13}/p_0			
Top skin at top surface	0.0000	0.0000	0.0000
Top skin at interface	3.9559	3.5542	19.390
Core at upper interface	3.9559	3.5542	1.2927
At mid surface	3.9638	4.0841	4.1832
Core at lower interface	3.5768	3.5542	1.2927
Bottom skin at interface	3.5768	3.5542	19.390
Bottom skin at bottom surface	0.0000	0.0000	0.0000

parison with the exact three-dimensional elasticity solution. Computations in the Table 1 have been achieve using a $N = 4$ mesh shown in the Fig. 3. This is sufficient to reach the convergence of stresses even for the transverse shear stresses, and therefore for the deflection, see Fig. 5. Actually, convergence properties for deflection is reached only with $N = 1$ mesh, see Fig. 4.

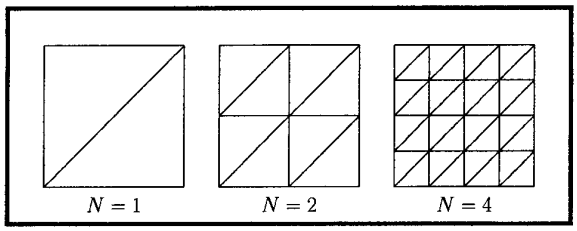

Fig. 4. Meshes used for convergence tests.

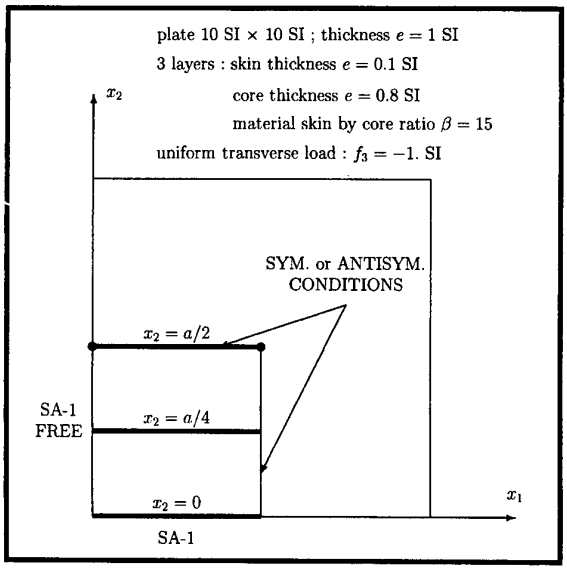

Fig. 3. Numerical test configuration for the sandwich plate

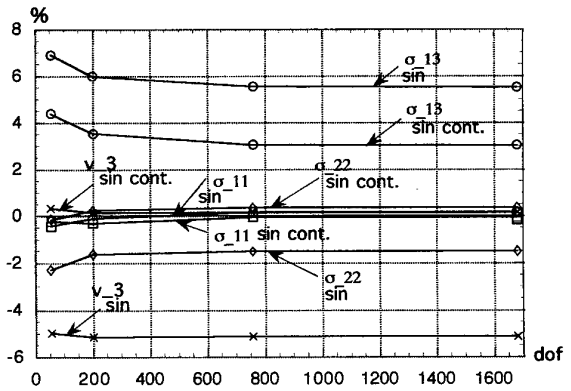

Fig. 5. Convergence test for displacement and stresses in a sandwich plate ($a/c = 10$) under and uniform normal tranverse load: SA-1 SA-1.

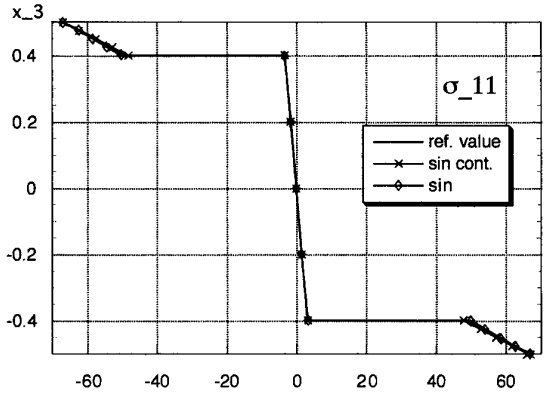

Fig. 6. Thickness distribution of σ_{11} at the center point $(a/2, a/2, x_3)$; SA-1−SA-1.

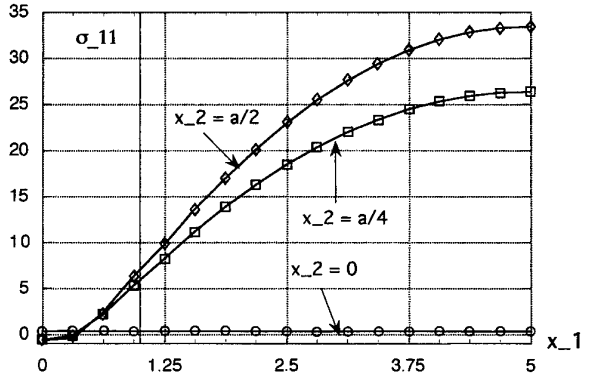

Fig. 9. Distribution of σ_{11} with respect to x_1 (lines $(x_1, x_2-e/2)$); FREE SA-1.

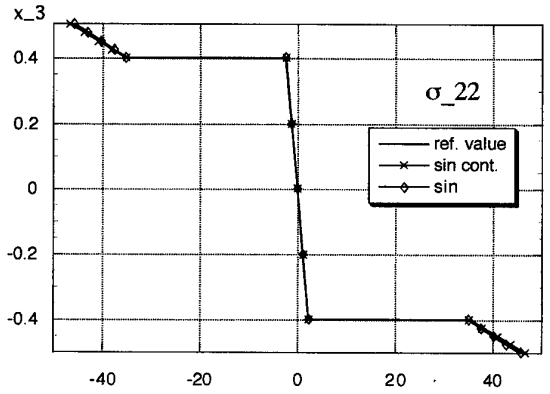

Fig. 7. Thickness distribution of σ_{22} at the center point $(a/2, a/2, x_3)$; SA-1−SA-1.

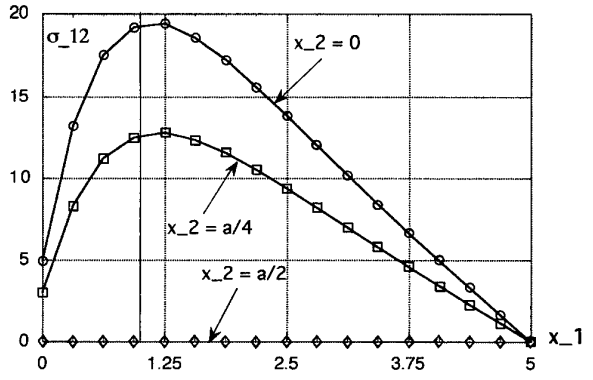

Fig. 10. Distribution of σ_{12} with respect to x_1 (lines $(x_1, x_2-e/2)$); FREE−SA-1.

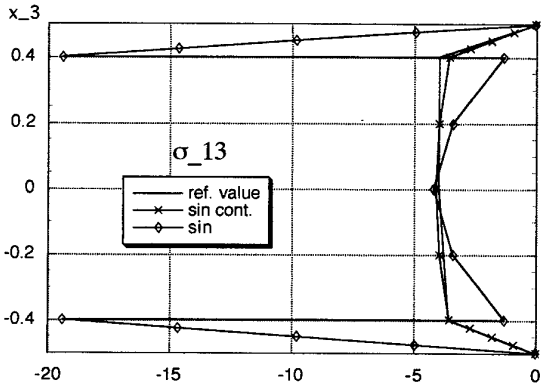

Fig. 8. Thickness distribution of σ_{13} at the middle point $(0, a/2, x_3)$ of the free side; SA-1−SA-1.

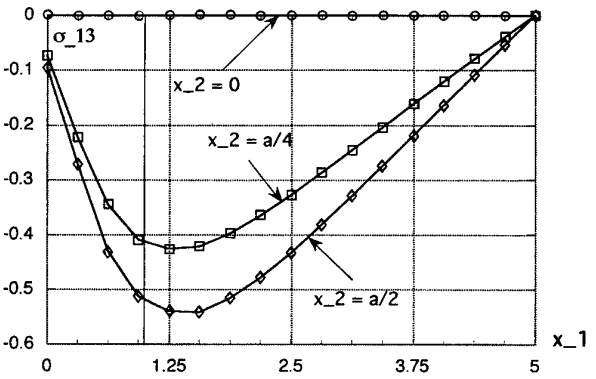

Fig. 11. Distribution of σ_{13} with respect to x_1 (lines $(x_1, x_2, 0)$); FREE SA-1.

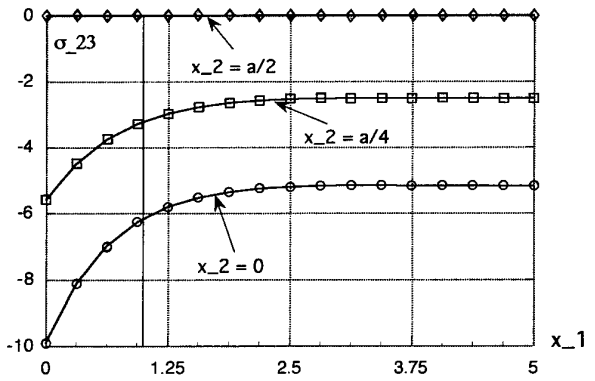

Fig. 12. Distribution of σ_{23} with respect to x_1 (lines (x_1, x_2, 0)); FREE–SA-1.

Distributions of stresses throughout the thickness at the center of the sandwich plate are given:

(1) Fig. 6 for the stress component σ_{11},
(2) Fig. 7 for the stress component σ_{22}.

Fig. 7 shows the distribution of the transverse shear stress σ_{13} throughout the thickness at the station (0, a/2) of the sandwich plate, see also Fig. 3.

Free edge effects

The problem considered is still the above square plate submitted to an uniform normal transverse load. Only boundary conditions are removed in order to analyze the effect of a free edge in statics, using the interlayer continuity SIN CONT model. Results are shown in Figs 9–12. The boundary conditions are: SA-1 for edges $x_2 = 0$ and a, FREE for edges $x_1 = 0$ and a, see Fig. 3.

Dynamics problem

The above sandwich square plate is studied in dynamics for free vibrations in the case of all simply supported edges (SA-1). Results are given in Table 2 for the models SIN CONT and SIN, and for different meshes in comparison with the three-dimensional solution. [10].

FINAL REMARKS

In this paper a new six node multilayered triangular finite element has been presented to analyze the behaviour of composite laminates. The novelty in this work is the use of a refined shear deformation theory including interlaminar continuity, both for displacements and transverse shear stresses, and satisfying exactly the boundary conditions at the top and bottom surfaces of a multilayered plate structure. In addition, the way to interpolate the generalized displacements using higher-order polynomials of C^1 continuity assures the field compatibility for membrane and transverse shear strains. Due to the C^1 continuity, it may be notice that all stresses are continuous at the corner nodes of two adjacent elements.

The element has good properties in the field of finite elements, and gives very good results compared to the exact three-dimensional elasticity solution for a sandwich plate.

Actual and future works are pointed toward edge effect sensitivity for this type of two-dimensional refined model, and buckling analysis.

REFERENCES

1. Noor, A.K. and Burton, W.S., Stress and free vibration analysis of multilayered composite plates. *Comp. and Struct.* 1989, **11**(3), 183–204.
2. Reddy, J.N., On refined computational models of composite laminates. *Int. J. Numer. Meth. Engng* 1989, **27**, 361–382.
3. Di Sciuva, M., A third order triangular multilayered plate finite element with continuous interlaminar stresses. *Int. J. Numer. Meth. Engng* 1995, **38**, 1–26.
4. Touratier, M., An efficient standard plate theory. *Int. J. Engng Sci.* 1991, **29**, 901–916.
5. Argyris, J.H., Fried, I. and Scharpf, D.W., The tuba family of plate elements for the matrix displacement

Table 2. Adimensional value of fundamental frequency of free vibrations

Mesh	Dof	SIN CONT	SIN
1	55	0.11202	0.11523
2	200	0.11202	0.11523
4	760	0.11202	0.11523
8	2960	0.11202	0.11523

Reference value: [10] 0.112034.

method. *Aero. J. Royal Aeronaut. Soc.* 1968, **72**, 701–709.
6. Ganev, H. G. and Dimitrov, Tch. T., Calculation of arch dams as a shell using IBM-370 computer and curved finite elements. In *Theory of Shells*, Amsterdam, North-Holland, 1980, pp. 691–696.
7. Beako, A. and Touratier, M., A rectangular finite element for analysing composite multilayered shallow shells in statics, vibration and buckling. *Int. J. Numer. Meth. Engng* 1993, **36**, 627–653.
8. Bernadou, M., *Méthodes d'Eléments Finis pour les Problémes de Coque Minces*. Collection R.M.A. Masson, Paris, 1994.
9. Dunavant, D.A., Hight degree efficient symmetrical gaussian quadrature rules for the triangle. *Int. J. Numer. Meth. Engng* 1985, **21**, 1129–1148.
10. Srinivas, S. and Rao, A.K., Bending, vibration and buckling of simply supported thick orthotropic rectangular plates and laminates. *Int. J. Solids Struct.* 1970, **6**, 1463–1481.

ELSEVIER

Composite Structures Vol. 38, No. 1–4, pp. 45–55
© 1997 Elsevier Science Ltd. All rights reserved
Printed in Great Britain
0263-8223/97/$17.00 + 0.00

PII:S0263-8223(97)00040-8

An investigation into the eigen-nature of cracked composite beams

A. Abd El-Hamid Hamada

Production Engineering and Mechanical Design Department, Faculty of Engineering, Menoufia University, Shebin El-Kom, Egypt

It is known that the presence of cracks in composite structures introduces local flexibility associated with the changes in the dynamic characteristics of composite structures. However the nature and variations of the natural frequencies due to the presence of cracks, are still under discussion and analysis.

The present work introduces an attempt to study the variations in the eigen-nature of cracked composite beams due to different crack depths and locations. A numerical and experimental investigation has been made. The numerical finite element technique is utilized to compute the eigen pairs of laminated composite beams through several state of cracks. The model is based on elastic–plastic fracture mechanics techniques in order to consider the crack tip plasticity in the analysis. A finite element model has been developed to formulate the stiffness matrices for single edge cracked structural elements using transfer matrix theory. These matrices take into account the effects of axial, flexural and shear deformations due to crack presence. The present model has been applied to investigate the effects of state of crack, lamina code number, boundary condition on the dynamic behavior of composite beams.

The experimental tests and frequency response spectrums (FRS) is displayed on [FFT] analyzer. In experimental work the eigen pairs versus several state of cracks with various code number are measured using inductive hammering technique. The results show that the changes of the eigen parameters provide a proper indicator for detection and predication the current state of crack. © 1997 Elsevier Science Ltd.

INTRODUCTION

The eigen nature of cracked laminated composite beams is one of the most serious problems in machine element structures. The investigation of dynamic criteria of these crack elements is of great interest due to its practical importance since cracks on a structural element change its local flexibility and damping capacity.

Early investigations into analysis of simple cracked structures formed from simple components such as uniformly cracked shafts and beams [1–5], where begun by recognizing the need for simplified modelling of cracks on elements. In the above research, the modelling under consideration was limited to simple stress–strain relations.

In recent years the determination of strain energy release rates and stress intensity factors using the finite element method has been presented in Ref. [6]. For more accurate analytical modelling of complex composite cracked structures, many finite element procedures were developed by many researchers [7–11]. These researches are directed towards improving the model of cracks either by using typical finite elements, by separating the nodes of the cracked elements with six to eight nodes, and by using a very dense grid finite element in the neigborhood of the crack tip due to the singular character of the local stresses and strains.

The present paper presents a numerical and experimental analysis of eigen parameters on a laminated composite beam with various orienta-

tions, which are carried out for different boundary conditions, and in the absence and presence of cracks.

The numerical finite element technique is utilized to compute the eigen pairs of laminated composite beams through several state of cracks. The model is based on elastic–plastic fracture mechanics techniques in order to consider the crack tip plasticity in the analysis. A finite element model has been developed to formulate the stiffness matrices for single edge cracked structural elements using transfer matrix theory. The model takes into account the effects of crack location and size, fiber orientation, and boundary fixation.

In the experimental work, various specimens of laminated composite beam made of fiber glass are investigated. Each specimen was made of five plies for various states of crack (different ratios of depth and location) for various code numbers via different boundary conditions within the overture frequency spectrum. The experimental tests and frequency response spectra were displayed on a [FFT] analyzer. The results show that the changes of the eigen parameters provide a proper indicator for the detection and prediction of the current state of the crack.

Finite element model

A finite element model is developed which represents a prismatic beam element containing an open single-edge crack. The model takes into consideration the effect of plasticity ahead of the cracked tip. For various cases of crack location and depth, it is possible to determine the changes in the static, dynamic and stability behaviour of the structural beam. The stiffness matrix for a single-edge cracked structural element has been derived using transfer matrix theory. These matrices take into account the effects of axial, flexural and shear deformation due to crack presence. Hence, this analysis can be employed to identify the order stressed regions in cracked-structures.

However, in practice most materials deform in a plastic manner once some critical combination of stresses is achieved. The plastic ahead of the crack tip will increase the compliance of the cracked-beam element. This may require modification on the element stress intensity factor to consider the effect of increased compliance due to crack tip plasticity.

Elastoplastic compliance of a cracked-beam element

The compliance of a cracked-beam element is affected by the crack-tip stretch caused by local yielding. Irwin [12] suggested that the effect of increased compliance due to the crack-tip yielding could be simulated by a hypothetical extension (r_p) of the crack tip. Irwin introduced the value of r_p for local mode I deformation by

$$r_p = \frac{1}{\pi}\left[\frac{k_I}{\sigma_{ys}}\right]^2 \tag{1}$$

where k_I

k_I elastic stress intensity = $Y\sigma\sqrt{a}$
σ applied nominal stress
a crack length
Y geometric correction factor
σ_{ys} yield strength of the material.

If the physical crack length is increased by $rp/2$. the following equation could still be used to calculate the near tip stress (σy) and the influence of the plastic zone would be approximately accounted for

$$\sigma_y = \frac{K_I}{\sqrt{2\pi r}} \tag{2}$$

which the expression $[k_I Y\sigma\sqrt{a}]$ adjusted Irwin becomes

$$k_{IP} = y\sigma\sqrt{a+r_p/2} \tag{3}$$

where k_{IP} = elasto plastic stress intensity factor.

Substituting the expressions of r and k into last equation we have

$$k_{IP} = F_P \cdot k_I \tag{4}$$

where F_P: plasticity adjustment factor given by

$$F_P = \left[1+\frac{Y^2}{2\pi}\left(\frac{\sigma}{\sigma_{ys}}\right)^2\right]^{\frac{1}{2}} \tag{5}$$

Here, the state of plane strain (σ_{ys}) is elevated to $\sqrt{3}\sigma_y$. The plasticity adjustment factor is used to determine the increase in the compliance of the cracked-beam element due to crack rip plasticity. Therefore, the change in the compliance

of the creaked-beam element due to crack presence is given by

$$\Delta c = \frac{b}{E'F^2}\int_0^{(a+r/2)} k_{IP}^2 \mathrm{d}(a+r_p/2) \tag{6}$$

where

E' equals equivalent modulus of elasticity and refrerring to Ref. 13 the results are calculated.
b beam width
F applied force (axial force, shear force or bending moment).

Axial force and bending moment contribute to mode I of stress intensity factor. Therefore, reciprocal effects between axial and flexural deformations at the cracked section must be considered. The change in each of axial compliance Δ_{cpp}, bending compliance Δ_{cmm}, reciprocal derived by a computer program to evaluate the local flexibility matrix for the crack segment, here as

$$[c] = \begin{bmatrix} \Delta c_{pp} & 0 & \Delta c_{pm} \\ 0 & \Delta c_{qq} & 0 \\ \Delta c_{mp} & 0 & \Delta c_{mm} \end{bmatrix} \tag{7}$$

The model of the cracked-beam element is divided to into three segments, namely, left crack and right segments. The left and right segments are standard beam elements with length L_1 and L_2, respectively. The crack segment is of zero length and connects left and right segments. Three degrees of freedom corresponding to axial force, shear force and bending moment are considered at each side of the crack segments as shown in Fig. 1.

The matrix $[c]$ relates the displacement vector to the corresponding force vector $\{\sigma\} = [c]\ \{p\}$ due to reciprocity, the matrix $[c]$ is symmetric, i.e. $\Delta c_{pm} = \Delta c_{mp}$

The transfer matrix of the crack segment, $[T_c]$ is related to the matrix $[c]$ as

$$[T_c] = \begin{bmatrix} [I] & [c] \\ [0] & [I] \end{bmatrix} \tag{8}$$

where [I] is (3×3) identity matrix, [0] is (3×3) null matrix, and $[c]$ is (3×3) local flexibility matrix.

Using the transfer matrix theory, the cracked-element transfer matrix $[T_{ce}]$ is given by

$$[T_{ce}] = [T_L][T_c][T_R] \tag{9}$$

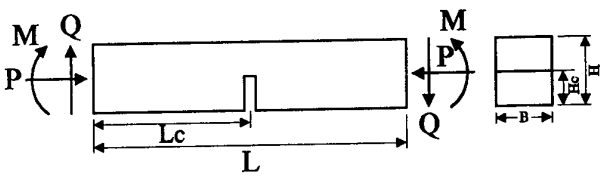

Geometry and loading of an element

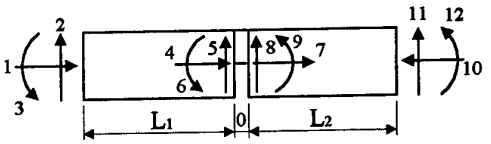

Cracked beam element model

Fig. 1. Geometry and loading of a rectangular cross-sectional element and cracked element model.

where $[T_L]$ and $[T_R]$ are the transfer matrix of the left and right segments, respectively. Various terms of $[T_L]$ and $[T_R]$ are given in computer program. This procedure is useful since small flexibility terms for small cracks do not affect the transfer matrix $[T_{ce}]$ if sufficient length of left and right segments are maintained. Moreover, for a crack very close to a node [14], we have the equation

$$k_{IP} Y \sigma \sqrt{a+r_p/2}$$

The crack element stiffness matrix $[k_c]$ of order (6×6) can be determined by partitioning the transfer matrix $[T_{ce}]$ into four 3×3 submatrices, and the matrix $[k_c]$ is given by

$$[k_c] = \begin{bmatrix} T_{12}^{-1} & T_{11} & & & T_{12}^{-1} \\ T_{21} & -T_{22} & T_{12}^{-1} & T_{22} & T_{12}^{-1} \end{bmatrix} \tag{10}$$

Various elements of the matrix $[k_c]$ are defined by computer program. This analysis is valid for open single-edge crack problems. The computer program BEAM2.BAS has developed to determine the stiffness matrix of the cracked-beam, including;

1. Stiffness matrix of beam without crack
2. Stiffness matrix of cracked beam (single-edge crack).

By using the program, the natural frequencies can be determined including computation of the

1. Mass matrix...
2. Eigen solution problem for various B.C.

Here the elements of stiffness matrix is given by

$$[k] = \frac{D_{ij}}{L^3} \times$$

$$\begin{bmatrix} \frac{AL^2}{I} & & & & & \text{Sym.} \\ 0 & 12 & & & & \\ 0 & 6L & 4L^2 & & & \\ \frac{-AL^2}{I} & 0 & 0 & \frac{AL^2}{I} & & \\ 0 & -12 & -6L & 0 & 12 & \\ 0 & 6L & 2L^2 & 0 & -6L & 4L^2 \end{bmatrix} \quad (11)$$

where A, L, I: cross section area, length and moment of inertia of the beam, respectively, for composite beam the equivalent bending stiffness matrix, D_{ij}[15] can be recast in the form

$$D_{ij} = D_{11} - \frac{D_{12}^2}{D_{22}} + \frac{[D_{12}D_{26} - D_{16}D_{22}]}{D_{22}[D_{26}^2 - D_{22}D_{66}]} \quad (12)$$

The elements of Inertia matrix of beam is given by

$$[M] = \frac{\rho AL}{420} \times$$

$$\begin{bmatrix} 140 & & & & & \text{Sym.} \\ 0 & 156 & & & & \\ 0 & 22L & 4L^2 & & & \\ 70 & 0 & 0 & 140 & & \\ 0 & 54 & 13L & 0 & 156 & \\ 0 & -13L & -13L & 0 & -22L & 4L^2 \end{bmatrix}$$

where ρ: density of composite beam material

Numerical calculations

A BEAM2.BAS computer program was developed to carry out the numerical results, which program has been employed to give stiffens matrix of beam element of single-edge cracked, and the inertia matrix of beam elements, finally calculation eigen freqencies for different boundary fixations, and various state of crack.

EXPERIMENTAL WORK

The test specimens are selected in the form of laminated beam dimensions 300×20 mm and thickness 5 mm. Six types of specimens with various Code number are constructed and manufactured using the hand layout technique with respect to the fiber direction. The mechan-

Table 1. Specifications of fiber and matrix used in the present study

Property type	Density (g/cm^3)	Tensile strength (MPa)	Elastic modulus (GPa)	Poission's ratio
E-Glass	2.5	3448	72	0.22
Polyester	1.2	34.5–103.5	3.95	0.3

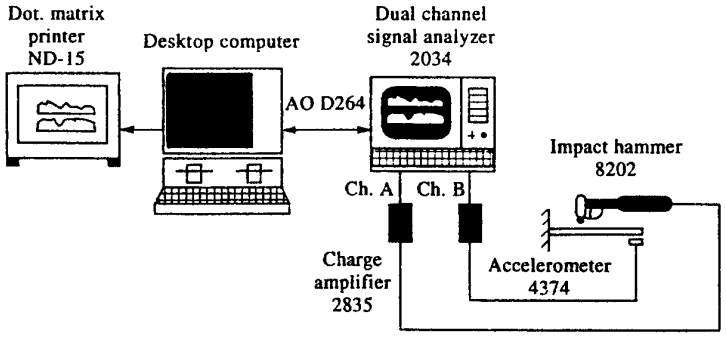

Fig. 2. Instrumentation set-up formed from excitation and measuring systems.

ical properties of fiber and polyester are listed in Table 1. The fiber volume fraction is 0.50%. The code numbers of five plies are $[0]_5$, [15/0/0/0/15] [45/0/0/0/45], [60/0/0/0/60], [75/0/0/0/75] and [90/0/0/0/90] with 1 mm thickness of each ply.

The experimental apparatus is shown in Fig. 2. The mounting of the specimens was either clamped or simply supported edges in the test rig. The boundary crack was initiated at the side of each specimen, with a saw cut and propagated successively for each state of crack. The depth and location of crack were checked directly by measurement at each test.

The excitation and measuring procedure including calibration, transducers using the dual channel signal analyzer [2034] in conjuction with the fast fourier transform (FFT), gives the mathematical connection between time and frequency, showing that the frequency response spectra (FRS) are similar to those illustrated in Ref [16]. The eigen frequencies and damping parameters measured for the first five natural frequencies and associated five damping parameters are carried out for each specimen in the uncracked reference state and the nine states of cracks. The three depth ratios and three location ratios for a single edge of the specimen are ($Hc/H = 0.10, 0.25, 0.35$) and $Lc/L = 0.15, 0.25, 0.35$), respectively. The experimental results are taken as an average of five measurements of each. The experimental measurements of the natural frequencies and damping parameters against the different states of crack for the three types of boundary conditions are listed in Table 3. The damping factor ξ of a particular resonance can be calculated from the width of the resonance peak in the magnitude of the (FRF) [17] and the form

$$\xi = \frac{1}{2Q}, \quad Q = w/wd$$

Hence the resonant frequency (wd) and the width (w) can be found from the magnitude diagrams using the reference cursor. The values

Table 2. Values of the first five frequencies in Hz for reference state of different lamina orientation and boundary conditions (finite element and experimental results)

Type of fixation	*c–F*		*s–s*		*c–c*	
Laminate	F. E	EX	F. E	EX	F. E	EX
[0]5	42.7	44	81.6	86	217.6	220
	163.6	167	259.2	265	381.8	384
	546.8	549	577.8	582	795	796
	1163.1	1169	1211	1215	1414	1416
	2211.6	2215	2418.8	2420	2688	2690
15/0/0/0/15	31.6	34	69.1	72	193.4	196
	127.3	131	233.2	235	312	315
	443.04	447	546.3	548	651	653
	1069.2	1075	1168	1172	1318	1320
	2114	2120	2377	2380	2333	2336
45/0/0/0/45	23.4	25	55.2	58	154.1	157
	109.8	115	181	184	245.1	249
	368.2	373	510	512	543.3	547
	824	829	1144	1148	1214.7	1218
	1509	1512	2125	2127	2338.1	2341
60/0/0/0/60	19.18	21	41.2	44	133.8	136
	92.4	96	159.9	162	221.1	224
	257.2	262	482.2	486	532.8	536
	644	649	1110.9	1116	1191.7	1194
	1468	1471	2105.8	2108	2309.3	2312
75101010/75	17.2	20	36.4	38	113	116
	91.3	94	144.9	148	208.1	212
	255.1	258	453.1	4 56	516.6	518
	641	645	1092.5	1096	1161.1	1164
	1459	1465	2098	2100	2292.9	2295
90/0/0/0/90	16.2	19	33.8	36	110.1	112
	92.1	94	139.2	142	205.5	208
	253	257	445.1	448	511.7	315
	641	645	1085.2	1088	1153.2	1156
	1456	1460	2086	2090	2288	2289

of the damping factor ξ was plotted against various states of crack as shown in Figs 5 and 6.

RESULTS AND DISCUSSION

In the tested specimens, the first five resonant frequencies of laminated composite beams for three fixations c–F, s–s and c–c are measured and computed numerically using a finite element technique for the six types of code numbers as shown in Table 2.

Experimental studies in the area of the eigennature of cracked composite beams are carried out by the measurement of five natural frequencies and the associated damping factors. Experimental results are obtained for the length ratio in the three states of crack location as $Lc/L = 0.15$, 0.25 and 0.35. The crack was initiated for each beam with a fine saw cut in the three states of crack-depth ratio ($Hc/H = 0.10$, 0.25 and 0.35). At each step the depth of crack is checked directly by measurement. It can be observed that the natural frequencies decrease

Table 3. Values of the fundamental frequency in Hz and damping factor $\xi \times 10^{-3}$ for different state of location and depth of cracks with different lamina orientation and boundary conditions (Experimental results)

Laminate	State of crack	[0]5	15/0/0/0/15	45/0/0/0/45	60/0/0/0/60	75/0/0/0/75	90/0/0/0/90
Boundary condition	*Lc/LHc/H*	15% 25% 35%	15% 25% 35%	15% 25% 35%	15% 25% 35%	15% 25% 35%	15% 25% 35%
	10%	Freq. 42 38 36	32 31 29	23 21 18	19 17 16	18 16 14	17 15 13
		Damp. Fac. 72 75 76	95 102 106	120 125 133	126 130 137	142 148 153	168 172 176
C–F	25%	Freq. 40 35 33	30 28 27	20 19 16	18 16 14	17 15 13	15 14 12
		Damp. Fac. 74 76 78	105 110 115	124 127 135	132 135 143	146 152 157	174 179 185
	35%	Freq. 37 33 31	29 26 24	18 17 13	15 13 12	15 13 11	12 11 10
		Damp. Fac. 77 79 80	109 114 120	129 131 139	138 140 147	149 154 160	180 186 192
	10%	Freq. 85 82 79	70 68 67	56 54 53	41 39 37	35 33 31	34 32 30
		Damp. Fac. 35 37 39	55 60 66	75 78 83	95 97 102	115 119 122	135 139 145
S–S	25%	Freq. 83 78 76	67 65 63	53 51 48	38 37 35	32 30 29	33 31 29
		Damp. Fac. 40 39 40	63 65 70	77 80 85	99 105 109	118 123 126	139 144 149
	35%	Freq. 80 75 72	64 62 61	49 47 46	36 34 32	28 27 26	30 28 27
		Damp. Fac. 40 42 43	71 74 78	81 84 89	104 109 115	121 126 130	144 148 155
	10%	Freq. 219 217 215	193 192 190	154 152 151	133 130 128	113 111 109	110 108 105
		Damp. Fac. 15 16 17	32 36 40	55 57 59	75 78 81	95 98 102	115 119 122
C–C	25%	Freq. 217 215 213	191 189 187	151 149 148	131 129 126	110 108 107	108 106 103
		Damp. Fac. 18 19 21	34 39 43	58 62 65	79 83 86	99 103 106	118 122 127
	35%	Freq. 216 214 211	190 188 185	147 146 144	129 127 124	109 107 105	105 102 101
		Damp. Fac. 20 22 23	37 41 46	60 64 68	84 89 92	104 106 108	123 126 129

monotonically as the current cross-distance of the crack decreases monotonically close to anti-nodes of the vibrating beam modes, and the depth of crack increases as shown in Table 3 and Figs 3 and 4.

The rates of change of the eigen frequencies via different fixations are relatively high compared with the rate of change due to the use of the various code numbers of fiber orientations as shown in Figs 3 and 4. In contrast to the feature of frequencies, the damping factors increase monotonically as the current depth of the crack increases and the current cross-distance decreases quasi-linearly can be observed in Figs 5 and 6.

In view of the stacking sequences, it is noticed that the orientations of $[0]_5$ layers is relatively high in natural frequencies compared

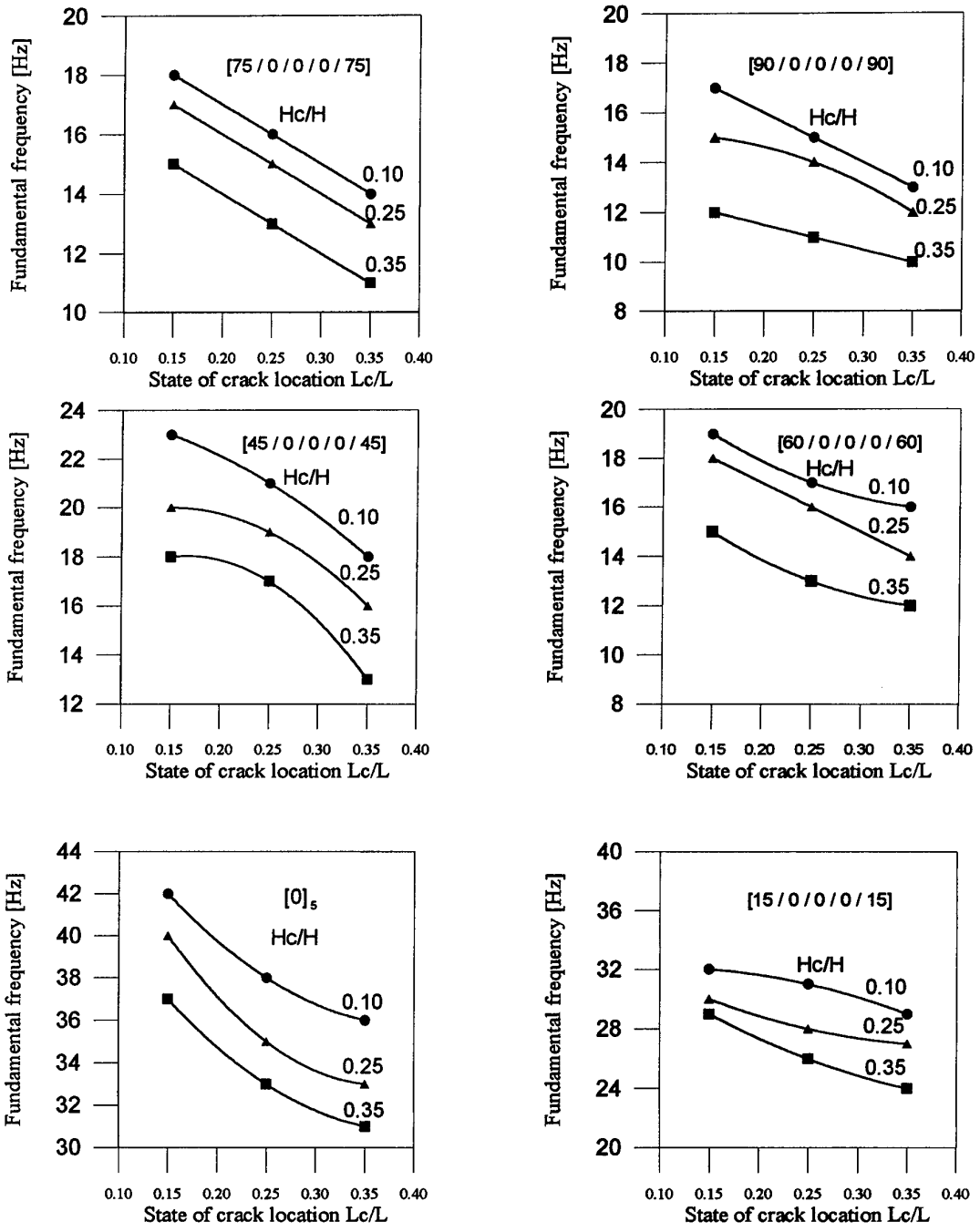

Fig. 3. Variations of the fundamental frequency and different location of the crack with various lamina orientation and depth of crack (*c–F*).

with the others. This is due to the maximum values of the flexural elastic modules and stiffness at this orientation.

With regard to changing the fiber direction of the outer most layers, this causes sharp changes in the values of the flexural elastic modulus, hence the frequency has a considerable effect and, by increasing the fiber orientation angle, the natural frequencies decrease as shown in Tables 2 and 3. These variations depend mainly on the magnitudes of the acute angles between the lamina orientations and the direction of the crack propogation. This means that the life span, in a typical crack, may be increased by increasing the acute angles. These results can be easily investigated by Comparing the meas-

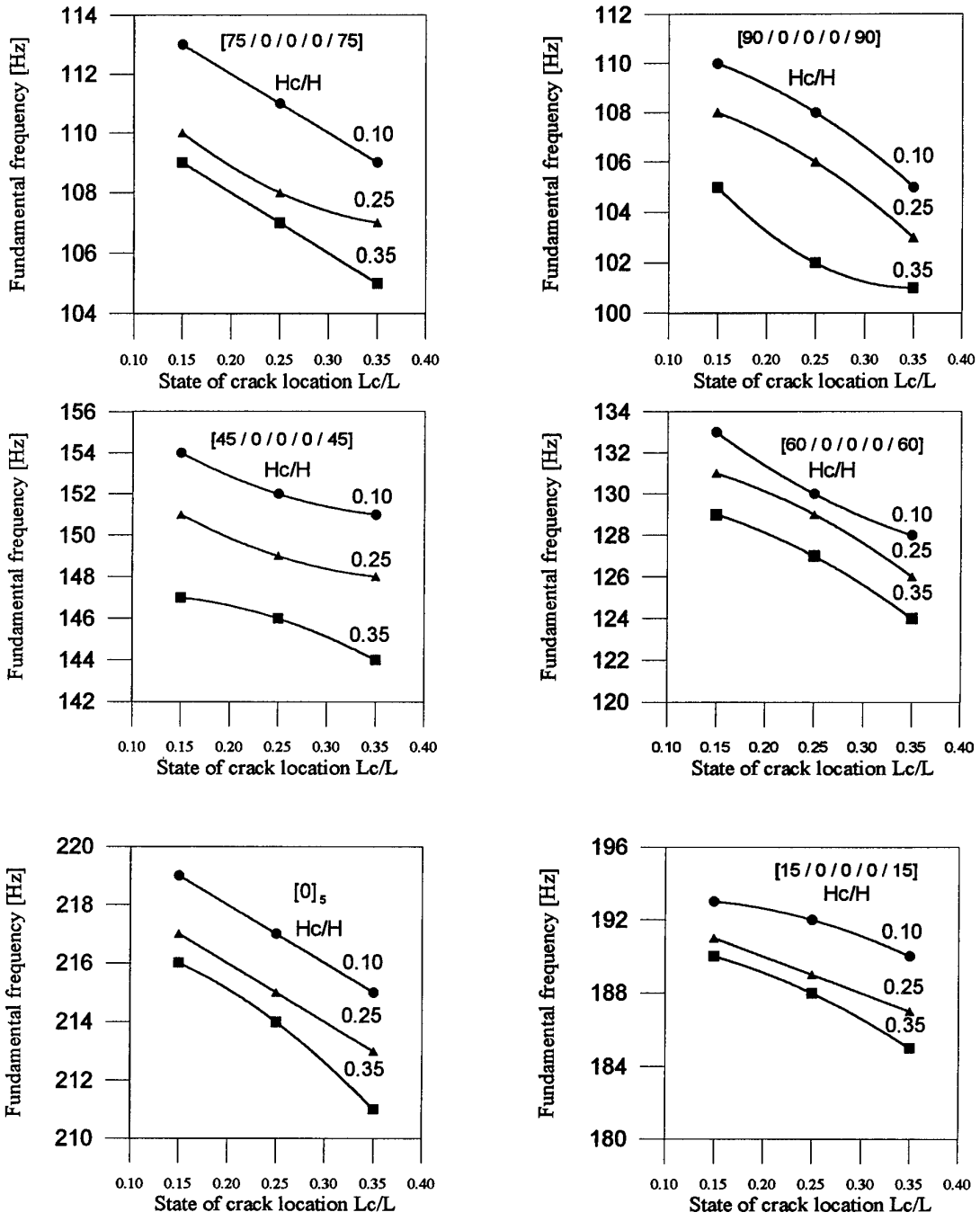

Fig. 4. Variations of the fundamental frequency and different locations of the crack with various lamina orientations and depth of crack (c–c).

urements of the laminate [15/0/0/0/15] to [90/0/0/0/90].

In view of crack location, it is observed that the damping capacity is higher and natural frequencies are lower at a crack location of 0.35 and a crack depth of 0.35, respectively. This comparison indicates that the effect of crack location may dominate the effect of the depth of the crack. In view of the state of fixation, it is observed that effect of the degree of constraints is dominant on the values of natural frequencies and damping factors, compared with the variation of the crack state (location, depth). The highest natural frequency and lowest damping factors occur at the state $Lc/L = 0.15$, $Hc/H = 0.10$ for clamped–clamped and the

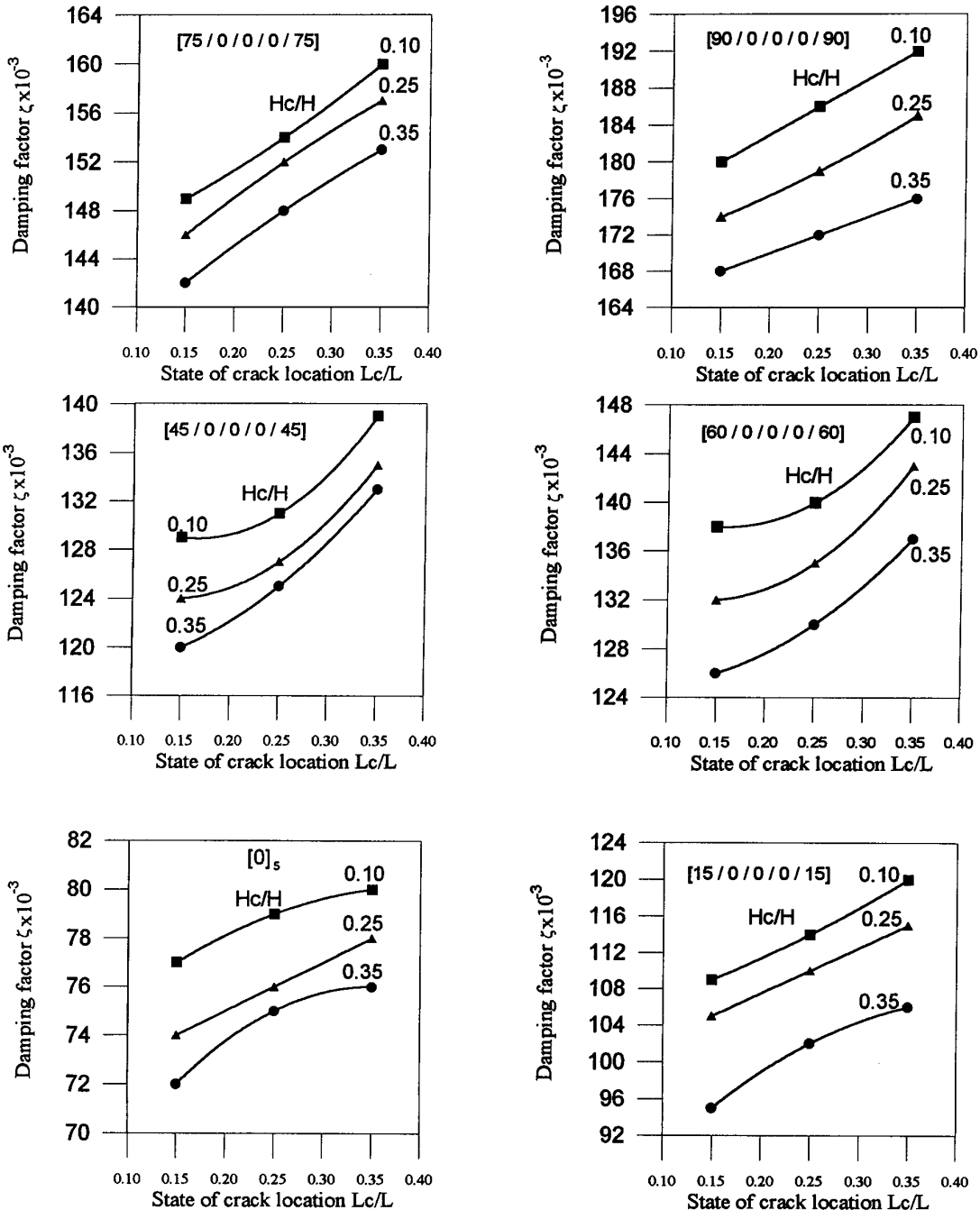

Fig. 5. Variations of the First damping factor $\xi \times 10^{-3}$ and different locations of the crack with various lamina orientations and depths of crack (*c–F*).

inverse occurs at the same state for clamped–free as shown in Table 3. It is noticed that the damping capacity depends to a certain extent on the mutual influence of the lamina code number and the type of fixation.

It can be noticed that the damping feature of specimen $[0]_5$ for clamped–clamped is a light damping compared with the moderate damping of specimen [90/0/0/0/90] for clamped–free as shown in Figs 5 and 6.

Conclusions

In the present work, an investigation into the eigen-nature of a cracked composite beam for various cases of the state of crack are investi-

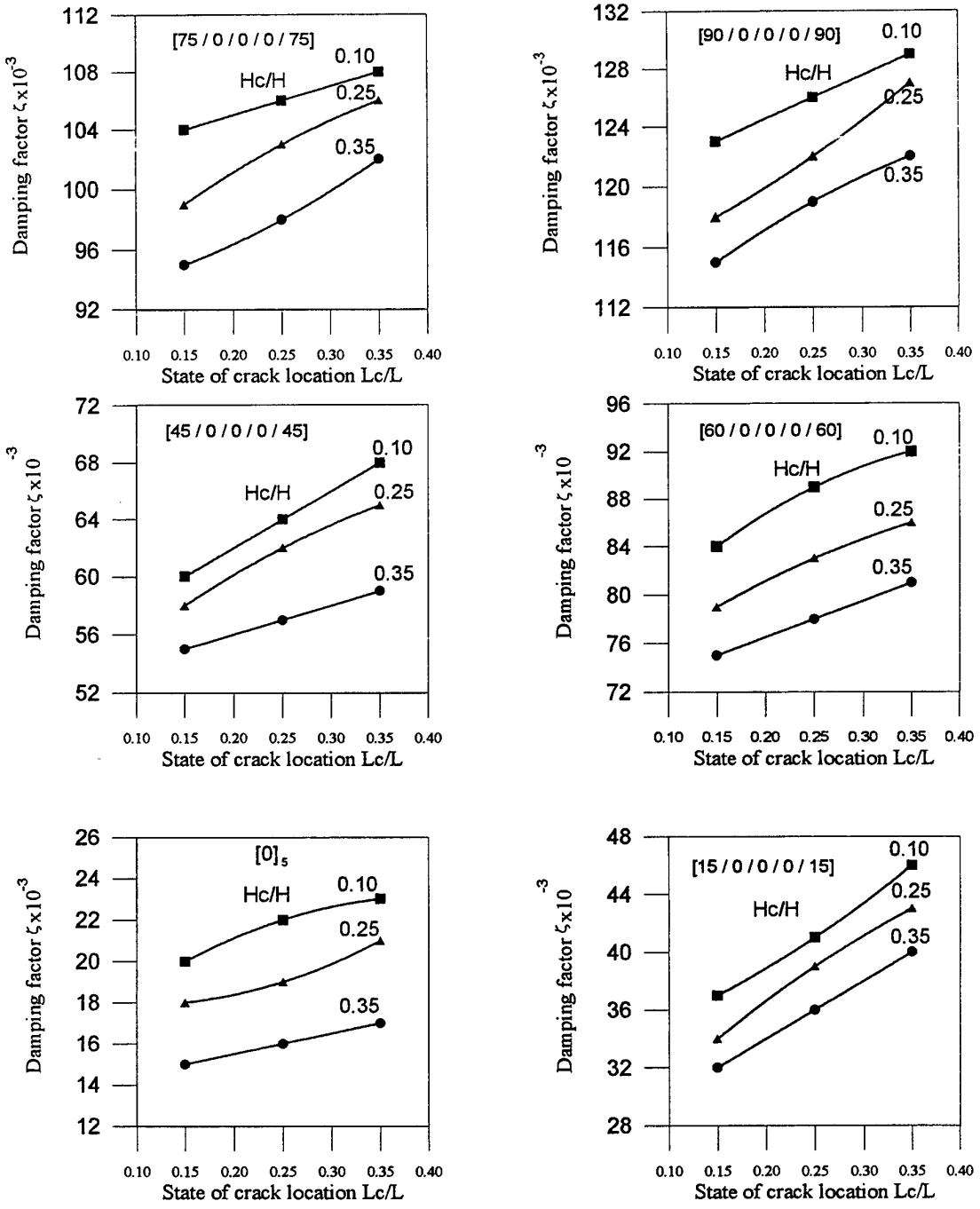

Fig. 6. Variations of the First damping factor $\xi \times 10^{-3}$ and different locations of the crack with various lamina orientations and depths of crack (c–c).

gated numerically and experimentally. A finite element model has been developed to formulate the stiffness matrices for cracked beam elements using a transfer matrix theory. The model is based on an elastic–plastic fracture mechanics technique considering the crack tip plasticity. The experimental measurements and computed values of natural frequencies are compared. The comparison indicates good agreement for various lamina orientations and fixations. The following conclusion can be drawn:

1. A finite element model based on elastic–plastic fracture mechanics technique considering the crack tip plasticity is a good key for formulating and estimating the state of the crack in composite beams.
2. The damping capacity of cracked composite beams increases quasi-linearly with increasing crack depth due to the dissipation of energy.
3. With the proper choice of lamina stacking sequence the maximum values of flexural elastic modulus and stiffness can be achieved. Hence the life time of a typical composite beam with a relatively small crack can be increased.
4. The crack location has a considerable effect on the stiffness and damping capacity of a composite beam. The perturbations of the eigen-nature are governed by the intensity of the crack and its location in the structure.
5. In contrast to the crack propagation in bulk material, the measurements of cracked composite specimens fabricated here indicated that fiber-glass prevents crack growth and is capable of increaseing the laminated composite structure strength to prevent the crack propagating to another lamina.
6. The present study provides an efficient non-destructive technique for the detection and prediction of the current state of the crack for any composite structure system.

REFERENCES

1. Erdogan, F., The crack problem for bonded non-homogeneous materials under antiplane shear loading. *J. Appl. Mech.*, 1985, **52**, 823–828.
2. Sekhar, A.S. and Prabhu, B.S., Crack detection and vibration characteristics of cracked shafts. *J. Sound Vibration*, 1992, **157**(2), 375–381.
3. Ibrahim, F.K., An elastoplastic cracked beam finite element for structural analysis. *J. Comput. and Struct.*, 1993, **49**(6), 81–988.
4. Shen, L.Y., Vibration of elastic structures with cracks. *J. Appl. Mech.*, 1993, **60**, 415–421.
5. Yokoyama, T. and Chen, M. C., An analytical technique for vibration analysis of edge cracked beams using a line-spring model. *Proc. of the 9th IFTOMN Conf.*, Milano, Italy, 1995, pp. 1522–1526.
6. El-Sayed, M. M. Stress intensity factors for edge-cracked bars in tension. *Proc. of the 7th AMME Conf.*, Egypt 28–30 May, 1996.
7. Aronsson, C.G. and Backlund, J., Tensile fracture of laminates with cracks. *J. Composite Mater.*, 1986, **20**, 287–306.
8. Ostachowicz, W.M. and Krawczuk, M., Vibration analysis of a cracked beam. *J. Comput. and Struct.*, 1990, **36**, (2), 245–250.
9. Khashaha, U. A., Notched and pin bearing strength of GFRP composite laminates. *Sixth Cario University International MDP Conf.*, Cairo, January, 1996, pp. 301–311.
10. Valliappan, S. and Wohua, Z., Analysis of structural components based on damage mechanics comcept. *Sixth Cairo University International, MDP Conf.*, 1996, pp. 265–279.
11. Krawczuk, M., A rectangular plate finite element with an open crack. *J. Comput. and Struct.*, 1993, **46**, (3), 487–493.
12. Irwin, G. and Tada, H., The Stress Analysis of Cracks Handbook, Hellertown, Pennsylvaina: Del Research Corporation, 1973.
13. Jones, R. M., *Mechanics of Composite Materials* Scripta Biik Co., Washington, 1975.
14. Gounaris, G. and Diamarogonas, A., A finite element of cracked prismatic, atic beam for structural analysis. *J. Comput. and Struct.*, 1988, **28**, 309–313.
15. Bangera, K., M and Chandrashekara, Vibration of symmetrically laminated clamped-free beam with a mass at the free end. *J. Sound and Vibration*, 1993, **160**, (1), 93–101.
16. Hamada, A., Vibration and damping analysis of beams with composite coats. *J. Composite Struct.*, 1995, **32**, 33–38.
17. Goldman, S., Vibration Spectrum Analysis: A practical Approach, Industrial Press, New York, 1991.

ELSEVIER

Composite Structures Vol. 38, No. 1–4, pp. 57–64
© 1997 Elsevier Science Ltd. All rights reserved
Printed in Great Britain
0263-8223/97/$17.00 + 0.00

PII:S0263-8223(97)00041-X

Composite wraps for ageing infrastructure: concrete columns

S. Hanna & R. Jones

Department of Mechanical Engineering, Monash University, Wellington Road, Clayton, Victoria 3168, Australia

The post-war boom years were when much of Australia's current infrastructure was constructed. However, there are now doubts as to the durability and structural integrity of this construction, and composite repairs may well be one method for addressing the problems of an ageing infrastructure. To this end the present paper evaluates the ability of externally bonded composite wraps to increase the load-carrying capacity of concrete columns. Tests are performed under a range of environmental conditions. Both glass and Kevlar wraps are considered. In this study the failure loads were found to be relatively unaffected by the environmental conditions with failure occurring when the wraps reached a critical strain level. © 1997 Elsevier Science Ltd.

INTRODUCTION

Concrete and structural steel are by far the most commonly used construction materials. This popularity is due both to low cost and the appropriate properties and characteristics these materials possess. However, concrete structures located in humid or marine environments, or where chemical attack is possible, often experience what has been termed 'concrete cancer' [1]. The problem starts by penetration of environmental agents (humidity and salts) through the concrete cover leading to the corrosion of reinforcements. This initiates swelling in the concrete and can result in spalling and loss of cover. The steel reinforcement may now be further exposed to the environment thereby accelerating the corrosion process. This corrosion affect is often termed concrete cancer. The remedial treatments employed to overcome this problem are greatly dependent on the extent of damage that has occurred. At an early stage, cathodic protection can provide an adequate means of protection against any further deterioration. When extensive damage has already occurred then (generally) only a few options remain. These options include either the demolition and rebuilding of the structure or adopting a conventional repair procedure. In the latter case an externally bonded repair or patch repair is frequently adopted [2–7]. Although composite materials have always been used in buildings (e.g. the use of straw to form mud bricks, etc.), in the twentieth century the construction industry has been relatively slow in adopting new materials. Concrete, steel and timber dominate the construction scene, and, although there is a large range of materials that offer (potentially) superior properties, there has been little success in using these materials on a large scale. The reason for this can be attributed to many factors, such as lack of hardware, expertise, design codes and cost.

Composite materials have the potential to provide a viable alternative to traditional concrete reinforcing material. Some selected advantages are:

- Resistance to chemical attack and corrosion resistance. In this case composites could provide an excellent alternative to steel reinforcements.
- Higher strength-to-weight ratio. Here lightweight repairs and reinforcing materials could replace heavier ones and the use of lighter materials also has the potential to decrease construction time and result in simpler repairs.

- Composite materials also have the potential to lead to more earthquake-resistant structures. Here composites could be used as an external confining reinforcement to concrete columns.

The beneficial effects of lateral reinforcement on the strength and deformation characteristics have been recognized since the early days of structural concrete. Early investigations showed that the use of circular reinforcing hoops or spirals could result in members twice as strong as similar members with only lateral reinforcement. Heavier spirals are thought to provide a significant safety factor against complete failure. Composites have the potential to be regarded as a substitute for conventional steel spirals. This would transfer the advantages of composites to wrapped members. Wrapping also has the potential to dramatically increase the toughness of concrete columns, and to provide an excellent resistance to harsh environmental conditions.

This paper illustrates the effectiveness of composite repairs via a series of laboratory tests. These tests focus on the ability of external wraps to concrete cylinders to increase the ultimate compression strength. At the same time a finite element analysis of these tests was performed so as to obtain an understanding of the failure mechanism(s).

COMPOSITE WRAPS TO CONCRETE COLUMNS

The vinyl ester resin used was prepared in batches consisting of resin, promoter and accelerator in the appropriate proportions. The mixed resins were consumed within two weeks of mixing. The promoter (cobalt naphthenate 6%) and the accelerator were thoroughly mixed into the resin by manual shaking of the resin container for 2 min. The catalyst, MEK peroxide, was added just prior to curing and mixed manually for 30 s. The concentrations of the catalyst, promoter and accelerator in the resin were 1%, 0.2% and 0.5% by weight, respectively. The GP polyester was prepared by mixing 3% catalyst, MEK peroxide, for 30 s into the resin just prior to use. In each case the fibres used in the repair were submerged in the resin before being wrapped around the cylinders using a simple manual device. The wrapped cylinders were then cured at 60°C for 9 h and subsequently left at room temperature for one week.

The tests were then performed using a 2000 kN compression testing machine under load control, and the deflection was measured using a compressometer fitted with two vertical and three radial dial gauges, each with a tolerance of 0.002 mm. In some samples strain gauges were used to measure strains at the concrete–wrap interface and at the surface of the wraps, in the vertical and the circumferential directions. The test specimens considered were standard test (concrete) cylinders (AS1012.8) with dimensions of 100 mm × 200 mm. The concrete cylinders were classified according to the Table 1 and the properties of fibres used in the composite wraps are given in Table 2. The test configuration was as shown in Fig. 1.

The properties of the vinyl ester resin, used as the matrix material, were $E = 3.25$ GPa, $G = 1.3$ GPa and $\nu = 0.32$. The wraps obtained using impregnated glass fibres had a 40% fibre content while those obtained using impregnated Kevlar fibres had fibre content of 34%. Use of a simple rule-of-mixtures approach yielded the properties for the fibre glass–vinyl ester composite wrap as $E_1 = 30.75$ GPa, $E_2 = 7$ GPa,

Table 1.

Cylinder bearing strength (MPa)	Static chord modulus (GPa)	Poisson's ratio
33	32	0.2
127	44.5	0.28

Table 2.

Fibre type	Fibre longitudinal tensile strength (MPa)	Fibre longitudinal modulus (GPa)	Fibre Poisson's ratio	Specific gravity	Strain to failure %
Kevlar 49	3600	124	0.35	1.45	2.0
E-fibre glass	3400	72	0.2	2.54	1.3 (measured value)

$v_{12} = 0.272$ and $G_{12} = 2.66$ GPa. For the Kevlar–vinyl ester composite wrap we obtained $E_1 = 44.3$ GPa, $E_2 = 6.34$ GPa, $v_{12} = 0.33$ and $G_{12} = 2.4$ GPa. Tests on simple uniaxial fibre glass–vinyl ester composite specimens gave $E_1 = 28.4$ GPa, $v_{12} = 0.33$ and $E_1 = 3.52$ GPa, $v_{12} = 0.435$ for the vinyl ester resin.

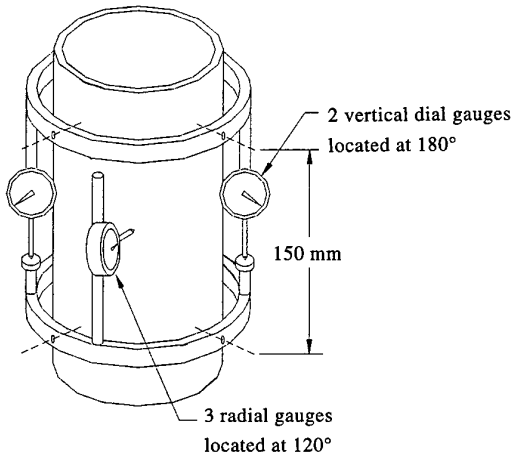

Fig. 1. Compression testing configuration.

Specimens' classification

In this test programme the test specimens were classified as described in Table 3. The specimen code number was designed to facilitate the identification of the samples. The first digit refers to the sequential number among the group of samples, the second digit refers to the weight of the fibres used, the letter F for fibre glass, and the letter K for Kevlar, the third digit represents concrete grade, and the last letter E stands for environmental exposure.

Specimens 1-0-127, 2-0-127, 1-0-33, 2-0-33, 3-0-33 were used as control specimens to obtain the maximum compression strength, (concrete) Young's modulus and Poisson's ratio and to monitor cracking progress and the failure mechanisms for unwrapped cylinders of different strengths. Specimens 1-100K-127 and 2-100K-127 were tested to evaluate the effectiveness of

Table 3. Classification of test specimens

Specimen sequential number	Sample code number	Wrap kind	Total wrap weight (g)	Concrete grade (MPa)	Environment	No. of days of exposure
1	1-0-127	No wraps	n/a	127	n/a	
2	2-0-127	No wraps	n/a	127	n/a	
3	1-300F-127	Fibre glass	300	127	n/a	
4	2-300F-127	Fibre glass	300	127	n/a	
5	1-100K-127	Kevlar	100	127	n/a	
6	2-100K-127	Kevlar	100	127	n/a	
6′ (Failed sample No. 2)	1-300K-127	Kevlar	100	127	n/a	
7	1-0-33	No wraps	n/a	33	n/a	
8	2-0-33	No wraps	n/a	33	n/a	
9	3-0-33	No wraps	n/a	33	n/a	
10	1-0-33E	No wraps	n/a	33	Soaked	45
11	2-0-33E	No wraps	n/a	33	Soaked	45
12	3-0-33E	No wraps	n/a	33	Soaked	45
13	1-200F-33	Fibre glass	200	33	n/a	
14	2-200F-33	Fibre glass	200	33	n/a	
15	3-200F-33	Fibre glass	200	33	n/a	
16	1-200F-33E	Fibre glass	200	33	Soaked	45
17	2-200F-33E	Fibre glass	200	33	Soaked	45
18	3-200F-33E	Fibre glass	200	33	Soaked	45
19	1-300F-33	Fibre glass	300	33	n/a	
20	2-300F-33	Fibre glass	300	33	n/a	
21	3-300F-33	Fibre glass	300	33	n/a	
22	1-300F-33E	Fibre glass	300	33	Soaked	45
23	2-300F-33E	Fibre glass	300	33	Soaked	45
24	3-300F-33E	Fibre glass	300	33	Soaked	45
25	1-100F-33	Fibre glass	100	33	n/a	
26	1-100F-33E	Fibre glass	100	33	Soaked, then wrapped	140
27	1-100F-33	Fibre glass	100	33	n/a	
28	4-200F-33E	Fibre glass	200	33	Soaked	140
29	4-300F-33E	Fibre glass	300	33	Soaked	140
30	4-200F-33	Fibre glass	200	33		
31	4-300F-33	Fibre glass	300	33		

Kevlar fibres in inducing confinement on the concrete cylinders and hence increasing the ultimate compression capacity. Specimen 1-300K-127 was tested to evaluate the effectiveness of Kevlar fibres in restoring strength to previously failed cylinders, i.e. to repair damaged structures. Specimens 1-300F-127 and 2-300F-127 were tested to evaluate fibre glass as a (cheaper) alternative to Kevlar specimens 1-200F-33, 2-200F-33, 3-200F-33, 1-300F-33, 2-300F-33, 3-300F-33 were tested to help determine the stress–strain relationship of wrapped concrete, and to establish the failure criterion of wrapped concrete. Specimen 1-100F-33 was tested to help understand the relationship between wrap thickness and the increase in the ultimate strength.

Specimens 1-0-33E, 2-0-33E, 3-0-33E were tested to determine the affect of the environmental on unwrapped concrete elastic properties and also as control specimens for the low-grade concrete subjected to environmental parameters. Specimens 1-200F-33E, 2-200F-33E, 3-200F-33E,1-300F-33E, 2-300F-33E, 3-300F-33E were tested to determine the degradation affect of environmental conditions on fibre-glass-wrapped cylinders. Specimens 4-200F-33E, 4-300F-33E were tested to determine the affect of environmental conditions, extended for a long duration, on the performance of fibre glass wraps. Specimens 1-100F-33E, 1-100F-33 were tested to evaluate the affect of different loading rates on the behaviour of wrapped concrete, particularly in the post-yield zone.

As part of the environmental test programme specimens were immersed in seawater with a salt content of 3.5% by weight and a pH value of 8.2–8.4. The specimens were also subjected to a circulating air current and fluctuating temperatures (20–43°C).

TEST RESULTS

The behaviour of wrapped cylinders under concentric loading up to failure could generally be divided into three regions: pre-yield zone, yield zone, and post-yield and failure zones (see Fig. 2). The behaviour of the test specimens in these three regions could be described as follows.

Region I. In this stage damage formation is believed to have started. Its existence appears

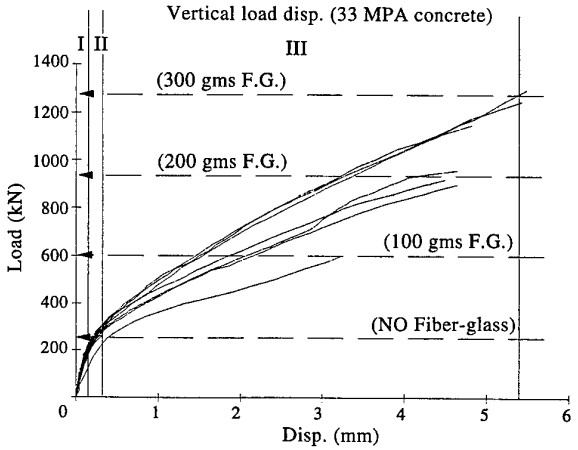

Fig. 2. Load versus displacement test results.

to have only a limited affect on the elastic properties. At this stage the behaviour of wrapped and unwrapped concrete specimens was almost identical.

Region II. In this region the load–deflection response was non-linear and as such was indicative of the onset of inelastic behaviour. It is believed that in this region microdamage may be joining thereby reducing the apparent stiffness of the concrete. In this region the load–deflection curve resembles that of the 'knee' in the stress–strain curve for metals. As such an apparent 'yield stress' can be defined, this yield stress roughly corresponds to the failure stress for the unwrapped concrete. At the end of this stage the similarity in the behaviour of unwrapped and wrapped concrete had ceased, and the concrete started transferring stresses to wraps, thereby allowing strain energy to be stored in wraps.

Region III. The inelastic behaviour (damage), which had previously been observed, continued and the slope of the load–deflection curve again became linear. The linearity in this region may also reflect the linear elastic behaviour of the wrapping materials. The ultimate strength of the concrete–wrap composite section was reached when the wraps reached a certain critical radial strain leading to failure of the wraps.

In Fig. 2 it can be noticed that a higher degree of confinement resulted in a higher post-yield slope. This was believed to be due to the fact that a more confined section produced a higher resistance to the vertical and radial deformations, which in turn increased the post-yield stiffness of wrapped concrete. It can be also noticed that the increase in the ultimate

strength was directly related to the stiffness of the wraps. Increasing the mass of the wraps from 200 to 300 g, which corresponded to a 33% increase in the thickness of the wrap, lead to a ≈33% increase in the ultimate load (see Fig. 2). This supports the hypothesis that the increase in the ultimate strength reflects the capacity of the wraps to both constrain the concrete and to store strain energy.

Modes of failure

Unwrapped cylinders. The loading and geometry of the test specimens were typical of a short column, with the main load being axial and with negligible eccentricities and bending moment affects. In general, high-strength concrete specimens had two modes of failure: shear failure with an inclination of about 25° to the vertical axis; and radial splitting failure; most evident in top and bottom faces (see Fig. 3). The loading was accompanied with cracking sounds which started at about 40% of ultimate load. The lower strength cylinders maintained a random cracking pattern with extensive splitting and with shear cracks being evident in the mid-section.

Fig. 3. A typical shear failure mode.

Wrapped high-strength concrete. High-strength concrete when wrapped with fibre glass or Kevlar fibres suffered shear failure. The higher stiffness of the concrete prohibited gradual fracture and tensile splitting associated with lower strength concrete. The fracture plane had an acute angle to the vertical with the crack front reaching both the top and bottom surfaces. Due to this failure mechanism, the concrete was unable to develop enough radial displacements to fully utilize the maximum potential of the wraps. At failure, the wraps remained essentially intact.

Failed then wrapped high-strength concrete. High-strength concrete cylinders which had been previously loaded to failure, and failed by tensile splitting, were repaired by wrapping with Kevlar fibres and retested. These specimens had a lower stress–strain slope reflecting the damaged state of the concrete. When retested the wraps prohibited further tensile splitting of the concrete and failure was due to shear failure extending from the top to the bottom concrete faces.

After failure, the differential surface movements could be seen from both top and bottom surfaces. The failure was accompanied with explosive sounds. The failed concrete was then sliced to obtain a clear view of the cracking pattern and to verify the failure mechanism. In general a single shear crack was clearly obvious in every section and created an acute angle with the vertical of about 26°.

Wrapped low-strength concrete. The low-strength concrete gave early signs inelastic behaviour. This lead to the gradual damage of the concrete as opposed to the sudden and brittle failure of high-strength concrete. The gradual and continuous fracture of the concrete allowed the concrete to achieve a substantial radial expansion and therefore transfer the stresses radially, possibly in a hydrostatic manner to wraps. The failure was ultimately governed by the ability of wraps to carry the radial stresses and achieve ultimate strain. Failure of the fibres lead to release of the radial (confining) stresses in this particular area leading to extensive splitting failure in concrete in this region.

Failed then wrapped low-strength concrete. The behaviour was essentially identical to the

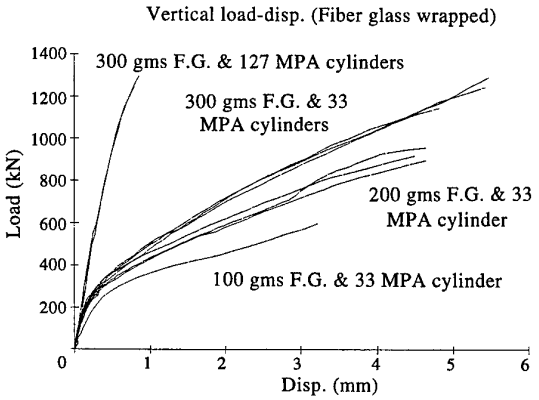

Fig. 4. Load–displacement curves for fibre glass wrap.

wrapped virgin (undamaged) concrete specimens.

The wraps did not markedly alter the vertical rigidity of the structure. However, through the use of external wrapping of 100 g of Kevlar fibres, impregnated in vinylester, the ultimate load was increased by 40%. Using 300 g of fibre glass yielded a 35% increase in strength for high-strength concrete; however the failure remained sudden and explosive.

When wraps were applied to low-strength concrete an increase in the ultimate strength of up to 600% was achieved (Figs 4 and 5).

The behaviour of wrapped cylinders is analogous to that of spiral reinforced columns. The spirals add little to the columns apparent 'yield point' strength and becomes effective only following the large increases in deformation that occur after the 'yielding' of the column.

In the presence of lateral confinement, the axial compressive loads initiated shear failure, while in its absence axial splitting failure took place for high-strength concrete while splitting

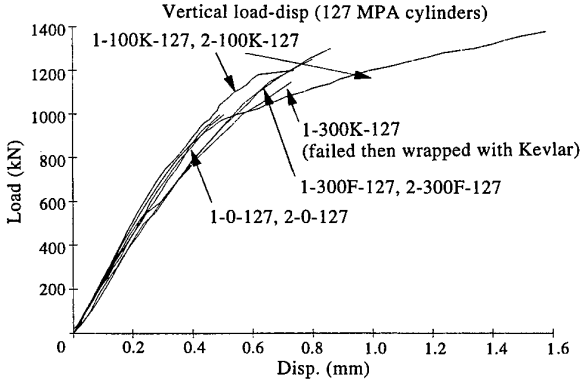

Fig. 5. Vertical displacement versus load curves.

tensile stresses was most common in lower strength concrete.

Failed, then Kevlar-wrapped, high-strength cylinders achieved approximately 125% of the strength of unwrapped cylinders. In the case of low-strength concrete this increase was up to 400%. (In both cases initial failure of concrete had almost no subsequent affect on behaviour, up to failure of the repaired specimens.) This highlights the potential of using wraps to restore strength to existing spalled or cracked columns. Indeed, as a result of this test programme it is believed that using wraps could also give additional toughness to concrete columns, and thereby greatly increase its ultimate strength and strain to failure.

The wrapped low-strength concrete specimens were able to achieve large displacements following the 'yield' point of the concrete. This resulted in a substantial contribution of wraps to load-carrying capacity. In contrast high-strength concrete achieved only limited post-yield displacements with a lower contribution of the wraps. Generally speaking shear failure was dominant in high-strength concrete, which tends to be global with brittle failure of the concrete occurring suddenly with little or no warning. This failure was evident in both wrapped and unwrapped cylinders. Low-strength concrete suffered localized fractures accompanied by radial expansion most evident in mid-section which suffered minimal restraining action due to friction forces at top and bottom platens.

Environmental effects

After 80 days the unwrapped cylinders had absorbed an average of 130 g of water to achieve an 8% moisture content of approximately 8% whilst wrapped cylinders absorbed an average of 115 g of water to achieve a moisture content of approximately 7%. The moisture content then continued to increase at a slower rate achieving a maximum of almost 9% after 120 days for unwrapped concrete. Despite the relatively high moisture content absorbed by cylinders, the test results performed after both 45 days of soaking and after 140 days were almost identical to those of the unsoaked cylinders (see Figs 6 and 7). The combined affect of moisture, salt and cyclic temperature had little (or no) affect on the behaviour of cylinders exposed to these environmental parameters.

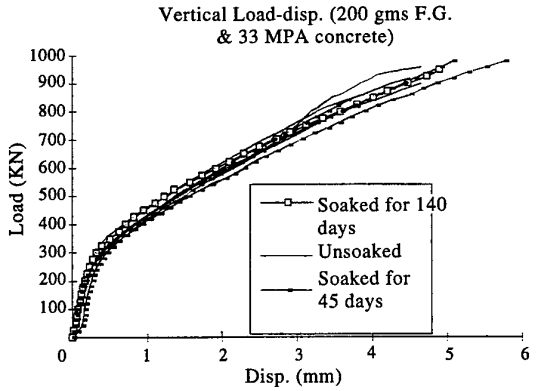

Fig. 6. Effect of environment.

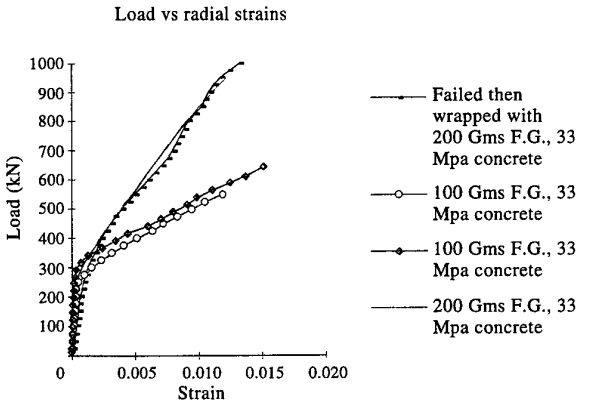

Fig. 8. Maximum radial strains, measured at mid-section, for 200 and 300 g wraps.

It should be noted here that the composite wraps themselves had a very slow rate of moisture absorption with specimens soaked for three months achieving a moisture content of approximately 3.4%. A pure resin samples achieved only 2.7%.

Failure analysis

As can be seen from the experimental test results (Fig. 8), it was found that in each case the wraps failed when a (maximum) radial strain of approximately 0.012 was reached. This was true regardless of the magnitude of vertical displacements, the thickness of the wraps or the level of environmental conditioning. Hence, it appears that failure analysis/prediction can be based on a simple maximum permissible strain criteria. Once the wraps failed the concrete could no longer carry the load and the specimen failed.

ANALYSIS

To aid in understanding of this process a finite element analysis of these tests was conducted with a range of models representing both the unwrapped and the wrapped structures. For simplicity the analysis used the Prandtl–Reuss equations for incremental plasticity. The stress–strain relationship in the concrete was assumed to be bilinear and, based on the previous test results, the yield stress of concrete was taken to be the failure stress of the uncracked concrete. As a first approximation the ratio of the post-yield slope (of the concrete) to its initial elastic modulus was taken to be the ratio of the post yield slope to the initial elastic slope for the 100 g wrap shown in Fig. 2. Due to geometric and loading symmetry, only a quarter of a cylinder was modelled.

The resultant load–deflection curves are given in Fig. 9 and Fig. 10. Here it can be seen that the results were in good agreement with

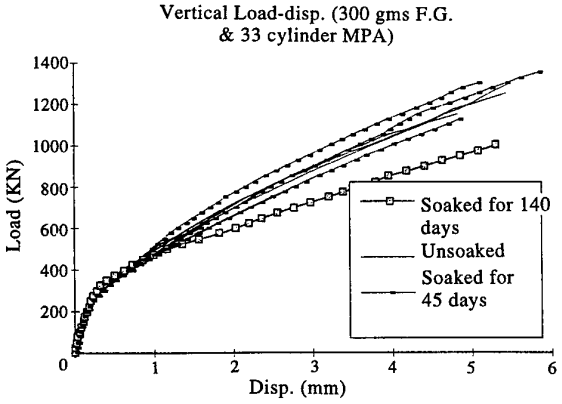

Fig. 7. Comparison of load–displacement results for soaked specimens.

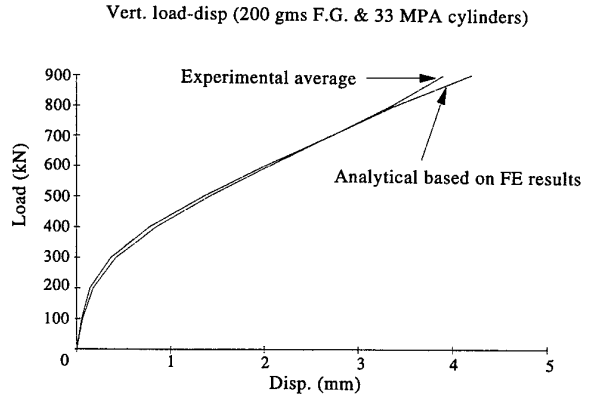

Fig. 9. Predicted vertical displacement versus load curve, 200 g wraps.

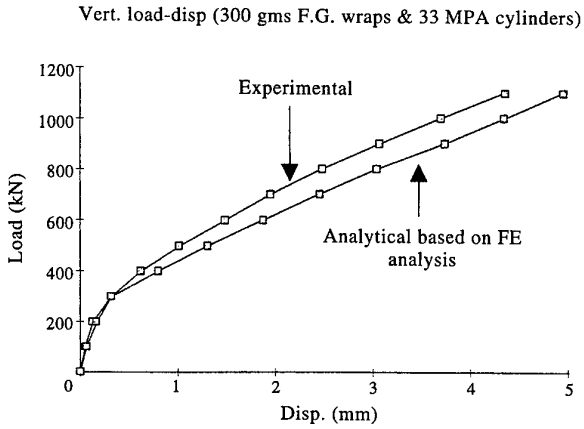

Fig. 10. Predicted vertical displacement versus load curve, 300 g wraps.

the experimental results. This highlights the ability of the finite element method to capture the gross behaviour of wrapped concrete structures. This analysis revealed that the fibres maintained an almost uniform tensile stress across the longitudinal profile. However, the in-plane shear stresses were maximum at the concrete–fibres interface. The maximum principle stresses obtained from the analysis were located at the outer fibres and decreased towards the centre. Kevlar fibres resulted in higher principle and shear stresses than glass fibres because of their higher stiffness.

In the wrapped concrete the principle stresses had higher magnitudes near the top and bottom faces. Unwrapped cylinders had much higher (radially oriented) maximum principle stresses than wrapped cylinders. This may explain the axial splitting of unwrapped concrete specimens.

CONCLUSION

This paper has discussed the potential for composite materials to assist in addressing problems associated with concrete cancer. To this end the present paper has outlined the results of an initial study into the behaviour of wrapped concrete columns. The experimental test programme, undertaken as part of this investigation, revealed that composite wraps were an effective means for increasing the strength of concrete columns.

The increase in strength was due to the confinement induced by the wrap. The failure load was determined by the maximum allowable strains in the wrap. The behaviour of the wrapped columns can be predicted using traditional finite element analysis tools.

While this work has concentrated on the ability of external composite wraps to increase residual strength additional work is required to evaluate the ability of wrapped columns to withstand large overloads without degradation in structural performance.

REFERENCES

1. Normad, R., Review of the performance of concrete coastal structures in the Gulf area. *Proceedings, International Conference on Concrete in the Marine Environment*. Concrete Society, London, 1986, pp. 101–113.
2. Brown, S., Fibre/epoxy composites strengthen bridge columns. *Proceedings of the Materials Engineering Congress (Materials Performance and Prevention of Deficiencies and Failures)*, 1992, pp. 691–694.
3. Meier, U., Deuring, M., Meier, H. and Schwegler, G., CFRP bonded sheets. *Fiber Reinforced Plastic (FRP) Reinforcement for Concrete Structures: Properties and Applications*, Nanni, A. (ed.). Elsevier, Amsterdam, 1993, pp. 423–435.
4. Dolan, C. W., FRP developments in the United States. *Fiber Reinforced Plastic (FRP) Reinforcement for Concrete Structures: Properties and Applications*, Nanni, A. (ed.). Elsevier, Amsterdam, 1993, pp. 129–155.
5. Taerwe, L. R., FRP developments and applications in Europe. *Fiber Reinforced Plastic (FRP) Reinforcement for Concrete Structures: Properties and Applications*, Nanni, A. (ed.). Elsevier, Amsterdam, 1993, pp. 99–113.
6. Larralde, J., Feasibility of FRP molded grating-concrete composites for one-way slab systems. *Proceedings of the Materials Engineering Congress (Materials Performance and Prevention of Deficiencies and Failures)*, 1992, pp. 645–653.
7. Mehta, P. K., *Concrete in the Marine Environment*. Elsevier, Amsterdam, 1991, pp. 17–28.

ELSEVIER

Composite Structures Vol. 38, No. 1–4, pp. 65–70
© 1997 Elsevier Science Ltd. All rights reserved
Printed in Great Britain
0263-8223/97/$17.00 + 0.00

PII:S0263-8223(97)00042-1

First-ply failure strength of laminated composite pressure vessels

T. Y. Kam, Y. W. Liu & F. T. Lee

Department of Mechanical Engineering, National Chiao Tung University, Hsin-Chu 30050, Taiwan, Republic of China

Strengths of laminated composite pressure vessels are studied via both analytical and experimental approaches. Experimental techniques are presented to determine the first-ply failure and burst strengths of laminated composite pressure vessels with different lamination arrangements. Different analytical methods, together with various failure criteria, are used to predict the first-ply failure strengths of the laminated pressure vessels. The accuracy of the theoretical prediction of first-ply failure strength is verified by the test data. The suitability of the failure criteria, as well as the limitations of the analytical methods are discussed. © 1997 Elsevier Science Ltd.

INTRODUCTION

The application of composites in pressure vessels and piping has drawn close attention in recent years [1–5]. Much work has been devoted to the manufacturing and design aspects of laminated composite pressure vessels [6–10]. In general, the design of laminated composite pressure vessels is achieved by the use of the first-ply failure approach, i.e. a suitable failure criterion is adopted to determine the first-ply failure load, and the classical lamination theory for stress analysis. The suitability of the adopted failure criterion and the classical lamination theory in determining the first-ply failure strength of laminated composite pressure vessels, however, has not been studied in detail nor validated by experimental data. For safety reasons, pressure vessels must be designed for high reliability. A meaningful reliability assessment of a laminated composite pressure vessel relies on the accurate prediction of the first-ply failure strength of the vessel. Therefore, more work must be devoted to the failure analysis of laminated composite pressure vessels if reliable as well as economical vessels are desired.

In this paper, first-ply failure of laminated composite pressure vessels is studied via both analytical and experimental approaches. Experiments are performed to determine the strengths of laminated composite pressure vessels with different lamination arrangements. The suitabilities of different failure criteria and analytical methods commonly used in determining first-ply failure strength of laminated composite pressure vessels are studied via the test data.

FIRST-PLY FAILURE ANALYSIS OF PRESSURE VESSELS

The pressure vessel is modeled as a symmetrically laminated cylindrical shell of thickness h, length L and radius R, where R refers to the radius of the middle surface. The shell is constructed of an even number of orthotropic layers of equal thickness, t. The fiber orientation θ is defined as the angle between the fiber direction and the longitudinal axis x. The stress resultants in the geometric coordinate axes are given by [11]

$$\underline{N} = \underline{A}\underline{\varepsilon} \tag{1}$$

where $\underline{N}$ is the vector of stress resultants, $\underline{A}$ is the matrix of extensional stiffnesses, $\underline{\varepsilon}$ is the vector of strains. The stress–strain relations for the kth orthotropic layer are given by

$$\underline{\sigma}^{(k)} = \underline{\bar{Q}}^{(k)}\underline{\varepsilon} \tag{2}$$

where $\underline{\sigma}^{(k)}$ is the vector of stresses for the kth ply, $\bar{Q}$ is the matrix of the transformed material stiffness constants. According to the principle of the strength of materials, the stress resultants of the pressure vessel subjected to internal pressure p are given by

$$N_x = \frac{pR}{2}, N_\phi = pR, N_{x\phi} = 0 \tag{3}$$

where N_x, N_ϕ are stress resultants in the axial and circumferential directions, respectively; $N_{x\phi}$ is the shear stress resultant which is zero due to the symmetry of the lamination. The first-ply failure analysis of the laminated composite pressure vessel is performed via the use of a suitable failure criterion. Herein, a number of phenomenological failure criteria are adopted in the analysis. For comparison purpose, the laminated composite pressure vessel is also analyzed using the finite element method which is formulated on the basis of the first-order shear deformation theory [12].

EXPERIMENTAL INVESTIGATION

A number of laminated composite cylindrical pressure vessels made of graphite/epoxy prepreg tapes were subjected to burst strength test. The properties of the composite material determined from experiment are listed in Table 1. The lamination arrangements and the dimensional properties of the pressure vessels are tabulated in Table 2. The experimental apparatus consists of a test rig for supporting the pressure vessel, an acoustic emission (AE) system (AMS3) with two AE sensors for detecting sound waves emitted from the pressure vessel during failure process, a data acquisition system, a digital pressure meter used for measuring oil pressure in the vessel, and two strain gauges attached to the surface of the vessel. A schematic description of the experimental setup is shown in Fig. 1. During testing, oil was pumped into the pressure vessel at low speed and the pressures at which first-ply and ultimate failures of the pressure vessel occurred were recorded. The first-ply failure pressure of

Table 1. Properties of graphite/epoxy laminate

Material constant	Value	Strength parameter	Value
E_1	88.53 GPa	X_T	1560 MPa
E_2	6.72 GPa	X_c	1760 MPa
G_{12}	4.03 GPa	Y_T	35.75 MPa
G_{23}	1.022 GPa	Y_c	178 MPa
ν_{12}	0.28	S	61 72 MPa
		R	46.21 MPa
		$X_{\epsilon T}$	1.174×10^{-2}
		$Y_{\epsilon T}$	0.35×10^{-2}

Table 2. Properties of pressure vessels

Lamination arrangement	Dimensions
$[54°/-54°]_s$	Outer radius $r_0 = 4$ cm
$[45°/-45°]_s$	Length $L = 23$ cm
$[90/0°]_s$	lamina thickness $t = 0.15$ mm
$[54°/-54°/54°]_s$	
$90°/0°/90°]_s$	
$[90°/0°/90°/0°]_s$	

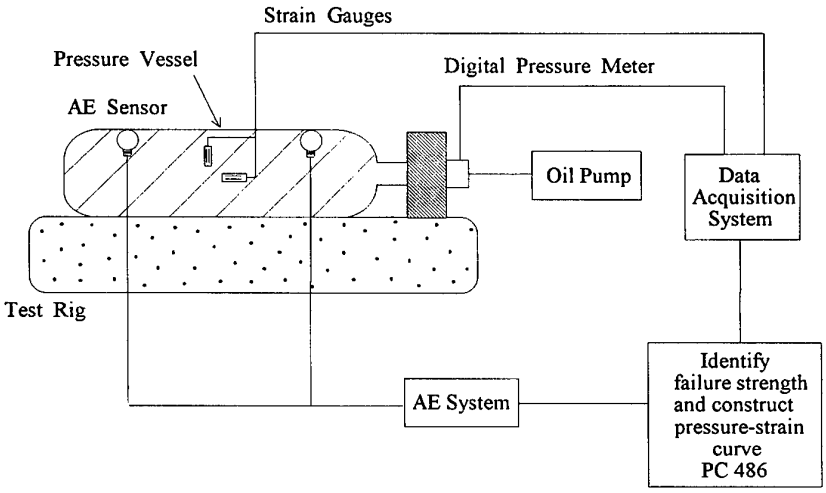

Fig. 1. A schematic description of the experimental setup.

the vessel was determined by identifying the first major energy rise in the energy–pressure diagram produced by the AE system. Figure 2, for instance, shows the energy–pressure relation of the $[54°/-54°/54°]_s$ pressure vessel generated by the AMS3 system. The ultimate burst strength of the vessel was identified from the measured pressure history. Deformation of the vessel was monitored via the strain gauges and the data acquisition system.

RESULTS AND DISCUSSION

Six laminated composite pressure vessels with different layups and various number of plies were tested to failure. The laminated composite pressure vessels subjected to burst test are also analyzed using the aforementioned analytical methods on the basis of different phenomenological failure criteria. The theoretical and experimental results are listed in Tables 3–8 for comparison. It is noted that when the number of plies in the laminated composite pressure vessels is equal to or less than 6, the first-ply failure pressures predicted by the analytical methods are in good agreements with the experimental ones. In particular, both the maximum stress and Hoffman criteria can yield very accurate theoretical first-ply failure pressures for the pressure vessels composed of 4 or 6 plies. As for the $[90°/0°/90°/0°]_s$ pressure vessel which is composed of 8 plies, there exists significant differences between the theoretical and experimental first-ply failure pressures which are greater than 20% as shown in Table 8. This implies that the present analytical methods are inadequate and more sophisticate methods such as those constructed on the basis of the higher order shear deformation theory are required for the stress analysis of moderately thick laminated composite pressure vessels. It is noted that for the laminated composite pressure vessels composed of same number of plies, the optimally designed pressure vessel possesses the highest first-ply failure strength as well as the ultimate burst strength. For instance, amongst the laminated composite pressure vessels composed of 4 plies (Tables 3–5) the $[54°/-54°]_s$ pressure vessel which has been opti-

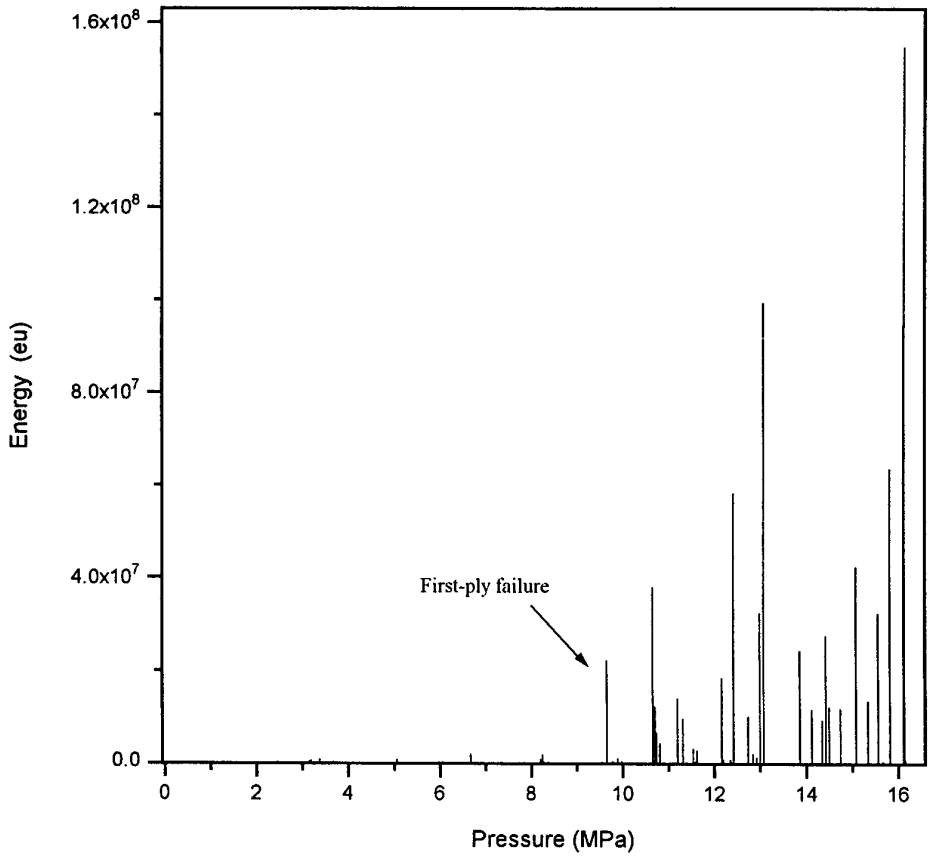

Fig. 2. Energy vs. pressure produced by tlle AE system for the $[54°/-54°/54°]_s$ pressure vessel.

Table 3. Failure strength of the [54°/−54°] pressure vessel

Failure criterion	Theoretical first-ply failure pressure P_t (MPa)	Experimental first-ply failure pressure P_f (MPa)	Experimental burst failure pressure P_b (MPa)	$\frac{\lvert P_f - P_t \rvert}{P_f}$ (%)	$\frac{P_f}{P_b}$ (%)
Maximum strain	9.32 (a)			29.81	
	9.44 (b)			31.47	
Maximum stress	7.61			5.99	
	7.64			6.41	
Hoffman	7.62	7.18	14.32	6.13	50.14
	7.65			6.55	
Tsai–Hill	7.75			7.94	
	7.78			8.36	
Tsai–Wu	7.97			11.00	
	8.03			11.83	

(a) first order shear deformation theory (finite element analysis), (b) classical plate theory.

mally designed yields the highest first-ply failure strength as well as the ultimate burst strength. It is also worth noting that for the same pressure vessel, the ultimate burst strength is usually much higher than the first-ply failure strength. Therefore, the pressure vessel will be safe enough if it is designed against the first-ply failure pressure.

Table 4. Failure strength of the [45°/−45°] pressure vessel

Failure criterion	Theoretical first-ply failure pressure P_t (MPa)	Experimental first-ply failure pressure P_f (MPa)	Experimental burst failure pressure P_b (MPa)	$\frac{\lvert P_f - P_t \rvert}{P_f}$ (%)	$\frac{P_f}{P_b}$ (%)
Maximum strain	5.21 (a)			50.14	
	5.34 (b)			53.89	
Maximum stress	3.40			2.02	
	3.43			1.12	
Hoffman	3.42	3.47	10.36	1.44	33.49
	3.45			0.58	
Tsai–Hill	4.35			25.36	
	4.39			26.51	
Tsai–Wu	4.03			16.14	
	4.06			17.00	

(a) first order shear deformation theory (finite element analysis), (b) classical plate theory.

Table 5. Failure strength of the $[90°/0°]_s$ pressure vessel

Failure criterion	Theoretical first-ply failure pressure P_t (MPa)	Experimental first-ply failure pressure P_f (MPa)	Experimental burst failure pressure P_b (MPa)	$\frac{\lvert P_f - P_t \rvert}{P_f}$ (%)	$\frac{P_f}{P_b}$ (%)
Maximum strain	7.07 (a)			24.47	
	7.11 (b)			25.17	
Maximum stress	6.04			6.33	
	6.06			6.69	
Hoffman	6.05	5.68	11.57	6.51	49.09
	6.07			6.87	
Tsai–Hill	6.21			9.33	
	6.24			9.86	
Tsai–Wu	6.42			13.03	
	6.46			13.73	

(a) first order shear deformation theory (finite element analysis), (b) classical plate theory.

Table 6. Failure strength of the [54°/−54°/54°] pressure vessel

Failure criterion	Theoretical first-ply failure pressure P_t (MPa)	Experimental first-ply failure pressure P_f (MPa)	Experimental burst failure pressure P_b (MPa)	$\frac{\lvert P_f - P_t \rvert}{P_f}$ (%)	$\frac{P_f}{P_b}$ (%)
Maximum strain	12.83 (a)			32.82	
	12.91 (b)			33.64	
Maximum stress	10.52			8.90	
	10.56			9.32	
Hoffman	10.53	9.66	16.07	9.01	60.11
	10.57			9.42	
Tsai–Hill	10.96			13.45	
	10.99			13.77	
Tsai–Wu	11.15			15.42	
	11.20			15.94	

(a) first order shear deformation theory (finite element analysis), (b) classical plate theory.

CONCLUSION

First-ply failure of laminated composite pressure vessels was studied via both theoretical and experimental approaches. Different methods were used to predict the first-ply failure pressures of the laminated composite pressure vessels on the basis of various failure criteria.

Table 7. Failure strength of the [90°/0°/90°] pressure vessel

Failure criterion	Theoretical first-ply failure pressure P_t (MPa)	Experimental first-ply failure pressure P_f (MPa)	Experimental burst failure pressure P_b (MPa)	$\frac{\lvert P_f - P_t \rvert}{P_f}$ (%)	$\frac{P_f}{P_b}$ (%)
Maximum strain	11.48 (a)			29.86	
	11.52 (b)			30.32	
Maximum stress	9.71			9.84	
	9.76			10.41	
Hoffman	9.73	8.84	10.07	13.41	65.92
	9.77			10.52	
Tsai–Hill	9.99			13.01	
	10.08			14.03	
Tsai–Wu	10.31			16.63	
	10.40			17.64	

(a) first order shear deformation theory (finite element analysis), (b) classical plate theory.

Table 8. Failure strength of the $[90°/0°/90°/0°]_s$ pressure vessel

Failure criterion	Theoretical first-ply failure pressure P_t (MPa)	Experimental first-ply failure pressure P_f (MPa)	Experimental burst failure pressure P_b (MPa)	$\frac{\lvert P_f - P_t \rvert}{P_f}$ (%)	$\frac{P_f}{P_b}$ (%)
Maximum strain	13.65 (a)			31.12	
	13.73 (b)			31.89	
Maximum stress	12.55			20.56	
	12.64			21.42	
Hoffman	12.57	10.41	20.75	21.96	47.40
	12.67			21.71	
Tsai–Hill	12.71			22.09	
	12.86			23.54	
Tsai-Wu	12.90			23.92	
	12.99			24.78	

(a) first order shear deformation theory (finite element analysis), (b) classical plate theory.

Experiments were carried out to verify the accuracy of the analytical methods. The analytical methods together with the maximum stress criterion or Hoffman failure criterion can predict accurate first-ply failure pressures for thin laminated composite pressure vessels. Both of the adopted analytical methods are inadequate for failure analysis of moderately thick laminated composite pressure vessels. Results on ultimate burst pressure for the pressure vessels were presented for comparison. Ultimate burst pressure is generally much higher than first-ply failure pressure of a laminated composite pressure vessel. It may be appropriate to use first-ply failure as a criterion for the design of laminated composite pressure vessels.

ACKNOWLEDGEMENTS

This research was supported by the National Science Council of the Republic of China under Grant No. NSC 85-2212-E009-021.

REFERENCES

1. Kulkarni, S. V. and Zweben, C. H. (eds), *Composites in pressure vessels and piping*. PVP-PB-021, ASME, 1977.
2. Darms, F.J., Space age pressure vessels. *In 36th Int. SAMPE Symposium and Exhibition* 1991, **36**, 818–826.
3. Young, K.S., Advanced composites storage containment for hydrogen. *Int. J. Hydrogen Energy* 1992, **17**, 505–507.
4. Lark, R. F., Recent advances in lightweight, filament-wound composite pressure vessel technology. In *Composites in Pressure Vessels and Piping* (eds Kulkarni, S. V. and Zweben, C. H.) PVP-PB-021, ASME, 1977, pp. 17–49.
5. Morris, E. E., Patterson, W. P., Landes, R. E. and Gordon, R., Composite pressure vessels for aerospace and commercial applications. In *Composites in Pressure Vessels and Piping* (eds Kulkarni, S. V. and Zweben, C. H.) PVP-PB-021, ASME, 1977, pp. 89–128.
6. Tauchert, T.R., Optimum design of a reinforced cylindrical pressure vessel. *J. Comp. Mat.* 1981, **15**, 390–402.
7. Fukunaga, H. and Uemura, M., Optimum design of helically wound composite pressure vessels. *J. Comp. Struct.* 1983, **1**, 31–49.
8. Eckold, G.C., A design method for filament wound GRP vessels and pipework. *Composites* 1985, **16**, 41–47.
9. Fukunaga, H. and Chou, T.W., Simplified design techniques for laminated cylindrical pressure vessels under stiffness and strength constraints. *J. Comp. Mat.* 1988, **22**, 1157–1169.
10. Adali, S., Sumers, E.B. and Verijenko, V.E., Optimization of laminated cylindrical pressure vessels under strength criterion. *Comp. Struct.* 1993, **25**, 305–312.
11. Tsai, S. W. and Hahn, H. T., *Introduction to Composite Materials*. Technomic, Wesport, CN, 1980.
12. Kam, T.Y. and Chang, R.R., Finite element analysis of shear deformable laminated composite plates. *J. Energy Resources and Technology, ASME* 1993, **115**, 41–46.

ELSEVIER

Composite Structures Vol. 38, No. 1–4, pp. 71–81
© 1997 Published by Elsevier Science Ltd. All rights reserved
Printed in Great Britain
0263-8223/97/$17.00 + 0.00

PII:S0263-8223(97)00043-3

The role of material nonlinearities in composite structures

W. K. Chiu[a], S. Galea[b] & R. Jones[a]

[a]*Department of Mechanical Engineering, Monash University, Wellington Road, Clayton, Victoria 3168, Australia*
[b]*Airframes and Engines Division, Aeronautical Research Laboratory, Defense Science and Technology Organisation, 506 Lorimer Street, Pt Melbourne, Victoria 3207, Australia*

In today's global market the optimal use of composites, to fulfil their potential for weight savings, is now being increasingly pursued as a means of obtaining a competitive advantage. However, the optimum design of composite structures and bonded composite joints requires a detailed understanding of the fundamental mechanical behaviour of composite materials and the adhesive systems. Whereas the time-dependent behaviour of the adhesive systems is reasonably well documented and has, to some degree, been accounted for in the design of bonded joints this has not yet occurred for advanced graphite–epoxy composites. Indeed, although it is recognised that the matrix-dominated response of many composite materials and structures is highly nonlinear, even at room temperature, this is often neglected in the design process. This restriction means that the full potential of the fibre matrix system may not be achieved. To this end the present paper, which focuses on the (matrix dominated) shear stress–shear strain behaviour of the AS4/3501-6 graphite–epoxy resin system, presents the results of an experimental investigation into the nonlinear behaviour of graphite–epoxy. © 1997 Published by Elsevier Science Ltd.

INTRODUCTION

In recent years there has been an increasing trend to use composite materials as primary load bearing structures. As with any new initiative safety considerations require a detailed understanding of the fundamental mechanical behaviour and the associated failure mechanisms. Furthermore, whereas in the past composites have been used mainly in the aerospace industry they are now being increasingly used across a broad range of other industries. This is particularly true in the newly emerging fields of composite, and adhesively bonded, pipelines and infrastructure rehabilitation [1]. In this context it has become apparent that the future economic lives of Australia's transportation and infrastructure complex is largely determined by the coupled effects of fatigue and corrosion. In reinforced concrete structures this combined effect is often termed 'Concrete Cancer' and is estimated to cost in excess of A$200 million per year. In South Australia it has been estimated that by the year 2010 this will have risen to absorb the entire State's construction budget. In the US there are currently in excess of 1500 structurally deficient bridges. Existing maintenance techniques have lead to significant closure/down times. The combination of 'down' time and maintenance costs have been estimated to be in excess of two billion dollars (US). To overcome this problem the use of composite reinforcement is now being considered.

In the aeronautical scene Australia has developed unique methods which utilise externally bonded composite patches to repair cracked, or damaged, structural components [2]. Although this repair methodology was first used to repair cracks in military aircraft it has recently been applied to civilian aircraft. Applications to Boeing and Airbus aircraft are described in Refs [3, 4], which outline a series of flight demonstrator programs. Composite

repair technology can also be used to maintain and extend the safe life of bridges and reinforced concrete structures, see Refs [1, 5, 6]. Indeed, Australian, Japanese and US companies are already focusing on this technique. There are three principal ways in which composites can be used to rehabilitate aging infrastructure:

(i) By using a modified cementious composite as a filler material.
(ii) As in (i) but with an external composite or metallic doubler also bonded over the damaged region.
(iii) Using a composite structural member to either replace the deficient component or to provide an alternative load path. In the latter case the member would be directly attached to the structure either mechanically or via an adhesive bond.

For damaged or degraded (infra) structures the challenge is to transmit a significant proportion of the load to the external wrap and to make the wrap tolerant to external damage. In both cases the (matrix dominated) shear performance of the composite wrap is often a limiting feature. Furthermore, for the purposes of certification it is necessary to understand all of the potential failure mechanisms. One recent review of the potential failure mechanisms of composite repairs was presented in Ref. [6]. Here it was shown that failure of the matrix material, i.e. interlaminar failure, can often drive the design process and limit the load bearing capability of the repair.

From the structural/design viewpoint the necessity, for composite repairs or composite joints, of transmitting the load from the composite to the underlying or connecting structure generally results in matrix dominated interlaminar shearing forces. Indeed, this was one of the primary causes of the disbonding of the structural reinforcement of the F111C wing pivot fitting, see Refs [6, 7]. Consequently, safety and certification concerns therefore dictate that the matrix dominated behaviour of graphite–epoxy composites be both understood and characterised.

To this end the present paper presents one such study into the nonlinear matrix dominated response of a composite material, AS4/3501-6. Particular attention is focused on the shear behaviour of the epoxy being used as the matrix material. This paper focuses on

— The effects of strain rate on the stress–strain behaviour.
— The effects of cyclic loading at various strain rates.
— Strain holds to demonstrate the stress relaxation phenomena.
— Creep experiments performed with load hold experiments.
— The effects of strain rate on the failure stresses and strains.
— The effects of strain rate on the interlaminar fracture toughness.

In this context it is important to note that similar experiments were also reported by Gates [8], where the rate-dependent behaviour of advanced composites was studied. In this work Gates investigated a different fibre matrix system (Hercules IM7 fibre and Amoco 8320 matrix, a thermoplastic material) and significant rate-dependent behaviour of this matrix material was reported [8].

This paper supports the general findings of Gates: rate-dependent stress–strain behaviour, rapid rates of stress decay during strain holds, significant creep characteristics, elevation of the apparent yield stress with loading rate, and failure loads and also reveals fracture energies which are dependent on the loading rate.

As a result of this investigation it is concluded that, in the initial design process, limiting the stress and strain levels in the composite to regimes where this complexity is not apparent will mean that the full potential of the fibre matrix system may not be achieved. If the design is not to be restricted then these complexities should be taken into account if an accurate assessment of the structural integrity of the composite structure/repair is required. This is particularly true for loading regimes which involve load, or displacement/strain, holds which can be expected in civil infrastructure applications [5] and which frequently occur in (structural) certification tests [6, 7] as well as in the proof pressure testing of pipelines.

This test programme also reveals that the failure load(s) can be load-history dependent. This is an interesting finding since, in many instances, the number of specimens required to obtain valid structural and material allowables have been based on statistics which assume load history independence. Consequently, the implications of this behaviour means that the number of specimen/structural tests required to

obtain a comprehensive data base needs to be revisited.

TEST SPECIMENS AND PROCEDURES

ASTM Standard D3518-76 tests

To determine the matrix dominated shear response tests were performed, using a 100 kN servohydraulic INSTRON test machine, in accordance with ASTM Standard D3518-76 on a 24 ply $((\pm 45)_{12})_s$ laminate. The geometry of the test specimens was as shown in Fig. 1 and was nominally $200 \times 50 \times 6.5$ mm. The test section was 115×50 mm. The specimens were manufactured from a large panel made from AS4/3501 graphite–epoxy. The lay up of the panel was $((\pm 45)_{12})_s$. As reported by Chiu *et al.* [9], it is desirable that the testing of the mechanical behaviour of the specimen be performed under local strain control. As a result, strain gauges were located in the centre of the test coupon to provide the local strain values and, more importantly, the signal to the strain controller of the Instron testing machine. This was required in order to test under strain rate control.

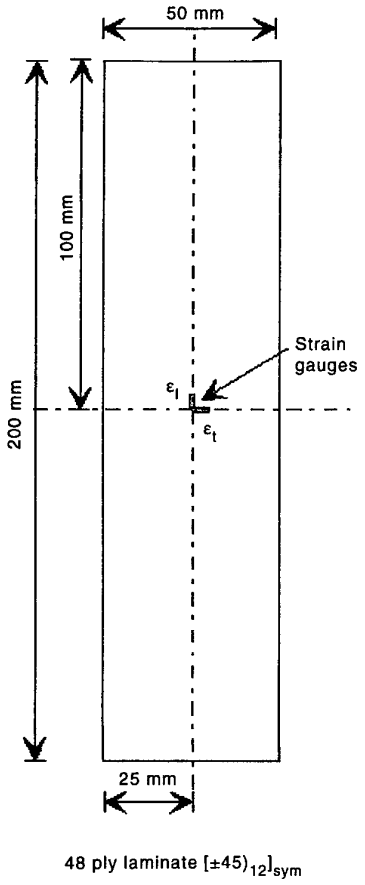

Fig. 1. Geometry of test specimen.

The tests were performed at room temperature (25–19°C) and at strain rates, ranging from 0.00001 s^{-1} to the machine maximum of 0.152 s^{-1}. During stress relaxation tests, the strain was held at a predetermined value. These tests consisted of loading the specimen to a nominal shear strain of 17000 $\mu\varepsilon$ and then applying a triangular cyclic loading of approximately $10{,}000 \pm 7000$ $\mu\varepsilon$ for a number of cycles.

Tests were also performed at a range of constant load rates, i.e. under load control, varying from 0.1 to 100 kN s^{-1}. The load hold tests were conducted at a load level where nonlinearity was observed in the monotonic tests.

RESULTS AND DISCUSSIONS

Strain rate controlled tests

Repeatability of test results is illustrated in Fig. 2, where two specimens were loaded at nominally similar strain rates. At strain rates of 0.00014 and 0.00017 s^{-1}, respectively.

The stress–strain behaviour of the graphite–epoxy at various strain rates is shown in Fig. 3. These curves demonstrate the dependencies of the stress–strain behaviour of the composite material on strain rates where, at high shear strain levels, the value of shear stress in the material may vary by up to 20% depending on the strain rate applied. For a general structure, in the area where local geometry changes occur, the local strain field changes rapidly. This can also be interpreted as a region of highly variant strain rates. Therefore, material in this location can follow a different stress–strain curve depending on its strain rate. This phenomena was studied numerically by Jones *et al.* [10], where it was shown that under these circumstances, analysis of the structure using traditional single stress–strain curves can result in gross errors in the estimation of the stress–strain values. A more accurate assessment of the structure can only be attained when the time-dependency of the material is incorporated in the analysis

The cyclic load results are shown in Fig. 4. Figure 4(a) shows that the hysteresis curve, for

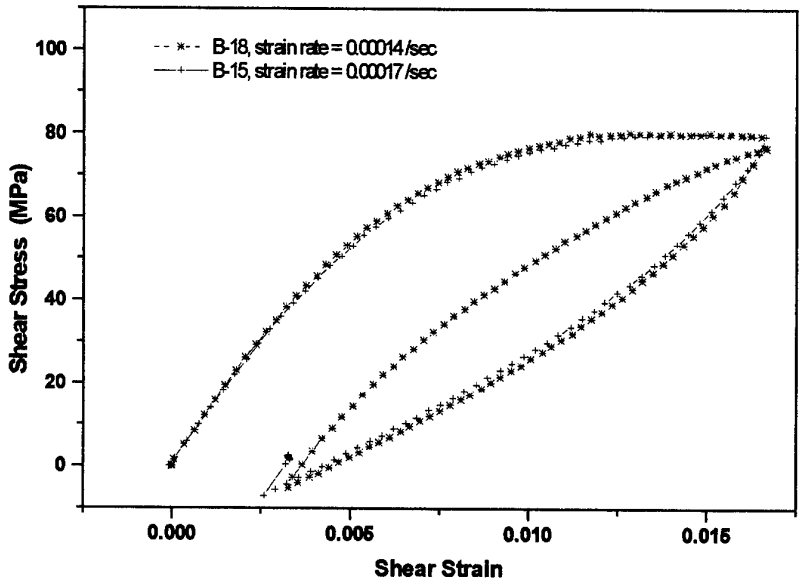

Fig. 2. Shear stress–shear strain behaviour of carbon fibre–epoxy resin system AS4/3501-6 for two test specimens at similar strain rates.

a shear strain rate of 0.00001 s^{-1}, has saturated at about the 5th cycle. Specimens loaded at higher rates require a greater number of cycles to reach saturation. Typically for the higher rates, greater than 0.00014 s^{-1}, about 10 cycles are required before saturation is achieved. It is also clear that although there are quite distinct hysteresis loops the (initial) loading and unloading curves appear to be parallel to the initial loading curve. This infers that the material non-linearity does not change the elastic modulus of the material.

The results from the stress relaxation experiments are shown in Fig. 5(a)–(c). The temporal stress decay during these experiments are shown in Fig. 6(a)–(c). As discussed by Chiu *et al.* [11, 12], during strain holds, the stress decays to an asymptotic limit. In this case, this limit is approximately 60 MPa. It can be seen that during a strain hold, depending on the initial

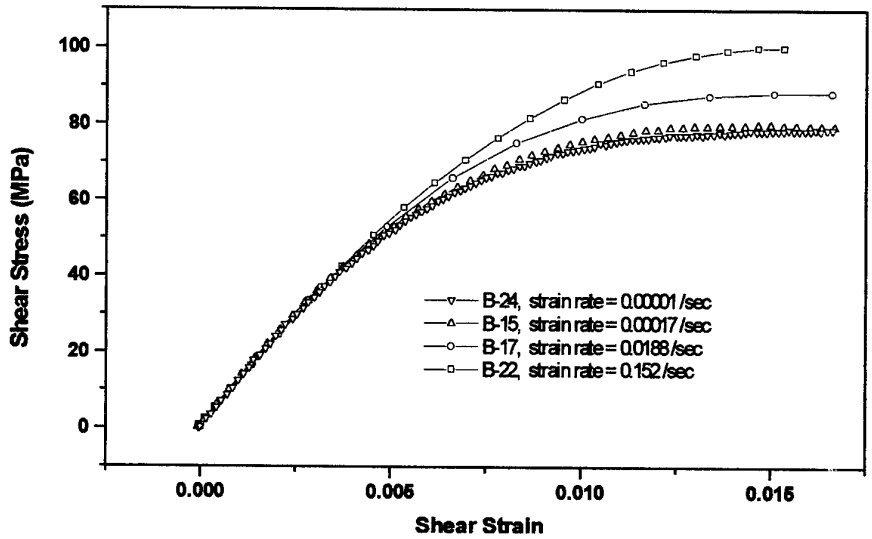

Fig. 3. Shear stress–shear strain behaviour of carbon fibre–epoxy resin system AS4/3501-6 at various strain rates.

loading rate, a stress decay of up to 30% can be obtained. Figure 6(a) shows that this 30% drop in shear stress (or load) was attained in less than 5 s. This demonstrates the highly nonlinear behaviour of the matrix material of this particular graphite–epoxy. This stress drop can be interpreted as a degradation of the matrix material as it represents a conversion of elastic

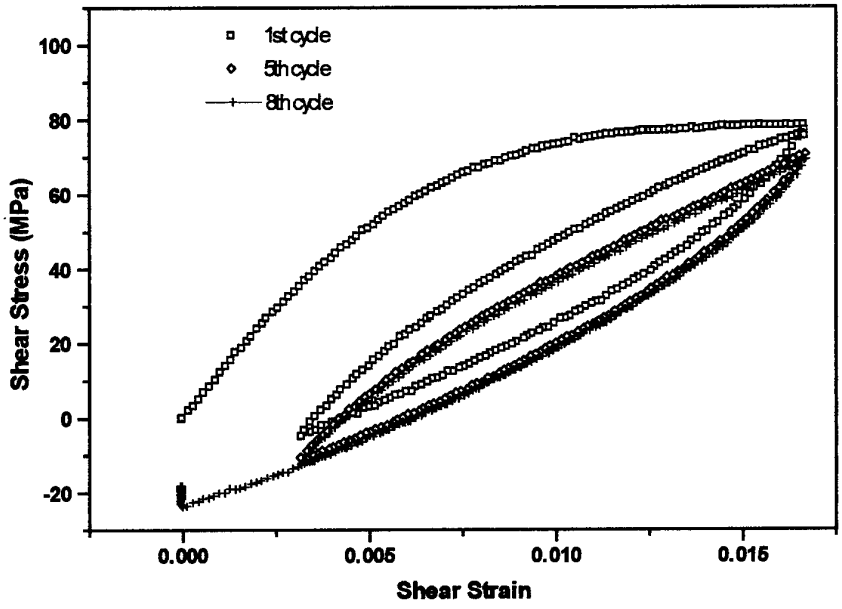

(a)

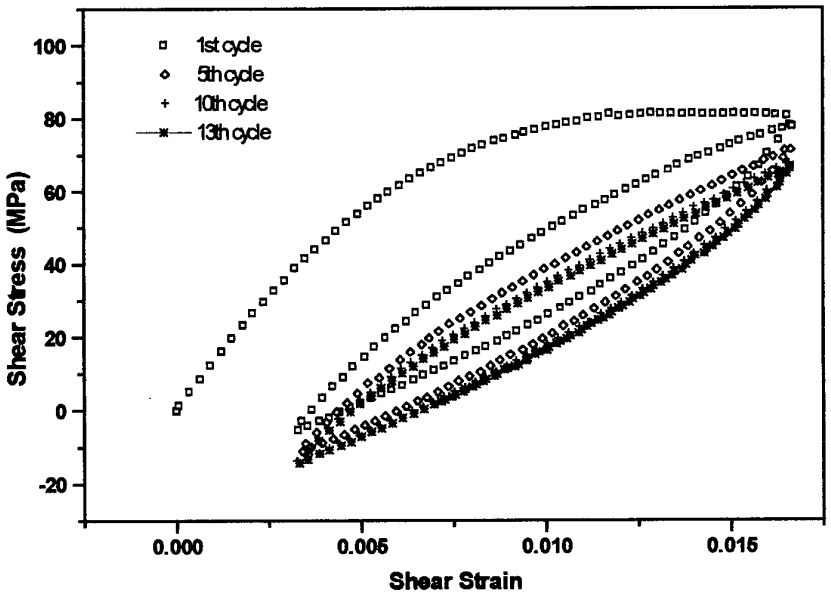

(b)

Fig. 4. Shear stress–shear strain behaviour of carbon fibre–epoxy resin system AS4/3501-6 under cyclic loading at various strain rates. (a) 0.00001 s^{-1}, (b) 0.00014 s^{-1},

energy to irrecoverable energy as the total strain is held at a constant value.

Figure 7(a)–(c) shows the creep characteristics of the matrix materials. These figures show that even at room temperature, the matrix exhibits significant time-dependent behaviour. It is expected that the creep rate is dependent on the load at which the test specimen is held at,

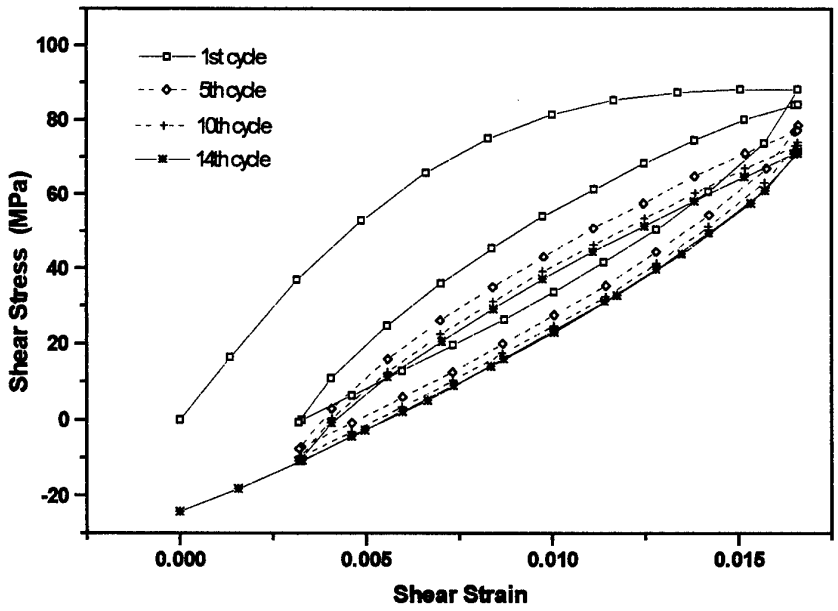

(c)

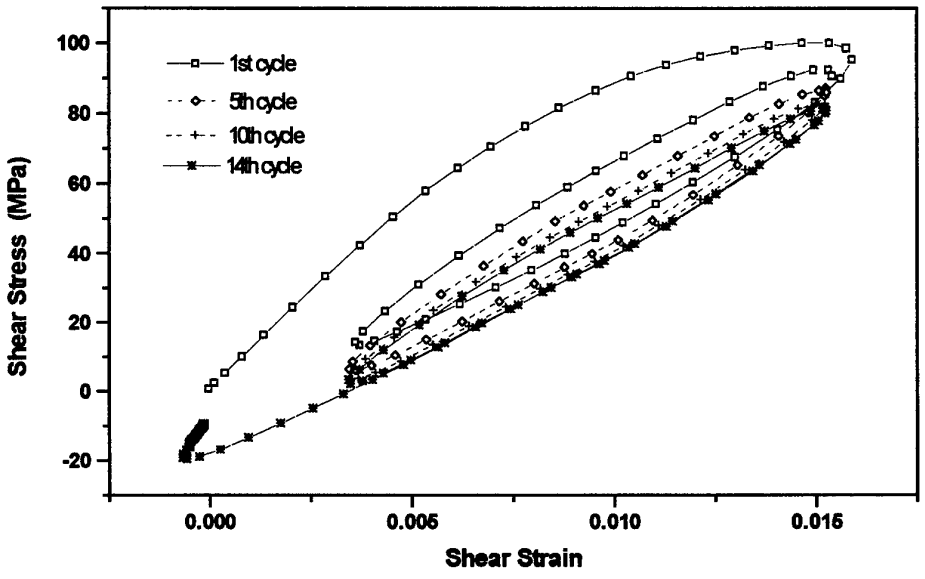

(d)

Fig. 4. Shear stress–shear strain behaviour of carbon fibre–epoxy resin system AS4/3501-6 under cyclic loading at various strain rates. (c) 0.0188 s^{-1} and (d) 0.152 s^{-1}.

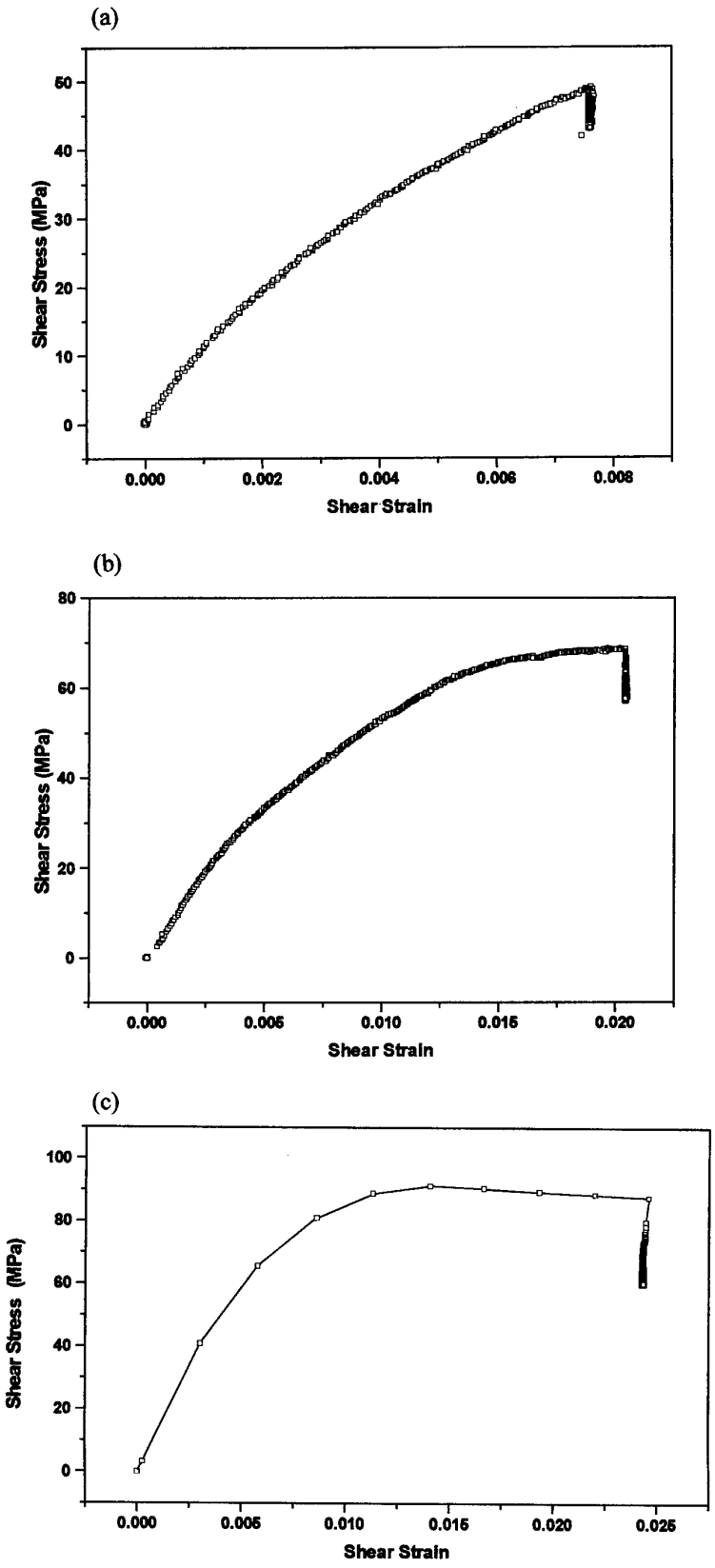

Fig. 5. Stress relaxation behaviour of carbon fibre–epoxy resin system AS4/3501-6 at various strain rates. (a) 0.000068 s^{-1}, (b) 0.000108 s^{-1} and (c) 0.135 s^{-1}.

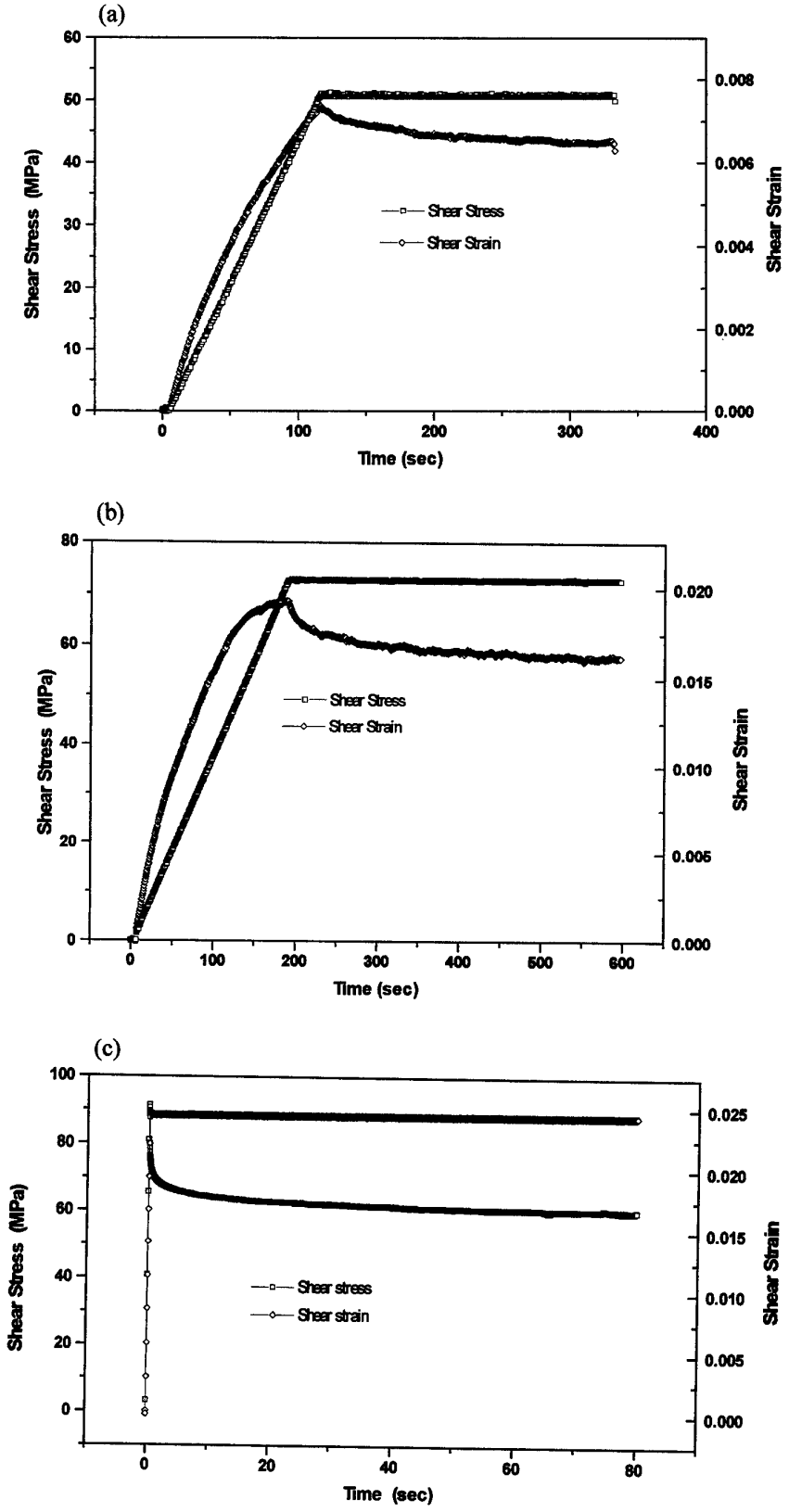

Fig. 6. Temporal stress decay during stress relaxation experiments. (a) 0.000068 s^{-1}, (b) 0.000108 s^{-1} and (c) 0.135 s^{-1}.

i.e. the higher the load, the higher the creep rate. Creep is, of course, a reflection of the degradation of the material. The load being held constant (i.e. elastic strain is constant) implies that the temporal development of strain contributes directly to the increase in inelastic strain. This may be interpreted as a accumulation of damage in the matrix material.

Load control tests

To compliment these tests a series of load control tests had also been performed, in accordance with ASTM Standard D3518-76, on a 16 ply $[(+45/-45)_4]_S$ laminate. In these series of tests the loading rates used were; *viz*: 0.4 kN s^{-1}, 4 kN s^{-1} and 270 kN s^{-1}. The resultant load displacement curves are shown in Fig. 8.

These tests revealed the following features:

(i) As the loading rate increased the apparent yield stress increased.

(ii) As the loading rate increased the failure stresses increased whilst the failure strain decreased.

Interlaminar fracture toughness tests

As a result of this work it was tempting to hypothesise that this rate dependency, both in the stress–strain response and in the failure loads,

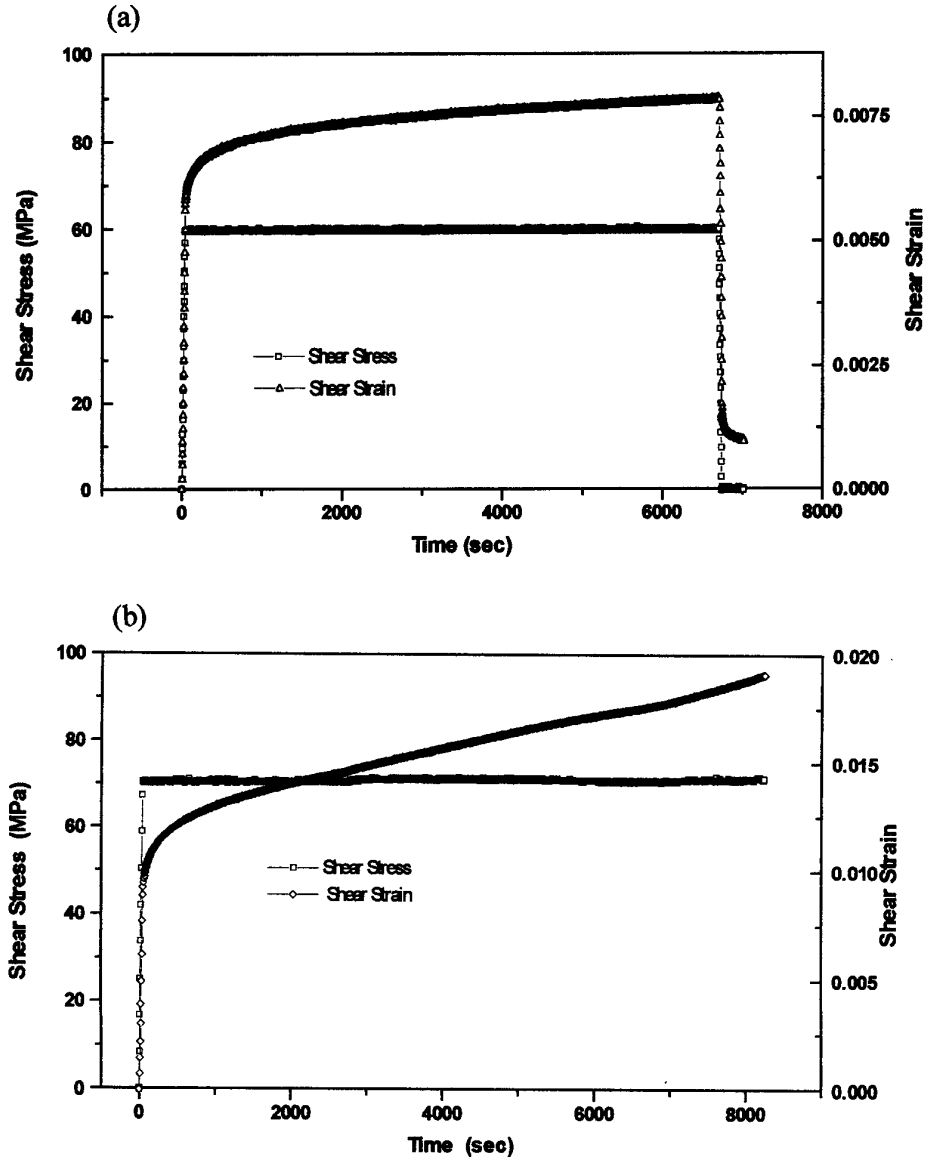

Fig. 7. Temporal strain development during load holds (creep test) at (a) 60 MPa and (b) 70 MPa.

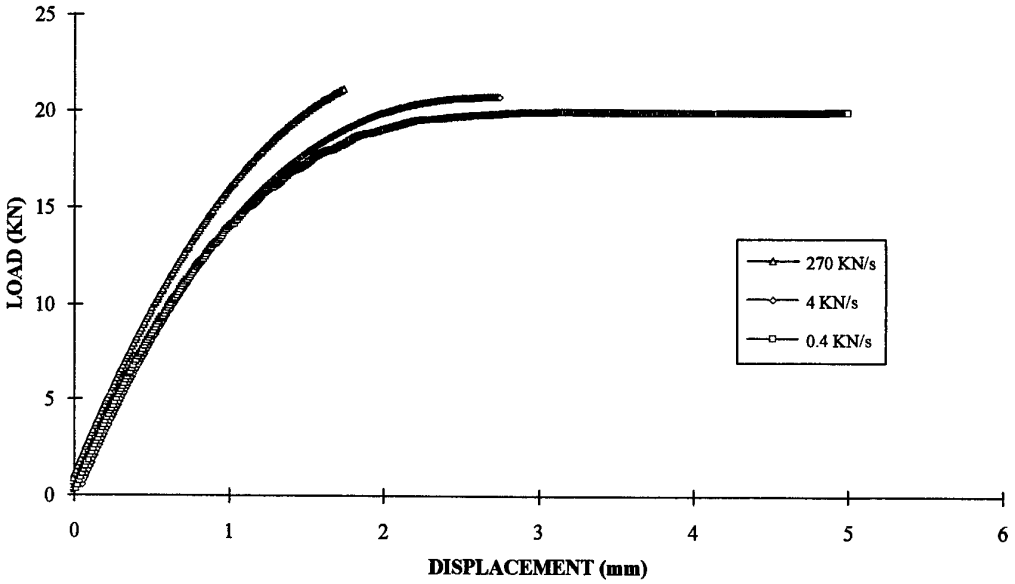

Fig. 8. Load displacement curves: load control.

should be reflected in the interlaminar fracture (failure) toughness being dependent on the loading rates. To this end a (preliminary) series of edge notch flexure tests were performed, see Ref. [12] for details of this test configuration. In this test programme the specimen layup was $[0_{12}]$ and had a 25 mm crack, i.e. a Teflon insert, between the 6th and the 7th plies. The test specimens were then loaded at three different crosshead speeds, i.e. 0.5 mm min^{-1}, 5 mm min^{-1} and 50 mm min^{-1}, and the load P deflection curves recorded, see Fig. 9.

Whilst this test programme was limited the results of this preliminary investigation were encouraging in that they supported the hypothesis of loading/strain rate dependency. In general as the displacement rate increased there was a significant increase in the failure load. A more detailed experimental programme aimed at clarifying this dependency is currently underway.

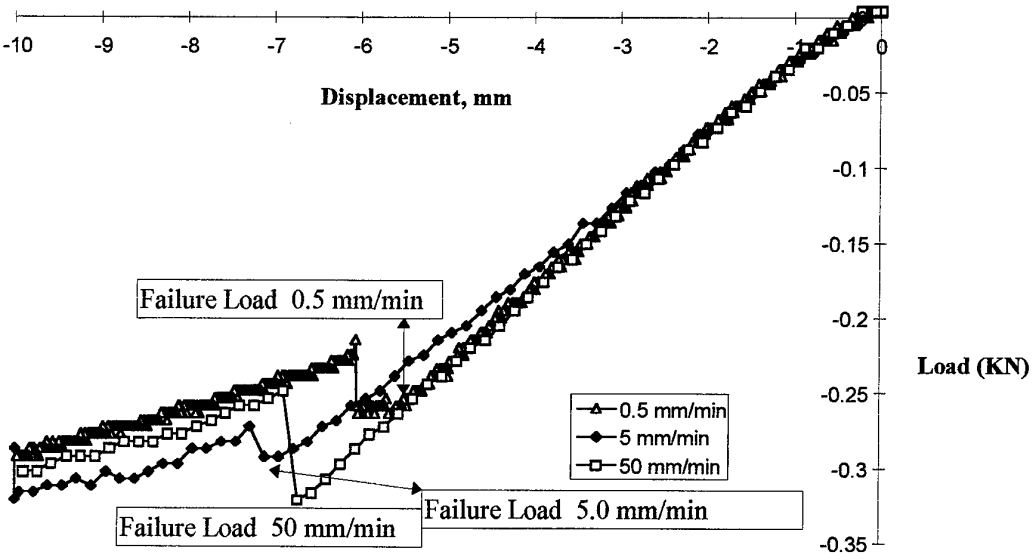

Fig. 9. Typical load displacement curves at three loading rates.

CONCLUSIONS

As a result of these experimental findings, the potential for graphite–epoxy composites to experience nonlinear time-dependent mechanical behaviour, even at room temperature, has been documented. In this investigation the rate-dependent stress–strain behaviour of the material was reflected in a rapid rate of stress decay during strain holds (in some cases, 30% in less than 5 s), significant creep characteristics, and in elevation of the apparent yield stress with loading rate. The failure loads, and strains (displacements), and the fracture energies were also dependent on the loading rate.

Whilst this behaviour is complex it is clear that limiting, in the initial design process, the stress and strain levels in the composite to regimes where this complexity is not apparent will mean that the full potential of the fibre matrix system may not be achieved. However, if the design is not to be restricted then these complexities should be taken into account if an accurate assessment of the structural integrity of the composite structure/repair is required. This is particularly true for loading regimes which involve load, or displacement/strain, holds which can be expected in civil infrastructure applications [5] and which frequently occur in (structural) certification tests [6,7] as well as in the proof pressure testing of pipelines.

In this test programme we have seen that the failure load(s) can be load-history-dependent. This is particularly interesting since in many instances the number of specimens required to obtain valid structural and material allowables has been based on statistics which assume load history independence. Consequently, the implications of this behaviour on the number of specimen/structural tests required to obtain statistically valid data needs to be evaluated.

REFERENCES

1. Nanni A., FRP reinforcement for prestressed and nonprestressed concrete structures. In *Fiber Reinforced Plastic (FRP) Reinforcement for Concrete Structures: Properties and Applications*, ed. Nanni, A., Elsevier, Amsterdam, 1993, pp. 3–12.
2. Baker, A. A. and Jones, R., *Bonded Repair of Aircraft Structure*, Martinus Nijhoff Publishers, The Hague, 1988.
3. Bartholomeus, R. A., Paul, J. J. and Roberts, J. D., Application of bonded composite Repair technology to Civilian Aircraft 747 Demonstrator Program. In *Proceedings International Conference on Aircraft Damage Assessment and Repair*, eds Jones, R. and Miller, N. J., Published by The Institution of Engineers Australia, ISBN (BOOK) 85825 537 5, July, 1991.
4. Jones, R., Bartholomeusz, R.A., Kaye, R. and Roberts, J.D., Bonded-composite repair of representative multisite damage in a full-scale fatigue-test article. *J Theoret. Appl. Fract. Mech.* 1994, **21**, 41–49.
5. Kobatake, K., Kimura, K. and Katsumata, H., A retrofitting method for reinforced concrete structures using carbon fiber. In *Fiber Reinforced Plastic (FRP) Reinforcement for Concrete Structures: Properties and Applications*, ed. Nanni, A., Elsevier, Amsterdam, 1993, pp. 435–450.
6. Jones, R., Chiu, W.K. and Hanna, S., Potential failure mechanisms of bonded composite repairs for metal and concrete. *J. Theoret. Appl. Fract. Mech.* 1994, **21**, 107–119.
7. Jones, R., Molent, L., Paul, L., Saunders, T. and Chiu, W. K., Development of a composite repair and the associated inspection intervals for the F111C stiffener runout region. In *FAA/NASA International Symposium on Advanced Structural Integrity Methods for Airframes Durability and Damage Tolerance, NASA Conference Publication*, 3274, Part 1, 1994, pp. 339–351.
8. Gates, T. S., Rate dependent stressstrain behaviour of advanced polymer matrix composites, *NASA Technical Memorandum 104070*, 1991.
9. Chiu, W.K., Rees, D., Chalkley, P.D. and Jones, R., Designing for damage tolerant composite repairs. *J. Composite Structures* 1994, **28**, 19–37.
10. Jones, R., Chiu, W. K. and Paul, J. J., Designing for damage tolerant joints. *Composite Structures* 1994, **25**, 201–208.
11. Chiu, W. K., Chalkley, P. D. and Jones, R., Effects of temperature on the stress–strain behaviour of film adhesives FM73. *Computers and Structures*, 1994, 17.
12. Tay, T.E., Williams, J.F. and Jones, R., Characterization of pure and mixed mode fracture in composite laminates. *J. Theoret. Appl. Fract. Mech.* 1987, **7**, 115–123.

ELSEVIER

Composite Structures Vol. 38, No. 1–4, pp. 83–89
© 1997 Elsevier Science Ltd. All rights reserved
Printed in Great Britain
0263-8223/97/$17.00 + 0.00

PII:S0263-8223(97)00044-5

On the response of MMC laminated plates to non-uniform temperature loading: the effect of temperature-dependent material properties

Esther Feldman & Irena Belostotsky

Department of Solid Mechanics, Materials and Structures, Faculty of Engineering, Tel Aviv University, Ramat Aviv 69978, Israel

Thermal response of antisymmetrically laminated metal matrix composite (MMC) plates subjected to non-uniform temperature field is analysed. Temperature dependence of both elastic and viscoplastic properties of the metallic matrix is taken into account; this suggests that a non-uniformly heated plate should be considered as a non-homogeneous structure. A micro-to-macro approach is employed to establish the instantaneous thermo-inelastic constitutive law at each point of the plate and to perform the structural analysis.

Results are presented for simply-supported and clamped graphite–aluminium plates. The effects of boundary conditions, lamination angle, length-to-thickness ratio and different types of spatial temperature distributions are illustrated. Comparisons with the results obtained using an approach that treats the effect of temperature-dependent material properties in a simplified manner are shown. Comparisons with the corresponding elastic solutions (which neglect the inelastic effects in the metallic matrix) are given. © 1997 Elsevier Science Ltd.

INTRODUCTION

Metal matrix composites (MMCs) possess some advantages that are very important for their use as structural materials; in particular, one of the main virtues of MMCs is that they are resistant to severe environments, and particularly to high temperatures. In the present study the thermal post-buckling behaviour of laminated MMC plates is addressed.

When a MMC plate is subjected to temperature change some special features of the metal matrix composites deserve consideration. First, the inelastic effects in the MMC structure cannot be disregarded, as thermo-mechanical behaviour of the metallic matrix at high temperatures is inherently time-dependent and hereditary. Second, both elastic and viscoplastic mechanical properties of the metallic matrix are highly temperature-dependent (see, for example, the monograph by Taya and Arsenault [1]). Therefore, an MMC plate exposed to a non-uniform temperature field must be treated as a non-homogeneous elasto-viscoplastic structure.

It is worth noting that among the studies concerned with the elastic thermo-mechanical response of composite plates and curved panels, the temperature-dependent material properties (TDMP) were included only in a few of them (see Chen & Chen [2] and Weller & Patlashenko [3]). From the results presented in these contributions it follows that the effect of TDMP on thermal post-buckling behaviour is significant. One would expect that when the elasto-viscoplastic behaviour of a structure is addressed, this effect might be of even greater importance.

Elasto-viscoplastic post-buckling response of antisymmetric angle-ply MMC plates under uniform thermal loading was analysed by Feldman & Aboudi [4]. Thermal buckling of non-uniformly heated symmetrically laminated MMC plates was studied by Feldman [5]. In both

papers, temperature-dependent material properties of the metallic matrix were taken into account.

In the present paper thermal post-buckling behaviour of non-uniformly heated antisymmetric angle-ply MMC plates is investigated. It is assumed that the thickness–temperature gradient is negligible, and that the temperature field, T, the plate is exposed to is a function of the in-plane coordinates x, y and the time t. The plate is treated as a non-homogeneous thermo-elasto-viscoplastic structure.

To analyse the response of non-uniformly heated plates, the micro-to-macro approach proposed by Feldman & Aboudi [4] to thermal post-buckling of inelastic laminated MMC plates is extended to include the behaviour of non-homogeneous structures. At the stage of a micromechanical consideration, the instantaneous overall thermo-elasto-viscoplastic constitutive law is obtained at every point of the plate using the micromechanical method of cells [6]. The micromechanically derived effective thermo-inelastic constitutive law is utilized to formulate a system of differential equations which govern the geometrically non-linear behaviour of a non-homogeneous plate. Two types of out-of-plane boundary conditions are examined, namely simply-supported and clamped.

Results are presented for Gr/Al plates subjected to a non-uniform temperature field $T = T(x,t)$. The effects of boundary conditions, length-to-thickness ratio, lamination angle and different types of spatial temperature distributions are illustrated. To evaluate the effect of temperature-dependent material properties the approach proposed in this study is compared to another one treating the effect of TDMP in a simplified manner. Comparisons with the corresponding elastic solutions, obtained by neglecting the inelastic effects in the metallic matrix, are shown.

FORMULATION AND SOLUTION PROCEDURE

Governing equations

In the present study, the moderately large deflection behaviour of geometrically imperfect MMC plates under quasi-static temperature loading is analysed in the framework of the classical plate theory. An antisymmetric angle-ply plate of length a, width b and thickness h is considered. Introducing the non-dimensional in-plane coordinates $\xi = x/a$, $\eta = y/b$, the non-dimensional coordinate in the normal z-direction $\zeta = z/h$, and the plate aspect ratio $\lambda = a/b$, the system of differential governing equations can be written in the form [7]

$$M_{\xi\xi,\,\xi\xi}+2\lambda M_{\xi\eta,\,\xi\eta}+\lambda^2 M_{\eta\eta,\,\eta\eta} + \frac{\lambda^2}{a^2}(\Phi_{,\eta\eta}w_{,\xi\xi}-2\Phi_{,\xi\eta}w_{,\xi\eta} +\Phi_{,\xi\xi}w_{,\eta\eta})=0 \tag{1}$$

$$\lambda^2\varepsilon^0_{\xi\xi,\,\eta\eta}+\varepsilon^0_{\eta\eta,\,\xi\xi}-\lambda\varepsilon^0_{\xi\eta,\,\xi\eta} = \frac{\lambda^2}{a^2}[-w_{,\xi\xi}w_{,\eta\eta}+(w_{,\xi\eta})^2+w^0_{,\xi\xi}w^0_{,\eta\eta}-(w^0_{,\xi\eta})^2] \tag{2}$$

Here w and w^0 are current and initial transverse displacements, respectively; Φ is the stress function; and $M_{\alpha\beta}$ ($\alpha, \beta = \xi, \eta$) are the moment resultants. The mid-plane strains $\varepsilon^0_{\alpha\beta}$ correspond to the von Karman kinematic relations

$$\varepsilon^0_{\xi\xi} = \frac{1}{a}u_{,\xi}+\frac{1}{2a^2}[(w_{,\xi})^2-(w^0_{,\xi})^2]$$

$$\varepsilon^0_{\eta\eta} = \frac{\lambda}{a}v_{,\eta}+\frac{\lambda^2}{2a^2}[(w_{,\eta})^2-(w^0_{,\eta})^2] \tag{3}$$

$$\varepsilon^0_{\xi\eta} = \frac{\lambda}{a}u_{,\eta}+\frac{1}{a}v_{,\xi}+\frac{\lambda}{a^2}[w_{,\xi}w_{,\eta}-w^0_{,\xi}w^0_{,\eta}]$$

where u and v are the in-plane displacements in the x- and y-directions, respectively.

The expressions for the middle plane strains and moment resultants in terms of Φ, w may be obtained using the corresponding constitutive relationships describing the thermo-inelastic behaviour of a plate. For an antisymmetrically laminated structure, these expressions have been derived in Feldman & Aboudi [4]. Substituting them into eqns (1) and (2) yields

$$[D^*_{11}(w-w^0)_{,\xi\xi}+\lambda^2 D^*_{12}(w-w^0)_{,\eta\eta}-\lambda B^*_{61}\Phi_{,\xi\eta}]_{,\xi\xi} +\lambda^2[D^*_{12}(w-w^0)_{,\xi\xi}+\lambda^2 D^*_{22}(w-w^0)_{,\eta\eta} -\lambda B^*_{62}\Phi_{,\xi\eta}]_{,\eta\eta}+2\lambda[2\lambda D^*_{66}(w-w^0)_{,\xi\eta} +\lambda^2 B^*_{16}\Phi_{,\eta\eta}+B^*_{26}\Phi_{,\xi\xi}]_{,\xi\eta}$$

$$+a^2(G^{P}_{\xi\xi,\,\xi\xi}+2\lambda G^{P}_{\xi\eta,\,\xi\eta}+\lambda^2 G^{P}_{\eta\eta,\,\eta\eta})$$
$$+a^2(G^{T}_{\xi\xi,\,\xi\xi}+2\lambda G^{T}_{\xi\eta,\,\xi\eta}+\lambda^2 G^{T}_{\eta\eta,\,\eta\eta})$$
$$-\lambda^2(\Phi_{,\eta\eta}w_{,\xi\xi}-2\Phi_{,\xi\eta}w_{,\xi\eta}+\Phi_{,\xi\xi}w_{,\eta\eta})=0 \qquad (4)$$

$$\lambda^2(\lambda^2 A^*_{11}\Phi_{,\eta\eta}+A^*_{12}\Phi_{,\xi\xi})_{,\eta\eta}+(\lambda^2 A^*_{12}\Phi_{,\eta\eta}$$
$$+A^*_{22}\Phi_{,\xi\xi})_{,\xi\xi}+\lambda^2(A^*_{66}\Phi_{,\xi\eta})_{,\xi\eta}$$
$$=2\lambda[B^*_{26}(w-w^0)_{,\xi\eta}]_{,\xi\xi}$$
$$+2\lambda^3[B^*_{16}(w-w^0)_{,\xi\eta}]_{,\eta\eta}$$
$$-\lambda[B^*_{61}(w-w^0)_{,\xi\xi}$$
$$+\lambda^2 B^*_{62}(w-w^0)_{,\eta\eta}]_{,\xi\eta}$$
$$+\lambda^2[(w_{,\xi\eta})^2-w_{,\xi\xi}w_{,\eta\eta}-(w^0_{,\xi\eta})^2+w^0_{,\xi\xi}w^0_{,\eta\eta}]$$
$$+a^2(\lambda\gamma^{P}_{\xi\eta,\,\xi\eta}-\lambda^2\gamma^{P}_{\xi\xi,\,\eta\eta}-\gamma^{P}_{\eta\eta,\,\xi\xi})$$
$$+a^2(\lambda\gamma^{T}_{\xi\eta,\,\xi\eta}-\lambda^2\gamma^{T}_{\xi\xi,\,\eta\eta}-\gamma^{T}_{\eta\eta,\,\xi\xi}) \qquad (5)$$

The stiffness matrices A^*, B^* and D^* (which are defined, for example, in Whitney [8]) are functions of the spatial coordinates ξ, η and the time t. The expressions for the plastic and thermal functions $G^{P}_{\alpha\beta}$, $\gamma^{P}_{\alpha\beta}$ and $G^{T}_{\alpha\beta}$, $\gamma^{T}_{\alpha\beta}$ may be found in Feldman [9].

Boundary conditions

Further, we shall analyse the thermal response of simply-supported (SS) and clamped (C) plates. The in-plane displacements u, v are supposed to be unrestricted in the tangential direction; the edges $\xi = 0$, 1 are immovable. As to the boundary conditions at the edges $\eta = 0$, 1, two possibilities are considered, namely: the edges $\eta = 0$, 1 are immovable in the y-direction (SS1 and C1 cases); the edges $\eta = 0$, 1 are unloaded (SS2 and C2 cases).

Introducing the average edge shortenings in both in-plane directions

$$\bar{\Delta}_x = \int_0^1 [u(1,\eta)-u(0,\eta)]\,d\eta;$$
$$\bar{\Delta}_y = \int_0^1 [v(\xi,1)-v(\xi,0)]\,d\xi$$

the boundary conditions may be formulated as follows

SS1 at $\xi=0$, 1: $\Phi_{,\xi\eta}=w=M_{\xi\xi}=\bar{\Delta}_x=0$;
at $\eta=0$, 1: $\Phi_{,\xi\eta}=w=M_{\eta\eta}=\bar{\Delta}_y=0$
SS2 at $\xi=0$, 1: $\Phi_{,\xi\eta}=w=M_{\xi\xi}=\bar{\Delta}_x=0$;
at $\eta=0$, 1: $\Phi_{,\xi\xi}=\phi_{,\xi\eta}=w=M_{\eta\eta}=0$
C1 at $\xi=0$, 1: $\Phi_{,\xi\eta}=w=w_{,\xi}=\bar{\Delta}_x=0$; (6)
at $\eta=0$, 1: $\Phi_{,\xi\eta}=w=w_{,\eta}=\bar{\Delta}_y=0$
C2 at $\xi=0$, 1: $\Phi_{,\xi\eta}=w=w_{,\xi}=\bar{\Delta}_x=0$;
at $\eta=0$, 1: $\Phi_{,\xi\xi}=\Phi_{,\xi\eta}=w=w_{,\eta}=0$

where the expressions for $\bar{\Delta}_x$, $\bar{\Delta}_y$ in terms of Φ, w, are derived in Feldman & Aboudi [4].

Solution procedure

To obtain a solution to the problem at hand, a micro-to-macro approach is adopted. At the stage of micromechanical analysis, the effective thermo-inelastic constitutive law of MMC material is established using the method of cells developed by Aboudi [6]. The fibers are assumed to be thermo-elastic, whereas the metallic matrix is represented as a thermo-plastic work-hardening material. The method of cells enables one to obtain, for a unidirectional MMC layer, the effective reduced stiffness matrix Q, the plastic deformations $\varepsilon^{P}_{\alpha\beta}$ and the effective coefficients of thermal expansion $\alpha_{\alpha\beta}$. Thereafter, the stiffness matrices A^*, B^* and D^*, as well as the plastic and thermal functions involved in eqns (4) and (5), may be calculated. It should be pointed out that, owing to TDMP, the above-mentioned micromechanical analysis is to be performed at every point of the plate at each increment of thermal loading.

At the structural analysis stage, an approximate solution to the boundary value problem, eqns (4–6), is represented in the form

$$\Phi(\xi,\eta,t)=-\frac{a^2}{\lambda^2}P_x(t)\frac{\eta^2}{2}-a^2P_y(t)\frac{\xi^2}{2}$$
$$+\sum_{p=1}^{P}\sum_{q=1}^{Q}F_{pq}(t)X_p(\xi)X_q(\eta)$$
$$w(\xi,\eta,t)=\sum_{m=1}^{M}\sum_{n=1}^{N}W_{mn}(t)\sin\pi m\xi\sin\pi n\eta$$
(for SS cases)
$$=\sum_{m=1}^{M}\sum_{n=1}^{N}W_{mn}(t)X_m(\xi)X_n(\eta)$$
(for C cases) (7)

where X_i ($i = 1, 2, \ldots$) are beam eigenfunctions satisfying boundary conditions $X_i(0)=X_i(1)=X_i'(0)=X_i'(1)=0$. The initial imperfection w^0 is expanded into the double Fourier series in accordance with the boundary conditions

$$w^0(\xi,\eta)=\sum_{m=1}^{M}\sum_{n=1}^{N}W^0_{mn}\sin\pi m\xi\sin\pi n\eta$$

(for SS cases)

$$= \sum_{m=1}^{M} \sum_{n=1}^{N} W^0_{mn} X_m(\xi) X_n(\eta)$$

(for C cases)

The coefficients in eqn (7), and the values of P_x, P_y (having the meanings of normal in-plane loads at the edges $x = 0$, a and $y = 0$, b), are obtained in an analogous manner as is performed in Feldman [5]. As a result, the following system of equations is arrived at

$$Q^{(0)}_{pq} + \sum_m \sum_n Q^{(1)}_{pqmn} W_{mn} + \sum_m \sum_n \sum_i \sum_j Q^{(2)}_{pqmnij} W_{mn} W_{ij} + \sum_m \sum_n \sum_i \sum_j \sum_k \sum_l Q^{(3)}_{pqmnijkl} W_{mn} W_{ij} W_{kl} = 0;$$

$$(p = 1, ..., M,\ q = 1, ..., N) \qquad (8)$$

Here $Q^{(0)}_{pq}, ..., Q^{(3)}_{pqmnijkl}$ are complicated expressions containing the geometrical parameters of the plate, the amplitudes of the initial imperfection $W^{(0)}_{mn}$, and various line and surface integrals involving the elements of the stiffness matrices as well as different plastic and thermal functions.

Thus, the system of eqn (8) describes the behaviour of a geometrically non-linear imperfect laminated plate, made of metal matrix composite material, and subjected to non-uniform temperature loading. In the absence of plastic deformations eqn (8) reduces to the system of equations from which the response of an imperfect thermo-elastic plate may be obtained.

To solve eqn (8), one needs to determine the coefficients $Q^{(0)}_{pq}, ..., Q^{(3)}_{pqmnijkl}$. Owing to the plastic effects, this is performed in an incremental procedure similar to those described by Feldman & Aboudi [4]. Once, at each loading increment, the coefficients of the system in eqn (8) have been calculated, the real roots of eqn (8) are to be found; they represent the amplitudes $W_{mn}(t)$ of the transverse displacement at the moment considered.

A simplified treatment of temperature-dependent material properties

With the intent of estimating the effect of temperature-dependent material properties (TDMP) on thermal response, we need to compare the approach proposed in this paper with another procedure that deals with this effect in a more simplified way. Such a simplified method to account for TDMP (which has been employed by Feldman [5]) is as follows. At each loading increment an average temperature of the plate surface $T_{av}(t)$ is introduced and the material properties of the composite are calculated at this temperature. Therefore, according to this approach, the material properties of each ply are 'smeared' over its surface, and the plate becomes effectively homogeneous: the parameters of its elastic and viscoplastic behaviour are no longer functions of the coordinates x, y.

It should be emphasized that this simplified procedure does not ignore totally the temperature dependence of material properties, because, as time goes on, the material parameters change with the change in T_{av}. However, at each increment of thermal loading the spatial distribution of the material properties is disregarded.

APPLICATIONS AND DISCUSSION

Results are presented for unidirectional and angle-ply graphite–aluminium plates with a fibre volume fraction $v_f = 0.3$, subjected to a non-uniform temperature field $T = T(x,t)$. The elastic T-50 graphite fibres are assumed to behave as transversely isotropic, with the following properties in the axial (denoted by subscript A) and transverse (denoted by subscript T) directions: Young's moduli $E_A = 388.2$ GPa, $E_T = 7.6$ GPa; Poisson's ratios $v_A = 0.41$, $v_T = 0.45$; shear modulus $G_A = 14.9$ GPa; and thermal expansion coefficients $\alpha_A = -0.68 \times 10^{-6}\,°C^{-1}$, $\alpha_T = 9.74 \times 10^{-6}\,°C^{-1}$.

The aluminium matrix is modelled as a thermo-viscoplastic work-hardening material, whose rate-dependent behaviour is described using the unified theory of plasticity given by Bodner & Partom [10]. In the framework of this theory, the material parameters of the aluminium alloy 2024-T4 at various temperatures are given in Table 1. The material parameters of the metallic matrix at any temperature within the interval $T \in [21, 371]$°C are obtained using piecewise linear interpolation of the data given in Table 1.

To illustrate the effect of non-uniform thermal loading, consider MMC plates exposed to a temperature field $T(\xi,t) = T_{ref} + T_0(t) \sin^n \pi\xi$; it is assumed that $T_{ref} = 21$°C throughout the

Table 1. Material constants of the 2024-T4 aluminum alloy: isotropic material in the elastic region; isotropic work-hardening material in the plastic region

T (°C)	E (GPa)	ν	α ($°C^{-1}$)	D_0 (s^{-1})	Z_0 (MPa)	Z_1 (MPa)	$\tilde{m}$	$\tilde{n}$
21.0	72.4	0.33	22.5×10^{-6}	10,000	340	435	300	10.0
148.9	69.3	0.33	22.5×10^{-6}	10,000	340	435	300	7.0
204.4	65.7	0.33	22.5×10^{-6}	10,000	340	435	300	4.0
260.0	58.4	0.33	22.5×10^{-6}	10,000	340	435	300	1.6
371.0	41.5	0.33	22.5×10^{-6}	10,000	340	435	300	0.6

Here E, ν and α are Young's modulus, Poisson's ratio and the thermal expansion coefficient, respectively; D_0 is the limiting strain rate, Z_0 is related to the 'yield stress' of a uniaxial stress–strain curve, Z_1 is proportional to the ultimate stress, $\tilde{m}$ determines the rate of work hardening and the rate-sensitivity is controlled by the parameter $\tilde{n}$.

plate. The value $n = 0$ corresponds to a uniform thermal loading; as the value of n increases, the temperature field becomes more and more localized. Note that information on the material properties of the aluminium alloy at $T > 371°C$ was not available; therefore, the process of thermal loading was terminated when the temperature at any point of the structure reached the value of 371°C. With the aim of comparing results relating to different types of non-uniform temperature distribution, the above-mentioned average temperature T_{av} of the plate surface is used. It is defined by

$$T_{av}(t) = \int_0^1 \int_0^1 T(\xi, \eta, t)\, d\xi\, d\eta \qquad (9)$$

The response of a plate is displayed as average temperature T_{av} vs the non-dimensional transverse displacement W/h, where W stands for the deflection at the centre of the middle plane. The initial geometrical imperfection of a simply-supported plate is assumed to have a sinusoidal form: $w^0(\xi, \eta) = W_0 \sin \pi\xi \sin \pi\eta$; for a clamped plate it is taken as $w^0(\xi, \eta) = W_0 X_1(\xi) X_1(\eta)$. It should be noted that, for all the cases considered below, the first term in eqn (7) for w was found to be a predominant one.

Consider first imperfect unidirectional plates with a lamination angle $\theta = 0°$, and the amplitude of initial geometrical imperfection $W_0/h = 0.01$. The response curves for simply-supported and clamped square plates ($a = b = 0.2$ m) subjected to the uniform and non-uniform heating are shown in Figs 1 and 2. Dashed lines represent the elastic solutions obtained by neglecting all of the inelastic effects; dashed–dotted lines display the results corresponding to the simplified approach to TDMP described above.

It is evident from the graphs that the type of non-uniform temperature distribution $T(x,t)$ that the plate is exposed to affects significantly its response, for all the boundary conditions considered. As Fig. 1 suggests, the thermal response of a thermo-viscoplastic plate differs essentially from the behaviour of its thermo-elastic counterpart. While the central deflection of the elastic structure continues to grow with the increase in temperature, the corresponding viscoplastic solution exhibits, as the temperature rises, an increase in W followed by a decrease in the central deflection. This effect has been discussed by Feldman [9]; it may be attributed to the fact that the in-plane forces acting on the viscoplastic plate at a given temperature are smaller than the forces corresponding to the elastic solution.

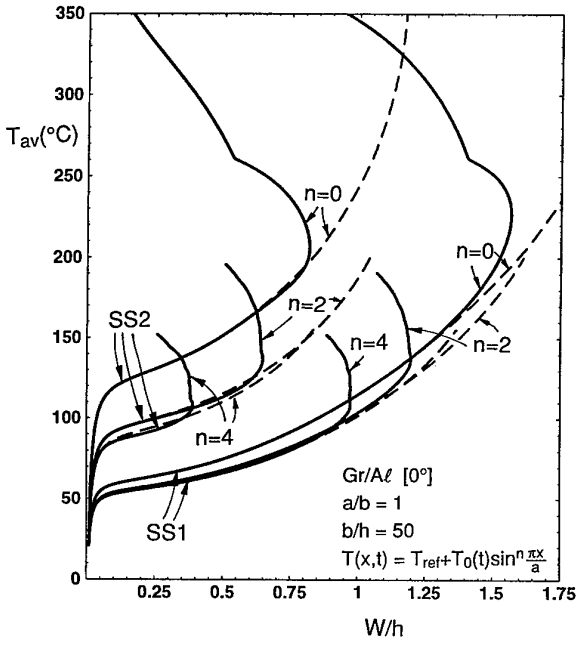

Figure 1. The effect of different types of spatial temperature distributions on the thermal response of a unidirectional simply-supported plate (boundary conditions SS1 and SS2). Dashed lines correspond to the elastic solutions.

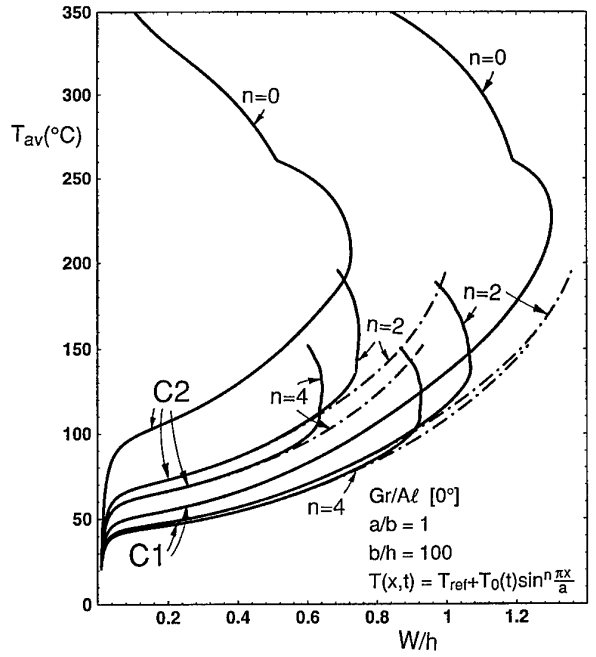

Figure 2. The effect of different types of spatial temperature distributions on the thermal response of a unidirectional clamped plate (boundary conditions C1 and C2). Dashed–dotted lines correspond to a simplified approach to the effect of temperature-dependent material properties.

One can see from Figs 1 and 2 that the in-plane boundary conditions considered in this study have a marked influence on the response curves. For a given set of out-of-plane boundary conditions and temperature loading $T(x,t)$, a plate with immovable edges in the y-direction, $y = 0,b$ (boundary conditions SS1 and C1), undergoes noticeably larger deflections than its counterpart with edges that are unloaded, $y = 0,b$ (boundary conditions SS2 and C2).

The effect of temperature-dependent material properties on the behaviour of a unidirectional plate is illustrated in Fig. 2 for the boundary conditions C1 and C2, and for several types of thermal loading $T(x,t)$. Figure 2 shows the response curves obtained using the method proposed in this paper alongside the graphs resulting from the simplified approach to TDMP (which disregards the spatial distribution of both elastic and viscoplastic material properties at each loading increment). Note that in the case of a uniform temperature change ($n = 0$) the two mentioned approaches obviously coincide. However, in the case of non-uniform heating these approaches lead to substantially different results, both in a quantitative and a qualitative sense.

The behaviour of a $[\pm 30°]$ angle-ply simply-supported plate, which is exposed to a non-uniform heating, $T(\xi, t) = T_{ref} + T_0(t) \sin^2 \pi\xi$, is displayed in Fig. 3. The graphs correspond to several values of width-to-thickness ratio b/h and to the boundary conditions SS1. Figure 3 allows the elastic solutions and the results obtained using both the approach proposed in this study and the simplified treatment of TDMP to be compared. It is seen that whereas the elastic and viscoplastic response curves differ essentially, only a slight dissimilarity may be observed between the elastic solution and its viscoplastic counterpart which treats the effect of temperature dependence of material properties in a simplified manner.

A character of stresses distribution is illustrated in Fig. 4, where the stresses σ_x at the surface $z = h/2$ of a $[\pm 30°]$ plate are presented. Owing to the symmetry, only a quarter of the plate surface is shown. The graphs $\sigma_x(\xi,\eta)$ are plotted at the average temperature $T_{av} = 195.5°C$; they correspond to a uniform temperature change $T(t) = T_{ref} + T_0(t)$ (Fig. 4a) and to localized heating $T(\xi, t) = T_{ref} + T_0(t) \sin^2 \pi\xi$ (Fig. 4b). For the case of localized thermal loading, the results obtained using the

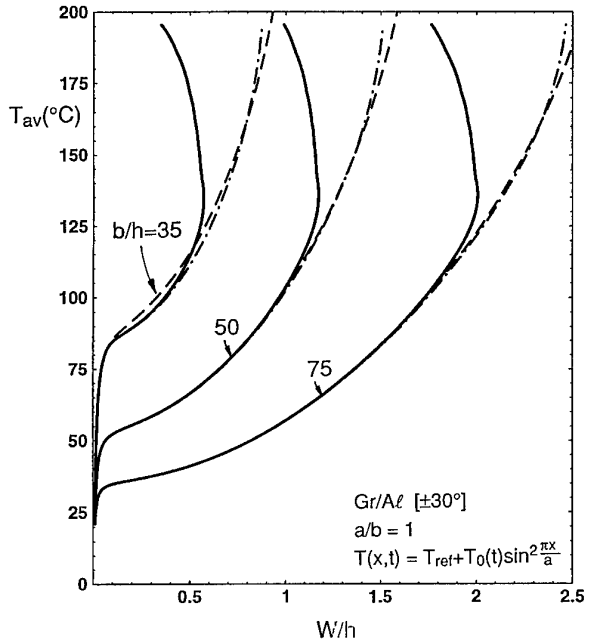

Figure 3. The effect of the length-to-thickness ratio on the thermal response of a $[\pm 30°]$ angle-ply plate (boundary condition SS1). Dashed and dashed–dotted lines correspond, respectively, to the elastic solutions and to a simplified approach to the effect of temperature-dependent material properties.

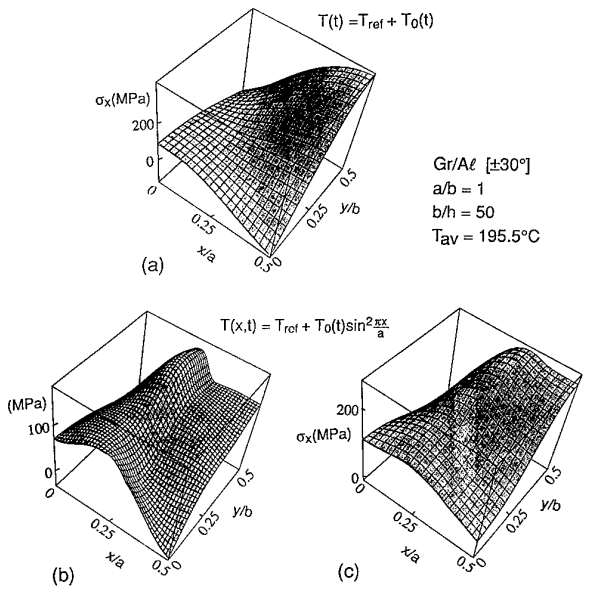

Figure 4. Distribution of a stress σ_x over the surface $z = h/2$ of a $[\pm 30°]$ angle-ply plate (boundary condition SS1). The graphs refer to three cases: (a) uniform thermal loading; (b) non-uniform thermal loading; and (c) non-uniform thermal loading and simplified approach to the effect of temperature-dependent material properties.

simplified treatment of TDMP are displayed in Fig. 4c. We note that the landscape of stress distribution in the non-uniformly heated plate is quite different to those corresponding both to the uniform heating and to the simplified approach to TDMP. Quantitatively, the stresses in case (b) are noticeably smaller than those in cases (a) and (c) in Fig. 4.

From the results obtained it may be concluded that thermal response is affected markedly by the type of spatial temperature distribution the plate is exposed to. The viscoplastic effects in the metallic matrix may have a significant influence on the behaviour of MMC plates. The effect of temperature-dependent material properties, both elastic and viscoplastic, should be taken properly into account.

ACKNOWLEDGEMENTS

The support of this research by the Ministry of Absorption of Israel is gratefully acknowledged.

REFERENCES

1. Taya, M. & Arsenault, R. J., *Metal Matrix Composites*. Pergamon Press, Oxford, 1989.
2. Chen, L.-W. and Chen, L.-Y., Thermal postbuckling behaviours of laminated composite plates with temperature-dependent material properties. *Composite Struct.* 1991, **19**, 267–283.
3. Weller, T. and Patlashenko, I., Postbuckling of infinite length cylindrical panels under combined thermal and pressure loading. *Int. J. Solids Struct.* 1993, **30**, 1649–1662.
4. Feldman, E. and Aboudi, J., Thermal postbuckling of metal matrix laminated plates. *J. Thermal Stresses* 1995, **18**, 197–218.
5. Feldman, E., The effect of temperature-dependent material properties on elasto-viscoplastic buckling behaviour of non-uniformly heated MMC plates. *Composite Struct.* 1995, **35**, 65–74.
6. Aboudi, J., *Mechanics of Composite Materials — A Unified Micromechanical Approach*. Elsevier, Amsterdam, 1991.
7. Simitses, G. J., *Dynamic Stability of Suddenly Loaded Structures*. Springer, New York, 1990.
8. Whitney, J. M., *Structural Analysis of Laminated Anisotropic Plates*. Technomic, Lancaster, PA, 1987.
9. Feldman, E., Postbuckling analysis of laminated plates made of discontinuous metal matrix composites. *Composite Struct.* 1995, **32**, 89–96.
10. Bodner, S.R. and Partom, Y., Constitutive equations for elastic–viscoplastic strain-hardening materials. *J. Appl. Mech.* 1975, **42**, 385–389.

ELSEVIER

Composite Structures Vol. 38, No. 1–4, pp. 91–98
© 1997 Elsevier Science Ltd. All rights reserved
Printed in Great Britain
0263-8223/97/$17.00 + 0.00

PII:S0263-8223(97)00045-7

Design, fabrication and testing of a composite bracket for aerospace applications

H. G. S. J. Thuis & C. Biemans

National Aerospace Laboratory, Voorsterweg 31, 8316 PR Marknesse, The Netherlands

In this paper the results of a programme, in which a composite bracket as a replacement for a metal forging was developed, will be presented. The finite-element method (FEM) in combination with an optimization module was used to design the bracket. Compared to its metal counterpart, the composite bracket demonstrated a weight reduction of 43%. Two composite brackets were fabricated by resin transfer moulding (RTM). One bracket was loaded statically to 1.38 × Design Ultimate Load. The bracket did not fail at this load level. © 1997 Elsevier Science Ltd.

INTRODUCTION

The use of composites in primary aerospace structures is increasing gradually. Until recently one of the most important reasons for using composites instead of metals for these structures was the reduction of weight. However, the last few years a change from 'Design for Minimal Weight' to 'Design to Cost' can be observed. The main goal of this 'Design to Cost' approach is to achieve a reduction in total life-cycle costs of a structure. A way to realize this cost reduction, among others, is to develop new composite materials and fabrication concepts for these materials. One of these fabrication techniques is 'resin transfer moulding' (RTM).

The RTM fabrication concept is based on the injection of resin into a mould cavity containing dry fibres (preform). During the injection process, air in the mould cavity is replaced by resin and the fibres are impregnated. The RTM process has been in use within the automotive industry for many years for limited-production run parts where the cost of tooling for pressed steel construction would be prohibitive, e.g. for sports cars and special purpose vehicles. RTM has also been in use in the aerospace industry for many years for secondary parts such as radomes and flap track fairings. However, until recently, RTM has not been used routinely in the aerospace industry for primary structures because of the lack of high-quality RTM resins and the lack of available material databases adequate for structural substantiation and certification.

Now that high-quality RTM resins are becoming commercially available, RTM is becoming increasingly popular in the aerospace industry. The main improvement of these new RTM resins (besides their improved mechanical properties) is that they have a low viscosity for a reasonable time, enabling large products with high fibre volume fractions to be produced without the use of excessively high injection pressures. Although RTM moulds often are very complex and expensive, RTM has several advantages compared to autoclave prepreg fabrication concepts which, at this moment, are the standard used in the aerospace industry. Some of these advantages are as follows.

- Net shaped products can be made, reducing the amount of trimming required for the cured product.
- Two-sided tooling concepts can be used assuring tight outer-dimensional tolerances, reducing the amount of shimming during assembly.
- No high capital investments (for instance an autoclave) are required.
- Both resin and fibres can be stored for long periods at room temperature.

- Three-dimensional double-curved products can be fabricated which cannot be made using standard autoclave fabrication techniques.

An example of a three-dimensional double-curved composite component is a bracket as a replacement for a metal forging. The potential advantages of these composite brackets are (besides a reduction in weight) a reduction in fabrication and maintenance costs. A major reduction in fabrication costs can be achieved because an RTM mould for such a part can be relatively simple in comparison to an often very complex and expensive forging die. The reduction in maintenance costs can be attributed to the excellent fatigue properties of composites.

In the investigation described in this paper a composite bracket for aerospace applications has been developed. The bracket was fabricated by RTM. To evaluate the composite design it was compared with an existing metal bracket as its counterpart. The main goal of the investigation was to demonstrate the feasibility of a composite bracket as a replacement for a metal version.

THE METAL BRACKET

The metal bracket, which was used as reference for this study, is presented in Fig. 1. The bracket is made of aluminium and has a weight of 314 g. In service the bracket will be connected to a backing structure by two 5/16-inch steel bolts and four 1/4-inch titanium high locks (see Fig. 2). Design Ultimate Load (DUL) for the metal bracket was 33.3 kN in tension and 34.0 kN in compression (see Fig. 2). These tension and compression loads are introduced via

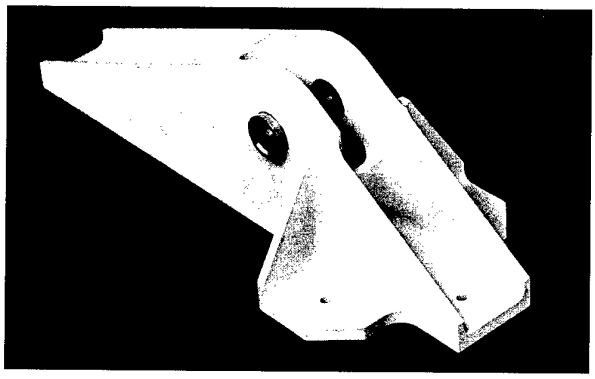

Fig. 1. Metal bracket.

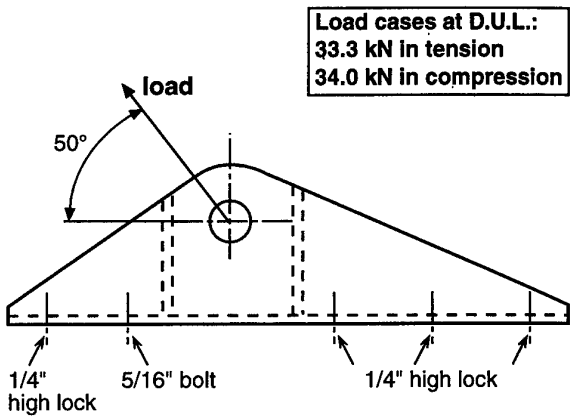

Fig. 2. Static load cases for the metal bracket.

two pin-loaded holes with diameters of 14.0 mm.

COMPOSITE MATERIALS USED

The following materials were used for the composite bracket.

(a) SA Injectex GF420-E01-100 2.5-D (420 g/m^2) carbon fabric with HTA fibres — this balanced fabric has an equal amount of fibres in the warp and weft direction. The mechanical properties of this fabric are not as good as for an unidirectional fabric but it has excellent drapability characteristics and can, therefore, be used in double-curved areas of the bracket.

(b) SA Injectex GU230-E01-100 unidirectional (230 g/m^2) carbon fabric with HTA fibres — this fabric has 90% of its fibres in the warp direction and 10% in the weft direction. Because of the unidirectional character of the fabric, the mechanical performance is excellent but drapability characteristics are poor. Therefore, this fabric can be used in single-curved areas of the bracket.

Low-temperature curing epoxy resin LY5052 and hardener HY5052 were used to impregnate the fibres.

The material properties of the materials used (needed as input for the finite-element analysis) were determined by testing tension ($250 \times 25 \times 3.5$ mm) and compression ($45 \times 40 \times 3.5$ mm) specimens. The specimens were fabricated by RTM and had a fibre volume fraction of 58%.

All tests were performed at ambient conditions. The results of these tests are presented in Table 1.

ANALYSES AND OPTIMIZATION OF THE COMPOSITE BRACKET

The purpose of the programme described in this paper was to demonstrate, in a relatively short period, the feasibility of a composite bracket as a replacement for a metal version. It was decided to use the same kind and number of pin-loaded holes, high locks and bolts in the composite bracket as were used in the metal bracket. The pin-loaded holes, used for load introduction, and the holes for the bolts and high-locks were not modelled in detail to keep the FEM model as simple as possible in order to minimize the time needed for modelling and post-processing.

The composite bracket had to be a functional replacement for the metal bracket. However, it was allowed that the global geometry of the composite bracket differed from the metal bracket. The finite-element code B2000 [1] was used for the analysis. The bracket was modelled using 354 nine-node anisotropic shell elements Q9.st (see Fig. 3). The pin-loaded holes were modelled by introducing the load in two nodes, one node on each side of the bracket. The bolts and high-locks were modelled using boundary conditions which lock all six degrees of freedom in the corresponding nodes in the base of the bracket. Because it was not certain whether a fibre volume fraction of 58% (which was used to determine the material properties) could be realized in the bracket the Design Ultimate Load levels were multiplied by a factor of 1.15.

The bracket was divided into six sections (see Fig. 4) with the following sublaminates:

Sections 1 and 6: $[45°,0°,45°]_{\text{sublaminate 1}}$, $[0°,90°,0°]_{\text{sublaminate 2}}$, $[45°,0°,45°]_{\text{sublaminate 5}}$
Section 2: $[45°,0°,45°]_{\text{sublaminate 1}}$, $[45°,0°,45°]_{\text{sublaminate 5}}$
Section 3: $[45°,0°,45°]_{\text{sublaminate 1}}$, $[0°,90°,0°]_{\text{sublaminate 2}}$, $[0°]_{\text{sublaminate 3}}$, $[90°]_{\text{sublaminate 4}}$, $[45°,0°,45°]_{\text{sublaminate 5}}$
Section 4: $[45°,0°,45°]_{\text{sublaminate 1}}$, $[0°]_{\text{sublaminate 3}}$, $[90°]_{\text{sublaminate 4}}$, $[45°,0°,45°]_{\text{sublaminate 5}}$

Table 1. Test results

	GU230	GF420
E_{1t}	110.0 GPa	59.0 GPa
E_{2t}	3.4 GPa	59.0 GPa
E_{1c}	110.0 GPa	57.0 GPa
E_{2c}	3.4 GPa	57.0 GPa
G_{12}	4.5 GPa	4.5 GPa
σ_{1t}	1500.0 MPa	591.0 MPa
σ_{2t}	70.0 MPa	591.0 MPa
σ_{1c}	633.0 MPa	388.0 MPa
σ_{2c}	70.0 MPa	388.0 MPa
ν_{12}	0.300	0.035
τ_{12}	89.0 MPa	89.0 MPa

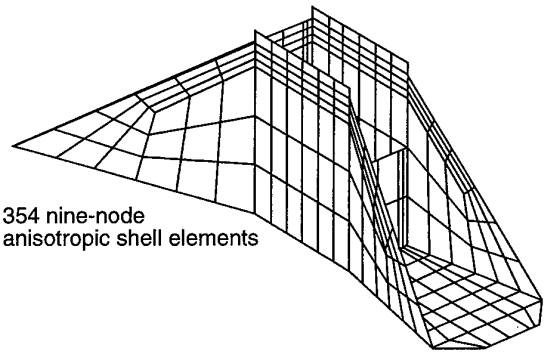

Fig. 3. Finite-element model.

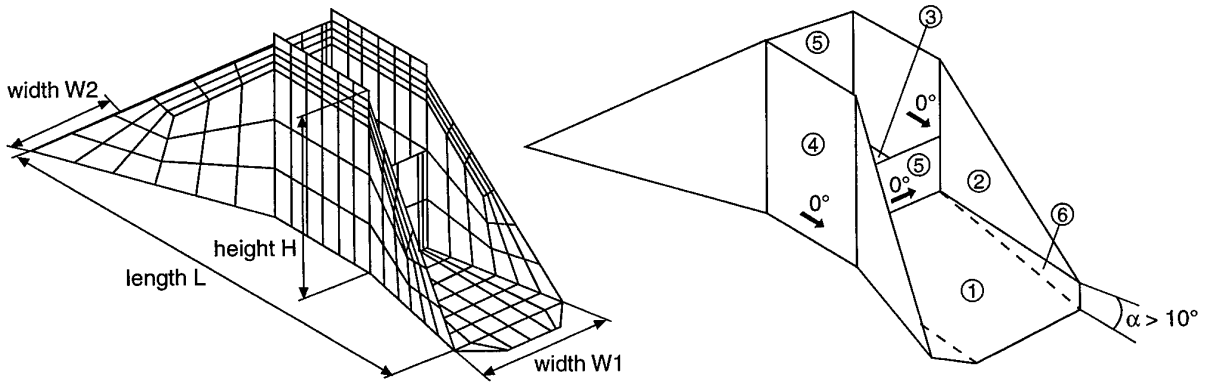

Fig. 4. Geometric design variables and sections 1–6.

Section 5: $[45°,0°,45°]_{\text{sublaminate 1}}$, $[0°]_{\text{sublaminate 3}}$, $[90°]_{\text{sublaminate 4}}$, $[45°,0°,45°]_{\text{sublaminate 5}}$.

The optimization module B2OPT [2] within B2000 was used to optimize the composite bracket. The optimization code minimizes the weight of the bracket while the design is subjected to constraints on stresses and geometric limits. For the optimization the following 10 design variables were defined (see Fig. 4):

- design variable 1 — height H;
- design variable 2 — width W_1;
- design variable 3 — width W_2;
- design variable 4 — length L;
- design variable 5 — number of 45° plies in sublaminates 1 and 5 of sections 1–6;
- design variable 6 — number of 0° plies in sublaminates 1 and 5 of sections 1–6;
- design variable 7 — number of 0° plies in sublaminate 2 of sections 1, 3 and 6;
- design variable 8 — number of 90° plies in sublaminate 2 of sections 1, 3 and 6;
- design variable 9 — number of 0° plies in sublaminate 3 of sections 3, 4 and 5;
- design variable 10 — number of 90° plies in sublaminate 4 of sections 3, 4 and 5.

Sublaminates 1 and 5 were composed of the 2.5-D fabric GF420-E01-100 (because this fabric is symmetric and balanced a 45° layer also can be regarded as a −45° layer, see design variable 5). Sublaminates 2–4 were composed of the unidirectional fabric GU230-E01-100.

The composite bracket had to be a functional replacement for the metal version. Therefore, side-constraints for the optimization were defined to ensure that the optimized bracket stayed within the available assembly window of the metal bracket. In order to avoid fibre wrinkling and ease fabrication of the bracket preform an experimental drape study was carried out to determine the drape limit of the fabrics used. This drape limit was transformed into a side-constraint for the optimization which defined that the angle between sections 1 and 2 of the bracket (see Fig. 4) had to be larger than 10°.

As mentioned before, the pin-loaded holes and holes for the high-locks and bolts were not modelled in detail. To design these holes in the bracket the following design stress levels were used [3]: $\sigma_{\text{bearing}} = 400$ MPa, $\tau_{\text{shear-out}} = 90$ MPa and $\sigma_{\text{tension}} = 388$ MPa. These stress levels, in combination with the diameters of the different holes, determine the dimensions required of the bracket near the holes (see Fig. 5). These minimum dimensions were used as side-constraints for the optimization. The side-constraints were set to values which ensured a bearing failure mode as this failure mode has a fail-safe character [3].

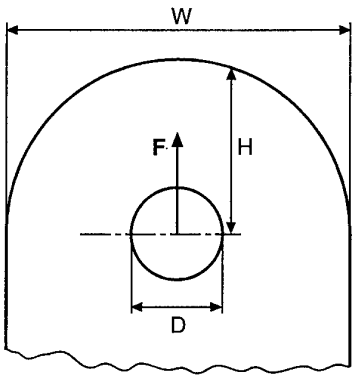

Fig. 5. Global sizing of a pin-loaded hole.

The Tsai–Hill stress criterion was used to predict laminate failure. A number of elements near the load introductions were left out in the determination of laminate failure as these elements were expected to give unrealistically high stresses as a result of the FEM model simplifications.

Figure 6(a) shows the stress distribution of the initial model before optimization. Note the stress concentrations near the load introduction areas. Figure 6(b) presents the stress distribution in the bracket after optimization. Note the change in geometry of the bracket and the uniform stress distribution. Figure 7(a) shows the (uniform) thickness distribution in the bracket before optimization. Figure 7(b) presents the thickness distribution of the bracket after optimization. Note the increase in thickness of the sublaminates to realize the uniform stress distribution and satisfy the side-constraints.

As a result of the optimization, the sublaminates in sections 1–6 had changed as follows.

Section 1 and 6: $[45_2°,0°,45_2°]_{\text{sublaminate 1}}$, $[0_3°,90°,0°,90°,0_3°]_{\text{sublaminate 2}}$, $[45_2°,0°,45_2°]_{\text{sublaminate 5}}$

Section 2: $[45_2°,0°,45_2°]_{\text{sublaminate 1}}$, $[45_2°,0°,45_2°]_{\text{sublaminate 5}}$

Section 3: $[45_2°,0°,45_2°]_{\text{sublaminate 1}}$, $[0_3°,90°,0°,90°,0_3°]_{\text{sublaminate 2}}$, $[0_3°,90°,0°,90°,0_3°,90°,0_3°]_{\text{sublaminates 3 and 4}}$, $[45_2°,0°,45_2°]_{\text{sublaminate 5}}$

Section 4: $[45_2°,0°,45_2°]_{\text{sublaminate 1}}$, $[90_2°,0_3°,90_2°,0°,90_2°,0_3°,90_2°]_{\text{sublaminates 3 and 4}}$, $[45_2°,0°,45_2°]_{\text{sublaminate 5}}$

Section 5: $[45_2°,0°,45_2°]_{\text{sublaminate 1}}$, $[90_2°,0°,90_2°,0°,90_2°,0°,90_2°]_{\text{sublaminates 3 and 4}}$, $[45_2°,0°,45_2°]_{\text{sublaminate 5}}$.

Figure 8 presents the dimensions of the bracket after optimization.

After optimization a buckling analyses was performed to check the stability of the bracket. Figure 9 presents the first buckling mode which occurred at 8.5 × Design Ultimate Load.

FABRICATION OF THE BRACKET

Figure 10 presents the different elements of the RTM mould. All elements of the mould were made of aluminium with the exception of the

Fig. 6. (a) Stress distribution before optimization. (b) Stress distribution after optimization.

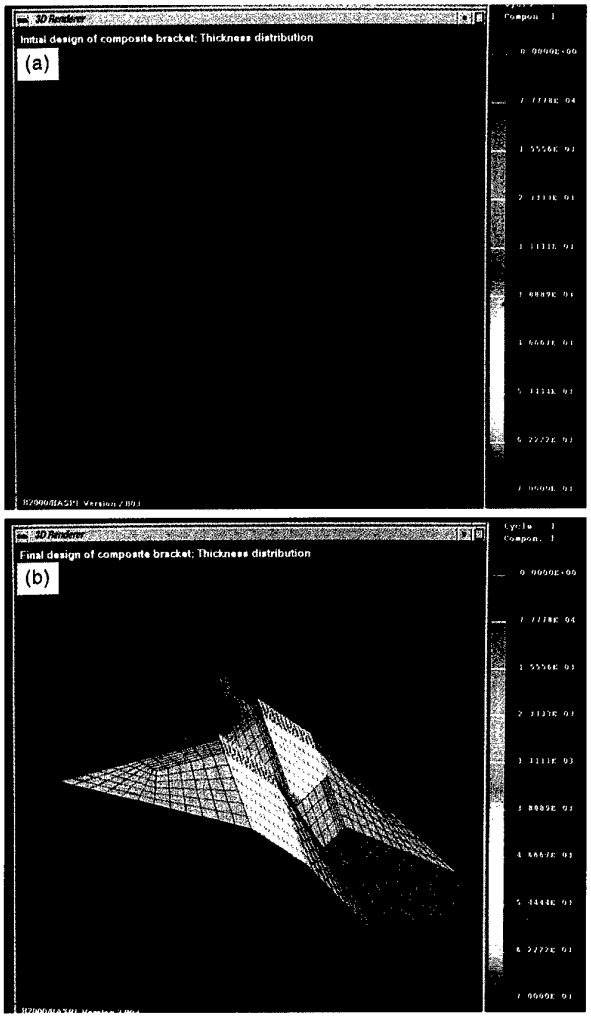

Fig. 7. (a) Thickness distribution before optimization. (b) Thickness distribution after optimization.

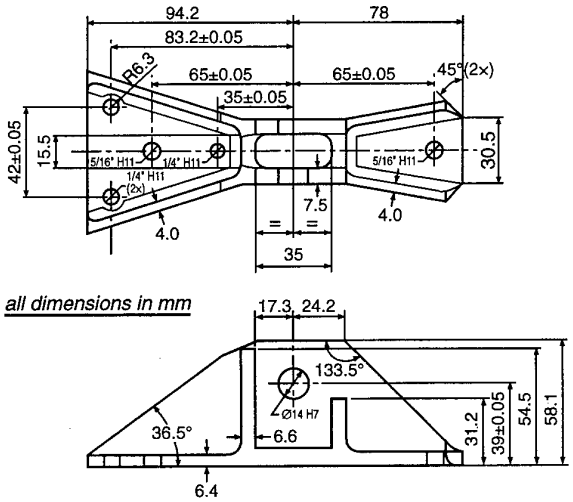

Fig. 8. Dimensions of the composite bracket after optimization.

central part which was made of the elastomer Techtron HPV. Techtron was selected because of its high coefficient of thermal expansion which eases demoulding of this mould element after post-curing the bracket. Because of the modular character of the mould, subpreforms could easily be prepared on the tapered mould elements and the Techtron central part. Then sublaminate 5 was preformed on the subpreforms to complete the preform of the bracket. The final preform was positioned on the mould base plate. Then the mould was closed by bolting the side plates to the base plate and positioning the top plate. Resin was injected through a hole in the Techtron central part via a central injection point in the top plate. Eight vents, located in the side walls, were used to evacuate the air during resin injection.

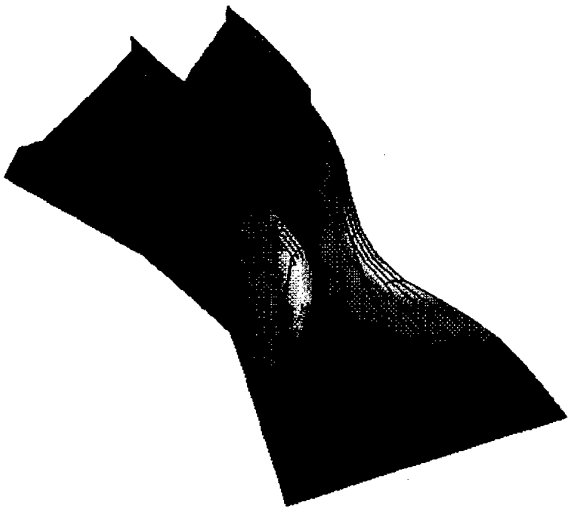

Fig. 9. First buckling mode at 8.5 × Design Ultimate Load.

Based on a cost estimation, it was decided not to fabricate the bracket net shaped but to machine the cured bracket to the required dimensions, as cutting the subpreforms to the net shaped dimensions without fibre distortion at the edges would become very difficult, time-consuming and expensive owing to the small dimensions of the bracket.

Two brackets were fabricated. During resin injection the mould had a temperature 50°C. Resin was injected without vacuum assistance. The RTM pump pressure needed to inject the resin varied from 1.5 bar at the beginning to 3.5 bar at the end of the RTM process. After

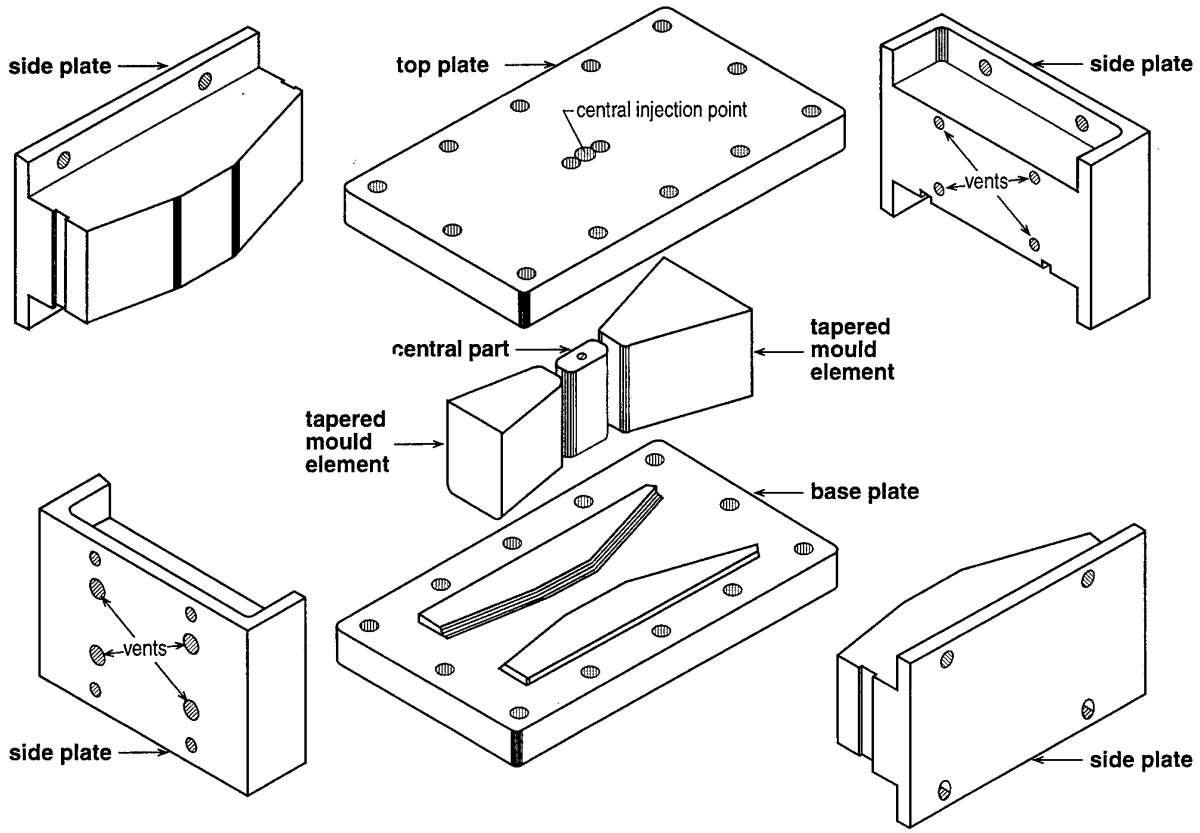

Fig. 10. Elements of the RTM mould.

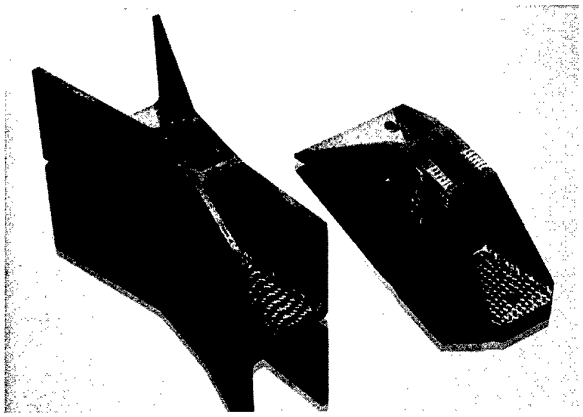

Fig. 11. Composite bracket before and after machining.

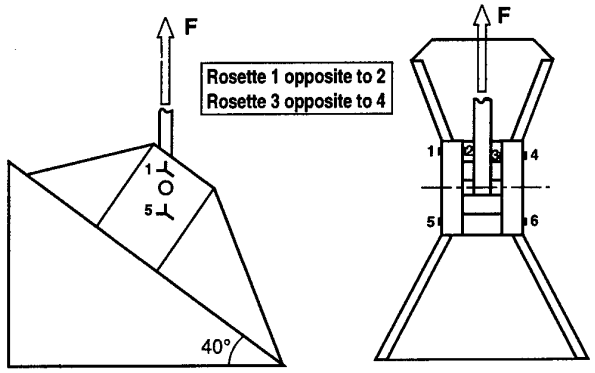

Fig. 12. Test set-up and instrumentation of the bracket.

4 min the preform was wetted. However, in order to ensure a complete impregnation of the fibres in the preform, the resin injection was continued for 20 m. A fibre volume fraction of 55% was achieved with a good laminate quality. The C-scans made indicated that there was no entrapped air or dry spots. Figure 11 shows the bracket before and after machining.

The weight of the bracket after machining was 173 g whereas the aluminium bracket weighed 314 g, which means that a weight reduction of 43% had been realized. Unfortunately, because no data were available on the costs of the metal bracket no cost comparison between the composite and the metal bracket could be made.

TESTING THE BRACKET AND TEST RESULTS

One of the two brackets fabricated was tested statically in tension and compression. During the tests the bracket was mounted in a test set-up on a slope making an angle of 40° (see Fig. 12). Six rosettes (type HBM 6/120RY11) were used to measure strains during the tests (see Fig. 12). The tension and compression loads were introduced to the bracket by a metal bar connected to a screw-driven test machine. Two steel bushes were positioned in the pin-loaded holes of the bracket to fix the metal bar. The tests performed were displacement controlled with a velocity of 0.1 mm/min. The bracket was subjected to the following test programme.

- Test 1 — 0.575 × Tension Design Ultimate Load
- Test 2 — 0.575 × Compression Design Ultimate Load
- Test 3 — 1.15 × Tension Design Ultimate Load
- Test 4 — 1.15 × Compression Design Ultimate Load
- Test 5 — 1.38 × Tension Design Ultimate Load
- Test 6 — 1.38 × Compression Design Ultimate Load.

The bracket was designed for 1.15 × (Design Ultimate Load)$_{\text{metal bracket}}$. During tests 5 and 6 the bracket was loaded to 1.2 × (1.15 Design Ultimate Load)$_{\text{metal bracket}}$. The bracket did not fail at this load level. The bracket was not loaded to failure at this stage because it will be subjected to a fatigue programme in the near future. Figure 13 presents the principle strains of rosettes 1 and 4 (see Fig. 12) measured during test number 3 (1.15 × design Ultimate Load test in tension), and principle strains of rosettes 5 and 6 (see Fig. 12) during test number 4 (1.15 × Design Ultimate Load in compression). Figure 12 indicates that for a certain load level the calculated strains are somewhat lower than the measured strains. This may have been caused by the mismatch in the fibre volume fractions between the specimens used to determine the material properties (58%), which were used as input for the FE analyses, and the fibre volume fraction of 55% obtained in the actual bracket.

CONCLUSIONS

A composite bracket for aerospace applications as a replacement for a metal bracket has been developed. The finite-element method in com-

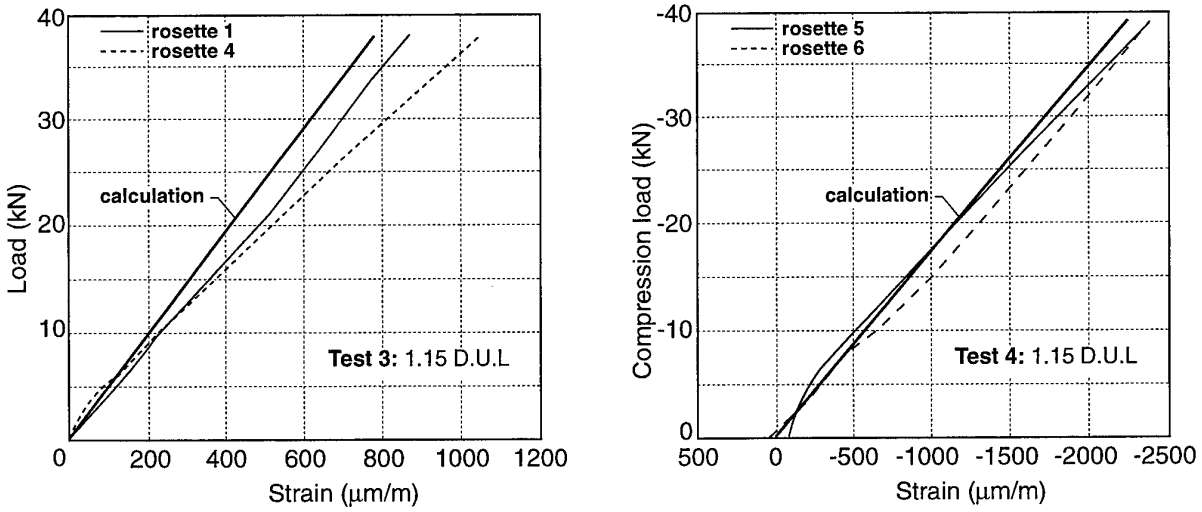

Fig. 13. Calculated and measured load–strain curves.

bination with an optimization module was used to design the bracket.

The weight of the composite bracket was 173 g whereas the aluminium bracket weighed 314 g, which means that a weight reduction of 43% has been realized. Because no data were available on the costs of the metal bracket no cost comparison between the composite and the metal bracket could be made.

An RTM mould and modular preforming concept to produce the composite bracket have been developed. Two composite brackets were fabricated. One bracket was subjected to a test programme in which the bracket was loaded to 1.38 × Design Ultimate Load in both tension and compression. The bracket did not fail at this load level.

REFERENCES

1. Merazzi, S., Modular finite element analysis tools applied to problems in engineering. Ph.D. thesis 1251, Ecole Polythenique Federale de Lausanne (EPFL), Lausanne, 1994.
2. Arendsen, P., *The B2000 Optimization Module: B2OPT.* NLR Technical Publication TP 94116 L, published as part of the GARTEUR AG13. Structural Optimization Action Group Report, 1993.
3. Thuis, H. G. S. J., Design stress levels and rough design rules for CFRP structures with concentrated load introductions — an experimental study. NLR technical report TR 97045 L, 1997.

ELSEVIER

Composite Structures Vol. 38, No. 1–4, pp. 99–110
© 1997 Elsevier Science Ltd. All rights reserved
Printed in Great Britain
0263-8223/97/$17.00 + 0.00

PII:S0263-8223(97)00046-9

Multiple eigenvalue optimization of composite structures using discrete third order displacement models

C. M. Mota Soares*, C. A. Mota Soares

IDMEC/I.S.T.-Instituto de Engenharia Mecânica-Instituto Superior Técnico, Av. Rovisco Pais, 1096, Lisboa, Codex, Portugal

&

V. M. Franco Correia

ENIDH-Escola Náutica Infante D. Henrique, Av. Eng. Bonneville Franco, Paço de Arcos, 2780 Oeiras, Portugal

This paper deals with the implementation and test of a non-smooth eigenfrequency based criterion to evaluate the directional derivatives applied to multilaminated plate structures, when non-differentiable multiple eigenfrequencies occur during the structural optimization process. The algorithm is applied to a family of C^0 Lagrangian higher order shear deformation theory discrete models. Angle ply design variables and vectorial distances from the laminate middle surface to the upper surface of each ply are considered as design variables. The efficiency and accuracy of the algorithm developed is discussed with an illustrative case. The analytical single and/or directional derivatives are compared to forward finite difference derivatives for the developed discrete models. © 1997 Elsevier Science Ltd.

INTRODUCTION

Laminated composite materials are being widely used in many industries mainly because they allow design engineers to achieve very important weight reductions when compared to traditional materials and also because more complex shapes can be easily obtained. The mechanical behavior of a laminate is strongly dependent on the fiber directions and because of this the laminate should be designed to meet the specific requirements of each particular application in order to obtain the maximum advantages of such materials. Accurate and efficient structural analysis, design sensitivity analysis and optimization procedures are very important to accomplish this task. Structural optimization with behavioral constraints, such as stress failure criterion, maximum deflection, natural frequencies and buckling load can be very useful in significantly improving the performance of the structures by manipulating certain design variables. Design sensitivity analysis is important to accurately know the effects of design variables changes on the performance of structures by calculating the search directions to find an optimum design. To evaluate these sensitivities efficiently and accurately it is important to have appropriate techniques associated to good structural models.

It is well known that the analysis of laminated composite structures by using the classical Kirchhoff assumptions can lead to substantial errors for moderately thick plates or shells. This is mainly due to neglecting the transverse shear deformation effects which become very important in composite materials with low ratios of transverse shear modulus to in-plane modulus. This can be attenuated by Mindlin's first order shear deformation theory [1,2], but this theory yields a constant shear strain variation through the thickness and therefore requires the use of shear correction factors [3] in order to approximate the quadratic distribution in the elasticity

*Address for correspondence: IDMEC/I.S.T.-Instituto de Engenharia Mecânica-Instituto Superior Técnico, Av. Rovisco Pais, 1096 Lisboa, Codex, Portugal.

theory. More accurate numerical models such as three-dimensional finite elements models can be used with adequate refined meshes in order to contemplate acceptable aspect ratios, but these models are computationally expensive. A compromising less expensive situation can be achieved by using single layer models, based on higher order displacement fields involving higher order expansions of the displacement field in powers of the thickness coordinate. These models can accurately account for the effects of transverse shear deformation yielding quadratic variation of out-of-plane strains and therefore do not require the use of artificial shear correction factors and are suitable for the analysis of highly anisotropic plates ranging from high to low length-to-thickness ratios.

Pioneering work on the structural analysis formulation based in higher order displacement fields can be reviewed in Lo *et al.* [4,5], where a theory which accounts for the effects of transverse shear deformation, transverse strain and nonlinear distribution of the in-plane displacements with respect to thickness coordinate is developed. Third order theories have been proposed and/or reviewed by several researchers [6–15].

Recently, Abrate [16] gave a perspective of work carried out by different researchers in the field of the optimum design of composite laminated plates and shells subjected to constraints on strength, stiffness, buckling loads and fundamental natural frequencies. Most of the papers reviewed are based on variational approximation methods. The use of higher order models as well as the problem of non-differentiability of multiple eigenvalues that may occur during the structural optimization process is not mentioned.

Multiple eigenfrequencies do appear frequently on complex structures. It is known [17–34] that multiple eigenvalues are not differentiable in the common sense and therefore analytical single design sensitivity analysis [35] cannot be used. When this problem occurs it can be overcome by evaluating the directional derivatives using the concept of generalized gradient [24]. An overview of recent developments in this area, mainly related to isotropic structures, can be found in Ollhoff *et al.* [30], Seyranian *et al.* [31] and Seyranian [34] among others.

In the present paper C^0 nine node Lagrangian higher order models applied to eigenfrequency sensitivity analysis of multilaminated thin-to-thick plate structures [36] is extended to contemplate the non-differentiability of multiple eigenfrequencies.

The design variables considered are the ply orientation angles of the fibers and the vectorial distances from the laminated middle surface to the upper surface of each layer. The sensitivities of eigenfrequency response with respect to the design variables are evaluated analytically. An illustrative numerical example is presented to validate the feasibility of the proposed design sensitivity approach to evaluate directional derivatives when multiple eigenvalues are involved.

HIGHER ORDER DISPLACEMENT FIELDS

In order to approximate the three-dimensional elasticity problem to a two-dimensional laminate problem, the displacement components $u(x,y,z,t)$, $v(x,y,z,t)$ and $w(x,y,z,t)$ at any point in the laminate space (Fig. 1) are expanded in Taylor's series powers of the thickness coordinate z. The following higher order displacement fields can be written [11]

HSDT 11

$$u(x,y,z,t) = u_0(x,y,t)+z\theta_x(x,y,t)+z^2u_0^*(x,y,t)+z^3\varphi_x^*(x,y,t)$$
$$v(x,y,z,t) = v_0(x,y,t)+z\theta_y(x,y,t)+z^2v_0^*(x,y,t)+z^3\varphi_y^*(x,y,t)$$
$$w(x,y,z,t) = w_0(x,y,t)+z\varphi_z(x,y,t)+z^2w_0^*(x,y,t) \quad (1)$$

HSDT 9

$$u(x,y,z,t) = u_0(x,y,t)+z\theta_x(x,y,t)+z^2u_0^*(x,y,t)+z^3\varphi_x^*(x,y,t)$$
$$v(x,y,z,t) = v_0(x,y,t)+z\theta_y(x,y,t)+z^2v_0^*(x,y,t)+z^3\varphi_y^*(x,y,t)$$
$$w(x,y,z,t) = w_0(x,y,t) \quad (2)$$

where u, v, w are the displacement components of generic point in the x, y, z directions, u_0, v_0, w_0 are the displacements of a generic point on the reference surface, t is the time, θ_x, θ_y are the rotations

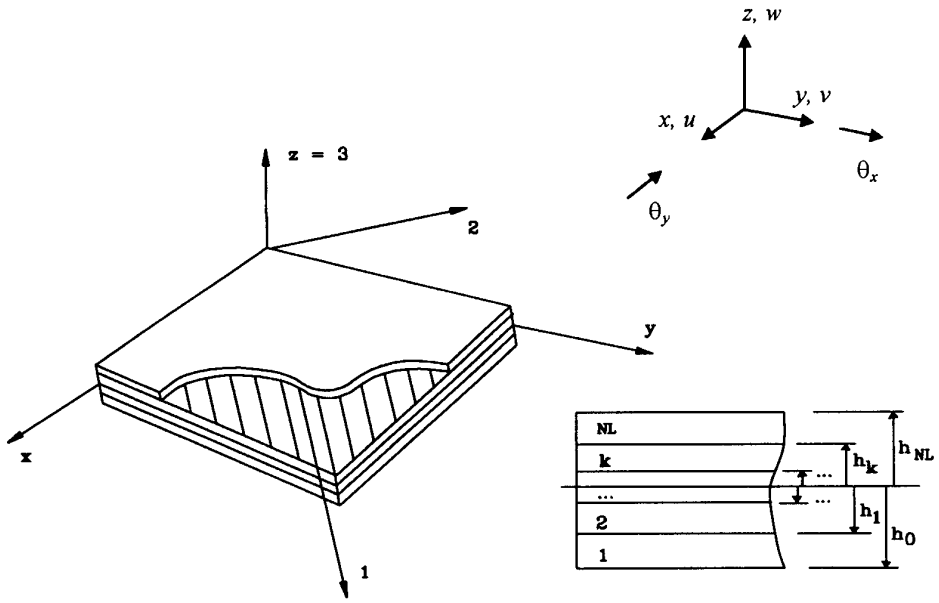

Fig. 1. Laminate geometry and coordinate systems (x, y, z) and (1, 2, 3).

of normal to the reference surface about the y and x axes respectively and φ_z, u_0^*, v_0^*, w_0^*, φ_x^*, φ_z^* are the higher order terms in the Taylor's series expansions, defined at the reference surface.

FINITE ELEMENT MODEL

The finite element formulation for the displacement field HSDT 11 represented by eqn (1) applied to 9-node Lagrangian quadrilateral elements, will be briefly described. The strain components are given by

$$\begin{Bmatrix} \varepsilon_{xx} \\ \varepsilon_{yy} \\ \varepsilon_{zz} \\ \gamma_{xy} \end{Bmatrix} = \begin{Bmatrix} \dfrac{\partial u_0}{\partial x} \\ \dfrac{\partial v_0}{\partial y} \\ \varphi_z \\ \dfrac{\partial u_0}{\partial y} + \dfrac{\partial v_0}{\partial x} \end{Bmatrix} + z \begin{Bmatrix} \dfrac{\partial \theta_x}{\partial x} \\ \dfrac{\partial \theta_y}{\partial y} \\ 2w_0^* \\ \dfrac{\partial \theta_x}{\partial y} + \dfrac{\partial \theta_y}{\partial x} \end{Bmatrix} + z^2 \begin{Bmatrix} \dfrac{\partial u_0^*}{\partial x} \\ \dfrac{\partial v_0^*}{\partial y} \\ 0 \\ \dfrac{\partial u_0^*}{\partial y} + \dfrac{\partial v_0^*}{\partial x} \end{Bmatrix} + z^3 \begin{Bmatrix} \dfrac{\partial \varphi_x^*}{\partial x} \\ \dfrac{\partial \varphi_y^*}{\partial y} \\ 0 \\ \dfrac{\partial \varphi_x^*}{\partial y} + \dfrac{\partial \varphi_y^*}{\partial x} \end{Bmatrix} \tag{3}$$

$$\begin{Bmatrix} \gamma_{yz} \\ \gamma_{xz} \end{Bmatrix} = \begin{Bmatrix} \theta_y + \dfrac{\partial w_0}{\partial y} \\ \theta_x + \dfrac{\partial w_0}{\partial x} \end{Bmatrix} + z \begin{Bmatrix} 2v_0^* + \dfrac{\partial \varphi_z}{\partial y} \\ 2u_0^* + \dfrac{\partial \varphi_z}{\partial x} \end{Bmatrix} + z^2 \begin{Bmatrix} 3\varphi_x^* + \dfrac{\partial w_0^*}{\partial y} \\ 3\varphi_x^* + \dfrac{\partial w_0^*}{\partial x} \end{Bmatrix} \tag{4}$$

The strains can be written as

$$\begin{Bmatrix} \varepsilon_{xx} \\ \varepsilon_{yy} \\ \varepsilon_{zz} \\ \gamma_{xy} \end{Bmatrix} = Z_{bm}\varepsilon_{bm}^*, \quad \begin{Bmatrix} \gamma_{yz} \\ \gamma_{xz} \end{Bmatrix} = Z_s\varepsilon_s^* \tag{5}$$

where Z_{bm} and Z_s are matrices containing powers of z coordinate (z^n with $n = 0, ..., 3$) defined in accordance with displacement fields and strain relations and ε^*_{bm} and ε^*_s are vectors containing the bending and membrane terms of the strain components and the transverse shear, respectively, given by

$$\varepsilon^*_{bm} = \left\{ \frac{\partial u_0}{\partial x}, \frac{\partial v_0}{\partial y}, \varphi_z, \frac{\partial u_0}{\partial y} + \frac{\partial v_0}{\partial x}, \frac{\partial u^*_0}{\partial x}, \frac{\partial v^*_0}{\partial y}, \frac{\partial u^*_0}{\partial y} + \frac{\partial v^*_0}{\partial x}, \frac{\partial \theta_x}{\partial x}, \frac{\partial \theta_y}{\partial y}, 2w_0, \frac{\partial \theta_x}{\partial y} + \frac{\partial \theta_y}{\partial x}, \frac{\partial \varphi^*_x}{\partial x}, \frac{\partial \varphi^*_y}{\partial y}, \frac{\partial \varphi^*_x}{\partial y} + \frac{\partial \varphi^*_y}{\partial x} \right\}^{\mathrm{T}} \tag{6}$$

$$\varepsilon^*_s = \left\{ \theta_y + \frac{\partial w_0}{\partial y}, \theta_x + \frac{\partial w_0}{\partial x}, 2v^*_0 + \frac{\partial \varphi_z}{\partial y}, 2u^*_0 + \frac{\partial \varphi_z}{\partial x}, 3\varphi^*_y + \frac{\partial w^*_0}{\partial y}, 3\varphi^*_x + \frac{\partial w^*_0}{\partial x} \right\}^{\mathrm{T}} \tag{7}$$

Using C^0 Lagrangian shape functions [1,37] the displacements and generalized displacements defined in the reference surface are obtained within each element, respectively, by

$$\begin{Bmatrix} u \\ v \\ w \end{Bmatrix} = Z_m \{u_0\ v_0\ w_0\ \theta_x\ \theta_y\ \varphi_z\ u^*_0\ v^*_0\ w^*_0\ \varphi^*_x\ \varphi^*_y\}^{\mathrm{T}} \tag{8}$$

$$\{u_0\ v_0\ w_0\ \theta_x\ \theta_y\ \varphi_z\ u^*_0\ v^*_0\ w^*_0\ \varphi^*_y\}^{\mathrm{T}} = \sum_{i=1}^{9} N_i q^e_i \tag{9}$$

where Z_m is a matrix containing powers of z coordinate defined in accordance with the displacement field, N_i are the Lagrange shape functions of node i and q^e_i is the displacement vector of node i which is related to the displacement vector of the element, q^e, by

$$q^e = \{...q^e_i...\}^{\mathrm{T}},\ i = 1, ..., 9 \tag{10}$$

The strains in eqns (6) and (7) are represented as

$$\begin{Bmatrix} \varepsilon^*_{bm} \\ \varepsilon^*_s \end{Bmatrix} = \begin{bmatrix} B_{bm} \\ B_s \end{bmatrix} q^e \tag{11}$$

where B_{bm} and B_s are the strain-displacement matrices, respectively, for bending and membrane and transverse shear, relating the degrees-of-freedom of the element with the strain components.

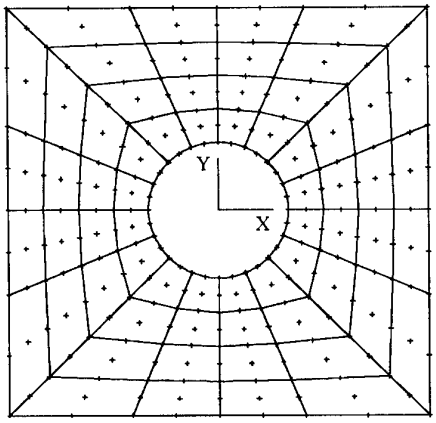

Fig. 2. Square plate with central circular hole — finite element mesh.

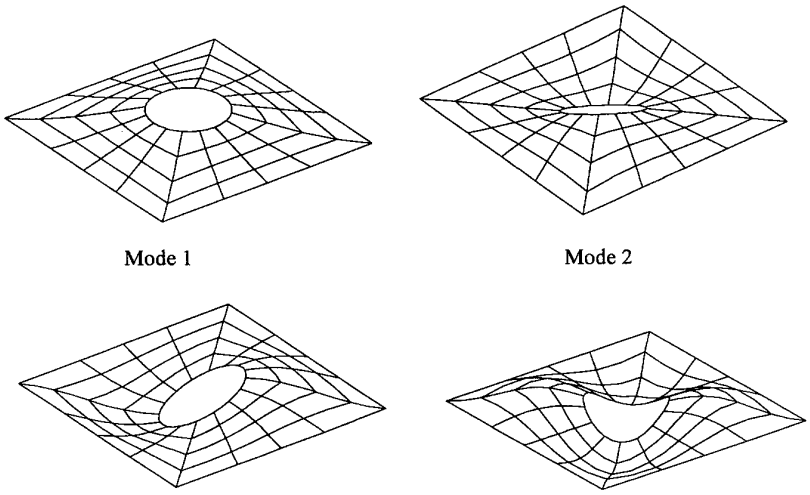

Fig. 3. Vibration modes for lamination sequence [45°/−45°].

Applying Hamilton's principle to the Lagrangian functional assuming small displacements and adding the contributions of all finite elements in the domain one obtains for free harmonic vibration the equilibrium equation of the finite element discretized structure

$$(K-\lambda_n M)q_n = 0,\ n = 1,\ \ldots,\ N \tag{12}$$

where K and M are respectively the structure stiffness matrix and mass matrix and N represents the total number of degrees of freedom. The solution of this eigenvalue problem consists of N eigenvalues $\lambda_n = \omega_n^2$ and corresponding eigenvectors q_n, where ω_n is the natural frequency of mode n. K and M matrices are obtained by assembling in the usual way the corresponding element matrices K_e, M_e.

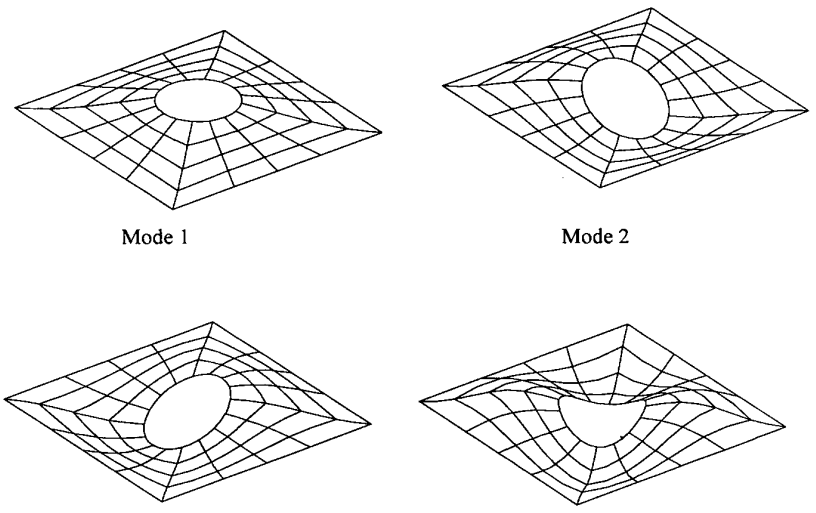

Fig. 4. Vibration modes for lamination sequence [30°/−60°].

Table 1. Eigenfrequency sensitivities in order to ply angles obtained with Q9-HSDT 11 model, for simply supported 2-ply [45°/−45°] square plate with central circular hole

Frequency (rad/s)		Direction (θ_1, θ_2)	Analytical sensitivities		Global finite difference[a]
			Multiple	Single	
146.0411	$d\omega_1/dc$	1,0	—	-0.163641×10^{-5}	-0.802172×10^{-2}
		0,1	—	0.163641×10^{-5}	0.229122×10^{-2}
259.5086	$d[\min(\omega_2, \omega_3)]/dc$	1,0	−44.7128	43.6214	−44.7136
		0,1	−44.7128	−43.6214	−44.7102
		$\frac{1}{\sqrt{5}}, \frac{2}{\sqrt{5}}$	−19.9962	−19.5081	−19.7928
259.5086	$d[\max(\omega_2, \omega_3)]/dc$	1,0	44.7128	−43.6214	44.7073
		0,1	44.7128	43.6214	44.7079
		$\frac{1}{\sqrt{5}}, \frac{2}{\sqrt{5}}$	19.9962	19.5081	19.79225
445.8111	$d\omega_4/dc$	1,0	—	-0.498112×10^{-6}	0.114643×10^{-2}
		0,1	—	0.498058×10^{-6}	-0.114643×10^{-2}

[a]Increment for forward finite difference derivatives $\delta = 0.000001°$.

Table 2. Eigenfrequency sensitivities in order to ply angles obtained with Q9-HSDT 11 model, for simply supported 2-ply [30°/−60°] square plate with central circular hole

Frequency (rad/s)		Direction (θ_1, θ_2)	Analytical sensitivities		Global finite difference[a]
			Multiple	Single	
130.0205	$d\omega_1/dc$	1,0	—	47.1639	47.1590
		0,1	—	47.1639	47.1527
254.0572	$d[\min(\omega_2, \omega_3)]/dc$	1,0	−26.7139	56.7199	−26.7067
		0,1	−26.7139	−18.3624	−26.7130
		$\frac{1}{\sqrt{5}}, \frac{2}{\sqrt{5}}$	5.20718	8.94208	5.31705
254.0572	$d[\max(\omega_2, \omega_3)]/dc$	1,0	65.0715	−18.3623	65.0594
		0,1	65.0715	56.7199	65.0622
		$\frac{1}{\sqrt{5}}, \frac{2}{\sqrt{5}}$	46.2549	42.5200	45.9627
426.0753	$d\omega_4/dc$	1,0	—	63.6208	63.6195
		0,1	—	63.6208	63.6212

[a]Increment for forward finite difference derivatives $\delta = 0.000001°$.

Table 3. Eigenfrequency sensitivities in order to ply angles obtained with Q9-HSDT 9 model, for simply supported 2-ply [45°/−45°] square plate with central circular hole

Frequency (rad/s)		Direction (θ_1, θ_2)	Analytical sensitivities		Global finite difference[a]
			Multiple	Single	
145.9545	$d\omega_1/dc$	1,0	—	-0.162070×10^{-5}	-0.200543×10^{-1}
		0,1	—	0.162070×10^{-5}	-0.160434×10^{-1}
259.3818	$d[\min(\omega_2, \omega_3)]/dc$	1,0	−44.7366	14.7842	−44.7446
		0,1	−44.7367	−14.7842	−44.7360
		$\frac{1}{\sqrt{5}}, \frac{2}{\sqrt{5}}$	−20.0068	−6.61170	−19.6851
259.3818	$d[\max(\omega_2, \omega_3)]/dc$	1,0	44.7367	−14.7842	44.7280
		0,1	44.7366	14.7842	44.7245
		$\frac{1}{\sqrt{5}}, \frac{2}{\sqrt{5}}$	20.0068	6.61170	19.6737
445.5345	$d\omega_4/dc$	1,0	—	-0.458874×10^{-6}	-0.114643×10^{-2}
		0,1	—	0.458800×10^{-6}	0.171964×10^{-2}

[a]Increment for forward finite difference derivatives $\delta = 0.000001°$.

The stiffness and mass matrices of the element are evaluated, respectively, as

$$K_e = \int_{-1}^{+1}\int_{-1}^{+1} \begin{bmatrix} B_{bm}^T \\ B_s^T \end{bmatrix} \left(\sum_{k=1}^{NL} \int_{h_{k-1}}^{h_k} \begin{bmatrix} Z_{bm}^T \\ Z_s^T \end{bmatrix} \bar{Q}_k \begin{bmatrix} Z_{bm} \\ Z_s \end{bmatrix} \mathrm{d}z \right) \begin{bmatrix} B_{bm} \\ B_s \end{bmatrix} \det J \, \mathrm{d}\xi \mathrm{d}\eta \tag{13}$$

$$M_e = \int_{-1}^{+1}\int_{-1}^{+1} N^T \left(\sum_{k=1}^{NL} \rho_k \int_{h_{k-1}}^{h_k} Z_m^T Z_m \, \mathrm{d}z \right) N \det J \, \mathrm{d}\xi \mathrm{d}\eta \tag{14}$$

where $\bar{Q}_k$ is the constitutive matrix in the (x, y, z) laminate axes for kth ply [6,7,38], N is the matrix of the Lagrange shape functions and (k the material density of kth layer. NL is the number of layers of the laminate, h_k is the vector distance from the middle surface of the laminate to the upper side of kth ply (Fig. 1). Finally, det J is the determinant of the Jacobian matrix of the transformation from (ξ, η) natural coordinates to element (x, y, z) coordinates.

The finite element model having the displacement field represented by eqn (1), will be referred to as Q9-HSDT 11. The element which displacement field is given by eqn (2) is developed easily from this parent element by deleting the appropriate degrees of freedom leading to the finite element discrete model referred to as Q9-HSDT 9. The C^0 9-node Lagrangian first order discrete model, referred to as Q9-FSDT 5, can also be obtained by deleting all high order terms and introducing shear correction factors [1–3,38].

SENSITIVITY ANALYSIS

For single eigenvalues, considering a vibration mode $\mathbf{q}_p$ which corresponds the natural frequency ω_p normalized through the relation $\mathbf{q}_p^T \mathbf{M} \mathbf{q}_p = 1$, the sensitivities of natural frequency with respect to changes in the design variable b_i are [35]

$$\frac{\mathrm{d}\omega_p}{\mathrm{d}b_i} = \frac{1}{2\omega_p} \mathbf{q}_p^T \left(\frac{\partial \mathbf{K}}{\partial b_i} - \omega_p^2 \frac{\partial \mathbf{M}}{\partial b_i} \right) \mathbf{q}_p \tag{15}$$

these sensitivities can be efficiently obtained at element level through

$$\frac{\mathrm{d}\omega_p}{\mathrm{d}b_i} = \frac{1}{2\omega_p} \sum_{l \in E} \mathbf{q}_p^{T^{e^l}} \left(\frac{\partial \mathbf{K}_e^l}{\partial b_i} - \omega_p^2 \frac{\partial \mathbf{M}_e^l}{\partial b_i} \right) \mathbf{q}_p^{e^l} \tag{16}$$

where E represents the set of elements in which the design variable b_i is defined.

In the case of multiple eigenvalues, if $\lambda_j = \lambda_{j+1} = ... = \lambda_{j+m}$ are the eigenvalues with $m+1$ multiplicity and $\mathbf{q}_j = \mathbf{q}_{j+1} = ... = \mathbf{q}_{j+m}$ are orthonormal eigenvectors of λ_j, then the directional derivatives in the direction $\mathbf{c} = \{c_1, ..., c_i, ..., c_{ndv}\}$, where $_{ndv}$ is the number of design variables, are obtained by calculating the eigenvalues of the χ matrix of dimension $(m+1) \times (m+1)$ whose elements are evaluated by [31,33]

$$\chi_{pq} = \sum_{i=1}^{ndv} c_i \left\{ \sum_{l \in E} \mathbf{q}_p^{T^{e^l}} \left(\frac{\partial \mathbf{K}_e^l}{\partial b_i} - \lambda_j \frac{\partial \mathbf{M}_e^l}{\partial b_i} \right) \mathbf{q}_p^{e^l} \right\}, \quad p, q = j, ..., j = m \tag{17}$$

where the vector $\mathbf{c}$ has the norm $\|\mathbf{c}\| = \sqrt{c_1^2 + ... + c_i^2 + ... + c_{ndv}^2} = 1$. Let us define the functions

$$f_1 = \max(\lambda_j, \lambda_{j+1}, ..., \lambda_{j+m}) \tag{18}$$

$$f_2 = \min(\lambda_j, \lambda_{j+1}, ..., \lambda_{j+m}) \tag{19}$$

If μ_1 and μ_2 are respectively the maximum and minimum eigenvalues of matrix χ then the directional derivatives of the functions f_1 and f_2 in the direction $\mathbf{c}$ are given by

$$\frac{\mathrm{d}f_1}{\mathrm{d}\mathbf{c}} = \mu_1 \text{ and } \frac{\mathrm{d}f_2}{\mathrm{d}\mathbf{c}} = \mu_2 \tag{20}$$

For comparison purposes the eigenfrequency directional derivatives in the direction **c** can be obtained by forward finite difference by

$$\frac{df}{d\mathbf{c}} = \frac{f(\mathbf{a}) - f(\mathbf{b})}{\delta} \tag{21}$$

The perturbed design represented by vector **a** is given by

$$\mathbf{a} = \mathbf{b} + \delta\mathbf{c} \tag{22}$$

where δ is a small positive design perturbation and $\mathbf{b} = \{b_1, ..., b_i, ..., b_{ndv}\}$ is the vector of design variables.

NUMERICAL APPLICATION

The free vibration problem of a 2-ply simply supported square plate with a central circular hole is considered. The side dimension of the plate is $a = 2$ m and the hole diameter is $a/3$. A finite element mesh with 288 elements and 64 nodes is used (Fig. 2). The simply supported boundary conditions for HSDT 11 model were taken as $u_0 = u_0^* = w_0 = w_0^* = \theta_x = \varphi_x^* = \varphi_z = 0$ at $y = \pm a/2$ and $v_0 = v_0^* = w_0 = w_0^* = \theta_y = \varphi_y^* = \varphi_z = 0$ at $x = \pm a/2$. The boundary conditions for HSDT 9 and FSDT 5 models can be obtained from HSDT 11 by deleting the appropriate terms.

Table 4. Eigenfrequency sensitivities in order to ply angles obtained with Q9-HSDT 9 model, for simply supported 2-ply [30°/−60°] square plate with central circular hole

Frequency (rad/s)		Direction (θ_1, θ_2)	Analytical sensitivities		Global finite difference[a]
			Multiple	Single	
129.9607	$d\omega_1/d\mathbf{c}$	1,0	—	47.0852	47.0931
		0,1	—	47.0851	47.0874
253.9611	$d[\min(\omega_2, \omega_3)]/d\mathbf{c}$	1,0	−26.8269	63.9992	−26.8150
		0,1	−26.8269	−25.8454	−26.8173
		$\frac{1}{\sqrt{5}}, \frac{2}{\sqrt{5}}$	5.06551	5.50448	5.37664
253.9611	$d[\max(\omega_2, \omega_3)]/d\mathbf{c}$	1,0	64.9806	−25.8454	64.9803
		0,1	64.9806	63.9991	64.9769
		$\frac{1}{\sqrt{5}}, \frac{2}{\sqrt{5}}$	46.1231	45.6841	45.7667
425.8654	$d\omega_4/d\mathbf{c}$	1,0	—	63.3884	63.3926
		0,1	—	63.3884	63.3926

[a]Increment for forward finite difference derivatives $\delta = 0.000001°$.

Table 5. Eigenfrequency sensitivities in order to ply angles obtained with Q9-FSDT 5 model, for simply supported 2-ply [45°/−45°] square plate with central circular hole

Frequency (rad/s)		Direction (θ_1, θ_2)	Analytical sensitivities		Global finite difference[a]
			Multiple	Single	
146.2792	$d\omega_1/d\mathbf{c}$	1,0	—	-0.165879×10^{-5}	0.401086×10^{-2}
		0,1	—	0.165879×10^{-5}	0.000000
259.8325	$d[\min(\omega_2, \omega_3)]/d\mathbf{c}$	1,0	−44.5991	−27.6453	−44.5967
		0,1	−44.5991	27.6453	−44.5985
		$\frac{1}{\sqrt{5}}, \frac{2}{\sqrt{5}}$	−19.9453	12.3634	−19.6192
259.8325	$d[\max(\omega_2, \omega_3)]/d\mathbf{c}$	1,0	44.5991	27.6453	44.6002
		0,1	44.5991	−27.6453	44.5956
		$\frac{1}{\sqrt{5}}, \frac{2}{\sqrt{5}}$	19.9453	−12.3634	19.6249
446.5281	$d\omega_4/d\mathbf{c}$	1,0	—	−56.2312	0.000000
		0,1	—	56.2316	-0.573212×10^{-3}

[a]Increment for forward finite difference derivatives $\delta = 0.000001°$.

Table 6. Eigenfrequency sensitivities in order to ply angles obtained with Q9-FSDT 5 model, for simply supported 2-ply [30°/−60°] square plate with central circular hole

Frequency (rad/s)		Direction (θ_1, θ_2)	Analytical sensitivities		Global finite difference[a]
			Multiple	Single	
130.1740	$d\omega_1/dc$	1,0	—	47.4291	47.4421
		0,1	—	47.4291	47.4426
254.2542	$d[\min(\omega_2, \omega_3)]/dc$	1,0	−26.3020	32.8684	−26.2925
		0,1	−26.3020	6.21572	−26.2982
		$\frac{1}{\sqrt{5}}, \frac{2}{\sqrt{5}}$	1.71635	20.2587	6.01434
254.2542	$d[\max(\omega_2, \omega_3)]/dc$	1,0	65.3861	6.21573	65.3894
		0,1	65.3861	32.8684	65.3980
		$\frac{1}{\sqrt{5}}, \frac{2}{\sqrt{5}}$	46.7205	32.1782	46.3563
426.5209	$d\omega_4/dc$	1,0	—	64.3679	64.3707
		0,1	—	64.3679	64.3724

[a]Increment for forward finite difference derivatives $\delta = 0.000001°$.

The material properties are: $E_1 = 138$ GPa, $E_2 = E_3 = 8.96$ GPa, $G_{12} = G_{13} = G_{23} = 7.1$ GPa, $\nu_{12} = \nu_{13} = \nu_{23} = 0.3$, $\rho = 2000$ kg/m^3 (mass density). The thickness of each ply is 0.01 m. Two lamination sequences are considered: [45°/−45] and [30°/−60°]. The 0° direction is aligned with the X axis. Both lamination sequences lead to repeated eigenfrequencies corresponding to the second and third vibration modes. The vibration modes for both lamination schemes are shown in Figs 3 and 4. Due to the high side-to-thickness ratio of 100 and low degree of anisotrophy (E_1/E_2 ratio) the natural frequencies and corresponding sensitivity results obtained with higher order and first order models are all in a good agreement.

The eigenfrequency sensitivities in order to ply angles θ_1 and θ_2 obtained with Q9-HSDT 11, Q9-HSDT 9 and Q9-FSDT 5 discrete models, for the above lamination sequences, are shown, respectively, in Tables 1–6. The multiple analytical directional derivatives (eqns (17)–(20)) evaluated along chosen directions **c** and the single design derivatives evaluated using eqn (16) and corresponding directional derivatives are compared with alternative values obtained with global forward finite difference (eqns (21) and (22)) with a perturbation $\delta = 0.000001°$ using the same discrete model.

Tables 7–9 show the eigenfrequency sensitivities in order to vectorial distances from middle surface of the laminate to the upper surface of

Table 7. Eigenfrequency sensitivities in order to vectorial distances h_k obtained with Q9-HSDT 11 model, for simply supported 2-ply [30°/−60°] square plate with central circular hole

Frequency (rad/s)		Direction (h_0, h_1, h_2)	Analytical sensitivities		Global finite difference[a]
			Multiple	Single	
130.0205	$d\omega_1/dc$	1, 0, 0	—	-0.64815×10^4	-0.648147×10^4
		0, 1, 0	—	-0.259227×10^{-4}	0.448799
		0, 0, 1	—	0.648158×10^4	0.648169×10^4
254.0572	$d[\min(\omega_2, \omega_3)]/dc$	1, 0, 0	-0.148266×10^5	-0.123981×10^5	-0.148263×10^5
		0, 1, 0	-0.446987×10^4	-0.386985×10^3	-0.446871×10^4
		0, 0, 1	0.103567×10^5	0.127851×10^5	0.103570×10^5
		$\frac{1}{\sqrt{6}}, \frac{1}{\sqrt{6}}, \frac{2}{\sqrt{6}}$	0.422810×10^4	0.521950×10^4	0.421704×10^4
254.0572	$d[\max(\omega_2, \omega_3)]/dc$	1, 0, 0	-0.103567×10^5	-0.127851×10^5	-0.103564×10^5
		0, 1, 0	0.446987×10^4	0.386985×10^3	0.447104×10^4
		0, 0, 1	0.148266×10^5	0.123981×10^5	0.148268×10^5
		$\frac{1}{\sqrt{6}}, \frac{1}{\sqrt{6}}, \frac{2}{\sqrt{6}}$	0.605292×10^4	0.506150×10^4	0.604523×10^4
426.0753	$d\omega_4/dc$	1, 0, 0	—	-0.211640×10^5	-0.211636×10^5
		0, 1, 0	—	0.516952×10^{-4}	1.67645
		0, 0, 1	—	0.211640×10^5	0.211645×10^5

[a]Increment for forward finite difference derivatives $\delta = 0.000001$ m.

Table 8. Eigenfrequency sensitivities in order to vectorial distances h_k obtained with Q9-HSDT 9 model, for simply supported 2-ply [30°/−60°] square plate with central circular hole

Frequency (rad/s)		Direction (h_0, h_1, h_2)	Analytical sensitivities		Global finite difference[a]
			Multiple	Single	
129.9607	$d\omega_1/dc$	1, 0, 0	—	-0.647778×10^4	-0.647767×10^4
		0, 1, 0	—	-0.258566×10^{-4}	0.449340
		0, 0, 1	—	-0.647778×10^4	0.647789×10^4
253.9611	$d[\min(\omega_2, \omega_3)]/dc$	1, 0, 0	-0.148196×10^5	-0.10825×10^5	-0.148194×10^5
		0, 1, 0	-0.446896×10^4	-0.352033×10^4	-0.446780×10^4
		0, 0, 1	0.103507×10^5	0.143453×10^5	0.103510×10^5
		$\frac{1}{\sqrt{6}}, \frac{1}{\sqrt{6}}, \frac{2}{\sqrt{6}}$	0.422565×10^4	0.585643×10^4	0.421460×10^4
253.9611	$d[\max(\omega_2, \omega_3)]/dc$	1, 0, 0	-0.103507×10^5	-0.143453×10^5	-0.103504×10^5
		0, 1, 0	0.446896×10^4	0.352033×10^4	0.447013×10^4
		0, 0, 1	0.148196×10^5	0.108250×10^5	0.148199×10^5
		$\frac{1}{\sqrt{6}}, \frac{1}{\sqrt{6}}, \frac{2}{\sqrt{6}}$	0.605009×10^4	0.441930×10^4	0.604241×10^4
425.8654	$d\omega_4/dc$	1, 0, 0	—	-0.211485×10^5	-0.211481×10^5
		0, 1, 0	—	0.516745×10^{-4}	1.67717
		0, 0, 1	—	0.211485×10^5	0.211489×10^5

[a]Increment for forward finite difference derivatives $\delta = 0.000001$ m.

kth ply — h_k, $k = 0, ..., 2$ obtained with Q9-HSDT 11, Q9-HSDT 9 and Q9-FSDT 5 discrete models for the lamination sequence [30°/−60°]. Again in this case the directional derivatives are compared with single derivatives and global forward finite difference with a perturbation $\delta = 0.000001$ m.

In both cases it can be observed a good agreement between the single analytical sensitivities and the global forward finite difference whenever the eigenvalue is unique. In the case of repeated eigenvalues the single analytical method gives wrong results. In this case a good agreement between the multiple analytical directional derivatives (eqns (17)–(20)) and global forward finite difference is obtained.

CONCLUSIONS

A non-smooth eigenfrequency based criterion has been applied to multilaminated plate structures in order to evaluate the directional derivatives when non-differentiable multiple eigenfrequencies occur. The algorithm has been applied to a family of C^0 Lagrangian higher

Table 9. Eigenfrequency sensitivities in order to vectorial distances h_k obtained with Q9-FSDT 5 model, for simply supported 2-ply [30°/−60°] square plate with central circular hole

Frequency (rad/s)		Direction (h_0, h_1, h_2)	Analytical sensitivities		Global finite difference[a]
			Multiple	Single	
130.1740	$d\omega_1/dc$	1, 0, 0	—	-0.649469×10^4	-0.649687×10^6
		0, 1, 0	—	-0.258359×10^{-4}	0.451860
		0, 0, 1	—	0.649469×10^4	0.649709×10^4
254.2542	$d[\min(\omega_2, \omega_3)]/dc$	1, 0, 0	-0.148339×10^5	-0.105351×10^5	-0.148552×10^5
		0, 1, 0	-0.447825×10^4	-0.411929×10^4	-0.447709×10^4
		0, 0, 1	0.103556×10^5	0.146544×10^5	0.103775×10^5
		$\frac{1}{\sqrt{6}}, \frac{1}{\sqrt{6}}, \frac{2}{\sqrt{6}}$	0.422765×10^4	0.354504×10^4	0.422541×10^4
254.2542	$d[\max(\omega_2, \omega_3)]/dc$	1, 0, 0	-0.103556×10^5	-0.146544×10^5	-0.103770×10^5
		0, 1, 0	0.447825×10^4	0.411929×10^4	0.447942×10^4
		0, 0, 1	0.148339×10^5	0.105351×10^5	0.148558×10^5
		$\frac{1}{\sqrt{6}}, \frac{1}{\sqrt{6}}, \frac{2}{\sqrt{6}}$	0.605589×10^4	0.430093×10^4	0.605703×10^4
426.5209	$d\omega_4/dc$	1, 0, 0	—	-0.211879×10^5	-0.212105×10^5
		0, 1, 0	—	0.515666×10^{-4}	1.68202
		0, 0, 1	—	0.211879×10^5	0.212114×10^5

[a]Increment for forward finite difference derivatives $\delta = 0.000001$ m.

order shear deformation theory discrete models suitable for the analysis of thin-to-thick multi-laminated structures.

The feasibility of the described method was validated through the numerical solution of an illustrative example. From the results shown for natural frequencies one can observe a good agreement between global forward finite difference sensitivities and analytical directional derivatives when multiple eigenfrequencies are involved. When multiple eigenfrequencies occur single analytical sensitivities evaluated by eqn (16) should not be used.

The frequent occurrence of multiple eigenfrequencies that can be observed from the simple test case carried out, emphasizes the need to introduce adequate algorithms into the structural optimization codes to overcome this non-differentiability problem.

ACKNOWLEDGEMENTS

This work was partially supported by EU project 'Diagnostic and Reliability of Composite Materials and Structures for Advanced Transportation Applications: HCM-CHRTX-CT93-0222'.

REFERENCES

1. Mindlin, R.D., Influence of rotary inertia and shear on flexural motions of isotropic elastic plates. *J. Appl. Mech., Trans. ASME*, 1951, **18**, 31–38.
2. Reddy, J.N., A review of refined theories of laminated composite plates. *Shock and Vibration Digest*, 1990, **22** (7), 3–17.
3. Whitney, J.M., Shear correction factors for orthotropic laminates under static load. *J. Appl. Mech.*, 1973, **40** (1), 302–304.
4. Lo, K. H., Christensen, R. M. and Wu, E. M., A high-order theory of plate deformation — Part 1: Homogeneous plates., *J. Appl. Mech.*, 1977, **44**, 663–668.
5. Lo, K. H., Christensen, R. M. and Wu, E. M., A high-order theory of plate deformation — Part 2: Laminated plates. *J. Appl. Mech.* 1977, **44**, 669–676.
6. Reddy, J.N., A simple higher-order theory for laminated composite plates. *J. Appl. Mech.*, 1984, **51**, 745–752.
7. Reddy, J.N., On refined computational models of composite laminates. *Int. J. Numerical Methods in Engng*, 1989, **27**, 361–382.
8. Reddy, J.N., An evaluation of equivalent single-layer and layerwise theories of composite laminates. *Composite Structures*, 1993, **25**, 31–35.
9. Phan, N.D. and Reddy, J.N., Analysis of laminated composite plates using a higher-order shear deformation theory. *Int. J. Numerical Methods in Engng*, 1985, **21**, 2201–2219.
10. Bhimaraddi, A. and Stevens, L.K., A higher-order theory for free vibration of orthotropic homogeneous and laminated rectangular plates. *J. Appl. Mech.*, 1984, **51**, 195–198.
11. Mallikarjuna and Kant, T., A critical review and some results of recently developed refined theories of fiber-reinforced laminated composites and sandwiches. *Composite Structures*, 1993, **23**, 293–312.
12. Kant, T. and Pandya, B.N., A simple finite element formulation of a higher-order theory for unsymmetric laminated composite plates. *Composite Structures*, 1988, **9**, 215–224.
13. Reddy, J.N. and Robbins, D.H. Jr., Theories and computational models for composite laminates. *Appl. Mech. Rev.*, 1994, **47**, (6), 147–169.
14. Robbins, D.H. Jr. and Reddy, J.N., Variable kinematic modeling of laminate composite plates. *Int. J. Numerical Methods in Engng*, 1996, **39**, 2283–2317.
15. Mallikarjuna, and Kant, T., Free vibration of symmetrically laminated plates using a higher-order theory with finite element technique. *Int. J. Numerical Methods in Engng*, 1989, **28**, 1875–1889.
16. Abrate, S., Optimal design of laminated plates and shells. *Composite Structures*, 1994, **29**, 269–286.
17. Haftka, R.T. and Adelman, R.M., Recent developments in structural sensitivity analysis. *J. Structural Optimization*, 1989, **1**, 137–151.
18. Grandhi, R.V., Structural optimization with frequency constraints — A review. *AIAA Journal*, 1993, **31** (12), 2296–2303.
19. Lancaster, P., On eigenvalue of matrices dependent on a parameter. *Numerische Matematik*, 1964, **6**, 377–387.
20. Masur, E.F. and Mróz, Z., Non-Stationary optimality conditions in structural design. *Int. J. Solids Structures*, 1979, **15**, 503–512.
21. Masur, E. F. and Mróz, Z., Singular solutions in structural optimization problems. *Variational Methods in the Mechanics of Solids*, Ed. Nemat-Nasser, Pergamon Press, Oxford, 1980, pp. 337–343.
22. Haug, E.J. and Rousselet, B., Design sensitivity analysis in structural mechanics II: Eigenvalue variations. *J. Structural Mechanics*, 1980, **8**, 161–186.
23. Choi, K. K. and Haug, E. J., Optimization of structures with repeated eigenvalues. *Optimal Design of Distributed Parameter Structures*, Eds Haug, E. and Cea, J., 1, Leyden: Sijthoff–Nordhoff, 1981, pp. 219–277.
24. Clarke, F., *Optimization and Non-smooth Analysis*, John Wiley and Sons, New York, 1983.
25. Ojalvo, I.U., Efficient computation of mode-shape derivatives for large dynamic systems. *AIAA Journal*, 1987, **25**, 1386–1390.
26. Ollhoff, N., Structural optimization by variational method. *Computer Aided Optimal Design: Structural and Mechanical Systems*, Ed. Mota Soares, C. A., Springer, Berlin, 1987, pp. 87–179.
27. Mills-Curran, W.C., Calculation of derivatives for structures with repeated eigenvalues. *AIAA Journal*, 1988, **26**, 867–871.
28. Dailey, R.L., Eigenvector derivatives with repeated eigenvalues. *AIAA Journal*, 1989, **27**, 486–491.
29. Overton, M.L., Large scale optimization of eigenvalues. *SIAM J. Optimization*, 1992, **2** (1), 88–120.
30. Ollhoff, N., Lund, E. and Seyranian, A. P., Sensitivity analysis and optimization of multiple eigenvalues in structural design problems. *AAIA/NASA/USAF/ ISSMO Symposium on Multidisciplinary Analysis and Optimization, part 1, paper AIAA-94-4319-CP, AIAA*, 1994, pp. 625–640.

31. Seyranian, A.P., Lund, E. and Ollhoff, N., Multiple eigenvalues in structural optimization problems. *Structural Optimization*, 1994, **8**, 207–227.
32. Ollhoff, N., Krog, L. A. and Lund, E., Optimization of multimodal structural eigenvalues. *WCSMO — 1, Structural and Multidisciplinary Optimization*, Eds Ollhoff, N. and Rozvany, G. I. N., Pergamon, Oxford, 1995, pp. 701–708.
33. Rodrigues, H.C., Guedes, J.M. and Bendsoe, M.P., Necessary conditions for optimal design of structures with a non-smooth based criterion. *Structural optimization*, 1995, **9**, 52–56.
34. Seyranian, A. P., Optimality conditions for multiple eigenvalues and new solutions to Lagrange problems. *WCSMO — 1, Structural and Multidisciplinary Optimization*, Eds Ollhoff, N. and Rozvany, G. I. N., Pergamon, Oxford, 1995, pp. 695–699.
35. Haftka, R. T., Gurdal, Z. and Kamat, M. P., *Elements of Structural Optimization*, 2nd edition, Kluwer Academic Publishers, The Netherlands, 1990.
36. Franco Correia, V. M., Mota Soares, C. M. and Mota Soares, C. A., Higher order models on the eigenfrequency analysis and optimal design of laminated composite structures. *Composite Structures* (to appear).
37. Zienkiewicz, O. C., *The Finite Element Method in Engineering Science*, 3rd edition, McGraw–Hill, London, 1987.
38. Vinson, J. R. and Sierakowski, R. L., *The Behavior of Structures Composed of Composite Materials*, Martinus Nijhoff, Dordrecht, The Netherlands, 1996.

ELSEVIER

Composite Structures Vol. 38, No. 1–4, pp. 111–117
© 1997 Elsevier Science Ltd. All rights reserved
Printed in Great Britain
0263-8223/97/$17.00 + 0.00

PII:S0263-8223(97)00047-0

Determination of the load-carrying capacity of steel fibre reinforced concrete beams

J. A. Purkiss, P. J. Wilson

School of Engineering, Aston University, Birmingham B4 7ET, UK

&

P. Blagojević

Faculty of Civil Engineering, University of Niš, Beogradska 18 000, Niš, Serbia

An earlier paper by Purkiss & Blagojević (*Composite Struct.*, **25**, 45–9, 1993) detailed the results from some load–deflection tests on two sets of beams. The first set were reinforced both with two number 8 mm high yield bars and with steel fibres. The second set as a comparison had only high yield bars.

The results reported indicated that at a given load the beams with fibres produced lower deflections and did not give such an extensive 'yield plateau' as those beams without fibres. Using a method proposed by Hsu *et al.* (*ACI Struct. J.*, **89**, 650–7, 1992), albeit modified to allow for the tension stiffening of the concrete and the use of a continuous function for the reinforcing bar stress–strain relationship, the theoretical deformations and crack widths may be calculated. The predicted load–deformation results are in good agreement with the experimental values for both sets of beams. The predicted crack widths were determined using the methods in both BS 8110 and ENV 1992-1-1. ENV 1992-1-1 gives good agreement for the beams with bars only and for the beams with fibres up to the point of first visible crack. This is not unexpected as the model used for the tensile zone in the concrete assumes immediate failure after the achievement of the flexural tensile strength. © 1997 Elsevier Science Ltd.

INTRODUCTION

Although the benefits of fibre reinforcement in concrete are reasonably well known, the analysis of such effects is less well known. This paper sets out an anylsis for the flexural behaviour of beams reinforced both with bars and with steel fibres.

EXPERIMENTAL DATA

As the results from the the experimental work have already been reported [1] only a very brief summary is provided.

The mix used was (by weight) 1:1.18:0.86 — OPC:10 mm coarse siliceous aggregate:zone 2 sand with a water/cement ratio of 0.4 (as batched) and, where appropriate, 1.5% volume fraction of Fibrex SS35 fibres (35 mm long with an equivalent diameter of 0.64 mm and an aspect ratio of 55). The control test results (cube strength, f_{cu}, and modulus of rupture, f_t) at 28 days were for the concrete with fibres f_{cu} = 68.9 MPa and f_t = 10.7 MPa, and for the no fibre concrete 66.9 MPa and 8.0 MPa, respectively.

The beams were 2 m long by 100 mm wide by 176 mm deep. The two 8 mm high yield bars (f_{yk} = 550 MPa) had an effective cover in both directions of 10 mm. The beams were loaded at third points over a span of 1.92 m by an hydraulic jack and spreader beam system. Deflections were measured at the midspan and under the load points. Electrical resistance strain gauge readings at the centre of the beam, and crack width measurements in the centre third, were also taken.

THEORETICAL ANALYSIS OF MOMENT CAPACITY

In order to carry out the analysis certain assumptions needed to be made on material behaviour (Fig. 1).

(1) The Bernoulli theory of bending was used.

(2) For the concrete in tension it was assumed that in the regrettable absence of complete data from the modulus of rupture tests the stress–strain was assumed to be linear with the same elastic modulus as in compression, and a maximum stress equal to the modulus of rupture. The concrete was taken to have no strength after the modulus of rupture was achieved. The stiffening effect of the tensile zone in the concrete was, however, included.

(3) Concrete in compression.

Concrete with no fibres. Equation (4) from the European Concrete Design Code (EC2) (ENV 1992-1-1: 1991 [2]) was used

$$\sigma_c = f_c \frac{kn - n^2}{1 + (k-2)n} \tag{1}$$

where $n = \varepsilon_c/\varepsilon_{c1}$ (ε_c is the compressive strain in the concrete and ε_{c1} is the strain at maximum stress taken as 2200 microstrain), f_c is the compressive cylinder strength of the concrete and the parameter k is defined as $1.1\,E_{c,\,nom}\varepsilon_{c1}/f_c$, where $E_{c,\,nom}$ is the mean value of Young's modulus for the concrete. As the experimental value of Young's modulus for plain concrete was not determined, the value given by eqn (3.5) of ENV 1992-1-1 was used

$$E_{c,\,nom} = 9.5(f_c + 8)^{1/3} \tag{2}$$

For the plain concrete $f_c = 46.2$ MPa, $E_c = E_{c,\,nom} = 35.95$ GPa and $k = 1.883$.

Concrete with fibres. The equation proposed in Hsu *et al.* [3] was used

$$\sigma_c = f_c \frac{\beta \dfrac{\varepsilon_c}{\varepsilon_0}}{\beta - 1 + \left(\dfrac{\varepsilon_c}{\varepsilon_0}\right)^{\beta}} \tag{3}$$

where β is a parameter dependant upon the type and shape of the fibre and for this case is given by

$$\beta = 1.093 + 7.4818\left(w_f \frac{l}{\phi}\right)^{-1.387} \tag{4}$$

where l/ϕ is the aspect ratio and w_f is the weight fraction of the fibres.

For the concrete in use $f_c = 48.1$ MPa, $\varepsilon_0 = 2543$ microstrain, $w_f = 0.0491$, $l/\phi = 55$ and $\beta = 2.98$.

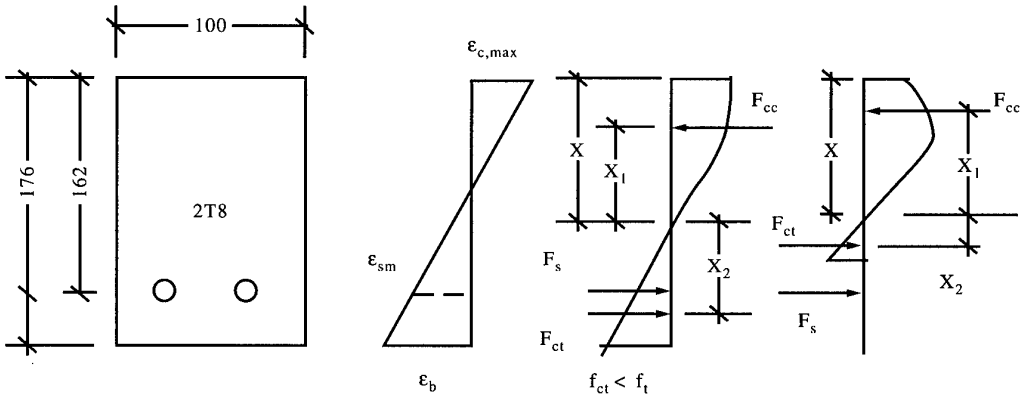

Fig. 1. Section geometry and stress block resultants.

(4) Reinforcement. From tests carried out at Aston on 8 mm high yield steel, the following equation was found to fit the data

$$\varepsilon_{sm} = \frac{\sigma_s}{0.201705} + 418.4\left(\frac{\sigma_s}{530.803}\right)^{17.9612} \quad (5)$$

where σ_s is the stress in the steel and ε_{sm} is the steel strain in microstrain.

At any point the following relationship must be satisfied

$$F_{ct} + F_s - F_{cc} = 0 \quad (6)$$

where F_{cc} is the resultant force due to the concrete compression zone, F_s is the force due to the steel reinforcement and F_{ct} is the force due to the tensile zone of the concrete.

The forces and the depth of the neutral x are dependant upon the strains in the section. An iterative solution is therefore necessary. The solution was achieved on a spreadsheet by setting a value of the strain in the extreme compression fibre $\varepsilon_{c,\,max}$ and iterating values of the neutral axis with the resulting steel and concrete tension strains until eqn (6) was solved to within 0.05×10^{-6} kN. The expressions for the concrete in compression for both the plain and fibre reinforced concrete are not capable of being integrated explicitly, so the trapezium rule was used. The stress–strain curve for the reinforcing steel also needs a numerical solution as the explicit variable is the steel strain. Two cases need to be considered for calculating the force in the tensile zone of the concrete, F_{ct}, and its point of action defined by the distance x_2 (Fig. 1).

For $\varepsilon_b < f_t/E_c$

$$F_{ct} = \frac{100\,(176-x)\varepsilon_b\,E_{c,\,nom}}{2} \quad (7a)$$

with

$$x_2 = \frac{2}{3}(176-x) \quad (8a)$$

and for $\varepsilon_b > f_t/E_c$

$$F_{ct} = \frac{100 f_t}{2}\,\frac{x f_t}{\varepsilon_{c,\,max}\,E_{c,\,nom}} \quad (7b)$$

with

$$x_2 = \frac{2}{3}\,\frac{x f_t}{\varepsilon_{c,\,max}\,E_{c,\,nom}} \quad (8b)$$

The position x_1 of the resultant force of the concrete compression zone is determined by evaluating the first moment of area of the stress block using numerical techniques and dividing by F_{cc}.

The moment M that can then be resisted by the section for a given value of $\varepsilon_{c,\,max}$ is given by

$$M = 162\,F_s + (x+x_2)\,F_{ct} - (x-x_1)\,F_{cc} \quad (9)$$

The full details of the proceedure are given in Wilson [4].

The total applied load P, ignoring the self-weight of the beam, is then determined as $3.125M$ (as the loading is at third points over a span of 1.92 m).

MIDSPAN DEFLECTION CALCULATION

Using a strain energy approach the midspan deflection δ is given by

$$\delta = 2\int_0^{L/2} \frac{M_0 m}{(EI)_s}\,ds \quad (10)$$

where $(EI)_s$ is the flexural rigidity at a point a distance s from the support, M_0 is the applied moment under a given load P, and m the moment due to a unit load at the centre.

$M_0/(EI)_s$ is the local curvature and is equal to $\varepsilon_{c,\,max}/x$ for a given load P, and the unit moment is given by $s/2$, thus eqn (10) becomes

$$\delta = \int_0^{L/2} \frac{s\varepsilon_{c,\,max}}{x}\,ds \quad (11)$$

The integral in eqn (11) is evaluated numerically on a spreadsheet to give the values of δ corresponding to a given applied load P. Thus, the load–deflection history is obtained.

CRACK WIDTH CALCULATION

Two approaches were considered.

(a) BS 8110 [5]

The design crack width w_d is given by

$$w_d = \frac{3a_{cr}\,\varepsilon_b}{1+2\left(\dfrac{a_{cr}-c_{min}}{h-x}\right)} \tag{12}$$

where ε_b is the strain in the extreme tension fibre (determined in this case with the effect of tension stiffness), a_{cr} is the distance from the surface of the bar to the centre of the beam soffit (= 36.5 mm), c_{min} is the minimum cover (= 10 mm) and h is the depth of the section (176 mm).

(b) ENV 1992-1-1 (EC2) [3]

The design crack width w_k is given by

$$w_k = \beta s_{rm}\varepsilon_{sm} \tag{13}$$

where s_{rm} is the average crack spacing and ε_{sm} is the mean strain in the reinforcement allowing for the effects of tension stiffening. The value of β is taken as 1.7 for determining the design, i.e. acceptible crack width. For the mean crack width, β is taken as unity [6].

The crack width spacing s_{rm} is determined from

$$s_{rm} = 50+0.25\,k_1k_2\frac{\phi}{\rho_r} \tag{14}$$

From EC2, for this case, $k_1 = 0.8$ (high bond bars), $k_2 = 0.5$ (flexure), $\phi = 8$ (bar size), $\rho_r = A_s/2.5(h-d)b = 2\times 50.3/(100\times 2.5(176-160)) = 0.0287$. Thus, $s_{rm} = 77.9$ mm. The average value of the crack spacing in the middle third of the beam observed in the tests was around 75 mm. The values of ε_{sm} are those from the section analysis, allowing for tension stiffening.

RESULTS

Load–deflection results

The calculated load–deflection results and the mean load–deflection results (from three tests) are plotted in Fig. 2(a) for the beams with no fibres and Fig. 2(b) for the beams with fibres. There is a very good correlation in both cases, except that for the beams with fibres a substantial yield plateau is generated in the theoretical response but which did not appear in the test results. The anomaly between the test results from beams with and without fibres remains unexplained (Wilson [4]). For beams with fibres only, Casanova & Rossi [7] indicate that there may be additional deflection due to the plastic hinge rotation at the root of the crack. Casanova & Rossi have only verified this for a single controlled crack at a notch but not for beams with additional steel reinforcement. Owing to the uncontrolled nature of the crack pattern within reinforced beams the extension of the theory by Casanova & Rossi may not be easy to confirm.

It should be noted that the predicted load at first crack is in reasonable correlation with the observed load, although it should however be pointed out that it is hard to determine the

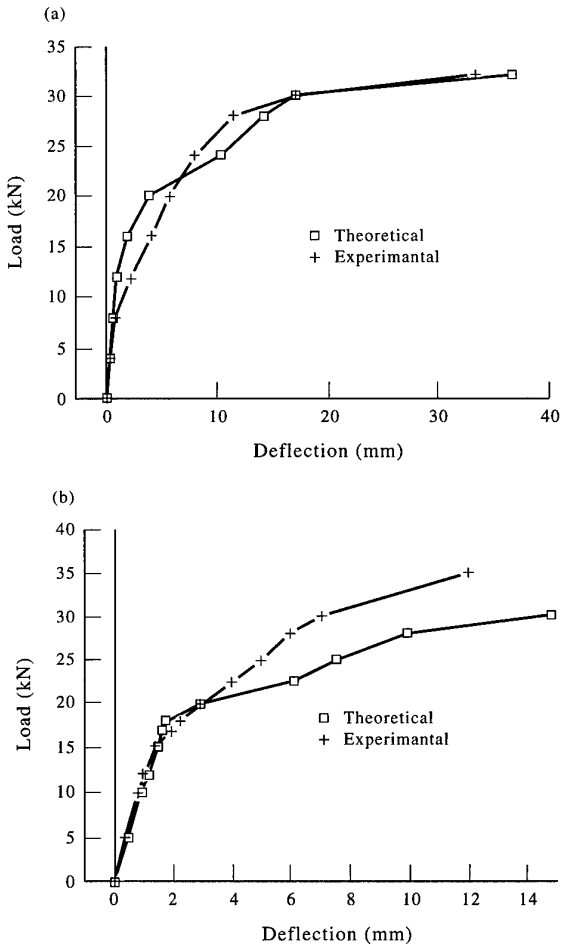

Fig. 2. Comparison between the theoretical and experimental load–deflection responses. (a) Beams with no fibres. (b) Beams with fibres.

exact load at which cracking occurs and the resultant observed load is likely to be a slight overestimate. The mean experimental load at first crack for the beams without fibres is 12 kN, and with fibres it is 18 kN. The calculated loads are 14.3 and 19.3 kN, respectively.

It should be noted that the predictions of the load at first crack show that there is a short period of instability in the values of strain and neutral axis depth until the crack stabilizes. This would not be observed in practice unless the strains were being continuously monitored and the response time of the experimental set-up was very low.

Strains

Table 1 gives values of strains measured in the actual tests, where gauges were attached to the bar reinforcement, and those calculated. Results from only one beam are available for beams without fibres and two beams with fibres. Below the load at which cracking occurs the two sets of values are close for both series of beams, except at extremely low values of loading. However, after cracking the calculated strains are generally much higher than the measured strains. This is due to the fact that the analysis assumes that once the section cracks this situation exists along the whole beam, whereas in practice the beam cracks discretely with the steel strains varying from zero at the face of the crack to a maximum half-way between cracks. This will also affect the strains in the concrete. Also, electrical resistance strain gauges effectively measure the mean strain over the length of the gauge, thus smearing the results. This applies to both the steel and the concrete strains.

Crack widths

Crack widths calculated using both design methods are compared, in Tables 2 and 3, with those reported by Purkiss & Blagojević [1]. To determine the mean crack widths the values in Table 1 should be multiplied by 0.6.

For beams with no fibres the BS 8110 approach underpredicts crack widths consistently by a factor of slightly less than 2, whereas the approach in EC2 using $\beta = 1.7$ gives a good correlation between the experimental and theoretical values. For the beams with fibres both methods give a good correlation below the loads to first crack of around 18 kN, although it should be remembered that that there may be large errors in the experimental values owing to the difficulty in making accurate measurements of small crack widths. After cracking the calculated results will not be reliable because the theoretical model used makes no allowance for post-cracking stiffness of the fibre matrix.

CONCLUSIONS

(1) Good correlation was found between the observed and calculated load–deflection curves for reinforced concrete beams with and without steel fibres.
(2) There was good agreement between the observed and calculated loads at crack initiation.
(3) Reasonable correlation was noted between the observed and calculated strains before cracking commenced. The correlation was less good post-cracking, although still acceptable.

Table 1. Crack widths

Load (kN)	Crack widths (mm)					
	No fibres			Fibres		
		Theoretical			Theoretical	
	Measured	BS 8110	EC2	Measured	BS 8110	EC2
11.0	0.16	0.09	0.14	0	0.01	0.02
13.0	0.19	0.11	0.17	0	0.02	0.03
15.0	0.22	0.13	0.20	0	0.02	0.03
17.0	0.25	0.16	0.23	0.03	0.02	0.04
19.0	0.28	0.17	0.26	0.05	0.02	0.04
20.0	0.31	0.18	0.27	0.06	0.17	0.26
22.5	0.33	0.21	0.32	0.10	0.20	0.31

Table 2. Comparison between measured and calculated strains — beam with no fibres

Load (kN)	Strains (microstrain)			
	Concrete		Reinforcement	
	Measured	Calculated	Measured	Calculated
0	0	0	0	0
4	60	67	65	46
8	267	120	710	96
12	449	182	1305	146
16	578	531	1771	1618
20	719	660	2443	2068
24	870	816	3645	2683
28	1100	1214	7915	5299
30	na	1759	14,458	10,131
31	1470	2259	15,148	15,029
32	1565	3500	na	25,128
33	1820	na	na	na

na indicates that for the measured strains values are not available as they were either not measured at that load or the gauges had failed. In the case of the calculated strains na indicates the analysis had been terminated before this point.

(4) There was good correlation between observed and calculated crack widths using the approach in ENV 1991-1-1 for the beams without fibres.
(5) The lower crack widths observed in the beams with fibres were not reflected in the calculations after cracking as it was not possible to incorporate a full model for the post-cracking steel fibre response in the calculations.

Table 3. Comparison between measured and calculated strains — beams with fibres

Load (kN)	Strains (microstrain)					
	Concrete			Reinforcement		
	Measured[a] (1)	(2)	Calculated	Measured[a] (1)	(2)	Calculated
0	0	0	0	0	0	0
5	30	70	102	47	65	79
10	108	157	205	132	167	160
11	na	172	225	na	188	176
12	136	204	247	174	242	193
13	160	232	266	204	300	208
14	na	265	287	na	390	225
15	202	352	308	331	503	241
16	na	364	329	na	614	257
17	275	407	351	449	695	275
18	310	450	370	516	808	290
19	na	402	392	na	910	307
20	390	459	684	781	1020	1516
22	na	642	866	na	1265	2236
22.5	485	na	885	1126	na	2302
24	na	752	955	na	1513	2589
25	570	na	1008	1425	na	2589
26	na	852	1086	na	1753	3256
28	na	947	1356	na	2031	5120
30	745	1037	1904	2069	2307	9959
32	na	1140	3241	na	2708	23328
34	na	1302	na	na	3693	na
35	960	na	na	3519	na	na
36	1010	1807	na	4379	10925	na

[a]There are two sets of experimental results from the beams with fibres labelled (1) and (2).
na indicates that for the measured strains values are not available as they were either not measured at that load or the gauges had failed. In the case of the calculated strains na indicates the analysis had been terminated before this point.

ACKNOWLEDGEMENTS

The authors wish to thank the Department of Civil Engineering, Aston University for making facilities available whilst the third author was on a period of study leave at Aston. They also wish to thank Messrs B. Fitzgerald for the contribution on the reinforcing stress–strain curve and M. Finlay for the basic test data on the steel fibre concrete.

REFERENCES

1. Purkiss, J.A. and Blagojević, P., Comparison between the short and long term behaviour of fibre reinforced and unreinforced beams. *Composite Struct.* 1993, **25**, 45–49.
2. ENV 1992-1-1: EuroCode 2 Design of Concrete Structures. Part 1. General Rules and Rules for Buildings. Committée European de Normalization, British Standards Institution, London, 1991.
3. Hsu, C-H.T., He, R.L. and Ezeldin, A.S., Load–deformation behavior of steel fiber reinforced concrete beams. *ACI Struct. J.* 1992, **89** (6), 650–657.
4. Wilson, P. J., Deflection and cracking analysis of steel fibre reinforced concrete beams. Final Year Project Report, Aston University, 1996.
5. BS 8110: Structural Use of Concrete, Part 2. Code of Practice for Special Circumstances. British Standards Institution, London, 1985 (revised 1989).
6. Beeby, A. W. & Narayan, R. S., *Designers' Handbook to EuroCode 2: Part 1.1. Design of Concrete Structures*. Thomas Telford, London, 1995.
7. Casanova, P. and Rossi, P., Analysis of metallic fibre-reinforced concrete beams submitted to bending. *Matér. Construct.* 1966, **29**, 354–361.

ELSEVIER

Composite Structures Vol. 38, No. 1–4, pp. 119–131
© 1997 Elsevier Science Ltd. All rights reserved
Printed in Great Britain
0263-8223/97/$17.00 + 0.00

PII:S0263-8223(97)00048-2

Buckling behaviour of laminated beam structures using a higher-order discrete model

M. A. Ramos Loja, J. Infante Barbosa

ENIDH — Escola Náutica Infante D. Henrique, Departamento de Máquinas Maritimas, Av. Bonneville Franco, Paçco de Arcos, 2780 Oeiras, Portugal

&

C. M. Mota Soares

IDMEC — Instituto de Engenharia Mecânica, Instituto Superior Técnico, Av. Rovisco Pais, 1096 Lisboa Codex, Portugal

A higher-order shear-deformation theory, assuming a non-linear variation for the displacement field, is used to develop a finite-element model to predict the linear buckling behaviour of anisotropic multilaminated or sandwich thick and thin beams. The model is based on a single-layer Lagrangean four-node straight-beam element. It considers stretching and bending in two orthogonal planes. The most common cross-sections and symmetric and asymmetric lay-ups are studied. The good performance of the present element is evident on the prediction of the buckling of several test cases of thin and thick isotropic or anisotropic beam structures. Comparisons show that the model is accurate and versatile. © 1997 Elsevier Science Ltd.

INTRODUCTION

Laminated beams are presently used as structural elements in general high-performance mechanical, aerospace, naval and civil applications, where high strength and high stiffness to weight ratios are desired. The beams are made of composite materials which have the ability of being tailored according to specified response constrained requirements to achieve optimum structural objectives. As part of the design process, it is required to predict accurately displacements, normal and transverse stresses, delamination, vibrational and buckling behaviour to establish the load and performance capabilities of this type of structural element. Owing to the large elongation to failure allowed by both fibre and resin, buckling is most of the time the governing failure for the most used pultruded structural members. In this paper a refined finite-element model for the linear buckling analysis of composite or sandwich beam structures is presented. The model is developed for symmetric and asymmetric lay-ups, and considers the most usual cross-sections used in design.

The present model is based on a higher-order displacement theory using displacement fields proposed by Lo *et al.* [1,2] for plates, and by Manjunatha & Kant [3], Vinayak *et al.* [4] and Prathap *et al.* [5] for rectangular cross-section beam structures in one-plane bending under static loading. The proposed theory enables the non-linear variation of displacements through the composite beam width/depth, thus eliminating the use of shear correction factors. These displacement fields are suitable for the analysis of highly anisotropic beams ranging from high to low length to depth and/or width ratios.

Pioneering work on the buckling analysis of composite beams can be reviewed in Kapania & Raciti [6]. Related work has been carried out by Bhimaraddi & Chandrashekhara [7], Hwu & Hu [8], Barbero & Tomblin [9], Barbero & Raftoyiannis [10], Wisnom and Häberle [11], Ray & Kar [12], Turvey [13], Rhodes [14] and Barbero *et al.* [15], among others. Recently, Sheinman *et al.* [16] developed a high-order ele-

ment for pre-buckling and buckling analysis of laminated rectangular cross-section beams and plane frame structures, considering a third-order expansion in the thickness direction for the in-plane displacement and a constant transverse displacement throughout the thickness. By deleting degrees of freedom they arrive at various alternative models. A parametric study of the locking phenomenon and the shear-deformation effects was carried out for isotropic and laminated structures. From the surveys one can find very few research publications related to the buckling of multilaminated composite/sandwich beams using higher-order displacement fields and, consequently, comparison with alternative formulations such as Euler–Bernoulli and Mindlin are also very rare, hence the motivation for the proposed work.

In the present study, the development of a higher-order discrete model (HSDT) for static and buckling analysis is presented. The model is based on a straight-beam finite element with four nodes and 14 degrees of freedom per node, considering bi-axial bending and stretching. The development takes into consideration non-symmetric lay-ups and the rectangular, I, T, channel and rectangular box beam cross-sections. The present discrete model is part of a package of finite-element programs for the optimization of two-dimensional composite or sandwich arbitrary beams. This package also includes Euler–Bernoulli (EBT) and Timoshenko (FSDT) beam elements. The performance of the model developed is discussed for several buckling applications.

DISPLACEMENT AND STRAIN FIELDS

The displacement field considered assumes, for the numerical finite-element model, a third-order expansion in the thickness and width co-ordinates for the axial displacement, and a second-order expansion for the transverse displacements. The displacement field can be represented in a compact form as

$$\boldsymbol{u} = \lambda \boldsymbol{q};\ \mathbf{u} = [u(x, z, y)\ v(x, y)\ w(x, z)]^{\mathrm{T}}$$

$$\lambda = \begin{bmatrix} 1 & 0 & 0 & 0 & z & -y & z^2 & -y^2 & 0 & 0 & 0 & 0 & z^3 & -y^3 \\ 0 & 1 & 0 & 0 & 0 & 0 & 0 & 0 & y^2 & 0 & y & 0 & 0 & 0 \\ 0 & 0 & 1 & 0 & 0 & 0 & 0 & 0 & 0 & z^2 & 0 & z & 0 & 0 \end{bmatrix}$$

$$\mathbf{q} = [u^0\ v^0\ w^0\ \theta_x^0\ \theta_y^0\ \theta_z^0\ u^{0*}\ u^{0**}\ v^{0*}\ w^{0*}\ \beta_y^0\ \beta_z^0\ \theta_y^{0*}\ \theta_z^{0*}]^{\mathrm{T}} \tag{1}$$

where $\boldsymbol{q}$ is the vector of generalized displacements, representing the appropriated Taylor's series terms defined along the x-axis and $z = 0$ and $y = 0$. The first six terms are related to displacements and rotations as defined in Fig. 1. The remaining parameters are higher-order terms in the Taylor series expansion. They represent higher-order transverse cross-sectional deformation modes which

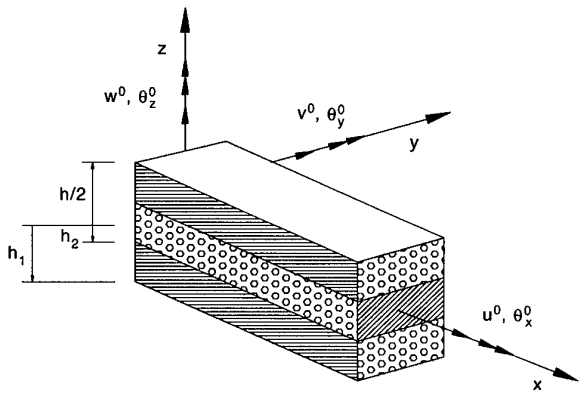

Fig. 1. Typical laminated beam geometry. Co-ordinate system.

are difficult to physical interpret. Considering the kinematic relations for linear elasticity and the HSDT displacement field (eqn (1)), the strain field is obtained as

$$\boldsymbol{\varepsilon} = \boldsymbol{\lambda}\boldsymbol{\varepsilon}^0;\ \boldsymbol{\varepsilon} = [\varepsilon_x\ \varepsilon_y\ \varepsilon_z\ \gamma_{xz}\ \gamma_{xy}]^{\mathrm{T}}$$

$$\boldsymbol{\lambda} = \begin{bmatrix} 1 & z^2 & -y^2 & 0 & 0 & z & z^3 & 0 & -y & -y^3 & 0 & 0 & 0 & 0 & 0 & 0 & 0 \\ 0 & 0 & 0 & 1 & 0 & 0 & 0 & z & 0 & 0 & 0 & 0 & 0 & 0 & 0 & 0 & 0 \\ 0 & 0 & 0 & 0 & 1 & 0 & 0 & 0 & 0 & 0 & y & 0 & 0 & 0 & 0 & 0 & 0 \\ 0 & 0 & 0 & 0 & 0 & 0 & 0 & 0 & 0 & 0 & 0 & 1 & z & z^2 & 0 & 0 & 0 \\ 0 & 0 & 0 & 0 & 0 & 0 & 0 & 0 & 0 & 0 & 0 & 0 & 0 & 0 & 1 & y & y^2 \end{bmatrix}$$

$$\boldsymbol{\varepsilon}^0 = [\varepsilon_x^0\ \varepsilon_x^{0*}\ \varepsilon_x^{0**}\ \varepsilon_y^0\ \varepsilon_z^0\ k_y\ k_y^*\ k_{xz}\ k_z\ k_z^*\ k_{xy}\ \phi_{xz}\ \phi_{xz}^*\ \phi_{xz}^{**}\ \phi_{xy}\ \phi_{xy}^*\ \phi_{xy}^{**}] \tag{2}$$

where

$$\varepsilon_x^0 = \frac{\partial u^0}{\partial x};\ \varepsilon_x^{0*} = \frac{\partial u^{0*}}{\partial x};\ \varepsilon_x^{0**} = \frac{\partial u^{0**}}{\partial x};\ \varepsilon_y^0 = \beta_y^0;\ \varepsilon_z^0 = \beta_z^0;\ k_y = \frac{\partial \theta_y^o}{\partial x};\ k_y^* = \frac{\partial \theta_y^{o*}}{\partial x};$$

$$k_{xz} = 2w^{o*}k_z = \frac{\partial \theta_z^o}{\partial x};\ k_z^* = \frac{\partial \theta_z^{o*}}{\partial x};\ k_{xy} = 2v^{o*};\ \phi_{xz} = \frac{\partial w^o}{\partial x} + \theta_y^o;\ \phi_{xz}^* = 2u^{o*}\frac{\partial \beta_z^o}{\partial x};$$

$$\phi_{xz}^{**} = 3\theta_y^{o*} + \frac{\partial w^{o*}}{\partial x};\ \phi_{xy} = \frac{\partial v^o}{\partial x} - \theta_z^o;\ \phi_{xy}^* = -2u^{o**} + \frac{\partial \beta_y^o}{\partial x};\ \phi_{xy}^{**} = -3\theta_z^{o*} + \frac{\partial v^{o*}}{\partial x} \tag{3}$$

CONSTITUTIVE RELATIONS

Considering the orthogonal referential *xyz*, the constitutive relation for an orthotropic beam layer, which can have an arbitrary fibre orientation, are related to the strains through the relations

$$\begin{bmatrix} \sigma_x \\ \sigma_y \\ \sigma_z \\ \tau_{xz} \\ \tau_{xy} \end{bmatrix} = \begin{bmatrix} \overline{Q}_{11} & \overline{Q}_{12} & \overline{Q}_{13} & 0 & \overline{Q}_{16} \\ \overline{Q}_{12} & \overline{Q}_{22} & \overline{Q}_{23} & 0 & \overline{Q}_{26} \\ \overline{Q}_{13} & \overline{Q}_{23} & \overline{Q}_{33} & 0 & \overline{Q}_{36} \\ 0 & 0 & 0 & \overline{Q}_{55}^* & 0 \\ \overline{Q}_{16} & \overline{Q}_{26} & \overline{Q}_{36} & 0 & \overline{Q}_{66} \end{bmatrix} \begin{bmatrix} \varepsilon_x \\ \varepsilon_y \\ \varepsilon_z \\ \gamma_{xz} \\ \gamma_{xy} \end{bmatrix} \tag{4}$$

Neglecting the shear stress τ_{yz}, one obtains for the elastic coefficient $\overline{Q}_{55}^*$ the expression

$$\overline{Q}_{55}^* = \overline{Q}_{55} - \overline{Q}_{45}^2/\overline{Q}_{44} \tag{5}$$

where the terms of matrix $\overline{Q}$, for the kth layer are explicitly given in Vinson & Sierakowski [1,17]. Integrating the stresses through the depth and width of the laminate one obtains the resultant forces and moments acting on it, as follows

$$[\mathbf{N}] = [N_x\ N_x^*\ N_x^{**}\ N_y\ N_z]^{\mathrm{T}} = \sum_{k=1}^{N} \int_{z_{k-1}}^{z_k} \int_{y_l}^{y_r} [\sigma_x\ \sigma_x\ \sigma_x\ \sigma_y\ \sigma_z]^{\mathrm{T}}\ [1\ z^2\ y^2\ 1\ 1]\ \mathrm{d}y\ \mathrm{d}z$$

$$[\mathbf{M}^{xz}] = [M_y\ M_y^*\ M_{xz}]^{\mathrm{T}} = \sum_{k=1}^{N} \int_{z_{k-1}}^{z_k} \int_{y_l}^{y_r} [\sigma_x\ \sigma_x\ \sigma_z]^{\mathrm{T}}\ [z\ z^3\ z]\ \mathrm{d}y\ \mathrm{d}z$$

$$[\mathbf{M}^{xy}] = [M_z\ M_z^*\ M_{xy}]^{\mathrm{T}} = \sum_{k=1}^{N} \int_{z_{k-1}}^{z_k} \int_{y_l}^{y_r} [\sigma_x\ \sigma_x\ \sigma_y]^{\mathrm{T}}\ [y\ y^3\ y]\ \mathrm{d}y\ \mathrm{d}z$$

$$[\mathbf{Q}^{xz}] = [S_{xz}\ S_{xz}^*\ S_{xz}^{**}]^{\mathrm{T}} = \sum_{k=1}^{N} \int_{z_{k-1}}^{z_k} \int_{y_l}^{y_r} \tau_{xz}\ [1\ z\ z^2]\ \mathrm{d}y\ \mathrm{d}z$$

$$[\mathbf{Q}^{xy}] = [S_{xy}\ S_{xy}^*\ S_{xy}^{**}]^{\mathrm{T}} = \sum_{k=1}^{N} \int_{z_{k-1}}^{z_k} \int_{y_l}^{y_r} \tau_{xy}\ [1\ y\ y^2]\ \mathrm{d}y\ \mathrm{d}z \tag{6}$$

where N is the number of layers. The constitutive relation then becomes

$$\begin{bmatrix} \mathbf{N} \\ \mathbf{M}^{xz} \\ \mathbf{M}^{xy} \\ \mathbf{Q}^{xz} \\ \mathbf{Q}^{xy} \end{bmatrix} = \begin{bmatrix} \mathbf{A} & \mathbf{B}^{xz} & \mathbf{B}^{xy} & 0 & \mathbf{C}_1^{xy} \\ \mathbf{B}^{xz^{\mathrm{T}}} & \mathbf{D}^{xz} & \mathbf{D}^{xyz} & 0 & \mathbf{C}_2^{xy} \\ \mathbf{B}^{xy^{\mathrm{T}}} & \mathbf{D}^{xyz^{\mathrm{T}}} & \mathbf{D}^{xy} & 0 & \mathbf{C}_3^{xy} \\ 0 & 0 & 0 & \mathbf{S}^{xz} & 0 \\ \mathbf{C}_1^{xy^{\mathrm{T}}} & \mathbf{C}_2^{xy^{\mathrm{T}}} & \mathbf{C}_3^{xy^{\mathrm{T}}} & 0 & \mathbf{S}^{xy} \end{bmatrix} \begin{bmatrix} \boldsymbol{\varepsilon}^0 \\ \mathbf{k}^{xz} \\ \mathbf{k}^{xy} \\ \boldsymbol{\phi}^{xz} \\ \boldsymbol{\phi}^{xy} \end{bmatrix} \tag{7}$$

$$\boldsymbol{\varepsilon}^0 = [\varepsilon_x^0\ \varepsilon_x^{0*}\ \varepsilon_x^{0**}\ \varepsilon_y^0\ \varepsilon_z^0]^{\mathrm{T}};\ \mathbf{k}^{xz} = [k_y\ k_y^*\ k_{xz}]^{\mathrm{T}};\ \mathbf{k}^{xy} = [k_z\ k_z^*\ k_{xy}]^{\mathrm{T}};\ \phi^{xz} = [\phi_{xz}\ \phi_{xz}^*\ \phi_{xz}^{**}]^{\mathrm{T}};\ \boldsymbol{\phi}^{xy} = [\phi_{xy}\ \phi_{xy}^*\ \phi_{xy}^{**}]^{\mathrm{T}} \tag{8}$$

Matrices $\mathbf{A}$, $\mathbf{B}^{ij}$, $\mathbf{D}^{ij}$, $\mathbf{S}^{ij}$, $\mathbf{D}^{ijk}$ and $\mathbf{C}_n^{ij}$ with ($ij = xz$, xy; $ijk = xyz$; $n = 1, \ldots, 3$) are explicitly given in Appendix A for multilaminated rectangular cross-sections. The corresponding matrices for T, I, channel and rectangular box beams, can be found in Loja [18].

FINITE-ELEMENT MODEL

In the present work a four-node straight-beam element is developed for static and buckling analysis. Lagrangean shape functions are used to interpolate the generalized displacements within the element, as follows

$$N_1 = -\frac{9}{16}\left(\xi+\frac{1}{3}\right)\left(\xi-\frac{1}{3}\right)(\xi-1) \quad N_2 = \frac{27}{16}(\xi+1)\left(\xi-\frac{1}{3}\right)(\xi-1)$$

$$N_3 = -\frac{27}{16}(\xi+1)\left(\xi+\frac{1}{3}\right)(\xi-1) \quad N_4 = \frac{9}{16}(\xi+1)\left(\xi+\frac{1}{3}\right)\left(\xi-\frac{1}{3}\right) \tag{9}$$

The generalized displacements (eqn (1)) can then be represented as

$$u^0 = \sum_{i=1}^{4} N_i\, u_i^0 \theta_z^{0*} = \sum_{i=1}^{4} N_i\, \theta_{z_i}^{0*} \tag{10}$$

One can then represent the displacement field, by

$$\mathbf{u}_{\mathrm{e}} = \lambda \mathbf{N} \mathbf{q}_{\mathrm{e}}$$
$$\mathbf{q}_{\mathrm{e}}^i = [u^0\ v^0\ w^0\ \theta_x^0\ \theta_y^0\ \theta_z^0\ u^{0*}\ u^{0**}\ v^{0*}\ w^{0*}\ \beta_y^0\ \beta_z^0\ \theta_y^{0*}\ \theta_z^{0*}]^{\mathrm{T}}\ (i = 1, 2, 3, 4) \tag{11}$$

where $\mathbf{N}$ is the shape function matrix and $\mathbf{q}_{\mathrm{e}}$ the element nodal displacement vector. By differentiating (eqn (10)) in accordance with the generalized strain field yields

$$\boldsymbol{\varepsilon}^0 = \mathbf{B}_{\mathrm{M}}\, \mathbf{q}_{\mathrm{e}};\ \mathbf{k}^{xz} = \mathbf{B}_{\mathrm{F}_{xz}}\, \mathbf{q}_{\mathrm{e}};\ \mathbf{k}^{xy} = \mathbf{B}_{\mathrm{F}_{xy}}\, \mathbf{q}_{\mathrm{e}};\ \phi^{xz} = \mathbf{B}_{\mathrm{S}_{xz}}\, \mathbf{q}_{\mathrm{e}};\ \phi^{xy} = \mathbf{B}_{\mathrm{S}_{xy}}\, \mathbf{q}_{\mathrm{e}} \tag{12}$$

where matrices $\mathbf{B}_{\mathrm{M}}$, $\mathbf{B}_{\mathrm{F}_{xz}}$, $\mathbf{B}_{\mathrm{F}_{xy}}$, $\mathbf{B}_{\mathrm{S}_{xz}}$ and $\mathbf{B}_{\mathrm{S}_{xy}}$ relate the degrees of freedom to the generalized strains, for membrane, flexure and shear.

The total potential energy for the eth element is

$$\Pi_e = \frac{1}{2}\left\{ \int_0^1 [\mathbf{N}\ \mathbf{M}^{xz}\ \mathbf{M}^{xy}\ \mathbf{Q}^{xz}\ \mathbf{Q}^{xy}] \begin{bmatrix} \boldsymbol{\varepsilon}^0 \\ \mathbf{k}^{xz} \\ \mathbf{k}^{xy} \\ \boldsymbol{\phi}^{xz} \\ \boldsymbol{\phi}^{xy} \end{bmatrix} \right\} \mathrm{d}x + \frac{1}{2} \int_V \sigma_{ij}^0 u_{s,i} u_{s,j}\, \mathrm{d}V - \mathbf{q}_{\mathrm{e}}^{xyz} \mathbf{Q}_{\mathrm{e}}^{xyz} \tag{13}$$

where the first and the second terms correspond to the first- and second-order strain elastic energy, σ_{ij}^0 denotes the stress components associated to the initial state of stress, which are previously calculated by means of a linear static analysis, V is the volume of the element, and the comma within the subscripts denotes the partial derivatives. The second term is expanded as shown in Moita *et al.*

[19] for plate structures, and $\mathbf{Q}_e$ is the element load vector. Substituting eqns (10) and (12) into eqn (13), one obtains

$$\Pi_e = \frac{1}{2}\mathbf{q}_e^T(\mathbf{K}_e+\mathbf{K}_e^G)\mathbf{q}_e - \mathbf{q}_e^T\mathbf{Q}_e \tag{14}$$

The application of the minimum potential energy variational principle yields the following equilibrium equations

$$\mathbf{K}_e\mathbf{q}_e+\mathbf{K}_e^G\mathbf{q}_e = \mathbf{Q}_e \tag{15}$$

where $\mathbf{K}_e$ and $\mathbf{K}_e^G$ are the element stiffness and geometric matrices. These matrices are respectively given as

$$\begin{aligned}\mathbf{K}_e = \int_{-1}^{+1} (&\mathbf{B}_M^T\,\mathbf{A}\mathbf{B}_M+\mathbf{B}_{F_{xz}}^T\,\mathbf{B}^{xz^T}\mathbf{B}_M+\mathbf{B}_M^T\,\mathbf{B}^{xz}\,\mathbf{B}_{F_{xz}}+\mathbf{B}_{F_{xy}}^T\,\mathbf{B}^{xy^T}\mathbf{B}_M+\mathbf{B}_M^T\,\mathbf{B}^{xy}\,\mathbf{B}_{F_{xy}}+\mathbf{B}_{F_{xz}}^T\,\mathbf{D}^{xz}\,\mathbf{B}_{F_{xz}}\\
&+\mathbf{B}_{F_{xy}}^T\,\mathbf{D}^{xy}\,\mathbf{B}_{F_{xy}}+\mathbf{B}_{F_{xz}}^T\,\mathbf{D}^{xyz}\,\mathbf{B}_{F_{xy}}+\mathbf{B}_{F_{xy}}^T\,\mathbf{D}^{xyz^T}\,\mathbf{B}_{F_{xz}}+\mathbf{B}_M^T\,\mathbf{C}_1^{xy}\,\mathbf{B}_{S_{xy}}+\mathbf{B}_{S_{xy}}^T\,\mathbf{C}_1^{xy^T}\,\mathbf{B}_M\\
&+\mathbf{B}_{F_{xz}}^T\,\mathbf{C}_2^{xy}\,\mathbf{B}_{S_{xy}}\\
&+\mathbf{B}_{S_{xy}}^T\,\mathbf{C}_2^{xy^T}\,\mathbf{B}_{F_{xz}}+\mathbf{B}_{F_{xy}}^T\,\mathbf{C}_3^{xy}\,\mathbf{B}_{S_{xy}}+\mathbf{B}_{S_{xy}}^T\,\mathbf{C}_3^{xy^T}\,\mathbf{B}_{F_{xy}}+\mathbf{B}_{S_{xz}}^T\,\mathbf{S}^{xz}\,\mathbf{B}_{S_{xz}}+\mathbf{B}_{S_{xy}}^T\,\mathbf{S}^{xy}\,\mathbf{B}_{S_{xy}})\,J\,\mathrm{d}\xi\end{aligned} \tag{16}$$

$$\mathbf{K}_e^G = \int_{-1}^{+1} \mathbf{G}^T\tau\mathbf{G}\,J\,\mathrm{d}\xi \tag{17}$$

Matrices τ and $\mathbf{G}$ are shown in Appendix B and Appendix C, respectively. The Jacobian operator, relating the natural co-ordinate derivatives to the local co-ordinate derivative, is $J = L/2$ for equally spaced nodes. Load vector $\mathbf{Q}_e$, when distributed loading is acting within the element, geometric element matrix $\mathbf{K}_e^G$ and terms relating to stretching, bending and bending–stretching of element stiffness matrix $\mathbf{K}_e$ are evaluated analytically in the ξ direction using symbolic manipulator Maple V. [20] The last two sub-matrices of eqn (16), relating to transverse shear elastic strain energy, are evaluated numerically using three Gauss points. The degrees of freedom θ_{x_i} ($i = 1, ..., 4$) are related with angles of twist on a plane normal to the x-axis of the element. Then, assuming that they do not affect displacements other than their own, the stiffness and geometric matrices for a four-node Lagrangean bar element in free torsion are superimposed onto eqns (16) and (17), in the usual assembly way. The equilibrium equations for the whole and discretized beam for static and linear buckling analysis are then

$$\mathbf{K}\mathbf{q} = \mathbf{Q} \tag{18}$$

$$\mathbf{K}\mathbf{q}_i+\lambda_i\mathbf{K}^G\mathbf{q}_i = 0 \tag{19}$$

where $\mathbf{Q}$ is the system load vector, $\mathbf{K}$ and $\mathbf{K}^G$ are the system stiffness and geometric matrices, $\mathbf{q}$ is the system displacement vector and $\mathbf{q}_i$ is the eigenvector associated with the λ_i eigenvalue, which is a function of the applied loading. The smallest λ_i corresponds to the critical buckling load parameter. Equations (18) and (19) can easily be solved once the boundary conditions are introduced.

NUMERICAL APPLICATIONS

The higher-order finite-element model (HSDT) is applied to several illustrative beams subjected to compressive axial loads. Buckling predictions are validated against results obtained by other researchers [23], and also with predictions of two available beam finite-element models based on Euler–Bernoulli formulation (EBT) and first-order shear-deformation theory (FSDT), and a higher-order shear-deformation plate finite-element model (HSDT) [19]. For all cases but one (see next section where discretization was considered for 10 beam finite elements.

Clamped–free isotropic T-beam

This example shows the influence of the slenderness ratio (length of column/least radius of gyration of the cross-section) on the critical load of a clamped–free isotropic wide-flange T-beam. The material and geometrical data are:

$E = 200.0$ GPa (Young's modulus);

$\nu = 0.3$ (Poisson's ratio);

$h_{web} = 0.102$ m;
$b_{flange} = 0.102$ m;
$t = 6.4 \times 10^{-3}$ m (where t is the thickness of web and flange).

In Table 1 one can observe the comparative influence of the slenderness ratio on the critical buckling load, for the different models, and the Euler critical load, given by $P_{crit} = \pi^2 EI/L^2$. As one can observe, for the different slenderness ratios, the EBT model gives very good results when compared with the closed form solution. If one considers low ratios, it is clear from Table 1 that the critical loads become lower than the analytical solutions for the FSDT and HSDT models. This fact is more evident in the HSDT case, which is not surprising because of its greater transverse shear-deformation influence.

Simply-supported isotropic beam

In this test case an isotropic rectangular cross-section beam is considered in order to study the shear-deformation effect on the buckling load. The material and geometric properties used are:

$E = 1.379 \times 10^9$ Pa;
$L = 0.0254$ m;
$h = 0.00254$ m (thickness);
$b = 0.003048$ m (width).

Table 2 shows predictions for the present (HSDT) model for several discretizations which are compared with the buckling loads obtained by Wennerström & Bäcklund [21] and with the mechanics of materials solution, including shear effects, which is evaluated using the expression [22] $P_{cr} = P_e/(1+P_e k/(Gbh))$, where $P_e = \pi^2 EI/L^2$ and $k = 5/6$. The HSDT model presents a good agreement for the different cases studied when compared with the closed form solution, leading to lower critical loads because of its greater flexibility.

Simply-supported composite I-beam

A simply-supported composite I-beam is considered. This test case intends to compare the critical loads of different commercially available laminated wide-flange I-beam sections. The following mechanical parameters are used:

$E_1 = 20.632$ GPa; $E_2 = 4.433$ GPa;
$G_{12} = 1.985$ GPa;
$\nu_{12} = 0.318$;
$E_3 = E_2$;
$G_{23} = G_{13} = G_{12}$;
$\nu_{13} = \nu_{23} = \nu_{12}$.

Table 3 shows the critical buckling load predictions for several I-sections. It can be seen that there is a good agreement between the HSDT model and the experimental values of Barbero & Tomblin [9] and the corresponding critical buckling loads evaluated by the Southwell asymptote technique of the experimental measurements [22,24].

Table 1. Effect of the slenderness ratio on the critical buckling load. T-column (kN)

Slenderness ratio	Euler load	EBT	FSDT ($k = 5/6$)	HSDT
30	2863.501	2863.506	2778.604	2243.168
50	1030.860	1030.862	1019.598	924.558
100	257.715	257.715	257.004	247.141
200	64.429	64.429	64.384	62.691
500	10.309	10.309	10.307	10.081
1000	2.577	2.577	2.577	2.525

EBT, Euler–Bernoulli theory; FSDT, first-order shear-deformation theory; HSDT, higher-order shear-deformation theory; k, shear correction factor.

Table 2. Convergence and influence of shear on critical loads (kN)

	Wennerström & Bäcklund [21] — FSDT		Present model — HSDT	
Elements	A	B	A	B
2	86.6758	73.8210	86.0859	73.0340
4	85.5166	72.9727	85.4426	72.9421
20	85.4477	72.9131	85.4321	72.9407
Analytical [21]	86.1043	73.3295		

FSDT, first-order shear-deformation theory; HSDT, higher-order shear-deformation theory.
A — $G = 0.6895 \times 10^9$ Pa (transverse elasticity modulus); B — $G = 0.6895 \times 10^8$ Pa.

Table 3. Critical buckling load, for wide-flange I-beams (kN)

Section (mm)	Length (m)	Experimental [9]	Southwell method [9]	Present method (HSDT)
102 × 102 × 6.4	4.48	12.08	12.46	11.60
102 × 102 × 6.4	2.98	27.21	28.10	26.09
152 × 152 × 6.4	6.03	23.10	23.66	21.15
152 × 152 × 6.4	3.58	64.15	67.11	59.49
152 × 152 × 9.5	6.03	33.38	34.11	31.42
152 × 152 × 9.5	3.89	78.80	82.22	75.02

HSDT, higher-order shear-deformation theory.

Simply-supported orthotropic beam

A simply-supported orthotropic beam with a rectangular cross-section is analysed, considering the following lay-ups: [0°], [0°/90°], [0°/90°/0°], [0°/90°/0°/90°]. The material properties of the beam are:

$E_1 = 181$ GPa; $E_1 = E_3 = 10.3$ GPa;
$G_{13} = G_{12} = 7.17$ GPa; $G_{23} = 6.21$ GPa;
$\nu_{12} = 0.28$; $\nu_{13} = 0.02$; $\nu_{23} = 0.40$.

Table 4 shows the results using the following multiplier $\lambda = p_{cr}/[h^2/L^2 \; E_2 h/(1-\nu_{12}\nu_{21})]$. The present results are compared with two alternative beam finite-element models proposed by Bhimaraddi & Chandrashekhara [7] using the displacement field (HSDT) [7]:

$$u(x, z) = u^0 + z\left(1 - \frac{4z^2}{3h^2}\right) \quad \theta_y^0 - z\frac{\partial w^0}{\partial x}$$

$$w(x, z) = w^0 \qquad (20)$$

and also the FSDT [7] formulation, respectively. As one can see from Table 4, the present model shows a good agreement with the two alternative solutions.

Orthotropic beam under different boundary conditions

An orthotropic, multilaminated, rectangular cross-section beam is studied to analyse its behaviour when subjected to different boundary conditions, and for various length to thickness ratios. The beam lay-up sequence is $[45°/-45°]_S$. The present model critical buckling load parameters are compared to the closed form solutions shown in Reddy [23] The material properties used are:

$E_1/E_2 = 25$;
$G_{13} = G_{12} = 0.5E_2$; $G_{23} = 0.2E_2$;
$\nu_{12} = 0.25$.

Table 5 shows the buckling load parameters, λ, which were obtained using the following multiplier $\lambda = P_{cr}L^2/E_2h^3$. From Table 5 one can see that there is good agreement between the present HSDT results and Reddy's solutions [23]. As expected, for lower length to thickness ratios, the present finite-element model gives lower critical buckling load predictions.

Table 4. Critical buckling load parameter, λ, for homogeneous and cross-ply beams ($L/h = 10$)

Model	0°	0°/90°	0°/90°/0°	0°/90°/0°/90°
HSDT [7]	11.5255	2.9172	11.0573	5.7511
FSDT [7]	11.5669	2.9297	11.0967	5.7740
HSDT (present method)	11.4179	2.7574	8.4274	5.5855

FSDT, first-order shear-deformation theory; HSDT, higher-order shear-deformation theory.

Table 5. Influence of the L/h ratio and boundary conditions on the critical buckling load parameter. Lay-up $[45°/-45°]_S$

L/h	Clamped–clamped		Clamped–free	
	Reddy [23]	Present HSDT	Reddy [23]	Present HSDT
100	5.737	5.847 (1.9%)	0.359	0.363 (1.1%)
20	5.478	5.515 (0.6%)	0.358	0.343 (−4.2%)
10	4.802	4.767 (−0.7%)	0.355	0.294 (−17.2%)

HSDT, higher-order shear-deformation theory.
Deviations (between brackets) calculated as: $(\lambda - \lambda^{24})/\lambda^{24} \times 100$.

Table 6. Critical buckling load parameter, λ, for angle-ply beams ($L/h = 10$)

Model	0°	15°	30°	45°	60°	75°	90°
HSDT [7]	11.5255	5.4619	2.4584	1.4050	0.9907	0.8414	0.8056
	(19.1%)	(0.5%)	(2.84%)	(6.3%)	(6.3%)	(6.7%)	(7.2%)
FSDT [7]	11.5669	10.4370	7.5251	4.1569	1.8142	0.9345	0.8092
	(19.5%)	(92.0%)	(214.8%)	(214.6%)	(94.7%)	(18.5%)	(7.6%)
HSDT [19]	9.6755	5.4352	2.3904	1.3212	0.9317	0.7884	0.7517
HSDT (present)	11.4179	10.2600	4.2349	1.4071	0.8095	0.7241	0.6996
	(18.0%)	(88.8%)	(77.2%)	(6.5%)	(−13.1%)	(−22.3%)	(−6.9%)

FSDT, first-order shear-deformation theory; HSDT, higher-order shear-deformation theory.
Deviations (between brackets) calculated as: $(\lambda-\lambda^{19})/\lambda^{19} \times 100$.

Simply-supported angle-ply beam

An angle-ply laminated beam, with the same properties as those of the previous test case, is studied to analyse the effect of the fibre orientation angle on the beam buckling behaviour. Table 6 presents the critical buckling loads on the xz plane, for the different fibre orientation angles considered, obtained with the different models using the multiplier $\lambda = p_{cr}/[h^2/L^2\ E_2 h/(1-\nu_{12}\nu_{21})]$. From Table 6 it can be seen that there is a fair agreement between the present HSDT predictions and the beam model of Bhimaraddi & Chandrashekhara [7], whose displacement field is given by eqn (20), and the results obtained using the plate model described in Moita *et al.* [19]. A full mesh discretization of 2×10 plate elements was been used. Moita *et al.*'s [19] plate finite-element model is based on a displacement field using a third-order expansion in the thickness co-ordinate for the in-plane displacement and a constant transverse displacement. The present HSDT results agree well with the FSDT [7] predictions for all ply orientations. No apparent reasons have been found for the discrepancies observed between the present model, the HSDT [7] beam model and the Moita *et al.* [19] plate model. The HSDT [7] and Moita *et al.* [19] models demonstrate a behaviour closer to that expected.

CONCLUSIONS

A single-layer Lagrangean beam finite-element model, based on a higher-order shear-deformation theory which assumes a non-linear variation for the displacement field, is proposed to study the buckling behaviour of anisotropic multilaminates of thick and thin sandwich beams. Its good performance is shown for most of the illustrative cases presented in this paper. From the extended numerical studies carried out, and comparisons with experimental and/or numerical alternative solutions available, it can be concluded that the proposed model efficiently predicts the buckling loads of beams, underestimating them compared with the EBT and FSDT models. For the simply-supported angle-ply beam (see the section on 'Simply-supported angle-ply beam'), and with no apparent reason, there are some discrepancies between the present HSDT buckling load predictions and the results obtained from the HSDT [7] beam model (eqn (20)) and the HSDT [19] plate model, which in fact perform better.

ACKNOWLEDGEMENTS

The authors are grateful for the financial support received from H.C.M. Project (CHRTX-CT93-0222), 'Diagnostic and Reliability of Composite Material and Structures for Advanced Transportation Applications', and Fundação Calouste Gulbenkian.

REFERENCES

1. Lo, K.H., Christensen, R.M. and Wu, E.M., A high-order theory of plate deformation. Part I: Homogeneous plates. *J. Appl. Mech., Trans. ASME* 1977, **44**, 663–668.
2. Lo, K.H., Christensen, R.M. and Wu, E.M., A high-order theory of plate deformation. Part II: Laminated plates. *J. Appl. Mech., Trans. ASME* 1977, **44**, 669–676.
3. Manjunatha, B.S. and Kant, T., New theories for symmetric/unsymmetric composite and sandwich beams with C^0 finite elements. *Composite Struct.* 1993, **23**, 61–73.
4. Vinayak, R.U., Prathap, G. and Naganarayana, B.P., Beam elements based on a higher order theory — I. Formulation and analysis of performance. *Comput. Struct.* 1996, **58**, 775–789.
5. Prathap, G., Vinayak, R.U. and Naganarayana, B.P., Beam elements based on a higher order theory — II. Boundary layer sensitivity and stress oscillations. *Comput. Struct.* 1996, **58**, 791–796.
6. Kapania, R.K. and Raciti, S., Recent advances in analysis of laminated beams and plates. Part I: shear effects and buckling. *AIAA J.* 1989, **27**, (7), 923–934.

7. Bhimaraddi, A. and Chandrashekhara, K., Some observations on the modelling of laminated composite beams with general lay-ups. *Composite Struct.* 1991, **19**, 371–380.
8. Hwu, C. and Hu, J.S., Buckling and postbuckling of delaminated composite sandwich beams. *AIAA J.* 1992, **30** (7), 1901–1909.
9. Barbero, E. and Tomblin, J., Buckling testing of composite columns. *AIAA J. Techn. Notes* 1992, **30** (11), 2798–2800.
10. Barbero, E.J. and Raftoyiannis, I.G., Euler buckling of pultruded composite beams. *Composite Struct.* 1993, **24**, 139–147.
11. Wisnom, M.R. and Häberle, J., Prediction of buckling and failure of unidirectional carbon fibre/epoxy struts. *Composite Struct.* 1994, **28**, 229–239.
12. Ray, K. and Kar, R.C., Parametric instability of a sandwich beam under various boundary conditions. *Comput. Struct.* 1995, **55**, 857–870.
13. Turvey, G.J., Effects of load position on the lateral buckling response of pultruded GRP cantilevers — comparisons between theory and experiment. *Composite Struct* 1996, **35**, 33–47.
14. Rhodes, J., A semi-analytical approach to buckling analysis of composite structures. *Composite Struct.* 1996, **35**, 93–99.
15. Barbero, E.J., Godoy, L.A. and Raftoyiannis, I.G., Finite elements for three-mode interaction in buckling analysis. *Int. J. Numer. Meth. Engng* 1996, **39**, 469–488.
16. Sheinman, I., Eisenberger, M. and Bernstein, Y., High-order element for prebuckling and buckling analysis of laminated plane frames. *Int. J. Numer. Meth. Engng* 1996, **39**, 2155–2168.
17. Vinson, J. R. & Sierakowski, R. L., *The Behavior of Structures Composed of Composite Materials*. Martinus Nijhoff, Dordrecht, The Netherlands, 1986.
18. Loja, M. A. R., Higher-order shear deformation models — development and implementation of stiffness coefficients for T, I, channel and rectangular box beams. Report IDMEC/IST, Project STRDA/C/TPR/592/92, Lisbon, 1995.
19. Moita, J.S., Mota Soares, C.M. and Mota Soares, C.A., Buckling behaviour of laminated composite structures using a discrete higher-order displacement model. *Composite Struct.* 1996, **35**, 75–92.
20. Maple V Release 4, *Waterloo Maple — Advancing Mathematics*. Waterloo Maple Inc., Waterloo, Ontario, Canada.
21. Wennerström, H. & Bäcklund, J., Static, free vibration and buckling analysis of sandwich beams. Report 86-3, Department of Aeronautical Structures and Materials, Royal Institute of Technology, Stockholm, Sweden, 1986.
22. Southwell, R.V., On the analysis of experimental observations in problems of elastic stability. *Proc. R. Soc. Lond.* 1932, **A135**, 601–616.
23. Reddy, J. N., *Mechanics of Laminated Composite Plates — Theory and Analysis*. CRC Press, Boca Raton, Florida, 1997.
24. Southwell, R.V., *An Introduction to the Theory of Elasticity*, 2nd edn. Oxford University Press, New York, 1941.

APPENDIX A

ELASTIC COEFFICIENT MATRICES FOR RECTANGULAR MULTILAYERED CROSS-SECTIONS

$$\mathbf{A}=\begin{bmatrix} \bar{Q}_{11}h_1b_1 & \bar{Q}_{11}h_3b_1 & \bar{Q}_{11}h_1b_3 & \bar{Q}_{12}h_1b_1 & \bar{Q}_{13}h_1b_1 \\ \bar{Q}_{11}h_3b_1 & \bar{Q}_{11}h_5b_1 & \bar{Q}_{11}h_3b_3 & \bar{Q}_{12}h_3b_1 & \bar{Q}_{13}h_3b_1 \\ \bar{Q}_{11}h_1b_3 & \bar{Q}_{11}h_3b_3 & \bar{Q}_{11}h_1b_5 & \bar{Q}_{12}h_1b_3 & \bar{Q}_{13}h_1b_3 \\ \bar{Q}_{12}h_1b_1 & \bar{Q}_{12}h_3b_1 & \bar{Q}_{12}h_1b_3 & \bar{Q}_{22}h_1b_1 & \bar{Q}_{23}h_1b_1 \\ \bar{Q}_{13}h_1b_1 & \bar{Q}_{13}h_3b_1 & \bar{Q}_{13}h_1b_3 & \bar{Q}_{23}h_1b_1 & \bar{Q}_{33}h_1b_1 \end{bmatrix}$$

$$\mathbf{B}^{xz}=\begin{bmatrix} \bar{Q}_{11}h_2b_1 & \bar{Q}_{11}h_4b_1 & \bar{Q}_{13}h_2b_1 \\ \bar{Q}_{11}h_4b_1 & \bar{Q}_{11}h_6b_1 & \bar{Q}_{13}h_4b_1 \\ \bar{Q}_{11}h_2b_3 & \bar{Q}_{11}h_4b_3 & \bar{Q}_{13}h_2b_3 \\ \bar{Q}_{12}h_2b_1 & \bar{Q}_{12}h_4b_1 & \bar{Q}_{23}h_2b_1 \\ \bar{Q}_{13}h_2b_1 & \bar{Q}_{13}h_4b_1 & \bar{Q}_{33}h_2b_1 \end{bmatrix} \quad \mathbf{B}^{xy}=\begin{bmatrix} \bar{Q}_{11}b_2h_1 & \bar{Q}_{11}b_4h_1 & \bar{Q}_{12}b_2h_1 \\ \bar{Q}_{11}b_2h_3 & \bar{Q}_{11}b_4h_3 & \bar{Q}_{12}b_2h_3 \\ \bar{Q}_{11}b_4h_1 & \bar{Q}_{11}b_6h_1 & \bar{Q}_{12}b_4h_1 \\ \bar{Q}_{12}b_2h_1 & \bar{Q}_{12}b_4h_1 & \bar{Q}_{22}b_2h_1 \\ \bar{Q}_{13}b_2h_1 & \bar{Q}_{13}b_4h_1 & \bar{Q}_{23}b_2h_1 \end{bmatrix}$$

$$\mathbf{D}^{xz}=\begin{bmatrix} \bar{Q}_{11}h_3b_1 & \bar{Q}_{11}h_5b_1 & \bar{Q}_{13}h_3b_1 \\ \bar{Q}_{11}h_5b_1 & \bar{Q}_{11}h_7b_1 & \bar{Q}_{13}h_5b_1 \\ \bar{Q}_{13}h_3b_1 & \bar{Q}_{13}h_5b_1 & \bar{Q}_{33}h_3b_1 \end{bmatrix} \quad \mathbf{D}^{xy}=\begin{bmatrix} \bar{Q}_{11}b_3h_1 & \bar{Q}_{11}b_5h_1 & \bar{Q}_{12}b_3h_1 \\ \bar{Q}_{11}b_5h_1 & \bar{Q}_{11}b_7h_1 & \bar{Q}_{12}b_5h_1 \\ \bar{Q}_{12}b_3h_1 & \bar{Q}_{12}b_5h_1 & \bar{Q}_{22}b_3h_1 \end{bmatrix}$$

$$\mathbf{S}^{xz}=\begin{bmatrix} \bar{Q}^{*}_{55}h_1b_1 & \bar{Q}^{*}_{55}h_2b_1 & \bar{Q}^{*}_{55}h_3b_1 \\ \bar{Q}^{*}_{55}h_2b_1 & \bar{Q}^{*}_{55}h_3b_1 & \bar{Q}^{*}_{55}h_4b_1 \\ \bar{Q}^{*}_{55}h_3b_1 & \bar{Q}^{*}_{55}h_4b_1 & \bar{Q}^{*}_{55}h_5b_1 \end{bmatrix} \quad \mathbf{S}^{xy}=\begin{bmatrix} \bar{Q}_{66}b_1h_1 & \bar{Q}_{66}b_2h_1 & \bar{Q}_{66}b_3h_1 \\ \bar{Q}_{66}b_2h_1 & \bar{Q}_{66}b_3h_1 & \bar{Q}_{66}b_4h_1 \\ \bar{Q}_{66}b_3h_1 & \bar{Q}_{66}b_4h_1 & \bar{Q}_{66}b_5h_1 \end{bmatrix}$$

$$\mathbf{D}^{xyz}=\begin{bmatrix} \bar{Q}_{11}h_2b_2 & \bar{Q}_{11}h_2b_4 & \bar{Q}_{12}h_2b_2 \\ \bar{Q}_{11}h_4b_2 & \bar{Q}_{11}h_4b_4 & \bar{Q}_{12}h_4b_2 \\ \bar{Q}_{13}h_2b_2 & \bar{Q}_{13}h_2b_4 & \bar{Q}_{23}h_2b_2 \end{bmatrix} \quad \mathbf{C}_2^{xy}=\begin{bmatrix} \bar{Q}_{16}b_1h_2 & \bar{Q}_{16}b_2h_2 & \bar{Q}_{16}b_3h_2 \\ \bar{Q}_{16}b_1h_4 & \bar{Q}_{16}b_2h_4 & \bar{Q}_{16}b_3h_4 \\ \bar{Q}_{36}b_1h_2 & \bar{Q}_{36}b_2h_2 & \bar{Q}_{36}b_3h_2 \end{bmatrix}$$

$$\mathbf{C}_1^{xy}=\begin{bmatrix} \bar{Q}_{16}b_1h_1 & \bar{Q}_{16}b_2h_1 & \bar{Q}_{16}b_3h_1 \\ \bar{Q}_{16}b_1h_3 & \bar{Q}_{16}b_2h_3 & \bar{Q}_{16}b_3h_3 \\ \bar{Q}_{16}b_3h_1 & \bar{Q}_{16}b_4h_1 & \bar{Q}_{16}b_5h_1 \\ \bar{Q}_{26}b_1h_1 & \bar{Q}_{26}b_2h_1 & \bar{Q}_{26}b_3h_1 \\ \bar{Q}_{36}b_1h_1 & \bar{Q}_{36}b_2h_1 & \bar{Q}_{36}b_3h_1 \end{bmatrix} \quad \mathbf{C}_3^{xy}=\begin{bmatrix} \bar{Q}_{16}h_1b_2 & \bar{Q}_{16}h_1b_3 & \bar{Q}_{16}h_1b_4 \\ \bar{Q}_{16}h_1b_4 & \bar{Q}_{16}h_1b_5 & \bar{Q}_{16}h_1b_6 \\ \bar{Q}_{26}h_1b_2 & \bar{Q}_{26}h_1b_3 & \bar{Q}_{26}h_1b_4 \end{bmatrix}$$

where

$$h_i\frac{(h_k^i-h_{k-1}^i)}{i};\ b_i\frac{(b_k^i-b_{k-1}^i)}{i}\quad (i=1,\ldots,7)$$

and k is the number of layers.

APPENDIX B

τ MATRIX

$$\tau=\begin{bmatrix} \tau_{11} & \tau_{12} \\ \tau_{21} & \tau_{22} \end{bmatrix}$$

$$\tau_{11}=\begin{bmatrix} N_x^0 & 0 & 0 & 0 & L_{xz}^0 & L_{xy}^0 & M_{xz}^0 & M_{xy}^0 & 0 & 0 & 0 & 0 \\ & N_x^0 & 0 & 0 & 0 & 0 & 0 & 0 & M_{xy}^0 & 0 & L_{xy}^0 & 0 \\ & & N_x^0 & 0 & 0 & 0 & 0 & 0 & 0 & M_{xz}^0 & 0 & L_{xz}^0 \\ & & & 0 & 0 & 0 & 0 & 0 & 0 & 0 & 0 & 0 \\ & & & & M_{xz}^0 & O_{yz}^0 & L_{xz1}^0 & O_{yz1}^0 & 0 & 0 & 0 & 0 \\ & & & & & M_{xy}^0 & P_{yz}^0 & L_{xy1}^0 & 0 & 0 & 0 & 0 \\ & & & & & & M_{xz1}^0 & P_{yz1}^0 & 0 & 0 & 0 & 0 \\ & & & & & & & M_{xy1}^0 & 0 & 0 & 0 & 0 \\ & & & & & & & & M_{xy1}^0 & 0 & L_{xy1}^0 & 0 \\ & & & & & & & & & M_{xz1}^0 & 0 & L_{xz1}^0 \\ & & & & & & & & & & M_{xy}^0 & 0 \\ \text{Sym.} & & & & & & & & & & & M_{xz}^0 \end{bmatrix}$$

$$\tau_{12}=\begin{bmatrix}
L^0_{xz1} & L^0_{xy1} & Q^0_{xz} & Q^0_{xy} & S^0_{xz} & S^0_{xy} & 0 & 0 & 0 & 0 & P^0_{xz} & P^0_{xy} \\
0 & 0 & 0 & 0 & 0 & 0 & S^0_{xy} & 0 & Q^0_{xy} & 0 & 0 & 0 \\
0 & 0 & 0 & 0 & 0 & 0 & 0 & S^0_{xz} & 0 & Q^0_{xz} & 0 & 0 \\
0 & 0 & 0 & 0 & 0 & 0 & 0 & 0 & 0 & 0 & 0 & 0 \\
M^0_{xz1} & O^0_{yz2} & S^0_{xz} & I^0_{yz} & P^0_{xz} & I^0_{yz1} & 0 & 0 & 0 & 0 & S^0_{xz1} & I^0_{yz2} \\
T^0_{yz} & M^0_{xy1} & I^0_{yz3} & S^0_{xy} & I^0_{yz4} & P^0_{xy} & 0 & 0 & 0 & 0 & H^0_{yx5} & S^0_{xy2} \\
L^0_{xz2} & P^0_{yz2} & P^0_{xz} & J^0_{yz} & S^0_{xz1} & J^0_{yz1} & 0 & 0 & 0 & 0 & P^0_{xz1} & J^0_{yz2} \\
T^0_{yz2} & L^0_{xy2} & J^0_{yz3} & P^0_{xy} & J^0_{yz4} & S^0_{xy1} & 0 & 0 & 0 & 0 & J^0_{yz5} & P^0_{xy1} \\
0 & 0 & 0 & 0 & 0 & 0 & S^0_{xy1} & 0 & P^0_{xy} & 0 & 0 & 0 \\
0 & 0 & 0 & 0 & 0 & 0 & 0 & S^0_{xz1} & 0 & P^0_{xz} & 0 & 0 \\
0 & 0 & 0 & 0 & 0 & 0 & P^0_{xy} & 0 & S^0_{xy} & 0 & 0 & 0 \\
0 & 0 & 0 & 0 & 0 & 0 & 0 & P^0_{xz} & 0 & S^0_{xz} & 0 & 0
\end{bmatrix}$$

$$\tau_{21}=\tau_{12}^{\mathrm{T}}$$

$$\tau_{22}=\begin{bmatrix}
M^0_{xz2} & T^0_{yz2} & S^0_{xz1} & H^0_{yz} & P^0_{xz1} & H^0_{yz1} & 0 & 0 & 0 & 0 & S^0_{xz2} & H^0_{yz2} \\
 & M^0_{xy2} & H^0_{yz3} & S^0_{xy1} & H^0_{yz4} & P^0_{xy1} & 0 & 0 & 0 & 0 & H^0_{yz5} & S^0_{xy2} \\
 & & N^0_z & 0 & L^0_z & 0 & 0 & 0 & 0 & 0 & M^0_z & 0 \\
 & & & N^0_y & 0 & L^0_y & 0 & 0 & 0 & 0 & 0 & M^0_y \\
 & & & & M^0_z & 0 & 0 & 0 & 0 & 0 & L^0_{z1} & 0 \\
 & & & & & M^0_y & 0 & 0 & 0 & 0 & 0 & L^0_{y1} \\
 & & & & & & M^0_y & 0 & L^0_y & 0 & 0 & 0 \\
 & & & & & & & M^0_z & 0 & L^0_z & 0 & 0 \\
 & & & & & & & & N^0_y & 0 & 0 & 0 \\
 & & & & & & & & & N^0_z & 0 & 0 \\
 & & & & & & & & & & M^0_{z1} & 0 \\
\text{Sym.} & & & & & & & & & & & M^0_{y1}
\end{bmatrix}$$

where the forces and moments resultants are given by

$$[N^0_x]\int_A \sigma^0_x \,\mathrm{d}A$$

$$[L^0_{xz}\ M^0_{xz}\ L^0_{xz1}\ M^0_{xz1}\ L^0_{xz2}\ M^0_{xz2}]=\int_A \sigma^0_x\,[z\ z^2\ z^3\ z^4\ z^5\ z^6]^{\mathrm{T}}\,\mathrm{d}A$$

$$[L^0_{xy}\ M^0_{xy}\ L^0_{xy1}\ M^0_{xy1}\ L^0_{xy2}\ M^0_{xy2}]=\int_A \sigma^0_x\,[y\ y^2\ y^3\ y^4\ y^5\ y^6]^{\mathrm{T}}\,\mathrm{d}A$$

$$[O^0_{yz}\ O^0_{yz1}\ O^0_{yz2}\ P^0_{yz}\ P^0_{yz1}\ P^0_{yz2}]=\int_A \sigma^0_x\,[yz\ y^2z\ y^3z\ z^2y\ z^2y^2\ z^2y^3]^{\mathrm{T}}\,\mathrm{d}A$$

$$[T^0_{yz}\ T^0_{yz1}\ T^0_{yz2}]=\int_A \sigma^0_x\,[z^3y\ z^3y^2\ z^3y^3]^{\mathrm{T}}$$

$$[N^0_y\ L^0_y\ M^0_y\ L^0_{y1}\ M^0_{y1}]=\int_A s^0_y\,[1\ y\ y^2\ y^3\ y^4]^{\mathrm{T}}$$

$$[N^0_z\ L^0_z\ M^0_z\ L^0_{z1}\ M^0_{z1}]=\int_A \sigma^0_z\,[1\ z\ z^2\ z^3\ z^4]^{\mathrm{T}}$$

$$[Q^0_{xy}\ S^0_{xy}\ P^0_{xy}\ S^0_{xy1}\ P^0_{xy1}\ S^0_{xy2}] = \int_A \int \sigma^0_{xy}\,[1\ y\ y^2\ y^3\ y^4\ y^5]^{\mathrm{T}}\,\mathrm{d}A$$

$$[I^0_{yz}\ J^0_{yz}\ H^0_{yz}\ I^0_{yz1}\ J^0_{yz1}\ H^0_{yz1}] = \int_A \int \sigma^0_{xy}\,[z\ z^2\ z^3\ zy\ z^2y\ z^3y]^{\mathrm{T}}\,\mathrm{d}A$$

$$[I^0_{yz2}\ J^0_{yz2}\ H^0_{yz2}] = \int_A \int \sigma^0_{xy}\,[zy^2\ z^2y^2\ z^3y^2]^{\mathrm{T}}$$

$$[Q^0_{xz}\ S^0_{xz}\ P^0_{xz}\ S^0_{xz1}\ P^0_{xz1}\ S^0_{xz2}] = \int_A \int s^0_{xz}\,[1\ z\ z^2\ z^3\ z^4\ z^5]^{\mathrm{T}}\,\mathrm{d}A$$

$$[I^0_{yz3}\ J^0_{yz3}\ H^0_{yz3}\ I^0_{yz4}\ J^0_{yz4}\ H^0_{yz4}] = \int_A \int \sigma^0_{xz}\,[y\ y^2\ y^3\ yz\ y^2z\ y^3z]^{\mathrm{T}}\,\mathrm{d}A$$

$$[I^0_{yz5}\ J^0_{yz5}\ H^0_{yz5}] = \int_A \int \sigma^0_{xz}\,[yz^2\ y^2z^2\ y^3z^2]^{\mathrm{T}}$$

APPENDIX C

G MATRIX

$$[G] = \begin{bmatrix}
\frac{\partial N_i}{\partial x} & 0 & 0 & 0 & 0 & 0 & 0 & 0 & 0 & 0 & 0 & 0 & 0 & 0 \\
0 & \frac{\partial N_i}{\partial x} & 0 & 0 & 0 & 0 & 0 & 0 & 0 & 0 & 0 & 0 & 0 & 0 \\
0 & 0 & \frac{\partial N_i}{\partial x} & 0 & 0 & 0 & 0 & 0 & 0 & 0 & 0 & 0 & 0 & 0 \\
0 & 0 & 0 & \frac{\partial N_i}{\partial x} & 0 & 0 & 0 & 0 & 0 & 0 & 0 & 0 & 0 & 0 \\
0 & 0 & 0 & 0 & \frac{\partial N_i}{\partial x} & 0 & 0 & 0 & 0 & 0 & 0 & 0 & 0 & 0 \\
0 & 0 & 0 & 0 & 0 & \frac{\partial N_i}{\partial x} & 0 & 0 & 0 & 0 & 0 & 0 & 0 & 0 \\
0 & 0 & 0 & 0 & 0 & 0 & \frac{\partial N_i}{\partial x} & 0 & 0 & 0 & 0 & 0 & 0 & 0 \\
0 & 0 & 0 & 0 & 0 & 0 & 0 & \frac{\partial N_i}{\partial x} & 0 & 0 & 0 & 0 & 0 & 0 \\
0 & 0 & 0 & 0 & 0 & 0 & 0 & 0 & \frac{\partial N_i}{\partial x} & 0 & 0 & 0 & 0 & 0 \\
0 & 0 & 0 & 0 & 0 & 0 & 0 & 0 & 0 & \frac{\partial N_i}{\partial x} & 0 & 0 & 0 & 0 \\
0 & 0 & 0 & 0 & 0 & 0 & 0 & 0 & 0 & 0 & \frac{\partial N_i}{\partial x} & 0 & 0 & 0 \\
0 & 0 & 0 & 0 & 0 & 0 & 0 & 0 & 0 & 0 & 0 & \frac{\partial N_i}{\partial x} & 0 & 0 \\
0 & 0 & 0 & 0 & 0 & 0 & 0 & 0 & 0 & 0 & 0 & 0 & \frac{\partial N_i}{\partial x} & 0 \\
0 & 0 & 0 & 0 & 0 & 0 & 0 & 0 & 0 & 0 & 0 & 0 & 0 & \frac{\partial N_i}{\partial x} \\
0 & 0 & 0 & 0 & N_i & 0 & 0 & 0 & 0 & 0 & 0 & 0 & 0 & 0 \\
0 & 0 & 0 & 0 & 0 & N_i & 0 & 0 & 0 & 0 & 0 & 0 & 0 & 0 \\
0 & 0 & 0 & 0 & 0 & 0 & N_i & 0 & 0 & 0 & 0 & 0 & 0 & 0 \\
0 & 0 & 0 & 0 & 0 & 0 & 0 & N_i & 0 & 0 & 0 & 0 & 0 & 0 \\
0 & 0 & 0 & 0 & 0 & 0 & 0 & 0 & N_i & 0 & 0 & 0 & 0 & 0 \\
0 & 0 & 0 & 0 & 0 & 0 & 0 & 0 & 0 & N_i & 0 & 0 & 0 & 0 \\
0 & 0 & 0 & 0 & 0 & 0 & 0 & 0 & 0 & 0 & N_i & 0 & 0 & 0 \\
0 & 0 & 0 & 0 & 0 & 0 & 0 & 0 & 0 & 0 & 0 & N_i & 0 & 0 \\
0 & 0 & 0 & 0 & 0 & 0 & 0 & 0 & 0 & 0 & 0 & 0 & N_i & 0 \\
0 & 0 & 0 & 0 & 0 & 0 & 0 & 0 & 0 & 0 & 0 & 0 & 0 & N_i
\end{bmatrix}$$

ELSEVIER

Composite Structures Vol. 38, No. 1–4, pp. 133–139
© 1997 Elsevier Science Ltd. All rights reserved
Printed in Great Britain
0263-8223/97/$17.00 + 0.00

PII:S0263-8223(97)00049-4

Study of damage evolution in composites using damage mechanics and micromechanics

Y. W. Kwon

Mechanical Engineering Department, Naval Postgraduate School, Monterey, California, USA

&

C. T. Liu

Phillips Laboratory, Edward AFB, California, USA

A numerical modeling technique was presented to simulate, predict and evaluate progressive damage or failure in a composite structure subjected to an external loading. To this end, a micro/macromechanical approach was proposed along with damage mechanics at the microlevel. The micro/macromechanical model utilized both the macromechanical analysis and the micromechanical analysis in tandem. The continuum damage mechanics was applied to the microlevel stresses–strains in order to predict damage evolution in a composite structure from the initiation of damage through to complete failure of the structure. Crack initiation and growth in a particulate composite with stress concentration was simulated using the proposed technique, and the results were compared to experimental data. The comparison showed a very good agreement. © 1997 Elsevier Science Ltd.

INTRODUCTION

Composite materials have been considered as substitutes for conventional materials for applications where specific strength and stiffness are the major concern. Examples include, but are not limited to, aerospace and military strutures. However, the design and analysis of composite structures challenges engineers because of the complicated nature of failure modes and mechanisms of composite materials. Therefore, prediction and evaluation of progressive damage in a composite structure is very important for structural design and/or analysis using advanced composite materials.

Modeling of damage or failure in composites was undertaken in the past, in general, using the macromechanical approach [1–7]. Because there are different damage or failure modes in a composite, depending on its physical constituents and lay-out, a damage or failure criterion was assumed for each case [8–16]. However, different damage or failure modes at the macromechanical level can be attributed to the same damage or failure mode at the micromechanical model. For example, fiber splitting, transvere matrix cracking and delamination result from the matrix damage or failure. Therefore, description of a damage or failure in terms of the micromechanical level can be more directive. At this level the damage or failure is classified in terms of the fiber/particle breakage, matrix cracking and/or interface debonding. However, the dimension of the micromechanical level is so much smaller than that of the macromechanical level. This makes it difficult to describe a progressive damage or failure in a general composite structure (i.e. macrolevel) using the microlevel damage or failure modes. As a result micromechanical studies generally have been focused on qualitative understanding of a damage or failure process in a composite

material, and prediction of the effective stiffness of an undamaged composite or a uniformly damaged composite [17–24].

In the present study, in order to relate the progressive damage at the microlevel to that at the structural level (i.e. macrolevel), the micro/macromechanical approach was proposed. In this approach the damage or failure of a structure is expressed in terms of the damage or failure of the constituent materials (i.e. microlevel). The micro/macromechanical approach can model, simulate and predict progressive damage or failure in a general composite structure including macrocrack initiation and growth, and reduction of strength and stiffness of the structure using the damage or failure of the constituent materials. This technique can provide engineers with a simulation-based design tool.

The next section describes the micro/macromechanical approach in detail. The approach is based on a micromechanical model and the damage mechanics. Thus, derivation of the micromodel and the damage mechanics is also provided later followed by some results and discussion as well as conclusions.

MICRO/MACROMECHANICAL APPROACH

The micro/macromechanical approach consists of two levels of analyses in tandem: macromechanical and micromechanical analyses. The two analysis modules are tied together through their inputs and outputs. The schematic diagram of the approach is illustrated in Fig. 1. For the macrolevel analysis, the finite-element technique [25] is utilized so that a general composite structure including plates and shells can be analyzed.

A finite-element analysis uses smeared, effective composite material properties which are determined from a microlevel analysis using a micromechanical model. In other words, the microlevel analysis computes the effective material properties from the constituent material properties. On the other hand, the smeared, composite-level stresses–strains from the finite-element analysis are decomposed into microstresses–microstrains at the constituent level (i.e. stresses–strains in the fiber, particle and matrix) using the micromechanical model. Then, the continuum damage mechanics is applied to the microstresses–microstrains to

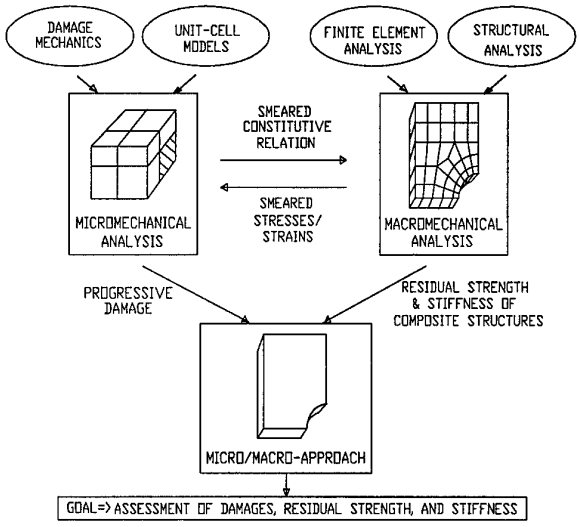

Fig. 1. Micro/macromechanical approach.

determine the damage initiation or growth in the constituent materials. Thus, fiber and/or matrix failure can be determined independently from the analysis. The damaged fibers, particles or matrix result(s) in reduced effective material properties for the subsequent finite-element analysis. Thus, the iteration of micro-/macroanalyses continues with progressive damage in the constituent materials until there is a complete failure in a structure (which denotes that a structure can no longer sustain a load) or until the final load is applied to a structure incrementally.

A detailed discussion about the micromechanical model and the damage mechanics are presented in subsequent sections. The microlevel analysis is performed, in general, at every element (or every numerical integration point) which can undergo damage. The elements may include the entire domain. However, the microlevel analysis is very computationally efficient because it is based on a simplified, analytical, three-dimensional micromechanical model. Therefore, the whole procedure in the micro/macromechanical approach is computationally efficient.

THREE-DIMENSIONAL MICROMECHANICAL MODEL

A micromechanical model for a fibrous composite was developed by Kwon *et al.* [24,26,27]. Thus, this section presents a micromechanical model for a particulate composite. The fibrous

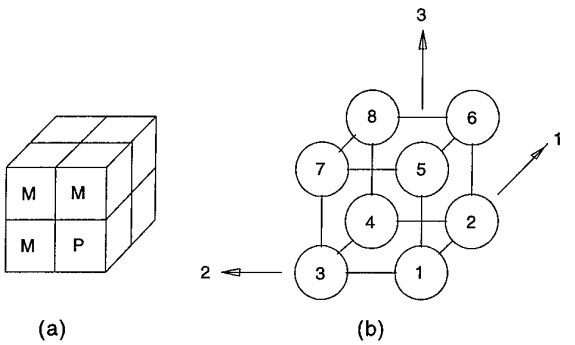

Fig. 2. Simplified, three-dimensional micromechanical model.

micromechanical model can be considered as a subset of the particulate micromechanical model. The simplified, micromechanical, unit-cell model is shown in Fig. 2(a). Figure 2(b) shows a clear view of the locations of eight subcells of the unit-cell seen in Fig. 2(a). Subcell 1 is the particle subcell and the rest are the binder (matrix) subcells. Planes 1–2, 2–3 and 3–1 are symmetric planes. For simplicity, it is assumed that each subcell has uniform stresses and strains. Equilibrium of subcell stresses at all interfaces must be satisfied as given below

$$\sigma_{11}^1 = \sigma_{11}^2,\ \sigma_{11}^3 = \sigma_{11}^4,\ \sigma_{11}^5 = \sigma_{11}^6,\ \sigma_{11}^7 = \sigma_{11}^8 \quad (1)$$

$$\sigma_{22}^1 = \sigma_{22}^3,\ \sigma_{22}^2 = \sigma_{22}^4,\ \sigma_{22}^5 = \sigma_{22}^7,\ \sigma_{22}^6 = \sigma_{22}^8 \quad (2)$$

$$\sigma_{33}^1 = \sigma_{33}^5,\ \sigma_{33}^2 = \sigma_{33}^6,\ \sigma_{33}^3 = \sigma_{33}^7,\ \sigma_{33}^4 = \sigma_{33}^8 \quad (3)$$

where the subscripts denote stress components along the axis shown in Fig. 2, and the superscript indicates the subcell number. Only normal stress components are considered in these equations. Similar equations can be written for shearing stress components. However, it is assumed that each subcell is an orthotropic or isotropic material so that normal stress–strain components are not coupled from shear components. Thus, the present development is only for the normal components of stresses–strains and a similar development can be made for the shearing stresses–strains.

It is assumed that subcells satisfy the following strain compatibility

$$l_p\varepsilon_{11}^1 + l_m\varepsilon_{11}^2 = l_p\varepsilon_{11}^3 + l_m\varepsilon_{11}^4 = l_p\varepsilon_{11}^5 + l_m\varepsilon_{11}^6 = l_p\varepsilon_{11}^7 + l_m\varepsilon_{11}^8 \quad (4)$$

$$l_p\varepsilon_{22}^1 + l_m\varepsilon_{22}^3 = l_p\varepsilon_{22}^2 + l_m\varepsilon_{22}^4 = l_p\varepsilon_{22}^5 + l_m\varepsilon_{22}^7 = l_p\varepsilon_{22}^6 + l_m\varepsilon_{22}^8 \quad (5)$$

$$l_p\varepsilon_{33}^1 + l_m\varepsilon_{33}^5 = l_p\varepsilon_{33}^2 + l_m\varepsilon_{33}^6 = l_p\varepsilon_{33}^3 + l_m\varepsilon_{33}^7 = l_p\varepsilon_{33}^4 + l_m\varepsilon_{33}^8 \quad (6)$$

in which

$$l_p = V_p^{1/3} \quad (7)$$

$$l_m = 1 - l_p \quad (8)$$

and V_p is the particle volume fraction of the composite.

The unit-cell stresses and strains are obtained from the volume average of subcell stresses and strains. In other words

$$\sigma_{ij} = \sum_{n=1}^{8} V^n \sigma_{ij}^n \quad (9)$$

$$\varepsilon_{ij} = \sum_{n=1}^{8} V^n \varepsilon_{ij}^n \quad (10)$$

Here, V^n is the volume fraction of the nth subcell over the unit-cell. Subscripts i and j vary from 1 to 3, and σ_{ij} and ε_{ij} are the average cell stresses and strains, respectively. Further, the constitutive equation between the subcell stresses and strains is

$$\sigma_{ij}^n = E_{ijkl}^n \varepsilon_{kl}^n \quad (11)$$

Manipulating these equations results in the following relationships explicitly

$$\sigma_{ij} = E_{ijkl}\varepsilon_{kl} \quad (12)$$

$$\varepsilon_{ij}^n = T_{ijkl}\varepsilon_{kl} \quad (13)$$

The detailed derivation is given by Kwon *et al.* [24,26,27] and is therefore omitted here. Equation (12) indicates the constitutive equation for the unit-cell. That is, E_{ijkl} is the smeared composite material property matrix determined from material properties of a particle and a matrix. This equation provides the route from the micromechanical analysis to the macromechanical analysis.

Equation (13) relates macrostrains (composite level strains) to microstrains (constituent level strains). Substituting the microstrains to eqn (11) yields microstresses. Thus, these equations make it possible to decompose macrostrains into microstrains, and likewise microstresses. The microstrains and microstresses are used for damage mechanics or failure criteria in the present analysis. Equation (13) yields the connection of the macromechanical analysis to the micromechanical analysis, the opposite to the process given in the previous paragraph.

In the unit-cell model, if any two contiguous subcells represent the fiber (for example, subcells '1' and '2'), the present model can also be

applied to a fibrous composite as developed by Kwon *et al.* [24,26,27].

CONTINUUM DAMAGE MODEL

Damage and failure in a composite structure is described in terms of those at the constituent level, i.e. fiber/particle fracture, matrix cracking and fiber(particle)/matrix debonding. The following derivation of continuum damage mechanics is for the matrix damage. However, a similar derivation may be obtained for fiber/particle damage. The present approach of continuum damage mechanics is a strain-based isotropic damage model as developed by Simo & Ju [28].

Introducing a scalar variable d as the damage parameter, the effective stress after damage can be expressed as

$$\bar{\sigma}_{ij} = \frac{\sigma_{ij}}{(1-d)} \tag{14}$$

where $\bar{\sigma}_{ij}$ and σ_{ij} are the effective and homogenized stress tensors, respectively. Further, the damage variable d is limited to between 0 and $d_c(<1)$, which denotes the damage saturation. It is assumed that the stress tensor can be obtained from the free energy as given below

$$\sigma_{ij} = \frac{\partial \Psi}{\partial \varepsilon_{ij}} = (1-d)\frac{\partial \Psi^o}{\partial \varepsilon_{ij}} \tag{15}$$

where Ψ^o is defined as $\frac{1}{2}E^o_{ijkl}\varepsilon_{ij}\varepsilon_{kl}$, and E^o_{ijkl} is the tensor of the undamaged material property.

The function for damage criterion is assumed to be

$$F = f(\varepsilon_{ij}, \sigma_{ij}) - \kappa \tag{16}$$

where κ is a constant for the damage threshold value which increases with the damage. If F is less than zero, damage does not occur, but damage occurs when $F = 0$. For the present damage model, function f is assumed to be

$$f(\varepsilon_{ij}) = \tilde{e} \tag{17}$$

where

$$\tilde{e} = \sqrt{2\Psi^o} \tag{18}$$

which is the equivalent strain measure as defined by Simo & Ju [28]. Equations (17) and (18) indicate that κ depends on the previous maximum state of strains. Thus, further damage begins to occur when the present state of strains reaches the previous maximum state of strains. This phenomenon was observed in some particulate composite materials such as a solid rocket propellant material [29].

Further, the damage evolution equation is defined as

$$\dot{d} = \dot{\kappa} g(\tilde{e}) \tag{19}$$

where the overdot denotes temporal derivative. Damage loading and unloading conditions can be stated as

$$\dot{\kappa} \geq 0 \tag{20}$$

$$F \leq 0 \tag{21}$$

$$\dot{\kappa} F = 0 \tag{22}$$

For unloading, $F<0$ and $\dot{\kappa} = 0$. Then $\dot{d} = 0$ from eqn (19). This indicates no more damage. On the other hand, if $\dot{\kappa}>0$, then $F = 0$ and $\dot{d} > 0$, i.e. damage is occurring.

In order to determine the damage tangent modulus, the time derivative is sustituted into eqn (15). Then

$$\dot{\sigma}_{ij} = (1-d)E^o_{ijkl}\dot{\varepsilon}_{kl} - \dot{d}\sigma^o_{ij} \tag{23}$$

where

$$\sigma^o_{ij} = \frac{\partial \Psi^o}{\partial \varepsilon_{ij}} \tag{24}$$

Use of previous equations finally results in the damage tangent modulus

$$E_{ijkl} = (1-d)E^o_{ijkl} - \frac{g}{\tilde{e}}\sigma^o_{ij}\sigma^o_{kl} \tag{25}$$

For the particulate composite under present study, function g is assumed to be constant. That is, the rate of damage evolution is linearly proportional to the rate of equivalent strain measure. Further, if the damage parameter d reaches its critical value d_c at a local zone, damage becomes saturated and a crack is assumed to initiate at the location. It is also assumed that the direction of crack propagation is determined from the direction of d_c in the material.

RESULTS AND DISCUSSION

A study was conducted to investigate the crack initiation in a particulate composite material using the micro/macromechanical approach and the damage mechanics as described in the previous sections. In order to evaluate the micromechanical model and the damage mechanics model, a uniaxial tensile test was conducted for the material. The micromechanical model requires the material properties of the particles and the matrix. For the present composite, the elastic modulus of the particles was 1.0×10^6 psi and that of the binding matrix was 110 psi. Thus, the particles are much stiffer than the matrix material. The particle volume fraction was 0.78. The predicted stress–strain curve agrees well with the experimental curve, as seen in Fig. 3.

The next study examined crack initiation from a notched specimen made of the same material as above. The specimens had dimensions of 3 in. wide by 3 in. long and 0.25 in. thick. Two circular holes of two different sizes were drilled at the center: one hole had a 0.25-in. diameter and the other had a 0.5-in. diameter. The specimens were subjected to tension with uniform displacement until a crack initiated from the hole. Numerical prediction was also undertaken for the crack initiation. A typical finite-element mesh is shown in Fig. 4. The mesh is refined around the hole.

For the specimen with a 0.25-in. diameter hole, the applied load vs displacement is plotted in Fig. 5 for both the experimental and numerical results until a crack initiates. The displacement is half the displacement between the two grips because of the symmetry of the specimen. The curve was linear up to a displacement of 0.11 in. and then became nonlinear. The crack occurred at a displacement of approximately 0.14 in. Damage initiated before the breaking point from the linearity in the curve. However, a small amount of damage at a local area around the notch tip of the hole had little effect on the damage tangent modulus. As the damage grew, the damage tangent modulus became significantly reduced from the virgin modulus and the curve deviated from linearity. The two curves obtained both from the

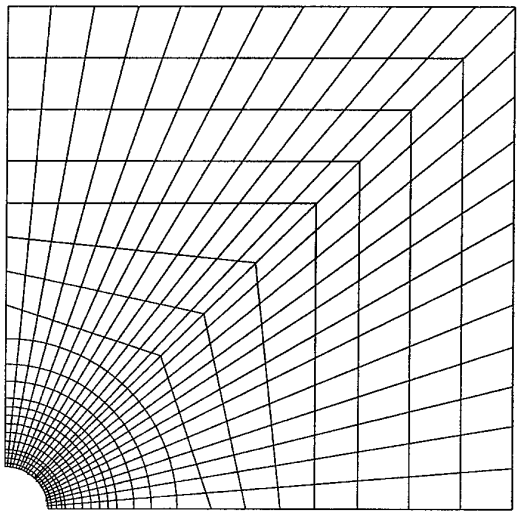

Fig. 4. Finite-element mesh for a specimen with a 0.5-in. diameter hole.

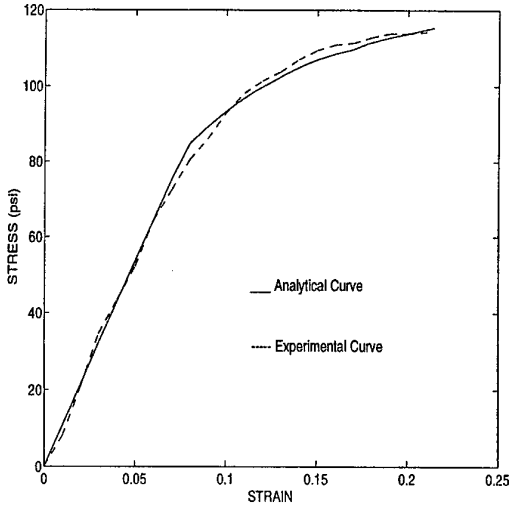

Fig. 3. Stress–strain curves.

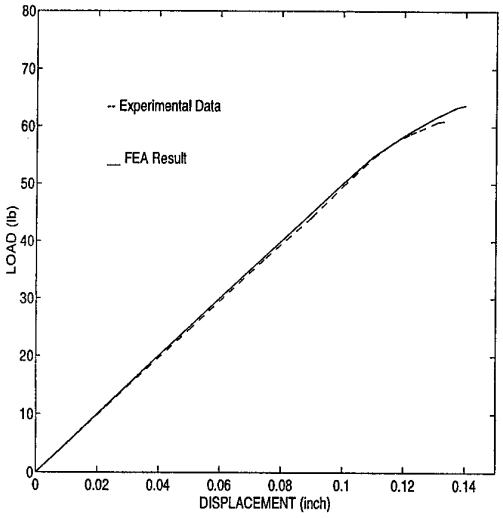

Fig. 5. Load–displacement curve for a specimen with a 0.25-in. diameter hole.

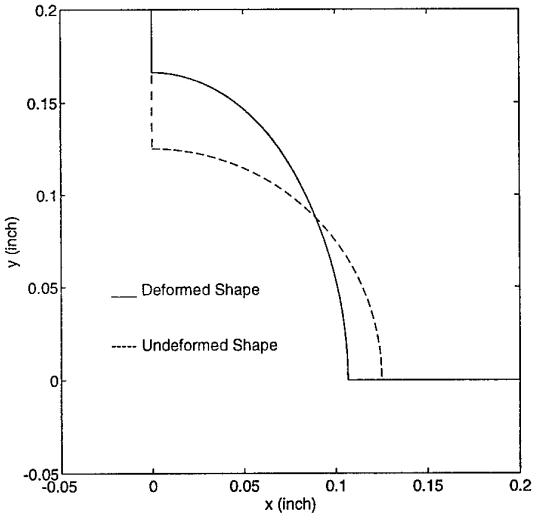

Fig. 6. Deformed shape of a specimen with a 0.25-in. diameter hole.

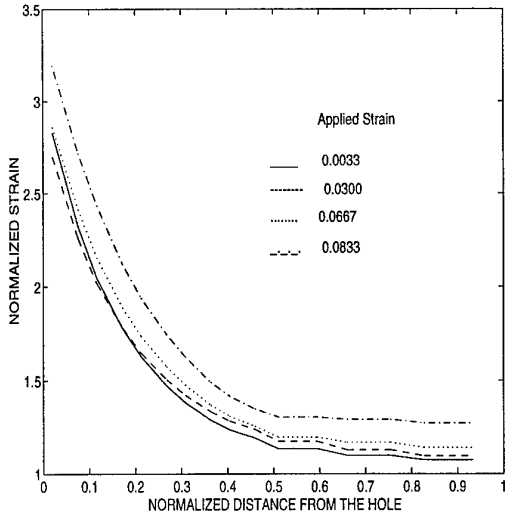

Fig. 7. Strain distribution along the minimum section.

experimental and the numerical studies show almost the same results.

Further, the predicted crack size was 0.048 in., while the measured crack size was between 0.043 and 0.051 in. Thus, the prediction lies within the experimental data. Figure 6 illustrates the predicted deformed shape of the initially circular hole. The circular hole became elliptic and the major diameter was about 60 longer than the minor diameter. This geometry was also confirmed by the experimental observations made by Yen & Liu [30]. The saturated damage zone did not increase for a while even when the applied strain to the specimen increased. As the applied strain increased further, the saturated damage zone then propagated. This phenomenon was also observed in the experiment. The experimental study showed that the critical crack hesitated for a while prior to propagation.

Figure 7 shows the distribution of normal strains in the load direction as a function of distance from the hole edge. The distance was normalized with respect to the hole radius, while the strain was normalized in terms of the applied strain. Before damage occurs, the strain concentration near the hole decreases along with the increase in the applied strain. This reduction is caused by the deformation of the circular hole into an ellipic shape with the major axis along the loading direction. The concentration factor for an elliptic hole is given by Timoshenko & Goodier [31] as $(1+2\,a/b)$, in which $2a$ is the axis of the ellipse normal to the loading direction and $2b$ is the axis in the loading direction. Therefore, this expression agreed with the present result. However, the normalized strain increases away from the hole as the load increases. (Compare the two curves in Fig. 7 for applied strains of 0.0033 and 0.0300, respectively.) On the other hand, as the damage initiates and propagates, the normalized strain increases because the damage tangent modulus decreases. In Fig. 7, the cases with applied strains of 0.0667 and 0.0833 show an increase in the normalized strain when compared to the other curves.

Similar comparisons were also made for the specimen with a 0.5-in. diameter hole. Figure 8

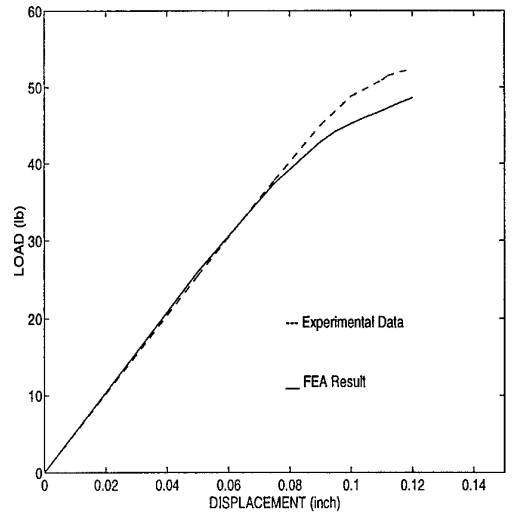

Fig. 8. Load–displacement curve for a specimen with a 0.5-in. diameter hole.

gives the load–displacement curve for comparison. The predicted crack size was 0.045 in., while the measured crack was between 0.035 and 0.067 in. Therefore, the prediction agreed well with the experimental data. The measured crack size for the 0.5-in. diameter hole had a larger variation than that for the 0.25-in. diameter hole.

CONCLUSIONS

A micro/macromechanical approach using the finite-element technique, a simplified micromechanical model and damage mechanics was developed to simulate the damage initiation and growth in a composite structure. The approach can model a general composite structure made of fibrous or particulate composite materials, and is also computationally efficient. The proposed approch was applied to investigate crack initiation in particulate composite specimens with a center hole. The numerically predicted results agreed well with the experimental data. Thus, the proposed approach is useful for the design and analysis of composite structures in terms of damage and failure.

REFERENCES

1. Tsai, S. W. & Hahn, H. T., *Introduction to Composite Materials*. Technomic Publishing Co., Westport, CT, 1980.
2. Gibson, R. F., *Principles of Composite Material Mechanics*. McGraw-Hill, New York, 1994.
3. Hill, R., A theory of the yielding and plastic flow of anisotropic metals. *Proc. R. Soc. Lond.* 1948, **A193**, 281–297.
4. Waddoups, M. E., Advanced composite material mechanics for the design and stress analyst. Report FZM-4763, General Dynamics, Fort Worth Division, 1967.
5. Tsai, S. W., Strength theories of filamentary structures. In *Fundamental Aspects of Fiber Reinforced Plastic Composites*, eds R. T. Schwarz & H. S. Schwartz. Wiley Interscience, New York, 1968.
6. Tsai, S. W. and Wu, E. M., A general theory of strength for anisotropic materials. *J. Composite Mater.* 1971, **5**, 58–80.
7. Hart-Smith, L. J., The role of biaxial stresses in discriminating between meaningful and illusory composite failure theories. *Composite Struct.* 1993, **25**, 3–20.
8. Hashin, Z., Failure criteria for unidirectional fiber composites. *J. Appl. Mech.* 1980, **47**, 329–334.
9. Chang, F. K. and Chang, K. Y., A progressive damage model for laminated composites containing stress concentrations. *J. Composite Mater.* 1987, **21**, 834–855.
10. Kelly, A. and Davies, G. J., The principles of the fibre reinforcement of metals. *Metall. Rev.* 1965, **10**, 1–77.
11. Rosen, B. W., Tensile strength of fibrous composites. *AIAA J.* 1964, **2**, 1985–1991.
12. Rosen, B. W., *Mechanics of Composite Strengthening*. In *Fiber Composite Materials*. American Society for Metals, Metals Park, OH, 1965, 37–75.
13. Kim, R. Y. and Soni, S. R., Experimental and analytical studies on the onset of delamination in laminated composites. *J. Composite Mater.* 1984, **18**, 70–80.
14. Whitney, J. M. and Nuismer, R. J., Stress fracture criteria for laminated composites containing stress concentrations. *J. Composite Mater.* 1974, **8**, 253–265.
15. Brewer, J. C. and Lagace, P. A., Quadratic stress criterion for initiation of delamination. *J. Composite Mater.* 1988, **22**, 1141–1155.
16. O'Brien, T. K., Characterization of delamination onset and growth in a composite laminate. In *Damage in Composite Materials*, ed. K. L. Reifsnider. American Society of Testing and Materials (ASTM) STP 775, 1982, pp. 140–67.
17. Ekvall, J. C., Elastic properties of orthotropic monofilament laminates. ASME Paper 61-AV-56, Aviation Conference, Los Angeles, CA, 1961.
18. Hashin, Z. & Rosen, B. W., The elastic moduli of fiber-reinforced materials. *J. Appl. Mech.*, ASME, Paper No. 63-WA-175, 1964, **31**, 223–232.
19. Dvorak, G. J. and Bahei-El-Din, Y. A., Plasticity analysis of fibrous composites. *J. Appl. Mech.* 1982, **49**, 327–335.
20. Aboudi, J., Micromechanical analysis of composites by the method of cells. *Appl. Mech. Rev.* 1989, **42** (7), 193–221.
21. Pecknold, D. A., A framework for 3-D nonlinear modeling of thick-section composites. DTRC-SME-90/92, Ship Materials Engineering Department Research and Development Report, David Taylor Research Center, 1990.
22. Adams, D., Elastoplastic behavior of composites. In *Mechanics of Composite Materials*, ed. G. P. Sendeckyi. Academic Press, New York, 1974, pp. 169–208.
23. Chamis, C. C., Micromechanics strength theories. In *Composite Materials, Volume 5: Fracture and Fatigure*, ed. L. J. Broutman. Academic Press, New York, 1974, Chap. 3.
24. Kwon, Y. W., Calculation of effective moduli of fibrous composites with or without micro-mechanical damage. *Composite Struct.* 1993, **25**, 187–192.
25. Kwon, Y. W. & Bang, H.-C., *The Finite Element Method Using Matlab*. CRC Press, Boca Raton, FL, 1997.
26. Kwon, Y. W. and Berner, J., Analysis of matrix damage evolution in laminated composite plates. *Engng Fract. Mech.* 1994, **48**, 811–817.
27. Kwon, Y. W. and Berner, J. M., Micromechanics model for damage and failure analyses of laminated fibrous composites. *Engng Fract. Mech.* 1995, **52**, 231–242.
28. Simo, J. C. and Ju, J. W., Strain- and stress-based continuum damage models — I. Formulation. *Int. J. Solids Struct.* 1987, **23**, 821–840.
29. Gurtin, M. E. and Francis, E. C., Simple rate-independent model for damage. *J. Spacecraft* 1981, **18**, 285–286.
30. Yen, S. C. M. & Liu, C. T., Investigating the local behaviors near the crack tip of a particular composite containing a circular hole. In *Third International Conference on Composites Engineering*, New Orleans, Louisiana, ed. D. Hui, 1996, pp. 953–4.
31. Timoshenko, S. P. & Goodier, J. N., *Theory of Elasticity*, 3rd edn. McGraw-Hill, New York, 1970.

ELSEVIER

Composite Structures Vol. 38, No. 1–4, pp. 141–149, 1997
© 1997 Elsevier Science Ltd. All rights reserved
Printed in Great Britain
0263-8223/97/$17.00 + 0.00

PII:S0263-8223(97)00050-0

Fibre-reinforced caissons for offshore applications

P. J. Boothby* & C. D. Johnstone

BG plc Research and Technology, Gas Research and Technology Centre, Ashby Road, Loughborough LE11 3GR, UK

Steel caissons currently used on offshore platforms for the uplift of seawater onto platform topsides, for example, are susceptible to corrosion, and some operators have had to replace corroded caissons during service. The use of fibre reinforced plastics (FRP), in particular glass-fibre (GRP), has been explored by a number of offshore operators as an alternative to steel, principally due to the resistance to corrosion of these materials. In addition, their relative light weight facilitates handling and installation that is particularly beneficial for retrofit applications.

However, the low flexural modulus of GRP compared to steel, combined with the large support spacings on conventional steel jacket structures in the splash zone region, means that standard GRP tubes designed for biaxial loading (i.e. with $\pm 55°$ reinforcement fibre winding angle) will exhibit greater deflections than their steel counterparts, when subjected to the various in-service wave loadings.

An investigation has therefore been conducted to determine the improvement in flexural modulus of GRP tubes manufactured with shallower reinforcement winding angles. Tubes manufactured with a range winding angles and different reinforcement types have been obtained and subjected to deflection tests. Experimental results are presented and compared with predictions of flexural modulus generated from laminate analyses software packages. © 1997 Elsevier Science Ltd.

INTRODUCTION

Caissons are large-diameter piping transportation systems suspended from offshore platforms for the import of seawater to, and the export of waste products from, the platform topside. They vary in size, from 250 to 1200 mm in diameter and from 20 to 100 m in length, depending on the function required and the size of the platform. Import caissons typically incorporate a central pumping and riser system to lift seawater to the platform topside for process, utility and fire applications. Export caissons normally contain a number of smaller pipes discharging treated effluent. A schematic of a caisson is shown in Fig. 1.

Steel caissons currently used are susceptible to corrosion, and require rigorous inspection, maintenance and repair/replacement procedures to ensure accordance with safety legislation, especially for fire water systems. These procedures are extremely expensive, often requiring underwater inspection, and can total as much as five times the original installation costs over the life of the caisson [1].

The use of fibre-reinforced plastics (FRP), in particular glass-reinforced plastic (GRP), has been explored by a number of offshore suppliers and operators as an alternative to steel, principally due to the corrosion resistance afforded by these materials. In addition, their relative light weight facilitates handling and installation, reducing the cost of retrofit applications. The substitution of a GRP caisson represents a 50% weight reduction over an equivalent steel caisson.

However, the relatively low flexural modulus of GRP, combined with the large support spacings through the splash zone on conventional

*Now at BG plc Transco, Norgas House, Killingworth, Newcastle upon Tyne, NE99 1GB.

steel jacket structures, means that standard GRP tubes designed for biaxial loading (i.e. with a $\pm 55°$ reinforcement fibre-winding angle) will deflect more than their steel counterparts when subjected to in-service wave loadings. Moreover, it is a design requirement that these deflections do not exceed prescribed limits or restrict the performance of the equipment housed within the caissons. An investigation has therefore been conducted to determine the increase in flexural modulus that can be achieved by manufacturing tubes with shallower reinforcement winding angles, and hybrid glass–carbon fibre reinforcement.

Glass-reinforced epoxy (GRE) tubes manufactured with a range winding angles and different reinforcement types were subjected to flexural-bending tests. The experimental results were then compared with predictions of flexural modulus generated from laminate analysis software packages. In addition, finite-element analysis was used to assess the magnitude of GRE caisson deflections when subjected to a critical in-service load; in this case, the 100-year wave load. The resulting data have been considered with regard to the geometry, loading, deflections and access of a typical caisson to indicate the feasibility of a GRP replacement.

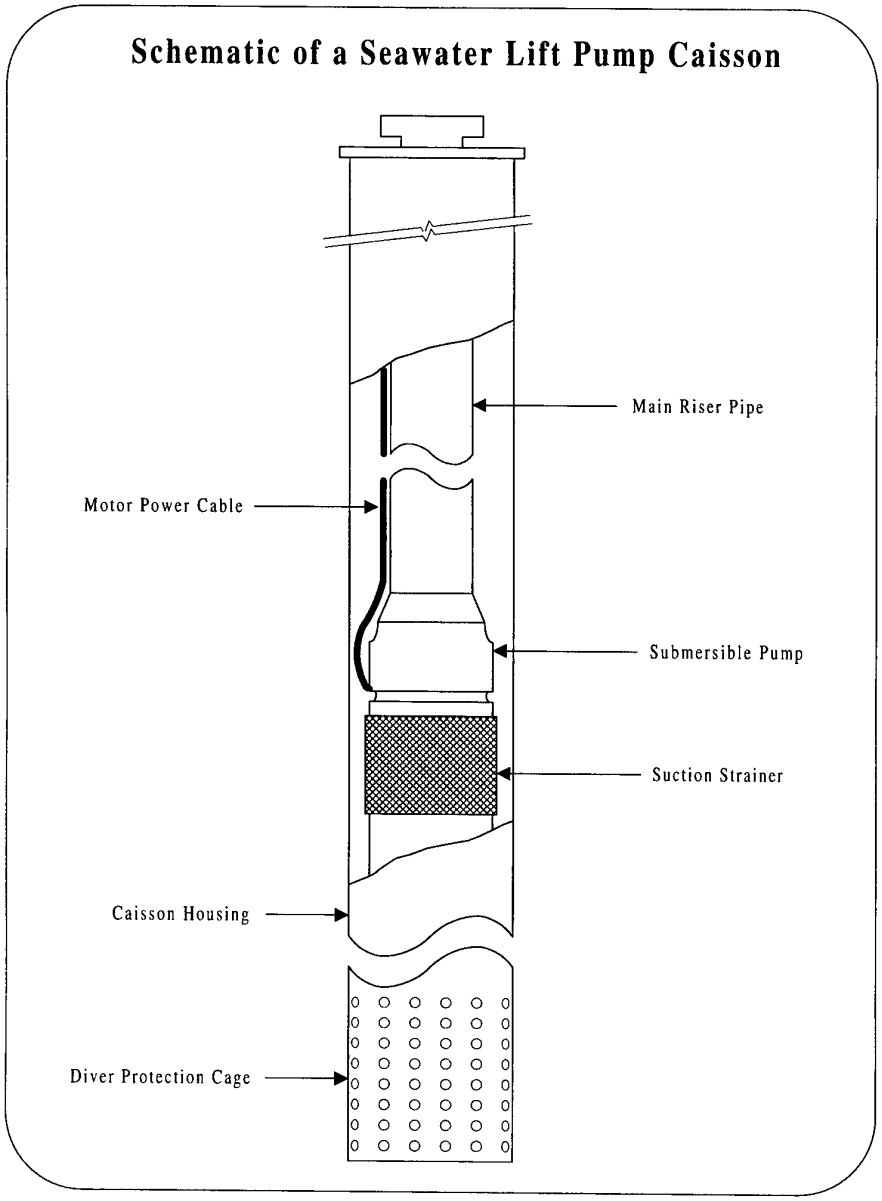

Fig. 1. Schematic of a seawater lift pump.

APPROACH

The GRP caisson study has been conducted in three stages.

Four-point flexural tests were performed on composite tubular specimens with a range of laminate constructions to determine flexural modulus. In addition to flexural modulus values, failure load, deflection and strain to failure were also recorded.

Predicted values of flexural modulus, obtained from commercially available software, were compared with the measured values from the flexural tests. Potentially, these software packages afford quick and easy methods of determining stiffness properties of composite materials with various laminate architectures, which can speed up the design process.

Finite-element analyses of actual caisson geometries were performed. Predictions of the maximum deflections and peak stresses made for both the steel and the GRP caissons, subjected to the 100-year wave load, were obtained. The purpose of this analysis was to determine the relative performance of steel and GRP caissons under in-service loading conditions. Two caissons diameters were selected for analysis: 610 and 1016 mm.

Experimental testing — four-point bend tests

Two types of GRE tubes were obtained from two manufacturers. Details of all the sample tubes are given in Table 1. Strain gauges were attached to the mid-point of the tubes at the top and bottom, dead centre, to measure failure strains. The four-point bend tests were carried out in each case until sample failure occurred. The length of the support spans for the bend tests were determined by scaling down a 22 m full-size span by the appropriate scale factor for each tube, namely 1:5 and 1:10. Test results are summarized in Table 2 [2].

Analytical predictions of flexural modulus for various laminate constructions

The following software tools were used to predict the relationship between flexural modulus and the laminate construction of GRP tubes.

Trilam II — Osbourne Composite Engineering Ltd;

Clamp — Hunting Engineering in-house program.

Both of these software packages use classical laminate analysis theory as their basis. Various laminate constructions were analysed, with the objective of optimizing flexural modulus. Variables included reinforcement winding angle, fibre volume fraction, number of layers, and resin and reinforcement types. Predicted flexural moduli for the different laminate constructions interrogated are given in Table 3.

The predicted values of flexural modulus compare favourably with those values obtained from flexural tests in all cases, except for the $\pm 10°$ hybrid (29% carbon–71% E-glass) specimen. A possible explanation for this could lie in the actual location of the carbon reinforcement fibres. To increase the carbon fibre reinforcement content from 14 to 29%, additional carbon layers were placed on the inside of the tube, with the effect that the contribution to the flexural modulus of the *internal* carbon reinforcing layers was negligible when compared to the carbon reinforcing layers placed on the outside of the tube. It would appear that the software

Table 1. Details of GRE sample tubes tested

Scale[a]	Internal diameter (mm)	Length (m)	Thickness (mm)	Winding angle (°)	Quantity tested	Details
1:5	208	4.9[b]	6	30	1	E-glass–epoxy (GRE)
1:5	208	4.9[b]	8	30	2	E-glass–epoxy (GRE)
1:10	106	2.5	4	10	3	E-glass–epoxy (GRE)
1:10	106	2.5	4	15	2	E-glass–epoxy (GRE)
1:10	106	2.5	6	15	2	E-glass–epoxy (GRE)
1:10	106	2.5	4	20	3	E-glass–epoxy (GRE)
1:10	106	2.5	4	10	3	Hybrid (29% carbon–71% E-glass)–epoxy
1:10	106	2.5	4	10	3	Hybrid (14% carbon–86% E-glass)–epoxy

[a]Scale indicates ratio of size of sample compared with full-sized caisson.
[b]4.9 m tubes were supplied with flanged ends.

Table 2. Results of four-point deflection tests

Winding angle (°)	Wall thickness (mm)	Material	Maximum load (kN)	Calculated maximum stress (MPa)	Flexural modulus (GPa)	Maximum displacement (mm)	Maximum strain TDC (axial) ($\mu\varepsilon$)	Maximum strain BDC (axial) ($\mu\varepsilon$)
208 mm diameter, 4.4 m span								
30	6	GRE	38.9	142	**24.5**	**130**	−5776	**5950**
30	8	GRE	64.9	148.3	**24.1**	**137**	−6150	**6605**
30	8	GRE	63.3	158.1	**24.4**	**135**	−6797	**6945**
106 mm diameter, 2.2 m span								
10	4	GRE	33.4	320	**32.9**	**96**	−9103	**10065**
10	4	GRE	*34.9*	*334*	**32.9**	***100***	*−8049*	***10708***
10	4	GRE	46.3	436.8	**31.8**	**134**	−13760	**13700**
15	4	GRE	45.3	427.6	**28.1**	**143**	−17270	**17930**
15	4	GRE	43.3	426.1	**29.3**	**137**	−19847	**13322**
15	6	GRE	71.6	453.7	**28.3**	**151**	−14274	**14740**
15	6	GRE	72	453.4	**26**	**152**	−21420	**14800**
20	4	GRE	27.3	262	**28.8**	**94**	−10466	**10080**
20	4	GRE	*28.0*	*268.3*	***28.1***	***103***	*−9078*	***10695***
20	4	GRE	32.5	313.5	**27.4**	**117**	−11411	**11247**
10	4	Hybrid (29% carbon)	49.7	430.9	**41.4**	**96**	−12770	**9144**
10	4	Hybrid (29% carbon)	43.1	390.4	**44.1**	**79**	−8540	**10330**
10	4	Hybrid (29% carbon)	36	333.6	**45.3**	**67**	−8821	**9870**
10	4	Hybrid (14% carbon)	52.2	420.2	**43.8**	**88**	−7405	**9215**
10	4	Hybrid (14% carbon)	52.2	434.6	**45.2**	**87**	−8340	**9460**
10	4	Hybrid (14% carbon)	47.4	382.5	**43.3**	**71**	−8184	**8889**

Italics indicate data recorded at maximum machine displacement before tube failure.

analysis packages simply calculate the stiffness of the laminate, and do not take into account any structural effects.

Analysis of offshore caissons

The Atkins Structural Analysis Systems (ASAS) finite-element package was used to simulate the effect of the load produced on a caisson by the 100-year wave. Two typical caisson sizes were chosen, with diameters of 610 and 1016 mm and an unsupported span of 22 m through the splash zone.

The maximum bending moment in the caisson occurs at the upper lateral restraint of the 22 m span, while the maximum deflection

Table 3. Comparison of predicted and measured flexural modulus

Winding angle (°C)	Wall thickness (mm)	Material	Flexural modulus (GPa)			
			Predicted[a]		Actual measured	
			Trilam	Clamp	Individual values	Mean
208 mm diameter						
30	6	GRE	24.1		24.5	24.5
30	8	GRE	24.4	—	24.1, 24.4	24.3
106 mm diameter						
10	4	GRE	33.1	32	31.8, 32.9, 32.9	32.5
15	4	GRE	31.2	29.8	28.1, 29.3	28.7
15	6	GRE	34.1	30.8	28.3, 26.0	27.2
20	4	GRE	31.8	27.5	27.4, 28.8, 28.1	28.1
10	4	Hybrid (29% carbon)	79.1	50.6	41.4, 44.1, 45.3	43.6
10	4	Hybrid (14% carbon)	40.9	38	43.8, 45.2, 43.3	44.1
55 (standard pipe)			10.4	—		11.7[b]

[a]Based on a 75% by weight reinforcement to resin ratio.
[b]Manufacturer's data.

occurs at the mid-point of the span, see Fig. 2. Graphs showing maximum bending stress and maximum deflections for the two caisson sizes are shown in Figs 3–6. For comparison, predicted deflections are given for steel and for GRP caissons with different levels of assumed flexural modulus.

The trends shown in Figs 4 and 6 are clear. Significant reductions in the maximum deflection of the caisson can be realized by increasing the flexural modulus. The tests described in the previous section show that GRP tubes manufactured with shallow winding angles have flexural moduli ranging from 24 to 33 GPa, and up to 44 GPa for the glass–carbon hybrid tubes. This represents a significant improvement in the flexural modulus for the standard $\pm 55°$ wound tube, namely 11.7 GPa [3]. Based on the rationale that a 50% weight saving would be achieved by using GRP tubes with a wall thickness around twice that of steel, the deflection data are summarized in Table 4.

The analysis predicts that the deflections for GRP caissons are approximately three times that for the associated steel caissons, albeit for different wall thicknesses. Also, the deflections are markedly lower for the larger diameter caissons, as would be expected. For the 1016 mm

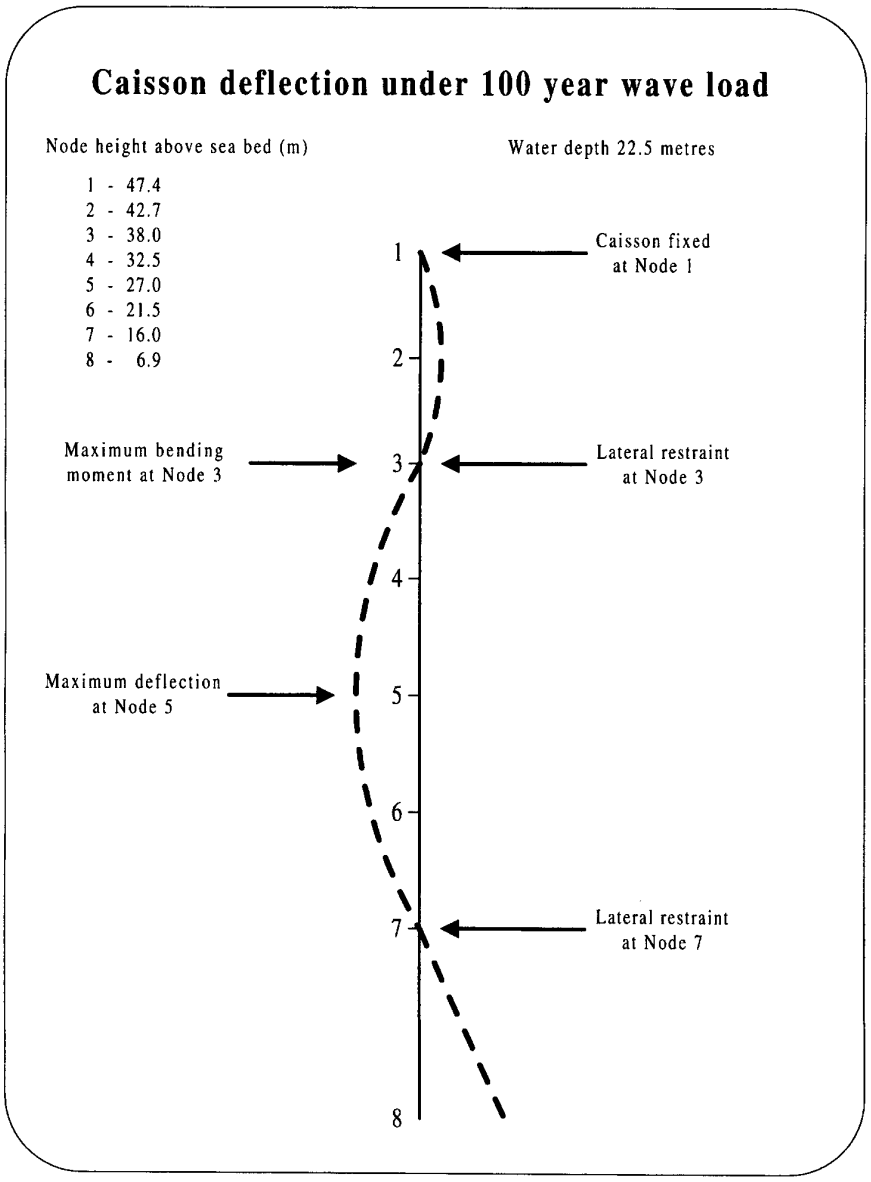

Fig. 2. Caisson deflection under the 100-year wave load.

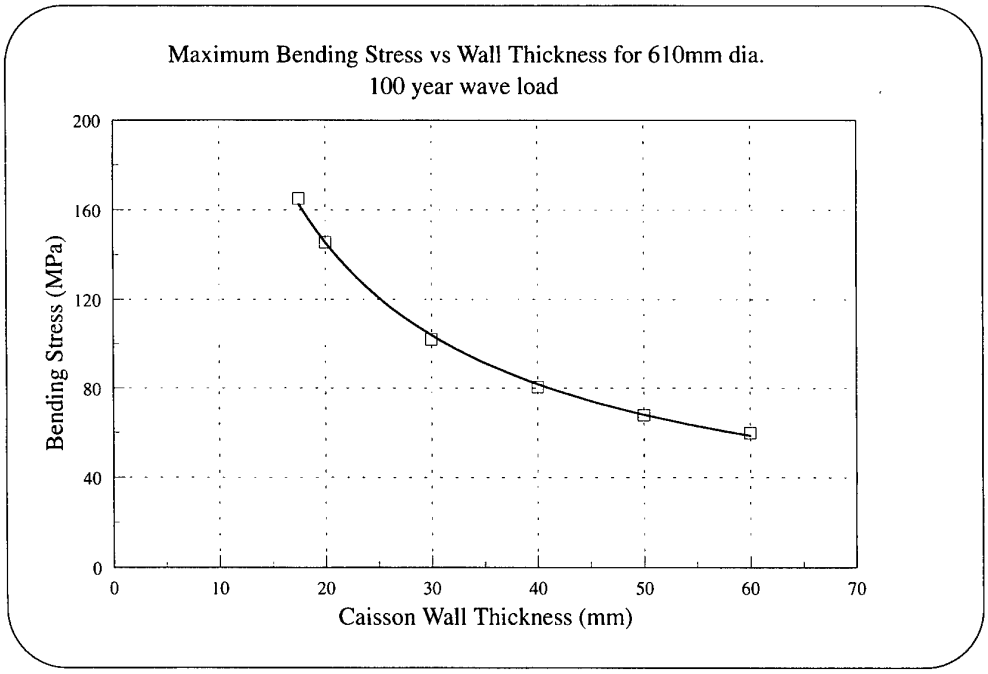

Fig. 3. Maximum bending stress vs wall thickness for a 610 mm diameter 100-year wave load.

diameter caisson, the relative slenderness of the internal riser and the location of the pump towards the bottom of the caisson are such that deflections of 83 mm should be accommodated easily, without damage to internal equipment. However, the maximum deflection of the 610 mm diameter GRP caisson (257 mm) may prove to be sufficiently large that the operational and/or safety requirements are compromised. Methods of limiting the maximum deflections of relatively slender caissons are best addressed on a case-by-case basis.

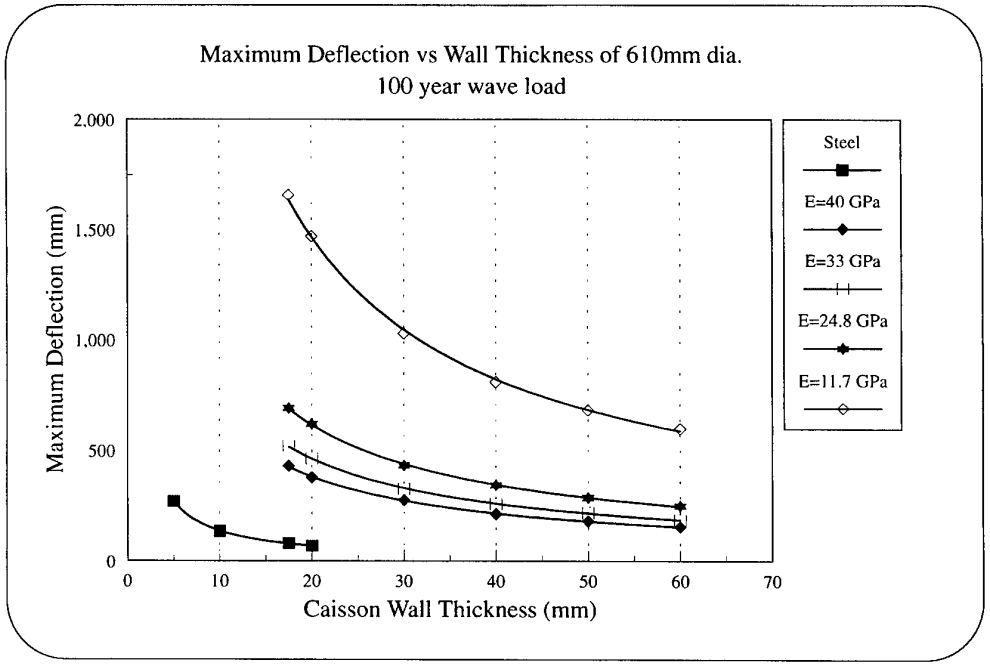

Fig. 4. Maximum deflection vs wall thickness for a 610 mm diameter 100-year wave load.

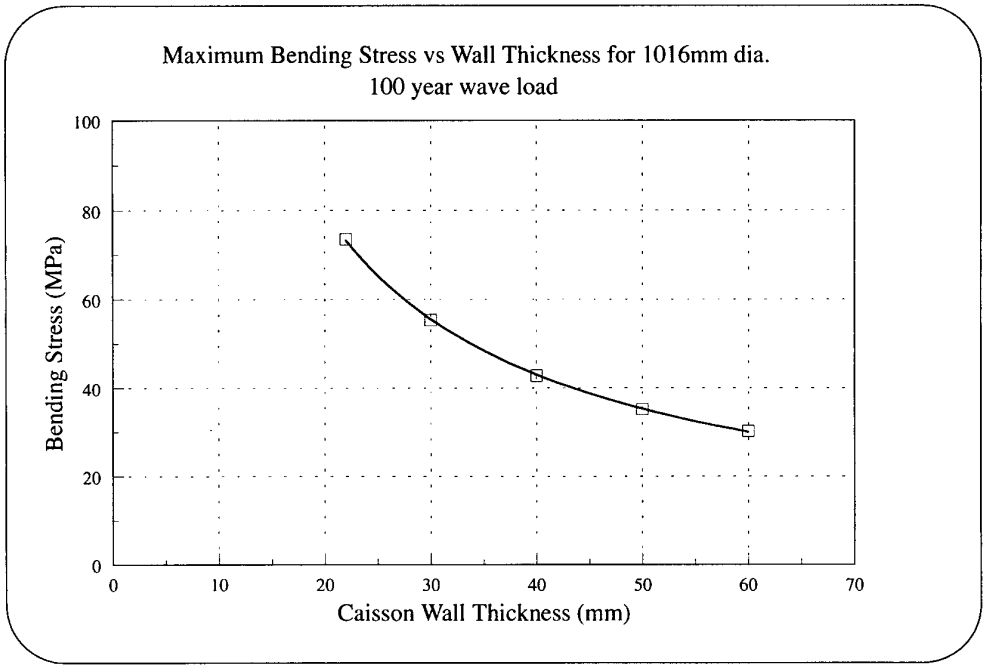

Fig. 5. Maximum bending stress vs wall thickness for a 1016 mm diameter 100-year wave load.

OBSERVATIONS FROM THE STUDY

Experimental measurements of flexural modulus

The measured values of flexural modulus for the GRE tubes ranged from 24.3 GPa ($\pm 30°$ winding angle) to 32.5 GPa ($\pm 10°$ winding angle). This represents a significant improvement compared with the flexural modulus of a standard $\pm 55°$ winding angle tube (i.e. 11.7 GPa).

A further improvement in flexural modulus to 44 GPa was obtained for the hybrid glass–

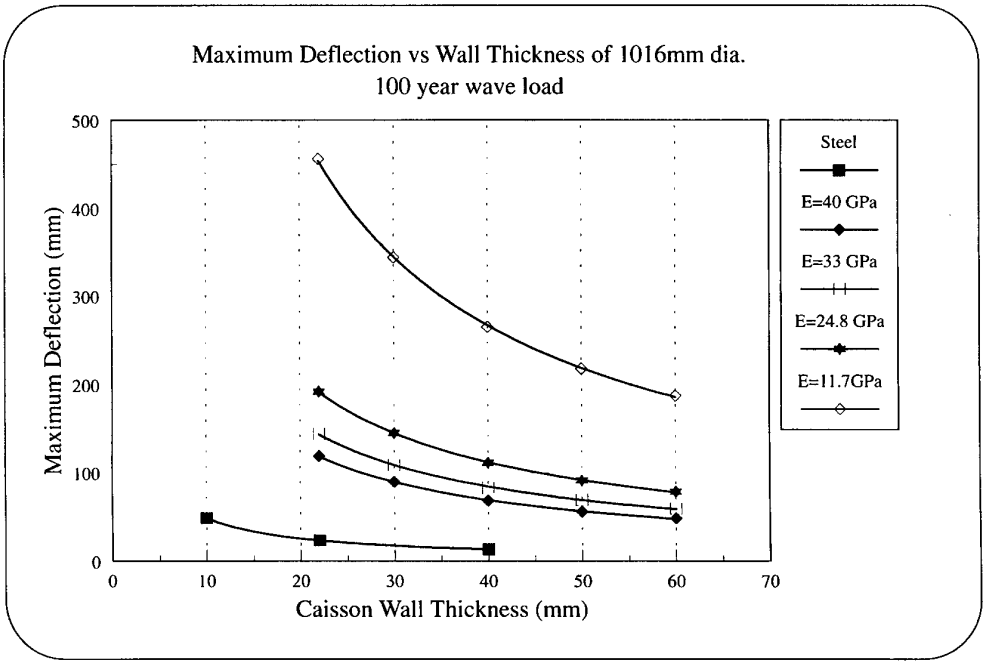

Fig. 6. Maximum deflection vs wall thickness for a 1016 mm diameter 100-year wave load.

Table 4. Deflection data

Material	Wall thickness (mm)	Maximum deflection (mm)	
		610 mm diameter	1016 mm diameter
Steel	17.5	80	
Steel	22		24
GRP (flexural modulus 33 GPa)	40	257	83
Hybrid (flexural modulus 40 GPa)	40	211	69

carbon tube. However, increasing the proportion of carbon in the reinforcement from 14 to 29% produced no change in measured flexural modulus, although the laminate analysis software predicts a significant increase.

Comparison of measured and predicted flexural modulus

Predicted moduli agreed reasonably well with the measured values for the all GRE tubes. Of the two programs compared, the Hunting Clamp program produced better agreement than the Trilam II software package, the latter tending to overestimate the flexural modulus.

Predicted moduli were less reliable for the hybrid tubes, resulting in a 7–14% underestimate for the lower carbon variant, and a large overestimate for the higher carbon variant. This could be attributed to the fact that the software analysis packages simply calculate the stiffness of the laminate, and do not take into account any stiffness effects afforded by the structure itself.

The reason for the discrepancy between the predicted and measured values for the $\pm 10°$ hybrid (29% carbon–71% E-glass) specimen may be explained by the details of the laminate construction. The extra carbon layers were placed on the inside of the tube, with the effect that the contribution of the *internal* carbon reinforcing layers to flexural modulus was negligible when compared to those placed on the outside of the tube.

It should also be recognized that there will be a cost implication of using carbon reinforcement as carbon fibre is an order of magnitude more expensive than E-glass. In addition, other aspects of performance would need to be evaluated, such as fatigue and impact tolerance.

Table 5. Determination of the fibre to resin ratio

Sample details		Fibre content	
Winding angle (°)	Wall thickness (mm)	% by volume	% by weight
10.0	4	56.2	75.4
20.0	4	56.7	76.1

Other properties

Tensile axial strains at failure varied as indicated:

$\pm 30°$ GRE tubes 0.6–0.7%;
$\pm 20°$ GRE tubes 1.0–1.1%;
$\pm 15°$ GRE tubes 1.3–1.5%;
$\pm 10°$ GRE tubes 1.0–1.4%;
$\pm 10°$ hybrid tubes 0.9–1.0%.

Burn-off tests were conducted to determine the fibre to resin ratio for selected tubes. Results are given in Table 5.

Comparison of the finite-element analysis with experimental data

The $\pm 10°$ GRE tubes failed at bending stresses of around 300–400 MPa. Corresponding failure strains are of the order of 1–1.4%. The analysis predicts a maximum bending stress of 43 MPa for the 1016 mm diameter, 40 mm wall thickness, caisson. Therefore, strain levels in the caisson will be an order of magnitude smaller than the failure strains, typically 0.1–0.14%, as stress and flexural modulus scale by the same magnitude. Therefore, a design strain level of 0.25% is sufficient to ensure the survival of the full-scale caisson against the 100-year wave load.

A GRP caisson of 1016 mm diameter and 40 mm wall thickness is approximately 50% of the weight of a traditional steel caisson of wall thickness 22 mm. The analysis predicts that the maximum deflection of the GRP caisson, when subjected to a 100-year wave, will be approximately three times that for the steel caisson.

The increase in deflection predicted by the analysis does not present any operational restrictions on the use of GRP materials for large-diameter caissons. Steel caissons have a lifetime corrosion allowance designed into the wall thickness, and as such are considerably *over-designed* with respect to structural loading. In view of the large distance over which the

caisson spans, up to 22 m in some cases, it is envisaged that the predicted maximum deflection for a 1016 mm diameter GRP caisson is still sufficiently small to ensure no damage to the equipment housed within it.

Manufacture of tubes

The practical manufacturing limit for shallow-angle winding of tubes lies in the range $\pm 10 - \pm 30°$. However, only a limited number of manufacturers are currently able to wind at the lower end of this range.

CONCLUSIONS

The results of the flexural-bending tests show that a significant increase in flexural modulus can be achieved by reducing the fibre winding angle of glass reinforcement. Also, by using glass–carbon hybrid reinforcement, the flexural modulus can be increased further. However, the use of such reinforcement material is prohibitively expensive for this application. Flexural moduli generated from the laminate analysis software packages compared reasonably well with the measured values for the all GRE tubes, and the measured tensile failure strains of the tubes were typical of GRP materials.

The maximum bending stress and maximum strain predicted by finite-element analysis for the 100-year wave loading condition were an order of magnitude lower than the failure stresses and strains measured in the flexural tests. The predicted maximum deflection of the GRP caisson is approximately three times that predicted for an equivalent steel caisson. However, steel caissons have a lifetime corrosion allowance designed into the wall thickness, and as such are considerably *over-designed* with regard to structural loading.

In summary, the use of GRP materials for caissons offers corrosion resistance and a 50% weight saving over traditional steel caissons. The findings of this study also conclude that, for large-diameter GRP caissons, the predicted maximum in-service deflection is sufficient not to damage equipment housed within it. As such, there are no perceived restrictions on the structural use of GRP for caissons, providing proper consideration is given to the criteria listed below.

— Caisson span and supporting structures.
— Predicted maximum deflection.
— Location internal equipment.
— Clearance issues, both internal and external.

ASSOCIATED WORK

The integrity of jointing methods for GRP tubes has been addressed by SLP Engineering and Ameron [4] under fatigue loading conditions, and has attained Lloyds certification for the *Bondstrand*® GRE system.

The effect of vortex shedding on caisson displacement and fatigue requires assessment. SLP Engineering have expertise in this area, having developed in-house software to perform vortex shedding analysis.

REFERENCES

1. *Balmoral Group News*, Issue 13, Spring 1994.
2. Static strength of GRE and CFRE pipes. TWI report, January 1996.
3. *Bondstrand*® *Product Data*. Ameron B.V., Fiberglass Pipe Division Europe.
4. Mike Bellamy, SLP Engineering Ltd. Private communication, 1996.

ELSEVIER

Composite Structures Vol. 38, No. 1–4, pp. 151–156, 1997
© 1997 Elsevier Science Ltd. All rights reserved
Printed in Great Britain
0263-8223/97/$17.00 + 0.00

PII:S0263-8223(97)00051-2

Axisymmetric vibration analysis of laminated hollow cylinders with ring stiffeners

Jianqiao Ye

Department of Civil Engineering, The University of Leeds, Leeds LS2 9JT, UK

This paper presents an axisymmetric vibration analysis of laminated hollow cylinders composed of monoclinic layers and stiffened by ring stiffeners. A successive approximation approach, which is based on a transfer matrix and then an equivalent stiffness matrix formulation, is used to enable three-dimensional solutions to be found. It is assumed that the ring stiffeners are attached to the lateral surfaces of the cylinder and only provide elastic supports in radial direction. These constraints are imposed by using Lagrange multipliers to couple the responses of a number of vibration modes of corresponding cylinders without stiffeners. Using this method the natural frequencies of a stiffened cylinder are found to be the eigenvalues of a constraint matrix and the predictions can be arbitrarily close to the exact three-dimensional solutions. © 1997 Elsevier Science Ltd.

INTRODUCTION

Laminated composite panels and cylinders are increasingly being used in mechanical, civil, aerospace and many other industries. As it is well known that the mechanical behaviour of such structures is far more complicated than that of ones made of homogeneous materials, three-dimensional stress analysis has received considerable attention over the last few years. For analytical vibration analysis of laminated cylinders, research results have been published concerning cylinders composed of either cross-ply or angle-ply laminates. These were mainly obtained on the basis of two alternative approaches: (a) the well-known method of Frobenius [1,2]; and (b) a new successive approximation method [3,4]. However, none of the these publications dealt with laminated cylinders with stiffeners.

As an initial study of three-dimensional free vibration analysis of stiffened laminated cylinders, this paper attempts solutions dealing with axisymmetric vibration of laminated hollow cylinders. The cylinders can be made of an arbitrary number of material layers and the lay-ups can be either cross-ply or angle-ply. The cylinders are stiffened using a number of ring stiffeners which are attached to their lateral surfaces. It is assumed in this study that the ring stiffeners only provide elastic support in the radial direction. A Lagrange multiplier approach, together with the successive approximation method that has been successfully used in connection with the vibration analysis of unstiffened plates and shells, is used to impose connections between cylinders and stiffeners. Using this method, a number of free vibration modes corresponding to an unstiffened cylinder are coupled to represent the real vibration modes of the stiffened cylinder. Theoretically, therefore, the exact three-dimensional solutions of the natural frequencies can be approached as long as sufficient vibration modes have been coupled. In practice, a satisfactory prediction of the exact solutions can always be obtained by coupling a suitably large number of the vibration modes.

The main purposes of this paper are not only to present an exact, three-dimensional and axisymmetric free vibration analysis of laminated cylinders but also to serve as a basis on which general vibrations of laminated cylinders can also be analysed in a similar manner.

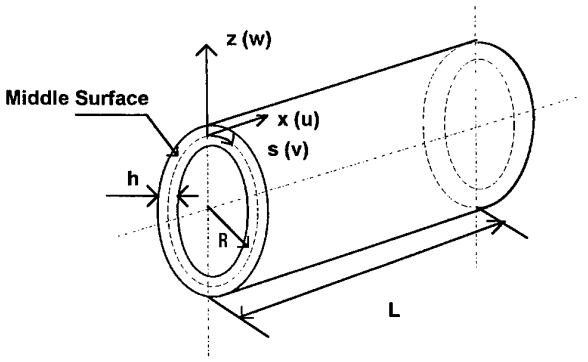

Fig. 1. Nomenclature of a hollow cylinder.

SUCCESSIVE APPROXIMATION OF A LAMINATED CYLINDER

Consider a hollow circular cylinder (Fig. 1) having an arbitrary constant thickness h, and denote with L and R its axial length and its middle-surface radius, respectively. The axial, circumferential and radial co-ordinates are denoted with x, s and z, respectively (the z co-ordinate is along the outward normal), while u, v and w represent the corresponding displacements. The cylinder may be divided into an arbitrary number of sub-layers, each of which is a co-axial cylinder. These sub-layers may have different thicknesses and material properties. It is assumed, however, that each of these sub-layers is made of an homogeneous monoclinic linearly elastic material, and the thicknesses of these sub-layers approach zero uniformly as the number of the division approaches infinite. The elastic behaviour of any of these sub-layers is described by Hook's law

$$\begin{Bmatrix} \sigma_x \\ \sigma_s \\ \sigma_z \\ \tau_{sz} \\ \tau_{xz} \\ \tau_{xs} \end{Bmatrix} = \begin{bmatrix} C_{11} & C_{12} & C_{13} & 0 & 0 & C_{16} \\ C_{12} & C_{22} & C_{23} & 0 & 0 & C_{26} \\ C_{13} & C_{23} & C_{33} & 0 & 0 & C_{36} \\ 0 & 0 & 0 & C_{44} & C_{45} & 0 \\ 0 & 0 & 0 & C_{45} & C_{55} & 0 \\ C_{16} & C_{26} & C_{36} & 0 & 0 & C_{66} \end{bmatrix} \begin{Bmatrix} \varepsilon_x \\ \varepsilon_s \\ \varepsilon_z \\ \gamma_{sz} \\ \gamma_{xz} \\ \gamma_{xs} \end{Bmatrix} \tag{1}$$

where C_{ij} are the stiffnesses of the materials.

The axisymmetric vibration of the cylinder is independent of the circumferential co-ordinate parameter, s. Owing to anisotropy, however, the following differences should be compared with the homogeneous orthotropic case. There is a coupling between the longitudinal and torsional deformations and, therefore, the circumferential displacement, v, and the shear strains, γ_{sz} and γ_{xs}, of the cylinder are all non-zero. Hence, the dynamic version of the Navier-type governing differential equations for each of these sub-layers have the form

$$\begin{aligned}
&C_{11}u_{,xx}+C_{55}R^{-1}(1+z/R)^{-1}u_{,z}+C_{55}u_{,zz}+(C_{13}+C_{55})w_{,xz}+(C_{12}+C_{55})R^{-1}(1+z/R)^{-1}w_{,x}+C_{16}v_{,xx}\\
&\qquad +C_{45}v_{,zz}=\rho u_{,tt}\\
&C_{66}v_{,xx}-C_{44}R^{-2}(1+z/R)^{-2}v+C_{44}R^{-1}(1+z/R)^{-1}v_{,z}+C_{44}v_{,zz}+C_{16}u_{,xx}\\
&\qquad +C_{45}u_{,zz}+(C_{36}+C_{45})w_{,xz}+2C_{45}R^{-1}(1+z/R)^{-1}u_{z}+(C_{26}+2C_{45})R^{-1}(1+z/R)^{-1}w_{,x}=\rho v_{,tt}\\
&(C_{13}+C_{55})u_{,xz}+(C_{13}-C_{12})R^{-1}(1+z/R)^{-1}u_{,x}+C_{55}w_{,xx}+C_{33}w_{,zz}\\
&\qquad -C_{22}R^{-2}(1+z/R)^{-2}w+C_{33}R^{-1}(1+z/R)^{-1}w_{,z}+(C_{45}+C_{36})v_{,xz}\\
&\qquad +(C_{36}-C_{26}-C_{45})R^{-1}(1+z/R)^{-1}v_{,x}=\rho w_{,tt}
\end{aligned} \tag{2}$$

For free vibration problems, the following stress boundary conditions are imposed on the lateral surfaces ($z=\pm h/2$) of the cylinder:

$$\sigma_z(\pm h/2)=0,\ \tau_{sz}(\pm h/2)=0 \text{ and } \tau_{xz}(\pm h/2)=0 \tag{3}$$

Owing to the appearance of the terms $(1+z/R)$, eqn (2) is made up of differential equations with

variable coefficients. However, on the basis of the analyses presented by Ye & Soldatos [3–4], all these terms in the equations are replaced by 1 for thin sub-cylinders ($h/R \ll 1$). Hence, eqn (2) is reduced to the following approximate equations with constant coefficients

$$\begin{aligned}
&C_{11}u_{,xx}+C_{55}R^{-1}u_{,z}+C_{55}u_{,zz}+(C_{13}+C_{55})w_{,xz}+(C_{12}+C_{55})R^{-1}w_{,x}+C_{16}v_{,xx}+C_{45}v_{,zz}=\rho u_{,tt}\\
&C_{66}v_{,xx}-C_{44}R^{-2}v+C_{44}R^{-1}v_{,z}+C_{44}v_{,zz}+C_{16}u_{,xx}+C_{45}u_{,zz}+(C_{36}+C_{45})w_{,xz}+2C_{45}R^{-1}u_{z}+(C_{26}+2C_{45})R^{-1}w_{,x}\\
&\qquad=\rho v_{,tt} \qquad (4)\\
&(C_{13}+C_{55})u_{,xz}+(C_{13}-C_{12})R^{-1}u_{,x}+C_{55}w_{,xx}+C_{33}w_{,zz}-C_{22}R^{-2}w+C_{33}R^{-1}w_{,z}+(C_{45}+C_{36})\\
&\qquad\times v_{,xz}+(C_{36}-C_{26}-C_{45})R^{-1}v_{,x}=\rho w_{,tt}
\end{aligned}$$

For axisymmetric vibration problems, the displacement model

$$\begin{aligned}
u(x,z;t)&=\bar{u}(x,z)T(t)=\sum_{m=1}^{q}U_m(z)\cos(m\pi x/L)\,e^{i\omega t}\\
v(x,z;t)&=\bar{v}(x,z)T(t)=\sum_{m=1}^{q}V_m(z)\cos(m\pi x/L)\,e^{i\omega t}\\
w(x,z;t)&=\bar{w}(x,z)T(t)=\sum_{m=1}^{q}W_m(z)\sin(m\pi x/L)\,e^{i\omega t} \qquad (5a)
\end{aligned}$$

represents a superposition of the first q normal modes of vibration and is associated with transverse stresses of the following form

$$\begin{aligned}
\tau_{xz}(x,z;t)&=\bar{\tau}_{xz}(x,z)T(t)=\sum_{m=1}^{q}X_m(z)\cos(m\pi x/L)\,e^{i\omega t}\\
\tau_{sz}(x,z;t)&=\bar{\tau}_{sz}(x,z)T(t)=\sum_{m=1}^{q}S_m(z)\cos(m\pi x/L)\,e^{i\omega t}\\
\sigma_{z}(x,z;t)&=\bar{\sigma}_{z}(x,z)T(t)=\sum_{m=1}^{q}Z_m(z)\sin(m\pi x/L)\,e^{i\omega t} \qquad (5b)
\end{aligned}$$

where ω is the vibration frequency of the cylinder. Equation (5b) satisfies exactly the following simply-supported boundary conditions at the two edges ($x=0$ and $x=L$)

$$w=\sigma_x=\tau_{xs}=0 \qquad (6)$$

Introduction of the displacement field (eqn (5a)) into eqn (4) and, for convenience, using $f_1(z)$, $f_2(z)$ and $f_3(z)$ to represent $U(z)$, $V(z)$ and $W(z)$, respectively, yields the following differential equation

$$f''_{km}(z)=\sum_{j=1}^{6}Z_{kj}F_j-C_{45}f''_{3-k,m}/C_{(6-k)(6-k)} \quad (k=1,2,3;\ f_{0m}=0) \qquad (7)$$

where F_j are the elements of the vector

$$\{F_m\}^{\mathrm{T}}=\{F_1\ F_2\ F_3\ F_4\ F_5\ F_6\}=\{f_{1m},\ f'_{1m},\ f_{2m},\ f'_{2m},\ f_{3m},\ f'_{3m}\} \qquad (8)$$

and the Z_{kj} can be found in the Appendix of Soldatos & Ye [4]. Using simple algebraic manipulations, eqn (7) can be further brought into the following form

$$\begin{aligned}
f''_{km}(z)&=\frac{C_{44}C_{55}}{C_{44}C_{55}-C_{45}^2}\sum_{j=1}^{6}\left\{Z_{kj}-\frac{C_{44}}{C_{(6-k)(6-k)}}Z_{kj}\right\}F_j \quad (k=1,2)\\
f''_{3m}(z)&=\sum_{j=1}^{6}Z_{3j}F_j \qquad (9)
\end{aligned}$$

Differential eqn (9) can equivalently be represented in the following matrix form

$$\{\mathbf{F}_m\}'=[\mathbf{G}_m]\{\mathbf{F}_m\} \qquad (10)$$

where the elements of [**G**] are calculated on the basis of eqns (8) and (9) and are, in general, dependent on the unknown natural frequency ω. Upon applying eqn (10) to all the sub-layers of the

cylinder, imposing appropriate continuity conditions on all interfaces and using the recursive formula introduced by Ye & Soldatos [3], the following equation is obtained

$$\{\mathbf{F}_m^{(N)}(h^{(N)}/2)\} = [\mathbf{H}_m]\{\mathbf{F}_m^{(1)}(-h^{(1)}/2)\} \tag{11}$$

where $\{F_m^{(N)}(h^{(N)}/2)\}$ and $\{F_m^{(1)}(-h^{(1)}/2)\}$ denote the values of $\{\mathbf{F}_m\}$ at the top and bottom lateral surfaces of the cylinder, respectively, and $[\mathbf{H}_m]$ is a frequency-dependent transfer matrix and has a dimension of 6×6.

The transfer matrix equation, eqn (11), can be represented by an equivalent stiffness matrix formulation after the following matrix transformation

$$\{\hat{\mathbf{F}}_m^{(N)}\} = [\mathbf{A}_{mn}]\{\mathbf{F}_m^{(N)}(h^{(N)}/2)\},\ \{\hat{\mathbf{F}}_m^{(1)}\} = [\mathbf{B}_m]\{\mathbf{F}_m^{(1)}(-h^{(1)}/2)\} \tag{12}$$

where

$$\{\hat{\mathbf{F}}^{(N)}\}^{\mathrm{T}} = [Z, X, S, U, V, W]_{z=h/2},\ \{\hat{\mathbf{F}}^{(1)}\}^{\mathrm{T}} = [Z, X, S, U, V, W]_{z=-h/2} \tag{13}$$

and the elements of the 6×6 matrices $[\mathbf{A}_m]$ and $[\mathbf{B}_m]$ are constants and can be calculated easily by using Hook's law and the strain–displacement relations. The column matrices appearing on the left-hand side of eqn (12) give the values of the stresses and displacements on the top and bottom lateral surfaces of the cylinder, respectively, and a combination of eqn (11) and (12) yields further

$$\{\hat{\mathbf{F}}_m^{(N)}\} = [\mathbf{A}_m][\mathbf{H}_m][\mathbf{B}_m]^{-1}\{\hat{\mathbf{F}}_m^{(1)}(-h^{(1)}/2)\} = [\hat{\mathbf{H}}_m]\{\hat{\mathbf{F}}_m^{(1)}(-h^{(1)}/2)\} \tag{14}$$

from which the following equations can finally be obtained

$$\{\mathbf{d}_m\} = [\mathbf{Q}_m]\{\hat{\mathbf{F}}_m^{(1)}\},\ \{\mathbf{s}_m\} = [\mathbf{R}_m]\{\hat{\mathbf{F}}_m^{(1)}\} \tag{15a}$$

where

$$\{\mathbf{d}\}^{\mathrm{T}} = [U(h^{(N)}/2), V(h^{(N)}/2), W(h^{(N)}/2), U(-h^{(1)}/2), V(-h^{(1)}/2), W(-h^{(1)}/2)]$$

$$\{\mathbf{s}\}^{\mathrm{T}} = [\mathrm{X}(\mathrm{h}^{(\mathrm{N})}/2), \mathrm{S}(\mathrm{h}^{(\mathrm{N})}/2), \mathrm{Z}(\mathrm{h}^{(\mathrm{N})}/2), \mathrm{X}(-\mathrm{h}^{(1)}/2), \mathrm{S}(-\mathrm{h}^{(1)}/2), \mathrm{Z}(-\mathrm{h}^{(1)}/2)] \tag{15b}$$

Obviously, the column matrices $\{\mathbf{d}_m\}$ and $\{\mathbf{s}_m\}$ consist of the values of the displacement and stress components, respectively, on the lateral surfaces of the cylinder. Elimination of $\{\hat{\mathbf{F}}_m^{(1)}\}$ from eqn (15a) yields the dynamic stiffness equation of the cylinder in the following form

$$\{\mathbf{s}_m\} = [\mathbf{R}_m][\mathbf{Q}_m]^{-1}\{\mathbf{d}_m\} = [\mathbf{K}_m]\{\mathbf{d}_m\} \tag{16}$$

where the 6×6 dynamic stiffness matrix $[\mathbf{K}_m]$ is symmetric and has frequency-dependent elements. Owing to the zero tractions on the lateral surfaces of an unstiffened cylinder, its natural vibration frequencies can be found as eigenvalues of the transcendental eigen-matrix $[\mathbf{K}_m]$. Numerical experience has shown that the natural frequencies obtained can approach the exact three-dimensional solutions as the thicknesses of all the sub-layers approach zero [3, 4].

VIBRATIONS OF LAMINATED CYLINDERS WITH ATTACHED RING STIFFENERS

For axisymmetric vibration of a laminated cylinder with attached ring stiffeners, the stiffeners can well be represented by a set of continuous springs that provide elastic supports in radial direction. The stiffnesses of these springs depend on the materials and the cross-sections of the stiffeners. Suppose that the coupling of the first q normal modes of eqn (5a) represent a vibration mode of a cylinder having a number of ring stiffeners attached to its lateral surfaces. Using the notations adopted in eqn (15b), two vectors that represent displacements and stresses on those lateral surfaces ($z = \pm h/2$) can, respectively, be formed as follows

$$\{\hat{\mathbf{D}}\} = \sum_{m=1}^{q} [\mathbf{N}_m(x)]\{\mathbf{d}_m\} \tag{17a}$$

$$\{\hat{\mathbf{T}}\} = \sum_{m=1}^{q} [\mathbf{N}_m(x)]\{\mathbf{s}_m\} \tag{17b}$$

where

$$\{\hat{\mathbf{D}}\}^{\mathrm{T}} = [\bar{u}(x, h/2), \bar{v}(x, h/2), \bar{w}(x, h/2), \bar{u}(x, -h/2), \bar{v}(x, -h/2), \bar{w}(x, -h/2)]$$

$$\{\hat{\mathbf{T}}\}_{xz}^{\mathrm{T}=[\bar{\tau}}(x, h/2), \bar{\tau}_{sz}(x, h/2), \bar{\sigma}_z(x, h/2), \bar{\tau}_{xz}(x, -h/2), \bar{\tau}_{sz}(x, -h/2), \bar{\sigma}_z(x, -h/2)]$$

$$[\mathbf{N}_m(x)] = Diag\left[\cos\left(\frac{m\pi x}{L}\right), \cos\left(\frac{m\pi x}{L}\right), \sin\left(\frac{m\pi x}{L}\right), \cos\left(\frac{m\pi x}{L}\right), \cos\left(\frac{m\pi x}{L}\right), \sin\left(\frac{m\pi x}{L}\right)\right] \tag{18}$$

Consider initially, for simplicity, a special case in which the cylinder has only one ring stiffener attached to its inner surface at $(x^*, -h/2)$, here x^* represents the x co-ordinate of the stiffener. As this ring stiffener can be modelled by a continuous spring attached to the cylinder at the same location, the following equation can be obtained from the last part of eqns (17b) and (19)

$$k\bar{w} = \sum_{m=1}^{q} [\mathbf{N}_m^*(x^*)]\{\mathbf{s}_m\} = \sum_{m=1}^{q} [\mathbf{N}_m^*(x^*)][\mathbf{K}_m]\{\mathbf{d}_m\} \tag{19}$$

where k is the rigidity of the stiffener that represents the force between the cylinder and the stiffener induced by a unit radial displacement of the interface, and $[\mathbf{N}_m^*]$ is the last row of $[\mathbf{N}_m]$. Introducing the last part of eqn (17a) into eqn (19) yields the following constraint equation

$$\sum_{m=1}^{q} [\mathbf{N}_m^*(x^*)]\{[\mathbf{K}_m] - k\mathbf{I}\}\{\mathbf{d}_m\} = 0 \tag{20}$$

where $\mathbf{I}$ is a unit matrix. It is worthwhile to mention that if the stiffener is attached to the outer surface of the cylinder, the corresponding constraint equation is

$$\sum_{m=1}^{q} [\mathbf{N}_m^*(x^*)]\{[\mathbf{K}_m] + k\mathbf{I}\}\{\mathbf{d}_m\} = 0 \tag{21}$$

Consider next that there are p ring stiffeners attached to either the inner or the outer surface of the cylinder at different locations. Upon denoting with $\mathbf{x}^*$, the vector consisting of the x co-ordinates of all the stiffeners, the general constraint equation has the following form

$$\sum_{m=1}^{q} [\mathbf{E}_m(\mathbf{x}^*)]\{\mathbf{d}_{mn}\} = \{\mathbf{0}\} \tag{22}$$

where $[\mathbf{E}_m(\mathbf{x}^*)]$ is a $p \times 6$ matrix, each row of which can be represented by either $[\mathrm{N}_m^*(x^*)]\{[\mathrm{K}_m] - k\mathrm{I}\}$ or $[\mathrm{N}_m^*(x^*)]\{[\mathrm{K}_m] + k\mathrm{I}\}$ calculated for different values of x^* and k.

Dynamic equilibrium considerations suggest that the total energy, V, of the cylinder equals the total work done by the external forces acting on the displacements of the lateral surfaces. Hence, the total energy of the panel can be written as follows

$$V = \frac{1}{2}\iint_A \{\hat{\mathbf{T}}\}^{\mathrm{T}}\{\hat{\mathbf{D}}\}\, \mathrm{d}A = \frac{1}{2}\int\int_A \left\{\sum_{m=1}^{q} [\mathbf{N}_m][\mathbf{K}_m]\{\mathbf{d}_m\}\right\}^{\mathrm{T}} \left\{\sum_{j=1}^{q} [\mathbf{N}_j]\{\mathbf{d}_j\}\right\} \mathrm{d}A \tag{23}$$

where A represents the area of the lateral surfaces. Applying the Lagrange multipliers method involves the minimization of a functional ϕ that equals V plus the product of the (arbitrary) Lagrangian multipliers and the constraints. Then the partial derivatives of ϕ with respect to elements of $\{\mathbf{d}_m\}$ are equated to zero. Thus, the function to be minimized is

$$\phi = \frac{1}{2}\int\int_A \left\{\sum_{m=1}^{q} [\mathbf{N}_m][\mathbf{K}_m]\{\mathbf{d}_m\}\right\}^{\mathrm{T}} \left\{\sum_{j=1}^{q} [\mathbf{N}_i]\{\mathbf{d}_i\}\right\} \mathrm{d}A + \{\lambda\}^{\mathrm{T}} \left\{\sum_{m=1}^{q} [\mathbf{E}_m(\mathbf{x}^*)]\{\mathbf{d}_m\}\right\} \tag{24}$$

The Lagrange multipliers vector, $\{\lambda\}$, represents the forces acting at the connections between the cylinder and the stiffeners due to the constraints. Performing the surface integration in eqn (24) and equating with zero the derivative of ϕ with respect to $\{\mathbf{d}_m\}$ yields the stationary values of ϕ as follows

$$[\mathbf{K}_m]\{\mathbf{d}_m\} + [\mathbf{E}_m]^{\mathrm{T}}\{\lambda^*\} = \{0\} \quad (m = 1, 2, \ldots, q) \tag{25}$$

where $\{\lambda^*\} = 2\{\lambda\}/\pi LR$.

Equations (22) and (25) can be written in the following compact matrix form

$$[\hat{\mathbf{K}}]\{\mathbf{D}\} = \{\mathbf{0}\} \tag{26}$$

where

$$[\hat{\mathbf{K}}] = \begin{bmatrix} [\mathbf{K}_1] & [\mathbf{0}] & \cdot & [\mathbf{0}] & \cdot & \cdot & [\mathbf{E}_1]^{\mathrm{T}} \\ [\mathbf{0}] & [\mathbf{K}_2] & \cdot & \cdot & \cdot & \cdot & [\mathbf{E}_2]^{\mathrm{T}} \\ \cdot & \cdot & \cdot & & & & \cdot \\ [\mathbf{0}] & \cdot & [\mathbf{K}_m] & & & & [\mathbf{E}_m]^{\mathrm{T}} \\ \cdot & \cdot & & & \cdot & & \cdot \\ \cdot & \cdot & & & & [\mathbf{K}_q] & [\mathbf{E}_q]^{\mathrm{T}} \\ [\mathbf{E}_1] & [\mathbf{E}_2] & \cdot & [\mathbf{E}_m] & \cdot & [\mathbf{E}_q] & [\mathbf{0}] \end{bmatrix}, \quad [\mathbf{D}] = \begin{Bmatrix} \{\mathbf{d}_1\} \\ \{\mathbf{d}_2\} \\ \cdot \\ \{\mathbf{d}_m\} \\ \cdot \\ \{\mathbf{d}_q\} \\ \{\lambda^*\} \end{Bmatrix} \tag{27}$$

Hence, the natural frequencies of a laminated cylinder having an arbitrary number of ring stiffeners can be found as roots of a transcendental equation which is produced by nullifying the determinant of the constrained dynamic stiffness matrix $\hat{\mathbf{K}}$. It becomes apparent, therefore, that upon employing a suitably large number, q, of normal vibration modes, these predictions can be arbitrarily close to the exact natural frequencies of the stiffened cylinder considered.

CLOSURE

A three-dimensional study of the axisymmetric dynamic behaviour of laminated cylinders composed of an arbitrary number of monoclinic layers and stiffened with ring stiffeners has been performed. The study was based on a recursive formulation of the successive approximation approach employed by Ye & Soldatos [3] and the Lagrangian multiplier technique. This method has been successfully applied in connection with vibration analysis of laminated cylinders and cylindrical panels having rigid point supports and clamped edges.

Some preliminary results have been obtained and show satisfactory predictions to the corresponding three-dimensional solutions. Nevertheless, it was decided that these results, along with other theoretical and numerical investigations, should be published in a more comprehensive form.

REFERENCES

1. Mirsky, I., Three-dimensional and shell theory analysis of axisymmetric vibrations of orthotroic shells. *J. Acoust. Soc. Am.*, 1966, **39**, 549–555.
2. Varadan, T.K. and Bhaskar, K., Bending of laminated orthotropic cylindrical shells — an elasticity approach. *Composite Struct.*, 1991, **17**, 141–156.
3. Ye, J.Q. and Soldatos, K.P., Three-dimensional vibrations of laminated cylinders and cylindrical panels with a symmetric or an antisymmetric cross-ply lay-up. *Composites Engng*, 1994, **4**, 429–444.
4. Soldatos, K.P. and Ye, J.Q., Axisymmetric static and dynamic analysis of laminated hollow cylinders composed of monoclinic elastic layers. *J. Sound Vibr.*, 1995, **184**, 245–259.

ELSEVIER

Composite Structures Vol. 38, No. 1–4, pp. 157–168, 1997
© 1997 Elsevier Science Ltd. All rights reserved
Printed in Great Britain
0263-8223/97/$17.00 + 0.00

PII:S0263-8223(97)00052-4

Interlaminar stresses in laminated composite plates, cylindrical/spherical shell panels damaged by low-velocity impact

S. Ganapathy & K. P. Rao

Department of Aerospace Engineering, Indian Institute of Science, Bangalore 560012, India

Prediction of damage caused by low-velocity impact in laminated composite plate cylindrical/spherical shell panels is an important problem faced by designers using composites. Not only the in-plane stresses but also the interlaminar normal and shear stresses play a role in estimating the damage caused. The work reported here is an effort in getting better predictions of damage in composite plate cylindrical/spherical shell panels subjected to low-velocity impact.

The low-velocity impact problem is treated as a quasi-static problem. First, the in-plane stresses are calculated by 2-D nonlinear finite element analysis using a 48 degrees of freedom laminated composite shell element. The damage analysis is then carried out using a Tsai–Wu quadratic failure criterion and a maximum stress criteria. Interlaminar normal and shear stresses are predicted after taking into account the in-plane damage caused by low-velocity impact. The interlaminar stresses are obtained by integrating the 3-D equations of equilibrium through the thickness. The deformed geometry is taken into account in the third equation of equilibrium (in the thickness direction). After evaluating the formulation and the computer program developed for correctness, the interlaminar stresses are predicted for composite plates/shell panels which are damaged by low-velocity impact. © 1997 Elsevier Science Ltd.

INTRODUCTION

Interlaminar stresses in composites arise due to the difference in elastic properties of the layers. Interlaminar stress prediction is essentially a three-dimensional (3-D) problem for which closed-form analytical solutions are not available. Hence, numerical methods, such as the finite element method, are used to predict the interlaminar stresses. A full 3-D finite element analysis of the problem is computationally expensive. The closed-form elasticity solution of interlaminar shear stress for multilayered bidirectional composites was given by Pagano and Hatfield [1]. Lajczok [2] has applied finite difference technique to the strains and curvatures obtained from MSC/NASTRAN thin plate solution to determine their derivatives. These quantities are incorporated into classical thin plate theory to calculate interlaminar shear stresses using equations of equilibrium. Tolson *et al.* [3] developed a 2-D finite element for composite laminate stress calculation which is used to predict the progressive failure. They have also used the equations of equilibrium for predicting interlaminar stresses. Lo *et al.* [4] have used a higher-order shear deformation theory based on assumed displacement fields to find the transverse stress components. They have shown that the transverse stresses obtained by integrating the equations of equilibrium are more accurate than those obtained directly from the constitutive relationships.

All the works described hitherto are based on small deformation theory. It is observed that thin laminated composite structures undergo large deformations due to low-velocity impact such as tool drop or runway debris hit. This in

turn affects both the magnitude and distribution of interlaminar stresses. Hence for predicting interlaminar stresses accurately, geometric nonlinearity must be taken into account in the analysis. Moreover, the inplane damage, namely matrix cracking and fiber breakage, caused by the low-velocity impact, affects the interlaminar stress distribution.

Reddy [5] has given a higher-order shear deformation theory of plates accounting for the von-Karman strains. He has mentioned that more accurate transverse shear stresses are obtained when equations of equilibrium of 3-D elasticity theory are used. Only linear analysis results are given. To the authors' knowledge, no work has been reported in the literature on prediction of interlaminar stresses in composite flat plates/shell panels taking into account the damage caused by low-velocity impact.

In the present work, the interlaminar stresses are predicted after taking into account the inplane damage caused by low-velocity impact. First a 2-D nonlinear finite element analysis is used to calculate the inplane stresses. A damage analysis is then carried out using the Tsai–Wu failure criterion. Subsequently 3-D equations of equilibrium are integrated through the thickness to get the interlaminar stresses.

NONLINEAR FINITE ELEMENT ANALYSIS

The low-velocity impact problem is treated as a quasi-static problem and the Hertzian law of load distribution is used. The inplane stresses are calculated using nonlinear finite element analysis. A four noded, 48 degrees of freedom doubly curved composite quadrilateral finite element developed by Venkatesh and Rao [6] is particularised to represent plate, cylindrical/spherical shell panel geometry. The element is of constant thickness and is based on Kirchhoff–Love shell theory. Only geometric nonlinearity is included in the analysis and the material is assumed to be linearly elastic. The Green's strain tensor is used in formulating the tangent stiffness matrix based on a total Lagrangian approach. The resulting nonlinear algebraic equations are solved by an incremental/iterative procedure using a standard Newton–Raphson method. The nonlinear inplane stresses are calculated at 7×7 Gauss points inside an element. The detailed formulation and solution technique used can be found in Ref. 7.

DAMAGE ANALYSIS

The inplane stresses thus obtained at Gauss points are used to predict the occurrence of damage with the Tsai–Wu quadratic failure criterion and the mode of damage, namely the matrix cracking and fiber breakage are identified using maximum stress failure criteria (see Ref. 7 for details). The material is degraded suitably at all failed Gauss points as follows:

- When the mode of failure is transverse matrix cracking or shear splitting, then $E_{22} = 0; G_{12} = 0$ and $\nu_{12} = 0$
- When fiber breakage occurs, then $E_{11} = 0; E_{22} = 0; G_{12} = 0$ and $\nu_{12} = 0$

where E_{11}, E_{22}, G_{12} and ν_{12} represent the inplane Young's modulus of the lamina in the fiber direction, inplane Young's modulus of the lamina in the transverse direction, inplane shear modulus of the lamina and inplane Poisson's ratio of the lamina, respectively. The nonlinear finite element analysis is carried out again taking into account the new material properties at failed Gauss points. This process is repeated until no further damage is observed.

INTERLAMINAR STRESS PREDICTIONS

The mid-plane strains and curvatures are obtained at element centers from nonlinear finite element analysis. A second order finite difference scheme is used to calculate the first and second derivatives of mid-plane strains and curvatures. The 3-D elasticity equations of equilibrium are integrated in the thickness direction to get the interlaminar stresses. The deformed geometry has been taken into account in the third equation of equilibrium (in the thickness direction).

Derivation for interlaminar stresses in axi-symmetric shell panels

The equations of equilibrium for an ith ply of an axi-symmetric shell panel is as follows [8]:

$$\frac{\partial \sigma_s^i}{\partial s}+\frac{\partial \tau_{s\theta}^i}{r\partial\theta}+\frac{\partial \sigma_{sz}^i}{\partial z}+(\sigma_s-\sigma_\theta)\frac{\sin\phi}{R_1\cos\phi}=0$$

$$\frac{\partial \tau_{s\theta}^i}{\partial s}+\frac{\partial \sigma_\theta^i}{r\partial\theta}+\frac{\partial \sigma_{\theta z}^i}{\partial z}+2\tau_{s\theta}\frac{\sin\phi}{R_1\cos\phi}=0 \tag{1}$$

$$\frac{\partial \sigma_{sz}^i}{\partial s}+\frac{\partial \sigma_{\theta z}^i}{r\partial\theta}+\frac{\partial \sigma_{zz}^i}{\partial z}-\left(\frac{\sigma_s}{R_1}+\frac{\sigma_\theta}{R_2}\right)+(\sigma_s^i\kappa_s+\tau_{s\theta}\kappa_{s\theta}+\sigma_\theta^i\kappa_\theta)=0$$

where R_1 and R_2 are the principal radii of curvatures and ϕ is the angle between the vertical and the tangent at any point on the shell panel. r is the radius of any parallel circle and is given as $R_2\cos\phi$ and κ_s, κ_θ and $\kappa_{s\theta}$ are the curvatures and are given as

$$\kappa_s=-\frac{\partial^2 w}{\partial s^2}-\frac{w}{R_1^2}$$

$$\kappa_\theta=-\frac{\partial^2 w}{r^2\partial\theta^2}-\frac{\partial w}{\partial s}\frac{\sin\phi}{r}-\frac{w}{R_2^2}-u\frac{\sin\phi}{r}\left(\frac{1}{R_2}-\frac{1}{R_1}\right)$$

$$\kappa_{s\theta}=-2\frac{\partial^2 w}{r\partial s\partial\theta}+\frac{\partial w}{r\partial\theta}\frac{\sin\phi}{r}-\left(\frac{1}{R_2}-\frac{1}{R_1}\right)\left(\frac{\partial u}{r\partial\theta}-\frac{\partial v}{\partial s}+\frac{v\sin\phi}{r}\right)$$

The above equations are derived with the approximation $(1+z/R_{1,2})\approx 1$. These equations can be particularised for flat plate, cylindrical shell panel and spherical shell panel easily. The interlaminar shear stresses are given as

$$\tau_{sz}^{i+1}=-\sum_{k=1}^{i}\left\{(z_{i+1}-z_i)F_s^i-\frac{1}{2}(z_{i+1}^2-z_i^2)G_s^i\right\} \tag{2}$$

$$\tau_{\theta z}^{i+1}=-\sum_{k=1}^{i}\left\{(z_{i+1}-z_i)P_s^i-\frac{1}{2}(z_{i+1}^2-z_i^2)R_s^i\right\} \tag{3}$$

where

$$F_s^i=\bar{Q}_{11}^i\varepsilon_{s,s}^o+\bar{Q}_{12}^i\varepsilon_{\theta,s}^o+Q_{16}^i\left(\gamma_{s\theta,s}^o+\frac{\varepsilon_{s,\theta}^o}{r}\right)+\bar{Q}_{26}^i\frac{\varepsilon_{\theta,\theta}^o}{r}+\bar{Q}_{66}^i\frac{\gamma_{s\theta,\theta}^o}{R_1\cos\phi}+\{(\bar{Q}_{11}^i-\bar{Q}_{12}^i)\varepsilon_s^o+(\bar{Q}_{12}^i-\bar{Q}_{22}^i)\varepsilon_\theta^o$$

$$+(\bar{Q}_{16}^i-Q_{26}^i)\gamma_{s\theta}^o\}\frac{\sin\phi}{r}$$

$$G_s^i = \bar{Q}_{11}^i \kappa_{s,s}^o + \bar{Q}_{12}^i \kappa_{\theta,s}^o + \bar{Q}_{16}^i \left(\kappa_{s\theta,s}^o + \frac{\kappa_{s,\theta}^o}{r} \right) + \bar{Q}_{26}^i \frac{\kappa_{\theta,\theta}^o}{r} + \bar{Q}_{66}^i \frac{\kappa_{s\theta,\theta}^o}{R_1 \cos\phi} + \{(\bar{Q}_{11}^i - \bar{Q}_{12}^i)\kappa_s + (\bar{Q}_{12}^i - \bar{Q}_{22}^i)\kappa_\theta + (\bar{Q}_{16}^i - Q_{26}^i)\kappa_{s\theta}\} \frac{\sin\phi}{r}$$

$$P_s^i = \bar{Q}_{16}^i \varepsilon_{s,s}^o + \bar{Q}_{26}^i \left(\varepsilon_{\theta,s}^o + \frac{\gamma_{s\theta,\theta}^o}{r} \right) + \bar{Q}_{66}^i \gamma_{s\theta,s}^o + Q_{12}^i \frac{\varepsilon_{s,\theta}^o}{r} + \bar{Q}_{22}^i \frac{\varepsilon_{\theta,\theta}^o}{R_1 \cos\phi} + \{\bar{Q}_{16}^i \varepsilon_s^o + \bar{Q}_{26}^i \varepsilon_\theta^o + \bar{Q}_{66}^i \gamma_{s\theta}^o\} \frac{2\sin\phi}{r}$$

$$R_s^i = \bar{Q}_{16}^i \kappa_{s,s}^o + \bar{Q}_{26}^i \left(\kappa_{\theta,s}^o + \frac{\kappa_{s\theta,\theta}^o}{r} \right) + \bar{Q}_{66}^i \kappa_{s\theta,s}^o + Q_{12}^i \frac{\kappa_{s,\theta}^o}{r} + \bar{Q}_{22}^i \frac{\kappa_{\theta,\theta}^o}{r} + \{\bar{Q}_{16}^i \kappa_s + \bar{Q}_{26}^i \kappa_\theta + \bar{Q}_{66}^i \kappa_{s\theta}\} \frac{2\sin\phi}{R_1 \cos\phi}$$

where $\bar{Q}_{kl}^i$ ($k, l = 1, 2, 6$) are the transformed modulus of the material of the ith ply. ε_x^o, ε_y^o, γ_{xy}^o are mid-plane strains due to extension and κ_x, κ_y, κ_{xy} are curvatures due to bending.It is assumed that the top and bottom surfaces of the laminate/shell panel are free from shear stresses. The condition at bottom surface is forced and integration is carried out from bottom ply. The condition at the top surface will be satisfied automatically.

The interlaminar normal stress is given as

$$\sigma_z^{i+1} = \frac{1}{2}(z_{i+1}^2 - 2z_{i+1}z_i + z_i^2) S_s^i + \frac{1}{6}(z_{i+1}^3 - 3z_{i+1}z_i^2 + 2z_i^3) T_s^i + (z_{i+1} - z_i) \sum_{k=1}^{i-1} \left\{ (z_{k+1} - z_k) S_s^k + \frac{1}{2}(z_{k+1}^2 - z_k^2) T_s^k \right\} + (z_{i+1} - z_i) U_s^i + \frac{1}{2}(z_{i+1}^2 - z_i^2) V_s^i + \sigma_z^i \tag{4}$$

where

$$S_s^i = \bar{Q}_{11}^i \varepsilon_{s,ss}^o + \bar{Q}_{12}^i \left(\varepsilon_{\theta,ss}^o + \frac{\varepsilon_{s,\theta\theta}^o}{r^2} \right) + \bar{Q}_{16}^i \left(\gamma_{s\theta,ss}^o + 2\frac{\varepsilon_{s,s\theta}^o}{r} \right) + \bar{Q}_{22}^i \frac{\varepsilon_{\theta,\theta\theta}^o}{r^2} + 2\bar{Q}_{66}^i \frac{\gamma_{s\theta,s\theta}^o}{r} + \bar{Q}_{26}^i \left(2\frac{\varepsilon_{\theta,s\theta}^o}{r} + \frac{\gamma_{s\theta,\theta\theta}^o}{r^2} \right) + \{(\bar{Q}_{11}^i - \bar{Q}_{12}^i)\varepsilon_{s,s}^o + (\bar{Q}_{12}^i - Q_{22}^i)\varepsilon_{\theta,s}^o (Q_{16}^i - Q_{26}^i)\gamma_{s\theta,s}^o\} \frac{\sin\phi}{r} + 2\left(\bar{Q}_{16}^i \frac{\varepsilon_{s,\theta}^o}{r} + \bar{Q}_{26}^i \frac{\varepsilon_{\theta,\theta}^o}{r} + \bar{Q}_{66}^i \frac{\gamma_{s\theta,\theta}^o}{r} \right) \frac{\sin\phi}{r}$$

$$T_s^i = \bar{Q}_{11}^i \kappa_{s,ss} + \bar{Q}_{12}^i \left(\kappa_{\theta,ss} + \frac{\kappa_{s,\theta\theta}}{r^2} \right) + \bar{Q}_{16}^i \left(\kappa_{s\theta,ss} + 2\frac{\kappa_{s,s\theta}}{r} \right) + \bar{Q}_{22}^i \frac{\kappa_{\theta,\theta\theta}}{r^2} + 2\bar{Q}_{66}^i \frac{\kappa_{s\theta,s\theta}}{r} + \bar{Q}_{26}^i \left(2\frac{\kappa_{\theta,s\theta}}{r} + \frac{\kappa_{s\theta,\theta\theta}}{r^2} \right) + \{(\bar{Q}_{11}^i - \bar{Q}_{12}^i)\kappa_{s,s} + (\bar{Q}_{12}^i - \bar{Q}_{22}^i)\kappa_{\theta,s} + (\bar{Q}_{16}^i - \bar{Q}_{26}^i)\kappa_{s\theta,s}\} \frac{\sin\phi}{r} + 2\left(\bar{Q}_{16}^i \frac{\kappa_s,\theta}{r} + \bar{Q}_{26}^i \frac{\kappa_\theta}{r} + \bar{Q}_{66}^i \frac{\kappa_{s\theta},\theta}{r} \right) \frac{\sin\phi}{r}$$

$$U_s^i = (\bar{Q}_{11}^i \varepsilon_s^o + \bar{Q}_{12}^i \varepsilon_\theta^o + \bar{Q}_{16}^i \gamma_{s\theta}^o)\kappa_s + (\bar{Q}_{12}^i \varepsilon_s^o + \bar{Q}_{22}^i \varepsilon_\theta^o + \bar{Q}_{26}^i \gamma_{s\theta}^o)\kappa_\theta + (\bar{Q}_{16}^i \varepsilon_s^o + \bar{Q}_{26}^i \varepsilon_\theta^o + \bar{Q}_{66}^i \gamma_{s\theta}^o)\kappa_{x\theta} + \frac{1}{R}\{(\bar{Q}_{11}^i + \bar{Q}_{12}^i)\varepsilon_s^o + (Q_{12}^i + \bar{Q}_{22}^i)\varepsilon_\theta^o + (\bar{Q}_{16}^i + \bar{Q}_{26}^i)\gamma_{s\theta}^o\}$$

$$V_s^i = (\bar{Q}_{11}^i\kappa_s + \bar{Q}_{12}^i\kappa_\theta + Q_{16}^i\kappa_{s\theta})\kappa_s + (\bar{Q}_{12}^i\kappa_s + \bar{Q}_{22}^i\kappa_\theta + \bar{Q}_{26}^i\kappa_{s\theta})\kappa_\theta + (\bar{Q}_{16}^i\kappa_s + \bar{Q}_{26}^i\kappa_\theta + \bar{Q}_{66}^i\kappa_{s\theta})\kappa_{s\theta}$$
$$+ \frac{1}{R}\{(\bar{Q}_{11}^i + \bar{Q}_{12}^i)\kappa_s + (\bar{Q}_{12}^i + \bar{Q}_{22}^i)\kappa_\theta + (\bar{Q}_{16}^i + \bar{Q}_{26}^i)\kappa_{s\theta}\}$$

Here the boundary conditions used are $\sigma_z^1 = 0$ at $z = z_1$ and $\sigma_z^{n+1} = q(s, \theta)$ *at* $z = z_{n+1}$, where $q(s, \theta)$ is the applied loading. The first boundary condition is forced and the second one is satisfied automatically.

Finite difference method

The mid-plane strains and curvatures at the center of each element are obtained from the finite element analysis. The first and second derivatives of these mid-plane strains and curvatures, which are required for the interlaminar stress calculation are obtained from the finite difference scheme. The forward difference method is used along the left and top edge, the backward difference method is used along the right and bottom edge and the central difference method is used elsewhere. The three different schemes used, for a general function $f(x, y)$, are as follows.

Forward difference method

$$\left[\frac{\delta f}{\delta x}\right]_{ij} = -\frac{(f_{i+2,j} - f_{i+1,j})}{(x_{i+2} - x_{i+1})}\frac{1}{(1+c_1)} + \frac{(f_{i+1,j} - f_{ij})}{(x_{i+1} - x_i)}\left(\frac{2+c_1}{1+c_1}\right) \tag{5}$$

where

$$c_1 = \frac{x_{i+2} - x_{i+1}}{x_{i+1} - x_i}$$

Backward difference method

$$\left[\frac{\delta f}{\delta x}\right]_{ij} = -\frac{(f_{i-2,j} - f_{i-1,j})}{(x_{i-2} - x_{i-1})}\frac{1}{(1+c_2)} + \frac{(f_{i-1,j} - f_{ij})}{(x_{i+1} - x_i)}\left(\frac{2+c_2}{1+c_2}\right) \tag{6}$$

where

$$c_2 = \frac{x_{i-2} - x_{i-1}}{x_{i-1} - x_i}$$

Central difference method

$$\left[\frac{\delta f}{\delta x}\right]_{ij} = \frac{[c_3^2 f_{i+1,j} - f_{ij}(c_3^2 - 1) + f_{i-1,j}]}{c_3(x_{i+1} - x_{i-1})} \tag{7}$$

where

$$c_3 = \frac{x_i - x_{i-1}}{x_{i+1} - x_i}$$

Effect of inplane damage

The interlaminar stresses are predicted by the same equations as given earlier. The only modification is that the degraded material properties are used in the damaged portion of a ply. Since the damage is predicted at all Gauss points and the interlaminar stresses are predicted at the center of each element, the damage which corresponds to the central Gauss point is taken as the damage of that element.

RESULTS AND DISCUSSIONS

First the computer code developed is evaluated thoroughly, for linear/nonlinear analysis of isotropic plates, cylindrical shell panels and axi-symmetric shells by comparing its results with those available in the literature. Subsequently the present method is applied for predicting interlaminar stresses in laminated composite plates, cylindrical/spherical shell panels, damaged by low-velocity impact.

Evaluation analysis

Simply supported isotropic plates subjected to a uniform load

A square isotropic plate of size 50 mm × 50 mm and 1 mm thick is considered first. The plate is simply supported along the edges and subjected to a uniform load of 1 MPa. The Young's modulus and Poisson's ratio of the material used are 210 GPa and 0.3, respectively. The boundary conditions used are defined as follows (refer to Fig. 1 for definition of a and b)

At $x = 0$, a: $u, v, w = 0$;

At $y = 0$, b: $u, v, w = 0$

The variation of shear stresses τ_{xz} and τ_{yz} with respect to x are shown in Fig. 2(a). The variation of τ_{xz} with respect to z is shown in Fig. 2(b). As seen from the graph, the agreement between the analytical results given by Timoshenko and Krieger [9] and the present results for the linear analysis is very good. The effect of nonlinearity is to reduce the magnitude of the shear stresses. Figure 2(c) and (d) shows the variation of normal stress with respect to x and z, respectively. The agreement between the analytical and the present results for linear analysis is good. The magnitude of the normal stress gets increased inside the plate when the nonlinearity is accounted for. However the boundary condition at the top surface, namely At $z = h/2$ $\sigma_z = q$ where q is the applied loading, is satisfied, if the equation of equilibrium in z-direction is written taking into account the deformations (see eqn (1)).

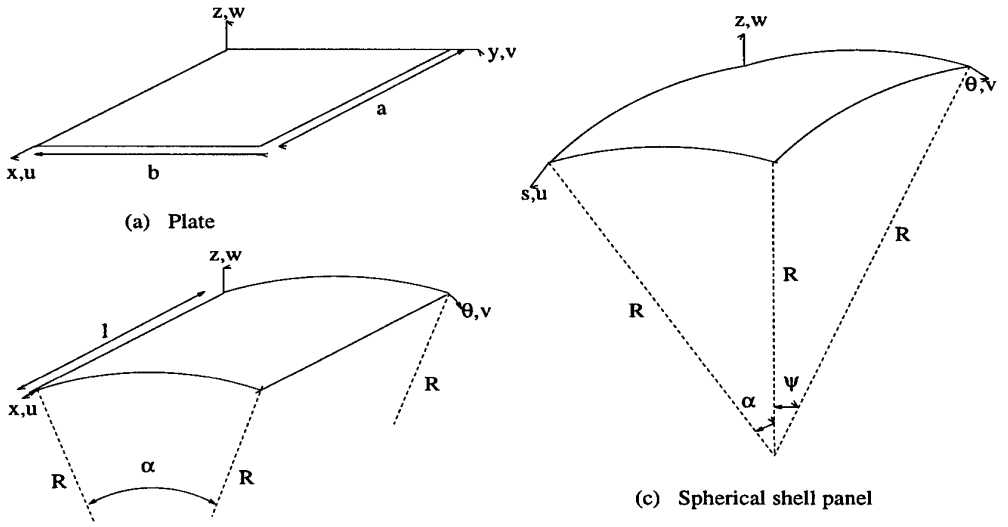

Fig. 1. Axes system.

Simply supported isotropic cylindrical shell panel subjected to a sinusoidal load

Next an isotropic cylindrical shell panel simply supported along the edges and subjected to sinusoidal loading is considered. The radius and length of the cylindrical shell are 250 mm and 20 mm, respectively. The shell is of 1 mm thickness and the angle subtended by the circular arc is 0.2 rad. The boundary conditions are given as (refer Fig. 1 for definition of l and α)

$x = 0, l$: $v, w = 0$;

At $\theta = 0, \alpha$: $u, w = 0$

The loading is defined as

$$q_o = \sin\left(\frac{\pi x}{l}\right)\sin\left(\frac{\pi\theta}{\alpha}\right)$$

The Young's modulus and Poisson's ratio of the plate material are 210 GPa and 0.3, respectively. The variation of shear stresses with respect to θ and z are given in Fig. 3(a) and (b), respectively. As seen from the graph, the results are matching very well with the analytical results given by Timoshenko and Krieger [9] for linear analysis. The maximum shear stresses have a

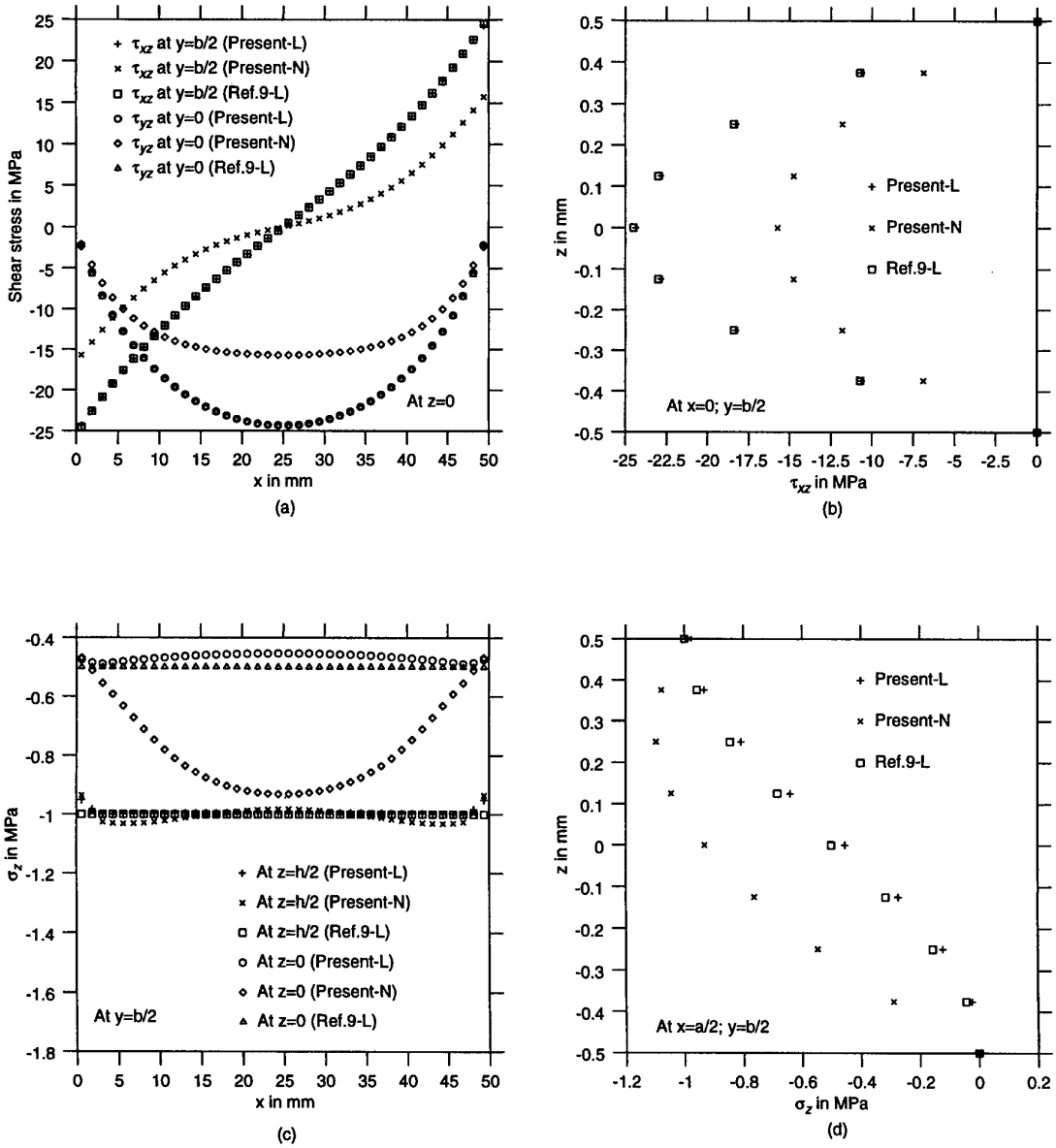

Fig. 2. Simply supported isotropic plate subjected to uniform load (L — linear; N — nonlinear).

higher value when the nonlinearity is accounted for. Figure 3(c) and (d) shows the variation of normal stress along θ and z, respectively. The agreement for the linear analysis with the analytical results is good. The magnitude of the normal stress reduces when nonlinearity is accounted for.

Clamped isotropic axi-symmetric spherical shell cap subjected to uniform pressure

The radius of the axi-symmetric spherical shell cap considered [9] is 56.3 in. and the included angle is $\psi = 78°$. The shell is 2.36 in. thick. The Poisson's ratio of the material is 0.2. An uniform load of 2840 psi is applied towards the center of the shell. Since the shell is an axisymmetric one, only a 5° segment of the shell is analyzed. The boundary conditions used are (refer to Fig. 1 for a definition of R and ψ)

$$\text{At } s = R\psi\text{: } u, v, w, w_s, w_\theta = 0;$$

$$\text{At } \theta = 0, 5°\text{: } u_\theta, v, w_\theta = 0$$

Figure 4(a) and (b) shows the variation of τ_{sz} with respect to s and z, respectively. The analytical solution for this problem is obtained by

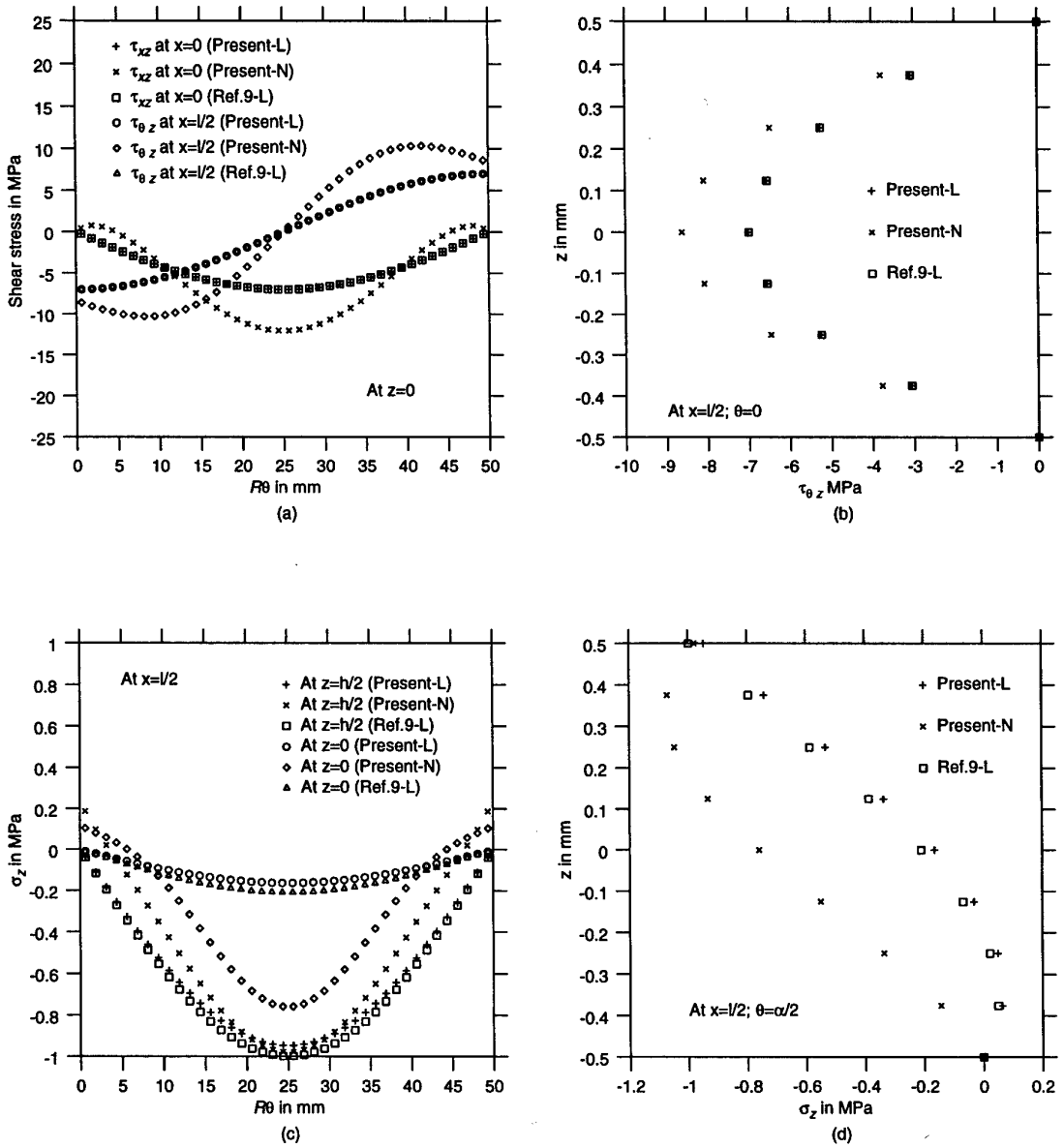

Fig. 3. Simply supported isotropic cylindrical shell panel subjected to sinusoidal load (L — linear; N — nonlinear).

using Geckler's approximation as given by Timoshenko and Krieger [9]. As seen in the graph, the difference between the present solution and the approximate analytical solution increases as s increases and it is maximum near the support. The nonlinear effect in this case is to reduce the magnitude of τ_{sz}. The difference between linear and nonlinear results are small because the load–deflection curve just crosses the linear regime. There is a small error in the boundary condition at the top surface both in the analytical and the present solution as shown in Fig. 4(b). The variation of σ_z with respect to s and z is shown in Fig. 4(c) and (d), respectively. Here also there is a small error in the boundary condition at the top surface.

Application to plates/shell panels damaged by low-velocity impact

In this section composite plates/shell panels are considered. The results are obtained using nonlinear finite element analysis.

Simply supported $[0_4/90_4]_s$ laminate

A 2 mm thick, square laminate of size 76.2 mm is considered. The laminate is simply supported along the edges. The central impact load is

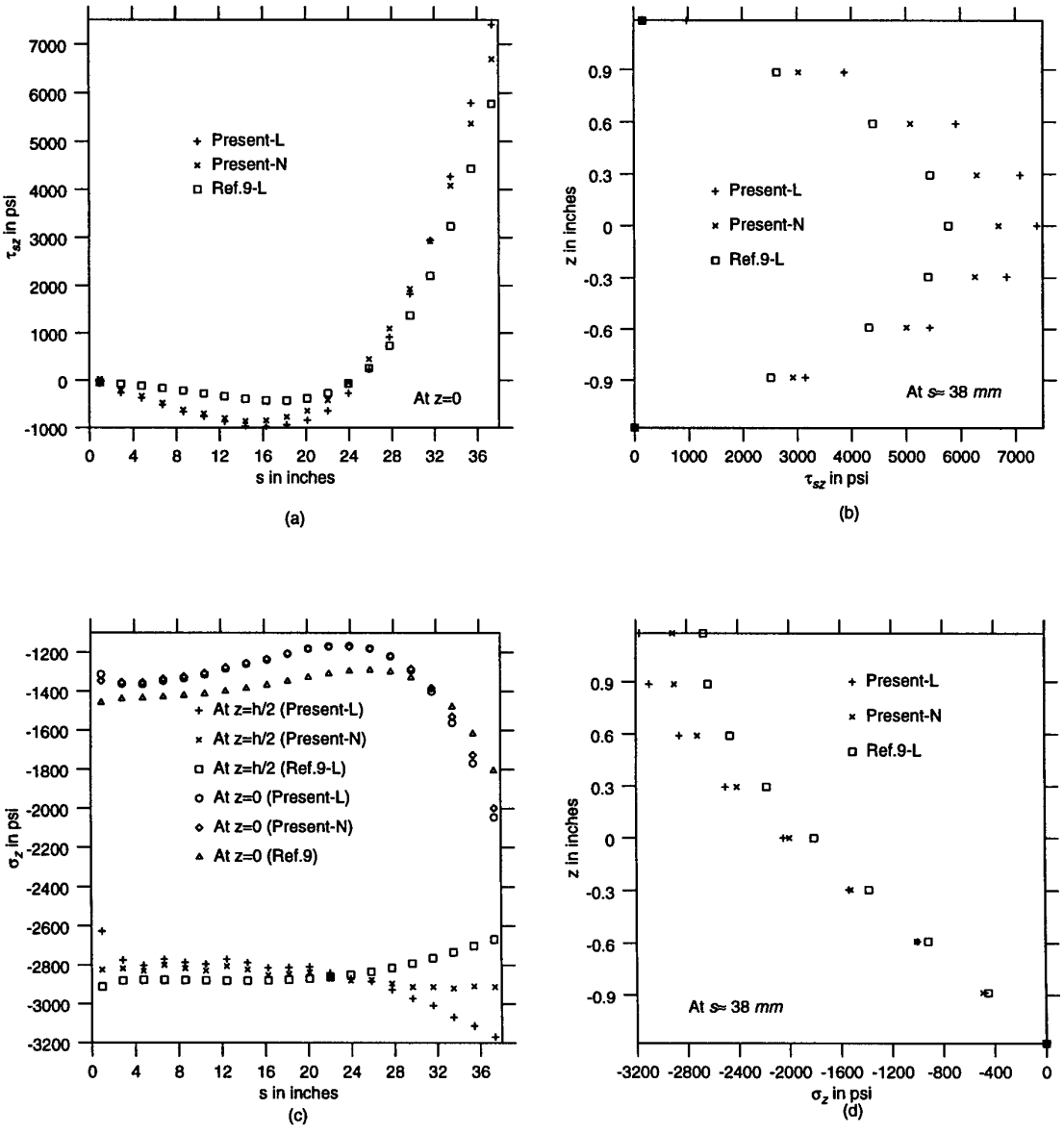

Fig. 4. Clamped isotropic axi-symmetric spherical shell subjected to uniform load (L — linear; N — nonlinear).

applied through a 6.35 mm nose diameter steel impactor to produce an impact energy of 1.1 J. The material used is graphite/bismalemide which has the following material properties

E_{11} = 177.8 GPa; E_{22} = 12.4 GPa;

G_{12} = 4.62 GPa; ν_{12} = 0.39

$X = X'$ = 1500 MPa; Y = 40 MPa;

Y' = 246 MPa; S = 68 MPa

where X, X' are the inplane tensile and compressive strengths of the lamina in the fiber direction, respectively, Y, Y' are the inplane tensile and compressive strengths of the lamina in the transverse direction, respectively, and S is the inplane shear strength of the lamina. The boundary conditions used are as follows

At $x = 0$, a: $v, w = 0$;

At $y = 0$, b: $u, w = 0$

Figure 5(a) and (b) shows the variation of interlaminar shear stresses with respect to x and z, respectively. As seen in the graph, the magnitude of stresses gets increased once the damage

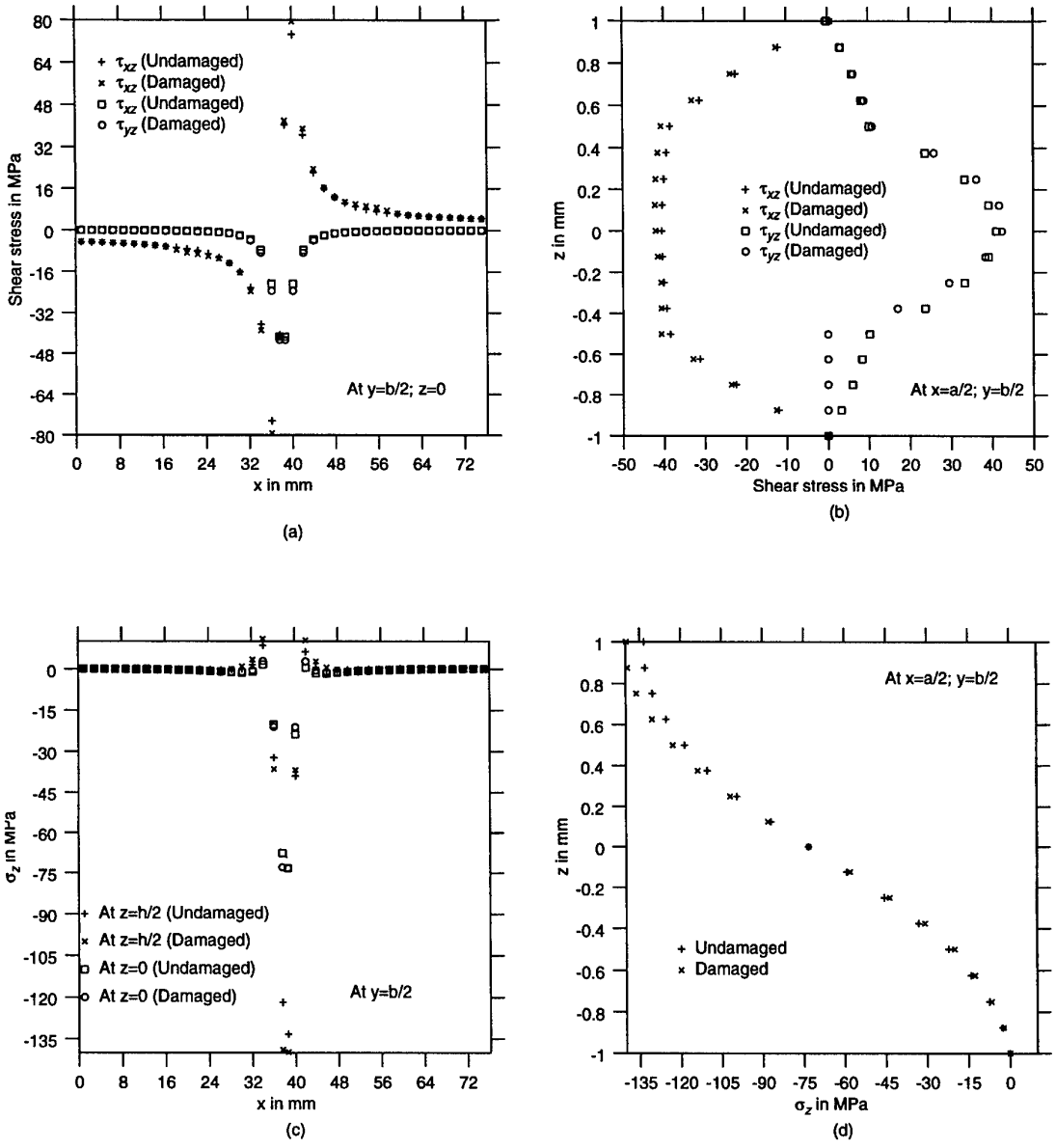

Fig. 5. Simply supported $[0_4/90_4]_s$ laminate subjected to impact load.

occurs. Since the damage is greater near the impact site, the stresses get modified in that zone only. The through-the-thickness stress distribution is affected drastically, especially for τ_{yz}, as shown in Fig. 5(b). The laminate becomes unsymmetric in the damage zone. The major mode of damage is matrix cracking and is along the fiber direction. This damage extends approximately up to 4 plies from the bottom surface. Hence τ_{yz} is zero in that region as its transverse properties are lost in that region. The interlaminar normal stress variation is shown in Fig. 5(c) and (d) with respect to x and z, respectively. Here also the stresses get increased near the impact site.

Simply supported $[0_4/90_4]_s$ cylindrical shell panel
The radius and length of the cylindrical shell panel considered next are 381 mm and 76.2 mm, respectively. The angle subtended by the circular arc is 0.2 rad. The shell panel is 2 mm thick. The material properties used are the same as in the previous example. An impact energy of 0.8 J is applied at the center of the shell panel through a spherical steel ball impactor of diameter 6.35 mm. The boundary conditions used are

At $x = 0, l$: $v, w = 0$;

At $\theta = 0, \alpha$: $u, w = 0$

Figure 6(a) and (b) shows the variation of interlaminar shear stresses and interlaminar normal stress with respect to z. The distribution of stresses is similar to that of the flat laminate but here the impact energy is less than that of the laminate.

Simply supported $[0_4/90_4]_s$ spherical shell panel
Next a spherical shell panel of radius 381 mm is considered. The α and ψ for the panel are both 0.2 rad. The shell panel is 2 mm thick. The loading and the material properties are the same as in the previous case. The boundary conditions used are

At $s = 0, R\psi$: $v, w = 0$;

At $\theta = 0, \alpha$: $u, w = 0$

Figure 7(a) and (b) shows the variation of interlaminar shear stresses and interlaminar normal stress with respect to z. Since the spherical shell panel is stiffer, the damage is greater when compared to the cylindrical shell panel and the flat laminate.

CONCLUSIONS

Interlaminar stresses are predicted for laminated composite plates, cylindrical/spherical shell panels, damaged by low-velocity impact. The impact problem is treated as a quasi-static problem. A nonlinear finite element analysis is carried out using a four noded, 48 degrees of freedom, doubly curved composite quadrilateral shell finite element. Kirchhoff–Love shell

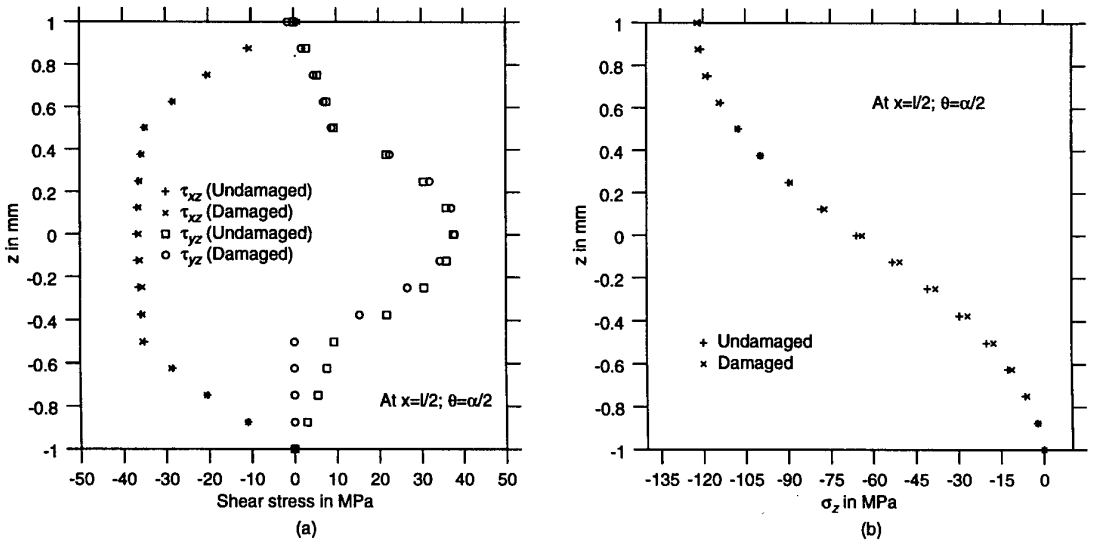

Fig. 6. Simply supported $[0_4/90_4]_s$ cylindrical shell panel subjected to impact load.

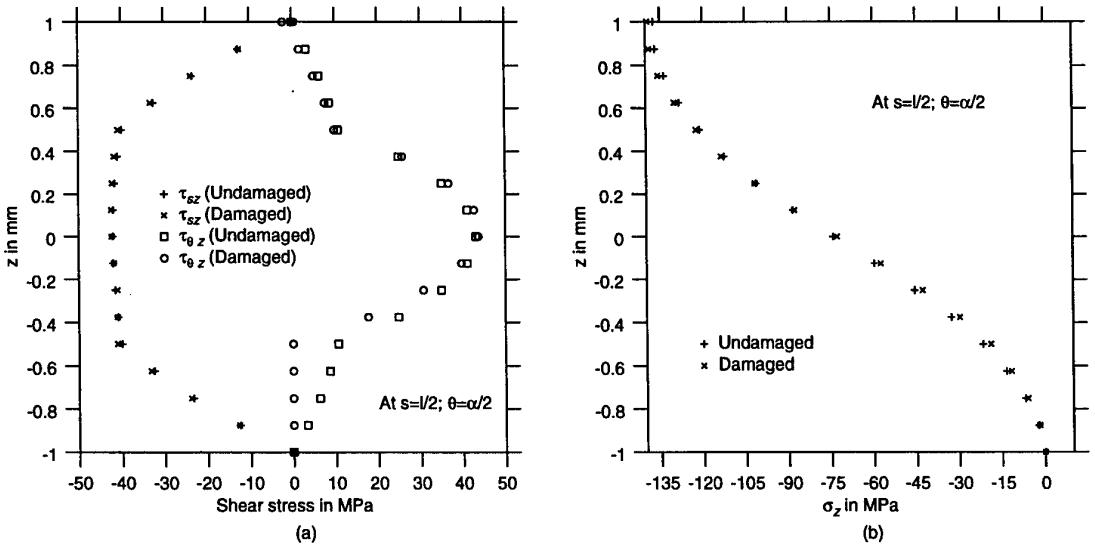

Fig. 7. Simply supported $[0_4/90_4]_s$ spherical shell panel subjected to impact load.

theory is used along with Green's strain tensor. The Tsai–Wu quadratic failure criterion and maximum stress failure criteria are used in the damage analysis. The 3-D elasticity equations of equilibrium are integrated through the thickness to get the interlaminar stresses.

The interlaminar stresses obtained from the present analysis can be used effectively in the study of delaminations in composite panels as well as in residual strength/stiffness studies.

REFERENCES

1. Pagano, N.J. and Hatfield, S.J., Elastic behavior of multilayered bidirectional composites. *AIAA J.* 1972, **10**, 931–933.
2. Lajczok, M.R., New approach in the determination of interlaminar shear stresses from the results of MSC/NASTRAN. *Computers and Structures* 1986, **24**, 651–656.
3. Tolson, S. and Zabaras, N., Finite element analysis of progressive failure in laminated composite plates. *Computers and Structures* 1991, **38**, 361–376.
4. Lo, K.H., Christensen, R.M. and Wu, E.M., Stress solution determination for higher order plate theory. *IJSS* 1978, **14**, 655–662.
5. Reddy, J.N., A refined nonlinear theory of plates with transverse shear deformation. *IJSS* 1984, **20**, 881–896.
6. Venkatesh, A. and Rao, K.P., A doubly curved quadrilateral finite element for the analysis of laminated anisotropic shells of revolution. *Computers and Structures* 1980, **12**, 825–832.
7. Ganapathy, S., Biswajit Tripathy and Rao, K. P., Damage and its growth in laminated composite circular/rectangular plates undergoing large deformations. *Composite Structures* 1995, **31**, 339–351.
8. Seide, P. *Small Elastic Deformations of Thin Shells*, Noordoff International Publishing, Leyden, 1975.
9. Timoshenko, S. P. and Krieger, S. W., *Theory of Plates and Shells*. Second edition, McGraw–Hill International Editions, 1983.

ELSEVIER

Composite Structures Vol. 38, No. 1–4, pp. 169–177, 1997
© 1997 Elsevier Science Ltd. All rights reserved
Printed in Great Britain
0263-8223/97/$17.00 + 0.00

PII:S0263-8223(97)00053-6

The stability of composite material stiffened conical shells under axial compression

Lingchuan Li

Department of Mechanical and Material Engineering, The University of Western Ontario, London, Ontario, Canada N6A 5B9

The stability of composite material stiffened conical shells under uniform axial compression and with classical clamped boundary conditions is investigated. The effects of stiffeners are uniformly distributed over the whole surface of the shell, and the shell is treated as an equivalent orthotropic shell. A method of solution is developed by using energy principles and Rayleigh–Rize approximations. It is shown that the approach proposed in this paper is practical, effective and satisfactory. © 1997 Elsevier Science Ltd.

INTRODUCTION

To increase the resistance of shells to buckling, they are strengthened by stiffeners and thus the critical load can be increased several times with only a little addition of material. Stiffened laminated composite material conical shells are finding widespread use in aerospace and other technical applications. Knowledge of the stability analysis of this kind of structure is essential for reliable lightweight structural design.

Extensive research on buckling behavior of many kinds of structures is reported in the open literature [1–6] and buckling of isotropic conical shells under compressive axial loads has been studied by many researchers [7–11]. A simple formula was developed for buckling of isotropic conical shells by Seide [7], and this formula is independent of boundary conditions and is best used for long shells. There have been fewer studies for orthotropic shells and stiffened laminated composite material conical shells [12].

The present study is an attempt to provide a suitable tool for the analysis of the stability of composite material stiffened conical shells subjected to axial compression. In the problem to be considered, the analysis is confined to the treatment of an equivalent orthotropic shell. The treatment distributes the stiffener effects uniformly over the shell and is capable of affording a good approximation to the elastic, stiffened shell if the reinforcing is sufficiently closely spaced. The critical buckling pressure for this kind of shell is obtained by using the energy principle, the variational principle and the Rayleigh–Ritz approximation.

ANALYTICAL FORMULATION

The shell geometry and the coordinate system are defined in Fig. 1.

Basic Assumptions

For the shell skin, it is assumed that the linear elastic theory for thin shell holds. For the stiffeners, it is assumed that: (1) the stiffeners are 'distributed' over the whole surface of the shell; (2) the normal strains ε_x and ε_φ vary linearly in the stiffener as well as in the sheet; (3) the stiffeners do not transmit shear; and (4) the torsional rigidity of the stiffener is ignored.

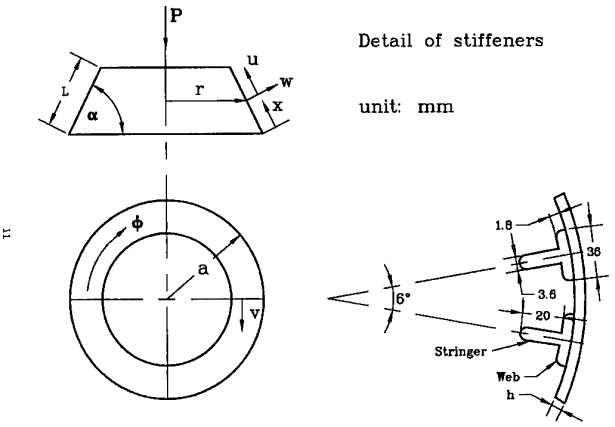

Fig. 1. The conical shell structure and the notation.

Middle surface strains and displacements

The expressions for the middle surface strains and curvatures of a deformed conical shell are given as follows: (Fig. 1)

$$\varepsilon_x = u_{,x} + \frac{1}{2} w_{,x}^2$$

$$\varepsilon_\varphi = (1/r)(v_{,\varphi} - u\cos\alpha + w\sin\alpha)$$

$$\varepsilon_{x\varphi} = v_{,x} + u_{,\varphi}/r + v\cos\alpha/r \kappa_\varphi = -w_{,xx}$$

$$\kappa_\varphi = (-1/r)(w_{,\varphi\varphi}/r - w_{,x}\cos\alpha$$

$$\kappa_{x\varphi} = -\kappa_{\varphi x} = (-1/r)(w_{,x\varphi} + w_{,\varphi}\cos\alpha/r) \tag{1}$$

The above is also called the strain–displacement relation.

The stress resultants and strain relationships, with no bending–twisting and no stretching–bending couplings, are given by

$$\begin{Bmatrix} N_x \\ N_\varphi \\ N_{x\varphi} \\ M_x \\ M_\varphi \\ M_{x\varphi} \end{Bmatrix} = \begin{bmatrix} A_{11} & A_{12} & 0 & 0 & 0 & 0 \\ A_{12} & A_{22} & 0 & 0 & 0 & 0 \\ 0 & 0 & A_{66} & 0 & 0 & 0 \\ 0 & 0 & 0 & D_{11} & D_{12} & 0 \\ 0 & 0 & 0 & D_{12} & D_{22} & 0 \\ 0 & 0 & 0 & 0 & 0 & D_{12} \end{bmatrix} \begin{Bmatrix} \varepsilon_x \\ \varepsilon_\varphi \\ \varepsilon_{x\varphi} \\ \kappa_x \\ \kappa_\varphi \\ \kappa_{x\varphi} \end{Bmatrix} \tag{2}$$

where, A_{ij} and D_{ij} are calculated from the elastic stiffness constants of the kth layer $(\bar{Q}_{ij})_k$ through

$$A_{ij} = \sum_{k=1}^{\bar{N}} (Q_{ij})_k (z_{(k)} - z_{(k-1)})$$

$$D_{ij} = \sum_{k=1}^{\bar{N}} (Q_{ij})(z_{(k)}^3 - z_{(k-1)}^3)/3 \tag{3}$$

and, the quantities N_x, N_φ, ..., $M_{x\varphi}$ are the force and monent resultants obtained by integrating the stresses σ_x, σ_φ, ..., $\sigma_{x\varphi}$ through the shell thickness.

According to the assumptions for stiffeners, the rigidities of stringer and web of the stiffener are uniformly distributed over the surface of the shell, and the stiffeners only bear pressure and bending. Thus, A_{11} and D_{11} of eqn (2) must be modified as

$$A_{11} = A_{11\ \text{shell}} + A_{11\ \text{stringer}} + A_{11\ \text{web}}$$

$$D_{11} = D_{11\ \text{shell}} + D_{11\ \text{stringer}} + D_{11\ \text{web}} \tag{4}$$

where

$$A_{11\ \text{stringer}} = \frac{E_1 A_1}{S}$$

$$A_{11\ \text{web}} = \frac{E_2 A_2}{S}$$

$$A_{11\ \text{stringer}} = \frac{E_1 I_1}{S}$$

$$A_{11\ \text{web}} = \frac{E_2 I_2}{S} \tag{5}$$

in which, E_1, E_2 and I_1, I_2 are moduli of elasticity and moment of inertia of stringer and web, respectively. S represents the distance between stiffeners at $x = L/2$. A_1 and A_2 are the cross section area of stringer and web, respectively.

From eqn (2), we can obtain

$$N_x = A_{11}\varepsilon_x + A_{12}\varepsilon_\varphi$$

$$N_\varphi = A_{12}\varepsilon_x + A_{22}\varepsilon_\varphi$$

$$N_{x\varphi} = A_{66}\varepsilon_{x\varphi} M_x = D_{11}\kappa_x + D_{22}\kappa_\varphi$$

$$M_\varphi = D_{12}\kappa_x + D_{22}\kappa_\varphi$$

$$M_{x\varphi} = -M_{\varphi x} = D_{66}\kappa_{x\varphi} \tag{6}$$

Energy relations

The potential energy for an elastic system is governed by the relation

$$V = U + \Omega \tag{7}$$

in which, U is the strain energy due to bending and stretching of the stiffened shell and Ω is the potential energy of the external force system. The strain energy of the stiffened shell may be expressed as the surface integral

$$U = \frac{1}{2}\int_s (N_x\varepsilon_x + N_\varphi\varepsilon_\varphi + N_{x\varphi}\varepsilon_{x\varphi} + M_x\kappa_x + M_\varphi\kappa_\varphi + 2M_{x\varphi}\kappa_{x\varphi})\mathrm{d}s \tag{8}$$

Infinitesimal theory of buckling

The infinitesimal theory of buckling requires that the variation of the change in potential energy of the system with respect to the allowable displacements must be zero. Expressed mathematically

$$\delta(\Delta V)=0 \tag{9}$$

where

$$\Delta V=\Delta U+\Delta\Omega \tag{10}$$

in which, ΔU and $\Delta\Omega$ are changes in the strain energy and the potential energy, respectively.

From the assumption of the linear elastic theory, we assume that the deformed shell prior to buckling is very close to its original shape, the expression, eqn (1), for the middle surface strains and curvatures may be considered to represent the change in strains and curvatures after buckling occurs. Hence, the displacements u, v, w, and the force and moment resultants N_x, N_φ, ..., $M_{x\varphi}$ are now taken as the additional displacements, forces and moments in the shell after buckling and eqn (8) as the changes in strain energy.

Since the middle surface strains and curvatures are measured from the position of incipient buckling, the potential energy expression must be modified to include the energy stored by the shell in a compressed but unbuckled state. The term to be added to the potential energy expression is given by

$$\Delta U_M=\int_s(\bar{N}_x\varepsilon_x+\bar{N}_\varphi\varepsilon_\varphi+\bar{N}_{x\varphi}\varepsilon_{x\varphi}+\bar{M}_x\kappa_x+\bar{M}_\varphi\kappa_\varphi+2\bar{M}_{x\varphi}\kappa_{x\varphi})\mathrm{d}s \tag{11}$$

in which, $\bar{N}_x$, $\bar{N}_\varphi$, ..., $\bar{M}_{x\varphi}$, are the membrane stresses and moments existing in the shell prior to buckling.

The shell is assumed under symmetric loading and initial bending stresses are neglected. Omitting the terms $\bar{N}_{x\varphi}$, $\bar{M}_x$, $\bar{M}_\varphi$, and $\bar{M}_{x\varphi}$, eqn (11) reduces to the form

$$\Delta U_M=\int_s(\bar{N}_x\varepsilon_x+\bar{N}_\varphi\varepsilon_\varphi)\mathrm{d}s \tag{12}$$

Under axial compression, we have following relations

$$\bar{N}x=-\frac{P}{2\pi r\sin\alpha} \tag{13}$$

By substituting eqns (1) and (6) into eqns (8) and (12) and retaining all second order terms, the total expression for the changes in strain energy of the stiffened shell becomes

$$\Delta U_T=\int_0^{2\pi}\int_0^L\bar{N}_x\left(u_{,x}+\frac{1}{2}w_{,x}^2\right)r\mathrm{d}x\mathrm{d}\varphi+\frac{1}{2}\int_0^{2\pi}\int_0^L\Big\{A_{11}u_{,x}^2+2A_{12}(v_{,\varphi}-u\cos\alpha+w\sin\alpha)$$

$$(u_{,x}/r)+A_{22}\left[\frac{1}{r}(v_{,\varphi}-u\cos\alpha+w\sin\alpha)\right]^2+A_{66}[v_{,x}+u_{,\varphi}/r$$

$$+v\cos\alpha/r]^2\Big\}r\mathrm{d}x\mathrm{d}\varphi+\frac{1}{2}\int_0^{2\pi}\int_0^L\Big\{D_{11}w_{,xx}^2+2D_{12}(w_{,\varphi\varphi}/r-w_{,x}\cos\alpha)(w_{,xx}/r)$$

$$+D_{22}\left[-\frac{1}{r}(w_{,\varphi\varphi}/r-w_{,x}\cos\alpha)\right]^2+2D_{66}\left[-\frac{1}{r}(w_{,x\varphi}+w_{,\varphi}\cos\alpha/r)\right]^2\Big\}r\mathrm{d}x\mathrm{d}\varphi \tag{14}$$

The terms in the expression $\Delta\Omega$ for the change in potential energy of the external force system are not presented herein. However, it is noted that terms in $\Delta\Omega$ which are linear u, v, w cancel with similar terms in the strain energy expression (eqn (14)) by the principal of virtual work. Thus, we only consider ΔU_T as ΔV for the following derivative.

Rayleigh–Ritz approximation

The related clamped boundary conditions can be written as

$$\left.\begin{array}{l} w=0 \\ w_{,x}=0 \\ v=0 \end{array}\right\} \text{ when } x=0,\ L \tag{15}$$

In applying the Rayleigh–Ritz approximate method, it is necessary to determine a set of displacements which accurately describe the deflected shape of the conical shell. Now, let us assume solutions for the displacements of the following forms

$$\begin{aligned} u &= A\cos n\varphi \cos(m\pi x/L) \\ v &= B\sin n\varphi \sin(m\pi x/L) \\ w &= C\cos n\varphi \sin(m\pi x/L) \end{aligned} \tag{16}$$

where, A, B and C are undetermined coefficients, and m and n are the number of waves in the axial and circumferential directions, respectively.

Substituting these equations into the simplified energy relation (14) and integrating yields a homogeneous quadratic function of A, B, and C, namely

$$\Delta V = a_{11}A^2+a_{12}AB+a_{13}AC+a_{22}B^2+a_{22}B^2+a_{23}BC+\left(a_{33}-\frac{PL\lambda^2}{8\sin\alpha}\right)C^2 \tag{17}$$

where

$$\lambda = m\pi/L \tag{18}$$

The coefficients in eqn (17) are defined in the Appendix.

The condition for the minimization of the potential energy of the system is obtained by setting the derivatives of eqn (17) with respect to the unspecified coefficients equal to zero. This operation yields a set of linear homogeneous equations for the coefficients of the displacements as follows

$$\begin{aligned} &2a_{11}A+a_{12}B+a_{13}C=0 \\ &a_{12}A+2a_{22}B+a_{23}C=0 \\ &a_{13}A+a_{23}B+2\left(a_{33}-\frac{PL\lambda^2}{8\sin\alpha}\right)C=0 \end{aligned} \tag{19}$$

The determinant of eqn (19) vanishes for nontrivial values of the critical load

$$\begin{vmatrix} 2a_{11} & a_{12} & a_{13} \\ a_{12} & 2a_{22} & a_{23} \\ a_{13} & a_{23} & 2\left(a_{33}-\dfrac{PL\lambda^2}{8\sin\alpha}\right) \end{vmatrix} = 0 \tag{20}$$

Theoretical result for conical shell

When the determinant, eqn (20), is expanded, the result for the composite material stiffened conical shell can be approximately expressed as

$$P_{cr} = \frac{8\sin\alpha}{L\lambda^2}a_{33} - \frac{8\sin\alpha(2a_{22}a_{13}^2+2a_{11}a_{23}^2-2a_{12}a_{13}a_{23})}{L\lambda^2(8a_{11}a_{22}-2a_{12}^2)} \tag{21}$$

In eqn (21), P_{cr} is only a function of the axial wave number m and circumferential wave number n after geometry and material parameters of the shell are given. For the minimum value of the general instability load, it is necessary to minimize eqn (21) with respect to the wave numbers, m and n. However, in this investigation, m is set equal to unity and n, allowed to vary continuously. This procedure assumes that the axial wave length extends over all of the stiffener element. It is especially available for the short conical shells.

NUMERICAL RESULTS AND DISCUSSION

The critical axial compression for general instability is computed for some typical cases. The geometry and material parameters of shells are given in Tables 1 and 2. The cases with different base angle α of the shell (Fig. 1) are investigated by the method proposed in this paper, and the numerical results are shown as Table 3. The torsional resistance of the stiffeners is neglected and the whole distance between the stiffeners is taken as the 'effective length' of the sheet. The moduli of elasticity of the sheet and stiffeners are considered equal.

For a particular conical shell with the base angle $\alpha = 60°$, we calculate its critical load P_{cr} by using an equivalent method in Ref. [13], and get $P_{cr} = 2.175 \times 10^6$ N. It is shown that the result obtained from proposed method is satisfactory, and has a good agreement with the result from other method. And from practical experience, one can understand that these results are reasonable for the short conical shells.

It can be seen, from Table 3, that P_{cr} and n increase when the base angle α becomes larger for shells with other fixed geometry parameters. It can be described, physically speaking, by saying that the larger the conical base angle α becomes, the larger the critical load tends to be. Thus, it may be safe to say that to increase the critical load of a composite material stiffened conical shell, one should try to consider the conical base angle α in an engineering design.

Table 1. Geometry

Shell	Stiffener
$L = 337.38$ mm	Thickness of stringer: 1.8 mm Height of stringer: 36 mm
$a = 1008.5$ mm	Thickness of web: 3.6 mm Height of web: 20 mm

Table 2. Material parameters

	Shell	Stringer of stiffener	Web of stiffener
Material	$E_{11} = 103{,}000$ N/mm^2	$E_1 = \sum_{K=1}^{N} \bar{Q}_{11\,\text{stringer}}$	$E_2 \sum_{K=1}^{N} \bar{Q}_{11\,\text{web}}$
Parameters	$E_{22} = 6850$ N/mm^2 $\nu_{12} = 0.31$ $\nu_{21} = 0.0206$ $G_{12} = 4050$ N/mm^2	$A_1 = 64.8$ mm^2 $I_1 = 17.469$ mm^4	$A_2 = 72.0$ N/mm^2 $I_2 = 77.76$ N/mm^4
Angle-ply	$[\pm 45/0_2/\pm 45/0_2/\mp 45]$	$[\pm 45/0_2/\pm 45/0_2/\pm 45]$	$[\pm 45/0_2/\pm 45/0_2/\pm 45]_2$
Ply thickness	0.18 mm	0.18 mm	0.18 mm

Table 3. Numerical results

α	S^* (mm)	P_{cr} (N)	n
15°	88.50	0.5650×10^6	10
30°	90.27	1.156×10^6	13
45°	93.07	1.720×10^6	15
60°	96.73	2.187×10^6	17
75°	100.99	2.492×10^6	19
80°	102.49	2.550×10^6	20

*S is the distance between stiffeners at $x = L/2$.

CONCLUSION

A relatively simple formula is derived for analysis of the stability of composite material stiffened conical shells subjected to axial compression. The formula contains two paramters, the axial wave number m and circumferential wave number n. The numerical analytical results show that the approach proposed in this investigation has good accuracy, and it can also be used in a practical analysis for long conical shell. For a simply supported conical shell, the following displacement functions are suggested

$$u = A \cos n\varphi \cos(m\pi x/L)$$

$$v = B \sin n\varphi \sin(m\pi x/L)$$

$$w = C \cos n\varphi \sin(m\pi x/L)$$

It is worth stressing that the conical base angle α has a significant influence on the critical buckling loads and the circumferential wave number. From this investigation, it is shown that the present method provides a widely practical tool in the stability analysis of composite material shell structures.

REFERENCES

1. Seide, P., A Donnell-type theory for asymmetrical bending and buckling of thin conical shells. *J. Appl. Mech.*, 1957, **24**, 547–552.
2. Serpico, J., Elastic stability of orthotropic conical and cylindrical shells subjected to axisymmetric loading conditions. *AIAA J.*, 1963, **1**, 128–137.
3. Singer, J., Buckling of orthotropic conical shells under external pressure. *J. Aero. Quar.*, May 1964, pp. 151–168.
4. Baruch, M. and Singer, J., General instability of stiffened circular conical shells under hydraulic pressure. *Aero. Quar.*, May 1965, pp. 187–204.
5. Tani, J., Buckling of truncated conical shells under combined axial load pressure and heating. *J. Appl. Mech.*, 1987, **52**, 402–408.
6. Kardomateas, G.A., Buckling of thick orthotropic cylindrical shells under external pressure. *J. Appl. Mech.*, 1993, **60**, 195–202.
7. Seide, P., Axisymmetrical buckling of circular cones under axial compression. *J. Appl. Mech.*, 1956, **23**, 625–628.
8. Lackman, L., Buckling of circular cones under axial compression. *J. Appl. Mech.*, 1960, **27**, 458–460.
9. Seide, J., Buckling of circular cones under axial compression. *J. Appl. Mech.*, 1961, **28**, 315–319.
10. Singer, J., Buckling of circular conical shells under uniform axial compression. *AIAA J.* 1965, **3**, 985–987.
11. Tani, J., Buckling of truncated conical shells under axial compression. *AIAA J.*, 1970, **8**, 568–571.
12. Tong, L.Y. and Wang, T.K., Buckling analysis of laminated composite conical shells. *Comp. Sci. Tech.*, 1993, **47**, 57–63.
13. Li Shunlin, *Handbook for Composite Materials*, Beijing, 1988

APPENDIX A

DEFINITION OF GEOMETRIC PARAMETERS

The coefficients in eqn (17) are defined as

$$a_{11} = \frac{1}{2}\left[\frac{\lambda^2 L\pi A_{11}}{2}\cdot K + A_{22}\pi\cos\alpha\cdot t_1 + A_{66}n^2\pi t_1/\cos\alpha\right]$$

$$a_{22} = \frac{1}{2}\left[A_{22}n^2\pi t_3/\cos\alpha + \frac{A_{66}\lambda^2\pi LK}{2} + A_{66}\pi\cos\alpha\cdot t_3\right]$$

$$a_{12} = \frac{1}{2}\left[-A_{12}\lambda n\pi L - 2A_{22}n\pi t_1 - A_{66}\lambda n\pi L - 2A_{66}n\pi t_4\right]$$

$$a_{13} = \frac{1}{2}\left[-2A_{22}\pi\sin\alpha\cdot t_4\right]$$

$$a_{23} = \frac{1}{2}[2A_{22}n\pi tg\alpha \cdot t_5]$$

$$a_{33} = \frac{1}{2}[A_{22}\pi tg\alpha \cdot t_6 + 2D_{11}\lambda^4 \pi LK - 4D_{12}\lambda^2 n^2 \pi \cdot t_7/\cos\alpha + D_{22}\pi n^4 t_8/\cos\alpha + 2D_{22}n^2\lambda\pi t_9$$

$$+ D_{22}\lambda^2 \pi t_{10}/\cos\alpha + 4D_{66}n^2\lambda\pi t_9 + 2D_{66}n^2\pi\cos\alpha \cdot t_8]$$

where

$$K = a - \frac{L}{2}\cos\alpha$$

$$t_1 = -\frac{1}{2}[\ln(1-\beta) + g_1]$$

$$t_2 = -\frac{1}{2}g_2$$

$$t_3 = -\frac{1}{2}[\ln(1-\beta) - g_1]$$

$$t_4 = -\frac{1}{4}(g_3 - g_4)$$

$$t_5 = -\frac{1}{4}(3g_5 - g_6)$$

$$t_6 = -\left[\frac{1}{8}\ln(1-\beta) - \frac{1}{2}g_1 + \frac{1}{8}g_7\right]$$

$$t_7 = -\left[\frac{1}{2}g_1 - \frac{1}{4}\ln(1-\beta) - \frac{1}{4}g_7\right]$$

$$t_8 = -\left[\frac{3}{16a^2} - \frac{3}{16(a - L\cos\alpha)^2} - \frac{1}{2}g_8 + \frac{1}{8}g_9\right]$$

$$t_9 = -\left(\frac{1}{2}g_{10} - \frac{1}{4}g_{11}\right)$$

$$t_{10} = -\frac{1}{2}[\ln(1-\beta) - g_7]$$

and

$$\beta = (L/a)\cos\alpha$$

$$g_1 = \cos(2m\pi/\beta)\int_{2m\pi/\beta}^{2m\pi/\beta-2m\pi}\frac{\cos y}{y}\,dy + \sin(2m\pi/\beta)\int_{2m\pi/\beta}^{2m\pi/\beta-2m\pi}\frac{\sin y}{y}\,dy$$

$$g_2 = \sin(2m\pi/\beta)\int_{2m\pi/\beta}^{2m\pi/\beta-2m\pi}\frac{\cos y}{y}\,dy - \cos(2m\pi/\beta)\int_{2m\pi/\beta}^{2m\pi/\beta-2m\pi}\frac{\sin y}{y}\,dy$$

$$g_3 = \cos(m\pi/\beta)\int_{m\pi/\beta}^{m\pi/\beta-m\pi}\frac{\cos y}{y}\,dy + \sin(m\pi/\beta)\int_{m\pi/\beta}^{m\pi/\beta-m\pi}\frac{\sin y}{y}\,dy$$

$$g_4 = \cos(3m\pi/\beta)\int_{3m\pi/\beta}^{3m\pi/\beta-3m\pi}\frac{\cos y}{y}\,dy + \sin(3m\pi/\beta)\int_{3m\pi/\beta}^{3m\pi/\beta-3m\pi}\frac{\sin y}{y}\,dy$$

$$g_5 = \sin(m\pi/\beta)\int_{m\pi/\beta}^{m\pi/\beta-m\pi}\frac{\cos y}{y}\,dy - \cos(m\pi/\beta)\int_{m\pi/\beta}^{m\pi/\beta-m\pi}\frac{\sin y}{y}\,dy$$

$$g_6 = \sin(3m\pi/\beta)\int_{3m\pi/\beta}^{3m\pi/\beta-3m\pi}\frac{\cos y}{y}\,dy - \cos(3m\pi/\beta)\int_{3m\pi/\beta}^{3m\pi/\beta-3m\pi}\frac{\sin y}{y}\,dy$$

$$g_7 = \cos(4m\pi/\beta)\int_{4m\pi/\beta}^{4m\pi/\beta-4m\pi}\frac{\cos y}{y}\,dy + \sin(4m\pi/\beta)\int_{4m\pi/\beta}^{4m\pi/\beta-4m\pi}\frac{\sin y}{y}\,dy$$

$$g_8 = \frac{4m^2\pi^2}{L^2\cos^2\alpha}\left[\cos(2m\pi/\beta)\int_{2m\pi/\beta}^{2m\pi/\beta-2m\pi}\frac{\cos y}{y^3}\,dy + \sin(2m\pi/\beta)\int_{2m\pi/\beta}^{2m\pi/\beta-2m\pi}\frac{\sin y}{y^3}\,dy\right]$$

$$g_9 = \frac{16m^2\pi^2}{L^2\cos^2\alpha}\left[\cos(4m\pi/\beta)\int_{4m\pi/\beta}^{4m\pi/\beta-4m\pi}\frac{\cos y}{y^3}\,dy + \sin(4m\pi/\beta)\int_{4m\pi/\beta}^{4m\pi/\beta-4m\pi}\frac{\sin y}{y^3}\,dy\right]$$

$$g_{10} = \frac{2m\pi}{L\cos\alpha}\left[\sin(2m\pi/\beta)\int_{2m\pi/\beta}^{2m\pi/\beta-2m\pi}\frac{\cos y}{y^2}\,dy - \cos(2m\pi/\beta)\int_{2m\pi/\beta}^{2m\pi/\beta-2m\pi}\frac{\sin y}{y^2}\,dy\right]$$

$$g_{11} = \frac{4m\pi}{L\cos\alpha}\left[\sin(4m\pi/\beta)\int_{4m\pi/\beta}^{4m\pi/\beta-4m\pi}\frac{\cos y}{y^2}\,dy - \cos(4m\pi/\beta)\int_{4m\pi/\beta}^{4m\pi/\beta-4m\pi}\frac{\sin y}{y^2}\,dy\right]$$

ELSEVIER

Composite Structures Vol. 38, No. 1–4, pp. 179–190, 1997
© 1997 Elsevier Science Ltd. All rights reserved
Printed in Great Britain
0263-8223/97/$17.00 + 0.00

PII:S0263-8223(97)00054-8

Compressible flow analysis of filling and post-filling in injection molding with phase-change effect

Kyeong-Hee Han & Yong-Taek Im

Computer Aided Materials Processing Laboratory, Department of Mechanical Engineering, Korea Advanced Institute of Science and Technology, Taejon 305-701, South Korea

In order to predict the shrinkage, warpage and mechanical properties of the injection molded parts, it is necessary to know the history of the flow field during injection-molding processes. In the present investigation a numerical simulation program was developed to predict the flow field in filling and post-filling stages of injection molding. To simulate the real molding conditions more accurately, a generalized Hele–Shaw model for a non-Newtonian fluid was assumed considering the effects of phase change and compressibility of the resin. A finite-element–finite-difference (FEM–FDM) hybrid scheme with control volume approach was employed as the solving technique. For modeling the viscosity of the resin, a modified Cross model was used with a double-domain Tait equation of state being employed in describing the compressibility of the resin during molding. The energy balance equation, including latent-heat dissipation for semi-crystalline materials, was solved in order to predict the solidified layer and temperature profile in detail. For verification of the numerical results obtained from the developed program, the simulation results were compared with the experimental results obtained from the test mold set designed in the current study using commercial-grade PP and the data available in the literature. Based on a comparison between experiments and simulations, it was found that the currently developed program was useful in unified simulations of filling and post-filling in injection-molding processes when considering the phase-change effect. © 1997 Elsevier Science Ltd.

INTRODUCTION

Injection molding is one of the most widely used manufacturing processes for producing thin thermoplastic parts. It consists of filling, packing and cooling stages. In the filling stage, in order to yield a good-quality product, molten polymer must fill the cavity without making any air entrapments, weld-lines or any other defects. After filling, additional polymer melt is pushed into the cavity to maintain a uniform pressure at the inlet and to compensate for any possible shrinkage caused by a phase change of the material. Thus, it is important to simulate the filling and post-filling stages as a continuous process to achieve good dimensional accuracy and mechanical properties of the final molded parts. In the present investigation, a simulation program for the filling and post-filling stages, considering this phase-change effect, was developed as a part of computer-aided engineering of injection molding.

After the pioneering work of Hieber & Shen [1], who developed a systematic approach for the filling analysis of injection molding by assuming a Hele–Shaw flow inside the thin cavity and by employing a finite-element–finite-difference (FEM–FDM) hybrid scheme for solving the pressure and temperature fields with the moving grid method, many more studies have been carried out [2–8]. Among these, Wang *et al.* [2] combined the control volume

with a flow analysis network (FAN) to advance the moving front during the filling stage. This approach reduced the computation time required for numerical analysis and made it easier to analyze filling in the case of complex cavities. In addition, Wang *et al.* [3] investigated the Spencer Gilmore or Tait state equations to consider a variable density for the post-filling analysis in Hele–Shaw flow modeling.

Recently, Chiang *et al.* [5,6] carried out a unified filling and post-filling simulation. They used unified governing equations for both the filling and post-filling stages. They employed one- and two-dimensional elements, respectively, to model complex thin cavities, and calculated the pressure distribution by applying a finite-element technique for each type of element. With this method, the pressure distributions during the filling stage were iteratively determined in order to satisfy the mass flow rate condition at each time step after the solution was obtained under constant pressure conditions. Thus, additional iteration is required and, furthermore, the strict mass flow rate condition at the inlet is probably not satisfied. The energy equation with latent-heat release for the semi-crystalline polymer was solved in their investigation [5,6] based on a fixed-domain method by modifying the specific heat according to the phase change of the material, although the exact location of the solid–liquid boundary cannot be predicted using this approach [9]. Therefore, another approach based on a moving-domain method was employed by Chen & Liu [4,7] to solve the same energy equation.

In the present investigation, a hybrid FEM–FDM was introduced for solving the coupled flow and temperature fields in filling and post-filling, taking account of both phase change and compressibility of the material. Mass conservation for the control volume defined was applied in obtaining flow fields for the convenience of computation. This approach eliminates the additional pressure iteration step mentioned earlier and allows the prescribed mass flow rate condition to be satisfied. It also enables us to use various types of elements, such as triangular, strip and cylindrical, to simulate fluid flow in runners and complex die cavities. The location of the solid–liquid boundary was calculated by solving the phase-change problem (Stefan problem) in the thickness direction based only on the moving-domain technique [10]. The variable-density effect was considered by applying the Tait state equation, with a Cross-type model being employed to represent the shear viscosity. The solution accuracies were tested by three different case studies. The first mold set was designed and manufactured in the current investigation, and the second and third molds were selected from Chiang *et al.* [6].

THEORETICAL BACKGROUND

The generalized Hele–Shaw (GHS) flow was assumed for flow analysis in a thin cavity. Considering the variable-density effect, governing equations for flow in the plane direction of Fig. 1 can be written as [1,11]

$$\frac{\partial \rho}{\partial t} + \frac{\partial}{\partial x}(\rho u) + \frac{\partial}{\partial y}(\rho v) + \frac{\partial}{\partial z}(\rho w) = 0 \tag{1}$$

$$\frac{\partial}{\partial z}\left(\eta \frac{\partial u}{\partial z}\right) - \frac{\partial p}{\partial x} = 0 \tag{2}$$

$$\frac{\partial}{\partial z}\left(\eta \frac{\partial v}{\partial z}\right) - \frac{\partial p}{\partial y} = 0 \tag{3}$$

where x and y denote the planar coordinates and z the gap-wise coordinate, while (u, v, w) are the velocity components in the (x, y, z) directions with t the time and p the pressure. $\rho(T, p)$ is the density and $\eta(\dot{\gamma}, T, p)$ the shear viscosity, where $\dot{\gamma}$ is the effective shear rate.

For the temperature field, phase change was assumed to occur at the crystalline temperature for semi-crystalline polymers and at the glass

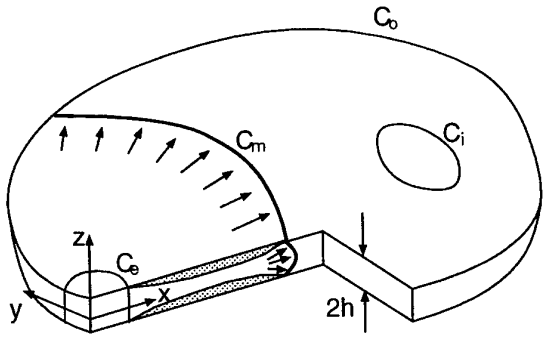

Fig. 1. Schematic diagram of material flow in the die cavity.

transition temperature for amorphous polymers, with both temperatures being dependent on pressure. So there is a definite boundary between solid and liquid, at which the latent heat is dissipated. Following this assumption, and neglecting thermal diffusion along the plane direction by comparing the order of magnitudes, the energy equation for each phase, liquid and solid, can be, respectively, expressed by

$$\rho C_{pl}\left(\frac{\partial T}{\partial t}+u\frac{\partial T}{\partial x}+v\frac{\partial T}{\partial y}\right)=k_l\frac{\partial^2 T}{\partial z^2}+\eta\dot{\gamma}^2 \quad (4)$$

$$\rho C_{ps}\frac{\partial T}{\partial t}=k_s\frac{\partial^2 T}{\partial z^2} \quad (5)$$

where T is the temperature, C_p the specific heat and k the thermal conductivity of the material, with subscripts l and s denoting the liquid and solid phase, respectively.

In addition the following interfacial energy balance equation should be applied at the liquid–solid boundary

$$\left[k_s\frac{\partial T_s}{\partial z}-k_l\frac{\partial T_l}{\partial z}\right]_{z=\delta}=\rho_s L\frac{\partial \delta}{\partial t} \quad (6)$$

where δ is the distance of the solid–liquid boundary from the center of the thickness and L is the latent heat of the material.

In the gap-wise direction, the flow was assumed to be symmetric at $z=0$ and non-slip conditions were applied at the wall, i.e. at $z=\pm h$. With these considerations, integrating eqns (2) and (3) in the z direction yields

$$\frac{\partial u}{\partial z}=-\frac{\Lambda_x z}{\eta},\quad \frac{\partial v}{\partial z}=-\frac{\Lambda_y z}{\eta} \quad (7)$$

where

$$\Lambda_x\equiv-\frac{\partial p}{\partial x},\ \Lambda_y\equiv-\frac{\partial p}{\partial y}$$

From this equation, the effective shear rate can be written as

$$\dot{\gamma}=\sqrt{\left(\frac{\partial u}{\partial z}\right)^2+\left(\frac{\partial v}{\partial z}\right)^2}=\frac{\Lambda z}{\eta} \quad (8)$$

where

$$\Lambda\equiv\sqrt{\Lambda_x^2+\Lambda_y^2}$$

Integrating eqn (7) in the z direction yields

$$u=\Lambda_x\phi,\ v=\Lambda_y\phi \quad (9)$$

where

$$\phi\equiv\int_z^h\frac{\tilde{z}}{\eta}\,d\tilde{z}$$

Then, the mass flow rate per unit length in the x and y directions can be obtained by integrating eqn (9) as follows

$$\dot{m}_x=2\int_0^h\rho u\,dz=2\tilde{S}\Lambda_x$$

$$\dot{m}_y=2\int_0^h\rho v\,dz=2\tilde{S}\Lambda_y \quad (10)$$

where

$$\tilde{S}\equiv\int_0^h\rho\phi\,dz$$

For boundary conditions of flow field in the plane direction (refer to Fig. 1), pressure was set to zero (atmospheric pressure) at the melt front (C_m) and the impermeability condition was imposed at locations where the polymer made contact with the wall surfaces or inserts ($C_o \cup C_i$). In addition, at the inlet, the constant mass flow rate condition was applied during the filling stage and the constant pressure condition during the post-filling stage, with the holding pressure being set in the injection-molding machine or measured pressure values at the inlet being used as the constant pressure condition. For the temperature field, as thermal diffusion along the plane direction was neglected in the present investigation, the temperatures needed to be specified only at the inlet and at the melt front. At the inlet the temperature was uniformly set to that of the barrel of the machine and at the melt front to that of the upstream core region to mimic the complex fountain flow effect.

To effectively describe the shear thinning effect, a Cross-type model was employed as follows [11]

$$\eta(\dot{\gamma}, T, p) = \frac{\eta_0(T, p)}{1+\left\{\frac{\eta_0(T, p)\dot{\gamma}}{\tau^*}\right\}^{1-n}} \tag{11}$$

Here, n is the power-law index, τ^* the stress level of the asymptotic transition region between the power-law and Newtonian fluids, and $\eta_0(T, p)$ the zero shear rate viscosity.

In representing η_0, the simplest form is the Arrhenius type [11] of temperature and pressure dependences such as

$$\eta_0(T, p) = B \exp\left(\frac{T_b}{T}\right) \exp(\beta p) \tag{12}$$

Another form for large temperature regions is the WLF (Williams, Landel and Ferry) functional form [11] such as

$$\eta_0(T, p) = D_1 \exp\left\{-\frac{A_1[T-T^*(p)]}{\tilde{A}_2+D_3 p+[T-T^*(p)]}\right\} \tag{13}$$

where $T^*(p) = D_2+D_3 p$.

Thus, for describing $\eta(\dot{\gamma}, T, p)$ eqns (11) and (12) yield a five-constants (n, τ^*, B, T_b, β) model, with eqns (11) and (13) being a seven-constants (n, τ^*, D_1, D_2, D_3, A_1, $\tilde{A}_2$) model. These two models were used in the current investigation and the values used in the numerical simulations are presented in Table 1.

Table 1. Viscosity model constants for PP

		Profax 6323	BJ 500
Seven-constants model	n	0.3135	—
	τ^* (Pa)	1.10×10^4	—
	D_1 (Pa·s)	1.96×10^{14}	—
	D_2 (°C)	−10.0	—
	D_3 (°C/Pa)	1.3×10^{-7}	—
	A_1	30.9	—
	$\tilde{A}_2$ (°C)	51.6	—
Five-constants model	n	—	0.204
	τ^* (Pa)	—	3.07×10^4
	B (Pa·s)	—	0.144
	T_b (K)	—	4830.0
	β (Pa^{-1})	—	4.39×10^{-9}

To describe the variable density, the Tait state equation [5] was used as follows

$$v(T, p) \equiv \frac{1}{\rho} = v_0(T)\left[1-C\ln\left(1+\frac{p}{B(T)}\right)\right] \tag{14}$$

where $C = 0.0894$. To accurately model density in both the liquid and the solid regions, $v_0(T)$ and $B(T)$ were represented by

$$v_0(T) = \begin{cases} b_{1,l}+b_{2,l}(T-b_5) \text{ if } T > T_t \\ b_{1,s}+b_{2,s}(T-b_5) \text{ if } T \le T_t \end{cases}$$

$$B(T) = \begin{cases} b_{3,l}\exp\{-b_{4,l}(T-b_5)\} \text{ if } T > T_t \\ b_{3,s}\exp\{-b_{4,s}(T-b_5)\} \text{ if } T \le T_t \end{cases}$$

$$T_t(p) = b_5+b_6 p$$

where T_t is the glass transition temperature for amorphous polymers or the melting temperature for semi-crystalline polymers. The 10 material constants ($b_{1,l}$–$b_{4,l}$, $b_{1,s}$–$b_{4,s}$, b_5, b_6) used in this investigation are shown in Table 2.

NUMERICAL

As the numerical approach to solve the GHS flow coupled with temperature is available elsewhere [11–13], the highlight of the present development will be described in the following.

Applying a finite-element formulation to the continuity equation, with mass flow rate as an integral form as in eqn (10), a pressure formulation can be obtained for each type of element. In order to satisfy the mass flow rate condition the iteration is, in general, required with this approach to adjust the pressure fields after the

Table 2. Specfic-volume model constants for PP

	Profax 6323	BJ500
$b_{1,l}$ (m^3/kg)	1.246×10^{-3}	1.319×10^{-3}
$b_{2,l}$ (m^3/kg·°C)	9.03×10^{-7}	1.156×10^{-6}
$b_{3,l}$ (Pa)	9.28×10^7	6.62×10^7
$b_{4,l}$ ($°C^{-1}$)	4.07×10^{-3}	3.76×10^{-3}
$b_{1,s}$ (m^3/kg)	1.16×10^{-3}	1.23×10^{-3}
$b_{2,s}$ (m^3/kg·°C)	3.57×10^{-7}	7.64×10^{-7}
$b_{3,s}$ (Pa)	2.05×10^8	9.73×10^7
$b_{4,s}$ ($°C^{-1}$)	2.49×10^{-3}	2.46×10^{-3}
b_5 (°C)	123.0	118.0
b_6 (°C/Pa)	2.25×10^{-7}	2.25×10^{-7}

solution is obtained under constant pressure conditions as explained in detail later.

To resolve this problem, the control volume (CV) technique will be used in the present investigation. It enables us to combine various types of elements such as triangular, cylindrical and strip elements, as introduced in Fig. 2, to effectively describe the complex mold shapes including runners. According to this approach, the pressure field will be determined from mass conservation applied to each CV constructed around each node. CV at each node was defined by summing the surrounding sub-volumes (SV) connecting the centroid of each element and the centers of the sides in each element, as shown in Fig. 3.

If node N is the $i(l)$th internal node of element l, which surrounds node N, mass conservation in CV(N) of node N can be written as

$$0=\left[\frac{\partial m_{CV}}{\partial t}+\int_{\partial CV}(\rho u_k)n_k\,dA\right]_N$$

$$=\sum_l\left(\frac{\partial}{\partial t}m_i^{(l)}+\dot{m}_i^{(l)}\right)-\dot{m}_N^{ext} \qquad (15)$$

where the index notation is used for the velocity (u_k) and normal vector (n_k) with duplicate index k implying summation. In addition, $m_i^{(l)}$ is the mass of SV(N, l) of the element l included in CV(N), $\dot{m}_i^{(l)}$ is the mass flow rate from SV(N, l) into element l, and $\dot{m}_N^{ext}$ is the mass flow rate into CV(N) from outside the calculation domain.

The value of $\dot{m}_N^{ext}$ is zero if node N is neither on the inlet nor on the melt front, the specified mass flow rate if node N is on the inlet, and undetermined if node N is on the melt front. Thus, the impermeability condition, where the melt is in contact with the inserts or the wall surface, and the constant mass flow rate condition at the inlet can be explicitly satisfied regardless of the type of element employed.

In most filling studies reported so far, a constant pressure condition was imposed at the inlet for each pressure iteration. To extract appropriate pressure boundary conditions from the given mass flow rate, additional iteration was indispensably required in which, as shown schematically in Fig. 4, the total mass flux along the melt front was calculated using the initial pressure condition, then compared to the given mass flow rate to adequately adjust the pressure condition. Such numerical iterations continued until the given mass flow rate was approximately satisfied. Furthermore, as the total mass flux along the melt front and the given mass flow rate are not exactly equal, as shown below, realistic injection-molding conditions cannot be satisfied by this kind of numerical iteration

$$\dot{m}_e=\frac{\partial m}{\partial t}+[\text{mass flux}] \qquad (16)$$

Here, m denotes the filled mass at time t and $\dot{m}_e$ the given mass flow rate condition.

As each element currently employed is linear, $\tilde{S}$ in eqn (10) is constant in the element, resulting in a constant mass flow rate per unit length. To calculate $\dot{m}_i^{(l)}$, the density can be integrated in SV(N, l), with assumed values for the pressure at node i, and the temperature at the

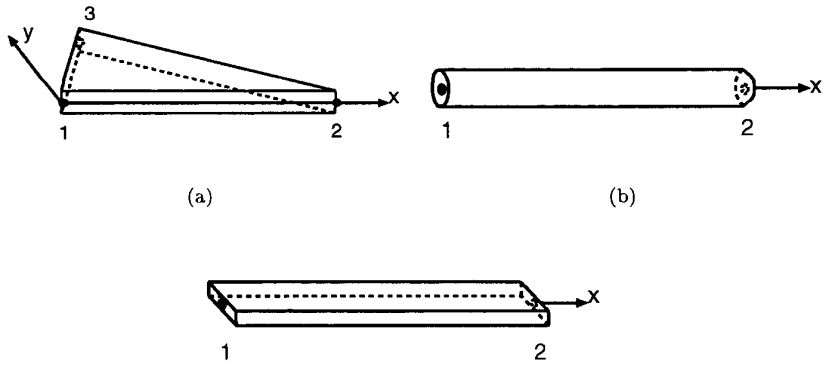

Fig. 2. Schematic diagram of linear (a) triangular, (b) cylindrical and (c) rectangular strip elements used in the simulations.

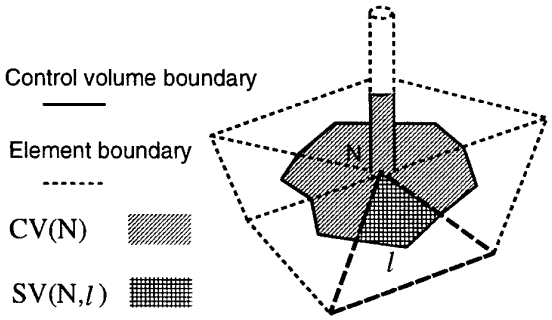

Fig. 3. Schematic diagram of the control volume used in the simulations.

centroid. The time derivative of density can be divided into the pressure derivative and the temperature derivative to ensure stability. Thus, discretizing eqn (15) yields a final equation of the following form [14]

$$\sum_{l}\sum_{k}\left(M_{ik}^{(l)}\frac{\partial p_k^{(l)}}{\partial t}+K_{ik}^{(l)}p_k^{(l)}\right)=\dot{m}_N^{\text{ext}}+\sum_{l}f_i^{(l)} \tag{17}$$

where i is defined as before in eqn (15) and k represents the free index of the internal nodal number.

In solving eqn (17), only the pressure condition at the melt front needs to be applied as impermeability and the mass flow rate conditions have already been satisfied. The time derivative was approximated using a backward difference scheme. Owing to non-linearity, successive under relaxation was adopted to solve the discretized finite-element equation.

The temperature field in the half thickness of the liquid phase (δ) was calculated at the center of each element where the velocity and viscous heating was accurately accounted. Nodal temperatures were obtained by averaging the elemental values of the surrounding elements by their sub-volumes and employing the upwind scheme to ensure numerical stability. Both the liquid and solid portions were divided into the same number of finite-difference grids in the thickness direction to solve the energy equation, taking into consideration the release of latent heat (see eqns (4–6)). The time derivative and conduction term were approximated using a backward difference scheme as in the following equation. The finite-difference equation for the ith layer in element l at time j can be obtained as follows

$$\beta T_{\mathrm{l,\,i-1,\,j+1}}-(1+2\beta)\mathrm{T}_{\mathrm{l,\,i,\,j+1}}+\beta\mathrm{T}_{\mathrm{l,\,i+1,\,j+1}} = -T_{l,\,i,\,j}+\Delta t_j\,\mathrm{CON}_{l,\,i,\,j}-\alpha\,\mathrm{VIS}_{l,\,i,\,j} \tag{18}$$

where

$$\alpha=\frac{\Delta t_j}{\rho C_{\mathrm{p}}},\quad \beta=k\frac{\Delta t_j}{\rho C_{\mathrm{p}}\Delta z^2}$$

The convection (CON) and the viscous heating (VIS) terms in the above equation were calculated from the previous temperature field and were set to zero in the solid phase.

The energy balance equation at the phase interface between solid and liquid, eqn (6), was also approximated as follows

$$k_{\mathrm{s}}\frac{T_{l,\,nl+1,\,j+1}-T_{\mathrm{m}}}{\Delta z_{\mathrm{s}}}-k_{\mathrm{l}}\frac{T_{\mathrm{m}}-T_{l,\,nl-1,\,j+1}}{\Delta z_{\mathrm{l}}} = \rho_{\mathrm{s}}L\frac{\delta_{l,\,j+1}-\delta_{l,\,j}}{\Delta t_j} \tag{19}$$

where Δz_{s} and Δz_{l} are the magnitudes of the finite-difference grid of the solid and liquid phases, respectively, and T_{m} is the melting temperature with nl indicating the location of the solid–liquid boundary.

As eqns (18) and (19) cannot start from a zero solid fraction, an analytical solution of the Stefan problem for a simplified case was used to provide the initial values.

The time increment in the filling stage was automatically determined by adopting a flow analysis network (FAN) combined with the control volume method, as described by Wang *et al.* [2]. In this approach, f is defined as the filled fraction and all nodes are classified as follows

$$\begin{cases}\text{filled node} & \text{if } f=1\\ \text{front node} & \text{if } 0<f<1\\ \text{unfilled node} & \text{if } f=0\end{cases} \tag{20}$$

Of the front nodes, the first to be filled was found from the calculated velocity fields. The

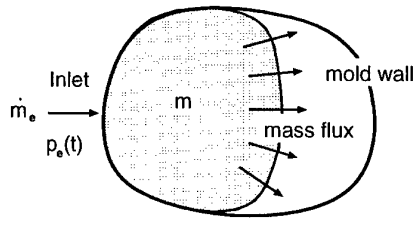

Fig. 4. Schematic diagram of the mass flow rate and mass flux.

time needed to fill this node was chosen as the next time increment.

At each time step, the temperature field was first calculated and then the pressure field was determined. The incremental time step was selected to be small enough so that iterations to couple the temperature and pressure fields were unnecessary.

EXPERIMENTAL

A Jaco III-H-3 injection-molding machine, which has a 46 ton clamping force, 101 cm^3 injection volume and 140 MPa maximum injection pressure was used for the experiments. To measure the cavity pressure a Kistler quartz pressure transducer type 6157BA was used. The mold wall temperature was measured using a J-type thermocouple. The signal from the pressure transducer was amplified by a Kistler charge amplifier type 5039A and stored in a PC.

The designed mold set (mold A) consists of four cavities and circular runners of 3 mm radius, as shown in Fig. 5. The material (PP; BJ500) used in this experiment and the raw material data were supplied by Samsung Chemicals Co. To extract appropriate constants for the material data, as summarized in Tables 1 and 2, the least-squares method combined with the steepest gradient method was employed. For thermophysical values of the material those of Profax 6323, as given in Table 3, were used in simulations because of the lack of data. The barrel temperature was set at 180°C, with the mold wall temperature measured as 40°C. Filling time set in the machine was 1.5 s, which was required for filling the whole mold including the

Table 3. Thermal properties of PP (Profax 6323)

C_{pl} (J/kg·K)	2.7×10^3
C_{ps} (J/kg·K)	2.0×10^3
k_l (W/m·°C)	0.175
k_s (W/m·°C)	0.22
L (J/kg)	2.34×10^5

sprue, runners and cavities. As the sprue was not considered in the analysis, the appropriate volumetric flow rate of 7.4×10^{-6} m^3/s was estimated from the sudden increases in measured values of P_1.

Two additional mold sets were adopted from Chiang *et al.* [6] for the purpose of verification studies. One (mold B) is for verification of the filling stage and the other (mold C) for a verification study of post-filling. Simulation results obtained from the currently developed program are compared with the experimental observations and simulation results available from Chiang *et al.* [6].

The mold schematic B is shown in Fig. 6. This mold consists of two cavities of the same shape, three rectangular gates, trapezoidal runners and a sprue. The runner system was designed to be unbalanced so that packing-type flow occurred in the upper cavity after it was filled. The trapezoidal runner was approximated by the equivalent cylindrical element, with the appropriate hydraulic radius as given in Chiang *et al.* [6]. The material properties of PP (polypropylene; Profax 6323/Himont) are summarized in Tables 1 and 2 based on the seven-constants viscosity model and the Tait state equation, the thermal constants are given in Table 3. For process variables, the temperatures of the barrel and the mold wall were set at 200 and 30°C, respectively, with a volumetric flow rate of 1.07×10^{-5} m^3/s. In order to satisfy

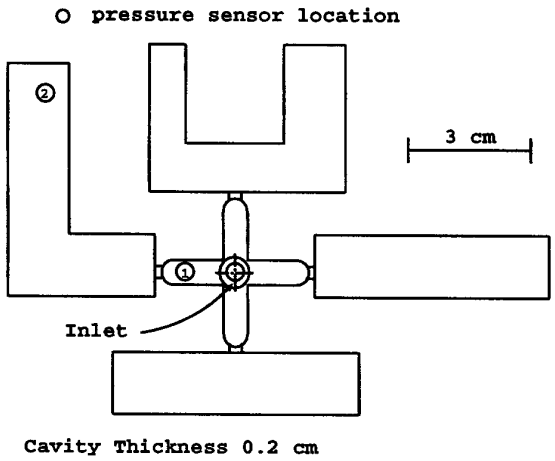

Fig. 5. Schematic diagram of mold A.

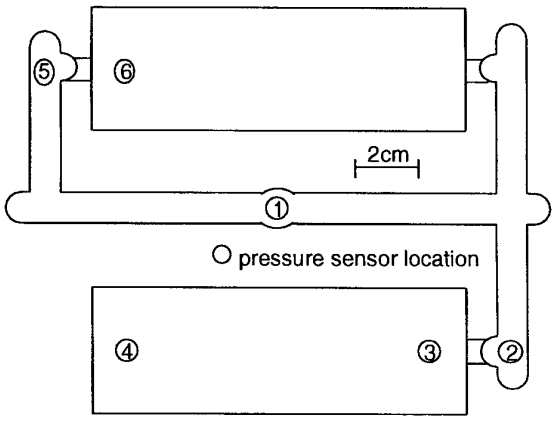

Fig. 6. Schematic diagram of mold B.

the given prescribed constant volumetric flow rate at the inlet in experiments, the constant mass flow rate was determined by multiplying the density of the material to the prescribed volumetric flow rate and applying it to the numerical simulations. A post-filling study was made for mold set C, as shown in Fig. 7. This mold consists of a rectangular cavity with a uniform thickness and a thick rectangular reservoir. This reservoir made the flow flat in the cavity. So the cavity was approximated in simulations using 24 identical rectangular strip elements. The material and process conditions used were the same as those in the previous calculations except that the mold wall temperature was set at 32°C. In the post-filling stage P_1 was used for the constant pressure condition at the inlet. For this material, the non-flow temperature was assumed to be 103°C, which was about 20°C less than the transition temperature.

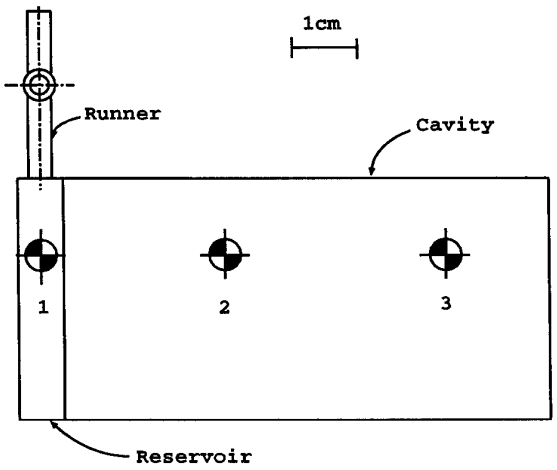

Fig. 7. Schematic diagram of mold C.

This was taken into consideration in simulations by replacing the viscosity value with infinity for temperatures below this non-flow temperature.

RESULT AND DISCUSSION

Figure 8 shows the calculated melt front advancement obtained for mold set A. The cavities were predicted to be filled in the order: lower, upper, right and left cavities. Pressure traces during the filling stage are shown in Fig. 9. For convenience, the time when P_1 begins to increase was set to zero in Fig. 9. Experimental and simulation results are seen to be very similar. But the locations of sudden increases are not accurately predicted according to Fig. 9. From the fact that this location coincides with the instant when the melt touches the cavity boundary, it can be construed that the rate of filling in each cavity was not predicted well. This might be due to the air ventilation condition in each cavity and the viscoelasticity of the polymer melt which was not considered in this analysis.

The comparison of pressures between prediction and measurement at the post-filling stage is made in Fig. 10 for a holding time of 6 s. In simulations, the pressure value at the inlet was chosen to be the measured values of P_1 based on the assumption that the pressure difference along the runner was not very noticeable in the post-filling stage, which is demonstrated in Fig. 10. For P_2, the pressure variations are similar, but the magnitudes differ by about 20%. This might be due to inaccurate thermal properties used in the present calculations.

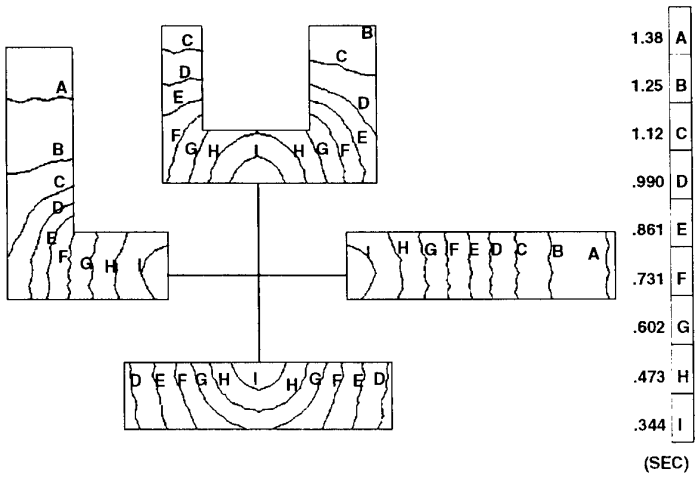

Fig. 8. Predicted melt front advancement for mold A.

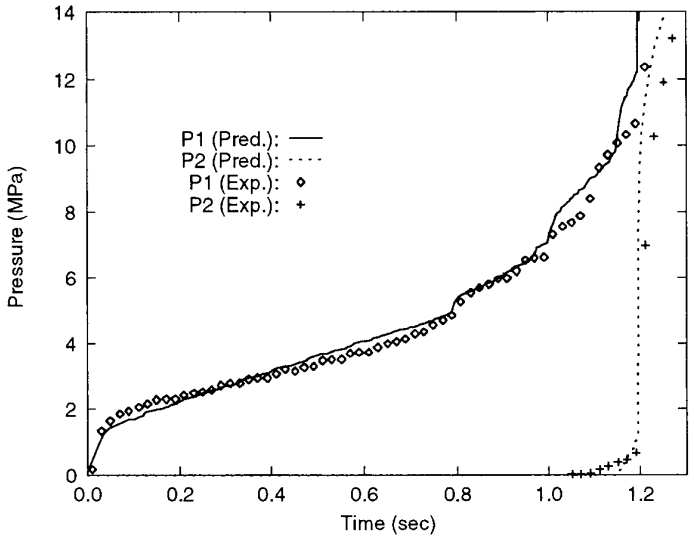

Fig. 9. Comparison of predicted and measured pressures in the filling stage for mold A.

For mold B, the simulation result of the melt front advancement is shown in Fig. 11. The melt entered the upper-left gate first and then the other gates after about 0.2 s. At 3.5 s the upper cavity is filled and packing-type flow occurs.

To study the effect of compressibility and phase change on filling, simulation results of the pressure difference between measuring locations at #1 and #5 ($\Delta P_{15} = P_1 - P_5$) are compared to the experimental results obtained from the same source [6] in Fig. 12. After the melt approaches the upper-right gate, ΔP_{15} decreases until the melt runs through all the gates. When the upper cavity is filled, ΔP_{15} decreases rapidly. Compared with the case where compressibility and phase change were not considered, the pressure difference becomes smoother when compressibility is considered and becomes higher if phase change is considered. However, the effect of phase change was not as large as that of compressibility.

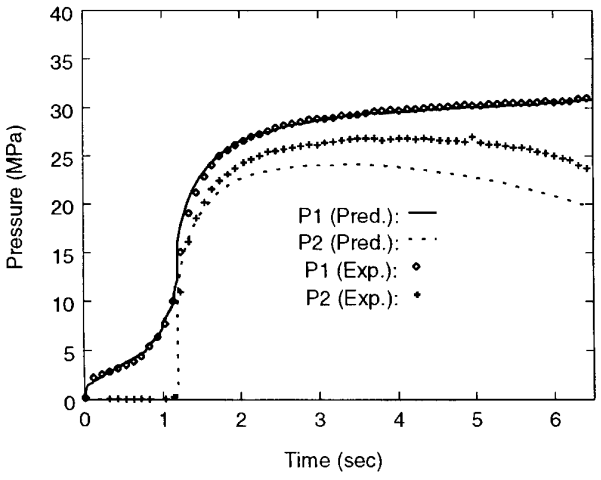

Fig. 10. Comparison of predicted and measured pressures in the filling and post-filling stages for mold A.

Simulation results of pressure distributions at various locations are compared with the available data from Chiang *et al.* [6] in Fig. 13(a) and (b). Figure 13(a) shows that the numerically calculated result is slightly higher than the one from Chiang *et al.* [6], and the trend of variation is closer to that of the experimental results. Comparing the level of reduction at 2.0 and 3.5 s shows that the current result is steeper. This is because of the constant mass flow rate boundary condition which was strictly applied in the present investigation, as previously mentioned. The pressure difference across the gate (ΔP_{23}) in Fig. 13(b) is still lower than for experimental results. This is probably due to juncture loss which was not considered in the governing equation.

For mold C, comparisons between the current simulations and numerical results obtained from Chiang *et al.* [6] are shown in Fig. 14(a) and (b), respectively, for the verification of the post-filling study.

In Fig. 14(a), the experimental results show that high pressure was maintained for about 10 s, and then the pressure decreased. This phenomenon was well predicted by the current simulation. Calculations also showed that the pressure decrease at 10 s was due to the whole solidification of one element, which was physically reasonable. After 12 s the pressure was not predicted well, but this was possibly due to the

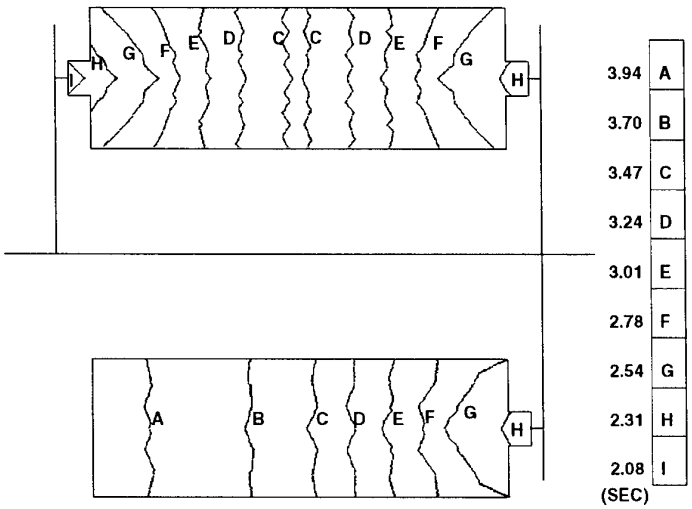

Fig. 11. Predicted melt front advancement for mold B.

lack of accuracy in the modeled thermal constants used in simulations.

In Fig. 14(b), trends in the pressure distributions were the same as in the reference data of Chiang *et al.* [6]. In addition, the unnecessary dip at around 6 s in the numerical prediction in Chiang *et al.* [6] does not occur in the current simulation. From these studies it was found that the currently developed program generated reasonable data for different cases.

CONCLUSIONS

For unified simulations of filling and post-filling processes in injection molding, a finite-element–finite-difference program was developed considering phase changes and compressibility effects of the material. Flow analysis network together with the control volume method enabled simulations to be available for complex mold cavities using various types of elements simultaneously. The constant mass flow rate condition could be applied explicitly at the inlet, resulting in a reduction of the calculation time. Simulations were performed for three different molds. For the filling analysis, the inclusion of the phase-change effect did not seem to produce any noticeable differences, while the consideration of compressibility led to more accurate results. For the post-filling stage, more accurate results were obtained by considering

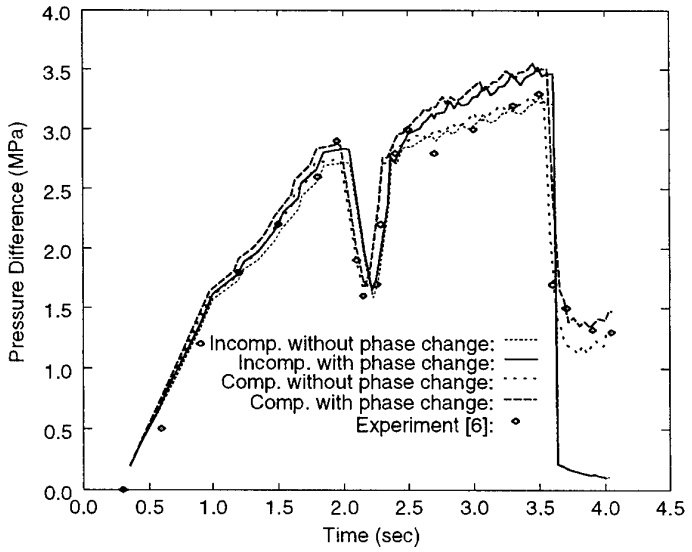

Fig. 12. Comparison of ΔP_{15} under various conditions for mold B.

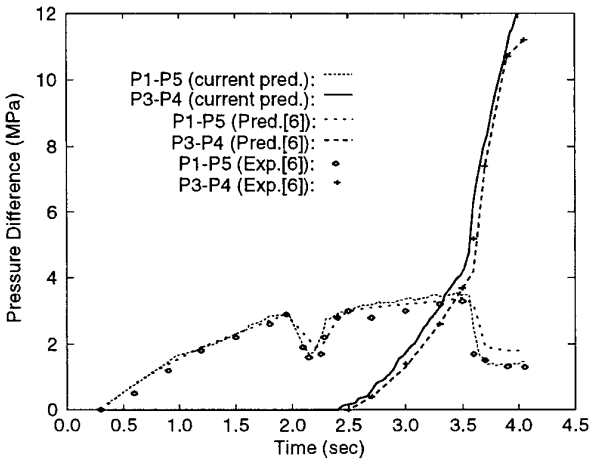

(a)

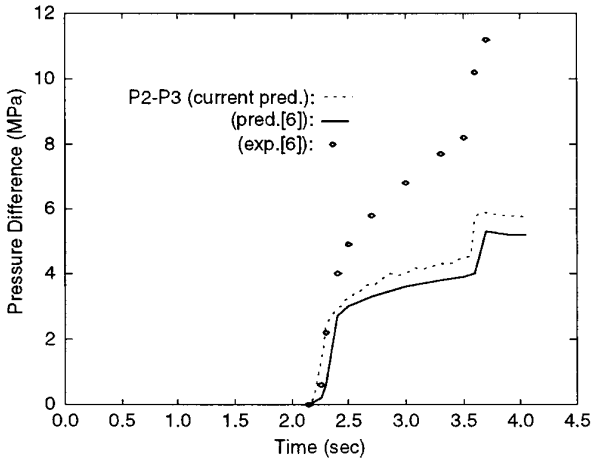

(b)

Fig. 13. Comparison of the simulation and the data available in Chiang *et al.* [6] for (a) ΔP_{15} and ΔP_{34} and (b) ΔP_{23} for mold B.

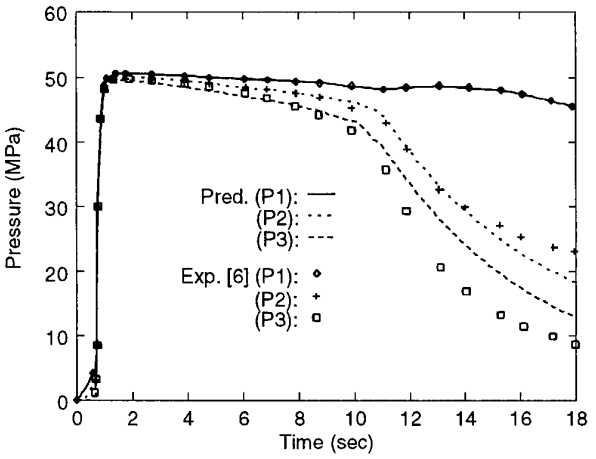

(a)

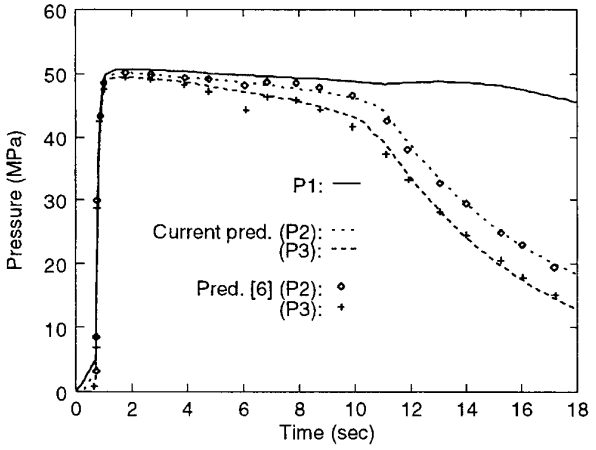

(b)

Fig. 14. Comparisons of pressure values obtained from the developed program with (a) measured values and (b) with simulation values from Chiang *et al.* [6] for mold C.

the phase-change effect during simulations. To further improve the reliability of the developed program, consideration of juncture loss and effects of air ventilation will be beneficial.

ACKNOWLEDGEMENTS

The authors are grateful for the grant from Korea Science and Engineering Foundation (KOSEF) through the Engineering Research Center for Net Shape and Die Manufacturing at Pusan National University under which this work was possible, and Samsung Chemicals Co. for providing PP materials.

REFERENCES

1. Hieber, C.A. and Shen, S.F., A finite-element/finite-difference simulation of the injection-molding filling process. *J. Non-Newt. Fluid Mech.*, 1980, **7**, 1–32.
2. Wang, K. K., Shen, S. F., Cohen, C., Hieber, C. A., Kwon, T. H. & Ricketson, R. C., Computer-aided design and fabrication of molds and computer control of injection molding. Progress Report No. 11, Cornell University, Ithaca, New York, 1985.
3. Wang, K. K., Shen, S. F., Cohen, C., Hieber, C. A. & Himasekhar, K., Integration of CAD/CAM for injection-molded plastic parts. Progress Report No. 14, Cornell University, Ithaca, New York, 1988.
4. Chen, B.S. and Liu, W.H., Numerical simulation and experimental investigation of injection mold filling with melt solidification. *Polym. Engng Sci.*, 1989, **29**, 1039–1050.
5. Chiang, H.H., Hieber, C.A. and Wang, K.K., A unified simulation of the filling and postfilling stages in

injection molding. Part I: Formulation. *Polym. Engng Sci.*, 1991, **31**, 116–124.
6. Chiang, H.H., Hieber, C.A. and Wang, K.K., A unified simulation of the filling and postfilling stages in injection molding. Part II: Experimental verification. *Polym. Engng Sci.*, 1991, **31**, 125–139.
7. Chen, B.S. and Liu, W.H., Numerical simulation of the post-filling stage in injection molding with a two-phase model. *Polym. Engng Sci.*, 1994, **34**, 835–846.
8. Najmi, L.A. and Lee, D.Y., Modeling of mold filling process for powder injection molding. *Polym. Engng Sci.*, 1991, **31**, 1137–1148.
9. Chen, Y.H., Im, Y.T. and Yoo, J.S., Finite element analysis of solidification of aluminum with natural convection. *J. Mater. Process. Tech.*, 1995, **52**, 592–609.
10. Yoo, J.S. and Rubinsky, B., A finite element method for the study of solidification processes in the presence of natural convection. *Int. J. Numer. Meth. Engng*, 1986, **23**, 1785–1805.
11. Isayev, A. I., *Injection and Compression Molding Fundamentals*. Marcel Dekker, New York, 1987.
12. Zienkiewicz, O. C., *The Finite Element Method*, 3rd edn. McGraw-Hill, New York, 1977.
13. Byon, S. K., Numerical simulation of filling stage during injection molding. Ph.D. thesis, KAIST, Taejon, Korea, 1994.
14. Han, K. H., Coupled analysis of compressible filling and post-filling process of injection molding with phase change. M.S. thesis, KAIST, Taejon, Korea, 1996.

ELSEVIER

Composite Structures Vol. 38, No. 1–4, pp. 191–201, 1997
© 1997 Elsevier Science Ltd. All rights reserved
Printed in Great Britain
0263-8223/97/$17.00 + 0.00

PII:S0263-8223(97)00055-X

Local buckling loads of sandwich panels made with laminated faces

M. A. Aiello & L. Ombres

Department of Materials Science, University of Lecce, Via per Monteroni, Lecce, Italy

The paper is devoted to assessing the optimal arrangements of hybrid laminated faces of sandwich panels in order to maximize local buckling loads corresponding to the wrinkling of compressed faces. The analysis is carried out by modelling compressed faces as thin unsymmetric laminates resting on elastic two-parameter foundations. The First-order Shear Deformation Theory, in conjunction with the Rayleigh–Ritz method, has been used to evaluate buckling loads of simply supported flat laminates subjected to in-plane biaxial compression and shear forces. A numerical investigation is intended to support evidence for the influence of laminate parameters (fibre orientation, geometrical dimensions) and foundation parameters (modulus of subgrade reaction and shear modulus); obtained results are reported and discussed in the paper. © 1997 Elsevier Science Ltd.

NOTATION

a, b, h	Laminate length, width and thickness, respectively
A_{ij}, B_{ij}, D_{ij}	Extensional, coupling and bending laminate stiffnesses
E_{11}, E_{22}	Young's moduli along the fibre direction and normal to the fibres, respectively
G_{12}, G_{13}, G_{23}	In-plane shear moduli
ν_{12}	Poisson's ratio
u, v, w	Displacements in the x, y and z directions, respectively
u_0, v_0, w_0	In-plane displacements of the middle plane of the laminate
$\varepsilon_{x0}, \varepsilon_{y0}, \varepsilon_{xy0}, \varepsilon_{xz}, \varepsilon_{yz}$	Laminate normal strains
ψ_x, ψ_y	Shear rotations
N_x, N_y, N_{xy}	In-plane applied loads
k_x, k_y, k_{xy}	Laminate curvatures
W, U	Elastic strain energy
L_2^*	Work of internal stresses
L_2	Work of external stresses
E	Total potential energy
λ	Load multiplier
ρ_i	Density of materials
k	Modulus of subgrade reaction
G_b	Shear modulus of the subgrade
n	$N_x b^2/E_{22}h^3$
ξ	N_y/N_x
ζ	N_{yx}/N_x
δ_k	$kb^4/E_{22}h^3$
δ_g	$G_b b^2/E_{22}h^3$

INTRODUCTION

Sandwich structural elements made with laminated faces are very widespread in the industrial fields of engineering as well as the mechanical, naval and aeronautical fields; however, they can also be useful in the field of civil engineering, particularly in lightweight constructions such as roof coverings [1].

Indeed, from a static point of view, the possibility of taking advantage of the anisotropy that

is a typical property of plastic composites materials makes the use of sandwich structures with laminated faces, in place of steel faces, a viable solution.

Sandwich panels consist of two thin outer sheets (faces), flat or profiled, generally made of a high strength material and a thick lightweight layer (core) of a low strength material which improves the bending stiffness of the panels.

At present, technological solutions commonly used in constructions consist of sandwich panels with metallic (steel or aluminium) or laminated faces and a core made of a metallic honeycomb, which is vertically stiff and very flexible with a negligible longitudinal rigidity, or, alternatively, a core made up of plastic foam or a non-metallic honeycomb which, generally, has a very low rigidity [2].

An analysis of the mechanical behaviour of sandwich panels must also take into account the instability phenomena caused by the high degree of slenderness of the panels and the very small thickness of the faces.

Instability phenomena may concern the whole panel but, often, take place in a localized zone of the panel affecting separate elements.

A typical local instability phenomenon is the wrinkling of the compressed faces of sandwich panels [3]. This wrinkling characterizes the local instability of sandwich panels where the core is made of a low density material. In this case, in the presence of flexural actions, the core may be insufficient to stabilize the panel; as a consequence, the faces become independent of each other and the compressed face can buckle locally because of its small thickness.

For this reason, analysis of the wrinkling type of local instability is carried out with reference to a single face of the panel connected to the core; this hypothesis is generally correct because the thickness of the core allows the interaction between opposite faces to be neglected.

Theoretical models used for the analysis of this wrinkling phenomenon are dependent on the type of core material and on its deformability; in fact, generally, the core is considered as an elastic medium supporting the outer face of the sandwich panel. The most correct theoretical model refers to a laminated plate supported by an elastic space; however, in order to reduce analytical difficulties, approximate models are currently used.

These models very useful from an engineering point of view as they consider the stabilizing action of the core proportional to the out-of-plane face displacement (Winkler model) also taking into account the shear deformability of the core (Pasternak model) [4].

The use of laminated faces allows the structural response of sandwich panels to be optimized on the basis of the state of stresses produced from external forces. It is possible, in fact, to design an optimal configuration of the laminate varying both in the fibre orientation in each layer and the geometrical dimensions of the laminate.

A very good performance is obtained by hybridization of the laminate, that is by the use of layers of different mechanical characteristics along the thickness of the laminate.

The influence of hybridization on the buckling load values of flat laminates subjected to in-plane axial and shear forces has recently been analysed from the literature [5]. Results obtained relating to hybrid symmetric and unsymmetric laminates, made with inner layers of a low-stiffness fibre-composite material and outer layers of a high-stiffness fibre-composite material, support the theory that advantages of hybridization increase when the anisotropy of outer layers is very high and that buckling loads of hybrid laminates are higher than those corresponding to homogeneous laminates of equal mass.

In this paper, on the basis of previous considerations, buckling load values corresponding to the wrinkling of sandwich panels with laminated faces are analysed in order to evaluate:

- the influence of the strong anisotropy that characterizes the structural system, in particular hybrid laminated faces;
- the better arrangement of laminated faces with varying fibre orientation and geometrical dimensions in order to maximize local buckling loads;
- the influence of characteristic properties of the core material.

The analysis is carried out by modelling the compressed face of a sandwich panel as a laminate resting on a two-parameter foundation; these parameters, modulus of the subgrade reaction and shear modulus, are defined on the basis of the geometrical dimensions and mechanical properties of the core.

Using the First-order Shear Deformation Theory, in conjunction with the Rayleigh–Ritz method, buckling loads of laminates, generally unsymmetric, are obtained by an energetic algorithm as a solution of a standard eigenvalue problem.

By numerical investigation, supposing the absence of delaminations, the best arrangement of laminates corresponding to maximum buckling loads, in the presence of in-plane biaxial compression and shear forces, is defined by varying parameters of both the laminates (geometrical dimensions, slenderness, mechanical properties of layers, etc.) and the subgrade (modulus of subgrade reaction, shear modulus). A comparison between obtained results and those corresponding to sandwich panels made with laminated homogeneous faces supports the theoretical advantage that the use of hybrid laminates can guarantee to increase local buckling loads of sandwich panels.

PROBLEM FORMULATION

Laminate modelling

The analysis was carried out assuming that global buckling of sandwich panels and local buckling of compressed faces are uncoupled. This hypothesis will not be completely correct if the core material is compressible in the vertical direction; in these cases, in fact, an interaction between the two faces of the sandwich panel exists [6–9].

Models that consider the coupling between global and local buckling are founded on a high-order theory and are defined by complex analytical procedures, often very onerous from a computational point of view.

For this reason the use of models that suppose the uncoupling of the two instabilities is very large, allowing very good provision for the real behaviour of structures with little computational effort.

In this paper the compressed faces of sandwich panels are modelled as flat plates resting on a two-parameter elastic foundation (Fig. 1).

These parameters take into account both the compressibility of the core by the modulus of the subgrade reaction k, and the shearing interaction between the loaded face and the core by the shear modulus G_b. In particular, the k value is determined by modelling the core material as

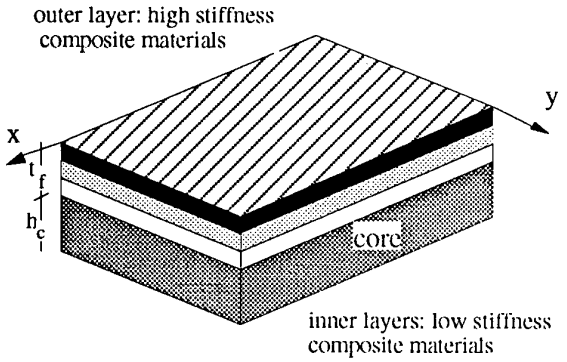

Fig. 1. Laminated faces of a sandwich plate resting on an elastic support.

a continuosly distributed linear tension–compression spring (Winkler model).

Values of k and G_b depend on the mechanical and geometrical properties of the core material, that is type and thickness; they have to be defined for each technological adopted solution. For cases analysed in the paper, the core material is assumed to be isotropic, homogeneous and linear-elastic.

Constitutive law of laminates

The constitutive law of a laminate made with orthotropic layers taking into consideration shear deformation is given by following relations:

$$\{N\} = [A]\{\varepsilon\} + [B]\{\kappa\}$$

$$\{M\} = [B]\{\varepsilon\} + [D]\{\kappa\}$$

$$\{Q\} = [F]\{v\}$$

where

$$\{N\} = \{N_x, N_y, N_{xy}\}$$

$$\{M\} = \{M_x, M_y, M_{xy}\}$$

$$\{Q\} = \{Q_x, Q_y\}$$

$$(A_{ij}, B_{ij}, D_{ij}) = \int_{-h/2}^{h/2[\min]} \bar{Q}_{ij}(1, z, z^2)\, \mathrm{d}z \quad (i, j = 1, 2, 6)$$

$$F_{ij} = \int_{-h/2}^{h/2} k^*_{ij} \bar{Q}_{ij}\, \mathrm{d}z \quad (i, j = 4, 5)$$

where k^*_{ij} are shear correction factors, Q_{ij} are functions of elastic constants and the ply angle, θ, differs from a layer to another, while

$$\{\varepsilon\} = \{\varepsilon_{x0}, \varepsilon_{y0}, \varepsilon_{xy0}\}$$

$$\{\kappa\} = \{\kappa_x, \kappa_y, \kappa_{xy}\}$$

$$\{v\} = \{\varepsilon_{yz}, \varepsilon_{xz}\}$$

with

$$\varepsilon_{x0} = u_{0,x};\ \varepsilon_{y0} = u_{0,y};\ \varepsilon_{xy0} = u_{0,y} + v_{0,x}$$

$$\kappa_x = -\psi_{x,x};\ \kappa_y = -\psi_{y,y};\ \kappa_{xy} = -(\psi_{x,y} + \psi_{y,x})$$

$$\varepsilon_{xz} = w_{,x} - \psi_x;\ \varepsilon_{yz} = w_{,y} - \psi_y$$

where u_0, v_0, ε_{x0}, ε_{y0} and ε_{xy0} are the displacements and strains at the middle plane of the laminate.

Energy expressions

The total strain energy of a laminate resting on an elastic foundation is expressed as

$$\Pi = W + U$$

where W is the strain energy of the laminate and U is the strain energy due to the foundation.

Considering a flat rectangular laminate of dimensions a and b along the x- and y-axis, respectively, the strain energy W is expressed as

$$W = \frac{1}{2}\int_S [\{\varepsilon\}^T[A]\{\varepsilon\} + \{\varepsilon\}^T[B]\{\kappa\} + \{\kappa\}^T[B]\{\varepsilon\} + \{\kappa\}^T[D]\{\kappa\} + \{v\}^T[F]\{v\}]\,dx\,dy$$

while the strain energy due to the two-parameter foundation is given by

$$U = \frac{1}{2}\int_0^a \int_0^b [kw_0^2 + G_b(w_{0,x}^2 + w_{0,y}^2)]\,dx\,dy$$

Buckling load analysis

The buckling load of a flat laminate is determined by an energetic approach founded on Dirichlet's principle, expressed as follows [5]

$$\delta_2 E = \Pi + \lambda(L_2^* - L_2) \qquad (1)$$

where $\Pi = W + U$ is the strain energy of the laminate, L_2^* is the work of internal stresses in the initial configuration for the second-order strain components, L_2 the work corresponding to the external loads for the second-order displacement components, $\delta_2 E$ is the second variation of the total potential energy and λ is the load multiplier.

For a flat rectangular laminate, the work L_2^* is expressed as

$$L_2^* = \frac{1}{2}\int_S [N_x(u_{0,x}^2 + v_{0,x}^2 + w_{,x}^2) + N_y(u_{0,y}^2 + v_{0,y}^2 + w_{,y}^2) + 2N_{xy}(u_{0,x}u_{0,y} + v_{0,x}v_{0,y} + w_{,x}w_{,y})]\,dx\,dy$$

The work L_2 is zero when external loads are constant or independent of u, v and w displacements.

For unsymmetric laminates in which the geometric middle plane is different to the neutral plane, the buckling load can be determined as a bifurcation load only if added conditions, that guarantee the flatness of the laminates, are imposed.

This problem has been investigated by Leissa [10,11] who defines the conditions under which unsymmetric laminates remain flat during the prebuckling stage when subjected to in-plane loads. Leissa separates the prebuckling response equations from the buckling equations and works out the conditions for the curvatures to vanish during the prebuckling stage (flatness conditions): if these conditions are satisfied, the bifurcation phenomenon will occur [11].

For a simply supported laminate subjected to in-plane loading, the flatness conditions involve the introduction of bending moments, M_x^0 and M_y^0, acting along the edges of the laminates in the initial configuration.

The values of M_x^0 and M_y^0 are determined using constitutive laws for the laminate with first-order components of displacement and shear rotations. Bending moments M_x^0 and M_y^0 furnish a value of L_2 that must be considered for the evaluation of $\delta_2 E$.

Substituting Π, L_2^* and L_2 expressions in eqn (1), the condition $\delta_2 E = 0$ gives the relations that allow the buckling loads of laminates to be determined.

The solution of the problem is obtained by the Rayleigh–Ritz method assuming linear variation of in-plane displacements u and v and constant transverse deflection w over the panel thickness

$$u(x, y, z) = u_0(x, y) + z\psi_x(x, y)$$

$$v(x, y, z) = v_0(x, y) + z\psi_y(x, y)$$

$$w(x, y, z) = w(x, y)$$

For a simply supported flat laminate the displacements that satisfy the geometric boundary conditions

$$v = w = \psi_y = 0 \quad \text{at } x = 0, a$$

$$u = w = \psi_x = 0 \quad \text{at } y = 0, b$$

are chosen in the form of following trigonometric series

$$u_0(x, y) = \sum_m \sum_n U_{mn} \cos(m\pi x/a) \sin(n\pi y/b)$$

$$v_0(x, y) = \sum_m \sum_n V_{mn} \sin(m\pi x/a) \cos(n\pi y/b)$$

$$\psi_x(x, y) = \sum_m \sum_n X_{mn} \cos(m\pi x/a) \sin(n\pi y/b) \quad (2)$$

$$\psi_y(x, y) = \sum_m \sum_n Y_{mn} \sin(m\pi x/a) \cos(n\pi y/b)$$

$$w(x, y) = \sum_m \sum_n W_{mn} \sin(m\pi x/a) \sin(n\pi y/b)$$

Substituting eqn (2) into the expressions of W and L_2, eqn (1) becomes

$$\{[L]^{-1}[K] + \lambda[I]\}\{q\} = 0 \quad (3)$$

that represents a system of linear equations of $5mn \times 5mn$ order. The solution to eqn (3) is obtained as solution of a standard eigenvalue problem that can be solved by available standard procedures. $[L]$ and $[K]$ are matrices of $5mn \times 5mn$ order that contain terms relative to strain energy and external work; the vector $\{q\}$ contains the series of coefficients U_{mn}, V_{mn}, W_{mn}, X_{mn} and Y_{mn} .

The buckling load coincides with the smallest eigenvalue of eqn (3). In the presence of biaxial compression and shear the solution is obtained considering the ratios

$$\xi = \frac{N_y}{N_x}; \zeta = \frac{N_{xy}}{N_x}$$

and evaluating the critical value of N_x.

NUMERICAL INVESTIGATIONS

Numerical analyses, founded on analytical relationships and procedures previously described, are carried out taking into consideration hybrid laminates resting on a two-parameter foundation. Hybrid configurations of laminates refer to compressed faces of sandwich panels; they are obtained considering laminated faces made with outers layers of a high-stiffness fibre-composite material and inner layers of a low-stiffness fibre-composite material.

Such configurations guarantee the best arrangement for obtaining maximum values for buckling loads [5]. The whole sandwich structure is considered symmetric while faces are unsymmetric; local buckling loads are then evaluated for unsymmetric flat hybrid laminates resting on elastic foundations.

Numerical results are carried out considering laminated faces made with one outer layer of a high-stiffness composite material and the inner layers of a low-stiffness composite material.

The material properties of the layers used in the numerical analysis are as follows.

Outer layer

Material M_{RI}: $E_{11} = 128$ GPa;
$E_{22} = 11$ GPa;
$G_{12} = 4.48$ GPa;
$G_{13} = 4.48$ GPa;
$G_{23} = 1.53$ GPa;
$\nu_{12} = 0.25$.

Material M_{RII}: $E_{11}/E_{22} = 40$;
$G_{12} = G_{13} = 0.6E_{22}$;
$G_{23} = 0.5E_{22}$;
$\nu_{12} = 0.25$.

Inner layers

Material M_I: $E_{11} = 38.6$ GPa;
$E_{22} = 8.27$ GPa;
$G_{12} = G_{13} = G_{23} = 4.14$ GPa;
$\nu_{12} = 0.26$.

Material M_{II}: $E_{11}/E_{22} = 10$;
$G_{12} = G_{13} = 0.5E_{22}$;
$G_{23} = 0.5E_{22}$;
$\nu_{12} = 0.28$.

The shear correction factor is assumed to be $k^* = 5/6$ for all calculations.

First, the analysis refers to laminates with constant thickness for which the optimal lamination angle values of the outer layer are defined by varying both the foundation parameters and the load combinations.

In Fig. 2 curves n–θ (where $n = Nb^2/E_{22}t_f^3$) for a foundationless laminate with a 90°/0°/90°/θ lay-up subjected to uniaxial compression are drawn by varying the amount of high-stiffness composite material ($\alpha = t_r/t_f$, where t_r is the thickness of the outer layer of the laminate).

For this configuration the optimal solution corresponds to $\theta = 42°$, confirming results of previous work [5].

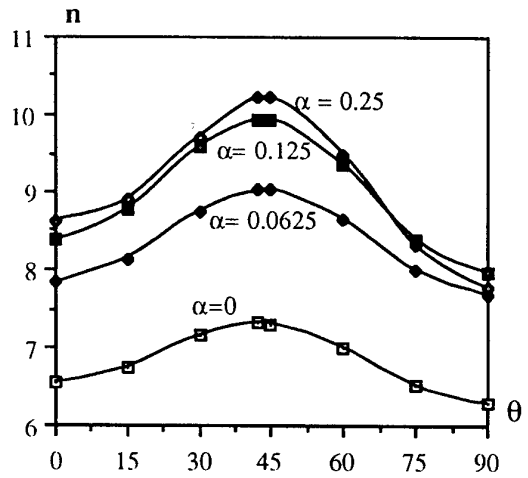

Fig. 2. Non-dimensional uniaxial buckling load vs lamination angle. Lay-up: 0°/90°/0°/θ. a/b = 1; b/t_f = 20. Outer layer: M_{RI}; inner layers: M_I.

For the same laminate configuration, curves n–θ are shown in Figs 3–5 for varying foundation parameters.

In particular Fig. 3 shows curves obtained by neglecting the shearing interaction; this situation corresponds to a Winkler model of foundations. Obtained results are very different to those illustrated in Fig. 2; in this case, in fact, the maximum buckling load is obtained for $\theta = 0°$ for all considered hybrid configurations.

Also, for $\theta > 45°$, by increasing the α value one obtains a drastic reduction in the buckling loads.

In Fig. 4, curves obtained by neglecting the subgrade reaction, k, are shown; results are

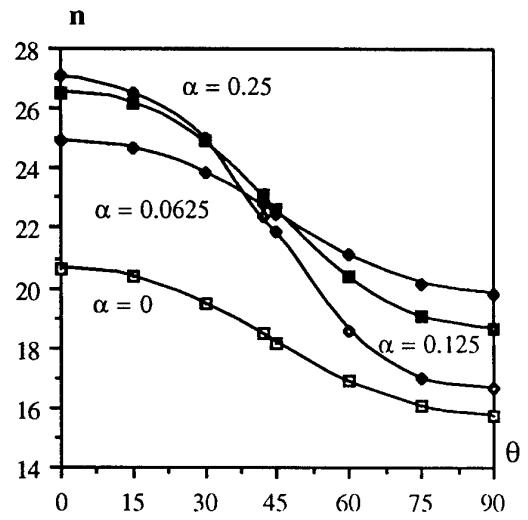

Fig. 3. Non-dimensional uniaxial buckling load vs lamination angle. Lay-up: 0°/90°/0°/θ. a/b = 1; b/t_f = 20. Foundation parameters: δ_k = 200; δ_g = 0. Outer layer: M_{RI}; inner layers: M_I.

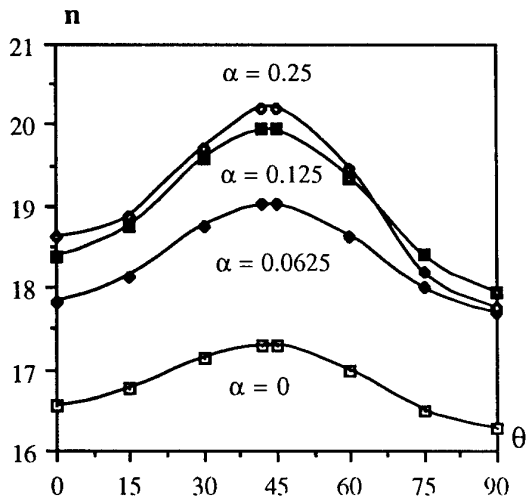

Fig. 4. Non-dimensional uniaxial buckling load vs lamination angle. Lay-up: 0°/90°/0°/θ. a/b = 1; b/t_f = 20. Foundation parameters: δ_k = 0; δ_g = 5. Outer layer: M_{RI}; inner layers: M_I.

similar to those corresponding to foundationless laminates, as illustrated in Fig. 2.

The maximum buckling load corresponds to $\theta = 42°$, and by increasing α values an improvement in the response of laminates can be noted.

Results obtained for hybrid laminates resting on a two-parameter foundation, as in the Pasternak type [4], are shown in Fig. 5.

It is possible to observe that the response of laminates is very similar to that corresponding to a Winkler foundation, as shown in Fig. 3.

The maximum buckling load corresponds to $\theta = 0°$; also, for hybrid configurations and $\theta > 45°$, by increasing the amount of high-stiff-

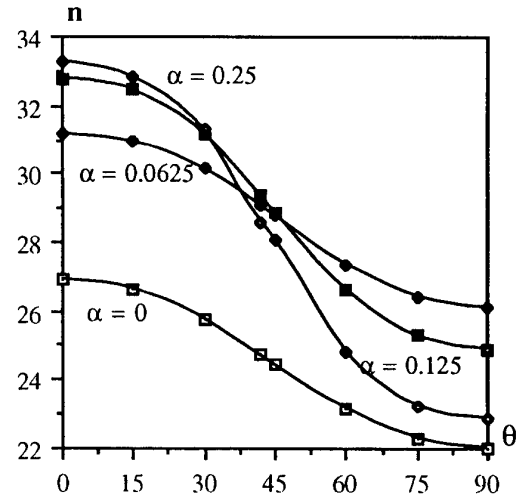

Fig. 5. Non-dimensional uniaxial buckling load vs lamination angle. Lay-up: 0°/90°/0°/θ. a/b = 1; b/t_f = 20. Foundation parameters: δ_k = 200; δ_g = 5. Outer layer: M_{RI}; inner layers: M_I.

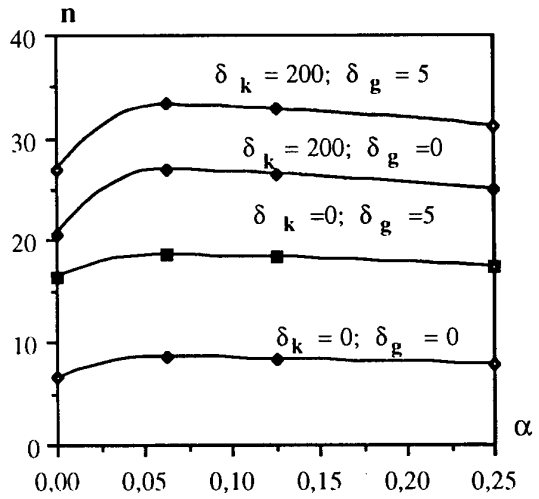

Fig. 6. Non-dimensional uniaxial buckling load vs $\alpha = t_r/t_f$. Lay-up: 0°/90°/0°/0°. $a/b = 1$; $b/t_f = 20$. Outer layer: M_{RI}; inner layers: M_I.

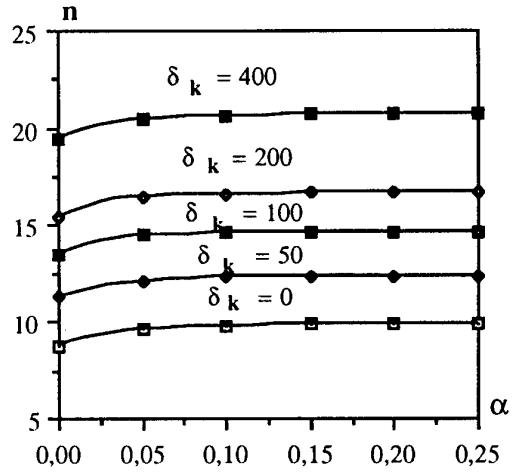

Fig. 8. Curves $n-\alpha$ for laminated faces resting on a two-parameter foundation (where $n = Nb^2/E_{22}h^3$). $a/b = 1$; $b/h = 20$; $\zeta = 0$; $\xi = 1$; $\delta_g = 5$. Lay-up: $(0°/30°/-30°/30°/\text{core})_s$. Outer layer: M_{RI}; inner layers: M_I.

ness composite material one can see a reduction in the buckling load values. In all situations, however, hybridization of laminates produces an increase in the buckling loads. In Fig. 6, $n-\alpha$ curves for varying foundation parameters and for a lamination angle of the outer layer equal to $0°$ are shown. For the cases examined it is possible to show that the best response of laminates is obtained for a small amount of outer layer reinforcing material.

The same considerations are taken into account when analysing the curves drawn in Figs 7 and 8; they represent the variation in buckling loads against foundation parameters for laminates under biaxial compression and uniaxial compression combined with shear.

The percentage variation in local buckling loads of hybrid laminated faces with respect to values corresponding to homogeneous laminated faces ($\alpha = 0$ for each examined situation) is reported in Tables 1 and 2.

When analysing the results it is evident that the hybridization of laminated faces increases

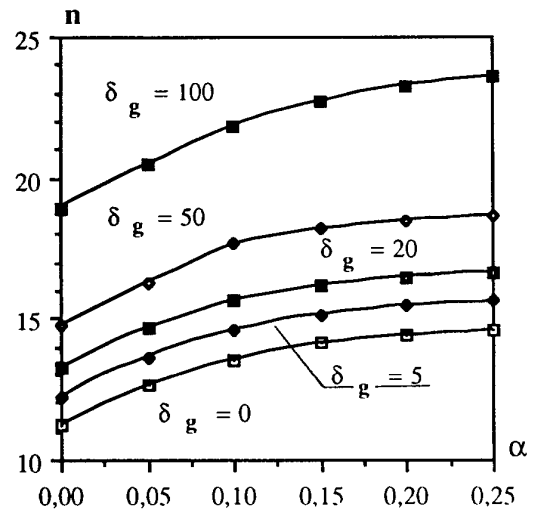

Fig. 7. Curves $n-\alpha$ for square laminated faces resting on a two-parameter foundation (where $n = Nb^2/E_{22}h^3$). $b/h = 20$; $\zeta = 0.5$; $\xi = 0$; $\delta_k = 400$. Lay-up: $(-30°/0°/90°/45°/\text{core})_s$. Outer layer: M_{RI}; inner layers: M_I.

Table 1. Percentage variation of local buckling loads. Square sandwich panels with hybrid laminated faces. Lay-up: $(0°/30°/-30°/30°/\text{core})_s$; $b/h = 20$; $\zeta = 0.5$; $\xi = 0$; $\delta_g = 5$

$\alpha\backslash\delta_k$	0	50	100	200	400
0.00	0.00	0.00	0.00	0.00	0.00
0.05	9.37	7.14	7.81	6.67	5.04
0.10	11.62	8.97	8.64	7.46	5.81
0.15	12.45	9.66	8.95	7.75	6.12
0.20	12.55	9.76	9.01	7.83	6.25
0.25	12.36	9.63	9.01	7.85	6.28

Table 2. Percentage variation of local buckling loads. Square sandwich panels with hybrid laminated faces. Lay-up: $(0°/30°/-30°/30°/\text{core})_s$; $b/h = 20$; $\zeta = 0.5$; $\xi = 0$; $\delta_k = 400$

$\alpha\backslash\delta_g$	0	5	10	20	50	100
0.00	0.00	0.00	0.00	0.00	0.00	0.00
0.05	12.31	11.58	10.98	10.03	8.04	6.24
0.10	20.81	19.29	18.04	19.30	15.28	11.40
0.15	25.74	23.80	22.19	22.99	19.86	14.71
0.20	28.44	26.29	24.51	25.09	22.80	16.85
0.25	29.78	27.55	25.70	26.19	24.65	18.20

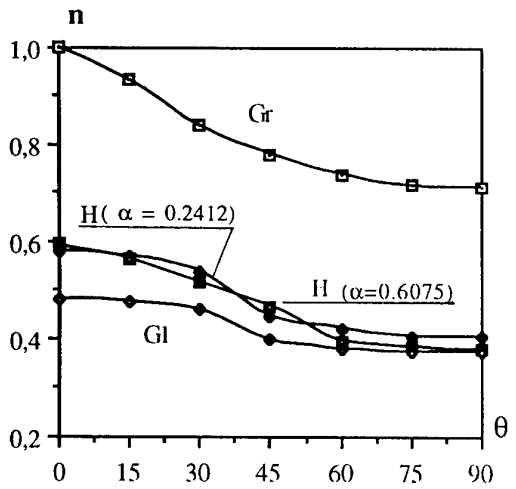

Fig. 9. Sandwich panels with equal mass: $n-\theta$ curves for laminated faces resting on a one-parameter foundation. $\delta_g = 0$; $a/b = 1$; $b/h = 20$. Lay-up: $(\theta/0°/90°/0°/\text{core})_s$.

the buckling loads; also, a small amount of reinforcing outer layer is sufficient in order to obtain a good response. In fact, by increasing α values for all assigned foundation parameters one obtains small increases in the buckling loads.

In Figs 9–11 results corresponding to laminates with equal mass are shown; in particular if h is the thickness of a hybrid laminate made using layers with ρ_i and ρ_j material density, using the condition $M_{hyb} = M_{hom}$, one obtains $h = h_i/[\mu+(1-\mu)\rho_i/\rho_j]$ where M_{hyb} and M_{hom} are the mass of the hybrid and homogeneous laminate, respectively, while μ is the ratio between the thickness of the material of density ρ_i and the total thickness of the hybrid laminate.

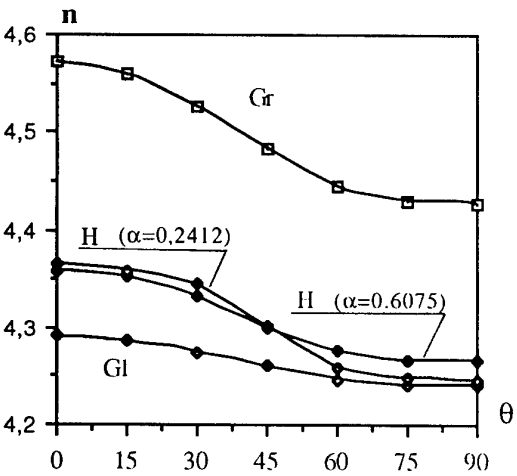

Fig. 10. Sandwich panels with equal mass: $n-\theta$ curves for laminated faces resting on a one-parameter foundation. $\delta_k = 0$; $a/b = 1$; $b/h = 20$. Lay-up: $(\theta/0°/90°/0°/\text{core})_s$.

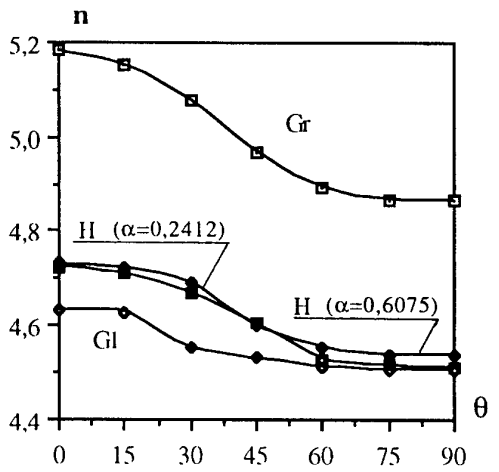

Fig. 11. Sandwich panels with equal mass: $n-\theta$ curves for laminated faces resting on a two-parameter foundation. $a/b = 1$; $b/h = 20$. Lay-up: $(\theta/0°/90°/0°/\text{core})_s$.

Results are shown as $n-\theta$ curves for uniaxial compression, where n is the ratio between buckling load values and those corresponding to the homogeneous laminate made up of four layers of graphite–epoxy composite material (M_{RI} material). The analysis is carried out for the following configurations:

Gr: M_{RI}–M_{RI}–M_{RI}–M_{RI};
H: M_I–M_I–M_I–M_{RI};
Gl: M_I–M_I–M_I–M_I.

Maximum buckling loads correspond to $\theta = 0°$ for all assumed configurations. The hybridization of laminated faces of sandwich panels furnishes an improvement of the local buckling response for $\theta < 45°$; also, an increase in the α value produces a small variation in the buckling load.

In order to evaluate the influence of load combinations on the buckling loads of laminated faces, curves $n-\theta$ for hybrid laminates with a constant thickness resting on a two-parameter foundation are shown in Fig. 12.

Results are obtained for the core material with the following mechanical parameters: $E_c = 3.86$ GPa, $G_c = 1.4846$ GPa, $\nu_c = 0.30$. The foundation parameters δ_k and δ_g are evaluated using the relationships of the Vlasov foundation model [12,13].

By varying the load combinations, maximum buckling loads are always attained for $\theta = 90°$; however, values corresponding to $\theta = 90°$ are very close to those ones corresponding to $\theta = 0°$.

In Fig. 13 local buckling interaction curves $n^*-\xi-\zeta$ for a $-45°/30°/0°/45°$ laminate resting

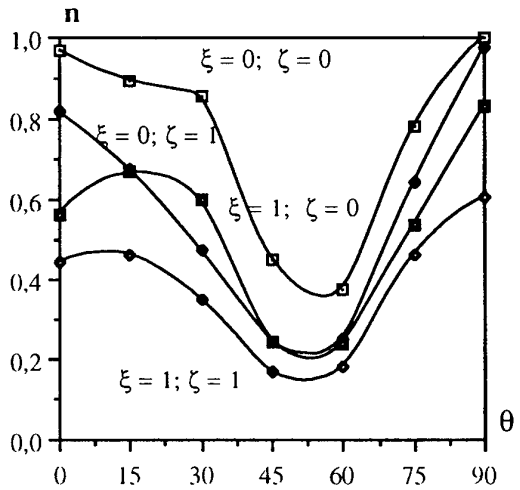

Fig. 12. Curves of $n-\theta$ for varying load combinations for square hybrid sandwich panels. $b/h = 20$; $b/t_f = 200$. Lay-up: $(\theta/30°/-30°/30°/\text{core})_s$. Outer layer: M_{RI}; inner layers: M_I.

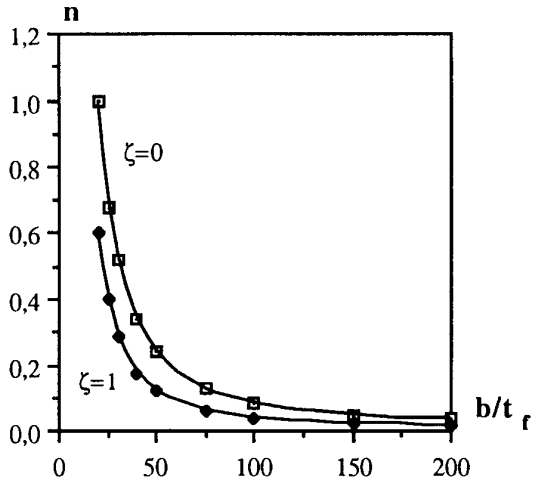

Fig. 14. Local buckling of square sandwich panels: curves $n-b/t_f$ for varying ζ. Lay-up: $(0°/30°/-30°/\text{core})_s$. Outer layer: M_{RII}; inner layers: M_{II}.

on a two-parameter foundation are shown. The non-dimensional value n^* is the ratio of the value of the buckling load to the value corresponding to the uniaxial compression load. The curves in Fig. 13 demonstrate the large reduction in buckling load values with increasing shear forces.

The influence of shear forces on the local buckling of sandwich panels can be observed with the analysing curves $n-b/t_f$ shown in Fig. 14; they are obtained for a three-layer laminate with a $0°/30°/-30°$ lay-up; non-dimensional values of buckling load are obtained as the ratio of buckling load to maximum uniaxial compression load. Results obtained confirm a very large decrease in the buckling load in the presence of shear forces for thick laminated faces; conversely, for thin laminated faces ($b/t_f > 100$), the presence of shear forces is not influential.

The influence of mechanical properties of the core material is evaluated using the ratio $\gamma = E_c/E_{11i}$ between the elastic modulus of the core, E_c, and of the inner layers, E_{11i}. Values of γ usually vary between 0.001 and 0.01 [7].

Curves $n-\bar{\gamma}$ (where $n = Nb^2/E_{22}h^3$ and $\bar{\gamma} = \gamma \times 10^3$), for varying b/h ratios (where h is the total thickness of the sandwich panels), are drawn in Fig. 15 for hybrid four-layer laminates with a $0°/-90°/45°/90°$ lay-up and $h_c/h = 0.8$ (where h_c is the core thickness).

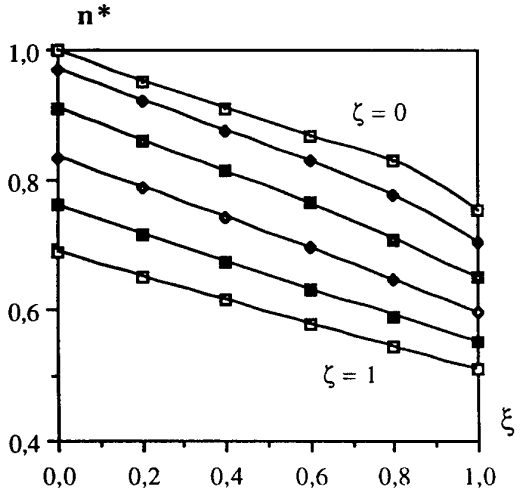

Fig. 13. Local buckling interaction curves $n^*-\zeta-\xi$ for square sandwich panels. $b/h = 10$; $b/t_f = 100$. Lay-up: $(-45°/30°/0°/45°/\text{core})_s$. Outer layer: M_{RI}; inner layers: M_I.

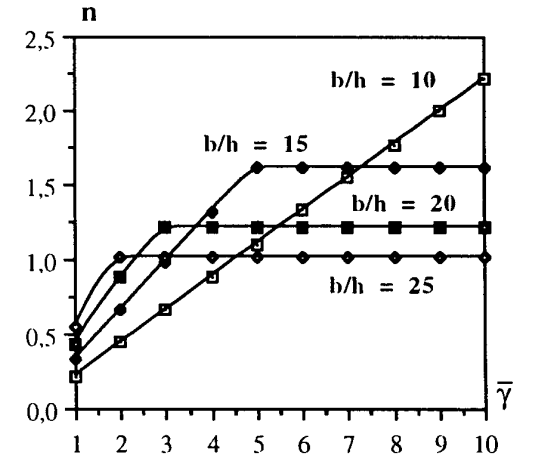

Fig. 15. Curves of $n-\bar{\gamma}$ for varying b/h ratios for square laminated faces of hybrid sandwich panels. Lay-up: $0°/-90°/45°/90°/\text{core}/\ 90°/45°/-90°/0°$. Outer layer: M_{RII}; inner layers: M_{II}.

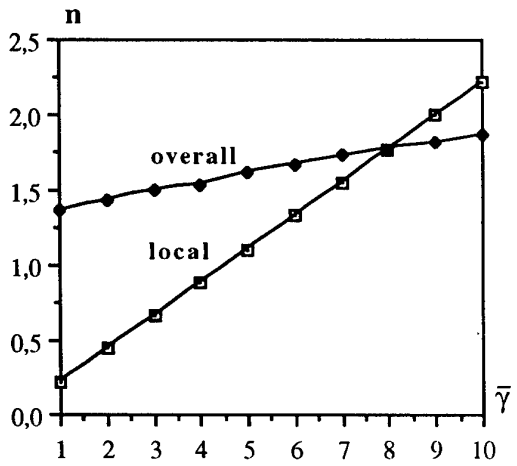

Fig. 16. Comparison between overall and local buckling loads of sandwich panels with varying γ values. Lay-up: 0°/−90°/45°/90°/core/90°/45°/−90°/0°. b/h = 10; a/b = 1. Outer layer: M_{RII}; inner layers: M_{II}.

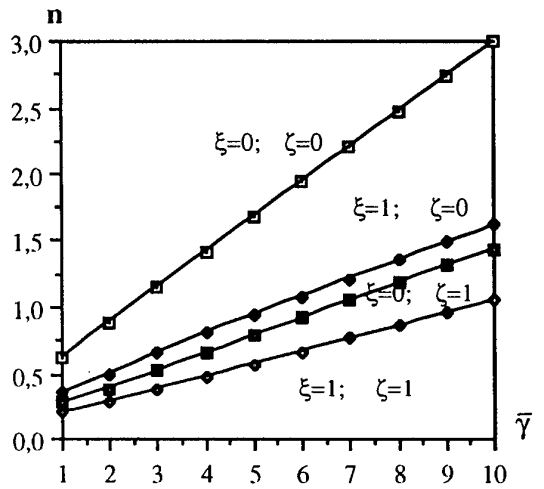

Fig. 18. Curves of $n-\bar{\gamma}$ for varying load combinations for square hybrid sandwich panels. b/h = 10; b/t_f = 100. Lay-up: $(30°/-30°/30°/0°/\text{core})_s$. Outer layer: M_{RII}; inner layers: M_{II}.

Analysis of the diagrams shows that local buckling of sandwich panels becomes nearly constant with increasing γ; in particular this situation is obtained for high values of γ for thick laminates ($b/h < 15$) and for low values of γ for moderately thick laminates. For sandwich panels with thin faces, local buckling is independent of the core material properties.

In Figs 16 and 17, curves $n-\bar{\gamma}$, relative to the overall buckling of the sandwich panels and the local buckling of compressed faces, are compared.

Overall buckling loads are evaluated considering the core as a layer of the whole sandwich panel in which the distribution of displacements are considered linear along the thickness: this hypothesis is correct because of the low value of the face thickness.

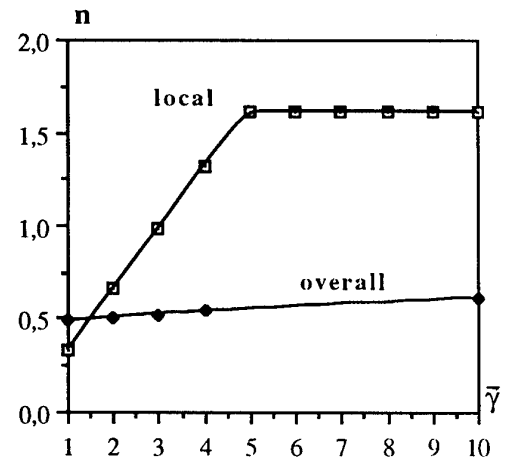

Fig. 17. Comparison between overall and local buckling loads of sandwich panels with varying γ values. Lay-up: 0°/−90°/45°/90°/core/90°/45°/−90°/0°. b/h = 15; a/b = 1. Outer layer: M_{RII}; inner layers: M_{II}.

Analysing results, it is evident that a coupling exists between the local and overall instability of the sandwich panels. Coupled instability is attained for γ values for different b/h ratios of the sandwich panels.

In Fig. 18, $n-\bar{\gamma}$ curves for a compressed face with a 30°/−30°/30°/0° lay-up are shown for varying load combinations. In the presence of biaxial compression and shear load, the buckling load of the faces is sensibly reduced.

In Fig. 19, for sandwich panels with a $(0°/90°/90°/0°/\text{core})_s$ lay-up, a comparison between local buckling corresponding to hybrid and homogeneous configurations of compressed faces is shown.

Curves are drawn by varying the ratio between the core thickness and the total thickness of the sandwich panel, h_c/h.

By analysing the curves it is possible to demonstrate that the advantages of hybridization are more evident for low values of the ratio h_c/h that correspond, for an assigned b/h value, to high value of the slenderness of the compressed faces (b/t_f).

CONCLUDING REMARKS

The local buckling of sandwich panels made up of hybrid laminated faces and a flexible core has been investigated in this paper. Local buckling

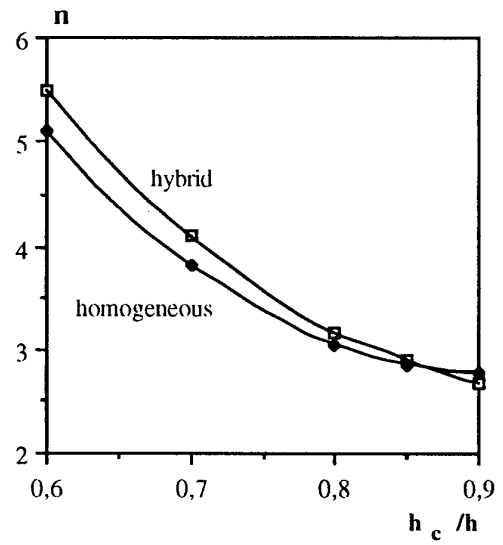

Fig. 19. Comparison between local buckling for sandwich panels with hybrid and homogeneous faces: curves of n vs h_c/h. $a/b = 1$; $b/h = 10$; $\gamma = 0.05$. Outer layer: M_{RII}; inner layers: M_{II}.

has been evaluated considering compressed faces as unsymmetric laminates resting on elastic foundations for which characteristic parameters have been determined on the basis of the mechanical properties and geometrical dimensions of the core.

The analysis has been carried out considering hybrid configurations of faces made with one outer layer of a high-stiffness composite material and inner layers of low-stiffness composite material.

The results of numerical investigations allow the following conclusions to be drawn.

The optimal configuration of the reinforcing outer layer of the sandwich faces is strongly conditioned from the mechanical properties of the core material; however, for examined cases, the maximum buckling load for each load combination is, generally, attained for a lamination angle of the outer layers equal to 0° or 90°.

The hybridization of faces produces an improvement in their instability behaviour. This result has been obtained even if the slenderness of the faces is very high.

Low percentages of reinforcing high-stiffness material are sufficient to obtain the optimal arrangement of laminated faces.

The mechanical properties of the core influence the local buckling of the faces only for low values of b/h ratios (thick and moderately thick sandwich panels).

The presence of shear forces, combined with in-plane compression loads, produces a reduction in buckling load.

A coupling between local and overall instability of the sandwich panels has been observed corresponding to low values of the b/h ratio.

REFERENCES

1. Schwartz, R. T. & Rosato, D. V., Structural-sandwich construction. In *Composite Engineering Laminates*, ed. A. G. Dietz. MIT Press, Cambridge, MA, 1969, pp. 165–194.
2. Davies, J.M., Sandwich panels. *Thin-walled Struct.* 1993, **16**, 179–198.
3. Chong, K.P. and Hartsoch, J.A., Flexural wrinkling in foam-filled sandwich panels. *J. Engng Mech. Div.* 1974, **100**, 95–110.
4. Xiang, Y., Kitipornchai, S. and Liew, K.M., Buckling and vibration of thick laminates on Pasternak foundation. *J. Engng Mech.* 1996, **122**(1), 54–63.
5. Aiello, M.A. and Ombres, L., Maximum buckling loads for unsymmetric thin hybrid laminates under in-plane and shear forces. *Composite Structures* 1996, **36**, 1–11.
6. Frostig, Y., Baruch, M. and Sheiman, I., High-order theory for sandwich-beam behaviour with transversely flexible core. *J. Engng Mech.* 1992, **118**(5), 1026–1043.
7. Frostig, Y. and Baruch, M., High-order buckling analysis of sandwich beams with transversely flexible core. *J. Engng Mech.* 1993, **119**(3), 476–495.
8. Hunt, G.W. and da Silva, L.S., Interactive bending behaviour of sandwich beams. *J. Appl. Mech.* 1990, **57**, 189–196.
9. Hunt, G.W., Hidden (a)symmetries of elastic and plastic bifurcation. *Appl. Mech. Rev.* 1986, **39**(8), 1165–1186.
10. Leissa, W.A., A review of laminated composite plate buckling. *Appl. Mech. Rev.* 1987, **40**(5), 575–591.
11. Leissa, W.A., Conditions for laminated plates to remain flat under inplane loading. *Composite Structures* 1986, **6**, 261–270.
12. Jones, R. and Xenophontos, J., The Vlasov foundation model. *Int. J. Mech. Sci.* 1977, **19**, 317–323.
13. Thomsen, O.T., Analysis of local bending effects in sandwich plates with orthotropic face layers subjected to localised loads. *Composite Structures* 1993, **25**, 511–520.

ELSEVIER

Composite Structures Vol. 38, No. 1–4, pp. 203–213, 1997
© 1997 Elsevier Science Ltd. All rights reserved
Printed in Great Britain
0263-8223/97/$17.00 + 0.00

PII:S0263-8223(97)00056-1

Composite nozzle dam in the steam generator of a nuclear reactor

Je Hoon Oh, Dai Gil Lee

Mechanical Design Laboratory with Advanced Materials, Department of Mechanical Engineering, Korea Advanced Institute of Science and Technology, ME 3221, Gusong-dong, Yusong-gu, Taejon-shi, Korea 305-701

&

Tae Ryong Kim

Advanced Research Group, Korea Atomic Energy Research Institute, Dukjin-dong, Yusong-gu, Taejon-shi, Korea 305-353

The period of normal shutdown and maintenance for a nuclear power plant can be remarkably shortened when the examination and maintenance of the tubes of a steam generator are simultaneously carried out with refueling. The nozzle dam in a steam generator is a closure to block the flow of coolant from the inlet–outlet nozzles in a steam generator. Recently, the installation and removal operations of the nozzle dam were attempted using a robot rather than the manual operation because of the radioactive hazard. For the operation using the robot the weight of the dam must be reduced because the robot's payload for assembling operations is usually small.

In this work, a lighter nozzle dam was designed and manufactured using a carbon–epoxy composite, a glass–epoxy fabric composite, an aluminium plate and honeycomb. The carbon–epoxy composite was used for the main structural material and the honeycomb was used to increase the bending stiffness, while the aluminium plate and the glass–epoxy fabric composite were used to reduce the stress concentration around bolt holes. Also, the variation in mechanical properties of composites with respect to radiation emission was investigated.

In order to verify the structural integrity of the nozzle dam installed on the nozzle ring with bolts, the stress analyses of the nozzle dam under hydrostatic pressure were performed using commercial finite-element software and the pressure test was performed. The stiffness of the composite nozzle dam was measured and compared to that obtained by finite-element analysis. © 1997 Elsevier Science Ltd.

INTRODUCTION

The examination and maintenance of the steam generator in a nuclear power plant should be carried out regularly, and a reduction in the period of normal shutdown and maintenance is extremely important. Therefore, the examination and maintenance operations of tubes in the steam generator are simultaneously carried out during refueling, which requires the flow of coolant from a reactor cavity to the steam generator to be blocked. The nozzle dam which is located at the inlet–outlet nozzles in the steam generator is a special closure to block the flow of coolant from the reactor. The installation and removal operations of the nozzle dam have usually been performed manually. Figure 1 shows the nozzle dam in the steam generator.

The manual installation of the nozzle dam induces radiation exposure to working personnel. Because the radiation exposure during its installation and removal sometimes becomes more than 15% of the whole radiation exposure absorbed in a nuclear plant, workers are reluctant to carry out the related work [1]. Moreover, the heavy weight of current nozzle dams, made of aluminium alloy, makes the installation and removal work much more difficult. In order to

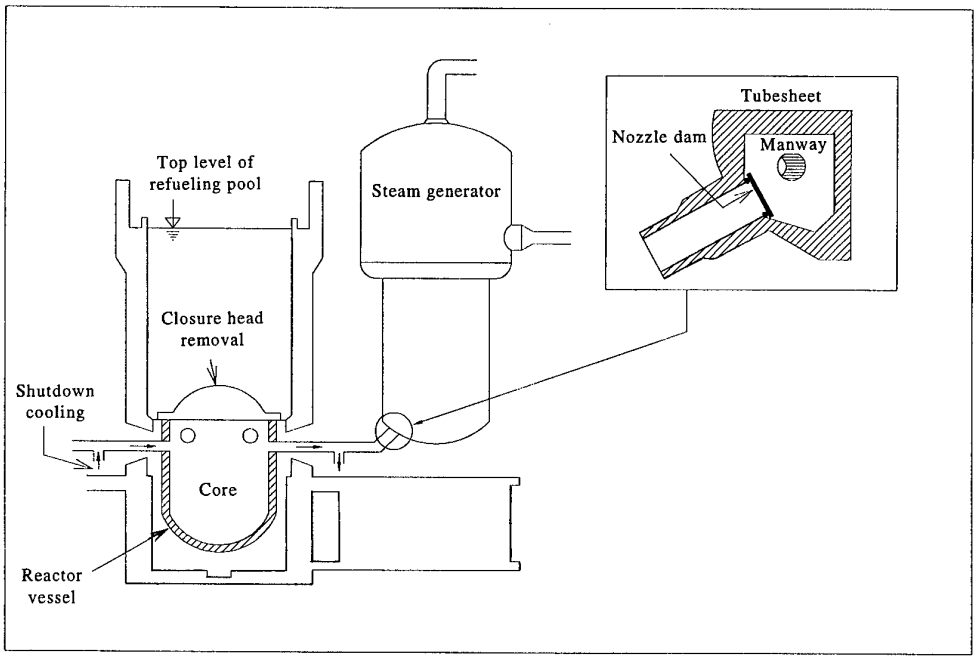

Fig. 1. Nozzle dam in the nuclear steam generator.

protect the workers from radiation exposure a new design concept for the nozzle dam should be developed, such as a lightweight one which can be installed in a shorter time or by a robot.

Three types of nozzle dams have been used in Korea, designed by Westinghouse, CE (Combustion Engineering) and NES (Nuclear Energy Service). The Westinghouse type is used in Kori nuclear power plant in Korea, while the CE and NES types are to be installed in Yonggwang 3 & 4 and Ulchin 3 & 4 in Korea, respectively, in the near future.

The Westinghouse-type nozzle dam is so heavy that oriental workers have great difficulty in installing and removing nozzle dams. It takes at least 30 min to install the nozzle dam using 20 bolts to provide both structural stability and sealing performance. In order to solve this problem, Trundle [2,3] has improved the installation technique by devising a new transport system for the heavy nozzle dam.

The CE-type nozzle dam for Yonggwang 3 & 4 is composed of one set of wet and dry nozzle dams, hence called double nozzle dams. The dams are installed by inserting pins into the holes on the nozzle wall of a steam generator. The nozzle dams have continually been improved, with Weisel [4] devising the single nozzle dam. McDonald [5] invented an instrument which enabled workers to install the nozzle dam outside the steam generator.

The NES-type nozzle dam for Ulchin 3 & 4 is conceptually similar to the CE-type single nozzle dam. It is composed of one centre section and two side sections, so that it can easily be transported through the small manway. It is installed by inserting pins into holes on a nozzle ring welded on the steam generator nozzle. The whole installation time of this nozzle dam is only a few minutes.

Another type of the nozzle dam, which is not used in Korea, is produced by BRAND utility

Table 1. Weights and materials for current nozzle dams

Nozzle dam type		Nozzle dam weight (N)		Material
		Centre section	Side section	
KORI nozzle dam		340	340	Aluminum alloy 5052-H32
BRAND nozzle dam		272	159	Aluminum alloy 2024-T351
NES Nozzle dam (Type C-2)	0.762 m	150	—	Aluminum alloy 2024-T351
	1.067 m	154	—	Aluminum alloy 2024-T351

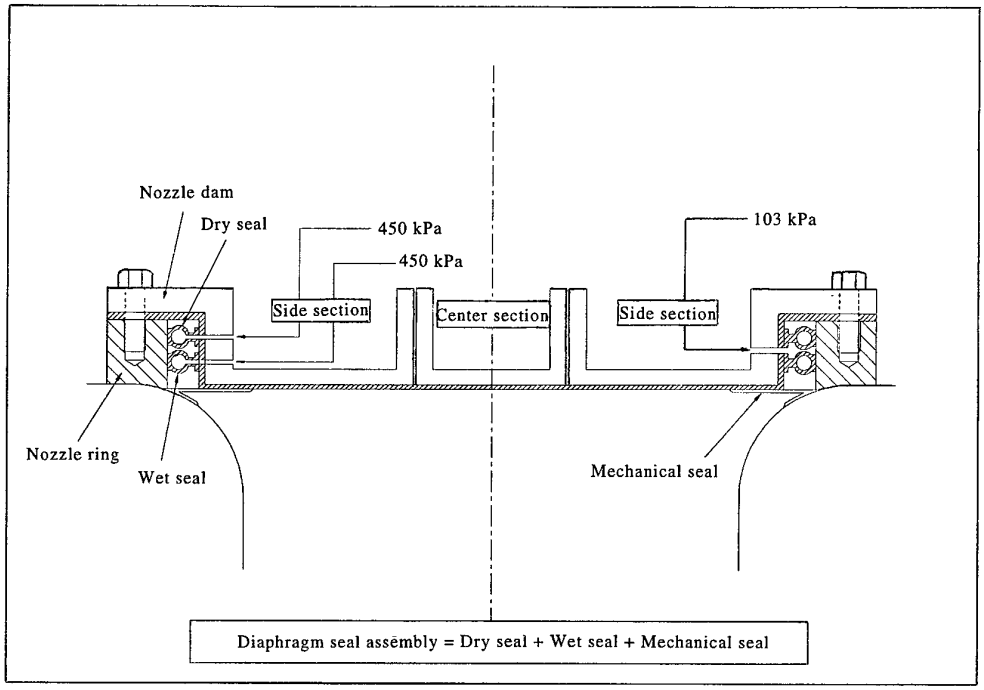

Fig. 2. Nozzle dam system composed of the nozzle dam, nozzle ring and diaphragm seal.

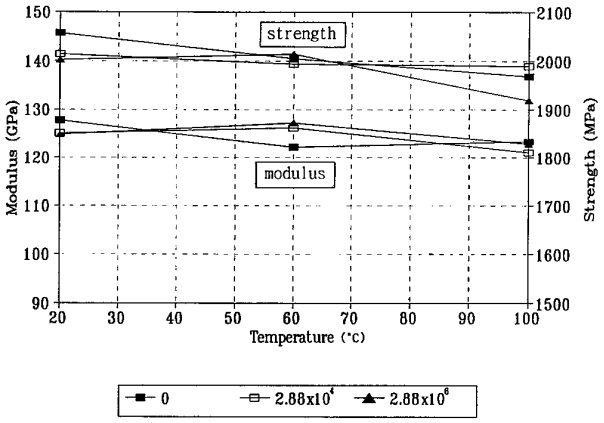

Fig. 3. Results of the tension test with respect to radiation emission and temperature.

Inc., USA. The thickness of the BRAND nozzle dam was determined by calculating the bending moment induced by the pressure of cooling water [6]. A separate sealing mechanism is used to reduce the number of bolts to be fastened and the BRAND nozzle dam can be installed by a robot using attached handling lugs [7]. It takes only a few minutes to install the BRAND nozzle dam.

However, there is great difficulty in installing the nozzle dam, whether manually or using a robot, because the nozzle dam is made of a heavy aluminium alloy. Table 1 gives the weights and materials for each nozzle dam. As shown in Table 1, the nozzle dams are very heavy for an oriental man or a robot to handle. Because the nozzle dam needs to be installed

Table 2. Mechanical properties of the nozzle dam used in the analysis

	Carbon–epoxy	Glass–epoxy (fabric)	Honeycomb	Aluminium
E_1 (GPa)	128.0	21.5	—	69
E_2 (GPa)	8.0	21.0	—	—
G_{12} (GPa)	6.0	4.0	—	—
G_{23} (MPa)	—	—	110	—
G_{13} (MPa)	—	—	69	—
v_{12}	0.30	0.11	—	0.3
X_T (MPa)	1900	428	—	—
Y_T (MPa)	60	425	—	—
S (MPa)	75	95	—	—
Ply thickness (mm)	0.125	0.20	—	—

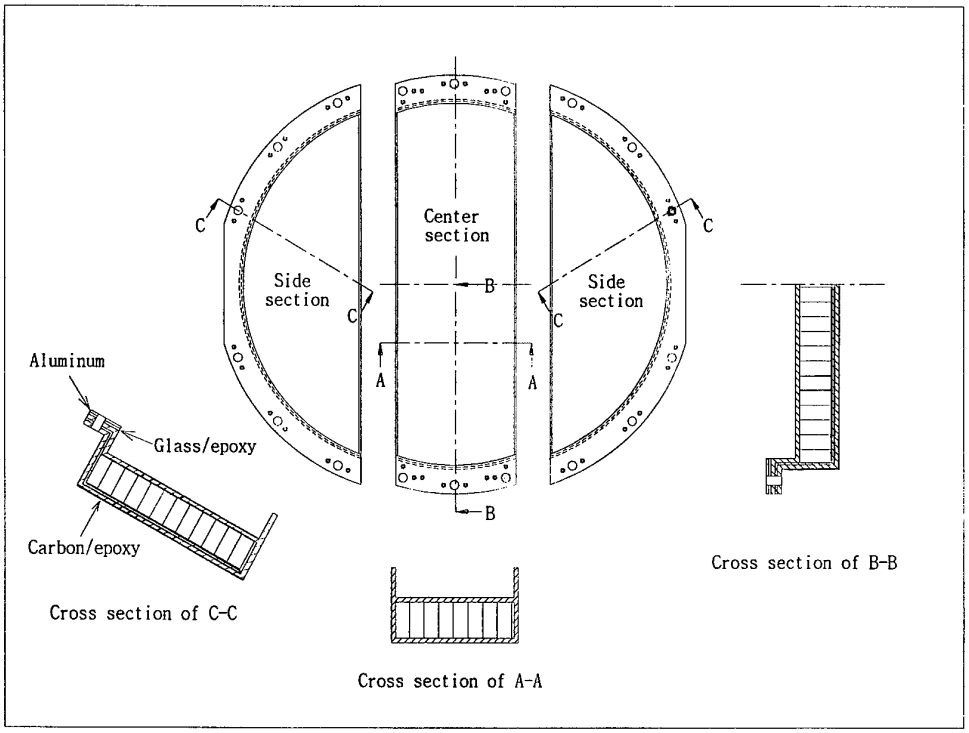

Fig. 4. Configuration of the composite nozzle dam.

within a confined area and in limited time, it would be of great benefit to reduce its weight.

In order to reduce the weight of the nozzle dam without sacrificing the structural safety, in this work the nozzle dam was designed and manufactured using fibre-reinforced composite materials as they have been widely used in aircraft and automotive structures due to their high specific modulus and high specific strength. If the nozzle dam is manufactured with fibre-reinforced composite materials, the time for installation and removal might be remarkably shortened or it could allow a robot to be used.

In this work the lighter nozzle dam was designed and manufactured using a carbon–epoxy composite, a glass–epoxy fabric composite, an aluminium plate and honeycomb. The carbon–epoxy composite was used for the main structural material and the honeycomb was used to increase the bending stiffness, while the aluminium plate and the glass–epoxy fabric composite were used to reduce the stress concentration around the bolt holes.

As there is a tendency for property degradation when composite materials are exposed to radiation emission, the effect of radiation on the mechanical properties of the carbon–epoxy composite material was tested with respect to radiation emission.

The stress analyses of the nozzle dam installed on the nozzle ring with bolts were performed by ANSYS, a commercial finite-element software, when the nozzle dam was subjected to hydrostatic pressure. In order to verify the structural integrity of the nozzle dam, the mock-up of the steam generator with the diaphragm seal assembly was manufactured and the pressure test was performed. The maximum

Table 3. Mechanical properties of the face and the core materials

	E_{11} (GPa)	E_{11}/E_{22}	G_{12}/E_{22}	ν_{12}	G_{13} (MPa)	G_{23} (MPa)
Graphite–epoxy (face material)	206.8	40	1.0	0.25	—	—
Glass fabric honeycomb (core material)	—	—	—	—	117.2	241.3

displacement of the composite nozzle dam was measured and compared to that obtained by finite-element analysis.

CHARACTERISTICS OF THE NOZZLE DAM SYSTEM

The nozzle dam system is composed of the nozzle dam, nozzle ring and diaphragm seal. Figure 2 shows the nozzle dam system. The nozzle dam located at the inlet–outlet nozzles blocks the flow of coolant from the reactor in a steam generator. The nozzle dam has to be carried through the manway. Because the diameters of the manway and the nozzle dam are 0.4 and 1.05 m, respectively, the nozzle dam was divided into one centre section and two side sections.

The nozzle ring is welded to the entrance of the nozzle of a steam generator and the nozzle dam is fastened to the nozzle ring with bolts.

In general, a water pressure of 110 kPa is applied to the nozzle dam. The diaphragm seal for the coolant is divided into a disk type and an inflatable seal type in which the latter uses compressed air, while the former uses many bolts of high clamping pressure. In the Kori nuclear power plant the disk-type diaphragm seal is used, which takes 30–40 min to install in the nozzle dam. In the inflatable seal type, the compressed air in the inflatable seal makes the seal adhere to the inner wall of the nozzle ring. It takes only a few minutes to install the nozzle dam when the inflatable seal type is used.

In this work, a lighter nozzle dam was designed for the Kori nuclear power plant using composite materials. In the Kori nuclear power plant, the weights of the centre section and the side section of the nozzle dam are both 340 N. There are 18 holes in the composite nozzle dam, of which 10 holes were used for bolts and the other eight holes for guide pins.

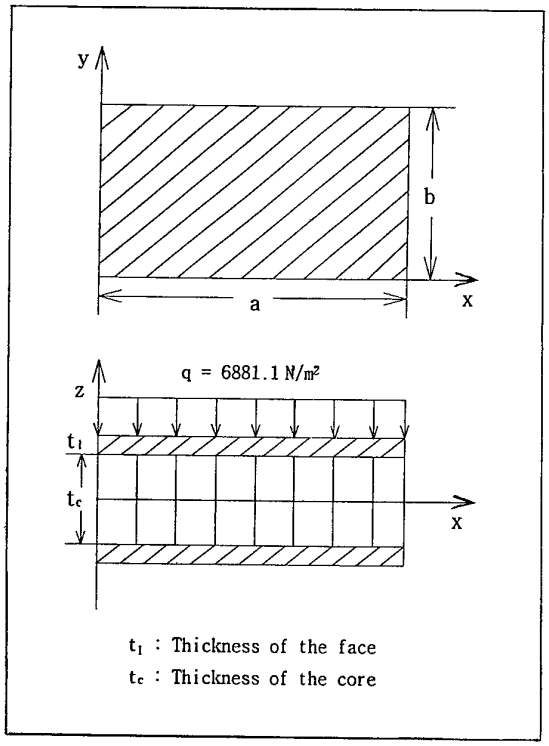

Fig. 5. Sandwich structure used in the verification of the model.

STATIC TEST OF CARBON–EPOXY WITH RESPECT TO RADIATION EMISSION AND TEMPERATURE

Radiation emission and environmental temperature may change material properties and induce swelling, hardening, softening and degradation. Therefore, the mechanical properties of dam materials should be tested with respect to radiation emission because the radiation emission is very high in the vicinity of the nozzle in the steam generator and the nozzle dam is used for a long time. In general, the temperature in the steam generator during the maintenance operation is about 60°C and the maximum temperature is less than 100°C. When the nozzle dam is installed on the nozzle ring in the

Table 4. Comparison of the analysis results from the sandwich model with those by Monforton & Ibrahim [8] (a = 1270 mm, t_c = 25.4 mm)

Aspect ratio (a/b)	t_c/t_f	ω_o [8] (m)	ω_o (this study) (m)	N_x [8] (N/m)	N_x (this study) (N/m)
1.0	4	5.121×10^{-4}	5.427×10^{-4}	21780	21391
2.5	10	1.421×10^{-4}	1.438×10^{-4}	26360	26336

t_c, thickness of the face; t_f, thickness of the honeycomb; ω_o, centre deflection of the sandwich plate.

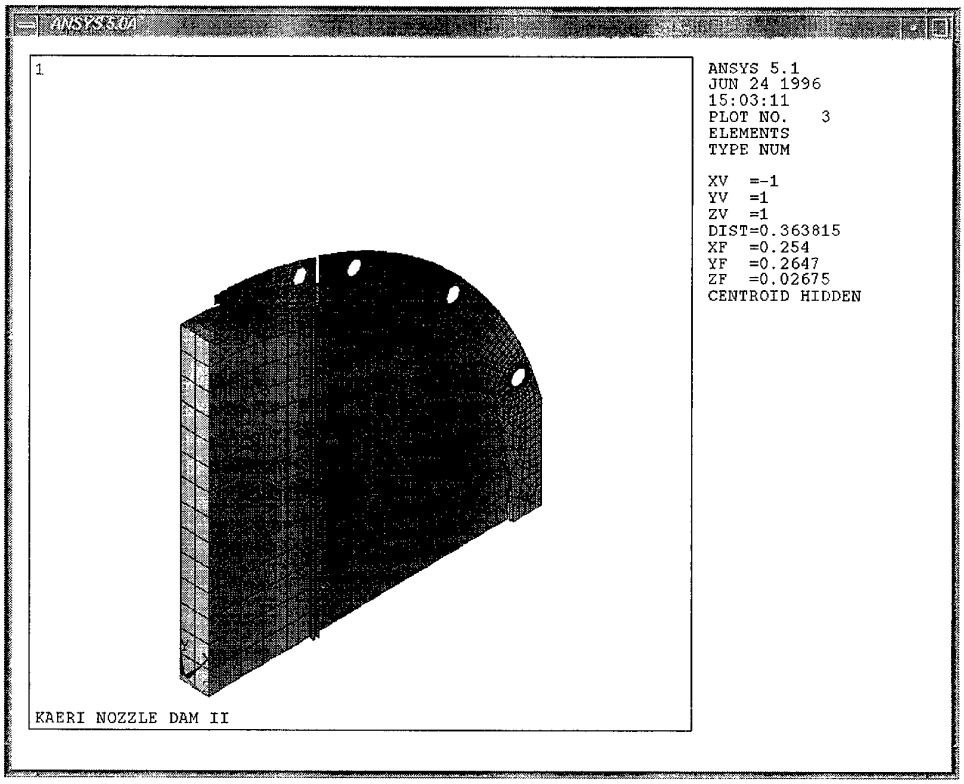

Fig. 6. Finite-element model used for the analysis.

steam generator it will be used for 30 days in radioactive conditions of 5–40 rads/h.

In order to investigate the effect of the radiation emission and temperature on the mechanical properties of the carbon–epoxy composite, tension, compression and shear tests were carried out using INSTRON with ASTM standard specimens after imposing radiation emission on the specimens.

When the nozzle dam is used for 30 days in radioactive conditions of 5–40 rads/h, the maximum radiation absorbed in the nozzle dam was obtained using the following equation

$$40 \text{ rads/h} \times 24 \text{ h/day} \times 30 \text{ days/month}$$

$$= 2.88 \times 10^4 \text{ rads/month}$$

The specimens were radio-activated using a γ-ray emission instrument in KAERI (Korea Atomic Energy Research Institute) with levels of 0, 2.88×10^4 and 2.88×10^6 rads at temperatures of 20, 60 and 100°C.

Figure 3 shows the result of the tension test of the unidirectional carbon–epoxy whose properties are given in Table 2 with respect to radiation emission and temperature. Each point in Fig. 3 is a mean value of five experiments. As shown in Fig. 3, the radiation did not affect the mechanical properties of the carbon–epoxy composite, however, the mechanical properties did decrease a little as the temperature increased. Therefore, it was concluded that carbon–epoxy was applicable as the main structural material for the nozzle dam.

DESIGN OF THE NOZZLE DAM

The design pressure for the nozzle dam was 110 kPa and compressed air at 448 kPa was injected into the diaphragm seal. Figure 4 shows the configuration of the three-piece composite nozzle dam.

The sandwich structure composed of carbon–epoxy face material and Nomex honeycomb of 1/8-in. core was employed for the nozzle dam structure to increase bending stiffness. The fabric glass–epoxy of 2 mm thickness and the aluminium plate of 2 mm thickness were

stacked around the bolt holes in the carbon–epoxy to reduce the stress concentration. The centre plate and the two side plates were fastened by two bolts and four bolts, respectively. Table 2 shows the material properties for the nozzle dam.

FINITE-ELEMENT MODELLING

The ply angle and thickness of the carbon–epoxy face material were determined using the Tsai–Wu failure criterion through a finite-element method. Before performing the analysis of the nozzle dam, a sandwich plate simply supported at four edges was analysed using ANSYS, a commercial finite-element analysis software, to verify the validity of the model of the nozzle dam. The result was compared with that of Monforton & Ibrahim [8]. The core material was modelled using solid elements with 20 nodes, and the face was modelled using shell elements with eight nodes. The ply angle and ply thickness can be assigned in the shell elements. The stacking sequence of the face material was $[90°/0°]_T$ and the core material was glass fabric honeycomb. Figure 5 shows the sandwich plate used for verification which is subjected to a uniform load of $q = 6881.1\ \text{N/m}^2$. Table 3 shows the mechanical properties of the face and the core materials.

Table 4 shows the results of FEM analysis as well as the results given by Monforton & Ibrahim [8]. From the results of the FEM analysis, it was found that the solid elements for the core model and the shell elements for the face model were appropriate for the sandwich structure.

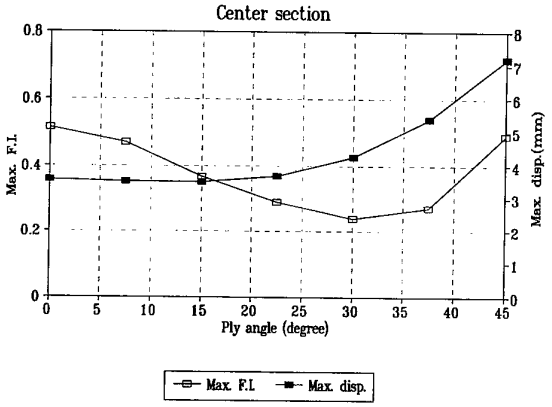

(a)

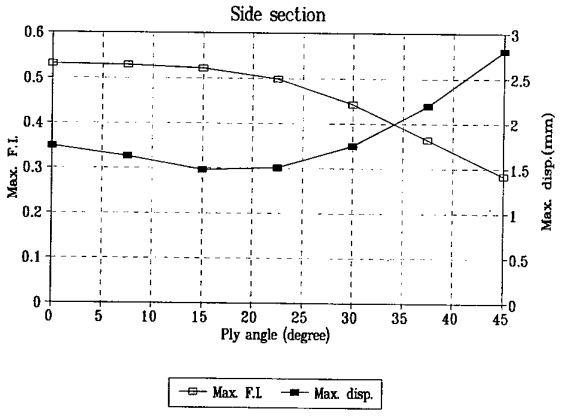

(b)

Fig. 7. Maximum failure index and maximum displacement with respect to ply angle: (a) centre section; (b) side section.

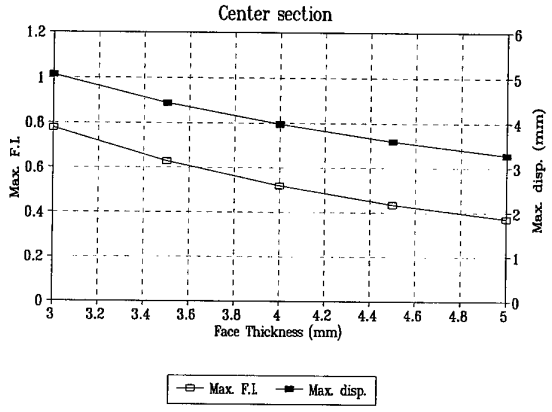

(a)

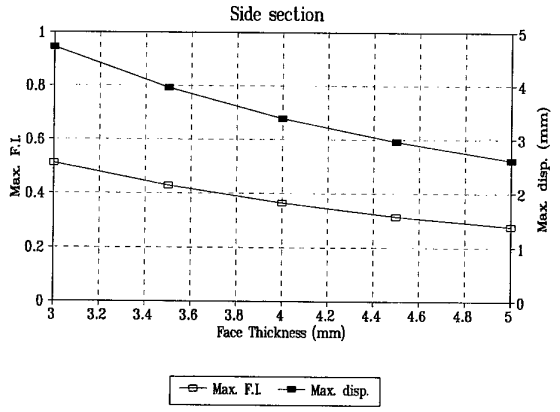

(b)

Fig. 8. Maximum failure index and maximum displacement with respect to the thickness of the face when the core thickness is 40 mm: (a) centre section; (b) side section.

The stresses of the nozzle dam were also calculated using ANSYS. Because of symmetry, only a quarter of the nozzle dam needed to be modelled. For the boundary conditions, all the displacements around the bolt holes were fixed and the design pressure of 110 kPa was applied to the nozzle dam and an air pressure of 448 kPa in the diaphragm seal was applied to the side wall. Figure 6 shows the finite-element model used in the analysis.

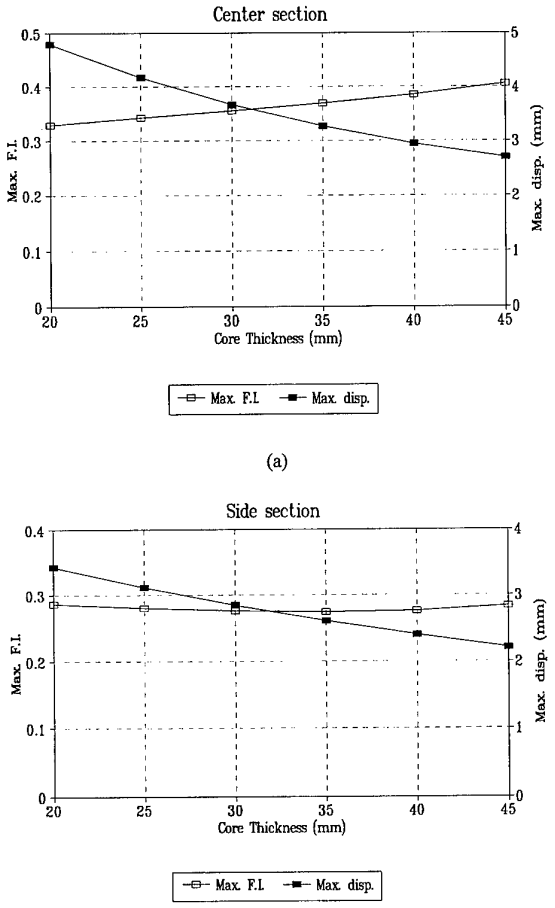

Fig. 9. Maximum failure index and maximum displacement with respect to the thickness of the core: (a) centre section; (b) side section.

Table 5. Determined ply angles and thicknesses

	Centre section	Side section
Ply angle of the carbon–epoxy (°)	±15	±45
Face thickness (mm)	5	5
Core thickness (mm)	40	40
Thickness of glass–epoxy (mm)	2	2
Thickness of aluminium (mm)	2	2

In order to determine the ply angle of the nozzle dam, the maximum Tsai–Wu failure index and the maximum displacement of each section were calculated with respect to ply angle when the face thickness and the core thickness were 4.5 and 40 mm, respectively. Figure 7 shows the maximum Tsai–Wu failure index and the maximum displacement of each section.

As the maximum failure index in the side section was lowest when the ply angle was ±45°, this ply angle was used for the side section. In this case, the maximum displacement of the side section was 2.8 mm. In the centre plate, when the ply angle was ±30°, the maximum failure index was lowest and the maximum displacement was 4.3 mm. However, the difference in maximum displacement between the centre plate and the side plate was large when the ply angle was ±30°. Because the large difference in displacements between the two plates would cause the diaphragm seal to fail, a ply angle of ±15° for the centre section was used because the maximum displacement was 3.5 mm in this case.

In order to determine the face thickness of each section, both the maximum failure index and the displacement of each section were calculated with respect to the thickness of the face when the core thickness was 40 mm. As shown in Fig. 8, the maximum failure index and displacement of the plates were decreased as the face thickness was increased. Considering the weight and safety factor of the nozzle dam, a face thickness of 5 mm was used for both sections.

The maximum failure index and the maximum displacement of the plates were also calculated with respect to the core thickness. Figure 9 shows the maximum failure index and the maximum displacement of the plates. In the centre section, as the core thickness increased, the maximum displacement was decreased but the maximum failure index was increased. In the side section, as the core thickness was increased, the maximum displacement was decreased but the maximum failure index was almost constant. Because the bending stiffness in the centre section was decreased as the core thickness was decreased, a core thickness of 40 mm for both sections was used although the

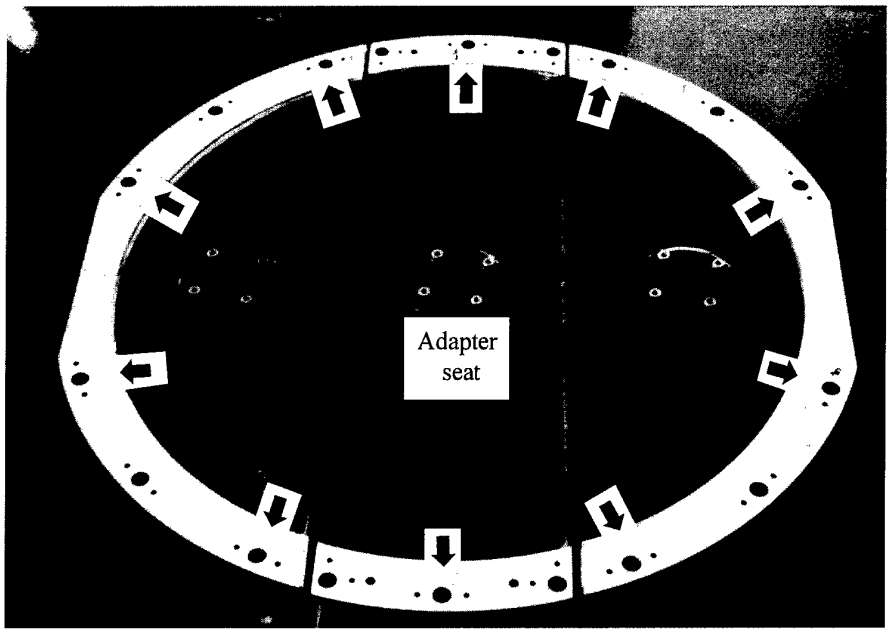

Fig. 10. Photograph of the prototype composite nozzle dam whose diameter is 1.06 m. The gripper of a robot holds the adapter portion and the arrow indicates the holes provided for the bolts.

maximum failure index was decreased as the core thickness was decreased. Table 5 shows the determined design parameters for the sections.

MANUFACTURING THE NOZZLE DAM

The face of the nozzle dam was manufactured using the pre-preg lay-up method and autoclave vacuum bag process. The face thickness and the core thickness of the centre plate and the side plate were 5 and 40 mm, respectively. The faces of the centre plate and the side plate had stacking sequences of $[\pm 15°]_{10S}$ and $[\pm 45°]_{10S}$, respectively. In order to reduce the stress concentration around the bolt holes, the glass fabric–epoxy composite of 2 mm thickness was stacked on the flange part of the carbon-epoxy

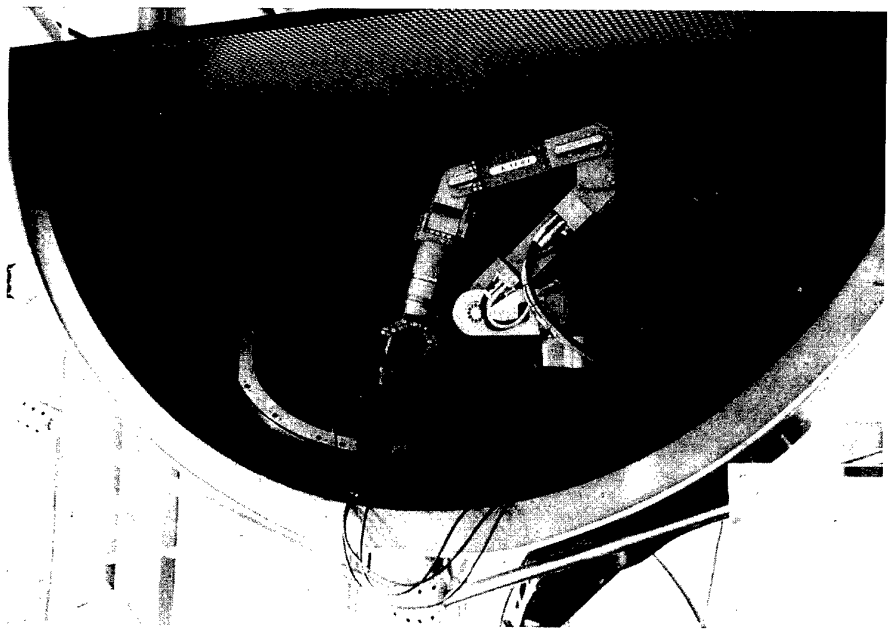

Fig. 11. Photograph of the composite nozzle dam installed in the mock-up of the steam generator.

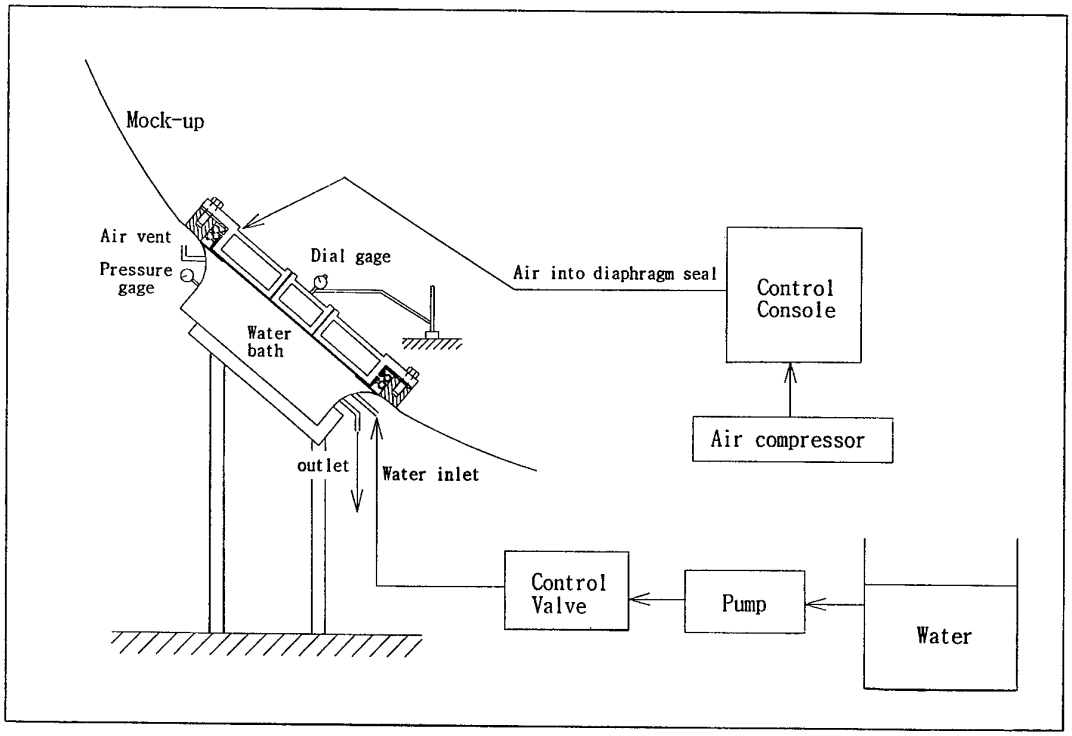

Fig. 12. Pressure test system of the nozzle dam.

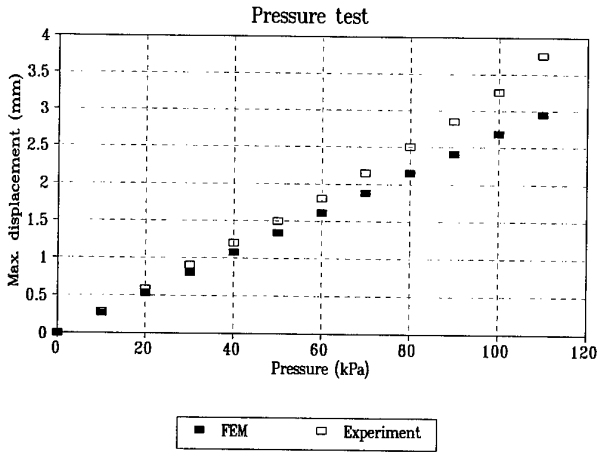

Fig. 13. Results of the pressure test and the finite-element analysis.

and then the aluminium plate of 2 mm thickness was bonded onto the glass fabric–epoxy composite.

The rib of the centre plate was tapered in order to reduce the interference between the centre plate and the side plate, which makes the installation of the nozzle dam by a robot possible. As there was a gap between the centre plate and the side plate, the two plates supported load independently. The robot handled the nozzle dam by gripping the adapters which were mounted both on the centre plate and the side plate of the nozzle dam.

The six 22-mm diameter holes were drilled on the centre and the side plates. Two bolts were used to fasten the centre plate while four bolts were used to fasten the side plate. The rest of the holes were for the guide pins. The two small 7-mm diameter holes around the 22-mm diameter holes were drilled for the bolt holder and the guide pin holder. The bolt holder and guide pin holder hold the bolts and pins with strings, which prevents the robot dropping bolts and pins into the bottom of the steam generator during the installation operation. Figure 10 shows the manufactured composite nozzle dam.

The centre plate and the side plate of the composite nozzle dam weighed 80 and 74 N, respectively. As the centre and side plates of the nozzle dam made of aluminium alloy weighed 340 N, the composite plates were only 25% and 22%, respectively, that of the aluminium alloy nozzle dam.

PRESSURE TESTING THE NOZZLE DAM

The pressure test for the nozzle dam was performed using a specially designed mock-up of

the steam generator to compare the calculated results with the tested results. Figure 11 is a photograph of the mock-up of the steam generator. In order to prevent water from leaking, the diaphragm seal was installed between the nozzle and the nozzle dam. As shown in Fig. 2, the diaphragm seal was composed of the dry seal, the wet seal and the mechanical seal. The sealing of the nozzle dam was established using compressed air at 448 kPa which was injected into the dry seal and the wet seal. The schematic diagram of the pressure test system is shown in Fig. 12.

Figure 13 shows the results of the pressure test and the calculated results for the centre section. The calculated value of the maximum transverse displacement of the centre section was 2.95 mm under a pressure of 110 kPa and the test result was 3.75 mm. As shown in Fig. 13, the test results were non-linear while the FEM results were linear, this is because linear material properties were used in the finite-element analysis. Therefore, at low pressure, the difference between the FEM result and the test result was small, but the difference increased as the pressure increased. It was therefore concluded that in order to perform a more accurate analysis, the non-linearity of the core material as well as the composite material should be included in the analysis.

The composite nozzle dam was tested under a pressure of 120 kPa. After the test the nozzle dam was disassembled from the mock-up and examined, no visible damage was found.

CONCLUSIONS

In this study a lighter nozzle dam was designed and manufactured using carbon–epoxy composite, glass–epoxy fabric composite, an aluminium plate and honeycomb. In order to investigate the effect of the radiation emission and temperature on the mechanical properties of the carbon–epoxy composites, tension, compression and shear tests were carried out and it was found that the radiation and a temperature lower than 100°C did not much affect the mechanical properties of the carbon–epoxy.

From the finite-element analysis, the ply angles of the centre section and the side section were determined to be $\pm 15°$ and $\pm 45°$, respectively; the thicknesses of the face and the core were determined to be 5 and 40 mm, respectively.

The prototype composite nozzle dam was manufactured using the autoclave vacuum bag process and tested using a specially designed mock-up of the steam generator. From the tests, it was found that the composite nozzle dam had a structural integrity although the weight of the composite nozzle dam was just 25% that of the aluminium nozzle dam.

REFERENCES

1. Meieran, H. B., Mobile robots continue to march (and crawl, roll, walk, slither, climb and swim) into action. *Nuclear Engng Int.*, Feb. (1991) **36**, 26–32.
2. Trundle, M. H., Nozzle dam remote installation system and technique. U.S. Patent No. 5006302, 1991.
3. Trundle, M. H., Nozzle dam translocating system. U.S. Patent No. 4959192, 1990.
4. Weisel, E. M., Multisectioned nozzle dam. U.S. Patent No. 5048570, 1991.
5. McDonald, F. X., Remotely installed steam generator nozzle dam system. U.S. Patent No. 4954321, 1990.
6. Evans, C., Segmented nozzle dam. U.S. Patent No. 4957215, 1990.
7. Meieran, H. B., Installing nozzle dams 100% remotely. *Nuclear Engng Int.*, March (1993) **38**, 17–19.
8. Monforton, G.R. and Ibrahim, I.M., Analysis of sandwich plates with unbalanced cross-ply faces. *Int. J. Mech. Sci.* 1975, **17**, 227–238.

ELSEVIER

Composite Structures Vol. 38, No. 1–4, pp. 215–227, 1997
© 1997 Elsevier Science Ltd. All rights reserved
Printed in Great Britain
0263-8223/97/$17.00 + 0.00

PII:S0263-8223(97)00057-3

Adhesively bonded lap-joints for the composite–steel shell structure of high-speed vehicles

Kum Cheol Shin, Young Goo Kim, Dai Gil Lee

Department of Mechanical Engineering, Korea Advanced Institute of Science and Technology, Gusong-dong, Yusong-gu, Taejon-shi, Korea 305-701

&

Jin Min Choi

Korea Institute of Machinery and Materials, PO Box 101, Yusong-gu, Taejon-shi, Korea 305-600

Recently the design and manufacture of lightweight train structures have become important in order to increase speed. Composite train structures have many advantages over conventional steel or aluminum train structures because of their high specific strength, modulus and high damping capacity, which is beneficial for NVH (noise, vibration and harshness).

From the structures of high-speed trains, the upper car-body is a good candidate for composite structures which increase the stability of trains due to the low gravity center of vehicles.

If the side body of the train is made of steel plates, then joining of composite structures to the steel structures is required.

In this work, the adhesive joining method between the composite upper car-body structure and the steel side plates was investigated. A 1/10-size model of a real train subjected to internal pressure was developed and tested statically and dynamically. © 1997 Elsevier Science Ltd.

INTRODUCTION

When speeding-up large vehicles, such as a train, it is important to reduce the weight of the car-body that contributes most of the weight of the vehicle. In order to decrease the weight of the car-body without sacrificing the safety of the vehicle, it is effective to change the materials making up the car-body. Fiber-reinforced composite materials have been widely used in aircraft and spacecraft structures because of their high specific strength, modulus and high damping capacity. If they are applied to the car-body, it is expected that not only the speed of the car-body is increased but also that noise and vibration are reduced.

Tagawa *et al.* used aluminum in their train structures and tested it under internal pressure, bending moments and twisting moments [1]. Suzuki *et al.* tested honeycomb and composite trains under bending moments and pressures [2]. Matsuoka & Nakamura suggested a method of joining the aluminum and composite materials using specimen tests and compared the effectiveness when they are applied to the train [3]. Lewis tested glass-reinforced plastic tubes to determine statically and dynamically the crash behavior of composite-structure trains with respect to many types of accidents [4]. Thorton & Jeryan performed axial compressive tests using quadrilateral composite tubes to determine the energy absorption of the composite-structure train [5]. Larrode *et al.* studied the manufacturing method of the composite-structure bus using FEM [6].

If an upper car-body is made of composite materials and the side plates of the car-body are made of steel, it is expected that both the speed

and stability of the car-body are improved because the weight of car is reduced and the gravity center of the vehicle is lowered. In this case, the joining of an upper composite car-body and the steel side plates is necessary. As the efficiency of composite structures is largely dependent on the joint used rather than the structure itself [7], the optimum joining of the composite car-body is imperative.

The forces trains are subjected to consist of internal pressure, and bending and twisting moments. To increase the speed of the train, a railroad track is designed to be straight with small curve and slope. Therefore, the dominant force of the high-speed train is the internal pressure because the difference between the inner and outer pressures of the car-body increases proportionally to car velocity squared, especially when traveling in a tunnel.

In this work, a 1/10-size composite–steel shell structure of the prototype train subjected to internal pressure was developed and tested. The adhesive joining method was used to assemble the upper composite roof to the side steel plates. The stress distribution of the joint was analyzed using a commercial finite-element software. Also, the prototype model was dynamically tested under fluctuating internal air pressure to investigate the fatigue strength of adhesive joints.

TEST SPECIMENS

Figure 1 shows the configuration and joining types of the composite–steel shell specimens, whose dimensions are $300 \times 350\ mm^2$, which is 1/10-size of the prototype train. Only 100 mm length of the specimen was chosen because the stress distribution of the train subjected to internal pressure was independent of the train length. The thickness of the composite roof for the weight reduction and stability of the train was chosen to be 2.4 mm, and steel plates were chosen for the side body of the train. For a reliable join of the composite and the steel an adhesive thickness of 0.1 mm was chosen [8]. Table 1 gives the properties of the carbon fiber–epoxy composite and the glass fiber–epoxy composite used in this work. Table 2 shows the properties of IPCO 9923, which is a rubber-toughened adhesive manufactured by IPCO National (CA, USA). Two bonding lengths of 10 and 20 mm for joining the composite roof to the steel side plates were tested. Three types of joining method, such as an adhesively bonded inner single lap-joint, an adhesively bonded outer single lap-joint and an adhesively bonded double lap-joint as shown in Fig. 1, were tested. The stacking sequences of the composite roof were $[\pm\theta]_{4S}$ ($\theta = 10$, 30, 45, 60 and 80°). For the adhesively bonded single lap-joint specimens, four different thicknesses

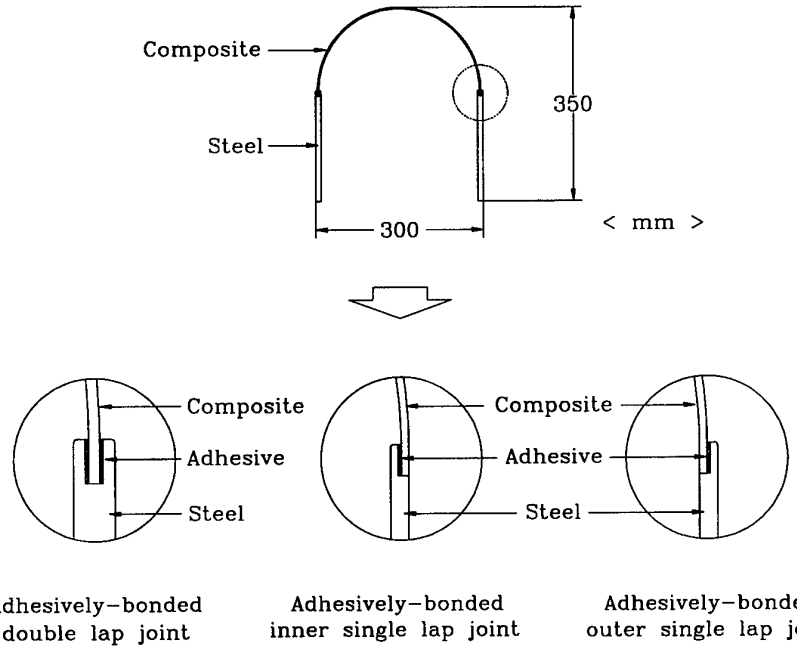

Fig. 1. Three types of lap joint specimens for the composite–steel shell structure.

Table 1. Properties of the composites[1]

	Carbon–epoxy composite	Glass–epoxy composite
E_L (GPa)	130.0	43.5
E_T (GPa)	8.0	5.0
G_{LT} (GPa)	6.0	5.0
ν_{LT}	0.28	0.25
X^t (MPa)	1800	1000
Y^t (MPa)	50	50
S (MPa)	75	50
Ply thickness (mm)	0.15	0.175
Density (kg/m^3)	1560	1980

[1] E_L, longitudinal tensile modulus; E_T, transverse tensile modulus; G_{LT}, shear modulus; ν_{LT}, Poisson's Ratio; X^t, longitudinal tensile strength; Y^t, transverse tensile strength; S, shear strength.

of the steel plates such as 4.0, 5.5, 7.0 and 10.0 mm were used. For the adhesively bonded double lap-joint specimens, 5.6, 8.6, 11.6 and 17.6 mm thick steel plates were used.

EXPERIMENTAL EQUIPMENT

The experimental equipment consists of a tester, a pneumatic circuit and an electric circuit. Figure 2 shows the tester on which the specimen was mounted. The rubber tube in the tester was used to apply internal pressure to the specimen. The wood in the tester was used to reduce the internal volume of the tester, which increased the loading frequency in the dynamic test. Figure 3 shows the configuration of the pneumatic and electric circuits that supply air into the rubber tube for static and dynamic tests. The function generator in Fig. 3 was used to supply fluctuating air pressure in the rubber tube.

After the composite roof was cured under the curing cycle for the composite, it was adhesively bonded to the two steel side plates using IPCO 9923 rubber-toughened adhesive. The tester was installed in a protective housing which had an aluminum lid and a lift. The lid was used for the shut-down of air pressure in case of composite roof failure. When the adhesive joint of the specimen or the specimen itself fails by the internal pressure, the composite roof clicks the limit switch, which shuts down the air supply to the tester.

Table 2. Properties of the adhesive (IPCO 9923)

Tensile modulus (GPa)	1.3
Poisson's ratio	0.41
Tensile strength (MPa)	45.0
Shear strength (MPa)	29.5
Lap shear strength (MPa)	13.7
Density (kg/m^3)	1200

FINITE-ELEMENT ANALYSES OF THE ADHESIVE JOINT

In order to investigate the stress distributions of the specimens subjected to internal pressure, finite-element analyses were performed using ANSYS 5.0, a commercial software. A layered version of the eight-node structural solid element (SOLID46) for the composite roof and an eight-node structural solid element (SOLID45) for the steel side plates and the adhesive layer were used. As the specimens had vertical symmetry, only half of the structure was analyzed. Figure 4 represents the element configuration and boundary conditions of the adhesively bonded inner single lap-joint specimen with 10 mm bonding length. The node numbers and element numbers for the analysis of the single lap-joint were 5742 and 4650, respectively. The IPCO 9923 epoxy adhesive had a strong nonlinear stress–strain behavior due to rubber toughening. Therefore, its behavior was modeled multi-linearly as shown in Fig. 5. The magnitude of the internal air pressure was 0.42 MPa.

For the failure prediction of the specimen, three failure criteria were used: Tsai–Wu and Ye-delamination for the composite roof, and von Mises yield criterion for the adhesive.

The Tsai–Wu failure criterion is described by the tensor polynomial [9]

$$F_i\sigma_i + F_{ij}\sigma_i\sigma_j = 1 \quad (i, j = 1, ..., 6) \tag{1}$$

In order to avoid failure, the left-hand side of eqn (1) must be <1, and failure is predicted when the left-hand side is ≥ 1.

The Tsai–Wu failure criterion was used to predict the in-plane failure of the composite roof in which $\sigma_3 = \sigma_{33} = 0$, $\sigma_4 = \tau_{23} = 0$, $\sigma_5 = \tau_{31} = 0$.

The Ye-delamination criterion was used to predict the interlaminar delamination failure of the composite roof.

The Ye-delamination criterion predicts the delamination failure [10] when

$$\left(\frac{\sigma_{33}}{Z_t}\right)^2 + \left(\frac{\sigma_{13}}{R}\right)^2 + \left(\frac{\sigma_{23}}{T}\right)^2 \geq 1 \text{ for } \sigma_{33} > 0$$

or

$$\left(\frac{\sigma_{13}}{R}\right)^2+\left(\frac{\sigma_{23}}{T}\right)^2 \geq 1 \text{ for } \sigma_{33}<0 \qquad (2)$$

where σ_{ii} $(i = 1, 2, 3)$ are the normal stress components in the principal material directions; σ_{ij} $(i, j = 1, 2, 3, i \neq j)$ are the shear-stress components; Z_t is the tensile strength of material in the thickness direction, and R and T are the corresponding shear strengths.

For the carbon composite roof, the following strength values were used to estimate the delamination failure: $Z_t = 50$ MPa, $R = 75$ MPa and $T = 18.8$ MPa.

The von Mises theory was used to predict the yield of the adhesive. The von Mises yield criterion predicts that the failure will occur when

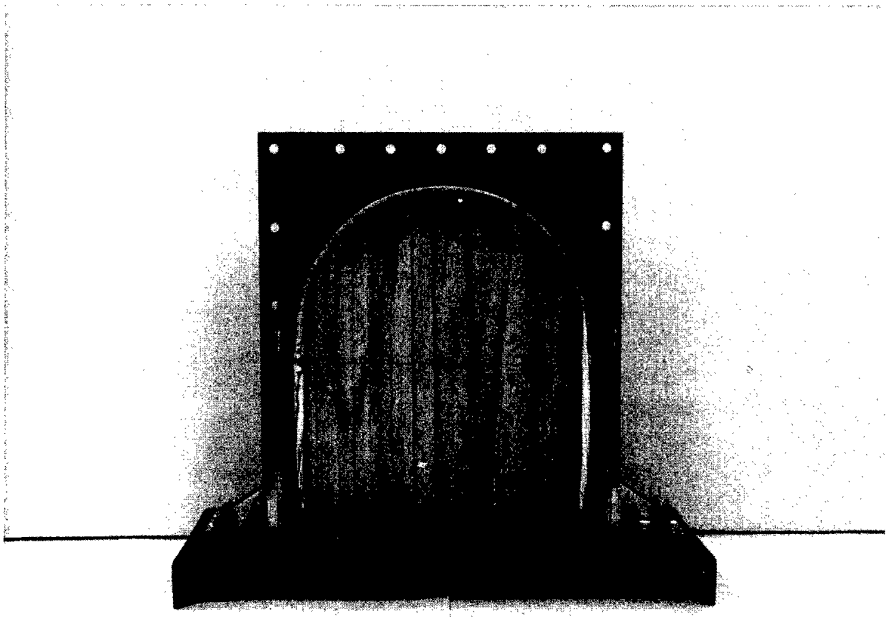

(a)

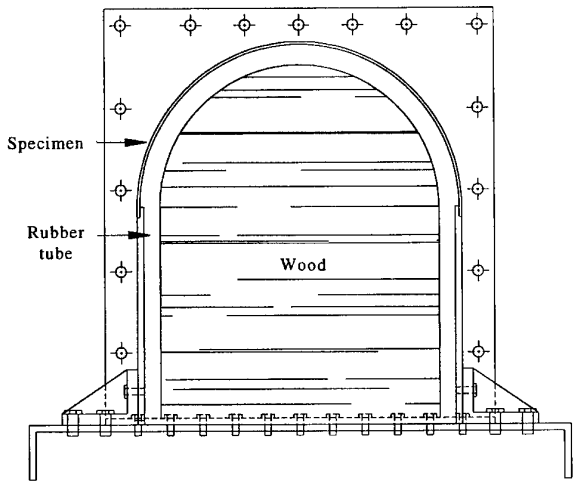

(b)

Fig. 2. Tester for the adhesively bonded lap joint for the composite–steel shell structure: (a) photograph and (b) schematic drawing.

the octahedral shear stress for any stress state equals or exceeds the octahedral shear stress for the simple tension-test specimen at failure [11]. The von Mises yield criterion is expressed as follows

$$\left[\frac{(\sigma_1-\sigma_2)^2+(\sigma_2-\sigma_3)^2+(\sigma_3-\sigma_1)^2}{2}\right]^{1/2}/\sigma_y \geq 1 \tag{3}$$

where σ_y is the yield strength of the adhesive.

The thickness of the steel side plates was determined from the bending stiffness of the prototype train section. Figure 6 shows the section of the prototype steel train.

The bending stiffness (EI) is expressed as follows.

$$EI = E\frac{bh^3}{12} \tag{4}$$

where E is the stiffness of the material, I is the second moment of inertia, b is the width of the section and h is the height of the section.

The side walls of real trains are usually manufactured with a hollow section. To estimate the thickness of the steel side plates, if the side walls of the real train had been manufactured with a solid section, the equivalent bending stiffness of the section was calculated as follows

$$E_h I_h = E_s I_s \tag{5}$$

where $E_h I_h$ is the stiffness of the steel hollow

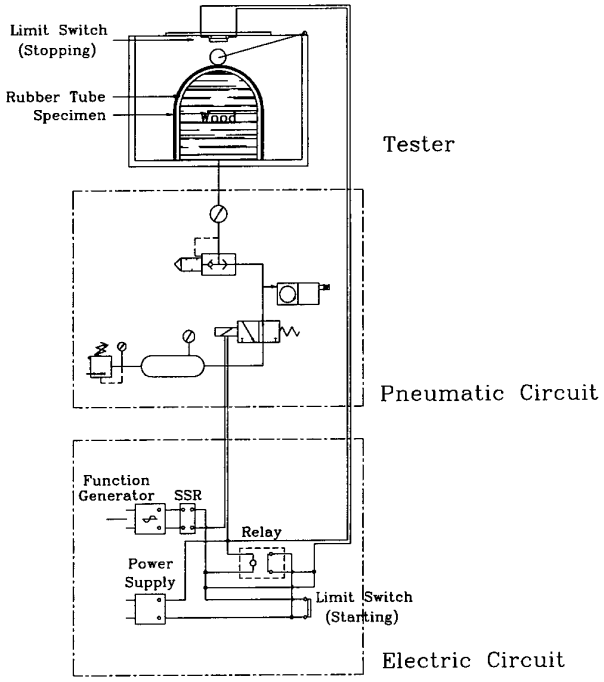

Fig. 3. Pneumatic and electrical circuits for the tester.

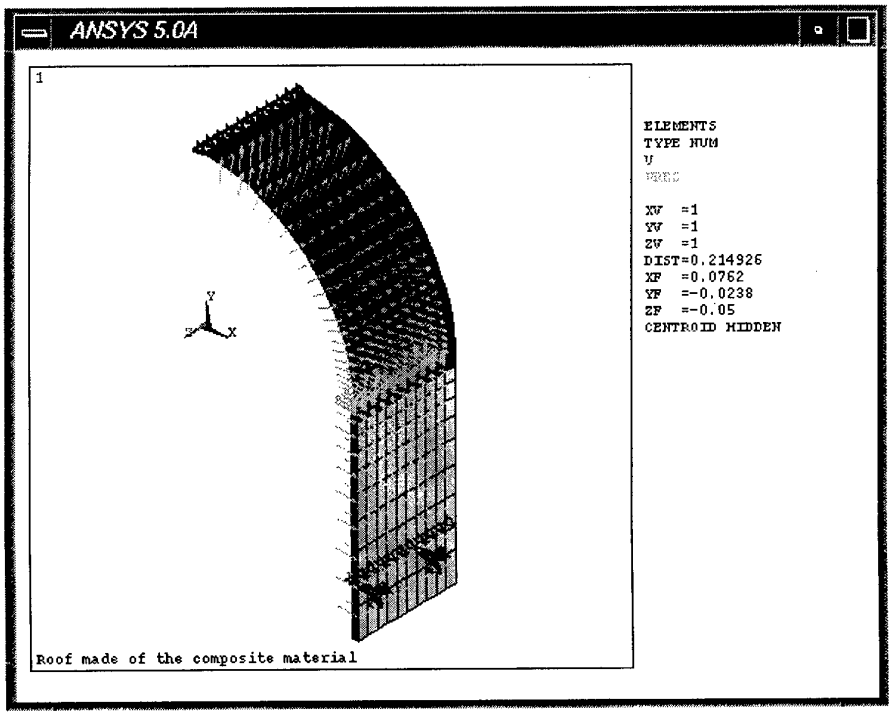

Fig. 4. Finite-element meshes and boundary conditions for the specimen.

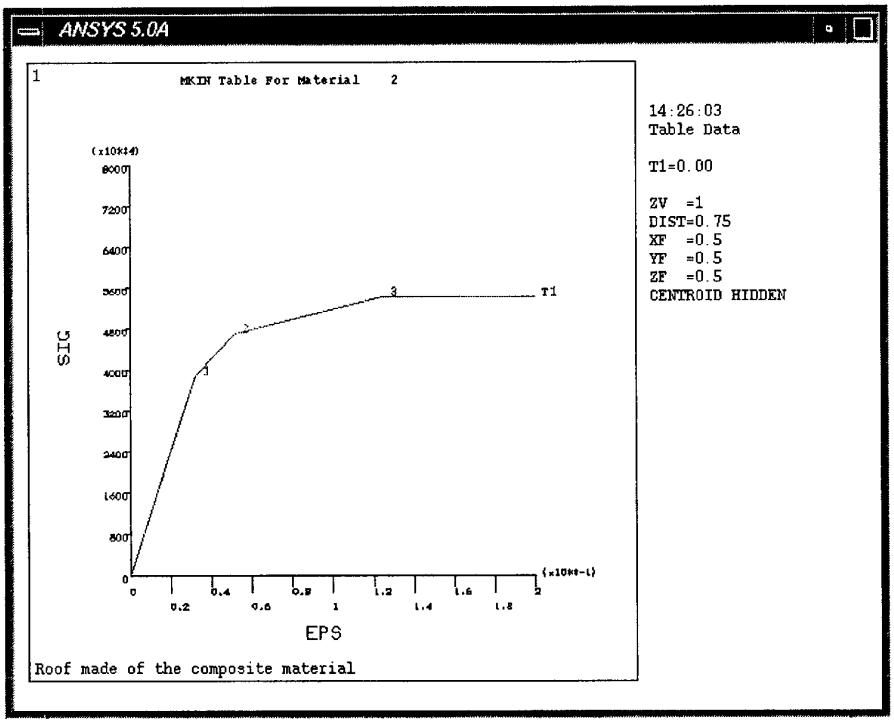

Fig. 5. Calculated multi-linear tensile stress–strain curve for the epoxy adhesive.

section of the prototype train and E_sI_s is the equivalent stiffness of the steel solid section of the prototype train.

Then the 1/10-size of the thickness of the prototype solid steel train was chosen as the thickness of the model section. Although the thickness of the 1/10-size train was 5.3 mm, a 5.5 mm thickness was chosen for the reliable manufacturing of the specimen.

Figure 7 shows the analysis results with respect to the stacking sequences for the adhesively bonded inner single lap-joint specimens, with 5.5 mm thick steel side plates, when the internal pressure was 0.42 MPa. The stacking sequences were $[\pm\theta]_{4S}$ ($\theta = 0$–$90°$).

In Fig. 7 the Ye-delamination index decreased as the stacking angle increased, and it was higher than both the Tsai–Wu failure index and the von Mises failure index at $\theta = 0$–$50°$. The Ye-delamination index was influenced by the peel stress and interlaminar shear stress of the joining area due to the internal air pressure.

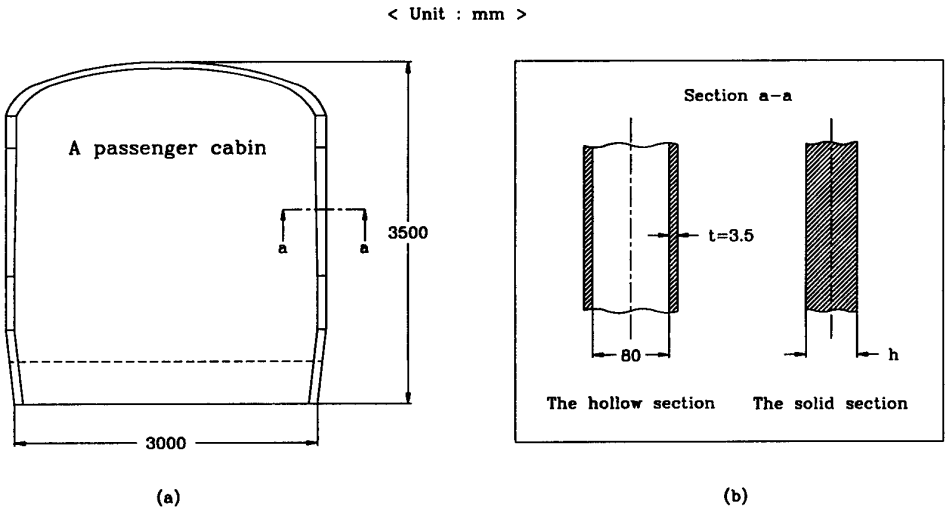

Fig. 6. Cross-section of the train; (b) cross-section of the a–a section.

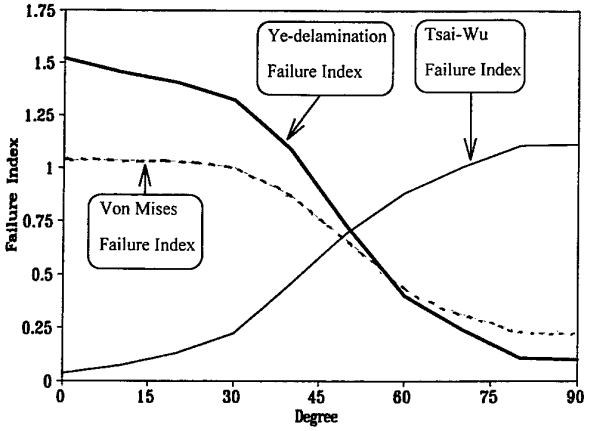

Fig. 7. Failure indices with respect to the stacking sequences for the adhesively bonded inner single lap-joint specimen (carbon–epoxy composite roof).

From these results, it was concluded that the specimen would fail by interlaminar delamination at $\theta = 0$–$50°$.

The Tsai–Wu failure index increased as the stacking angle increased. At $\theta = 50$–$90°$, the Tsai–Wu failure index was higher than both the Ye-delamination index and the von Mises failure index, and it was concluded that the specimen would fail by in-plane failure. The Tsai–Wu failure index was greatly influenced by hoop stress that was distributed on the composite roof because the hoop strength of the composite roof was low when the stacking angle was large. Because the von Mises failure index was relatively low compared with both the Ye-delamination index and the Tsai–Wu failure index, it was concluded that the adhesive would not fail.

Figure 8 shows the analysis results with respect to the stacking sequences for the adhesively bonded outer single lap-joint specimens with 5.5 mm thick steel side plates. The stacking sequences were the same as those for the adhesively bonded inner single lap-joint specimens.

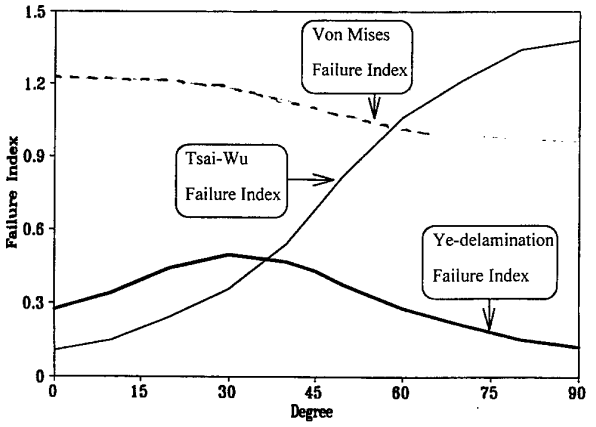

Fig. 8. Failure indices with respect to the stacking sequences for the adhesively bonded outer single lap-joint specimen (carbon–epoxy composite roof).

The Ye-delamination index was lower than the von Mises failure index at all stacking sequences and lower than the Tsai–Wu failure index at the stacking sequences $[\pm\theta]_{4S}$ ($\theta = 40$–$90°$). In this joining type, low peel stress and interlaminar shear stresses were found. From these results it was concluded that the specimen would not fail by interlaminar delamination. The Tsai–Wu failure index was larger than the other indices at the stacking sequences $[\pm\theta]_{4S}$ ($\theta = 60$–$90°$). At these stacking sequences the hoop strength of the composite roof was low when the stacking angle was large. Therefore, the specimen would fail by in-plane failure. The von Mises failure index was larger than the other indices at the stacking sequences $[\pm\theta]_{4S}$ ($\theta = 0$–$60°$). At these stacking sequences high interfacial shear stresses between the adhesive and the composite roof were found. From these results it was concluded that the specimen would fail by the failure of the adhesive itself or the interfacial failure between the adhesive and the composite roof.

From the analysis results, with respect to the stacking sequences, it was concluded that a suitable stacking angle was at $\theta = 40$–$60°$, irrespective of the type of join.

In order to investigate whether the 5.5 mm thick steel side plates were suitable for the stacking angle of $\theta = 40$–$60°$, the analyses for the specimens with the stacking sequence $[\pm 45°]_{4S}$ were performed with respect to the thicknesses of the steel side plates.

Figure 9 shows the analysis results with respect to the thickness ratios for the adhesively bonded inner single lap-joint specimens. The thickness ratio was defined as follows

$$t_R = \frac{\text{Thickness of the steel side plates}}{\text{Thickness of the composite roof}} \qquad (6)$$

The Ye-delamination index was larger than the Tsai–Wu failure index and the von Mises failure index at all thickness ratios. The Ye-delamination index was influenced by the peel stress and the interlaminar shear stress when the thickness ratio, t_R, was less than 2.29 and greatly influenced by the interlaminar shear stress when t_R was larger than 2.29. Therefore, the specimen with the 5.5 mm thick steel side

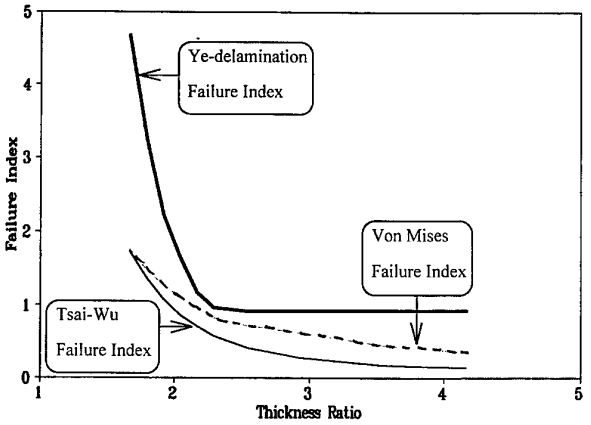

Fig. 9. Failure indices with respect to the thickness ratios for the adhesively bonded inner single lap-joint specimen (carbon–epoxy composite roof; stacking sequence: $[\pm 45°]_{4S}$).

plates was appropriate for the stacking sequence of $[\pm 45°]_{4S}$, from which it was concluded that the specimens would fail by interlaminar delamination.

Figure 10 shows the analysis results with respect to the thickness ratios for the adhesively bonded outer single lap-joint specimens.

The von Mises failure index was larger than both the Tsai–Wu failure index and the Ye-delamination index at all thickness ratios. The von Mises failure index was influenced by the peel stress and the interfacial shear stress between the adhesive and the composite roof when t_R was less than 2.29 and greatly influenced by the interfacial shear stress when t_R was larger than 2.29. Therefore, the specimen with the 5.5 mm thick steel side plates was appropriate for the stacking sequence $[\pm 45°]_{4S}$, from which it was concluded that the specimens

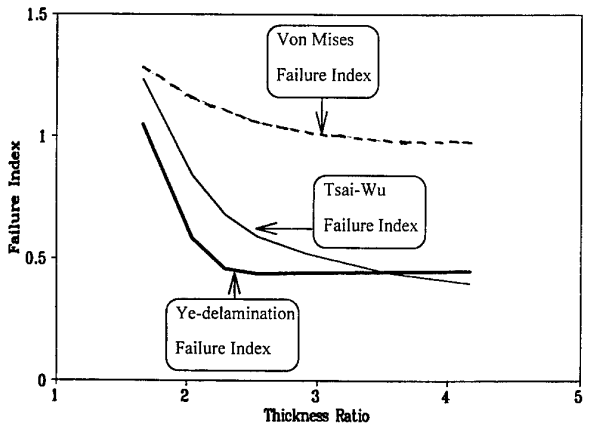

Fig. 10. Failure indices with respect to the thickness ratios for the adhesively bonded outer single lap-joint specimen (carbon–epoxy composite roof; stacking sequence: $[\pm 45°]_{4S}$).

would fail by interfacial failure between the adhesive and the composite roof.

From the analysis results with respect to the thickness ratios, it was concluded that the effective thickness ratio for the adhesively bonded inner single lap-joint specimen and the adhesively bonded outer single lap-joint specimen was 2.29.

EXPERIMENTAL RESULTS AND DISCUSSION

Static test

Three different failures, interlaminar delamination, interfacial and in-plane failure, were observed in the tests. Figure 11 shows photographs of the failed specimens for each failure types. The failure in Fig. 11(a) was caused by interlaminar delamination due to the high peel stress between the plies of the composite roof. The peel stress was produced by the bending moment due to the internal pressure. The failure in Fig. 11(b) was caused by the high peel stress between the adhesive and the composite roof in the joining section. The peel stress was also produced by the bending moment due to the internal pressure. The failure in Fig. 11(c) was caused by the low hoop strength of the composite roof. The low hoop strength was caused by the large stacking angle of the composite roof.

Table 3 compares the failure characteristics of two different types of adhesively bonded single lap-joints when the stacking sequence and thickness ratio were $[\pm 45°]_{4S}$ and 2.29, respectively, which gave the highest strength in the analyses. Looking at the sections of the fractured specimens, it was found that the adhesively bonded inner single lap-joint specimens failed as a result of interlaminar delamination. The joining area of the composite roof was subjected to a bending moment due to the internal pressure, which produced a peel stress in the lower side of the joint and a compressive stress in the upper side of the joining area. Interlaminar shear stresses were also produced in the joining area. The composite roof failed in the delamination mode because of the peel stress and the interlaminar shear stress in the lower side of the joining area. However, the interface between the adhesive and the composite roof, as well as the adhesive itself, was not affected. On the contrary, the adhesively bon-

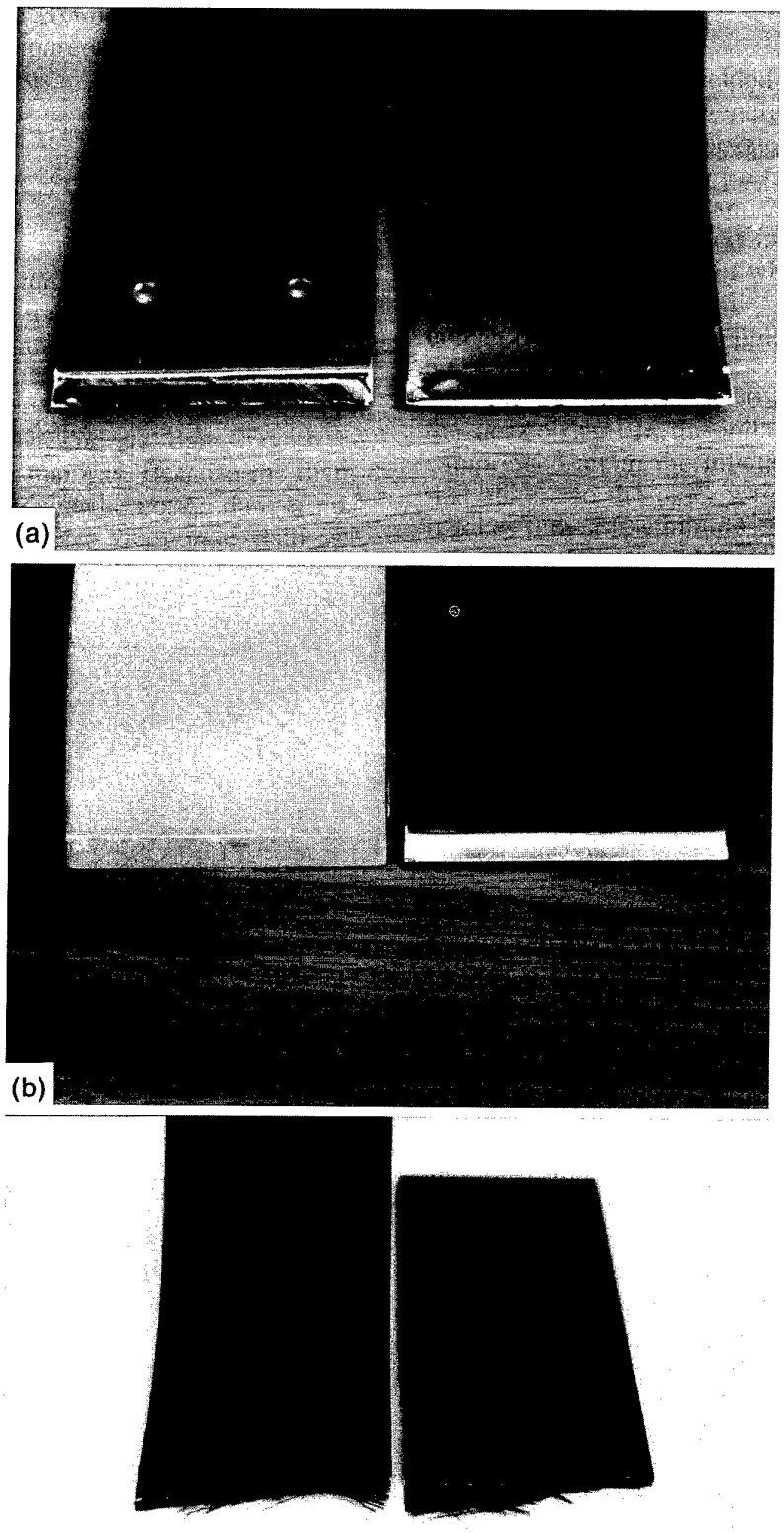

Fig. 11. Specimens fractured by: (a) interlaminar delamination (carbon–epoxy composite roof; stacking angle: $[\pm 45°]_{4S}$): (b) interfacial failure between the adhesive and the composite roof (glass–epoxy composite roof; stacking angle: $[\pm 45°]_{4S}$); (c) in-plane failure (carbon–epoxy composite roof; stacking angle: $[\pm 80°]_{4S}$).

Table 3. Failure pressure of the adhesively bonded single lap-joints

Type of specimen	Bonding length (mm)	Inner single lap-joint (MPa)	Outer single lap-joint (MPa)
Carbon composite	10	0.42 (interlaminar delamination)	0.13 (interfacial failure)
	20	> 0.75 (no failure)	0.18 (interfacial failure)
Glass composite	10	0.40 (interlaminar delamination)	0.08 (interfacial failure)
	20	> 0.75 (no failure)	0.16 (interfacial failure)

ded outer single lap-joint specimens failed because of the interfacial failure between the adhesive and the composite roof caused by the high peel stress and the interlaminar shear stress due to the bending moment. The peel and interlaminar shear stresses were relatively small in the composite roof. Therefore, it was concluded that the adhesively bonded inner single lap-joint type was a better joining method than the adhesively bonded outer single lap-joint type.

Table 3 shows the failure pressures of the adhesively bonded single lap-joints. From Table 3 it was concluded that the joint strength of the glass–epoxy specimens was almost same as that of the carbon–epoxy specimens. Therefore, further tests were concentrated on the adhesively bonded inner single lap-joint specimens with the carbon–epoxy composite roof. The maximum internal pressure was limited to 0.75 MPa for test safety.

Figure 12 shows the test results with respect to the stacking sequences of the composite roof of the adhesively bonded inner single lap-joint specimens with 10 and 20 mm bonding lengths and 5.5 mm thick steel side plates. From Fig. 12, the strength of the specimens was low at the $[\pm 10°]_{4S}$ stacking angle because of the high bending stiffness of the composite roof. The strength of the specimens was increased as the stacking angle was increased until the $[\pm 45°]_{4S}$ stacking angle and decreased beyond this stacking angle because the bending stiffness of the composite roof was comparable to that of the steel side plates. From these results it was concluded that the high bending stiffness of the composite roof produced a high peel stress at the joining area. Therefore, interlaminar delamination failure occurred up until the $[\pm 60°]_{4S}$ stacking angle and composite failure occurred at the $[\pm 80°]_{4S}$ stacking angle due to the low hoop strength of the composite roof.

Figure 13 shows the test results with respect to the stacking angles of the adhesively bonded double lap-joint specimens. The strength of the specimens was similar to that of the adhesively

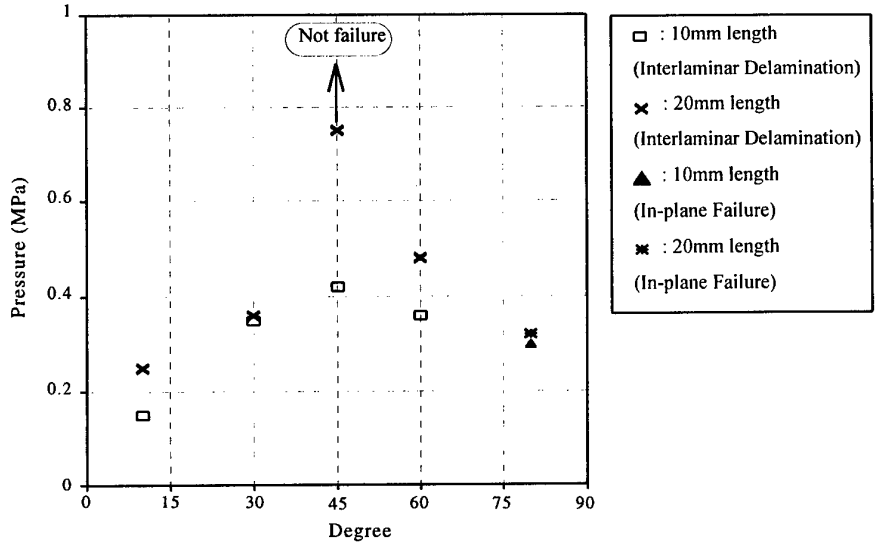

Fig. 12. Test results with respect to the stacking angles of the composite roof for the adhesively bonded inner single lap-joint specimen (carbon–epoxy composite roof; thickness ratio: 2.29).

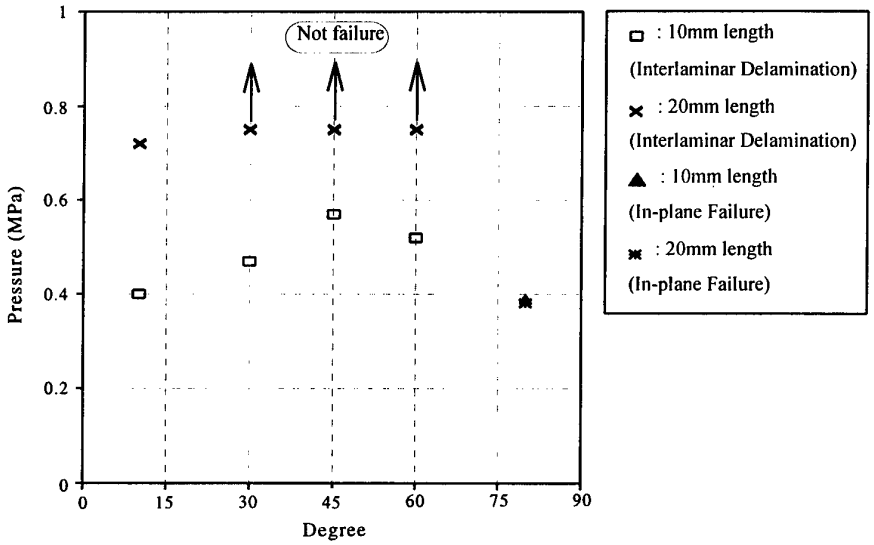

Fig. 13. Test results with respect to the stacking angles of the composite roof for the adhesively bonded double lap-joint specimen (carbon–epoxy composite roof; thickness ratio: 3.58).

bonded inner single lap-joint specimens. The strength was at a maximum at the $[\pm 45°]_{4S}$ stacking angle. Interlaminar delamination failure occurred up until the $[\pm 60°]_{4S}$ stacking angle and composite failure occurred at the $[\pm 80°]_{4S}$ stacking angle.

The specimens were also tested with respect to the thickness ratios of the steel side plates. Figure 14 shows the test results with respect to the thickness ratios of the adhesively bonded inner single lap-joint specimens. From Fig. 14, the strength of the specimens was very low at $t_R = 1.67$. Because the bending stiffness of the steel side plates was small at $t_R = 1.67$, the steel side plates were observed to be quite significantly bent. Therefore, it was concluded that the low strength of the specimen at $t_R = 1.67$ was caused by the high peel stress of the joining area. But as the bending stiffness of the steel side plates was comparable to that of the composite roof at $t_R = 2.29$, the strength of the specimens was much increased due to the low peel stress. Above $t_R = 2.29$, the peel stress of the joining area did not much affect the strength of the specimens but the interlaminar shear stresses did affect the strength of the specimens. Because the interlaminar shear stress did not vary much when the thickness was

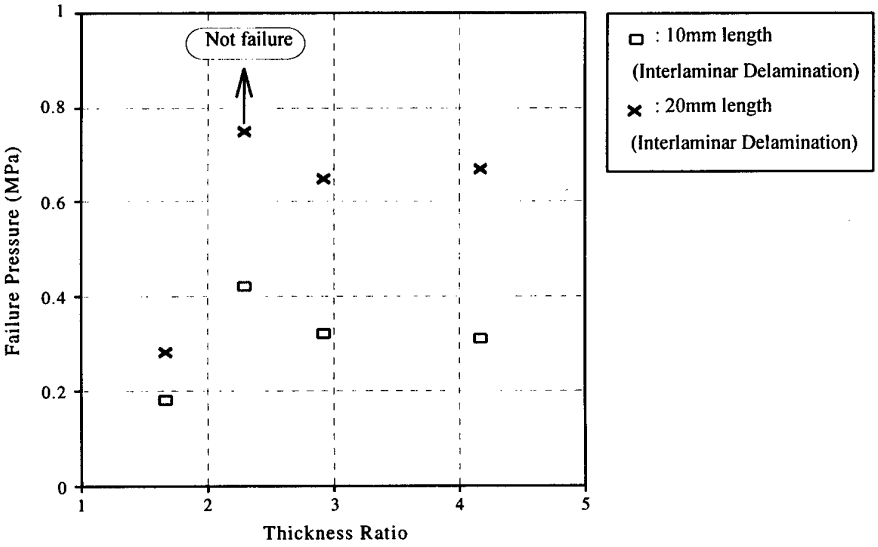

Fig. 14. Test results with respect to the thickness ratios for the adhesively bonded inner single lap-joint specimen (carbon–epoxy composite roof; stacking angle: $[\pm 45°]_{4S}$).

large, the strength of the specimens was almost constant when the thickness ratio was greater than 2.92.

Figure 15 shows the test results with respect to the thickness ratios of the adhesively bonded double lap-joint specimens. The strength of the adhesively bonded double lap-joint specimens was similar to that of the adhesively bonded inner single lap-joint specimens. The strength of the specimens was a maximum at $t_R = 3.58$ which is when interlaminar delamination failure occurred.

Dynamic test

One of the most important subjects in the design of car-body structure is to sustain the outer pressure fluctuation. As the speed of trains increases, the outer pressure fluctuation increases proportionally to car velocity squared when the train passes through tunnel. Therefore, requirements were established for car-body design as follows [1].

1. For static air pressure load: −0.02 to 0.013 MPa. (Two trains pass each other in a tunnel at a velocity of 550 km/h.)
2. For cyclic air pressure load range: −0.017 to 0.011 MPa. Number of cycles: 100,000. (Two trains pass each other in a tunnel at a velocity of 500 km/h.)

In Korea, Saemaul Express Trains make one round trip a day between Seoul and Pusan with 17 tunnels, which is about 450 km with a speed of about 100 km/h. For the dynamic internal pressure test, the cyclic air pressure load range and the number of cycles were established as follows.

1. For cyclic air pressure load range: 0–0.1 MPa (a more severe test condition than the general requirement).
2. The number of cycles: TU × TB × DA × YE × $n \fallingdotseq$ 200,000 cycles (a more severe test condition than the general requirement), where TU (the number of tunnels) = 17, TB (there and back) = 2, DA (days per year) = 365, YE (estimated life of the train in years) = 10, n (safety factor) = 1.6.

The specimens with the carbon composite roof and the glass composite roof were dynamically tested under 0.1 MPa internal pressure with a 10 s period. The composite roof specimens that were adhesively bonded with 10 and 20 mm bonding lengths did not fail until 200,000 cycles were completed. Therefore, it was concluded that all of the specimens were suitable for the car-body subjected to dynamic pressure.

CONCLUSIONS

In order to investigate the adhesive joining method between the composite roof and the steel side plates of trains, 1/10-size models of the real train were designed and tested under static and dynamic internal pressures. From the tests, the following conclusions were made.

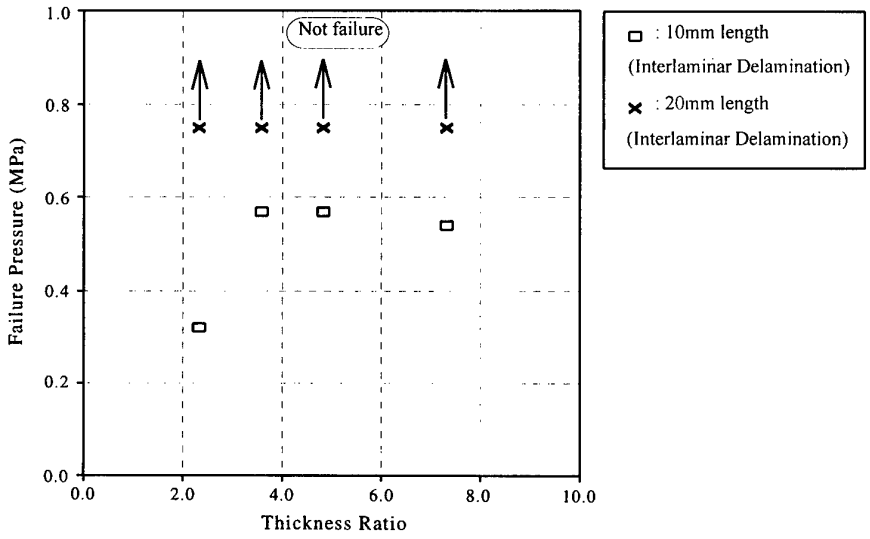

Fig. 15. Test results with respect to the thickness ratios for the adhesively bonded double lap-joint specimen (carbon–epoxy composite roof; stacking angle: $[\pm 45°]_{4S}$).

1. The optimal joining method between the composite roof and the steel side plates was an adhesively bonded inner single lap-joint type.
2. The stacking sequence $[\pm\theta]_{4S}$ ($\theta = 40$–$60°$) of the composite roof was chosen for the optimum stacking sequence when the thickness ratio was 2.29. At the stacking sequence $[\pm 45°]_{4S}$, it was found that the optimum thickness ratios for the adhesively bonded inner single lap-joint specimen and the adhesively bonded double lap-joint specimen were 2.29 and 3.58, respectively.
3. From the static and dynamic test results, the joining strengths of the specimens made with carbon fiber and glass fiber composite roofs were similar.

REFERENCES

1. Tagawa, N., Yamashiro, H. and Kadota, K., Development of new car-body structure for high speed train. *Proc. Int. Conf. on Speed-up Technology for Railway and Maglev Vehicles*, 1993, **1**, 477–481.
2. Suzuki, T., Satoh, K. and Akutsu, K., Weight reduction of a railway car-body shell by applying new materials. *Proc. Int. Conf. on Speed-up Technology for Railway and Maglev Vehicles*, 1993, **1**, 459–463.
3. Matsuoka, S. and Nakamura, T., Development of carbon fiber reinforced plastic car-body shell. *Proc. Int. Conf. on Speed-up Technology for Railway and Maglev Vehicles*, 1993, **1**, 464–468.
4. Lewis, J.H., Development of crash-worthy vehicle structures for railways. *Proc. World Congr. on Railway Research*, 1994, **2**, 893–900.
5. Thornton, P.H. and Jeryan, R.A., Crash energy management in composite automotive structures. *Int. J. Impact Engng*, 1988, **7**, 167–180.
6. Larrode, E., Miravete, A. and Fernandez, F.J., A new concept of a bus structure made of composite materials by using continuous transversal frames. *Composite Struct.*, 1995, **32**, 345–356.
7. Reinhart, T. J., *Composites*. ASM International, Metals Park, OH, 1987, pp. 479–95.
8. Lee, S.J. and Lee, D.G., Optimal design of the adhesively-bonded tubular single lap joint. *J. Adhesion*, 1995, **50**, 165–180.
9. Gibson, R. F., *Principals of Composite Material Mechanics*. McGraw-Hill, New York, 1994, pp. 110–12.
10. Chen, W.H. and Lee, S.S., Numerical and experimental failure analysis of composite laminates with bolted joints under bending loads. *J. Composite Mater.*, 1995, **29**, 15–36.
11. Shigley, J. E. & Mischke, C. R., *Mechanical Engineering Design*, 5th edn. McGraw-Hill Mechanical Engineering Series, New York, 1989, pp. 243–6.

ELSEVIER

Composite Structures Vol. 38, No. 1–4, pp. 229–239, 1997
© 1997 Elsevier Science Ltd. All rights reserved
Printed in Great Britain
0263-8223/97/$17.00 + 0.00

PII:S0263-8223(97)00058-5

Composite side-door impact beams for passenger cars

Seong Sik Cheon,[a] Dai Gil Lee[a] & Kwang Seop Jeong[b]

[a]*Department of Mechanical Engineering, Korea Advanced Institute of Science and Technology, Taejon 305-701, Korea*
[b]*Department of Textile Engineering, Yeungnam University, Kyongsan 712-749, Korea*

The fuel efficiency and emission gas regulation of passenger cars are two important issues nowadays. The best way to increase fuel efficiency without sacrificing safety is to employ fibre-reinforced composite materials in the body of cars because fibre-reinforced composite materials have higher specific strengths than those of steel.

In this study, the side-door impact beam for passenger cars was developed using glass-fibre-reinforced composite materials as metals usually have a lower capacity of impact absorption energy at low temperature compared with that of glass-fibre-reinforced composite materials. Static tests were carried out to determine the optimum fibre stacking sequences and cross-sectional thickness for the composite impact beams taking consideration of the weight saving ratio compared to the high strength steel.

Dynamic tests were carried out at several different temperatures using the pneumatic impact tester, which was developed to investigate the dynamic characteristics of impact beams at a speed of 30 mph. Also, finite-element analyses were performed using ABAQUS, a commercial software to compare the simulated characteristics of the impact beams with the experimental results.

From the comparison, it was found that the results from the finite-element analyses showed good agreement with the experimental results, although several assumptions were made in the finite-element analyses. © 1997 Elsevier Science Ltd.

INTRODUCTION

Fibre-reinforced composite materials have been used in aircraft and space vehicles as they have high specific strength (strength/density) and high specific stiffness (stiffness/density) [1]. They also have high damping [2] and impact characteristics [3]. As the price of composites has fallen, they are now widely used for sport goods, leisure supplies, machine tools and in the structure of automobiles [4,5]. Reports from the United States and Canada predicted that plastics and composites would be widely applied to body panels, bumper systems, flexible components, trims, driveshaft and transparent parts of cars [6–8]. Also, rotors manufactured using RTM (resin transfer moulding) for air compressors or superchargers of cars have been used to substitute for metal rotors which are difficult to machine [9]. Composites have also been used to substitute flexspline materials in harmonic drives or traction drives [10,11]. In industrial robots, in particular, stiffness is very important and an increase in the robot stiffness leads to an increase in the body weight, which reduces the payload of a robot. Therefore, composites were tried in the body of SCARA-type [12] or anthropomorphic robots [13]. As mentioned above, substitutions using composites for existing metal structures have been widely tried and successfully achieved in several cases.

The weight of cars has been continuously reduced to increase the fuel efficiency, which sacrifices the safety of cars. The best way to increase the fuel efficiency of cars without sacrificing safety is to employ fibre-reinforced composite materials in the body of cars because the fibre-reinforced composite materials have a

higher specific strength compared to that of metals. Because glass-fibre-reinforced and aramid-fibre-reinforced composites have high impact energy absorption characteristics, a car body made of these composite materials would bring about an increase in fuel mileage and a reduction in human body injuries when accidents occur.

In this study side-door impact beams, which require a large impact energy absorption capability, were manufactured using glass-fibre–epoxy composites. Design parameters such as fibre stacking sequence and cross-sectional thickness were selected and determined in order to manufacture composite impact beams. Moreover, various cross-sectional shapes of composite impact beams were designed to prevent local collapse as composites have a tendency to buckled at low level of external load owing to local collapse by concentric loads. Moulds for composite impact beams were fabricated and the prototype composite impact beams were manufactured. Three-point static bending tests were performed for the steel and composite impact beams.

Although the static energy absorption of composite beams was low, because composites usually have low failure strains compared with those of metals, the dynamic impact energy absorption of composites are high due to fibre pull-out, matrix cracking and delamination.

Because the dynamic energy absorption of side-door impact beams is more important than the static energy absorption, a pneumatic impact tester, whose impact velocity was 30 mph, was developed to investigate the dynamic behaviour of steel and composite impact beams. With the developed impact tester, the dynamic energy absorption of steel and composite impact beams was investigated at several low temperatures, as well as room temperature.

Also, numerical analyses using ABAQUS/Standard, a commercial finite-element analysis package developed by H.K.S. Inc. (Hibbitt, Karlsson and Sorensen Inc.), were performed to compare the numerical results with the experimental ones.

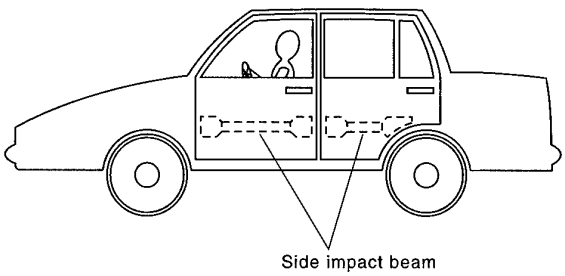

Fig. 1. Shape and mounting configuration of the side-door impact beams.

DESIGN PARAMETERS FOR COMPOSITE IMPACT BEAMS

Figure 1 shows the shape and mounting configuration of the side-door impact beams. The lengths of the front-door impact beam and the rear-door impact beams for compact passenger cars were 803 mm and 507 mm, respectively.

To manufacture the composite impact beams, design parameters such as the type of composite materials, stacking sequences [14], shape and the thickness of cross-sections should be determined. Table 1 shows the mechanical properties of high strength steel and glass-fibre–epoxy composites [3]. Consulting the Charpy impact energy absorption in Table 1, the glass-fibre–epoxy composite was selected for the impact beam material. Also, compositions of high strength steel (AISI 4340) for steel impact beams are shown in Table 2 [15]. The stacking sequences of the beam were determined using the results of the three-point static bending tests.

Table 1. Properties of high strength steel and glass-fibre–epoxy composites

	High strength steel (AISI 4340) [3]	Glass-fibre–epoxy composites
Charpy impact (kJ/m^2) [3]	214	622
Density (kg/m^3)	7870	1980
E_x (GPa)	210	43.5
E_y (GPa)	210	5
v_{xy}	0.3	25
G_{xy} (GPa)	80.8	5
X^t (GPa)	1.5	1.0

Table 2. Compositions of AISI 4340 steel [15]

	C	Mn	P	S	Si	Ni	Cr	Mo
AISI 4340	0.38–0.43	0.60–0.80	0.035	0.040	0.15	1.65–2.00	0.70–0.90	0.20–0.30

Five different stacking sequences, such as $[0°]_{nT}$, $[\pm 15°]_{nT}$, $[0_2°/90°]_{nT}$, $[0_3°/90°]_{nT}$ and $[0_{16}°/90_4°]_T$, for the glass-fibre–epoxy composite impact beams were selected. The mass of each of the 507 mm impact beams was 0.25 kg and the cross-sectional shapes of each of the impact beams was circular. The outside and inside diameters of the composite impact beam were 31.8 mm and 26.3 mm, respectively. The longitudinal or axial direction was designated to be 0°. The three-point static bending tests were carried out using Instron 4206 to determine the optimum stacking sequences for the composite impact beams. The jig span and diameter of the loading cylinder for the three-point static bending tests were 250 mm and 25.4 mm, respectively. Figure 2 shows the results of the three-point static bending tests.

From Fig. 2 it was found that $[0°]_{nT}$ angle could not effectively sustain external load because of its low strength under hoop stress. In the case of $[0_{16}°/90_4°]_T$, the 0° fibre could not withstand the hoop stress after the 90° fibre yielded. Therefore, it was found that the 90° fibre should be uniformly placed through the entire cross-section of the composite impact beams. The stacking sequences of $[\pm 15°]_{nT}$ and $[0_2°/90°]_{nT}$ showed similar behaviour; however, the latter was desirable because of the ease of cutting and handling the prepreg. Finally, an additional 0° layer was included to enhance the bending stiffness, resulting in the stacking sequence $[0_3°/90°]_{nT}$.

Composites have a tendency to buckle by concentrated loads which give rise to local collapse, consequently fracture would occur at relatively low external loads. Therefore, various cross-sectional shapes, such as shown in Fig. 3, for prohibiting local collapse were devised.

The impact beam (a) in Fig. 3 has a hollow circular cross-section, (b) has a regular square cross-section, (c) is a composite wrapped onto a low carbon circular steel tube, (d) is a composite wrapped onto a low carbon regular square steel tube, (e) is centre-part enhanced, (f) is a regular square cross-section strengthened by a rib and (g) is an I-type cross-section composite impact beam. Two different thicknesses for the impact beams were used to make the weights of the impact beams 50% and 70% weight ratios with respect to the high strength steel impact beams whose outer and inner diameters were

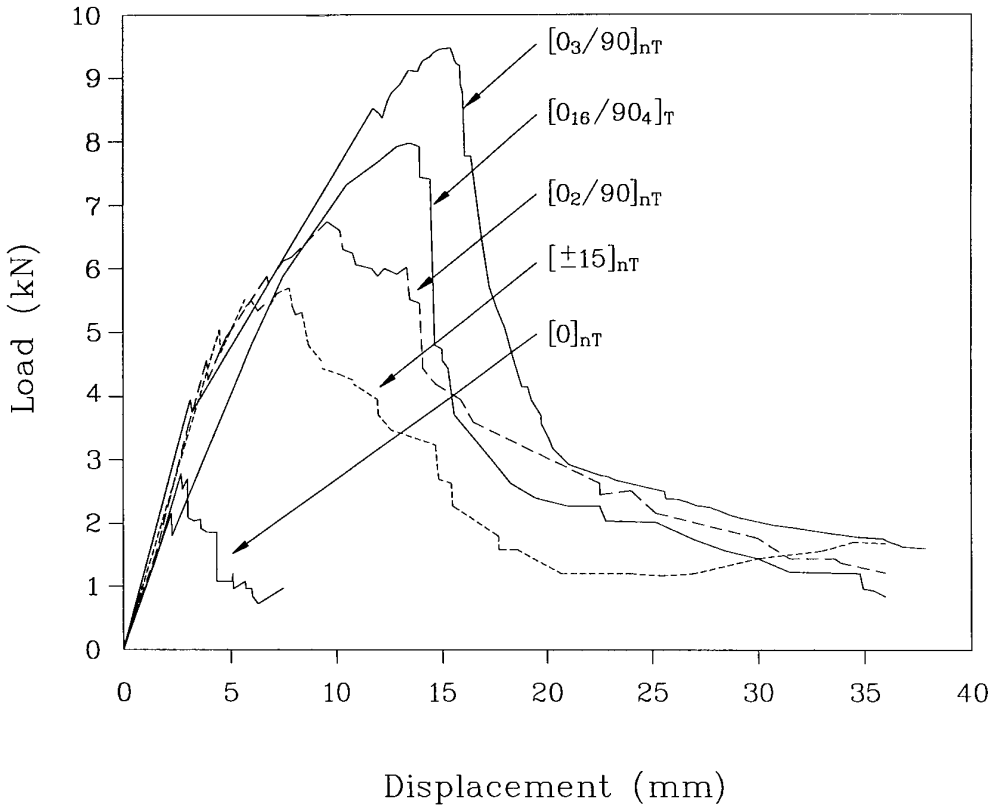

Fig. 2. Load vs displacement diagram of composite impact beams with respect to stacking sequences.

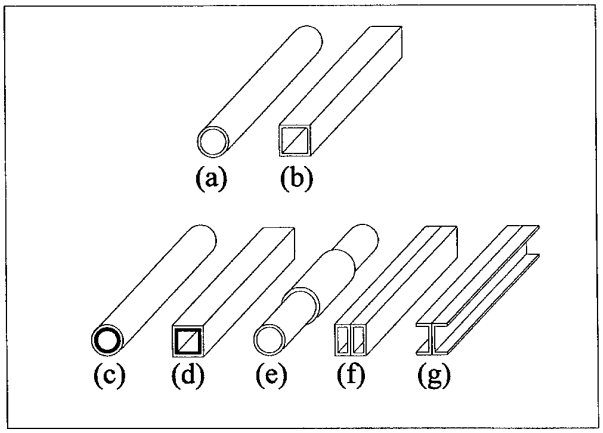

Fig. 3. Various cross-sectional shapes for the composite impact beams.

31.8 and, 27.4 mm, respectively. The mass and length of the high strength steel impact beam were 0.825 kg and 507 mm, respectively.

MANUFACTURE OF THE COMPOSITE IMPACT BEAMS

Moulds for the various cross-sectional shapes were designed and manufactured. The UGN 150 type uni-directional glass-fibre–epoxy prepreg fabricated by Sun Kyung Industry (Suwon, Korea) was used for the manufacture of composite impact beams by the autoclave–vacuum bag degassing method.

Figure 4 shows the manufacturing sequence for the circular composite impact beam. First, a non-porous Teflon sheet was wrapped on a steel mandrel as shown in Fig. 4(a). Then, the prepreg was cut to the appropriate size and angle and was stacked on the Teflon-sheet-wrapped mandrel, as shown in Fig. 4(b). After removing the mandrel, as shown in Fig. 4(c), the rolled prepreg was placed inside the bottom mould, as shown in Fig. 4(d). After assembling the upper and lower moulds, with bolts as shown in Fig. 4(e), the prepreg inside mould was cured in an autoclave after bagging the whole assembly with a vacuum bag, as shown in Fig. 4(f).

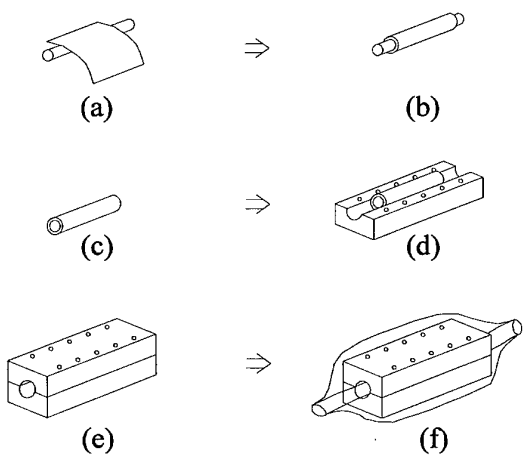

Fig. 4. Schematic diagram of the manufacturing sequence for the circular composite impact beams.

Figure 5 is a photograph of the manufactured circular cross-sectional composite impact beam which was adhesively bonded to the mounting brackets. After painting, the yellow–green colour of the glass-fibre–epoxy composite was changed to black.

The regular square composite impact beams were manufactured using the mould with a regular square cross-sectional shape. The manufacturing methods for the regular square cross-section composite beam strengthened by the rib, as well as the I-type cross-section composite impact beam, are shown in Fig. 6.

The regular square cross-section composite impact beam strengthened by the rib was manufactured by co-curing [16–18] a prepreg layer inserted between the interface and two prepreg layers both placed on the top and the bottom surfaces of the two rectangular composites already manufactured. A similar manufacturing method was used for the I-type cross-sectional composite impact beams.

Figure 7 shows the cure cycle used for the manufacture of the composite impact beams.

As shown in Fig. 7, the 30 min dwelling stage at 80°C was employed to promote consolidation between the plies of prepreg. Then the inside temperature of the autoclave was increased to 120°C to cure the prepreg. During the entire cure cycle a vacuum state was maintained inside the vacuum bag, while a 0.6 MPa air pressure was applied outside the vacuum bag. A photograph of the cross-sections of the manufactured composite impact beams of the types shown in Fig. 3(a), (b), (f) and (g) are shown in Fig. 8. The cross-sections of the impact beams were painted to enhance their visability.

STATIC BENDING TEST AND NUMERICAL ANALYSIS

The jigs and loading cylinders were prepared based on the FMVSS (Federal Motor Vehicle

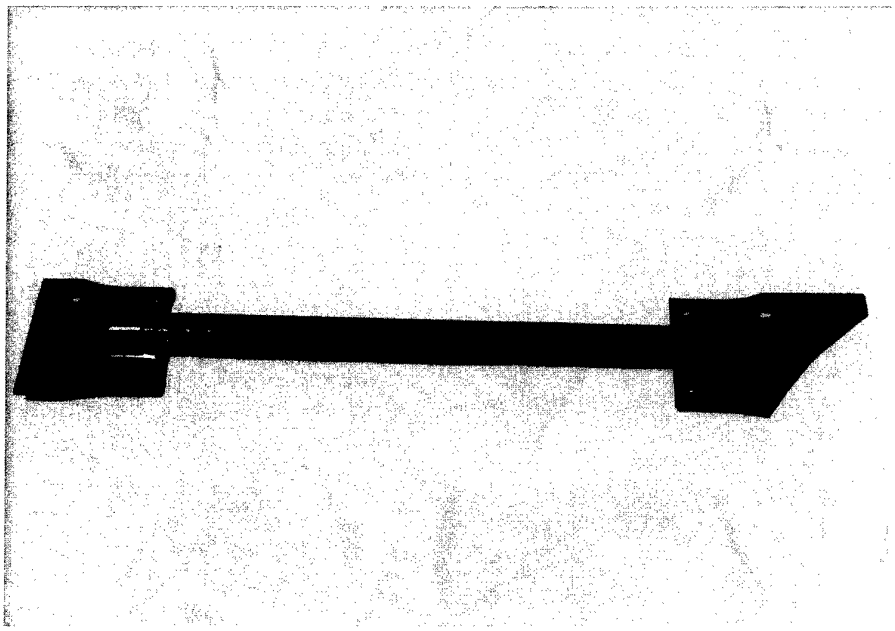

Fig. 5. Photograph of the circular cross-sectional composite impact beam bonded to the mounting brackets.

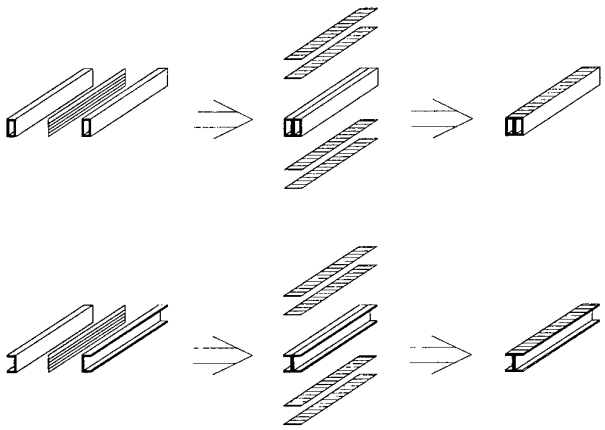

Fig. 6. Schematic diagram of the manufacturing methods for the regular square cross-section impact beam strengthened by the rib, as well as the I-type cross-section composite impact beams.

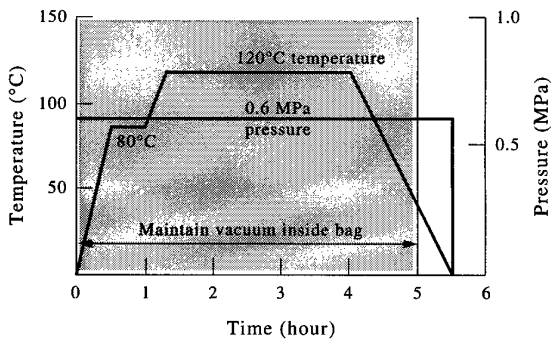

Fig. 7. Cure cycle for the glass-fibre–epoxy composites.

Safety Standards) 214 regulation which regulates the static properties of the side-doors of passenger cars. Figure 9 shows the jig for the three-point bending test of the impact beams.

As shown in Fig. 9, the jig span was set at 470 mm (18.5 in.), and two 25.4 mm (1 in.) diameter cylinders were used to support the impact beam. The load was given by an Instron 4206 through a 304.8 mm (12 in.) diameter half cylinder at the midpoint of the impact beam. The stacking sequence of all the composites was $[0_3°/90°]_{nT}$. Prototype composite impact beams were manufactured and tested with a weight ratio of 50% and 70% with respect to steel impact beams. From the experiments, it was found that the load-carrying capacity of the high strength steel impact beams was 27.3 kN, while the load-carrying capacity of the circular composite impact beams was 16.2 kN. The composite impact beam was collapsed locally by the concentrated load which was prominent at the circular cross-section. The regular square cross-section composite impact beams were able to resist a 25.3 kN external load because the contact area of the regular cross-section was larger than the circular cross-section. The impact beam manufactured by wrapping composite prepreg onto the circular low carbon steel yielded at low external load of 12.5 kN, which has not only low load-carrying capacity but also low weight saving effect due to the embedded steel. The composite impact beam which had an

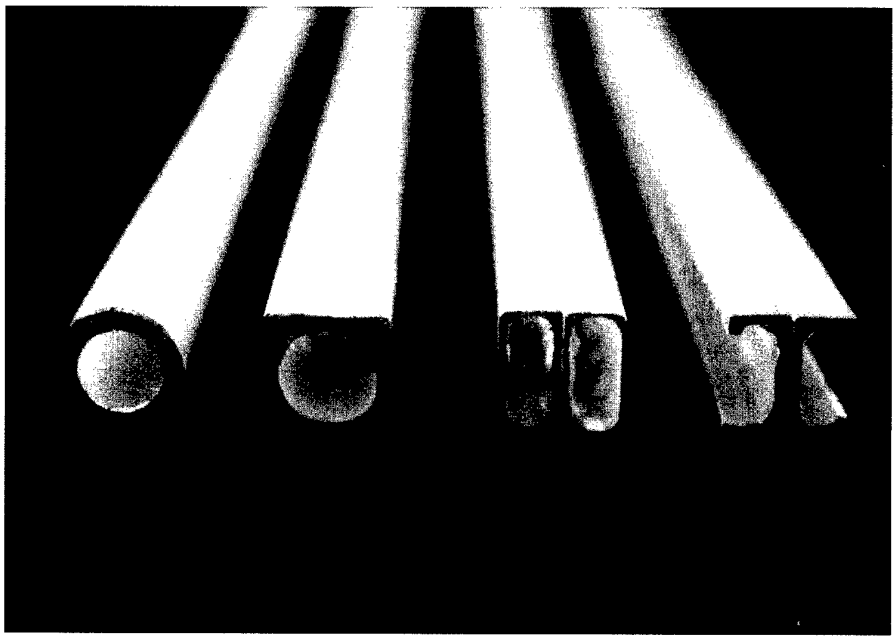

Fig. 8. Photograph of the cross-sections of the composite impact beams.

enhanced centre part also yielded at a relatively low external load of 17 kN. The centre-part size of the impact beam could not be increased beyond a certain limit because of the limitation of the mounting space. Therefore, the composite impact beam whose centre part was enhanced was shown to be irrelevant. The regular square cross-section composite impact beams strengthened by the rib could resist an external load of 27.1 kN, which is similar to that of the impact beam made of high strength steel. The I-type cross-section composite impact beams yielded at 25 kN, which was similar to the impact beams with the regular square cross-section. Figure 10 shows the static load-carrying capacity of the impact beams.

The load-carrying capacities of the impact beams were numerically analysed [19] using ABAQUS/Standard. The employed element both for the high strength steel and for the glass-fibre–epoxy composites was C3D8R (solid three-dimensional, eight nodes, reduced integration, hour-glass control) to prevent both shear locking and hour-glass mode. Only a quarter of the cross-section of the impact beam was modelled to include the contact phenomenon between the impact beam and the loading cylinder. The loading cylinder was assumed to

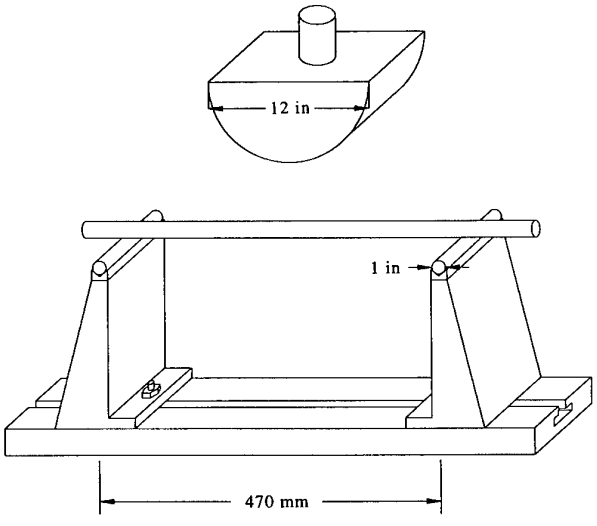

Fig. 9. Jig for the three-point static bending test.

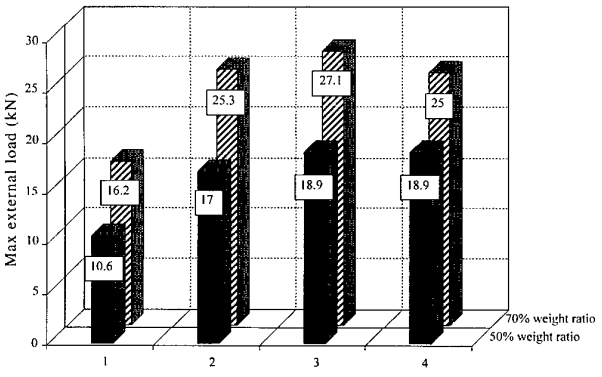

Fig. 10. Static load-carrying capacity of the composite impact beams of $[0_3°/90°]_{nT}$ stacking sequence. 1, Circular cross-section; 2, regular square cross-section; 3, regular square cross-section strengthened by a rib; and 4, I-type cross-section.

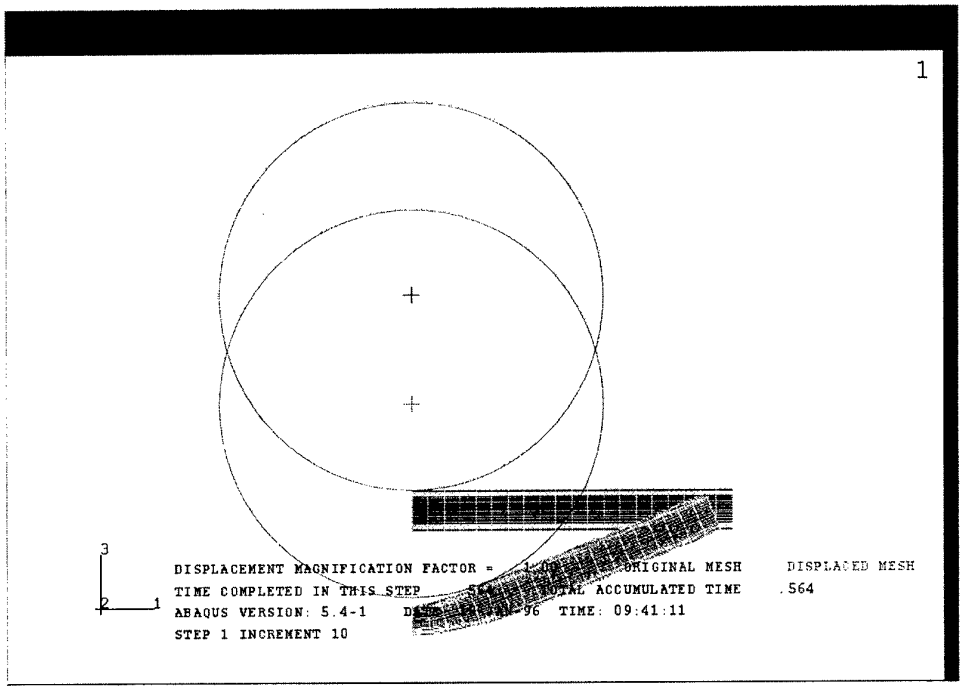

Fig. 11. Deformed shape of the steel impact beam.

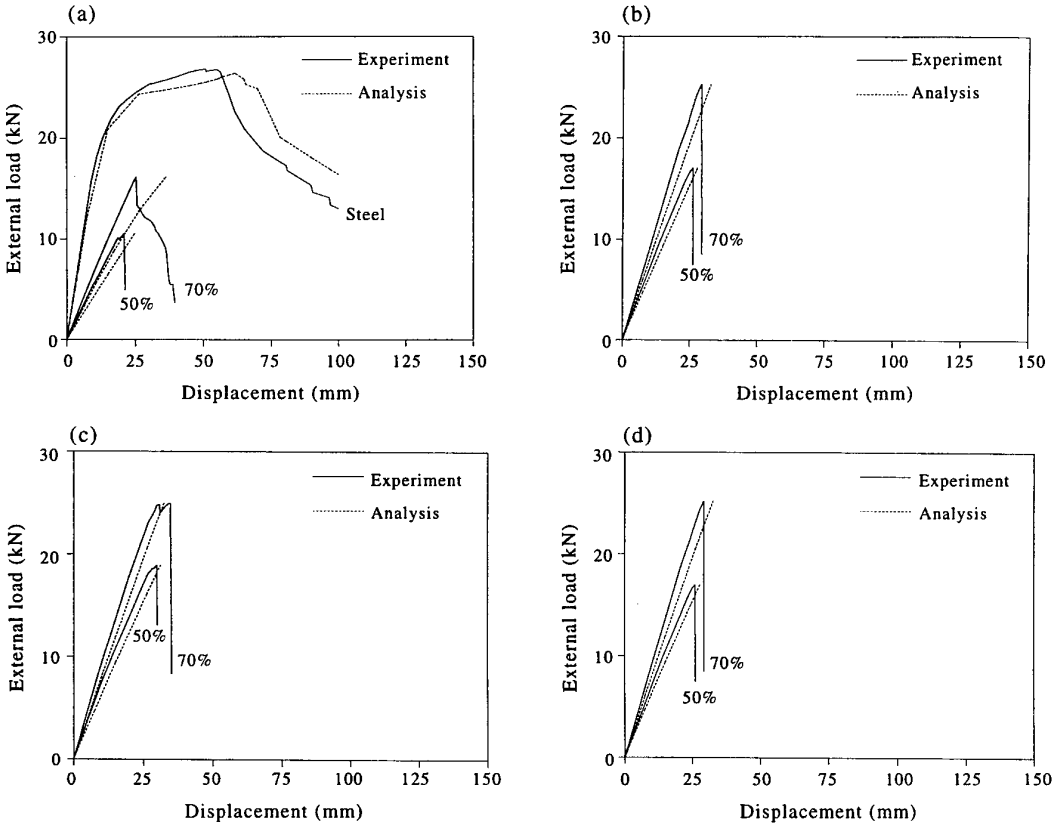

Fig. 12. Comparison between the static test results and the finite-element analyses. (a) Circular cross-section, (b) regular square cross-section; (c) regular square cross-section strengthened by a rib; and (d) I-type cross-section.

be rigid. The friction force between the contact surfaces was assumed to be negligible. The orthotropic composite properties as shown in Table 1 were used taking into consideration the stacking sequences. The deformed shape of the steel impact beams from finite-element analyses is shown in Fig. 11 as a representative sample.

Figure 12 shows the results of the finite-element analysis where they showed a relatively good agreement with experimental results. The low- and high-level lines represent 50% and 70% weight ratios, respectively, with respect to the steel. Also, the solid and the dashed lines represent experiment and analysis, respectively.

From the experiments and analyses, it was found that the composite impact beam of the regular square cross-section strengthened by the rib had a comparable static strength compared to the high strength steel impact beam. However, the composite impact beam had a low energy absorption capability because composites usually do not have plastic regions after yielding. However, as impact beams undergo dynamic loads in a car crash, the dynamic impact energy absorption capability [20] of impact beams is more important than the static energy absorption capability. In addition, the new FMVSS 214 regulation, revised in 1993, introduced these dynamic tests between cars.

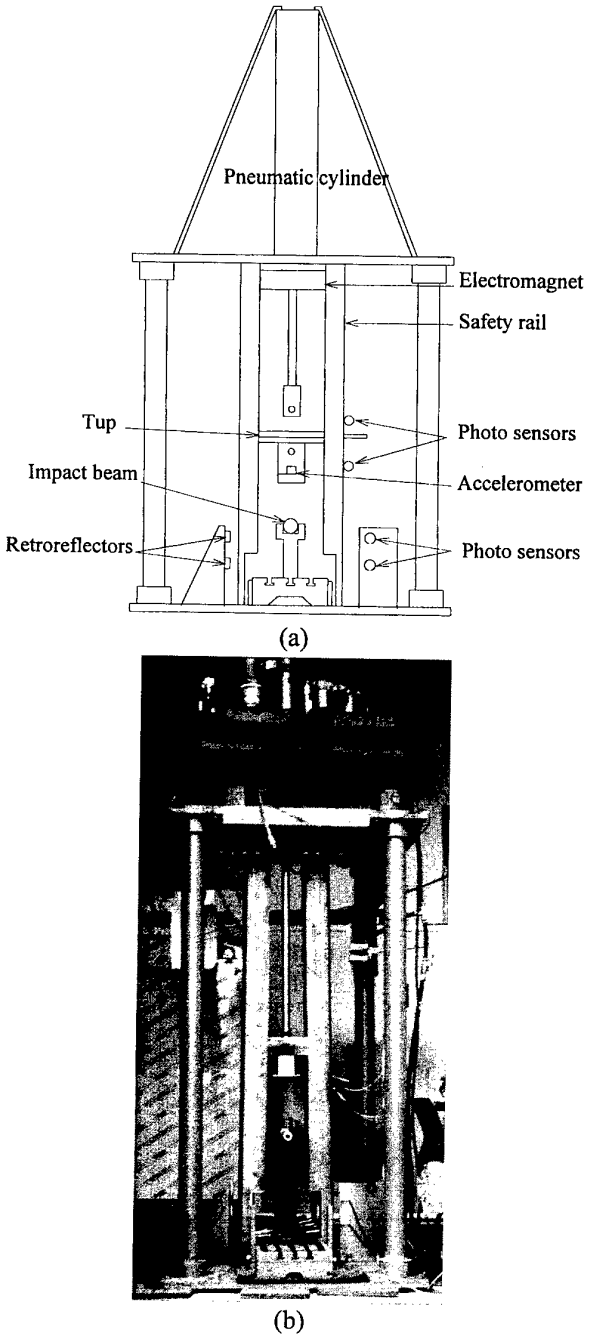

Fig. 13. Dynamic impact tester accelerated by a pneumatic cylinder. (a) Schematic diagram. (b) Photograph.

DEVELOPMENT OF AN IMPACT TESTER

An impact tester, whose impact velocity was increased by a pneumatic cylinder, was developed to investigate the dynamic characteristics of impact beams, as shown in Fig. 13.

The 25 mm nose radius impact tup of the dynamic impact tester is accelerated when the electromagnet which holds the piston in the pneumatic cylinder is switched off. When the air pressure in the cylinder was 0.5 MPa, the velocity of the 13 kg impact tup was greater than 30 mph. During the impact process, velocities of the impact tup before and after impact were measured with four photo-sensors. The upper two photo-sensors were used to measure the time difference through 50 mm of movement, while the lower two photo-sensors were used to measure the time difference through 100 mm of movement. Because the lower two photo-sensors were infrared emitted–retroreflector-type, the interval between them was set to 100 mm considering the space for the retroreflective mirror mounting, whose diameter was 85 mm. On the other hand, as the upper two photo-sensors were optical-fibre-type without mirrors, their interval was set at 50 mm.

The acceleration of the impact tup was also measured with an accelerometer attached at the impact tup. The signals from the photo-sensors and the accelerometer were processed by an IBM 486 computer through an A/D converter.

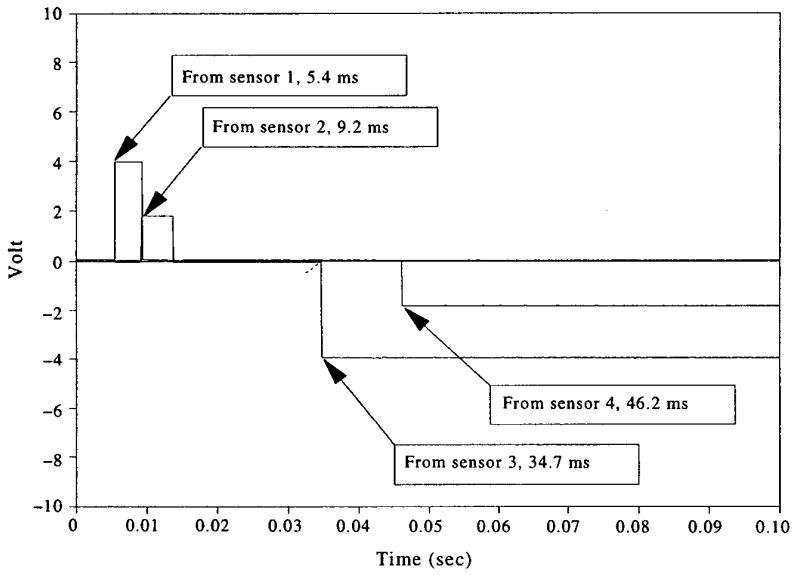

Fig. 14. Signal from the photo-interrupt sensors.

The mass of the impact tup was adjusted in the range of 10–15 kg to vary the impact magnitude. Also, the impact velocity was adjusted in the range of 1–25 m/s by varying the pressure inside the cylinder. The measured signals from the accelerometer were low-pass filtered with a 100 kHz cut-off frequency.

DYNAMIC IMPACT TESTS

The high strength steel circular impact beam whose outer diameter and inner diameter were 30 and 27.4 mm, respectively, was impact tested. The high strength steel, which was heat-treated through its thickness, had an ultimate tensile strength of 1.5 GPa. The mass and length of the high strength circular impact beam were 0.50 kg and 507 mm, respectively. The simply supported jig span of 360 mm was used during impact tests. When the tup mass and the cylinder pressure were 13 kg and 0.5 MPa, respectively, the velocity of the tup was 13.1 m/s (29 mph, 47 km/h), which was close to the standard velocity of 30 mph for the side crash test of FMVSS 214. In the tests, about 1100 J of dynamic energy was given to each specimens.

In dynamic tests, because the composite impact beams of 0.25 kg (50% weight ratio) showed a sufficient dynamic energy absorption capability, only 0.25 kg composite impact beams were tested. Figure 14 shows the time differences checked by the four photo-interrupt-sensors during dynamic testing of the high strength steel impact beams at 25°C.

From Fig. 14, the measured initial velocity of the impact tup was 13.1 m/s ($V_i = 50$ mm/3.819 ms), and the measured velocity after impact on the high strength steel impact beam was 8.75 m/s ($V_f = 100$ mm/11.43 ms). Therefore, the energy absorption rate, which is defined as $1 - V_f^2/V_i^2$, was 55%. The glass-fibre–epoxy composite impact beam, which had a 0.25 kg mass, was found to absorb 53% of the given impact energy at a room temperature of 25°C. Therefore, it was found that a 50% weight saving could be obtained when the composite impact beams were used instead of steel ones, based on the dynamic energy absorption capability. Moreover, composite impact beams showed very similar dynamic energy absorption capabilities regardless of their cross-sectional shapes, although the static strengths were much more dependent on the cross-sectional shapes

Table 3. Dynamic energy absorption rate of four sections of composite impact beams

Cross-sectional shape	Circular type (0.25 kg)	Regular square (0.25 kg)	Regular square+rib (0.25 kg)	I (0.25kg)
Energy absorption rate	53.2%	52.9%	52.5%	53.3%

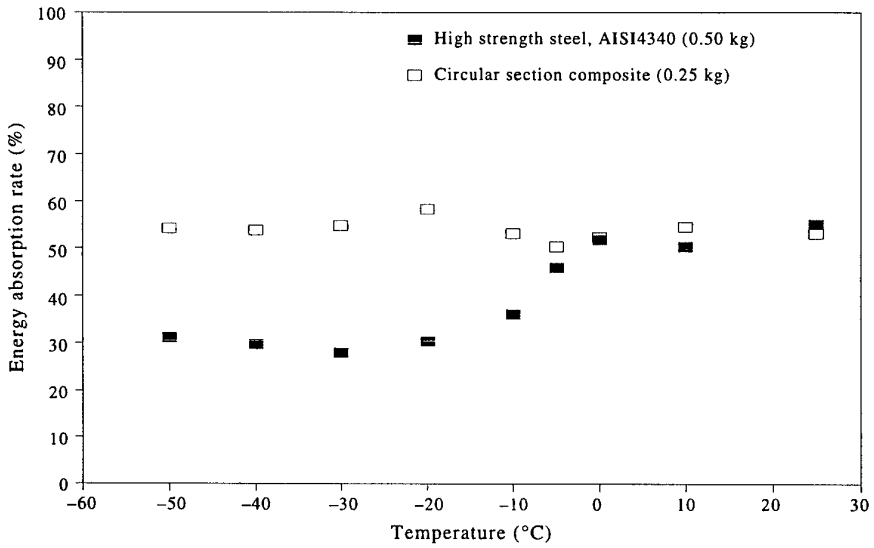

Fig. 15. Dynamic energy absorption results with respect to temperature.

on the composite impact beams, as shown in Table 3. Therefore, it was decided that in this study only circular composite impact beams were to be investigated.

In order to investigate the temperature dependence of the impact beams, the impact tests were performed at several low temperatures. Figure 15 shows the impact energy absorption of the impact beams with respect to environmental temperatures. The low environmental temperature was established by placing the impact beams inside a box containing dry ice, and the outside temperature of the impact beam was measured by a touch-probe-type thermometer.

From Fig. 15, it was revealed that the energy absorption of the steel impact beams went down as the environmental temperature dropped; however, the composite impact beam had an almost constant energy absorption capability. As it was expected that the slope of energy absorption rate was steep between 0 and -10°C, an impact test was performed at -5°C. From the test it was estimated that the nil ductility temperature [21] of the steel impact beam might exist between -5 and -10°C.

CONCLUSIONS

In this study composite side-door impact beams were designed and manufactured. From the three-point static bending tests it was found that the composite impact beams with a circular cross-section had a tendency to be buckled by relatively low concentrated loads, which gave rise to local collapse and fracture. However, the regular square cross-section composite impact beams, especially strengthened by the rib, could resist external loads comparable with that of the high strength steel impact beams. The glass-fibre–epoxy composite impact beam has a 30% weight reduction compared to the high strength steel impact beam based on the static bending tests.

A pneumatic impact tester was developed to investigate the dynamic characteristics of the impact beams at several different environmental temperatures. From the dynamic tests it was found that the composite impact beam had better impact energy absorption capability than the high strength steel impact beams. The cross-sectional shape of the impact beams had little influence on the impact energy absorption capability. The impact energy absorption capability of the high strength steel impact beams dropped abruptly at environmental temperatures below -10°C, from which it was concluded that the nil ductility temperature of the high strength steel impact beam might exist at a temperature around -10°C. The glass-fibre–epoxy composite impact beam has a 50% of weight reduction compared to the high strength steel impact beam based on the dynamic tests.

From the experiments it was concluded that the composite impact beams not only reduce the weight of the impact beams by more than 50% but also had a constant impact energy

absorption capability with respect to environmental temperature variation.

ACKNOWLEDGEMENTS

This work was supported by KOSEF (Korea Science and Engineering Foundation) under grant No. 95-02-00-14. Their support is gratefully acknowledged.

REFERENCES

1. Choi, J. K. and Lee, D. G., Torque transmission capabilities of bonded polygonal lap joints for carbon fiber epoxy composites. *J. Adhesion*, 1995, **48**, 235–250.
2. Kim, H. S., Park, K. Y. and Lee, D. G., A study on the epoxy resin concrete for the ultra-precision machine tool bed. *J. Mater. Process. Technol.*, 1995, **48**, 649–655.
3. Mallick, P. K., *Fiber Reinforced Composites*. Marcel Dekker, 1988, pp. 248–62.
4. Gibson, R. F., *Principles of Composite Material Mechanics*. McGraw-Hill, New York, 1994, pp. 13–31.
5. Thornton, P.H., Energy absorption in composite structures. *J. Composite Mater.*, 1979, **13**, 247–262.
6. Automotive Plastics Report 92. Market Search Inc., Section 1, 1992, p. 17.
7. Beardmore, P., Composite structures for automobiles. *Composite Struct.*, 1986, **5**, 163–176.
8. Mallick, P. K. & Newman, S., *Composite Materials Technology*. Hanser, 1990, pp. 211–35.
9. Kim, Y. G., Lee, D. G. and Oh, P. K., Manufacturing of the composite screw rotors by resin transfer molding. *J. Mater. Process. Technol.*, 1995, **48**, 641–647.
10. Jeong, K. S., Lee, D. G. and Oh, S. H., Development of the composite flexspline for a cycloid-type harmonic drive using net shape manufacturing method. *Composite Struct.*, 1995, **32**, 557–565.
11. Kim, D.H., Jeong, K.S., Lee, D.G. and Oh, S.H., Manufacturing of the traction drive with the glass fiber epoxy composite materials. *J. Mater. Process. Technol.*, 1995, **48**, 333–339.
12. Lee, D.G., Kim, K.S. and Kwak, Y.G., Manufacturing of a SCARA type direct-drive robot with graphite fiber epoxy composite materials. *Robotica*, 1991, **9**, 219–229.
13. Lee, D.G., Jeong, K.S., Kim, K.S. and Kwak, Y.G., Development of the anthropomorphic robot with carbon fiber epoxy composite materials. *Composite Struct.*, 1993, **25**, 313–324.
14. Strait, L.H., Karasek, M.L. and Amateau, M.F., Effects of stacking sequence on the impact resistance of carbon fiber reinforced thermoplastic toughened epoxy laminates. *J. Composite Mater.*, 1992, **26**, 1725–1741.
15. *Metals Handbook*, 10th edn, Vol.1. ASM International, 1990, p. 152.
16. Jones, R., Chiu, W.K. and Paul, J., Designing for damage tolerant bonded joints. *Composite Struct.*, 1993, **25**, 201–207.
17. He, S. and Rao, M.D., Residual stresses and delamination problems induced by cocuring of damped composite laminates. *J. Composite Mater.*, 1994, **28**, 112–129.
18. Kim, H.S., Lee, S.J. and Lee, D.G., Development of a strength model for the cocured stepped lap joints under tensile loading. *Composite Struct.*, 1995, **32**, 593–600.
19. Li, S., Soden, P.D., Reid, S.R. and Hinton, M.J., Indentation of laminated filament-wound composite tubes. *Composites*, 1993, **24**, 407–421.
20. Thornton, P.H. and Jeryan, R.A., Crash energy management in composite automotive structures. *Int. J. Impact Engng*, 1988, **7**, 167–180.
21. Hertzberg, R. W., *Deformation and Fracture Mechanics of Engineering Materials*, 2nd edn. John Wiley & Sons, Chichester, 1989, pp. 333–9.

ELSEVIER

Composite Structures Vol. 38, No. 1–4, pp. 241–250, 1997
© 1997 Elsevier Science Ltd. All rights reserved
Printed in Great Britain
0263-8223/97/$17.00 + 0.00

PII:S0263-8223(97)00059-7

Flexural–torsional buckling of pultruded fiber reinforced plastic composite I-beams: experimental and analytical evaluations

Julio F. Davalos,[a] Pizhong Qiao[a] & Hani A. Salim[b]

[a]*Department of Civil and Environmental Engineering, West Virginia University, Morgantown, WV 26506-6103, USA*
[b]*Department of Civil Engineering, University of Missouri-Columbia, Columbia, MO 65211, USA*

In this paper a comprehensive experimental and analytical approach is presented to study flexural–torsional buckling behavior of full-size pultruded fiber-reinforced plastic (FRP) I-beams. Two full-size FRP I-beams with distinct material architectures are tested under midspan-concentrated loads to evaluate their flexural–torsional buckling responses. To monitor rotations of the cross-section and the onset of critical buckling loads, transverse bars are attached to the beam cross-section and are subsequently connected to LVDTs; strain gages bonded at the edges of the top flange are also used. The analysis is based on energy principles, and the total potential energy equations for the instability of FRP I-beams are derived using nonlinear elastic theory. The equilibrium equation in terms of the total potential energy is solved by the Rayleigh–Ritz method, and simplified engineering equations for predicting the critical flexural–torsional buckling loads are formulated. A good agreement is obtained between the experimental results, proposed analytical solutions and finite-element analyses. Through the combined experimental and analytical evaluations reported in this study, it is shown that the testing setup used can be efficiently implemented in the characterization of flexural–torsional buckling of FRP shapes and the proposed analytical design equations can be adopted to predict flexural–torsional buckling loads. © 1997 Elsevier Science Ltd.

INTRODUCTION

Pultruded fiber-reinforced plastic (FRP) composite shapes are increasingly used in civil engineering structures, due to their favorable properties such as light weight, corrosion resistance and electromagnetic transparency. FRP shapes are commonly fabricated using fiberglass and either polyester or vinylester resins. Because of the low modulus of elasticity of glass fibers and the common thin-walled sectional geometry, pultruded FRP beams are susceptible to buckling under service loads.

Owing to the high strength-to-stiffness ratio of pultruded FRP composites, buckling is the most likely mode of failure before the ultimate load reaches the material failure for FRP shapes. A long slender beam under bending loads about the strong axis may buckle by a combined twisting and lateral (sideway) bending of the cross-section. This phenomenon is known as flexural–torsional (lateral) buckling. Numerous analyses [1–4] have been presented for steel beams, where the material is homogeneous and isotropic. Several researchers have carried out studies on theoretical and experimental evaluations of lateral buckling for FRP structural shapes and have developed some design methodologies for these members. The flexural–torsional buckling behavior of pultruded E-glass FRP I-beams has been experimentally investigated by Mottram [5], and the observed results compared well with numerical predictions using a finite-difference method. Mottram [5] emphasized that there is a potential danger in analysis and design of FRP beams without including

shear deformation. A series of lateral buckling tests on small-scale pultruded E-glass FRP beams were carried out by Turvey [6] and Brooks & Turvey [7,8]. The effects of load position and boundary condition on the lateral buckling response of FRP I-sections were investigated, and the results were correlated with approximate formulae by Nethercot & Rockey [9] and finite-element eigenvalue analysis. They attributed the disparity between experiment and analysis to factors not included in the models, such as initial deflections, prebuckling displacements and geometric nonlinearities. Although significant contributions have been provided by previous investigators, there is a need to develop combined experimental and analytical studies to characterize the buckling behaviors of full-size FRP sections and to propose engineering design analysis equations for flexural–torsional buckling of FRP beams.

In this paper a comprehensive experimental and analytical approach is used to study flexural–torsional buckling behavior of pultruded FRP I-beams. Two full-size FRP wide-flange I-beams with two different material architectures are tested to study their flexural–torsional buckling responses under midspan-concentrated loads and, to induce global buckling without distortion of the beam cross-section (flexural–torsional buckling), wooden stiffeners are inserted between the flanges and web at midspan. Through displacement measurements with LVDTs and strain measurements at the edges of the top flange, bifurcation responses and rotations of the midspan cross-sections are evaluated. Energy principles and nonlinear elastic plate theory are applied to formulate the engineering equations of flexural–torsional buckling loads for FRP I-beams. The predictions of simplified equations for flexural–torsional critical buckling loads correlate closely with experimental results and finite-element analyses. The present study intends to bridge a gap between sophisticated modeling of composite materials and the requirement of a simple but accurate tool for engineering design.

EXPERIMENTAL EVALUATIONS OF FLEXURAL–TORSIONAL BUCKLING OF FRP I-BEAMS

In this study two full-size FRP wide-flange I-beams, which were manufactured based on optimum designs [10], are tested to evaluate their flexural–torsional buckling responses [11]. The beams tested are full-size $304.8 \times 304.8 \times 12.7$ mm ($12 \times 12 \times 1/2$ in.) I-beam sections with two different material architectures: (1) beams WF-A (Fig. 1) consist of rovings, continuous strand mats (CSM) and $\pm 45°$ angle-ply stitched fabrics (SF); and (2) beams WF-AC (Fig. 2) consist of rovings, continuous strand mats (CSM), $\pm 45°$ angle-ply stitched fabrics (SF) and 0°/90° cross-ply stitched fabrics (SF). The span length considered is $L = 4.42$ m (14.5 ft), and both beams are tested under midspan-concentrated loads.

Experimental setup

For the experimental evaluation of flexural–torsional buckling of the WF I-beams [11], wooden stiffeners were inserted between the flanges and web at midspan to prevent distortions of the beam cross-sections. The beams were restrained at the supports to closely simulate a roller condition and at the same time avoid out-of-plane twisting. Using transverse bars attached to the beam midspan cross-section (as shown in Fig. 3), LVDTs were installed to measure the rotation angles of the cross-section at critical buckling loads. Also, strain gages were installed

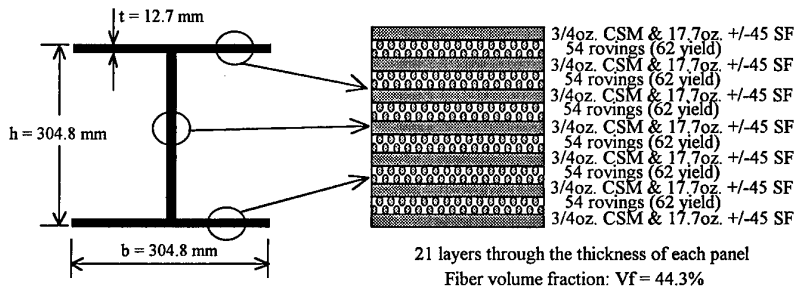

Fig. 1. Dimensions and panel fiber architectures of WF-A beams.

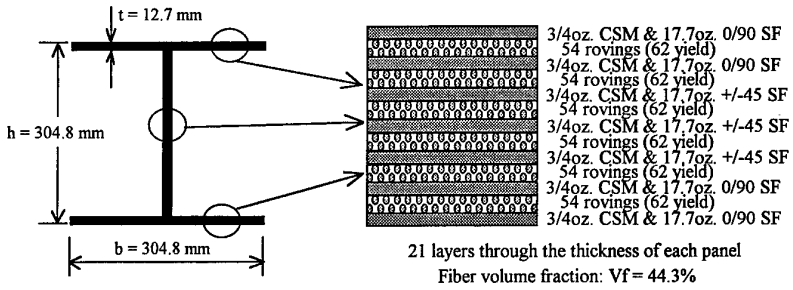

Fig. 2. Dimensions and panel fiber architectures of WF-AC beams.

on the compression flanges to detect the onset of lateral buckling. The load was applied to the top flange and lateral supports were placed close to the beam to prevent catastrophic failures. The hydraulic ram was rigidly attached to a supporting frame and, therefore, the load was not capable of acting as a 'follower load' when flexural–torsional buckling occurred and the whole cross-section rotated suddenly. At the onset of buckling, this loading arrangement had a restraining effect against rotation of the cross-section as flexural–torsional buckling proceeded and induced a restoring torque making the critical load slightly higher than for the case of a true follower load.

Experimental response of flexural–torsional buckling

The experimental physical occurrence of flexural–torsional buckling is shown in Fig. 4, where all attached bars rotated in the same direction under torsional response of the cross-section. The LVDTs' readings of the tip vertical displacements of the transverse bars, described in Fig. 3, are shown in Fig. 5 for the WF-A I-beam and in Fig. 6 for the WF-AC I-beam, respectively. Strain responses along the two edges of the top flange at the midspan cross-sections are also plotted in Fig. 7 for the WF-A beam and Fig. 8 for the WF-AC beam. As indicated in Figs 5–8, a bifurcation response point from load–displacement or load–strain curves can be observed when the applied load reached the critical buckling load for each individual beam.

ANALYTICAL EVALUATIONS OF THE FLEXURAL–TORSIONAL BUCKLING OF FRP I-BEAMS

The analyses of flexural–torsional (lateral) buckling are based on energy considerations, and the total potential energy equations governing instability are derived using nonlinear plate theory.

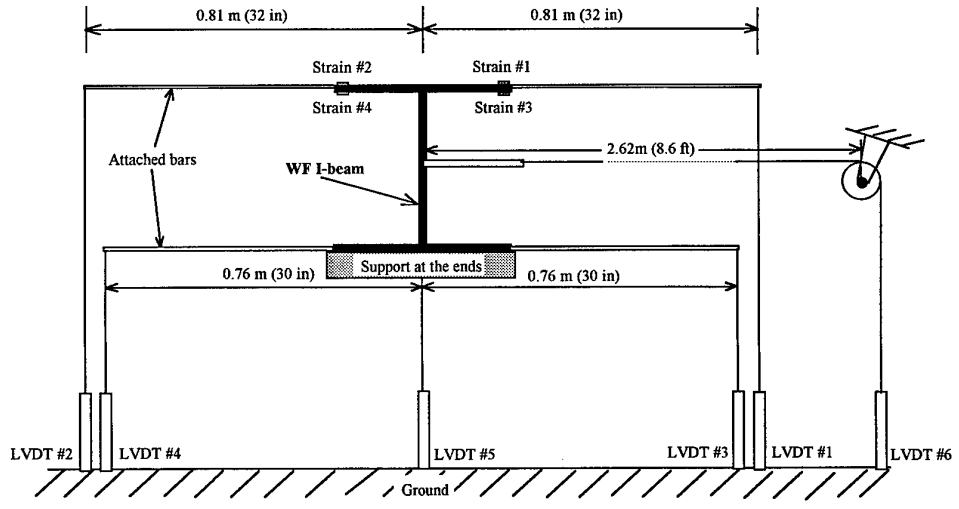

Fig. 3. Arrangement of LVDTs and strain gages at the midspan cross-section of the WF I-beams.

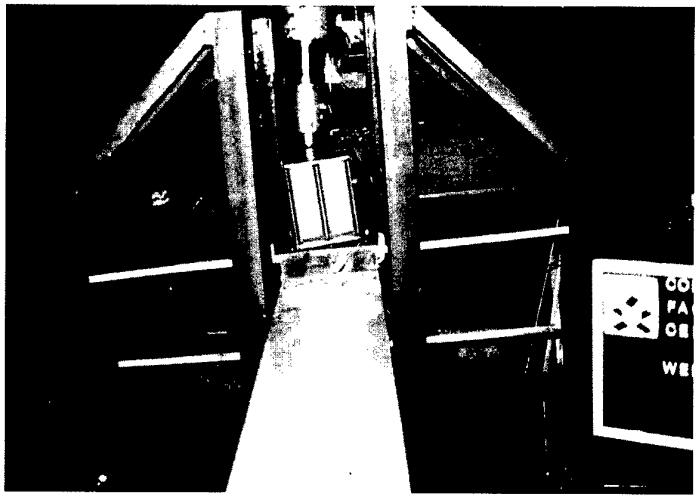

Fig. 4. Experimental phenomenon of flexural–torsional buckling of a WF I-beam.

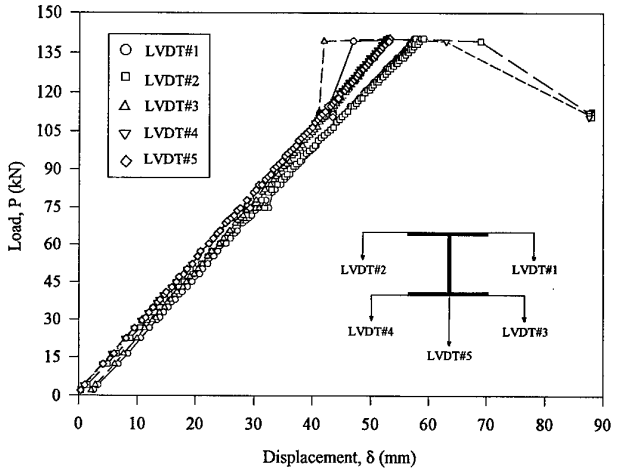

Fig. 5. Load–displacement curve for flexural–torsional buckling of a WF-A I-beam.

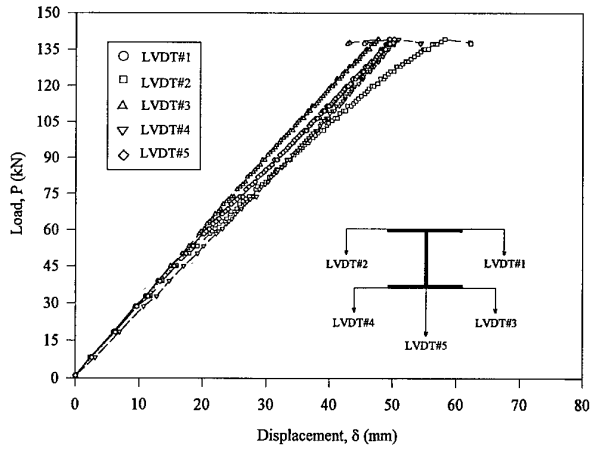

Fig. 6. Load–displacement curve for flexural–torsional buckling of a WF-AC I-beam.

Derivation of total potential energy

The total potential energy of the system (e.g. I-beams) is the sum of the strain energy and potential energy of the applied loads. To establish equilibrium using the total potential energy (Π) in a displaced buckling mode, the prebuckling work, which is the product of the applied loads and their corresponding displacements, can be ignored in stability analysis. In conformance with the basic approximations for thin-plate theory, the strain energy in a deformed plate is

$$U = \frac{1}{2} \iiint_V (\sigma_x \varepsilon_x + \sigma_y \varepsilon_y + \tau_{xy} \gamma_{xy})\, dV \qquad (1)$$

For I-beam sections consisting of two flanges

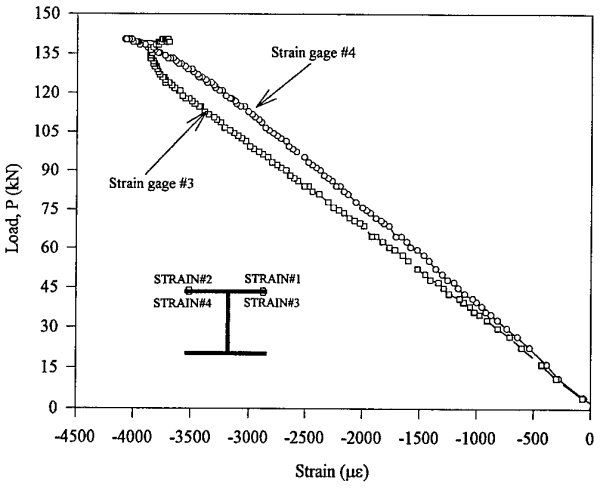

Fig. 7. Load–strain curve for flexural–torsional buckling of a WF-A I-beam.

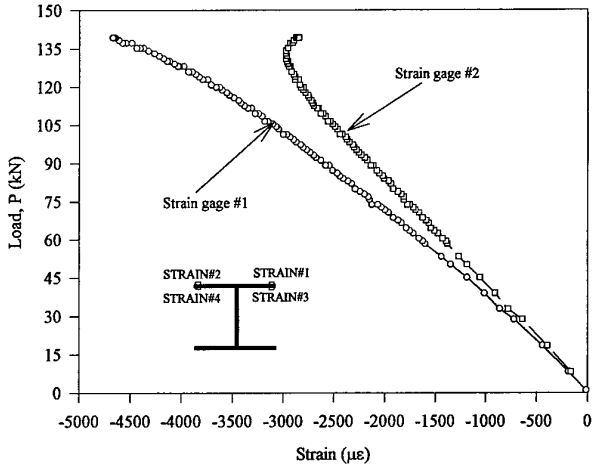

Fig. 8. Load–strain curve for flexural–torsional buckling of a WF-AC I-beam.

and one web, the total strain energy in a buckled beam is given by

$$U = U^{tf} + U^{w} + U^{bf} \tag{2}$$

where the superscripts tf, w and bf refer to top flange, web and bottom flange, respectively.

As the displacement–gradient components are not small compared to unity, the strains for the buckling problem are expressed in nonlinear terms. It is assumed that the strains and curvatures are much less than unity everywhere in the plate. For a plate in the x–y plane, the in-plane finite strains of the midsurface of the plate are given by Malvern [12] as

$$\varepsilon_x = \frac{\partial u}{\partial x} + \frac{1}{2}\left[\left(\frac{\partial u}{\partial x}\right)^2 + \left(\frac{\partial v}{\partial x}\right)^2 + \left(\frac{\partial w}{\partial x}\right)^2\right]$$

$$\varepsilon_y = \frac{\partial v}{\partial y} + \frac{1}{2}\left[\left(\frac{\partial u}{\partial y}\right)^2 + \left(\frac{\partial v}{\partial y}\right)^2 + \left(\frac{\partial w}{\partial y}\right)^2\right]$$

$$\gamma_{xy} = \frac{\partial v}{\partial x} + \frac{\partial u}{\partial y} + \frac{\partial u}{\partial x}\frac{\partial u}{\partial y} + \frac{\partial v}{\partial x}\frac{\partial v}{\partial y} + \frac{\partial w}{\partial x}\frac{\partial w}{\partial y} \tag{3}$$

Based on von Karman plate theory, only the displacement gradients $\partial w/\partial x$ and $\partial w/\partial y$ are considered to have significant values and, therefore, the nonlinear terms $(\partial w/\partial x)^2$ and $(\partial w/\partial y)^2$ in eqn (3) remained. For a stability problem, the displacement gradients $\partial v/\partial x$ and $\partial u/\partial y$ may become relatively large due to in-plane rotations, especially for the flanges; whereas the terms $\partial u/\partial x$ and $\partial v/\partial y$, and particularly their quadratic forms, are significantly smaller than the other terms and can be ignored. Hence, eqn (3) reduces to

$$\varepsilon_x = \frac{\partial u}{\partial x} + \frac{1}{2}\left[\left(\frac{\partial v}{\partial x}\right)^2 + \left(\frac{\partial w}{\partial x}\right)^2\right]$$

$$\varepsilon_y = \frac{\partial v}{\partial y} + \frac{1}{2}\left[\left(\frac{\partial u}{\partial y}\right)^2 + \left(\frac{\partial w}{\partial y}\right)^2\right]$$

$$\gamma_{xy} = \frac{\partial v}{\partial x} + \frac{\partial u}{\partial y} + \frac{\partial w}{\partial x}\frac{\partial w}{\partial y} \tag{4}$$

The curvatures of the midplane are defined as

$$\kappa_x = \frac{\partial^2 w}{\partial x^2} \quad \kappa_y = \frac{\partial^2 w}{\partial y^2} \quad \kappa_{xy} = 2\frac{\partial^2 w}{\partial x \partial y} \tag{5}$$

For buckling analysis of I-beams under bending, the deformation before perturbation is ignored. Based on the coordinate system shown in Fig. 9, the buckled displacement fields are expressed as follows [4]

$$u_w = 0,\ v_w = 0,\ w_w = w(x, y),$$

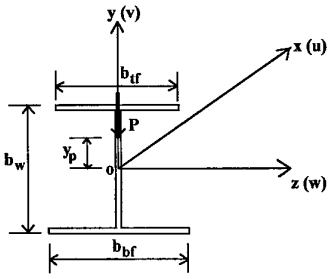

Fig. 9. Displacement field and coordinator system of an I-beam.

for the web (in the $x-y$ plane) (6a)

$$u_{tf}=u_{tf}(x, z),\ v_{tf}=v_{tf}(x, z),\ w_{tf}=w_{tf}(x),$$

for the top flange (in the $x-z$ plane) (6b)

$$u_{bf}=u_{bf}(x, z),\ v_{bf}=v_{bf}(x, z),\ w_{bf}=w_{bf}(x),$$

for the bottom flange (in the $x-z$ plane) (6c)

For the top flange (x–z plane), the strains and curvatures in eqns (4) and (5) become

$$\varepsilon_{tfx}=\frac{\partial u_{tf}}{\partial x}+\frac{1}{2}\left[\left(\frac{\partial w_{tf}}{\partial x}\right)^2+\left(\frac{\partial v_{tf}}{\partial x}\right)^2\right]$$

$$\varepsilon_{tfz}=\frac{\partial w_{tf}}{\partial z}+\frac{1}{2}\left[\left(\frac{\partial u_{tf}}{\partial z}\right)^2+\left(\frac{\partial v_{tf}}{\partial z}\right)^2\right]$$

$$\varepsilon_{tfxz}=\frac{\partial w_{tf}}{\partial x}+\frac{\partial u_{tf}}{\partial z}+\frac{\partial v_{tf}}{\partial x}\frac{\partial v_{tf}}{\partial z} \tag{7}$$

and

$$\kappa_x=\frac{\partial^2 v_{tf}}{\partial x^2}\quad \kappa_z=\frac{\partial^2 v_{tf}}{\partial z^2}\quad \kappa_{xz}=2\frac{\partial^2 v_{tf}}{\partial x\partial z} \tag{8}$$

In the present study, the above equations are applied in the buckling analysis of pultruded FRP I-beams. Most pultruded FRP sections [13] are produced as symmetric laminated structures (no stretching–bending coupling, $B_{ij}=0$), and the off-axis plies of pultruded panels are balanced symmetric (no extension–shear and bending–twist couplings: $A_{16}=A_{26}=D_{16}=D_{26}=0$). The panel mechanical properties are independently obtained either from experimental coupon tests or theoretical predictions using micro/macromechanics models [13].

For a laminate in the x–y plane, the in-plane midsurface strains and curvatures are expressed in terms of the compliance coefficients and panel resultant forces as [14]

$$\begin{Bmatrix}\varepsilon_x\\ \varepsilon_y\\ \gamma_{xy}\\ \kappa_x\\ \kappa_y\\ \kappa_{xy}\end{Bmatrix}=\begin{bmatrix}\alpha_{11}&\alpha_{12}&\alpha_{16}&\beta_{11}&\beta_{12}&\beta_{16}\\ \alpha_{12}&\alpha_{22}&\alpha_{26}&\beta_{12}&\beta_{22}&\beta_{26}\\ \alpha_{16}&\alpha_{26}&\alpha_{66}&\beta_{16}&\beta_{26}&\beta_{66}\\ \beta_{11}&\beta_{12}&\beta_{16}&\delta_{11}&\delta_{12}&\delta_{16}\\ \beta_{12}&\beta_{22}&\beta_{26}&\delta_{12}&\delta_{22}&\delta_{26}\\ \beta_{16}&\beta_{26}&\beta_{66}&\delta_{16}&\delta_{26}&\delta_{66}\end{bmatrix}\begin{Bmatrix}N_x\\ N_y\\ N_{xy}\\ M_x\\ M_y\\ M_{xy}\end{Bmatrix} \tag{9}$$

and considering the top flange of an I-beam (Fig. 9) to act as a beam element, the transverse resultant forces are neglected

$$N_z^{tf}=M_z^{tf}=0 \tag{10}$$

Referring to the coordinate system of Fig. 9 and applying eqn (9) to the x–z plane, we obtain

$$N_x^{tf}=\frac{\varepsilon_{tfx}}{\alpha_{11}},\quad N_{xz}^{tf}=\frac{\gamma_{tfxz}}{\alpha_{66}},$$

$$M_x^{tf}=\frac{\kappa_{tfx}}{\delta_{11}},\quad M_{xz}^{tf}=\frac{\kappa_{tfxz}}{\delta_{66}} \tag{11}$$

where N_x and N_{xz} are the membrane forces per unit length, and M_x and M_{xz} are the bending and twisting moments per unit length. The compliance coefficients $[\alpha]$ and $[\delta]$ are obtained by inversion of the stiffness matrices $[A]$ and $[D]$. Then the total strain energy of the flange becomes

$$U^{tf}=\frac{1}{2}\iint_{\text{Area}}(N_x^{tf}\varepsilon_{tfx}+N_{xz}^{tf}\gamma_{tfxz}+M_x^{tf}\kappa_{tfx}+M_{xz}^{tf}\kappa_{tfxz})\,dx\,dz \tag{12}$$

Ignoring the fourth-order terms, the total strain energy of the top flange is simplified as

$$U^{tf}=\frac{1}{2}\iint_{\text{Area}}\left\{N_x\left[\left(\frac{\partial v_{tf}}{\partial x}\right)^2+\left(\frac{\partial w_{tf}}{\partial x}\right)^2\right]+2N_{xz}\frac{\partial v_{tf}}{\partial x}\frac{\partial v_{tf}}{\partial z}\right\}dx\,dz$$

$$+\frac{1}{2}\iint_{\text{Area}}\left\{\frac{1}{\alpha_{11}}\left(\frac{\partial u_{tf}}{\partial x}\right)^2+\frac{1}{\alpha_{66}}\left[\left(\frac{\partial w_{tf}}{\partial x}\right)+\left(\frac{\partial u_{tf}}{\partial z}\right)\right]^2+\frac{1}{\delta_{11}}\left(\frac{\partial^2 v_{tf}}{\partial x^2}\right)^2+\frac{1}{\delta_{66}}\left(\frac{\partial^2 v_{tf}}{\partial x\partial z}\right)^2\right\}dx\,dz \tag{13}$$

where

$$N_x=\frac{1}{\alpha_{11}}\frac{\partial u_{tf}}{\partial x}\quad N_{xz}=\frac{1}{\alpha_{66}}\left(\frac{\partial w_{tf}}{\partial x}+\frac{\partial u_{tf}}{\partial z}\right)$$

The total strain energy of the bottom flange can be obtained in a similar way as

$$U^{bf} = \frac{1}{2}\iint_{Area}\left\{N_x\left[\left(\frac{\partial v_{bf}}{\partial x}\right)^2+\left(\frac{\partial w_{bf}}{\partial x}\right)^2\right] +2N_{xz}\frac{\partial v_{bf}}{\partial x}\frac{\partial v_{bf}}{\partial z}\right\}dx\,dz + \frac{1}{2}\iint_{Area}\left\{\frac{1}{\alpha_{11}}\left(\frac{\partial u_{bf}}{\partial x}\right)^2 + \frac{1}{\alpha_{66}}\left[\left(\frac{\partial w_{bf}}{\partial x}\right)+\left(\frac{\partial u_{bf}}{\partial z}\right)\right]^2 + \frac{1}{\delta_{11}}\left(\frac{\partial^2 v_{bf}}{\partial x^2}\right)^2+\frac{1}{\delta_{66}}\left(\frac{\partial^2 v_{bf}}{\partial x\partial z}\right)^2\right\}dx\,dz \tag{14}$$

Considering the web as a plate and the deformation field of eqn (6a), the total strain energy of a web panel is expressed as

$$U^{w} = \frac{1}{2}\iint_{Area}\left[N_x\left(\frac{\partial w_w}{\partial x}\right)^2+N_y\left(\frac{\partial w_w}{\partial y}\right)^2 +2N_{xy}\frac{\partial w_w}{\partial x}\frac{\partial w_w}{\partial y}\right]dx\,dy + \frac{1}{2}\iint_{Area}\left[D_{11}^{w}\left(\frac{\partial^2 w_w}{\partial x^2}\right)^2+D_{22}^{w}\left(\frac{\partial^2 w_w}{\partial y^2}\right)^2 +2D_{12}^{w}\frac{\partial^2 w_w}{\partial x^2}\frac{\partial^2 w_w}{\partial y^2} +4D_{66}^{w}\left(\frac{\partial^2 w_w}{\partial x\partial y}\right)^2\right]dx\,dy \tag{15}$$

The equilibrium equation ($\Pi = U = 0$) in terms of the total potential energy is then solved by the Rayleigh–Ritz method.

Stress resultants in I-beam panels

For a simply supported I-beam subjected to a midspan-concentrated vertical load, simplified stress resultant distributions on the corresponding panels are assumed based on beam theory, and the location, or height, of the applied load is accounted for in the analysis. For FRP I-beams of uniform thickness, the membrane forces are expressed in terms of the applied midspan-concentrated load P. The expressions for the flanges are

$$N_x^{tf} = \frac{Pb_w t}{4I}x \quad (0\le x\le L/2)$$

$$N_x^{tf} = \frac{Pb_w t}{4I}(L-x) \quad (L/2\le x\le L)$$

$$N_x^{bf} = -\frac{Pb_w t}{4I}x \quad (0\le x\le L/2)$$

$$N_x^{bf} = -\frac{Pb_w t}{4I}(L-x) \quad (L/2\le x\le L)$$

$$N_z^{tf} = N_z^{bf} = N_{xz}^{tf} = N_{xz}^{bf} = 0 \tag{16a}$$

Similarly for the web

$$N_x^{w} = \frac{Pt}{2I}xy \quad (0\le x\le L/2)$$

$$N_x^{w} = \frac{Pt}{2I}(L-x)y \quad (L/2\le x\le L)$$

$$N_y^{w} = 0 \quad (0\le x<L/2;\ L/2<x\le L)$$

$$N_{xy}^{w} = -\frac{P}{2b_w} \quad (0\le x\le L/2)$$

$$N_{xy}^{w} = \frac{P}{2b_w} \quad (L/2\le x\le L) \tag{16b}$$

where

$$I = \left(\frac{1}{2}b_f b_w^2+\frac{1}{12}b_w^3\right)t$$

To account for the location of the applied load along the web panel, the transverse stress resultant on the web panel is represented as

$$N_y^{w} = -\frac{P(y+y_P)}{b_w} \quad (x = L/2 \text{ and } -b_w/2\le y\le b_w/2) \tag{16c}$$

where y_P is the distance from the centroidal axis to the location of the applied load (Fig. 9).

Displacement field of buckled I-beam panels

Assuming that the top and bottom flanges do not distort (i.e. the displacements are linear in the z direction) and considering compatibility conditions at the flange–web intersections, the buckled displacement fields (Fig. 9) for the web, top and bottom panels of the I-section are derived. For the web (in the x–y plane):

$$u_w = 0,\ v_w = 0,\ w_w = w(x, y) \tag{17a}$$

For the top flange (in the x–z plane)

$$u_{tf} = u_{tf}(x, z) = -z(w_{tf})_{,x},$$
$$v_{tf} = v_{tf}(x, z) = -z\theta_{tf},$$
$$w_{tf} = w_{tf}(x) \tag{17b}$$

For the bottom flange (in the x–z plane)

$$u_{bf} = u_{bf}(x, z) = -z(w_{bf})_{,x},$$
$$v_{bf} = v_{bf}(x, z) = -z\theta_{bf},$$
$$w_{bf} = w_{bf}(x) \tag{17c}$$

For flexural–torsional (lateral) buckling of I-section beams, the cross-section of the beam is considered as undistorted. As the web panel is not allowed to distort and remains straight in flexural–torsional buckling, the rotation of the web and sideway deflection are coupled. The following displacement functions for the web centroidal axis displacement (w) and the beam rotation (θ) are selected as

$$w = C_1 \sin(\pi x/L) \quad \theta = C_2 \sin(\pi x/L) \tag{18}$$

The displacements and rotations (referring to eqns (17a–c) of panels then become

$$w_w = w + y\theta$$

$$w_{tf} = w + \frac{h}{2}\theta$$

$$w_{bf} = w - \frac{h}{2}\theta$$

$$\theta_{tf} = \theta_{bf} = \theta \tag{19}$$

where h is the height of beam.

Simplified equation for flexural–torsional (lateral) buckling

By applying the Rayleigh–Ritz method and solving for the eigenvalues of the potential energy equilibrium equation, the critical buckling load, P_{cr}, for a midspan point load applied at the centroid of the cross-section is obtained. As an example, based on the above formulation, a design equation for the critical buckling load, P_{cr}, is obtained as

$$P_{cr} = 2\pi^3 h[(6D_{11}+a_{11}h^2) \times [(\pi h)^2(2D_{11}+4d_{11} + a_{11}h^2)+48(2D_{66}+d_{66})L^2]]^{1/2}3(\pi^2+4)L^3 \tag{20}$$

where $a_{11} = 1/\alpha_{11}$ and $[\alpha_{ij}] = [A_{ij}]^{-1}$ (or $a_{11} = E_x t$, where E_x can be obtained from coupon tests); $d_{11} = 1/\delta_{11}$, $d_{66} = 1/\delta_{66}$ and $[\delta_{ij}] = [D_{ij}]^{-1}$ (or $d_{11} = E_x t^3/12$, $d_{66} = G_{xy}t^3/12$, where E_x and G_{xy} can be obtained from coupon tests); D_{11} and D_{66} are obtained from the $[D_{ij}]$ matrix; h is the width and height of I-beam (in the above equation, the width is assumed to be equal to the height, h). The stretching stiffness coefficients $[A_{ij}]$ and bending stiffness coefficients $[D_{ij}]$ used in this study are obtained from micro/macro-mechanics models. In Figs 10 and 11 the critical flexural–torsional buckling loads (P_{cr}) for WF-A and WF-AC beams (see details about the

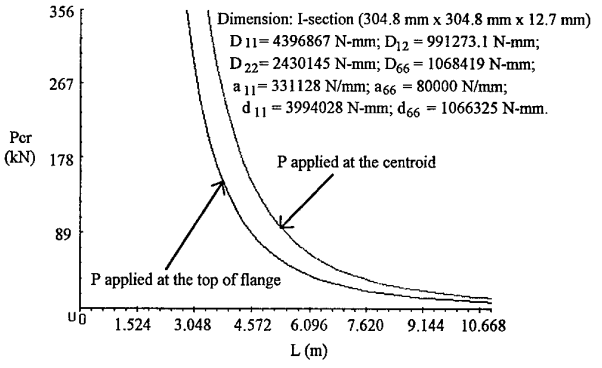

Fig. 10. Critical flexural–torsional buckling load envelope for a WF-A I-beam.

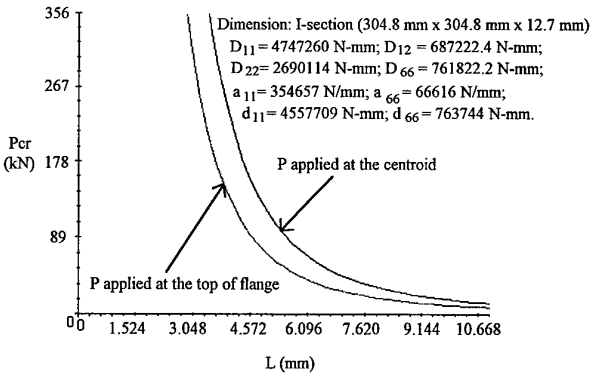

Fig. 11. Critical flexural–torsional buckling load envelope for a WF-AC I-beam.

Table 1. Comparison of flexural–torsional buckling load for a pultruded FRP WF-A beam

Load application	P_{cr} (kN)		
	Analytical solution	Finite element	Experimental
Centroid of section	163.128	163.297	—
Halfway between top flangeand centroid	124.413	125.681	133.554
Top of flange	96.578	101.767	—

material lay-up for these beams in Figs 1 and 2) are plotted vs the span length, L. The predictions of the proposed formulation are correlated with experimental results presented in the next section.

EXPERIMENTAL AND ANALYTICAL CORRELATIONS

As discussed in the previous section, the displacement functions for flexural–torsional buckling for the web central displacement (w) and rotation of the beam (θ) are given in eqn (18). By solving for the eigenvalues of the energy equation, the critical buckling load, P_{cr}, for a midspan point load applied at the centroid of the cross-section of an I-beam is given by eqn (20) (as shown in Fig. 10 for a WF-A section and Fig. 11 for a WF-AC section). To verify the prediction accuracy of the explicit solutions, the test beams were also analyzed with the commercial finite-element program ANSYS [15], using Mindlin eight-node isoparametric layered shell elements (SHELL 99). The results given in Tables 1 and 2 indicate that the predicted analytical values from eqn (20) agree well with the FE and average experimental values.

CONCLUSIONS

In this paper a combined experimental and analytical method is used to characterize the flexural–torsional (lateral) buckling response of pultruded FRP I-beams. Two full-size FRP wide-flange I-beams are tested under midspan-concentrated loads to evaluate their flexural–torsional and lateral–distortional buckling responses. Using transverse bars attached to the beam midspan cross-section, LVDTs are installed to measure the rotations of the cross-section at critical buckling loads. Similarly, strain gages bonded at the edges of the top flange are used to detect the onset of buckling. The experimental setup used in this study can be applied to other FRP shapes to detect the onset of flexural–torsional as well as lateral–distortional buckling.

Based on energy principles, the total potential energy equations for the instability of pultruded FRP I-sections are derived using nonlinear elastic theory. The flexural–torsional responses are analyzed using this approach and simplified engineering equations for flexural–torsional buckling are formulated. The models exhibit a satisfactory accuracy as verified both by experimental data and by finite-element analysis results.

A good agreement is obtained in this study between the proposed analytical approach, experimental results and finite-element analyses, and, through the combined analytical and experimental program reported in this paper, it is shown that the proposed analytical solutions can be adopted to predict flexural–torsional buckling loads and used to formulate simplified design equations for pultruded FRP I-sections. As there are no simplified and yet rigorous

Table 2. Comparison of flexural–torsional buckling load for a pultruded FRP WF-AC beam

Load application	P_{cr} (kN)		
	Analytical solution	Finite element	Experimental
Centroid of section	171.952	166.857	—
Halfway between top flange and centroid	130.585	128.970	137.790
Top of flange	101.015	101.168	—

guidelines for predicting flexural–torsional buckling of pultruded FRP I-beams, it is significant that this paper develops an experimentally verified engineering equation that can be readily adopted by pultrusion manufacturers and practicing engineers.

REFERENCES

1. Hancock, G. J., Local, distortional, and lateral buckling of I-beams. *J. Struct. Div. ASCE*, 1978, **104**, (ST11), 1787–1798.
2. Roberts, T. M., Second order strains and instability of thin-walled bars of open cross-section. *Int. J. Mech. Sci.*, 1981, **23** (5), 297–306.
3. Roberts, T. M. and Jhita, P. S., Lateral local and distortional buckling of I-beams. *Thin-Walled Struct.*, 1983, **1** (5), 289–308.
4. Ma, M. and Hughes, O., Lateral distortional buckling of monosysmmetric I-beams under distributed vertical load. *Thin-Walled Struct.*, 1996, **26**, (2), 123–145.
5. Mottram, J. T., Lateral-torsional buckling of a pultruded I-beam. *Composites*, 1992, **32**, (2), 81–92.
6. Turvey, G. J., Effects of load position on the lateral buckling response of pultruded GRP cantilevers — comparisons between theory and experiment. *Composite Struct.*, 1996, **35** (1), 33–47.
7. Brooks, R. J. and Turvey, G. J., Lateral buckling of pultruded GRP I-section cantilevers. *Composite Struct.*, 1995, **32** (1–4), 203–215.
8. Turvey, G. J. & Brooks, R. J., Lateral buckling tests on pultruded GRP I-section beams with simply supported-simply supported and clamped-simply supported end conditions. In *Proc. First Int. Conf. on Composites in Infrastructure*, Tucson, Arizona, 1996, pp. 651–64.
9. Nethercot, D. A. and Rockey, K. C., A unified approach to the elastic lateral buckling of beams. *Struct. Engng*, 1971, **49** (7), 321–330.
10. Davalos, J. F., Qiao, P. and Barbero, E. J., Multiobjective material architecture optimization of pultruded FRP I-beams. *Composite Struct.*, 1996, **35** (3), 271–281.
11. Qiao, P., Analysis and design optimization of fiber-reinforced plastic (FRP) structural beams. Ph.D. dissertation, West Virginia University, Morgantown, WV, 1997.
12. Malvern, L. E., *Introduction to the Mechanics of a Continuous Medium*. Prentice–Hall, Englewood Cliffs, NJ, 1969.
13. Davalos, J. F., Salim, H. A., Qiao, P., Lopez-Anido, R. and Barbero, E. J., Analysis and design of pultruded FRP shapes under bending. *Composites, Part B: Engng J.*, 1996, **27B**, (3/4), 295–305.
14. Jones, R. M., *Mechanics of Composite Materials*. Hemisphere, New York, 1975.
15. *ANSYS User's Manual*. Swanson Analysis Systems Inc., Houston, PA, 1992.

ELSEVIER

Composite Structures Vol. 38, No. 1–4, pp. 251–260, 1997
© 1997 Elsevier Science Ltd. All rights reserved
Printed in Great Britain
0263-8223/97/$17.00 + 0.00

PII:S0263-8223(97)00060-3

Improvement of the dynamic properties of a steel–composite hybrid flexspline of a harmonic drive

Se Hoon Oh

Department of Mechanical Design and Production Engineering, Chungang University, Dongsak-gu, Seoul, Korea 156-756

&

Seung Hwan Chang & Dai Gil Lee

Department of Mechanical Engineering, Korea Advanced Institute of Science and Technology, ME3221, Gusong-dong, Yusong-gu, Taejon-shi, Korea 305-701

The harmonic drive is a special gear-drive speed reduction system whose operation principle is based on elastic deformation rather than rigid-body motion of the general gearing system. From the components of the harmonic drive, the flexspline is the key element for the transmission of motion. It must be flexible in the radial direction, but must be stiff in the torsional direction to accurately transmit rotational motion. Because the contradictory dual role of the flexspline cannot be satisfied effectively with conventional isotropic materials, but can be achieved with anisotropic composite materials, in this paper the cup section of the flexspline was hybridly manufactured by laying-up composite material on the inside surface of the steel cup section.

The static and dynamic characteristics of the hybrid flexspline were investigated with respect to the fibre volume fraction, stacking sequence and the mass ratio of the composite to steel. © 1997 Elsevier Science Ltd.

INTRODUCTION

The harmonic drive has many advantages, such as a high-speed reduction ratio, high rotational accuracy, high torque transfer per weight, high efficiency, little backlash and a very compact size. Therefore, the harmonic drive is widely adopted in precision mechanisms such as in industrial robots, CNC machine tools and communication equipment where little backlash and a high-speed reduction ratio are required.

The harmonic drive is composed of a rigid circular spline, elliptical wave generator and a flexible spline, which is called the flexspline. The input torque of the harmonic drive is usually applied to the shaft of the wave generator, which is pressure fitted to the open end of the flexspline, and the output torque is transmitted to the shaft at the closed end of the flexspline. In the case where the natural frequency of the radial direction of the flexspline coincides with the driving frequency of the wave generator a resonance vibration occurs. Therefore, the vibration characteristics such as natural frequency and damping ratio of the flexspline are very important. Figure 1 shows the shapes of the conventional cup-type steel flexspline which was investigated in this work.

Because the operation principle of the harmonic drive is based on elastic deformation rather than rigid-body motion, the flexspline must be flexible in the radial direction but must be stiff in the torsional direction. Therefore, the harmonic drive has dynamic drawbacks: the motion is not perfectly smooth but has a small ripple which has the same frequency as the

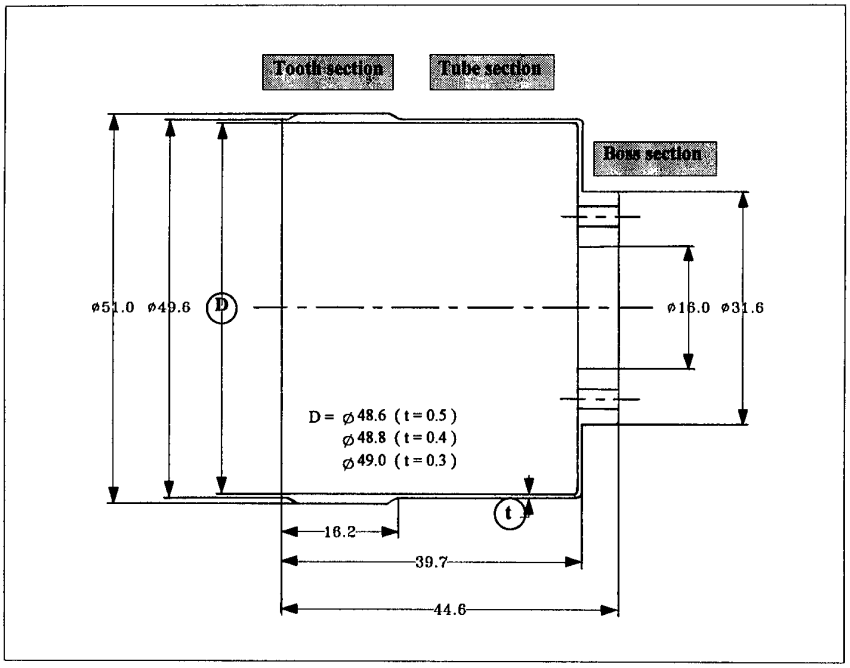

Fig. 1. Shape of the conventional cup-type steel flexspline investigated in this work.

wave generator. The ripple can produce noise or vibration when the natural frequency of the flexspline becomes the same as the exciting frequency. Also, the torsional stiffness of the flexspline is small because it is designed as a thin cup shape to decrease the radial stiffness. These phenomena cannot be avoided when the flexspline is made of conventional isotropic materials such as steel and aluminium.

In order to solve these problems, the flexspline was designed and manufactured using carbon fibre–epoxy composite because the carbon fibre–epoxy composite material has a high specific stiffness, a high specific strength and a high damping capacity [1–3]. According to previous studies on the composite flexspline, it was found that the composite flexspline had sufficient torque transmission capability and excellent vibration characteristics.

The vibration characteristics of composite cylindrical shells depend on the stacking sequence of composites. From the many studies on composite shells, several studies relating to the composite flexspline are cited in this paper. Jones & Morgan [4] investigated vibration characteristics of cross-ply composite shells. Ditaranto [5] derived the sixth-order equation of motion, taking into consideration the shear deformation of a beam, and also derived an auxiliary equation to explain the damping effect of the viscoelastic materials on the vibration. Sharma & Darvizeh [6] analysed free vibration problems of specially orthotropic thin cylindrical shells with various boundary conditions using Rayleigh–Ritz variational procedure. Kostas [7] studied the buckling and free vibration problems of thin composite antisymmetric angle ply shells and concluded that the effect of coupling between bending and extension on free vibration frequencies died out rapidly as the number of layers increased.

In this study, in order to enhance the damping capacity of the flexspline and to increase the manufacturing productivity of the flexspline, the hybrid type flexspline was manufactured using both composites and steel. The inside of the hybrid flexspline was reinforced with carbon fibre–epoxy composite and glass fibre–epoxy composite either by co-cure bonding or by epoxy adhesive bonding. The design concept of the hybrid flexspline is that the steel part of the flexspline transmits the major portion of required torque, while the composite part increases the natural frequency and damping capacity of the flexspline.

The static and dynamic characteristics of the hybrid flexspline were measured and compared to those of the steel flexspline with respect to

Table 1. Properties of the steel

Tensile modulus (GPa)	200
Shear modulus (GPa)	80
Poisson's ratio	0.27
Tensile strength (MPa)	1000
Density (kg/m^3)	7850

the thickness of the steel tube, the stacking sequence of the composites and the thickness of the adhesive.

MANUFACTURE OF THE HYBRID FLEXSPLINE

The properties of the steel, composite materials and epoxy resin that were used for the hybrid flexspline are shown in Tables 1–3, respectively.

The co-cured hybrid flexspline was manufactured by laying-up composite prepregs on the inside of a steel tube and curing in an autoclave with a cure cycle as shown in Fig. 2. The inside surface of the steel tube was abraded using #80 mesh sandpaper giving a better adhesion of the composite to the steel.

The required pressure for the consolidation of the prepreg and the adhesion of the composite to the steel tube was given by a silicon mandrel. The pressure of the silicon mandrel was adjusted by upper and lower plates which gave axial compression to the silicon rubber. The stacking sequences of the composites for the manufacture of the hybrid flexspline were $[\pm 30°]_T$, $[\pm 45°]_T$, $[\pm 60°]_T$, $[\pm 30°]_S$, $[\pm 45°]_S$ and $[\pm 60°]_S$.

Table 2. Properties of the composites

	Carbon fibre–epoxy composite	Glass fibre–epoxy composite
E_L (GPa)	130.0	43.5
E_T (GPa)	8.0	5.0
G_{LT} (GPa)	6.0	5.0
ν_{LT}	0.28	0.25
X^t (MPa)	1800	1000
Y^t (MPa)	60.0	50.0
S (MPa)	75.0	50.0

Table 3. Properties of the epoxy resin (IPCO 9923)

Tensile modulus (GPa)	1.3
Shear modulus (GPa)	0.46
Poisson's ratio	0.41
Tensile strength (MPa)	45.0
Shear strength (MPa)	29.5
Lap shear strength (MPa)	13.7
Density (kg/m^3)	1200

Figure 3 shows a photograph of the co-cured hybrid flexspline and the silicon rubber mandrel.

The hybrid flexspline was also manufactured by using adhesive bonding to compare the performance of the two flexsplines. The epoxy resin used for adhesive bonding was IPCO 9923 (from IPCO National Ltd, USA) and its properties are given in Table 3. The inside surface of the steel tube was abraded with #80 mesh sandpaper before adhesive bonding, and bonding thicknesses of 0.1, 0.5 and 1.0 mm were used. For control of the bonding thickness and the concentricity of the adherends, the guide section of a cylindrical fixture was inserted in the

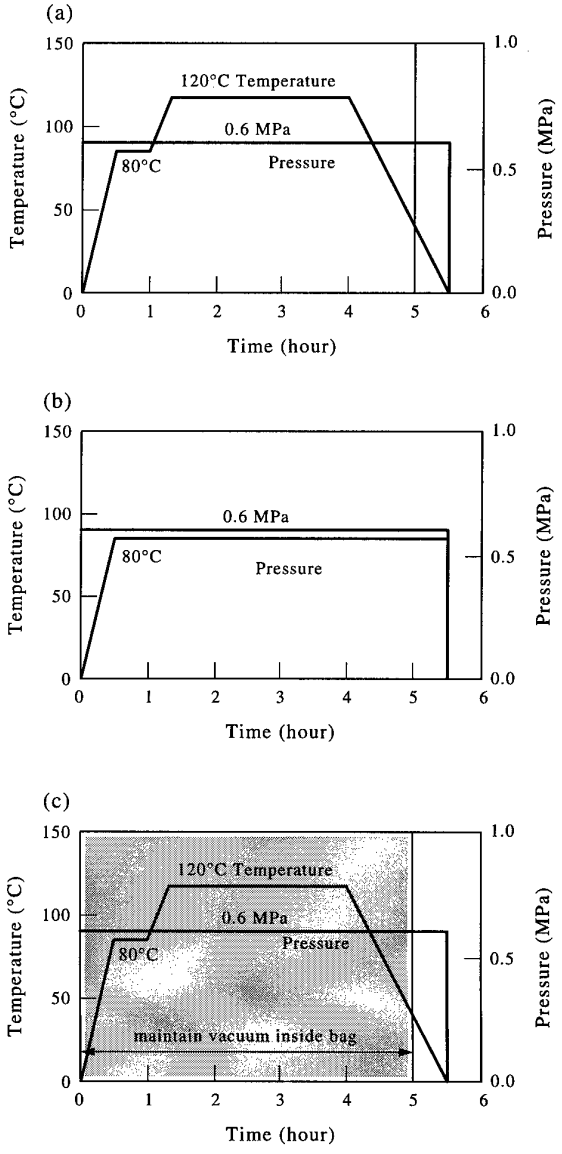

Fig. 2. Cure cycle for the composite materials, the epoxy resin and the silicon rubber.

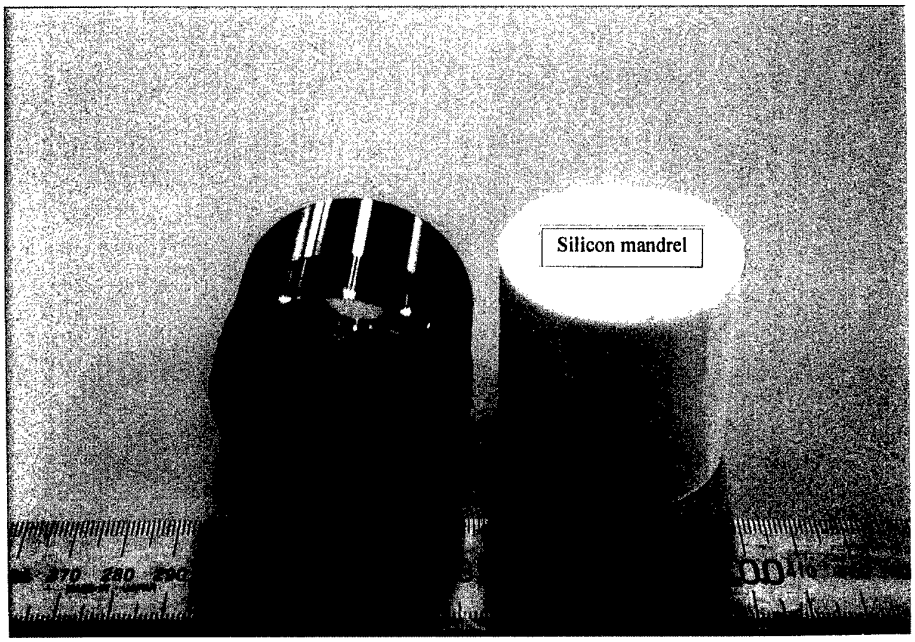

Fig. 3. Photograph of the co-cured hybrid flexspline and the silicon rubber mandrel.

hole of the boss section of the flexspline. Figure 4 shows the cylindrical fixture for the concentric adhesive bonding of the hybrid flexspline. The epoxy adhesive was cured using a cure cycle as shown in Fig. 2 in an autoclave and the composite tube was cured using a vacuum bag degassing–moulding process. Figure 5 shows the flexspline manufactured by using epoxy adhesive bonding.

MEASUREMENT OF THE SPRING CONSTANT OF THE HYBRID FLEXSPLINE

The stiffness of the flexspline in the radial direction must be low for smooth operation. Because the stiffness of the hybrid flexspline in the radial direction might be increased too much due to the reinforcement of the composite, the spring constant of the flexspline was

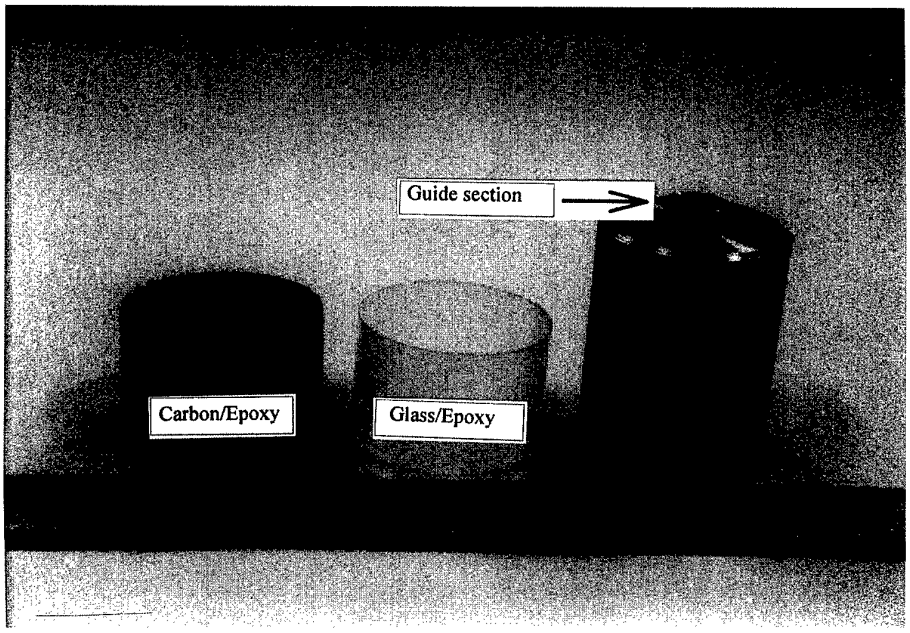

Fig. 4. Composite tube and cylindrical fixture for concentric bonding.

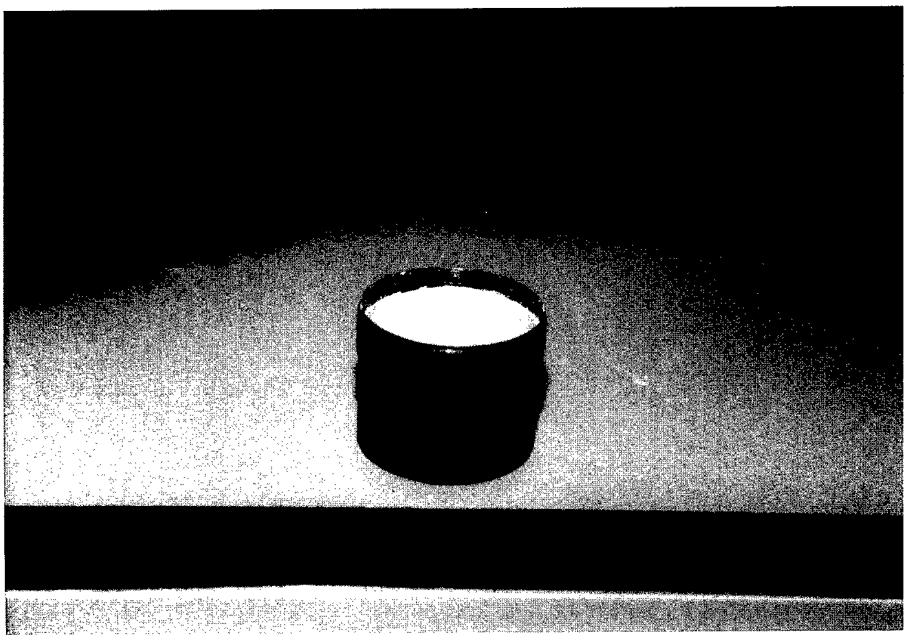

Fig. 5. Hybrid flexspline manufactured by epoxy adhesive bonding.

measured by compressing the flexspline with INSTRON 4206, as shown in Fig 6. Figure 7 shows the measured stiffness of the flexspline in the radial direction with respect to stacking sequence and bonding type such as co-cure bonding and adhesive bonding. The adhesive thickness of the adhesively bonded hybrid flexspline in Fig. 7 was 0.1 mm.

From the test results it was found that the stiffness of the flexspline was strongly dependent on the type of composite, the stacking sequence and the number of plies as the thickness of the steel tube was decreased. When a 0.3 mm thick steel tube was reinforced by co-cure bonding with the carbon fibre–epoxy composite, with a $[\pm 60°]_S$ stacking sequence, the radial stiffness was increased by about $+100\%$, while that of the hybrid flexspline reinforced by co-cure bonding with the glass fibre–epoxy composite, with a $[\pm 60°]_S$ stacking

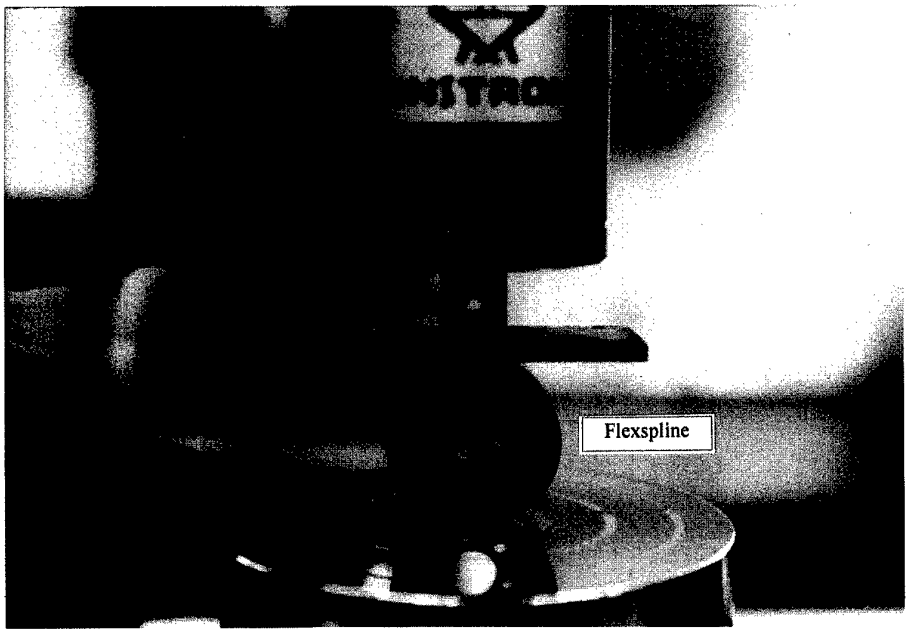

Fig. 6. Apparatus for measuring the spring constant of the flexspline.

sequence, was increased about 30% compared with that of the unreinforced steel flexspline. When the steel tube was reinforced by adhesive bonding with the glass fibre–epoxy composite, with a $[\pm 60°]_S$ stacking sequence, the stiffness was increased about 100% when the bonding thickness was 0.1 mm, while that of the carbon fibre–epoxy composite reinforced with same stacking sequence was increased about 300%. Therefore, it was concluded that the glass fibre–epoxy composite material and the small stacking angle from the axis of the flexspline were beneficial because the flexspline must be flexible in the radial direction.

VIBRATION CHARACTERISTICS OF THE HYBRID FLEXSPLINE

The vibration characteristics of the hybrid flexspline were measured using an impulse–frequency response test. The test apparatus consisted of a dual-channel fast Fourier transform analyser (B&K 2032), a charge amplifier

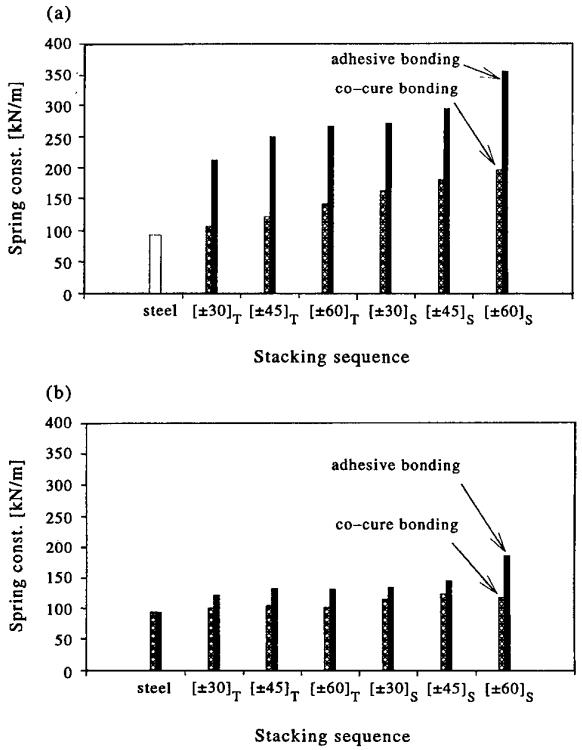

Fig. 7. Comparison of measured spring constants of the flexsplines with respect to the stacking sequence and bonding type (co-cure bonding and epoxy adhesive bonding): (a) reinforced with the carbon fibre–epoxy composite; and (b) reinforced with the glass fibre–epoxy composite.

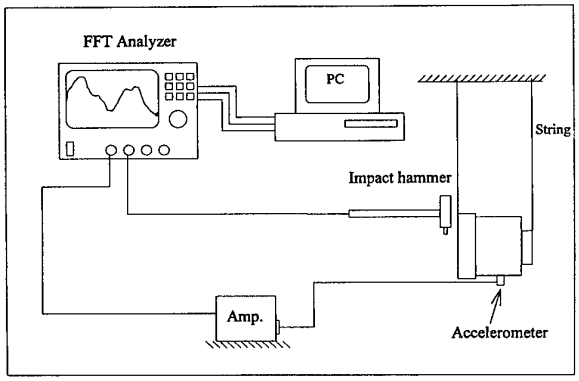

Fig. 8. Impulse–frequency response test of the flexspline.

(B&K 2626), an impulse hammer (B&K 8202), an accelerometer (B&K 4374), a force transducer (B&K 8200) and a personal computer with an HP-IB board for data acquisition. The fundamental natural frequency and damping ratio were measured by giving radial impulses on the flexspline suspended with strings, as shown in Fig. 8. Figure 9 shows the fundamental natural frequency and damping of the co-cured hybrid flexspline, and Fig. 10 shows the fundamental natural frequency and damping of the adhesively bonded hybrid flexspline reinforced with the glass fibre–epoxy composite with respect to stacking sequence, number of ply and thickness of the steel tube.

As shown in Fig. 9, the fundamental natural frequency of the co-cured hybrid flexspline was increased and the damping ratio was decreased as the stacking angle was increased. The vibration characteristics of the hybrid flexspline was greatly dependent on the properties of the composite materials as the thickness of the steel tube was decreased. When the thickness of the steel tube was 0.3 mm, for the hybrid flexspline reinforced with the glass fibre–epoxy composite with a stacking sequence of $[\pm 30°]_S$, the fundamental natural frequency in the radial direction was increased by 8%; however, the damping ratio was increased by about 140% compared with those of the unreinforced steel flexspline of 0.3 mm thickness.

As shown in Fig. 10, for the adhesively bonded hybrid flexspline reinforced with the glass fibre–epoxy composite with a stacking sequence of $[\pm 30°]_S$, the fundamental natural frequency in the radial direction was increased by 23–47% when the bonding thickness varied from 0.1 to 1.0 mm; however, the damping ratio was increased by 630% when the bonding thickness

was 0.1 mm, compared with those of the unreinforced steel flexspline of 0.3 mm thickness.

From the test results it was found that the damping ratio of the adhesively bonded hybrid flexspline was superior to that of the co-cured hybrid flexspline and the damping ratio of the hybrid flexspline reinforced with a glass fibre–epoxy composite was higher than that of the hybrid flexspline reinforced with a carbon fibre–epoxy composite. Therefore, the adhesively bonded hybrid flexspline reinforced with the glass fibre–epoxy composite was more beneficial.

TORQUE TEST

The torque transmission capabilities of the hybrid flexsplines, manufactured either by co-curing or by adhesive bonding with bonding thickness of 0.1 mm, were tested. The flexspline which consisted of the glass fibre–epoxy composite with a stacking sequence of $[\pm 30°]_T$ and a steel tube of thickness 0.3 mm was tested because this type of flexspline is supposed to have the lowest torque transmission capability.

Figure 11 shows the apparatus (MTS 319.10) for the torque test of the flexspline. During the torque test, the six bolts clamping the boss section of the hybrid flexspline failed at the applied torque of 430 Nm. As the rated torque transmission capability of the flexspline was 110 Nm, further tests were not performed. Therefore, it was concluded that the hybrid flexsplines had a sufficient torque transmission capability.

FINITE-ELEMENT ANALYSIS OF THE HYBRID FLEXSPLINE

The fundamental natural frequency in the radial direction was calculated by finite-element method using ANSYS5.0, a commercial software. Also, the torque transmission capability of the hybrid flexspline was calculated by finite-element method and compared to the experimental results when it was subjected to the maximum rated torque of the flexspline.

The eight-node 3-DOF SOLID 45 elements of ANSYS were used for the modelling of isotropic materials such as steel and epoxy, and the eight-node 3-DOF SOLID 46 elements

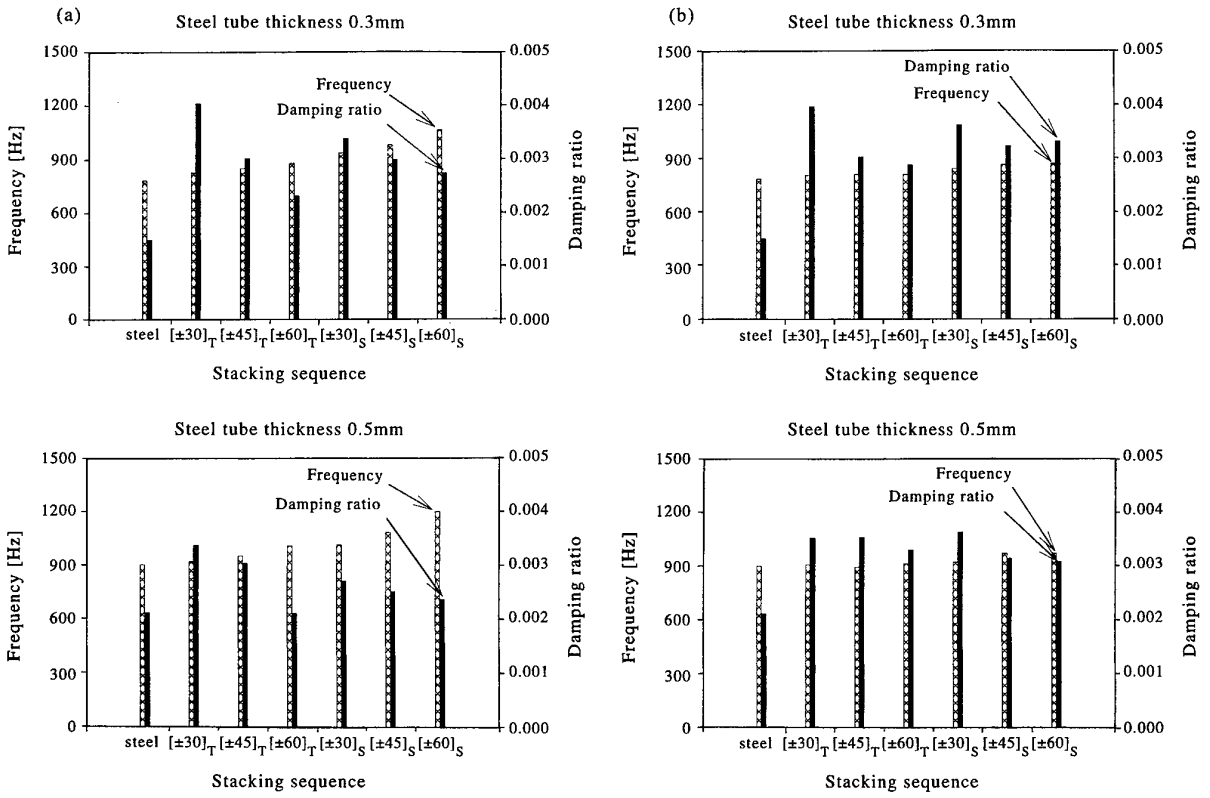

Fig. 9. Vibration characteristics of the co-cured hybrid flexspline: (a) reinforced with the carbon fibre–epoxy composite; and (b) reinforced with the glass fibre–epoxy composite.

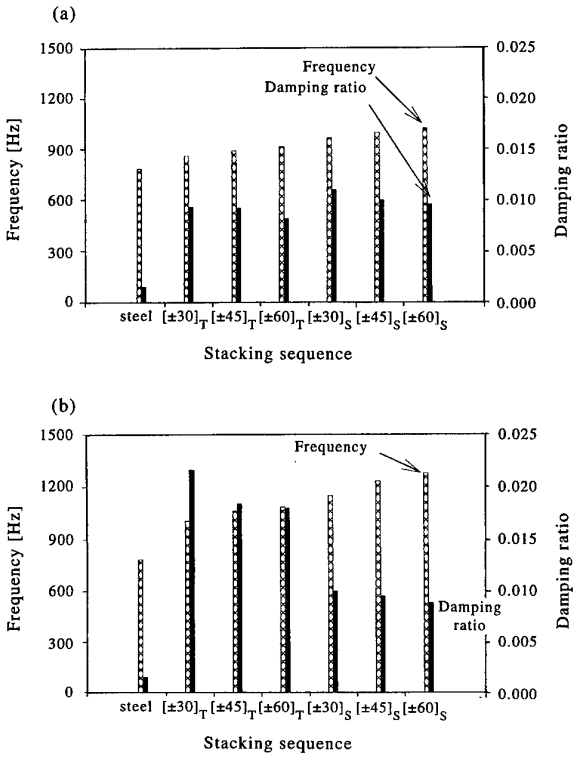

Fig. 10. Vibration characteristics of the adhesively bonded hybrid flexspline reinforced with the glass fibre–epoxy composite. Bonding thickness of (a) 0.1 mm and (b) 1.0 mm.

were used for the modelling of anisotropic materials such as the carbon fibre–epoxy composite and the glass fibre–epoxy composite, as shown in Fig. 12.

Owing to axi-symmetry, only a quarter of the flexspline was modelled, and the tooth part was modelled as a rectangular cross-section which has the same area as a trapezoid consisting of an addendum circle for the upper side and a dedendum circle for the lower side of the tooth.

For the torque analysis, the element nodes were fixed in the radial and axial directions to prevent out-of-plane deformation, and the boss section was fixed. The torque was applied to the outer nodes of the tooth section in the θ-direction.

Although the tooth shape of the flexspline was assumed to be rectangular, the error in the fundamental natural frequency between the calculated and the experimentally determined was less than 10%, as shown in Fig. 13.

When the co-cured hybrid flexspline was composed of a 0.3 mm steel tube and the glass fibre–epoxy composite, with a stacking sequence of $[\pm 30°]_T$, the maximum stresses in the steel tube and the composite tube were 0.67 GPa and 21.3 MPa in the composite part (failure index = 0.10), respectively. When the adhesively bonded hybrid flexspline was reinforced with the glass fibre–epoxy composite, with the same stacking sequence, the maximum

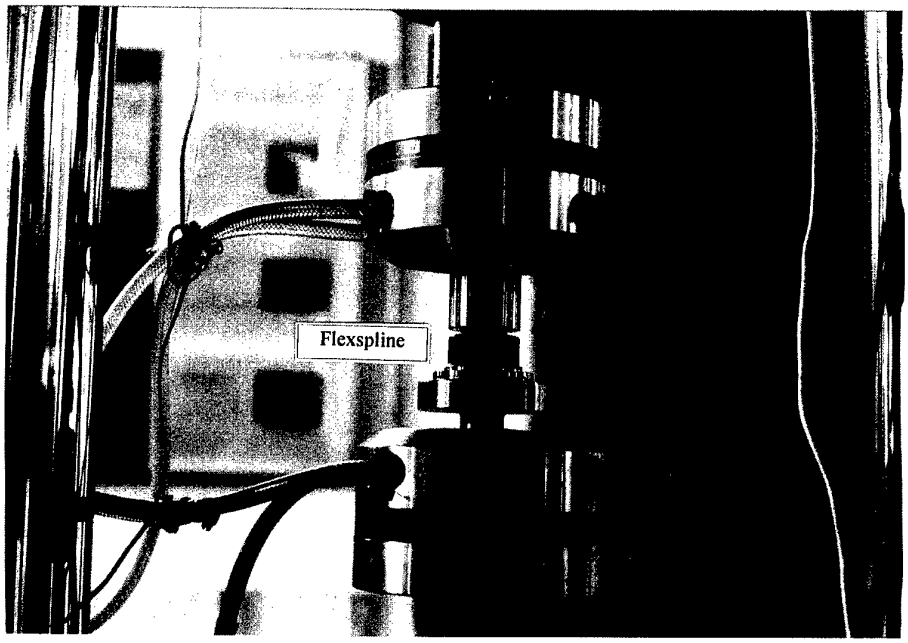

Fig. 11. The apparatus for the torque test of the flexspline.

stress of the steel part was slightly decreased as the bonding thickness was increased. When the bonding thickness was 1.0 mm, the maximum stresses in the steel tube and the composite tube were 0.661 GPa and 20.1 MPa (failure index = 0.09), respectively. Therefore, it was concluded that the hybrid flexspline reinforced with the glass fibre–epoxy composite had good torque transmissibility.

CONCLUSIONS

In this paper the hybrid flexspline of a harmonic drive was designed and manufactured with steel and fibre-reinforced composite materials to improve the dynamic properties of the steel flexspline. The carbon fibre–epoxy composite and the glass fibre–epoxy composite were either co-cure bonded or adhesively bonded to the inside surface of the steel tube to produce the hybrid flexspline.

From the experimental and numerical results it was found that the adhesively bonded hybrid flexspline had better dynamic characteristics than those of the co-cured and unreinforced flexsplines. For the adhesively bonded hybrid flexspline reinforced with the glass fibre–epoxy composite, with a stacking sequence of $[\pm 30°]_S$, the damping capacity was increased by 630%, while the fundamental frequency and the radial stiffness was increased by only 23% and 43%, respectively, compared to those of the unreinforced steel flexspline when the bonding thickness was 0.1 mm. Also, it was found that the hybrid flexspline had enough torque transmission capability compared to the steel flexspline.

Therefore, it may be concluded that the adhesively bonded hybrid flexspline reinforced with the glass fibre–epoxy composite, with a

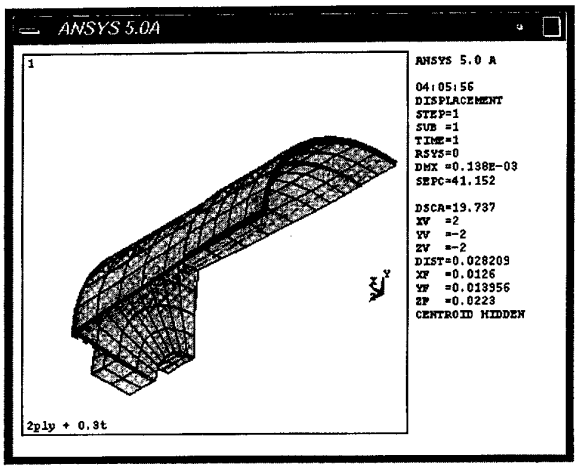

(a)

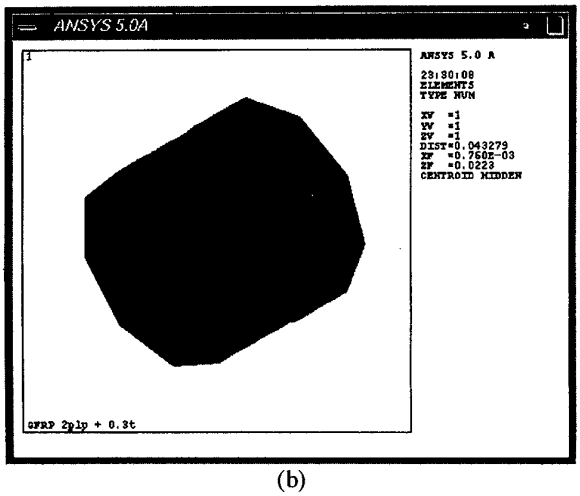

(b)

Fig. 12. Finite-element model for the hybrid flexspline: (a) modelling for modal analysis; and (b) modelling for torque analysis.

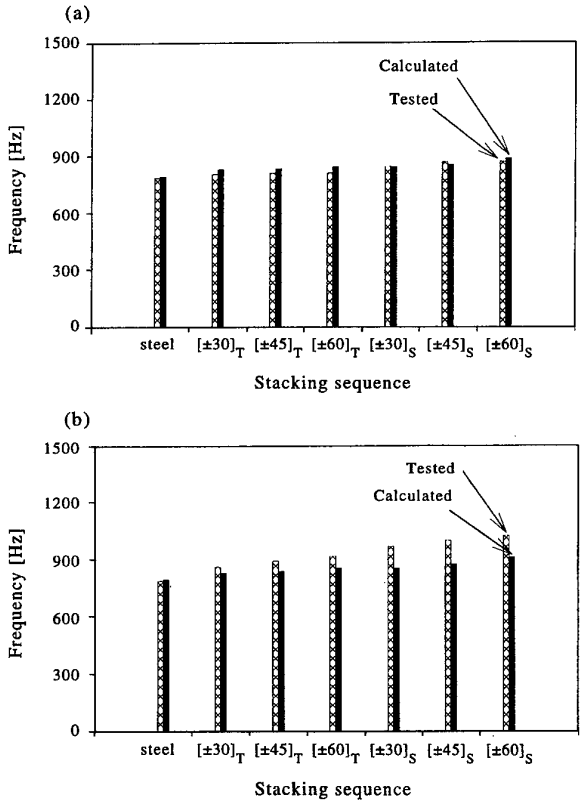

Fig. 13. Comparison between the test results and the calculated results when the steel thickness was 0.3 mm: (a) co-cured flexspline reinforced with the glass fibre–epoxy composite; and (b) adhesively bonded flexspline reinforced with the glass fibre–epoxy composite.

stacking sequence of $[\pm 30°]_S$, was most appropriate for a harmonic drive.

ACKNOWLEDGEMENTS

The authors thank Kwang Shin Co. and KAIST for manufacturing the harmonic drives. This research was supported by Chungary University research grants.

REFERENCES

1. Jeong, K.S., Lee, D.G. and Kwak, Y.K., Adhesive joining technology for manufacturing of the composite flexspline for a harmonic drive. *J. Adhesion*, 1996, **55**, 329–350.
2. Jeong, K.S., Lee, D.G. and Oh, S.H., Development of the composite flexspline for a cycloid-type harmonic drive using net shape manufacturing method. *Composite Struct.*, 1995, **32**, 557–565.
3. Oh, H.S., Jeong, K.S. and Lee, D.G., Design and manufacture of the composite flexspline of a harmonic drive with adhesive joining. *Composite Struct.*, 1994, **28**, 307–314.
4. Jones, R.M. and Morgan, S.H., Buckling and vibration of cross-ply laminated circular cylindrical shells. *AIAA J.*, 1975, **13**(5), 664–671.
5. Ditaranto, R.A., Theory of the vibratory bending for elastic and viscoelastic finite length beams. *J. Appl. Mech., Trans. ASME*, 1965, **32**, 881–886.
6. Sharma, C.B. and Darvizeh, M., Free vibration of specially orthotropic, multilayered, thin cylindrical shells with various end conditions. *Composite Struct.*, 1987, **7**, 123–138.
7. Kostas, P.S., On the buckling and vibration of antisymmetric angle-ply laminated circular cylindrical shells. *Int. J. Engng Sci.*, 1983, **21**, 217–232.

ELSEVIER

Composite Structures Vol. 38, No. 1–4, pp. 261–271
Printed in Great Britain
0263-8223/97/$17.00 + 0.00

PII:S0263-8223(97)00061-5

A three-dimensional modelling technique for predicting the linear elastic property of opened-packing woven fabric unit cells

P. Tan,[a,b] L. Tong[a] & G. P. Steven[a]

[a]*Department of Aeronautical Engineering, University of Sydney, Sydney, NSW 2006, Australia*
[b]*Cooperative Research Center for Aerospace Structures, P.O. Box 30, 351 Milperra Road, Bankstown, NSW 2200, Australia*

Woven fabric has been recognized as one of the widely used materials in the aerospace industry. In order to effectively utilize this material, it is necessary to evaluate its mechanical properties. In this paper a three-dimensional multi-scaled modelling technique has been developed to investigate the linear elastic properties of single-ply opened-packing woven fabrics for pure tension and shear responses. This technique is accomplished by introducing a number of new three-dimensional macro- and micro-blocks. Thus, this technique can be considered as a full three-dimensional modelling technique. In order to verify the capability of this method, some theoretical and finite-element analysis (FEA) numerical studies were carried out for four types of opened-packing woven fabric unit cells. It was shown that there exists a good agreement between the theoretical results and those predicted using the FEA models. The trends of the stiffness and engineering elastic constants with n_g, which denotes a warp (or weft) yarn is interlaced with every n_gth weft (or warp) yarn, were also investigated. For the in-plane elastic properties, the present results correlate well with those available in the literature. © 1997 Elsevier Science Ltd.

INTRODUCTION

To tailor woven fabric composite materials to the exact requirements of their functions in the components or structures, it is necessary to determine their mechanical properties. Measurements of these properties are difficult and the costs involved can be very high, especially when studying effects of manufacturing and geometrical parameters. Theoretical and finite-element analysis (FEA) modelling are cost-effective alternatives of determining these properties, and thus provide savings in both manpower and time [1,2].

It is known that [3–8] a woven fabric is usually considered as an assemblage of unit cells interconnected at a discrete number of nodal points. Hence, mechanical properties for woven fabrics can be predicted based on those for the relevant unit cells.

In this paper, a three-dimensional modelling technique applicable to theoretical and FEA analysis is presented for predicting the linear elastic properties for opened-packing woven fabric unit cells. This technique involves artificial division of a woven fabric unit cell into macro-blocks, which are further divided into micro-blocks. The fabric reinforcing geometry for a micro-block is easier to determine, model and analyse.

In the theoretical model, the linear elastic properties of the three-dimensional micro-blocks are easy to obtain theoretically utilizing elastic mechanics theory. Those for the macro-blocks can be evaluated using an 'XY model' or 'YX model' and the relevant elastic properties of the micro-blocks. The 'XY model' and 'YX model' will be described in the following section. The procedure for evaluating elastic properties of the macro-blocks can also be

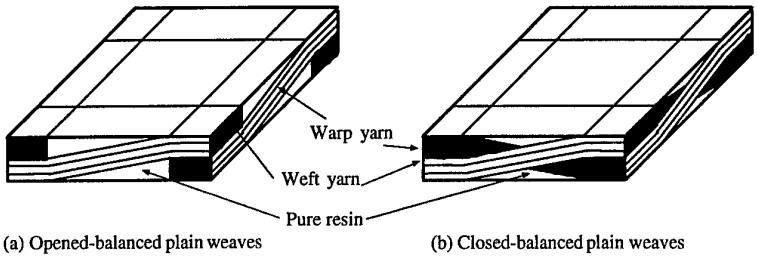

Fig. 1. A schematic of unit-cell architecture for the artificial plain weaves.

utilized to estimate those for woven fabric unit cells. In FEA modelling, using the FEA software Strand6 [9], the linear elastic properties for micro-blocks, macro-blocks and woven fabric unit cells can also be obtained. It is shown that there exists a good correlation between the theoretical results and those calculated using FEA models.

To be cost-effective on establishing and running FEA models, it is suggested that a mechanical property data bank be established for the micro- and macro-blocks. Thus, for the blocks that have the same geometrical parameters and mechanical properties of composite constituents, we can select the same elastic property data from the data bank rather than run the models again.

THEORETICAL MODELLING

In this section, the linear elastic properties for woven fabric unit cells will be investigated using the 'XY model' and 'YX model', respectively. This investigation was carried out based on four types of artificial woven fabric unit-cell architectures (i.e. plain, twill, 5- and 8-harness satin weaves).

Constructions and assumptions of the artificial woven fabric unit-cell architecture

Owing to the complicated architecture of woven fabric, it is difficult to describe a unit-cell geometry at the same scale as woven fabric micro-geometry. Hence, the geometrical models for woven fabrics are established at the yarn level. In these models, each yarn contains a few thousand fibres and all fibres are assumed to follow the same path as the corresponding yarn. To evaluate the elastic properties with minimum effort, four simplified three-dimensional unit-cell models are proposed for the four types of woven fabrics. As shown in Fig. 1, for plain woven fabrics it is noted that the cross-section shapes of yarns in the unit-cell models are assumed to be rectangular for opened-packing woven fabrics (see Fig. 1a) and hexagonal for closed-packing woven fabrics (see Fig. 1b). Each yarn in a unit cell is divided into three segments along its longitudinal direction, i.e. two straight yarn segments and one undulated yarn segment. In the present work the discussion is restricted to non-hybrid, opened-packing woven fabrics.

For all four types of artificial woven fabric unit-cell models, the following assumptions are introduced to simplify the analysis.

- The woven fabrics are assumed to be balanced, i.e. within a woven fabric unit cell, the fibre volume fraction and mechanical properties along the warp direction are exactly the same as those in the weft direction.
- Both warp and weft yarns exhibit linear elastic behaviours prior to failure. The elastic properties of yarns are taken to be identical to those of fibres.
- The warp and weft yarns are packed perfectly. Thus, the overall fibre volume fraction is equal to the ratio of the yarn geometrical volume to the whole unit-cell geometrical volume. The void of resin and nesting resin on the interlacing areas between a warp yarn and a weft yarn are ignored.
- The undulated segments for both warp and weft yarns are idealized to be inclined straight yarns.
- The micro-blocks, macro-blocks and woven unit cells are assumed to be orthotropic and homogeneous in the woven fabric unit-cell global coordinate system, while resin is assumed to be isotropic and homogeneous.

Theoretical modelling for plain weaves

An opened-packing plain weave unit cell is shown in Fig. 2(a) using a bold square, where a small square covered with light lines indicates that the warp yarn crosses over the weft yarn at that intersection can be considered to be an assemblage of three types of micro-blocks, as shown in Fig. 2(b). They are the straight cross-ply micro-block (SCPMIB), the undulated yarn micro-block (UMIB) and the pure resin micro-block (PRMIB) (see Fig. 2c). The micro-block SCPMIB is composed of two straight fibre yarn segments which are cross-banded, while the micro-block UMIB consists of an undulated fibre yarn segment and pure resin. The constituent of the micro-block PRMIB is pure resin.

For the micro-block SCPMIB, the stress–strain relations in the global coordinate system for a plain weave unit cell can be expressed as follows

$$\sigma_i = C_{ij}\varepsilon_j \tag{1}$$

where the stiffness constants C_{ij} $(i, j = 1\text{–}6)$ are given by

$$C_{11} = C_{11}^{\mathrm{T}}V^{\mathrm{T}} + C_{11}^{\mathrm{B}}V^{\mathrm{B}} \tag{2}$$

$$C_{12} = C_{12}^{\mathrm{T}}V^{\mathrm{T}} + C_{12}^{\mathrm{B}}V^{\mathrm{B}} \tag{3}$$

$$C_{13} = C_{33}\left(\frac{C_{13}^{\mathrm{T}}V^{\mathrm{T}}}{C_{33}^{\mathrm{T}}} + \frac{C_{13}^{\mathrm{B}}V^{\mathrm{B}}}{C_{33}^{\mathrm{B}}}\right) \tag{4}$$

$$C_{22} = C_{22}^{\mathrm{T}}V^{\mathrm{T}} + C_{22}^{\mathrm{B}}V^{\mathrm{B}} \tag{5}$$

$$C_{23} = C_{33}\left(\frac{C_{23}^{\mathrm{T}}V^{\mathrm{T}}}{C_{33}^{\mathrm{T}}} + \frac{C_{23}^{\mathrm{B}}V^{\mathrm{B}}}{C_{33}^{\mathrm{B}}}\right) \tag{6}$$

$$C_{33} = \frac{C_{33}^{\mathrm{T}}C_{33}^{\mathrm{B}}}{V^{\mathrm{T}}C_{33}^{\mathrm{B}} + V^{\mathrm{B}}C_{33}^{\mathrm{T}}} \tag{7}$$

$$C_{44} = \frac{C_{44}^{\mathrm{T}}C_{44}^{\mathrm{B}}}{V^{\mathrm{T}}C_{44}^{\mathrm{B}} + V^{\mathrm{B}}C_{44}^{\mathrm{T}}} \tag{8}$$

$$C_{55} = \frac{C_{55}^{\mathrm{T}}C_{55}^{\mathrm{B}}}{V^{\mathrm{T}}C_{55}^{\mathrm{B}} + V^{\mathrm{B}}C_{55}^{\mathrm{T}}} \tag{9}$$

$$C_{66} = C_{66}^{\mathrm{T}}V^{\mathrm{T}} + C_{66}^{\mathrm{B}}V^{\mathrm{B}} \tag{10}$$

in which V^{T} and V^{B} are the volume fractions for the top and bottom fibre ply, respectively; C_{ij}^{T}, C_{ij}^{B}, and C_{ij} are, respectively, the stiffness constants for the top fibre ply, the bottom fibre ply and the micro-block SCPMIB.

For the micro-block UMIB, shown in Fig. 2(c), the stiffness constants C_{ij} under the yarn principal direction coordinate system can be evaluated using eqns (2)–(10), and then the stiffness constants C'_{ij} under the plain weave unit-cell global coordinate system can be obtained by

$$[C'_{ij}] = [T^{-1}][C_{ij}][T] \tag{11}$$

where $[C_{ij}]$ is the stiffness matrix referred to in the local coordinate system and $[C'_{ij}]$ is the stiffness matrix in the global coordinate system, and

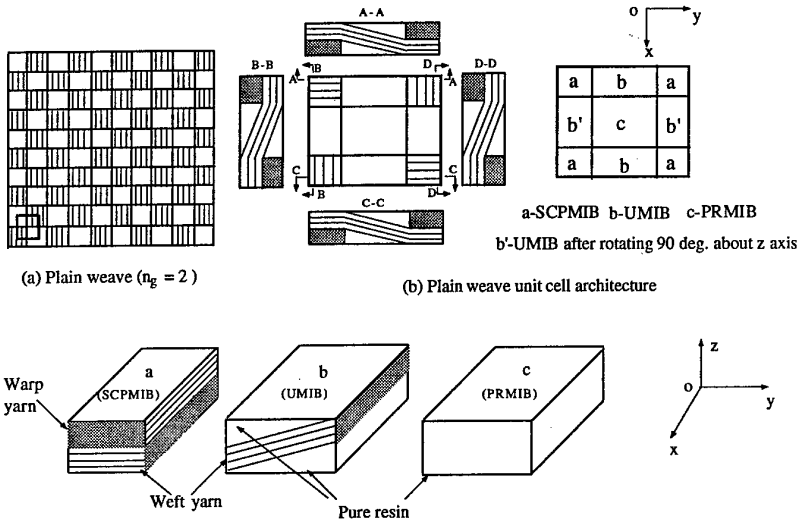

Fig. 2. A schematic of plain weaves.

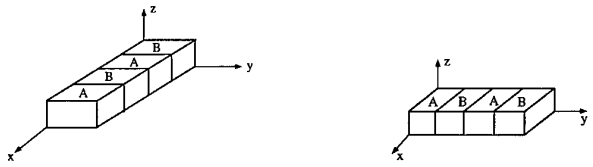

(a) "X model" (b) "Y model"

Fig. 3. The schematic of (a) the 'X model' and (b) the'Y model'.

$[T]$ is the Hamiltonian tensor transformation matrix.

For the micro-block PRMIB, the relevant stiffness constants can be evaluated in terms of the Young's modulus and Poisson's ratio of the resin.

Evidently, the stiffness constants for the micro-blocks SCPMIB, UMIB and PRMIB, evaluated above, can be further used to determine the elastic properties of a plain weave unit cell using the 'X model' and the 'Y model'. In the 'X model' all micro-blocks are assembled into a strip along the x-axis (shown in Fig. 3a), while in the 'Y model' all micro-blocks are assembled into a strip in the y-direction (shown in Fig. 3b).

Using concepts of both the 'X model' and 'Y model', and the elastic mechanics theory, we derive the following formulae for the stiffness constants of a strip assembled by micro-block elements.

1. Equations derived using the 'X model'

$$C_{11}^{S}=\frac{C_{11}^{A}C_{11}^{B}}{N^{A}V^{A}C_{11}^{B}+N^{B}V^{B}C_{11}^{A}} \tag{12}$$

$$C_{12}^{S}=C_{11}^{S}\left[\frac{N^{A}C_{12}^{A}V^{A}}{C_{11}^{A}}+\frac{N^{B}C_{12}^{B}V^{B}}{C_{11}^{B}}\right] \tag{13}$$

$$C_{13}^{S}=C_{11}^{S}\left[\frac{N^{A}C_{13}^{A}V^{A}}{C_{11}^{A}}+\frac{N^{B}C_{13}^{B}V^{B}}{C_{11}^{B}}\right] \tag{14}$$

$$C_{22}^{S}=N^{A}C_{22}^{A}V^{A}+N^{B}C_{22}^{B}V^{B} \tag{15}$$

$$C_{23}^{S}=N^{A}C_{23}^{A}V^{A}+N^{B}C_{23}^{B}V^{B} \tag{16}$$

$$C_{33}^{S}=N^{A}C_{33}^{A}V^{A}+N^{B}C_{33}^{B}V^{B} \tag{17}$$

$$C_{44}^{S}=N^{A}C_{44}^{A}V^{A}+N^{B}C_{44}^{B}V^{B} \tag{18}$$

$$C_{55}^{S}=\frac{C_{55}^{A}C_{55}^{B}}{N^{A}V^{A}C_{55}^{B}+N^{B}V^{B}C_{55}^{A}} \tag{19}$$

$$C_{66}^{S}=\frac{C_{66}^{A}C_{66}^{B}}{N^{A}V^{A}C_{66}^{B}+N^{B}V^{B}C_{66}^{A}} \tag{20}$$

2. Equations derived using the 'Y model'

$$C_{11}^{S}=N^{A}C_{11}^{A}V^{A}+N^{B}C_{11}^{B}V^{B} \tag{21}$$

$$C_{12}^{S}=C_{22}^{S}\left[\frac{N^{A}C_{12}^{A}V^{A}}{C_{22}^{A}}+\frac{N^{B}C_{12}^{B}V^{B}}{C_{22}^{B}}\right] \tag{22}$$

$$C_{13}^{S}=N^{A}C_{13}^{A}V^{A}+N^{B}C_{13}^{B}V^{B} \tag{23}$$

$$C_{22}^{S}=\frac{C_{22}^{A}C_{22}^{B}}{N^{A}V^{A}C_{22}^{B}+N^{B}V^{B}C_{22}^{A}} \tag{24}$$

$$C_{23}^{S}=C_{22}^{S}\left[\frac{N^{A}C_{23}^{A}V^{A}}{C_{22}^{A}}+\frac{N^{B}C_{23}^{B}V^{B}}{C_{22}^{B}}\right] \tag{25}$$

$$C_{33}^{S}=N^{A}C_{33}^{A}V^{A}+N^{B}C_{33}^{B}V^{B} \tag{26}$$

$$C_{44}^{S}=\frac{C_{44}^{A}C_{44}^{B}}{N^{A}V^{A}C_{44}^{B}+N^{B}V^{B}C_{44}^{A}} \tag{27}$$

$$C_{55}^{S}=N^{A}C_{55}^{A}V^{A}+N^{B}C_{55}^{B}V^{B} \tag{28}$$

$$C_{66}^{S}=\frac{C_{66}^{A}C_{66}^{B}}{N^{A}V^{A}C_{66}^{B}+N^{B}V^{B}C_{66}^{A}} \tag{29}$$

where N^{A} and N^{B} are the numbers of micro-blocks A and B within a strip, respectively; and V^{A} and V^{B} are the volume fractions of micro-blocks A and B, respectively; C_{ij}^{A}, C_{ij}^{B} and C_{ij}^{S} are the stiffness constants for micro-block A, micro-block B and a strip, respectively.

Similarly, the stiffness constants for a plain weave unit cell can also be evaluated using the 'Y model' or 'X model' and the relevant strip stiffness constants. Thus, we need to introduce two models known as the 'XY model' and 'YX model' for evaluating the stiffness constants for a plain weave unit cell. In the 'XY (or YX) model' all micro-blocks of a strip along the x (or

y) direction are assembled, then all of these strips are assembled in the y (or x) direction. So we can use the 'X (or Y) model' to evaluate the stiffness constants of a strip and then, based on these constants obtained, the 'Y (or X) model' will be applied to estimate the stiffness constants of a plain weave unit cell.

Theoretical modelling for twill weaves

For twill weaves, the relevant unit cell, shown by a bold square in Fig. 4(a), is constructed by assembling three types of macro-blocks denoted as A, B and C. The geometry and elastic properties of macro-block A is exactly the same as those for a unit cell in opened-packing plain weaves shown in Fig. 2(b). The geometry of macro-blocks B and C are shown in Fig. 4(b) and (c), respectively. Comparing Fig. 4(b) with Fig. 4(c), it is noted that both macro-blocks B and C are assembled by micro-blocks a, b, c and d, where the geometry and elastic properties for micro-blocks a, b and c are exactly the same as those for micro-blocks SCPMIB, UMIB and PRMIB in a plain weave unit cell, respectively. The geometry of micro-block d, called the straight yarn micro-block (SMIB), is shown in Fig. 4(d). This micro-block consists of a straight fibre yarn and pure resin. Its stiffness constants can be evaluated using eqns (2)–(10). Because the stiffness constants for micro-blocks SCPMIB, UMIB, PRMIB and SMIB are known, it is possible to determine the stiffness constants of macro-blocks A, B and C using the 'XY model' or 'YX model'. When the stiffness constants of macro-blocks A, B and C are known, the stiffness constants for a twill weave unit cell can also be predicted using the 'XY model' or the 'YX model'.

Theoretical modelling for 5- and 8-harness satin weaves

For 5-harness satin weaves, the relevant unit cell illustrated in Fig. 5(a) by a bold square is constructed by assembling macro-blocks B, C, D, E and F, and the structures for macro-blocks D, E and F are shown in Fig. 5(b)–(d). The stiffness constants for both macro-blocks E and F, which are obtained using the 'XY model' or 'YX model', are equal to those for macro-block B in twill weaves under the global coordinate system. Macro-block D shown in Fig. 5(b) is assembled by micro-blocks SCPMIB, PRMIB and SMIB. The stiffness constants for macro-

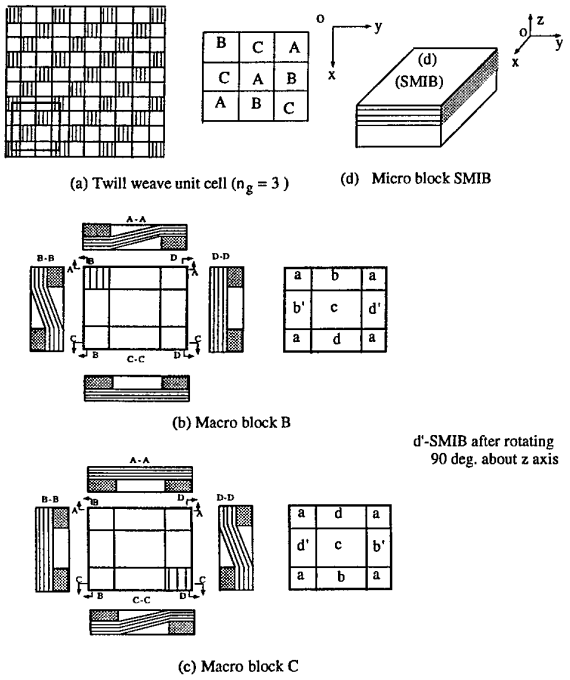

Fig. 4. A schematic of the twill weave.

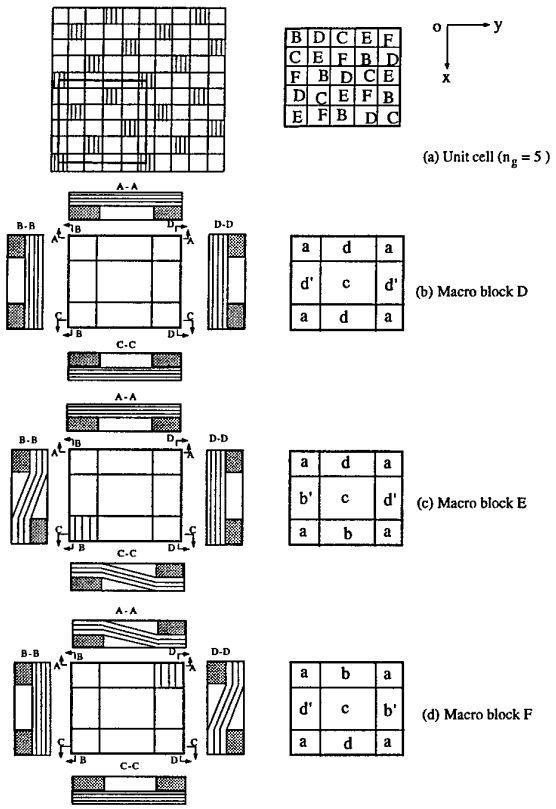

Fig. 5. A schematic of the 5-harness satin weaves.

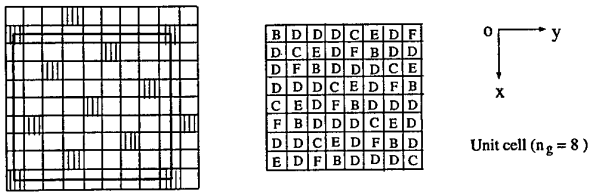

Fig. 6. A schematic of the 8-harness satin weaves.

block D can be determined by following a similar procedure to that for macro-block B. Similarly for 8-harness satin weaves, the unit cell indicated by a bold square in Fig. 6 is also constructed by assembling macro-blocks B, C, D, E and F. Thus, the stiffness constants for both 5- and 8-harness satin weave unit cells can be evaluated using similar procedures to that for the twill weave unit cell.

FINITE ELEMENT ANALYSIS MODELLING

A number of three-dimensional finite element models, including various types of micro-blocks, macro-blocks and unit-cells models, were developed using 20-node three-dimensional brick elements in Strand6 [9]. Orthotropic and homogeneous material properties were used. Linear deformations, namely pure extension and pure shear, are applied to the models using Lagrange constants. These pure extension and shear deformations are considered to be homogeneous. The average forces required to create such deformations can be recovered from the relevant finite element models by summing the values of the Lagrange Multipliers.

Boundary conditions and loadings

To evaluate the stiffness constants for all three-dimensional micro-blocks, macro-blocks and woven fabric unit cells, six separate strain vectors are applied to them using Lagrange Multipliers. Six separate FEA analysis cases (i.e. cases (a)–(f) below) are required to run on the same architecture FEA model for the corresponding six separate strain vectors: case (a) $\varepsilon_x = 0.001$; case (b) $\varepsilon_y = 0.001$; case (c) $\varepsilon_z = 0.001$; case (d) $\gamma_{xy} = 0.001$; case (e) $\gamma_{yz} = 0.001$ and case (f) $\gamma_{zx} = 0.001$. The relevant boundary conditions for each case are obtained using the usual form of the linear strain–displacement relationships [10,11] (e.g. $DX|_{x=lx} = 0.001 l_x$, $DX|_{x=0} = 0$, $DY|_{y=0} = DY|_{y=ly} = DZ|_{z=0} = DZ|_{z=lz} = 0$ for case (a)). Based on the average normal and shear stresses obtained for each case, the required stiffness constants can be determined (e.g. $C_{11} = \sigma_x/\varepsilon_x$, $C_{21} = \sigma_y/\varepsilon_x$, $C_{31} = \sigma_z/\varepsilon_x$ for case (a)).

RESULTS AND DISCUSSION

In this section the theoretical and FEA models developed previously will be used to evaluate the stiffness and engineering elastic constants for all four types of artificial woven fabric unit cells. In addition, the in-plane engineering elastic constants for plain weave will be compared with those obtained by Naik & Shembekar [6].

The geometry details are listed in Table 1 for all four types of micro-blocks and Table 2 for all four types of woven fabric unit cells, where l_x, l_y and l_z are lengths of a block or a unit cell in the x, y and z directions, respectively. The elastic constants for yarns and resin used in this investigation are listed in Table 3 [6].

Comparing the theoretical and FEA results for both stiffness and engineering elastic constants, it is found that there exists a good agreement. For both stiffness and engineering elastic constants, the absolute differences between the theoretical analysis and FEA simulating results range from 0 to 4 GPa. In addition, by studying the constraints used in FEA models, it is noted that for cases (a)–(c), C_{ij} values ($i, j = 1$–3) are evaluated under the iso-stress conditions. Hence, the lower bounds are obtained [6,7,12–15]. This is the reason why C_{ij} values ($i, j = 1$–3) obtained from FEA models are close to the lower bounds evaluated using the theoretical models. For the rest of the cases, the FEA models run under the iso-strain conditions. Thus, the FEA results are close to the upper bounds predicted from the theoretical models. Note that the number of finite elements in the FEA models does not affect the effective stiffness constants significantly, but the predictive stiffness constants are very sensitive to the choice of boundary conditions.

From comparisons of the C_{ij} values obtained from both theoretical and FEA models for all four types of woven fabrics, it is found that an increase in n_g generally results in an increase in C_{11} because of less undulation. This finding is consistent with that reported by Chou & Ko

Table 1. Geometry for four types of micro-blocks[1]

	SCPMIB (mm)	UMIB (mm)	PRMIB (mm)	SMIB (mm)
l_x	0.25	0.25	0.5	0.25
l_y	0.25	0.5	0.5	0.5
l_z	0.1	0.1	0.1	0.1

[1]SCPMID, straight cross-ply micro-block; UMID, undulated yarn micro-block; PRMIB, pure resin micro-block; SMID, straight yarn micro-block.

[12]. The variation trends of the stiffness and engineering elastic constants with n_g are illustrated in Figs 7 and 8, respectively.

Figure 7 shows that an increase in n_g also causes an increase in C_{22} and slight decreases in C_{13}, C_{23}, C_{44} and C_{55}. When n_g increases C_{12} and C_{66} increase slightly. C_{33} remains constant as n_g changes. From Fig. 8, it is noted that an increase in n_g generally results in increases in in-plane Young's modulus, E_1 and E_2, and decreases in out-of-plane Poisson's ratio, v_{13} and v_{23}, and out-of-plane shear modulus, G_{13} and G_{23}. Some of these variations can be attributed to the decrease in waviness as n_g increases. These findings are consistent with the report that with decreased waviness E_1 increases and G_{23} and v_{13} decrease [16]. With the increases in n_g in-plane Poisson's ratio, v_{12}, increases slightly, which is consistent with v_{12} increasing with decreased waviness [16] and plain weaves generally having a lower in-plane Poisson's ratio than the satin weaves [5]. In-plane shear modulus, G_{12}, is almost unchanged when n_g changes, while it is reported by Ishikawa *et al.* [17] that the in-plane shear modulus increases as n_g increases. Whitcomb [16] also reported that G_{12} increases with decreased waviness. The effects of n_g on out-of-plane Young's modulus, E_3, are not significant, which is expected. Hence, it may be concluded that with increases in n_g the in-plane Young's modulus and Poisson's ratio increase, but the out-of-plane shear modulus and Poisson's ratio decrease. The out-of-plane Young's modulus and in-plane shear modulus almost remain constant when n_g changes. Thus, for the structural components requiring higher in-plane stiffness and tensile strength, it is suggested that woven fabrics with a higher n_g are chosen.

For the plain weave unit cell comparisons of the in-plane Young's moduli, shear moduli and Poisson's ratio between the present results and those reported by Naik & Shembekar [6] are also presented on the basis of same three dimensions (i.e. l_x, l_y and l_z), lamina thickness, h, fabric thickness, h_t, the undulated length of yarn, l_u (see Fig. 9), and the close overall fibre volume fraction V_f^o. The relevant data and results are listed in Table 4.

It is noted that the in-plain Young's moduli obtained from both the FEA and theoretical models are in good agreement with those obtained from Naik & Shembekar's WF parallel model and one-dimensional mosaic parallel model [6] and the experimental results. For the in-plane shear modulus, G_{12}, the present results predicted by theoretical models also correlated well with those calculated using Naik & Shembekar's models and mosaic models [6]. However, the value predicted by FEA model is 50% larger than those predicted by the theoretical model. The reason for this is that the

Table 2. Geometry of the unit cell for four types of woven fabrics

	Plain weave (mm)	Twill weave (mm)	5-harness satin (mm)	8-harness satin (mm)
l_x	1	3	5	8
l_y	1	3	5	8
l_z	0.1	0.1	0.1	0.1

Table 3. Elastic properties for warp (weft) yarn and resin

	Materials	E_1	E_2	E_3	v_{12}	v_{13}	v_{23}	G_{12}	G_{13}	G_{23}
Yarn (GPa)	T-300 carbon	230	40	40	0.26	0.26	0.26	24	24	14.3
Resin (GPa)	Epoxy resin	3.5	3.5	3.5	0.35	0.35	0.35	1.3	1.3	1.3

FEA model runs under the iso-strain condition which gives an upper bound while the presented theoretical models are developed under the iso-stress condition which gives the lower bounds. The in-plane Poisson's ratio determined by the FEA and the presented theoretical models only correlate well with that obtained using Naik & Shembekar's two-dimensional WF models [6].

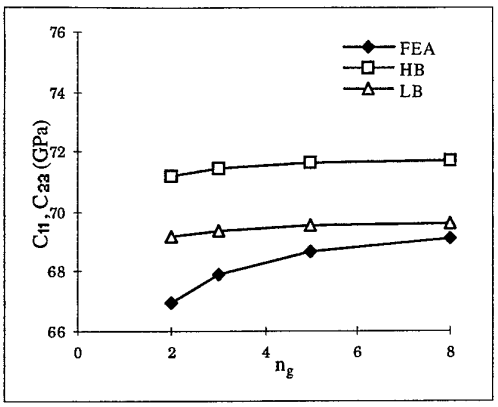

(a) Effect of n_g on C_{11} and C_{22}

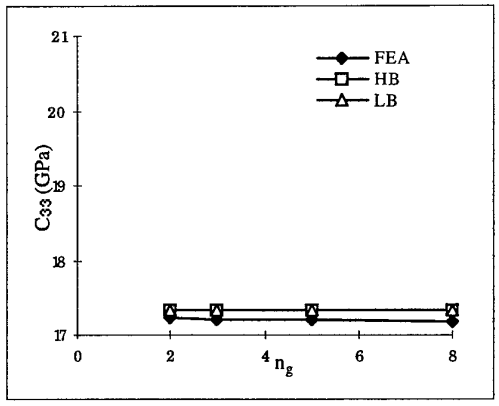

(b) Effect of n_g on C_{33}

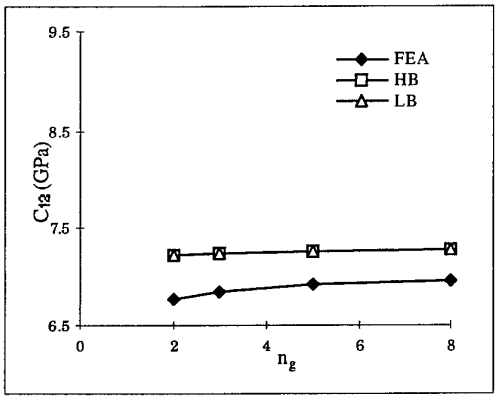

(c) Effect of n_g on C_{12}

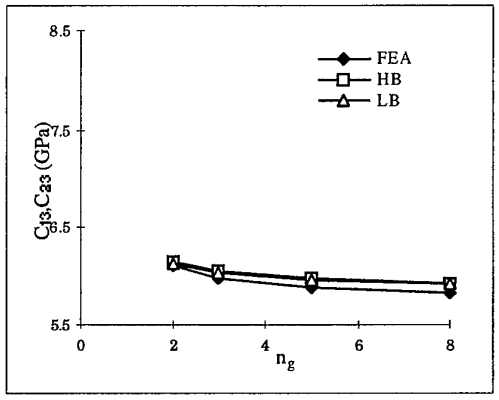

(d) Effect of n_g on C_{13} and C_{23}

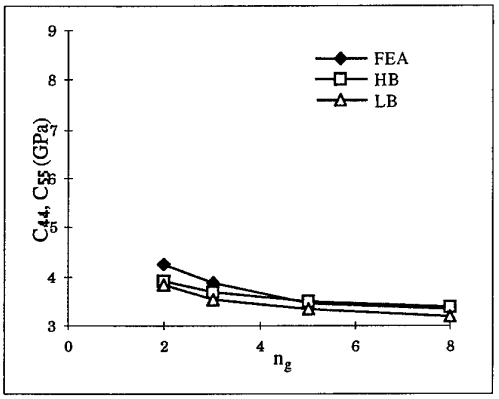

(e) Effect of n_g on C_{44} and C_{55}

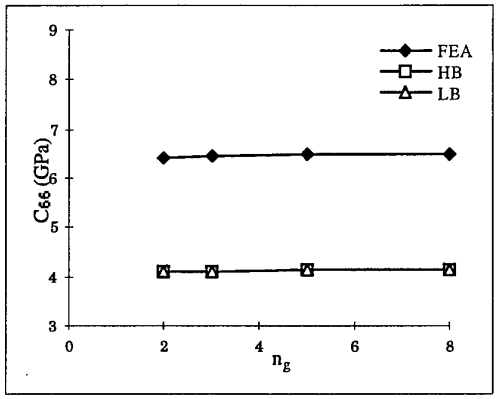

(f) Effect of n_g on C_{66}

FEA: FEA model HB: Higher bound LB: Lower bound

Fig. 7. Effects of n_g on the stiffness constants for woven fabrics. Effect of n_g on: (a) C_{11} and C_{22}; (b) C_{33}; (c) C_{12}; (d) C_{13} and C_{23}; (e) C_{44} and C_{55}; and (f) C_{66}. FEA, FEA model; HB, higher bound; LB, lower bound.

CONCLUSIONS

This paper proposed a multi-scaled three-dimensional modelling technique that has been theoretically verified to be a logical and general method, and can be used to evaluate the elastic properties of various types of woven fabrics. The elastic properties of a woven fabric lamina

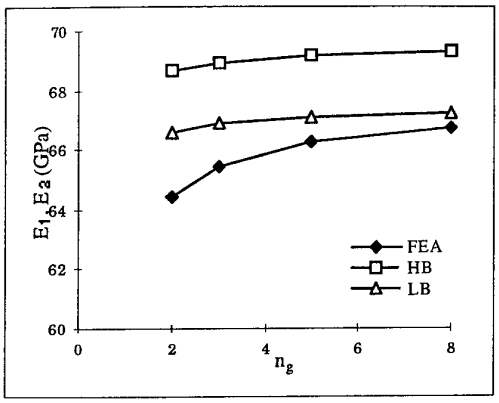

(a) Effect of n_g on E_1 and E_2

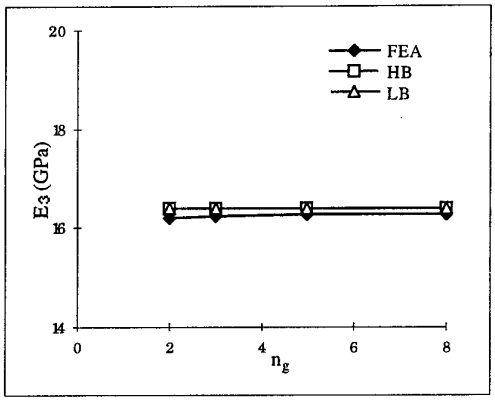

(b) Effect of n_g on E_3

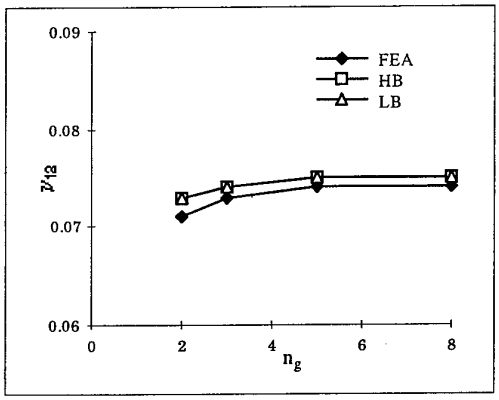

(c) Effect of n_g on ν_{12}

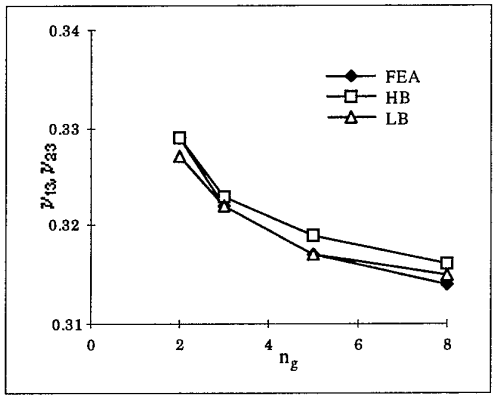

(d) Effect of n_g on ν_{13} and ν_{23}

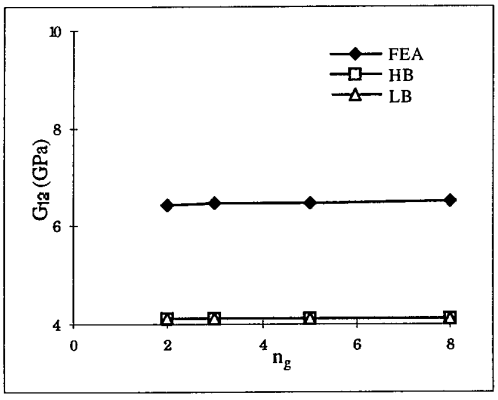

(e) Effect of n_g on G_{12}

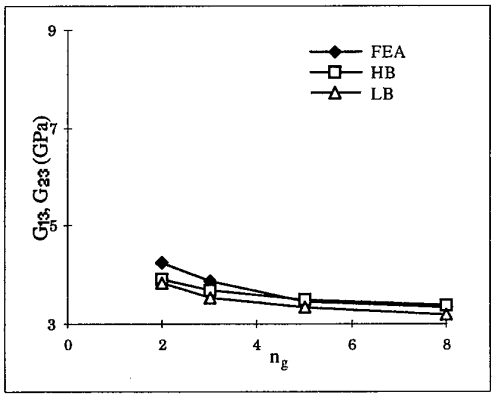

(f) Effect of n_g on G_{13} and G_{23}

FEA: FEA model HB: Higher bound LB: Lower bound

Fig. 8. Effects of n_g on elastic constants for woven fabrics. Effect of n_g on: (a) E_1 and E_2; (b) E_3; (c) v_{12}; (d) v_{13} and v_{23}; (e) G_{12}; and (f) G_{13} and G_{23}. FEA, FEA model; HB, higher bound; LB, lower bound.

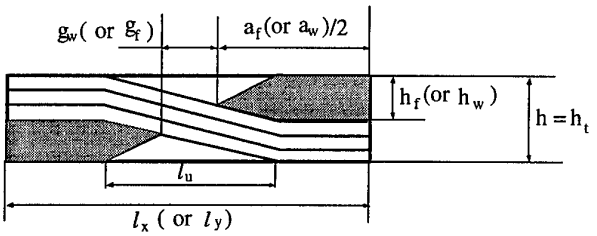

Fig. 9. The geometry of the plain weave unit cell. The nomenclature used in Table 4 is given here.

can be evaluated based on those of the relevant unit cells. The data for the unit cells can be obtained using the FEA models, in which the woven fabric unit cells are assembled by selecting the required micro-blocks for plain weave and macro-blocks for other types of weaves. The stiffness and elastic constants for these blocks can be obtained from the corresponding FEA modelling or data bank established.

The theoretical models, i.e. the 'XY model' and 'YX model', presented in this paper can be further extended to estimate the elastic properties for the woven fabric laminates. Hence, two new theoretical models called as 'XYZ model' and 'YXZ model' will be developed for studying the mechanical properties of the composite laminates. In these two models, all micro-blocks of a strip along the x (or y) direction are assembled, then all these strips are assembled in the y (or x) direction to form a plane. Later, these planes for different lamina are assembled along the z direction. Hence, a new block called the plate-block will be introduced into these models.

In general, a single micro-block can be used as an assembling unit for different types of macro-blocks, and a macro-block can be an assembling unit for different woven fabric unit cells, and a plate-block will be an assembling unit for different woven fabric laminates. From this point of view, this three-dimensional FEA technique is an effective and efficient method for reducing the time spent on building FEA models and carrying out the relevant calculations as the elastic properties for these blocks may be obtained from the data bank.

ACKNOWLEDGEMENTS

P. Tan is supported by an Australian Postgraduate Award (APA) and a Supplementary Scholarship in the Aeronautical Engineering Department of the University of Sydney.

REFERENCES

1. Hewitt, J.A., Brown, D. and Clarke, R.B., Computer modelling of woven composite materials. *Composites, Part A*, 1995, **26**(2), 134–140.
2. Sun, C.T. and Vaidya, R.S., Prediction of composite properties from a representative volume element. *Composites Sci. Technol.*, 1996, **56**, 171–179.
3. Whitcomb, J., Srirengan, K. & Chapman, C., Model technique for three-dimensional stress analysis of plain weave composites. In *The Tenth International Conference on Composite Materials*, Woodland Publishing Limited Whistler, British Columbia, Canada, 1995, pp. 29–36.
4. Ning, Q.G. and Chou, T.W., Closed-form solutions of the in-plane effective thermal conductivities of the woven-fabric composites. *Composites Sci. Technol.*, 1995, **55**, 41–48.
5. Whitney, T.J. and Chou, T.W., Modelling of 3-D angle-interlock textile structural composites. *J. Composite Mater.*, 1989, **23**, 891–911.
6. Naik, N.K. and Shembekar, P.S., Elastic behaviour of woven fabric composites: I — lamina analysis. *J. Composite Mater.*, 1992, **26**(15), 2197–2225.
7. Naik, N. K., *Woven Fabric Composites*. Technomic, 1994.
8. Dasgupta, A., Agarwal, R.K. and Bhandarkar, S.M., Three-dimensional modelling of woven-fabric composites for effective thermo-mechanical and thermal properties. *Composites Sci. Technol.*, 1996, **56**, 209–223.
9. STRAND6, *Reference Manual and User Guide*. G+D Computing Pty Ltd, Sydney, Australia, 1993.
10. Whitney, J. M., Daniel, I. M. & Pipes, R. B., *Experimental Mechanics of Fiber Reinforced Composite Materials*. Society for Experimental Stress Analysis, USA, 1982.
11. Daniel, I. M. & Ishai, O., *Engineering Mechanics of Composite Materials*. Oxford University Press, Oxford, 1994
12. Chou, T. W. & Ko, F. K., *Textile Structural Composites. Volume 3. Composite Materials Series*. Elsevier Science, Amsterdam, 1989.
13. Ishikawa, T. and Chou, T.W., Elastic behavior of woven hybrid composites. *J. Composite Mater.*, 1982, **16**, 2–19.
14. Chou, T. W., *Microstructural Design of Fibre Composites*. Cambridge University Press, Cambridge, 1992.

15. Ishikawa, T., Anti-symmetric elastic properties of composite plates of satin weave cloth. *Fibre Sci. Technol.*, 1981, **15**, 127–145.
16. Whitcomb, J. D., Three-dimensional stress analysis of plain weave composites. NASA report, NASA TM-101672, 1989
17. Ishikawa, T., Matsushima, M. and Hayashi, Y., Experimental confirmation of the theory of elastic moduli of fabric composites. *J. Composite Mater.*, 1985, **19**(5), 443–458.

ELSEVIER

Composite Structures Vol. 38, No. 1–4, pp. 273–280, 1997
© 1997 Published by Elsevier Science Ltd. All rights reserved
Printed in Great Britain
0263-8223/97/$17.00 + 0.00

PII:S0263-8223(97)00062-7

Stress expressions of single-lap adhesive joints of dissimilar adherends

Z. J. Wu,[a] A. Romeijn[b] & J. Wardenier[b]

[a]*Department of Engineering Mechanics, Tsinghua University, Beijing 100084, People's Republic of China*
[b]*Faculty of Civil Engineering, Delft University of Technology, 2600 GA Delft, The Netherlands*

The present investigation provides the correct expressions of adhesive stresses in Goland and Reissner's solution. An improvement on the inconsistent plane stress and plane strain relations using in Goland and Reissner's original paper is achieved. A set of generalized equations are suggested for the adhesive analysis in dissimilar adherends with different thicknesses and lengths. Some comments on the proposed European code of polymer composites structural design are also given. © 1997 Published by Elsevier Science Ltd.

INTRODUCTION

Adhesive bonding techniques have been widely used in flight and space vehicle structures. Now it is also being used increasingly in civil engineering, for example, in designing fiber reinforced plastics (FRP) bridges and structures, in stiffening, joining, and repairing precast, prestressed concrete structures.

Consequently, the importance of adhesive bonding in technology [1] has been recognized, and a considerable amount of theoretical and experimental research has been carried out on adhesive structures. For example, in simple lap joint theories which predict the state of stress in the thin adhesive which bonds the adherend plates, Goland and Reissner presented the first modern lap joint theory [2]. Subsequently, numerous authors [3–5] have proposed theories which have improved upon Goland and Reissner's basic formulation. The common feature of all these theories is that simplified assumptions are made concerning the behaviour of the adherends and of the adhesive. These assumptions remove the stress singularities which occur at the edges of the interfaces and the adherends and yield tractable differential equations which can be solved to yield the stresses in the adhesive. Maximum adhesive stresses from these solutions can then be used in joint design. Carpenter [6] had made a comprehensive comparison of numerous lap joint theories for adhesive bonded joints and founded that predicted maximum adhesive shear stress is insensitive to underlying assumptions and that maximum adhesive peel stress is relatively unaffected by most assumptions.

However, the classic theory of Goland and Reissner neglects shear deformation of the adherends, inconsistently uses plane stress and plane strain for the adherends, and uses an inconsistent shear strain equation for the adhesive. The maximum peel stress from this theory is expected varying less 30% compared with that prediction by a consistent lap joint theory which considers shear deformation of the adherends [6]. Although there exists a little stress difference between classic Goland and Reissner theory and some improved theories, the Goland and Reissner theory is widely accepted today because of it's simplification of the model. Furthermore, it can provide explicit analytical expressions for the shear and peel stresses, which is very useful to designers in engineering. Some so-called consistent solutions can only be realized by very complicated numerical calculations [7]. This is why the Goland and Reissner theory was recommended

as a basis of simplified design procedure for adhesive lap joints in the recent publication *Structural Design of Polymer Composite Eurocomp Design Code and Handbook* [8]. However, it should be noted that Goland and Reissner's solution for the stress in the adhesive is incorrectly written and has unfortunately been used in this form by many authors [8–10] including the *Structural Design of Polymer Composite Eurocomp Design Code and Handbook*. Carpenter [11] has pointed out one of these errors in Goland and Reissner's paper. Adams *et al.* [12], had cited Sneddon's result [13] of Goland and Reissner theory. To our surprise, some terms and signs were also incorrectly left out in the parameter and solution expressions in Sneddon's paper.

The present investigation does not give a new solution to the adhesive joint problem. It will provide the correct expressions of adhesive stresses in Goland and Reissner's solution. An improvement on the inconsistent plane stress and plane strain relations using in Goland and Reissner's original paper is achieved and applied to composite adhesive joints. Several differential equations are suggested for the analysis of joint-edge loads in dissimilar adherends with different thicknesses and lengths. It

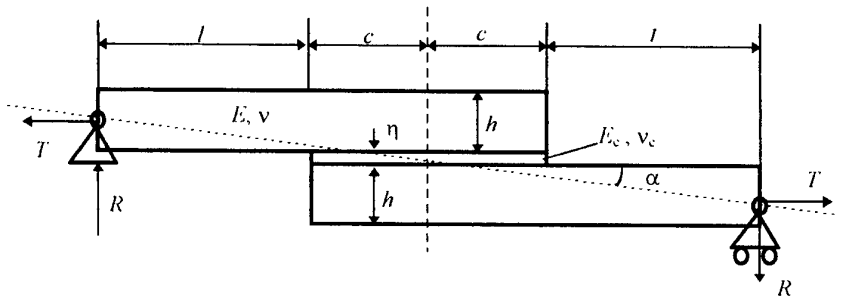

(a) geometric and material parameters

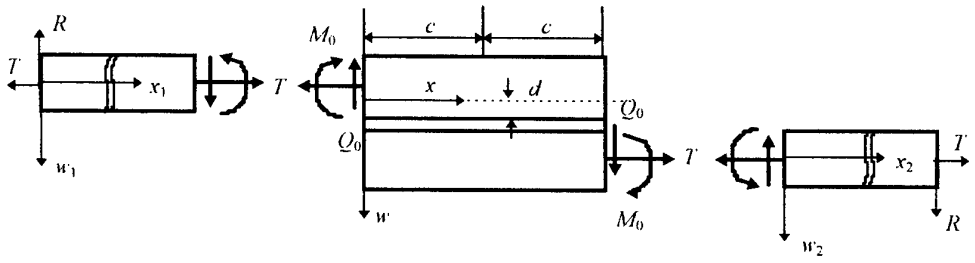

(b) free-body diagrams under loading

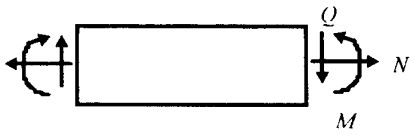

(c) positive conventions for the internal forces

Fig. 1. Schematic representation of a single-lap joint, (a) geometric and material parameters, (b) free-body diagrams under loading, (c) positive conventions for the internal forces.

can be used for the stress analysis of adhesive joints of FRP adherends.

THEORETICAL FORMULATIONS OF CLASSIC ANALYSIS

In classic analysis, the geometrical and material parameters of the single-lap joint of two rectangular adherends (sheets) are shown in Fig. 1(a), in which α represents a force-eccentricity angle, l the length of the outer adherend, $2c$ the length of the overlap, h the thickness of the adherend, and η the thickness of the adhesive layer. The elastic modulus and Poisson's ratio are E and v, respectively, for the isotropic adherends, and E_c and v_c for the adhesive. When the single-lap joint is subjected to a stretching load, T, it is convenient to introduce two coordinate systems (x_1, w_1) and (x, w) in order to study the deformations [shown in Fig. 1(b)].

Obviously

$$R=\alpha T, \text{ and } \alpha=\frac{h+\eta}{2(l+c)} \tag{1}$$

Setting M_1 equal to the bending moment in the sheet 1 and M equal to the moment in the joint, each per unit of width, then

$$M_1=T(\alpha x_1-w_1)\ (0\le x_1\le l) \tag{2}$$

$$M=T\left[\alpha(l+x)-w-\frac{h+\eta}{2}\right](0\le x\le c) \tag{3}$$

The positive conventions chosen for the moments M_1 and M and for the transverse shearing forces per unit of width Q_1 in the sheet 1 and Q in the joint, to be given in the later work, are shown in Fig. 1 (c).

According to the theory for the small bending of thin cylindrically bent plates, the differential equations for the transverse deflections of the sheet and joint become

$$\begin{cases}\dfrac{d^2w_1}{dx_1^2}=-\dfrac{M_1}{D_1}=-\dfrac{T}{D_1}(\alpha x_1-w_1) & (0\le x_1\le l)\\[2ex] \dfrac{d^2w}{dx^2}=-\dfrac{M}{D}=-\dfrac{T}{D}\left[(\alpha(l+x)-w-\dfrac{h+\eta}{2}\right] & (0\le x\le c)\end{cases} \tag{4}$$

where D_1 and D are the flexural rigidities of the sheet and joint, respectively, and

$$D_1=\frac{Eh^3}{12(1-v^2)},\ D=\frac{Eh^3}{3(1-v^2)}$$

$$+\left(\frac{1}{2}h\eta^2+h^2\eta\right)\frac{E}{1-v^2}+\frac{E_c\eta^3}{12(1-v_c^2)} \tag{5}$$

The solutions of eqn (4) have the form of

$$\begin{cases}w_1=A_1ch\mu_1x_1+B_1sh\mu_1x_1+\alpha x_1 & (0\le x_1\le l)\\ w=Ach\mu x+Bsh\mu x+\alpha(l+x)-\dfrac{h+\eta}{2} & (0\le x\le c)\end{cases} \tag{6}$$

where

$$\mu_1=\sqrt{\frac{T}{D_1}},\ \mu=\sqrt{\frac{T}{D}} \tag{7}$$

The four constants A_1, B_1, A, B of formula (6) are determined by the four boundary conditions

$$w_1(0)=0,\ w_1(l)=w(0),\ w(l)=0,\ \frac{d_1(l)}{dx_1}=\frac{dw(0)}{dx} \tag{8}$$

and

$$A_1 = 0,\ B_1 = -\frac{h+\eta}{2}\ \frac{ch\mu c}{sh\mu_1 l \cdot ch\mu c + \frac{\mu_1}{\mu} ch\mu_1 l \cdot sh\mu c}$$

The constants A, B are not needed in the subsequent calculations. The moment and shearing force at the end of the overlap then become

$$M_0 M_1|_{x_1=l} = T[\alpha l - w_1(l)] = \frac{(h+\eta)T}{2}\ \frac{sh\mu_1 l \cdot ch\mu c}{sh\mu_1 l \cdot ch\mu c + \frac{\mu_1}{\mu} ch\mu_1 l \cdot sh\mu c} \quad (9)$$

$$Q_0 = Q_{1\,x_1=l} = \frac{dM_1}{dx_1}_{x_1=l} = T\left[a - \frac{dw_1(l)}{x_1}\right]$$

$$= \frac{(h+\eta)T}{2}\ \frac{\mu_1 ch\mu_1 l \cdot ch\mu c}{sh\mu_1 l \cdot ch\mu c + \frac{\mu_1}{\mu} ch\mu_1 l \cdot sh\mu c} \quad (10)$$

If we introduce a dimensionless parameter k, i.e.,

$$k = \frac{sh\mu_1 l \cdot ch\mu c}{sh\mu_1 l \cdot ch\mu c + \frac{\mu_1}{\mu} ch\mu_1 l \cdot sh\mu c} \quad (11)$$

then

$$M_0 = \frac{(h+\eta)T}{2} k,\ Q_0 = \frac{(h+\eta)T}{2} k \cdot \frac{\mu_1 ch\mu_1 l}{sh\mu_1 l} \quad (12)$$

If the adhesive layer was thin compared to the thickness of the sheet ($\eta \ll h$) so that the presence of the adhesive layer was neglected, η and E_c are eliminated from the formulation. By applying the approximations

$$sh\mu_1 l \approx ch\mu_1 l \quad (13)$$

to the isotropic balanced single-lap joint, the edge moment, M_0, and shearing force, Q_0, can be written as

$$M_0 = \frac{T}{2} k,\ Q_0 = \mu_1 M_0 \quad (14)$$

where

$$\mu_1 = \sqrt{\frac{12(1-\nu^2)T}{Eh^3}} \quad (15)$$

$$k = \frac{1}{1 + 2\sqrt{2}\,\mathrm{th}\left(\frac{\mu_1 c}{2\sqrt{2}}\right)} \quad (16)$$

Formula (13) is exactly equation (15) in Goland and Reissner paper.

STRESSES IN JOINT FOR FLEXIBLE ADHESIVE LAYER

In this section, the assumption is made that the deformations of adherend arise only from the longitudinal stress, σ_x. Since the transverse normal strain and shear strain in the adherends (sheets) are relatively small compared to those in the adhesive, a cylindrically bent-plate formulation was developed with values of M_0, T and Q_0 given in Section 2. The adhesive shear and transverse normal stresses (τ_0 and σ_0) were assumed constant through the thickness of the thin adhesive layer. Figure 2(a) and (b) show elements for the sheets 1 and 2, respectively, with the sign conventions chosen for the moments and forces indicated.

The equilibrium equations for the elements of the joints are

$$\begin{cases} \dfrac{dM_1}{dx} = Q_1 - \tau_0 & \dfrac{h+\eta}{2} \\ \dfrac{dQ_1}{dx} = -\sigma_0, & \dfrac{dN_1}{dx} = -\tau_0 \end{cases} \quad (17)$$

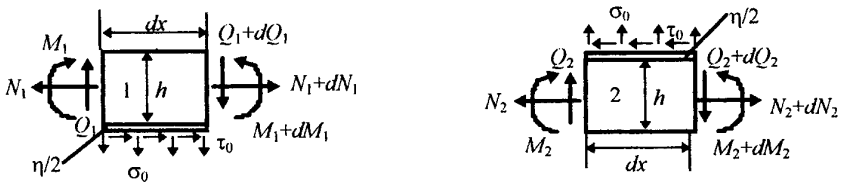

(a) sheet 1 (upper) (b) sheet 2 (lower)

Fig. 2. Elements of sheets in joint, (a) sheet 1 (upper), (b) sheet 2 (lower).

$$\begin{cases} \dfrac{dM_{21}}{dx} = Q_2 - \tau_0 & \dfrac{h+\eta}{2} \\ \dfrac{dQ_2}{dx} = -\sigma_0, & \dfrac{dN_2}{dx} = \tau_0 \end{cases} \tag{18}$$

Where the subscripts 1 and 2 designate quantities pertaining to the sheets 1 and 2, respectively. Denoting the transverse deflections of the sheets 1 and 2 in joint by w_1 and w_2 as shown in Fig. 1, the differential equations for the transverse deflections are

$$\frac{d^2w_1}{dx^2} = -\frac{M_1}{D_1}, \quad \frac{d^2w_2}{dx^2} = -\frac{M_2}{D_2} \tag{19}$$

where

$$D_2 = D_1 = \frac{Eh^3}{12(1-\nu^2)}$$

given as before.

Let u_1 and u_2 represent the longitudinal displacements of lower surface in sheet 1 and upper surface in sheet 2 at the boundaries adjacent to the adhesive, then the stress–strain relations give

$$\begin{cases} \dfrac{du_1}{dx} = \dfrac{1-\nu^2}{E}\left(\dfrac{N_1}{h} + \dfrac{6M_1}{h^2}\right) \\ \dfrac{du_2}{dx} = \dfrac{1-\nu^2}{E}\left(\dfrac{N_2}{h} - \dfrac{6M_2}{h^2}\right) \end{cases} \tag{20}$$

It is compatible with the plane strain assumption of the sheets deformations. Goland and Reissner gave an inconsistent relations by leaving out $(1-\nu^2)$ in eqn (20).

The assumption that the adhesive is elastic leads to the relations

$$\begin{cases} \tau_0 = G_c \dfrac{u_2 - u_1}{\eta} \\ \sigma_0 = E_c \dfrac{w_2 - w_1}{\eta} \end{cases} \tag{21}$$

which is compatible with the directions of τ_0 and σ_0 shown in Fig. 2.

The edge conditions for the two sheets [Fig. 1(b)] are

$$x = c, \begin{cases} M_1 = 0, & Q_1 = 0, & N_1 = 0 \\ M_2 = -M_0, & Q_2 = Q_0, & N_2 = T \end{cases} \tag{22}$$

$$x = -c, \begin{cases} M_1 = M_0, & Q_1 = Q_0, & N_1 = T \\ M_2 = 0, & Q_2 = 0, & N_2 = 0 \end{cases} \tag{23}$$

From eqns (17)–(21), two differential equations for τ_0 and σ_0 can be obtained

$$\frac{d^3\tau_0}{dx^3} - \beta^2 \frac{d\tau_0}{dx} = 0 \tag{24}$$

$$\frac{d^4\sigma_0}{dx^4} + 4\left(\frac{\gamma}{h}\right)^4 \sigma_0 = 0 \tag{25}$$

where

$$\beta^2 = \frac{1-\nu^2}{E} \cdot \frac{8G_c}{\eta h}, \quad \gamma^4 = \frac{6(1-\nu^2)E_c h}{E\eta} \tag{26}$$

The boundary conditions (22) and (23) are reduced to:

For τ_0

$$x=\pm c,\ \frac{d\tau_0}{dx}=\pm\frac{G_c}{\eta}\cdot\frac{1-\nu^2}{E}\left(\frac{T}{h}+\frac{6M_0}{h^2}\right) \tag{27}$$

and

$$\int_{-c}^{c}\tau_0 dx=T \tag{28}$$

For σ_0

$$x=\pm c,\ \frac{d^2\sigma_0}{dx^2}=\frac{E_c}{\eta D_1}M_0 \tag{29}$$

$$x=\pm c,\ \frac{d^3\sigma_0}{dx^3}=\mp\frac{E_c}{\eta D_1}Q_0 \tag{30}$$

On the basis of the eqns (27)–(30), the solutions for eqns (24) and (25), i.e., the distributions of the shearing and the normal stresses are, respectively

$$\frac{\tau_0 c}{T}=\frac{1}{8}\left[\frac{\beta c}{h}(1+3k)\frac{ch\left(\frac{\beta c}{h}\cdot\frac{x}{c}\right)}{sh\frac{\beta c}{h}}+3(1-k)\right] \tag{31}$$

$$\frac{\sigma_0\cdot c^2}{th}=\frac{1}{\Delta}\left[\left(R_1\lambda^2\frac{k}{2}+\lambda k'\sin\lambda sh\lambda\right)\sin\lambda\frac{x}{c}\cdot sh\lambda\frac{x}{c}+\left(R_2\lambda^2\frac{k}{2}+\lambda k'\lambda ch\lambda\right)\cos\lambda\frac{x}{c}\cdot ch\lambda\frac{x}{c}\right] \tag{32}$$

where

$$k'=k\cdot c\sqrt{\frac{3(1-\nu^2)T}{Eh^3}}\frac{ch\mu_1 l}{sh\mu_1 l} \tag{33}$$

$$\lambda=\frac{c}{h}\cdot\gamma$$

$$R_1=ch\lambda\sin\lambda+sh\lambda\cos\lambda$$

$$R_2=sh\lambda\cos\lambda-ch\lambda\sin\lambda$$

$$\Delta=\frac{1}{2}(sh2\lambda+\sin 2\lambda)$$

Compared with the results of Goland and Reissner paper, Goland and Reissner failed to give a correct expression of β and γ shown in formula (26). The factor $(1-\nu^2)$ was incorrectly left out in both β^2 and γ^4 expressions. It is also important to note that Goland and Reissner's derivation (see equations (38) and (48) of the Goland and Reissner paper) was inconsistent with the sign of Q_0 in the boundary conditions. The effect of the inconsistency on σ_0 was removed by a second inconsistency in the development of their analysis from their equations (48)–(53). Sneddon [13] pointed out the inconsistency in Goland and Reissner's formulation of the boundary conditions and removed it [but did not correct equation (48) in the Goland and Reissner paper]. Sneddon also removed the second inconsistency in the derivation but used the original equation (48), and obtained an expression similar to eqn (32) of the present paper but with negative signs for the k' terms. Subsequently many researchers have used the Sneddon expression, for example, Adams *et al.* [32,12]. In the recent publication *Structural Design of Polymer Composite Eurocomp Design Code and Handbook* [8], Sneddon's result has even been adopted as a theoretical basis of adhesive joint design. Hence, the problem should be pointed out now. To the author's knowledge, a fine explanation to the problem just mentioned was first given by Tsai [9]. Unfortunately, Tsai's paper [9] only repeated the derivation of Goland and Reissner original results. One year later, he made a change to the expression of γ^4 and gave the correct formula [10]. However, the expression of β^2 was still incorrect, based on plane strain assumption of adherends deformations.

FORMULATION OF ADHESIVE JOINTS OF DISSIMILAR ADHERENDS

Because the original research of Goland and Reissner's paper is only available for the single-lap joints of two isotropic sheets of equal thickness t, and length $l+2c$ (where $2c$ is the lap-jointed length and both adherend sheets has the same material property), the results can hardly be used for the dissimilar adherends. So far, we note that the most refined analytical

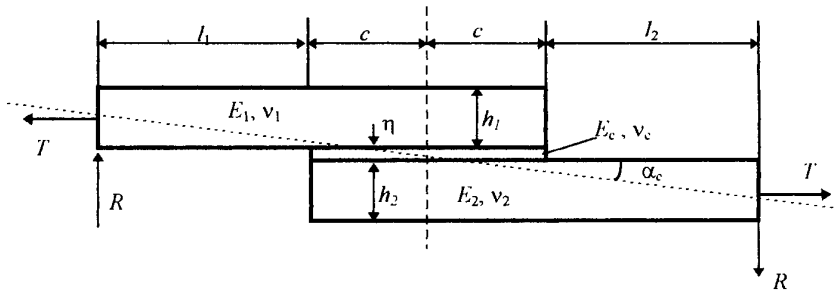

Fig. 3. Geometric and material parameters of joint.

model on the adhesive joint problem of dissimilar adherends is based on the laminated anisotropic plate theory [14]. The entire coupled system is then obtained through assuming the peel stress between the two adherends and shear stress distribution throughout the thickness of the adhesive. It is, in fact, a kind of generalized Goland and Reissner theory. Not much progress on this aspect is made. Here, we suggest several differential equations used for the analysis in dissimilar adherends with different thicknesses and lengths.

The problem considered is two rectangular sheets of different materials, unequal thickness, h_1 and h_2, and length (l_1+2c) and (l_2+2c), respectively (Fig. 3). The bond between the two sheets is established by means of an adhesive layer with thickness η. Let E_1, ν_1 be the Young's modulus and Poisson's ratio of one sheet; E_2, ν_2 those of the other; and E_c, ν_c those of the adhesive layer. The main problem is the determination of joint-edge loads and the stress distribution in the joint region.

To determine the loads acting on the edges of the joint, three coordinate systems (x_1, w_1), (x_2, w_2) and (x, w) like Fig. 1(b) were introduced. According to the theory for small bending of cylindrically bent plates, the differential equations for the transverse deflections are

$$\begin{cases} \dfrac{d^2w_1}{dx_1^2} = -\dfrac{M_1^*}{D_1} = -\dfrac{T}{D_1}(\alpha_c x_1 - w_1) & (0 \le x_1 \le l_1) \\ \dfrac{d^2w}{dx^2} = -\dfrac{M}{D} = -\dfrac{T}{D}\left[\alpha_c(l_1+x) - w - \dfrac{h_1}{2} + d\right] & (0 \le x \le 2c) \\ \dfrac{d^2w_2}{dx_2^2} = -\dfrac{M_2^*}{D_2} = -\dfrac{T}{D_2}\left[\alpha_c(l_1+2l+x_2) - w_2 - \dfrac{h_1+h_2}{2} + d\right] & (0 \le x_2 \le l_2) \end{cases} \tag{34}$$

These equations have solutions of the form

$$\begin{cases} w_1 = A_1 ch\mu_1 x_1 + B_1 sh\mu_1 x_1 + \alpha_c x_1 \\ w = Ach\mu x + Bsh\mu x + \alpha_c(l_1+x) - \dfrac{h_1}{2} + d \\ w_2 = A_2 ch\mu_2 x_2 + B_2 sh\mu_2 x_2 + \alpha_c(l_1+2l+x_2) - \dfrac{h_1+h_2}{2} \end{cases} \tag{35}$$

where

$$\mu_1 = \sqrt{\frac{T}{D_1}},\ \mu_2 = \sqrt{\frac{T}{D_2}},\ \mu = \sqrt{\frac{T}{D}},$$

$$a_c = \frac{h_1+h_2}{2(l_1+2c+l_2)} \tag{36}$$

$$D_1 = \frac{E_1 h_1^3}{12(1-v_1^2)}, D_2 = \frac{E_2 h_2^3}{12(1-v_2^2)}$$

$$D = \frac{E_1}{3(1-v_1^2)}[(h_1 - \mathrm{d})^3$$

$$+\mathrm{d}^3] + \frac{E_2}{3(1-v_2^2)}[(h_2-\mathrm{d})^3+\mathrm{d}^3]$$

$$\mathrm{d} = \frac{1}{2}\left(\frac{E_1 h_1^2}{1-v_1^2} - \frac{E_2 h_2^2}{1-v_2^2}\right)$$

$$\left(\frac{E_1 h_1}{1-v_1^2} + \frac{E_2 h_2}{1-v_2^2}\right)$$

in which d is the distance between the neutral and adhesive planes of the joint portion (Fig. 4).

The constants A_1, B_1, A_2, B_2, A, B can be evaluated from the six boundary conditions

$$\begin{aligned} &w_1(0) = 0 \qquad w_2(l_2) = 0 \\ &w_1(l_1) = w(0) \qquad \frac{\mathrm{d}w_1(l_1)}{\mathrm{d}x_1} = \frac{\mathrm{d}w(0)}{\mathrm{d}x} \\ &w(2c) = w_2(0) \qquad \frac{\mathrm{d}w(2c)}{\mathrm{d}x} = \frac{\mathrm{d}w_2(0)}{\mathrm{d}x_2} \end{aligned} \tag{37}$$

Thus, the deflections of the joint can be uniquely determined. The edge-loads can then be obtained from the differential eqn (34). For example, M_1 and M_2 shown in Fig. 4 are, respectively

$$M_1 = M_1^*|_{x_1 - l_1} = -D_1 \frac{\mathrm{d}^2 w_1}{\mathrm{d}x_1^2}|_{x_1 = l_1} \tag{38}$$

$$M_2 = M_2^*|_{x_2 = 0} = -D_2 \frac{\mathrm{d}^2 w_2}{\mathrm{d}x_2^2}|_{x_2 = 0} \tag{39}$$

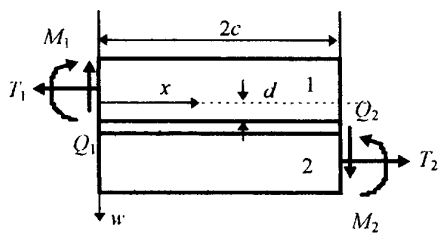

Fig. 4. Schematically shown of joint-edge loads and the position of the neutral axis.

Once the edge loads (moments, shear forces etc.) are known, The stress distributions in adhesive layer can be easily detected by using the similar procedure as shown in Section 3. Here, we do not want to repeat this tedious work. Interested readers can refer to the paper of Shun Cheng *et al.* [34,5].

ACKNOWLEDGEMENTS

This work was partly supported by National Natural Science Foundation of China. Financial support from Delft University of Technology, the Netherlands, are much appreciated.

REFERENCES

1. Yuceoglu, U. and Updike, D.P., Stress analysis of bonded plates and joints. *J. Eng. Mech.*, 1980, **106**, (1), 37–56.
2. Goland, M., Buffalo, N.Y. and Reissner, E., The stresses in cemented joints. *J Appl. Mech.*, 1944, **11**, A17–A27.
3. Hart-Smith, L. J., *Adhesive-bonded single-lap joints*, NASA, CR-112236, 1973.
4. Williams, J.H. Jr., Stresses in adhesive between dissimilar adherends. *J. Adhesion*, 1975, **7**, 97–107.
5. Cheng, S., Chen, D. and Shi, Y., Analysis of adhesive-bonded joints with non-identical adherends. *J. Eng. Mech.*, 1991, **117**, (3), 605–623.
6. Carpenter, W.C., A comparison of numerous lap joint theories for adhesively bonded joints. *J. Adhesion*, 1991, **35**, 55–73.
7. Delale, F., Erdogan, F. and Aydinoglu, M.N., Stresses in adhesively bonded joints: A closed form solution. *J. Composite Mater.*, 1981, **15**, 249–271.
8. Clarke, J. L. (ed.), *Structural Design of Polymer Composites-EUROCOMP Design Code and Handbook*, St Edmundsbury Press, UK, 1996.
9. Tsai, M.Y. and Morton, J., An evaluation of analytical and numerical solutions to the single-lap joint. *Int. J. Solids Structures*, 1994, **31**, (18), 2537–2563.
10. Tsai, M.Y. and Morton, J., An experimental investigation of nonlinear deformations in single-lap joints. *Mech. of Mater.*, 1995, **20**, 183–194.
11. Carpenter, W. C. and Patton, G. C., Comparison of the maximum stress and the stress intensity approaches in the analysis of bonded joints. *Advances in Adhesively Bonded Joints*, eds. Mall, S., Liechti, K. M. and Vinson, J. R., ASME 1988 Winter Annual Meeting in Chicago, Illinois, Nov. 27–Dec. 2, 1988, pp. 23–31.
12. Adams, R.D. and Peppiatt, N.A., Stress analysis of adhesively bonded lap joints. *Strain Analysis*, 1974, **9**, 185–196.
13. Sneddon, I. N., The distribution of stresses in adhesive joints, Chapter in *Adhesion*, ed. Eley, D. D., Oxford University Press, 1961, pp. 207–253.
14. Yang, C. and Pang, S.S., Stress–strain analysis of single-lap composite joints under tension. *J. Eng. Mater. and Tech.*, 1996, **118**, 247–255.

ELSEVIER

Composite Structures Vol. 38, No. 1–4, pp. 281–294, 1997
© 1997 Published by Elsevier Science Ltd. All rights reserved
Printed in Great Britain
0263-8223/97/$17.00 + 0.00

PII:S0263-8223(97)00063-9

Simplified linear and non-linear analysis of stepped and scarfed adhesive-bonded lap-joints between composite laminates

Flemming Mortensen & Ole Thybo Thomsen

Institute of Mechanical Engineering, Aalborg University, Pontoppidanstraede 101, DK-9220 Aalborg East, Denmark

This paper presents a newly developed unified approach for the analysis and design of adhesive-bonded stepped and scarfed lap-joints. The adherends are modelled as beams or wide plates in cylindrical bending, and are considered as generally orthotropic laminates using classical laminate theory. Consequently, adherends made as asymmetric and unbalanced composite laminates can be included in the analysis. The adhesive layer is modelled in two ways. The first approach assumes the adhesive layer to be a linear elastic material, and the second approach takes into account the inelastic behaviour of many adhesives. The governing equations are formulated in terms of sets of first-order ordinary differential equations, which are solved numerically using the 'multi-segment method' of integration. © 1997 Published by Elsevier Science Ltd.

INTRODUCTION

The use of polymeric fibre-reinforced composite materials has gained widespread acceptance as an excellent way to obtain stiff, strong and very lightweight structural elements. However, load introduction into composite structural elements through joints, inserts and mechanical fasteners is associated with considerable difficulties. The primary reason for this is the layered structure of composite laminates, which results in poor strength properties with respect to loading by interlaminar shear and transverse normal stresses. Thus, the interaction between composite elements and adjoining parts often proves to be among the most critical areas of a structural assembly.

Joining of composite structures can be achieved through the use of bolted, riveted or adhesive-bonded joints. The performances of the mentioned joint types are severely influenced by the characteristics of the layered composite materials, but adhesive-bonded joints provide a much more efficient load transfer than mechanically fastened joint types.

From a purely structural point of view, the most effective adhesive joint types are stepped and scarfed lap-joints, where both types can be single- or double-sided. These types of joints are most often used when severe loads are to be transferred between structural components made of composite materials.

Accurate analysis of adhesive-bonded joints, for instance using the finite-element method, is an elaborate and computationally demanding task (see Crocombe & Adams [1], Harris & Adams [2] and Frostig *et al.* [3]), and there is a specific need for analysis and design tools that can provide accurate results with little computational effort involved. Such tools would be very useful for preliminary design purposes, i.e. in the stages of design where fast estimates of stress and strain distributions as well as joint strengths are needed.

The main objective of the present paper is to consider a unified approach for the analysis of stepped and scarfed adhesive-bonded lap-joints. Even though the approach is shown for the analysis of stepped and scarfed adhesive-bonded lap-joints, it can equally well be used for

the analysis of any of the following commonly used joint types: single lap-joints, scarfed single lap-joints, bonded double lap-joints, double lap-joints, double-sided stepped lap-joints and double-sided scarfed lap-joints (see Mortensen & Thomsen [4]).

In the analysis the adherends are modelled as beams or wide plates in cylindrical bending and are considered as generally orthotropic laminates using classical laminate theory. Consequently, adherends made as asymmetric and unbalanced composite laminates can be included in the analysis. The adhesive layer is modelled as continuously distributed linear tension–compression and shear springs. As non-linear effects in the form of adhesive plasticity play an important role in the load transfer, the analysis allows inclusion of non-linear adhesive properties. The load and boundary conditions can be chosen arbitrarily. Analysis procedures for all the adhesive-bonded joints mentioned above have been developed and are being implemented in the new composites analysis and design software package ESAComp (see Saarela *et al.* [5]). ESAComp, which is being developed for the European Space Agency, provides an easy-to-use environment for preliminary evaluation and analysis of plies and laminates, as well as structural composite components. The developed analysis tools for adhesive-bonded joints will be completely integrated in the ESAComp environment, which offers complete access to the ESAComp design system [5].

MATHEMATICAL FORMULATION

The stepped and scarfed lap-joint configurations, each composed of two similar or dissimilar generally orthotropic laminates subjected to general loading conditions, are shown in Fig. 1.

The adherend thicknesses are t_1 and t_2 outside the overlap zones for both joint types. Inside the overlap zone the adherend thicknesses for the stepped lap-joint are

$$t_1(x)=t_1^m;\quad t_2(x)=t_2^m;\quad m=\text{step number},\quad 0\le x\le L \tag{1}$$

For the scarfed lap-joint the adherend thicknesses inside the overlap zone are changed linearly

$$t_1(x)=t_1-\left(\frac{t_1}{L}\right)x;\quad t_2(x)=\left(\frac{t_2}{L}\right)x;\quad 0\le x\le L \tag{2}$$

where t_1 and t_2 are the thicknesses of the adherends outside the overlap zone.

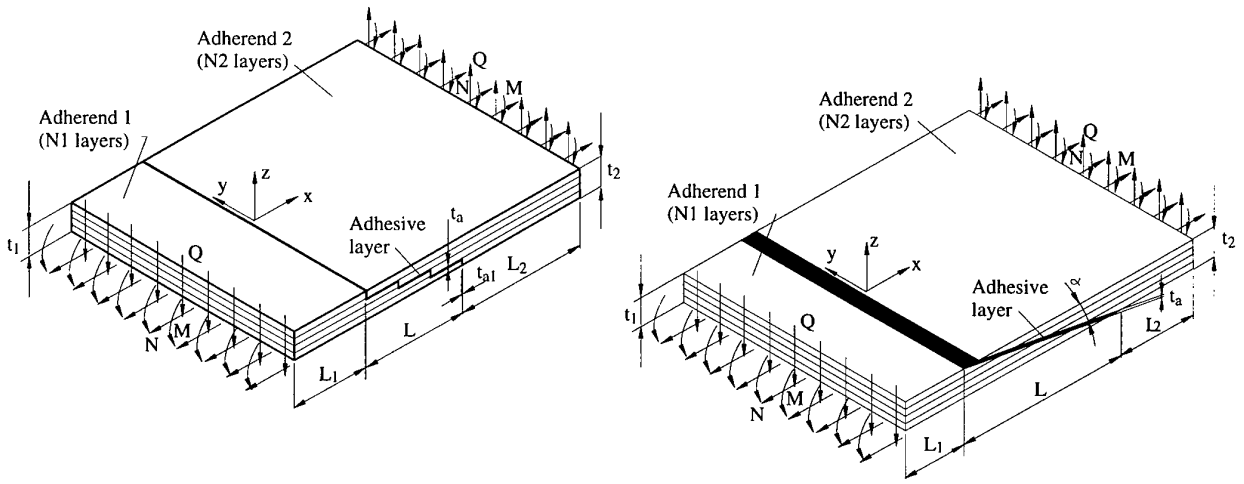

Fig. 1. Schematic illustration of an adhesive stepped lap-joint and an adhesive scarfed lap-joint (both single-sided) subjected to general loading conditions.

Basic assumptions for the structural modelling

The basic assumptions adopted for the structural modelling are the following.

The adherends:

- beams or wide plates in cylindrical bending, which are described by use of ordinary 'Kirchhoff' plate theory;
- generally orthotropic laminates using classical laminate theory (e.g. asymmetric and unbalanced composite laminates can be included in the analysis);
- the laminates are assumed to obey linear elastic constitutive laws;
- the strains are small, and the rotations are very small.

The adhesive layer:

- modelled as continuously distributed linear tension–compression and shear springs;
- inclusion of non-linear adhesive properties, by using a tangent modulus approach for the non-linear stress–strain relationship in conjunction with a modified von Mises yield criterion.

Load and boundary conditions:

- can be chosen arbitrarily.

The system of governing equations is set up for two different cases, i.e. the adherends are modelled as wide plates in cylindrical bending or as narrow beams.

Modelling of adherends as plates in cylindrical bending

For the purposes of the present investigation, and with references to Fig. 1, cylindrical bending can be defined as a wide plate (in the y direction), where the displacement field can be described as a function of the longitudinal coordinate only. As a consequence of this, the displacement field in the width directions will be uniform. Thus, the displacement field can be described as

$$u_0^i = u_0^i(x), \quad v_0^i = v_0^i(x), \quad w^i = w^i(x) \tag{3}$$

where u_0 is the midplane displacement in the longitudinal direction, v_0 is the midplane displacement in the width direction and w is the displacement in the transverse direction (all with respect to the middle surfaces of the laminates), and where $i = 1, 2$ corresponds to laminates 1 and 2, respectively (see Fig. 1). As a consequence of this, the following holds true

$$u^i_{0,\,y} = v^i_{0,\,y} = w^i_{,y} = w^i_{,yy} = 0 \tag{4}$$

It should be noted that the concept of 'cylindrical bending' is not unique, and that other definitions than the one used in the present formulation can be adopted (see Whitney [6]).

Substitution of the quantities in eqn (4) into the constitutive relations for a laminated composite material [4,6] gives the constitutive relations for a laminate (i) in cylindrical bending

$$\begin{aligned}
N^i_{xx} &= A^i_{11}u^i_{0,\,x} + A^i_{16}v^i_{0,\,x} - B^i_{11}w^i_{,xx}, & M^i_{xx} &= B^i_{11}u^i_{0,\,x} + B^i_{16}v^i_{0,\,x} - D^i_{11}w^i_{,xx} \\
N^i_{yy} &= A^i_{12}u^i_{0,\,x} + A^i_{26}v^i_{0,\,x} - B^i_{12}w^i_{,xx}, & M^i_{yy} &= B^i_{12}u^i_{0,\,x} + B^i_{26}v^i_{0,\,x} - D^i_{12}w^i_{,xx} \\
N^i_{xy} &= A^i_{16}u^i_{0,\,x} + A^i_{66}v^i_{0,\,x} - B^i_{16}w^i_{,xx}, & M^i_{xy} &= B^i_{16}u^i_{0,\,x} + B^i_{66}v^i_{0,\,x} - D^i_{16}w^i_{,xx}
\end{aligned} \tag{5}$$

where A^i_{jk}, B^i_{jk} and D^i_{jk} ($j, k = 1, 2, 6$) are the extensional, coupling and the flexural rigidities. N^i_{xx}, N^i_{yy} and N^i_{xy} are the in-plane stress resultants, and M^i_{xx}, M^i_{yy} and M^i_{xy} are the moment resultants. For the stepped lap-joint the rigidities A^i_{jk}, B^i_{jk} and D^i_{jk} ($j, k = 1, 2, 6$) have different values within each step depending on the thickness of the adherends and the plies within each step. For the scarfed lap-joint the rigidities within the overlap zone are each changed as a function of the longitudinal direction in accordance with their definition, i.e. A^i_{jk} is changed linearly, B^i_{jk} is changed parabolically and D^i_{jk} is changed cubically ($j, k = 1, 2, 6$).

From the basic assumptions, the following kinematic relations for the laminates are derived

$$u^i = u^i_0 + z\beta^i_x, \quad \beta^i_x = -w^i_{,x}, \quad \beta^i_y = 0 \tag{6}$$

Stepped lap-joints

With reference to Fig. 1 the equilibrium equations for the stepped lap-joint are specified in three regions: $-L_1 \le x \le 0$, $0 \le x \le L$ and $L \le x \le L+L_2$.

Referring to Fig. 2, the equilibrium equations can be written as follows

$$\left.\begin{Bmatrix} N^i_{xx,x}=0 \\ N^i_{xy,x}=0 \\ Q^i_{x,x}=0 \\ M^i_{xx,x}=Q^i_x \\ M^i_{xy,x}=Q^i_y \end{Bmatrix}\right. \begin{array}{l} i=1 \text{ for } -L_1 \le x \le 0, \\ i=2 \text{ for } L \le x \le L+L_2. \end{array} \left\{\begin{array}{ll} N^1_{xx,x}=-\tau_{ax}, & N^2_{xx,x}=\tau_{ax} \\ N^1_{xy,x}=-\tau_{ay}, & N^2_{xy,x}=\tau_{ay} \\ Q^1_{x,x}=-\sigma_a, & Q^2_{x,x}=\sigma_a \\ M^1_{xx,x}=Q^1_x-\tau_{ax}\dfrac{t^m_1+t_a}{2}, & M^2_{xx,x}=Q^2_x-\tau_{ax}\dfrac{t^m_2+t_a}{2} \\ M^1_{xy,x}=Q^1_y-\tau_{ay}\dfrac{t^m_1+t_a}{2}, & M^2_{xy,x}=Q^2_y-\tau_{ay}\dfrac{t^m_2+t_a}{2} \end{array}\right\} 0 \le x \le L \quad (7)$$

where t^m_1 and t^m_2 are the thicknesses of the adherends within the mth step. Within each gap of length t_{a1} in the overlap zone (see Fig. 1) the thickness of the adhesive layer is large compared to the overall thickness of the adhesive layer t_a, and therefore the adhesive in these gaps is assumed not to participate in the load transfer.

The coupling between the two adherends is established through the constitutive relations for the adhesive layer, which as a first approximation is assumed to be homogeneous, isotropic and linear elastic. The constitutive equations for the adhesive layer are established by a spring model, where the adhesive layer is assumed to be composed of continously distributed shear and tension–compression

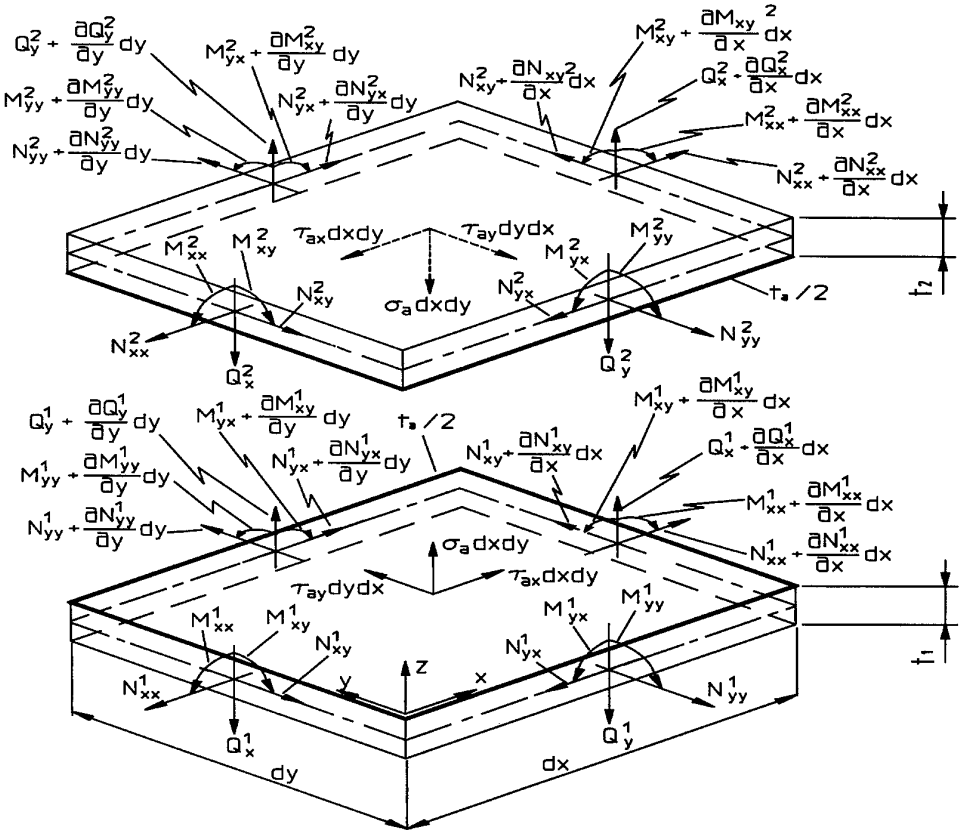

Fig. 2. Equilibrium elements for a stepped lap-joint in the overlap zone; $0 \le x \le L$.

springs. The constitutive equations of the adhesive layer are suggested in accordance with Thomsen [7,8] and Tong [9]

$$\tau_{ax}=\frac{G_a}{t_a}(u_2-u_1)=\frac{G_a}{t_a}\left(u_0^2-\frac{t_2}{2}\beta_x^2-u_0^1-\frac{t_1}{2}\beta_x^1\right)$$

$$\tau_{ay}=\frac{G_a}{t_a}(v_2-v_1)=\frac{G_a}{t_a}(v_0^2-v_0^1) \tag{8}$$

$$\sigma_a=\frac{E_a}{t_a}(w^2-w^1)$$

where G_a is the shear modulus and E_a is the elastic modulus of the adhesive layer.

As a consequence of the modelling of the adhesive layer it is not possible to fulfil the condition of zero shear stresses at the free edges of the adhesive (see Fig. 1). However, in real adhesive joints no free edges at the ends of the overlap zone are present. Instead a fillet of surplus adhesive, a so-called 'spew fillet', is formed at the ends of the overlap. This spew fillet allows the transfer of shear stresses at the overlap ends. Modelling the adhesive layer by spring models has been compared with other known analysis methods such as finite-element analysis [1,3] and High-order Theory Approach [3] (including the spew fillet), and the results show that the overall stress distribution and the predicted values are in very good agreement.

From the equations derived it is possible to form a complete set of system equations for the stepped lap-joint problem. Thus, a combination of eqns (5)–(8), in the areas $-L_1\le x\le 0$ and $L\le x\le L+L_2$ (outside the overlap) yields

$$\left.\begin{aligned}
&u^i_{0,x}=k_{1i}N^i_{xx}+k_{2i}N^i_{xy}+k_{3i}M^i_{xx}, && N^i_{xx,x}=0\\
&w^i_{,x}=-\beta^i_x, && Q^i_{x,x}=0\\
&\beta^i_{x,x}=k_{4i}N^i_{xx}+k_{5i}N^i_{xy}+k_{6i}M^i_{xx}, && M^i_{xx,x}=Q^i_x\\
&v^i_{0,x}=k_{7i}N^i_{xx}+k_{8i}N^i_{xy}+k_{9i}M^i_{xx}, && N^i_{xy,x}=0
\end{aligned}\right\}\quad i=1,2 \tag{9}$$

The coefficients k_{1i}–k_{9i} ($i=1, 2$) contain laminate stiffness parameters and appear when $u^i_{0,x}$, $v^i_{0,x}$ and $w^i_{,xx}$ are isolated from N^i_{xx}, N^i_{xy} and M^i_{xx} in eqn (5). Equation (9) constitutes a set of eight linear coupled first-order ordinary differential equations. Within the overlap zone, i.e. for $0\le x\le L$, a combination of eqns (5)–(8) yields

$$\begin{aligned}
&u^1_{0,x}=k_{11}N^1_{xx}+k_{21}N^1_{xy}+k_{31}M^1_{xx},\\
&w^1_{,x}=-\beta^1_x,\\
&\beta^1_{x,x}=k_{41}N^1_{xx}+k_{51}N^1_{xy}+k_{61}M^1_{xx},\\
&v^1_{0,x}=k_{71}N^1_{xx}+k_{81}N^1_{xy}+k_{91}M^1_{xx},
\end{aligned}\qquad
\begin{aligned}
&u^2_{0,x}=k_{12}N^2_{xx}+k_{22}N^2_{xy}+k_{32}M^2_{xx}\\
&w^2_{,x}=-\beta^2_x\\
&\beta^2_{x,x}=k_{42}N^2_{xx}+k_{52}N^2_{xy}+k_{62}M^2_{xx}\\
&v^2_{0,x}=k_{72}N^2_{xx}+k_{82}N^2_{xy}+k_{92}M^2_{xx}
\end{aligned}$$

$$N^1_{xx,x}=\frac{G_a}{t_a}u_0^1+\frac{G_at_1}{2t_a}\beta_x^1-\frac{G_a}{t_a}u_0^2+\frac{G_at_2}{2t_a}\beta_x^2,\qquad N^2_{xx,x}=-\frac{G_a}{t_a}u_0^1-\frac{G_at_1}{2t_a}\beta_x^1+\frac{G_a}{t_a}u_0^2-\frac{G_at_2}{2t_a}\beta_x^2$$

$$N^1_{xy,x}=\frac{G_a}{t_a}v_0^1-\frac{G_a}{t_a}v_0^2,\qquad N^2_{xy,x}=-\frac{G_a}{t_a}v_0^1+\frac{G_a}{t_a}v_0^2$$

$$M^1_{xx,x}=Q^1_x+\frac{G_a(t_1+t_a)}{2t_a}u_0^1+\frac{G_at_1(t_1+t_a)}{4t_a}\beta_x^1-\frac{G_a(t_1+t_a)}{2t_a}u_0^2+\frac{G_at_2(t_1+t_a)}{4t_a}\beta_x^2,$$

$$M^2_{xx,x}=Q^2_x+\frac{G_a(t_2+t_a)}{2t_a}u_0^1+\frac{G_at_1(t_2+t_a)}{4t_a}\beta_x^1-\frac{G_a(t_2+t_a)}{2t_a}u_0^2+\frac{G_at_2(t_2+t_a)}{4t_a}\beta_x^2$$

$$Q^1_{x,x} = \frac{E_a}{t_a} w^1 - \frac{E_a}{t_a} w^2, \qquad Q^2_{x,x} = -\frac{E_a}{t_a} w^1 + \frac{E_a}{t_a} w^2 \tag{10}$$

Within each gap in the overlap zone the governing equations are the same as those of each adherend outside the overlap, i.e. eqn (9). Equation (10) constitutes a set of 16 linear coupled first-order ordinary differential equations. A solution vector containing the fundamental variables for each adherend can be defined such that

$$\{y^i\} = \{u^i_0, w^i, \beta^i_x, v^i_0, N^i_{xx}, N^i_{xy}, M^i_{xx}, Q^i_x\} \quad i = 1, 2 \tag{11}$$

These variables will be determined through the analysis. In addition, the quantities

$$\{y^i_{res}\} = \{N^i_{yy}, M^i_{yy}, M^i_{xy}, Q^i_y\} \quad i = 1, 2 \tag{12}$$

can be determined from the equilibrium equations and the constitutive relations.

To solve the problem the boundary conditions and continuity conditions have to be stated

$$x = -L_1, L+L_2\text{: prescribed: } \left.\begin{matrix} u^i_0 \text{ or } N^i_{xx},\ w^i \text{ or } Q^i_x \\ \beta^i_x \text{ or } M^i_{xx},\ v^i_0 \text{ or } N^i_{xy} \end{matrix}\right\} \quad i = 1, 2$$

$x = 0$: adherend 1: Continuity across junction

adherend 2: $N^2_{xx} = N^2_{xy} = M^2_{xx} = Q^2_x = 0$

$x = L$: adherend 1: $N^1_{xx} = N^1_{xy} = M^1_{xx} = Q^1_x = 0$

adherend 2: Continuity across junction

Continuity across each step:

adherend 1: $u^{1*}_0 = u^1_0 - \beta^1_x t^*_1$

$M^{1*}_{xx} = M^1_{xx} + N^1_{xx} t^*_1$

$M^{1*}_{xy} = M^1_{xy} + N^1_{xy} t^*_1$

adherend 2: $^{2*}_{0} = u^2_0 - \beta^2_x t^*_2$

$M^{2*}_{xx} = M^2_{xx} + N^2_{xx} t^*_2$

$M^{2*}_{xy} = M^2_{xy} + N^2_{xy} t^*_2$ (13)

where $t_1{}^*$ and $t_2{}^*$ are the distances between the centerlines of the adherend laminates at each step. The boundary conditions for adherend 2 at $x = 0$ and for adherend 1 at $x = L$ are derived from the assumption that the adherend edges are free and do not participate in the load transfer (see Fig. 1).

Scarfed lap-joints

For the scarfed lap-joint problem the constitutive relations, the kinematic relations and the equilibrium equations outside the overlap zone are the same as for the stepped lap-joint. Inside the overlap zone the constitutive relations are the same as for the stepped lap-joint, except that the stiffness parameters change as functions of the longitudinal coordinate due to the linear change of adherend thicknesses. The equilibrium equations are also different inside the overlap zone due to the linear change of the adherend thicknesses. With reference to Fig. 3, the equilibrium equations for the scarfed lap-joint within the overlap zone (region; $0 \le x \le L$, see Fig. 1) can be written as follows

$$N^1_{xx,x} = -\tau_{ax}, \qquad N^2_{xx,x} = \tau_{ax}$$

$$
\left.\begin{aligned}
&N^1_{xy,x} = -\tau_{ay}, && N^2_{xy,x} = \tau_{ay}\\
&Q^1_{x,x} = -\sigma_a, && Q^2_{x,x} = \sigma_a\\
&M^1_{xx,x} = Q^1_x - \tau_{ax}\left(\frac{t_1(x)+t_a}{2}\right) + N^1_{xx}\frac{t_1}{2L}, && M^2_{xx,x} = Q^2_x - \tau_{ax}\left(\frac{t_2(x)+t_a}{2}\right) + N^2_{xx}\frac{t_2}{2L}\\
&M^1_{xy,x} = Q^1_y - \tau_{ay}\left(\frac{t_1(x)+t_a}{2}\right) + N^1_{xy}\frac{t_1}{2L}, && M^2_{xy,x} = Q^2_y - \tau_{ay}\left(\frac{t_2(x)+t_a}{2}\right) + N^2_{xy}\frac{t_2}{2L}
\end{aligned}\right\} \quad 0 \le x \le L \qquad (14)
$$

where the relationship between τ_{ax}, σ_a in eqn (14) and τ_{an}, σ_{an} shown in Fig. 3 is established through equilibrium

$$\tau_{ax} = \tau_{an} + \sigma_{an}\tan\alpha, \quad \sigma_a = \sigma_{an} - \tau_{an}\tan\alpha \qquad (15)$$

The quantities $t_1(x)$ and $t_2(x)$ are the linear variations of the thicknesses of the adherends defined in eqn (2), and t_1 and t_2 are the thicknesses of the adherends outside the overlap zone.

As for the stepped lap-joint the complete set of system equations for the scarfed lap-joint problem can be formed by a combination of the derived equations. The system equations for the scarfed lap-joint are the same as for the stepped lap-joint outside the overlap, i.e. in the areas $-L_1 \le x \le 0$ and

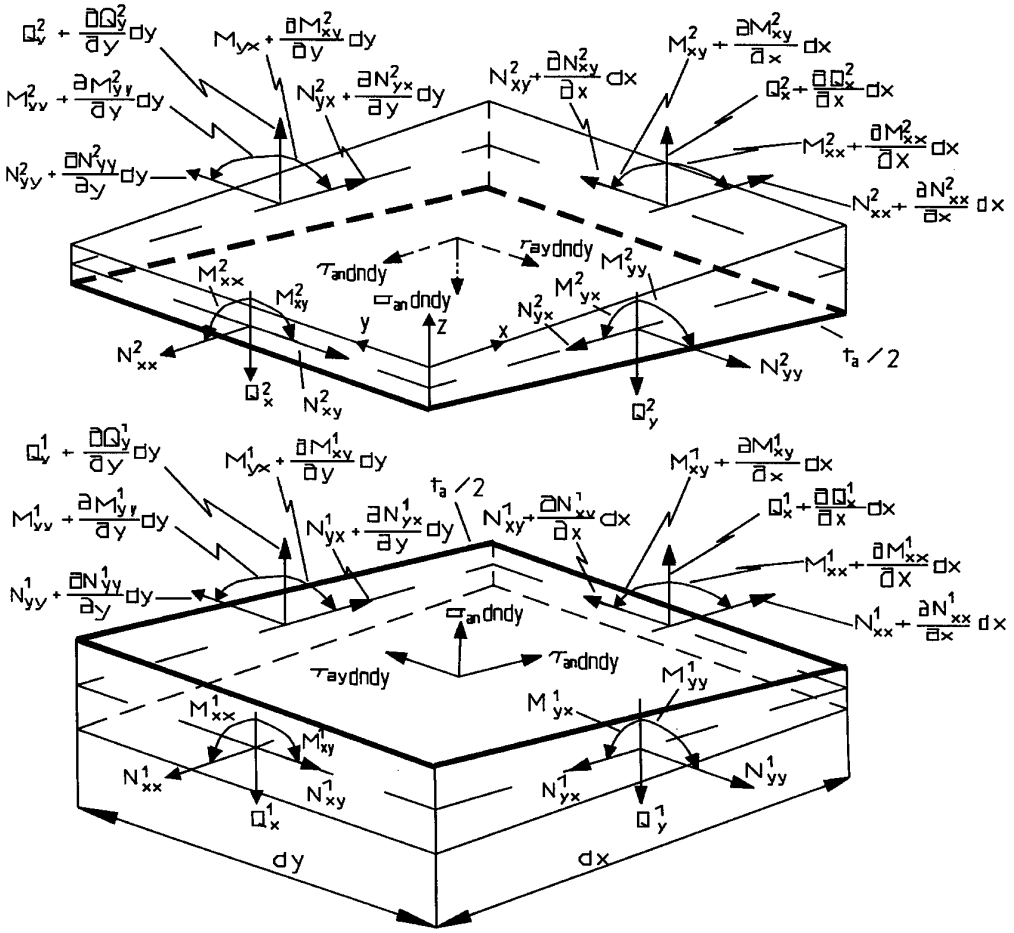

Fig. 3. Equilibrium elements in the overlap zone for a scarfed lap-joint; $0 \le x \le L$.

$L \leq x \leq L+L_2$. Within the overlap zone, i.e. for $0 \leq x \leq L$, combination of eqns (5), (6), (8) and (14) yields

$$u^1_{0,x} = k_{11}N^1_{xx} + k_{21}N^1_{xy} + k_{31}M^1_{xx}, \qquad u^2_{0,x} = k_{12}N^2_{xx} + k_{22}N^2_{xy} + k_{32}M^2_{xx}$$

$$w^1_{,x} = -\beta^1_x, \qquad w^2_{,x} = -\beta^2_x$$

$$\beta^1_{x,x} = k_{41}N^1_{xx} + k_{51}N^1_{xy} + k_{61}M^1_{xx}, \qquad \beta^2_{x,x} = k_{42}N^2_{xx} + k_{52}N^2_{xy} + k_{62}M^2_{xx}$$

$$v^1_{0,x} = k_{71}N^1_{xx} + k_{81}N^1_{xy} + k_{91}M^1_{xx}, \qquad v^2_{0,x} = k_{72}N^2_{xx} + k_{82}N^2_{xy} + k_{92}M^2_{xx}$$

$$N^1_{xx,x} = \frac{G_a}{t_a}u^1_0 + \frac{G_a t_1(x)}{2t_a}\beta^1_x - \frac{G_a}{t_a}u^2_0 + \frac{G_a t_2(x)}{2t_a}\beta^2_x \qquad N^2_{xx,x} = -\frac{G_a}{t_a}u^1_0 - \frac{G_a t_1(x)}{2t_a}\beta^1_x + \frac{G_a}{t_a}u^2_0 - \frac{G_a t_2(x)}{2t_a}\beta^2_x$$

$$N^1_{xy,x} = \frac{G_a}{t_a}v^1_0 - \frac{G_a}{t_a}v^2_0, \qquad N^2_{xy,x} = -\frac{G_a}{t_a}v^1_0 + \frac{G_a}{t_a}v^2_0$$

$$M^1_{xx,x} = Q^1_x + \frac{G_a(t_1(x)+t_a)}{2t_a}u^1_0 + \frac{G_a t_1(x)(t_1(x)+t_a)}{4t_a}\beta^1_x - \frac{G_a(t_1(x)+t_a)}{2t_a}u^2_0 + \frac{G_a t_2(x)(t_1(x)+t_a)}{4t_a}\beta^2_x + \frac{t_1}{2L}N^1_{xx},$$

$$M^2_{xx,x} = Q^2_x + \frac{G_a(t_2(x)+t_a)}{2t_a}u^1_0 + \frac{G_a t_1(x)(t_2(x)+t_a)}{4t_a}\beta^1_x - \frac{G_a(t_2(x)+t_a)}{2t_a}u^2_0 + \frac{G_a t_2(x)(t_2(x)+t_a)}{4t_a}\beta^2_x + \frac{t_2}{2L}N^2_{xx},$$

$$Q^1_{x,x} = \frac{E_a}{t_a}w^1 - \frac{E_a}{t_a}w^2, \qquad Q^2_{x,x} = -\frac{E_a}{t_a}w^1 + \frac{E_a}{t_a}w^2 \tag{16}$$

Coefficients k_{1i}–k_{9i} ($i = 1, 2$) are functions of the longitudinal coordinate, as the stiffness parameters are functions of the longitudinal coordinate within the overlap for the scarfed lap-joint. To solve the problem the boundary conditions again have to be stated

$$x = -L_1, L+L_2\text{: prescribed: } \left.\begin{matrix} u^i_0 \text{ or } N^i_{xx},\ w^i \textit{ or } Q^i_x \\ \beta^i_x \text{ or } M^i_{xx},\ v^i_0 \text{ or } N^i_{xy} \end{matrix}\right\} \quad i = 1, 2$$

$x = 0$: adherend 1: Continuity across junction

adherend 2: $N^2_{xx} = N^2_{xy} = M^2_{xx} = Q^2_x = 0$

$x = L$: adherend 1: $N^1_{xx} = N^1_{xy} = M^1_{xx} = Q^1_x = 0$

adherend 2: Continuity across junction

(17)

The governing equations can be derived in a similar way for the double-sided stepped lap and scarfed lap-joints. In these cases a set of 24 linear coupled first-order ordinary differential equations will appear within the overlap zone. In addition, other continuity conditions have to be specified.

Modelling of adherends as beams

Modelling of the adherends as narrow beams can be considered as a special case of cylindrical bending. When the adherends are modelled as beams the width direction displacements are not considered, and only the longitudinal and vertical displacements are included. Thus, the displacement field in eqn (3) is reduced to

$$u_0 = u_0(x), \quad w = w(x) \tag{18}$$

For this case the constitutive relations for a composite beam are reduced to

$$N^i_{xx} = A^i_{11} u^i_{0,x} - B^i_{11} w^i_{,xx}, \tag{19}$$

$$M^i_{xx} = B^i_{11} u^i_{0,x} - D^i_{11} w^i_{,xx}$$

The kinematic relations (eqn (6)), the equilibrium equations (eqns (7) and (24)) and the constitutive relations for the adhesive layer (eqn (8)) are the same as for cylindrical bending cases except that all variables associated with the width direction are nil.

The problem is reduced to a set of six coupled first-order ordinary differential equations for each adherend outside the overlap zone, and 12 inside the overlap zone. For this problem, the solution vector containing the fundamental variables for each adherend is defined by

$$\{y^i\} = \{u^i_0,\ w^i,\ \beta^i_x,\ N^i_{xx},\ M^i_{xx},\ Q^i_x\} \quad i = 1, 2 \tag{20}$$

The boundary conditions can be stated as for the cylindrical bending case (eqns (13) or (17)) except that v_0 or N_{xy} do not have to be specified on the boundaries x = constant.

Multi-segment method of integration

The set of governing equations, i.e. eqns (9) and (10) for the stepped lap-joint and eqns (9) and (16) for the scarfed lap-joint, together with the boundary conditions, eqn (13) or eqn (17), constitute a multiple-point boundary value problem which for both problems can be expressed in the following general form

$$\{y^1(x)\}_{,x} = [\mathbf{A}_{11}(x)]\{y^1(x)\} + \{\mathbf{B}_1(x)\}$$
$$-L_1 \le x \le 0$$

$$\begin{Bmatrix}\{y^1(x)\}\\ \{y^2(x)\}\end{Bmatrix}_{,x} = \begin{bmatrix}[\mathbf{A}^*_{11}(x)] & [\mathbf{A}^*_{12}(x)]\\ [\mathbf{A}^*_{21}(x)] & [\mathbf{A}^*_{22}(x)]\end{bmatrix}\begin{Bmatrix}\{y^1(x)\}\\ \{y^2(x)\}\end{Bmatrix}$$

$$+\begin{Bmatrix}\{\mathbf{B}_1(x)\}\\ \{\mathbf{B}_2(x)\}\end{Bmatrix} \quad 0 \le x \le L$$

$$\{y^2(x)\}_{,x} = [\mathbf{A}_{22}(x)]\{y^2(x)\} + \{\mathbf{B}_2(x)\}$$
$$L \le x \le L + L_2 \tag{21}$$

The boundary conditions at $x = -L_1$, $x = 0$, $x = L$, $x = L + L_2$ (see Fig. 1) are stated by specifying linear combinations of the fundamental variables

$$x = -L_1\colon [\mathbf{T}_0]\{y^1(-L_1)\} = \{\mathbf{U}_0\}$$

$$x = 0\colon [\mathbf{T}_1]\begin{Bmatrix}\{y^1(0)\}\\ \{y^2(0)\}\end{Bmatrix} = \{\mathbf{U}_1\}$$

$$x = L\colon [\mathbf{T}_2]\begin{Bmatrix}\{y^1(L)\}\\ \{y^2(L)\}\end{Bmatrix} = \{\mathbf{U}_2\}$$

$$x = L + L_2\colon [\mathbf{T}_3]\{y^1(L + L_2)\} = \{\mathbf{U}_3\} \tag{22}$$

It should be emphasized that eqn (22) does not involve any restrictions on the boundary conditions, and that any natural boundary conditions may be stated in this form. The multiple-point boundary value problem constituted by eqn (21) and eqn (22) is solved using the 'multi-segment method of integration' (see Kalnins [10]). This method is based on a transformation of the original 'multiple-point' boundary value problem into a series of initial value problems. The principle behind the method is to divide the original problem into a finite number of segments, where the solution within each segment can be accomplished by means of direct integration. Fulfilment of the boundary conditions, as well as fulfilment of continuity requirements across the segment junctions, is assured by formulation and solving a set of linear algebraic equations.

NON-LINEAR ADHESIVE FORMULATION

Most polymeric structural adhesives exhibit inelastic behaviour, in the sense that plastic residual strains are induced even at low levels of external loading. Thus, the assumption of linear elasticity of the adhesive is an approximation.

The concept of effective stress–strain is one way of approaching this problem, and it assumes, for a ductile material, that plastic residual strains are large compared with the creep strains at normal loading rates. Therefore a plastic yield hypothesis can be applied, and the multi-directional state of stress can be related to a simple unidirectional stress state through a function similar to that of von Mises.

However, it is widely accepted that the yield behaviour of polymeric structural adhesives is dependent on both deviatoric and hydrostatic stress components. A consequence of this phenomenon is a difference between the yield stresses in uniaxial tension and compression. This behaviour has been incorporated into the analysis by the application of a modified von Mises criterion suggested by Gali *et al.* [11]

$$s = C_S (J_{2D})^{1/2} + C_V J_1$$

$$C_S = \frac{\sqrt{3}(1+\lambda)}{2\lambda}$$

$$C_V = \frac{\lambda - 1}{2\lambda}$$

$$\lambda = \frac{\sigma_c}{\sigma_t} \tag{23}$$

where s is the effective stress, J_{2D} is the second invariant of the deviatoric stress tensor, J_1 is the first invariant of the general stress tensor and λ is the ratio between the compressive and tensile yield stresses. For $\lambda = 1$, eqn (23) is reduced to the ordinary von Mises criterion. At the failure load level, the first part of eqn (23) is transformed into the expression

$$s_{ult} = C_{S,\,ult} (J_{2D})_{ult}^{1/2} + C_{V,\,ult} (J_1)_{ult} \tag{24}$$

where the subscript 'ult' denotes 'ultimate'. Equation (24) describes the failure envelope for the general case of a ductile material, and in three-dimensional stress space eqn (24) represents a paraboloid with its axis coincident with the line $\sigma_1 = \sigma_2 = \sigma_3$.

The effective strain e is given by:

$$e = C_S \frac{1}{1+v} (I_{2D})^{1/2} + C_V \frac{1}{1-2v} (I_1) \tag{25}$$

where v is Poisson's ratio, I_{2D} is the second invariant of the deviatoric strain tensor and I_1 is the first invariant of the general strain tensor.

The non-linear adhesive properties are included by implementing an effective stress–strain relationship derived experimentally from tests on adhesive bulk specimens [7,9]. Thus, it is assumed that the bulk and *in situ* mechanical properties of the structural adhesive are closely correlated (see Gali *et al.* [11] and Lilleheden [12]).

Based on a tangent modulus approach for the the non-linear effective stress–strain relationship for the adhesive, the solution procedure for determining the stress distribution in the adhesive layer can be described by the following steps.

1. Calculate the effective strains, e_1, and stresses, s_1^* (eqns (23) and (25)), for each point of the adhesive layer using the linear elastic solution procedure and assuming a uniform elastic modulus, E_1, for the adhesive.
2. If the calculated effective stresses, s_1^*, are above the proportional limit, denoted by s_{prop}, determine the effective stresses s_1 for each point of the adhesive layer according to the corresponding effective strains, e_1, calculated in step (1).
3. Calculate the difference $\Delta s_1 = s_1^* - s_1$ between the 'calculated' and the 'experimental' effective stresses, and determine the specific tangent modulus, E_2^t, defined by

$$E_2^t = \{1 - \delta(\Delta s_1 / s_1)\} E_1 \tag{26}$$

   where δ is a weight factor which determines the change of the modulus in each iteration.
4. Re-run the procedure (steps (1) and (2)) with the elastic modulus, E_1, for each adhesive point modified as per step (3).
5. Compare the 'calculated' effective stresses, s^*, for each adhesive point with the 'experimental' values, s, obtained from the effective stress–strain curve.
6. Repeat steps (4) and (5) until the difference between the 'calculated' and 'experimental' stresses (Δs) drops below a specified fraction (2%) of the 'experimental' stress value.

Convergence is usually achieved within a few iterations.

EXAMPLES AND DISCUSSION

To show the applicability of the developed linear and non-linear solution procedures two examples will be presented. The first example presents the results obtained for a stepped lap-joint assuming linear elastic adhesive behaviour. The second example presents the results obtained for a scarfed lap-joint assuming linear elastic as well as non-linear adhesive properties. The basic adherends properties, i.e. outside the overlap zone, and the adhesive properties assumed in the examples are given by (see Fig. 1 for reference) the following.

Plies:	graphite–epoxy $E_1 = 164.0$ GPa, $E_2 = E_3 = 8.3$ GPa, $G_{12} = G_{31} = G_{23} = 2.1$ GPa, $\nu_{12} = \nu_{13} = \nu_{23} = 0.34$, $t = 0.125$ mm
Laminate 1:	graphite–epoxy $[0°, 30°, 60°]_4$, $t_1 = 1.5$ mm;
Laminate 2:	graphite–epoxy $[60°, 30°, 0°]_4$, $t_2 = 1.5$ mm;
Adhesive:	epoxy AY103, $E_a = 2800$ MPa, $\nu_a = 0.4$, $t_a = 0.05$ mm; $\lambda = 1.3$, $s_{prop} = 27.0$ MPa, $s_{ult} = 71.5$ MPa, $e_{ult} = 0.049$
Lengths:	$L_1 = L_2 = 30.0$ mm, $L = 20.0$ mm;
Load and B.C.:	$x = -L_1$: $u_0^1 = w^1 = v_0^1 = M_{xx}^1 = 0$; $x = L + L_2$: $w^2 = v_0^2 = M_{xx}^2 = 0$, $N_{xx}^2 = 0.2$ kN/mm
Modelling:	Wide plates in cylindrical bending
Stepped lap:	$t_{a1} = 1.0$ mm; length of each step = 7.0 mm
Scarfed lap:	$\alpha = 4.33°$

The adhesive layer stresses are normalized with respect to the prescribed tension load on the loaded edge, which is given by

$$\sigma_N = N/t_2 b \tag{27}$$

where N is value of the axial tension load.

Linear analysis of a stepped lap-joint

The stepped lap-joint is made with three steps in the overlap (see Fig. 1). Within each step three plies of the laminates are dropped. The lay-up of the laminates is made such that a 0° ply is always facing the adhesive layer. Figure 4 shows the distribution of the normalized adhesive layer shear stresses.

As a consequence of the inclusion of the coupling effects in the laminates it is seen that width direction shear stresses (τ_{ay}) are induced. Figure 5 shows the distribution of the normalized adhesive layer transverse normal stresses.

From Figs 4 and 5 it is seen that the peak stresses are located close to the ends of the overlap.

Linear and non-linear analysis of a scarfed lap-joint

The vertical displacements of the adherends are shown in Fig. 6, and the width direction displacements are shown in Fig. 7.

The width direction displacements v_0^1 and v_0^2 shown in Fig. 7 occur because of the inclusion of the coupling effects in the laminates, i.e. because the adherend laminates are asymmetric and unbalanced. Figure 8 shows the distribution of the normalized adhesive layer stresses.

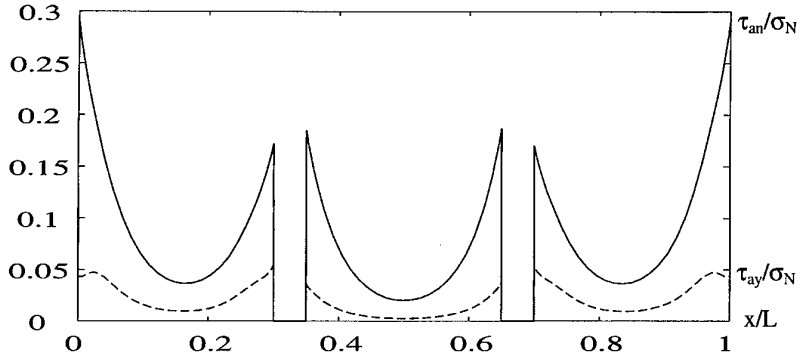

Fig. 4. Normalized adhesive layer shear stresses, τ_{ax}/σ_N and τ_{ay}/σ_N.

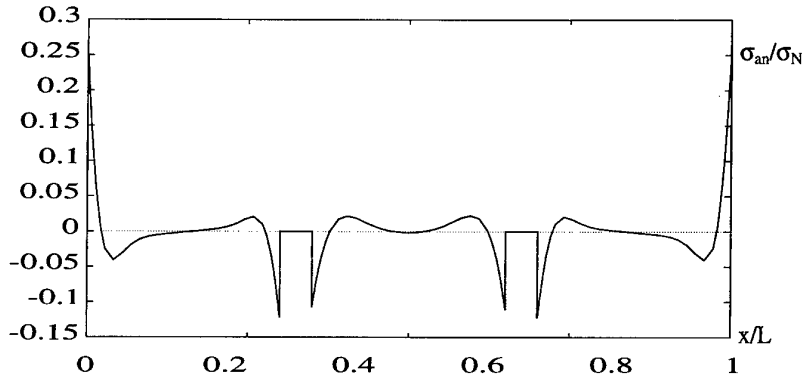

Fig. 5. Normalized adhesive layer transverse normal stresses σ_a/σ_N.

As a consequence of the inclusion of the coupling effects in the laminates, it is seen that width direction shear stresses (τ_{ay}) are induced. As for the stepped lap-joint, it is seen that the peak stresses are located close to the ends of the overlap.

The stress–strain curve for the AY103 adhesive (from Ciba–Geigy) used is obtained from bulk specimens [7]. Using the non-linear material properties for this adhesive, together with the modified von Mises criterion, results in the adhesive layer stress distribution shown in Fig. 9.

Comparison of the adhesive stress distributions obtained for the linear case in Fig. 8 and for the non-linear case in Fig. 9 shows that

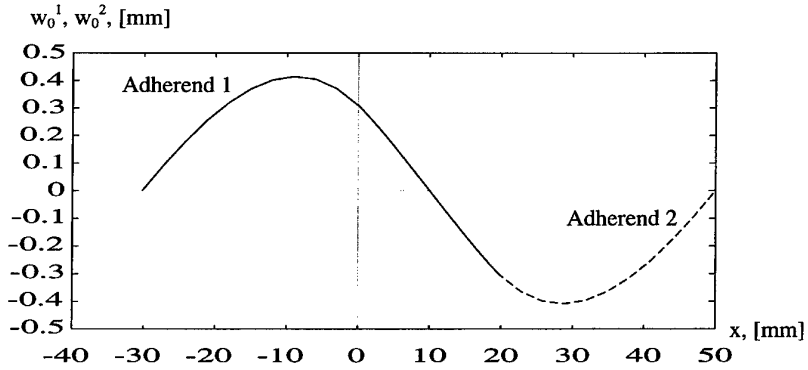

Fig. 6. Vertical displacements w^1 and w^2.

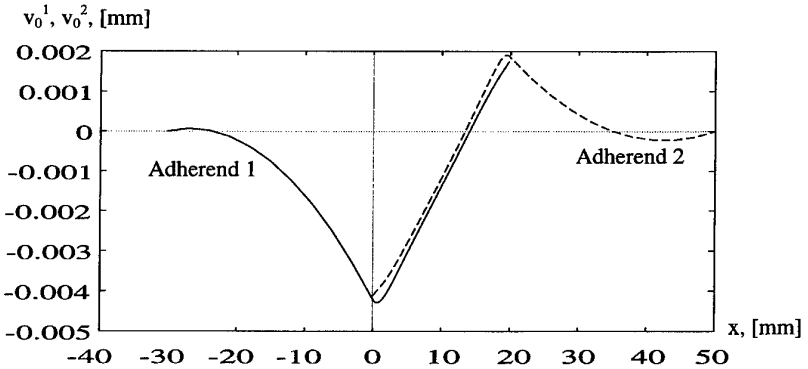

Fig. 7. Width direction displacements v_0^1 and v_0^2.

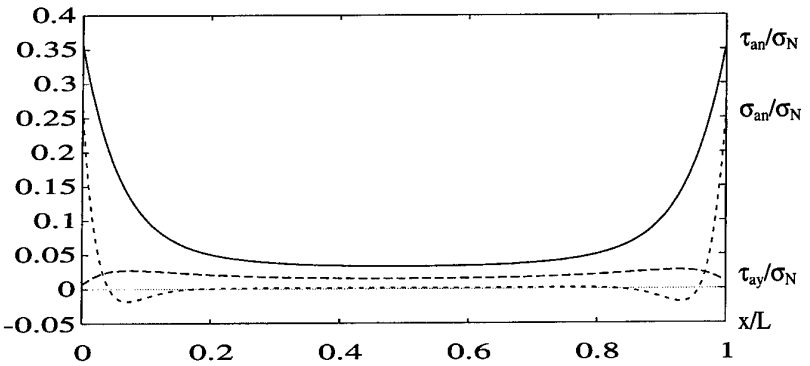

Fig. 8. Normalized adhesive layer stresses, τ_{ax}/σ_N, τ_{ay}/σ_N and σ_a/σ_N, obtained using the linear solution procedure.

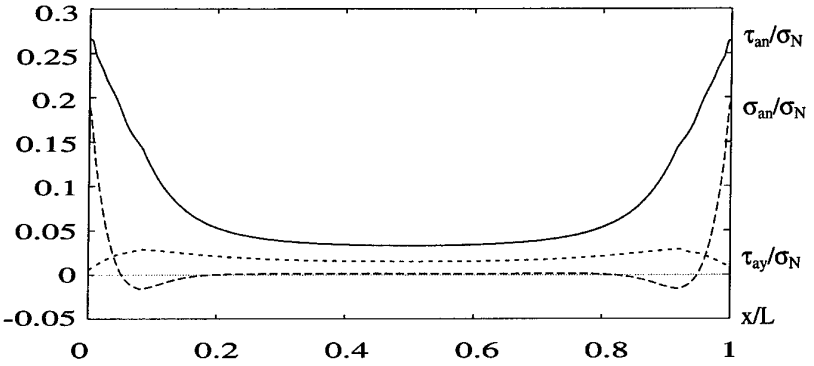

Fig. 9. Normalized adhesive layer stresses, τ_{ax}/σ_N, τ_{ay}/σ_N and σ_a/σ_N, obtained using the non-linear solution procedure.

inclusion of the non-linar effects reduce the maximum predicted adhesive layer stresses by about 25%. Based on these results, it is concluded that inclusion of adhesive non-linarity is very important as adhesive plasticity can occur even at low levels of external loading

CONCLUSION

A general method for the analysis of stepped and scarfed adhesive-bonded lap-joints between composite laminates has been presented. The analysis accounts for coupling effects induced by adherends made as asymmetric and unbalanced laminates. The analysis allows specification of any combination of boundary conditions and external loading, and it allows inclusion of the non-linear behaviour of many structural adhesives. The analysis can be carried out with the adherends modelled as narrow beams or wide plates in cylindrical bending.

The developed analysis procedures have proven to be robust, reliable and computionally effective, and the obtained results are very accurate.

REFERENCES

1. Crocombe, A. D. and Adams, R. D., Influence of the spew fillet and other parameters on the stress distribution in the single lap joint. *J. Adhesion*, 1981, **13** (2), 141–155.
2. Harris, J. A. and Adams, R. D., Strength prediction of bonded single lap joints by non-linear finite element methods. *Int. J. Adhesion Adhesives*, 1984, **4**, 65–78.
3. Frostig, Y. Thomsen, O. T. & Mortensen, F., Analysis of adhesive bonded joints, square-end and spew-fillet closed-form higher-order theory approach. Submitted, 1997.
4. Mortensen, F. & Thomsen, O. T., A simple unified approach for the analysis and design of adhesive bonded composite laminates. *Proc. Eleventh Int. Conf. on Composite Materials*, 1997.
5. Saarela, O., Palanterä, M., Häberle, J. & Klein, M., ESAComp: A powerful tool for analysis and design of composite materials. *Proc. of Int. Symp. on Advanced Materials for Lightweight Structures*, ESA-WPP-070. ESTEC, Noordwijk, The Netherlands, 1994, pp. 161–9.
6. Whitney, J. M., *Structural Analysis of Laminated Anisotropic Plates*. Technomic, Lancaster, PA, 1987.

7. Thomsen, O. T., Elasto-static and elasto-plastic stress analysis of adhesive bonded turbular lap joints. *Composite Struct.*, 1992, **21**, 249–259.
8. Thomsen, O. T., Rits, W., Eaton, D. C. G. and Brown, S., Ply drop-off effects in CFRP/honeycomp sandwich panels — theory. *Composite Sci. Technol.*, 1996, **56**, 407–422.
9. Tong, L., Bond strength for adhesive-bonded single lap joints. *Acta Mech.*, 1996, **117**, 101–113.
10. Kalnins, A., Analysis of shell of revolution subjected to symmetrical and non-symmetrical loads. *Trans. ASME, J. Appl. Mech.*, 1964, **31**, 467–476.
11. Gali, S., Dolev, G. and Ishai, O., An effective stress/strain concept in mechanical characterization of structural adhesive bonding. *Int. J. Adhesion Adhesives*, 1981, **1**, 135–140.
12. Lilleheden, L., Properties of adhesive *in situ* and in bulk. *Int. J. Adhesion Adhesive*, 1994, **14** (1), 31–37.

ELSEVIER

Composite Structures Vol. 38, No. 1–4, pp. 295–307, 1997
© 1997 Elsevier Science Ltd. All rights reserved
Printed in Great Britain
0263-8223/97/$17.00 + 0.00

PII:S0263-8223(97)00064-0

Analysis and design of fiber reinforced plastic composite deck-and-stringer bridges

Hani A. Salim,[a] Julio F. Davalos,[b] Pizhong Qiao[b] & Sam A. Kiger[a]

[a]*Department of Civil Engineering, University of Missouri-Columbia, Columbia, MO 65211, USA*
[b]*Department of Civil and Environmental Engineering, West Virginia University, Morgantown, WV 26506, USA*

A comprehensive study on analysis and design of fiber reinforced plastic (FRP) composite deck-and-stringer bridges is presented. The FRP decks considered consist of contiguous thin-walled box sections and are fabricated by bonding side-by-side pultruded thin-walled box beams, which are placed transversely over FRP composite stringers. In this study, we review the modeling and experimental verification of FRP structural beams, including micro/macro-mechanics predictions of ply and laminate properties, beam bending response, shear-lag effect, and local and global buckling behaviors. A simplified design analysis procedure for cellular FRP bridge decks is developed based on a first-order shear deformation macro-flexibility (SDMF) orthotropic plate solution. The present approach can allow the designers to analyze, design and optimize material architectures and shapes of FRP beams, as well as various bridge deck configurations, before their implementation in the field. Experimental studies of cellular FRP bridge decks are conducted to obtain stiffness coefficients, and an example of a cellular FRP deck on optimized winged-box FRP stringers under actual track-loading is presented to illustrate the analytical method. The experimental–analytical approach presented in this study is used to propose simplified engineering design equations for new and replacement highway FRP deck-and-stringer bridges. © 1997 Elsevier Science Ltd.

INTRODUCTION

Many of the bridges in the United States are deteriorating, particularly concrete bridge decks. According to the US Congress, 42% of the nation's highway bridges are considered deficient [1]. Owing to the corrosive nature of steel rebars used in concrete bridge decks, the service-life of these bridges is reduced. The rehabilitation and replacement of bridge decks requires intensive planning, analysis and design of alternative materials and systems. The advantages of fiber reinforced plastic (FRP) composites over conventional materials motivate their use in highway bridge rehabilitation and replacement applications. The favorable properties of FRPs include low weight, corrosion resistance, high specific stiffness and strength, and ease of installation and fabrication. In addition, the material architecture and geometric shape of FRPs can be tailored for specific applications. FRP decks are considered a potential solution to the problem of deteriorating bridge decks.

Current applications of composite structural components include buildings, pedestrian bridges, platforms and highway bridges. In the literature, there are several efforts to build and test FRP decks for highway bridges. The success of the use of FRP decks for highway bridge applications will depend, among other things, on the accuracy and simplicity of the analytical tools available. When designing steel or concrete bridges, engineers have access to design guidelines to meet certain established criteria. In contrast, when dealing with FRP bridge decks, engineers have to use expensive tools, such as the finite-element method, to optimize and analyze the superstructure. The use of sophisticated analyses can be time consuming and, therefore, a simple but yet accurate analysis procedure is needed to be able to predict the

response of FRP decks for highway bridge applications.

In this study, we propose to construct FRP decks from single-cell thin-walled box sections bonded together using adhesive (Fig. 1). In order to fully understand the behavior of the whole system, the analytical–experimental evaluation of the component single-cell box sections is essential; therefore, the developments on analysis, design and optimization for structural composite beams are first reviewed. The review includes: micro-mechanics predictions of ply stiffness; macro-mechanics predictions of laminate (panel) stiffness; beam stiffness coefficients computed using the Mechanics of Laminated Beams (MLB) model; beam response in bending accounting for shear deformation for box, winged-box (WB) and wide-flange (WF) sections; shear-lag study of beam flange panels; local and global buckling behaviors of FRP beams; first-ply-failure; and design optimization of beam shapes. The combined analysis, design optimization and experimental evaluation can be used to propose a comprehensive engineering design approach for FRP beams and to develop new innovative shapes for bridge applications.

Consistent with design methods for highway bridges given by AASHTO [2], step-by-step design guidelines for FRP decks are needed. The development of design equations can be based on a first-order shear deformation macro-flexibility (SDMF) orthotropic plate solution, as proposed by the authors. In this paper, a one-term approximation of a SDMF series solution for deck-and-stringer orthotropic bridges is used to develop simple expressions for load distribution factors, which in turn reduce the analysis of a deck-and-stringer bridge system to the analysis of a beam section. It is significant that the present equations include important parameters that represent, as accurately as possible, the response characteristics of the structure, such as material properties of the deck and stringers, the bridge aspect ratio, and the number and spacing of the stringers.

First, we present a comprehensive overview of analysis and design optimization of FRP beams and, subsequently, we introduce the SDMF analysis for FRP deck-and-stringer bridges, from which we derive an explicit expression for wheel-load distribution factors. The experimental investigation of a cellular FRP bridge deck test sample includes push-down shear, transverse and longitudinal bending, and torsion tests. Further on-going research efforts on FRP bridges are described in this paper.

REVIEW OF EXPERIMENTAL–ANALYTICAL EVALUATION AND OPTIMAL DESIGN OF FRP BEAMS

Because of the complexity of composite materials, analytical and design tools developed for conventional materials cannot always be

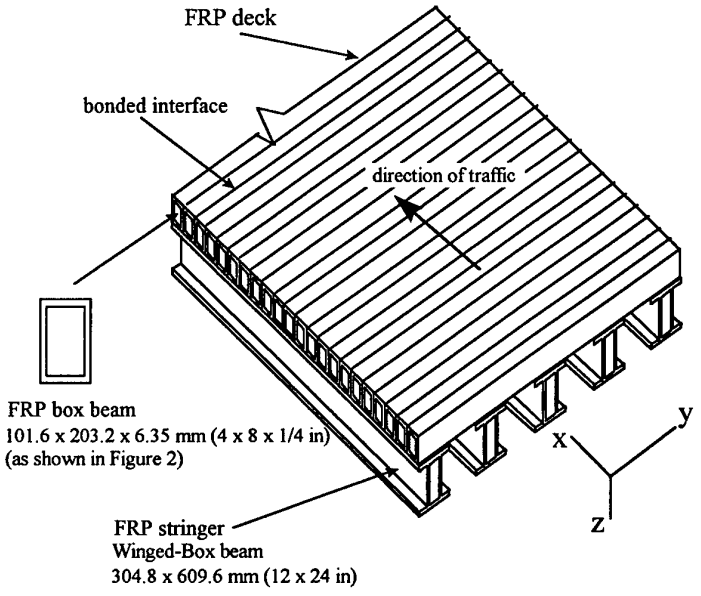

Fig. 1. Schematic of an FRP deck on FRP stringers.

readily applied to FRP shapes, and numerical methods, such as finite elements, are often difficult and expensive to use and require specialized training. Therefore, to expand the structural applications of pultruded FRP beam sections and create a new family of efficient FRP shapes for civil engineering structures, a practical and comprehensive engineering design and analysis tool for FRP shapes is needed. In this section we review analytical and experimental studies on FRP beams, and we suggest a practical design and optimization method for structural composite beams.

Prediction of ply–laminate stiffnesses

Although pultruded FRP shapes are not laminated structures in a rigorous sense, they are pultruded with material architectures that can be simulated as laminated configurations. A typical pultruded section mainly includes the following three types of layers [3] (see Figs 2 and 3): (1) continuous strand mats (CSM); (2) angle-ply stitched fabrics (SF); and (3) unidirectional fibers or roving layers. Each layer is modeled as a homogeneous, linearly elastic and generally orthotropic material. Based on the fiber volume fraction (V_f) and the manufacturer's specification, the ply stiffnesses are computed from micro-mechanics models for composites with periodic micro-structure [4]. For more details on the V_f computation and micro-mechanics model see Davalos *et al.* [3]. Once the ply stiffnesses for each laminate or panel of a FRP beam are computed, the stiffnesses of a laminate can be computed from macro-mechanics [5]. The micro/macro-mechanics models reviewed in this study have been shown to correlate well with experimental results for coupon samples [3,6,7].

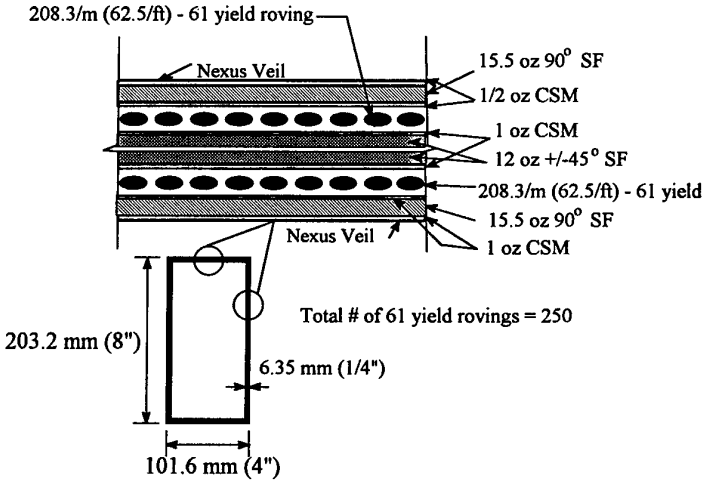

Fig. 2. Material lay-up of a typical FRP box beam section.

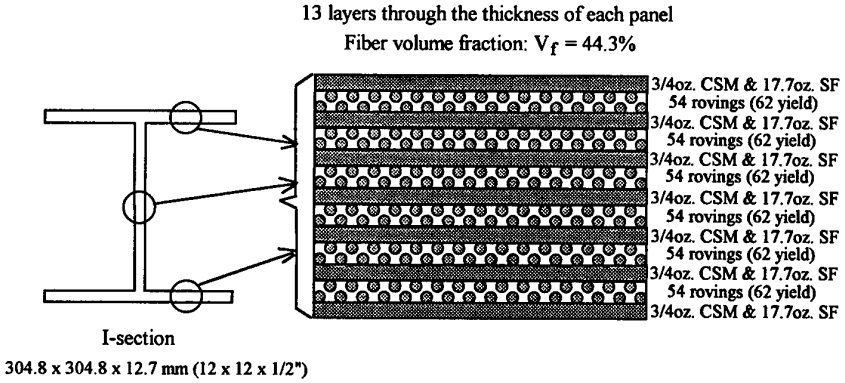

Fig. 3. Dimensions and panel fiber architectures of a WF-beam.

Predictions of beam stiffness coefficients and member response

The response of FRP shapes in bending is evaluated using the mechanics of thin-walled laminated beams (MLB) model [8]. In the MLB model the stiffness coefficients (axial, A; bending, D; axial–bending coupling, B; and shear, F) of a beam are computed by adding the contribution of the stiffnesses of the component panels, which in turn are obtained from the effective beam moduli. Displacement and rotation functions can be obtained by solving Timoshenko's beam theory equilibrium equations, and the ply strains and stresses can be obtained from classical lamination theory (CLT) [5]. The MLB model is suitable for straight FRP beam columns with at least one axis of geometric symmetry. As indicated in Table 1, the MLB analytical prediction of deflections and strains correlated well with experimental results for the $101.6 \times 203.2 \times 6.35$ mm ($4 \times 8 \times 1/4$ in.) box beam section of Fig. 2 (see Salim *et al.* [6]). Based on the MLB model, engineering design equations for FRP beams under bending [9] have been formulated, and they can be easily adopted by practicing engineers and composite manufacturers for the analysis, design and optimization of structural FRP beams.

Local and global buckling of FRP shapes

Because of the low modulus of elasticity of glass fibers and the common thin-walled sectional geometry, FRP beams may be susceptible to buckling even under service loads. Owing to the high strength-to-stiffness ratio of pultruded FRP composites, buckling is the most likely mode of failure before the ultimate material strength is reached. We developed a comprehensive analytical approach to study the local buckling behaviors of pultruded FRP shapes [10]. The local buckling analysis for discrete laminated plates or panels of FRP shapes is formulated and the effects of restraint at the flange–web connection are considered. For the flange panels under compression, simplified expressions for predictions of plate buckling strength are proposed by approximately solving transcendental equations as

$$N_x = \frac{\pi^2}{b_2}\left[\sqrt{q}\left(2\sqrt{D_{11}D_{22}}\right)+p\left(D_{12}+2D_{66}\right)\right] \qquad (1)$$

where N_x is the critical stress resultant, D_{ij} are bending stiffness coefficients, and p and q depend on the coefficient of restraint (ζ). For example, the values of p and q are illustrated in Fig. 4 for the flanges of the $101.6 \times 203.2 \times 6.35$ mm ($4 \times 8 \times 1/4$ in.) box beam section (Fig. 2), where $\zeta = 0$ corresponds to a clamped condition and $\zeta = \infty$ represents a hinged condition. The details on the determination of the coefficient of restraint (ζ) are given by Qiao & Davalos [10]. For the web panels under shear loading, the analysis is based on an energy approach, and the equilibrium equation in terms of the total potential energy is solved by the Rayleigh–Ritz method. The simplified design equation [eqn (1)] and the relationship between the parameters p and q and the coefficient of restraint ζ developed by Qiao & Davalos [10] can assist practitioners to perform local buckling analyses of customized FRP shapes as well as to optimize innovative sections.

A combined analytical and experimental evaluation of flexural–torsional and lateral–distortional buckling of fiber-reinforced plastic (FRP) composite I-beams was recently conducted by Davalos & Qiao [11]. Based on energy principles and nonlinear elastic theory, simplified engineering equations for flexural–torsional buckling were formulated. A good agreement was obtained among the analytical predictions, experimental results and finite-element analyses, and through the combined

Table 1. Experimental and analytical predictions of deflections and strains for a $101.6 \times 203.2 \times 6.35$ mm ($4 \times 8 \times 1/4$ in.) box section

Loading		Maximum deflection (mm/kN)			Maximum strain ($\mu\varepsilon$/kN)		
		Experiment	MLB model	Ratio	Experiment	MLB model	Ratio
Four-point	edge	0.114	0.122	1.070	82.31	82.64	1.004
	flat	0.354	0.373	1.051	123.56	122.58	0.992
Three-point	edge	0.796	0.830	1.043	105.67	116.36	1.101
	flat	2.427	2.512	1.035	177.93	184.16	1.035

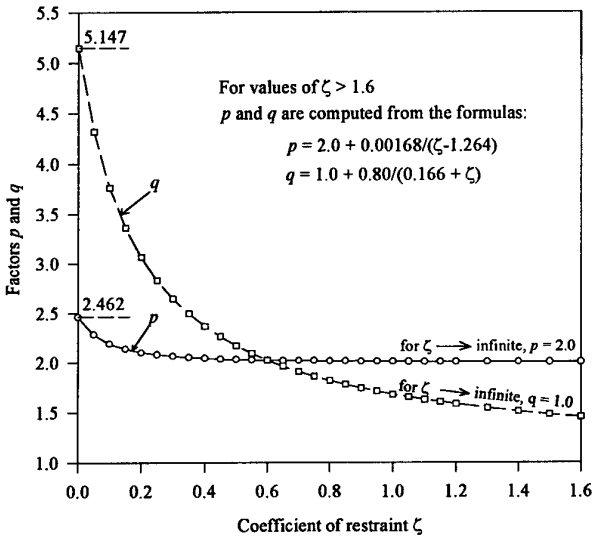

Fig. 4. Local buckling predictions for the flange of the box section in Fig. 2. (Factors p and q vs the coefficient of restraint ζ.)

analytical and experimental program considered by the authors it was shown that the proposed analytical solutions can be adopted to predict flexural–torsional and lateral–distortional buckling loads and used to formulate simplified design equations for pultruded FRP I-sections.

First-ply-failure

The Tsai–Hill failure criterion can be used to predict the first-ply-failure load (P_{FPF}) of FRP beams as [12]

$$\frac{P}{P_{FPF}} = \sqrt{\left(\frac{\sigma_1}{X}\right)^2 + \left(\frac{\sigma_2}{Y}\right)^2 - \frac{\sigma_1\sigma_2}{X^2} + \left(\frac{\tau_{12}}{S}\right)^2} \quad (2)$$

where σ_1, σ_2 and τ_{12} are the components of in-plane ply stresses in material coordinates, and X, Y and S are the corresponding ply strengths.

FRPBEAM computer program

Based on the modeling assumptions and analytical tools for FRP beams discussed above, the computer program FRPBEAM (flowchart shown in Fig. 5) was developed by Qiao *et al.* [13] to model, analyze and design FRP beams, from the evaluation of ply stiffnesses by micromechanics to the overall beam response by

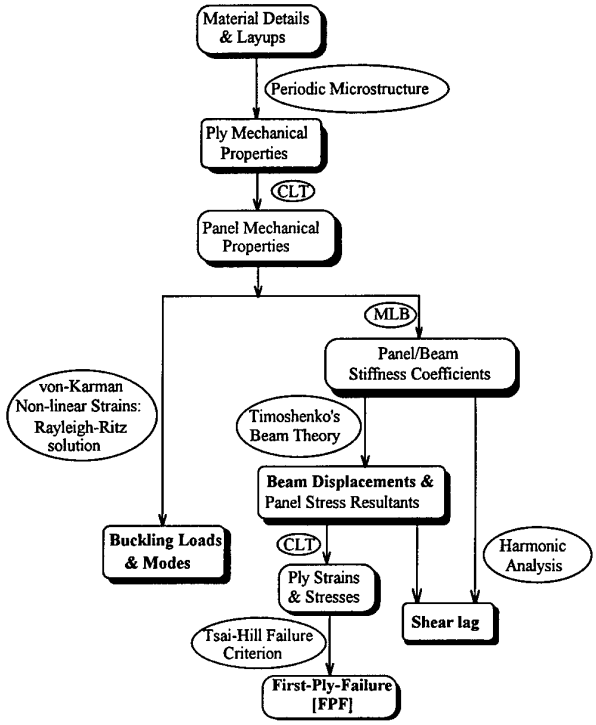

Fig. 5. Computational flowchart for program FRPBEAM [13].

Mechanics of Laminated Beams (MLB). The MLB subroutine can accurately predict displacements and strains of pultruded FRP beams [14].

Shear-lag in flange components of beams

In contrast to the assumption of constant stress across the width of a section used in elementary beam bending theory, the stress distributions across the flanges of beams can be nonuniform due to shear-lag, which results from the in-plane shear flexibility of the flange panels. The shear-lag effect can be important in design as it can lead to a significant decay of normal stresses at locations away from the intersections of flanges and webs. On the other hand, shear-lag can also reduce the bending stiffness of a given member from what is expected by ordinary beam theory. Salim & Davalos [15] presented a model for predicting shear-lag effects in FRP box sections and this model was extended to the analysis of FRP WF sections [16]. The flanges of a box or a WF section are first isolated and loaded by the longitudinal shear flow transmitted from the webs and by the normal stress resultant per unit width. This procedure is incorporated into the Mechanics of Laminated

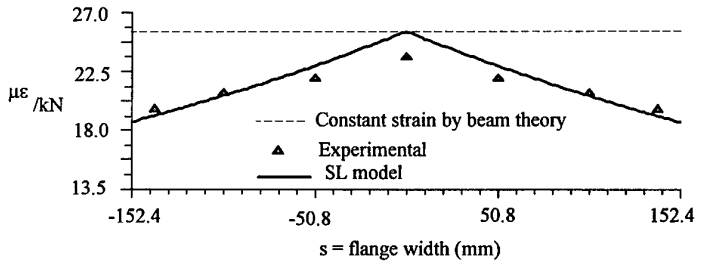

Fig. 6. Shear-lag effects of the WF beam in Fig. 3.

Beams (MLB) model [8] to predict the nonlinear distribution of stresses on the flanges that result from shear-lag effects. The predictions of the present shear-lag model correlated closely with experimental results for FRP box beams [15] and for wide-flange I-beams [16], as illustrated in Fig. 6.

Design optimization of FRP shapes

Unlike the extensive work reported for the optimal design of laminated composites plates and shells, the material architecture and shape optimization of thin-walled laminated composites beams is still under investigation and is less developed. Qiao *et al.* [17] proposed an optimization method to minimize the cross-sectional area for new pultruded FRP beams. The beam members were subjected to transverse loading, and the optimization constraints included deflection limit, material failure and elastic buckling. A global approximation technique was combined with a power law to generate the constraint equations at a number of design points. Davalos *et al.* [18] improved the above work and presented a design and optimization approach for structural composite beams. An optimized winged-box section was proposed as a new structural shape with significantly better performance than a counterpart WF beam of the same cross-sectional area. A multiobjective (multicriteria) design optimization of material architecture (ply fiber orientations and ply fiber percentages) for pultruded FRP shapes was subsequently developed [12], and a wide-flange I-section beam, which is one of the most commonly used structural shapes, was chosen to illustrate the analysis and design optimization. The beam maximum deflection, buckling resistance and material failure were considered as multiple objectives (criteria) in the optimization process. The optimal solutions were obtained through a multiobjective scheme, and a recommended practical design was proposed [12] which was used to manufacture the actual section shown in Fig. 3.

An optimized winged-box (WB) section was recently proposed by Qiao *et al.* [19], and the final cross-sectional dimensions and material architecture are given in Fig. 7. This WB beam section is used for the bridge main stringers of the example presented in this study (Fig. 1). The review given above on a comprehensive study for the analysis, design and optimization of FRP beams can be used to formulate engineering design equations and develop various innovative shapes for infrastructure applications.

DESIGN OF AN FRP DECK-AND-STRINGER BRIDGE

For an FRP bridge deck (Fig. 1), equivalent orthotropic properties such as longitudinal (D_y), transverse (D_x) and in-plane (H_{xy}) stiffnesses are needed to accurately model the structure. These properties are determined from the apparent stiffnesses of the FRP deck. The deck longitudinal stiffness, along the axis of the single cells, can be characterized by considering each repetitive cell as a representative beam, and the apparent bending stiffness of the cell, D_y, is predicted using the Mechanics of Laminated Beams (MLB) model [3,8]. The deck transverse stiffness, D_x, and in-plane shear stiffness, H_{xy}, are defined analytically and experimentally (Fig. 8).

The design of a deck-and-stringer bridge is usually reduced to the analysis of a single beam section, loaded by a concentrated load corresponding to an equivalent fraction of the applied truck load. This equivalent load is defined by load-distribution factors that approximate the overall behavior of the bridge superstructure. In this section, the first-order Shear Deformation Macro-Flexibility (SDMF)

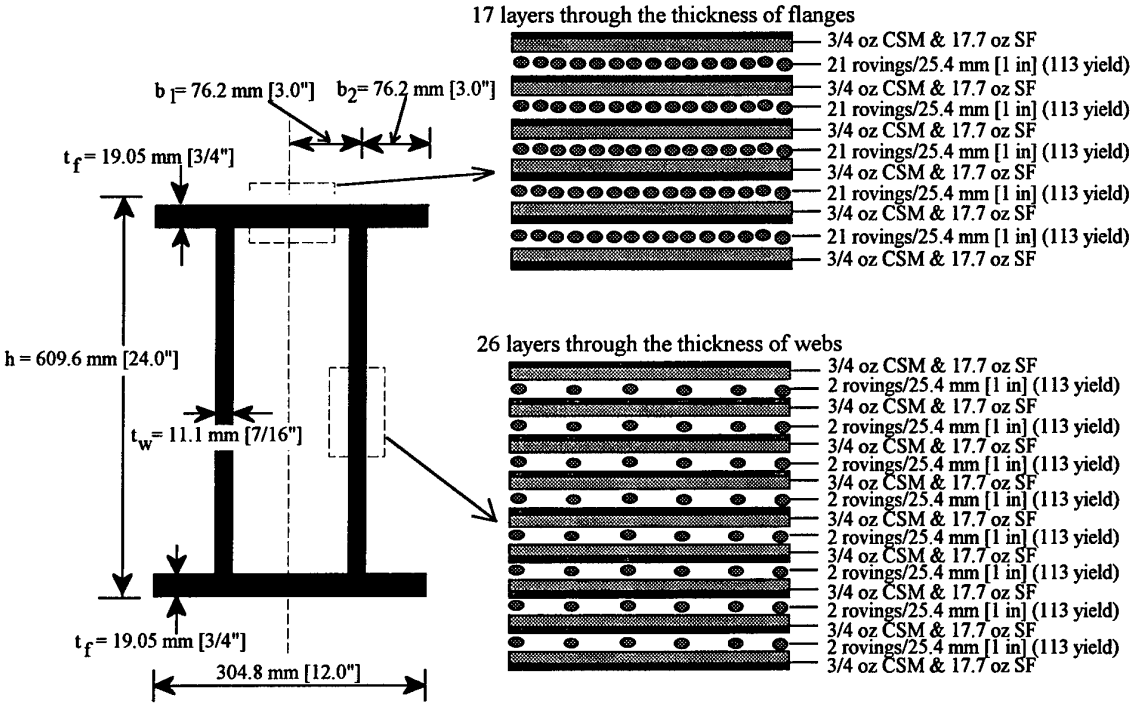

Fig. 7. Dimensions and panel fiber architectures of an optimized winged-box beam [19].

analysis is first presented, and an explicit expression for wheel-load distribution factor is derived, followed by a proposed design methodology for FRP composite deck-and-stringer bridges. Experimental results for stiffnesses of a cellular FRP bridge deck are correlated with the analytical solutions proposed by the authors.

SDMF analysis

For a rectangular plate element the equilibrium forces and moments, and the sign convention, for the deformations are shown in Fig. 9. The assumptions for shear deformation plate theory are analogous to Timoshenko's beam theory.

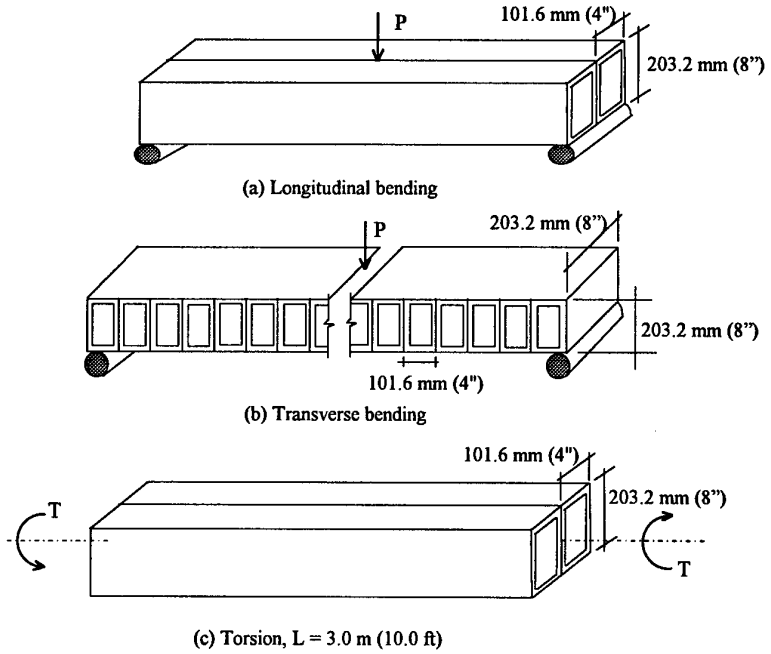

Fig. 8. Experimental deck stiffness coefficients.

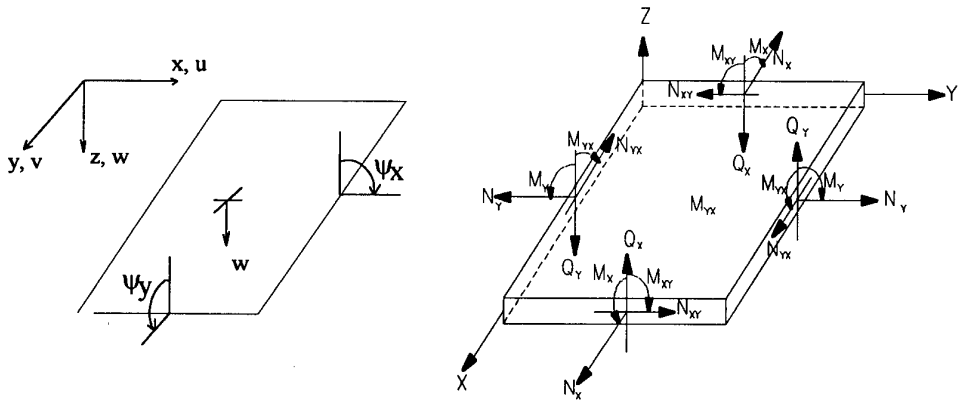

Fig. 9. Sign convention for deformation and plate stress resultants.

The displacement field of the plate is given by [20]

$$u(x,y,z) = u_0(x,y) + z\psi_x(x,y)$$
$$v(x,y,z) = v_0(x,y) + z\psi_y(x,y)$$
$$w(x,y,z) = w_0(x,y) \quad (3)$$

where u_0, v_0, w_0 denote displacement components of a point along the x, y, z coordinates, and ψ_x and ψ_y denote the rotations of a line element, originally perpendicular to the longitudinal plane, about the y and x axes, respectively. Using the total potential energy principle, the equilibrium equations for first-order shear deformation theory can be obtained, as available in Reddy [20]. The result is five differential equations for five unknowns, u_0, v_0, w_0, ψ_x and ψ_y. However, in this case w_0, ψ_x and ψ_y are decoupled from u_0 and v_0.

For certain boundary conditions one can develop solutions by using double series expansions. The closed-form solution for the response of a bridge-type system (Fig. 10), with two opposite sides simply supported and the other two stiffened by edge beams, is developed by a macro-flexibility (MF) analysis [21]. The rectangular deck-stringer system can be subjected to arbitrary static transverse loads (no torsional moments and/or in-plane forces). The stringers are equally spaced and have identical section and material properties. The analysis is general with respect to: (1) size and stiffness of the deck; and (2) type of loading (uniform and/or concentrated). The solution for symmetric loading condition only is given in this paper.

The basic steps in the flexural analysis of ribbed plates by the macro-flexibility approach are: (1) following the formulation proposed by Salim *et al.* [21], obtain the solution for the plate stiffened by exterior stringers only (see Fig. 10b); (2) obtain the solution for an interior rib (stringer) subjected to the interaction forces $R(x,r)$ (Fig. 10c); (3) as the solutions of the previous steps have the interaction forces $R(x,r)$ as the only unknown, determine $R(x,r)$ by satisfying the compatibility conditions for the deflection of the plate along the interior ribs; and (4) once the deflection functions are

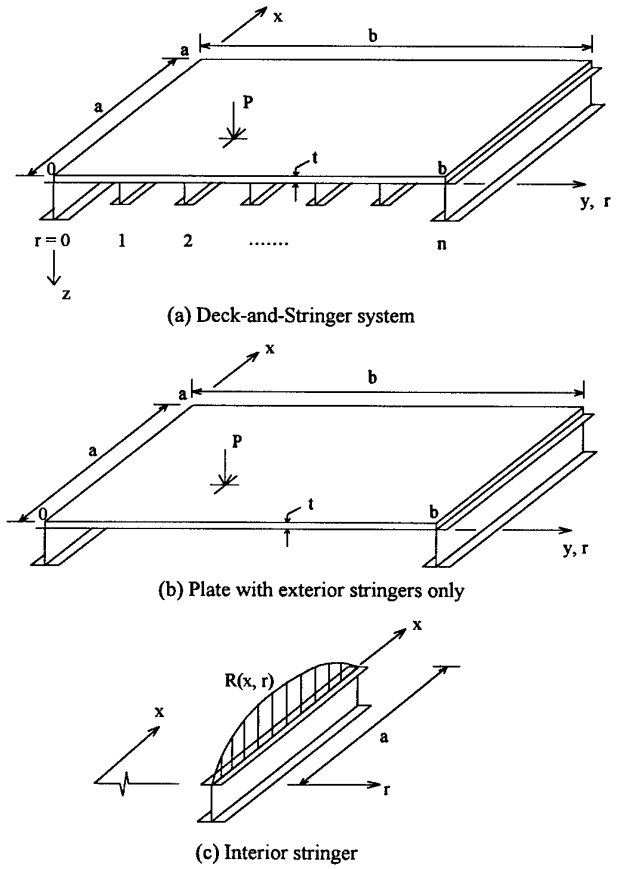

Fig. 10. SDMF flexural analysis model.

obtained for the plate and for the stringers, obtain moments for an isolated deck-and-stringer 'composite' beam section. Following these steps, the macro-flexibility solution for symmetric load case is derived. The solution for a stiffened plate is developed first, followed by the solution for an interior stringer.

Solution for a plate stiffened by edge beams

A Fourier polynomial series is employed in this approach to obtain the solutions for the plate equation. The solutions for w_0, ψ_x and ψ_y for a symmetric loading are

$$w_0(x,y)=\sum_{i,j=1}^{\infty} W_{ij}\sin(\alpha x)(\cos(\beta y)+W_0)$$

$$\psi_x(x,y)=\sum_{i,j=1}^{\infty} X_{ij}\cos(\alpha x)(\sin(\beta y)+X_0)$$

$$\psi_y(x,y)=\sum_{i,j=1}^{\infty} Y_{ij}\sin(\alpha x)\cos(\beta y) \tag{4}$$

where $\alpha = i\pi/a$ and $\beta = j\pi/b$, W_0 and X_0 are edge deflection coefficients, and W_{ij}, X_{ij} and Y_{ij} are the coefficients to be determined to complete the solution. By applying orthogonality conditions [21] we obtain, for any given i and j, the following equations

$$\begin{bmatrix} K_{11} & K_{12} & K_{13} \\ K_{21} & K_{22} & K_{23} \\ K_{13} & K_{23} & K_{33} \end{bmatrix} \begin{Bmatrix} W_{ij} \\ X_{ij} \\ Y_{ij} \end{Bmatrix} = \begin{Bmatrix} -Q_{ij} \\ 0 \\ 0 \end{Bmatrix} \tag{5}$$

where Q_{ij} is the load parameter and K_{ij} are the coefficients

$$K_{11}=\alpha^2 A_{55}+\beta^2 A_{44}+\frac{4\alpha^2}{\beta b}A_{55}W_0K_{12}$$

$$=\alpha A_{55}+\frac{4\alpha}{\beta b}A_{55}X_0K_{13}$$

$$=\beta A_{44}K_{21}=\alpha A_{55}+\frac{4\alpha}{\beta b}A_{55}W_0K_{23}$$

$$=\alpha\beta(D_{12}+D_{66})K_{33}$$

$$=\alpha^2 D_{66}+\beta^2 D_{22}+A_{44}K_{22}$$

$$=\alpha^2 D_{11}+\beta^2 D_{66}+A_{55}+\frac{4\alpha^2}{\beta b}D_{11}X_0+\frac{4}{\beta b}A_{55}X_0$$

The stiffness coefficients A_{ij} and D_{ij} relate stress resultants and strains and curvatures. The constants W_0 and X_0 are obtained by satisfying the boundary conditions of the orthotropic plate, and are given as

$$W_0=\frac{A_{44}}{\alpha^4}\left(\frac{\alpha^2}{\kappa F}+\frac{1}{D}\right)\left(\frac{Y_{ij}}{W_{ij}}+\beta\right)$$

and

$$X_0=-\frac{A_{44}}{\alpha^3 D}\left(\frac{Y_{ij}+\beta W_{ij}}{X_{ij}}\right) \tag{6}$$

where κ, F and D are, respectively, the shear correction factor, shear stiffness and bending stiffness of the exterior stringer (beam). At this stage all the constants have been determined to allow us to completely define the deflection and moments at any point in the plate of Fig. 10b for any type of loading.

Solution for an interior stringer

The effect of the interior stringers is now added in order to evaluate the deflection function and moments of any interior stringer. For any interior stringer at any location r ($r = 0, 1, 2, \ldots n$), the governing differential equations are [20]

$$\frac{\partial}{\partial x}\left[\kappa F\left(\psi^{\mathrm{R}}(x,r)+\frac{\partial w^{\mathrm{R}}(x,r)}{\partial x}\right)\right]=R(x,r) \tag{7}$$

$$D\frac{\partial^2\psi^{\mathrm{R}}(x,r)}{\partial x^2}-\kappa F\left(\psi^{\mathrm{R}}(x,r)+\frac{\partial w^{\mathrm{R}}(x,r)}{\partial x}\right)=0 \tag{8}$$

where $w^{\mathrm{R}}(x,r)$ is the generalized deflection function for any interior rib (stringer), $\psi^{\mathrm{R}}(x,r)$ is the generalized rotation of any interior rib and $R(x,r)$ is the generalized interaction force at the rib line (Fig. 10c).

The generalized deflection function of any interior stringer is defined for any symmetric loading as

$$w^{R}(x,r) = R_{11}\left(\frac{a}{\pi}\right)^{4}\left(\frac{\alpha^2}{\kappa F}+\frac{1}{D}\right) \times \sin\frac{\pi x}{a}\left[\sin\frac{\pi r}{n}+W_0\right] \quad (9)$$

where

$$R_{11} = \frac{Q_{11}}{\left(\frac{a}{\pi}\right)^{4}\left(\frac{1}{\kappa F}+\frac{1}{\alpha^2 D}\right)\frac{Q_{11}}{W_{11}}+\frac{n}{b}\left(1+\frac{4W_0}{\pi}\right)} \quad (10)$$

Wheel-load distribution factor

The macro-flexibility solution is used to define a wheel-load distribution factor for any of the stringers. The basic steps in the formulation are: (1) to obtain the edge deflection coefficients W_0 and X_0 from eqn (6); and (2) to compute the distribution factor for any ith interior stringer as the ratio of the interaction forces, $R(x,r)$, for the ith stringer to the sum of interaction forces for all stringers. The wheel-load distribution factor under symmetric loading is given as

$$W_{f}^{sym}(r) = \frac{W_0+\sin\frac{\pi r}{n}}{(n+1)W_0+\frac{2}{\pi}n} \quad (11)$$

where n is the number of stringer spacings. The maximum wheel-load factor under symmetric loading becomes

$$(W_{f}^{sym})_{max} = \frac{1+W_0}{(n+1)W_0+\frac{2}{\pi}n} \quad (12)$$

Design methodology for FRP composite bridges

For the design of FRP composite deck-and-stringer bridges, the one-term SDMF solution is used to define a wheel-load distribution factor which reduces the design of the bridge to the design of a single deck-and-stringer 'composite' beam section. The stiffness coefficients of the unit-cell beams that compose the bridge deck are used to evaluate the deck stiffness coefficients of eqn (5). For example, D_{11} is obtained from the bending stiffness D of a single box beam [3]. The coefficient D_{22} is the bending stiffness of a unit width of the deck in the transverse direction, and is obtained experimentally. The value of D_{66} is considered as the in-plane torsional stiffness of an individual box beam which can be obtained both analytically and experimentally [22]. The stiffness coefficients of the stringers, D and κF, can also be obtained both analytically and experimentally [3].

Once all the stiffness coefficients of the deck and the stringers are defined, either analytically or experimentally, the edge coefficients (W_0 and X_0) are computed from eqn (6) and are used to compute the maximum wheel-load distribution factor from eqn (12). Then, an isolated deck-and-stringer 'composite' beam section of span L is loaded at the center by an equivalent concentrated load, P_e, which produces a maximum moment, M_A, equal to the maximum AASHTO [2] lane moment for a given truck loading (e.g. HS-20 or HS-25)

$$P_e = M_A\left(\frac{4}{L}\right) \quad (13)$$

This load P_e is then modified by a maximum wheel-load distribution, $(W_f)_{max}$, and the number of lanes, N_L, to produce the design concentrated load, P_d

$$P_d = P_e N_L (W_f)_{max} \quad (14)$$

which induces a corresponding design moment, M_d. The maximum live load moment, M_{LL}, and deflection, δ_{LL}, including impact, for an interior stringer are computed from

$$M_{LL} = \frac{P_d L}{4}(1+\mathrm{DLA}) \quad (15)$$

$$\delta_{LL} = P_d\left(\frac{L^3}{48D} + \frac{L}{4\kappa F}\right)(1+DLA) \qquad (16)$$

where DLA is the dynamic load allowance, not yet defined for FRP bridges but can be assumed to be similar to those suggested for timber bridges [21].

Experimental investigation of an FRP bridge deck

Under this research effort a $3.0 \times 3.0 \times 0.2$ m (10×10 ft $\times$ 8 in.) deck is fabricated by bonding box beams of $101.6 \times 203.2 \times 6.35$ mm ($4 \times 8 \times 1/4$ in.) (Fig. 2) produced by pultrusion (Creative Pultrusions Inc., Alum Bank, PA, USA). Single- and double-cell box beams were tested in bending under three- and 4-point loadings to assess their bending and shear stiffnesses (Fig. 8a). The box beams were also tested in torsion to obtain their in-plane shear stiffness using the applied torque and relative angle of twist measurements (Fig. 8c). A $0.3 \times 0.2 \times 2.0$ m ($12 \times 8 \times 80$ in.) transverse beam was built by bonding 20 0.3 m (1.0 ft) box sections together (Fig. 8b). The transverse beam was tested under three- and four-point bending for various spans to obtain the bending and shear stiffnesses in the transverse direction of the deck. The experimental–analytical stiffnesses to be used in the analysis of a deck-and-stringer system are given in Table 2. As F_x is relatively small, it can be ignored in design.

Design application

To illustrate the design procedure, a single-lane short-span bridge of 4.5 m (15 ft) width and 7.5 m (25 ft) span is designed using the $101.6 \times 203.2 \times 6.35$ mm ($4 \times 8 \times 1/4$ in.) box sections (Fig. 2) for the deck assembly and FRP winged-box beams of 304.8×609.6 mm (12×24 in.) (Fig. 7) for the stringers. The required material properties [19] for the stringers are: $D = 2.903 \times 10^7$ kN-m^4/m^2 (1.248×10^{10} kip-in.^{4}/in.^{2}); and $F = 8.73 \times 10^7$ kN-m^2/m^2 (1.940×10^7 kip-in.^{2}/in.^{2}). A deflection limit of $L/500$ is used. The loading considered is AASHTO HS-20 [2], and the stringer spacing is used as the design variable.

Table 2. Stiffnesses of the FRP deck

Stiffness	Experimental	Analytical
D_y (kN-m^4/m^2)	627.571	525.957
F_y (kN-m^2/m^2)	14949.0	16555.5
D_x (kN-m^4/m^2)	15.949	—
F_x (kN-m^2/m^2)	69.3	—
H_{xy} (kN-m^4/m^2)	2.838	2.742

The edge deflection coefficient is evaluated from eqn (6) as $W_0 = 0.270$, and the deflection limit from eqns (12), (14) and (16) is written as a function of the number of stringers $(n+1)$

$$\delta_{LL} = \frac{L}{500} = M_A\left(\frac{4}{L}\right)N_L\left(\frac{1+W_0}{(n+1)W_0 + \frac{2}{\pi}n}\right)\left(\frac{L^3}{48D} + \frac{L}{4\kappa F}\right)(1+DLA) \qquad (17)$$

The DLA factor is taken as 0.20, which is recommended for timber bridges [23]. From AASHTO [2] $M_A = 279.99$ kN-m (207.4 kip-ft). In this case $N_L = 1.0$, and κ is taken as 1.0. Solving for the number of stinger spacing we get $n = 4.25$ and, therefore, we use $n = 5$, which corresponds to 0.9 m (36 in.) center-to-center spacing of the stringers, and a total of six longitudinal stringers should therefore be used.

We can now go back and evaluate P_d from eqn (14) and, subsequently, we compute the maximum moment from eqn (15) as $M_{LL} = 90.263$ kN-m (789.7 kip-in.) and, based on this value, the maximum stress in the stringer becomes $\sigma_{max} = 18.865$ MPa (2.734 ksi), which is below the allowable value.

Other considerations

The local deflection, stresses, punching shear and local buckling in a deck section between two adjacent stringers need to be investigated. Equally important is the connection between the deck and the stringers, and also the side-by-side connection of the FRP cells, which may need to be designed with a locking mechanism to properly transfer shear.

Summary

In this section we presented a one-term macro-flexibility series solution, including transverse shear deformations, for the approximate analysis of orthotropic, simply supported, stiffened

plates. The formulation is applied to FRP decks, and is used to define a wheel-load distribution factor. The wheel-load distribution factor is used to define design equations for FRP decks on stringers, and the analysis of the superstructure is reduced to the design of a beam. The present formulation can be extended to include asymmetric loading [21,22]. Based on partial experimental results, an illustrative example for a short-span FRP bridge is presented. To validate the present model, experimental and finite-element studies are being conducted and results will be presented at a later date.

CONCLUSIONS

In this paper, a new design concept for short-span FRP composite bridges is presented. FRP sections are bonded to construct a cellular FRP bridge deck, and optimized FRP winged-box (WB) beams are considered as the bridge stringers. An overview of the analysis, design optimization and experimental verification of the FRP beam components is given, and the present analytical tools for FRP beams can be used to propose efficient engineering design equations. Based on the present first-order SDMF orthotropic plate solution, a simplified design analysis procedure is proposed, and it can be used for the analysis and design optimization of various case studies of FRP deck-and-stringer bridges. Partial experimental results validate the proposed analytical models. The experimental and analytical results presented in this study can assist in the development of efficient FRP sections and simplified design equations for new and replacement highway bridge decks.

REFERENCES

1. Aref, A. and Parsons, I. D., Design and analysis procedures for a novel fiber reinforced plastic bridge deck. In *Advanced Composite Materials in Bridges and Structures*. CSCE, Montreal, 1996, pp. 743–50.
2. *Standard Specifications for Highway Bridges*. American Association of State Highway and Transportation Officials (AASHTO), Washington, DC, 1989.
3. Davalos, J. F., Salim, H. A., Qiao, P., Lopez-Anido, R. and Barbero, E. J., Analysis and design of pultruded FRP shapes under bending. *Composites, Part B: Engng J.*, 1996, **27**, (3/4), 295–305.
4. Luciano, R. and Barbero, E. J., Formulas for the stiffness of composites with periodic microstructure. *Int. J. Solids Struct.*, 1994, **31**, 2933–2944.
5. Jones, R. M. *Mechanics of Composite Materials*. Hemisphere, New York, 1975.
6. Salim, H.A., Davalos, J.F., Qiao, P. and Barbero, E.J., Experimental and analytical evaluation of laminated composite box beams. *Proc. 40th Int. SAMPE Symposium*, 1995, **40**, 532–539.
7. Davalos, J. F., Qiao, P., and Salim, H. A., Characterization of pultruded FRP wide-flange beams. In *4th ASCE Materials Engineering Conference*, Washington, DC, 1996, pp. 223–32.
8. Barbero, E. J., Lopez-Anido, R. and Davalos, J. F., On the mechanics of thin-walled laminated composite beams. *J. Composite Mater.* , 1993, **27**, (8), 806–829.
9. Davalos, J. F., Qiao, P., and Salim, H. A., An engineering approach for design of FRP beams. In *ASCE Structural Congress*, Portland, OR, 1997, pp. 1479–83.
10. Qiao, P. and Davalos, J. F., Local buckling of composite FRP shapes by discrete plate analysis. *Composites, Part B: Engineering J.*, submitted (1997).
11. Davalos, J. F. and Qiao, P., Analytical and experimental study of lateral and distortional buckling of FRP I-beams. *ASCE J. Composites Construct.*, **2**, (4) (in press).
12. Davalos, J. F. and Qiao, P. and Barbero E. J., Multiobjective material architecture optimization of pultruded FRP I-beams. *Composites Construct.*, 1996, **35**, 271–281.
13. Qiao, P., Davalos, J. F. and Barbero, E. J., *FRPBEAM: A Computer Program for Analysis and Design of FRP Beams*. CFC-94-191, Constructed Facilities Center, West Virginia University, Morgantown, WV, 1994.
14. Qiao, P. Analysis and design optimization of fiber-reinforced plastic (FRP) structural beams. Ph.D. dissertation, Department of Civil and Environmental Engineering, West Virginia University, Morgantown, WV, 1997.
15. Salim, H. A. and Davalos, J. F., Shear lag analysis in composite box beams. In *Proc. 1st Int. Conf. on Composites in Infrastructure*, University of Arizona Press, Tucson, AZ, 1996, pp. 628–37.
16. Davalos, J. F., Salim, H. A. and Qiao, P., Shear lag in wide-flange FRP composite shapes. In *Proc. 3rd Int. Conf. on Composites Engineering (ICCE/3)*, University of New Orleans Press, New Orleans, LA, ed. D. Hui, 1996.
17. Qiao, P., Davalos, J. F. and Barbero, E. J., Optimal design of pultruded FRP shapes for structural applications. In *Proc. 1st Int. Conf. on Composites in Infrastructure*, University of Arizona Press, Tucson, AZ, 1996, pp. 676–88.
18. Davalos, J. F., Qiao, P. and Salim, H. A., A practical design and optimization method for structural composite beams. In *Proc. Composites Institute's 51st Conference and EXP. '96*. SPI, Cincinnati, OH, 1996, pp. (24-D) 1–8. (Best Design Paper Award.)
19. Qiao, P., Davalos, J. F., and Barbero, E. J., Design optimization of fiber reinforced plastic composite shapes. *J. Composite Mater.*, **31**, (19) in press.
20. Reddy, J. N., *Energy and Variational Methods in Applied Mechanics*. John Wiley, New York, 1984.
21. Salim, H. A., Davalos, J. F., GangaRao, H. V. S. and Raju, P., An approximate series solution for design of deck-and-stringer bridges. *Int. J. Engng Anal. Design*, 1995, **2**, 15–31.

22. Salim, H. A., Modeling and application of thin-walled composite beams in bending and torsion. Ph.D. dissertation, Department of Civil and Environmental Engineering, West Virginia University, Morgantown, WV, 1996.

23. Davalos, J. F., Salim, H. A. and Dickson, B. W., Development and field testing of the Camp Arrowhead modular stress-laminated T-system timber bridge. Transportation Research Record 1426, TRB, NRC, Washington, DC, 1993, pp. 44–9.

ELSEVIER

Composite Structures Vol. 38, No. 1–4, pp. 309–319, 1997
© 1997 Elsevier Science Ltd. All rights reserved
Printed in Great Britain
0263-8223/97/$17.00 + 0.00

PII:S0263-8223(97)00065-2

Manufacture of one-piece automotive drive shafts with aluminum and composite materials

Durk Hyun Cho, Dai Gil Lee

Department of Mechanical Engineering, Korea Advanced Institute of Science and Technology, Gusong-dong, Yusong-gu, Taejon-shi, Korea 305-701

&

Jin Ho Choi

Department of Mechanical Design Engineering, Gyeong Sang National University, Chinju-shi, Gyeongnam, Korea 660-701

The natural bending frequency of a torque transmission shaft can be increased without reducing the torque transmission capability if the shaft is made using both carbon fiber composite and aluminum: the former increases the natural bending frequency and the latter sustains the applied torque. The high natural bending frequency of a shaft makes it possible to manufacture the drive shaft of passenger cars in one piece.

In this work, a hybrid one-piece drive shaft composed of carbon fiber–epoxy composite and aluminum tube was manufactured by co-curing the carbon fiber on the aluminum tube.

The fabricational thermal residual stresses due to the coefficient difference of thermal expansions of aluminum and carbon fiber composite were eliminated by applying a compressive preload to the aluminum tube before the co-curing operation.

From the dynamic tests, it was found that the first natural bending frequency and the minimum static torque transmission capability of the hybrid shaft were 9000 rpm and 3550 Nm, respectively, and the shaft did not fail until 10^7 cycles under a dynamic load of ± 500 Nm. © 1997 Elsevier Science Ltd.

INTRODUCTION

An automotive drive shaft, or propeller shaft, as shown in Fig. 1 transmits power from the engine to the differential gears of rear wheel-drive vehicles. The torque transmission capability of the drive shaft for passenger cars, small trucks and vans should be larger than 3500 Nm and the fundamental natural bending frequency of the drive shaft should be higher than 6500 rpm to avoid whirling vibration [1]. The whirling of the drive shaft which is a resonance vibration occurs when the rotational speed is equal to the fundamental natural bending frequency, which is inversely proportional to the square of the shaft length and proportional to the square root of specific stiffness.

Since the fundamental natural bending frequency of one-piece drive shafts made of steel or aluminum cannot be higher than 6500 rpm when the length of the drive shaft is longer than 1.0 m, the steel drive shaft is usually manufactured in two pieces. However, the two-piece steel drive shaft has a complex and heavy structure and produces noise and vibrations that are transmitted to the vehicle through a center bearing.

The fundamental natural frequency of the carbon fiber composite drive shaft can be twice as high as that of steel or aluminum because the

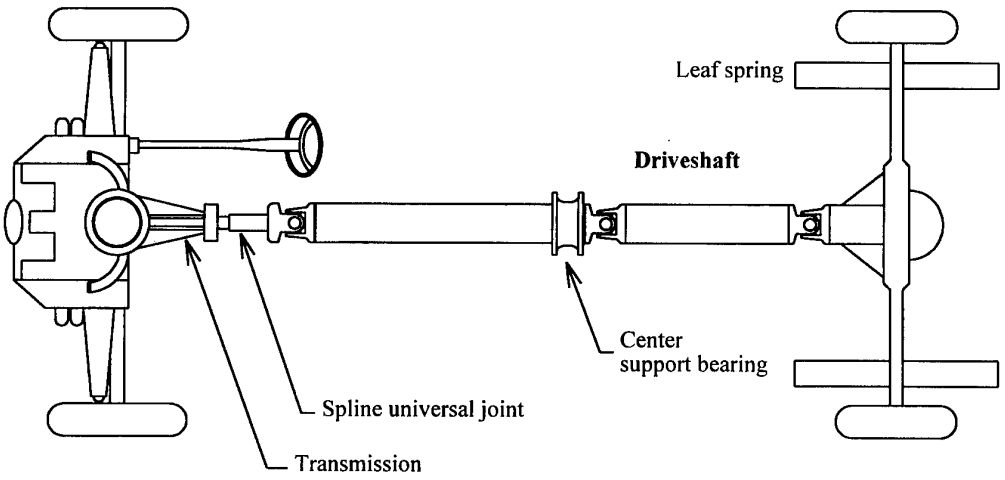

Fig. 1. Schematic diagram of the drive shaft for a rear wheel driving vehicle.

carbon fiber composite material has more than 4 times the specific stiffness than steel or aluminum [2], which makes it possible to manufacture the drive shaft of passenger cars in one piece [3].

The composite drive shaft has many other benefits such as reduced weight and less noise and vibration. However, the composite drive shaft requires reliable joining of the composite shaft to the steel or aluminum yoke of a universal joint [4,5], which is often the most difficult task.

The first composite drive shaft was developed by the Spicer U-Joint Division of Dana Corporation for the Ford econoline van models in 1985. The General Motors pickup trucks which adopted the Spicer product enjoyed a demand three times that of projected sales in its first year (1988) [1]. Until now, three different manufacturing methods for the composite drive shaft were developed: Dana–MMFG, Hercules and Ciba–Geigy methods. Figure 2 shows the representative manufacturing methods for the composite drive shaft. In the Hercules and Ciba–Geigy designs, the filament wound carbon/glass–epoxy composite tube was assembled to steel yokes with a blind fastener or a compression ring with adhesive. In Dana–MMFG manufacturing method, glass fibers were filament-wound in the hoop direction on an aluminum tube and 0° carbon fibers were coated by pultrusion. Forged aluminum yokes were beam welded to the aluminum tube. For the Dana–MMFG method, there is a high tendency that the thermal residual stresses would be produced in the aluminum tube and composites.

Although the co-curing of composite to metal reduces process times, only a few related studies on the co-cure joining for composite structures are available. In damping enhancement of aerospace and military structures subjected to dynamic loading, however, there are several attempts to co-cure join one or more layers of high damping visco-elastic material to the structures [6,7].

In this work, the drive shaft was hybridly manufactured using both carbon fiber–epoxy

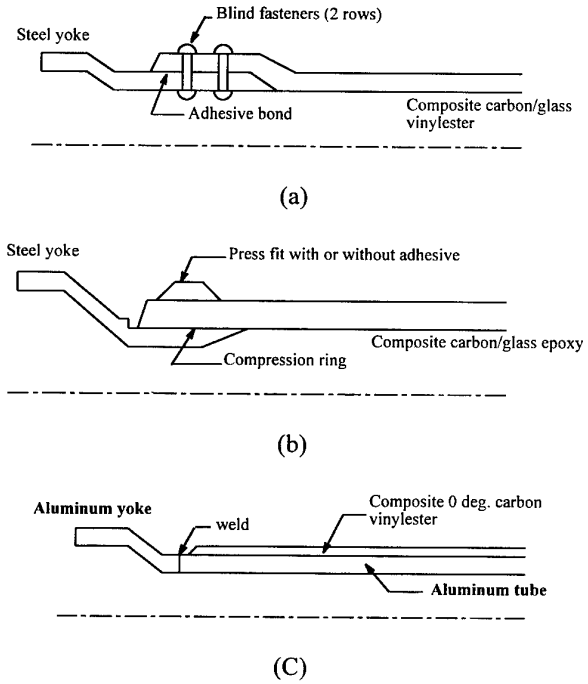

Fig. 2. Joining methods between the composite drive shafts and yokes: (a) Hercules design (b) Ciba–Geigy design (c) Dana–MMFG design.

composite and aluminum, in which the carbon fiber–epoxy composite increases the natural bending frequency and the aluminum sustains the required torque transmission capability. This method eliminates the joining problem between composite and metal because the yoke of a universal joint can be welded to the aluminum shaft or joined using a serration. Also, a preload was given to the aluminum shaft before co-curing the composite to the aluminum shaft to reduce the thermal residual stresses. The static torque transmission capability, natural frequency and damping of the manufactured hybrid drive shaft were tested. Also, a whirling test of the drive shaft was performed.

DESIGN OF THE HYBRID DRIVE SHAFT

The one-piece hybrid drive shaft was designed using both aluminum and carbon fiber–epoxy composite in which the major role of the aluminum was to transmit the required torque while the role of the carbon fiber epoxy composite material was to increase the natural bending frequency. For the drive shafts of passenger cars, small vans and trucks, the minimum value of the torque transmission capability and the natural bending frequency are 3500 Nm and 6500 rpm, respectively. Taking into account these requirements, the dimensions of the aluminum tube and the number of stacking plies of the composite were calculated. Since the outer diameter of the drive shaft was limited to 80 mm for passenger cars, the outer and inner diameters of the aluminum shaft were determined to be 74 and 70 mm, respectively. One ply of glass fiber epoxy fabric was firstly laid-up on the aluminum tube to eliminate galvanic corrosion between aluminum and carbon fiber and eight plies of carbon fiber epoxy prepregs with a stacking sequence of $[\pm 5]_{4T}$ from the shaft axis were laid-up on the glass epoxy fabric. The carbon fiber–epoxy prepreg was USN150 manufactured by Sunkyung Industry (Suwon, Korea), whose properties were similar to T300/5208. Table 1 and Table 2 show the mechanical properties of carbon fiber epoxy composites and the aluminum tube (6061-T6).

For the high natural bending frequency of the shaft, the stacking angle of the fiber from the shaft axis should be small. In this work, the stacking sequence of $[\pm 5]_{4T}$ was employed because the transverse tensile strength of the composite with the stacking sequence of $[0]_{8T}$ was too low. Table 3 shows the laminate properties calculated by the classical lamination theory [8] using the unidirectional properties of

Table 1. Properties of the unidirectional carbon fiber–epoxy composite (USN 150)

E_L	131.6 GPa
E_T	8.20 GPa
G_{LT}	6.12 GPa
v_{LT}	0.281
ρ	1560 kg/m^3
X_t	2000 MPa
X_c	100 MPa
Y_t	60.9 MPa
Y_c	130 MPa
S	74.8 MPa
α_L	-0.9 μs/°C
α_T	27 μs/°C
Thickness of ply	0.15 mm

Table 2. Properties of the aluminum tube (6061-T6)

E	72 GPa
G	27 GPa
α_T	23.0 μs/°C
ρ	2695 kg/m^3
Tensile strength	350 MPa
Yielding strength	325 MPa
Shear strength	210 MPa

Table 3. Laminated properties of the carbon fiber–epoxy prepreg

Stacking angle	$[\pm 5]_{4T}$
E_1	129.30 GPa
E_2	8.30 GPa
G_{12}	6.96 GPa
α_1	-1.06 μs/°C
α_2	26.57 μs/°C

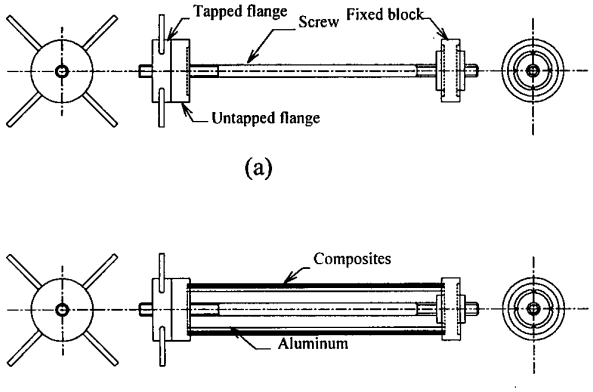

Fig. 3. The compressive jig. (a) Schematic diagram of the compressive jig. (b) Hybrid drive shaft compressed by the jig.

the carbon fiber–epoxy prepreg. The torque transmission capability of the hybrid drive shaft was calculated by the following equations.

$$T = T_{al} + T_{co} \tag{1}$$

$$T_{al} = \frac{G_{al} \cdot J_{al}}{G_{al} \cdot J_{al} + G_{co} \cdot J_{co}} T \tag{2}$$

$$\frac{\tau_y \cdot J_{al}}{r_o} = T_{al} \tag{3}$$

where, T, T_{al} and T_{co} are the torque transmission capabilities of the hybrid shaft, the aluminum shaft, and the composite shaft, respectively, G shear modulus, J second moment of inertia, τ_y the shear strength of aluminum and r_o the outer radius of the aluminum shaft. When the thickness of the carbon fiber–epoxy composite was 1.2 mm and the outer and inner diameters of the aluminum shaft were 74 and 70 mm, respectively, the calculated torque capability was 3770 Nm, which was larger than 3500 Nm.

The first natural bending frequency ω of the hybrid drive shaft was calculated by the follow-

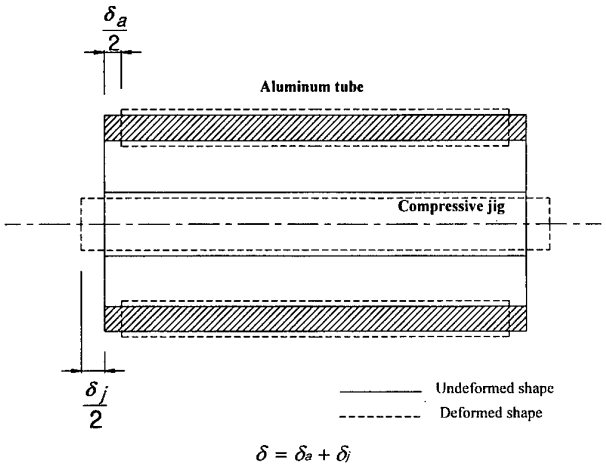

Fig. 4. Total compressive displacements (δ) of a jig composed of δ_a and δ_j.

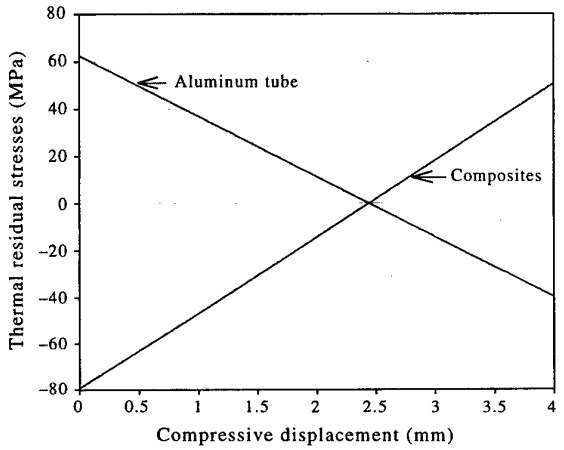

Fig. 5. Compressive displacement vs. thermal residual stresses in the co-cured drive shaft.

Table 4. Stresses in the four steps of co-curing with the stacking angle $[\pm 5]_{4T}$ of the composite

Step	Temperature	σ_a (MPa)	σ_c (MPa)	σ_j (MPa)
1	20°C	−106.66	—	68.26
2	120°C	−173.21	—	130.38
3	20°C	−84.84	−152.39	112.95
Final	20°C	0.01	−0.02	—

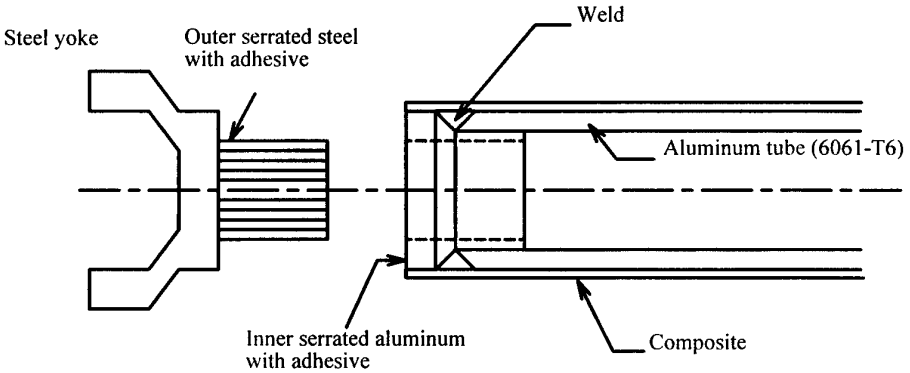

Fig. 6. Schematic diagram of the joining method with serrations.

ing equations with simply supported boundary conditions

$$\bar{\omega} = \frac{9.869}{l^2}\sqrt{\frac{E_{al}\cdot I_{al}+E_{co}\cdot I_{co}}{\rho_{al}+\rho_{co}}} \text{ (rad/s)} \qquad (4)$$

where, l is the length of the shaft, E Young's modulus, I mass moment of inertia and ρ mass per unit length. When the length of the shaft was 1.35 m, the calculated fundamental natural bending frequency of the shaft was 9055 rpm.

METHOD OF ELIMINATING THE FABRICATIONAL THERMAL RESIDUAL STRESSES

The residual thermal stresses are induced at the interface between the composites and the aluminum of the hybrid drive shaft during co-curing operation due to the large difference of coefficient of thermal expansion. The aluminum tube expands as the temperature rises until the curing temperature of 120°C without constraint by composites. After co-curing composites to the aluminum tube, the hybrid drive shaft was cooled down to the room temperature of 20°C. Since the coefficient of thermal expansion of the composite shaft in the axial direction is near zero when the stacking angle of the composite is less than 15° from the axis of the shaft, the tensile stress in the axial direction occurs in the aluminum shaft and the axial compressive stress occurs in the carbon fiber composite when the shaft is cooled down.

When the stacking angle of composites was $[\pm 5]_{4T}$, the calculated residual thermal stresses, by the method of solid mechanics in the aluminum tube and the composite, were 62.46 MPa and −79.42 MPa, respectively. The residual thermal stresses were calculated on the assumption that the radial and hoop stress components in the co-cured shaft were not produced because the difference of the CTEs of the two materials in the radial and hoop directions was small. However, the large shear stress in the axial direction occurs at the interface of the two materials due to the large difference of the CTEs of the two materials. This large shear stress at the interface of the hybrid shaft lowers the torque transmission capability of the co-

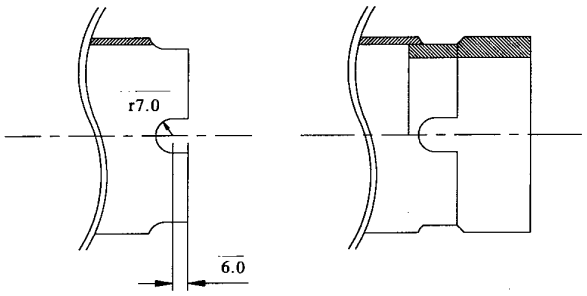

Fig. 7. Configurations of the end part of the aluminum tube with four slots.

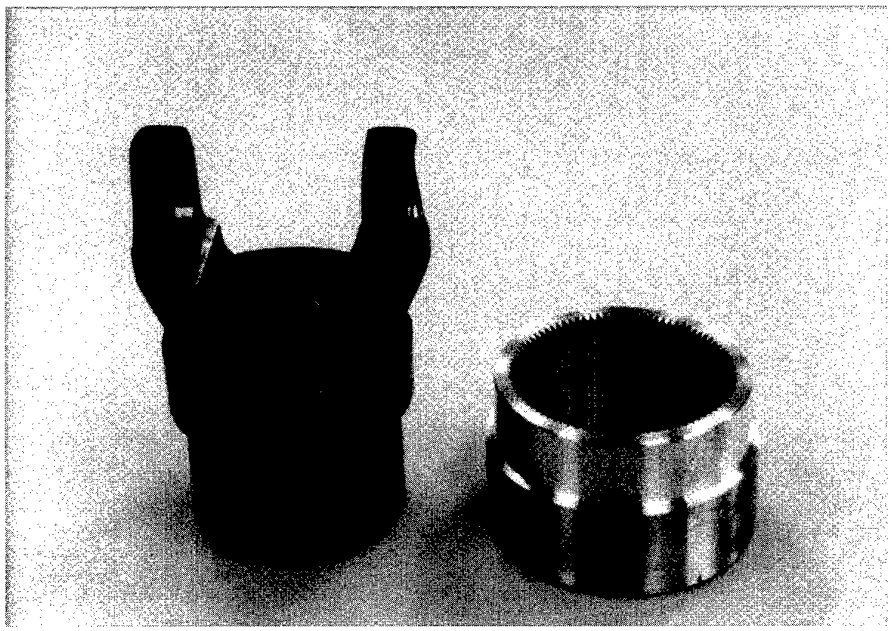

Fig. 8. Photograph of the inner serration and the outer serration.

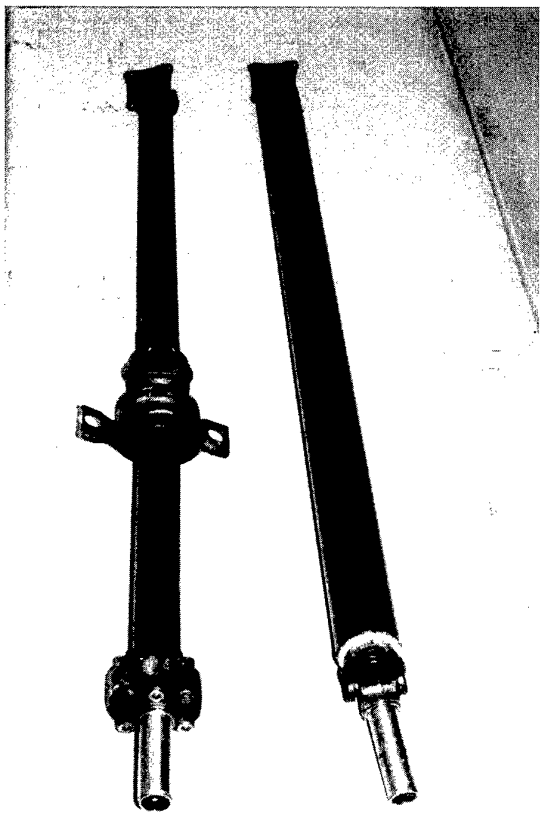

Fig. 9. Photograph of the two-piece steel drive shaft and the one-piece hybrid drive shaft manufactured.

cured hybrid drive shaft. In this work, to reduce the residual thermal stresses produced at the interface of the two materials of the hybrid shaft during the co-curing operation, a compressive preload was applied to the aluminum tube before the co-curing operation. To apply a compressive preload to the aluminum tube, a compressive jig similar to a vice was used. Figure 3 shows the compressive jig composed of a steel screw of 1 mm pitch thread, a fixed block, an untapped flange and a tapped flange with a thrust bearing.

The method for eliminating the residual thermal stresses in the hybrid drive shaft by applying a preload is described by the following four steps. In the first step, the carbon fiber–epoxy prepreg was laid-up on the surface of the preloaded aluminum tube. In the second step, the composite was co-cured on the surface of the preloaded aluminum tube. In the third step, the co-cured shaft was cooled down to the room temperature of 20°C without removing the preload in the aluminum tube. Both the composite and the aluminum tube were under compressive stress in the third step. In the fourth step, the preload by the compressive jig was removed, then the residual thermal stresses of the composite and the aluminum tube were eliminated.

The applied compressive displacement was calculated by the following method considering the axial stress component (σ_z). If the displace-

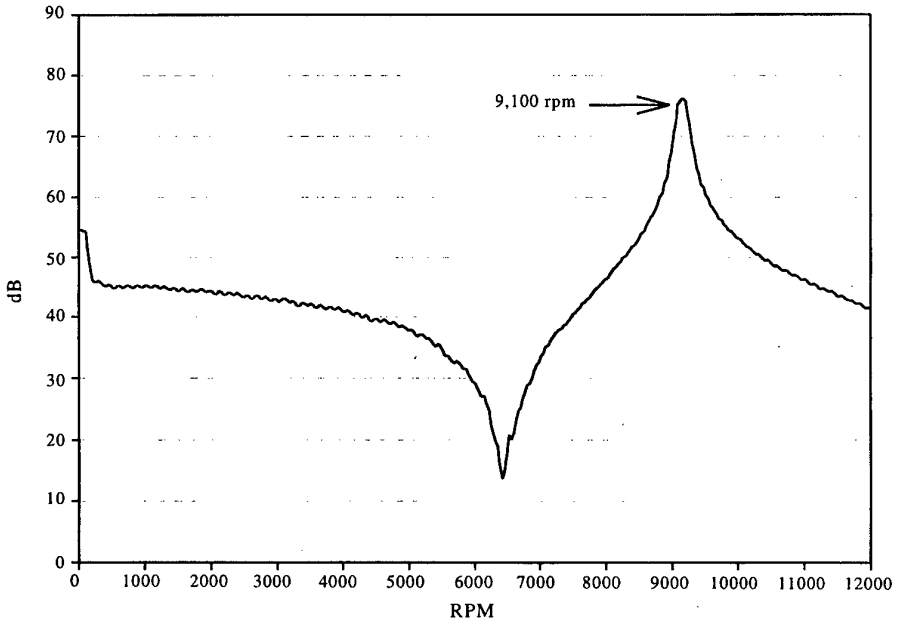

Fig. 10. Frequency response plot of the vibration of the hybrid drive shaft.

ments of the aluminum tube and the jig, both of length l, are δ_a and δ_j, respectively, then the total displacement δ produced by the rotation of the tapped flange in the compressive jig is $\delta = \delta_a + \delta_j$ as shown in Fig. 4. Therefore, the total displacement δ can be expressed as follows

$$\frac{\delta}{l} = \frac{\delta_j}{l} + \frac{\delta_a}{l} = \varepsilon_j - \varepsilon_a = \frac{\sigma_j}{E_j} - \frac{\sigma_a}{E_a} \tag{5}$$

where, ε_j and ε_a are the axial strains of the jig and the aluminum tube, respectively, and σ_j and σ_a the axial stresses of the jig and the aluminum tube, respectively, and E_j and E_a the Young's moduli of the jig and the aluminum tube, respectively.

From the force equilibrium between the aluminum tube and the jig, the following equation holds

$$A_a\sigma_a + A_j\sigma_j = 0 \tag{6}$$

where A_a and A_j are the areas of aluminum tube and the jig, respectively.

Using eqns (5) and (6), the tensile stress in the jig and the compressive stress in the aluminum tube in the first step can be calculated in terms of δ as follows

$$\sigma_j)_1 = \frac{E_jE_aA_a}{E_jA_j + E_aA_a}\,\frac{\delta}{l} \tag{7}$$

$$\sigma_a)_1 = -\frac{E_jE_aA_j}{E_jA_j + E_aA_a}\,\frac{\delta}{l} \tag{8}$$

In the second step, the jig and the aluminum tube expand the same amount due to the temperature increase ΔT. Then, the stress–strain–temperature relationship can be written as follows

$$\frac{\sigma_a}{E_a} + \alpha_a\Delta T = \frac{\sigma_j}{E_j} + \alpha_j\Delta T \tag{9}$$

Using eqns (6) and (9), the axial stresses in the jig and the aluminum tube in the second step can be calculated as follows

$$\sigma_j)_2 = (\alpha_a - \alpha_j)\Delta T\,\frac{E_jE_aA_a}{E_jE_j + E_aA_a} \tag{10}$$

$$\sigma_a)_2 = -(\alpha_a - \alpha_j)\Delta T\,\frac{E_jE_aA_j}{E_jE_j + E_aA_a} \tag{11}$$

In the third step, the jig, the aluminum tube and the composite are cooled down to the room temperature. Therefore, the force equilibrium among the three materials is

$$\sigma_aA_a + \sigma_jA_j + \sigma_cA_c = 0 \tag{12}$$

where σ_c and A_c are the axial stress and the area of the composite, respectively.

In the third step, the length changes of the three materials or strains are same

$$\frac{\sigma_a}{E_a} + \alpha_a\Delta T = \frac{\sigma_j}{E_j} + \alpha_j\Delta T = \frac{\sigma_c}{E_c} + \alpha_c\Delta T \tag{13}$$

From eqns (12) and (13), the axial stresses in the three materials were calculated as follows

$$\sigma_a)_3 = \left(\frac{E_aA_a\alpha_a + E_jA_j\alpha_j + E_cA_c\alpha_c}{E_aA_a + E_jA_j + E_cA_c} - \alpha_a\right)E_a\Delta T \tag{14}$$

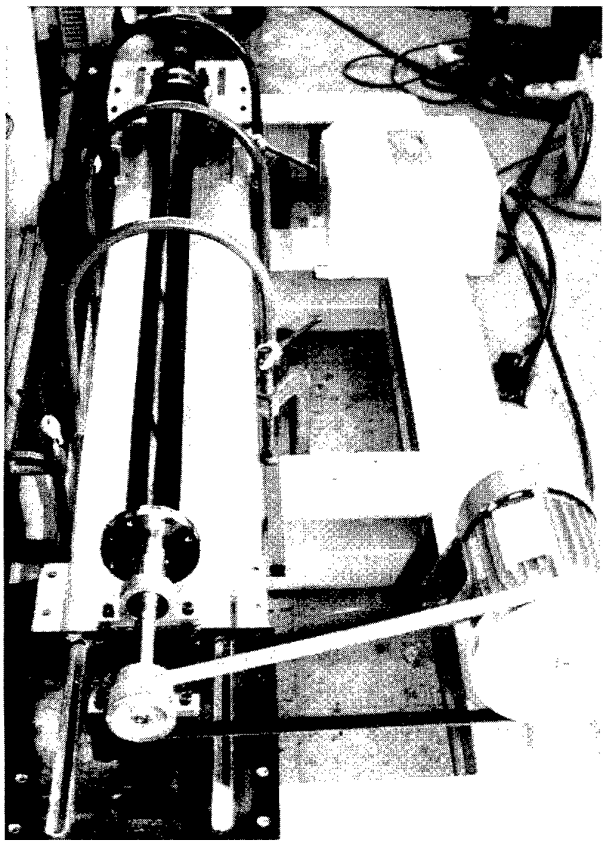

Fig. 11. Photograph which shows the whirling test of the one-piece hybrid drive shaft.

$$\sigma_j)_3 = \left(\frac{E_a A_a \alpha_a + E_j A_j \alpha_j + E_c A_c \alpha_c}{E_a A_a + E_j A_j + E_c A_c} - \alpha_j \right) E_j \Delta T \tag{15}$$

$$\sigma_c)_3 = \left(\frac{E_a A_a \alpha_a + E_j A_j \alpha_j + E_c A_c \alpha_c}{E_a A_a + E_j A_j + E_c A_c} - \alpha_c \right) E_c \Delta T \tag{16}$$

Finally in the fourth step, the preload by the compressive jig was released. When the jig was removed, it was assumed that the preload of the compressive jig was transferred to the composites and the aluminum tube. Therefore, in the fourth step the following equations hold

$$\sigma_j A_j = \sigma_a A_a + \sigma_c A_c \tag{17}$$

$$\frac{\sigma_a}{E_a} = \frac{\sigma_j}{E_j} \tag{18}$$

From eqns (17) and (18), the axial stresses were calculated as follows

$$\sigma_a)_4 = \frac{E_a}{E_a A_a + E_c A_c} A_j \cdot \sigma_j)_4 \tag{19}$$

$$\sigma_c)_4 = \frac{E_c}{E_a A_a + E_c A_c} A_j \cdot \sigma_j)_4 \tag{20}$$

where

$$\sigma_j)_4 = \sigma_j)_1 + \sigma_j)_2 + \sigma_j)_3 \tag{21}$$

Then the final stresses in the aluminum tube

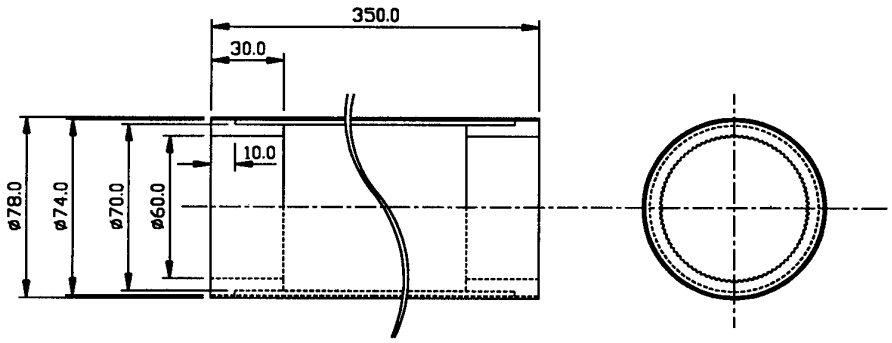

(a)

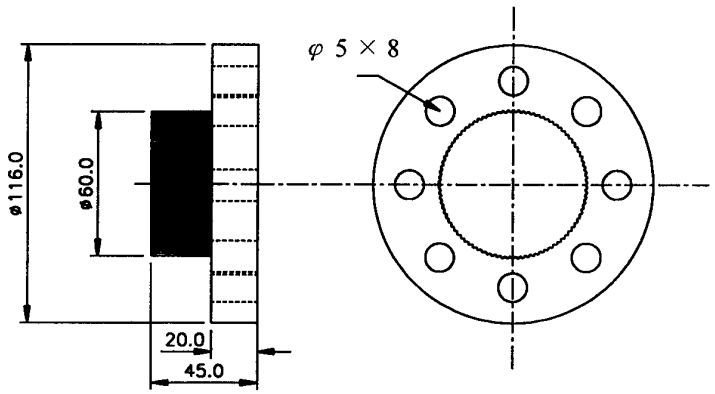

(b)

Fig. 12. Dimension of the static torque specimen. (a) Hybrid drive shaft. (b) Outer serrated adapter for the installation in the static torque tester.

Table 5. Torque transmission capabilities of the hybrid drive shafts

Specimen	Torque (Nm)
1	3600
2	3650
3	3550
4	3620

and composites are the sum of the stresses calculated in the previous steps

$$\sigma_a)_{\text{final}} = \sigma_a)_1 + \sigma_a)_2 + \sigma_a)_3 + \sigma_a)_4 \quad (22)$$

$$\sigma_c)_{\text{final}} = \sigma_c)_3 + \sigma_c)_4 \quad (23)$$

Using above equations, the residual thermal stress distributions when the stacking angle of composites was $[\pm 5]_{4T}$ was calculated with respect to the compressive displacement (δ) as shown in Fig. 5. The residual thermal stresses in the aluminum and the composite were almost zero when the compressive displacement δ of the jig was 2.445 mm, in which the compressive displacement δ_a of the aluminum tube was 2.0 mm and the tensile displacement δ_j of the jig was 0.445 mm. Table 4 shows the stresses and temperatures of each loading step. Table 4 shows the fabricational thermal stresses in the hybrid shaft when the compressive displacement of the aluminum tube was 2.0 mm. In Table 4, a very small tensile stress of 0.01 MPa in the aluminum tube and a very small compressive stress of -0.02 MPa in the composite were produced in the final stage.

MANUFACTURING

The hybrid drive shaft consists of the co-cured shaft and the two yokes. The inner-serrated aluminum bushes were welded at the both ends of the aluminum tube as shown in Fig. 6. To increase the weld strength, four slots in the aluminum tube along the circumference as shown in Fig. 7 were machined and welded. The steel yoke consists of the outer serrated part, a universal joint and a spline universal joint. Figure 8 shows a photograph of the inner and outer ser-

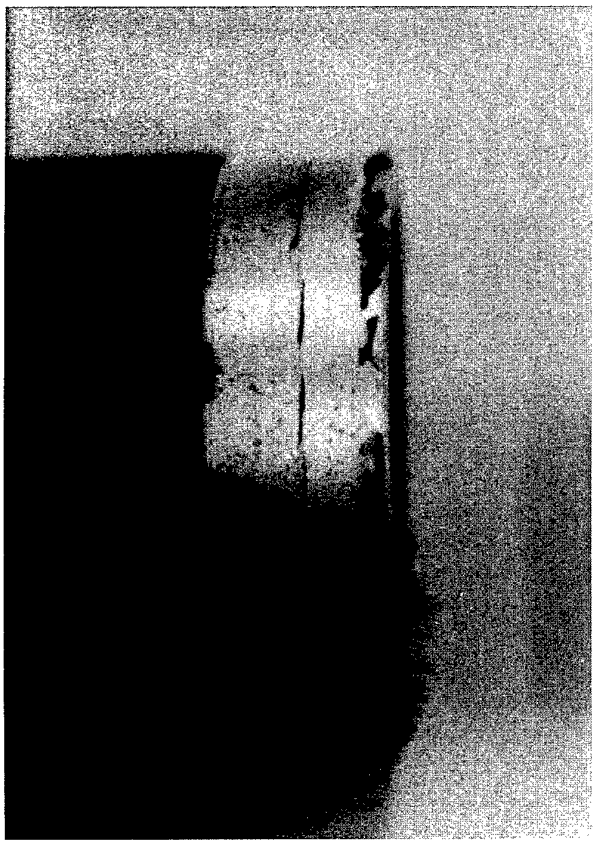

Fig. 13. Fractography of the hybrid drive shaft after static torque test.

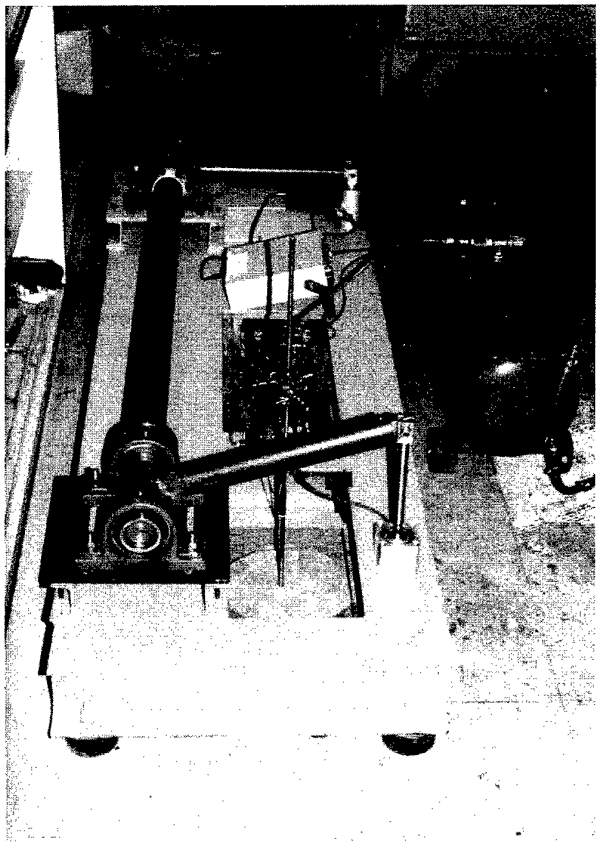

Fig. 14. Photograph which shows the fatigue test of the one-piece hybrid drive shaft.

rations with 90 teeth. The former serration was machined with a slotter and the latter was machined with a hobbing machine.

The hybrid drive shaft was manufactured by co-curing after wrapping one-ply glass fabric and eight ply carbon fiber–epoxy prepreg on the surface of a treated aluminum tube with the predetermined preload. The outer serration part of the universal joint was assembled with interference fit into the inner serration part of the hybrid drive shaft. Figure 9 shows a photograph of the existing two-piece steel drive shaft and the one-piece hybrid drive shaft manufactured. The hybrid drive shaft was 50% lighter than the steel drive shaft.

EXPERIMENTS

Whirling Test

The vibration characteristics of the hybrid drive shaft were measured by impulse–frequency response test using a fast Fourier transform analyzer (B&K 2023). Figure 10 shows the impulse–frequency responses of the hybrid drive shaft. The fundamental natural bending frequency was 9100 rpm and the error between the measured value and the calculated value (9055 rpm) was about 5.0%. The damping ratio was 0.01, which was about seven times larger than that of the steel drive shaft.

For the whirling test of the hybrid drive shaft, an apparatus shown in Fig. 11 was designed and manufactured. The whirling tester was composed of a three pole AC electric motor (220 V, 3.7 kW), a frequency converter for the control of motor velocity, bearing units (NSK P5) for high rotational speed and a jig for fixing the hybrid drive shaft. The rotational velocity of the hybrid drive shaft was controlled from 0 to 10000 rpm by the frequency converter and measured by a stroboscope. From the whirling test, it was observed that the resonance whirling vibration did not occur until 9000 rpm.

Static torque test

For the static torque test, the short length hybrid drive shafts rather than the full size drive shafts were used. Figure 12 shows the dimensions of the hybrid drive shaft and the outer serrated adapter for mounting on the static tester. The test specimens were manufactured by the same method for the full size hybrid drive shaft. The outer serrated adapter made of S45C steel was tight-fitted into the inner serrated aluminum bush of the hybrid drive shaft with an interference fit. Table 5 shows the maximum torque transmission capabilities of the four test specimens in which the minimum torque transmission capability of the hybrid drive shaft was 3550 Nm. From these test results, it was concluded that the hybrid drive shaft had a suitable torque transmission capability for passenger cars, vans and small trucks. All the fractures of the hybrid drive shafts occurred at the circumferential weld line between the aluminum tube and the inner serrated bush as shown in Fig. 13.

Dynamic torque test

The dynamic torque test of the prototype hybrid drive shaft was performed by the fatigue tester that was composed of a double acting pneumatic cylinder (FESTO ADV-100), a 5/2 way solenoid valve (FESTO JMFH-5-1/4), a load cell and a sequence control unit. The torque of the fatigue tester was produced by rotating the moment arm by the double acting pneumatic cylinder. The applied torque to the hybrid drive shaft was measured by the load cell fixed at the frame of the fatigue tester. The frequency of loading of the fatigue tester was controlled by varying the duration of electric current in the solenoid valve using a function generator. Figure 14 shows the hybrid drive shaft mounted on the fatigue tester. From the fatigue test, it was found that the hybrid drive shaft did not fail until 10^7 cycles under dynamic torque of ± 500 Nm.

CONCLUSIONS

In this paper, the one-piece hybrid drive shaft composed of carbon fiber–epoxy composite and an aluminum tube was designed and manufactured to reduce weight and vibration. The hybrid shaft was manufactured by co-curing the composite to the aluminum shaft with an applied preload to the aluminum before co-curing to reduce thermal residual stresses. The vibration characteristics of the hybrid drive shaft were measured by impulse–frequency responses and whirling tests. The static and dynamic torque tests of the hybrid drive shaft

was also performed. From the tests, the following conclusions were made:

1. The hybrid drive shaft was 50% lighter than the existing steel drive shafts.
2. The fundamental natural bending frequency of the hybrid drive shaft was 9100 rpm and the shaft rotated without whirling until 9000 rpm.
3. The minimum static torque transmission capability of the hybrid drive shaft was 3550 Nm.
4. The hybrid drive shaft was not failed until 10^7 cycles under a dynamic torque of ± 500 Nm

ACKNOWLEDGEMENTS

The authors appreciate financial supports for this research by Hwa Shin Industry in Ansan, Korea.

REFERENCES

1. Mallick, P. K., Newman, S., *Composite Materials Technology*, Hanser Publishers, New York, 1990, Chapter 6.
2. Lee, D.G., Kim, K.S. and Kwak, Y.K., Manufacturing of a SCARA-type direct-drive robot with graphite/epoxy composite materials. *Robotica* 1991, **9**, 219–229.
3. Kulkarni, S. V., Zweben, C. H. and Pipes, R. B., *Composite Materials in the Automobile Industry*, The ASME winter annual meeting, San Francisco, California, December 10–15, 1978.
4. Schmelz, F., Seherr-Thoss, C. and Aucktor, E., *Universal Joints and Driveshafts*, Chap. 4, Springer–Verlag, Berlin, 1992.
5. Reimpell, J. and Stoll, H., *The Automotive Chassis*, Society of Automotive Engineers, 1996, Chap. 1.
6. Rao, M.D. & He, S. Dynamic analysis and design of laminated composite beams with multiple damping layers. *AIAA Journal*, **31**(4) (1993) 736–745; *AIAA J. Composite Materials*, **24**(4) (1993) 92–102.
7. He, S. and Rao, M.D., Residual stresses and delamination problems induced by co-curing of damped composite laminates. *J. Composite Materials* 1994, **28**, 112–129.
8. Jones, R. M., *Mechanics of Composite Materials*. McGraw–Hill, New York, 1975, pp. 72–75.

ELSEVIER

Composite Structures Vol. 38, No. 1–4, pp. 321–328, 1997
© 1997 Elsevier Science Ltd. All rights reserved
Printed in Great Britain
0263-8223/97/$17.00 + 0.00

PII:S0263-8223(97)00066-4

Development of guide rollers using electroplated carbon fiber–epoxy composite for thin polymer film processing

Kyung Guen Bang, Jin Kyung Choi, Hyun Surk Kim, Dai Gil Lee*

Department of Mechanical Engineering, Korea Advanced institute of Science and Technology, ME3221, Kusong-dong, Yusong-gu, Taejon-shi, Korea 305-701

&

Han Su Jeon

Department of Mechanical Design and Production Engineering, Chungang University, Dongsak-gu, Korea 156-756

Since thin polymer films can not sustain the large tension generated from the rotational inertia of a guide roller during start and stop periods of film processing and can be easily damaged by the rough surface of the guide roller, the guide roller should have low rotational inertia, low friction coefficient, high bending stiffness and fine surfaces.

The carbon fiber–epoxy composite material electroplated with chromium has excellent properties for the structure of the guide roller due to its high specific modulus and high damping, which reduces induced vibrations.

In this paper, the design and manufacturing methods as well as the static, dynamic and frictional characteristics of the carbon fiber–epoxy composite rollers electroplated with chromium were investigated using analytical and experimental methods to improve the performance of the high speed guide roller. © 1997 Elsevier Science Ltd.

INTRODUCTION

Rollers are widely used in the metal rolling and polymer film manufacturing processes to control thickness, to guide the paths of products and to wind films [1]. Rollers have been designed and manufactured using steel or aluminum with the aim of minimizing the deflection caused by processing pressure and its own weight. However, the high speed production of thin polymer film has been hindered by the heavy weight and inertia of rollers, because thin polymer films can not sustain the large tension generated from the rotational inertia of the guide roller, especially during the start and stop periods of film processing. Thin films can be easily damaged by the rough surface of the guide roller. Therefore, the guide roller should have low rotational inertia, low friction coefficient, high bending stiffness and fine surfaces. Also, the material for the guide roller should have high damping to reduce the vibration which might be induced during operation.

One method to increase the dynamic stiffness of the guide roller is to use a material which has both high static stiffness and high damping. However, it is very difficult to increase the dynamic stiffness of conventional materials because they usually have high stiffness with low damping and vice versa. Composite materials, on the other hand, can be made to have both high static stiffness and damping because composite materials can be composed of two materials, one of which has high Young's mod-

*Department of Mechanical Engineering, Korea Advanced Institute of Science and Technology, ME3221, Kusong-dong, Yusong-gu, Taejon-shi, Korea 305-701

ulus and the other has high damping. The resulting performance will reflect the best characteristics of each material [2].

However, the fiber reinforced composite material has low hardness and high surface roughness due to the projection of the fiber when the surface was ground or machined by another method. Therefore, it is necessary to coat the surface of the composite with hard materials such as chromium for a guide roller. Since the conductivity of carbon fiber–epoxy composite is anisotropic and low compared to other high conductivity metals, it is not easy to directly electroplate the carbon fiber composite with chromium [3]. It is necessary to coat paste which includes a good conductor such as silver or copper on the composite surface before electroplating.

Several attempts to increase the roller performance have been performed through experiments and analyses. Conroy studied the design of the large roller press and discussed the bearing housing and roller alignment [4]. Yang derived governing equations for rotating arbitrary axi-symmetric rollers with various types of boundary and initial conditions. He obtained the analytical solutions for the case of a circular cylinder [5]. Good developed models to calculate the internal stress in wound rolls of web material in which a new boundary condition were presented to calculate the internal stresses [6]. Ulku investigated fiber breakage at different roller speeds and the relationship between the breakage and friction of yarns made of cotton, polyester, viscose and acrylic fibers [7]. Lee *et al.* developed the carbon fiber composite spindle system to enhance the dynamic and thermal stability of the spindle system [8]. Several attempts to use high damping materials as an additive layer have also been conducted. However, the use of a damping material was limited by the geometric and boundary conditions and also by the lubrication and bearing mounting requirements.

In this paper, the design and manufacturing methods as well as the static and dynamic characteristics of the carbon fiber–epoxy composite guide rollers electroplated with chromium were investigated using analytical and experimental methods to improve the performance of the guide roller system.

EXPERIMENTAL SETUP FOR THE HIGH SPEED GUIDE ROLLER SYSTEM

For the development of the composite guide roller, the bearing types and the stacking sequence of composite materials must be selected first. Then the bearing arrangement and the roller shape are determined for the optimum performance of the guide roller system. For the first stage of development, the experimental setup for the prototype guide roller system as shown in Fig. 1 was designed and manufactured. The bearings were mounted on the shaft with interference fit to obtain high stiffness. Table 1 shows the specifications and circularity for the roller system. The 60-series deep groove ball bearings manufactured by FAG in Germany, whose specifications are shown in Table 2 were selected for the roller.

The low friction grease, Arcanol 174, manufactured by FAG in Germany, was used for bearing lubrication. The high strength carbon fiber–epoxy USN150 manufactured by Sunkyung, Korea, was used for the guide roller. Table 3 shows the mechanical properties of the carbon fiber–epoxy composite.

Figure 2 shows a photograph of the experimental setup before assembling the high speed ball bearings. This setup was used to measure the static, dynamic and thermal characteristics of the guide roller system.

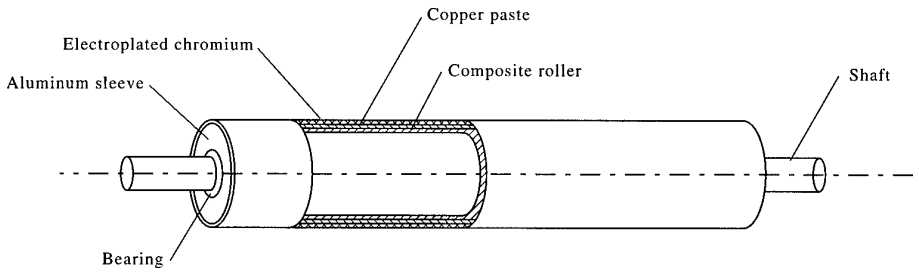

Fig. 1. Experimental setup for the prototype composite guide roller system.

Table 1. Specifications and circularity of the roller

Roller diameter (mm)	100
Roller length (mm)	800
Surface roughness (μm)	$\leq$0.5
Circularity (μm)	$\leq$20

MANUFACTURING OF THE CARBON FIBER–EPOXY COMPOSITE GUIDE ROLLER

Since heat generated from bearings and moisture might degrade the properties of composite materials, two aluminum sleeves for bearing mounts were manufactured as shown in Fig. 3. The two aluminum sleeves and the carbon fiber–epoxy composite roller were bonded with epoxy adhesive. Table 4 shows the properties of the epoxy adhesive used.

Since the hardness of carbon fiber–epoxy composites is low and the surface roughness can not be reduced beyond a certain value due to the projection of fibers on the surface of the composites when they are machined, the surface of the composites must be coated with hard material to be used as the guide rollers for thin polymer film processing. In this work, the surface of the carbon fiber–epoxy composite was electroplated with chromium. Since the carbon fiber–epoxy composite has anisotropic and inhomogeneous conductivity and does not have enough conductivity for electroplating with chromium, some conductors such gold, silver and copper must be coated on the carbon fiber–epoxy composite. In this work, the copper paste, ACP-060 manufactured by ASAHI in Japan, was uniformly painted on the surface of the composite. Table 5 shows the properties of the copper paste used and Fig. 4 shows a photograph of the carbon fiber–epoxy roller painted with the copper paste before electroplating with chromium.

The carbon fiber–epoxy composite painted with the copper paste has been electroplated in a chromium bath for 18 h. Then, the carbon fiber–epoxy composite roller electroplated with chromium was ground to the final dimensions.

The stacking sequence of composite materials was determined to satisfy the high flexural modulus for high natural frequency and low deflection. In this work, the specifications of power and speed were 10 kW and 3800 rpm, respectively, and the maximum bending compliance at the center of the shaft should be less than 0.1 μm/N. The required torque capacity T of the roller is obtained by the following equation

$$T = \frac{60H}{2\pi n} \tag{1}$$

where, H is the motor power and n is the rpm of the shaft.

From Eq. (1), the maximum required torque capacity of the roller was 95 Nm when the roller was driven at 1000 rpm. With this torque capacity, the fundamental natural frequency of the roller should be larger than 3800 rpm. Figure 5 shows the calculated natural frequencies in the bending mode of the roller versus stacking sequence of $[\pm\theta]_{nT}$ with simply supported boundary condition. The natural frequency of the composite shaft in bending mode decreases with the increase of the stacking angle θ.

When the stacking sequence $[\pm 5]_{nT}$ from the axis of the shaft was chosen, the fundamental natural bending frequency was higher than 45 000 rpm and the maximum compliance at the center of the roller shaft was smaller than 0.1 μm/N. For the easy separation of the composite roller shaft from the mandrel, a taper angle of 1/1600 was given to the mandrel. Since the maximum driving frequency of the roller motor and the allowable maximum compliance were 3800 rpm (63.3 Hz) and 0.1 μm/N, respectively, this stacking sequence was found acceptable.

The material damping of metal is dependent on frequency. The damping factors of steel and aluminum usually decrease with frequency and are less than 0.001–0.005 when the frequency is greater than 100 Hz. Since the damping factor of the carbon fiber–epoxy composite is around

Table 2. Specifications of the deep groove ball bearing (FAG, Germany)

Bearing model	Inner diameter (mm)	Dynamic load rating (kN)	Static load rating (kN)	Limit speed (rpm)	
				Oil–air lubrication	Grease lubrication
6004	20	9.3	5	20000	17000

Table 3. Properties of the unidirectional carbon fiber–epoxy composite

Tensile Modulus (GPa)	131.6
Transverse Modulus (GPa)	8.2
Shear Modulus (GPa)	6.1
Poisson's Ratio	0.3
Tensile Strength (GPa)	1.78
Transverse Strength (MPa)	50
Shear Strength (MPa)	88
Fiber Volume Fraction (%)	60
Density (kg/m^3)	1600

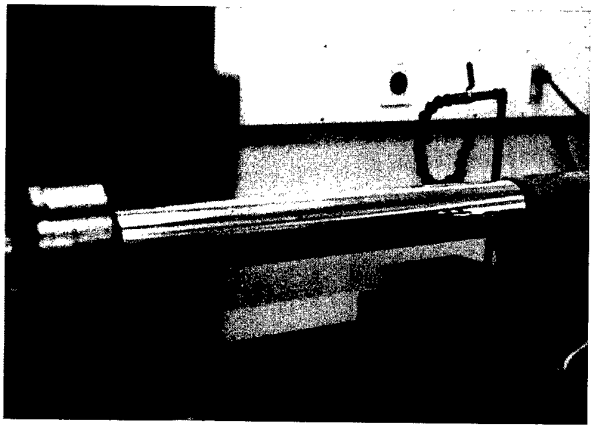

Fig. 2. Experimental setup for measuring static and dynamic characteristics of the roller system.

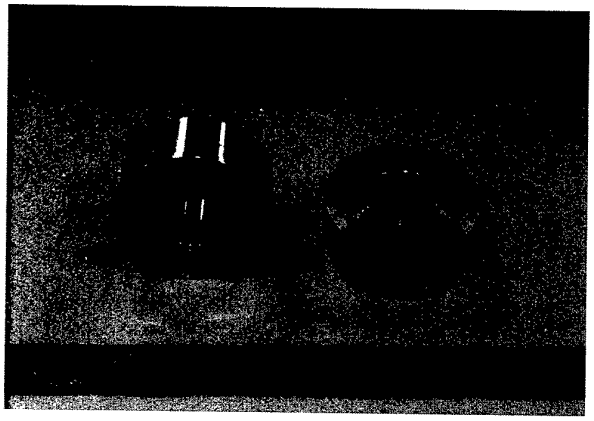

Fig. 3. Two aluminum sleeves for bearing mounting.

Table 4. Properties of the epoxy adhesive (IPCO 9923)

Lap shear strength (MPa)	13.7 (ASTM D-1002-72)
Tensile modulus (GPa)	1.3
Tensile strength (MPa)	45
Shear modulus (GPa)	0.46
Poisson's ratio	0.41

Table 5. Properties of the copper paste (ASAHI, Japan)

Viscosity (ps at 25°C)	400–600
Specific gravity (g/cc at 25°C)	3.2
Curing conditions	30 min at 150°C
Hardness (H)	3
Sheet resistance (Ω/mm^2)	0.1
Humidity aging (%)	$\pm$30
Solder resistance (%)	$\pm$30

0.01 and less dependent on frequency, the damping factor of the carbon fiber–epoxy composite is about 2–10 times higher than that of the cast iron or steel when the vibration frequency is higher than 100 Hz [1,9].

The torque transmission capabilities of the adhesively bonded joints between the composite roller shaft and the aluminum sleeves are dependent on the bonding length and the adhesive thickness [10]. Figures 6 and 7 show the calculated torque transmission capabilities with respect to bonding length and adhesive thick-

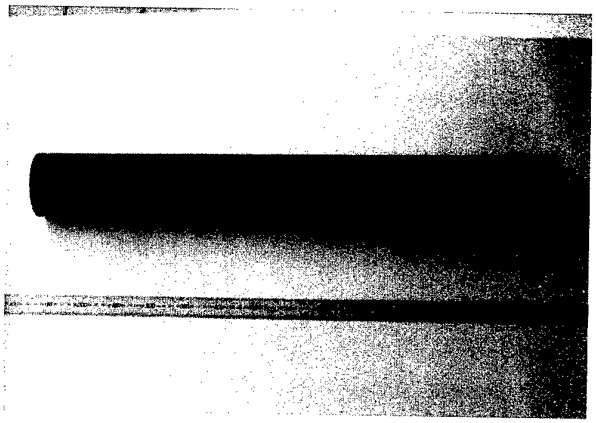

Fig. 4. Carbon fiber–epoxy roller painted with the copper paste before electroplating with chromium.

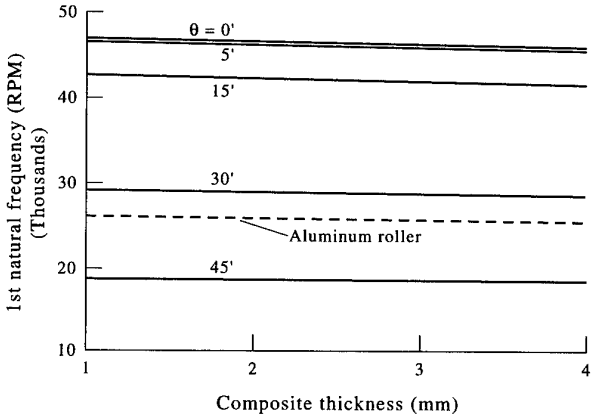

Fig. 5. Variations of the fundamental natural frequency of the composite roller in bending mode versus stacking sequence $[\pm\theta]_{nT}$.

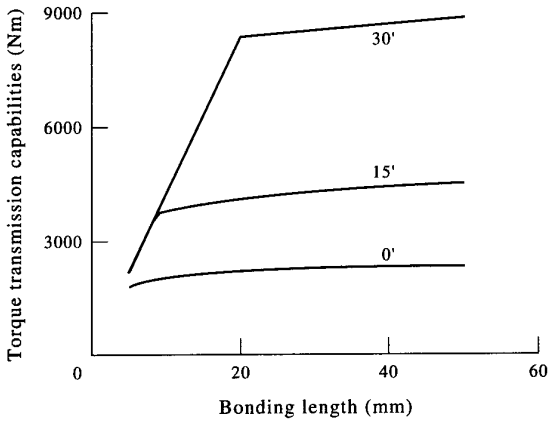

Fig. 6. Torque transmission capabilities of the composite roller wrt bonding length and stacking sequence when the bonding thickness is 0.5 mm.

ness. Since the maximum torque generated by the driving motor was 95 Nm, it was found that the 30 mm bonding length and 0.5 mm adhesive thickness were more than enough.

Figure 8 shows the coefficient of thermal expansion versus stacking sequence calculated by classical laminated plate theory. From Fig. 8, the transverse coefficient of thermal expansion of the composite was 26.5 μm/m °C, which was similar to that of aluminum (23.6 μm/m °C) when the stacking sequence was $[\pm 5]_{nT}$.

STATIC AND DYNAMIC CHARATERISTICS OF THE COMPOSITE ROLLER SYSTEM

Since the static stiffness of the roller determines both the accuracy and natural frequencies of the roller system, the estimation of the static stiffness of the roller system is important in the design stage.

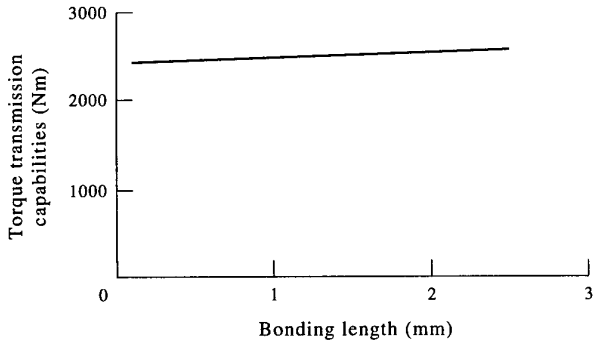

Fig. 7. Torque transmission capabilities of the composite roller wrt adhesive thickness when the bonding length and the stacking sequence are 30 mm and $[\pm 5]_{nT}$, respectively.

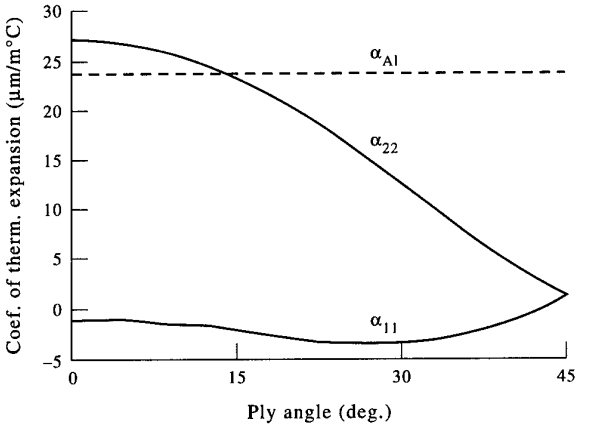

Fig. 8. Coefficient of thermal expansion of the composite versus stacking sequence.

The analytic expression for the roller stiffness was attempted by simplifying the roller system of Fig. 1. The simplified roller system for analysis is shown in Fig. 9. The bearings were replaced by equivalent springs. Under these assumptions, the maximum deflection δ of the center of the roller system was expressed as follows [11].

$$\delta = \frac{\bar{\omega} l}{4}\left(\frac{1}{k_1}+\frac{1}{k_2}\right)+\frac{5\bar{\omega} l^4}{384EI} \tag{2}$$

Where, $\bar{\omega}$ is the distributed load per length, l the roller span, EI the flexural rigidity of the roller and k_1, k_2 the stiffness constants of the front and rear bearings, respectively.

In order to assess the validity of the displacement equation of the roller, the displacement was also calculated using ANSYS, a commercial finite element analysis software. In the finite element analysis, the nodes were generated using one dimensional beam elements. Figure 10 shows the deflection of the roller system when the distributed load of 1 kN was applied at the center of the roller. Table 6 shows the calculated displacements.

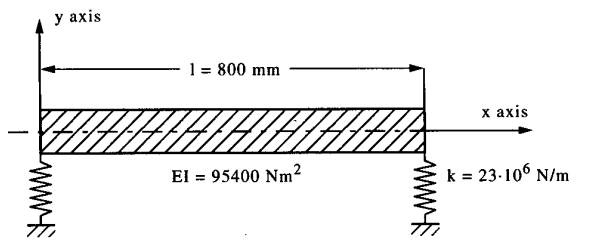

Fig. 9. Simplified roller system for analysis.

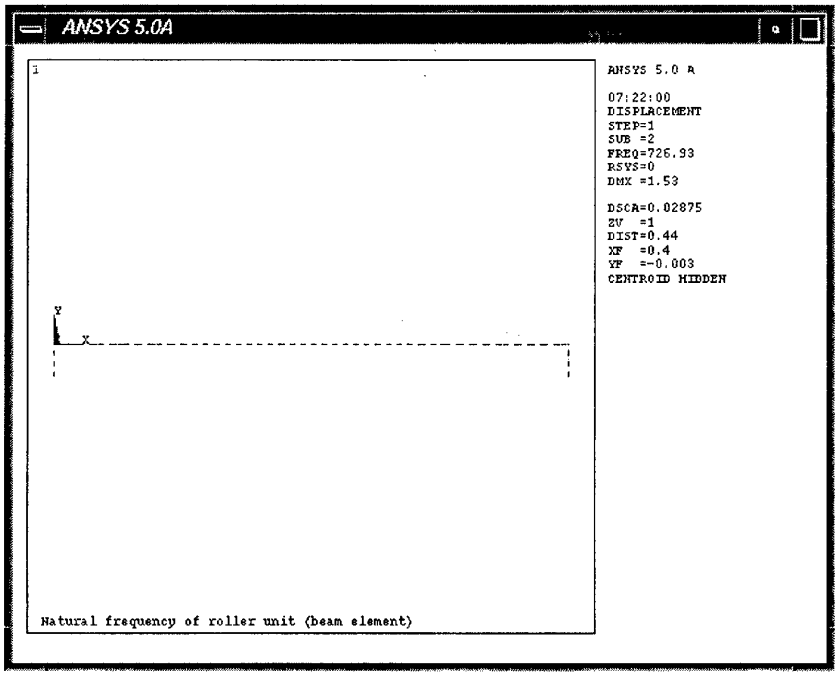

Fig. 10. Deflection of the roller system when the distributed load of 1 kN was applied on the roller.

During the rolling operation, it is generally known that two different vibrations of the roller system occur: the rigid body motion of the roller which is supported by bearings and the bending motion of the roller on the bearing foundation. Under the assumption of the two vibration modes, the natural frequencies of the composite roller system can be calculated either by analytic or numerical methods. The Rayleigh–Ritz method, which is an analytic method, calculates the natural frequencies using appropriate functions which represent the vibration modes [12]. In this work, the Rayleigh–Ritz method was applied to the composite roller system as shown in Fig. 9. The displacement Y of the roller was assumed by the following equation.

$$Y = C_1 x + C_2 \sin \frac{\pi x}{l} \tag{3}$$

Where, C_1 represents the displacement of the roller in the rigid body motion and C_2 represents the bending motion of the roller supported by the bearings. Then, the square of the natural frequency ω is expressed as follows

$$R(\omega) = \omega^2 = \frac{\int EI\left(\frac{d^2Y}{dx^2}\right)^2 dx + k_1 Y^2 + k_2 Y^2}{\int_\rho AY^2 dx} = \text{const.} \tag{4}$$

Table 6. Deflections of the center of the roller when the distributed load of 1 kN is applied

	From Eq. 2	FEM result	Error (%)
Displacement at the center of the roller	0.056 mm	0.058 mm	3.4

The numerical value of the first natural frequency of the composite roller system calculated by Eqs. 3 and 4 was 745 Hz. However, the Rayleigh–Ritz method becomes very complicated for higher natural frequencies and consequently the calculation error will be larger. Also, the natural frequencies of the composite roller system was calculated using FEM. In the numerical analysis, one dimensional beam elements were used and the front and the rear bearings were replaced by equivalent springs. Figure 11 shows the first mode shape of the bearing system which occurs at 727 Hz.

To compare the analytical result with the experimental result, the amplitude of the acceleration at the center of the roller system was measured with an accelerometer through FFT (Fast Fourier Transform) signal analyzer. Table 7 shows the natural frequencies calculated by several methods. From the calculation of the natural frequencies by FEM, it was found that the FEM with one dimen-

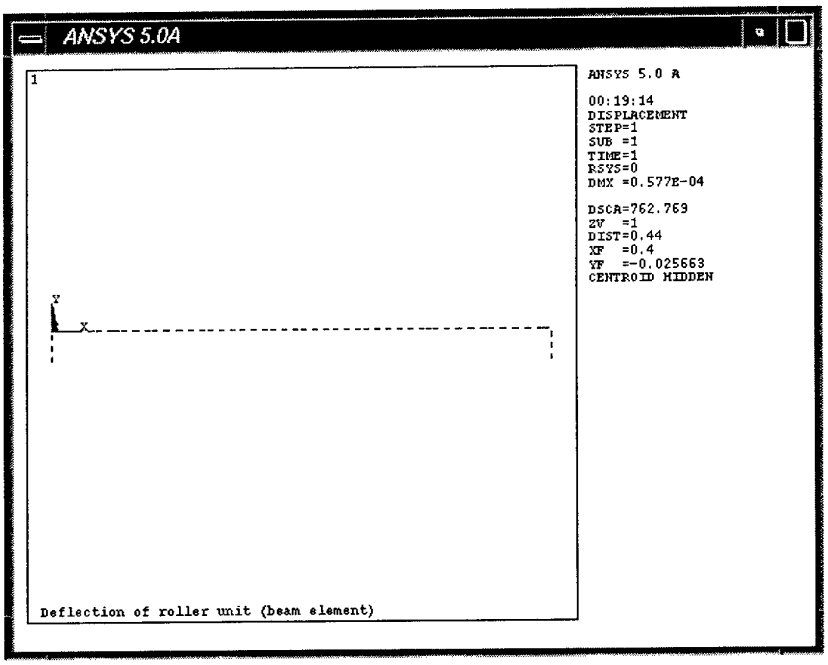

Fig. 11. First mode shape of the roller system.

sional beam element gave more accurate result than the Rayleigh–Ritz method.

PERFORMANCE OF THE ROLLER SYSTEMS

In general, aluminum shafts have been used without machining for long and large rollers because it is not easy to bore out the inner surface of a long pipe with the required accuracy. Then, the balancing of large aluminum shafts has been important issue. These problems can be solved with the composite roller because it is easily balanced owing to its light weight and can be moulded with hollow shape using mandrels. Table 8 shows several advantages of the composite roller compared with the existing aluminum roller.

Since both the natural frequency and damping ratio of the composite roller were increased, the dynamic stiffness of the roller system which is defined as the product of stiffness and damp-

Table 7. Fundamental natural frequencies of the roller system

Methods	First natural frequency	Error (%)
Rayleigh–Ritz method	745 Hz	8.8
FEM	One dimensional beam element: 727 Hz	6.1
Experiment	685 Hz	–

Table 8. Comparison of the composite roller system with the steel roller shaft

	Existing aluminum system	Composite roller system	Notes
Roller section shape	Hollow	Hollow	
Maximum deflection	0.058 mm/kN	0.058 mm/kN	Same
Machining, balancing and handling	Difficult	Easy	
Natural frequency (Simply supported)	425 Hz	685 Hz	Increase of 1.6 times
Damping ratio	0.004	0.015	Increase of 3.8 times
Mass (Excluding both sleeves)	1.81kg	0.92kg	Decrease of 2.0 times

ing, was also increased. Moreover, due to its light weight the assembly of the composite roller shaft was much easier than the existing aluminum roller shaft.

CONCLUSIONS

In this paper, the high speed roller for thin polymer film processing was designed and manufactured with carbon fiber–epoxy composite material. The surface of the composite roller was electroplated with chromium to increase surface hardness. The static and dynamic characteristics of the composite roller system were investigated using analytical and experimental methods when the maximum deflection of the composite roller was equal to that of the existing aluminum roller. From the investigation, it was found that the natural frequency and the damping ratio of the composite roller were increased by 1.6 and 3.8 times, respectively, compared with those of the existing aluminum roller. Also the weight of the composite roller was 50% that of the aluminum roller. Therefore, it was concluded that the productivity in thin film processing could be increased significantly by using the composite roller system.

REFERENCES

1. Larke, E. C., *The Rolling of Strip, Sheet and Plate*. Chapman and Hall, London, 2nd Ed., Chap. 1, 1967.
2. Choi, J. K. and Lee, D. G., Experimental investigation of the static torque transmission capabilities of the adhesively bonded single lap joints. *J. Material Processing Technology*, 1995, **48**, 341–347.
3. Lowenheim, F. A., *Electroplating*. McGraw–Hill, New York, 1978, pp. 169–250.
4. Conroy, G. H., Progress in roller press design technology. *Trans. IEEE on Industry Applications*, 1994, **30**, 561–567.
5. Yang, R. J., Steady motion of a thread over a rotating roller. *J. Applied Mechanics of Trans. ASME*, 1994, **61**, 16–22.
6. Good, J. K., Wu, Z. and Fikes, M. W. R., The internal-stresses in wound rolls with the presence of a nip roller. *J. Applied Mechanics of Trans. ASME*, 1994, **61**, 182–185.
7. Ulku, S., Ozipek, B. and Acar, M., Effect of opening roller speed on the fiber and yarn properties in open-end friction spinning. *Textile Research J.* , 1995, **65**, 557–563.
8. Lee, D. G., Sin, H. C. and Suh, N. P., Manufacturing of a graphite epoxy composite spindle for a machine tool. *Ann. CIRP*, 1985, **34**, 365–369.
9. Welbourn, D. B. and Smith, J. D., *Machine Tool Dynamics*, Cambridge University Press, Chap. 5, 1970.
10. Lee, S. J. and Lee, D. G., An iterative solution for the torque transmission capability of adhesively-bonded tubular single loap joints with nonlinear shear properties. *J. Adhesion*, 1995, **53**, 217–227.
11. Crandall, S. H. and Dahl, N. C., *An Introduction to the Mechanics of Solids*, McGraw–Hill, New York, 2nd Ed., 1978, pp. 164–172.
12. Rao, S. S., *Mechanical Vibrations*. Addison–Wesley, New York, 1984.

ELSEVIER

Composite Structures Vol. 38, No. 1–4, pp. 329–341, 1997
© 1997 Elsevier Science Ltd. All rights reserved
Printed in Great Britain
0263-8223/97/$17.00 + 0.00

PII:S0263-8223(97)00067-6

Optimum bolted joints for hybrid composite materials

Je Hoon Oh, Young Goo Kim & Dai Gil Lee*

Mechanical Design Laboratory with Advanced Materials, Department of Mechanical Engineering, ME3221 Korea Advanced Institute of Science and Technology, Gusong-dong, Yusong-gu, Taejon-shi, Korea 305-701

The optimum bolted joints for hybrid composite materials composed of glass–epoxy and carbon–epoxy under tensile loading were investigated. The design parameters considered for the bolted joints were ply angle, stacking sequence, the ratio of glass–epoxy to carbon–epoxy, the outer diameters of washers and the clamping pressure. As bearing failure was desirable for bolted joints, the geometry of the bolted joint specimen was designed to undergo bearing failure only.

By inspecting the fracture surfaces of the specimens it was found that delamination on the loaded periphery of the holes and extensive damage on the edge region constrained by a washer occurred. To assess the delamination of the hybrid composite materials, three-dimensional stress analysis of the bolted joint was performed using a commercial finite-element software and compared with the experimental results. © 1997 Elsevier Science Ltd.

INTRODUCTION

The fiber-reinforced composites have been used widely in aircraft and spacecraft structures, as well as in sports and leisure goods, because they have high specific stiffness, high specific strength, high damping and a low coefficient of thermal expansion. These properties cannot be obtained from conventional metals such as steel and aluminum [1,2]. In addition, the structures made of composites have a high natural frequency as well as a light weight, therefore they are increasingly employed in rotating structures such as power transmission shafts of aircrafts and automotives [3], in machine elements such as machine tool spindles [4] and robot arms [5].

When composites are employed as structural materials, joining of composites to other materials is necessary because manufacturing the whole structure using only composites is not generally feasible. Therefore, the joint used in composite structures, with only a few exceptions, determines the structural efficiency because it usually becomes the weakest part of the structure [6,7]. There are two types of joints: mechanical and adhesively bonded joints. The mechanical joint has several advantages over the adhesively bonded joint, which requires careful surface treatment of the adherend, is affected by service environment and is difficult to dismantle for inspection and repair, although it does distribute load over a larger area than the mechanical joint. However, the mechanical joint requires holes to be drilled for bolts and rivets, which causes unavoidable stress concentrations as well as a weight penalty due to the bolts and rivets [8].

Three different types of fasteners, such as self-tapping screws, rivets and bolts, are usually used in mechanical joints. Among these fasteners, the bolted joint was found to be most efficient for the mechanical fastening of composites [9]. However, the analysis of mechanical joints has not been very satisfactory because of the friction between bolts and holes, the material non-linearity and the presence of three-dimensional stresses and strains. Thus, many investigators have experimentally studied

*Author to whom correspondence should be addressed.

the behavior of mechanical joints of CFRP and GFRP.

Collings [9] investigated the effect of stacking angle on the bearing strength with respect to three different composites. Eriksson [10] showed that bearing strength was strongly affected by a lateral constraint of the material surrounding the loaded hole. Quinn & Matthews [11] reported a significant effect of the stacking sequence on the bearing strength of GFRP. Herrington & Sabbaghian [12] studied the effect of radial clearance between the bolt and washer on the bearing strength of the composite bolted joints and showed that bearing strength increased as the radial clearance decreased. They also found that the ratios of width-to-diameter (w/d) and edge distance-to-diameter (e/d) influenced the failure mode, and the bearing strength was increased and approached a limiting value as the ratios were increased [13–15]. Kim & Whitney [16] found that elevated temperature and increased moisture content of the laminate reduced the bearing strength. Akay [17] studied the static and dynamic bearing strengths of uni-directional and woven carbon–epoxy composite when test pieces were hygrothermally treated.

Most models for the strength prediction of bolted composite laminates adopted elastic two-dimensional plane-stress analysis using a finite-element method [18–21]. Chen *et al.* [22] used the incremental restricted variational principle and the transformation matrix, derived from three-dimensional contact kinematic conditions, to carry out a three-dimensional contact stress analysis of a composite laminate with bolted joints. Graham *et al.* [23] performed a two-dimensional contact stress analysis assuming that bolts and washers were rigid and that bolts had a perfect fit. Smith *et al.* [24] established a simple three-dimensional model to predict the strength of bolted composite laminates, and studied the effects of the coefficient of friction between washers and laminates.

Although hybrid composites composed of carbon–epoxy and glass–epoxy are in widespread use in automotive and aerospace propeller shafts, leaf springs and fly wheels due to their improved mechanical behavior, such as their high specific stiffness, high specific strength, high impact energy, cost reduction, good corrosion resistance and easy fabrication [25], most studies have been focused on the behavior of mechanically fastened joints for non-hybrid composites such as carbon–epoxy and glass–epoxy. Therefore, there are few data available on the joints for hybrid composites [26].

In this work, the optimum bolted joints for hybrid composite materials composed of glass–epoxy and carbon–epoxy under tensile loading were investigated. The geometry of the bolted joint specimen was designed to induce bearing failure because bearing failure is preferable for the bolted joint. The design parameters were ply angle, stacking sequence, ratio of glass–epoxy to carbon–epoxy, outer diameter of the washer and clamping pressure.

The optimum ply angle for hybrid composites was determined using the static test results for the bolted joints of carbon–epoxy and glass–epoxy composites with respect to ply angle. Then the joint specimens for the hybrid composites were tested under tensile loading with different stacking sequences and ply number ratios of glass–epoxy to carbon–epoxy composite. The effects of the outer diameter of the washer and the clamping pressure of the bolt on the bearing strength were also investigated.

In order to investigate the delamination of the hybrid composite materials three-dimensional stress analyses for the bolted joint were performed using a commercially available finite-element software and then compared with the experimental results.

EXPERIMENTS

Because the failure of bolted joints should not occur catastrophically, in this work the specimen geometry was designed to induce bearing failure. For this purpose, both the ratio of width-to-diameter and of edge distance-to-diameter were set at 5. The geometry of the bolted joint is shown in Fig. 1.

In order to determine the ply angle of the hybrid composites the static tests of the bolted joints for carbon–epoxy and glass–epoxy were performed with respect to the ply angle. The number of plies for both the carbon–epoxy and the glass–epoxy composite were 20. The stacking sequences for both the composites were $[0_2/(0/90)_3/90_2]_S$ and $[0_2/(\pm\theta)_3/90_2]_S$ ($\theta = 15$, 30 and 45°).

The carbon–epoxy composite and the glass–epoxy prepregs used were USN150 and UGN150, respectively, both manufactured by Sunkyung Industry (Suwon, Korea). Table 1

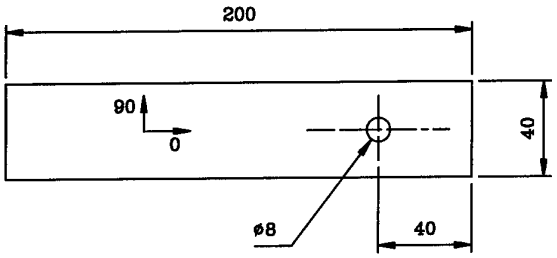

w/d = 5 e/d = 5
Number of plies = 20 plies

Fig. 1. Geometry of the specimen.

shows the uni-directional mechanical properties of the composite materials and Fig. 2 shows the curing cycle for the composite materials.

A glass fabric–epoxy composite was used for the tabs on the composite specimens, and the tensile tests were performed using the loading fixture illustrated in Fig. 3. The 8 mm bolt with class 10.9 was used for the bolted specimens. Washers, 2 mm thick, with the same inner diameter as the bolt and a 20 mm outer diameter were used. The specimens, clamped using finger-tightened bolts, were tested at room temperature with an Instron 4206, a static material testing machine with a test speed of 1 mm/min. Five specimens were tested for each point.

Table 1. Material properties of the carbon–epoxy (USN150) and glass–epoxy (UGN150) composites

	Carbon–epoxy (USN150)	Glass–epoxy (UGN150)
E_L (GPa)	130.0	43.5
E_T (GPa)	8.0	5.0
G_{LT} (GPa)	6.0	5.0
ν_{LT}	0.28	0.25
X_t (MPa)	1800	1000
Y_t (MPa)	60	50
S (MPa)	75	50
Ply thickness (mm)	0.15	0.125

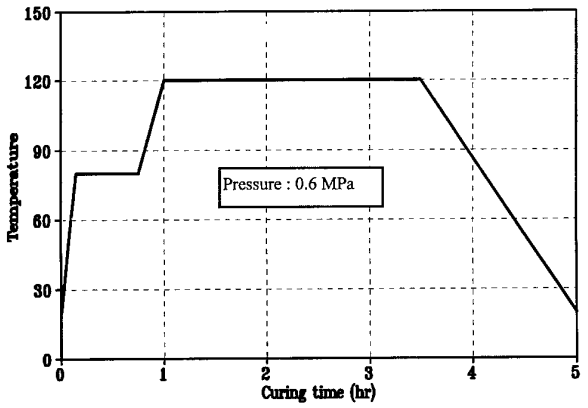

Fig. 2. Cure cycle for composite materials.

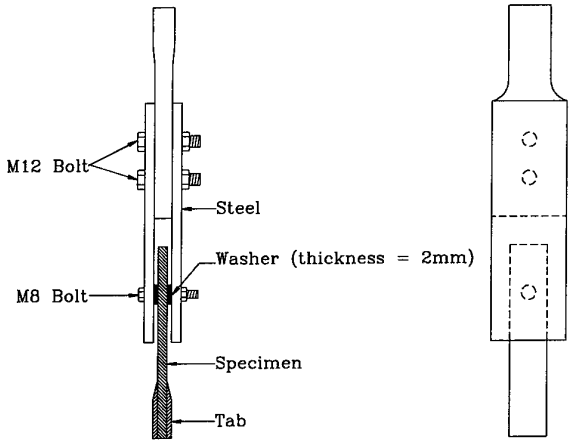

Fig. 3. Schematic diagram of loading fixture.

Typical load–displacement curves are shown in Fig. 4, where the first peak loads (A) indicate the local delaminations around the holes under the washers. The damage development in the vicinity of the hole boundary at the peak point (A) was measured using an ultrasonic C-scan as shown in Fig. 5. From the result of the C-scan, it was found that damage developed along the loaded half of the hole circumference. The load was continuously increased because the swelling of the composite in the thickness direction, due to the Poisson effect, induced the clamping

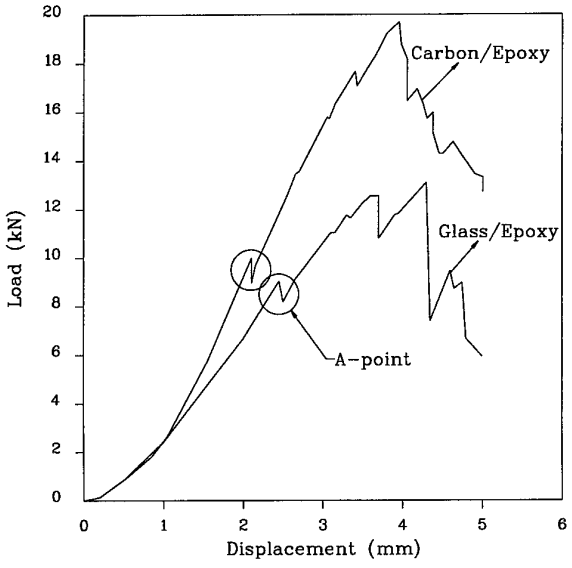

Fig. 4. A typical load–displacement curve for the carbon–epoxy bolted joint and the glass–epoxy bolted joint.

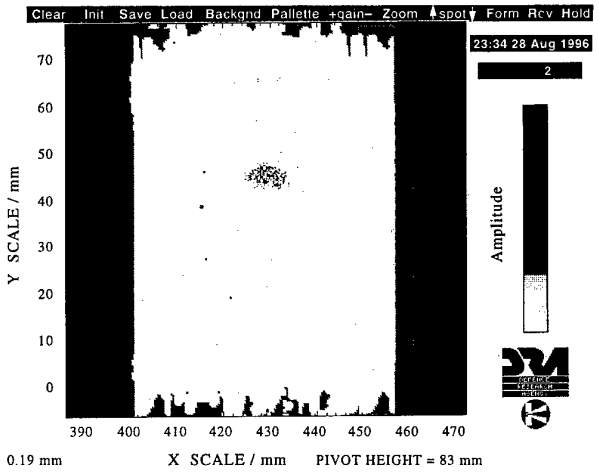

Fig. 5. Results of the ultrasonic C-scan of the bolted joint.

pressure in the region of the laminate constrained by the washer, which delayed the delamination of the specimens. Therefore, in this work, the ultimate failure load rather than the first peak load was taken as the joint strength load because the joint was not fractured at the first peak load (A) and the rate of the increase of the load was not decreased.

The ultimate bearing strength, σ_b, was defined by the following equation

$$\sigma_b = \frac{P}{dt} \tag{1}$$

where P is the ultimate failure load, d is the hole diameter and t is the thickness of the laminate.

Static tests of joints for the carbon–epoxy and glass–epoxy composites

In order to determine the optimum ply angle for hybrid composites, the bolted joints for the carbon–epoxy and glass–epoxy composites were first tested with respect to the ply angle. Table 2 shows the stacking sequences for the carbon–epoxy and glass–epoxy composites. From the static test results of the carbon–epoxy composite with a stacking sequence of $[0_2/(0/90)_3/90_2]_S$ and $[0_2/(\pm\theta)_3/90_2]_S$ ($\theta = 15$, 30 and 45°), it was found that the bearing strength was increased as the ply angle θ was increased. When the stacking sequence was $[0_2/(0/90)_3/90_2]_S$, the combined modes of tensile and shear-out failure occurred, and the bearing failure mode

Table 2. Stacking sequences of the carbon–epoxy and glass–epoxy composites

Material	Stacking sequence	E_L^{L1} (GPa)
Carbon–epoxy	$[0_2/(0/90)_3/90_2]_S$	69.3
	$[0_2/(\pm15)_3/90_2]_S$	95.8
	$[0_2/(\pm30)_3/90_2]_S$	69.8
	$[0_2/(\pm45)_3/90_2]_S$	46.1
Glass–epoxy	$[0_2/(0/90)_3/90_2]_S$	24.4
	$[0_2/(\pm15)_3/90_2]_S$	33.1
	$[0_2/(\pm30)_3/90_2]_S$	26.1
	$[0_2/(\pm45)_3/90_2]_S$	19.2

[1] E_L^L, Laminate longitudinal modulus.

occurred when the stacking sequence was $[0_2/(\pm\theta)_3/90_2]_S$ ($\theta = 15$, 30 and 45°). Figure 6a shows the bearing strength and failure modes of carbon–epoxy with respect to the ply angle. On inspecting the fracture surfaces of the specimens, delamination of the carbon–epoxy specimen on the loaded side of the holes and extensive damage at the washer edge outside the constrained region were found. From the test results, it was found that delaminations were more critical to the joint failure than in-plane damage.

In order to investigate the effect of a 90° ply on the joint strength, the specimen with a stacking sequence of $[0_3/(\pm45)_3/+45]_S$ was tested and the result was compared with that of $[0_2/(\pm45)_3/90_2]_S$. The bearing strengths of the specimens with $[0_3/(\pm45)_3/+45]_S$ and $[0_2/(\pm45)_3/90_2]_S$ were 859 and 880 MPa, respectively, where the bearing strength was higher when a 90° ply was contained in the laminates.

From the static test results of a glass–epoxy composite with a stacking sequence of $[0_2/(0/90)_3/90_2]_S$ and $[0_2/(\pm\theta)_3/90_2]_S$ ($\theta = 15$, 30 and 45°), it was found that the bearing strengths of the two specimens were similar. The specimen with $[0_2/(0/90)_3/90_2]_S$ failed in the combined modes of bearing and shear-out failures. The specimen with $[0_2/(\pm15)_3/90_2]_S$ was failed in the combined modes of bearing, tension and shear-out failures, while the specimens with a $[0_2/(\pm\theta)_3/90_2]_S$ ($\theta = 30°$ and 45°) joint failed in bearing failure mode. Figure 6b shows the bearing strength and failure modes of the glass–epoxy composite with respect to the stacking sequence.

Similar to the case of the carbon–epoxy composite, delamination of the glass–epoxy specimen on the loaded side of the holes and extensive damage at the washer edge outside the constrained region were found. During the

tests it was found that the area of the specimen between the hole and the edge was deformed considerably out of the laminate plane due to the low modulus of the glass–epoxy composite. This out-of-plane buckling mode was also observed by Kretsis & Matthews [27].

Static tests of the joints for the hybrid composites

From the static tests of the carbon–epoxy and glass–epoxy composites, it was found that carbon–epoxy with $[0_2/(\pm 45)_3/90_2]_S$ yielded the highest bearing strength and the glass–epoxy with $[0_2/(\pm 30)_3/90_2]_S$ and $[0_2/(\pm 45)_3/90_2]_S$ yielded similar high bearing strengths. Therefore, for the hybrid composites, the stacking sequence was $[0C/\pm 45G/\pm 45C/90C]_S$ (C: carbon–epoxy, G: glass–epoxy) containing carbon plies in the 0°, 90° and ±45° directions and glass plies in the ±45° direction.

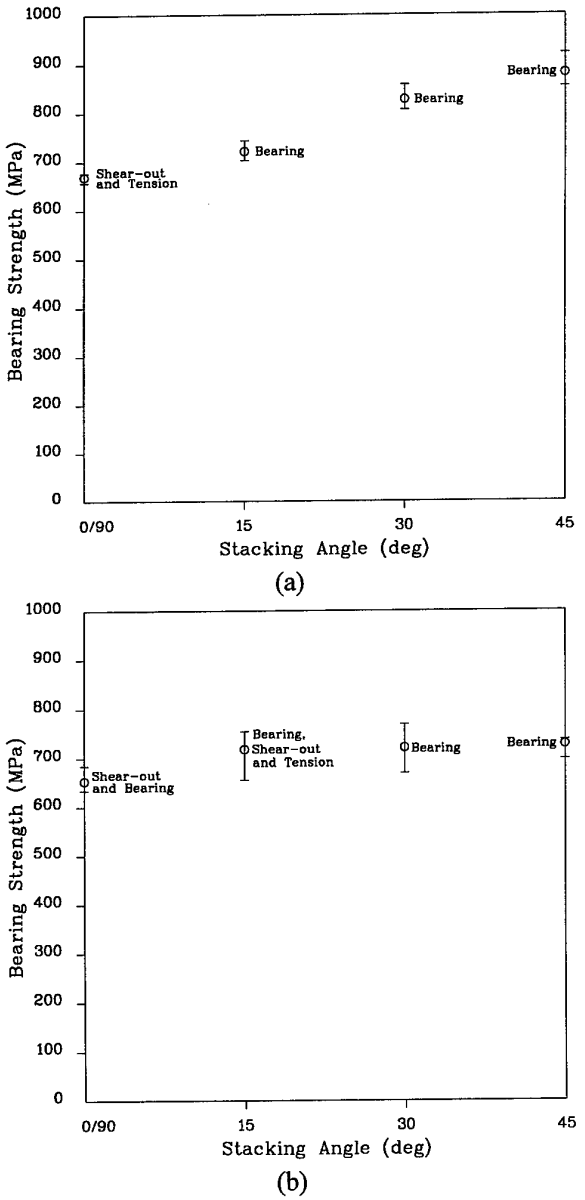

Fig. 6. Joint bearing strengths of the CFRP and GFRP with respect to the stacking angle of $[0_2/(\pm\theta)_3/90_2]_S$. (a) CFRP. (b) GFRP.

In order to investigate the effects both of the clamping pressure of the bolt and the outer diameter of the washer on the bearing strength, the stacking sequence and the ratio of carbon–epoxy to glass–epoxy which gives the highest bearing strength was used in the test of specimens. As the thickness of carbon–epoxy was different to that of glass–epoxy, as shown in Table 1, the percentage of ply number is different to the volume fraction. Therefore, the volume fractions of the glass–epoxy with ply number percentages of 20, 40 and 60 are 17.2, 35.8 and 55.6%, respectively. Table 3 shows the stacking sequences of the hybrid composites which have the stacking sequence type $[0C/\pm 45G/\pm 45C/90C]_S$. The specimens with 14 different stacking sequences were tested when the volume fractions of glass–epoxy were 17.2 and 35.8%, while the specimens with seven different stacking sequences were tested when the volume fraction of glass–epoxy was 55.6%.

When the volume fraction of the glass–epoxy was 17.2% (0C: 20.7%, ±45G: 17.2%, ±45C: 41.4%, 90C: 20.7%), type G yielded the highest bearing strength (941 MPa) and type H yielded the lowest bearing strength (834 MPa), the difference being 107 MPa as shown in Fig. 7.

From Fig. 7a and b, it was found that the bearing strength was dependent on the location of the ±45G and ±45C plies. The difference in bearing strengths between types A–G composites and types H–N composites was about 60 MPa, although the only difference in the two types of composites was the location of the ±45G plies. Therefore, it was concluded that the location of the ±45G plies was important for the bolted joint in composite materials.

When the 90C plies were located in the vicinity of the ±45G plies (type F) and the ±45C plies were located in the vicinity of the ±45G plies (type M), the bearing strength of type F was higher than that of type M. Similarly, type B as shown in Fig. 8a, where the ±45G plies are located between the 0C and the ±45C plies, had a lower bearing strength than

that of type I as shown in Fig. 8b, where the $\pm$45G plies were located between the $\pm$90C and the $\pm$45C plies. Therefore, it was concluded that the interlaminar stress concentration was decreased due to the smaller difference in stiffness of each ply when the $\pm$45G plies were located between the 90C and the $\pm$45C plies.

When the volume fraction of the glass–epoxy was 35.8% (0C: 21.4%, $\pm$45G: 35.8%, $\pm$45C: 21.4%, 90C: 21.4%), type G yielded the highest bearing strength (917 MPa) and type F yielded the lowest bearing strength (792 MPa), as shown in Fig. 9.

When the volume fraction of the glass–epoxy was 55.6% (0C: 22.2%, $\pm$45G: 55.6%, $\pm$45C: 0%, 90C: 22.2%), type G yielded the highest bearing strength (788 MPa) and type C yielded the lowest bearing strength (695 MPa), as shown in Fig. 10.

Figure 11 shows the bearing strength with respect to the volume fraction of glass–epoxy in the hybrid composites. As shown in Fig. 11, the bearing strength decreased for all the stacking sequences as the volume fraction of glass–epoxy was increased. In case of type A, the bearing strengths of joints for the pure carbon–epoxy and the pure glass–epoxy are also presented in Fig. 11. Although glass–epoxy is cheaper and more impact-resistant than carbon–epoxy, it is important to determine an appropriate volume fraction of glass–epoxy as the bearing strength of the joint decreases as the volume fraction of glass–epoxy increases.

When the stacking sequence of the hybrid composite was $[0G/\pm45C/90G]_S$, where the volume fractions for glass–epoxy and carbon–epoxy were 35.8 and 64.2%, respectively (0G: 17.9%, $\pm$45C: 64.2%, 90G: 17.9%), the specimens with seven different stacking sequences, as shown in Table 4, were tested.

In this case it was found that the bearing strength increased as the volume fraction of the $\pm$45C plies was increased, which is a similar

Table 3. Stacking sequences of the hybrid composites $[0C/\pm45G/\pm45C/90C]_S$

Stacking pattern[1]	Type	Stacking sequence
$[0C/\pm45G/\pm45C/90C]_S$0C: 20.7% $\pm$45G: 17.2% $\pm$45C: 41.4%90C: 20.7%	A	$[(0C)_2/(\pm45C)_2/\pm45G/(90C)_2]_S$
	B	$[(90C)_2/(\pm45C)_2/\pm45G/(0C)_2]_S$
	C	$[(\pm45C)_2/\pm45G/(0C)_2/(90C)_2]_S$
	D	$[(90C)_2/(0C)_2/(\pm45C)_2/\pm45G]_S$
	E	$[(0C)_2/(90C)_2/(\pm45C)_2/\pm45G]_S$
	F	$[(\pm45C)_2/(0C)_2/(90C)_2/\pm45G]_S$
	G	$[+45C/-45C/+45C/(0C)_2/-45C/+45G/-45G/(90C)_2]_S$
	H	$[(0C)_2/\pm45G/(\pm45C)_2/(90C)_2]_S$
	I	$[(90C)_2/\pm45G/(\pm45C)_2/(0C)_2]_S$
	J	$[\pm45G/(\pm45C)_2/(0C)_2/(90C)_2]_S$
	K	$[(90C)_2/(0C)_2/\pm45G/(\pm45C)_2]_S$
	L	$[(0C)_2/(90C)_2/\pm45G/(\pm45C)_2]_S$
	M	$[\pm45G/\pm45C/(0C)_2/(90C)_2/\pm45C]_S$
	N	$[+45G/-45G/+45C/(0C)_2/-45C/+45C/-45C/(90C)_2]_S$
$[0C/\pm45G/\pm45C/90C]_S$0C: 21.4% $\pm$45G: 35.8% $\pm$45C: 21.4%90C: 21.4%	A	$[(0C)_2/\pm45C/(\pm45G)_2/(90C)_2]_S$
	B	$[(90C)_2/\pm45C/(\pm45G)_2/(0C)_2]_S$
	C	$[\pm45C/(\pm45G)_2/(0C)_2/(90C)_2]_S$
	D	$[(90C)_2/(0C)_2/\pm45C/(\pm45G)_2]_S$
	E	$[(0C)_2/(90C)_2/\pm45C/(\pm45G)_2]_S$
	F	$[\pm45C/\pm45G/(0C)_2/(90C)_2/\pm45G]_S$
	G	$[+45C/-45C/+45G/(0C)_2/-45G/+45G/-45G/(90C)_2]_S$
	H	$[(0C)_2/(\pm45G)_2/\pm45C/(90C)_2]_S$
	I	$[(90C)_2/(\pm45G)_2/\pm45C/(0C)_2]_S$
	J	$[(\pm45G)_2/\pm45C/(0C)_2/(90C)_2]_S$
	K	$[(90C)_2/(0C)_2/(\pm45G)_2/\pm45C]_S$
	L	$[(0C)_2/(90C)_2/(\pm45G)_2/\pm45C]_S$
	M	$[(\pm45G)_2/(0C)_2/(90C)_2/(\pm45C)]_S$
	N	$[+45G/-45G/+45G/(0C)_2/-45G/+45C/-45C/(90C)_2]_S$
$[0C/\pm45G/\pm45C/90C]_S$0C: 22.2% $\pm$45G: 55.6% $\pm$45C: 0%90C:22.2%	A	$[(0C)_2/(\pm45G)_3/(90C)_2]_S$
	B	$[(90C)_2/(\pm45G)_3/(0C)_2]_S$
	C	$[(\pm45G)_3/(0C)_2/(90C)_2]_S$
	D	$[(90C)_2/(0C)_2/(\pm45G)_3]_S$
	E	$[(0C)_2/(90C)_2/(\pm45G)_3]_S$
	F	$[(\pm45G)_2/(0C)_2/(90C)_2/\pm45G]_S$
	G	$[+45G/-45G/+45G/(0C)_2/-45G/+45G/-45G/(90C)_2]_S$

[1]C, Carbon–epoxy; G, glass–epoxy.

trend to that found for $[0G/\pm45G/\pm45C/90G]_S$. Therefore, the specimens with $[0G/\pm45C/90G]_S$ (0G: 17.9%, $\pm45C$: 64.2%, 90G: 17.9%), which had a high of volume fraction of $\pm45C$ plies, were tested. Type G yielded the highest bearing strength (974 MPa) and type C yielded the lowest bearing strength (839 MPa), as shown in Fig. 12.

As it was found that the bearing strength of $[0_2/(\pm45)_3/90_2]_S$ was similar to that of $[0_2/(\pm30)_3/90_2]_S$ from the static test of glass–epoxy, type G of $[0C/\pm30G/\pm45C/90C]_S$ was also tested and compared to $[0C/\pm45G/\pm45C/90C]_S$. As shown in Fig. 13, when the volume fractions of the glass–epoxy were 17.2 and 35.8%, the bearing strength of the joint containing $\pm30G$ was a little higher than that of the $\pm45G$, while the bearing strength of the joint containing $\pm30G$ was a little lower than that of the $\pm45G$ when the volume fraction of the glass–epoxy was 55.6%.

The hybrid composites of type G $[0G/\pm45C/90G]_S$ (0G: 17.9%, $\pm45C$: 64.2%, 90G: 17.9%), which had the highest bearing strength, were tested with respect to the clamping pressure of the bolt and the outer diameter of the washer, when the inner diameter of the washer was same as that of the bolt and the outer diameter of the washer was 20 mm. After lubricant was applied to the bolt threads to reduce the variation of preload, the clamping pressure was given

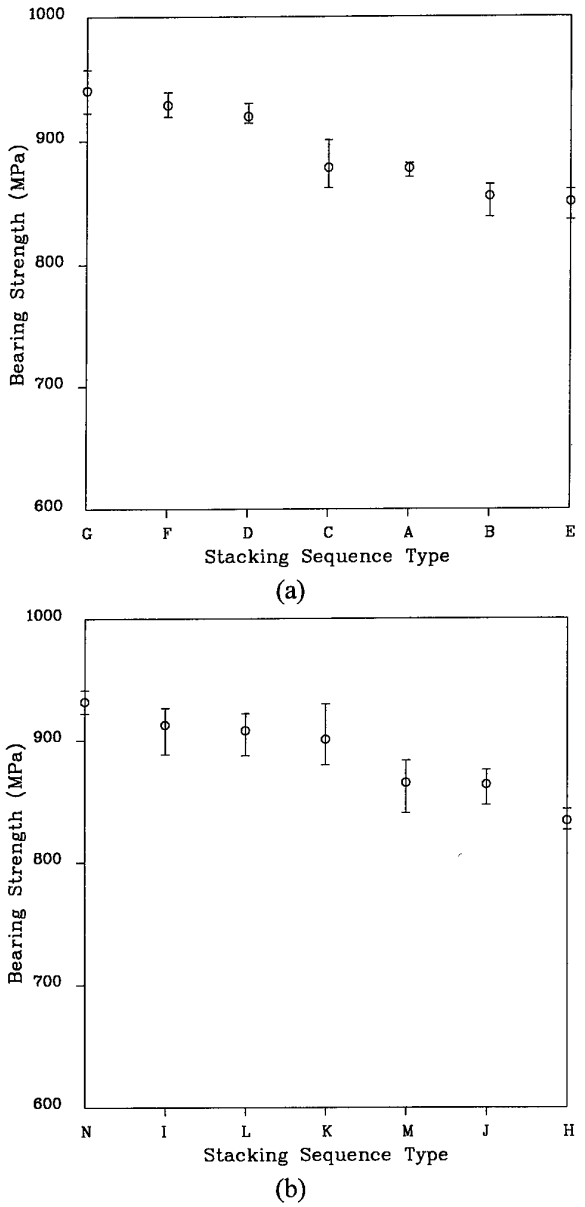

Fig. 7. Joint bearing strengths of the hybrid joints with respect to stacking sequences ($[0C/\pm45G/\pm45C/90C]_S$ (0C, 90C: 20.7%, $\pm45G$: 17.2%, $\pm45C$: 41.4%)). (a) Type A–type G. (b) Type H–type N.

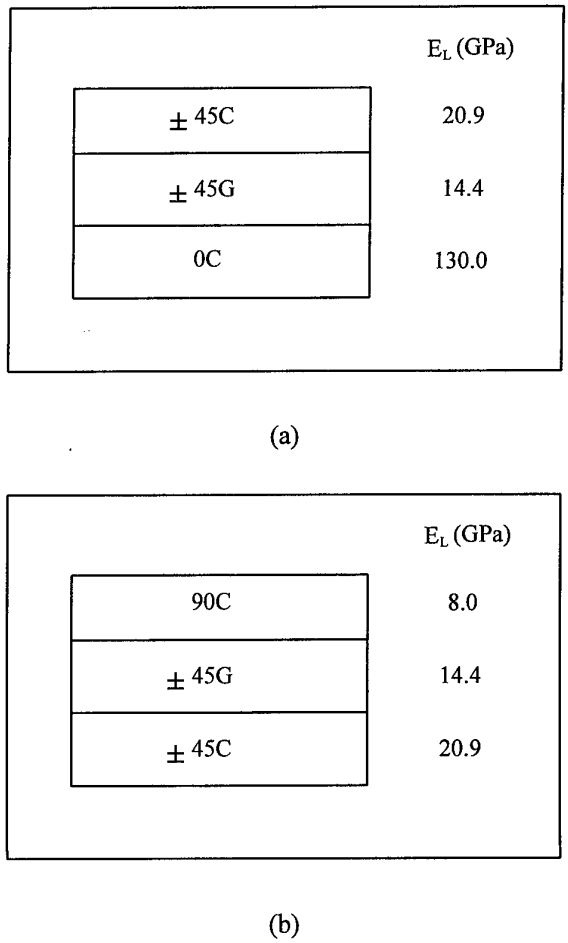

Fig. 8. Effective longitudinal modulus of the plies in the vicinity of the $\pm45G$ ply. (a) Case of low bearing strength (type B). (b) Case of high bearing strength (type I).

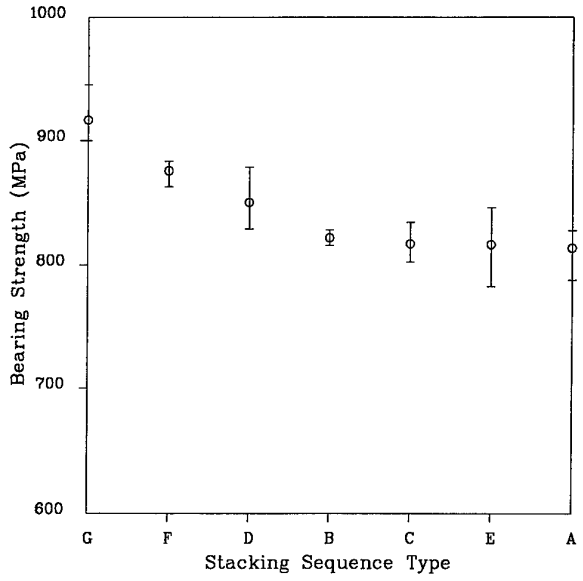

(a)

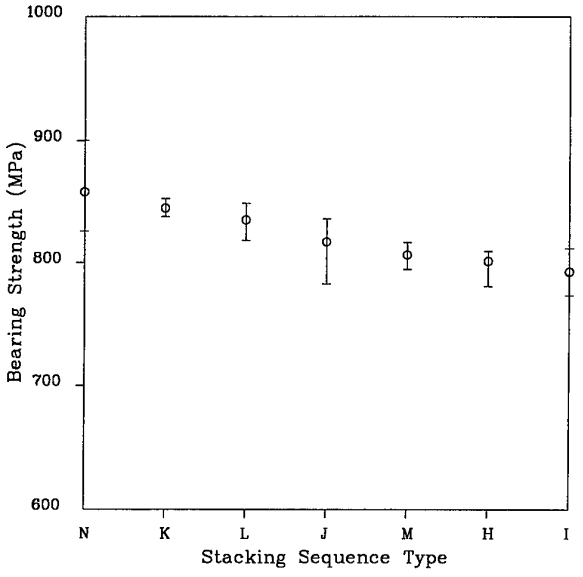

(b)

Fig. 9. Joint bearing strengths of the hybrid joints with respect to stacking sequences ($[0C/\pm45G/\pm45C/90C]_S$ (0C, 90C: 21.4%, $\pm45G$: 35.8%, $\pm45C$: 21.4%)). (a) Case of type A–type G. (b) Case of type H–type N.

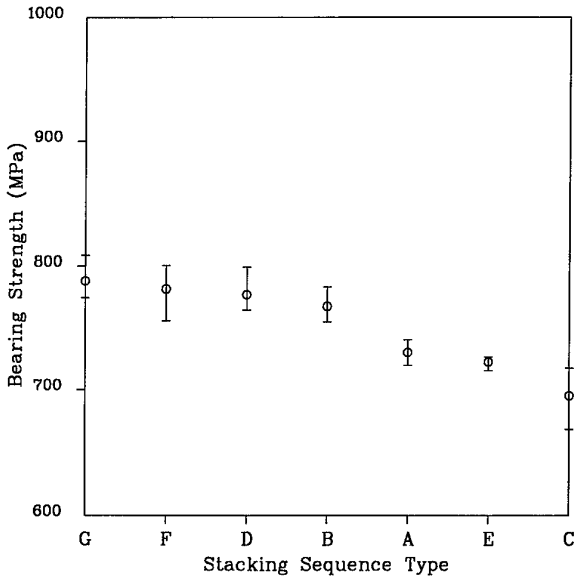

Fig. 10. Joint bearing strengths of the hybrid joints with respect to stacking sequences ($[0C/\pm45G/\pm45C/90C]_S$ (0C, 90C: 22.2%, $\pm45G$: 55.6%, $\pm45C$: 0%)).

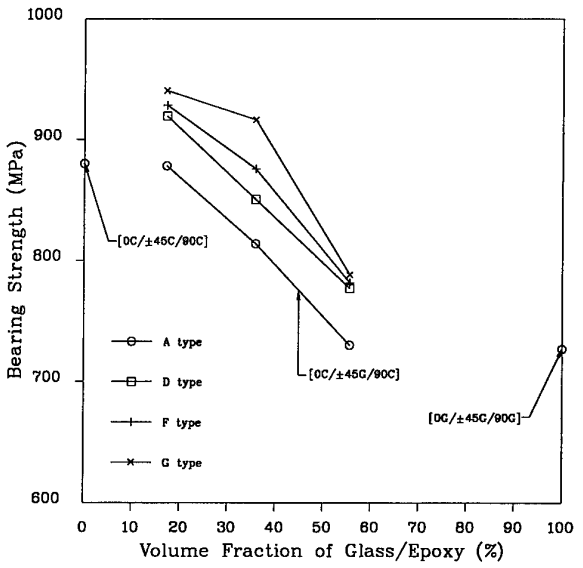

Fig. 11. Bearing strengths with respect to the volume fraction of the glass–epoxy and laminate type.

Table 4. Stacking sequences of the hybrid composites $[0G/45C/90G]_S$

Stacking pattern[1]	Type	Stacking sequence
$[0G/\pm45C/90G]_S$	A	$[(0G)_2/(\pm45C)_3/(90G)_2]_S$
0G: 17.9%	B	$[(90G)_2/(\pm45C)_3/(0G)_2]_S$
$\pm45C$: 64.2%	C	$[(\pm45C)_3/(0G)_2/(90G)_2]_S$
90G: 17.9%	D	$[(90G)_2/(0G)_2/(45C)_3]_S$
	E	$[(0G)_2/(90G)_2/(\pm45C)_3]_S$
	F	$[(\pm45C)_2/(0G)_2/(90G)_2/\pm45C]_S$
	G	$[+45C/-45C/+45C/(0G)_2/-45C/+45C/-45C/(90G)_2]_S$

[1]C, Carbon–epoxy; G, glass–epoxy.

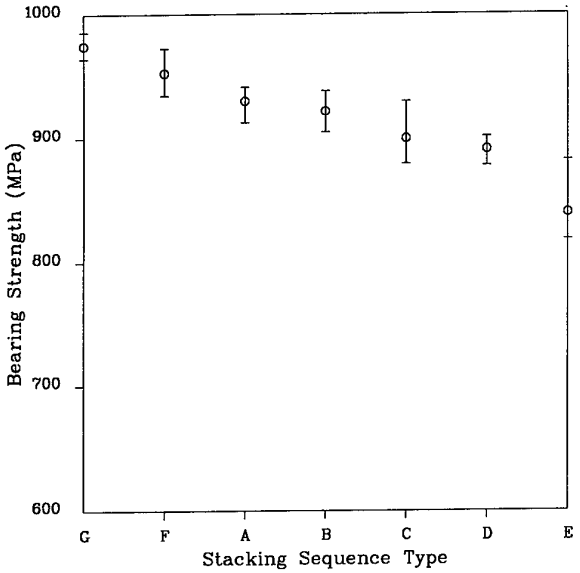

Fig. 12. Joint bearing strengths of the hybrid joints with respect to stacking sequence ($[0G/\pm45C/90G]_S$ (0G, 90G: 17.9%, ±45C: 64.2%)).

by a torque wrench [28]. The torque T (N·m) required for a given axial preload F(N) is calculated as follows [29]

$$T = KF\frac{d}{1000} \tag{2}$$

where K is the torque factor (0.2 on average) and d is the nominal bolt diameter (mm). Then eqn (2) becomes

$$\sigma_{press} = \frac{T}{\frac{\pi}{4}Kd(d_w^2 - d^2)} \tag{3}$$

or

$$\sigma_{press}\ (\text{MPa}) = 2.37T\ (\text{N·m}) \tag{4}$$

where d_w is the outer diameter of the washer. The torque range used was 0–40 N·m, which was 0–95 MPa in terms of the axial load. Figure 14 shows the bearing strength with respect to clamping pressure. As shown in Fig. 14, the bearing strengths of the hybrid composites were increased as the clamping pressure was increased up to 71.1 MPa, and it then converged to a constant value which was 1.3 times higher than the value without preload.

The bolted joints for the hybrid composites were tested by varying the outer diameter of the washer, ranging from 1.5d (12 mm) to 4.5d (36 mm) when the inner diameter of the washer and the clamping pressure of the bolt were 8 mm and 23.7 MPa, respectively. As shown in Fig. 15, as the outer diameter of the washer was increased up to 2.5d (20 mm), the bearing strength was increased and then saturated. When the outer diameter of the washer was smaller than 2.5d (20 mm) bearing failure occurred; however, tension failure occurred

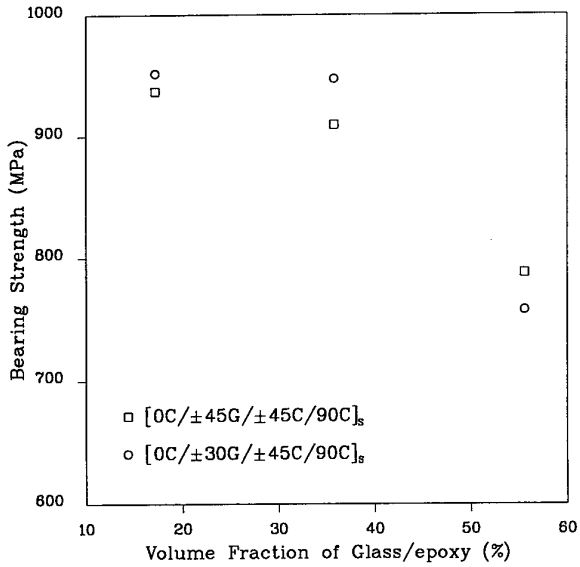

Fig. 13. Bearing strengths of the $[0C/\pm45G/\pm45C/90C]_S$ and $[0C/\pm30G/\pm45C/90C]_S$ with respect to the volume fraction of the glass–epoxy. (All cases are type G.)

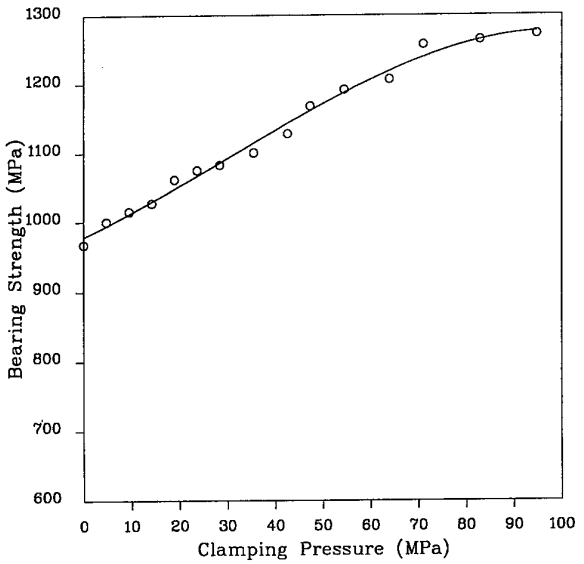

Fig. 14. Bearing strength with respect to the clamp-up pressure for type G of $[0G/\pm45C/90G]_S$ (washer outer diameter = 20 mm).

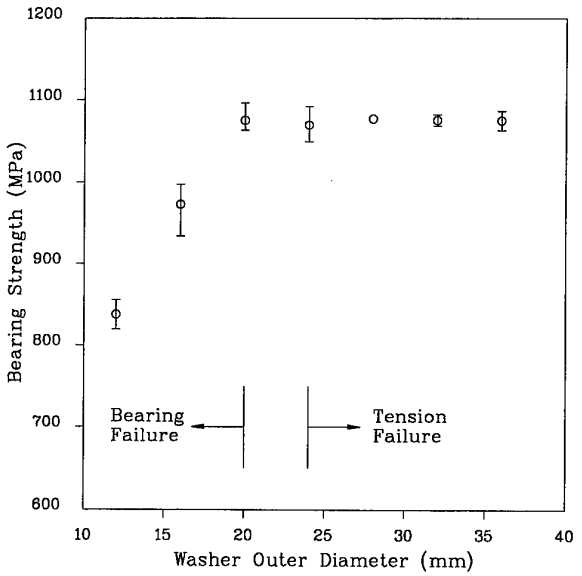

Fig. 15. Bearing strength with respect to the outer diameter of the washer for type G of $[0G/\pm 45C/90G]_S$ (clamping pressure = 23.7 MPa).

when the outer diameter was larger than $3d$ (24 mm) because the gap distance (w') between the washer edge and the specimen edge was reduced, as shown in Fig. 16, as the washer size was increased.

STRESS ANAYSIS

Because delamination on the loaded side of the holes and the extensive damage at the washer outside edge were found from the joint tests of the hybrid composites, delamination of the bolted joints for the hybrid composite materials was investigated using ANSYS, a commercial finite-element software, and compared with the experimental results. A cosine load distribution was used for the contact force between the composites and the bolt. The solid 46 element of the ANSYS element library, which enables the assignment of the ply angle, stacking sequence and ply thickness, was used for the stress analysis. Figure 17 shows the finite-element model for the bolted joint. Owing to symmetry, only a quarter of the laminate was modeled and the finger-tightened washer effect was simulated by constraining the z-direction displacements of the elements under the washer.

The delamination of the hybrid composites was predicted using the Ye-delamination failure

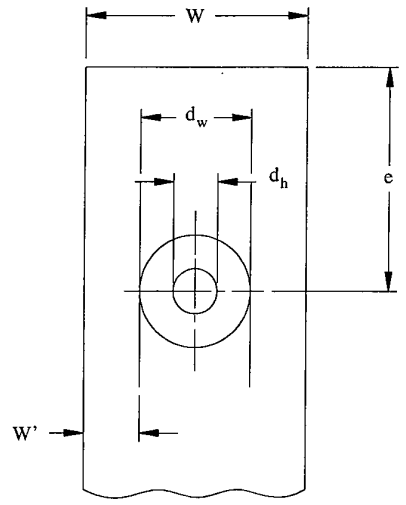

Fig. 16. Geometry of the hole and washer.

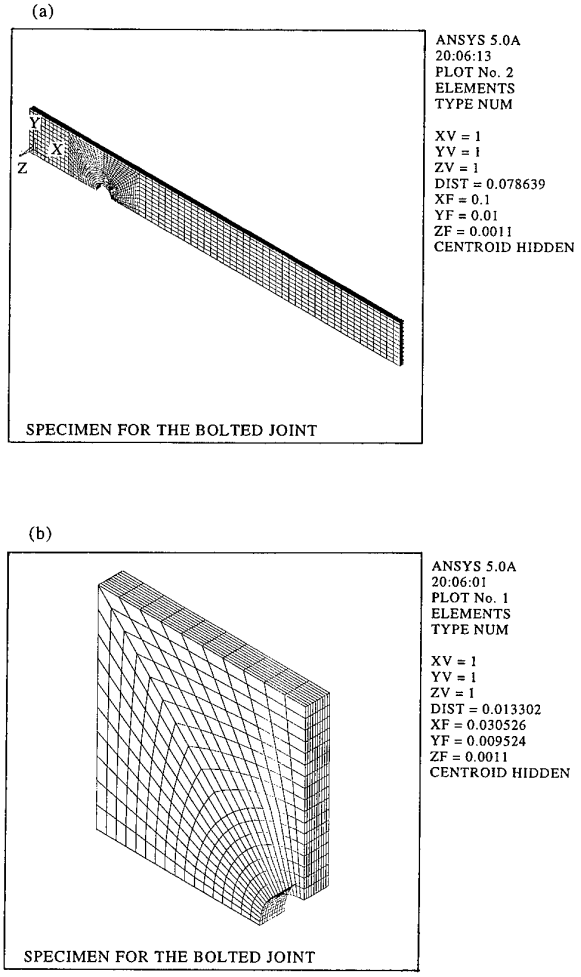

Fig. 17. Finite-element model for the bolted joint.

criterion, which is depicted in the following [30]

$$\left(\frac{\sigma_{33}}{Z_t}\right)^2+\left(\frac{\sigma_{13}}{R}\right)^2+\left(\frac{\sigma_{23}}{T}\right)^2\geq 1 \text{ for } \sigma_{33}>0 \tag{5a}$$

or

$$\left(\frac{\sigma_{13}}{R}\right)^2+\left(\frac{\sigma_{23}}{T}\right)^2\geq 1 \text{ for } \sigma_{33}<0 \tag{5b}$$

where Z_t is the interlaminar tensile strength, and R and T are the interlaminar shear strengths in the 1–3 and 2–3 directions, respectively. The material properties in Table 1 were used and the interlaminar tensile strength was assumed to be equal to the transverse tensile strength, Y_t. The interlaminar shear strengths R and T were assumed to be equal to the in-plane shear strength, S, and the out-of plane shear moduli, G_{13} and G_{23}, were assumed to be equal to the in-plane shear modulus, G_{LT}.

The load condition of stress analyses was the cosine distribution, of which the x-directional resultant force was 10 kN.

The hybrid composites of $[0G/\pm 45C/90G]_S$ with seven different stacking sequences were analyzed and compared with the experimental results. The analysis results predicted the first peak load (A in Fig. 4), however, it could not predict the maximum failure load. Figure 18a and b show experimental and FEM results.

For a more accurate prediction of the joint strength it might be necessary to include the effects of the material non-linearity, the friction between the washer and the laminate, as well as between the bolt and the laminate, and the stiffness reduction due to failure during analysis.

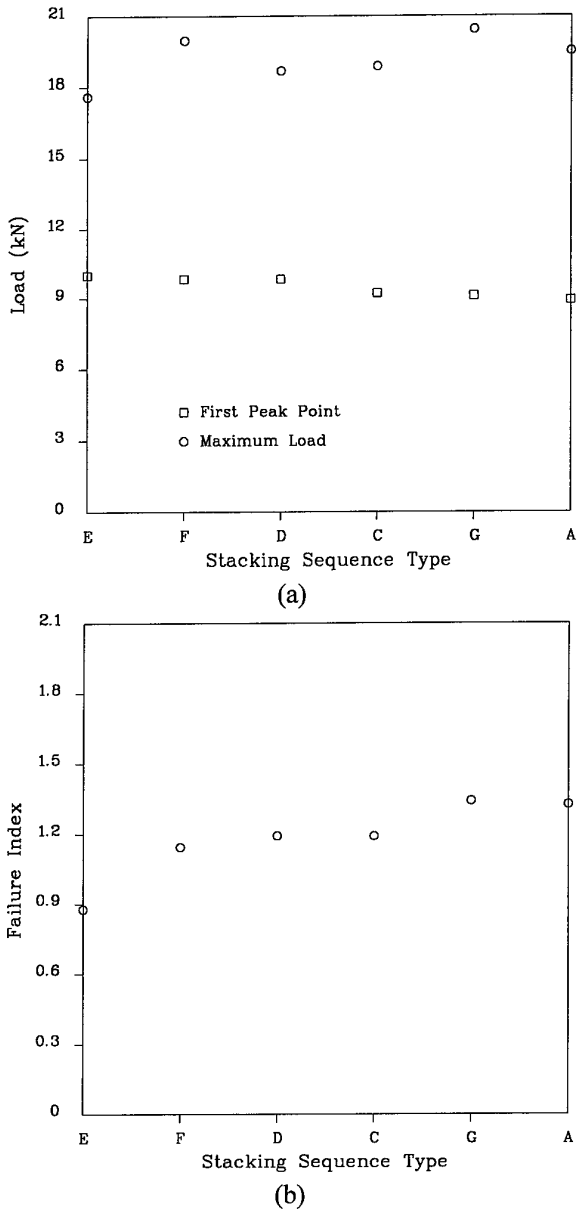

Fig. 18. Comparison of experimental results with the FEM calculated failure index result of the joints when the external load was 10 kN ($[0G/\pm 45C/90G]_S$ (0G, 90G: 17.9%, $\pm 45C$: 64.2%)). (a) Experimental results. (b) FEM results.

CONCLUSIONS

In this work, the optimum conditions of bolted joints for the hybrid composite materials composed of glass–epoxy and carbon–epoxy under tensile loading were investigated. The design parameters investigated were ply angle, stacking sequence, the ratio of glass–epoxy to carbon–epoxy, the outer diameter of the washer and the clamping pressure. From the test results the following conclusions were made.

1. A peak load occurred before the maximum failure load, which was due to delamination of the laminate under the washer. At the maximum failure load, delamination on the loaded side of the hole and the extensive buckling of plies at the washer outside edge were found.
2. From the static test results of the hybrid composites with stacking sequences of $[0C/\pm 45G/\pm 45C/90C]_S$ and $[0G/\pm 45C/90G]_S$ (C: carbon–epoxy, G: glass–epoxy), it was found that the bearing strength increased as

the ± 45 plies were distributed evenly in the thickness direction, irrespective of the ratio of glass–epoxy to carbon–epoxy and the stacking pattern.

3. The bolted joint of $[+45C/-45C/+45C/(0G)_2/-45C/+45C/-45C/(90G)_2]_S$, which has a 35.5% volume fraction of glass–epoxy, yielded the highest bearing strength. In this case, the bearing strength increased as the clamping pressure of the bolt increased up to 71.1 MPa, then the bearing strength saturated to a constant value. When the washer outer diameter was 20 mm, the failure mode was changed from bearing to tension. Therefore, the stacking sequence of $[+45C/-45C/+45C/0G_2/-45C/+45C/-45C/90G_2]_S$ would be the most suitable one. Also the clamping pressure should be larger than 70 MPa and the outer diameter of the washer should be 20 mm, respectively.
4. The finite-element analysis predicted the first peak load, however, it could not predict the maximum failure load. For a more accurate prediction of the joint strength it might be necessary during the analysis to include the effects of the material non-linearity, the friction between the washer and the laminate, and between the bolt and the laminate, and the stiffness reduction due to failure.

ACKNOWLEDGEMENTS

This research was supported financially by the Korean Ministry of Science and Technology under the international collaboration research between KAIST and France (FRAMASOFT+CSI).

REFERENCES

1. Mallick, P. K., *Fiber-reinforced Composites*. Marcel Dekker, New York, 1988, pp. 3–4.
2. Schwartz, M. M., *Composite Materials Handbook*. McGraw-Hill, New York, 1984, Chap. 7.
3. Reugg, C. & Habermeir, J., Composite propeller shafts design and optimization. In *Advanced Composite Material Proc. ICCM 3*, Vol. 2, ed. A. Bunsell *et al.*, Pergamon Press, Oxford, 1980, pp. 1740–55.
4. Lee, D. G., Sin, H. C. and Suh, N. P., Manufacturing of a graphite epoxy composite spindle for a machine tool. *Ann. CIRP*, 1985, **27**, (1), 365–369.
5. Lee, D. G., Kim, K. S. and Kwak, Y. K., Manufacturing of a SCARA type direct-drive robot with graphite fiber epoxy composite material. *Robotica*, 1991, **9**, 219–229.
6. Reinhart, T. J., *Composites — Engineered Materials Handbook*, Vol.1. ASM International, 1987, pp. 665–728.
7. Vinson, J. R. & Sierakowski, R. L., *The Behavior of Structure Composed of Composite Materials*. Martinus Nijhoff, 1989, pp. 239–83.
8. Matthews, F. L., *Joining Fibre-reinforced Plastics*. Elsevier Applied Science, London, 1987.
9. Collings, T. A., On the bearing strength of CFRP laminates. *Composites*, 1982, **13**, 241–252.
10. Eriksson, I., On the bearing strength of bolted graphite/epoxy laminates. *J. Composite Mater.*, 1990, **24**, 1246–1249.
11. Quinn, W. J. and Matthews, F. L., The effect of stacking sequence on the pin-bearing strength in glass fibre reinforced plastics. *J. Composite Mater.*, 1977, **11**, 139–142.
12. Herrington, P. D. and Sabbaghian, M., Effect of radial clearance between bolt and washer on the bearing strength of composite bolted joints. *J. Composite Mater.*, 1992, **26**, 1826–1843.
13. Godwin, E. W. and Matthews, F. L., A review of the strength of joints in fibre-reinforced plastics. Part I. mechanically fastened joints. *Composites*, 1980, **11**, 155–160.
14. Collings, T. A., The strength of bolted joints in multi-directional CFRP laminates. *Composites*, 1977, **8**, 43–54.
15. Smith, P. A., Pascoe, K. J., Polak, C. and Stroud, D. O., The behavior of single-lap bolted joints in CFRP laminates. *Composite Struct.*, 1986, **6**, 41–55.
16. Kim, R. Y. and Whitney, J. M., Effect of temperature and moisture on the pin-bearing strength of composite laminates. *J. Composite Mater.*, 1976, **10**, 149–151.
17. Akay, M., Bearing strength of as-cured and hygrothermally conditioned carbon fiber/epoxy composites under static and dynamic loading. *Composites*, 1992, **23**, 101–108.
18. Waszczak, J. P. and Cruse, T. A., Failure mode and strength prediction of anisotropic bolt bearing specimens. *J. Composite Mater.*, 1971, **5**, 421–425.
19. Agarwal, B. L., Static strength prediction of bolted joints in composite material. *AIAA J.*, 1980, **18**, 1371–1375.
20. Soni, S. R., Failure analysis of composite laminates with a fastener hole. In *Joining of Composite Materials*, ASTM STP 749, ed. K. T. Kedward. American Society for Testing and Materials, 1981, pp. 145–64.
21. Chang, F. K., Scott, R. A. and Springer, G. S., Failure of composite laminates containing pin-loaded holes — method of solution. *J. Composite Mater.*, 1984, **18**, 255–278.
22. Chen, W. H., Lee, S. S. and Yeh, J. T., Three-dimensional contact stress analysis of a composite laminate with bolted joint. *Composite Struct.*, 1995, **30**, 287–297.
23. Graham, U., Wisnom, M. R. and Webber, J. P. H., A novel finite element investigation of the effects of washer friction in composite plates with bolt-filled holes. *Composite Struct.*, 1994, **29**, 329–339.
24. Smith, P. A., Ashby, M. F. and Pascoe, K. J., Modelling clamp-up effects in composite bolted joints. *J. Composite Mater.*, 1987, **21**, 878–897.
25. Hancox, N. L., *Fibre Composite Hybrid Materials*. Applied Science, London, 1981.
26. Matthews, F. L., Roshan, A. A. and Phillips, L. N., The bolt bearing strength of glass/carbon hybrid composites. *Composites*, 1982, **13**, 225–227.

27. Kretsis, G. and Matthews, F. L., The strength of bolted joints in glass fiber/epoxy laminates. *Composites*, 1985, **16**, 92–102.
28. Bickford, J. H., *An Introduction to the Design and Behavior of Bolted Joints*. Marcel Dekker, New York, 1981.
29. Edwards, K. S., Jr & Robert, B. McKee, *Fundamentals of Mechanical Component Design*. McGraw-Hill, New York, 1991.
30. Chen, W. H. and Lee, S. S., Numerical and experimental failure analysis of composite laminates with bolted joints under bending loads. *J. Composite Mater.*, 1995, **29**, 15–36.

ELSEVIER

Composite Structures Vol. 38, No. 1–4, pp. 343–350, 1997
© 1997 Elsevier Science Ltd. All rights reserved
Printed in Great Britain
0263-8223/97/$17.00 + 0.00

PII:S0263-8223(97)00069-X

Investigation on cutting mechanism in small diameter drilling for GFRP (thrust force and surface roughness at drilled hole wall)

K. Ogawa,[a] E. Aoyama,[b] H. Inoue,[c] T. Hirogaki,[d] H. Nobe,[e] Y. Kitahara,[f] T. Katayama[b] & M. Gunjima[a]

[a]*Doshisha University, Kyoto 610-03, Japan*
[b]*Faculty of Engineering, Doshisha University, Kyoto 610-03, Japan*
[c]*Faculty of Engineering, University of Osaka Prefecture, Osaka 590, Japan*
[d]*School of Engineering, University of Shiga Prefecture, Shiga 522, Japan*
[e]*Akamatsu Forging Ltd, Osaka 537-01, Japan*
[f]*Osaka Prefectural Industrial Technology Research Institute, Osaka 590-02, Japan*

This study describes the relation between the cutting force and the surface roughness of a drilled hole wall in small-diameter drilling of GFRP for a printed wiring board. In order to investigate the characteristics of small diameter drilling for GFRP, the surface of the drilled hole wall is observed by SEM, and the surface roughness along the feed direction is measured at various edge position angles of the drilled hole. The cutting force during drilling is measured. Moreover, the thrust force is devided into two components (the static component and the dynamic component). It is shown that the dynamic components are related with the surface roughness of the drilled hole wall. In conclusion, it is found that the major cutting edge of the drill is more influential in the quality of the drilled hole wall than the chisel edge of the drill in small diameter drilling of PWB. © 1997 Elsevier Science Ltd.

INTRODUCTION

Recently, one requirement has been that the packaging density of printed wiring boards (PWB) be improved because high packaging density technology has allowed downsizing. For example, from a general public of view, televisions and telephones are typical cases of downsizing, so that their use has changed from stationary to portable. From an industrial point of view, computing speed and memory size are increasing. Therefore, high-quality micromachinings are necessary for PWB. Especially, it is necessary that a great number of through-holes can be drilled with high reliability to make a circuit. So it is required to clarify the cutting mechanism of small diameter drilling in order to improve the quality of the drilled hole on PWB. On the other hand, printed wiring boards are often made of glass fibre reinforced plastics (GFRP). There are a few studies which have mainly dealt with the machined surface conditions of FRP [1–8]. But there are few studies which have dealt with the cutting force during drilling the small diameter hole. Hence, in this study, the relation between the thrust force and the surface roughness at the drilled hole wall is given attention in order to investigate the cutting mechanism in small diameter drilling for GFRP.

First, to investigate the drilled hole quality in detail, the surface roughness of the hole wall along the feed direction is measured, and the hole surface is observed by SEM. It is found that the surface roughness has different characteristics at the each edge position angle.

Second, the thrust force is measured to research the cutting mechanism in small diameter drilling for PWB under various cutting speeds and feed rates. The investigation is

carried out from the point of view of the relation between the thrust force and the process of drilling. As a result, it is found that there is a large variation in the thrust force because of the different forces between for resin and for fibres in the laminate. So, to evaluate the cutting mechanism, we utilize a method of dividing the thrust force into two components, its mean value (named the static component) and the magnitude of variation (named the dynamic component). It is found that the dynamic component and the static component are affected by the cutting speed and the feed rate.

Third, drilling for various pre-hole workpieces is carried out to research a distribution of those force components along the radius direction of the point (the chisel edge and the major cutting edge) of the small diameter drill. The static component and the dynamic component increase as the pre-hole diameter decreases. Especially, when the pre-hole diameter is smaller than the chisel edge diameter, the static component increases greatly. However, the increase rate of the dynamic component is not as large as that of the static component in such small pre-hole diameters. As a result, it is clear that the static component mainly occurs at the chisel edge of the drill and the dynamic component is mainly occurs at the major cutting edge of the drill. Therefore, it is found that the static component influences on a cutting phenomenon occur at the chisel edge of the drill and the dynamic component influences on a cutting phenomenon occur at the major cutting edge of the drill.

Finally, to investigate the influence of the thrust force on the surface roughness at the drilled hole wall, the surface roughness is measured in detail under various drilling conditions. It is found out that the surface roughness is affected by the cutting speed and the feed rate. Compared with results of the thrust force measurement, it is clarified that the surface roughness is related to the dynamic component more than the static component in small diameter drilling, i.e. the dynamic component is influential in the surface roughness.

EXPERIMENTAL EQUIPMENT AND MATERIALS

An NC-drilling machine is used in the experiments. Cemented carbide drills for PWB are used, and the diameter is 1.0 mm. The drilling conditions are 5000–12000 rpm spindle speeds and 5–63 μm/rev feed rates.

Drilled GFRP is glass (39% in weight)–epoxy resin, plain woven cloth and thickness 1.6 mm. This workpiece is a copper clad laminate (consisting of eight plies) for PWB. The filaments are 9 μm, and the width of yarn is about 500 μm in the laminate. An aluminum plate is used as a top stiffener and a bakelite plate is used as a bottom stiffener to prevent burr and delamination at the hole entrance and exit, as is usual with small diameter drilling for PWB.

The thrust force (a feed direction component of the cutting forces) is measured by a piezoelectric dynamometer mounted on the table of the drilling machine and the force is recorded through a charge-amplifier on a data-recorder. The hole surface is observed by a scanning electron microscope (SEM), and the surface roughness (maximum peak-to-valley; R_{max}) of the hole wall is measured along the feed direction by a stylus profile meter.

RESULTS AND DISCUSSION

Influence of drilling conditions on surface roughness

In general, it is necessary to take into account the fibre angle 0–180°, the relative angle between the cutting direction and the fibre direction. Therefore, in the case of the plain woven cloth, the edge position angle γ (0–180°), as shown in Fig. 1, is defined in this paper. The relationship between the edge position angle γ and the fibre angle θ is also shown in this figure. Hence, when regarding the direction of warp yarn and weft yarn, it is necessary to asses the damage along the half circumference of the drilled hole.

Figure 2 shows the relationship between the edge position angle and the hole surface roughness measured along the feed direction. From this figure, the surface roughness value becomes maximum at edge position angles of 30° and 120°, compared with other angles. There is little difference in the surface roughness values between the two edge position angles (30/120°). Therefore, it is not necessary to take account of the directions of warp and weft yarns. After this, we take notice of the surface roughness at the edge position angle 30°.

Figure 3 shows the high magnification SEM photograph of the drilled surface at the edge position angle 30°. In this figure, fibre buckling is observed. At this edge position angle, there are two fibre angles (30/120°). The buckling occurs at the 30° fibre angle, and not at 120°. Therefore, the surface roughness increases at the edge position angle of 30°.

Figure 4 shows the relationship between the cutting speed and the surface roughness. Figure 5 shows the relationship between the feed rate and the surface roughness. The surface roughness increases slightly in proportion to the cutting speed as shown in Fig. 4. On the other hand, the surface roughness increases largely in proportion to the feed rate as shown in Fig. 5. Therefore, it is found that the feed rate is more influential in the surface roughness of a drilled hole wall than the cutting speed.

Cutting force during drilling

As stated in Section 3.1, the surface roughness of the drilled hole wall increases as the cutting speed and the feed rate increase, but the feed rate is more influential than the cutting speed.

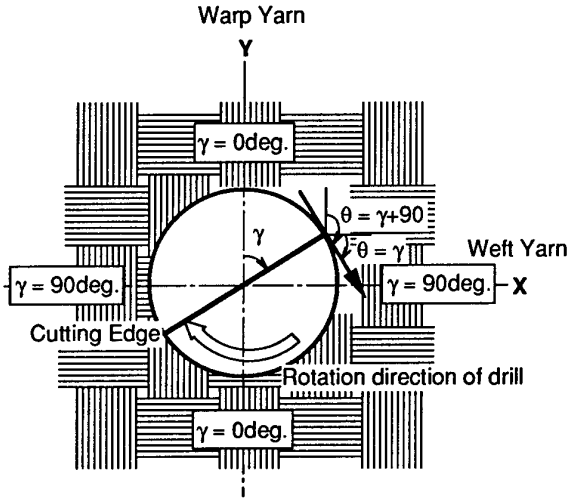

Fig. 1. The definintion of the edge position angle (γ°) and the fiber angle (θ°).

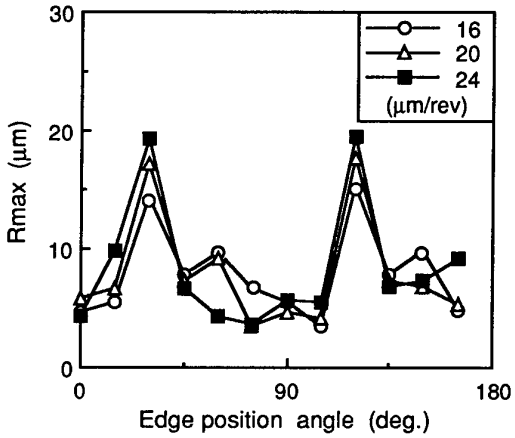

Fig. 2. The edge position angle and the surface roughness (maximum peak-to-valley; R_{max}).

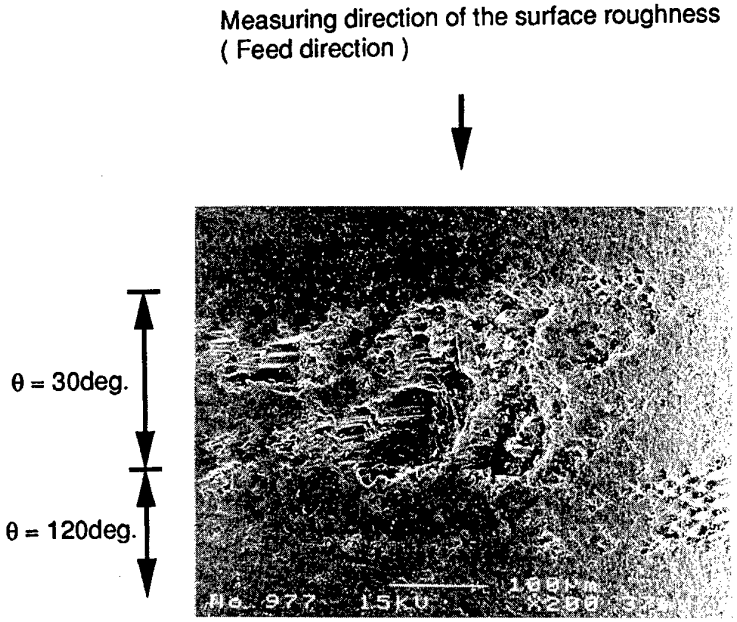

Fig. 3. The high magunifacation SEM photograph of the drilled srface (Cutting speed = 15.7 m/min, Feed rate = 20 μm/rev, γ = 30°).

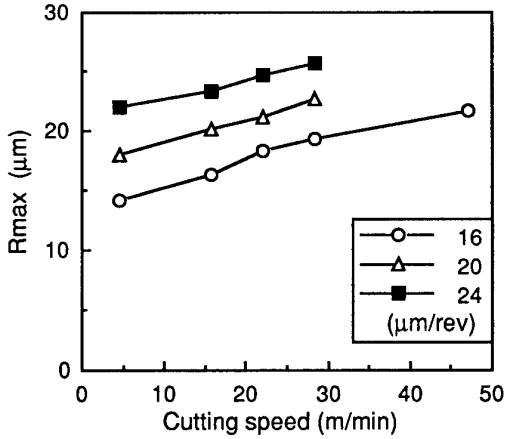

Fig. 4. The cutting speed and the surface roughness ($\gamma = 30°$).

On the other hand, the surface roughness increases due to the difference of the cutting states between fibre angle 30° and 120° at the edge position angle 30°. It is considered that the difference of the cutting states represents cutting forces. Thus, thrust force is considered as an influential factor in the surface roughness.

Figure 6 shows the thrust force during drilling in PWB. From this figure, it is found that the drill cuts the aluminum plate as a top stiffener, the upper copper foil, the laminate of GFRP (eight plies), the lower copper foil and the bakelite plate as a bottom stiffener in this order, and the thrust force has some peaks during that time. In particular, it is considered that variations in thrust force during drilling of the laminate part are caused by the different cutting characteristics of two materials of GFRP. In order to estimate the thrust force quantitatively, the mean value of the thrust

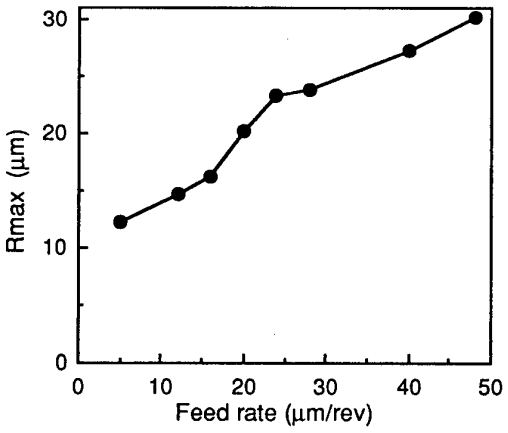

Fig. 5. The feed rate and the surface roughness (cutting speed = 15.7 m/min, $\gamma = 30°$).

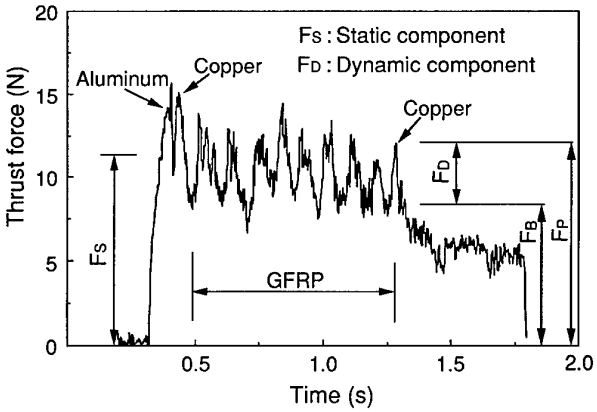

Fig. 6. The thrust force during drilling (cutting speed = 15.7 m/min, feed rate = 24 μm/rev).

forces is defined as the static component (we named F_S) and the magnitude of variations is defined as the dynamic component (we named F_D), moreover, peaks and valleys in eight variations are defined, respectively, as the maximum value (we named F_P) and as the minimum value (we named F_B). Those definitions are shown in Fig. 6.

Drilling condition and thrust force

In this section, the thrust force is measured in drilling various pre-hole diameters workpieces in order to evaluate the influence of the chisel edge on F_S and F_D. Figure 7(a) and (b) shows the relationship between the pre-hole diameter and F_S, F_D, respectively. F_S increases as the pre-hole diameter decreases as shown in Fig. 7(a). In particular, F_S increases sharply at the pre-hole diameter 0.4 mm or less. It can be seen that F_S at the chisel edge occurs most because the chisel edge diameter of the drill is about 0.4 mm. On the other hand, F_D increases slightly at the pre-hole diameter 0.4 mm or less as shown in Fig. 7(b). It can be seen that the major cutting edge of the drill is influential in F_D.

Figure 8 shows F_S and F_D under various feed rates, and Fig. 9 shows them under various cutting speeds. From Fig. 8, it is found that F_S and F_D increase as feed rate increases. On the other hand, as the cutting speed increases, F_D increases slowly, but F_S decreases a little as shown in Fig. 9. So, F_P and F_B are evaluated in detail to research the influential factors of F_S and F_D under various drilling conditions. Figure 10 shows F_P, F_B in drilling GFRP and F_S in drilling an epoxy plate under various feed

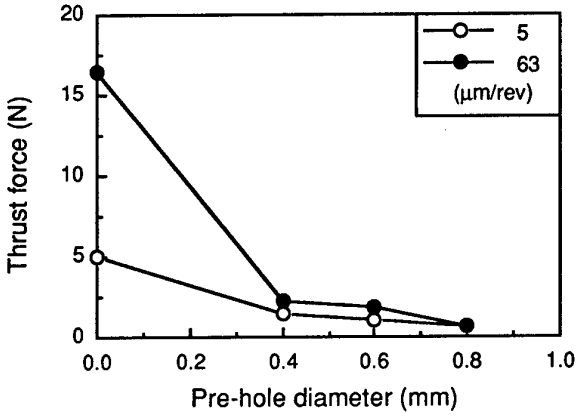

(a) Fs

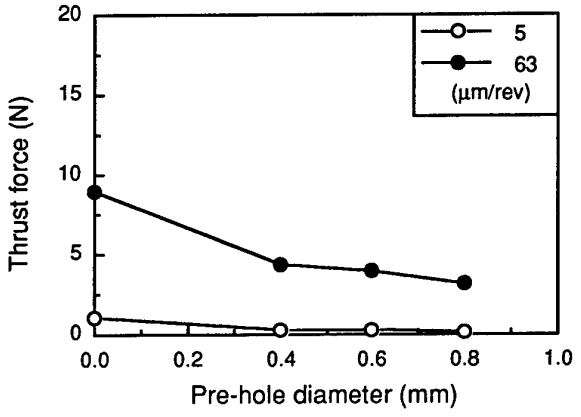

(b) FD

Fig. 7. The pre-hole diameter and the thrust force (cutting speed = 15.7 m/min).

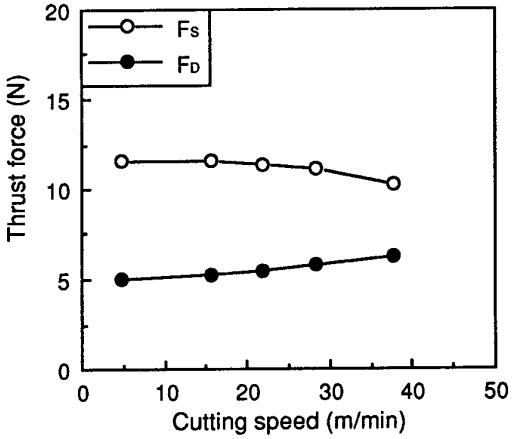

Fig. 9. The cutting speed and the thrust force (feed rate = 24 μm/rev).

rates. In the case of the epoxy plate, there are little differences of F_P and F_B (no existence of F_D). From that figure, the thrust force of drilling in the epoxy plate is almost same as F_B. Therefore, it can be mentioned that F_B is related with the thrust force for resin parts of GFRP in the case of this workpiece. On the other hand, it is considered that F_P is related with the thrust force for fibres. As shown in the relationship between F_P and F_B, both of them grow as the feed rate increases. Moreover, F_P increases more rapidly than F_B. Therefore, both F_P and F_B increase almost linearly with the increase of the cutting area, such as drilling for metals. The cutting force per unit area for fibres is larger than that for resin. Hence, the increase of F_S with increased feed rate is due to the increase of F_P and F_B with increased feed rate. On the other hand, the increase of F_D with increased feed rate is the reason the difference

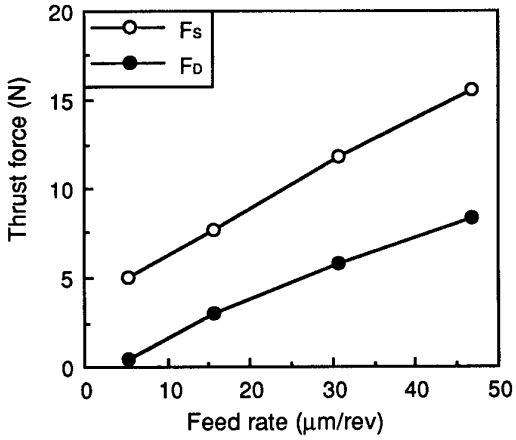

Fig. 8. The feed rate and the thrust force (cutting speed = 15.7 m/min).

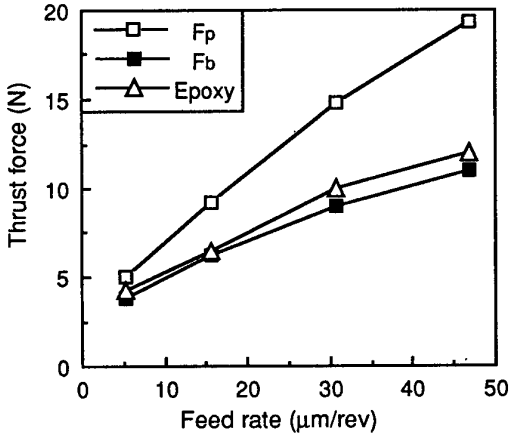

Fig. 10. The feed rate and the thrust force (cutting speed = 15.7 m/min).

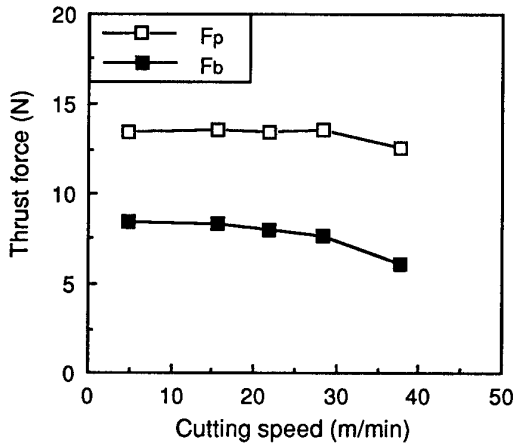

Fig. 11. The cutting speed and the thrust force (feed rate = 24 μm/rev).

of F_P and F_B increases with increased feed rate because the cutting force per unit area of F_P and F_B is different.

Figure 11 shows F_P and F_B under various cutting speeds. F_P changes little and F_B decreases a little with increased cutting speed. The influence of cutting temperature is considered as a reason for this result. It is difficult that the heat, which occurs by friction between drill and a workpiece, transmits into the workpiece, because the thermal conductivity of the glass fibre and the epoxy resin is smaller than that of steels by 2 or 3 orders of magnitude. Moreover, the cutting temperature rises rapidly with the friction heat and the increase in the cutting speed. Therefore, it is considered that the reason for almost no changes of F_P is that the fibre is little effected by cutting temperature because of the high melting point of the fibre. On the other hand, the resin is softened by the influence of the cutting temperature because of its low melting point. As a result, it is considered that F_B is reduced. Hence, it is found that F_S is reduced with increased cutting speed, because F_B decreases, and F_P is almost constant against the increase in cutting temperature. It is also found that F_D increases with increasing cutting speed because the difference of F_P and F_B is larger at high temperatures.

Influence of thrust force on surface roughness

In Section 3.3, the fact that the drilling conditions effect the thrust force is clarified. Therefore, in this section, we continue the evaluation of the influence of the thrust force on the surface roughness.

Figure 12(a) shows the relationship between F_S and the surface roughness and Fig. 12(b) shows the relationship between F_D and the surface roughness. These figures indicate that the surface roughness increases with increasing thrust force. Moreover, F_S and F_D are in proportion to the surface roughness. From Fig. 12, it is found that F_S and F_D increase more when the feed rate is increased under the constant cutting speed than when the cutting speed is increased under the constant feed rate. In conclusion, it is found that the surface roughness is more affected by feed rate than by the cutting speed.

The relationship between the surface roughness and the thrust force is evaluated in the case of pre-hole existence or not. Figure 13(a) and (b) show the relationships between F_S, F_D and the surface roughness, respectively. From

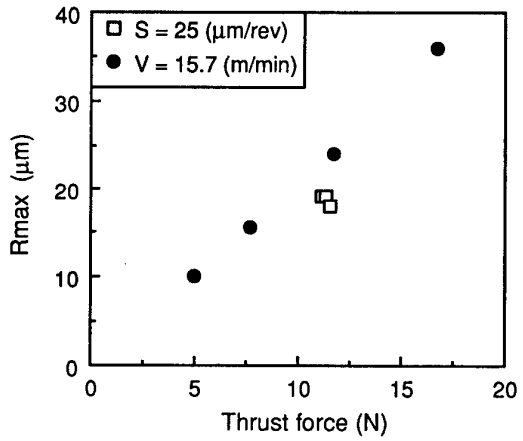

(a) Fs

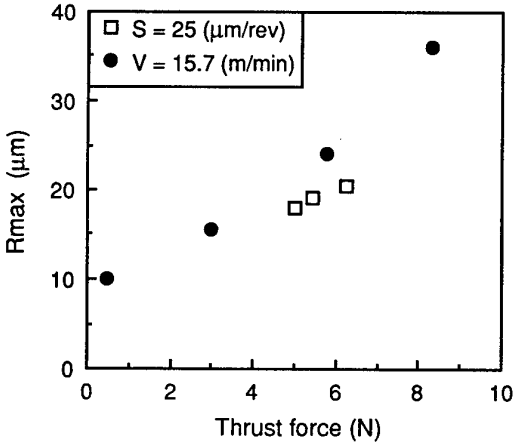

(b) FD

Fig. 12. The thrust force and the surface roughness.

Fig. 13(a), it is found that the surface roughness increases with an increase in F_S, but there are two different lines in the case of pre-hole existence or not. On the other hand, from Fig. 13(b), it is found that the surface roughness increases with an increase in F_D, and there is a line in the case of pre-hole existence or not. Therefore, F_D is more influential in the surface roughness than F_S. In conclusion, it is considered that the difference of the thrust force for fibres and resin, that is, the difference of the cutting phenomena for fibres and resin is influential in the surface roughness. Compared with results of the thrust force measurement, it is clarified that the surface roughness is related with F_D more than F_S in small diameter drilling. F_D is influential in the surface roughness, because the major cutting edge of the drill has an effect on the surface roughness at the drilled hole wall more than the chisel edge.

In conclusion, it is found that the major cutting edge of the drill is more influential in the quality of the drilled hole wall than the chisel edge of the drill in small diameter drilling for PWB. Therefore, it is clarified that, in order to improve the quality of the drilled hole, it is effective to reduce F_D occurring at the major cutting edge of the drill.

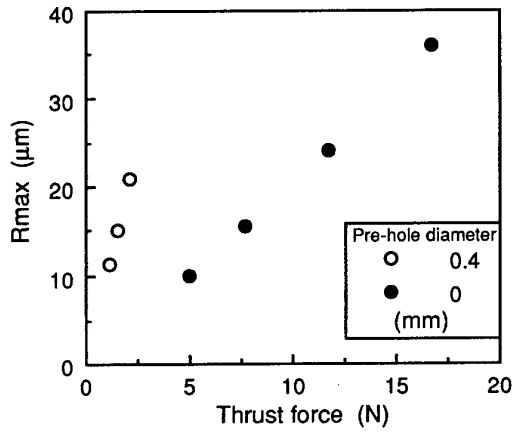

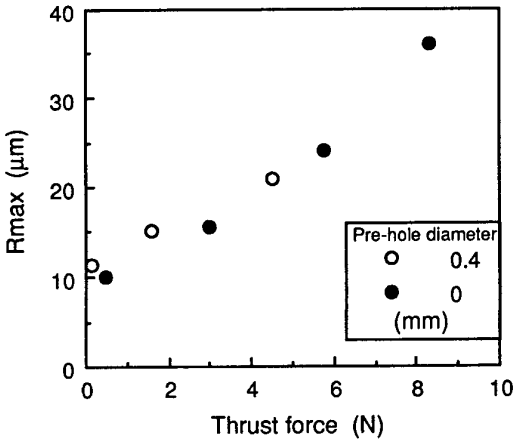

Fig. 13. The thrust force and the surface roughness.

CONCLUSION

Drilling experiments are carried out to investigate the cutting mechanism in small diameter drilling for GFRP. In particular, surface roughness of drilled hole walls and the thrust force in drilling are paid attention. The results are as follows:

1. The characteristics of the cutting force (the thrust force) have been clarified by dividing the force into two components, the static component F_S and the dynamic component F_D. That is, influential factors on the thrust force has been clarified from the point of view of radius direction distribution of the drill and drilling conditions.
2. The feed rate is more influential in the surface roughness of the drilled hole wall than the cutting speed. Therefore, it is effective to reduce the feed rate so as to improve the drilled hole quality.
3. It is found that F_D is very influential in the surface roughness, because this component indicates the difference of cutting characteristics between fibres and resin of GFRP. Therefore, in order to improve the quality of the drilled hole, it is effective to reduce F_D occurring at the major cutting edge of the drill.

REFERENCES

1. Jain, S. and Yang, D.C.H., Effects of feed rate and chisel edge on delamination in composites drilling. *Trans. ASME, J. Eng. for Industry*, 1993, **115**, 398–405.
2. Ho-Cheng, H. and Dharan, C.K., Delamination during drilling in composite laminates. *Trans. ASME, J. Engng for Industry*, 1990, **112**, 236–239.
3. Ramulu, M., Wern, C.W. and Garbini, J. L., Effect of fiber direction on surface roughness measurements of machined graphite/epoxy composite. *Comp. Manuf.*, 1993, **4**, 39–51.

4. Wern, C.W., Ramulu, M. and Colligan, K., A study of the surface texture of composite drilled holes. *J. Mat. Proc. Tech.*, 1993, **37**, 337–389.
5. Chambers, A. R., Factors influencing the surface quality of drilled holes in carbon fiber reinforced polymer. *Proc. ECCM 6*, Bordeaux, 1993, pp. 185–190.
6. Jamil, S. J., Evaluation of surfaces quality of drilled holes in composite materials after high speed drilling. *Proc 2nd International Conf. On the Behaviour of Materials in machining*, York, 1991, pp. 70–76.
7. Radhakrishnan, T. and Wu, S.M., Trans. ASME, J. Engng for industry, 1981, **103**, 119–125.
8. Srinivasan, M., N, Hough, C. L, Bolton, R. W. and Davis, F. M., Evaluation of drilled hole quality in printed circuit boards. *Trans. ASME, J. Engng for Industry*, 1995, **117**, 248–252.

ELSEVIER

Composite Structures Vol. 38, No. 1–4, pp. 351–359, 1997
© 1997 Elsevier Science Ltd. All rights reserved
Printed in Great Britain
0263-8223/97/$17.00 + 0.00

PII:S0263-8223(97)00070-6

Optimal design of composite hood with reinforcing ribs through stiffness analysis

Dae-Young Kwak,[a,c]* Jin-Ho Jeong,[b] Jae-Seung Cheon[c] & Yong-Taek Im[c]

[a]*Kia Motor Company, Kwangmyungshi, Kyunggido 781-1, South Korea*
[b]*Hyundai Motor Company, Namyangmyun, Whasunggun, Kyunggido 445-850, South Korea*
[c]*Computer Aided Materials Processing Laboratory, Department of Mechanical Engineering, Korea Advanced Institute of Science and Technology, Taejon 305-701, South Korea*

Fiber glass reinforced composites like sheet molding compounds (SMC) have recently been widely used in the fabrication of two-piece automobile hoods for passenger cars. In the present investigation, a one-piece composite hood with reinforcing ribs was optimally designed and manufactured by resin transfer molding in order to reduce manufacturing cost. In order to obtain the optimal design, stiffness analyses for deflections due to self-weight, oil canning, and torsion test conditions were carried out by applying the ABAQUS/Standard program. Based on these analyses, the thickness dimension of the composite hood required to maintain a stiffness comparable to a conventional steel hood was determined. For optimization studies of the weight reduction of the currently proposed one-piece composite hood with reinforcing ribs, IDESIGN program was employed. Based on a recursive quadratic programming technique, the thickness dimensions of the reinforcing ribs were optimized. The deflection ratios between fiber glass reinforced composite and conventional steel hoods were minimized in the optimization studies. From the present studies, it was found that the weight saving effect obtained by introducing the optimally designed one-piece composite hood was 37% compared to the conventional steel hood. This ranged approximately from 30 to 40% for composite hoods manufactured by resin transfer molding, depending on the composite materials used. Through these studies, it was confirmed that the one-piece composite hood was a preferable design and manufacture, compared to currently used composite hood made in two pieces, in terms of weight reductions and manufacturing cost without losing the stiffness required.
Copyright © 1997 Elsevier Science Ltd.

INTRODUCTION

Recent environmental issues require less fuel consumption with better efficiency. Due to such a requirement, one of the major design constraints for passenger cars is to reduce their weight. Weight reduction can be achieved by either redesigning its structure and size or introducing new light-weight materials for body components without sacrificing the safety of the vehicles [1].

Since the optimal design of reinforcement geometry and arrangements for better stiffness is of importance in automotive structure design, numerous studies for weight reduction have been carried out so far. Radaj *et al.* [2], conducted finite element structural design analysis and Melosh [3] carried out static and dynamic analyses of bottom frame for Ford using NASTRAN. Also, optimization analysis of automotive structure design with a beam element was conducted by Bennett *et al.* [4]. A simplified stick model was proposed by Choon *et al.* [5] for structural analysis.

In order to apply new light-weight materials in the manufacture of body components instead of steel, it is necessary to estimate the new required dimension of the same part without loss of safety or stiffness. Fenyes [6] studied the applications of high-strength steel, aluminum

*Corresponding author.

and graphite–epoxy for weight savings in automobiles. In particular, it is well known that the use of engineering plastics, which was limited to bumpers and inner components in the past, is being expanded to outer components [7–9].

With the rapid development of computer technology and numerical methods, the field of optimization is actively being studied by many researchers. In general, the optimization problem in structure design in the automotive industry can be divided into two processes: a determination process of cross-section, shape, and configuration; and a total optimization process based on the design variables selected. Numerous optimization algorithms and programs to solve such problems have been developed so far. IDESIGN [10] is one such program, which can solve the optimization problems interactively. It consists of several algorithms such as cost function boundings (CFB), recursive quadratic programming (RQP), linearization method of Pshenichny (LINRM), and the conjugate gradient method [11]. Thus, it is adequate for applications to various engineering fields.

The major purpose of this study is to design a hood in one piece with rib-type reinforcements made of sheet molding compounds (SMC), thermoset based composites reinforced with fiber-glass. Currently, SMC hoods are manufactured in two pieces and bonded together by applying adhesives [7]. In order to achieve this goal, simplified structural analysis was conducted by applying the ABAQUS/Standard program to determine deflections due to self-weight, oil canning, and torsion for a conventional hood made of aluminum killed steel under the assumption that the material properties were isotropic. Similar studies were carried out for composite materials by changing the thickness of the hood. By comparing the numerical data for deflection levels obtained from simulations, the weight saving effect was investigated between aluminum killed steel and composite materials. In order to optimize the weight reduction of the one-piece plastic hood, IDESIGN was applied based on the RQP method by selecting the thickness of the reinforcements as a primary design variable and the deflection ratios between aluminum killed steel and plastic hoods as object functions. The total weight of the hood was given as a constraint. Based on the optimization results, the one-piece composite hood was made by applying resin transfer molding. It was found that the weight saving ranged from 30 to 40% through the present investigation.

STIFFNESS ANALYSIS

Stiffness analysis process

In order to estimate the necessary hood thickness made of composite materials such as SMC, structural analysis of a conventional aluminum killed steel hood was made to establish the reference data for the stiffness requirement. In general, stiffness analysis is conducted by estimating and comparing the deflections subjected to external loads. For self-weight and torsion analyses, the global stiffness of the hood is compared by examining maximum deflection values, whereas in oil canning analysis, the localized stiffness is compared. In the present investigation, self-weight, torsion, and oil canning analyses were undertaken for global and local stiffness comparisons using the ABAQUS/Standard program.

The geometry of the hood was idealized for computational simplicity into a one-piece hood with stiffening ribs as shown in Fig. 1(a) and (b). In Fig. 1(b), the arrangement is shown and in Table 1, the dimensions of each reinforcing rib are summarized. Due to geometric symmetry only half of the hood was used in simulations. Although the material properties were anisotropic, they were assumed to be isotropic for numerical simplicity. The material properties used in the present investigation are summarized in Table 2 for aluminum killed steel and SMC [12].

The boundary and loading conditions used in the self-weight and oil canning analyses are approximated as depicted in Fig. 2(a) and (b), respectively. In these figures, A–A′ represents the line of symmetry, B the points of simple supports, and C the hinged boundary points. For the self-weight analysis, the gravitational body force was the only external loading applied. However, the gravitational effects were neglected in oil canning and torsion analyses. A concentrated load of 50 N was applied at point D in oil canning analysis. For torsion analysis, concentrated loads of 40 N were applied at the given point C as shown in Fig. 2(c). Here, A–A′ is the line of skew-symmetry and B is the fixed point.

ANALYSIS RESULTS

A number of thickness variations were used for self-weight, oil canning, and torsion analyses. The numerical results obtained from simulations for aluminum killed steel and SMC are compared in Table 3 and Fig. 3 in consideration

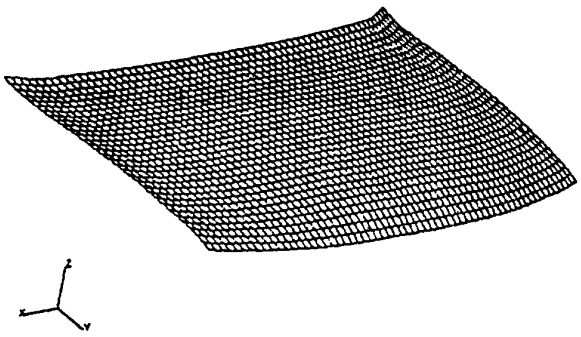

(a)

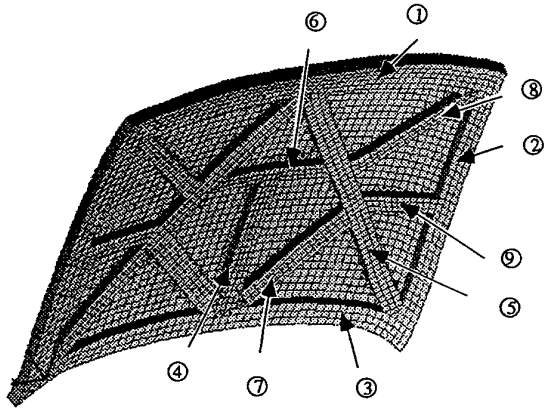

(b)

Fig. 1. Schematic diagrams of (a) automobile hood and (b) structure of reinforcements used.

Table 1. The dimension of each reinforcing rib in Fig. 1(b)

Reinforcing ribs	Width (mm)	Initial thickness
Rib 1	150	
Rib 2	70	
Rib 3	90	
Rib 4	80	
Rib 5	65	$2t_{steel}$ ($= 2 \times 0.7$ mm)
Rib 6	55	
Rib 7	100	
Rib 8	50	
Rib 9	60	

Table 2. Physical properties of high strength steel and SMC

	High strength steel	SMC
Young's modulus (MPa)	210×10^3	14×10^3
Poisson's ratio	0.29	0.49
Yield strength (MPa)	91.3	55.0
Density (kg/m^3)	7833	1700

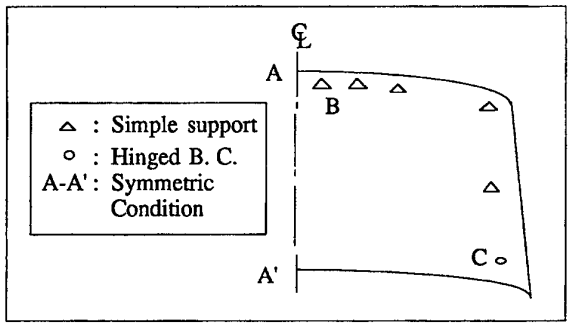

(a)

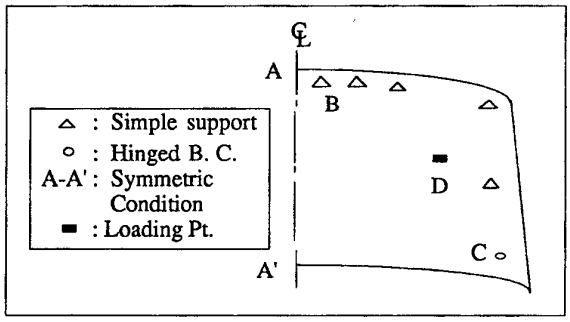

(b)

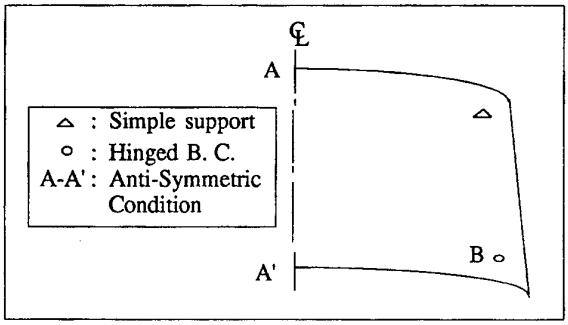

(c)

Fig. 2. The boundary conditions used for (a) self-weight, (b) oil canning, and (c) torsion deflection analyses.

Table 3. Deflection results obtained for stiffness analyses

Thickness ratio	Weight ratio	Weight reduction (%)	Deflection ratio		
			Self-weight	Oil canning	Torsion
2.0	0.435	56.5	1.628	2.344	3.195
2.2	0.478	55.2	1.508	1.732	2.529
2.4	0.522	47.8	1.414	1.270	2.307
2.6	0.565	43.5	1.334	0.969	1.664
2.8	0.608	39.2	1.265	0.772	1.378
3.0	0.652	34.8	1.205	0.635	1.153
3.2	0.696	30.4	1.151	0.501	0.974

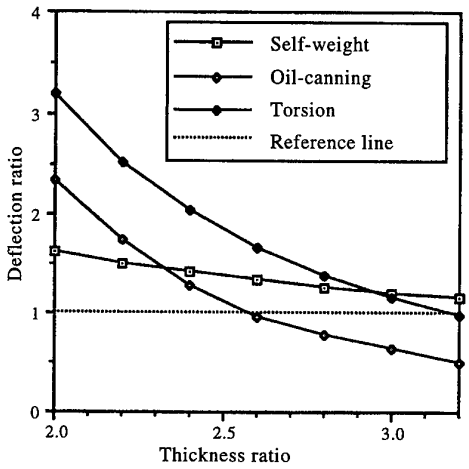

Fig. 3. Comparison of deflection curves obtained from self-weight, oil canning, and torsion analyses.

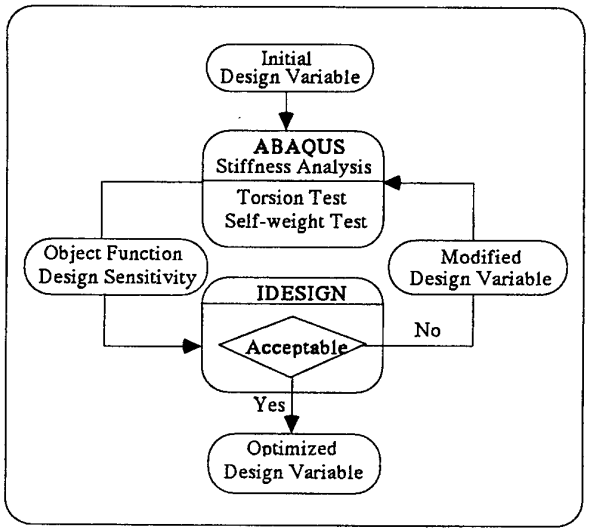

Fig. 4. Flow chart of the optimization process.

of weight reduction and stiffness levels. The thickness ratio, percentage of weight reduction, and deflection ratio used in Table 3 were defined as follows:

$$\text{Thickness Ratio} = \frac{\text{Thickness of SMC hood}}{\text{Thickness of aluminum killed steel hood}} \quad (1)$$

$$\text{Weight Reduction (\%)} = \left\{1 - \frac{\text{Weight of SMC hood}}{\text{Weight of aluminum killed steel hood}}\right\} \times 100 \quad (2)$$

$$\text{Deflection Ratio} = \frac{\text{Maximum deflection value of SMC hood}}{\text{Maximum deflection value of aluminum killed steel hood}} \quad (3)$$

As shown in Table 3, the deflection ratios obtained under the present simulation conditions are 1.151, 0.501, and 0.974 for self-weight, oil canning, and torsion studies, respectively, when the thickness ratio used was 3.2. From the results, it can be construed that the thickness ratio of 3.2 was safe enough based on the stiffness consideration. This result leads to a weight reduction of 30% when SMC was used as a replacement for aluminum killed steel. In Fig. 3, as the deflection curves are lower than the reference deflection ratio line for oil canning and torsion tests, it can be found that the

stiffness of the SMC hood is better than that of aluminum killed steel.

OPTIMAL DESIGN

Optimal design process

In order to enhance the weight reduction effect and to achieve a more efficient stiffness distribution within the prescribed design conditions, the optimization analyses were carried out by selecting the thickness of the reinforcing ribs as a primary design variable. The thickness of the outer hood without reinforcements was assumed to be three times thicker than the one of aluminum killed steel based on the results obtained from previous stiffness analyses.

The optimization was carried out for three cases according to the selection of object functions as follows. The deflection ratios between one-piece SMC and conventional aluminum killed steel hoods due to self-weight and torsion were used as object functions in the first and second cases of optimization, respectively. In the third case, the weighted deflection ratio obtained from self-weight and torsion analyses was selected as an object function. The total weight of the SMC hood and the minimum and maximum thicknesses of the reinforcing ribs were identically constrained for all three optimization cases.

The optimization modeling for each case was formulated as follows.

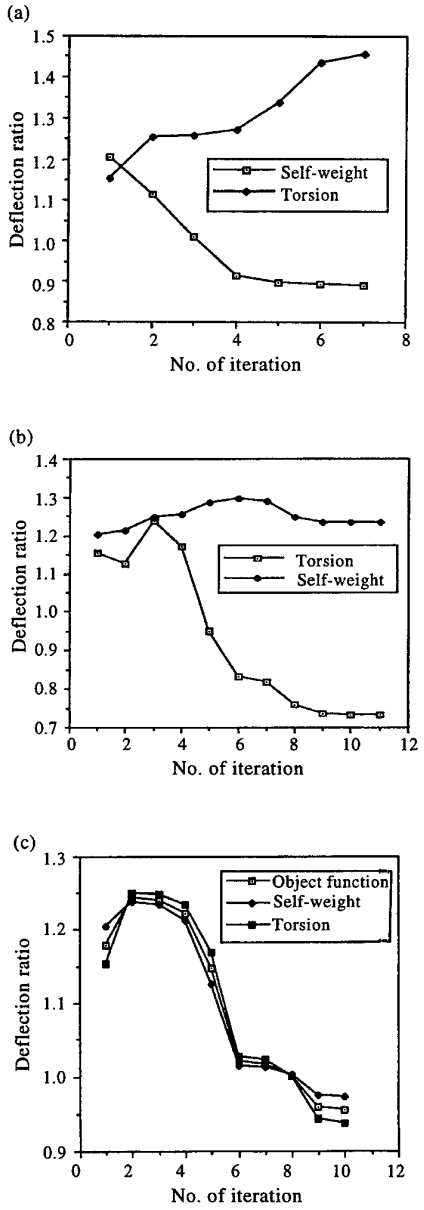

Fig. 5. Comparison of deflection curves obtained from self-weight and torsion analyses with optimized thicknesses for three case studies: (a) case (i), (b) case (ii), and (c) case (iii).

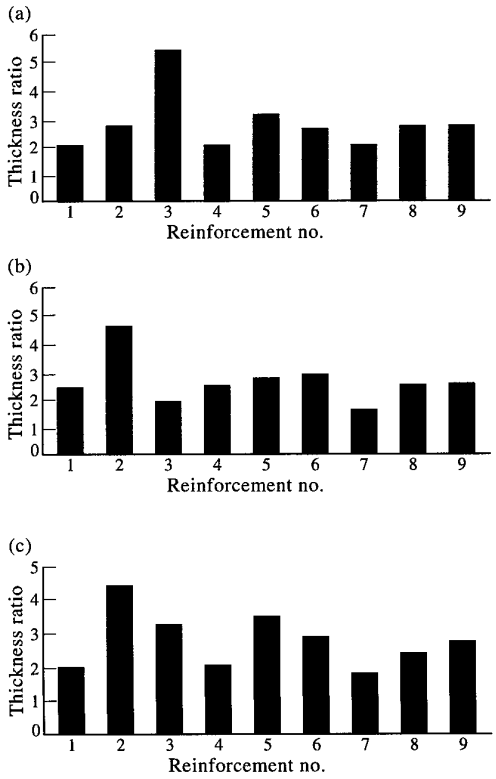

Fig. 6. Resultant thickness ratios of reinforcements based on different optimization processes due to (a) self-weight, (b) torsion, and (c) weighted self-weight and torsion analyses.

Case (i): find the t_i ($i = 1, 2, ..., 9$) values which will minimize the equation

$$f = \frac{(\delta_{\text{weight}})_{\text{SMC}}}{(\delta_{\text{weight}})_{\text{steel}}} \tag{4}$$

subject to

$$M_{\text{Total}} \leq M_{\text{Critical}} (= 0.65\, M_{\text{steel}}) \tag{5}$$

$$(t_i)_{\text{Minimum}} (= 2t_{\text{steel}}) \leq (t_i) \leq (t_i)_{\text{Maximum}} (= 6.5 t_{\text{steel}}) \tag{6}$$

Case (ii): find the t_i ($i = 1, 2, ..., 9$) values which will minimize the equation

$$f = \frac{(\delta_{\text{torsion}})_{\text{SMC}}}{(\delta_{\text{torsion}})_{\text{steel}}} \tag{7}$$

subject to

$$M_{\text{Total}} \leq M_{\text{Critical}} (= 0.65\, M_{\text{steel}}) \tag{8}$$

$$(t_i)_{\text{Minimum}} (= 2t_{\text{steel}}) \leq (t_i) \leq (t_i)_{\text{Maximum}} (= 6.5 t_{\text{steel}}) \tag{9}$$

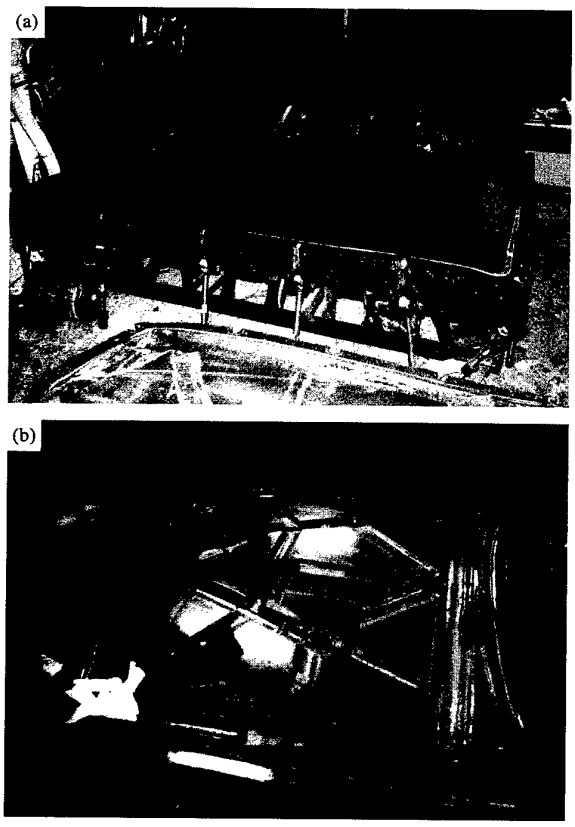

Fig. 7. Photographs of (a) upper and (b) lower moulds used for RTM.

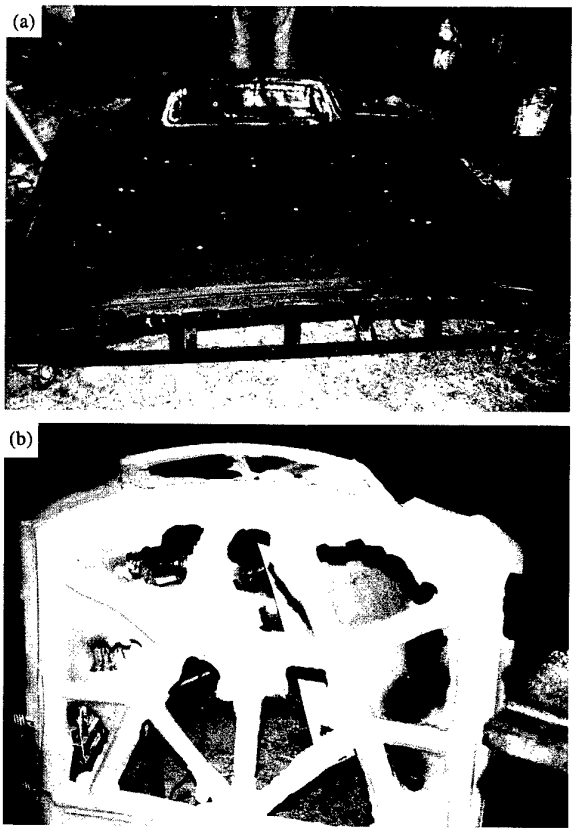

Fig. 8. Photographs of (a) foam core mould and (b) foam core manufactured by RTM.

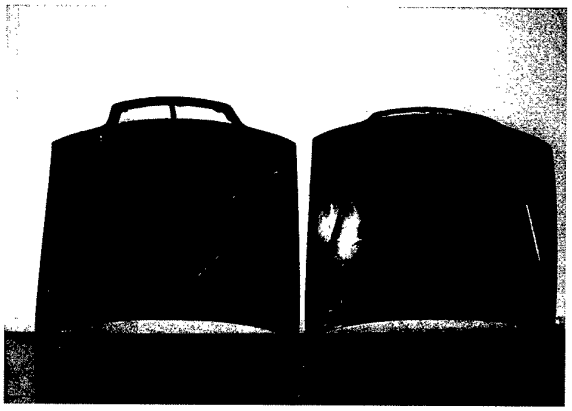

Fig. 9. Photograph of top and bottom surfaces of the one-piece composite hood manufactured by RTM.

Table 4. The materials used in manufacturing composite hoods by RTM and the measured weight reduction ratios for each case

	Resin type (product name)	Weight reduction (%)
1	Epoxy (Epolite 2410/2183 (100:44))	32%
2	Vynilester Resin (AROTAN Q6530)	35%
3	Novolac Type Vynilester Resin (SR-841L)	32%
4	Epoxy (Epolite 2410/2310 (100:14))	31%
5	Phenol Versatil	40%
6	Unsaturated Polyester Resin (R401)	35%
7	Epoxy (Epolite 2410/2180 (100: 7.5))	37%
8	Unsaturated Polyester Resin (R459)	34%
9	Epoxy (Epolite 2434/2347)	30%

Case (iii): find the t_i ($i = 1, 2, ..., 9$) values which will minimize the equation

$$f = \alpha\left\{\frac{(\delta_{\text{weight}})_{\text{SMC}}}{(\delta_{\text{weight}})_{\text{steel}}}\right\} + (1-\alpha)\left\{\frac{(\delta_{\text{torsion}})_{\text{SMC}}}{(\delta_{\text{torsion}})_{\text{steel}}}\right\}, \alpha = \frac{1}{2} \tag{10}$$

subject to

$$M_{\text{Total}} \leq M_{\text{Critical}} (= 0.65\, M_{\text{steel}}) \tag{11}$$

$$(t_i)_{\text{Minimum}} (= 2t_{\text{steel}}) \leq (t_i) \leq (t_i)_{\text{Maximum}} (= 6.5 t_{\text{steel}}) \tag{12}$$

where t_i, δ, and M are the thicknesses of the reinforcing ribs as illustrated in Fig. 1(b), deflection value obtained from the structural analysis and the total weight of the hood. α represents the weighting factor used in optimization.

In order to solve the above optimization problems, the recursive quadratic programming method provided in IDESIGN was used. The flow chart of optimization process used in the present study is given in Fig. 4. As can be seen, the deflection ratio was computed using the ABAQUS/Standard program in the same manner as previously mentioned for stiffness analyses. The object function values were separately determined for three different cases according to their definitions as previously introduced. These object function values were provided as input for IDESIGN and the modified design variables, t_i, were used for structural analyses again until desired values were obtained.

Sensitivities of the object function and the constraint were calculated by applying the linear perturbation method as follows

$$\frac{\partial f}{\partial t_i} = \frac{f(t_i + \Delta t_i) - f(t_i)}{\Delta t_i} \tag{13}$$

$$\frac{\partial M_{\text{Total}}}{\partial t_i} = \frac{M_{\text{Total}}(t_i + \Delta t_i) - M_{\text{Total}}(t_i)}{\Delta t_i} \tag{14}$$

Optimal design results

In Fig. 5(a), (b) and (c), the deflection ratios calculated by three different optimization cases, (i), (ii), and (iii), as introduced previously, are depicted at every iteration number. As seen in Fig. 5(a), the object function value, namely the deflection ratio obtained from self-weight analyses became lower than the reference value of one as the number of iterations increased, whereas the deflection ratio obtained from torsion analyses increased. This result showed that only the self-weight deflection ratio was minimized, while the torsion deflection ratio was not controlled. For case (ii), in contrast to the results of case (i), only the torsion deflection ratio was minimized. In this case, the self-weight deflection ratio was bounded, but the desired value less than the reference value of one was not obtained. From these results, it is found out that it was necessary to include the deflection ratios obtained from both the self-weight and torsion analyses into the object function.

In order to satisfy the reference value for stiffness in both cases of optimization due to

self-weight and torsion, weighting factors were introduced in the third case of optimization. When the same weighting factor of 0.5 was imposed on both self-weight and torsion deflection ratios, deflection ratios of 0.9742 and 0.9381 were obtained, respectively, as shown in Fig. 5(c). Thus, it can be construed that both self-weight and torsion deflection ratios are satisfied by imposing a weighting factor of 0.5 on each deflection ratio. According to this figure, object function values and deflection ratios converged as the number of iterations increased for this case. Also, for all three cases, a weight reduction of 37% in the SMC hood was achieved compared to the aluminum killed steel hood. Therefore, both the stiffness and weight reduction were improved through optimization compared to the initial design obtained from structural analyses only.

Figure 6 shows the bar graphs of the resultant reinforcement thickness ratios for three cases of optimization, (i), (ii), and (iii). As shown in Fig. 6(a) and (b), reinforcements 3 and 2 have dominant influences on the self-weight and torsion deflection ratios, respectively. However, for case (iii), as can be seen in Fig. 6(c), the dominant components are reinforcements 2, 3, 5, and 6. Thus, different reinforcement design was necessary, depending on the selection of the object function.

MANUFACTURING THE COMPOSITE HOOD

Through the optimal design process, a one-piece type composite hood was designed. For the purpose of checking the manufacturability of the designed hood, composite hoods were manufactured by a resin transfer molding (RTM) process. For this purpose, RTM moulds were manufactured in three parts, the upper and lower RTM moulds and the foam core. The RTM moulds were made of epoxy. By using a foam core, a one-piece composite hood with rib-type reinforcements could be manufactured.

The widths of the reinforcing ribs were the same as the values given in Table 1, but the thicknesses were determined from the third case of the optimization results. Figure 7 shows photographs of the upper and lower moulds and the foam core mould and manufactured foam core for rib-type reinforcements can be seen in Fig. 8. A photograph of one of the one-piece composite hoods manufactured by resin transfer molding is shown in Fig. 9. The weights of the manufactured hoods were measured, and based on these, it was found that the actual weight reduction ranged from 30 to 40%. Table 4 summarizes the materials used in manufacturing the composite hoods and the actual weight reductions for each case.

CONCLUSIONS

The following conclusions were obtained from the present investigation.

1. A weight reduction of around 30% was achieved by applying SMC as a substitute for aluminum killed steel, when the thickness ratio was 3.2.
2. The optimization results showed that an additional 7% weight reduction can be obtained compared to the initial design. This leads to a better design in terms of weight saving without sacrificing the stiffness of the hood.
3. According to experimental observations, the final weight reduction ranged between 30 and 40%, which is very close to the value obtained from the optimization.
4. A one-piece composite hood designed in the present investigation can reduce the manufacturing cost by removing the bonding process.

ACKNOWLEDGEMENTS

The authors are thankful for the grants from the Ministry of Science and Technology and the Ministry of Trade and Industry under which this work was possible.

REFERENCES

1. Kim, C.W. and Kim, J.H., Light weight vehicle design by stick model. *KSAE Trans.*, 1990, **12**, 97–106.
2. Radaj, D., Zimmer, A. and Geissler, H., Finite element analysis, an automobile engineer's tool. *SAE Trans.*, 1974, **740338**, 228–243.
3. Melosh, R.J., Finite element analysis of automobile structures. *SAE Trans.*, 1974, **740319**, 1341–1355.
4. Bennett, J.A. and Nelson, M.F., An optimization capability for automotive structures. *SAE Trans.*, 1979, **790972**, 2186–2198.
5. Choon, T.C., Mohammadtrab, H. and Ei-Essawi, M., Generic stick model of a vehicle structure. *SAE Trans.*, 1986, **860825**, 235–241.

6. Fenyes, P.A., Structural optimization with alternate materials — minimum mass design of the primary structures. *SAE Trans.*, 1981, **810228**, 992–1001.
7. *Automotive Plastics Report*, Market Search, Toledo, Ohio, USA, 1992.
8. Kim, K.T. and Im, Y.T., Experimental study on physical properties of compression molded SMC parts under plane strain condition. *Composite Structures*, 1996, **35**, 131–141.
9. Jeong, J. H. and Im, Y. T., Estimation of sink mark depth in compression molded SMC parts with substructures, *J. Composite Materials* (in press).
10. Arora, J. S., *Introduction to Optimum Design*, McGraw–Hill, New York, 1989.
11. Arora, J. S., *Theoretical Manual for IDESIGN* Report No. ODL-85.9, The University of Iowa, 1985.
12. *Engineering Materials Handbook 1, Composites*, ASM International, 1989.

ELSEVIER

Composite Structures Vol. 38, No. 1–4, pp. 361–371, 1997
© 1997 Elsevier Science Ltd. All rights reserved
Printed in Great Britain
0263-8223/97/$17.00 + 0.00

PII:S0263-8223(97)00071-8

Mechanical properties prediction of textile-reinforced composite materials using a multiscale energetic approach

D. Bigaud & P. Hamelin

Mechanical Engineering and Material Laboratory, Université Claude-Bernard, Lyon, France

A computer aided design tool and a numerical procedure allowing the prediction of textile reinforced composite behaviour are presented in this paper. Specifying a geometrical description, the software used allows the rebuildong of both simple or sophisticated textile structures. It also aims to become a pre-processing work for the subsequent mechanical analysis. Fabric unit cells (fibres+matrix) are regarded as a three-dimensional aggregate of subcells on which we apply a multi-scale energetic approach. First elements to validate the elastic prediction are provided by results obtained on a woven fabric material. The progressive failure procedure is validated by comparisons between simulation and experiment on 3D braided composites. © 1997 Elsevier Science Ltd.

INTRODUCTION

The potentialities of woven, non-woven, knitted or braided fabrics used as reinforcements for polymer matrix composite materials are increasing. Today, their use within laminates in aerospatial and ship building fields, or as soft membranes and repairing elements in the civil engineering area, are common. However, the multi-functional character of those materials, which are perfectly adapted for structural element design, is not thoroughly used. This is essentially the result of the difficulties in predicting their performance. The main problem of modelling the textile composite's mechanical properties lies in dealing with the large stress and strain variations within a textile accurately.

A textile composite is a very heterogenous structure. Therefore, it must be considered (as it is often modelled) as a three-dimensional assembly of transverse isotropic unidirectional rods. As far as polymer matrix composites are concerned, the anisotropic factor ($E_{axial}/E_{transverse}$) of those rods is substantial, between 20 and 30 for a carbon/epoxy composite for example. As a consequence, the stress and strain fields within these differents elements depend greatly on the constituent's repartition, on their size and on their spatial arangement. In other words, it depends on the textile architecture.

Many approaches exist to describe the global geometry of a composite. A simplifying description—we can speak about geometrical homogeneization—is necessary in order to develop a mechanical model. Many of them only provide good results for specific textile geometry, according to a certain kind of loading. Most of the existing models seem to be inaccurate because of the introduction of new reinforcements such as multi-directional or three-dimensional fabrics.

This paper has two objectives. The first is to describe a computer program developed in order to model the textile architecture geometry. The second is to present a numerical procedure allowing the estimation of the elastic and failure behaviour of composites with a textile reinforced polymer matrix. Finally, the

model is compared with results provided from experiments carried out on woven and braided fabric composites.

PRESENTATION OF TIS3D

The graphical technics implicated in computer aided design tools find an appropriate field of applications in the description of textile structures. In a sophisticated representation, we can find a substantial amount of information which we have to deal with and use efficiently.

The computer aided design software developed by the Mechanical engineering and Material Laboratory (L2M) is called TIS3D. One of its main features is to reconstitute basic volumes that represent usual textile structures. The geometrical description according to a reduced number of parameters allows the study of woven, knitted, braided, 2D or 3D reinforcements of homogeneized geometries (Fig. 1).

Once the unit cell is defined, a regular volume element meshing is superposed on the 'real' geometry (Fig. 2(a)–(b)).

Each element is specified as a 'meso-element' and is characterized by an individual material orientation obtained by minimizing the distance between its own center and the yarn path.

This meso-element is then considered as an assembly of eight micro-elements, the properties of which depend on their belonging or not to the yarn volume (Fig. 3). If all or part of the micro-element is in the yarn volume, its properties are those of the fibre-matrix mixture with the average orientation of the meso-element.

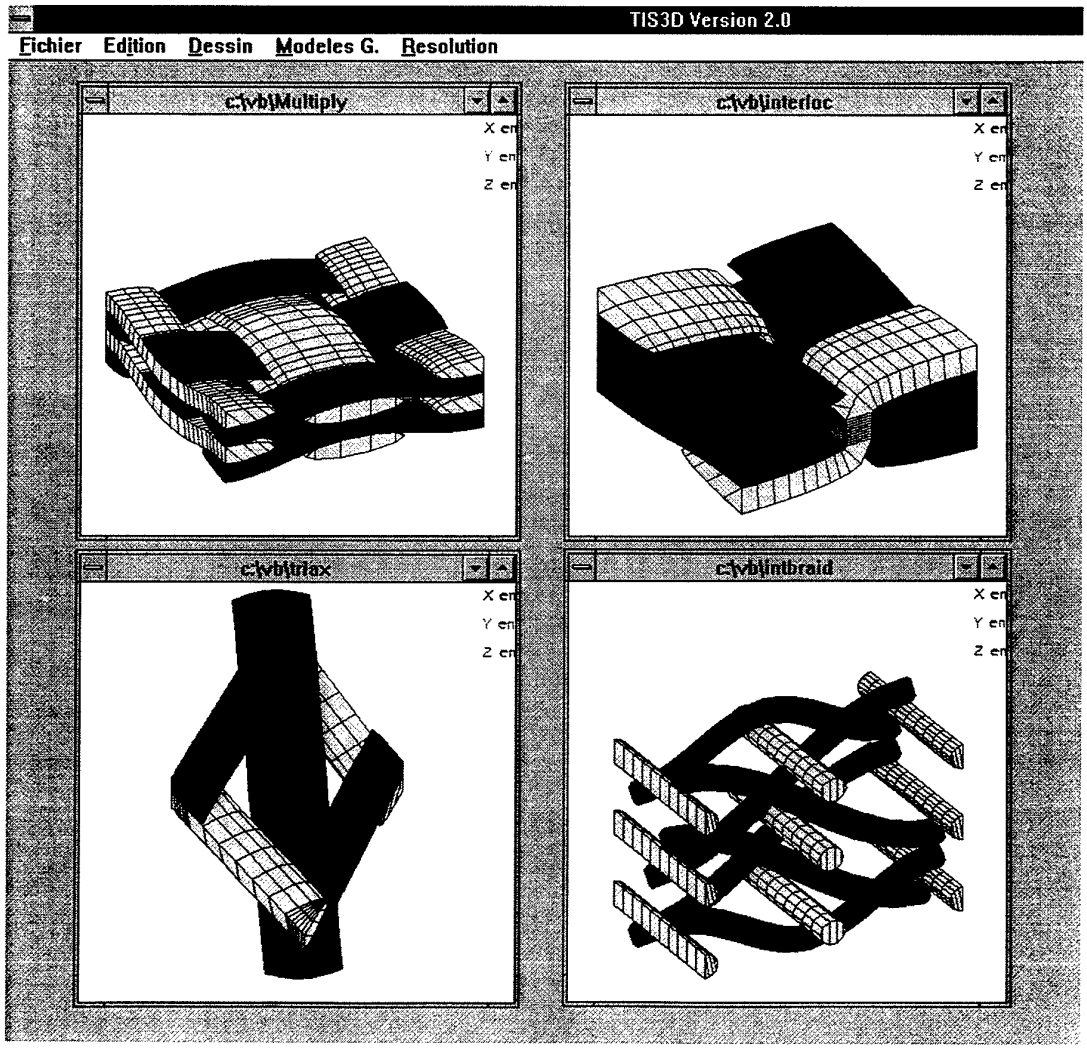

Fig. 1. Architectures generated by Tis3D — from left to right, top to bottom: multi-layered woven fabric, interlock woven fabric, triaxial braided fabric, interlock braided fabric.

On the contrary, if the micro-element does not belong to the yarn volume, its properties are similar to those for the matrix.

Finally, the analysis of the unit cell mechanical behaviour consists of studying that of an aggregate of multi-scale elements with individual properties.

For the mechanical prediction we must then consider three analysis scales:

- a microscopic scale at the level of which we have to determine the tow properties according to those of the constituents (fiber+ matrix),
- a mesoscopic scale at the level of which we define properties of a meso-element (eight micro-elements),
- finally, the macroscopic scale at the level of which we consider the mechanical properties of the unit cell (aggregate of meso-elements).

THEORETICAL ASPECTS

General aspect

An energetic approach is used for each analysis level. At the microscopic scale, we idealize the fibre+matrix mixture by a bidimensional network of cells (Fig. 4). This modelling has already been proposed by Aboudi [1].

The main idea of this method consists of minimizing the complementary energy U_{cj} from the j-assembly defined as the average energy in each i-cell (i = fiber or matrix)

$$U_{cj} = \frac{1}{2} \sum_{i=1}^{i=4} v_i \{\sigma_i\}^{\mathrm{T}} [s]_i \{\sigma\}_i$$

$$= \frac{1}{2} \{\sigma\}^{\mathrm{T}}_{j-\mathrm{micro}} [s]_{j-\mathrm{micro}} \{\sigma\}_{j-\mathrm{micro}} \qquad (1)$$

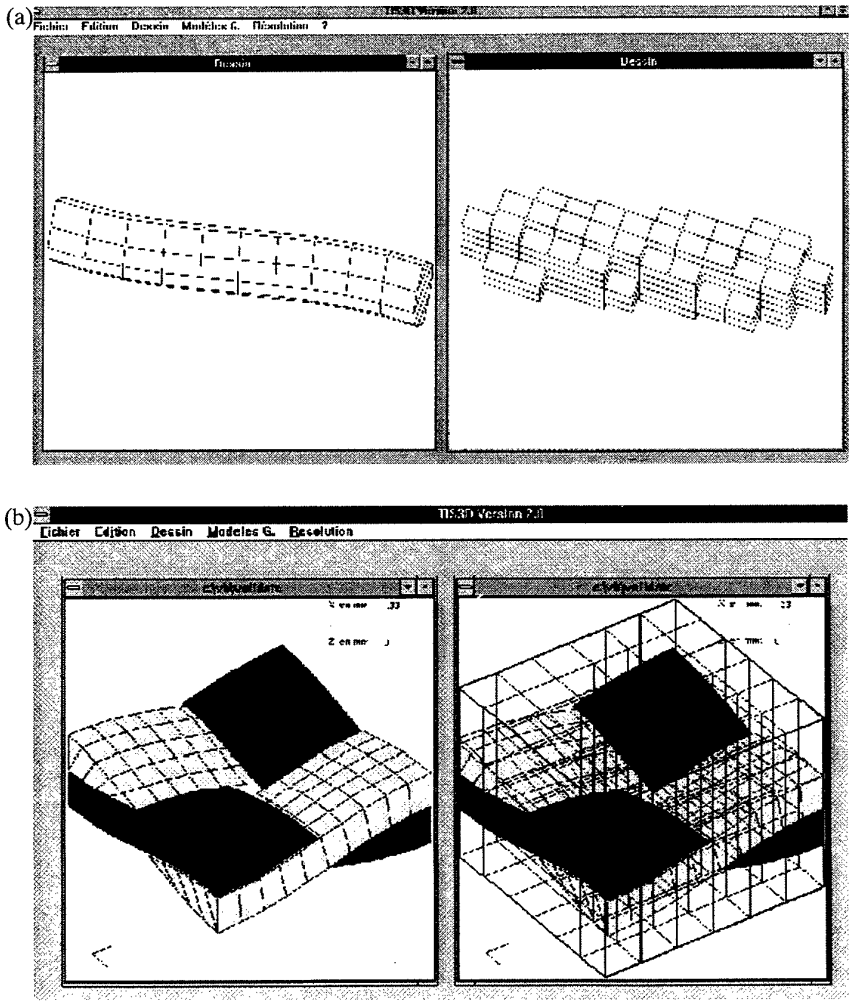

Fig. 2. Meso-element meshing: (a) yarn partial meshing; (b) unit cell total meshing.

where v_i is the volume ratio of the i-cell and $[s]_\alpha$ represents the compliance matrix of the α entity.

Through Lagrangian multipliers [2] and imposing the conditions of continuity and averaging of stresses specified in eqn (2), it is possible to determine the linear relationships between the local tensors $\{\sigma\}_i$ and the tensor of micro-element stresses $\{\sigma\}_{j\text{-micro}}$ as matrices of stresses localization $[L_i^\sigma]_{j\text{-micro}}$ (eqn (3))

$$\langle\sigma\rangle = \frac{1}{4}\sum_{i=1}^{i=4}(\sigma)_i$$

$$(\sigma_y)_1 = (\sigma_y)_3;\ (\sigma_y)_2 = (\sigma_y)_4$$

$$(\sigma_z)_1 = (\sigma_z)_2;\ (\sigma_z)_3 = (\sigma_z)_4$$

$$(\tau_{yz})_1 = (\tau_{yz})_3;\ (\tau_{yz})_2 = (\tau_{yz})_4$$

$$(\tau_{xz})_1 = (\tau_{xz})_2;\ (\tau_{xz})_3 = (\tau_{xz})_4$$

$$(\tau_{xy})_1 = (\tau_{xy})_3;\ (\tau_{xy})_2 = (\tau_{xy})_4 \qquad (2)$$

$$\{\sigma\}_i = [L_i^\sigma]_{j-\text{micro}}\{\sigma\}_{j-\text{micro}} \qquad (3)$$

The compliance matrix $[s]_{j\text{-micro}}$ of the j-assembly is then easily explained

$$[s]_{j-\text{micro}} = \sum_{i=1}^{i=4} v_i[s]_i[L_i^\sigma]_{j-\text{micro}}$$

$$= v_{\text{fi}}[s]_f[L_1^\sigma]_{j-\text{micro}} + \sum_{i=2}^{i=4} v_i[s]_m[L_i^\sigma]_{j-\text{micro}} \qquad (4)$$

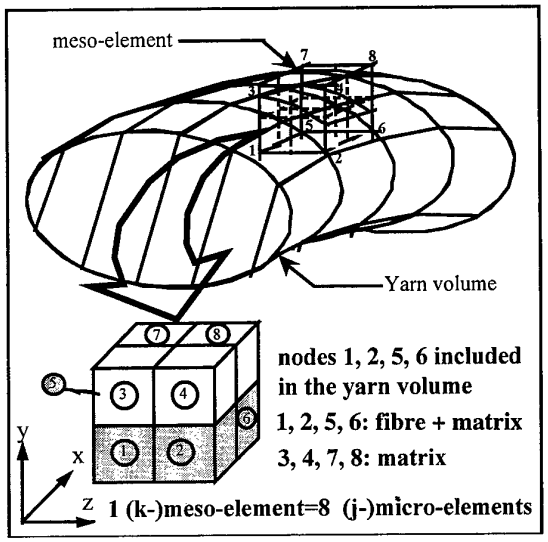

Fig. 3. A meso-element as an assembly of eight micro-elements.

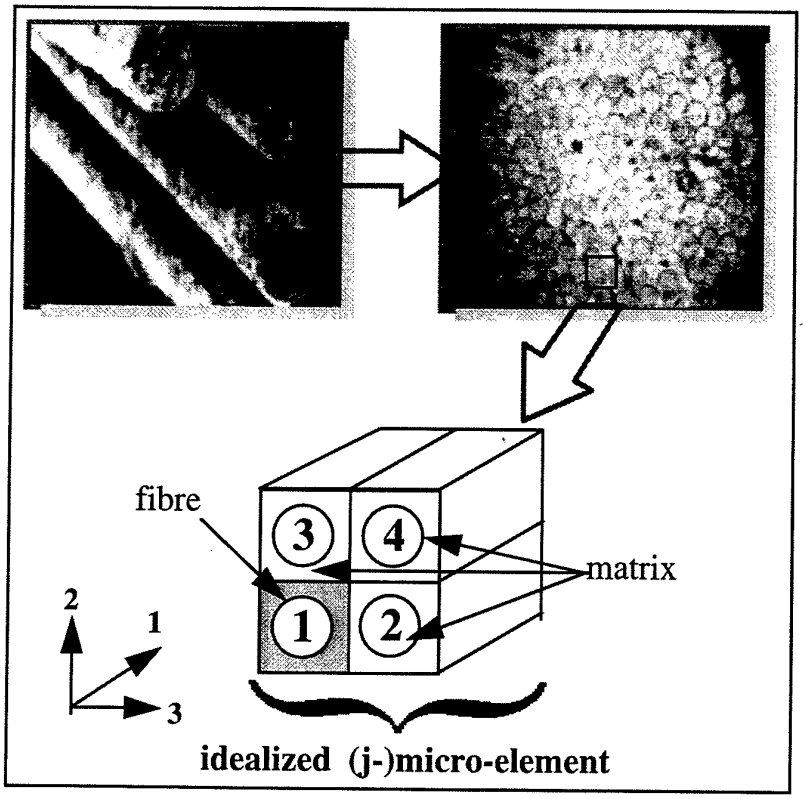

Fig. 4. Geometrical idealization of the fibre–matrix mixture.

with m: matrix, f: fibre, $v_2 = v_3 = \sqrt{V_{fl}} - V_{fl}$ $v_4 = 1 - 2\sqrt{V_{fl}} + V_{fl}$, V_{fl} is the fibre packing ratio.

At the mesoscopic scale, we consider a volume element composed of eight subdivisions of identical volumes (Fig. 3). The subdivision properties are then defined as

$$[S]_{j-\text{micro}} = [s]_{\text{matrix}} \tag{5a}$$

if the subdivision does not belong to the yarn volume

$$[S]_{j-\text{micro}} = [T_\sigma]^{-1}[s]_{\text{fibre}-\text{micro}}[T_\varepsilon]$$

in the opposite case. Or else

$$[C]_{j-\text{micro}} = [s]^{-1}_{\text{matrix}}$$

$$[C]_{j-\text{micro}} = [[T_\sigma]^{-1}[s]_{\text{fibre}-\text{micro}}[T_\varepsilon]]^{-1} \tag{5b}$$

where $[T_\sigma]$, $[T_\varepsilon]$ are the stress and the strain transformation matrices.

Then, still using the Lagrangian multipliers method and conditions of continuity and averaging of stresses or strains, the approach consists of supplying the lower and the upper bounds of each volume meso-element stiffness (or compliance) properties, respectively, minimizing the complementary (U_c) and strain (U_s) energy. Thus, we define

$$[C]_{k-\text{meso}} \leq \sum_{j=1}^{8} V_j [C]_{j-\text{micro}} [L^\varepsilon_j]_{k-\text{meso}} U_s \min i$$

$$[S]_{k-\text{meso}} \leq \sum_{j=1}^{8} V_j [S]_{j-\text{micro}} [L^\sigma_j]_{k-\text{meso}} U_c \min i \tag{6a}$$

with $[L^\varepsilon_j]_{k\text{-meso}}$ and $[L^\sigma_j]_{k\text{-meso}}$ derived from expression (6b).

$$\{\varepsilon\}_{j-\text{micro}} = [L^\varepsilon_j]_{k-\text{meso}} \{E\}_{k-\text{meso}} U_s \min i$$

$$\{\sigma\}_{j-\text{micro}} = [L^\sigma_j]_{k-\text{meso}} \{\Sigma\}_{k-\text{meso}} U_c \min i \tag{6b}$$

where $\{\varepsilon\}_{j\text{-micro}}$, $\{\sigma\}_{j\text{-micro}}$, $\{E\}_{k\text{-meso}}$, $\{\Sigma\}_{k\text{-meso}}$ are the micro-element and meso-element strains and stresses.

At the macroscopic level, the latter approach is extended to a three-dimensional assembly of regular volume meso-elements (see Fig. 2) to eventually estimate the bounds of the unit cell elastic properties.

$$[C]_{\text{macro}} \leq \sum_{k=1}^{N_x N_y N_z} V_k [C]_{k-\text{meso}} [L^\varepsilon_k]_{\text{macro}} U_s \min i$$

$$[S]_{\text{macro}} \leq \sum_{k=1}^{N_x N_y N_z} V_k [S]_{k-\text{meso}} [L^\sigma_k]_{\text{macro}} U_c \min i \tag{7a}$$

where $v_k = 1/N_x N_y N_z$; $N_x N_y N_z$ represents the number of meso-elements, with

$$\{E\}_{k-\text{meso}} = [L^\varepsilon_k]_{\text{macro}} \{E\}_{\text{macro}} U_s \min i$$

$$\{\Sigma\}_{k-\text{meso}} = [L^\sigma_k]_{\text{macro}} \{\Sigma\}_{\text{macro}} U_c \min i \tag{7b}$$

where $\{E\}_{\text{macro}}$ and $\{\Sigma\}_{\text{macro}}$ are the unit-cell strains and stresses.

Result of the method

The key point of the method which consists of explaining the relations between internal and external stresses (or strains) through localization matricies, allows us, first, to determine the bounds for the elastic characteristics of a textile reinforcement unit cell. Then, it is possible to estimate the internal stress and strain states according to an imposed external stress $\{\Sigma\}_{\text{macro}}$ or an imposed external strain $\{E\}_{\text{macro}}$ up to the microscopic scale.

For example, we propose in eqns (8a)–(8d) the bounding of stress and strain tensors at the microscopic scale (that of a micro-element) for an imposed external stress and then for an imposed strain. The knowledge of micro-element stress and strain states is directly exploitable to anticipate the composite failure behaviour.

At this scale, we can include several criteria taking into account the matrix cracking and the fibre failure. As each of the different criteria are applied to the assembly of subcells which compose the unit cell, progressive damage functions can also be determined.

Details on numerical procedure for progressive failure simulation

The method used to simulate progressive failure of textile composites is based on the relations (8). The analysis according to an imposed macroscopic stress or an imposed strain are similar in so far as the yield criterion used is the same for both configurations. In the present paper, the maximum stress criterion will be used to study the failure behaviour of 3D braided composites. However, it is possible to use a maximum strain or a quadratic criterion. The procedure for progressive failure simulation according to an imposed uniaxial stress and using a maximum stress criterion is detailed below.

First of all, each stiffness $[C]_{j\text{-micro}}$ or compliance $[S]_{j\text{-micro}}$ matrix is calculated by a first elastic analysis on the undamaged composite. Once this calculation is achieved, we consider a macroscopic stress (for example, a unity) in the studied direction. The micro-elements internal stresses are then deduced in the local axis associated with the fibre direction. The minimal tension, compression or shear normalized stress (strength on real stress) is investigated in order to give the macroscopic stress value that would yield to the first micro-element failure. The constitutive matrix of the micro-element is then reduced by the selective RC method (rows and columns of the matrix $[C]_{\text{macro}}$ set to zero according to the stress allowable which was exceeded). The elastic analysis is continued, taking into account the change of $[C]_{j\text{-micro}}$ (or $[S]_{j\text{-micro}}$).

Table 1. Glass and epoxy properties [MPa]

	Glass	Epoxy
$E_{11} = E_{22} = E_{33}$	73000	3130
$G_{12} = G_{13} = G_{23}$	30000	1170
$\nu_{12} = \nu_{13} = \nu_{23}$	0.20	0.34

APPLICATION TO A WOVEN FABRIC–PREDICTION OF ELASTIC BEHAVIOUR

The validation of the numerical procedure in case of elastic prediction is provided through experiments carried out on woven fabric composites. We study the cases of a plain-woven and five-harness-satin-woven fabrics. Both textile composites are glass/epoxy materials. The constituent properties and the main geometrical characteristics of the unit cells are given in Tables 1 and 2 and Fig. 5.

Table 2. Geometrical data [mm]

	Unit cell						Tow	
	t_m*	H*	D_{weft}*	D_{warp}*	V_{fl}	V_{fg}	a*	b*
Plain	0.005	0.205	0.65	0.65	0.81	0.514	0.3	0.05
Satin	0.005	0.205	3.25	3.25	0.81	0.538	0.3	0.05

*t_m: matrix thickness, H: height of the unit cell, D_{weft} and D_{warp}: distance along weft and warp directions, V_{fl}: tow fibre packing ratio, V_{fg}: composite fibre volume ratio, a and b: yarn geometric parameters (Fig. 5).

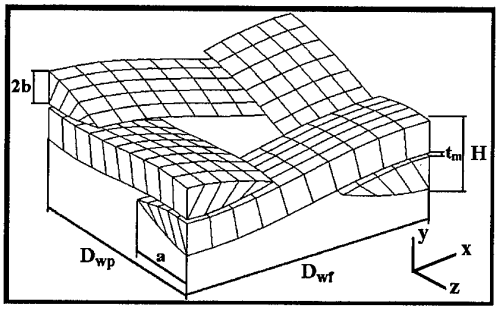

Fig. 5. Plain-woven fabric unit cell geometrical parameters.

According to an imposed stress

$$[L_j^{\sigma}]_{k-\text{meso}}\left[\sum_{j=1}^{j=8} v_j[S]_{j-\text{micro}}[L_j^{\sigma}]_{k-meso}\right]^{-1}[L_k^{\varepsilon}]_{\text{macro}}$$

$$\left[\sum_{k=1}^{N_xN_yN_z} v_k\cdot\left\{\sum_{j=1}^{j=8} v_j[C]_{j-\text{micro}}[L_j^{\varepsilon}]_{k-\text{meso}}\right\}\cdot[L_k^{\varepsilon}]_{\text{macro}}\right]^{-1}\{\Sigma\}_{\text{macro}}\le\{\sigma\}_{j-\text{micro}}$$

$$\{\sigma\}_{j-\text{micro}}\le[L_j^{\sigma}]_{k-\text{meso}}\cdot\left\{\sum_{j=1}^{j=8} v_j[C]_{j-\text{micro}}[L_j^{\varepsilon}]_{k-meso}\right\}\cdot[L_k^{\varepsilon}]_{\text{macro}}\cdot$$

$$\left(\sum_{k=1}^{N_xN_yN_z} v_k\cdot\left\{\sum_{j=1}^{j=8} v_j[S]_{j-\text{micro}}[L_j^{\sigma}]_{k-\text{meso}}\right\}\cdot[L_k^{\sigma}]_{\text{macro}}\right)\{\Sigma\}_{\text{macro}} \tag{8a}$$

$$[L_j^{\varepsilon}]_{k-\text{meso}}[L_k^{\sigma}]_{\text{macro}}\left[\sum_{k=1}^{N_xN_yN_z} v_k\cdot\left\{\sum_{j=1}^{j=8} v_j[C]_{j-\text{micro}}[L_j^{\varepsilon}]_{k-\text{meso}}\right\}\cdot[L_k^{\varepsilon}]_{\text{macro}}\right]^{-1}\{\Sigma\}_{\text{macro}}\le\{\varepsilon\}_{j-\text{micro}}$$

$$\{\varepsilon\}_{j-\text{micro}}\le[L_j^{\varepsilon}]_{k-\text{meso}}\cdot[L_k^{\varepsilon}]_{\text{macro}}\cdot\left(\sum_{k=1}^{N_xN_yN_z} v_k\cdot\left\{\sum_{j=1}^{j=8} v_j[S]_{j-\text{micro}}[L_j^{\sigma}]_{k-\text{meso}}\right\}\cdot[L_k^{\sigma}]_{\text{macro}}\right)\{\Sigma\}_{\text{macro}} \tag{8b}$$

According to an imposed strain

$$[L_j^{\sigma}]_{k-\text{meso}}[L_k^{\sigma}]_{\text{macro}}\left[\sum_{k=1}^{N_xN_yN_z} v_k\cdot\left\{\sum_{j=1}^{j=8} v_j[S]_{j-\text{micro}}[L_j^{\sigma}]_{k-\text{meso}}\right\}\cdot[L_k^{\sigma}]_{\text{macro}}\right]^{-1}\{\Sigma\}_{\text{macro}}\le\{\sigma\}_{j-\text{micro}}$$

$$\{\sigma\}_{j-\text{micro}}\le[L_j^{\sigma}]_{k-\text{meso}}\cdot[L_k^{\sigma}]_{\text{macro}}\cdot\left(\sum_{k=1}^{N_xN_yN_z} v_k\cdot\left\{\sum_{j=1}^{j=8} v_j[C]_{j-\text{micro}}[L_j^{\varepsilon}]_{k-\text{meso}}\right\}\cdot[L_k^{\varepsilon}]_{\text{macro}}\right)\cdot\{E\}_{\text{macro}} \tag{8c}$$

$$[L_j^{\varepsilon}]_{k-\text{meso}}\left[\sum_{j=1}^{j=8} v_j[C]_{j-\text{micro}}[L_j^{\varepsilon}]_{k-meso}\right]^{-1}[L_k^{\sigma}]_{\text{macro}}$$

$$\left[\sum_{k=1}^{N_xN_yN_z} v_k\cdot\left\{\sum_{j=1}^{j=8} v_j[S]_{j-\text{micro}}[L_j^{\sigma}]_{k-\text{meso}}\right\}\cdot[L_k^{\sigma}]_{\text{macro}}\right]^{-1}\{\Sigma\}_{\text{macro}}\le\{\varepsilon\}_{j-\text{micro}}$$

$$\{\varepsilon\}_{j-\text{micro}}\le[L_j^{\varepsilon}]_{k-\text{meso}}\cdot\left\{\sum_{j=1}^{j=8} v_j[S]_{j-\text{micro}}[L_j^{\sigma}]_{k-meso}\right\}\cdot[L_k^{\sigma}]_{\text{macro}}$$

$$\left(\sum_{k=1}^{N_xN_yN_z} v_k\cdot\left\{\sum_{j=1}^{j=8} v_j[C]_{j-\text{micro}}[L_j^{\varepsilon}]_{k-\text{meso}}\right\}\cdot[L_k^{\varepsilon}]_{\text{macro}}\right)\cdot\{E\}_{\text{macro}} \tag{8d}$$

For the plain-woven fabric, a unit-cell quarter is meshed with 864 meso-elements ($12(x)\times12(y)\times6(z)$). As for the five-harness-satin-woven fabric, which has a more heterogeneous geometry, it is meshed with 3456 elements ($24(x)\times24(y)\times6(z)$). More refined meshing does not improve the elastic prediction.

Table 3 gives comparisons between the results obtained by the experiments (only for the plain woven fabric), our numerical procedure (average of results provided by both the U_s and U_c approaches) and an exact method (F.E.M.) [4]. We can see that the results obtained by the

numerical procedure can be accepted. Indeed, the difference from the exact solution does not exceed 1% as for the E_x and E_z moduli and 11% as for the E_y modulus. However, we have to be cautious as far as the Poisson ratios are concerned (24% for ν_{xz}, 11% for ν_{yx}). The satin-woven fabric can be considered in the same way. The results confirm that the moduli predictions can be accepted (1% as for the E_x and E_z moduli and 6% as for the E_y modulus). However, the discrepancies observed for the Poisson ratios are lower (about 18% for ν_{xz} and 9% for ν_{yx}).

Table 3. Comparisons between experimental and numerical results

	Plain			Satin	
	Exact	Tis3D	Exp.	Exact	Tis3D
$E_x = E_z$	25200	24700	24860	25800	25540
E_y	11000	12380	14000	11100	11800
G_{xz}	5230	5140	6140	5700	5560
$G_{yx} = G_{yz}$	3260	3640	4000	3400	3740
ν_{xz}	0.140	0.178	0.194	0.150	0.181
$\nu_{yx} = \nu_{yz}$	0.310	0.348	0.360	0.320	0.352

APPLICATION TO A 3D COMPOSITES—PREDICTION OF PROGRESSIVE FAILURE

We propose to test the validity of our numerical procedure for the failure behaviour from experiments carried out on Carbon/PA12 3D rectangular cartesian braided fabrics. The carbon yarns are spun and coated with the matrix.

Material properties

The mechanical properties of the constituents are summed up in Table 4. The fibre packing ratio is equal to 0.7.

Data used to study the braided composite failure behaviour are voluntarily restricted (in a first approach and considering the tensile loading) to axial tension and compression and braiding yarn shear strengths at the micro-elements scale. These data are presented in Table 5.

This restrictive choice is deduced from experimental observations usually done concerning the 3D composites failure. Referring to Cox [5], their failure results from phenomena combining axial tension and compression and yarn shear (kink band formation) failures, which the resin resistance does not affect.

Table 4. Carbon and PA12 properties [MPa]

	Carbon	PA-12
E_{11}	230000	1300
E_{22}	15000	1300
E_{33}	15000	1300
G_{12}	50000	480
G_{13}	50000	480
G_{23}	12000	480
ν_{12}	0.33	0.36
ν_{13}	0.33	0.36
ν_{23}	0.33	0.36

Table 5. Tow maximum strengths

Axial tensile strength	Axial compression strength	Shear strength
$\sigma_o = 912$ MPa $s = 6.612$ $L_o = 35$ mm $\alpha = 0.610$	810 MPa	90 MPa

The tensile strength is described through a three-parameter Weibull distribution with the cumulative distribution function (CDF) given below (eqn (9)).

$$F(\sigma) = 1 - \exp\left[-\left(\frac{L}{L_0} \right)^{\alpha} \left(\frac{\sigma}{\sigma_0} \right)^{s} \right] \qquad (9)$$

where s is the shape parameter, σ_o the shape parameter, L_o the gauge length reference and α describes the effect of the gauge length on the CDF.

The determination of these three parameters is carried out by testing four yarn groups of different lengths consolidated at 220 °C and submitted to a 7-bar pressure for one hour. This is a simulation of the consolidation cycle of the 3D braided composites. Each group are composed of 15–23 specimens with a gauge length of 35–140 mm. In Fig. 6, we present the CDF curves for F versus σ/σ_o allowing us to determine two parameters of the Weibull law. Figure 7 shows the evolution of $(\sigma_o(L)/\sigma_o(L_o))$

ratio (normalized scale parameter) according to the gauge length ratio L/L_o. It is then possible to determine the third CDF parameter, giving the tensile strength distribution law however long the specimen is.

The axial compression and shear strength values given are averages. As for axial compression, tests are carried out on 2 mm-long specimens and the variations observed on them are quite negligible. As for shear, we also observe few variations since it is impossible to include scale phenomena (tests are carried out on tows with an identical section).

Geometrical properties

In order to determine the unit cell geometry of the 3D rectangular cartesian braided composites, we make a painstaking sectioning of specimens (Fig. 8). It allows us to rebuild the path of each braiding yarn along a repetition unit and thus to identify 10 constituent subcells

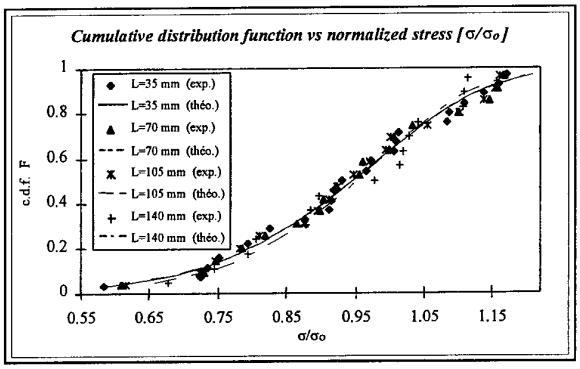

Fig. 6. Cumulative distribution functions of single Carbon/PA12 tows made for various gauge length.

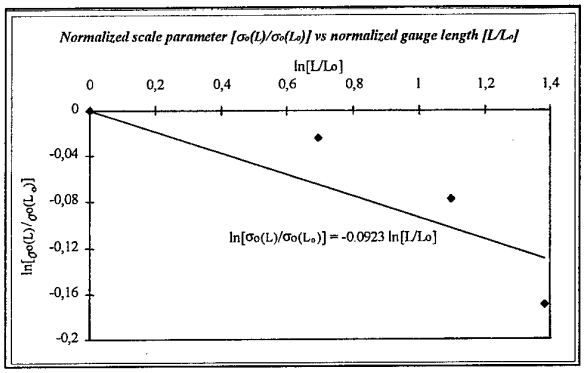

Fig. 7. Normalized scale parameter $[\sigma_o(L)/\sigma_o(L_o)]$ versus normalized gauge length $[L/L_o]$ — determination of the third Weibull distribution parameter α.

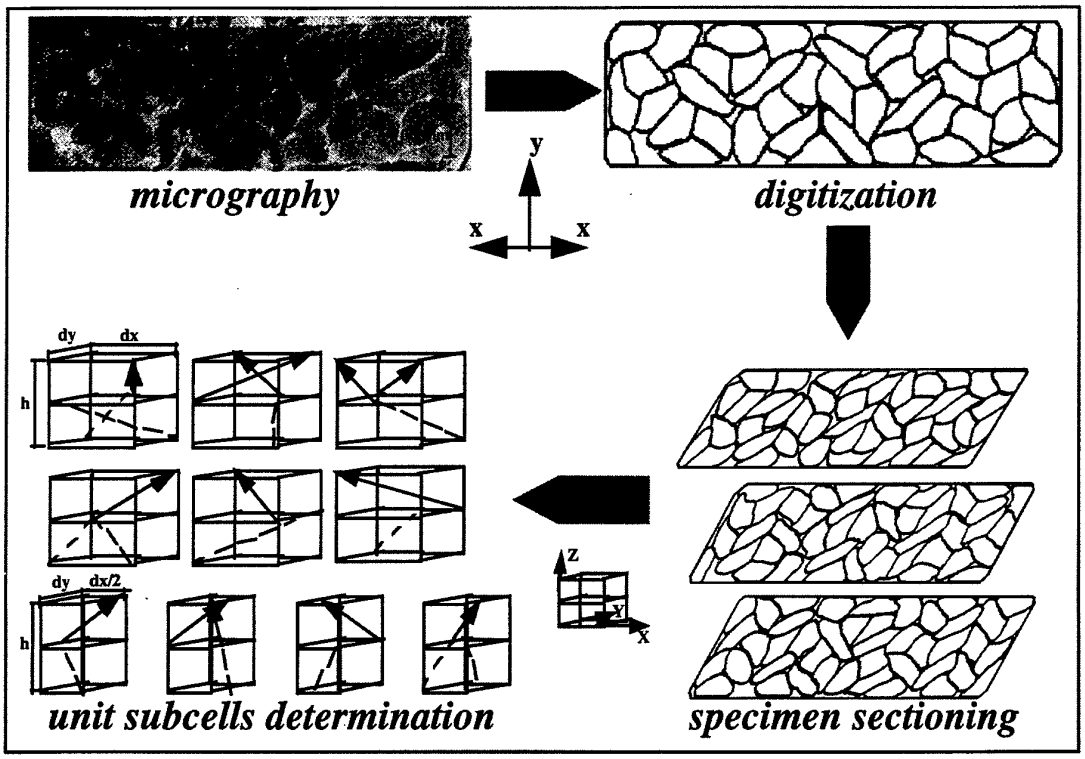

Fig. 8. 3D braided fabric unit cell construction by specimen sectioning.

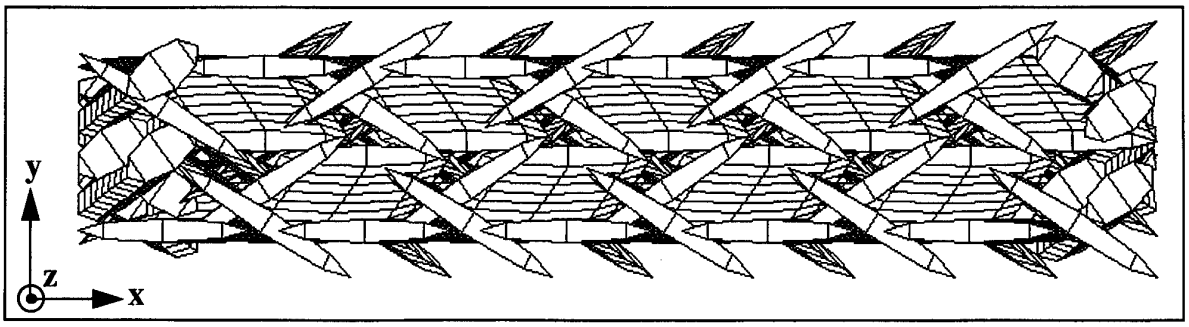

Fig. 9. 3D cartesian braided fabric unit cell.

from the braided composite unit cell (Fig. 9). The orientations of each of the yarn elements within the subcells as well as the composite fibre volume ratio can be determined from the process parameters.

Progressive failure according to a tensile loading

Forty-three-yarn-braided-fabrics are loaded to failure (along the z-axis direction). The dimensions of the specimens are $100 \times 10 \times 2$ mm ($L \times l \times e$). The average braiding angle is equal to 27°. The average fibre volume ratio, determined according to the ASTM D 3171 norm, is 0.517.

The Fig. 10 shows a comparison between five experimental and two simulated progressive damage functions. The simulations are derived from the eqn (8a) (maximum stress criterion) and considering that the macroscopic strain $\{E\}_{\text{macro}}$ according to the imposed macroscopic stress $\{\Sigma\}_{\text{macro}}$ is directly given by

$$\{E\}_{\text{macro}} = [S]_{\text{macro}} \cdot \{\Sigma\}_{\text{macro}} \qquad (10)$$

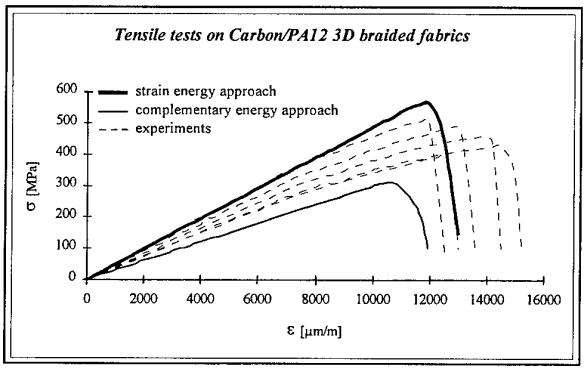

Fig. 10. Comparisons between experimental and simulated damage functions.

this expression is determined from the eqns (6b) and (7b).

The two simulation curves are based on a 1536-meshing ($24(x) \times 8(y) \times 8(z)$) of the unit cell shown in Fig. 9.

We note that in the case of a complementary energy approach the first simulated micro-element failure occurs more rapidly in terms of stress (310 MPa according to U_c and 560 MPa according to U_s). The failure of the whole braided composite is then predicted before that determined from the strain energy approach which seems rather logical according to expressions (8). We can also notice that strains to failure are almost similar (10%).

As far as the experimental curves are concerned, we remark that strength values are included between the bounds predicted by both of our approaches. However the simulated strain to failure values are lower than the experimental ones. This is probably due to the original formulation of the strength problem which is based on a maximum stress criterion and that in principle strain criteria are not taken into account. We can also explain it by the fact that, by definition, 3D braided architecture implies important strains to failure, often considered as structural strains, which can hardly be modelled at the present time.

Finally, it seems necessary to add that the failure description included between two functions is justified if we consider the various dispersions observed on a group of specimens.

CONCLUSIONS

An efficient numerical procedure based on the knowledge of textile geometry is proposed in order to simulate the elastic and failure behaviour of textile-reinforced composites.

The elastic prediction is shown to be quite close to a usual F.E.M. in the case of woven fabric composites. Failure seems to have quite an encouraging future since they can deal with complex architectures.

In the future, this numerical procedure will allow us to optimize and compare the properties of braided structural elements with these of metal elements.

ACKNOWLEDGEMENTS

Mr Bigaud's research was supported by the French Research Ministry and the Rhône-Alps Region.

REFERENCES

1. Aboudi, J., Micromechanical analysis of composites by the method of cells. *Appl. Mech. Reviews* 1989, **47**, (7), 193–221.
2. Chen, D. and Cheng, S., Analysis of composite materials: a micromechanical approach. *J. Reinforced Plastics and Composites* 1993, **12**, 1323–1338.
3. Lene, F., Hassim, A. and Paumelle, P., Homogenized behaviour of woven fabric composites, *Proceedings of 'Comportement des composites 'a renforts tissus — Comportement dynamique des composites'*, Ed. Pluralis, 1991, pp. 69–82.
4. Chouchaoui, C. S., Modélisation du comportement des matériaux composites à renforts tissés et à matrice organique. *Thesis submitted at Université de technologie de Compiègne*, 1995.
5. Cox, B. N. and Flanagan, G., *Handbook of Analytical Methods for Textile Composites*, Rockwell Science Center, 1996.

ELSEVIER

Composite Structures Vol. 38, No. 1–4, pp. 373–381, 1997
© 1997 Elsevier Science Ltd. All rights reserved
Printed in Great Britain
0263-8223/97/$17.00 + 0.00

PII:S0263-8223(97)00072-X

The influence of FRP inserts on the energy absorption of a foam-cored sandwich panel

M. S. Found,[a] A. M. Robinson[b] & J. J. Carruthers[b]

[a]*Department of Mechanical Engineering, The University of Sheffield, Mappin Street, Sheffield S1 3JD, UK*
[b]*Advanced Railway Research Centre, The University of Sheffield, Regent Court, 30 Regent Street, Sheffield S1 4DA, UK*

This paper describes an experimental investigation into the energy absorption properties of a foam-cored sandwich panel with integral fibre-reinforced plastic (FRP) tubes and frusta. The panels were tested under quasi-static flatwise compression and a number of different insert geometries were examined. By using X-ray analysis it was found that those panels with inserts which failed by stable progressive brittle fracture exhibited the best specific energy absorptions. Inserts which failed catastrophically led to much lower values. Conical inserts were found to offer the most repeatable performance as their geometry assisted in ensuring consistency of manufacture. © 1997 Elsevier Science Ltd.

INTRODUCTION

Considerable research interest has been shown in the use of composite materials for crashworthiness applications because it has been demonstrated that they can be designed to provide energy absorption capabilities which are superior to those of metals when compared on a weight-for-weight basis [1,2]. It has been found that, in general, fibre-reinforced plastics (FRPs) do not exhibit the ductile failure processes associated with metals. Instead, the brittle nature of most fibres and resins tends to generate a brittle mode of failure. Provided that the crushing mechanisms can be controlled so that the FRP fails in a stable, progressive manner, very high levels of energy can be absorbed.

In recent years, some progress has been made in establishing the influence of material, geometric and experimental parameters on the energy absorption capability of FRP tubes, with perhaps Hull [3] providing the definitive work in this field. However, the practical application of this knowledge has been limited by the simplistic nature of the geometries investigated. Although tubes can be considered structurally representative up to a point, the question remains of how best to reproduce the high energy absorptions demonstrated in the laboratory within real applications. Furthermore, design methodologies and manufacturing techniques need to be developed which will enable the viable production of actual crashworthy structures. This is especially important if FRP components are to be competitive with their metallic counterparts.

This paper describes one approach to the development of structural crashworthy composites. It is based on the use of a foam-cored sandwich panel with integral energy absorbing FRP inserts. The function of the FRP inserts, which were in the form of tubes and hollow conical frusta, was to control the failure loads (and hence the energy absorption capability) of the panels. Resin transfer moulding (RTM) was used to fabricate the test specimens. The overall objective of this investigation was to establish a fundamental understanding of the energy absorption behaviour of the panels and, in particular, the influence of the FRP inserts. By identifying the principal failure mechanisms and ascertaining their relative contribution to the overall energy absorption, recommendations for optimising the performance of such structures can be proposed.

MATERIAL DESIGN AND SPECIFICATION

A cut-away illustration of the structural concept behind the panels studied in this investigation is shown in Fig. 1. The basic sandwich consisted of a rigid closed-cell polyurethane foam of nominal density 120 kg/m^3 surrounded by facings of glass-reinforced unsaturated polyester (GRP). Moving outwards from the core, the face plate laminates were comprised of a layer of 450 g/m^2 continuous fibre mat, a layer of 2336 g/m^2 [0/45/90/−45] non-crimp quadriaxial mat and a 80 g/m^2 surface veil. Each facing had a thickness of 3 mm, and that of the foam core was 25 mm.

Incorporated within the core of each specimen were four GRP inserts fabricated from [±45] braided glass fibres in an unsaturated polyester resin. These ran through the entire thickness of the core with their longitudinal axes perpendicular to the face plates of the sandwich. Their positions within each specimen are shown in Fig. 2. The fibres at the ends of each braided insert were merged with those of the face plate laminates (between the continuous fibre and quadriaxial mats) so as to provide a mechanical tie between opposing facings. It has previously been shown [4] that this arrangement inhibits separation of the face plates, even after core debonding. Furthermore, it been found [4] to enhance the mechanical properties of a panel, particularly with respect to shear stiffness and strength.

A number of different insert geometries were tested, although there was no variation within a given specimen. Details are provided in Table 1. The geometries of the conical frusta were chosen in accordance with Mamalis *et al.* [5], recommendations for designing FRP frusta which fail by high energy progressive crushing. Similar mean diameters were then selected for the tubular inserts. In general, all the conical inserts in a given specimen were oriented in the same direction (i.e. all the wide ends were adjacent to the same face plate). However, for some of the 20.6 mm wide outside diameter frusta, two diagonally opposing inserts were inverted (i.e. each face plate was adjacent to two wide ends and two narrow ends). Furthermore, a number of the specimens with 20.6 mm wide outside diameter frusta were manufactured without any braid ends passing into the face plate laminate (i.e. there were no mechanical ties between opposing facings). A conventional sandwich panel, without any inserts, was also tested for the purpose of comparison.

MANUFACTURE OF SPECIMENS USING RESIN TRANSFER MOULDING

Resin transfer moulding (RTM) typically involves the assembly of a dry fibre/foam preform which is then placed in a closed mould and injected with a low viscosity liquid resin. The advantages of RTM which make it particularly suitable for manufacturing energy absorbing sandwich panels include:

1. The ability to produce complex geometries.

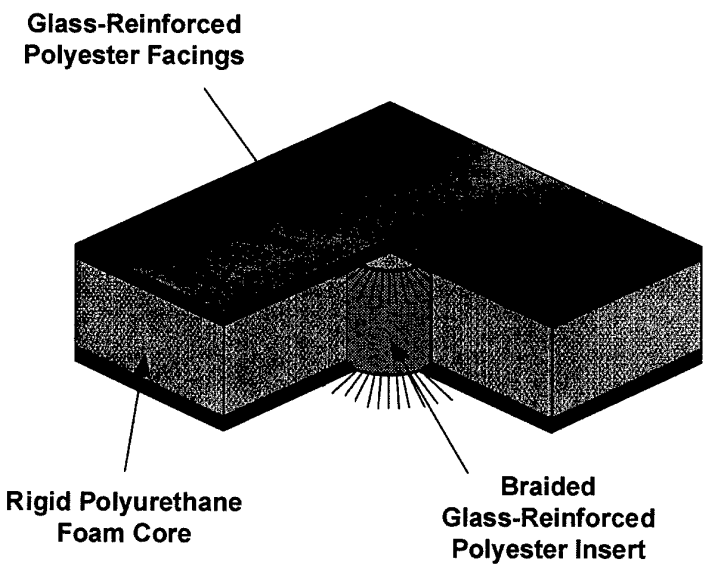

Fig. 1. General structural design of the energy absorbing composite sandwich structures.

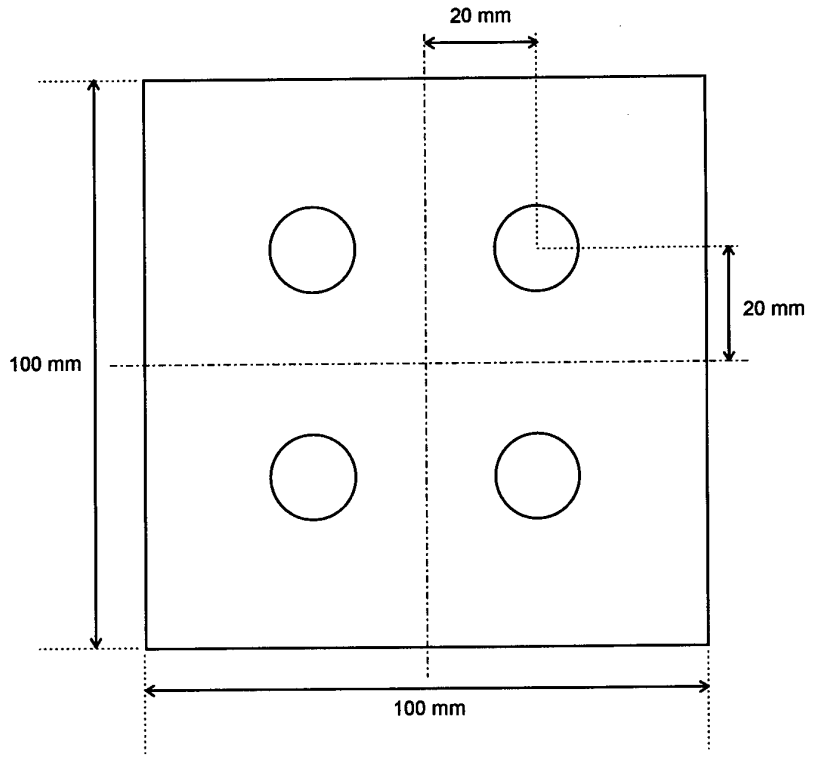

Fig. 2. Arrangement of the four GRP inserts within the cores of the test specimens.

2. The consistency of the finished products.
3. The opportunities it provides for the local tailoring of reinforcements.
4. The opportunities it provides for integrated design.
5. The closed mould reduces emissions and promotes a healthy work place.
6. It is cost-effective for small–medium sized production runs.

The first stage in the manufacture of the test specimens involved the production and preparation of the rigid polyurethane foam core material. This was moulded in solid blocks of dimensions $800 \times 130 \times 25$ mm using a procedure which has been described elsewhere [6]. From these blocks, smaller $125 \times 125 \times 25$ mm core specimens were cut. These were then abraded (to improve adhesion with the face plates) and drilled in accordance with Fig. 2 and Table 1; the diameters of the drilled holes were equal to the external dimensions of the GRP tubes and frusta. Solid cylindrical and conical polyurethane foam plugs were also produced to fill the gaps inside the GRP inserts. The geometries of these plugs were equal to the internal dimensions of the GRP tubes and frusta.

Having prepared the rigid polyurethane foam, the tubular glass braid was then cut into 60 mm lengths. Each piece was passed through a hole in the foam core and filled with a foam plug. These integrated cores were then laid-up in groups of six, together with their glass mat facings, within a $375 \times 250 \times 31$ mm wooden

Table 1. The different geometries of GRP insert investigated

Insert type	Semi-apical angle	Length (mm)	Inside diameter (mm)	Outside diameter (mm)	Estimated fibre volume fraction (%)
None	—	—	—	—	—
Tube	—	25	14	15	59
Tube	—	25	14	16	29
Hollow conical frustum	10°	25	Wide end = 19.4	Wide end = 20.6	49
Hollow conical frustum	10°	25	Wide end = 19.4	Wide end = 21.5	24

moulding frame on a steel base plate. Holes were cut in the continuous fibre mat to allow the passage of the tubular braid. Once through this layer, the ends of the braid were splayed radially to promote bonding with the rest of the face plate laminate.

When the dry fibres and foams had been satisfactorily positioned within the wooden frame, the whole arrangement was firmly clamped between two steel moulding plates. These plates were heated to a temperature of around 30–35°C in order to promote cure and to ensure the low viscosity of the resin. The polyester resin was then injected through a port located in the centre of the top moulding plate. Injection continued until the resin had reached the small ventilation holes in each of the four lower corners of the mould and no more trapped air was escaping. Upon removal of the injection head, the mould was sealed and the specimens were left to cure for around an hour. The finished six-specimen moulding was then unclamped, removed from the wooden frame and cut into individual $100 \times 100 \times 25$ mm test specimens. This process was repeated for each of the specimen types listed in Table 1.

TESTING AND ANALYSIS PROCEDURES

The specimens were compressed in the flatwise direction between two parallel rectangular platens using a Mayes 100 kN capacity servo-electric test machine. All the specimens were crushed at a uniform rate of 5 mm/min and the load–displacement characteristic was recorded in each case.

One specimen of each type listed in Table 1 was also examined using X-ray analysis. Because glass fibres have higher mass absorption coefficients than either polyurethane foam or polyester resin, radiography provided an ideal method for visualising the response of the GRP inserts at progressively increasing crush distances. In particular, it eliminated the need for specimen dissection, a process which would have been likely to displace the fibres from their original crushed positions.

FAILURE MECHANISMS OF THE TEST SPECIMENS

Under flatwise compression, all specimens exhibited a linear–elastic response at small crush distances ($< \approx 1$ mm). This was due to the bending and stretching of the cells within the rigid polyurethane foam and the elastic compression of the GRP tubes and frusta. Those specimens with GRP inserts displayed a stiffer elastic response than those without.

At large crush distances ($> \approx 15$ mm), the collapse load of all specimens increased rapidly with displacement. The cores of the sandwich panels had become fully crushed, and their useful energy absorption capability was exhausted. Core densification had been reached.

Between these two extremes (i.e. for crush distances of ≈ 1–15 mm), the load–displacement response of the sandwich panels was found to vary considerably with insert geometry. In general, three different types of behaviour were observed: a uniform response, a uniform response with an initial peak load, and a non-uniform response (Fig. 3). Each is considered in turn below.

Uniform response

This was the characteristic behaviour of the sandwich panels with no GRP inserts. Between the elastic and densification regions there was a long collapse plateau in which the load increased only slowly with displacement. Such a response is typical of polymer foams [7], and is associated with the gradual collapse of the cells within the foam. The implication is that, in the absence of any inserts, the properties of the sandwich panels under flatwise compression were dictated by the bulk core material. The principal energy absorption mechanism was the plastic collapse of the cell walls.

Uniform response with an initial peak

This was the characteristic behaviour of the sandwich panels with the following types of insert:

- 16 mm outside diameter tubes.
- 20.6 mm wide outside diameter frusta, half of which were inverted.
- 20.6 mm wide outside diameter frusta, with no braid ends passing into the face plate laminate.
- 21.5 mm wide outside diameter frusta.

These specimens all exhibited a pronounced peak load at the end of the elastic region.

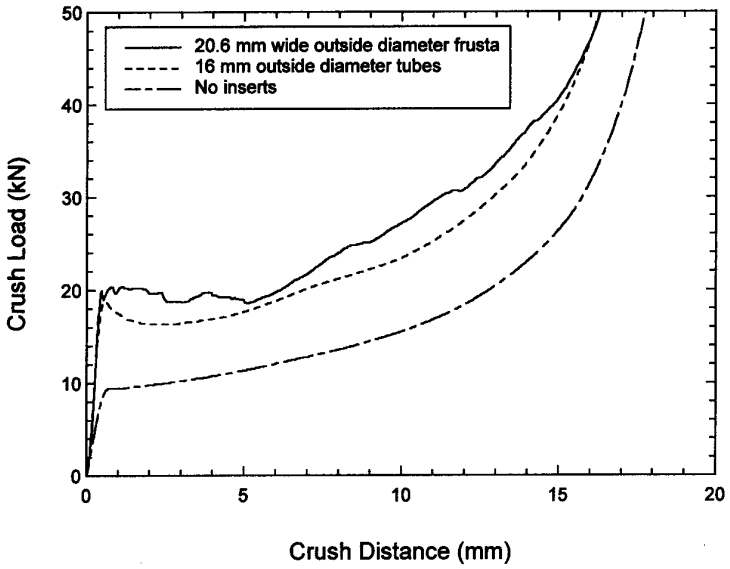

Fig. 3. A comparison of the load–displacement characteristics of representative specimens from each of the three general failure categories. The 20.6 mm wide outside diameter frusta in the specimen shown were all oriented in the same direction.

Audible cracking accompanied the termination of the peak load, suggesting failure of the FRP inserts. The load then dropped and assumed a largely uniform response, similar to that typical of foams, but at a higher average crush level.

These observations would tend to indicate an initial catastrophic failure of the GRP inserts rather than the onset of controlled progressive crushing. X-ray analysis supported this hypothesis. Figure 4 shows the sequence of failure for a 16 mm outside diameter tube. The images clearly show the development of a central circumferential fracture. This then generates a telescopic collapse mode in which the bottom half of the tube slides up inside the top half. Apart from the initial fracture, there is no further evidence of brittle failure. This explains the uniformity in the load–displacement characteristic.

The principal energy absorption mechanisms of these specimens included the plastic collapse of the cells within the rigid polyurethane foam, the matrix cracking and fibre breakage associated with the initial fracture of the GRP inserts, and the frictional effects caused by the fractured halves sliding over one another.

It is believed that the majority of the specimens which failed in a catastrophic manner did so because of inconsistencies in the fibre distribution within the GRP tubes and frusta. Unstable failure was initiated from a local non-uniformity in the material or geometry. These inconsistencies were caused by displacement of the braided fibres during the injection of the resin. For the specimens with the 16 mm outside diameter tubes and the 21.5 mm wide outside diameter frusta, this can be attributed

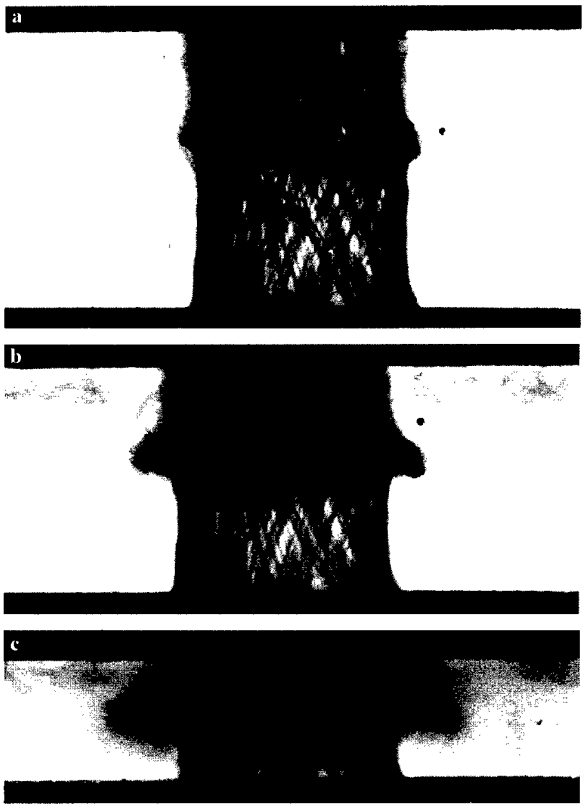

Fig. 4. X-ray analysis showing the sequence of failure for a 16 mm outside diameter tube. Images are shown at crush distances of 2, 6 and 13 mm.

to the large gaps between the inner foam plugs and the outer foam core. The braided glass fibres were free to wander within these gaps and this resulted in considerable deviations in their geometry. Inconsistencies in the fibre distribution were also observed for those inserts without any braid ends passing into the face plate laminate. The very short lengths of braid used to make these specimens tended to result in a lack of cohesion in the fibre weave. The only specimens which were found to have a consistent fibre distribution and yet still failed in a catastrophic manner were those in which half the conical inserts were inverted. It is believed that the inherent asymmetry of this arrangement prevented the onset of stable progressive crushing.

Non-uniform response

This was the characteristic behaviour of the remainder of the specimens, i.e. those with 15 mm outside diameter tubes and 20.6 mm wide outside diameter frusta (oriented in the same direction, with braid ends passing into the face plate laminate). Following initial failure, the load–displacement characteristics of these specimens exhibited pronounced serrations. Furthermore, there was audible cracking throughout the crush event.

These observations are consistent with the progressive crushing of the inserts. Figures 5 and 6 show the sequence of failure for a 15 mm outside diameter tube and a 20.6 mm wide outside diameter frustum. Both clearly show *controlled* brittle failure from one end of the insert. The serrations in the load–displacement characteristic are caused by the stick–slip nature of the brittle fracture process.

It is interesting to note that the GRP frusta all crushed progressively from their wide ends. This is contrary to what is commonly observed [8]; crushing usually occurs from the narrow end of frusta where the stress is locally highest. It is believed that this apparent deviation from the norm was a result of the tubular braid used to fabricate the inserts. This had a nominally constant diameter. Therefore, when formed into a conical geometry, there was a locally higher fibre volume fraction at the narrow end of the frustum and a correspondingly lower one at the wide end. The reduced level of reinforcement at the wide end caused failure to be initiated from this point.

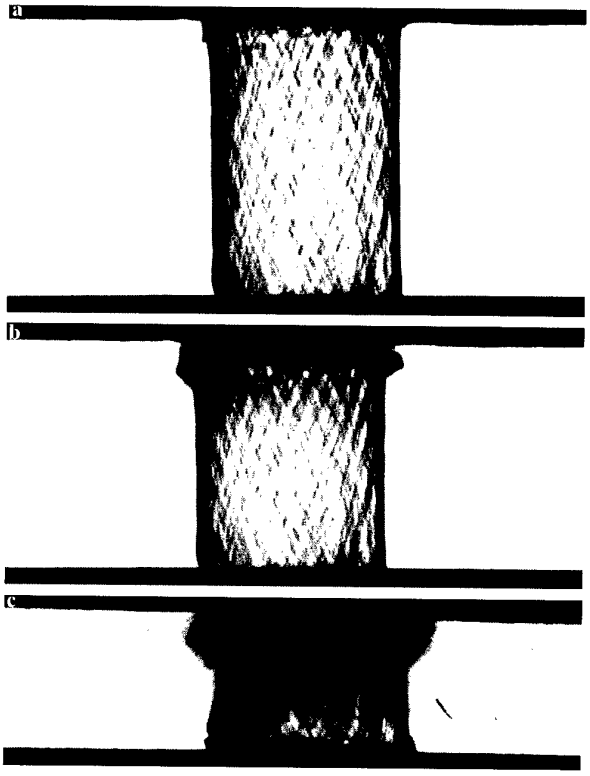

Fig. 5. X-ray analysis showing the sequence of failure for a 15 mm outside diameter tube. Images are shown at crush distances of 2, 6 and 13 mm.

The principal energy absorption mechanisms of the progressive crushing specimens included the plastic collapse of the cells within the rigid polyurethane foam, and the matrix cracking, fibre–matrix debonding and fibre breakage associated with the brittle failure of the inserts.

ENERGY ABSORPTION CAPABILITY OF THE TEST SPECIMENS

Having established the failure mechanisms of the different types of sandwich panel, their energy absorption capabilities were then assessed. The amount of energy absorbed by each specimen was calculated from the area under its load–displacement characteristic. Only useful energy absorption was considered; that beyond crush distances of 15 mm was not taken into account.

Figure 7 shows the variation of absolute energy absorption with insert geometry. The columns represent mean values for specimens with a given type of insert, and the error bars indicate recorded extremes. It can be seen that all panels with GRP tubes and frusta absorbed

more energy than those without. Specimens with 20.6 mm wide outside diameter frusta (oriented in the same direction, with braid ends passing into the face plate laminate) exhibited the highest mean energy absorption, with an increase of 69% over the sandwich panels with no inserts.

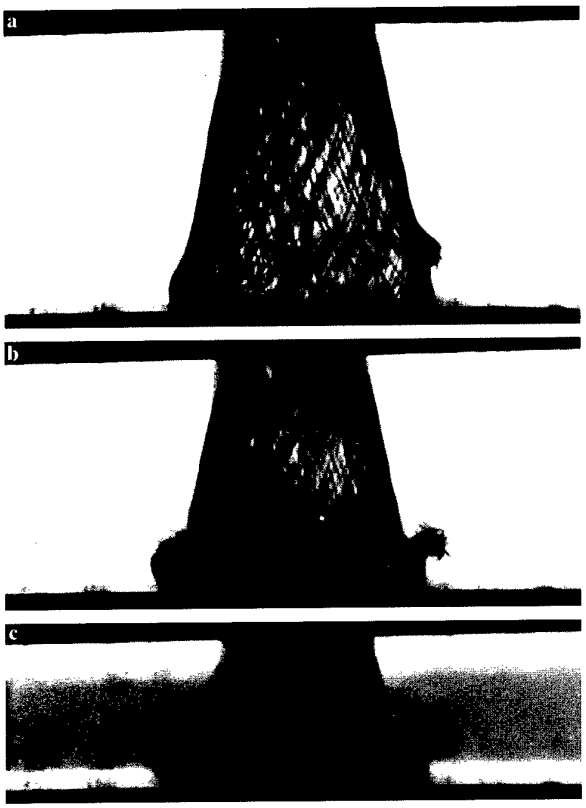

Fig. 6. X-ray analysis showing the sequence of failure for a 20.6 mm wide outside diameter frustum. Images are shown at crush distances of 2, 6 and 13 mm.

However, more meaningful assessments of relative energy absorption performance are often provided by normalised measures. These allow direct comparisons to be made between specimens of different materials and geometries. Therefore, mass specific energy absorptions were also calculated and a comparison is shown in Fig. 8. It can be seen that a very different trend to that shown earlier is revealed. Only two of the insert geometries provided significant improvements over the basic sandwich construction. In other words, for the majority of the specimens, any increase in energy absorption by virtue of the inserts was offset by their higher mass.

The two insert geometries which did show improvements were the 15 mm outside diameter tubes and the 20.6 mm wide outside diameter frusta (oriented in the same direction, with braid ends passing into the face plate laminate). Sandwich panels with these types of insert showed increases in mean specific energy absorption of 12% and 34%, respectively. It should be recalled that these were the only geometries which were found to crush in a stable, progressive manner. Therefore, the energy absorption potential of the brittle fracture processes was exploited very efficiently. Those specimens which failed in a catastrophic manner were much less efficient and resulted in

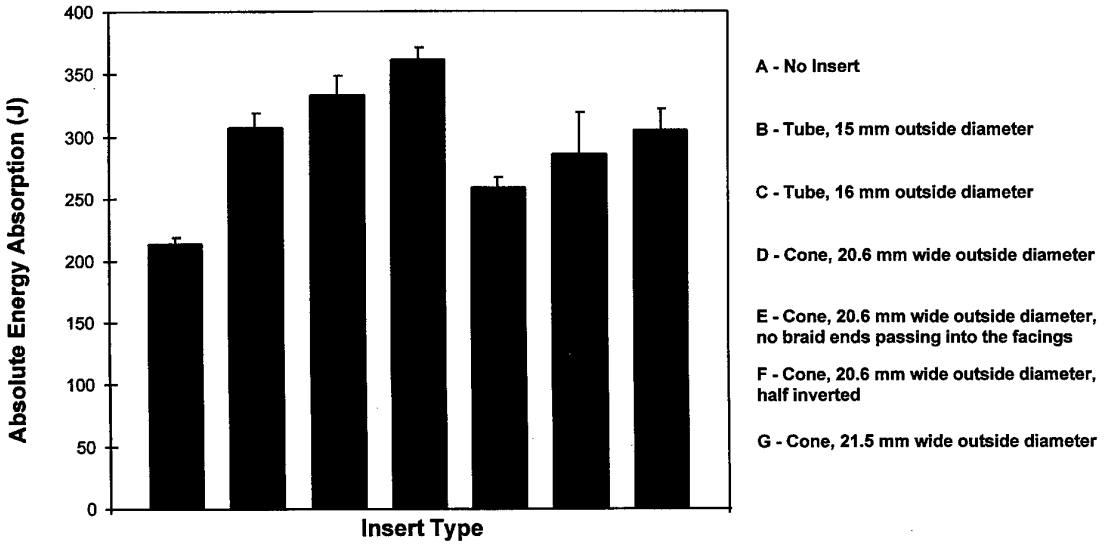

Fig. 7. A comparison of the absolute energy absorption for the different types of sandwich panel.

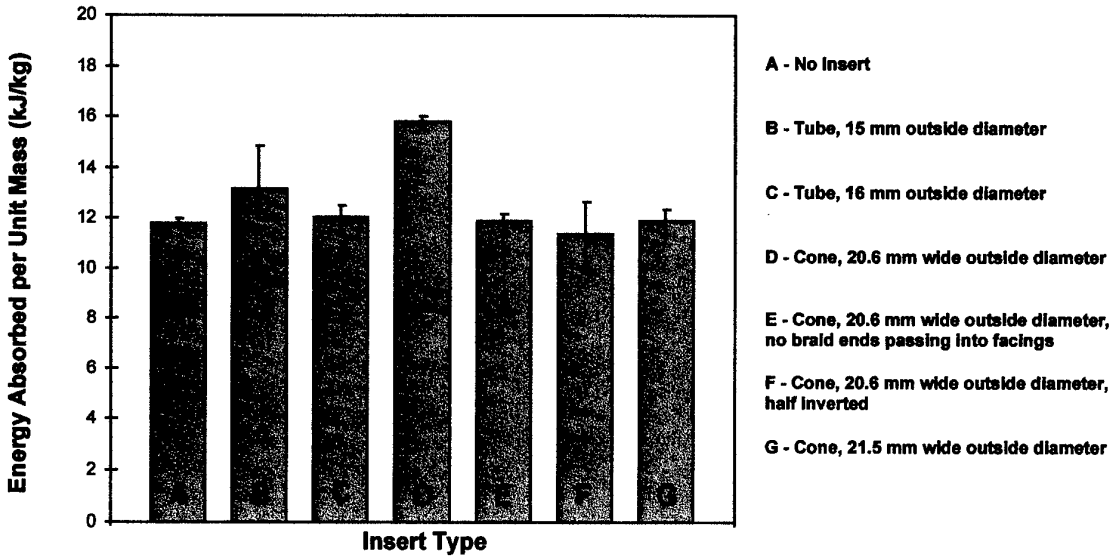

Fig. 8. A comparison of the energy absorbed per unit mass for the different types of sandwich panel.

correspondingly lower values of specific energy absorption.

As for the repeatability of the results, it can be seen from the error bars in Fig. 8 that the specimens with GRP inserts generally exhibited a much wider spread in recorded specific energy absorptions than those without. This is significant because repeatability is an important aspect of crashworthy design; a minimum level of performance must be guaranteed and, on a larger structural scale, there will be a need to predict and ensure a preferred sequence of collapse. However, the 20.6 mm wide outside diameter frusta (with braid ends passing into the face plate laminate) did provide a level of consistency which was comparable to the sandwich panels without any inserts. It is believed that this was due to the manufacturing benefits of this particular geometry. In particular, the conical foam plugs were more straightforward to produce than their tubular counterparts because their shape facilitated easy removal from their moulds. Furthermore, there were a number of factors associated with these specimens which assisted in maintaining the position of the braided glass fibres during lay-up and injection. These included the relatively small gaps between the inner foam plugs and the outer foam cores, the braid ends passing into the face plate laminate, and the inherent conical geometry. All of these helped to ensure that the GRP inserts had a high consistency in their fibre distribution, and hence in their mechanical properties.

CONCLUSIONS

Foam cored sandwich panels with integral GRP tubes and frusta have been tested under quasi-static flatwise compression. Those panels with inserts which failed by stable progressive brittle fracture exhibited the best energy absorption characteristics. The main prerequisite for ensuring this mode of failure was consistency in the fibre distribution within the GRP tubes and frusta. Otherwise, the inserts tended to fail catastrophically at a local non-uniformity in material or geometry. Conical inserts were found to offer the most repeatable energy absorption performance as their geometry assisted in ensuring consistency of manufacture.

The development of representative scale structures based on this, and similar, material systems will form the next stage of this work as part of the *HYCOTRANS* project, a European consortium which has been formed to develop crashworthy composite bodyshells for rail vehicles and coaches [9]. In particular, much work is still required on the optimisation of insert geometries and configurations for a range of loading conditions, not just flatwise compression. Less labour intensive insert designs would also be advantageous.

ACKNOWLEDGEMENTS

The authors would like to thank John Crossland of Fibrelite Composites Ltd, Steve Kemp of Foam Technology Ltd and Martin Spooner of Tech Textiles Ltd for their support of this work.

REFERENCES

1. Thornton, P.H., Energy absorption in composite structures. *J. Composite Materials*, 1979, **13**, 247–262.
2. Schmueser, D.W. and Wickliffe, L.E., Impact energy absorption of continuous fiber composite tubes. *J. Engng Materials and Tech.*, 1987, **109**, 72–77.
3. Hull, D., A unified approach to progressive crushing of fibre-reinforced composite tubes. *Composites Sci. Tech.*, 1991, **40**, 377–421.
4. Richardson, M.O.W., Robinson, A.M., Eichler, K. and Moura Branco, C., Mechanical behaviour of a new stress dissipating composite sandwich structure. *Cellular Polymers*, 1994, **13**, 305–317.
5. Mamalis, A.G., Manolakos, D.E. and Viegelahn, G.L., Sin Min Yap and Demosthenous, G. A., On the axial crumpling of fibre-reinforced thin-walled conical shells. *Int. J. Vehicle Design*, 1991, **12**, 450–467.
6. Carruthers, J.J. and Robinson, A.M., Rigid polyurethane foam as an energy absorbing core for composite components manufactured by resin transfer moulding (RTM) part I: determination of properties. *Cellular Polymers*, 1997, **16**, 1–13.
7. Gibson, L. J. and Ashby, M. F., *Cellular Solids: Structure and Properties*. Pergamon Press, Oxford (1988).
8. Price, J.N. and Hull, D., Axial crushing of glass fibre-polyester composite cones. *Composites Sci. and Tech.*, 1987, **28**, 211–230.
9. Hibbert, L., Composites come up on the rails. *Professional Engng*, 1997, **10** (4), 14–15.

ELSEVIER

Composite Structures Vol. 38, No. 1–4, pp. 383–394, 1997
© 1997 Published by Elsevier Science Ltd. All rights reserved
Printed in Great Britain
0263-8223/97/$17.00 + 0.00

PII:S0263-8223(97)00073-1

Nonlinear closed-form high-order analysis of curved sandwich panels

E. Bozhevolnaya & Y. Frostig*

Institute of Mechanical Engineering, Aalborg University, Pontoppidanstraede 101, DK-9220 Aalborg East, Denmark

Closed-form high-order theory of sandwich panels, including transverse flexibility and shear rigidity of a core, as well as geometrical nonlinearity of unsymmetric faces is generalized for sandwich panels of constant curvature. Variational calculus is used to derive the set of governing equations describing a stress-deformation response of the panel to arbitrary loads. Boundary conditions are presented both in the local and global formulations. The procedure for the numerical solution of the governing nonlinear differential equations is based on the finite-difference method with deferred corrections. The solution technique is illustrated through numerical examples. Influence of the geometrical nonlinearity on the overall behaviour of the sandwich panel and localized effects are demonstrated. © 1997 Elsevier Science Ltd.

INTRODUCTION

Sandwich panels and shells are becoming increasingly used in high-performance crafts and building facilities. Various theoretical models of sandwich structures have been developed in recent years, and a summary of the general approaches can be found in a few textbooks by Plantema [1], Allen [2] and Zenkert [3]. Although these textbooks are devoted mainly to flat sandwich panels, similar principles are adopted in the analysis of curved panels and shell structures.

Reissner [4] was the first who took into account the transverse shear resistance of sandwich plates. Further development of the first-order shear-deformation theory was due to Mindlin [5]. The Reissner–Mindlin model became a foundation for a large group of research accomplishments (see, for example, Di Sciuva and Carrera [6]). The thickness of the sandwich panel is assumed to be constant, thus the normal stresses are neglected. As a consequence, local effects such as debonding and delamination phenomena, the presence of concentrated loads and geometric discontinuities are beyond the capability of the proposed approach.

To overcome the inaccuracies of the first-order shear-deformation theory, higher-order displacements fields were suggested (see, for example, Lo *et al.* [7]). However, these attempts were of limited use as difficulties arose in obtaining the solutions for governing equations under prescribed boundary conditions. Reddy [8] introduced a specific form of the displacement fields that does not increase the order of the system of governing equatons to be solved, but at the same time accounts for a higher-order shear-strain distribution through the thickness of the plate. The application of higher-order shear-deformation theories in FEM modelling has been considered by many (see, for example, Meyer-Piening [9]).

A classification of the computational models supplied with the detailed literature survey has been conducted by Noor *et al.* [10]. It should be stressed that these computational models are based on *a priori* assumptions regarding displacements fields in the sandwich layers. Such a

*Visiting Professor. On Academic leave from Technion-Israel Institute of Technology, Faculty of Civil Engineering, 32000 Israel.

hypothesis suits very well as far as the overall behaviour of a sandwich structure is concerned, but fails if localized phenomena are examined.

Recently, Frostig *et al.* [11–20] have developed a consistent rigorously closed-form high-order theory for sandwich panels and plates that can be extended to curved panels and shells. The theory does not impose any preliminary restrictions on the deformation distributions through the thickness and, as a consequence, the high-order effects are obtained as a part of the solution. The theory is valid for any type of loading, point load as well as distributed, allows discontinuities in loads and geometry and incorporates the transverse flexibility of the sandwich core along with its shear rigidity. Localized effects can be described within the frames of this approach. Boundary conditions may be global or local, i.e. the conditions for the various skins at the same section may be different. The theory has been used to model buckling, vibrations problems, delamination cases, tapered beam and stress concentration in general.

The literature survey reveals that, so far, there is no rigorous nonlinear theory developed for arbitrary loaded sandwich curved panels of general design with a 'soft' core and under arbitrary boundary conditions. Thus, this paper is an extension of the linear closed-form high-order theory to the nonlinear analysis of sandwich curved panels with transversely flexible core assuming a geometrical nonlinearity of the sandwich faces.

MATHEMATICAL MODEL

The proposed model is related to a cylindrically curved sandwich panel consisting of an inner core and two outer face layers. Geometry of the panel, coordinates and sign convention appear in Fig. 1. Here, and in the following text, indices t and b refer to the top (upper) and bottom (lower) faces of the panel. The faces of the sandwich are not identical and have a constant thickness and a constant curvature of their centroidal lines d_i and r_i (i = t,b), respectively. The local coordinate systems for each face (z_i, s_i), with their origins on the face centroidal surfaces, are introduced. Note that these curvilinear systems become polar through the substitution $s_i = r_i\varphi$, where φ is a polar angle.

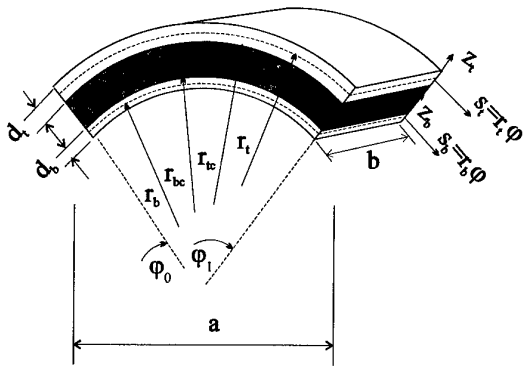

Fig. 1. Geometry of the model.

The local coordinate system for the core is polar (r, φ) and has its origin in the centre of the panel curvatures.

The following assumptions form the basis of the presented model.

The faces may have a different thickness d_t and d_b and they are small in comparison with the panel span a or radii of curvature of the faces. The ratio between the panel span and its radii can be arbitrary. The core is considered to be a two-dimensional elastic medium with resistance to shear and radial stresses. Circumferential (tangential) stresses in the core are neglected. The allowed deformations in the core are small (Fig. 2), thus the kinematic relations become linear. Note that no *a priori* assumptions on the deformation fields through the thickness of the core are made. The core is fully bonded with the faces. Faces are treated as thin elastic panels that follow Bernoulli assumptions. However, circumferential deformations in the faces are in the class of intermediate deformations, i.e. substantial rotations are allowed.

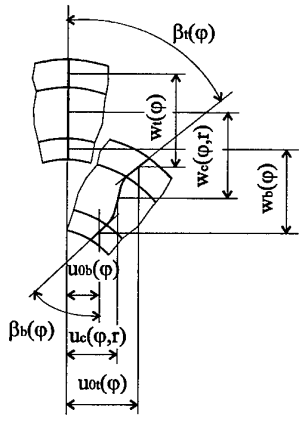

Fig. 2. Deformation in the faces and core.

External loading is exerted on the centroidal surfaces of the faces only. Different kinds of boundary conditions may be implemented for the various faces at the same section. Local boundary conditions are applied to the faces and core separately. If some extraneous rigid members are introduced to connect sandwich components at the edges of the panel, global boundary conditions are applied.

The variational principle based on the minimization of the total potential energy of a deformed system is used to derive the governing equations and the boundary conditions. Total potential energy of the deformed panel consists of the strain energy of the deformed panel U and potential energy of the external forces V.

The variation of the strain energy U is given by

$$\delta U = \int_{V_{top}} \sigma_t \delta\varepsilon_t \, dv_t + \int_{V_{bot}} \sigma_b \delta\varepsilon_b \, dv_b + \int_{V_c} (\sigma_{rr}\delta\varepsilon_{rr} + \tau_c \delta\gamma_{r\varphi}) \, dv_c \tag{1}$$

where σ_i, ε_i ($i = t, b$) are circumferential (tangential) stresses and strains in the faces; σ_{rr}, τ_c and ε_{rr}, $\gamma_{r\varphi}$ are radial and shear stresses and strains in the core, respectively; V_{top}, V_{bot}, V_c are the appropriate volumes of the faces and core to perform integration; $dv_i = r_i d_i b \, d\varphi$ ($i = t, b$), $dv_c = bdr \, d\varphi$ are elementary volumes relating to polar coordinates (see Fig. 1).

External loads acting on the panel are shown in Fig. 3. Here, q_t, q_b, n_t, n_b is a pressure and tangential loading distributed circumferentially; $\bar{P}_{jt}$, $\bar{P}_{jb}$, $\bar{N}_{jt}$, $\bar{N}_{jb}$ are concentrated forces in the radial and circumferential directions; m_t, m_b, $\bar{M}_{jt}$, $\bar{M}_{jb}$ are distributed and concentrated moments.

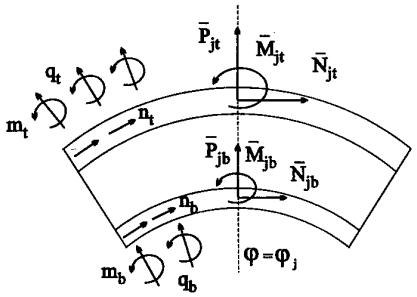

Fig. 3. External loads: distributed and concentrated.

The variation in the potential energy of the external forces V is equal to

$$\delta V = -\int_{L_{top}} (q_t \delta w_t + n_t \delta u_{0t} - m_t \delta\beta_t) \, ds_t - \int_{L_{bot}} (q_b \delta w_b + n_b \delta u_{0b} - m_b \delta\beta_b) \, ds_b - \sum_j \int_{L_{top}} (\bar{P}_{jt}\delta w_t + \bar{N}_{jt}\delta u_{0t} - \bar{M}_{jt}\delta\beta_t) \, \delta_D(s_t - s_j) \, ds_t - \sum_j \int_{L_{bot}} (\bar{P}_{jb}\delta w_b + \bar{N}_{jb}\delta u_{0b} - \bar{M}_{jb}\delta\beta_b) \, \delta_D(s_b - s_j) \, ds_b \tag{2}$$

where w_i, u_{0i}, β_i ($i = t, b$) are radial, circumferential displacements and rotations of the centroids of the faces (see Fig. 2); $\delta_D(s_i - s_j)$ is the Dirac function and s_j is a circumferential coordinate of an applied concentrated load. Integration in eqn (2) is performed along the lengths of the face centroids L_{top} and L_{bot} (cf. Fig. 1).

Deformation of the panel element is shown in Fig. 2. Note that deformation of the faces depends only on the circumferential coordinate φ, while deformations of the core are also functions of the radial variable.

The kinematic relations for the faces in polar coordinates using a moderate type of deformation (see pp. 124–5 of Brush and Almroth [21]) are

$$u_i = u_{0i} + z_i\beta_i, \quad \varepsilon_i = \varepsilon_{0i} + z_i\kappa_i, \quad \beta_i = \frac{u_{0i} - w_{i,\varphi}}{r_i} \quad (i = t, b) \tag{3}$$

where

$$\varepsilon_{0i} = \frac{u_{0i,\varphi} + w_i}{r_i} + \frac{(u_{0i} - w_{i,\varphi})^2}{2r_i^2}, \qquad \kappa_i = \frac{\beta_{i,\varphi}}{r_i} = \frac{u_{0i,\varphi} - w_{i,\varphi\varphi}}{r_i^2}$$

The second term in the expression for the circumferential in-plane strain ε_{0i} introduces geometrical nonlinearity and is due to rotaton of the centroids of the faces.

The kinematic relations for the core in polar coordinates are

$$\varepsilon_{rr} = w_{c,r},\ \gamma_{r\varphi} = u_{c,r} + \frac{w_{c,\varphi} - u_c}{r} \tag{4}$$

As the core and faces are assumed to be fully bonded along their mutial interfaces the following compatibility conditions exist at the upper face–core interface $r = r_{tc}$

$$w_c = w_t,\ u_c = u_{0t} - \frac{d_t}{2}\beta_t \tag{5}$$

and at the lower interface $r = r_{bc}$

$$w_c = w_b,\ u_c = u_{0b} + \frac{d_b}{2}\beta_b \tag{6}$$

In the faces, in-plane resultants and moments are

$$N_i = b\int_{-d_i/2}^{d_i/2} \sigma_i\, dz,\ M_i = b\int_{-d_i/2}^{d_i/2} \sigma_i z\, dz\ (i = t, b) \tag{7}$$

The adopted sign convention and the internal resultants acting in the faces and in the element of the core are shown in Fig. 4. Note that the total stress resultants are presented in the faces: in-plane circumferential resultants, N_i, shear resultants, Q_i, and moments, M_i (i = t, b). The upper face from below and the lower face from above are affected by the shear stress, $\tau_c(r_{ic})$, and the radial normal stress, $\sigma_{rr}(r_{ic})$, because of the cooperation of the faces with the core.

Equilibrium/field equations and boundary conditions

Minimization of the total potential energy of the deformed system $\delta\Pi = \delta U + \delta V \Rightarrow 0$ (cf. eqns (1) and (2)), together with compatibility equations (eqns (5) and (6)) and kinematic relations (eqns (3), (4) and (7)) results in the following set of equalibrium/field equations for a loaded curved sandwich panel

$$N_{t,\varphi} + \frac{M_{t,\varphi}}{r_t} - N_t\frac{(u_{0t} - w_{t,\varphi})}{r_t} - N_t \times \frac{(u^*_{0t} - w^*_{t,\varphi})}{r_t} - br_{tc}\left(1 - \frac{d_t}{2r_t}\right)\tau_c(r = r_{tc}) + r_t n_t - m_t = 0 \tag{8}$$

$$N_{b,\varphi} + \frac{M_{b,\varphi}}{r_b} - N_b\frac{(u_{0b} - w_{b,\varphi})}{r_b} - N_b\frac{(u^*_{0b} - w^*_{b,\varphi})}{r_b} + br_{bc}\left(1 + \frac{d_b}{2r_b}\right) \times \tau_c(r = r_{bc}) + r_b n_b - m_b = 0 \tag{9}$$

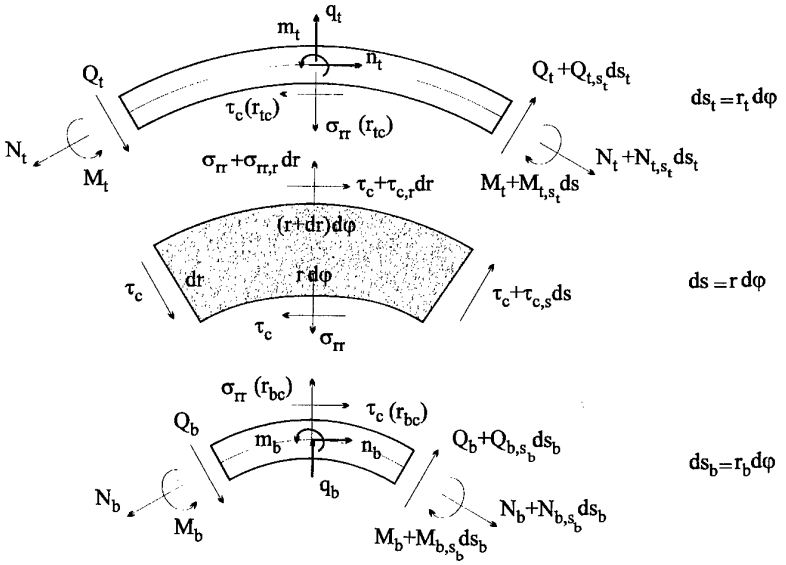

Fig. 4. Internal resultants and stresses in the faces and core.

$$\frac{M_{t,\varphi\varphi}}{r_t} - N_t - \left(N_t \frac{(u_{0t} - w_{t,\varphi})}{r_t}\right)_{,\varphi} - \left(N_t \frac{(u^*_{0t} - w^*_{t,\varphi})}{r_t}\right)_{,\varphi} + br_{tc}\frac{d_t}{2r_t} + \tau_{c,\varphi} \times (r = r_{tc}) - br_{tc}\sigma_{rr}(r = r_{tc}) + r_t q_t - m_{t,\varphi} = 0 \quad (10)$$

$$\frac{M_{b,\varphi\varphi}}{r_b} - N_b - \left(N_b \frac{(u_{0b} - w_{b,\varphi})}{r_b}\right)_{,\varphi} - \left(N_b \frac{(u^*_{0b} - w^*_{b,\varphi})}{r_b}\right)_{,\varphi} + br_{bc}\frac{d_b}{2r_b} + \tau_{c,\varphi} \times (r = r_b) + br_{bc}\sigma_{rr}(r = r_{bc}) + r_b q_b - m_{b,\varphi} = 0 \quad (11)$$

$$\tau_{c,\varphi} + r\sigma_{rr,r} + \sigma_{rr} = 0 \quad (12)$$

$$2\tau_c + r\tau_{c,r} = 0 \quad (13)$$

The first four equations of this system are equilibrium equations (in the radial and circumferential directions) of differential elements of the upper and lower faces. It should be mentioned, referring to Fig. 4, that the terms $\sigma_{rr}(r = r_{ic})$, $\tau_c(r = r_{ic})$ $(i = \mathrm{t}, \mathrm{b})$ in eqns (8)–(11) are radial and shear stresses of the core in the face–core interfaces. The last two equations of this system (eqns (12) and (13)) describe the equilibrium of the two-dimensional elastic core medium in polar coordinates. The local boundary conditions at the edges of the curved panel φ_0 and φ_1 are derived simultaneously with the governing equations from the variation of the total potential energy as follows

$$\lambda\left(N_i + \frac{M_i}{r_i}\right) - \left(\bar{N}_i - \frac{\bar{M}_i}{r_i}\right) = 0 \text{ or } u_{0i} = \bar{u}_{0i} \quad (14)$$

$$\lambda\left(\frac{M_{i,\varphi}}{r_i} - N_i \frac{u_{0i} - w_{i,\varphi}}{r_i} - N_i \frac{u^*_{0i} - w^*_{i,\varphi}}{r_i} + b\frac{r_{ic}d_i}{2r_i}\tau_c(r = r_{ic}) + m_i\right) - \bar{P}_i = 0 \text{ or } w_i = \bar{w}_i \quad (15)$$

$$-\lambda M_i - \bar{M}_i = 0 \text{ or } w_{i,\varphi} = \bar{w}_{i,\varphi} \quad (16)$$

$$\tau_c = 0 \text{ or } w_c = \bar{w}_c(r) \quad (17)$$

where $\lambda = -1$ at the left edge of the panel $\varphi = \varphi_0$, and $\lambda = +1$ at the right edge of the panel $\varphi = \varphi_1$ (see Fig. 1).

Because in most practical applications sandwich panels have rigid inserts (stiffeners, membranes) at their edges, global boundary conditions have to be implemented. These extraneous rigid members force boundary conditions for the faces and the core to be related to each other and also to the global boundary conditions. In the general form the global boundary conditions for the curved sandwich panel with rigid inserts at their edges can be written as follows

$$w_t = w_b \quad (18)$$

$$w_{t,\varphi} = w_{b,\varphi} \quad (19)$$

$$w_{t,\varphi} = \frac{u_{0b}r_t - u_{0t}r_b}{c + d_t/2 + d_b/2} \quad (20)$$

$$\lambda(M_t + M_b + N_t r_t + N_b r_b) + \bar{M}_G - \bar{N}_G r_G = 0$$

or

$$\bar{u}_{0G} = \frac{u_{0t}(c + d_b)/2 + u_{0b}(c + d_t)/2}{c + d_t/2 + d_b/2} \quad (21)$$

$$\lambda\left(M_t + M_b + N_t\left(\frac{c + d_t}{2}\right) - N_b\left(\frac{c + d_b}{2}\right)\right) + \bar{M}_G = 0$$

or

$$\bar{w}_{G,\varphi} = \frac{u_{0b}r_t - u_{0t}r_b}{c + d_t/2 + d_b/2} \quad (22)$$

$$\lambda\left(\frac{M_{t,\varphi}}{r_t}+\frac{M_{b,\varphi}}{r_b}+b\frac{r_{tc}d_t}{2r_t}\tau(r=r_{tc})+b\frac{r_{bc}d_b}{2r_b}\tau(r=r_{bc})-m_t-m_b\right)$$

$$-\lambda\left(\frac{N_t}{r_t}(u_{0t}-w_{t,\varphi}+u^*_{0t}-w^*_{t,\varphi})+\frac{N_b}{r_b}(u_{0b}-w_{b,\varphi}+u^*_{0b}-w^*_{b,\varphi})\right)$$

$$-\bar{P}_G=0 \text{ or } w_t=\bar{w}_G \tag{23}$$

$$\tau_c=0 \text{ or } w_t=w_b=w_c=\bar{w}_G \tag{24}$$

where $\lambda=-1$ at the left edge of the panel $\varphi=\varphi_0$, and $\lambda=+1$ at the right edge of the panel $\varphi=\varphi_1$ (see Fig. 1); $c=r_{tc}-r_{bc}$ is the thickness of the sandwich core; $r_G=(r_{tc}+r_{bc})/2$ is the radius of fixation of the stiffener; $\bar{P}_G$, $\bar{N}_G$, $\bar{M}_G$ are external concentrated loads applied to the supports of the panel; $\bar{u}_{0G}$, $\bar{w}_G$, $\bar{w}_{G,\varphi}$ are prescribed deformations and rotation of the edge stiffener.

Stresses and deformations in the core

The shear and radial stresses in the core with the help of kinematic relations, eqn (4), give the following constitutive relations for the core

$$\tau_c=G_c\gamma_{r,\varphi}=G_c\left(u_{c,r}-\frac{u_c-w_{c,\varphi}}{r}\right),$$

$$\sigma_{rr}=E_c\varepsilon_{rr}=E_cw_{c,r} \tag{25}$$

where E_c and G_c are the Young's and shear modulii of elasticity of the core, respectively. Analysis of the governing equations (eqns (8)–(13)) shows that the equilibrium equations of the two-dimensional core medium (eqns (12) and (13)) can be integrated separately. Substituting the above-defined radial stress $\sigma_{rr}(r, \varphi)$ into the second constitutive relation for the core (eqn (25)), and performing integration with respect to r, one obtains radial displacement in the core, $w_c(r, \varphi)$, which has to satisfy compatibility conditions in the radial directions (eqns (5) and (6)) at the upper and lower interfaces. The relations for the shear and radial stresses of the core are

$$\tau_c(r,\varphi)=\frac{\tau}{r^2},\ \sigma_{rr}(r,\varphi)=\frac{\tau_{,\varphi}}{r}\left(\frac{1}{r}+\gamma_0\right)+\frac{\gamma_1}{r}(w_b-w_t) \tag{26}$$

where

$$\gamma_0=\frac{r_{tc}-r_{bc}}{r_{tc}r_{bc}\ln(r_{bc}/r_{tc})},\quad \gamma_1=\frac{E_c}{\ln(r_{bc}/r_{tc})} \tag{27}$$

Note that in eqn (26) unknowns τ, w_t and w_b are functions of the circumferential coordinate φ only. Using eqn (26) the stresses at the face–core interfaces, which appear in the first four governing equations (eqn (8)–(11)), can be determined.

To obtain circumferential displacements in the core, $u_c(r, \varphi)$, one has to integrate the first constitutive relation for the core (eqn (25)) with respect to r taking into account the first of the relations from eqn (26). Afterwards it is necessary to fulfil the second of the compatibility conditions (eqn (5)) and use simultaneously the relations (eqn (3)) for the face rotations, β_i (i = t, b).

Finally, radial and circumferential displacements of the core are

$$w_c(r,\varphi)=w_b+\frac{1}{E_c}\left[\tau_{,\varphi}\left(\frac{1}{r_{bc}}-\frac{1}{r}+\gamma_0\ln\left(\frac{r}{r_{bc}}\right)\right)+\gamma_1\ln\left(\frac{r}{r_{bc}}\right)\times(w_b-w_t)\right],\ u_c(r,\varphi)$$

$$=r\left(\frac{u_{0t}}{r_{tc}}-\frac{d_t(u_{0t}-w_{t,\varphi})}{2r_tr_{tc}}\right)-\frac{\tau}{2G_c}\left(\frac{r_{tc}^2-r^2}{r_{tc}^2r}\right)+w_{b,\varphi}\frac{r_{tc}-r}{r_{tc}}$$

$$+\frac{\tau_{\varphi\varphi}}{E_c}\left[\frac{r_{tc}-r}{r_{tc}r_{bc}}-\left(\frac{r_{tc}^2-r^2}{2r_{tc}^2 r}\right)\right.$$

$$\left.+\gamma_0\left(\frac{r_{tc}-r}{r_{tc}}+\ln\frac{r}{r_{bc}}-\frac{r}{r_{tc}}\ln\frac{r_{tc}}{r_{bc}}\right)\right]$$

$$+\frac{(w_{t,\varphi}-w_{b,\varphi})}{\ln(r_{bc}/r_{tc})}$$

$$\times\left[\frac{r_{tc}-r}{r_{tc}}+\ln\frac{r}{r_{bc}}-\frac{r}{r_{tc}}\ln\frac{r_{tc}}{r_{bc}}\right] \quad (28)$$

The solution of the last two field equations (eqns (8)–(13)) represents the stresses (eqn (26)) and deformations (eqn (28)) in the sandwich core in terms of the five unknown functions of the variable φ: τ, w_t, w_b, u_{0t} and u_{0b}.

Governing equations

Internal resultants in the faces (eqn (7)), in the case of isotropic or composite laminated faces with a symmetric lay-up, can be expressed through the circumferential stresses, $\sigma_i = E_i\varepsilon_i$, which together with kinematic relations (eqn (3)) leads to the following constitutive relations for the faces of sandwich panel

$$N_i = E_i A_i\left(\frac{u_{0i,\varphi}+w_i}{r_i}+\frac{(u_{0i}-w_{i,\varphi})^2}{2r_i^2}\right),$$

$$M_i = E_i I_i\frac{(u_{0i,\varphi}-w_{i,\varphi\varphi})}{r_i^2} \quad (i=\mathrm{t},\mathrm{b}) \quad (29)$$

where E_i are the Young's modulii of the faces; $A_i = d_i b$ are areas of the cross-sections of the faces and $I_i = bd_i^3/12$ represents their moments of inertia.

Continuing the analysis of the field equations (eqns (8)–(13)), one can express the remaining equations (eqns (8)–(11)) through the same unknown functions that appear in eqns (26) and (28). Making use of constitutive relations (eqn (29)) and expressions for the shear stresses at the interfaces (eqn (26)), four governing equations in terms of five unknowns τ, w_t, w_b, u_{0t} and u_{0b} can be derived. Note, that the number of unknowns is larger than the number of equations. However, in all the above deriviations the compatibility condition of the circumferential displacement at the lower face–core interface, $u_c(r=r_{bc})$, i.e. the second part of eqn (6), has not yet been utilized. Substituting eqn (28) for u_c and eqn (3) for β into this equation, the fifth governing equation with the same unknowns, τ, w_t, w_b, u_{0t} and u_{0b} is obtained. Finally, the set of governing equations is

$$\alpha_1 u_{0t,\varphi\varphi}+\alpha_2 w_{t,\varphi}-(\alpha_1-\alpha_2)w_{t,\varphi\varphi\varphi}$$
$$+\frac{\alpha_2}{r_t}(u_{0t}-w_{t,\varphi})(u_{0t,\varphi}-w_{t,\varphi\varphi})$$
$$-N_t\frac{(u_{0t}-w_{t,\varphi})}{r_t}-N_t\frac{(u_{0t}^*-w_{t,\varphi}^*)}{r_t}$$
$$-\gamma_t\tau(\varphi)+r_t n_t-m_t=0 \quad (30)$$

$$\beta_1 u_{0b,\varphi\varphi}+\beta_2 w_{b,\varphi}-(\beta_1-\beta_2)w_{b,\varphi\varphi\varphi}$$
$$+\frac{\beta_2}{r_b}(u_{0b}-w_{b,\varphi})(u_{0b,\varphi}-w_{b,\varphi\varphi})$$
$$-N_b\frac{(u_{0b}-w_{b,\varphi})}{r_b}-N_b\frac{(u_{0b}^*-w_{b,\varphi}^*)}{r_b}$$
$$+\gamma_b\tau(\varphi)+r_b n_b-m_b=0 \quad (31)$$

$$\alpha_2 u_{0t,\varphi}+\frac{\alpha_2(\alpha_1-\alpha_2)}{\alpha_1}w_{t,\varphi\varphi}+\frac{\alpha_2(\alpha_1-\alpha_2)}{\alpha_1}$$
$$\times w_{t,\varphi\varphi\varphi\varphi}+(\alpha_2-b\gamma_1)w_t+b\gamma_1 w_b$$
$$+\frac{\alpha_2(\alpha_1-\alpha_2)}{\alpha_1 r_t}$$
$$\times((u_{0t}-w_{t,\varphi})(u_{0t,\varphi}-w_{t,\varphi\varphi}))_{,\varphi}$$
$$+\frac{\alpha_2}{2r_t}(u_{0t}-w_{t,\varphi})^2$$
$$+\frac{\alpha_2}{\alpha_1}\left[\left(N_t\frac{(u_{0t}-w_{t,\varphi})}{r_t}\right)_{,\varphi}\right.$$
$$\left.+\left(N_t\frac{(u_{0t}^*-w_{t,\varphi}^*)}{r_t}\right)_{,\varphi}\right]$$
$$+\frac{\alpha_2}{\alpha_1}\gamma_t\tau_{,\varphi}(\varphi)+b\gamma_0\tau_{,\varphi}(\varphi)+\frac{(\alpha_1-\alpha_2)}{\alpha_1}$$

$$\times r_t n_{t,\varphi} - r_t q_t + \frac{\alpha_2}{\alpha_1} m_{t,\varphi} = 0 \quad (32)$$

$$\beta_2 u_{0b,\varphi} + \frac{\beta_2(\beta_1-\beta_2)}{\beta_1} w_{b,\varphi\varphi} + \frac{\beta_2(\beta_1-\beta_2)}{\beta_1} \times w_{b,\varphi\varphi\varphi\varphi} + (\beta_2 - b\gamma_1) w_b + b\gamma_1 w_t + \frac{\beta_2(\beta_1-\beta_2)}{\beta_1 r_b} ((u_{0b} - w_{b,\varphi}) \times (u_{0b,\varphi} - w_{b,\varphi\varphi}))_{,\varphi} + \frac{\beta_2}{2r_b}(u_{0b} - w_{b,\varphi})^2 + \frac{\beta_2}{\beta_1}\left[\left(N_b \frac{(u_{0b} - w_{b,\varphi})}{r_b}\right)_{,\varphi} + \left(N_b \frac{(u^*_{0b} - w^*_{b,\varphi})}{r_b}\right)_{,\varphi}\right] - \frac{\beta_2}{\beta_1}\gamma_b \tau_{,\varphi}(\varphi) - b\gamma_0 \tau_{,\varphi}(\varphi) + \frac{(\beta_1-\beta_2)}{\beta_1} \times r_b n_{b,\varphi} - r_b q_b + \frac{\beta_2}{\beta_1} m_{b,\varphi} = 0 \quad (33)$$

$$-\gamma_t u_{0t} + \gamma_b u_{0b} + (\gamma_t + b\gamma_0) w_{t,\varphi} - (\gamma_b + b\gamma_0) w_{b,\varphi} + \frac{b\gamma_0\gamma_2}{G_c}\tau(\varphi) - \frac{b\gamma_0}{E_c}\left(\gamma_2 + \frac{(r_{tc} - r_{bc})}{r_{tc} r_{bc}}\right)\tau_{,\varphi\varphi}(\varphi) = 0 \quad (34)$$

where

$$\gamma_t = \frac{b}{r_{tc}}\left(1 - \frac{d_t}{2r_t}\right), \quad \gamma_b = \frac{b}{r_{bc}}\left(1 + \frac{d_b}{2r_b}\right),$$

$$\gamma_2 = \frac{(r_{tc} + r_{bc})\ln(r_{bc}/r_{tc})}{2r_{tc} r_{bc}}, \quad \alpha_1 = \frac{EA_t r_t^2 + EI_t}{r_t^3},$$

$$\alpha_2 = \frac{EA_t}{r_t}, \quad \beta_1 = \frac{EA_b r_b^2 + EI_b}{r_b^3}, \quad \beta_2 = \frac{EA_b}{r_b}$$

The set of governing equations (eqn (30)–(34)) is a system of ordinary differential equations. The five unknown functions of the variable φ are: the radial, w_t, w_b, and circumferential, u_{0t}, u_{0b}, displacements of the centroids of the upper and lower panel faces, and the shear function, τ, that is related to the shear stress in the core, τ_c, by the first part of eqn (26). The order of the system (eqns (30)–(34)) is 14, that coincides with the number of boundary conditions whether in local (cf. eqns (14)–(17)) or in global (cf. eqns (18)–(24)) cases.

NUMERICAL STUDY

The numerical procedure consists of converting the set of five governing equations (eqns (30)–(34)) into a set of first-order ordinary differential equations. Thus the obtained set contains 14 equations. Further replacing of the derivatives by their finite-difference counterparts transforms the set of ordinary differential equations into a system of nonlinear algebraic equations. The linear part of this system is solved and used as an initial guess in the iteration procedure followed. The Newton iteration method with deferred corrections, elaborated by Pereyra [22], is employed to solve the full system of nonlinear algebraic equations. Convergency of the numerical procedure is improved by gradually increasing the relative weight of the nonlinear part of system.

Numerical examples are presented here to illustrate the ideas behind the theory developed and demonstrate the effect of the nonlinearity introduced. A sandwich beam with aluminium 2024-T3 faces and a Divinycell H-160 core is considered. The geometrical parameters of the beam are as follows (see Fig. 1): $b = 30$ mm, $d_t = 1$ mm, $d_b = 1$ mm, $r_{tc} = 812.5$ mm, $r_{bc} = 787.5$ mm and $a = 500$ mm. The beam is subjected to a radially uniform load on the upper face only.

Two kinds of supports are considered: simple supports at the edges (S–S) and clamped edges of the beam (C–C). To prevent damage of the sandwich beam, the simply supported beam has been supplied with infinitely rigid edge stiffeners hinged at their midheights. The global boundary conditions were applied.

The shear stresses at the upper, $\tau_c(r = r_{tc})$, and lower, $\tau_c(r = r_{bc})$, face–core interfaces are

presented in Fig. 5. The shear-stress distribution through the thickness of the core is not constant, as it is known to be for flat panels. Shear changes abruptly in the vicinity of the edges and increases smoothly to zero at the beam mid-span. Attenuation of the shear stresses due to nonlinearity is of the order of the difference between shear at the upper and lower interface, and is particularly pronounced in the area where these stresses have their extrema: at $\varphi_{loc} \simeq 0.025$ or $l \simeq 20$ mm. This distance is of the order of the beam height and determines a zone of stress concentrations.

Distributions of the circumferential normal stresses in the aluminium faces are affected by the stress concentration in the vicinity of the beam edges. The relations $\sigma_t(\varphi)$ and $\sigma_b(\varphi)$ are shown in Fig. 6. The labels 'top' and 'bottom' in this figure correspond to the outer upper and outer lower fibres of the faces, respectively, and the label 'interface' corresponds to the lower fibre of the upper face and the upper fibre of the lower face. Being very close to each other along most of the length of the beam, the circumferential face stresses change abruptly close to the supports. In the case of a clamped beam, the outer fibre of the upper face is in tension, while the inner fibre of this face is in compression. The lower face is entirely in compression. Existing stresses are close to the yield stress that is indicated for severe bending moments in that zone. Nevetheless, the average stresses at the beam edges are far from critical and the relations $\bar{\sigma}_t(\varphi)$ and $\bar{\sigma}_b(\varphi)$ for the face centroids

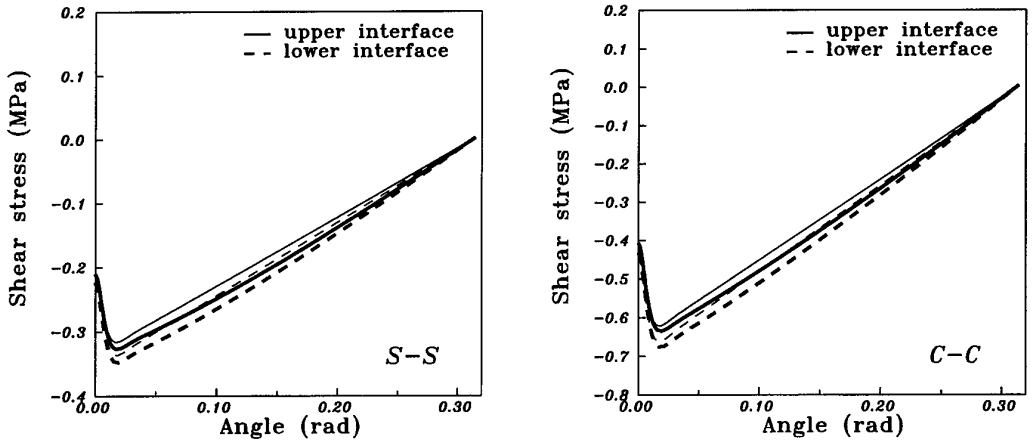

Fig. 5. Shear stresses in the core at the face-core interfaces: (a) simply supported and (b) clamped beam edges. $q_t = -9$ N/mm, $q_b = 0$. (Thin lines, linear model; thick lines, nonlinear model.)

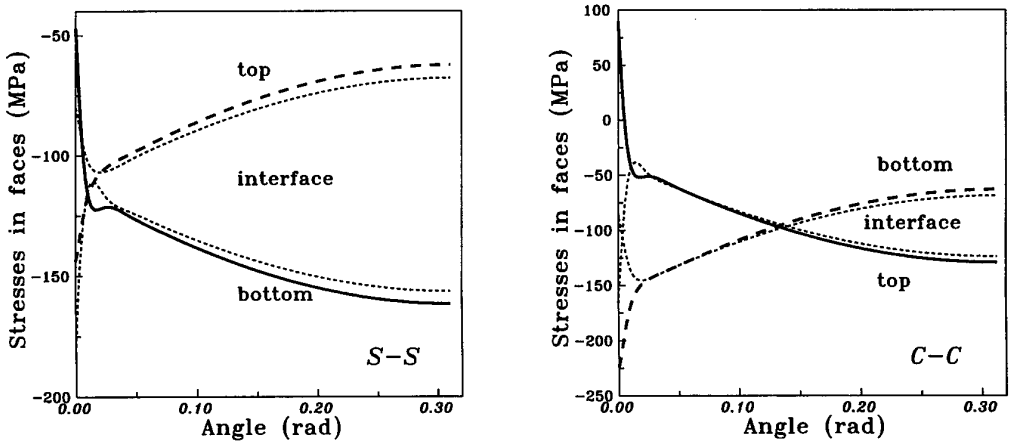

Fig. 6. In-plane stresses in the sandwich faces: (a) simply supported and (b) clamped beam edges. $q_t = -9$ N/mm, $q_b = 0$. (Nonlinear model.)

are smooth and monotonous along the entire length of the beam. It is known, however, that failure of sandwich structures occurs more often due to debonding of the core from the adjacent faces close to the supports, inserts, concentrated loads, geometrical discontinuties, etc. The behaviour of the radial shear stresses σ_{rr} in the core is shown in Fig. 7. To avoid damage these stresses should be less than the core strength. The radial shear stresses in the face–core interfaces are denoted as peeling stresses. Owing to the uniform loading exerted on the upper face of the beam, the compressive radial stress developes mainly in the core beyond zones of localized effect: at $\varphi > \varphi_{loc} = 0.025$. At the same time, drastic changes in the peeling stresses occur in the vicinity of the supports at the characteristic length $l = 20$ mm (see the enlargement of this area in Fig. 8). The peeling stresses at the upper interface are tensile in the S–S and C–C cases. In Fig. 8 a comparison of linear and nonlinear models is demonstrated.

Radial displacements of the sandwich faces are shown in Fig. 9. The nonlinear model yields larger displacements than the linear model. Radial displacements of the lower faces are slightly smaller than those of the upper faces, which indicates the compressibility of the core. The influence of nonlinearity introduced into the model is illustrated in Fig. 10, where the radial midpoint displacement of the upper beam face w_t at $\varphi = 0.3125$ vs uniform loading

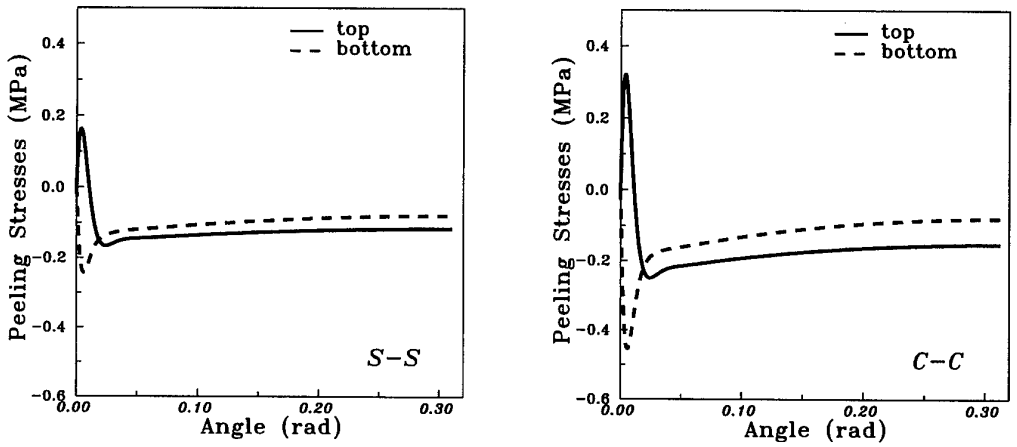

Fig. 7. Peeling stresses in the face-core interfaces: (a) simply supported and (b) clamped beam edges. $q_t = -9$ N/mm, $q_b = 0$. (Nonlinear model.)

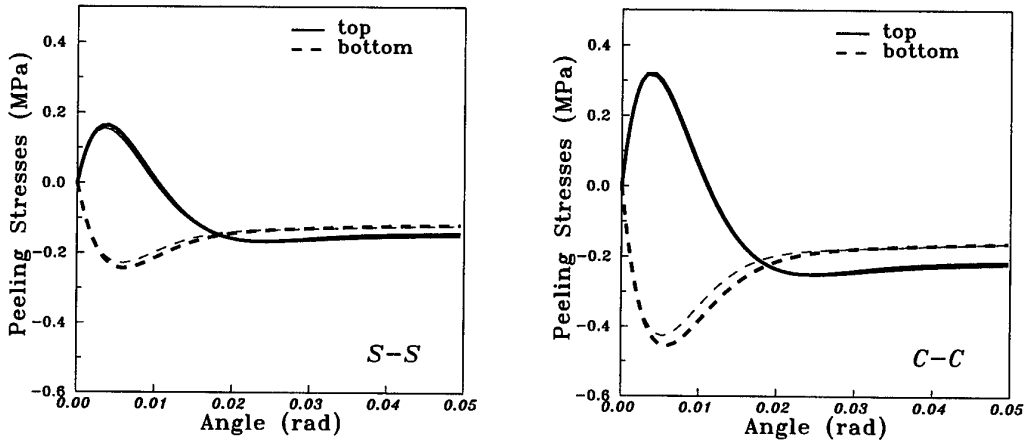

Fig. 8. Transverse radial stresses at the face-core interfaces in the vicinity of the beam edges: (a) simply supported and (b) clamped beam edges. $q_t = -9$ N/mm, $q_b = 0$. (Thin lines, linear model; thick lines, nonlinear model.)

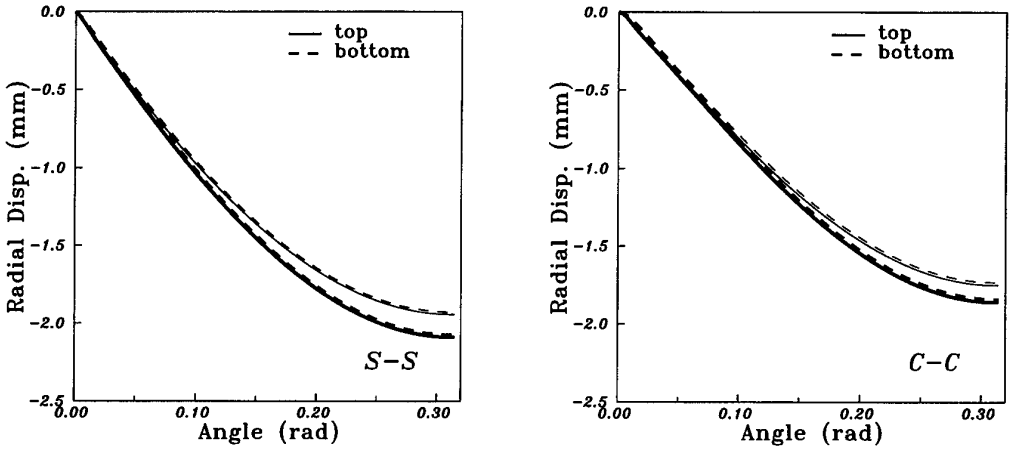

Fig. 9. Radial displacements of the faces: (a) simply supported and (b) clamped beam edges. $q_t = -9$ N/mm, $q_b = 0$. (Thin lines, linear model; thick lines, nonlinear model.)

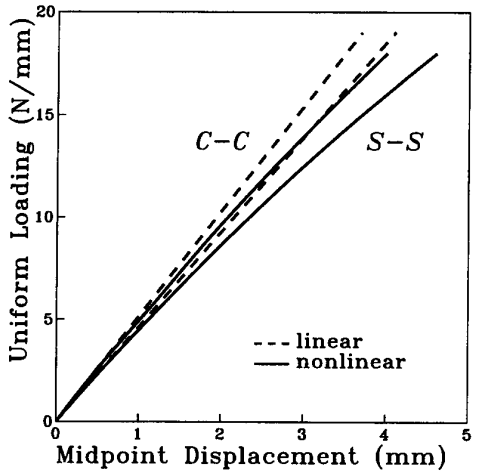

Fig. 10. Displacement of the upper face vs uniform loading.

q_t are shown. The deviation of nonlinear curves from the appropriate linear relations are larger for the S–S beam than for the C–C beam.

CONCLUSIONS

The nonlinear model presented describes the stress-deformation response of an arbitrary loaded sandwich panel of constant curvature. The model accounts for the geometrical nonlinearity in the sandwich faces and the transverse shear and normal compliances of core. No *a priori* assumptions on the displacement fields in the core are made. Using the variational principle, the set of governing equations and the boundary conditions in global and local formulations are derived. An appropriate numerical procedure is developed and the numerical analysis is performed. The nonpolynomial displacement distributions through the panel thickness are obtained as an inherent part of the solution. Attenuation of the results due to the nonlinearity introduced is demonstrated. The model is shown to be suitable for describing the overall behaviour as well as the localized effects in the arbitrary loaded sandwich panel of constant curvature.

REFERENCES

1. Plantema, F. J., *Sandwich Construction*. John Wiley and Sons, New York, 1966.
2. Allen, H. G., *Analysis and Design of Structural Sandwich Panels*. Pergamon Press, Oxford, 1969.
3. Zenkert, D., *An Introduction to Sandwich Construction*. Chameleon Press, London, 1995.
4. Reissner, E., Finite deflections of sandwich plates. *J. Aerospace Sci.*, 1948, **15**, (7), 435–440.
5. Mindlin, R. D., Influence of rotary interia and shear on flexural motions of isotropic elastic plates. *ASME J. Appl. Mech.*, 1951, **18**, 31–38.
6. Di Sciuva, M. and Carrera, E., Static buckling of moderately thick, anisotropic, laminated and sandwich cylindrical shell panels. *AIAA J.*, 1990, **28**, (10), 1783–1793.
7. Lo, K. H., Christensen, R. M. and Wu, E. M., A high-order theory of plate deformation. *ASME J. Appl. Mech.*, 1977, **44**, 669–676.
8. Reddy, J. N., A simple higher-order theory for laminated composite shells. *J. Appl. Mech.*, 1984, **51**, 745–752.
9. Meyer-Piening, H.-R., Remarks on higher order sandwich stress and deflection analyses. In *Sandwich Constructions — 1. Proc. of the 1st Int. Conf. on Sandwich Constructions*, Stockholm, Sweden. Hameleon Press, London, 1989, pp. 107–127.

10. Noor, A. K., Burton, W. S. and Bert, C. W., Computational models for sandwich panels and shells. *Appl. Mech. Rev.*, 1996, **49**, 155–199.
11. Frostig, Y., Behavior of delaminated sandwich beams with transversely flexible core-high order theory. *Comput. Struct.*, 1992, **20**, 1–16.
12. Frostig, Y., Baruch, M., Vilnai, O. and Sheinman, I., High-order theory for sandwich-beam behavior with transversely flexible core. *ASCE J. Engng Mech., EM Div.*, 1992, **118**, (5), 1026–1043.
13. Frostig, Y. and Baruch, M., High-order buckling analysis of sandwich beams with transversely flexible core. *ASCE J. Engng Mech., EM Div.*, 1993, **119**, (3), 476–495.
14. Frostig, Y., On stress concentration in the bending of sandwich beams with transversely flexible core. *Composite Struct.*, 1993, **24**, 161–169.
15. Frostig, Y., High-order behavior of sandwich beams with flexible core and transverse diaphragms. *ASCE J. Engng Mech., EM Div.* , 1993, **119**, (5), 955–972.
16. Frostig, Y. and Baruch, M., Free vibration of sandwich beams with a transversely flexible core: a high order approach. *J. Sound Vibr.*, 1994, **176**, (2), 195–208.
17. Peled, D. and Frostig, Y., High-order bending of sandwich beams with transversely flexible core and nonparallel skins. *ASCE J. Engng Mech., EM Div.*, 1994, **120**, (6), 1255–1269.
18. Frostig, Y. and Shenhar, I., High-order bending of sandwich beams with a transversely flexible core and unsymmetrical laminated composite skins. *Composite Engng*, 1995, **5**, (4), 405–414.
19. Peled, D. and Frostig, Y., High-order bending of piecewise uniform sandwich beams with a tapered transition zone and a transversely flexible core. *Comput. Struct.*, 1995, **31**, 151–162.
20. Frostig, Y. and Baruch, M., Localized load effects in high-order bending of sandwich panels with transversely flexible core. *ASCE J. Engng Mech., EM Div.* , 1996, **122**, (11), 1069–1087.
21. Brush, D. O. and Almroth, B. O., *Buckling of Bars, Plates and Shells*. McGraw-Hill, New York, 1975.
22. Pereyra, V., An adaptive finite difference Fortran program for first order nonlinear differential ordinary boundary problems. In *Codes for Boundary-value Problems in Ordinary Differential Equations. Proc. of Working Conf.*, Vol. 76, ed. B. Childs *et al.* Springer, New York, 1979, pp. 67–88.

ELSEVIER

Composite Structures Vol. 38, No. 1–4, pp. 395–403, 1997
© 1997 Elsevier Science Ltd. All rights reserved
Printed in Great Britain
0263-8223/97/$17.00 + 0.00

PII:S0263-8223(97)00074-3

The effect of tooling geometry on a new continuous fabrication system for SMC using roll forming

Tsuneo Hirai

INTEC-HIRAI Ltd. and Doshisha University, Kyoto-fu, Japan

&

Mitomo Hirai

Osaka Prefectural College of Technology, Osaka-fu, Japan

In an effort to further decrease the power requirement caused by the spherical stress tensor in SMC compression moulding, further developments in roll forming have been pursued. A continuous cross section such as a channel beam is produced by longitudinal rolling in progressive stages. As the product has a shear centre away from the centroid when the component is used as a structural part, the forming process must avoid the development of stress concentrations resulting from unsuitable orientation of reinforcements. © 1997 Elsevier Science Ltd.

INTRODUCTION

SMC compression moulding is used extensively today in manufacturing the panels and structural parts of transportation vehicles. In an effort to further decrease the power requirement caused by the spherical stress tensor, while maintaining cycle time, fabrication by roll forming has been developed. A continuous uniform cross section is produced by longitudinal rolling in progressive stages. As the product has a shear centre away from the centroid, the forming process employed should avoid the stress concentrations arising in shear due to the orientation of reinforcement. For the case of pultrusion as a continuous moulding process, it is necessary to employ special techniques to ensure adequate strength in the web against shear stress caused by the fibre orientation to prevent unstable plastic buckling. To overcome these problems, it is necessary to develop new techniques for the micro-specific interfaces in continuous processes with investigations of the mechanical properties of the products from various forming conditions. The principal purpose of the study is to develop a design procedure for a new roll forming process considering tooling geometry to optimise interface conditions. Basic information on the deformation behaviour is obtained for channel-shaped profiles using various coupled rolls with different diameter ratios to active optimum tool geometry, and also a T-shaped profile process is applied to investigate a filling flow behaviour by quasi two-dimensional analysis due to phenomena of rigid rotation along interfaces.

It is necessary to adopt single shaft driving for the two rolls due to US Patent considerations, but this leads to an effective result to preventing unstable plastic buckling due to the interface problem.

EXPERIMENTAL ROLL FORMING USING A PROTOTYPE MACHINE

The rolling machine should be made with high longitudinal rigidity to maintain the accuracy at

intersection points of each beam element with synchronisation of all the drive shafts. It is necessary to adopt single shaft driving for the above mentioned rolls due to US Patent, and it is effective in preventing buckling due to interface problem.

Although the method of uniaxial driving is generally used, a traction driving method is adopted at the coupling rolls between the forming device and the hardening furnace and after hardening. The various parts of the equipment can be adjusted and rolls and adapted variants changed during investigation. The general layout showing essential futures of the machine designed in 1991 are shown in Figs 1 and 2 and the design of one rolling stage is shown in Fig. 3. A profile of a channel-shaped product is shown in Fig. 4. It is possible to select suitably dimensioned flange parts to overcome forming faults, but they have to be of a suitable design for refined tooling geometry. The fundamental stage assembly is shown in Fig. 5, which is very effective in getting suitable distribution of materials at the interface. Driving the material by a slightly smaller diameter roller, giving a deviation of the neutral axis, and also by an upper roller with an incremental reduction creates resistance in the distortion controlled filling behaviour. This should be considered as a basic feature of roll forming.

As a forming material, Class A SMC is used, made up from resin/filling/glass fibre 26.5/46.5/27 wt.%, respectively, and with a thickness of about 2 mm.

As the filling increases at the flange, it should be possible to use a special filling material to hold with considerable resistance under the thin strip. Alternatively, to make control easy, it should be possible to apply a surface driving velocity to the filling flow using a harmonic drive motor on the front and rear coupling rolls.

INTERFACE ASPECTS AT PREPREG SMC CAUSED BY HETEROGENEITY

Prepreg SMC is essentially heterogeneous, consisting of reinforcement, matrix and voids. The blanks used for roll forming are laminates of SMC where the outer surfaces of each ply are resin-rich, creating so called macroscopic interfaces. Each ply in a laminate has orientated strands (fibres) with random microscopic interfaces. It offers advantages over isotropic materials with the possibility of achieving properties not possible with conventional materials.

An important aspect is that the flow behaviour depends on the microscopic interfaces occurring at changes of orientation of the

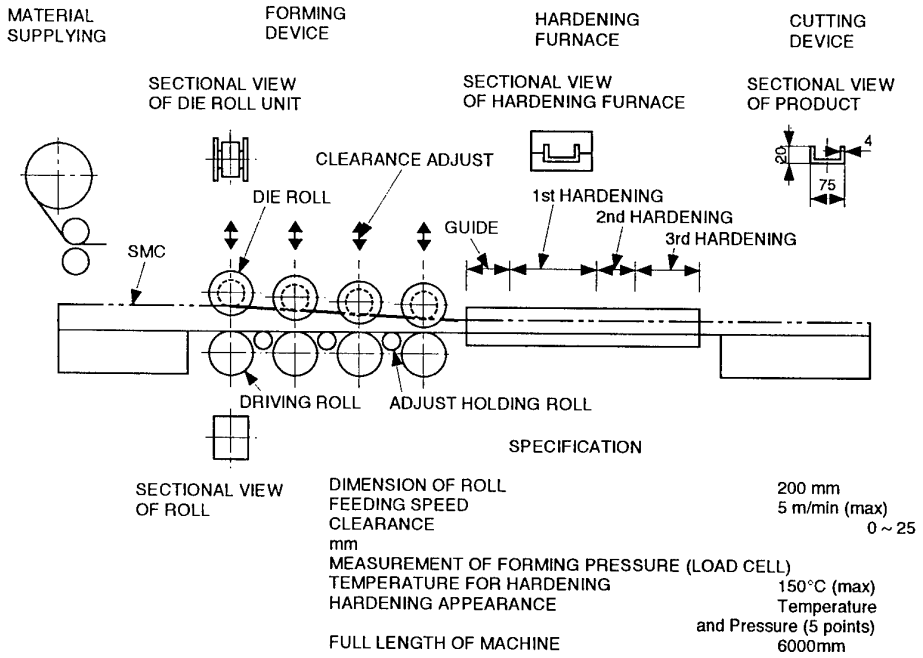

Fig. 1. Roll forming machine used in the trial.

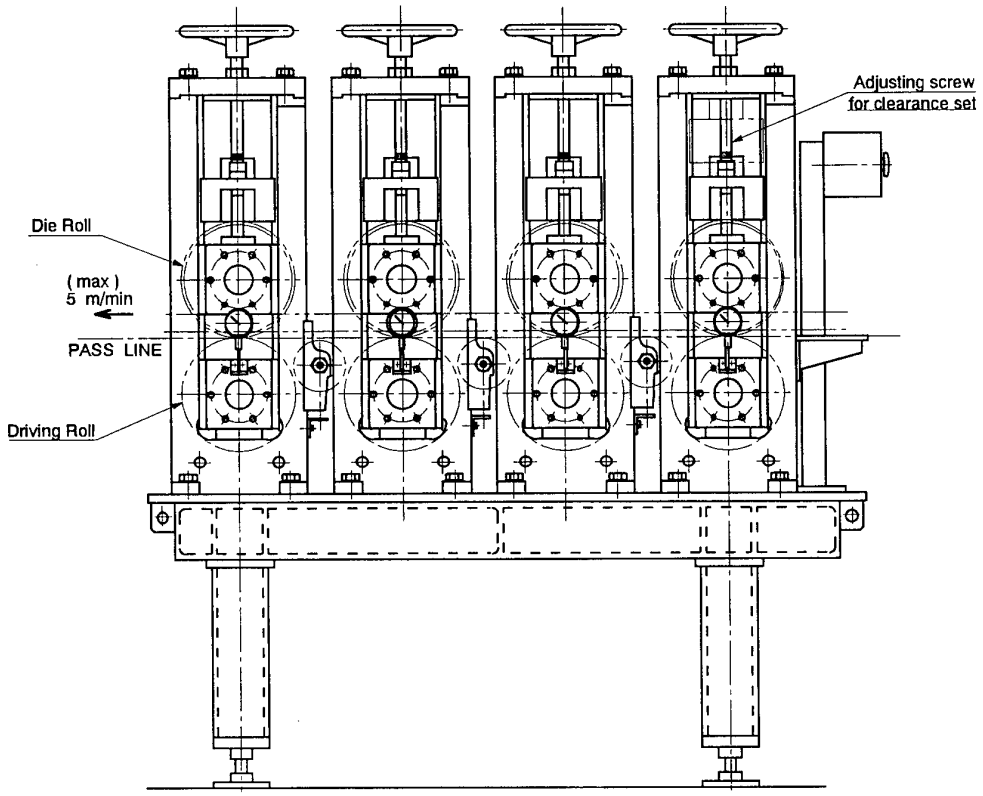

Fig. 2. Forming device of roll forming machine.

reinforcement. There are many microscopic interfaces to affect flow lying in the plane of SMC. The complex filling behaviour is influenced by the existence of interfaces during roll forming, as shown in Fig. 6. As the rolling behaviour is initially seen to be unstable, the deformation during an incremental reduction gives the eigenmode at macroscopic interfaces based on the boundary loading conditions on the blank. The subsequent deformation is dependent on the distribution of microscopic interfaces, and it is necessary to investigate the effects of heterogeneity. Hence the volume fraction condition of the intersection and orientation of reinforcement must be investigated as a possible influence on filling behaviour.

The approach in optimizing the forming process is to look for the factors affecting filling behaviour by systematic experiments. Initially it is considered in relation to feed rate (incre-

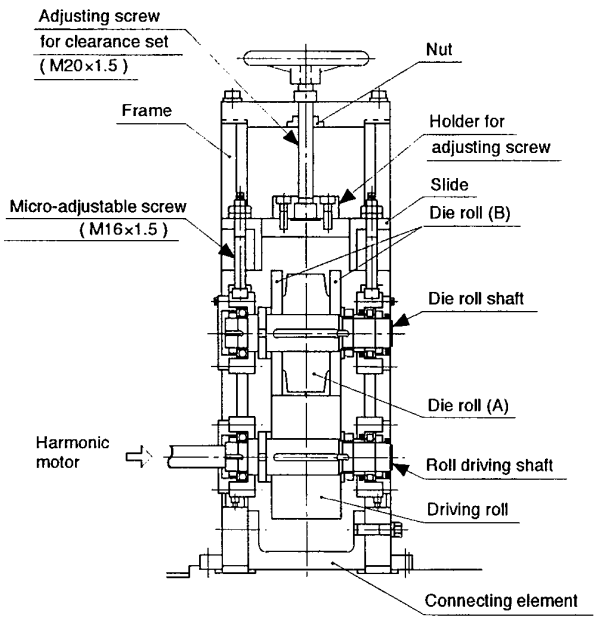

Fig. 3. Design figure of one stage for roll forming machine.

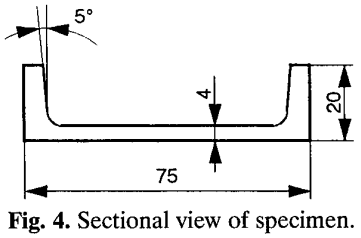

Fig. 4. Sectional view of specimen.

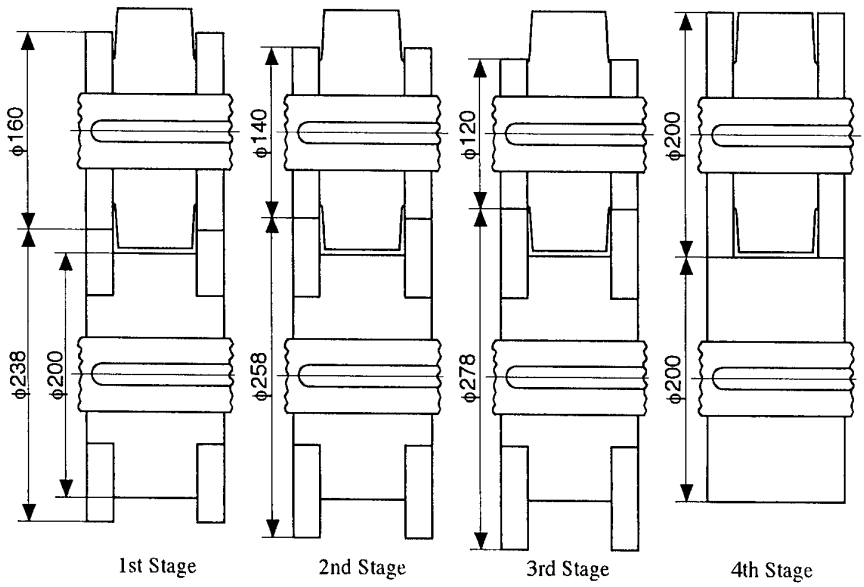

Fig. 5. Shaping die roll and driving cylindrial roll coupling assembly.

mental reduction speed/driving speed) and the experimental results show that the composite behaves in an opposite way to conventional materials.

Although fabrication methods using the process of the roll-flower shows an advantage in production rate and flange moulding accuracy, there still remains the problem of unstable plastic buckling due to quasi two-dimensional orientated flow patterns and the many patents on the system.

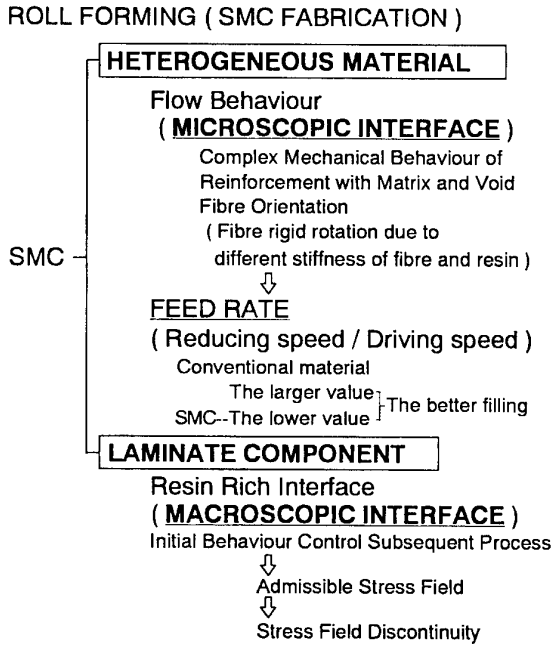

Fig. 6. Macro- and microscopic interfaces due to heterogeneous material and laminate component under roll forming process.

FILLING EFFECT ON TOOLING GEOMETRY AND INTERFACE DEPENDENCE ON BIDIRECTIONAL REINFORCEMENT

Because the SMC is a laminate, the initial rolling behaviour of the macroscopic interfaces between plies with resin-rich surfaces should be considered. As the interface could be assumed discontinuous, compared with the prepreg material, the deformation under the admissible stress field and stress field discontinuity in the cross section was analysed to obtain the eigenmodes. The principal stress at each interface under various rolling conditions is obtained during initial stages as shown in Fig. 7. The experimental conditions are very important in investigating the effect of the microscopic interfaces for a particular product. As shown in Fig. 5, the die rolls are designed with an 8 mm smaller radius in this paper and only one shaft at the coupling rolls is driven, being different to a conventional roll machine. But this applied design may be better to create interfaces in SMC.

The eigenmode for the material under incremental reduction in roll forming is very important in the filling flow into the flange. The principal stress shows a deformation pattern for each ply. For example, the lowest ply in

Fig. 7(a) suggests a difficulty in achieving filling into the flange due to separation from the lamina. The result is evidenced by many short pick points of glass fibre standing out from the bottom of the product after relaxation of the resin material.

The approach in optimising the roll forming process is to look for the factors affecting filling behaviour by systematic experiments. Initially it is considered in relation to feed rate (incremental reduction speed/driving speed) and the experimental results show that the composite behaves opposite to conventional materials [1].

Filling behaviour into rib canal

The filling effect on flow behaviour should be considered for the rigid rotation of reinforcement. The distribution aspect of the microscopic interfaces plays an important role in the filling behaviour during the deformation process.

The first problem is to control the flow and filling behaviour during the fabrication process, caused by rigid rotation due to the different stiffnesses of fibres and resin at the microscopic interfaces. As the flow analysis was carried out continuously by a progressive step-by-step method, the results after flow analysis along the centre line of a rib channel shows the swing of the vectors at the entrance to the T profile, which can be observed in Fig. 8 with the velocity vectors along the axis of symmetry from a to b point in Fig. 8(a), shifting to a simple flowing process a to be considered as a tendency according to incremental steps. It is evident from the results that the unsteady flow is quite significant for early steps and not significant later, dependent on roll diameter. The behaviour during the incremental roll pass shows a changing step of orientation of the velocity vectors as indicated in Fig. 9. As a simple example homogeneous material such as Plasticine shows, similar dependence on the roll diameter exists in analytical and experimental

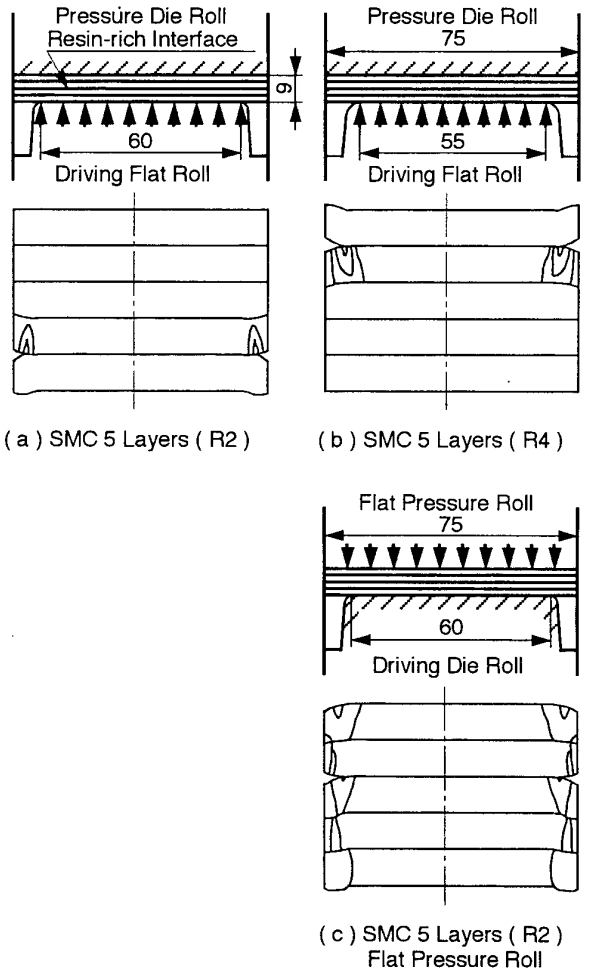

Fig. 7. Principal stress distribution on channel-shape with free space at both ends along the macrospecific interfaces under incremental reduction. (a) SMC 5 layers (R2) (b) SMC 5 layers (R4) (c) SMC 5 layers (R2) flat pressure roll.

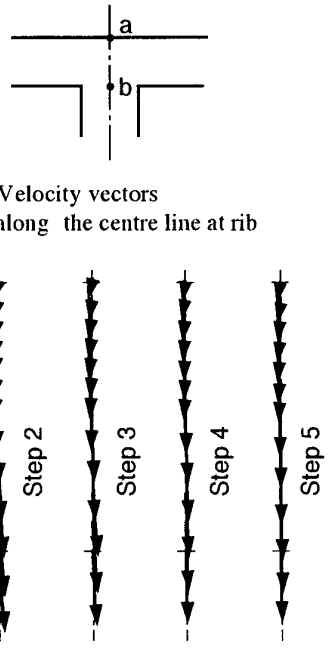

(a) Velocity vectors along the centre line at rib

(b) Snaking velocity vectors along the centre line

Fig. 8. Velocity vectors along the centre line at rib part. (a) Velocity vectors along the centre line at rib. (b) Snaking velocity vectors along the centre line at rib part.

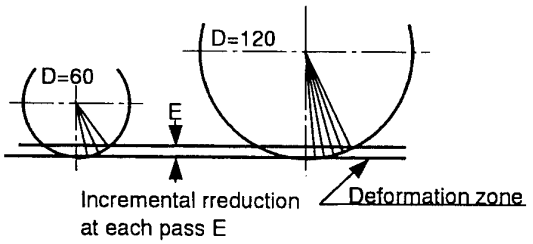

Fig. 9. Progress of incremental reducing steps due to the diameter of roll.

results irrespective of feed rate, as shown in Fig. 10. A higher rate of filling at a higher feed rate has been obtained for a ring rolling process [2], and to some extent for the TMC (Thick SMC) composites, as there is unsteady flow for a short period which decreases as flow proceeds due to the interfaces resulting from its soft rigidity. The results of fibre content in the plate part are verified by experiment, which indicates a higher ratio of filling at a higher feed rate and a slightly higher rigidity of material when the roller has more limited diameter.

UP-SET COMBINATION BY DIE-ROLL DRIVING

It has proven to be very difficult to channel material into a flange canal, as observed in the initial conditions shown by Fig. 7(c). Some filaments appeared at both sides of the web in the bottom of the channel, depending on deviation of the neutral axis of the cross section shown as in Fig. 11. The process should be carried out to give a heavy distortion of the material

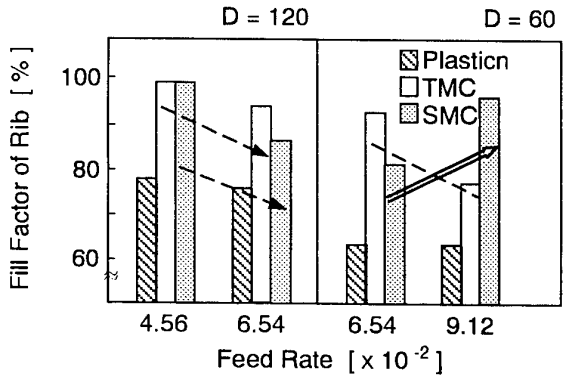

Fig. 10. Fill factor of rib glass fibre under various feed rate.

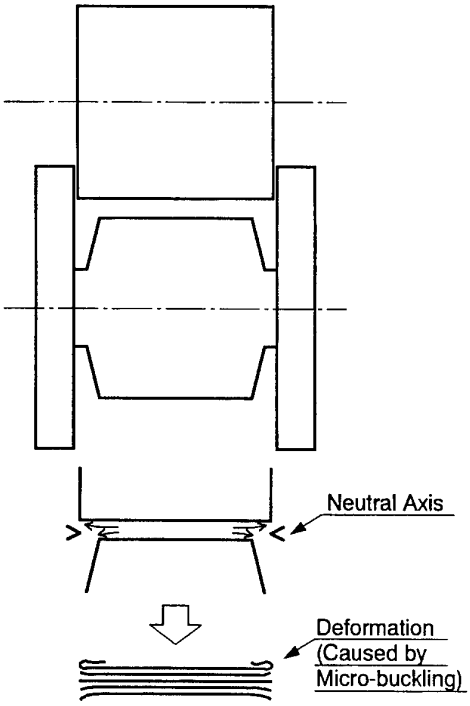

Fig. 11. Case of die roll driven.

dependent on additional flanges in the upper roll, to increase the moment of inertia as shown in Fig. 12. Although additional material at both end flange positions is applied to improve filling in the previous case, the result is no good after several rolling operations due to the deviation of the neutral axis following belt transmission theory. One result is shown in Fig. 13.

RESULTS SYNTHESES

Experimental conditions on the coupled roller assembly investigated by bending behaviour are very important in investigating the effect of microscopic interfaces for a particular product, as shown in Table 1. The basic deformation behaviour depends on the applied rolling conditions. The physical properties of the SMC are

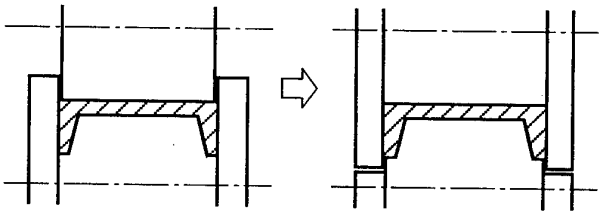

Fig. 12. Additional flanges into upper roll to increase the moment of inertia.

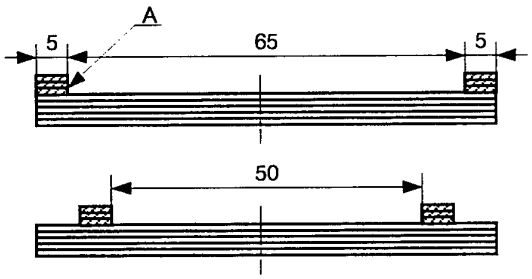

Fig. 13. Transportation aspect of an additional limited narrow material upon the opposite side of filling canal.

dependent on its heterogeneous nature and the laminate component. Because the SMC is a laminate, the initial rolling behaviour of the macroscopic interfaces between plies with resin-rich surfaces should be considered. As the interface could be assumed to be discontinuous compared with the prepreg material, the deformation under the admissible stress field and the stress field discontinuity in the cross section was analysed to obtain eigenmodes. The principal stresses at each interface under various rolling conditions during the initial stages are shown in Fig. 7.

For a structural component, the first problem is to control the flow and filling behaviour during the fabrication process, which is influenced by the rigid rotation due to different stiffnesses of fibre and resin at the microscopic interfaces covering each ply range. Mechanical behaviour under loading depends on the distribution of the interfaces. In the simplest case, the effects of feed rate on the flow pattern is a very important aspect of the rolling process, as well as the properties of products made under various conditions of roll forming, at the same feed rate, since the filling behaviour depends on an eigenmode at the initial incremental reduction, due to the laminate component of SMC.

Voids which are present in SMC are not all eliminated with increasing moulding pressure and can remain as fibrous voids. Thin channel components are subject to normal stress and shear flow stress concentrations under bending loads. The product can suffer sudden buckling due to the stress concentration. It might appear that fibrous voids aligned parallel to the sectional surface during roll forming could prevent sudden buckling caused by delamination of the interface since it relaxes the over stress. On the contrary the stress concentration gives rise to a dangerous debonding due to the plastic buckling in the case of void lines distributed randomly. This behaviour can be appreciated from Fig. 14.

The anisotropic mechanical charactertics for the web of channel-shaped products along the longitudinal and lateral directions related to the strength have been investigated for the various fabrication methods [3]. Although high modulus and strength are evident for a higher value of radius of curvature at the corner ($R = 4$ mm), dangerous buckling is produced for the case shown as R4A in the figure. For the case of R2A with a smaller radius, sudden delamination of the interface might occur at the high peak stress without showing buckling behaviour. Characteristics evident in the products of roll forming will indicate the presence of interfaces, dependent on heterogeneous properties. The best filling behaviour is obtained for the case of 0.25 mm incremental reduction, but the value of 0.1 mm is used in this experiment to make fabrication of any form possible. At the higher value of (5 m/min), there is a pronounced buckling mode as shown in Fig. 15, R2B. Since a channel-shaped sectional beam has a shear flow, the component is loaded by bending and torsional moment. It is most important to prevent torsional collapse laterally caused by buckling at the corners between web and flange. Therefore, it is undesirable to have small values of maximum shear strain. The principal strains and principal axes should be analysed by in-plane and out-of-plane deformation using pairs of gauges to obtain the maximum and minimum normal strains and also the maximum tangential strains to estimate the equivalent strain. The summarised results are indicated in Fig. 16, and are very convenient to select the moulding method and shape of product. The mechanical properties of channel-shaped beams made by roll forming using composite materials are shown in the figure by the equivalent strain and shearing resistance. The highest strength product is made by the pultrusion process with robing cloth, but this is not expected to show torsional resistance. Although the anisotropic characteristics due to the fabrication method of normal strain are shown by R2C and the component should be roll-formed by the distortion process of SMC, the product has a small residual shear strain under the bending test. This is caused by the optimum distribution of microscopic interfaces with more distortion in this process compared with other products because of the uniaxial driving process.

Table 1. Experimental conditions

Conditions	R2A	R2B	R2C	R4A
Incremental reduction (mm)	0.1			
Driving speed (m/min)	1	5	1	
Roll type	Upper driving roll	DS	FC	DS
	Lower driving roll	FC	DS	FC
Corner radius of die shape (mm)	2			4

The next best would be R2A based on the equivalent strain being the principal strain, but it's macroscopic interfaces should be considered for the filling behaviour under initial incremental reduction because of the torsional resistance. The mechanical properties are compared near the peak point of linearity in Fig. 15.

The main feature in this development has been the reduction in forming load. The load has been measured at the upper roller and is shown in Fig. 17. The maximum fabrication pressure under a small area between the coupling rolls is 3.5 MPa. This value may not produce fracture in glass fibre compared with the practical experience with SMC compression moulding.

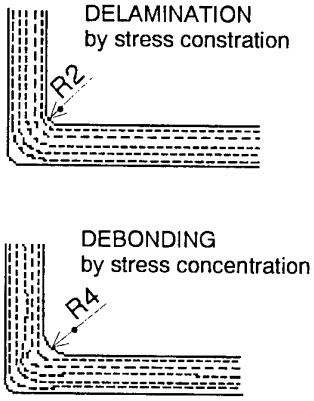

Fig. 14. Voids aspects in the sectional view of product.

CONCLUSION

Having established the optimum conditions in the forming sequence from the experimental study, suitable boundary conditions can be

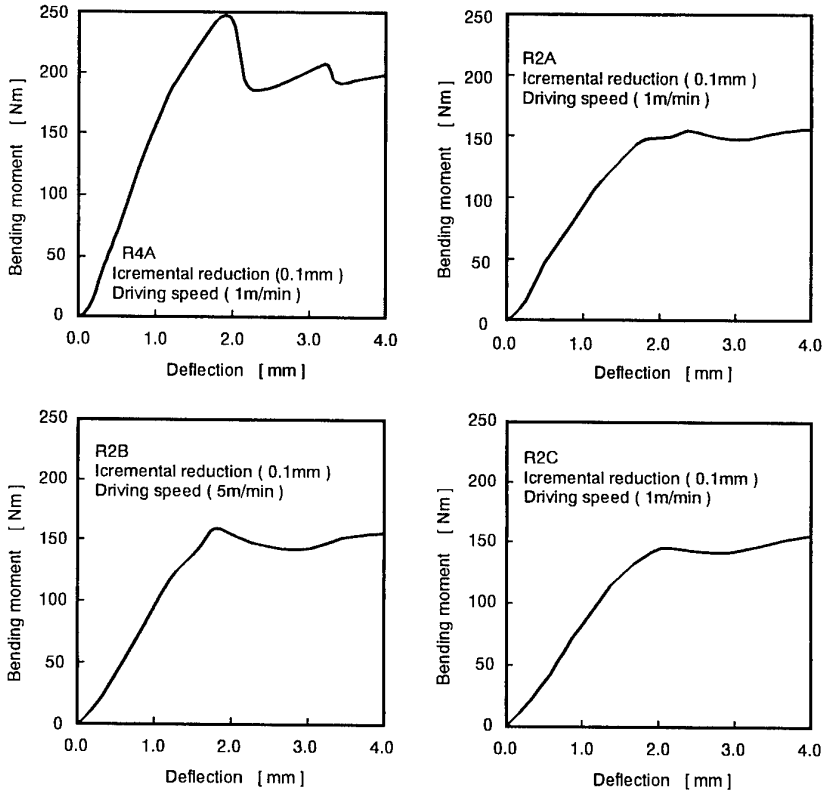

Fig. 15. Bending moment–deflection diagrams for channel-shaped component made by roll forming.

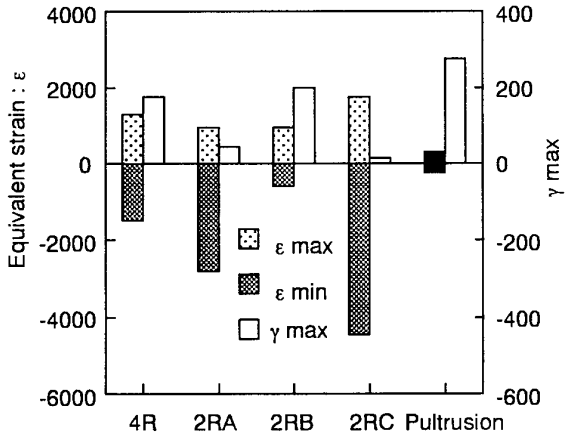

Fig. 16. Equivalent strain due to Tresca's assumption and maximum shear strain.

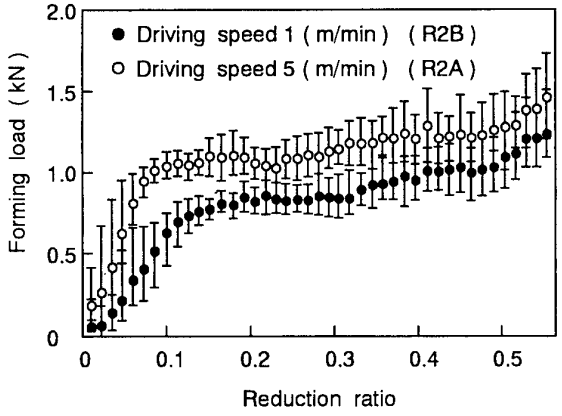

Fig. 17. Forming load for multi-stage roll forming machine.

obtained to produce shaped channel beam components. The important feature is that filling is achieved by suppressing the longitudinal deformation between the stages. This paper might help to determine the most suitable shaped product. The most suitable fabrication using rolling could be derived from the process applied to the method and the objective distribution of interfaces in the materials.

REFERENCES

1. Hirai, T., Hawkyard, J. B., Maekawa, T. and Katayama, T., Rheological interpretation in profile ring rolling. In *Advanced Technology of Plasticity*, Proc. of Third ICTP, Germany, Vol. 2, 1990, pp. 653–658.
2. Hirai, T., Roll forming of SMC and TMC, considering the resin-fibre interface. *Composite Structures* 1995, **32**, 541–548
3. Hirai, T., Hayakawa, Y. and Hakotani, M, SMC moulding using progressive rolling to reduce forming load. In *Materials and Technologies*, ed. Visconti, C., Woodhead, Italy, 1994.

ELSEVIER

Composite Structures Vol. 38, No. 1–4, pp. 405–411, 1997
© 1997 Elsevier Science Ltd. All rights reserved
Printed in Great Britain
0263-8223/97/$17.00 + 0.00

PII:S0263-8223(97)00075-5

Reduction in tensile and flexural strength of unidirectional glass fibre-epoxy with increasing specimen size

M. R. Wisnom & J. W. Atkinson

University of Bristol, Department of Aerospace Engineering, Bristol, UK

Size effects in tensile failure were investigated by means of tensile and four-point bending tests. Tapered tensile specimens with plies dropped off internally showed a reduction in strain at failure with increasing gauge length. Scaled bending tests also showed a reduction in strain with increasing specimen size. These two effects and the relationship between the tensile and flexural results could all be fitted satisfactorily with a Weibull strength model. © 1997 Elsevier Science Ltd.

INTRODUCTION

The tensile strength of composites tends to reduce with increasing stressed volume. Such size effects have been reported for example for tensile loading of glass fibre [1] and carbon fibre [2], and for flexural loading of carbon [3] and glass fibre composites [4]. This is an important phenomenon because allowable stresses based on small coupons are often used to design large structures. It is also of more fundamental interest in understanding failure in these materials.

Size effects in composites are usually explained on the basis of Weibull statistical theory in terms of the probability of finding larger defects when the stressed volume is greater [2]. Weibull theory also indicates that higher strength would be expected under flexural loading than in tension, and this has been observed experimentally [5,6]. Whilst Weibull strength theory works well for brittle materials, it is less clear whether it is applicable when failure occurs progressively as often happens in tensile failure of unidirectional composites, especially in bending. Also there are indications that strength may be more dependent on length than volume [2, 7]. An alternative explanation has been proposed for the higher strength in bending than tension based on a fibre bundle model [8]. This model predicts a size effect depending on specimen length rather than volume.

It is difficult to resolve these questions conclusively because of the many problems in obtaining accurate and reliable experimental results. For example, constant section specimens are often used to measure tensile strength. However, these tend to fail near the grips, and therefore underestimate the true strength of the material. A recent study showed that by carefully tapering the ends of the specimens, values of strength 14% higher could be obtained [9]. In flexural tests beam theory is often used to determine stresses. Deviations due to large deflections and also due to material non-linear stress–strain response for carbon fibre can introduce significant errors into the stresses calculated [10], making the validity of comparisons questionable in some cases. A further problem is the difficulty of excluding effects due to different test techniques or material processing, for example when comparing tests on single tows and on laminates.

In this study an investigation of size effects was carried out for unidirectional glass fibre-epoxy prepreg material with all specimens manufactured under the same conditions from the same batch of material. Strain gauges were

used to obtain reliable results for tensile strains at failure. Size effects in tension were studied using a newly developed tapered test specimen with different gauge lengths. Size effects in bending were investigated with scaled four-point bending tests. The results in tension and bending were compared, and the ability of Weibull statistical strength theory to fit the data was assessed.

EXPERIMENTAL

Materials

All tests were performed on material from the same batch of unidirectional Ciba E glass/913 epoxy prepreg. The volume fraction was measured by resin burn-off, giving a value of about 56%. All plates for tensile testing were cured using the standard cure cycle at 120°C. Specimens up to 64 plies thick were used for flexural testing. To avoid any problems due to exotherms, all plates for flexural specimens were subjected to an additional dwell of 45 min at 90°C.

Tensile test specimen

Standard straight-sided tensile test coupons tend to fail at the ends due to stress concentrations and stresses through the thickness caused by the load introduction at the grips. This can be overcome by waisting the specimen through the thickness, but it leaves broken fibres on the surface, and very often failure initiates from these, leading to delamination along the length. It was therefore decided to use tapered specimens with plies dropped off internally. Calculations based on previous work [11] suggested that these should not fail by delamination prior to tensile failure. There are still local stress concentrations at the ends of the dropped plies, but these only extend over a very small volume of material.

A tapered plate was manufactured by dropping off plies symmetrically within the layup. The centre section was eight plies thick, increasing to 15 plies at the ends. The ply drop nearest the centre was of a single ply at the mid-plane. Subsequent plies were dropped in pairs, one on each side of the centreline. The ply drops were spaced 5 mm apart, with continuous interleaving plies. The arrangement is shown in Fig. 1.

The tapered plate was laid up between flat aluminium plates by including additional plies on the other side of the release cloth to make up the thickness, as shown in Fig. 2. In the centre section it is necessary to make up one-half ply thickness on either side, and this was done by including a layer of bagging film on the surfaces of the plate. This method of making

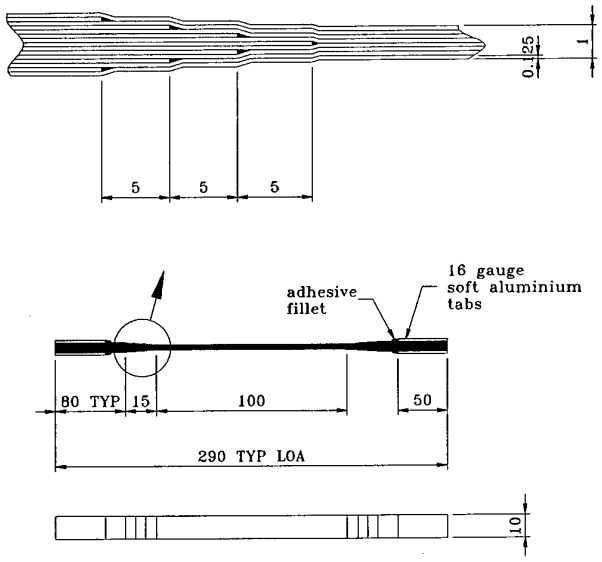

Fig. 1. Geometry of short stepped tensile specimen (mm).

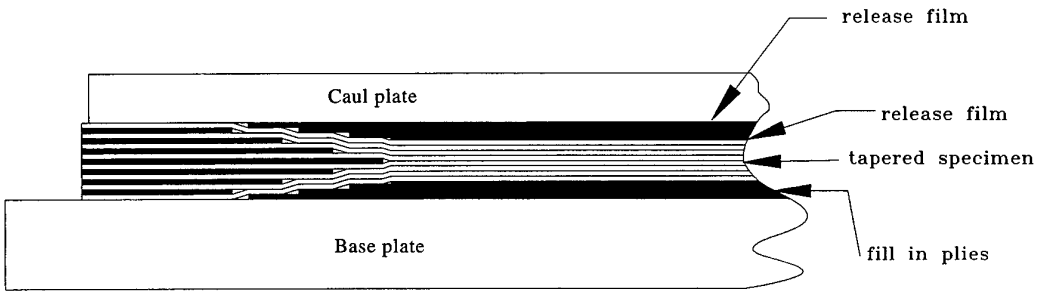

Fig. 2. Manufacturing method for tensile specimens.

tapered plates has been used previously, and found to provide very good consolidation provided care is taken to position the fill-in plies accurately. The release cloth used left a textured finish on the surface of the specimens.

Figure 1 shows the baseline test piece geometry. Specimens of width 10 mm were cut out of the plate using a diamond wheel. The gauge length was 100 mm. Some specimens had soft aluminium tabs bonded at the ends, and others were simply wrapped in emery paper to protect the ends from the grips. Initial tests did not show any evidence of failure initiating at the grips, and tests with and without tabs gave similar results. Subsequent tests were therefore performed without tabs.

Tensile tests at different gauge lengths

A series of tests was performed on the standard 100 mm gauge length specimens, and on ones with 300 and 1000 mm gauge lengths. All details of the specimen geometry and manufacturing process were the same apart from the lengths.

Strain gauges were bonded to the centre of both sides of the specimens. Tests were carried out in a Zwick screw-driven test machine under displacement control. The rate was changed to produce failure in similar times. Displacement rates of 0.048, 0.116 and 0.48 mm/s were used for the 100, 300 and 1000 mm specimens, respectively.

Specimens were loaded to failure, and values of load, strain and cross-head displacement were logged on a computer data acquisition system.

Scaled flexural tests

Four-point bending tests were carried out on 16-ply unidirectional glass fibre-epoxy. Smooth release film was used to produce a flat surface. Specimens 60 mm × 5 mm were cut out with a diamond wheel saw, and tested with an outer span of 45 mm, and inner span of 15 mm. The rig had fixed loading and support noses of diameter 10 mm, with a layer of greased rubber placed under the loading noses. The test rig is shown in Fig. 3.

Strain gauges of 1-mm length were attached to both surfaces at the centre. Tests were carried out under displacement control to produce failure in about 60 s, a similar rate to that used on the tensile tests. Loads, strains and crosshead displacement were logged on the computer.

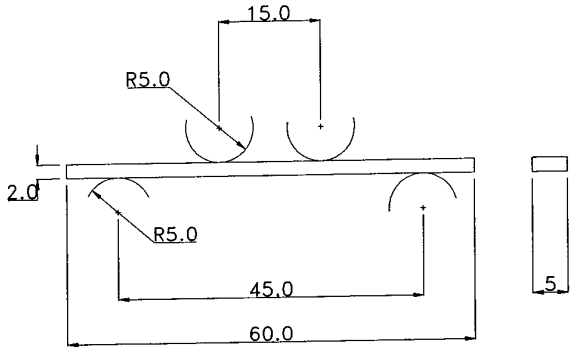

Dimensions in mm.

Fig. 3. Small bending rig.

Two further sets of tests were carried out with all dimensions of the specimens and test rigs increased by factors of 2 and 4 compared with the initial set. The thicknesses of the specimens from the 32- and 64-ply panels did not scale perfectly, with mean measured values of 4.30 and 9.21 mm compared with 2.19 mm for the 16-ply panel. The number of layers of rubber under the loading noses was also increased in proportion to maintain the same distribution of local stresses at the loading points. The size of the strain gauges was not changed between the different tests.

RESULTS AND DISCUSSION

Tensile tests

For the 100-mm specimens the response was initially linear. Towards the end of the test, the load started to increase less rapidly, eventually reaching a peak and then dropping before catastrophic failure. The strain was increasing throughout the test. Figure 4 shows a typical load–strain response based on the average of the two gauge readings.

Failed specimens showed extensive splitting and fibre failure throughout the gauge length. On all specimens longitudinal splitting and delamination extended right back as far as the grips, but in most cases there was little evidence of fibre failure here, and so it is believed that failure did not initiate at the grips. There was no clean delamination between the continuous and dropped plies of the type that might be

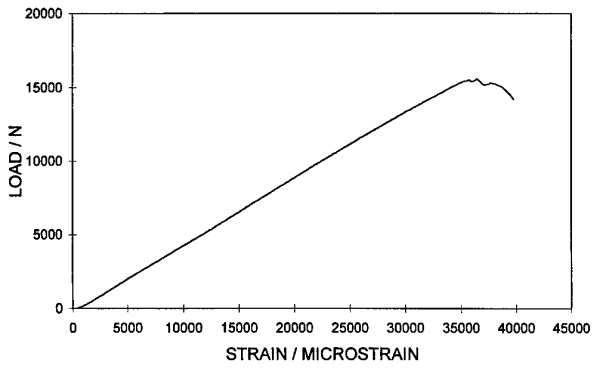

Fig. 4. Response of typical 100 mm gauge length tensile specimen.

expected if this was the cause of failure. On some specimens damage was greatest within the gauge length, whereas on others it was more concentrated around the start of the tapered sections.

The fact that the strain increased whilst the load dropped means that there must have been broken fibres in the gauge length prior to final failure. Damage at this stage was internal, with generally no visible evidence of fibre failure, but it is not possible to determine whether it initiated randomly along the gauge length or at the start of the taper due to the stress concentration at the dropped plies.

The longer specimens all behaved similarly, although there was a tendency for there to be less damage distributed along the gauge length, and more concentrated near the start of the tapers. There was also less drop in load after the maximum tensile strain had been reached for the 300-mm specimens, and virtually no drop in load at all for the 1000-mm ones.

Table 1 shows the results for the three different length specimens in terms of the strains at maximum load and maximum strains at failure. The values are the averages of the gauges on both sides of the specimen except for a few cases where one of the gauges failed prematurely. The strains for the 100-mm specimens are higher than the longer ones, especially the maximum strains, but there is little difference between the results for the 300- and 1000-mm long specimens.

The strain at maximum load is considered to be the best measure of tensile failure strain, as this corresponds to the strength of the material when tested under load control. The reduction in strain at maximum load from the 100- to 1000-mm specimens is 7.2%, a significant difference. However, there is not a consistent trend between all three sets of results. The expected differences are relatively small compared with the coefficients of variation, and it may be that scatter in the results is obscuring the trend for reducing strain with increasing gauge length.

Alternatively it could be that failure for the longer two sets of specimens is controlled by the stress concentration at the start of the tapered section, and this is why the strains at failure are similar. If this is the case it is not clear why the shorter specimens should be stronger since the tapers at the end of the gauge length are nominally identical.

One possible explanation is the effect of the strain energy stored in the specimens, which increases with length. When failure initiates, the greater release of energy for the longer specimens makes it more likely that failure will propagate. This is also consistent with the longest ones failing at the maximum load, whereas the shortest ones survived to considerably higher strains after the load had peaked.

Despite the care taken with specimen design and testing, these tests did not resolve conclusively the questions of size effects in tension, or the relative importance of length and volume on strength. The results illustrate the difficulties in carrying out tensile tests and trying to measure relatively small effects. Fortunately a

Table 1. Summary of results for tensile tests

Gauge length (mm)		Tensile strain at maximum load (microstrain)	Maximum tensile strain (microstrain)	Maximum load (kN)	No. of specimens
100		36710	39070	15.36	9
	c.v.	3.4%	3.6%	3.8%	
300		33650	34120	14.54	15
	c.v.	4.6%	5.2%	6.8%	
1000		34060	34120	14.46	10
	c.v.	5.8%	5.5%	5.2%	

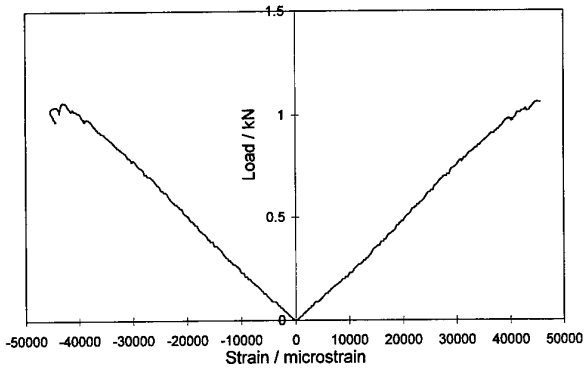

Fig. 5. Response of typical small flexural specimen.

clearer picture emerged from the four-point bending tests discussed next.

Flexural tests

Failure occurred in tension in all cases, with fibres breaking in the centre section between the loading points and splitting off from the surface to produce a brush-like appearance. Failure initiated at the surface, and then continued progressively through the thickness until the deflections became very large and the test was stopped. Figure 5 shows a typical response for one of the smallest specimens. The tensile gauge failed when the fibres on the surface fractured. In some cases this was the point of maximum strain, whilst in other cases the maximum strain was registered shortly before gauge failure, suggesting that damage had initiated close enough to the gauge to affect its reading. In all but one case the maximum strain was recorded at or before the maximum load. The compressive gauges continued to read beyond this point, with strains generally increasing while the load reduced.

The medium and large specimens behaved very similarly, and in all cases the maximum strain occurred before the maximum load. As with the smaller specimens this sometimes corresponded to the point of gauge failure, and sometimes the strain dropped slightly before the gauge broke. Again the compressive strains continued to increase, but there was less tendency for the load to drop, especially for the largest specimens. This could be explained by failure occurring on a ply by ply basis, where the effect of one ply failing and splitting off would have much less effect on the load on a 64-ply specimen than it would on one with only 16 plies.

Table 2. Summary of results for flexural tests

Number of plies	Maximum tensile strain (microstrain)	c.v. (%)	Number of specimens
16	43950	2.3	7
32	42210	5.9	6
64	37110	5.7	6

The maximum tensile strain was considered to be the most reliable measure of failure strain, and the mean results are shown in Table 2. There is a significant size effect, with a 16% drop in strain from the smallest to the largest specimens. This is very similar to the size effect previously found in bending of unidirectional carbon fibre-epoxy with the same matrix [3], where a 14% reduction in tensile strain at failure was measured going from scaled specimens of 25 to 100 plies.

Very high strains were measured on the compressive surface of the specimens, up to 47920 microstrain for one of the small ones. However, there was no indication of any damage on the surface despite the high strains.

The maximum strains for failure under flexural loading can be compared with the strains at maximum load under tensile loading. This is probably the best basis for comparison, although in the bending tests there was considerable fibre failure before the maximum load was reached whereas in the tensile tests there was not. There is a significant difference between the bending and tensile failure strains, with the lowest set of results for the largest bending tests being higher than the highest set of results for the shortest tensile specimens. In view of the considerable care taken in the specimen design and testing, this is believed to reflect a real difference between failure under flexural and tensile loading, rather than being due to the different testing techniques.

Fit with Weibull theory

Weibull statistical strength theory predicts a size effect for scaled specimens and a higher strength in bending than tension. In this section it is applied to the experimental results to see how well it is able to fit the data.

For a two-parameter Weibull model, the probability of survival for a specimen subject to a strain field ε over a volume V is

$$P(s) = \exp[-\int(\varepsilon/\varepsilon_o)^m \, dV] \quad (1)$$

where ε_o is the characteristic strain and m is the Weibull modulus.

For tensile specimens the strain field can be assumed constant over the gauge length. The tapered part can be neglected, since the taper is short compared with the gauge length and the stress drops rapidly as the thickness increases. Also the stress concentration at the first ply drop only extends over a very small volume and will be neglected. Strains ε_1 and ε_2 for specimens of different volumes V_1 and V_2 can be compared using eqn (1) and assuming equal probability of failure

$$\varepsilon_1/\varepsilon_2 = (V_2/V_1)^{1/m} \tag{2}$$

A log–log plot of failure strain against volume should therefore give a straight line.

In the bending tests there is a variable strain distribution. In order to compare the results with the tensile tests it is therefore necessary to calculate an equivalent volume $\bar{V}$ which gives the same probability of failure when subject to a constant tensile strain $\bar{\varepsilon}$ as the actual strain distribution ε acting over the volume V. This requires integration of the strain distribution using eqn (1).

Based on beam theory the strain can be assumed to vary linearly through the thickness, with a constant distribution along the length l between the loading noses. The surface strain can be assumed to vary linearly from zero to the maximum value over the distance d between the support and loading noses. Integrating eqn (1) over the half thickness of the specimen where the strains are tensile and equating to the uniform tension case gives

$$\bar{V} = wt\left[\frac{l}{2(m+1)} + \frac{d}{(m+1)^2}\right] \tag{3}$$

Figure 6 shows all the results for the tensile and flexural tests plotted on a log–log scale. The strains at maximum load from the tensile tests are plotted against the actual gauge length volume. The maximum strains from the flexural tests are plotted against the equivalent volume $\bar{V}$ calculated from eqn (3) using the nominal specimen thicknesses. The error bars correspond to one standard deviation on either side of the mean results.

A least squares line has been put through the data, and gives a very good fit, passing within the error bars of all six sets of data. The slope

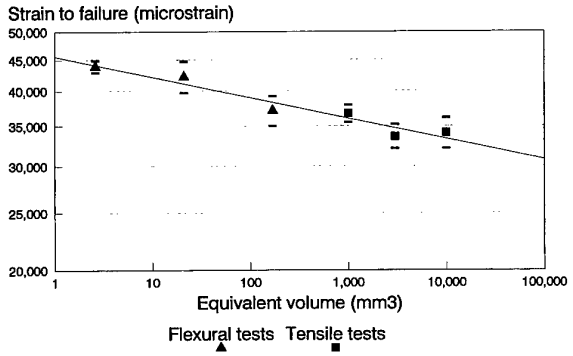

Fig. 6. Weibull fit to data.

of the graph gives a Weibull modulus of 29.3, and this was the value used in eqn (3) to correct the volumes of the bending specimens. This is similar to values obtained in other studies on unidirectional composites. For example, a Weibull modulus of 25 was obtained from scaled bending tests of unidirectional carbon fibre-epoxy [3].

There are some questions about the applicability of Weibull theory to tensile failure of unidirectional composites due to the progressive nature of failure as opposed to the catastrophic propagation from a critical defect implied by Weibull strength theory. Nevertheless, it has been shown to be successful in fitting the experimentally observed phenomena. The length effect in tensile tests, the size effect in bending tests and the difference in tensile strength in tension and bending have all been reconciled using a single set of Weibull parameters. Despite the remaining uncertainties, from a practical point of view it is reasonable to use Weibull theory to predict failure and set allowable stresses accounting for specimen size and non-uniform stress distributions.

CONCLUSIONS

A new type of tapered tensile test specimen has been developed which produced failure away from the grips at high strains. A tensile value of 36 700 microstrain was obtained with a 100-mm gauge length. This dropped to 34 100 for specimens with a gauge length of 1000 mm, a 7.2% reduction. Four-point bending tests failed in tension, with higher strains at failure than under tensile loading. A size effect was observed in scaled tests, with failure strain decreasing with increasing specimen size. Maximum values of

43900 were obtained for 16-ply specimens, decreasing to 37100 for 64-ply specimens, a reduction of 16%. All six sets of data fitted a Weibull strength model with a Weibull modulus of 29.3. The same set of Weibull parameters was able to reconcile the length effect in the tensile tests, the size effect in the bending tests and the difference between tensile strength in tension and bending.

ACKNOWLEDGEMENTS

This work was funded by EPSRC/MOD under contract No. GR/H75017 in collaboration with Westland Helicopters and DRA Farnborough.

REFERENCES

1. Kies, J. A., The strength of glass fibers and failure of filament wound pressure vessels. NRL report No. 6034, US Naval Research Laboratory, Washington, 1964.
2. Hitchon, J.W. and Phillips, D.C., The effect of specimen size on the strength of CFRP. *Composites*, 1978, **9**, 119–124.
3. Wisnom, M.R., The effect of specimen size on flexural strength of unidirectional carbon fibre-epoxy. *Composite Struct.*, 1991, **18**, 47–63.
4. Phillips, H.J., Shenoi, R.A. and Lewis, S.M., Effect of specimen size on the strength scaling of GFRP laminates. *Materials Lett.*, 1994, **21**, 229–238.
5. Bullock, R.E., Strength ratios of composite materials in flexure and in tension. *J. Composite Mater.*, 1974, **8**, 200–206.
6. Whitney, J.M. and Knight, M., The relationship between tensile strength and flexure strength in fiber-reinforced composites. *Exp. Mech.*, 1980, **XXXVII**, (1), 211–216.
7. Wisnom, M.R., Relationship between size effect and strength variability in unidirectional carbon fibre-epoxy. *Composites*, 1991, **22**, 47–52.
8. Wisnom, M.R., The relationship between flexural and tensile strength of unidirectional carbon fibre-epoxy. *J. Composite Mater.*, 1992, **26**, 1173–1180.
9. Wisnom, M. R. and Maheri, M. R., Tensile strength of unidirectional carbon fibre-epoxy from tapered specimens. *Second European Conference on Composites Testing and Standardisation*, Hamburg, September 1994, pp. 239–247.
10. Wisnom, M. R., Limitations of linear elastic bending theory applied to four point bending tests of unidirectional carbon fibre-epoxy. *Proceedings of the AIAA Structures, Structural Dynamics and Materials Conference*, Long Beach, CA, April 1990, pp. 740–747.
11. Wisnom, M.R., Jones, M.I. and Cui, W., Failure of tapered composites under static and fatigue tension loading. *AIAA Jnl*, 1995, **33**, (5), 911–918.

ELSEVIER

Composite Structures Vol. 38, No. 1–4, pp. 413–420, 1997
© 1997 Elsevier Science Ltd. All rights reserved
Printed in Great Britain
0263-8223/97/$17.00 + 0.00

PII:S0263-8223(97)00076-7

Vibration control of an active laminated beam

Paolo Gaudenzi, Rolando Carbonaro & Renato Barboni

Università di Roma La Sapienza, Dipartimento Aerospaziale, Roma, Italy

The dynamic response of a carbon fibre reinforced plastic $[0/+45/-45/0]_s$ active laminated beam covered by piezoelectric layers is considered. A simple collocated displacement control strategy is implemented by letting the active layers work as actuators and sensors and by constructing an analogue control circuit the characteristics of which are given in some detail. The open- and closed-loop steady-state response of the cantilever beam are then experimentally tested in the range of 40–2000 Hz and the effectiveness of the control mechanism is successfully demonstrated. © 1997 Elsevier Science Ltd.

INTRODUCTION

Recently, considerable attention has been directed to the use of piezoelectric materials as actuators and sensors in the development of advanced fully integrated active structures [1].

Many studies have focused on the description of the interaction between the piezoelectric part and the host structure both in the static and in the dynamic conditions by means of analytical methods and finite element techniques [1–4].

Increasing efforts have been addressed to the problem of vibration control and suppression [5–8]. In fact the practical opportunity to effectively face the problem of reducing the level of the dynamic response of a flexible structure represents one of the most interesting areas of application of the so-called 'intelligent structures' technology. The possibility of applying a distributed control on a flexible structure by means of piezoelectric materials was illustrated by Bailey and Hubbard [5] and demonstrated, both from the analytical and the experimental point of view, by Hagood *et al.* [6]. Hanagud *et al.* [7] have shown the use of optimal control strategy based on the minimization of a quadratic performance index for the vibration of an elastic cantilever. Denoyer and Kwak [8] applied positive position feedback control and LQG control for the vibration suppression of a slewing cantilever.

It is especially clear from the works of Hagood *et al.* [6] and Denoyer and Kwak [8] that the use of electrically active actuators and sensors requires not only the necessary development of a reliable optimal control strategy, but also a special attention to the construction of the control chain and the relevant electronics. The design of the feedback electronic circuits represents a fundamental step in the realization of the entire controlled system. Indeed an electronic circuit which is not well matched at its output or input can substantially modify its expected response in terms of bandwidth and phase. In particular, because of its large capacitance, the electronic interfacing of a piezoelectric device, both as a sensor and an actuator, is a critical point of the electronic design. In such a design concept the role of connections between the different sub-systems (passive structure, sensors and actuators, control circuit, power supply) is a key issue for the feasibility and the reliability of the system.

The already well-established technology of laminated composites provides an extraordinary opportunity for developing and constructing real systems which can practically meet the technical requirements of an active structure. In fact, the concept of laminated structures offers a natural environment for introducing in different layers the various functions which are present in the system. Active actuating or sensing piezoelectrics can be introduced at a certain point of the stacking sequence and connected to a layer where the electronics for control are constructed.

This paper aims to describe the implementation of a vibration control capability on a laminated composite beam using piezoelectric materials as active actuating and sensing layers and analogue circuitry as the control devices. The use of commercially available piezoelectric devices is demonstrated to allow the construction of an active laminated structure. Simple open- and closed-loop experiments, based on a simple and effective displacement control technique, show significant reduction for the first two modes of a cantilever structure excited at its tip by an external disturbing action.

THE ACTIVE LAMINATED BEAM

A composite $[0/+45/-45/0]_s$ cantilever carbon fibre reinforced plastic (CFRP) beam with two active layers of piezoelectric material covering approximately 50% of the top and bottom surfaces is considered (Fig. 1). The characteristics of the laminate and the geometry of the beam are illustrated in Table 1 and shown in Fig. 1.

The piezoelectric layers (whose characteristics are shown in Table 2) are symmetrically glued to the beam by means of a two-phase epoxy resin cured at room temperature. The polarization directions are also shown in Fig. 1. The position of the piezo-devices was chosen in such a way to activate and sense the dynamic response of the beam at the first and second mode. To achieve this aim the results obtained in ref. [9] for an isotropic beam structure are used to establish the position and the length of the piezo. Both active layers can work either as a sensor or as an actuator. In the present case these layers are made from commercially available devices and are connected to the host structure after the composite's curing process has been concluded. It is possible to consider a process in which the curing of the composite includes also the active layers. In this case, however, some serious difficulties may arise, especially in the case of internal active layers, as to the wiring and the electric connections to the control sub-system. The electronic circuit itself, if inserted in one layer of the laminate, can produce some problems. This paper is not addressing such issues, which are of primary importance in the feasibility study of active composite structures.

A SIMPLE CONTROL STRATEGY

Due to the converse piezoelectric effect a polarized piezoelectric device strains if excited by an applied voltage and, due to the piezoelectric direct effect, generates a voltage if mechanically deformed. Then a piezo is able to produce an induced strain or to monitor a strain (or stress) field by means of the interaction of its mechanical and electrical properties [4]. In the former case the piezo operates as an actuator and in the second one as a sensor device.

With the beam considered here, the piezoelectric layer was placed on the top of the laminated host structure and was supposed to work as an actuator while the second one, placed at the same position but on the opposite side of the beam thickness, acts as a sensor. The objective of the control action is to reduce the vibrations induced on the beam by some external steady-state actions. In our case an electromagnetic exciter produces sinusoidal

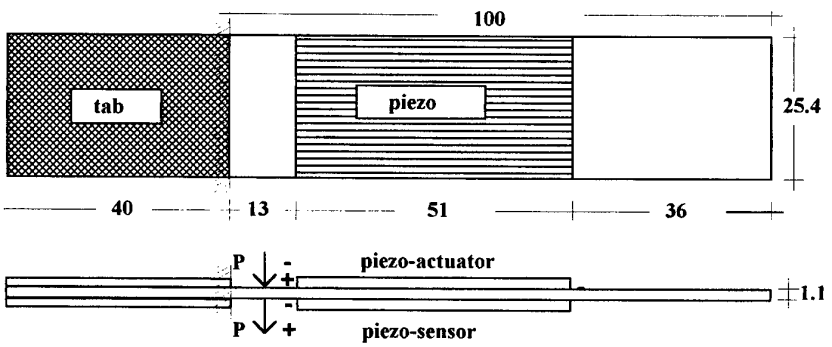

Fig. 1. Geometry of the active cantilever beam (all measurements are in mm). The polarization directions of the double-bonded piezo-devices are also indicated.

transverse forces at the tip of the beam which are tuned from 40 to 2000 Hz; the range of the first three bending modes of the beam.

Due to this excitation, the sensing piezo is subjected to a strain field which is proportional to the surface electric charge which appears on both the electrodes covering the upper and lower surfaces of the device. By amplifying and feeding back this charge to the actuator which is placed on the opposite side of the beam, an electric voltage is produced that causes the (actuating) piezo to strain in a fashion which opposes to the bending motion. The presence of the charge on the electrodes of the sensor is proportional to the average of the strain field at the top surface of the laminated beam which is covered by the piezoeletric sensor itself. For this reason special attention should be paid to the position of the actuator along the beam axis or to the dimensions of the active part of it, as explained in ref. [9].

This control mechanism, being the strain related to displacements by means of spatial (and not time) derivatives, can be thought of as a displacement (or position) like control strategy which performs its action by increasing the stiffness of the structure.

Table 1. $[0/+45/-45/0]_s$ laminate characteristics and lamina elastic characteristics

E_{11}	250 GPa
$E_{22} = E_{33}$	7.8 GPa
$G_{12} = G_{13} = G_{23}$	4.5 GPa
$\nu_{12} = \nu_{13} = \nu_{23}$	0.3
Density	1644 kg/m^3

EXPERIMENTAL HARDWARE

A block diagram of the controlled system is shown in Fig. 2. As can be seen from the figure, the feedback signal is obtained interfacing the piezo-sensor to a charge amplifier. As will be explained in more detail later, this allows one to obtain, with the necessary sensitivity, a voltage signal which is proportional to the average strain in the area of the beam covered by the actuator (that is to the surface charge produced in that area due to the direct piezoelectric effect). The feedback circuit is then completed

Table 2. Piezo characteristics of model QP10N by ACX Inc.

Young's modulus	18.95 GPa
d_{31}	-7.257×10^{-10} m/V
ε	16.112 nF/m
Device size	50.8 mm × 25.4 mm × 0.381 mm
Piezo-wafer size	45.97 mm × 20.57 mm × 0.25 mm
Operating voltage range	0–200 V
Maximum operating frequency	20000 Hz
Device capacitance	0.06 μF
Full-scale strain extension	± 352 $\mu\varepsilon$
Extension gain	1.76 $\mu\varepsilon$/V

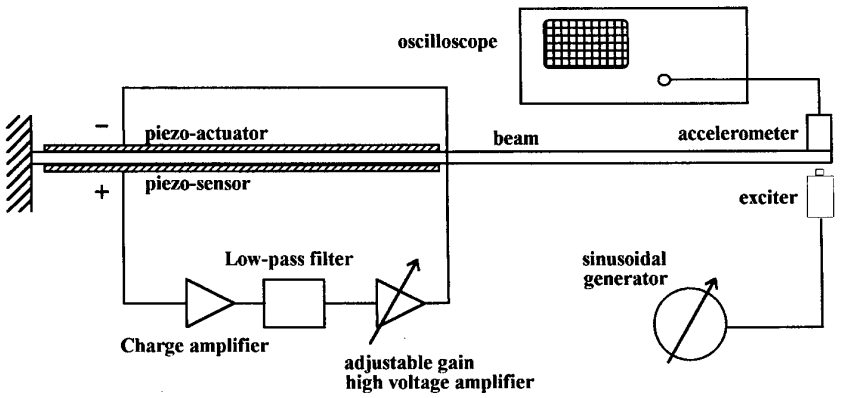

Fig. 2. Experimental apparatus.

by a filtering circuit which is necessary in order to stabilize the system response and a high-voltage amplifier which increases the level of the field induced in the piezo-actuator.

Besides the aforementioned feedback loop circuits the experimental apparatus includes measurement devices which were utilized to carry out the harmonic responses of the system:

1. an electromagnetic exciter (Brüel and Kjaer type 3930) producing the external action at the beam tip which represents the disturbance that has to be suppressed;
2. a frequency oscillator (Brüel and Kjaer type 1017) generating sinusoidal signals in the 2 to 2 kHz frequency range to drive the exciter;
3. a dual-trace oscilloscope (Tektronics type 2246A) with frequency, phase and amplitude measure displaying capability;
4. an accelerometer bonded at the tip of the cantilever.

The circuits which form the feedback loop will be described in detail below.

The charge amplifier

The piezo-sensor is a charge generator with the generated charge proportional to the sensed strain. Its equivalent circuit consists of an ideal charge generator Q_p and a shunt capacitor C_p (see Fig. 3). The open circuit voltage V_p, which is a measure of the device sensitivity, is defined as in eqn (1)

$$V_p = \frac{Q_p}{C_p} \tag{1}$$

When the piezo-sensor is connected to an amplifier by a coaxial cable other shunt capacitances are added to C_p as shown in Fig. 3. The

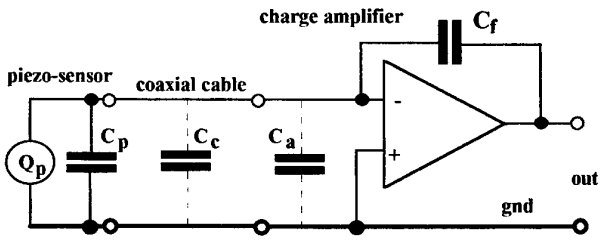

Fig. 3. Ideal charge amplifier.

total shunt capacitance will be the following eqn (2)

$$C_T = C_p + C_c + C_a \tag{2}$$

In eqn (2) C_c and C_a represent the distributed capacitance of the cable and the input capacitance of the amplifier respectively. The effect of these added capacitances is to reduce the device sensitivity. As a consequence if the piezo-sensor is interfaced to a voltage amplifier its output voltage signal is strongly influenced by from the presence of these capacitances. For this reason a charge amplifier is preferred for interfacing the piezo-sensor.

The circuit diagram of the ideal charge amplifier is shown in Fig. 3. When a piezo-sensor is connected to the input of this amplifier the charge Q_p is divided in part on input capacitance and in part on the feedback capacitor C_f and it is possible to write

$$Q_p = C_T V_{\text{in}} + (V_{\text{in}} - V_{\text{out}}) C_f \tag{3}$$

But the output voltage of the amplifier is $V_{\text{out}} = A V_{\text{in}}$ where A is the open loop gain of the amplifier. Then eqn (3) can be transformed in the following eqn (4)

$$Q_p = C_T V_{\text{in}} - V_{\text{in}}(A-1) C_f \tag{4}$$

Because the gain A is very high ($A > 10^5$), it is possible to write eqn (5)

$$Q_p \cong = V_{\text{in}} A C_f = -V_{\text{out}} C_f \tag{5}$$

As a consequence of this last result, all of the piezo-sensor generated charge Q_p is pushed into the feedback capacitor C_f and the output voltage of the amplifier depends only on the charge intensity. In such a way a voltage signal proportional to the average strain detected by the piezo-sensor can be obtained.

The circuit used in the tests was made by means of a serial connection of two distinct circuits: a charge amplifier and an inverting voltage amplifier. The complete circuit diagram is shown in Fig. 4. The two operational amplifiers used are integrated into the same chip (TL082, dual operational amplifiers, by Texas Instruments [10]).

In the charge amplifier section of Fig. 4 it is possible to note the presence of the feedback capacitor C_f and other components that were added to eliminate the effects of the input offset voltage and input bias current [11] of the

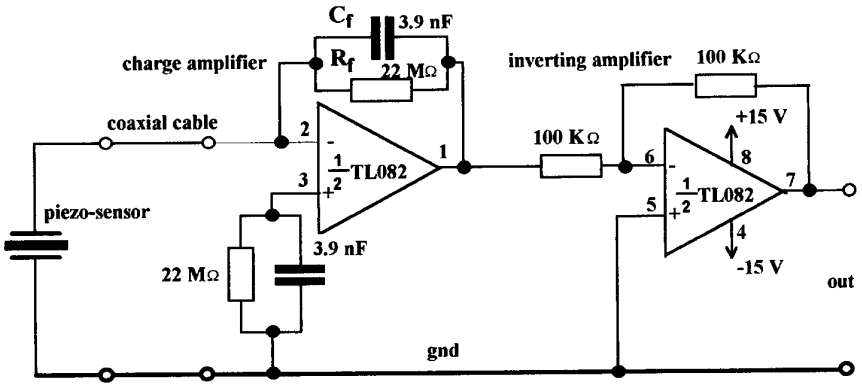

Fig. 4. Real charge amplifier.

real operational amplifier. The presence of these components and in particular the presence of the resistance R_f causes a frequency-dependent behaviour of the charge amplifier. Our circuit behaves like an ideal charge amplifier only when the frequency of the input signal is over a cut-off value determined by eqn (6) ($f_c \cong 2$ Hz in the present case).

$$f_c = \frac{1}{2\pi R_f C_f} \tag{6}$$

In order to have the right phase in the feedback control, the 180° phase shifting of the charge amplifier is to be eliminated. For this reason an inverting voltage amplifier was connected to the charge amplifier.

The transfer function of the complete circuit can be supposed as a constant between the 40 and 2 kHz frequency range of the experimental tests because the lower cut-off frequency is f_c while the higher one is equal to the high cut-off frequency of the operational amplifiers that is about 3 MHz.

The low-pass filter

The function of the low-pass filter is to stabilize the controlled system by reducing the closed-loop gain out of the frequency band of the experimental tests (between 40 and 2 kHz) (Fig. 5). It is a typical two-pole active low-pass filter characterized by a cut-off frequency fixed at 2000 Hz. The value of the cut-off frequency f_c was chosen in such a way as to have no influence on the phases of the modes into the frequency band of the tests.

The high voltage amplifier

The high voltage amplifier is an inverting amplifier of type 1224/5 manufactured by Quick Pack, Active Control eXpert. Its principal characteristics are: maximum output voltage ± 200 V at a peak current of 200 mA; adjustable inverted gain from $\times 1$ to $\times 20$, continuous; output impedance 1 Ω. Because the bandwidth of this amplifier is 5 kHz in value, also the relevant transfer function can be supposed as a constant between the 40 and 2 kHz frequency range of the experimental tests.

EXPERIMENTAL RESULTS

The active beam described in Fig. 2 along with its control chain can be thought of as a single input–single output control system. The input and the output of the system are represented respectively from the input of the piezo-actuator and the output of the piezo-sensor. The

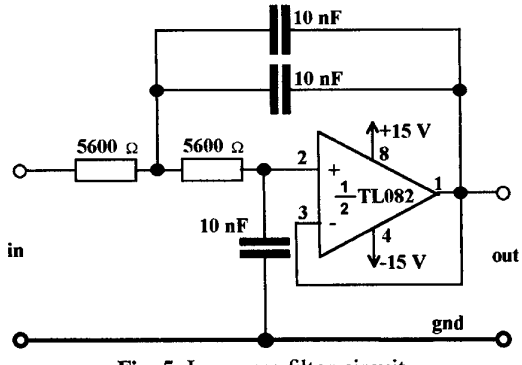

Fig. 5. Low-pass filter circuit.

series connection of dedicated electronic circuits which connects the output and the input of the system forms the feedback loop.

In the displacement control the feedback circuit generates an actuating voltage signal $V_{act}(t)$ proportional to the sensing displacements. This signal drives the piezo-actuator in such a way to obtain a displacement field which is opposite respect to that one produced from the disturbance external action. It can be demonstrated that this type of control performs its action by increasing the stiffness of the structure.

The flexural modal frequencies were first experimentally determined by measuring the harmonic response relative to the acceleration of the beam tip without control; the test gave a value of 81 Hz for the first modal frequency and of 542 Hz for the second one. The problem of system stability was then analysed measuring the amplitude and the phase of the open-loop transfer function. The measuring was done by assuming that the input voltage of the high voltage amplifier was the input and the charge amplifier output voltage was the output. The amplitude (in dB units) and phase diagrams for this function obtained for a fixed value of the gain of the power amplifier are shown in Fig. 6.

The phase of the open-loop transfer function has a value about equal to 0° out of the resonance and becomes about −160° in correspondence to every resonance frequency. Referring to the usual stability criteria (Nyquit's

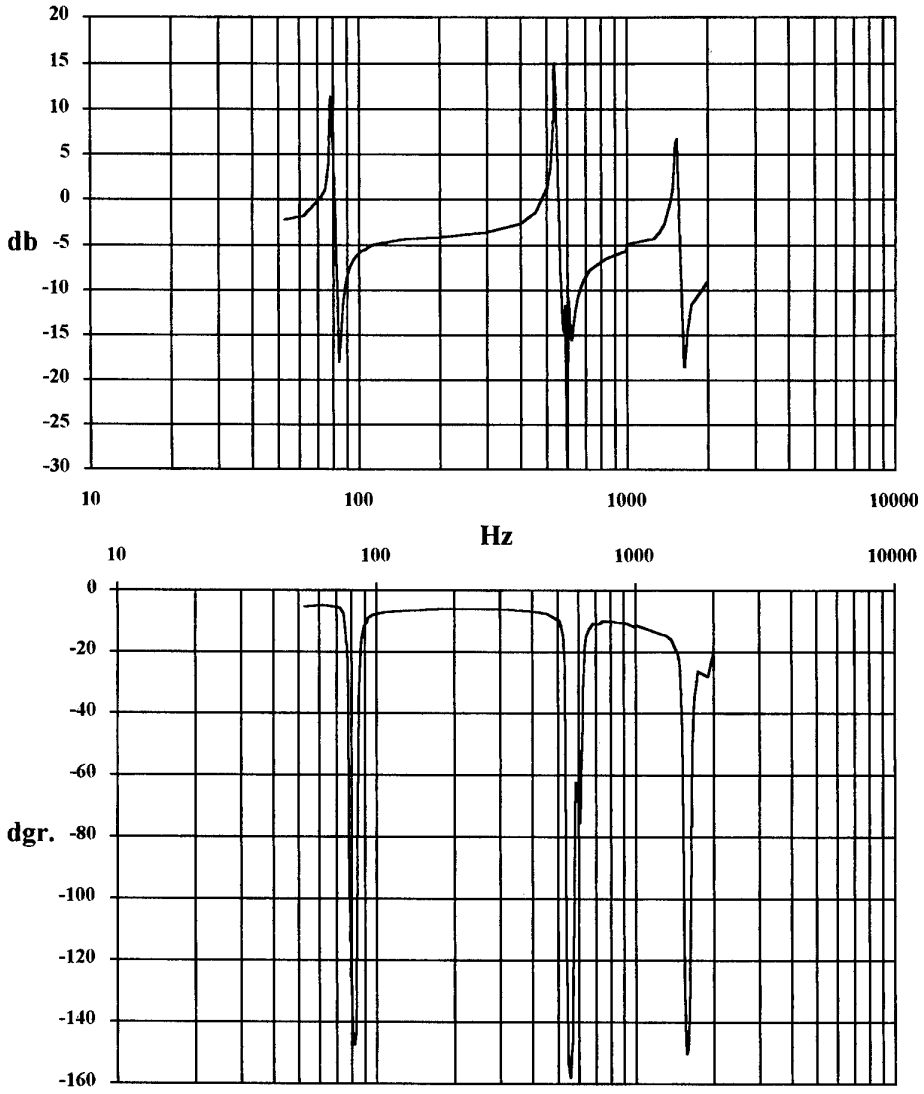

Fig. 6. Amplitude and phase diagrams of the power amplifier to charge amplifier open-loop transfer function.

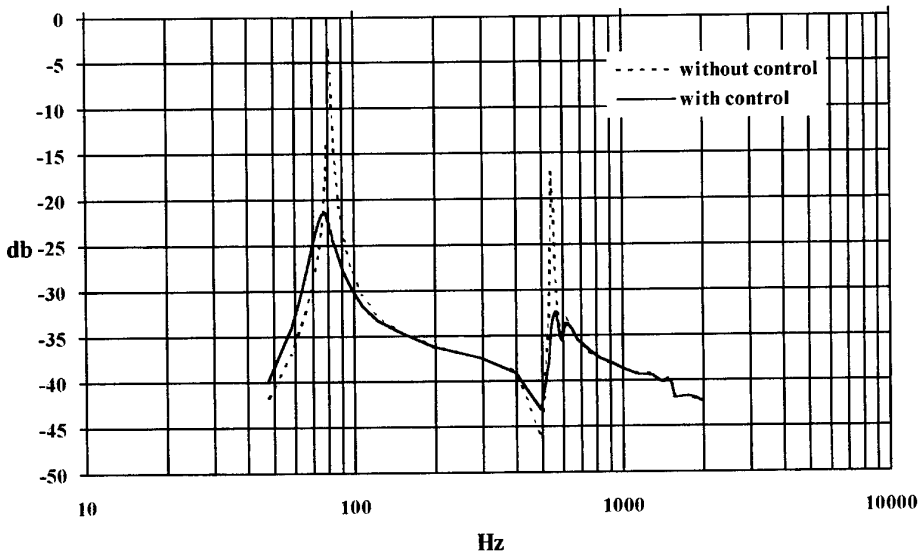

Fig. 7. Amplitude of the exciter input voltage to beam-tip acceleration transfer function with displacement control.

criterion) and on the basis of these results the controlled system is inherently stable, as expected, between the 40 and 2 kHz frequency range.

Nevertheless instability problems were present in the closed-loop system, shown by spontaneous oscillations at 20 kHz, the same value indicated by the piezo-device data sheet as the maximum operating frequency. For this reason, a second-order low-pass filter with a cut-off frequency of 2 kHz was introduced into the feedback loop. In this way all the harmonic components of the feedback signal over this frequency were cut-off. By this adjustment the closed-loop system became stable and it was possible to increase the gain over the previous fixed value and to measure the closed-loop response whose amplitude diagram is shown in Fig. 7.

The diagram in Fig. 7 is plotted in decibel units assuming as reference and output signals the exciter input voltage and the accelerometer output, respectively. The attenuation of the external action effects is strong for both modes, indeed we have 18.1 and 15.3 dB, respectively for the first and the second modes. Shifts of the resonance frequencies between the two states of deactivated/activated control were also noted. Indeed, the frequency of the first resonance is decreased from 81 to 78 Hz, while the second is increased from 542 to 555 Hz. These frequency shifts happen because of the concurrent action of the stiffness increasing and the changing pole values when the control loop is closed.

CONCLUSIONS

The possibility of constructing an active composite beam with sensing and actuating capability is demonstrated. A simple collocated control strategy is implemented by means of analogue circuitry which allows one to consider the sensitivity and instability problems that were met for frequency ranges of up to 2000 Hz of the dynamic response of the beam. A reduction of 18 dB for the first mode and of 15 dB for the second mode in the case of steady-state external harmonic disturbances is obtained. The experimental results show that piezoelectric actuators and sensors can be used effectively for vibration control and suppression of a composite laminated beam.

ACKNOWLEDGEMENT

The financial support of the Italian Ministry for Research (MURST contract 301/1994, Dr P. Gaudenzi supervising) is gratefully acknowledged.

REFERENCES

1. Crawley, F. and de Luis, J., Use of piezoelectric actuators as elements of intelligent structures. *AIAA Jnl*, 1987, **25**, (10), 1373–1385.
2. Chaudhry, Z. and Rogers, C.A., The pin-force model revisited. *J. Intell. Mater. Syst. Struct.*, 1994, **5**, 347–353.

3. Strambi, G., Barboni, R. and Gaudenzi, P., Pin-force and Euler–Bernoulli models for analysis of intelligent structures. *AIAA Jnl*, 1995, **33**, (9), 1746–1749.
4. Gaudenzi, P. and Bathe, K., An iterative finite element procedure for the analysis of piezoelectric continua. *J. Intell. Mater. Syst. Struct.*, 1995, **6**, 266–273.
5. Bailey, T. and Hubbard, J. E. Jr., Distributed piezoelectric polymer active vibration control of a cantilever beam. *J. Guidance Cont. Dyn.*, 1985, **8**, (5), 605–611.
6. Hagood, N.W., Chung, W.H. and Von Flotow, A., Modelling of piezoelectric actuator dynamics for active structural control. *J. Intell. Mater. Syst. Struct.*, 1990, **1**, 327–354.
7. Hanagud, S., Obal, M.W. and Calise, A.J., Optimal vibration control by the use of piezoceramic sensors and actuators. *J. Guid. Contr. Dyn.*, 1992, **15**, (5), 1199–1206.
8. Denoyer, K.K. and Kwak, M.K., Dynamic modelling and vibration suppression of a slewing structure utilizing electric sensors and actuators. *J. Sound Vibr.*, 1996, **189**, (1), 13–31.
9. Barboni, R., Fantini, E., Gaudenzi, P. and Mannini, A., On the optimal placement of pzt actuators for the control of the dynamic response of a beam. *20th ICAS*, Sorrento, Italy, September 1996, Vol. 2, pp. 1890–1900.
10. Texas Instruments, *Operational Amplifiers and Comparators Data Book*, Vol. A, 1995.
11. Millman, J. and Halkias, C. C., *Integrated Electronics and Digital Systems*. McGraw-Hill, New York, 1972.

ELSEVIER

Composite Structures Vol. 38, No. 1–4, pp. 421–433, 1997
© 1997 Elsevier Science Ltd. All rights reserved
Printed in Great Britain
0263-8223/97/$17.00 + 0.00

PII:S0263-8223(97)00077-9

Analysis of a glass-fibre sandwich panel for car body constructions

P. Gaudenzi, A. Pascucci, R. Barboni

Università di Roma La Sapienza, Dipartimento Aerospaziale, Roma, Italy

&

A. Horoschenkoff

Daimler-Benz AG, Research and Technology, Munich, Germany

The analysis of a glass-fibre sandwich panel for railway applications is considered. The influence of a special fire-resistant treatment on the mechanical properties of the structure is analysed for static and cycling loadings. The main design and simulation issues are first highlighted. The failure loads of the composite panel are then evaluated from a numerical and an experimental point of view both for the laminated skin of the sandwich and for the entire structure. © 1997 Elsevier Science Ltd.

INTRODUCTION

The possible use of composite materials in secondary and primary structures has recently received more and more attention within the framework of railway applications [1–3]. In particular, some interest has been devoted to the adoption of sandwich panels made using composite laminated skins with an insulating core for the construction of railway carriages.

In fact, several advantages of such a technology compared to more traditional ones can be easily identified:

- weight reduction;
- integrated acoustic insulation;
- integrated thermal insulation;
- reduction in the finishing work required;
- reduction in the number of assembly phases required.

While these advantages may offer cost savings, some drawbacks are expected due to:

- joining difficulties;
- manufacturing process still in its 'infancy' stage;
- difficulties of quality control;
- maintenance aspects (repair and recyclability).

One of the most important requirements of the component is its fire resistance and whether there is an emission of toxic gases in the event of fire.

In this paper, the design and testing of glass-fibre sandwich panels for car body constructions is analysed. The structure is first described in some detail. Then the main design and simulation issues are highlighted and some numerical predictions are presented. In particular, the loss of symmetry of the skin laminate and the non-linearity of its constitutive behaviour due to the treatment of the matrix for fire resistance are investigated.

DESCRIPTION OF THE PANEL

The analysed sandwich is a segment of the wide wall of a carriage. Each face of the sandwich panel is a fibre-reinforced laminate, whose thickness is $t_f = 4$ mm; the thermosetting matrix is vinylester with the addition of aluminium trioxide powder (ATH), used to improve the fire resistance, while the composite reinforcement is

glass fabric. The core is polymeric foam, with a thickness of $t_c = 40$ mm; the skins are adhesively bonded to the core materials (epoxy-based adhesive). One skin essentially consists of two outer plies, which are the fire-resistant part of the skin, and of three plies, which are the carrying part of the skin (it is placed in proximity to the core). The two parts of the skin are distinguished by the amount of ATH in the matrix and by the fibre reinforcement. The thermosetting matrix mixed with ATH has better fire resistance, but lower mechanical properties. Hence, the powder weight is three times greater in the outer plies than in the inner plies.

The stacking sequence of the skin is illustrated in Fig. 1, while the characteristics of the plies are described in Table 1. In Table 1 it can be noted that the fibre content is higher in the inner laminate, in accordance with the defined task. Owing to the presence of fire-resistant layers, the laminate is not symmetric. Furthermore, the lower fibre content and the lower toughness of the matrix, caused by ATH, results in other critical effects, such as the reduction of stiffness and strength of the laminate and the non-linearity of the stress–strain relation.

INFLUENCE OF ATH ON MECHANICAL BEHAVIOUR

The ATH powder is an inorganic substance, Al_2O_3, used to increase the fire resistance of the polymeric material in which it is inserted. The principle is based on an endothermic reaction produced at about 200°C, which generates water molecules and aluminium oxides. In addition, the ATH powder is relatively cheap compared to other modifiers and it does not cause any manufacturing problems, but, however, its use does result in some disadvantages: a substantial reduction in both strength and stiffness. Laminates (made of nine layers with the same fibre direction) constituted with glass fabric, vinylester matrix and several amounts of ATH have been produced: 0 ATH, ATH is not used; 60 ATH, ATH weight = 60% of the matrix weight; and 180 ATH, ATH weight = 180% of the matrix weight

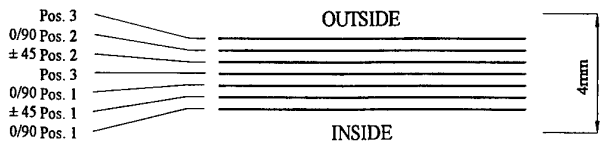

Fig. 1. Stacking sequence scheme of the laminate.

The laminates were subjected to fire-resistance tests, the results of which are illustrated in Table 2.

Tensile and shear tests have been performed; it has been noted that Young's modulus is substantially constant in two intervals. The Young's moduli of both intervals and the knee strain (strain range between them) decrease with increasing ATH content. Engineering constants, ultimate strains and strengths of several laminates, resulting from different ATH powder fractions, are illustrated in Tables 3 and 4.

ANALYTICAL STUDY

Structural characteristics of the laminate (skin)

The structural characteristics of the laminate, which is the sandwich skin, have been computed by means of the classical lamination theory. The experimental data, illustrated in Tables 3 and 4, have been used to assign the properties of plies in the principal directions; the layer properties in the weft direction were reduced by 10% compared to the ones in the warp direction. Hence, checking of normal strain in local references with increasing load has been used to consider the two intervals in which the Young's moduli are constant.

Because the constitutive behaviour of each fabric layer is non-linear, the local in-plane stresses, σ_1, σ_2 and τ_{12}, of every ply have a non-

Table 1. Material characteristics of the laminate

Position	Number	Main characteristic	Kind of fibre	Name	Matrix	Weight fibre content (%)
3	2	Separate layer	—	—	VE-ATH 180	—
2	2	Fire-resistant layer	Glass fabric	800L	VE-ATH 180	60
1	3	Load-carrying layer	Glass fabric	W1480	VE-ATH 60	70

Table 2. Fire test results for laminates with different ATH contents

Time interval (s)	0 ATH	60 ATH	180 ATH
First flame formation	25	170	—
Failure (gas formation)	90	180	500

linear dependence on the external tensile load (Figs 2–4). The diagram is arrested at the first ply failure load of the laminate. The nomenclature of the laminate used in such graphs is such that the plies are numbered from inside to outside (see Fig. 1).

For each of the cases considered (traction, bending, shear and torsion) the shear-stress component is always responsible for the first-ply failure. For tensile and bending load cases the first broken layer is the fire-resistant lamina at ($\pm 45°$), while for the shear and torsion load cases the first ply to fail is the fire-resistant lamina at (0°, 90°). Calculated first-ply failure and ultimate loads of the laminate are illustrated in Table 5. The first-ply failure load is about 50–60% of the ultimate load of the laminate; for the tensile load it appears as normal strain of the middle plane, $\varepsilon_x = 0.79\%$.

In the tensile case, a strong decrease in Young's modulus for a mean stress $\sigma_x = 40$ N/mm^2 and a strain $\varepsilon_x = 0.2\%$ can be observed. However, Young's modulus is reduced constantly with increasing load for the bending case and it negligibly decreases for shear and torsion loads. In Table 6, the reductions in the engineering coefficients of the laminate, loaded up to first-ply failure, are summarized.

Failure modes of the sandwich

The loads, causing fracture of the face in the cases of traction, constant bending and in-plane shear, have been calculated by means of the classical lamination theory. In addition, the core shear failure and wrinkling loads have been determined. The numerical results for a test sandwich panel (110×80 cm) are summarized in Table 7.

The critical compressive loads on the test sandwich panel have been performed by means of the finite-element program ADINA [7] by using the composite shell element; the skin (whose properties were experimentally determined) is considered to be an orthotropic layer while the core is treated as an isotropic medium. The mesh used for the sandwich panel has six elements for each edge, every element having eight nodes and each node has six degrees of freedom, which totals 1728 degrees of freedom. In Table 8 critical loads for several cases of boundary conditions are shown.

The critical shear load for the simply supported plane, calculated using the FE method, has the value $N_{xy} = 6{,}232{,}500$ N.

It can be noted that for each load (N_x, M_x, N_{xy} and M_{xy}) sandwich failure occurs at levels which are lower than the ones due to local or global instability.

Finally, the four-point bending results have been determined analytically: the value of the distance between the inner and outer supports, above which first-ply failure occurred and below which core shear failure occurred, is $L = 93.5$ cm, which corresponds to a load, P, of 4610 N.

EXPERIMENTS

Structural characteristics of the laminate (skin)

First, tensile, three-point bending and shear tests were performed on the laminate being considered; Figs 5 and 6 show the graphs (normal stress vs strain) of tensile and bending experiments, respectively, while Tables 9 and 10 describe the results.

In addition, the ultimate shear stress has also been determined: $\tau_{xy\,(\text{ultimate})} = 99.2$ N/mm^2.

Table 3. Tensile tests results for laminates with different ATH contents

	0 ATH	60 ATH	180 ATH
$\Delta\varepsilon_x$ (phase 1) (%)	0–0.25	0–0.18	0–0.13
$\Delta\varepsilon_x$ (knee) (%)	0.25–0.63	0.18–0.35	0.13–0.25
$\Delta\varepsilon_x$ (phase 2) (%)	0.63–2.05	0.35–1.55	0.25–1.13
E_x (phase 1) (N/mm^2)	27,600	26,500	25,000
E_x (phase 2) (N/mm^2)	21,100	18,100	13,900
$\varepsilon_{x\,(\text{ultimate})}$ (%)	2.32	2.33	2.49
$\sigma_{x\,(\text{ultimate})}$ (N/mm^2)	498.5	419.1	315.9

In Fig. 7, experimental forms of Young's modulus with increasing load for the tensile and the bending cases are illustrated.

The form of Young's modulus for the tensile case presents a strong discontinuity compared to the bending case, for which the Young's modulus decreases fairly constantly.

Table 4. Shear tests results for laminates with different ATH contents

	0 ATH	60 ATH	180 ATH
G_{xy} (N/mm^2)	4800	4590	3620
$\tau_{xy\,(ultimate)}$ (N/mm^2)	60.0	52.0	37.5

For both the tensile and the bending cases, specimens were subjected to increasing loads up to a level causing first-ply failure, with the objective of identifying the reason for the non-linear behaviour of the composite; Figs 8–11 show both surfaces of the laminate for traction and bending, respectively. The formation of microcracks in the matrix, which are arranged in a transverse direction to the load, could be observed on the surfaces of the laminates. This

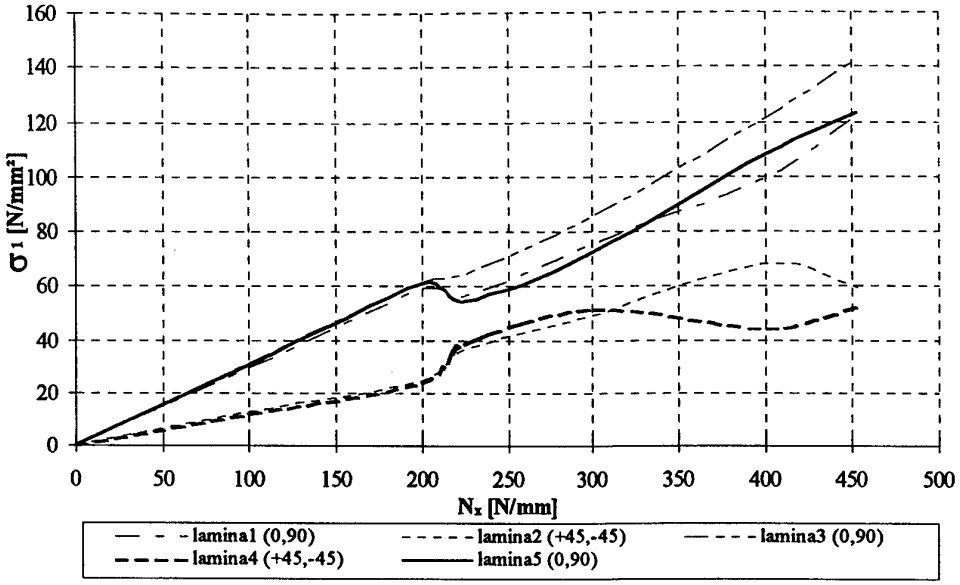

Fig. 2. Normal stress (in the warp direction) of each layer vs tensile load.

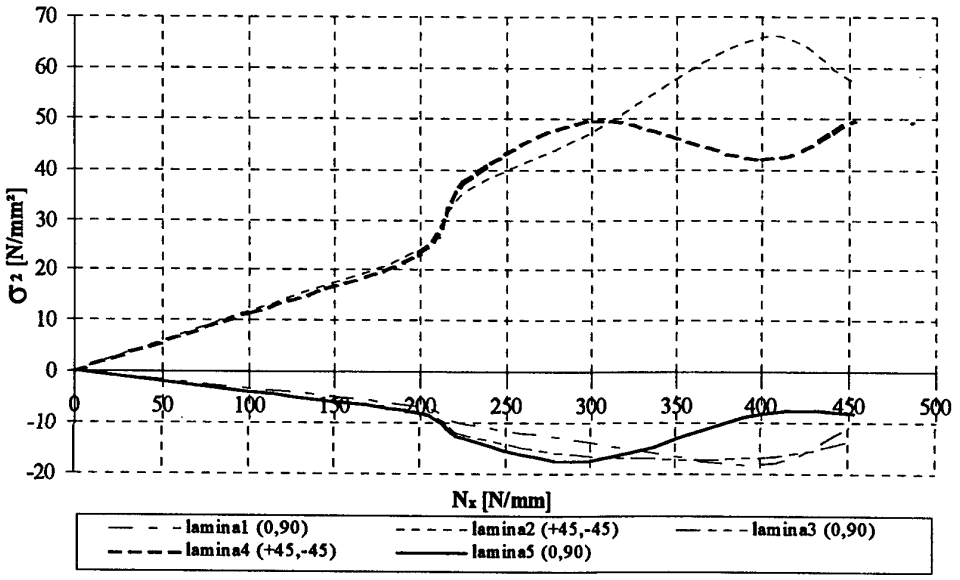

Fig. 3. Normal stress (in the weft direction) of each layer vs tensile load.

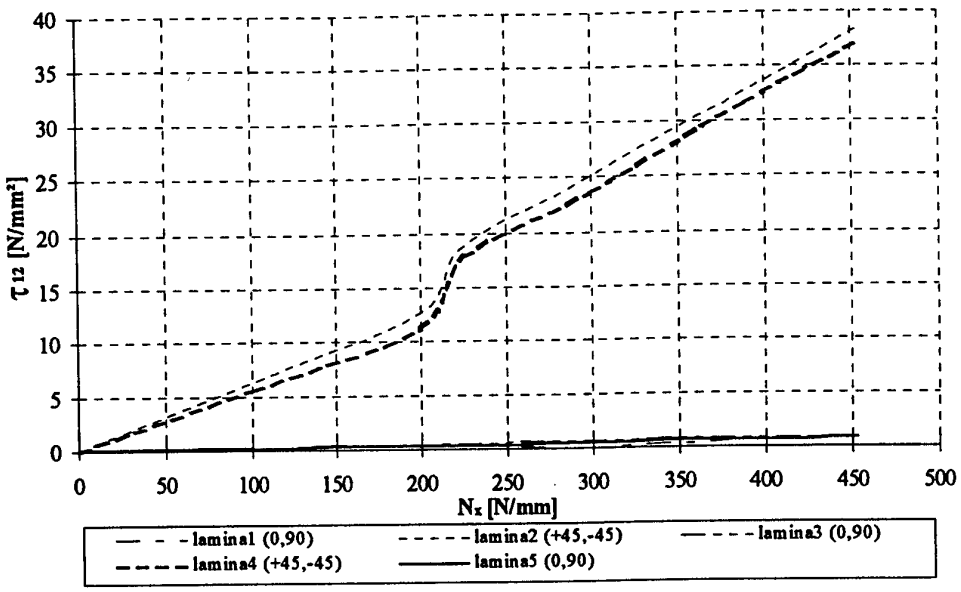

Fig. 4. In-plane shear stress of each layer vs tensile load.

Table 5. Ultimate and first-ply failure loads on the laminate

	First-ply failure load	Ultimate load
Traction N_x (N/mm)	453	805
Bending M_x (N)	619	—
In-plain shear N_{xy} (N/mm)	187	327
Torsion M_{xy} (N)	140	—

structural damage clearly reduces the mechanical properties. In the tensile case, the fire-resistant layer shows a higher density of cracks compared to the load-carrying ply; this means that the ATH makes the matrix brittle. In addition, on the surface of the load-carrying ply, it is possible to see the first phase of the formation of damage; the formation of cracks is focused in the intersection zone of the warp and

Table 6. Reduction in engineering coefficients between initial conditions and loads causing first-ply failure

	ΔE_x (%)	ΔE_y (%)	ΔG_{xy} (%)	Δv_{xy} (%)
N_x (0–453 N/mm)	32.0	18.2	23.7	9.7
M_x (0–619 N)	30.0	21.0	14.0	2.7
N_{xy} (0–187 N/mm)	5.5	6.2	23.0	27.9
M_{xy} (0–140 N)	2.9	3.2	14.0	14.7

Table 7. Failure loads on the test sandwich panel

	Face fracture	First-ply failure	Shear core failure	Wrinkling
Traction N_x (N)	1,492,100	749,000	—	1,719,900
Bending M_x (Nm)	30,100	15,800	—	42,200
Transversal shear N_{xx} (N)			35,900	—
In-plane shear N_{xy} (N)	503,800	137,800	—	—

Table 8. Critical compressive load on the test sandwich panel with several boundary conditions (N)

	The others free	The others simply supported	The others clamped
Loaded edges clamped	1,292,900	1,963,600	2,883,700
Loaded edges simply supported	352,460	1,518,500	2,389,400
Loaded edges clamped and simply supported	696,100	1,518,500	2,440,700
Load edges clamped and free	911,000	—	—

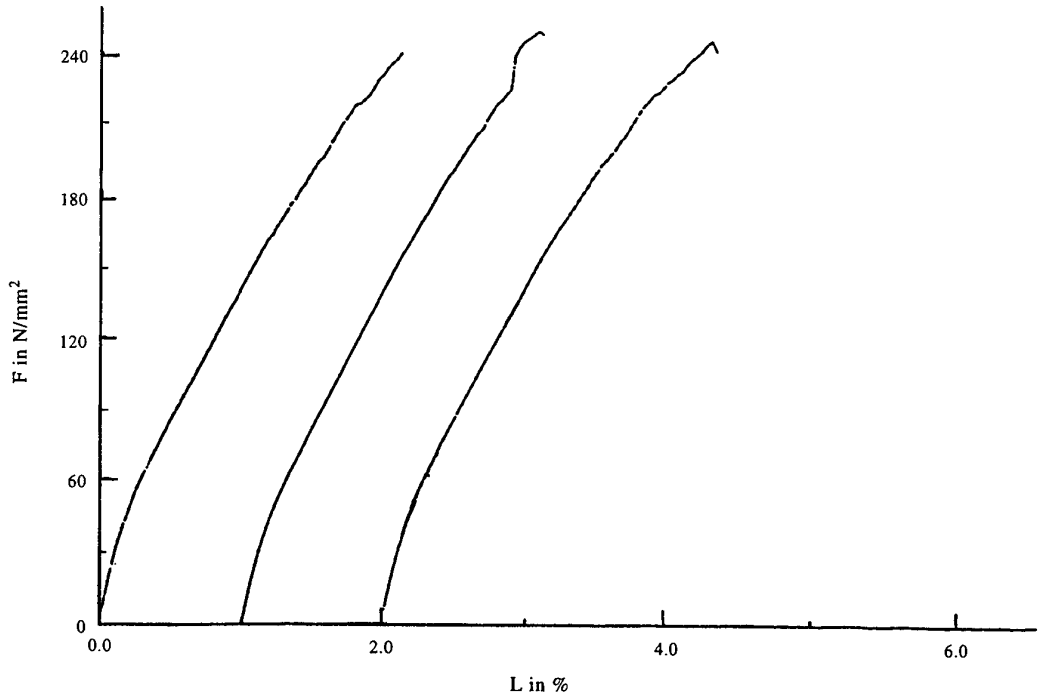

Fig. 5. Tensile test on the laminate, normal stress vs normal strain.

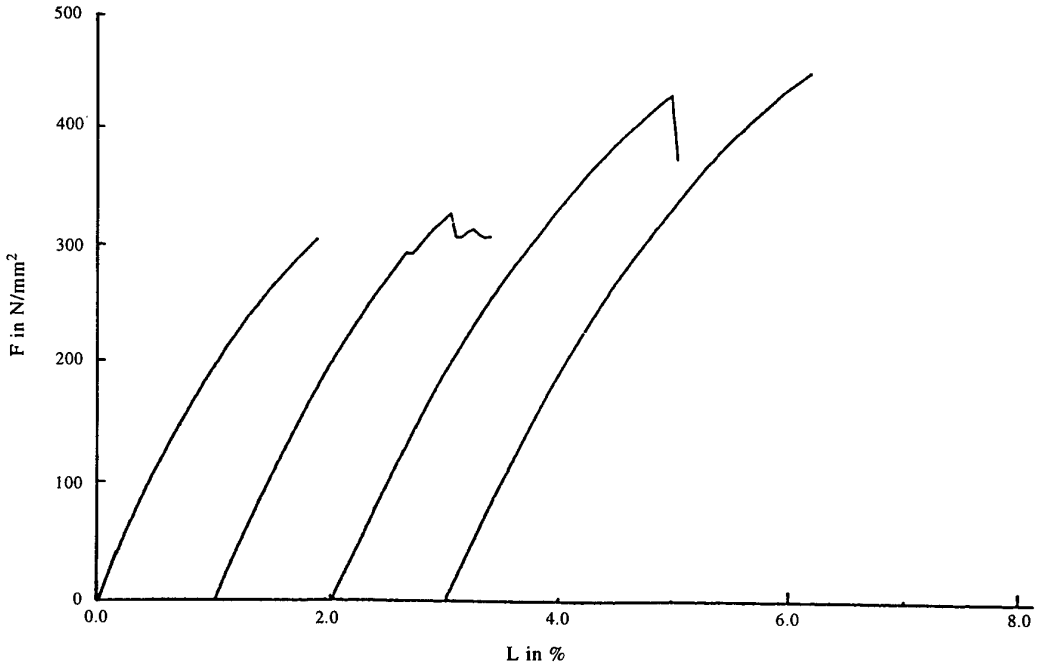

Fig. 6. Three-point bending test on the laminate, normal stress of the edge vs corresponding normal strain.

Table 9. Tensile test on the laminate, main strains, stresses and Young's moduli

	(%)		N/mm²		N/mm²
$\varepsilon_{x\,(\text{ultimate})}$	2.29	$\sigma_{x\,(\text{ultimate})}$	244.4	$E_{x\,(\text{DIN})}$ (10–50%)	13,728
$\Delta\varepsilon_x$ (phase 1)	0–0.18	$\Delta\sigma_x$ (phase 1)	0–40	E_x (phase 1)	21,200
$\Delta\varepsilon_x$ (knee)	0.18–0.34	$\Delta\sigma_x$ (knee)	40–60	E_x (phase 2)	11,033
$\Delta\varepsilon_x$ (phase 2)	0.34–1.30	$\Delta\sigma_x$ (phase 2)	60–162		

Table 10. Three-point bending test on the laminate, ultimate strain, stress of the edge and secant Young's modulus

	(%)		N/mm^2		N/mm^2
$\varepsilon_{x\,(\text{ultimate})}$	2.53	$\sigma_{x\,(\text{ultimate})}$	384.0	$E_{x\,(\text{DIN})}$ (10–50%)	19,108

weft fibres, particularly among the weft fibres in the proximity of the external surface.

Then, the first-ply failure was studied in detail for the tensile and bending cases; in fact, specimens subject to first-ply failure load were analysed with a C-scan, in addition to taking micrographs of their cross-sections (see Figs 12 and 13).

The micrographs show cracks in the fire-resistant ply, with the principal direction orientated ($\pm 45°$) with respect to the global reference, which complies with analytical results.

In addition, specimens were subjected to a cycling tensile load with decreasing maximum normal strain, in steps of $\Delta\varepsilon_x = 0.02\%$, starting

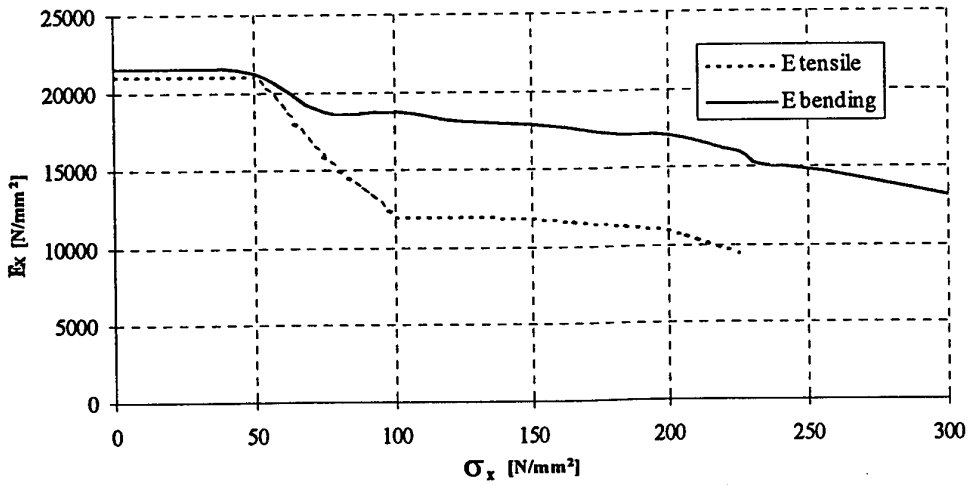

Fig. 7. Secant Young's moduli for the tensile and bending cases vs the mean stress through the cross-section and the normal stress at the edge, respectively.

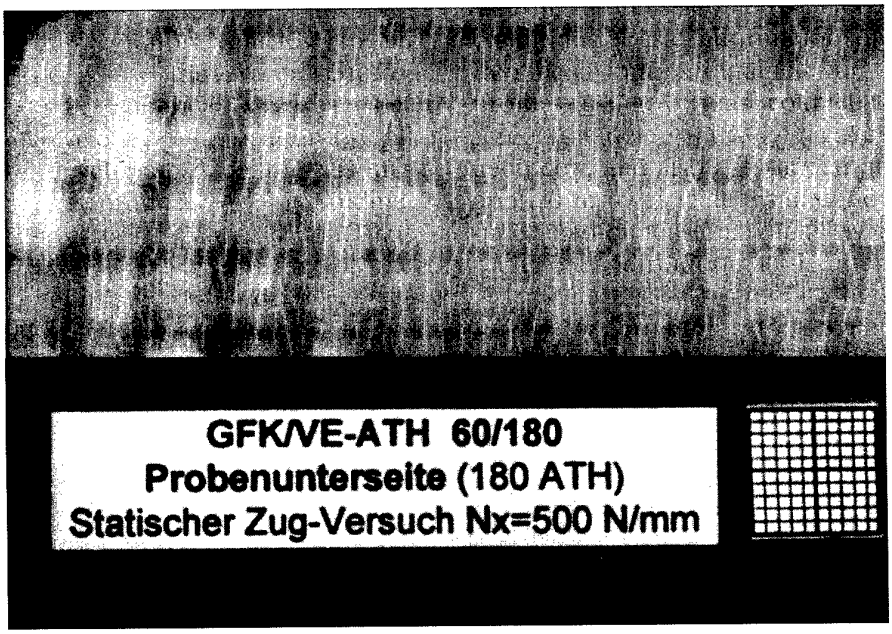

Fig. 8. Tensile test, the surface of the fire-resistant layer, of which the calculated strain is $\varepsilon_x = 0.895\%$.

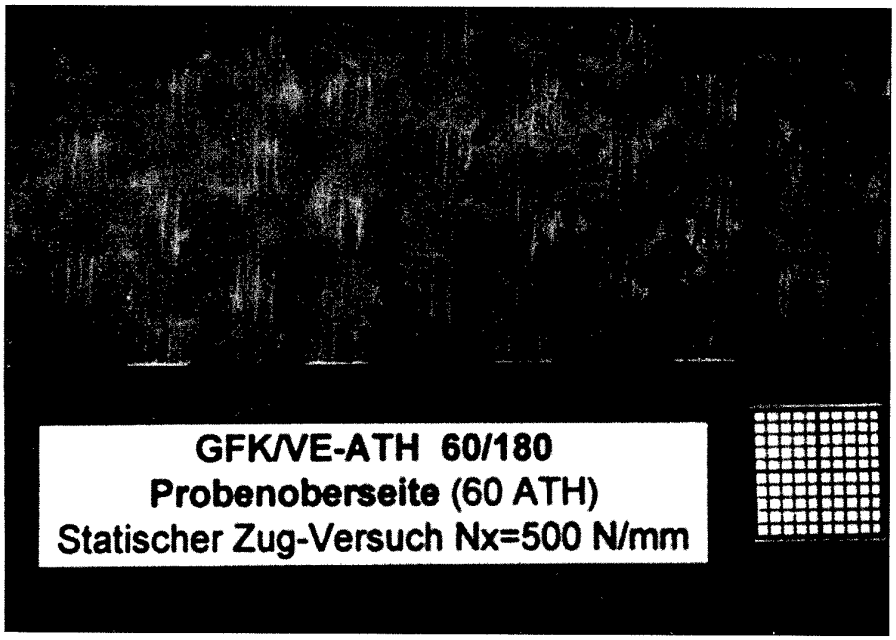

Fig. 9. Tensile test, the surface of the load-carrying layer, of which the calculated strain is $\varepsilon_x = 0.681\%$.

at $\varepsilon_x = 0.18\%$ (extreme strain limit of the first phase where the stiffness behaviour is linear). Thus, as shown in Fig. 14, the elastic limit of the laminate has been defined as a deformation ε_x of 0.09%/0.1%; such a specimen does not exhibit any damage on the surface.

As the fatigue limit has been determined for a ε_x of 0.4%, the increase in damage of the laminate, subjected to few load cycles, has been qualitatively studied. In Fig. 15, three graphs (stress vs strain) relating to tensile tests for one, five and 10 cycles are illustrated; it can be noticed that the highest deformation occurs for $\varepsilon_x = 0.35\%$, which is within the strain range of damage tolerance. The laminate absorbs most of the energy in the first cycle compared to the following ones; however, the formation of microcracks is still not saturated even after 10

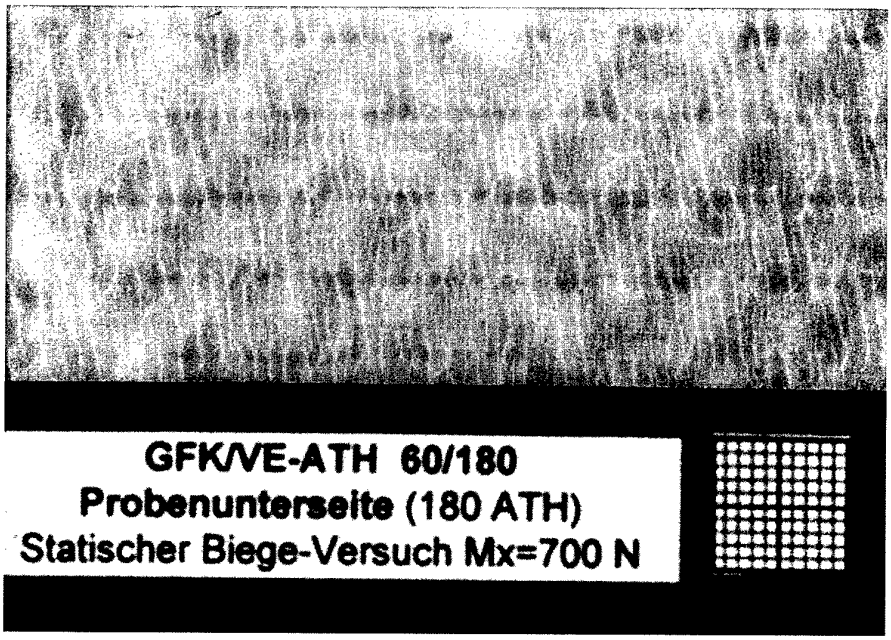

Fig. 10. FPB test, the surface of the fire-resistant layer, of which the calculated strain is $\varepsilon_x = 1.418\%$.

Fig. 11. FPB test, the surface of the load-carrying layer, of which the calculated strain is $\varepsilon_x = 1.128\%$.

cycles. In addition, the stress–strain relation becomes linear with increasing number of cycles; the stiff contribution of the matrix quickly vanishes and after 10 cycles the Young's modulus, E_x, is 17,400 N/mm^2.

Reduction of residual deformation of the laminate

Because the laminate is not symmetric, residual strains are present. Several square laminated plates (with a 30 cm side) have been manufactured and the curvatures have been measured; the mean values of which are: $k_x = 0.215\ \text{m}^{-1}$, $k_y = 0.197\ \text{m}^{-1}$ and $k_{xy} = 0.278\ \text{m}^{-1}$.

Fire-resistant layers could be added in the proximity of the outer side of the load-carrying plies to obtain symmetry, but other disadvantages occur: a large increase in weight and the formation of cracks for weak loads on the surface adjacent to the adhesive ply.

Hence a concept has been elaborated to introduce an interlayer (thin ply with casually orientated glass-fibres) which is able to reduce the coupling between in-plane and out-of-plane action. First, the stiffness properties of the

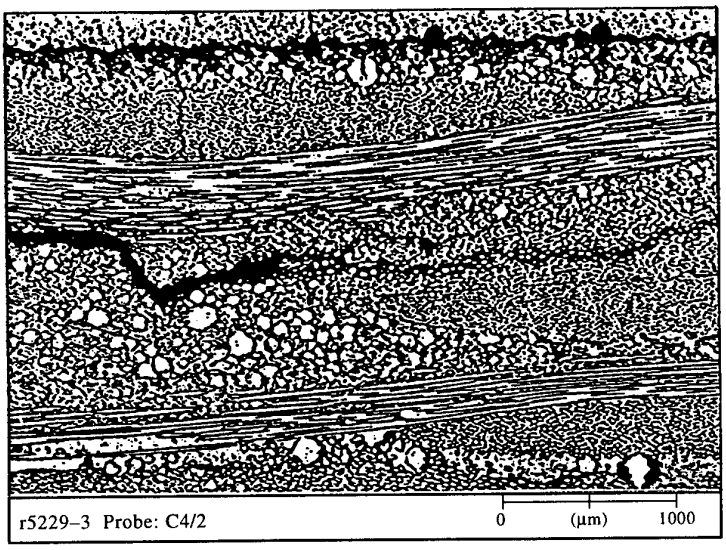

Fig. 12. Tensile test, micrograph of the cross-section of the laminate.

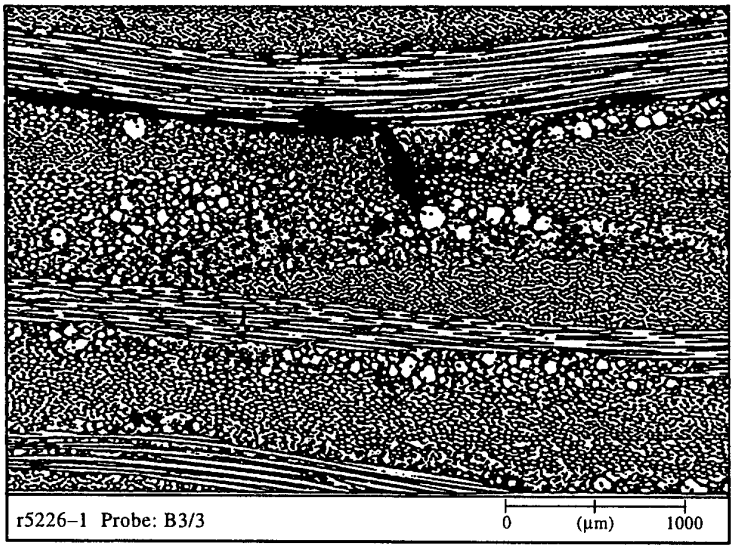

Fig. 13. TPB test, micrograph of the cross-section of the laminate.

interlayer were determined experimentally. Thus, the coefficients of the coupling matrix as a function of position and thickness of the interlayer have been analysed.

A substantial reduction of coupling coefficients has been obtained for the laminate with an interlayer (whose thickness is $t = 0.85$ mm) placed between the load-carrying layers (between the outer one with a (0°, 90°) orientation and the one with a ($\pm 45°$) orientation). Finally, the laminate was built with the new stacking sequence; a large reduction of curvatures has been measured: $\Delta k_x = 41.7\%$, $\Delta k_y = 57.3\%$ and $\Delta k_{xy} = 93.7\%$.

However, no interlayer was used for further investigations as a reduction of curvature is

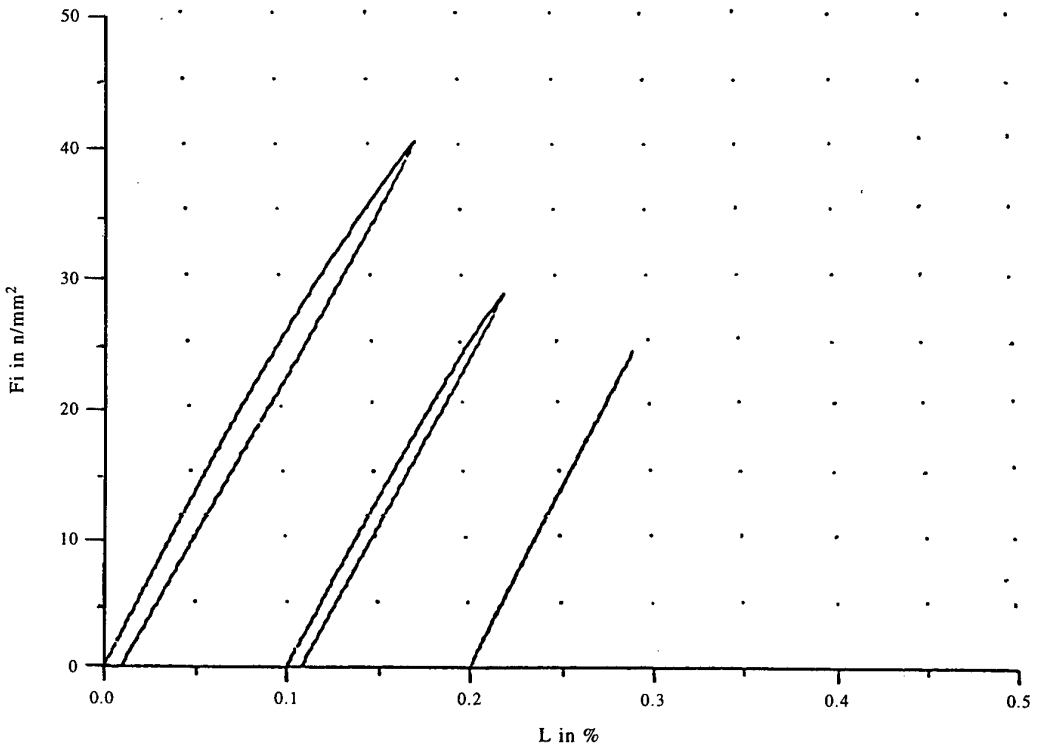

Fig. 14. Normal stress vs strain of laminates subjected to a cycling tensile load.

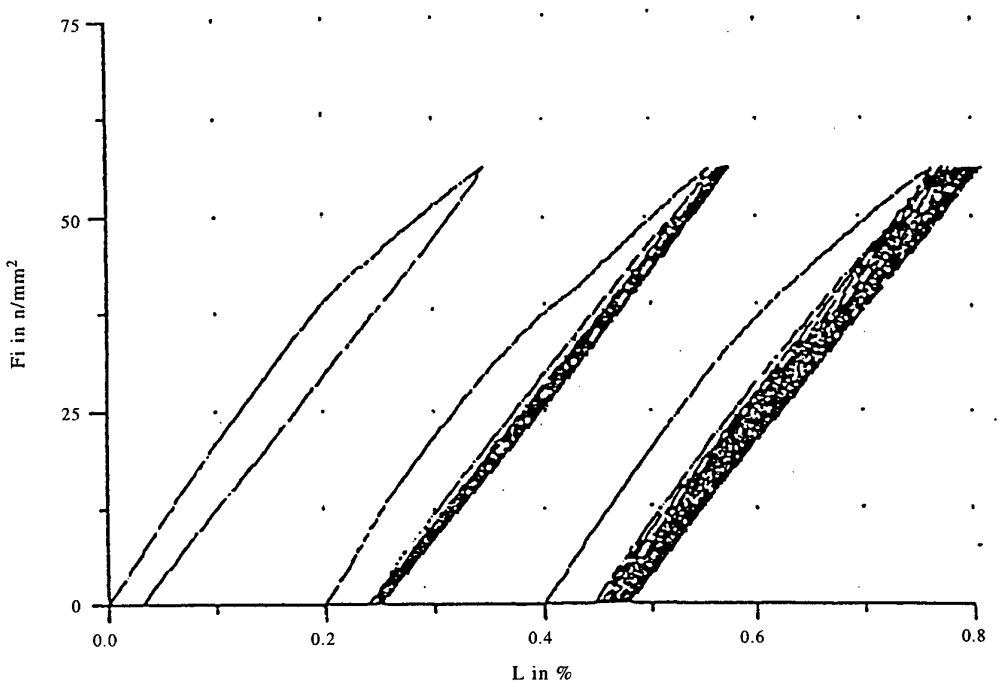

Fig. 15. Normal stress vs strain diagrams of laminates subjected to a cycling tensile load with one, five and 10 cycles, respectively.

obtained by means of an excessive increase of the skin thickness and of the corresponding weight.

Four-point bending test

Sandwich beams have been designed and realized; the main manufacturing steps are summarized below.

1. Construction of two laminates (with dimensions of 850×400 mm). The Bag Molding technique was used; hence, after preparing the tool plate, glass fabrics (six pieces with a (0°, 90°) orientation and four with a ($\pm 45°$) orientation of fibres), peel plies, bleeder ply and vacuum bag were cut and the matrixes were prepared, according to the weight contents of Table 11. Hence, the lay-up according to the stacking sequence in Fig. 1 was implemented; subsequently, the vacuum bag assembly process was realized by heating up to $T = 100°C$, staying constant at $T = 100°C$ for 1 h and letting cool down up to 40°C (approximately 0.5 h). The pressure is kept at 7 bar during the entire process.
2. Using an electric saw, the edges of the laminates (which constitute impurity) were removed and the core panel cut.
3. Adhesion between faces and core. The laminates were warmed at a low temperature $T \cong 50$–$60°C$, then the adhesive paste was smeared on the side of the load-carrying layer of the laminate. Subsequently, the faces and core were fixed together with no adhesive tapes; in addition, the sandwich panel was vacuum-bagged, as shown in Fig. 16, and the adhesive resin was polymerized by means of the following curing process: $T = 60°C$; $p = 1$ bar; $\Delta t = 2$ h.
4. Using an electric saw, four sandwich beams were cut, having the dimensions: $L = 800$ mm (length of beam); $b = 80$ mm (width); $h = 48$ mm (thickness); $t_f = 4$ mm (thickness of face); $t_c \cong 40$ mm (thickness of core); $t_a \cong 0.5$ mm (thickness of adhesive layer).

Table 11. Weight content of the layers

Position	Fibre (g)	Matrix (g)	TBPB hardening (g)	TBEH hardening (g)	ATH (g)
1	810	347	3.5	6.9	208.3
2	540	360	3.6	7.2	648.0

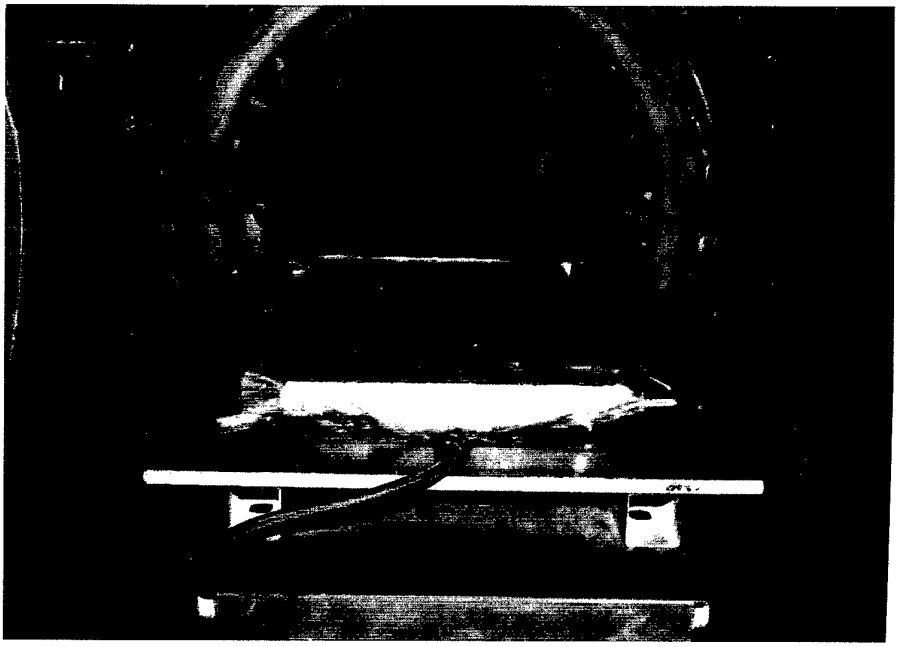

Fig. 16. Vacuum bag process during the bonding phase.

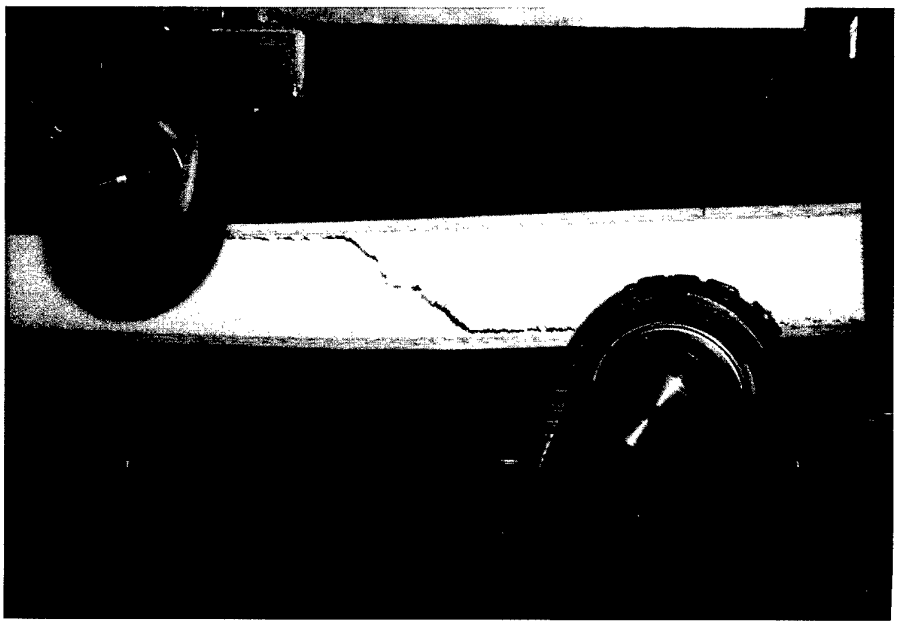

Fig. 17. Failure of the sandwich beam.

5. Finally, two strain rosettes were placed on the skins in the middle cross-section to measure the deformation ε_x.

The equipment for the four-point bending test was regulated so that the distance between the outer supports was $L_{out} = 700$ mm and the distance between the inner supports was $L_{in} = 300$ mm. Three beams were tested; as expected, failure occurred in the core. The separation surface is oblique and it was placed between the inner and outer supports; Fig. 17 shows the beam crack at the instant of failure; it clearly shows how the faces slide over each other (shear deformation). The experimental graphs, load vs normal strain of the skin in the middle cross-section, give information on the flexural rigidity, whose value is $D = 40{,}000$ N/

mm^2; the failure load is $P = 4570$ N and the failure normal strain at the edge of the middle section is $\varepsilon_x = 0.03\%$. The maximum normal strain of the skins is lower than the elastic limit of the laminate; in fact, the specimens tested do not show damage of the skins, and the flexural rigidity remains constant.

ACKNOWLEDGEMENTS

The authors wish to express their appreciation to Mr Wenzl for his contribution to the fire-resistance tests on the laminate. In addition, special thanks are given to all the laboratory staff at the Daimler-Benz AG, Research and Technology, Department F2K-F, in Ottobrunn (Munich, Germany), where the present work was developed during a stay of A. Pascucci. As to the part of the work developed in Rome and concerning the numerical calculations and, partly, the interpretation of the experimental results, the support of CNR contract No. 96.02342.CT07 (Dr P. Gaudenzi supervising) is gratefully acknowledged.

REFERENCES

1. Batchelor, J., Use of fibre reinforced composites in modern railway vehicles. *Mater. Engng*, 1981, **2**, 172–182.
2. Ruhmann, D.C., The design, fabrication and testing of the Glasshopper prototype covered hopper rail cars. *Composite Struct.*, 1994, **6**, 207–213.
3. Takao, K., Yoshimura, M., Tagawa, N., Matsudaira, Y. & Nagano, K., Development of the superconducting Maglev vehicles for the Yamanashi test line. In *4th Japan International SAMPE*, Japan, 1995.
4. Jones, R. M., *Mechanics of Composite Materials*. McGraw-Hill, New York, 1975.
5. Vinson, J. R. & Sierakowski, R. L., *The Behaviour of Composed Structures of Composite Materials*. Kluwer Academic, 1990.
6. Zenkert, D., An introduction to sandwich construction. KTH Department of Lightweight Structures, Sweden, 1993.
7. ADINA Theory and Modelling Guide. Report ARD 87-8. ADINA R & D Inc., 1987.

ELSEVIER

Composite Structures Vol. 38, No. 1–4, pp. 435–445, 1997
© 1997 Elsevier Science Ltd. All rights reserved
Printed in Great Britain
0263-8223/97/$17.00 + 0.00

PII:S0263-8223(97)00078-0

Effects of temperature on the creep behaviour of woven and stitched composites

R. G. Bathgate,[a] C. H. Wang[b] & Feiyi Pang[a]

[a]*School of Engineering and Technology, Deakin University, Geelong, Vic. 3217, Australia*
[b]*Aeronautical and Maritime Research Laboratory, DSTO, 506 Lorimer Street, Fishermens Bend, Vic. 3207, Australia*

This paper presents an investigation of the tensile creep behaviour of woven fibre composite stitched, through the thickness, with cotton or carbon threads along the loading direction. Creep tests were conducted at various temperatures. It was found that the through-thickness stitching significantly improved the creep deformation and creep rupture resistance of these composites. The creep data were analysed using the 'time–temperature–stress superposition principle' theory (TTSSP). The long-term behaviour of the material could then be predicted by means of a master curve. Finite-element analyses of the composites was also carried out and the stitching was found to considerably reduce the interlaminar stresses. © 1997 Elsevier Science Ltd.

INTRODUCTION

Polymers generally exhibit a viscoelastic response when subjected to load at ambient or elevated temperatures. This time-dependent response becomes significant as the temperature approaches the glass transition temperature, T_g. Therefore, in many structural applications, an understanding of the effect of temperature on mechanical properties is essential.

A study of the viscoelastic behaviour of a thermosetting, glass-filled polyester was reported by Janas & McCullough [1]. An early study [2] on methylmethacrylate, below its glass transition temperature, showed that the amount and rate of creep were significantly influenced by the thermal history. One method that has been widely adopted to predict long-time creep behaviour, using accelerated tests, is the 'time–temperature–stress superposition' principle (TTSSP) [3–6]. The TTSSP is essentially based on the fact that creep deformation curves for different thermomechanical conditions are of the same shape. In addition, increases in temperature and/or stress will shift creep deformation curves to the left on a log-time scale, indicating that these parameters accelerate creep deformation in much the same manner. Therefore, by collecting short-time creep deformation data at elevated temperatures (or stresses), long-time creep behaviour at lower temperatures (or stresses) can be predicted.

The aim of the present investigation was to study the influence of temperature on the viscoelastic creep response of stitched and unstitched composites. Previous studies [7,8] have found that the creep of woven composites, at room temperature, can be significantly reduced by the introduction of a stitching process during manufacture. In particular, composites stitched with thick carbon threads were the most resistant to creep compared with other stitching yarns. Based on the superposition principle of the theory of viscoelasticity (TTSSP), the long-term viscoelastic behaviour was predicted from short-term behaviour using an accelerated characterization procedure. To investigate the changes in the stress distribution as a result of stitching, finite-element analysis was also performed for both unstitched and stitched structures.

MATERIALS AND EXPERIMENTS

The composite was manufactured by stitching woven cloth lay-ups followed by a standard resin injection technique. Five layers of bi-directional carbon fibre cloth were placed between two layers of bi-directional E-glass cloth. The matrix employed was a unfilled epoxy-resin known as EPOCAST 50-A/946, which was made by mixing thoroughly 100 parts by weight of Epocast 50-A with 15 parts by weight of hardener 946. The resulting mixture had a low viscosity. The carbon preform was a (0°/90°) plain weave cloth with a thickness of 0.35 mm/ply and a weight of 0.46 kg/m^2. Fifty per cent of the fibres were in the warp direction and 50% in the weft direction. The final fibre–matrix ratio of the cured composite was 3:2 (i.e. 60% fibre and 40% matrix by weight).

The stitching operation was performed on the fabric before resin injection. A modified lock stitch was used as shown in Fig. 1(a). As the thread experienced significant bending during stitching, a relatively high flexibility was desired. To assess whether a low stiffness thread would achieve the same effect in terms of suppressing creep strain, both cotton and carbon threads were used in the present work. Table 1 summarizes the dimensions and mechanical properties of the cotton and carbon threads.

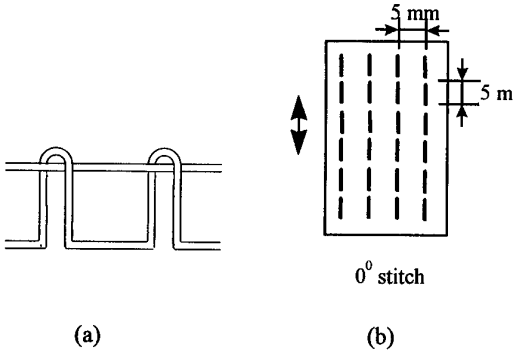

Fig. 1. (a) Lock stitch pattern and (b) loading direction.

Table 1. Characterization of stitch yarn

	Cotton yarn (Tex = 300)	Carbon yarn (Tex = 200)	Thick carbon (Tex = 800)
Tensile strength (MPa)	350	3400	3400
Modulus (GPa)	2.857	238	238

The stitching process was repeated along the loading direction as shown in Fig. 1.

After the stitching process was completed, a standard resin injection procedure was applied to obtain the stitched composites. The specimens were finally cured as recommended: 3 days at room temperature followed by a post-curing process of 2 h at 80°C. The resulting composites had a volume fraction of approximately 0.5, half of which was aligned parallel to the axis of the specimens and the rest perpendicular to that axis.

Specimens were cut using a water-cooled diamond saw. The size of each specimen was 200 mm long, 15 mm wide and 1.5 mm thick, and the edges were smoothed using fine emery paper. The specimens were cut in such a way that two stitching lines were symmetrical to the centre-line of the specimen. At each end, 50 mm of the specimen was held in the grips, leaving a test area of 100 mm long and 15 mm wide. Tensile creep tests were conducted at temperatures of 35, 55 and 70°C, and rupture testing was conducted at 80°C using a workshop constructed lever arm tester. At each temperature 30, 50 and 70 MPa stress levels were applied to specimens which were: unstitched, cotton stitched (pitch = 5 mm), carbon stitched (pitch = 5 mm) and thick carbon stitched (pitch = 10 mm).

The temperature variation was kept constant with ± 1.5°C during the tests. The oven consisted of aluminium plates, fixed on both sides of the specimen, which incorporated power resistors to provide the heat. The temperature was monitored by a thermocouple and digital voltmeter system, and was automatically controlled during testing. A uniform temperature distribution was achieved throughout the gauge section at the test temperature for 30 min prior to loading. A dial gauge was employed to measure the specimen extension. At least two specimens were tested at each condition.

RESULTS AND DISCUSSION OF CREEP STRAIN RATE TESTING

The experimental creep curves for unstitched specimens at 35, 55 and 70°C are shown in Fig. 2(a)–(c), where the creep strains, corresponding to different constant stresses, were plotted against time. Here the strains were the total longitudinal strains, ε. It is clear that the

creep strain increased with increases in temperature and stress.

The effects of various stresses and temperatures on the creep behaviour of cotton stitched composites can be seen in Fig. 3(a)–(c). Considerable reduction in creep strain was observed in the cotton stitched specimens when compared with similar unstitched lay-ups.

The creep responses of carbon thread stitched composites are shown in Fig. 4(a)–(c). Even more reduction in the creep strain at a given stress level was observed compared with the cotton stitched composites.

To examine further the influence of thread tensile stiffness on creep, experiments were carried out for specimens stitched with a thicker carbon thread. The results are shown in Fig. 5(a)–(c). It is seen that some further reduction in creep occurred when compared with the thin carbon thread results. At a given stress level, it is observed that the creep rate increased with increasing temperature.

A comparison is made, in Fig. 6, of the effects of stitch threads at various temperatures. Clearly, for the same pitch density, thick carbon thread is shown to be most effective. Nevertheless, cotton thread was reasonably effective.

In this study the time–temperature–stress superposition principle (TTSSP) was employed to provide a method by which long-term behaviour could be predicted from short-term tests. To perform TTSSP, creep data at various

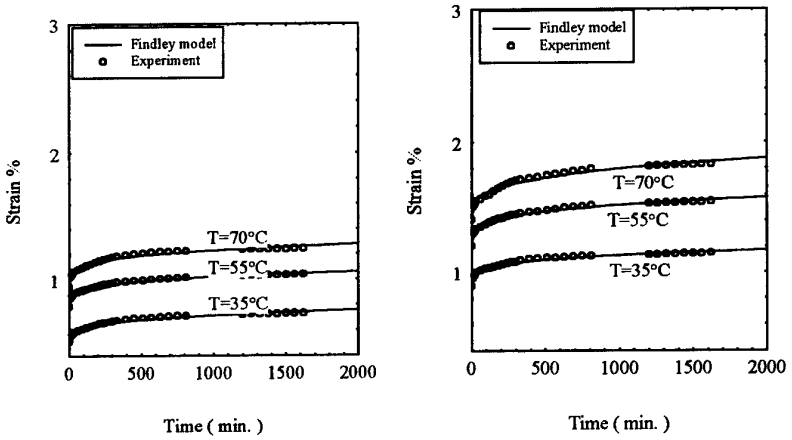

(a) σ=30MPa

(b) σ=50MPa

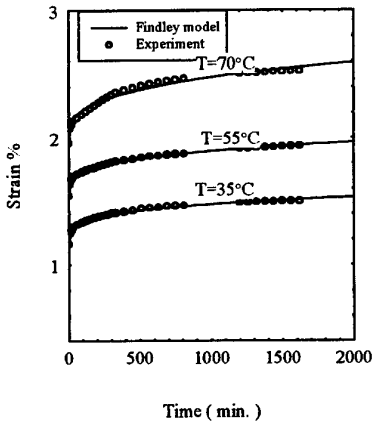

(c) σ=70MPa

Fig. 2. Effects of temperature on unstitched composite creep behaviour. (a) $\sigma = 30$ MPa, (b) $\sigma = 50$ MPa and (c) $\sigma = 70$ MPa.

conditions of stress and temperature were first plotted on a log-time scale. These curves were then shifted vertically and horizontally to form a smooth continuous curve, called the master curve, which represented the long-time viscoelastic response at a given reference condition. In the following, an equation is introduced which allows the analytical determination of the amount of shift necessary to construct a master curve.

For a given specific thermomechanical condition, the Findley equation [3] can be written as

$$\varepsilon(\sigma, T, t) = \varepsilon_0(\sigma, T) + B(\sigma, T)t^n \quad (1)$$

where T is the temperature and σ is the stress, and n, B and ε_0 are functions of the stitching thread, temperature and applied stress. Based on the concept of the TTSSP previously described, eqn (1) can be expressed in terms of the creep response at a given reference condition (σ_0 and T_0)

$$\varepsilon(\sigma, T, t) = a_v[\varepsilon_0(\sigma_0, T_0) + B(\sigma_0, T_0)\,(t/a_h)^n] \quad (2)$$

where

$$a_v = \varepsilon_0(\sigma, T)/\varepsilon_0(\sigma_0, T_0) \quad (3)$$

$$a_h = \{\,[\varepsilon_0(\sigma_0, T_0)B(\sigma, T)]/[\varepsilon_0(\sigma, T)B(\sigma_0, T_0)]\,\}^{-1/n} \quad (4)$$

From eqn (2), the creep strain data at a given thermomechanical condition can be shifted to

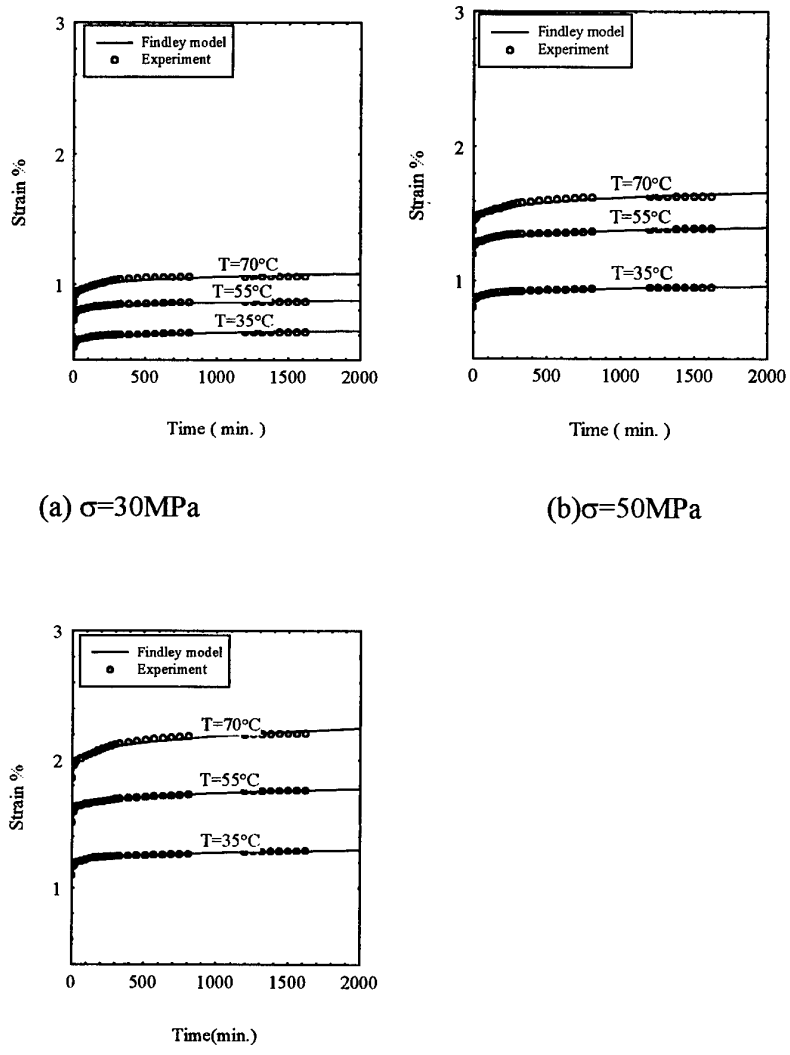

Fig. 3. Effects of temperature on cotton stitched composite creep behaviour. (a) $\sigma = 30$ MPa, (b) $\sigma = 50$ MPa and (c) $\sigma = 70$ MPa.

represent the creep strain at a reference condition. The appropriate shifts of the creep strain curve plotted on a log-time scale are vertical, $\log a_v$, and horizontal, $\log a_h$.

It should be pointed out that in eqn (2) the time exponent, n, is assumed to be independent of both stress and temperature. To perform the TTSSP, creep strain data at different environmental conditions were fitted with the time exponent obtained for the reference condition (σ_0, T_0). To obtain a master curve, using the prescribed analytical characterization procedure, the Findley equation parameters ε_0 and B in eqn (1) for the reference time exponent, n, must be used. The reference conditions chosen for this study were $T = 35°C$ and $\sigma = 30$ MPa. The vertical and horizontal shift factors were calculated using eqns (3) and (4). Construction of the master curves for unstitched, cotton thread stitched, carbon fibre stitched and thick carbon fibre stitched are shown in Fig. 7(a)–(d).

CREEP RUPTURE TESTING

The experimental results obtained for stage I and II creep represent the behaviour that may occur under service conditions with low and

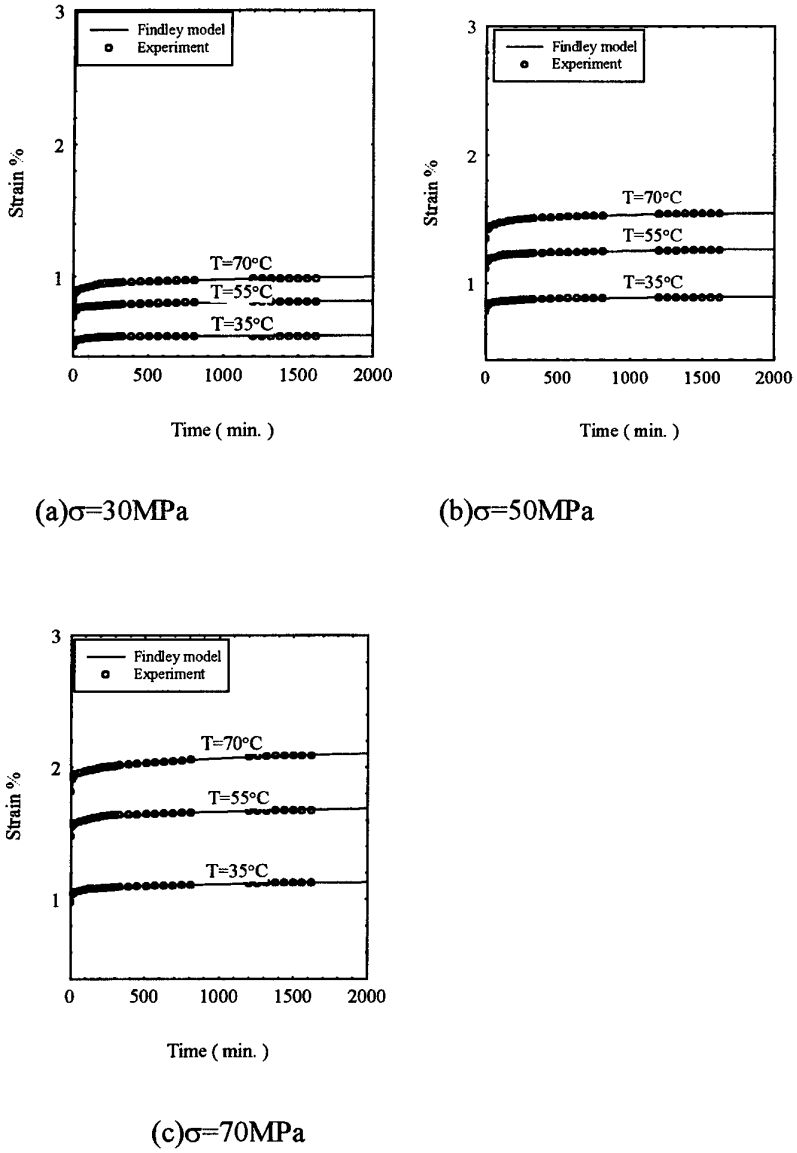

Fig. 4. Effects of temperature on carbon stitched composite creep behaviour. (a) $\sigma = 30$ MPa, (b) $\sigma = 50$ MPa and (c) $\sigma = 70$ MPa.

medium applied stresses. As the applied stress increases, failure in the form of creep rupture may result. If composite materials are to be used reliably for extended periods, it is important to know not only how much the material deforms but also if and when the material will fail. To this end, experiments were carried out by increasing the applied stress level to between 85 and 95% of the tensile strength and increasing the temperature to 80°C. Figure 8 shows these creep to rupture curves.

The creep curves exhibited various stages. Directly upon loading, the unstitched specimens experienced instantaneous stretch, which was followed by the primary stage creep, as shown in Fig. 8(a). The creep rate declined gradually in this region and eventually reached a constant value in the secondary stage. The third or final stage took place in a relatively short period covering only several minutes in the experiments performed. At the same applied stress and temperature ($T = 80°C$, $\sigma_i/\sigma_b = 0.8$) the curve for the cotton stitched composite, shown in Fig. 8(b), exhibited a slower creep rate and longer time to fracture compared with the unstitched specimens. Figure 8(c) shows the carbon stitched composite creep to rupture curves. Compared with the unstitched and cotton stitched composites, under the same stress level, the carbon stitched specimens generally took longer to fail. A further increase in the rupture life was observed for thick carbon

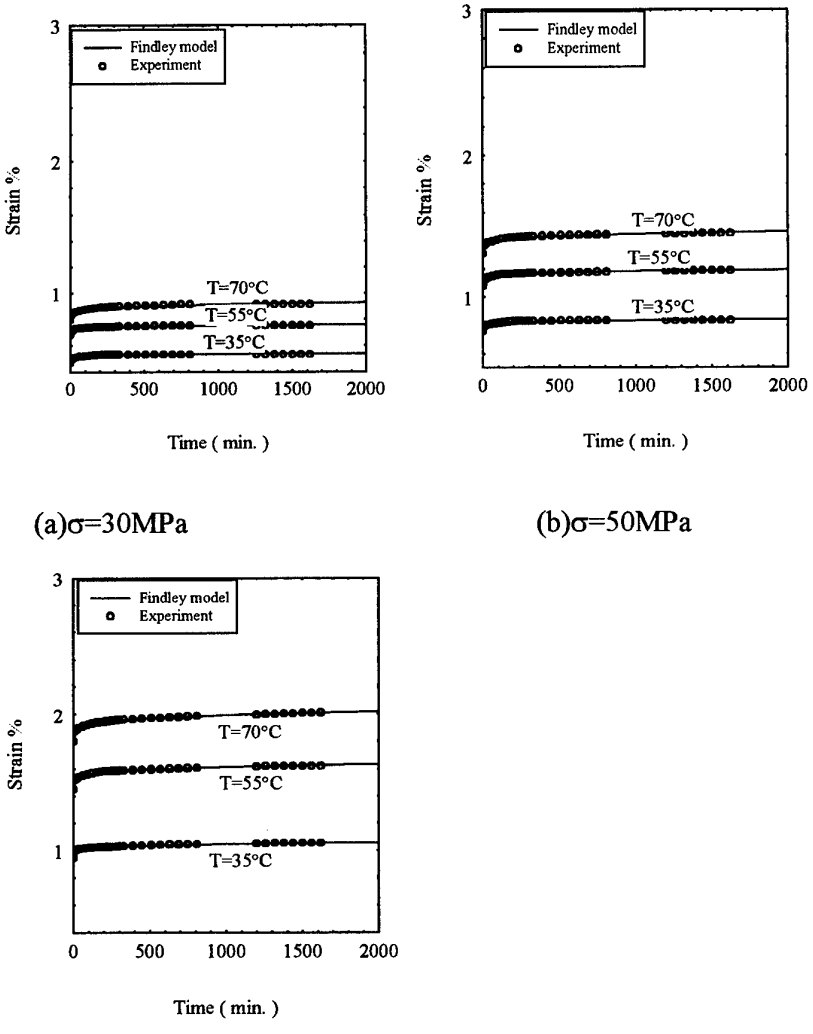

Fig. 5. Effects of temperature on thick carbon stitched composite creep behaviour. (a) $\sigma = 30$ MPa, (b) $\sigma = 50$ MPa and (c) $\sigma = 70$ MPa.

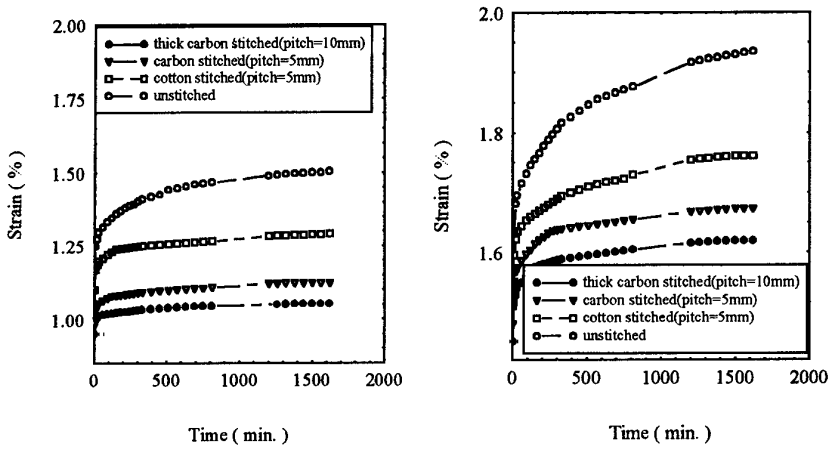

(a) (b)

Fig. 6. Effects of stitching and type of stitch fibre on creep behaviour. (a) $T = 35°C$ and $\sigma = 70$ MPa. (b) $T = 55°C$ and $\sigma = 70$ MPa.

thread stitched composites, as shown in Fig. 8(d).

Compared with cotton threads and carbon threads, thick carbon threads can enhance the creep rupture time for a given stress, see Fig. 9(a) and (b). It should be noted that the tensile strength (σ_b) used in the normalization is dependent also on the stitching thread used and stitching density. It is also clear that for a given creep rupture life, at a certain temperature condition, the maximum stress level that a plain woven composite can sustain can been considerably increased by stitching with thick carbon threads.

In addition to the creep rates, the creep strain at failure was also determined for each specimen. As illustrated in Fig. 8(a)–(d), the creep strain at failure increased as the applied stress decreased. Figure 10 shows creep failure strain as a function of failure time.

It has been suggested that the creep lifetime of many materials can be correlated using a Monkman–Grant type of relationship which relates the failure time, t_f, to the creep rate, $\dot{\varepsilon}$.

$$t_f = C\dot{\varepsilon}^{-m} \tag{5}$$

where C and m are material and environmental constants. Equation (5) has been shown to be valid for various metals, ceramic composites and polymer composites, with a single curve being able to describe the behaviour of a material independent of stress state and temperature. An exponent of $m = 1$ implies a constant strain at failure and assumes that creep in the primary and tertiary stages is negligible, whereas an exponent greater than unity means that the failure strain should increase as the strain rate decreases. Figure 11 shows the creep rate for the unstitched and stitched composites as a function of the time to failure. Clearly, the time to failure was independent of the applied stress, temperature and materials (stitched or unstitched). This means that all of the creep rupture data (unstitched and stitched) could be correlated using this one universal curve, thus providing a creep rupture criterion that can be identified relatively easily. Thereafter, C and m were constants independent of stitching and temperature.

A more useful relationship would be one that relates the time to failure to the applied stress and temperature. Because the results of this study have shown that the time to failure when plotted against creep rate is independent of the stress state and the microstructure of stitched composites, eqn (5) and Norton's law [2] can be combined to provide an expression that gives the time to failure as a function of the applied stress

$$t_f = CA_0^{-m} e^{-\alpha m/T} \sigma^{-mn} \tag{6}$$

where C and m are constants independent of geometry and temperature. However, constants

A_0, α and n are dependent on temperature and stitching.

FINITE-ELEMENT ANALYSIS

To gain further insight into the mechanism of stitching, a finite-element analysis was performed for plain weave textile composites. Unit cells, as shown in Fig. 12, for stitched and unstitched models were constructed using two-dimensional, plane strain elements. For the first attempt, the fibre architecture within the unit cell (pitch = 5 mm) was simplified to a two-dimensional idealization. The three phases are assigned the appropriate in-plane elastic properties corresponding to 0° fibres, 90° fibres and the matrix. The impregnated fibre tows (warp and weft yarns) were modelled with constant rectangular cross-sections, rather than elliptical sections. Curvature of the tows, due to interlacing, was represented by parallel and diagonal straight lines. A unit tensile stress, σ_{app}, was applied to each side of the unit cell as shown in Fig. 12.

The distributions of the resulting interlaminar shear stress, τ_{xy}, and interlaminar normal stress, σ_{yy}, along line AB are shown in Fig. 13(a) and (b). These two stresses are believed to control the viso-elastic–plastic deformation and cracking of the matrix, and interfibre cracking of the 90° fibre tows. As the creep of the fibres is normally negligible, especially at low temperatures, any creep in the matrix would lead to a straightening of the 0° fibre tows under the action of an applied tensile stress. As can be

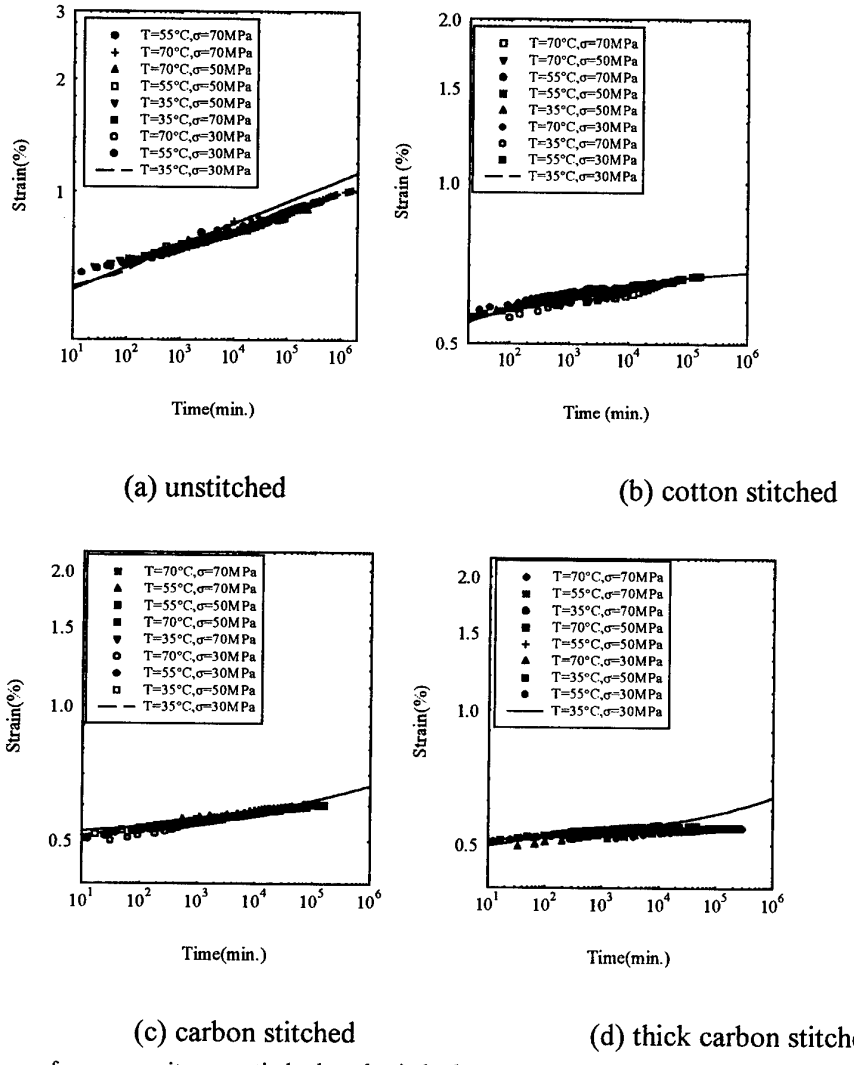

(a) unstitched (b) cotton stitched

(c) carbon stitched (d) thick carbon stitched

Fig. 7. Master curves for composites, unstitched and stitched, at $T = 35°C$ and $\sigma = 30$ MPa reference temperature and stress. (a) Unstitched, (b) cotton stitched, (c) carbon stitched and (d) thick carbon stitched.

seen in Fig. 13, both the interlaminar shear and the normal stresses have been significantly reduced as a result of stitching. In particular, there is a three-fold reduction in the shear stress and a two-fold reduction in the normal stress. The amount of reduction in these stresses is approximately equal to the increase in the stress required to cause the same amount of creep after stitching in a given time. In other words, the enhanced creep resistance of stitched composites can be attributed to reductions in the interlaminar shear and normal stresses. This indicates that the main mechanism for the significant improvement in creep performance by stitching is the reduction in interlaminar stresses.

CONCLUSIONS

1. For the stitched and unstitched composites investigated, the influence of temperature on the creep response has been experimentally studied.
2. The creep response of stitched woven composites has been characterized by isothermal creep tests with various stress levels via the time–stress superposition principle.
3. A universal relationship between creep rate and rupture life has been found to exist for all the woven composites examined.
4. Finite-element analysis has revealed that through-thickness stitching significantly reduces the interlaminar stresses, hence

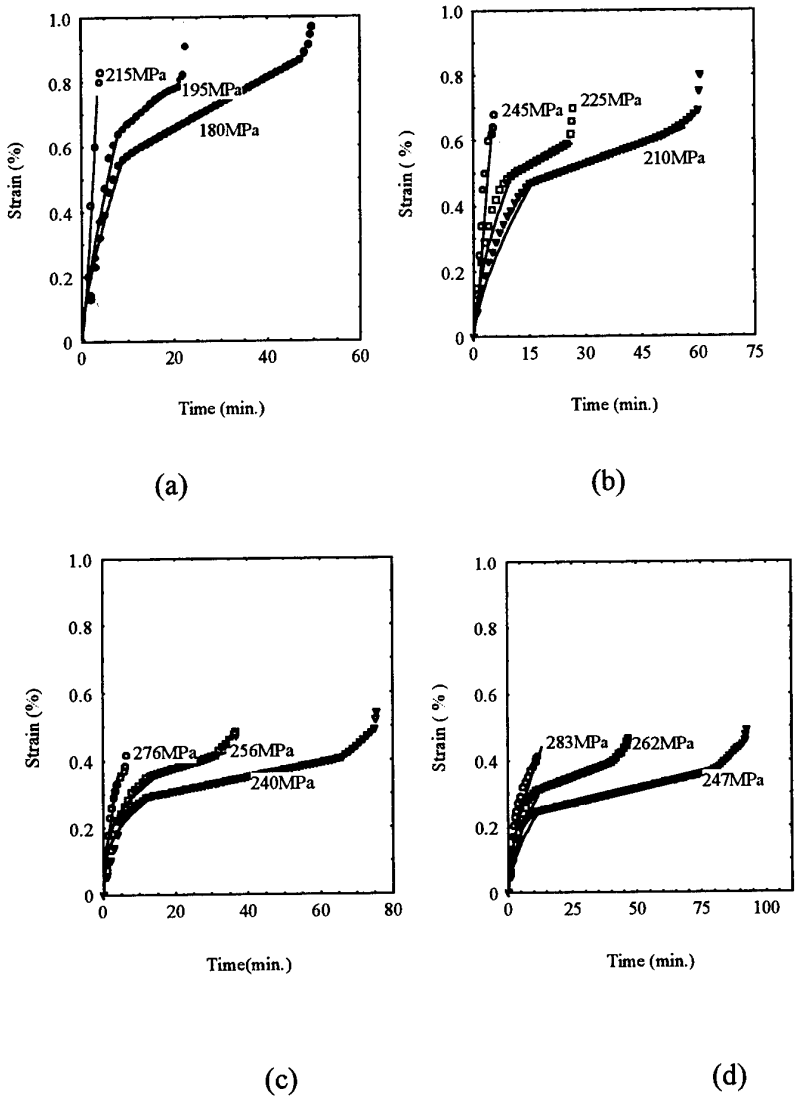

Fig. 8. Rupture behaviour of (a) unstitched, (b) cotton stitched, (c) carbon stitched and (d) thick carbon stitched composites.

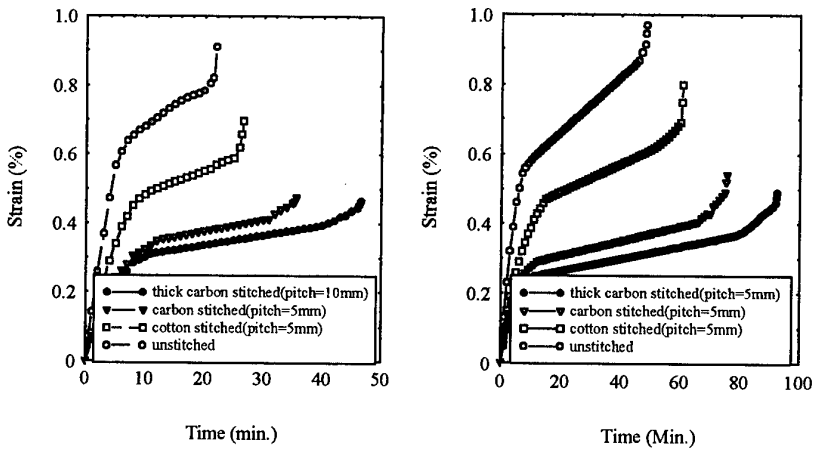

(a)σ_i/σ_b=0.7, T=80°C (b)σ_i/σ_b=0.63, T=80°C

Fig. 9. Effects of stitching and type of stitch fibre on creep rupture behaviour. (a) $\sigma_i/\sigma_b = 0.7$ and $T = 80°C$. (b) $\sigma_i/\sigma_b = 0.63$ and $T = 80°C$.

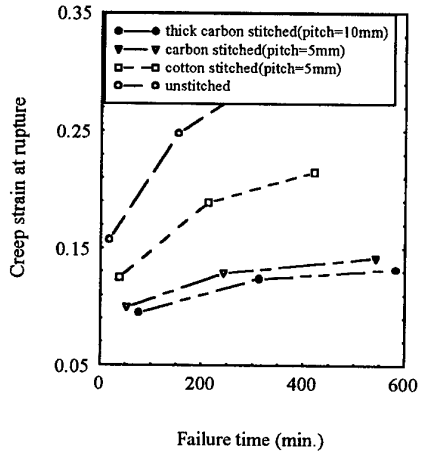

Fig. 10. Creep failure strain as a function of failure time (80°C).

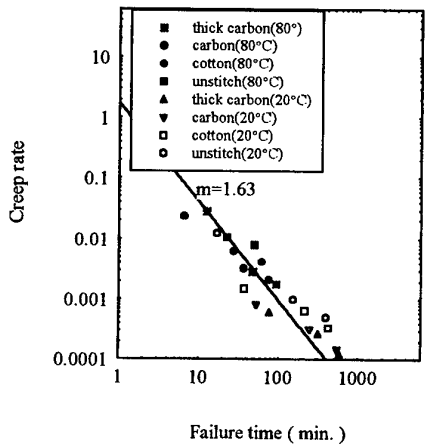

Fig. 11. Master rupture curves for woven stitched composites.

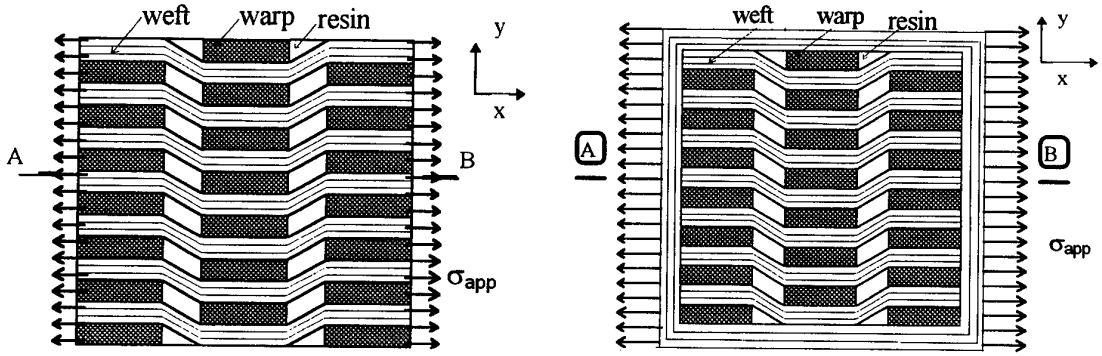

Fig. 12. Finite-element mesh for an unstitched and stitched unit cell (not to scale).

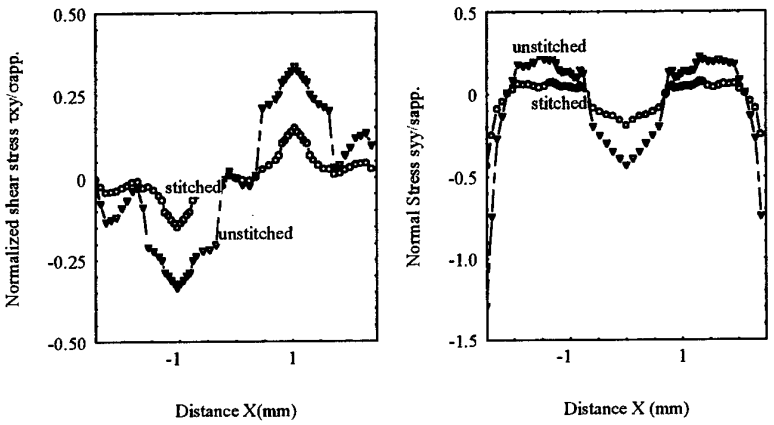

(a) (b)

Fig. 13. Distribution of: (a) the shear stress along AB; and (b) normal stress along AB.

accounting for the beneficial effects of stitching on the creep resistance of woven composites.

REFERENCES

1. Janas, V.F. and McCullough, R.L., The effects of physical aging on the viscoelastic behavior of a thermoset polyester. *Composite Sci. Technol.*, 1987, **30**, 99–118.
2. Mcloughlin, J.R. and Tobolsky, A.V., Effect of rate of cooling on stress relaxation of polylmethyl methacrylate. *J. Polym. Sci.*, 1951, **7**, 658
3. Yen, S.C. and Williamson, F.L., Accelerated characterization of creep response of an off-axis composite material. *Composite Sci. Technol.*, 1990, **38**, 103–118.
4. Griffith, W. I., Morris, D. H. & Brinson, H. F., The accelerated characterization of viscoelastic composite materials. Report No. VPI-E-80-15, Virginia Polytechnic Institute and State University, Blacksburg, VA, 1980.
5. Yeow, Y. T., The time temperature behavior of graphite epoxy laminates. Ph.D. dissertation, Virginia Polytechnic Institute and State University, Blacksburg, VA, 1978.
6. Yen, S. C. & Morris, D. H., Accelerated characterization of the creep behavior of SMC-R50. In *Proc. 40th Annual Conf. of Society of the Plastics Industries, Reinforced Plastics/Composites Institute*. SPI, New York, 1985, Session 5-F, pp. 1–3.
7. Pang, F., Wang, C. H. & Bathgate, R. G., A creep study on stitched fiber/resin composite. In *Proc. of 1st Australasian Congress on Applied Mechanics*. Institution of Engineers Australia, 1996, pp. 357–61.
8. Pang, F., Wang, C. H. & Bathgate, R. G., Creep response of woven fiber composites: effect of stitching. *Composite Sci. Technol.*, 1997, **57**, 91–98.

ELSEVIER

Composite Structures Vol. 38, No. 1–4, pp. 447–452, 1997
© 1997 Elsevier Science Ltd. All rights reserved
Printed in Great Britain
0263-8223/97/$17.00 + 0.00

PII:S0263-8223(97)00079-2

Reliability formulation for composite laminates subjected to first-ply failure

T. Y. Kam & E. S. Chang

Mechanical Engineering Department, National Chiao Tung University, Hsin-Chu 300, Taiwan, Republic of China

Methods formulated on the basis of the concept of first-ply failure and the structural reliability theory are presented for the reliability analysis of laminated composite plates. In the reliability formulation, an appropriate phenomenological failure criterion is used to establish the limit state equation of the laminated composite plates, and different numerical techniques are employed to evaluate the reliability of the plates. Experimental investigations of lamina strengths and first-ply failure loads of laminated composite plates were performed. Baseline probability distributions of lamina strength parameters constructed from the test data are used to study the reliability of the laminated plates. The accuracy of the proposed models in reliability assessment of the laminated plates are verified by the experimental results on first-ply failure load distributions. © 1997 Elsevier Science Ltd.

INTRODUCTION

Laminated composite plates are important components in the construction of aircrafts, automobiles, and mechanical and marine structures. In general, these structures are operated in severe environments and subjected to complex loadings. To ensure no sudden catastrophe for the structures, the reliability of the structures must be thoroughly investigated before use. In order to have a meaningful reliability evaluation, realistic reliability models must be adopted in the reliability analysis of the laminated composite structures. Recently, a number of researchers have proposed different methods for studying the reliability of composite laminates [1–6]. For instance, Kam *et al.* [5] presented a load space formulation technique for the reliability analysis of laminated composite plates. In the previous reliability studies of laminated composite plates, however, only the theoretical aspect was considered and no experimental data were presented to verify the accuracy of their proposed methods.

In this paper, methods formulated on the basis of the first-ply failure concept are presented for the reliability analysis of laminated composite plates with random strength parameters. Phenomenological failure criteria are used to construct the limit state equation of the laminated composite plates. Different numerical techniques are adopted to derive the reliability of the laminated composite plates from the probability distributions of the lamina strength parameters. The feasibility and accuracy of the proposed methods are validated by the experimental data.

FAILURE ANALYSIS OF LAMINATED COMPOSITE PLATES

Stress analysis of a laminated composite plate is accomplished via the finite-element method, which is constructed on the basis of the first-order shear-deformation theory [7]. The element contains five degrees of freedom (three displacements and two shear rotations) per node. In the evalution of the element stiffness matrix, a nine-node Lagrangian element with reduced integration using the 2×2 Gauss rule is adopted. Stresses at node points of an element are determined from those at the integration points via the extrapolation method. Five inde-

pendent stress components at any point in the laminated plate are considered in the finite-element analysis. The first-ply failure load of the laminated composite plate is defined as the strength of the plate. The first-ply failure analysis of the laminated plate is performed via the use of a phenomenological failure criterion. Currently, there are a number of phenomenological failure criteria available for the failure analysis of composite laminates [8]. In general, the failure criteria can be classified into two categories, namely, independent and dependent failure criteria. For instance, maximum stress and Tsai–Wu failure criteria belong to the categories of independent and dependent failure criteria, respectively. Herein, maximum stress and Tsai–Wu criteria are adopted in the first-ply failure analysis of laminated composite plates. The maximum stress criterion states that the ratios of stresses in the principal material directions to the respective strengths must be less than 1, otherwise failure is said to have occurred, that is

$$R_i = \frac{\sigma_i}{X_i} < 1 \ (i = 1, 2, 4, 5, 6) \tag{1}$$

where R_i are stress ratios; σ_1 and σ_2 are normal stress components; σ_4, σ_5 and σ_6 are shear stress components; X_1 and X_2, are the lamina normal strengths in the 1, 2 directions; and X_4, X_5 and X_6 are the shear strengths in the 23, 13 and 12 planes, respectively; $X_5 = X_6$. When σ_1, σ_2 are of a compressive nature they should be compared with X_{1C}, X_{2C} which are normal strengths in compression along the 1, 2 directions, respectively. The Tsai–Wu criterion can be expressed as

$$F_i\sigma_i + F_{ij}\sigma_i\sigma_j \geq 1 \tag{2}$$

with

$$F_1 = \frac{1}{X_T} - \frac{1}{X_C}; \quad F_2 = \frac{1}{Y_T} - \frac{1}{Y_C}$$

$$F_{11} = \frac{1}{X_T X_C}; \quad F_{22} = \frac{1}{Y_T Y_C}$$

$$F_{44} = \frac{1}{R^2}; \quad F_{55} = \frac{1}{S^2}$$

$$F_{12} = \frac{1}{2\sqrt{X_T X_C Y_T Y_C}} \tag{3}$$

where $X_T = X_1$, $Y_T = X_2$, $R = X_4$, $S = X_5$, $X_C = X_{1C}$ and $Y_C = Y_{2C}$.

RELIABILITY FORMULATION

In the reliability formulation for laminated composite plates strength parameters of the constituent composite laminae are treated as independent baseline random variables. The constituent laminae of the laminated composite plates are assumed to possess the same material properties and strength parameters. Herein, the reliability model for composite laminates with random strength parameters subjected to first-ply failure is formulated on the basis of the structural reliability theory. The failure probability, P_f, of a composite laminate is expressed as

$$P_f = \int\cdots\int_{g>0} f_{X_i}(x_i)\cdots f_{X_q}(x_q)\, dx_i \cdots dx_q \tag{4}$$

where g is the limit state equation of the laminated plate; X_i are independent random strength parameters; $f_{X_i}(x_i)$ are baseline probability density functions; and the integration is performed over the failure region, $g > 0$. In general, the limit state equation represents a surface in the strength space where the surface separates the survival and failure regions. Figure 1 shows the limit state curve, $g(x_1, x_2) = 0$, in the strength plane. Herein, the limit state equation of the plate is constructed using either the maximum stress or the Tsai–Wu failure criteria.

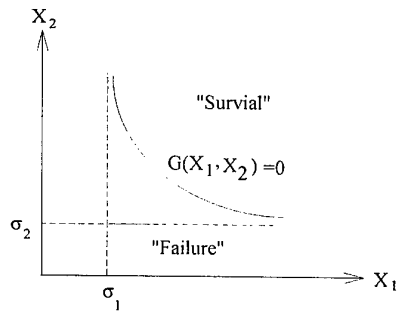

Fig. 1. Two-dimensional limit state curve constructed on the basis of dependent criteria.

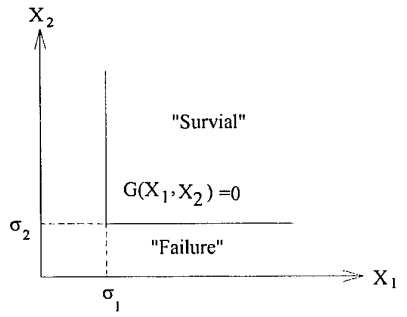

Fig. 2. Two-dimensional limit state curve constructed on the basis of maximum stress criterion.

Maximum stress criterion (independent)

In view of eqn (1) the limit state equation is expressed as

$$g = \prod_{i=1,\, i\neq 3}^{6} (R_i - 1) = 0 \tag{5}$$

where $\prod$ is the notation of multiplication. For the two-dimensional case, the limit state curve in the strength plane is shown in Fig. 2. In view of eqn (4), the reliability of the laminated plate, P_S, is written as

$$P_S = \prod_{i=1,\, i\neq 3}^{6} \int_{\sigma_i}^{\infty} f_{x_i}(x_i)\, \mathrm{d}x_i \tag{6}$$

where σ_i are the largest stress components in the laminated plate. Equation (6) can be solved easily via the use of numerical integration.

Tsai–Wu criterion (dependent)

In this model, the stress state of the most critical point in the laminated plate is used to construct the limit state equation of the plate. In view of eqn (2), the limit state equation is expressed as

$$g = F_i\sigma_i + F_{ij}\sigma_i\sigma_j - 1 = 0 \tag{7}$$

Unlike the independent failure criteria, the solution of eqn (4) will be difficult if not untractable for dependent failure criteria. Herein, the modified β-method [9] is used to evaluate the reliability of the plate.

Table 1. Statistics of strength parameters

Strength parameter	Mean value (MPa)	Coefficient of variation (CV) (%)
$X_1 = X_T$	1537.2	2.1
$X_2 = Y_T$	42.7	6.3
$X_4 = R$	79.67	5.7
$X_5 = T$	102.42	5.7
$X_6 = S$	102.42	5.7
$X_{1C} = X_C$	1722.1	2.1
$X_{2C} = Y_C$	213.95	6.3

EXPERIMENTAL VERIFICATION

Experiments of centrally loaded laminated composite square plates of length $a = 100$ mm and ply thickness $h_i = 0.121$ mm were performed to verify the accuracy of the proposed reliability models. The laminated composite plates under consideration were made of graphite–epoxy (Q-1115) perpreg tapes supplied by the Toho Co., Japan. The properties of the composite material were determined from experiments conducted in accordance with the relevant ASTM standards [10] and their mean values are given as: $E_1 = 139.4$ GPa, $E_2 = 7.65$ GPa, $G_{12} = G_{13} = 4.35$ GPa, $G_{23} = 1.02$ GPa and $\nu_{12} = 0.29$.

The statistics of the lamina strength parameters are listed in Table 1spherical head and a fixture for clamping the specimen. The fixture

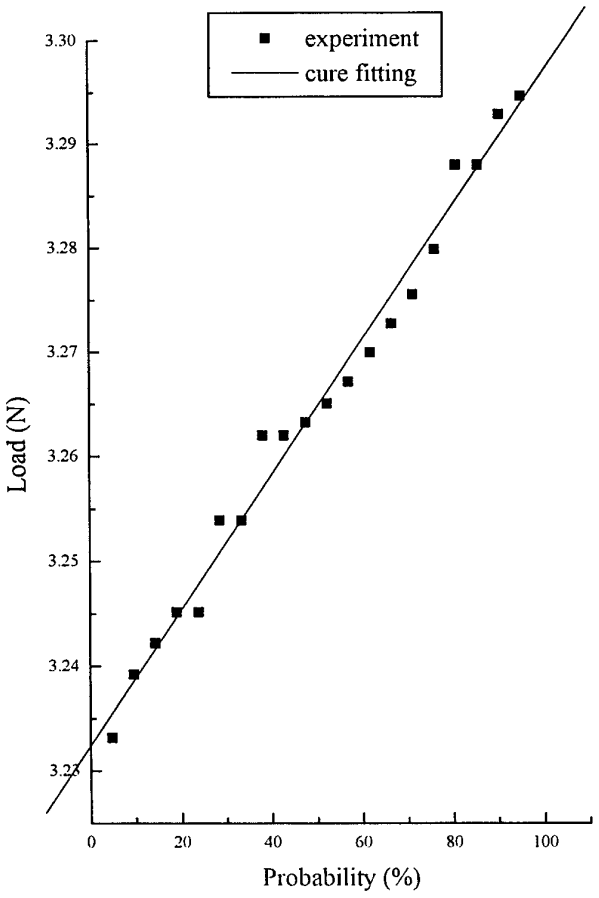

Fig. 3. First-ply failure load data of the $[0°/90°_2/0°_9]$ plate fitted by lognormal distribution.

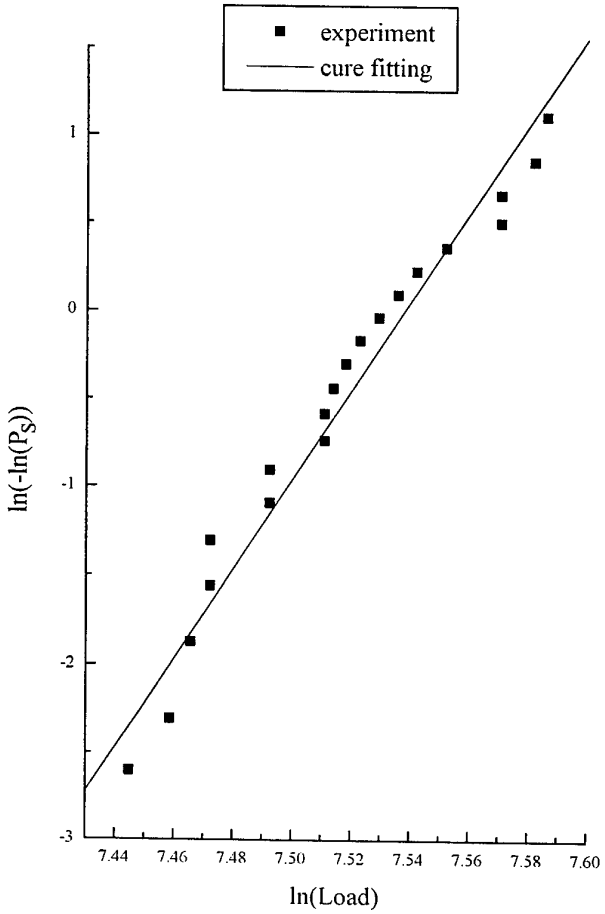

Fig. 4. First-ply failure load data of the $[0°/90°_2/0°_9]$ plate fitted by Weibull distribution.

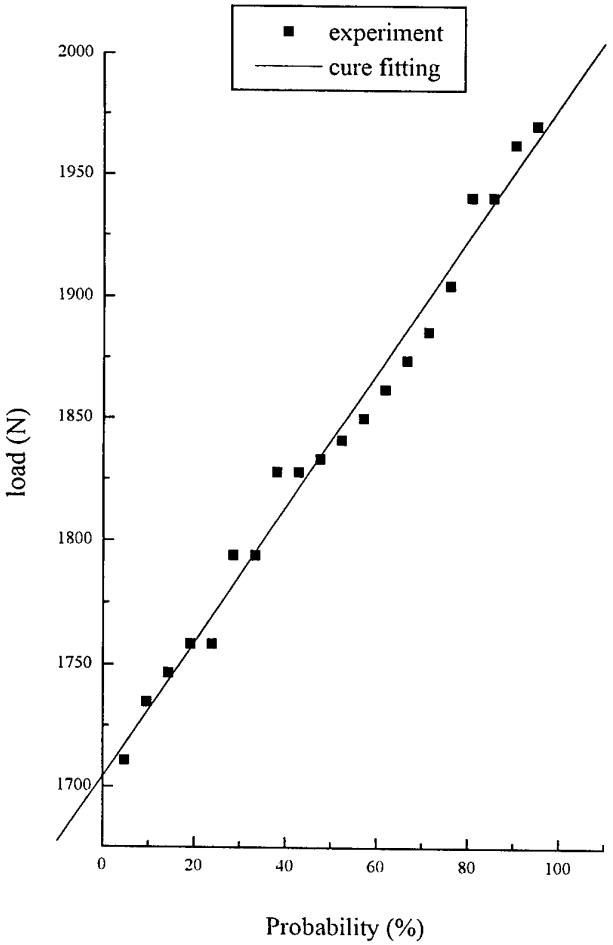

Fig. 5. First-ply failure load data of the $[0°/90°_2/0°_9]$ plate fitted by normal distribution.

Table 2. Statistical parameters of experimental probability distributions of first-ply failure load

Plate	Normal		Weibull		Lognormal	
	Mean $\bar{P}$	σ_P	Scale parameter	Shape parameter	$E[\ln P]$	$\sigma_{\ln P}$
$[0°/90°_2/0°_6]_S$	1841.1	75.7	1878.14	25.1877	3.26	0.0178
$[0°_6/90°_6]_S$	1207.7	65.6	1240.53	18.493	3.08	0.0237
$[45°/-45°_2/45°_6]_S$	2091.6	117.88	2148.21	18.4856	3.32	0.0248
$[45°_6/-45°_6]_S$	1296.3	72.93	1331.58	18.3931	3.11	0.0246

Note: σ = standard deviation; $E[\ ]$ = expected value.

Table 3. Experimental plate reliabilities derived from various probability distributions

Plate	$P(N)$	Reliability		
		Normal	Weibull	Lognormal
$[0°/90°_2/0°_6]_S$	1725	0.9241	0.8914	0.9376
$[0°_6/90°_6]_S$	1125	0.9306	0.8992	0.9344
$[45°/-45°_2/45°_6]_S$	1900	0.9529	0.9018	0.9639
$[45°_6/-45°_6]_S$	1175	0.9638	0.9047	0.9762

Table 4. Theoretical plate reliabilities derived from various baseline probability density distributions

Plate	$P(N)$	Independent reliability model			Dependent reliability model		
		Normal	Weibull	Lognormal	Normal	Weibull	Lognormal
$[0°/90°_2/0°_6]_S$	1725	0.876	0.8232	0.8495	0.851	0.817	0.827
$[0°_6/90°_6]_S$	1125	0.9233	0.865	0.904	0.904	0.843	0.871
$[45°/-45°_2/45°_6]_S$	1900	0.9362	0.8758	0.9173	0.9333	0.8747	0.9095
$[45°_6/-45°_6]_S$	1175	0.9493	0.889	0.933	0.9207	0.862	0.8945

was made up of two square steel frames. During testing the laminated plate was clamped using the two steel frames, which were connected together by four bolts. A stroke control approach was adopted in constructing the load–deflection relation for the laminated plate. The loading rate was slow enough for inertia effects to be neglected. During loading, two acoustic emission sensors were used to measure the stress waves released at the AE sources in the laminated plate. The measured acoustic emissions were converted by the AMS3 (AE) system to a set of signal describers such as peak amplitude, energy, rise time and duration, which were then used to identify the first-ply failure load of the laminated plate [7].

RESULTS AND DISCUSSION

First-ply failure load data of laminated composite plates with different lamination arrangements, namely $[0°/90°_2/0°_9]_S$, $[0°_6/90°_6]_S$ $[45°/-45°_2/45°_9]_S$ and $[45°_6/-45°_6]_S$, obtained from experiments are fitted by various probability distributions via the probability papers. For instance, Figs 3–5 show the first-ply failure load data of the $[0°/90°_2/0°_9]_S$ plate fitted by normal, Weibull and lognormal distributions, respectively. It is noted that Weibull distribution can yield the most conservation values for plate reliability when small failure probability, e.g. $P_f < 0.1$, is considered. The statistical parameters of the experimental probability distributions of the first-ply failure loads for the laminated plates are listed in Table 2. The experimental reliability of the laminated composite plates, which are subjected to a center point load, P, of different magnitudes, derived from various probability distributions are listed in Table 3. It should be noted that the $[45°/-45°_2/45°_9]_S$ plate, which has been optimally designed, yields the highest reliability. The reliability of the laminated composite plates is also determined using the aforementioned reliability models and baseline probability density functions. Table 4 lists the theoretically predicted reliabilities for the plates with different lamination arrangements. The differences between the experimental and theoretical plate reliabilities are given in Table 5. It is noted that in general the differences between the experimental and theoretical results are small (less than 12%) irrespective to the types

Table 5. The difference between theoretical and experimental reliabilities of composite plates[1]

Plate			Independent reliability model			Dependent reliability model		
Lay-up	$P(N)$	Experiment distribution	Normal	Weibull	Lognormal	Normal	Weibull	Lognormal
$[0°/90°_2/0°_6]_S$	1725	Normal	5.2	10.9	8.1	7.9	11.6	10.5
		Weibull	1.7	7.6	4.7	4.5	8.3	7.2
		Lognormal	6.5	12.2	9.4	9.2	12.8	11.8
$[0°_6/90°_6]_S$	1125	Normal	0.8	7.0	2.8	2.8	9.4	6.4
		Weibull	2.7	3.8	0.5	0.5	6.3	3.1
		Lognormal	1.2	7.4	3.2	3.2	9.8	6.8
$[45°/-45°_2/45°_6]_S$	1900	Normal	1.7	8.1	3.7	2.0	8.2	4.5
		Weibull	3.8	2.9	1.7	3.5	3.0	0.8
		Lognormal	2.8	9.1	4.8	3.1	9.2	5.6
$[45°_6/-45°_6]_S$	1175	Normal	1.5	7.8	3.2	4.5	10.6	7.2
		Weibull	4.9	1.7	3.1	1.7	4.7	1.1
		Lognormal	2.7	8.9	4.4	5.7	11.7	8.3

[1]$\text{Difference} = \left(\dfrac{\text{experiment} - \text{theory}}{\text{experiment}} \right)\%$.

of probability distributions used in modeling the distributions of the lamina strength parameters and first-ply failure load. In particular, when the baseline probability density functions are normal and the distribution of first-ply failure load is Weibull, the differences can be less than 5% for the laminated composite plates irrespective to the method used in the reliability analysis.

CONCLUSIONS

Different methods were presented for the reliability assessment of laminated composite plates. The methods were constructed on the basis of the concept of first-ply failure and the structural reliability theory. The feasibility and accuracy of the present methods were validated by the experimental distributions of first-ply failure loads of laminated composite plates with different lamination arrangements. The effects of different types of baseline probability density functions on the system failure probability of laminated composite plates were studied. It was found that the use of Weibull distribution in the reliability design of laminated composite plates could yield more conservative results. The use of normal distribution for modeling the lamina strength parameters in the reliability analysis could yield very accurate results for the plates when their first-ply failure loads were modeled as Weibull variates. Both analytical methods are suitable for the reliability analysis of laminated composite plates.

ACKNOWLEDGEMENTS

This research was supported by the National Science Council of the Republic of China under grant No. NSC 86-2623-D-009-008.

REFERENCES

1. Cassenti, B. N., Probabilistic static failure of composite material. *AIAA J.*, 1984, **22** (1), 103–110.
2. Cederbaum, G., Elishakoff, I. and Librescu, L., Reliability of laminated plates via the first-order second method. *J. Composite Struct.*, 1990, **15**, 161–167.
3. Engelstad, S. P. and Reddy, J. N., Probabilistic nonlinear finite element analysis of composite structures. *AAIA J.*, 1992, **31** (2), 362–369.
4. Kam, T. Y. and Lin, S. C., Reliability analysis of laminated composite plates. *Proc. NSC, Part A*, 1992, **16**, 163–171.
5. Kam, T. Y., Lin, S. C. and Hsiao, K. M., Reliability analysis of nonlinear laminated composite plate structures. *J. Composite Struct.*, 1993, **25**, 503–510.
6. Sun, C. T. and Yamada, S. E., Strength distribution of a unidirectional fiber composite. *J. Composite Mater.*, 1978, **12**, 169–176.
7. Kam, T. Y., Sher, H. F., Chao, T. N. and Chang, R. R., Predictions of deflection and first-ply failure load of thin laminated composite plates via the finite element approach. *J. Solids Struct.*, 1996, **33**, 375–398.
8. Tsai, S. W. & Hahn, H. T., *Introduction to Composite Materials*. Technomic, Lancaster, PA, 1980.
9. Ang, A. H.-S. & Tang, W. H., *Probability Concepts in Engineering Planning and Design*, Vol. II. Rainbon-Bridge, 1984.
10. *ASTM Standards and Literature References for Composite Material*, 2nd edn. American Society for Testing and Materials, 1990.

ELSEVIER

Composite Structures Vol. 38, No. 1–4, pp. 453–462, 1997
© 1997 Elsevier Science Ltd. All rights reserved
Printed in Great Britain
0263-8223/97/$17.00 + 0.00

PII:S0263-8223(97)00080-9

Free and forced vibration analysis of thin, laminated, cylindrically curved panels

N. S. Bardell,* J. M. Dunsdon & R. S. Langley

Department of Aeronautics and Astronautics, University of Southampton, Highfield, Southampton SO17 1BJ, Hampshire, UK

A comprehensive vibration study of thin, laminated, cylindrically curved shell panels (based on the shell theory of Love with a modification by Arnold and Warburton) is conducted by using the h–p version of the finite-element method (FEM). Polynomially enriched stiffness and mass matrices are derived from classical shell theory using Symbolic Computing, and then stored in algebraic form for a single, generic element. A number of such elements may then be combined to form the global stiffness and mass matrices for a more general co-axial and/or co-circumferential assembly. Any of the classical edge conditions, or point corner supports, may be accommodated in the analysis; forcing may be applied through one or more point forces acting normal to the shell surface. Excellent agreement has been found with the work of other investigators, and some new results are presented for a multiply supported curved panel made from the aluminium–glass-fibre hybrid *GLARE*. The h–p method is shown, by example, to offer an efficient means of conducting typical repetitive sensitivity analyses, such as varying the fibre orientation and the stacking sequences of a given panel. © 1997 Elsevier Science Ltd.

INTRODUCTION

The use of laminated fibre-reinforced composite materials in thin-walled structural applications has had a major impact on the entire design process for two-dimensional stress-bearing systems. Nowhere has this impact been greater than in the birthplace of the modern composite — the aerospace industry — where current design capabilities range from aeroelastic tailoring to minimum weight structures. This advantageous state of affairs owes much to the vast amount of research and development that has been, and continues to be, expended in gaining a better understanding of the mechanical behaviour of composite materials under static and dynamic loading actions. The research effort reviewed here [1–16] contains only a representative overview of this vast subject area; an exhaustive survey is beyond the scope of this discussion.

*Westland Lecturer in Helicopter Engineering, and author to whom correspondence should be addressed.

This paper continues the programme of work first carried out by the authors on laminated coplanar plate assemblies [1] using the h–p version of the finite-element method [17–20], which is a state-of-the-art numerical modelling technique. The main aim of this work is to validate the use of h–p techniques for simple, singly curved, laminated components, and explore the efficiency gains that might be realized through adopting this methodology. The feature of forced vibration response is also considered.

Three problems are addressed in this work. The first is a simple convergence benchmark test for the natural frequencies of a thin, laminated, cylindrically curved shell, supported on shear diaphragms on all four edges [7,12]. The second is a free and forced vibration analysis of a clamped panel [10], with the emphasis on investigating the effect of different ply orientations and stacking sequences. Finally, some new free and forced vibration results are presented for a curved, multi-bay panel made from the

layered aluminium and glass-fibre hybrid *GLARE*. This panel is internally sub-divided by an orthogonal array of line simple supports, and supported around its boundaries by a mixture of point supports, and clamped and free edges.

Love's shell theory [15], with the modification introduced by Arnold & Warburton [16], is used as the basis for the h–p finite-element formulation developed here.

METHOD OF ANALYSIS

Background to the h–p version of the FEM

The h–p version of the FEM may be regarded as the marriage of the conventional h version and p version; convergence is sought by *simultaneously* refining the mesh and increasing the degree of the elements [17–19]. For the type of problem under consideration here, in which the motion in all three co-ordinate directions is coupled, it is advantageous to represent both the out-of-plane displacements and the in-plane displacements by the *same* set of assumed modes. There are two good reasons for this: (i) it greatly reduces the computational effort required to calculate the element stiffness and mass matrices; and (ii) it simplifies the element assembly process.

An ascending hierarchy of K-orthogonal polynomials, used in conjunction with Hermite cubics, furnishes a complete set of admissible functions with full C_1 continuity. (A full description of these assumed modes is given by Bardell *et al.* [1].) The hierarchical modes contribute only to the internal displacement field of the element, and do not therefore affect the displacement along the element edge or at the element nodes. However, products formed between any of the K-orthogonal polynomials and the Hermite cubics will constitute what amounts to edge degrees of freedom along the element boundaries. Adjacent elements may be joined by ensuring compatibility of both nodal *and* edge displacements. The use of C_1 continuity functions to describe the *in-plane* displacement field is justified on the grounds that it is only necessary to match the *displacements* u and v across an element interface to thus ensure C_0 continuity; no attempt is made to enforce *first derivative* continuity (i.e. $\partial u/\partial \eta$, $\partial v/\partial \eta$, $\partial u/\partial \xi$, $\partial v/\partial \xi$) — which effectively describes the in-plane strain at a point — across an element interface, because this would over-prescribe the connectivity. In this manner, all the edge-to-edge interfaces are fully conforming in the conventional sense.

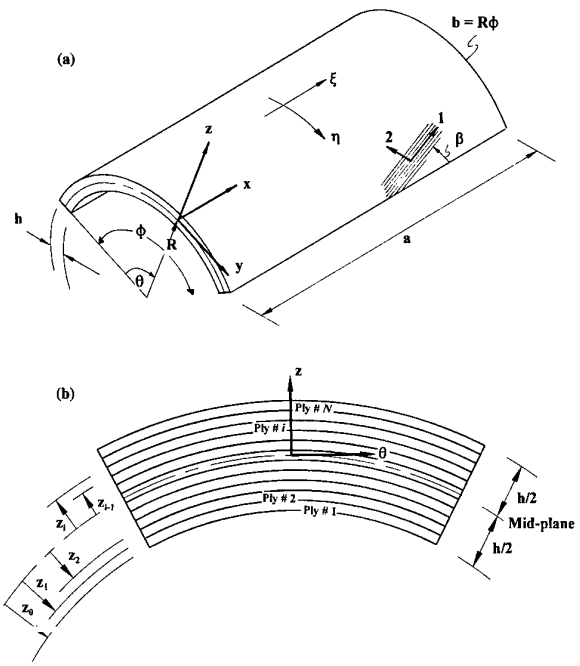

Fig. 1. (a) The geometry of the laminated curved shell element. (b) The stacking notation for the layers of the shell element.

Derivation of the laminate stiffness and mass matrices

With reference to Fig. 1, consider a general point, distance z from the geometric mid-plane, within the ith layer of an N-layer, laminated, cylindrically curved, rectangular planform shell finite element. The laminate is of total thickness h, mean radius of curvature R, considered thin, i.e. $h \ll R$, bounded along its edges by the lines $x = 0$, $x = a$, $\theta = 0$ and $\theta = \phi$, and each layer is assumed to be generally orthotropic, homogeneous, elastic, of uniform thickness and perfectly bonded to its neighbours. The usual thin-shell assumption is made that plane-sections remain plane under combined bending and stretching of the laminate. According to Love [15] and Arnold & Warburton [16], the strain–displacement relationships at a general point within the ith layer, are

$$\varepsilon_{xx} = \frac{\partial u}{\partial x} - z\frac{\partial^2 w}{\partial x^2}$$

$$\varepsilon_{\theta\theta} = \frac{1}{R}\frac{\partial v}{\partial \theta} + \frac{w}{R} - z\left(\frac{1}{R^2}\frac{\partial^2 w}{\partial \theta^2} + \frac{1}{R^2}\frac{\partial v}{\partial \theta}\right)$$

$$\gamma_{x\theta} = \frac{1}{R}\frac{\partial u}{\partial \theta} + \frac{\partial v}{\partial \theta} - 2z\left(\frac{1}{R}\frac{\partial^2 w}{\partial x \partial \theta} + \frac{1}{R}\frac{\partial v}{\partial x}\right) \tag{1}$$

where u, v and w refer to the mid-plane displacements. It should be noted that no account is taken of shear deformation within the layers of this particular model.

On introducing the non-dimensional co-ordinates ξ, η which are related to the element Cartesian co-ordinates through $\xi = 2x/a - 1$ and $\xi = 2R\theta/b - 1$, the strain–displacement relationship can be rendered in the matrix form

$$\begin{bmatrix}\varepsilon_{xx}\\ \varepsilon_{\theta\theta}\\ \gamma_{x\theta}\end{bmatrix} = \begin{bmatrix} \frac{2}{a}\frac{\partial}{\partial \xi} & 0 & -z\frac{4}{a^2}\frac{\partial^2}{\partial \xi^2} \\ 0 & \frac{2}{b}\left(1-\frac{z}{R}\right)\frac{\partial}{\partial \eta} & -\frac{1}{R} - z\frac{4}{b^2}\frac{\partial^2}{\partial \eta^2} \\ \frac{2}{b}\frac{\partial}{\partial \eta} & \frac{2}{a}\left(1-2\frac{z}{R}\right)\frac{\partial}{\partial \xi} & -z\frac{8}{ab}\frac{\partial^2}{\partial \xi \partial \eta} \end{bmatrix} \begin{bmatrix} u(\xi,\eta)\\ v(\xi,\eta)\\ w(\xi,\eta)\end{bmatrix} \tag{2}$$

This can be written more concisely as

$$\{\varepsilon\} = [\Delta]\{\delta\} \tag{3}$$

The state of displacement of the laminate mid-plane may approximately be represented by a finite series of the previously assumed modes in the ξ- and η-directions, namely

$$u(\xi,\eta) = \sum_{rx=1}^{p_{ux}} \sum_{sx=1}^{p_{uy}} X_{rx,\,sx} f_{rx}(\xi) f_{sx}(\eta) \tag{4a}$$

$$v(\xi,\eta) = \sum_{ry=1}^{p_{vx}} \sum_{sy=1}^{p_{vy}} Y_{ry,\,sy} f_{ry}(\xi) f_{sy}(\eta) \tag{4b}$$

$$w(\xi,\eta) = \sum_{rz=1}^{p_{wx}} \sum_{sz=1}^{p_{wy}} Z_{rz,\,sz} f_{rz}(\xi) f_{sz}(\eta) \tag{4c}$$

where $X_{rx,\,sx}$, $Y_{ry,\,sy}$, and $Z_{rz,\,sz}$ are the (unknown) generalized co-ordinates of the problem, and each summation may be taken over any number of p assumed modes. Equations (4a), (4b) and (4c) can be written more succinctly in matrix notation as

$$\{\delta\} = [N]\{q\} \tag{5}$$

where $\{q\} = \{X_{rx,\,sx},\ Y_{ry,\,sy},\ Z_{rz,\,sz}\}^{\mathrm{T}}$. Substituting eqns (4a), (4b) and (4c) into eqn (3) yields

$$\{\varepsilon\} = [\Delta][N]\{q\} \tag{6}$$

As the material of each layer of the plate is considered to be generally orthotropic, with its directional elastic properties depending upon the fibre orientation angle β (see Fig. 1), the constitutive relationship for the ith layer can be written

$$\{\sigma\}_i = [D]_i\{\varepsilon\} \tag{7}$$

where $\{\sigma\}_i = \{\sigma_x,\ \sigma_y,\ \tau_{xy}\}_i^{\mathrm{T}}$, and $[D]_i$ is the well-known [21] 3×3 array of elastic coefficients for a generally orthotropic material. Note that for use in the forced response analysis, a single layer-wise value of the loss factor η_i is assigned to all the elastic moduli to reflect the presence of hysteretic damping in each layer of material [22]. Whilst it is recognized that such an approach is highly simplistic — there are, in fact, 18 different damping loss factors that can be prescribed in a laminated composite [22] — it is justifiable on the grounds that the main purpose of this work is to illustrate the applicability of the methodology to such problems.

Panel strain energy

In element-local, non-dimensional, co-ordinates, the strain energy of the complete N-layer laminate is given [21] by

$$U = \frac{1}{2}\{q\}^{\mathrm{T}}\frac{ab}{4}\sum_{i=1}^{N}\int_{-1}^{+1}\int_{-1}^{+1}\int_{z_{i-1}}^{z_i}([\Delta][N])^{\mathrm{T}} \times [D]_i[\Delta][N]R\,\mathrm{d}z\,\mathrm{d}\eta\,\mathrm{d}\xi\{q\} \tag{8}$$

The terms between the row and column vectors denote the laminate element stiffness matrix $\boldsymbol{K}^{\mathrm{E}}$.

Panel kinetic energy
Likewise, in element-local, non-dimensional, co-ordinates, the kinetic energy of the complete N-layer laminate is given by

$$T = \frac{1}{2}\{\dot{q}\}^{\mathrm{T}} \frac{ab}{4} \sum_{i=1}^{N} \rho_i \int_{-1}^{+1} \int_{-1}^{+1} \int_{z_{i-1}}^{z_i} [N]^{\mathrm{T}} \times [N] R \, \mathrm{d}z \, \mathrm{d}\eta \, \mathrm{d}\xi \{\dot{q}\} \tag{9}$$

Evidently, the terms between the row and column vectors denote the laminate element mass matrix $\boldsymbol{M}^{\mathrm{E}}$. Both $\boldsymbol{K}^{\mathrm{E}}$ and $\boldsymbol{M}^{\mathrm{E}}$ are of the overall order $[(p_{wx} \times p_{wy}) + (p_{ux} \times p_{uy}) + (p_{vx} \times p_{vy})]$, and are comprised of nine sub-matrices.

Potential energy of the external loading action
Only harmonic point forces, acting normal to the shell surface (positive radially outwards), are considered here. The gain in potential energy of such a force P located at $(\xi_{\mathrm{P}}, \eta_{\mathrm{P}})$ and with phase μ is given by

$$V = -P\mathrm{e}^{j\mu} w(\xi_{\mathrm{P}}, \eta_{\mathrm{P}}) \tag{10}$$

Equations of motion
The equations of motion of the system can be formulated using Lagrange's equation, which states

$$\frac{\partial U}{\partial \boldsymbol{q}} + \frac{\partial}{\partial t}\left(\frac{\partial T}{\partial \dot{\boldsymbol{q}}}\right) - \frac{\partial T}{\partial \boldsymbol{q}} = -\frac{\partial V}{\partial \boldsymbol{q}} \tag{11}$$

where U, T and V are defined above. By substituting these expressions into eqn (11), and assuming harmonic motion, the equations of motion of the shell can be expressed in the form

$$-\omega^2 \boldsymbol{M}\boldsymbol{q} + \boldsymbol{K}(1 + j\eta)\boldsymbol{q} = \boldsymbol{F} \tag{12}$$

where $\boldsymbol{M}$ and $\boldsymbol{K}$ are the global mass and stiffness matrices, and the vectors $\boldsymbol{q}$ and $\boldsymbol{F}$ contain the generalized co-ordinates and generalized forces. Note: the absence of any in-plane forces will render the two sub-sets of the generalized force vector corresponding to $X_{rx,\,sx}$ and $Y_{ry,\,sy}$ zero, i.e. $\boldsymbol{F}^{\mathrm{E}} = [0, 0, F_{rz,\,sz}]^{\mathrm{T}}$.

Element assembly
The matrix multiplication and integration required to evaluate the element stiffness and mass matrices shown in eqns (8) and (9), and the generalized force vector shown in eqn (10), was performed symbolically (for a maximum of 10 assumed in-plane and out-of-plane modes in both the x- and y-directions) by using the Computer Algebra package *MAPLE* [23]. This enables all the entries in $\boldsymbol{K}^{\mathrm{E}}$, $\boldsymbol{M}^{\mathrm{E}}$ and $\boldsymbol{F}^{\mathrm{E}}$ to be pre-computed in exact, fractional, algebraic format, and then down-loaded to the main analysis program where they are stored at a familial level. In this way, no numerical rounding errors are introduced into the calculation of the element matrices; also, only one significant computational expense is ever incurred by keeping $\boldsymbol{K}^{\mathrm{E}}$, $\boldsymbol{M}^{\mathrm{E}}$ and $\boldsymbol{F}^{\mathrm{E}}$ completely generic. The h–p method of assembling the elements to obtain the global stiffness and mass matrices, and generalized force vector, is accomplished by identifying, and then adding together, all the like terms from any number of adjacent elements which correspond to common nodal and edge degrees of freedom along their interface. The only restriction on the boundary geometry possible with the method in its current state of development is that it must be possible to divide the structure into an assembly of rectangular planform elements of identical curvature.

Boundary conditions
Specific boundary conditions may be applied to the model simply by removing those rows/columns from $\boldsymbol{K}$ and $\boldsymbol{M}$, and rows from $\boldsymbol{F}$, which correspond to fixed degrees of freedom — hence any combination of shear diaphragm, simple support, clamped or free edges, or corner point supports can be accommodated in the analysis. In the current work, a shear diaphragm (S-D) permits an in-plane translation across the support but prevents w-wise motion normal to it; a simple support (S-S) permits rotation of the plate normal about the supporting edge, but prevents all three (u, v and w) translational freedoms.

The frequency equation for free vibration
By assuming harmonic motion and the absence of any external forcing agency or internal damping, the governing equations of motion can be written in the standard form

$$[\boldsymbol{K} - \omega^2 \boldsymbol{M}]\boldsymbol{q} = \boldsymbol{0} \tag{13}$$

which can be solved as a matrix-eigenvalue problem. The solution to eqn (13) yields the natural frequencies. Corresponding to each eigenvalue is an eigenvector, which may be used

in conjunction with eqn (4c) to recover the associated out-of-plane normal modes of the panel under consideration.

The equation of motion for forced response

By assuming harmonic motion, the governing equations of forced motion can be expressed thus

$$[(1+j\eta)\boldsymbol{K}-\omega^2\boldsymbol{M}]\boldsymbol{q}=\boldsymbol{F} \tag{14}$$

The solution to eqn (14) can be found by specifying ω and then pre-multiplying the right-hand side by the inverse of the left-hand side, thus

$$\boldsymbol{q}=[(1+j\eta)\boldsymbol{K}-\omega^2\boldsymbol{M}]^{-1}\boldsymbol{F} \tag{15}$$

The (complex) vector $\boldsymbol{q}$ may then be used in conjunction with eqn (4c) to recover the associated out-of-plane displacement $w(\xi, \eta)$ of each element in the model, and hence permit the construction of a frequency–response receptance plot w/F. If w is determined at the point of excitation, then a point receptance is obtained; if w is determined at some point other than the excitation point, then a transfer receptance is obtained.

RESULTS

Comparison with the work of others

Confidence has been gained in the h–p methodology through a number of validation exercises. The first comparison case is based on the work of Sinha and Rath [5], Soldatos [8] and Bercin [12], who all determined the fundamental frequencies of a shear diaphragm supported curved panel defined by $b/R = 0.5$, $R/h = 40$, with various a/b. The variety of different methods and shell theories used provide a good set of benchmark results, although it should be noted that relative to the radius, this shell is quite thick, and hence it is likely that shear-deformation effects will influence the frequencies of all the modes. The panel is constructed from two layers of angle ply material; the principal fibre direction of the inner layer is aligned with the circumferential direction, and the principal fibre direction of the outer layer is aligned with a generator of the shell, i.e. [90°/0°]. The material properties for each layer are as follows: $E_1/E_2 = 25$, $G_{12}/E_2 = 0.5$, and the major Poisson's ratio $\nu_{12} = 0.25$. The fundamental non-dimensional natural frequencies $\Omega = \omega a^2(\rho/E_2h^2)^{1/2}$ have been calculated for a variety of aspect ratios a/b which are shown in Table 1.

It is immediately apparent that the fundamental frequencies converge monotonically from above to give answers consistent with those reported by other investigators. The maximum discrepencies (which fall consistently between the results of Soldatos [8] and Bercin [12]) are well within the limits attributable to the different shell theories and methodologies employed, and are consistent with the fact that Bert & Kumer [6] included shear-deformation effects within their model.

For the $a/b = 1$ case, the results arising from the $h = 4$ mesh idealization are consistently lower than those from either the $h = 1$ or $h = 9$ case. This apparent anomaly can be explained by reference to this particular mode of vibration, which is the (1, 1) mode. It just so happens that dividing the shell into four equal elements enables the available shape functions within those elements to ape the actual deformation of this particular mode better than either of the other two idealizations, and hence yield a more accurate answer. This 'feature' arises because

Table 1. Convergence study for the fundamental natural frequencies $\Omega = \omega a^2(\rho/E_2h^2)^{1/2}$ of a two-layer curved panel supported on shear diaphragms ($b/R = 0.5$, $R/h = 40$, with various a/b)

a/b	$h=1$			$h=4$			$h=9$		Sinha & Rath [5]	Soldatos [8]	Bercin [12]
	$p=6$	$p=8$	$p=10$	$p=5$	$p=7$	$p=9$	$p=6$	$p=8$			
1	11.6988	11.6967	11.6967	11.6967	11.6943	11.6896	11.6962	11.6949	11.65	11.84	12.01
2	7.3296	7.3280	7.3280	7.3285	7.3279	7.3277	7.3279	7.3279	7.37	7.25	7.43
3	6.5462	6.5444	6.5444	6.5450	6.5444	6.5444	6.5444	6.5444	6.59	6.39	6.59
4	6.2842	6.2824	6.2824	6.2830	6.2824	6.2824	6.2824	6.2824	6.33	6.11	6.30
5	6.1702	6.1683	6.1683	6.1689	6.1683	6.1683	6.1683	6.1683	6.21	5.99	6.20
MO[1]	64	132	224	148	364	676	539	1131	—	—	—

[1]The term MO denotes the final matrix order, or total number of DOFs, of the problem under consideration.

Table 2. The first six natural frequencies $\Omega = (\rho h\omega^2 b^4/D_0)^{1/2}$ of various clamped laminated curved panels (where the factor $D_0 = E_{11}h^3/12(1-\nu_{12}\nu_{21})$). h–p results arising from one super-element with $p = 10$ ($R/h = 500$, $a/b = 1$, $b/h = 100$, MO = 164)

	Symmetric cross-ply $[0°/90°]_S$		Antisymmetric cross-ply $[0°/90°]$		Symmetric cross-ply $[\beta/-\beta/-\beta/\beta]$					
					$\beta = 0°$	$\beta = 30°$	$\beta = 45°$	$\beta = 60°$	$\beta = 60°$	$\beta = 90°$
	h–p	Chun & Lam [10]	h–p	Chun & Lam [10]	h–p	h–p	h–p	h–p	Chun & Lam [10]	h–p
Ω_1	47.99	*48.19*	35.09	*35.48*	28.27	31.49	38.89	48.87	*49.06*	60.98
Ω_2	55.46	—	42.24	—	31.20	38.83	46.26	52.89	—	63.88
Ω_3	60.97	*60.96*	51.09	*51.57*	42.61	56.37	55.70	60.17	*60.25*	64.20
Ω_4	70.75	—	52.31	—	60.55	57.61	66.38	67.86	—	70.77
Ω_5	72.82	*72.83*	65.28	*65.61*	65.04	71.09	78.66	77.74	*77.71*	71.50
Ω_6	88.85	—	73.46	—	68.76	79.57	89.02	87.90	—	82.21

the internal p-boost in the $h = 4$ mesh does not constitute a sub-set of the p-boost in the $h = 9$ case.

For shells with a higher value of R/h than that just considered, for which shear-deformation effects could be neglected with confidence in the first few modes of vibration, consistent and reliable answers should be forthcoming. To test this hypothesis, a further study was conducted based on the work of Chun and Lam [10], who analysed a variety of differently laminated cylindrically curved panels that were clamped around all four edges. In particular, a panel characterized by $R/h = 500$, $a/b = 1$, $b/h = 100$ was modelled using one super-element with each of the series representing the u, v and w displacements boosted to a maximum polynomial enrichment of 10, i.e. $h = 1$, $p = 10$. The material properties are assumed to be the same for all the layers, and are $E_1/E_2 = 15.4$, $G_{12}/E_2 = 0.8$, and the major Poisson's ratio $\nu_{12} = 0.3$.

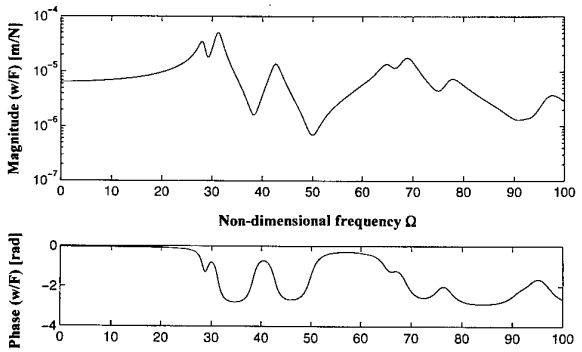

Fig. 2. The point receptance and phase for a clamped $[0°/-0°/-0°/0°]$ panel subjected to a unit harmonic force applied at $\xi = -0.37$ and $\eta = 0.43$.

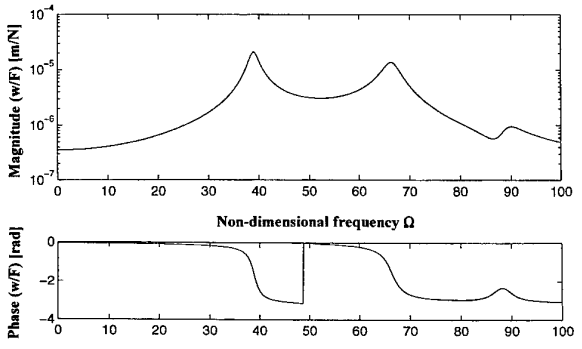

Fig. 3. The transfer receptance and phase for a clamped $[45°/-45°/-45°/45°]$ panel subjected to a unit harmonic force applied at $\xi = -0.37$ and $\eta = 0.43$, and monitored at the panel centre.

To illustrate the efficacy of the current technique, a variety of different symmetric angle ply lay-ups were considered, and the first six non-dimensional natural frequencies, $\Omega = (\rho h\omega^2 b^4/D_0)^{1/2}$, where $D_0 = E_{11}h^3/12(1-\nu_{12}\nu_{21})$, of each of these panels are presented in Table 2. The agreement with Chun and Lam [10] is excellent, especially when it is understood that some of the latter authors' results are not fully converged and therefore will marginally overestimate the correct frequency values. This study also shows that the curvature, as well as stacking sequence and principal fibre direction, influences significantly the general trend of the results at low frequencies. For example, the $[0°/-0°/-0°/0°]$ case is a panel with the principal fibre directions in each layer parallel with a generator of the shell, i.e. it will favour wave motion around the circumference in preference to along its length, and therefore will vibrate with the lowest frequencies of all the cases considered here. However, the $[90°/-90°/-90°/90°]$ case, which might be

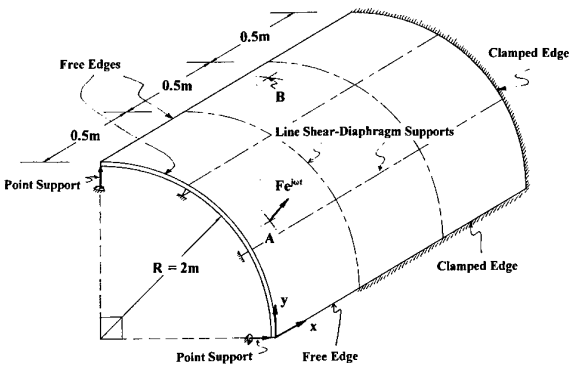

Fig. 4. The geometry and mesh design of a *GLARE* internally supported curved panel.

thought to be the stiffest panel within this study, will not vibrate solely along its lengthwise direction as might be expected, on account of the additional stiffness afforded that direction by the panel curvature. It is also worth noting that the [30°/−30°/−30°/30°] case and the [60°/−60°/−60°/60°] case do not give identical frequencies, as they would for a flat plate. Again, this is because the 60° case has a greater proportion of its principal fibre direction aligned with the curvature than the 30° case, and hence affords the panel more stiffeness in the circumferential sense.

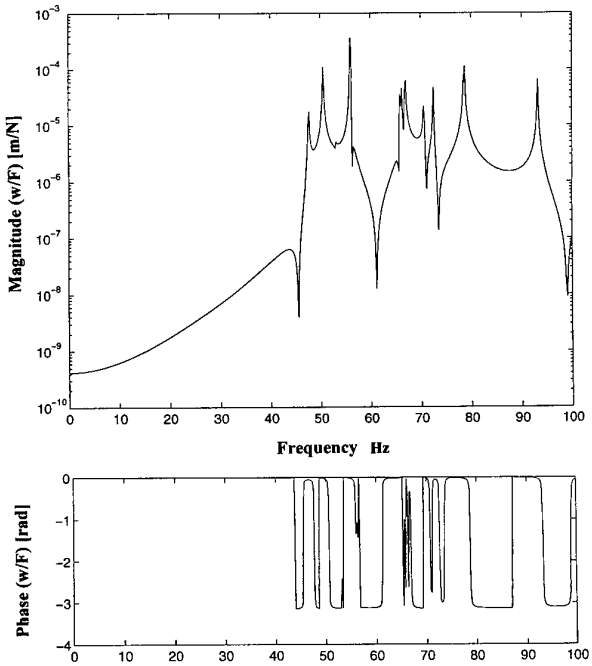

Fig. 5. The transfer receptance and phase for the panel shown in Fig. 4, when it is subjected to a unit harmonic force applied at (0.07 m, 1.217 m) and monitored at (0.89 m, 2.904 m).

Some forced response calculations have been performed for the basic panel with two different symmetric angle-ply lay-ups. The first case concerns a [0°/−0°/−0°/0°] lay-up subjected to a unit harmonic force applied at $\xi = -0.37$ and $\eta = 0.43$. (This location was chosen at random such that it would be unlikely to coincide with any nodal lines.) The (simplified) damping loss factor associated with each layer was 0.05, and the response was measured at the point of application of the force. The magnitude and phase of the point receptance, plotted over a non-dimensional frequency range from 0 to 100, are shown in Fig. 2. The location of the resonant peaks accords with the free vibration results, apart from the absence of mode 4 at $\Omega = 60.55$. It is likely that this particular mode is hardly excited by the applied force, a conjecture borne out by the corresponding 'kink' in the phase diagram in the vicinity of this particular frequency.

The second case concerns a [45°/−45°/−45°/45°] lay-up subjected to a unit harmonic force applied at $\xi = -0.37$ and $\eta = 0.43$, and monitored at the panel mid-point. The magnitude and phase of the transfer receptance are shown in Fig. 3. The location of the resonant peaks again accords with the free vibration results for the modes at $\Omega = 38.89$ and at $\Omega = 66.38$. The remaining modes within the frequency range under consideration all have nodal lines at the centre of the panel, and hence are not observed at this monitoring location.

Further results

Having accumulated some experience with the *h–p* curved laminate element, one further example was considered to illustrate the versatility of the methodology. This concerns the vibrational behaviour of a 1.5 m length of panel with an included angle of 90° and a 2.0 m radius. The panel is divided internally by line shear diaphragms, such that one shell element with $p = 10$ can be used to model each of the nine so-formed sub-panels. See Figure 4. It is assumed the panel is fabricated from *GLARE* with the following lay-up [Al, 0°, Al, 90°, Al]$_S$. The material properties are (i) Aluminium foil: thickness 0.2 mm, E = 72 GPa, ρ = 2780 kg/m^3, ν = 0.30, η_{al} = 0.001; (ii) Glass fibre prepreg: thickness 0.125 mm, E_1 = 50 GPa, E_2 =

4.0 GPa, G_{12} = 1.25 GPa, ρ = 2000 kg/m^3, ν_{12} = 0.35 η_{gfp} = 0.05.

The panel was excited by a unit harmonic force located near the 'free end' at A (0.07 m, 1.217 m), and the response was monitored at B (0.89 m, 2.904 m), where distances are measured relative to the set of global axes indicated in Fig. 4. The magnitude and phase of the transfer receptance are presented in Fig. 5, and clearly show a congregation of resonant peaks

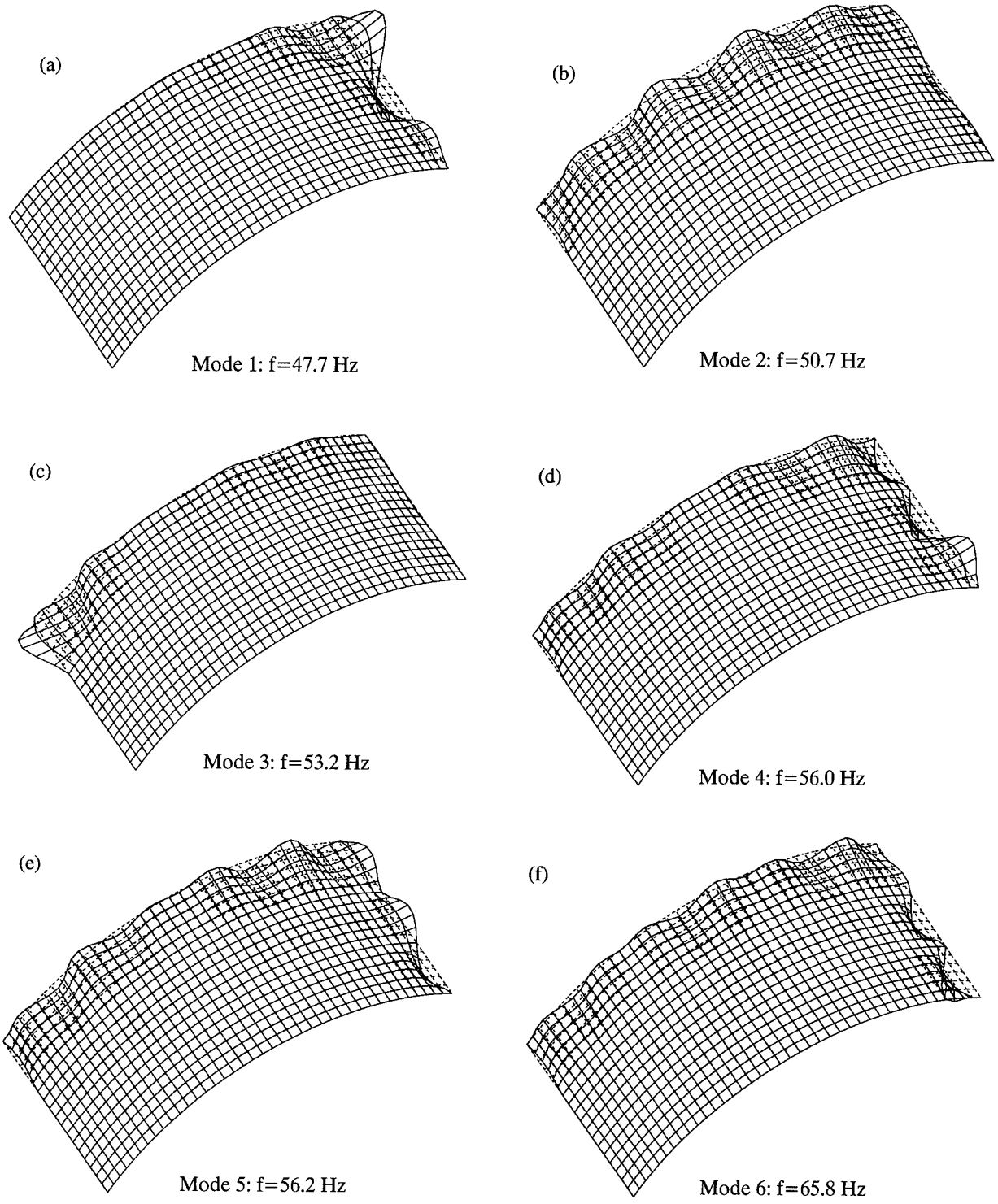

Fig. 6. The first six natural modes of the panel shown in Fig. 4.

just above 50 Hz. The corresponding natural modes are shown in Fig. 6, confirming that a lot of modal activity takes place within a very narrow frequency band width. Clearly, the motion of the panel is dominated by localized modes caused by the internal sub-divisions and supported edges. Only in modes 2, 5 and 6 can anything resembling a more global mode be seen to establish itself around the less highly constrained 'free' edges of the panel.

The usefulness of such a model at the design stage cannot be underestimated when the complex interaction between panel geometry, boundary conditions, radius of curvature, angle ply properties and stacking sequence all have to be considered, and parameter studies undertaken.

CONCLUSIONS

The *h–p* version of the FEM has been developed to study the vibration characteristics of laminated cylindrically curved panels. The element stiffness and mass matrices have been derived and stored in symbolic form for a single, generic element. By removing the need to carry out numerical integration at the element assembly stage every time a new model is constructed, execution times are kept to a minimum, and no rounding errors are introduced. Experience to date indicates that the optimal blend of mesh refinement and polynomial enrichment should be such that the coarsest *h*-mesh commensurate with the boundary conditions is used in conjunction with a high degree of *p*-enrichment. Excellent correlation has been found with the work of other investigators, and considerable savings on the final size of the matrix-eigenvalue frequency problem have been demonstrated. Should a typical sensitivity analysis be required, in which variations of ply angle and stacking sequence are considered the prime design variables, it is essential that an efficient analysis tool is available. The *h–p* methodology advanced here would seem to fulfil this demanding criterion.

ACKNOWLEDGEMENTS

The financial assistance of EPSRC, contract No. GR/J 06306, is gratefully acknowledged. The pictorial illustrations were kindly produced by Mr R. E. W. Creffield, of the Department of Aeronautics and Astronautics.

REFERENCES

1. Bardell, N.S., Dunsdon, J.M. and Langley, R.S., Free vibration analysis of thin rectangular laminated plate assemblies using the *h–p* version of the finite element method. *Composite Struct.*, 1995, **32**, 237–246.
2. Dong, S.B., Free vibration of laminated orthotropic cylindrical shells. *J. Acoust. Soc. Am.*, 1968, **44** (6), 1628–1635.
3. Dong, S.B. and Tso, F.K.W., On a laminated orthotropic shell theory including transverse shear deformation. *J. Appl. Mech.* , 1972, **39**, 1091–1097.
4. Sun, C.T. and Whitney, J.M., Axisymmetric vibrations of laminated composite cylindrical shells. *J. Acoust. Soc. Am.*, 1974, **55** (6), 1238–1246.
5. Sinha, P.K. and Rath, A.K., Vibration and buckling of cross-ply laminated circular cylindrical panels. *Aeronaut. Qt.*, 1975, **26**, 211–218.
6. Bert, C.W. and Kumar, M., Vibration of cylindrical shells of bimodulus composite materials. *J. Sound Vibr.*, 1982, **81**, 107–121.
7. Soldatos, K.P., Free vibrations of antisymmetric angle ply laminated circular cylindrical panels. *Qt. J. Mech. Appl. Math.*, 1983, **36**, 207–221.
8. Soldatos, K.P., A comparison of some shell theories used for the dynamic analysis of cross-ply laminated circular cylindrical panels. *J. Sound Vibr.*, 1984, **97**, 305–319.
9. Narita, Y., Ohta, Y. and Saito, M., Finite element study for natural frequencies of cross-ply laminated cylindrical shells. *Composite Struct.*, 1993, **26**, 55–62.
10. Chun, L. and Lam, K.Y., Dynamic analysis of clamped laminated curved panels. *Composite Struct.*, 1995, **30**, 389–398.
11. Chakravorty, D., Bandyopadhyay, J.N. and Sinha, P.K., Finite element free vibration analysis of point supported laminated composite cylindrical shells. *J. Sound Vibr.*, 1995, **181**, 43–52.
12. Bercin, A.N., Natural frequencies of cross-ply laminated singly curved panels. *Mech. Res. Commun.*, 1996, **23** (2), 165–170.
13. Leissa, A. W., *Vibration of Shells*. NASA SP 288. US Government Printing Office, Washington, DC, 1973.
14. Qatu, M.S., Review of shallow shell vibration research. *Shock Vibr. Dig.*, 1992, **24** (9), 3–15.
15. Love, A. E. H., *A Treatise on the Mathematical Theory of Elasticity*, 1st edn. Cambridge University Press, Cambridge, 1892.
16. Arnold, R.N. and Warburton, G.B., The flexural vibrations of thin cylinders. *Proc. Inst. Mech. Engrs (Series A)*, 1948, **167**, 62–80.
17. Zienkiewicz, O.C., Gago, J.P., De, S.R. and Kelly, D.W., The hierarchical concept in finite element analysis. *Comput. Struct.*, 1983, **16**, 53–65.
18. Peano, A., Hierarchies of conforming finite elements for plane elasticity and plate bending. *Comput. & Math. Appl.*, 1976, **2**, 211–224.
19. Babuska, I. and Guo, B., The *h–p* version of the finite element method, Part I: The basic approximation results. *Computat. Mech.*, 1986, **1**, 21–41.
20. Demkowicz, L., Oden, J.T., Rachowicz, W. and Hardy, O., Toward a universal *h–p* adaptive finite element strategy, Part I. Constrained approximation and data structure. *Comput. Meth. Appl. Mech. Engng*, 1989, **77**, 79–112.

21. Vinson, J. R. & Chou, T.-W., *Composite Materials and Their use in Structures*. Applied Science, London, 1975.
22. Sun, C. T. & Lu, Y. P., *Vibration Damping of Structural Elements*. Prentice-Hall, Englewood Cliffs, NJ, 1995.
23. Char, B. W., Geddes, K. O., Gonnet, G. H., Leong, B. L., Monagan, M. B. & Watt, S. M., *MAPLE V Language Reference Manual*. Springer, Berlin, 1993.

ELSEVIER

Composite Structures Vol. 38, No. 1–4, pp. 463–475, 1997
© 1997 Elsevier Science Ltd. All rights reserved
Printed in Great Britain
0263-8223/97/$17.00 + 0.00

PII:S0263-8223(97)00081-0

Free vibration analysis of coplanar sandwich panels

N. S. Bardell,* J. M. Dunsdon & R. S. Langley

Department of Aeronautics and Astronautics, University of Southampton, Highfield, Southampton SO17 1BJ, Hampshire, UK

A comprehensive vibration study of simple three-layer sandwich plates, based on the *h–p* version of the finite element method, is presented. The methodology incorporates a new set of trigonometric functions to provide the element *p*-enrichment — these functions exhibit good convergence characteristics, and enable the medium frequency regime to be explored at minimum computational expense. Elements may be joined together to model more general coplanar assemblies, and the trade-off between *h*-division and *p*-enrichment is discussed. Excellent agreement has been found with the work of other investigators, and new results are presented for (i) a completely free, symmetric section, rectangular sandwich panel whose core thickness is varied as a function of the overall plate thickness whilst the mass per unit area is maintained constant, and (ii) a cantilevered, T-planform, asymmetric section, sandwich plate. The results from this latter case are compared with those forthcoming from a proprietary finite element package; outstanding agreement is obtained, and a reduction of over 30% in the total number of degrees of freedom is demonstrated. © 1997 Elsevier Science Ltd.

INTRODUCTION

The origins of laminated or sandwich panel construction can be traced to the aircraft industry, where the need for high strength-to-weight ratio structures has been, and always will be, a driving factor in innovative design. In its simplest form, sandwich construction typically comprises three layers of materials: two thin sheets of high-strength material between which a relatively thick core layer of low average strength and density is intercalated. The various types of different faceplates, core materials, and constructional variations found in sandwich structures are described in detail by Allen [1].

This general subject area has been well researched over the past 50 years, and although a comprehensive literature survey is beyond the scope of this paper, some of the more significant publications merit a brief mention at this juncture. The early work on sandwich plates [2–5] was carried out in the 1950s and 1960s long before the availability of large-scale computing, and therefore concentrated on developing and solving increasingly sophisticated sandwich plate equations that arose from generalizing ever more of the governing assumptions. The merit of this analytical approach was the good physical insight it provided into the mechanical behaviour of these structures. By the early 1970s, some results arising from nascent finite element formulations [6] had been produced, and since then, a vast amount of work [7–9] has appeared in this general subject area. Ha [10] and Noor *et al.* [11], have recently produced comprehensive and timely reviews of the entire spectrum of work related to sandwich plates and shells; the latter item contains over 800 relevant references! It is apparent that since the 1970s, the greatest proportion of analysis has been of an approximate nature based on variational approaches, with most of the numerical solutions being determined by one or another type of finite element or finite strip methodology.

The present study has arisen from a larger programme of work intended to explore the use

*Westland Lecturer in Helicopter Engineering.

of sandwich construction as the primary structural medium in the vicinity of future ASTOVL aircraft jet engine exhaust nozzles. For this reason, the scope of the work has deliberately been limited to metallic panels having isotropic faceplates and generally orthotropic honeycomb cores.

Mathematical models of such structural forms must take account of the shear deformable nature of the core material, which, in a displacement-type of formulation, is usually accounted for by the use of additional degrees of freedom (DOF) to represent the shear deformation [10]. It is well known that approximately four conventional finite elements are required to capture one half-wavelength of vibration in a given direction [12] — in a two-dimensional plate model, this would amount to some 16 elements being needed to resolve the fundamental (1,1) mode of a square panel, and over 50 elements to recover the 2,2 mode. Considering that most 'sandwich elements' are often constructed from three separate layers, each with four nodes and three DOF per node, then it soon becomes apparent that the total number of DOF in a model capable of capturing, say, the first 10 modes of vibration, is extremely large, and will most likely prove prohibitively expensive for recursive analyses such as optimization or sensitivity studies, or predicting the response at medium frequencies. It is against this background that the h–p version of the finite element method (FEM) [13–17] is presented, since this formulation promises substantial efficiency gains without loss of accuracy when compared with the conventional FEM. Hence the main purpose, and indeed novelty, of this paper is to validate the use of h–p techniques for predicting the natural frequencies and modes of sandwich panels.

METHOD

Assumptions

As with all work of this kind, a set of initial assumptions [10] must be made with the aim of capturing the essential properties of the physical sandwich panel, whilst permitting an analytically tractable solution to be obtained. For the problem under consideration, this set may be summarized thus:

(i) There is no significant direct strain in the core perpendicular to the plane of the face plates. Hence, both the face plates and the core deflect by the same amount normal to the plate surface.

(ii) There is no significant shear strain across the depths of the face plates. Hence, only the core will carry the shear strain, which is assumed *uniform* through the core depth.

(iiii) The face plates are considered to be isotropic, and to possess both axial and flexural stiffness.

(iv) The core is considered to be generally orthotropic, and to possess both axial and flexural stiffness.

(v) The sandwich plate is assumed to behave elastically, and is subject to small displacements.

In what follows, the lower faceplate will be referred to as layer 1, the core as layer 2, and the upper faceplate as layer 3. The mid-plane of layer 2 is taken as the global reference datum from which all subsequent deformations are measured. (Note that this reference datum will not coincide with the geometric mid-plane of a panel whose faceplates are not of equal thickness.)

Assumed deformation pattern

Consider a particle at a general point x, y, z_2 within layer 2. In its deformed state, the position of this particle is related to the layer 2 mid-plane displacements by

$$u_2(x, y, z_2) = u_0 + z_2\psi \tag{1a}$$

$$v_2(x, y, z_2) = v_0 + z_2\phi \tag{1b}$$

$$w_2(x, y, z_2) = w_0 \tag{1c}$$

where u_0, v_0, and w_0 are the displacements of the layer 2 mid-plane, and ϕ and ψ are the rotations due to shear deformation of layer 2 about the x- and y-axes, respectively (see Fig. 1). Equations (1) can be rendered in matrix format as

$$\begin{bmatrix} u_2 \\ v_2 \\ w_2 \end{bmatrix} = \begin{bmatrix} 1 & 0 & 0 & z_2 & 0 \\ 0 & 1 & 0 & 0 & z_2 \\ 0 & 0 & 1 & 0 & 0 \end{bmatrix} \begin{bmatrix} u_0 \\ v_0 \\ w_0 \\ \psi \\ \phi \end{bmatrix} \tag{1d}$$

i.e.

$$\delta_2 = \mathbf{R}_2 \delta_0 \tag{1e}$$

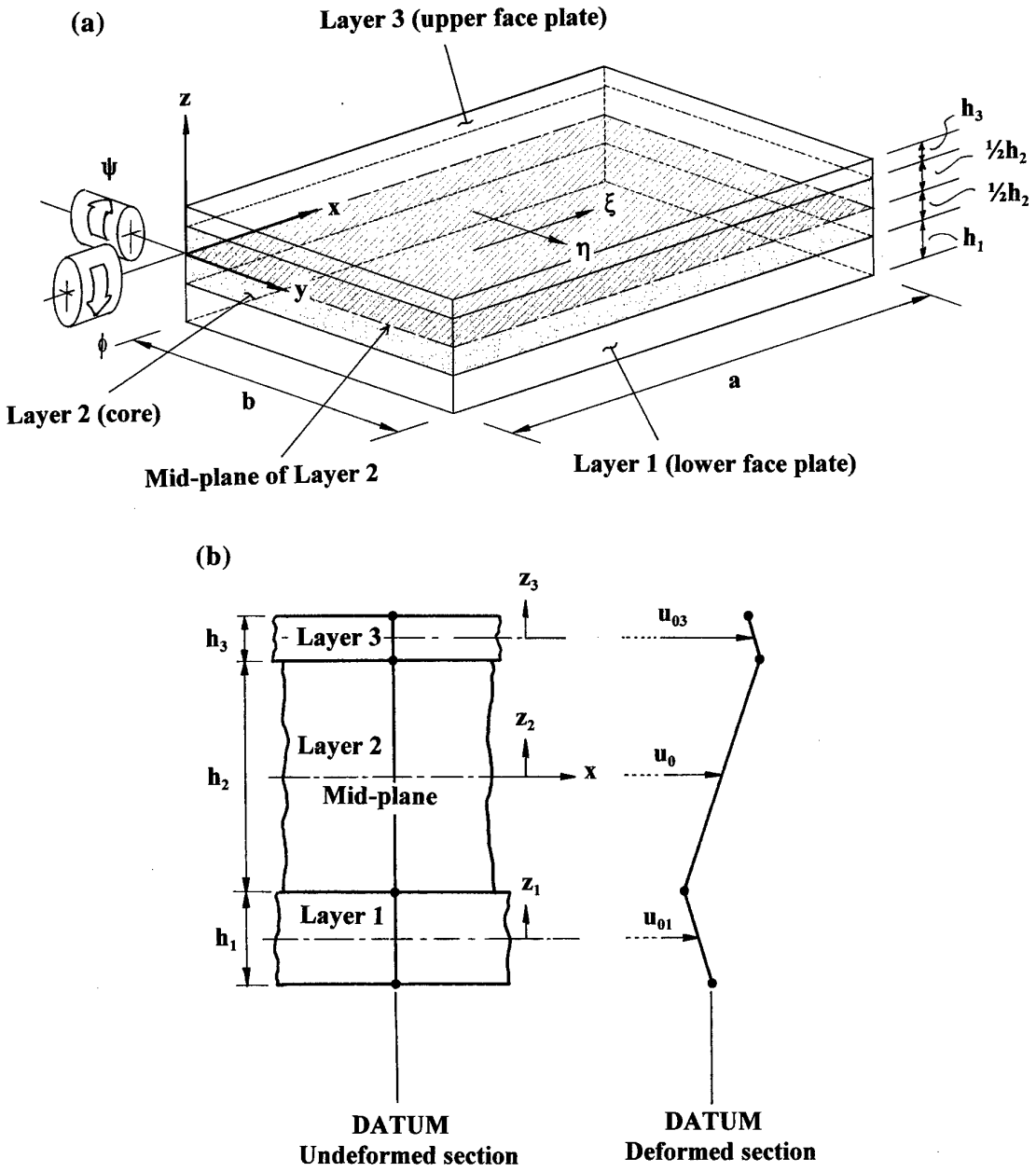

Fig. 1. (a) The sandwich plate element. (b) The assumed deformation pattern (shown in the x-direction).

where δ_0 is the column vector of the layer 2 mid-plane 'master' displacements. By similar reasoning, the displacement of a particle at a general point x, y, z_3 within layer 3 is related to the layer 3 mid-plane by

$$u_3(x, y, z_3) = u_{03} - z_3 \partial w_{03}/\partial x \tag{2a}$$

$$v_3(x, y, z_3) = v_{03} - z_3 \partial w_{03}/\partial y \tag{2b}$$

$$w_3(x, y, z_3) = w_{03} = w_0 \tag{2c}$$

where u_{03}, v_{03}, and w_{03} are the displacements of the layer 3 mid-plane (see Fig. 1). Compatibility between layers 2 and 3 is enforced by ensuring that every particle on the upper surface of layer 2 occupies the same position as every particle on the lower surface of layer 3, i.e., there is no relative slippage permitted between the core and faceplate. Hence, equating eqns (1a–c) with z_2 set equal to $h_2/2$, to eqns (2a–c) with z_3 set equal to $-h_3/2$, respectively, the following compatibility relationship is established

$$\begin{bmatrix} u_{03} \\ v_{03} \\ w_{03} \end{bmatrix} = \begin{bmatrix} 1 & 0 & -\frac{h_3}{2}\frac{\partial}{\partial x} & h_2 & 0 \\ 0 & 1 & -\frac{h_3}{2}\frac{\partial}{\partial y} & 0 & h_2 \\ 0 & 0 & 1 & 0 & 0 \end{bmatrix} \begin{bmatrix} u_0 \\ v_0 \\ w_0 \\ \psi \\ \phi \end{bmatrix}; \tag{3a}$$

$$\begin{bmatrix} u_{03} \\ v_{03} \\ w_{03} \end{bmatrix} = \begin{bmatrix} 1 & 0 & -\frac{h_3}{a}\frac{\partial}{\partial \xi} & h_2 & 0 \\ 0 & 1 & -\frac{h_3}{b}\frac{\partial}{\partial \eta} & 0 & h_2 \\ 0 & 0 & 1 & 0 & 0 \end{bmatrix} \begin{bmatrix} u_0 \\ v_0 \\ w_0 \\ \psi \\ \phi \end{bmatrix} \tag{3b}$$

The latter expression is obtained when the element-local, non-dimensional, coordinates $\xi = 2x/a - 1$ and $\eta = 2y/b - 1$ are introduced. Equation (3b) can be written more compactly as

$$\delta_{03} = \mathbf{R}_3 \delta_0 \tag{3c}$$

In a similar manner, enforcing compatibility between layers 2 and 1 yields

$$\begin{bmatrix} u_{01} \\ v_{01} \\ w_{01} \end{bmatrix} = \begin{bmatrix} 1 & 0 & \frac{h_1}{2}\frac{\partial}{\partial x} & -h_2 & 0 \\ 0 & 1 & \frac{h_1}{2}\frac{\partial}{\partial y} & 0 & -h_2 \\ 0 & 0 & 1 & 0 & 0 \end{bmatrix} \tag{4a}$$

$$\begin{bmatrix} u_{03} \\ v_{03} \\ w_{03} \end{bmatrix} = \begin{bmatrix} 1 & 0 & \frac{h_1}{a}\frac{\partial}{\partial \xi} & -h_2 & 0 \\ 0 & 1 & -\frac{h_1}{b}\frac{\partial}{\partial \eta} & 0 & -h_2 \\ 0 & 0 & 1 & 0 & 0 \end{bmatrix} \begin{bmatrix} u_0 \\ v_0 \\ w_0 \\ \psi \\ \phi \end{bmatrix} \tag{4b}$$

Equation (4b) can be written more compactly as

$$\delta_{01} = \mathbf{R}_1 \delta_0 \tag{4c}$$

Strain–displacement relationships

The strain–displacement relationships [18], rendered in terms of the element-local, non-dimensional, coordinates for layers 1 and 3, related to their own mid-planes, are

$$\begin{bmatrix} \varepsilon_{xx} \\ \varepsilon_{yy} \\ \gamma_{xy} \end{bmatrix}_{1,3} = \begin{bmatrix} \frac{2}{a}\frac{\partial}{\partial\xi} & 0 & -z_{1,3} & \frac{4}{a^2}\frac{\partial^2}{\partial\xi^2} \\ 0 & \frac{2}{b}\frac{\partial}{\partial\eta} & -z_{1,3} & \frac{4}{b^2}\frac{\partial^2}{\partial\eta^2} \\ \frac{2}{b}\frac{\partial}{\partial\eta} & \frac{2}{a}\frac{\partial}{\partial\xi} & -z_{1,3} & \frac{8}{ab}\frac{\partial^2}{\partial\xi\partial\eta} \end{bmatrix} \begin{bmatrix} u_{01,03} \\ v_{01,03} \\ w_{01,03} \end{bmatrix} \tag{5a}$$

$$\varepsilon_{1,3} = \mathbf{F}\delta_{01,03} \tag{5b}$$

In order to relate the faceplate displacements to the core mid-plane displacements, it is necessary to use eqns (3c) and (4c) such that $\varepsilon_1 = \mathbf{F}\mathbf{R}_1\delta_0$ and $\varepsilon_3 = \mathbf{F}\mathbf{R}_3\delta_0$, i.e.

$$\varepsilon_1 = \Lambda_1 \delta_0 \tag{6a}$$

and

$$\varepsilon_3 = \Lambda_3 \delta_0 \tag{6b}$$

where $\Lambda_1 = \mathbf{F}\mathbf{R}_1$ and $\Lambda_3 = \mathbf{F}\mathbf{R}_3$. The strain–displacement relationship for the shear deformable core can be written [18] in terms of the element-local, non-dimensional, coordinates as

$$\begin{bmatrix} \varepsilon_{xx} \\ \varepsilon_{yy} \\ \gamma_{yz} \\ \gamma_{xz} \\ \gamma_{xy} \end{bmatrix}_2 = \begin{bmatrix} \frac{2}{a}\frac{\partial}{\partial\xi} & 0 & 0 & z_2\frac{2}{a}\frac{\partial}{\partial\xi} & 0 \\ 0 & \frac{2}{b}\frac{\partial}{\partial\eta} & 0 & 0 & z_2\frac{2}{b}\frac{\partial}{\partial\eta} \\ 0 & 0 & \frac{2}{b}\frac{\partial}{\partial\eta} & 0 & 1 \\ 0 & 0 & \frac{2}{a}\frac{\partial}{\partial\xi} & 1 & 0 \\ \frac{2}{b}\frac{\partial}{\partial\eta} & \frac{2}{a}\frac{\partial}{\partial\xi} & 0 & z_2\frac{2}{b}\frac{\partial}{\partial\eta} & z_2\frac{2}{a}\frac{\partial}{\partial\xi} \end{bmatrix} \begin{bmatrix} u_0 \\ v_0 \\ w_0 \\ \psi \\ \phi \end{bmatrix} \tag{7a}$$

$$\varepsilon_2 = \Lambda_2 \delta_0 \tag{7b}$$

Layer constitutive relations

The standard constitutive relations [18] for the isotropic face plates, and the generally orthotropic core, are written as follows:

$$\begin{bmatrix}\sigma_{xx}\\ \sigma_{yy}\\ \tau_{xy}\end{bmatrix}_{1,3} = \begin{bmatrix} \dfrac{E}{(1-\nu^2)} & \dfrac{\nu E}{(1-\nu^2)} & 0 \\ \dfrac{\nu E}{(1-\nu^2)} & \dfrac{E}{(1-\nu^2)} & 0 \\ 0 & 0 & G \end{bmatrix}_{1,3} \begin{bmatrix}\varepsilon_{xx}\\ \varepsilon_{yy}\\ \gamma_{xy}\end{bmatrix}_{1,3}$$

$$\begin{bmatrix}\sigma_{xx}\\ \sigma_{yy}\\ \tau_{yz}\\ \tau_{zx}\\ \tau_{xy}\end{bmatrix}_2 = \begin{bmatrix} \dfrac{E_x}{(1-\nu_{xy}\nu_{yx})} & \dfrac{\nu_{yx}E_x}{(1-\nu_{xy}\nu_{yx})} & 0 & 0 & 0 \\ \dfrac{\nu_{xy}E_y}{(1-\nu_{xy}\nu_{yx})} & \dfrac{E_y}{(1-\nu_{xy}\nu_{yx})} & 0 & 0 & 0 \\ 0 & 0 & G_{yz} & 0 & 0 \\ 0 & 0 & 0 & G_{zx} & 0 \\ 0 & 0 & 0 & 0 & G_{xy} \end{bmatrix} \begin{bmatrix}\varepsilon_{xx}\\ \varepsilon_{yy}\\ \gamma_{yz}\\ \gamma_{zx}\\ \gamma_{xy}\end{bmatrix}_2$$

$$\sigma_{1,3} = \mathbf{D}_{1,3}\varepsilon_{1,3} \tag{8a}$$

and

$$\sigma_2 = \mathbf{D}_2\varepsilon_2 \tag{8b}$$

Choice of assumed displacement functions; background to the *h–p* version of the FEM

The *h–p* methodology adopted is similar to that presented elsewhere by the authors [19], so only the essential details are given here. In brief, the *h–p* version of the FEM may be regarded as the marriage of the conventional *h*-version and *p*-version; convergence is sought by simultaneously refining the mesh and increasing the degree of the elements [13–17]. For the type of problem under consideration here, in which the motion in all five DOF is coupled, it is advantageous to represent all the displacement fields by the *same* set of assumed modes. This greatly reduces the computational effort required to calculate the element stiffness and mass matrices, and simplifies the element assembly process.

To this end, an ascending hierarchy of special trigonometric functions [20], used in conjunction with Hermite cubics, will furnish a complete set of admissible displacement functions $f(\xi$ or $\eta)$ (see Table 1). The motivation for using trigonometric, as opposed to the usual *K*-orthogonal polynomial [19] hierarchical functions, is on account of their improved performance when modelling medium frequency deformations [21].

The hierarchical modes contribute only to the internal displacement field of the element, and do not therefore affect the displacement along the element edge or at the element nodes. However, products formed between any of the trigonometric functions and the Hermite cubics will constitute what amounts to edge freedoms along the element boundaries. Adjacent elements may be joined by ensuring compatibility of both nodal and edge displacements. The use of what effectively amounts to C_1 continuity functions to describe the in-plane and shear deformation displacement fields — which possess C_0 continuity — is justified on the grounds that no attempt is made to enforce *first derivative continuity* of any of these quantities across an element interface.

Hence the in-plane, out-of-plane, and shear deformation master displacements can be represented as the following series expressions

$$u_0(\xi, \eta) = \sum_{rx=1}^{p_{ux}} \sum_{sx=1}^{p_{uy}} X_{rx,sx} f_{rx}(\xi) f_{sx}(\eta) \tag{9a}$$

$$v_0(\xi, \eta) = \sum_{ry=1}^{p_{vx}} \sum_{wy=1}^{p_{vy}} Y_{ry,sy} f_{ry}(\xi) f_{sy}(\eta) \tag{9b}$$

$$w_0(\xi, \eta) = \sum_{rz=1}^{p_{wx}} \sum_{sz=1}^{p_{wy}} Z_{rz,sz} f_{rz}(\xi) f_{rz}(\eta) \tag{9c}$$

$$\psi(\xi, \eta) = \sum_{r\psi=1}^{p_{\psi x}} \sum_{s\psi=1}^{p_{\psi y}} \Psi_{r\psi,s\psi} f_{r\psi}(\xi) f_{s\psi}(\eta) \tag{9d}$$

$$\phi(\xi, \eta) = \sum_{r\phi=1}^{p_{\phi x}} \sum_{s\phi=1}^{p_{\phi y}} \Phi_{r\phi,s\phi} f_{r\phi}(\xi) f_{s\phi}(\eta) \tag{9e}$$

This can be expressed in a more compact matrix notation as

$$\delta_0 = \mathbf{Nq} \tag{9f}$$

where $\boldsymbol{q}^T = [X_{rx,sx}, Y_{ry,sy}, Z_{rz,sz}, \Psi_{r\varphi,s\varphi}, \Phi_{r\phi,s\phi}]$, and $\boldsymbol{N}$ is a rectangular matrix with five rows.

Table 1. The first ten assumed displacement functions

Function number	Hermite cubics set $f_r(\xi)$	Trigonometric set $f_r(\xi)$
r=1	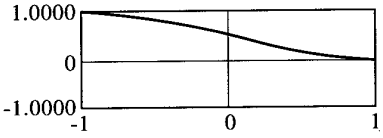	r=5 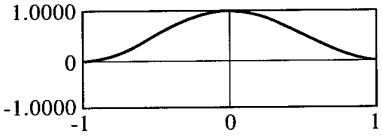
r=2	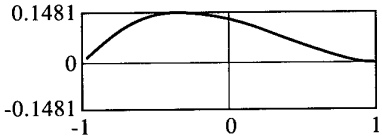	r=6 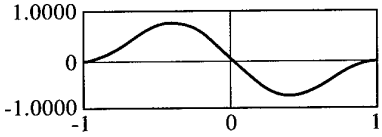
r=3	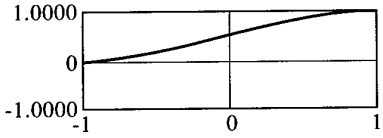	r=7 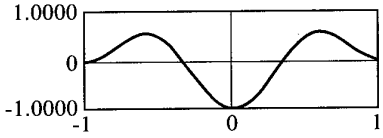
r=4	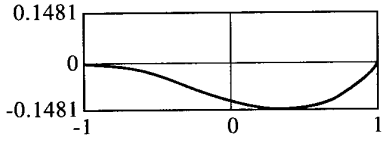	r=8 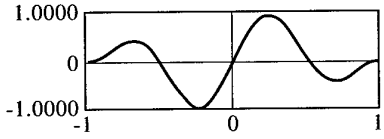
	For r>4, the following set of trigonometric functions is used as hierarchical functions.	r=9 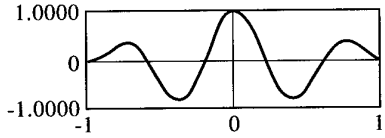
	$f_r(\xi) = \sin\left(\frac{\pi}{2}(r-4)(\xi+1)\right) \sin\left(\frac{\pi}{2}(\xi+1)\right)$	r=10 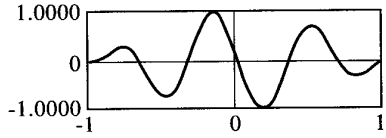

Panel energies

The strain energy of the panel, which is given by

$$U = \frac{1}{2} \sum_{i=1}^{3} \int_{V_i} \varepsilon_i^{\mathrm{T}} \mathbf{D}_i \varepsilon_i \, \mathrm{d}V_i \tag{10}$$

can be constructed from eqns (1)–(9) thus

$$U = \frac{1}{2} \mathbf{q}^{\mathrm{T}} \left[\sum_{i=1}^{3} \int_{-1}^{+1} \int_{-1}^{+1} \int_{-h_i/2}^{+h_i/2} (\Lambda_i N)^{\mathrm{T}} \mathbf{D}_i \Lambda_i \mathbf{N} \frac{ab}{4} \, \mathrm{d}z_i \, \mathrm{d}\xi \, \mathrm{d}\eta \right] \mathbf{q} \tag{11}$$

The terms within parentheses are recognized as the element stiffness matrix $\mathbf{K}^E$.

Similarly, the kinetic energy of the panel element is given by

$$T = \frac{1}{2} \sum_{i=1}^{3} \int_{V_i} \rho_i \dot{\delta}_i^{\mathrm{T}} \dot{\delta}_i \, \mathrm{d}V_i \tag{12}$$

Substituting eqns (1e), (3c), (4c) and (9) into eqn (12) yields

$$T = \frac{1}{2} \dot{\mathbf{q}}^{\mathrm{T}} \left[\sum_{i=1}^{3} \int_{-1}^{+1} \int_{-1}^{+1} \int_{-h_i/2}^{+h_i/2} \rho_i (\mathbf{R}_i \mathbf{N})^{\mathrm{T}} \mathbf{R}_i \mathbf{N} \frac{ab}{4} \, \mathrm{d}z_i \, \mathrm{d}\xi \, \mathrm{d}\eta \right] \dot{\mathbf{q}} \tag{13}$$

The terms within parentheses are recognized as the element mass matrix $\mathbf{M}^E$. Note that in-plane inertia and rotary deformation effects are contained within this expression on account of the coupling that exists between the various displacements characterizing each layer.

The matrix multiplication and integration required to evaluate the element stiffness and mass matrices shown in eqns (11) and (13) was performed numerically using a Gauss–Legendre quadrature scheme. This scheme, which was implemented using commercially available software [22], dynamically allocates the number of integration points required to ensure a predetermined level of accuracy.

Interelement compatibility is achieved simply by matching the appropriate generalized 'master' coordinates at common element nodes and along common edges, as explained earlier. This procedure ensures the elements are fully conforming — in the conventional sense — and, moreover, facilitates assembly of the global stiffness and mass matrices $\mathbf{K}^G$ and $\mathbf{M}^G$.

Boundary conditions

Specific boundary conditions may be applied to the model simply by removing those rows/columns from $\mathbf{K}^G$ and $\mathbf{M}^G$ which correspond to fixed 'master' degrees of freedom — hence any combination of shear diaphragm, simple support, clamped or free edges, or corner point supports, can be accommodated in the analysis. In the current work, the support conditions are imposed at the layer 2 mid-plane, so some care has to be taken in defining exactly what each category means. A shear diaphragm permits an in-plane translation across the support, and full rotation about the mid-plane, but prevents w-wise motion normal to it; a simple support permits full rotation of the panel about its mid-plane, but prevents all three translational freedoms there; a clamped support prevents all three translational freedoms, and shear deformation within layer 2.

Equations of motion

By assuming simple harmonic motion, and the absence of any forcing agency, the governing equations of motion for free vibration can be obtained by deriving Lagrange's equation from the expressions already obtained for the strain and kinetic energies of the complete model. This yields the standard matrix-eigenvalue form of the problem

$$[\mathbf{K}^G - \omega^2 \mathbf{M}^G]\{\mathbf{q}\} = \mathbf{0} \tag{14}$$

The solution to eqn (14) gives the natural frequencies in radian units, rendered here in an appropriate form depending on the analysis. Corresponding to each eigenvalue is an eigenvector which may be used in conjunction with eqn (9) to recover the associated displacement of each element in the model, and hence the complete mode of the panel under consideration.

COMPARISON WITH OTHER WORK

Convergence study

In order to gain confidence with the h–p formulation presented here, it is important to validate the convergence behaviour of the model. The example chosen as a suitable benchmark was presented by Zhou and Li [9], who determined the natural frequencies of an aluminium honeycomb sandwich panel with all four edges simply supported by using a spline finite point method (SFPM). The panel dimensions are $a = 182.9$ cm and $b = 121.9$ cm, giving an aspect ratio of $a/b = 1.5$. The material properties are quoted in Table 2a.

Three different trade-off studies were conducted using various combinations of the h- and p-parameters. These results are presented in Table 2b, alongside the results of Zhou and Li [9], and some further, exact, and experimental, results presented by Raville and Veng [23]. It is immediately obvious that the results from the current method converge monotonically and from above, as expected, and that very good agreement is obtained with the work of other investigators — the current results deviate from the exact solution by a maximum of only 1.7% in the sixth mode. The relatively slow convergence of the low frequency results stems from the use of the trigonometric assumed displacement functions; this feature has been noted by their progenitors [20]. Clearly, the single super-element, with the highest possible amount of p-enrichment, can be seen to give the most accurate results for the least overall number of DOF. This finding is commensurate with previous work in this subject area [19]. Considering that Zhou and Li [9] used specific beam modes as their assumed displacement functions, and would have to generate different sets for different combinations of boundary conditions, the versatility of the present h–p methodology is clearly self-evident. This exercise, and other such studies not reported here, give confidence in the validity of the h–p formulation as applied to the title problem.

Further results

Two further examples are now presented to illustrate the versatility of the methodology, and to add some new results to the available literature. In both cases, the material properties quoted in Table 2a are used, i.e. the structures are both aluminium honeycomb sandwich panels, with the core ribbon direction aligned with the element y-axis.

Example (1): Consider a solid, uniform, isotropic, rectangular panel ($a = 1$ m, $b = 0.5$ m), of total thickness 5 mm, with all four edges completely free. (The free edge case is one of the more challenging test cases for any approximate methodology, and has been chosen here in order to fill this particular lacuna.) The mass per unit area of this panel is 13.84 kg/m^2. A parameter study was conducted to examine the effect on the panel's natural frequencies of increasing the core depth as a percentage of its total thickness, whilst maintaining a constant mass. For this study, the face plate thicknesses were considered equal, so $h_1 = h_3$.

Let α represent the fraction of the core depth relative to the total thickness. Then $h_2 = \alpha(2h_1+h_2)$ or, after a little manipulation, $h_2 = 2\alpha h_1/(1-\alpha)$. Keeping the mass per unit area constant guarantees that $2\rho_1 h_1 + \rho_2 h_2 = 13.84$, which, on substituting for h_2, means that $2\rho_1 h_1 + 2\rho_2 \alpha h_1/(1-\alpha) = 13.84$, or, $h_1 = 6.92(1-\alpha)/[\rho_1(1-\alpha)+\rho_2\alpha]$. By varying α between 0 and 0.95, it is possible to see what

Table 2a. Material properties for an aluminium honeycomb sandwich panel

	Thickness (mm)	Elastic modulus (GPa)	Poisson's ratio	Shear modulus (GPa)			Density (kg/m^3)
Layers 1 & 3	0.41	68.95	0.33	25.92			2768
Layer 2	6.35	0	0	$G_{xy}=0$	$G_{zx}=0.0517$	$G_{yz}=0.1345$	121.8

effect the introduction of a particular depth of honeycomb core will have on the natural frequencies of this panel.

Figure 2 shows the first six elastic frequencies (the rigid-body modes are not included in this numbering scheme) in cycles per second, plotted as a (continuous) function of α. What is immediately apparent is the rise in frequency in all six modes as the percentage depth of the core increases. This is due to the relative increase in the flexural stiffness of the plate caused by the increasing depth of sandwich core. To quantify this, if it was desired to raise the fundamental frequency of the original solid plate (25.8 Hz) without increasing the structural mass, it would be germane to replace the solid plate by a sandwich panel — the fundamental frequency could be *doubled* by making the thickness of both face plates 2.4 mm and the core depth 3.2 mm (corresponding to $\alpha = 0.4$), or increased *10-fold* by making the thickness of both face plates 1.6 mm and the core depth 38.2 mm (corresponding to $\alpha = 0.92$). Similar improvements can be obtained for the higher modes, with greater frequency rises being obtained for greater core depth fractions. Clearly, there is some scope here to 'design out' unwanted resonances, knowing the operating environment of the panel. This example clearly shows the reason why sandwich construction is so highly favoured by the aerospace industry when dealing with weight-critical applications. (Note that the current model cannot be relied on to produce accurate results as $\alpha \to 1$ because certain assumptions no longer remain valid.)

Example (2): Consider the T-planform, cantilevered, honeycomb sandwich plate shown in Fig. 3. The top and bottom face plates are of

Table 2b. Convergence properties of the current *h–p* method. Simply supported honeycomb sandwich panel after [9]. Material properties are given in Table 2a

Current $h-p$ version h=1		Current $h-p$ version h=4		Current $h-p$ version h=9		[9] SFPM	[23] Exact	[23] Experiment
	f_1=23.30		f_1=23.18		f_1=23.20	23.29	23	—
	f_2=44.98		f_2=44.27		f_2=44.37	44.47	44	45
p=2	f_3=73.52	p=1	f_3=71.59	p=0	f_3=71.80	71.15	71	69
120 DOF	f_4=89.12	248 DOF	f_4=80.43	260 DOF	f_4=83.56	78.78	80	78
	f_5=93.53		f_5=91.64		f_5=91.94	91.57	91	92
	f_6=133.72		f_6=125.95		f_6=128.26	125.10	126	125
	f_1=23.11		f_1=23.10		f_1=23.09			
	f_2=44.01		f_2=44.02		f_2=43.98			
p=8	f_3=71.14	p=3	f_3=71.15	p=2	f_3=71.12			
588 DOF	f_4=78.54	608 DOF	f_4=78.60	608 DOF	f_4=78.52			
	f_5=91.03		f_5=91.06		f_5=91.00			
	f_6=124.15		f_6=124.22		f_6=124.09			
	f_1=23.07		f_1=23.07		f_1=23.05			
	f_2=43.94		f_2=43.94		f_2=43.91			
p=12	f_3=71.08	p=5	f_3=71.09	p=4	f_3=71.06			
1100 DOF	f_4=78.42	1128 DOF	f_4=78.43	1844 DOF	f_4=78.37			
	f_5=90.90		f_5=90.91		f_5=90.85			
	f_6=123.92		f_6=123.93		f_6=123.82			

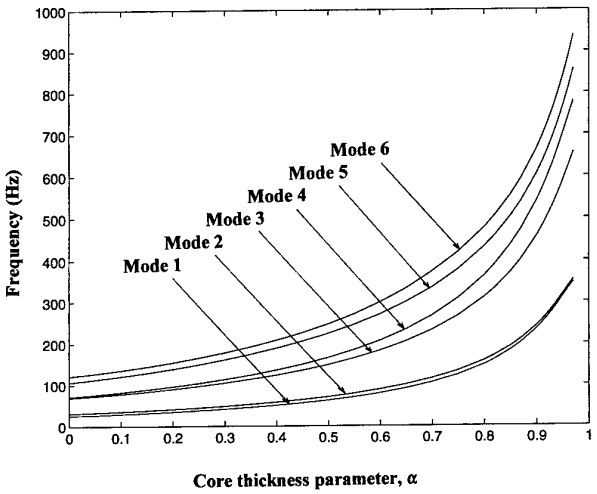

Fig. 2. Parameter study to examine the effect on the first six natural frequencies of a completely free rectangular panel by increasing the sandwich core depth as a fraction, α, of its total thickness, whilst maintaining a constant mass.

thickness 2 and 4 mm, respectively, while the core depth is 30 mm. To determine the first six natural frequencies and modes of this structure represents a significantly more challenging problem than has hitherto been reported, and indeed was chosen to demonstrate the general efficacy of the current technique. An *h–p* model was constructed using just four *h*-elements (denoted by the dashed lines in Fig. 3), each boosted to $p = 8$, since experience indicated that this level of refinement should produce fully converged frequency results for the low frequency modes. The total number of DOF used in this model was 2460.

In order to provide some measure of validation and confidence in the *h–p* results, a detailed model of this panel was also constructed using the proprietary finite element package ANSYS [24]. The face plates and core

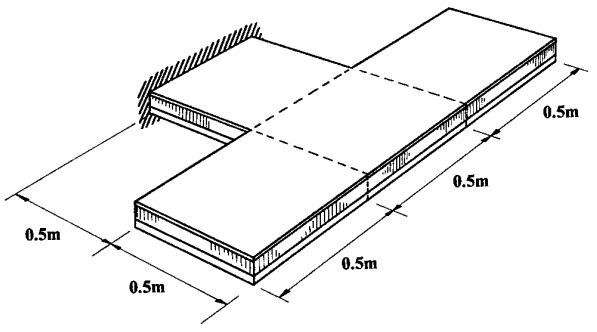

Fig. 3. Schematic of a T-planform, asymmetric section, cantilevered, sandwich panel.

were modelled individually from quadrilateral brick elements, each having eight nodes with three DOF per node, giving each 'sandwich' element a total of 48 DOF. Some 256 elements (3460 DOF) were necessary to obtain converged results for the panel.

Results from both methodologies are shown in Fig. 4. Outstanding agreement is obtained across all six modes, with less than 1% difference being observed between the *h–p* and ANSYS results. Perhaps of greater significance, however, is the fact that the *h–p* results were obtained using some 30% fewer DOF than the ANSYS model. The benefit of such savings, when translated into reduced computational costs, could become important when modelling sandwich-type structures significantly more complicated than the example presented here.

CONCLUSIONS

A detailed formulation of an *h–p* sandwich panel finite element, based on a novel set of trigonometric assumed displacement functions, has been presented in this paper. The convergence properties of this element have been established for different combinations of the *h*- and *p*-parameters, thereby assuring its integrity for more general use. To illustrate the efficacy of the method, two new sets of results have been added to the literature: (i) a detailed parameter study that examined the effect on the natural frequencies of a completely free panel by increasing the core depth as a percentage of its total thickness, while maintaining a constant mass, and (ii) the determination of the first six natural frequencies and modes for a T-planform, asymmetric section, cantilevered, honeycomb sandwich plate. These studies have shown, amongst other things, that the *h–p* formulation offers considerable savings on the final size of matrix–eigenvalue problem when compared with conventional finite element-type analyses. This feature could usefully be employed should typical parameter studies, or repetitive calculations arising from an optimization algorithm, be required at the design stage.

ACKNOWLEDGEMENTS

The financial assistance of EPSRC, contract number GR/J 06306, is gratefully acknow-

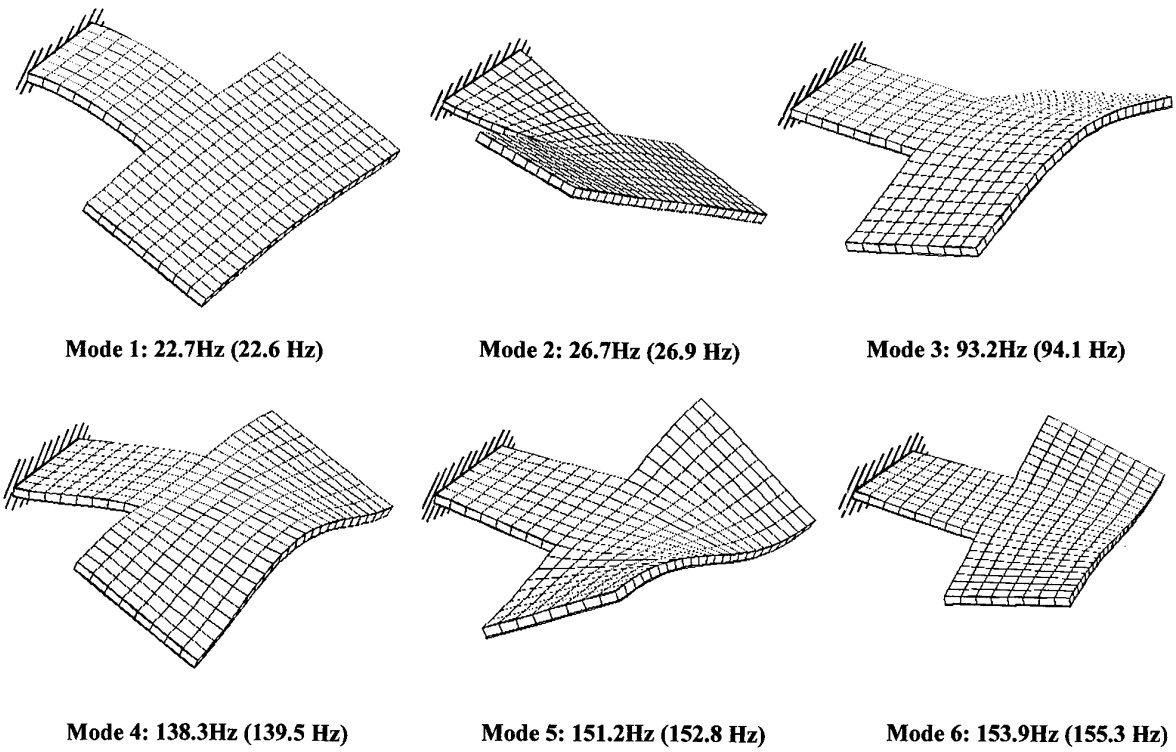

Fig. 4. The first six natural frequencies and modes of the sandwich panel illustrated in Fig. 3 determined by the current h–p methodology. ANSYS results are shown in parentheses.

ledged. Mr P. R. Cunningham and Mr R. E. W. Creffield, of the Department of Aeronautics and Astronautics, kindly assisted in the preparation of the ANSYS model and the illustrations, respectively.

REFERENCES

1. Allen, H. G., *Analysis and Design of Sandwich Panels*. Pergamon Press, Oxford, 1969.
2. Reissner, E., Small bending and stretching of sandwich type shells. NACA report 975, 1950.
3. Mindlin, R. D., Flexural vibrations of elastic sandwich plates. Columbia University technical report 35, 1959.
4. Yu, Y.Y., Flexural vibrations of elastic sandwich panels. *J. Aeronaut. Space Sci.,* 1960, **27**, 272–282.
5. Mead, D. J. and Pretlove, A. J., On the vibrations of cylindrically curved elastic sandwich plates. Part I — With the solution for flat plates; Part II — With the solution for cylindrical plates. Aeronautical Research Council reports and memoranda, No. 3363, 1962.
6. Ahmed, K.M., Static and dynamic analysis of sandwich structures by the method of finite elements. *J. Sound Vibr.,* 1971, **18**, (1), 75–91.
7. Soovere, J., Dynamic response of acoustically excited stiffened honeycomb panels. University of Southampton, PhD thesis, 1984.
8. Lee, L.J. and Fan, Y.J., Bending and vibration analysis of composite sandwich plates. *Comput. Struct.,* 1995, **60**, (1), 103–112.
9. Zhou, H.B. and Li, G.Y., Free vibration analysis of sandwich plates with laminated faces using spline finite point method. *Comput. Struct.,* 1996, **59**, (2), 257–263.
10. Ha, K.H., Finite element analysis of sandwich plates: an overview. *Comput. Struct.,* 1990, **37**, (4), 397–403.
11. Noor, A.K., Burton, W.S. and Bert, C.W., Computational models for sandwich panels and shells. *Appl. Mech. Rev.,* 1996, **49**, (3), 155–199.
12. Zienkiewicz, O. C., *The Finite Element Method*, 3rd edn. McGraw-Hill, 1977.
13. Zienkiewicz, O.C., Gago, J.P., De, S.R. and Kelly, D.W., The hierarchical concept in finite element analysis. *Comput. Struct.,* 1983, **16**, (1–4), 53–65.
14. Peano, A., Hierarchies of conforming finite elements for plane elasticity and plate bending. *Comput. Math. Applic.,* 1976, **2**, 211–224.
15. Guo, B. and Babuska, I., The h–p version of the finite element method, Part 1: The basic approximation results. *Comput. Mech.,* 1986, **1**, 21–41.
16. Guo, B. and Babuska, I., The h–p version of the finite element method, Part 2: General results and applications. *Comput. Mech.,* 1986, **1**, 203–220.
17. Demkowicz, L., Oden, J.T., Rachowicz, W. and Hardy, O., Toward a universal h–p adaptive finite element strategy, Part 1: Constrained approximation and data structure. *Comput. Meth. Appl. Mech. Engng,* 1989, **77**, 79–112.
18. Soedel, W., *Vibrations of Shells and Plates*. Marcel Dekker, New York, 1981.
19. Bardell, N.S., Dunsdon, J.M. and Langley, R.S., Free vibration analysis of thin rectangular laminated plate assemblies using the h–p version of the finite element method. *Composite Struct.,* 1995, **32**, 237–246.

20. Beslin, O. and Nicolas, J., A hierarchical functions set for predicting very high order plate bending modes with any boundary conditions. Journal of Sound and Vibration, 1997, **202**, 633–655.
21. West, L. J., Bardell, N. S., Dunsdon, J. M. and Loasby, P. M., Some limitations associated with the use of *K*-orthogonal polynomials in hierarchical versions of the finite element method. *Proceedings of the Sixth International Conference on Recent Advances in Structural Dynamics*, 1997, Vol. I, 217–232.
22. NAG FORTRAN Library D01 AKF Mark 16, NAG Ltd, Wilkinson House, Jordan Hill Road, Oxford, UK.
23. Raville, M.E. and Veng, C.E.S., Determination of natural frequencies of vibration of a sandwich plate. *Exp. Mech.,* 1967, **7**, 490–493.
24. ANSYS Inc., 201 Johnson Road, Houston, PA 15342-1300, USA.

ELSEVIER

Composite Structures Vol. 38, No. 1–4, pp. 477–481, 1997
© 1997 Elsevier Science Ltd. All rights reserved
Printed in Great Britain
0263-8223/97/$17.00 + 0.00

PII:S0263-8223(97)00082-2

Free vibration and flutter of damaged composite panels

R. M. V. Pidaparti

Department of Mechanical Engineering, Purdue University at Indianapolis (IUPUI), IN 46202, USA

A finite element method is investigated for studying the free vibration and supersonic flutter analysis of arbitrary damaged composite panels. The finite element method employs a 48 degrees of freedom (DOF) general plate element and uses the classical lamination theory, microstructural continuum damage theory and linearized piston theory. Two different damage models were investigated. Finite element results are obtained to illustrate the effect of damage on the eigenvalues and flutter boundaries. The results obtained indicate that between the two models considered, damage model 1 has a strong influence on both free vibration and flutter boundaries. © 1997 Elsevier Science Ltd.

INTRODUCTION

Composite materials are being used in aerospace engineering applications to minimize weight and increase stiffness by tailoring the structures, and also to meet performance requirements. Composite structures develop damage in the form of matrix cracks, delamination, fiber-matrix debond and fiber breakage due to the manufacturing process or fatigue loading during service. It is important to study the flutter behavior of such damaged panels due to the complex interaction of aerodynamic, inertial and structural forces. Flutter takes place at a critical air speed and it is important to capture this accurately for damaged panel configurations otherwise it might lead to catastrophic failures.

Several authors have investigated the flutter behavior of undamaged panels, see for example, Refs [1–3], among others. The flutter behavior of composite plates and shells was recently studied by Pidaparti and Yang [4] and Liaw and Sun [5] using general plate and shell finite elements. Mei [6] studied non-linear and temperature effects on the panel flutter. Chen and Lin [7] studied the supersonic flutter behavior of isotropic thin cracked panels using the hybrid finite element method. Lin *et al.* [8] studied the panel flutter problems of thin plate-like composite panels with patched cracks using a finite element method. Recently, Strganac *et al.*, in a series of papers, investigated the aeroelastic behavior of damaged composite plate and beam structures [9–11]. In their studies results are presented for aeroelastic systems with examples of evolving microstructural damage. They concluded that the development of appropriate damage models is important as the change in stress field affects the accumulation of damage and the resulting aeroelastic stability boundaries.

It appears plausible to explore the influence of different damaged-material models to study the aeroelastic behavior of aging/damaged aircraft structural components. This paper presents an investigation of damaged composite panels under supersonic flow using the recently developed general plate finite element [4]. Two different damage models were investigated. The present formulation and computer program were validated by solving examples of a no-damage case for which alternative solutions are available. To illustrate the effect of different damage models, the example of a symmetrically laminated composite plate was studied and the free vibration and flutter results are presented and discussed.

FINITE ELEMENT ANALYSIS

A general quadrilateral plate finite element [4] is extended to include the different damaged-material models for composite materials. The finite element was formulated based on the classical lamination theory and linearized piston theory for the flutter analysis of laminated composite panels. The general plate finite element is quadrilateral in shape and has four nodal points each with 12 DOFs.

The laminated anisotropic behavior was included using the classical lamination theory. The plate is assumed to be made of an arbitrary number of layers. Each layer is assumed to be orthotropic with its principal material axes at an angle to the local coordinate axes. The stress–strain relation for each layer is transformed to the reference coordinate system. The stress and moment resultants are then related to the middle surface strains and the change of curvatures. Details of the element developments are available in Ref. [4].

The derivation of the aeroelastic equations was obtained using Hamilton's principle. The aeroelastic system of equations results in an eigenvalue problem corresponding to a value of the aerodynamic pressure parameter. The aeroelastic system of equations for a panel under the influence of stiffness, inertia and aerodynamic forces may be written in the matrix form as

$$\{[K]+\beta[A]-\lambda[M]\}\{q\}=\{0\} \tag{1}$$

where β is the aerodynamic parameter, and λ is the eigenvalue of the panel. In eqn (1), the stiffness matrix is $[K]$, mass matrix is $[M]$ and the aerodynamic matrix is $[A]$. When $\beta=0$, the eigenvalues are real, positive and definite, giving the free vibration characteristics. If the aerodynamic damping factor is neglected, the flutter boundary is obtained when the two relative lowest eigenvalues coalesce at a critical value of the aerodynamic parameter. The critical values of the flutter boundaries are the eigenvalue and the aerodynamic pressure parameter.

DAMAGED-MATERIAL MODELS

Two different types of damaged-material models were investigated in this study. Both damaged-material models follow the continuum damage mechanics theory with an internal state variable to describe the state of damage in the material. It is assumed that damage is at the ply level and the properties are changed as a result of damage present in that lamina. The damage parameter is related to the density of microcracks present in the composite material in a particular direction.

The stress–strain relationship for a damaged laminate is described in terms of the constitutive properties for each lamina in the principal material directions. The details of each material model are described below.

Model 1

The elastic stiffness reduction in each lamina in the two orthogonal directions is a function of damaged areas through a damage parameter (α_i) in those two directions. The damaged orthotropic lamina's elastic properties in the principal material direction are defined in terms of undamaged elastic properties [12] as

$$E_i^d=E_i(1-\alpha_i)^2 \tag{2}$$

$$G_{ij}^d=G_{ij}\frac{(1-\alpha_i)^2(1-\alpha_j)^2}{(1-\alpha_i)^2+(1-\alpha_j)^2} \tag{3}$$

$$\nu_{ij}^d=\nu_{ij}\frac{(1-\alpha_i)}{(1-\alpha_j)} \tag{4}$$

where the material properties with superscript d are the damaged material properties, while those properties without superscript are the undamaged properties. The subscripts i or $j=1$ and 2 denote the principal material directions of the composite plate.

Model 2

A different damage parameter (ξ) introduced by Talreja [13] was used in the present study. This damage parameter describes the density of damage at the ply level. The constitutive properties of the damaged orthotropic lamina in the principal material direction are defined in terms of undamaged lamina elastic properties as

$$E_1^d=E_1+2\xi[C_3+C_8(\nu_{12})^2-C_{16}\nu_{12}] \tag{5}$$

$$E_2^d=E_2+2\xi[C_8+C_3(\nu_{21})^2-C_{16}\nu_{21}] \tag{6}$$

$$\nu_{12}^d=\nu_{12}+\xi[(1-\nu_{12}\nu_{21})/E_2](C_{16}-2C_8\nu_{12}) \tag{7}$$

$$G_{12}^{d} = G_{12} + 2\xi C_{13} \tag{8}$$

The terms C_3, C_8, C_{13}, and C_{16} in the above equations are experimentally derived material constants [13].

Given the undamaged lamina properties and the damage parameter, the damaged lamina properties can be estimated by using eqns (2)–(4) and eqns (5)–(8). These damaged lamina properties were used in the finite element simulation to estimate the damaged stiffness of the composite plate due to microdamage.

RESULTS AND DISCUSSION

A computer program was developed to include the different damaged-material models into the finite element formulation for supersonic flutter analysis of damaged composite panels. Finite element simulations were carried out to find the results of eigenvalues and flutter bounds. Results were obtained for an example of a $[0/90]_s$ laminated graphite–epoxy (AS4/3502) composite square plate with simply-supported boundary conditions. Each lamina is assumed to be 0.00544 in. thick.

The material properties used for undamaged and damaged composite plates are taken from Refs [2–8, 11] as follows

$E_1 = 19.8$ Mpsi
$E_2 = 1.45$ Mpsi
$G_{12} = 0.7$ Mpsi
$\nu_{12} = 0.3$
$C_3 = -0.627$ Mpsi
$C_8 = -0.329$ Mpsi
$C_{16} = -0.564$ Mpsi
$C_{13} = 0$ (due to symmetry of laminate) and
$\rho = 1.4488 \times 10^{-4}$ lb s^2/in^4.

The results of the aerodynamic pressure parameter (β) and the eigenvalues for various values of damage parameter (α for material model 1 and ξ for material model 2) corresponding to flutter conditions are obtained and presented for the $[0/90]_s$ laminated composite square plate.

The first two eigenvalues as a function of the damage parameter for the two damaged-material models (1 and 2) are shown in Fig. 1. It can be seen that as the damage parameter increases, the eigenvalues decrease. Damaged-material model 1 predicts lower eigenvalues as compared to damaged-material model 2. The difference between eigenvalues for two damaged-material models increases as the damage parameter is increased. For example, at a damage parameter of 0.4, there is a difference of 13.5% and 18.4% for modes 1 and 2, respectively.

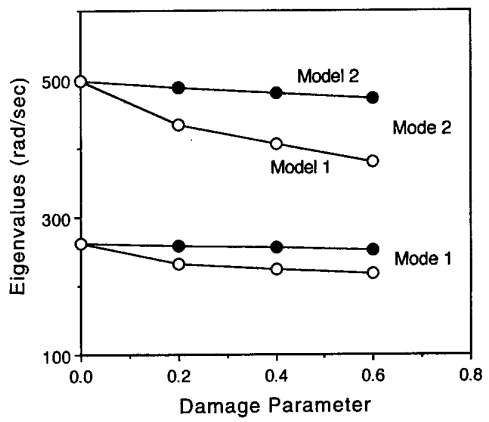

Fig. 1. Eigenvalues as a function of the damage parameter for the two material models considered in this study.

Figures 2 and 3 show the coalescence of the first four eigenvalues as a function of aerodynamic parameter (β) for the case of a damaged composite plate (0.2) for material models 1 and 2, respectively. It can be seen from both the figures that flutter occurs by coalescence of modes 1 and 2. However, material model 1 predicts a lower value for the critical dynamic pressure as compared to material model 2. The relationship between the aerodynamic parameter and the damage parameter for both material models is shown in Fig. 4. It can be seen from Fig. 4 that for the same value of the damage parameter, model 1

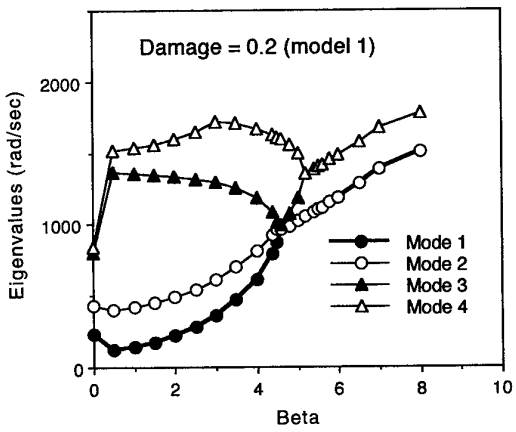

Fig. 2. Coalescence of eigenvalues as a function of the aerodynamic parameter for the damaged composite plate ($\alpha = 0.2$) using material model 1.

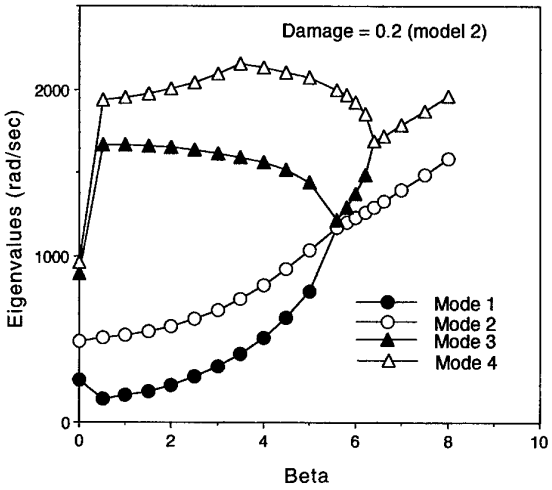

Fig. 3. Coalescence of eigenvalues as a function of the aerodynamic parameter for the damaged composite plate ($\xi = 0.2$) using material model 2.

predicts a lower value for the critical dynamic pressure as compared to material model 2.

Figure 5 shows the comparison of eigenvalue coalescence for the damaged composite plate (0.4) using the two different material models considered in this study. It can be seen that the critical flutter dynamic pressure for the damaged composite plate decreases around 22.6% and 3.5% for the material models 1 and 2, respectively, as compared to the no-damage case. It is evident that damage decreases the critical flutter dynamic pressure by different amounts. The results presented in Figs 1–5 illustrate the effects of two different damaged-material models on eigenvalues and

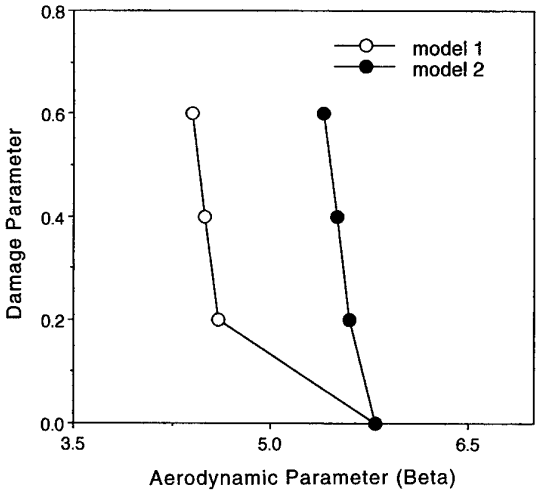

Fig. 4. Relationship between the damage parameter and the aerodynamic parameter for the two material models considered.

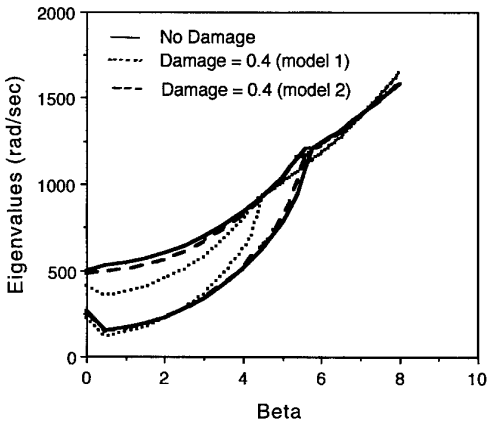

Fig. 5. Comparison of the eigenvalue coalescence between the damaged and undamaged composite plate with the two different material models considered in this study.

flutter bounds. The present approach can be easily extended for parametric studies of various parameters affecting the damage in the composite plates.

CONCLUDING REMARKS

Free vibration and supersonic flutter analysis of selected laminated composite damaged panels is investigated. The finite element method employs a 48 DOF general plate element and uses the classical lamination theory, microstructural continuum damage theory and linearized piston theory. Numerical results are obtained for a [0/90] symmetrically laminated composite plate using two different damaged-material models.

Amongst the damaged-material models considered in this study, model 1 predicts lower values for eigenvalues and flutter bounds as compared to model 2. The limited results presented indicate that the damage parameter has a strong influence on both free vibration and flutter boundaries. Currently, results are being obtained to study the influence of various damage parameters on the flutter bounds for various composite panels.

REFERENCES

1. Dowell, E.H., Panel flutter: a review of the aeroelastic stability of plates and shells. *AIAA J.*, 1970, **8**, (3), 385–399.
2. Srinivasan, R.S. and Babu, B.J., Free vibration and flutter of laminated quadrilateral plates. *Comput. Structures*, 1987, **27**, (2), 297–304.

3. Lin, K.J., Lu, P.J. and Tam, J.Q., Flutter analysis of composite panels using high-precision finite elements. *Comput. Structures*, 1989, **33**, (2), 561–574.
4. Pidaparti, R.M.V. and Yang, H.T., Flutter analysis of stiffened laminated composite plates and shells in supersonic flow. *AIAA J.*, 1993, **31**, (6), 1109–1117.
5. Liao, C.L. and Sun, Y.W., Supersonic flutter analysis of plates and shells. *AIAA J.*, 1993, **31**, (8), 1897–1905.
6. Mei, C., A finite element approach for non-linear panel flutter. *AIAA J.*, 1977, **15**, (8), 1107–1110.
7. Chen, W.H. and Lin, H.C., Flutter analysis of thin cracked panels using the finite element method. *AIAA J.*, 1985, **23**, (5), 795–801.
8. Lin, K.J., Lu, P.J. and Tarn, J.Q., Flutter analysis of anisotropic panels with patched cracks. *AIAA J.*, 1994, **23**, (5), 234–266.
9. Kim, Y. I. and Strganac, T. W., Aeroelastic stability of damaged composite structures. *AIAA Paper 92-2392*, April 1992.
10. Strganac, T. W., Kim, Y. I. and Kurdila, A. J., Non-linear flutter of composite plates with damage evolution. *AIAA Paper 93-1546*, April 1993.
11. Strganac, T.W. and Kim, Y.I., Aeroelastic behavior of composite plates subject to damage growth. *J. Aircraft*, 1996, **33**, (1), 68–73.
12. Valliappan, S., Murti, V. and Wohua, Z., Finite element analysis of anisotropic damage mechanics problems. *Engng Fract. Mech.*, 1990, **35**, 1061–1071.
13. Talreja, R., A continuum mechanics characterization of damage in composite materials. *Proc. Royal Soc. London*, 1985, **A399**, (1817), 195–216.

ELSEVIER

Composite Structures Vol. 38, No. 1–4, pp. 483–487, 1997
© 1997 Elsevier Science Ltd. All rights reserved
Printed in Great Britain
0263-8223/97/$17.00 + 0.00

PII:S0263-8223(97)00083-4

Thermogravimetric and binder removal analysis of injection moulded reinforced ceramic composite

R. K. Y. Li, C. M. L. Wu & T. L. Wong

Department of Physics and Materials Science, City University of Hong Kong, 83 Tat Chee Avenue, Kowloon, Hong Kong

The study of the binder removal processes for injection moulded ceramic composite compacts was studied with the aid of a thermogravimetric analyser. It has been observed that a number of factors, such as the heating rate, the heating environment and the heating profile have an effect on the rate of binder removal. The matrix of the composite was alumina and the reinforcement was silicon carbide whiskers. It was confirmed that the presence of silicon carbide whiskers in the injection moulded compacts provided additional oxygen diffusion paths to enhance oxidative degradation. It was also found that the heating profile used for binder removal had a strong influence on the formation of internal cracks in the moulded components. © 1997 Elsevier Science Ltd.

INTRODUCTION

There are many shape-forming processes for ceramic materials but most of them involve powder compacting. One of these techniques is injection moulding which has the ability of mass production with high dimensional accuracy [1–4]. As ceramic injection moulding provides many manufacturing advantages, it seems that this technology can be extended to ceramic matrix composite materials [5–8]. The steps involved in the ceramic shape-forming by injection moulding include the following:

(a) selecting a ceramic powder for the process;
(b) mixing the powder with a suitable binder;
(c) producing homogeneous granular pellets of mixed powder and binder;
(d) injection mould the pellets to form the component;
(e) remove the binder from the formed part (debinding);
(f) densifying the debinded compact by a high temperature sintering process.

Most investigators in Refs [3,4,9,10] agreed that the incidence of defects in a ceramic moulding after binder removal is closely related to the rate of weight loss of the polymeric binder during decomposition. For pyrolytic removal of the polymeric binder from the ceramic injection moulding, the thermogravimetric behaviour may be influenced by the heating rate, ambient environment, sample size, heating profile, etc. [10–13].

In our earlier investigation on the injection moulding of alumina/silicon carbide whisker (Al_2O_3/SiC_w) composites [14], we have derived a suitable binder for the ceramic composite. In this paper, we shall report on the investigation of the binder removal behaviour for the injection moulding compacts (IMC) of Al_2O_3/SiC_w composites.

EXPERIMENTAL DETAILS

Alumina powder (Grade A152, Alcoa Chemicals Ltd.) and SiC_w (Grade SCW-1, Tateho Chemical Industries) were selected as matrix and reinforcement materials, respectively, in this investigation. The polymeric binder system consists of

(a) polystyrene (Grade 25, Kaofu Chemical) as the major binder,

(b) stearic acid (Riedel–deHaen Laboratory Chemicals), and
(c) a lubricant (N34, Eastman Chemical).

The selection of N34 as the lubricant was based on results of our earlier investigation [14].

The compounding of the alumina/SiC_w/binder systems was the same as described earlier [14]. Basically, compounding was done using a Brabender counter-rotation twin-screw compounder. Alumina/whisker/binder (A/W/B) blends with different weight compositions were compounded. Their designation and composition used in this work are given in Table 1. The compounded blends were pelletized and injection moulded into rectangular bars as described earlier [14], and were referred to as IMC.

The main emphasis of this work is to study the thermal decomposition behaviour of the IMC. Thermogravimetric analysis was carried out using a Seiko TG/DTA 220 Thermal Analysis System. Samples of approximately 10 mg in weight were cut from the IMCs and were used for measurements.

RESULTS AND DISCUSSION

Thermograms for the binder constituents

In order to study the decomposition behaviour of the binder constituents, thermogravimetric analysis was carried out at a heating rate of 10°C/min and under static air environment. Figure 1 shows the thermograms for the stearic acid, polystyrene and N34. For the stearic acid used, its decomposition started at about 200°C, followed by a rigorous weight loss to nearly 0 wt% at about 300°C. For polystyrene, decomposition started at about 300°C and ended at about 425°C. For the N34 lubricant, decomposition started at about 300°C; 65 wt% of the lubricant was rapidly lost within a temperature range of 75°C. The remaining 35 wt% decomposed gently to completion at about 550°C.

Knowledge of the thermogram for the binder constituents will allow us to predict the decomposition behaviour of the binder in the IMCs. Figure 2 compares the experimental thermogram for an A152 IMC with a rule-of-mixture prediction of the following form:

$$W_c(T) = W_{PS}(T) \times m_{PS} + W_{SA}(T) \times M_{SA} + W_{\text{lub}}(T) \times m_{\text{lub}} \quad (1)$$

where $W_c(T)$ is the total weight of the polymeric binder remaining in the IMC at temperature T; $W_{PS}(T)$, $W_{SA}(T)$, and $W_{\text{lub}}(T)$ are the weight of polystyrene, stearic acid, and lubricant, respectively, remaining in the IMC at temperature T; and m_{PS}, m_{SA}, and m_{lub} are the wt% of polystyrene, stearic acid, and lubricant, respectively, in the binder system before binder removal.

In the current study, the values of m_{PS}, m_{SA}, and m_{lub} are equal to 0.67, 0.11 and 0.22, respectively. It can be seen from Fig. 2 that eqn (1) gives a prediction to the decomposition of the binder system in the IMC with acceptable accuracy.

Effects of whisker content

Figure 3 shows the thermograms of the IMCs with various whisker contents. All the thermograms were obtained at a heating rate of 10°C/min and in a static air environment. The thermograms showed that they had the same initial binder decomposition temperature and nearly the same final decomposition temperature. These curves mainly differ in the starting temperature (T_s) at which the most rapid rate of weight loss occurred. T_s can be determined by plotting the rate of change of the thermograms against temperature (DTG). The DTG curves are shown in Fig. 4. Close inspection showed that A152 had the highest T_s value whereas samples containing SiC_w (i.e. 5SC, 15SC and 30SC as described in Table 1) had lower T_s values in comparison.

Generally, both thermal and oxidation degradation can occur if a polymer is heated under

Table 1. Weight composition of the ceramic/binder blends

Ceramic/binder blend (wt%)	A152	5SC	15SC	30SC
Alumina	85	81.6	74.5	63.3
SiC whisker	0	3.4 (5 vol%)	10.5 (15 vol%)	21.7 (30 vol%)
Polystyrene	10	10	10	10
Stearic acid	1.7	1.7	1.7	1.7
Lubricant	3.3	3.3	3.3	3.3

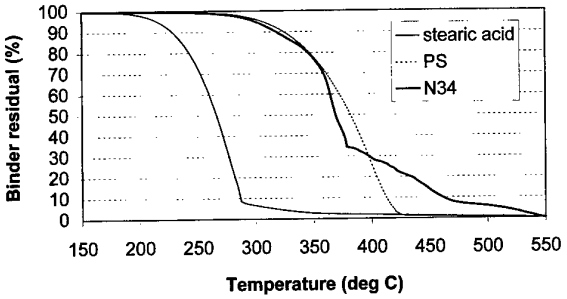

Fig. 1. Thermogravimetric curve of individual polymeric binder system constituents.

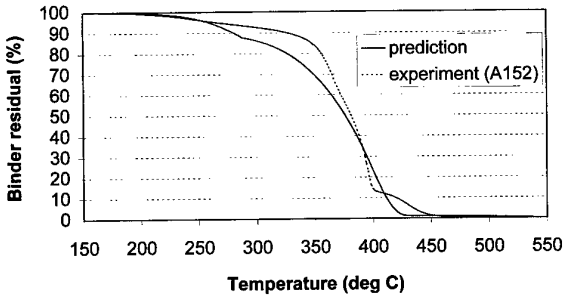

Fig. 2. Thermogravimetric curve of alumina injection moulding.

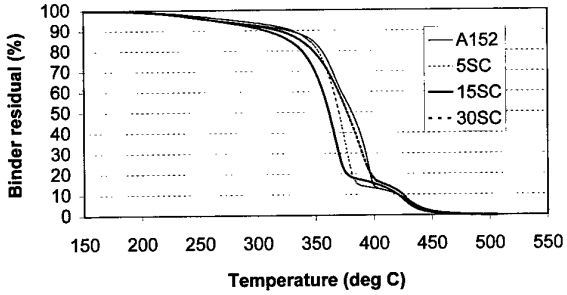

Fig. 3. Thermogravimetric curves of alumina injection moulding in static air.

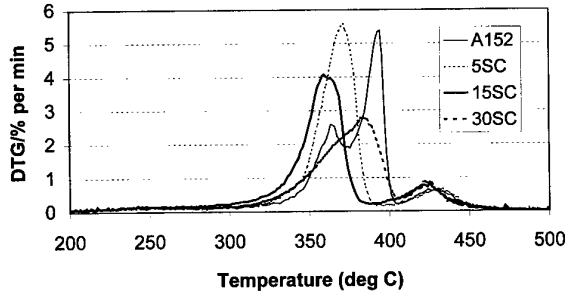

Fig. 4. DTG behaviour of alumina injection moulding in static air.

an oxidizing atmosphere such as static air. Thermal degradation is the process at which long molecular chains are broken into shorter molecular chains when they acquire sufficient activation energy. It is therefore temperature controlled and is a bulk reaction process. For oxidation degradation of polymers, this occurs under an oxidizing atmosphere. Therefore the rate of weight loss of polymers through oxidation degradation is controlled by the diffusion rate of oxygen into the bulk sample.

The incorporation of SiC_w increases internal porosity throughout the IMC during compaction [1,10]. The increase in internal porosity provides more diffusion paths for the oxygen to diffuse into the core of the bulk sample and consequently enhance the weight loss of the binder system due to oxidation degradation. This explains the increasing shift of the thermograms to lower temperatures when a sample contains more and more SiC_w (see Fig. 3).

In order to show that the difference of the thermograms between the samples with and without SiC_w is due to the presence of more oxygen diffusion paths, TGA measurements were also taken for the IMCs in a non-oxidizing (N_2) environment at a heating rate of 10°C/min. The measured thermograms are shown in Fig. 5. It is noted that the thermograms nearly overlap each other and this shows that the excess oxygen diffusion paths for the SiC_w are no longer functional in a non-oxidizing environment. Thus it proved that the shifting of the thermograms of the samples with SiC_w is due to the presence of more oxygen diffusion paths in air than a non-oxidizing environment.

Effect of heating rate

Figure 6 shows the thermograms for A152 under five heating rates. It can be seen that the

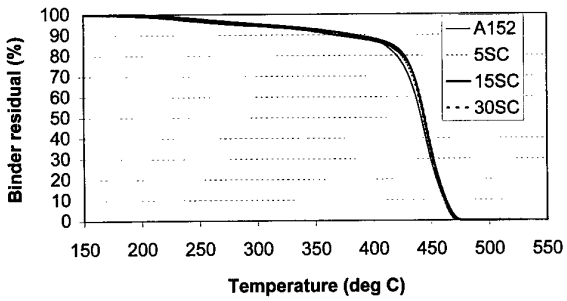

Fig. 5. Thermogravimetric curves of alumina injection moulding in flowing nitrogen gas.

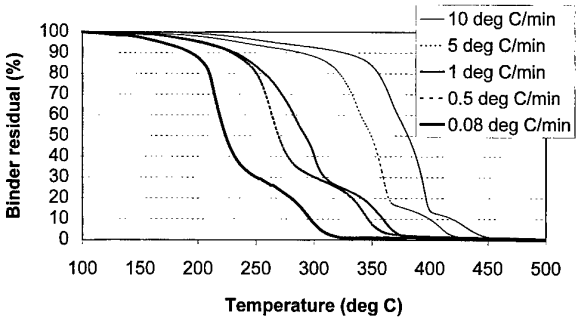

Fig. 6. Thermogravimetric curves of alumina injection moulding under various heating rates.

thermogram is shifted more to the left of the temperature axis with decreasing heating rate. Similar results can also be found in the IMCs containing SiC_w (see Fig. 7). The observation is consistent with the results obtained by Shukla and Hill [10].

Effect of heating profile on binder removal

Thermogravimetric measurements on the binder removal behaviour of the A152 IMC were conducted at three different heating profiles. The three profiles used are shown schematically in Fig. 8. Heating profile A is

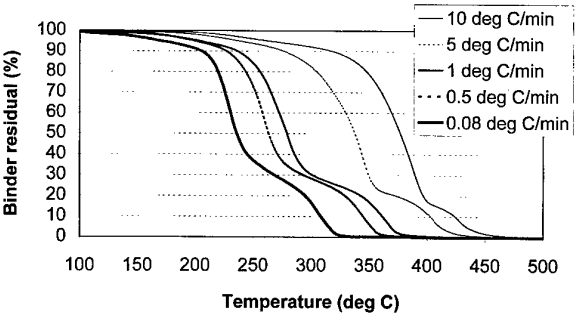

Fig. 7. Thermogravimetric curves of alumina injection moulding with 30 vol% SiC whisker under various heating rates.

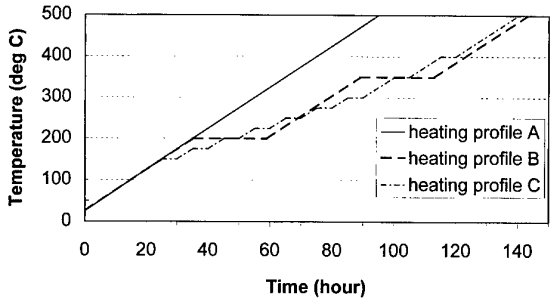

Fig. 8. Heating profiles.

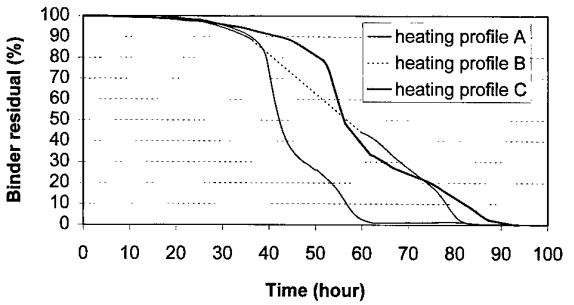

Fig. 9. Binder weight loss of alumina moulding against time using various heating profiles.

monotonous increasing from 25 to 500°C at a heating rate of 5°C per hour. For heating profile B, the starting temperature, ending temperature and heating rate were the same as profile A but there exist two steps at 200 and 350°C and the holding time for each step was 24 hours. Heating profile C was similar to that of profile B but it possessed more steps and the holding time for each step was 5 h.

Figure 9 shows the variation of binder residue with time in the A152 IMC using heating profiles A, B and C. It can be seen that profile B provides a much more gentle decrease than profiles A and C. Between profiles A and C, profile C had a more gentle overall decrease than profile A. It is believed that the incidence of defects or cracks in IMC during binder removal is closely related to the rate of weight loss of the binder [3,4,9,10]. Therefore, a steady rate of weight loss over a wide temperature range is more preferable than a sudden decomposition. As a result, both heating profiles B and C are preferred to profile A because they can provide smaller rate of weight loss over the temperature range.

Figure 10 shows the optical micrograph of a sample of the A152 IMC after binder removal using heating profile A. Cracks were clearly observed. However, cracks were not observed in similar samples when binder removal was conducted using profiles B or C.

CONCLUSIONS

An Al_2O_3/SiC_w composite manufactured by injection moulding method was studied. In particular, the binder removal processes for ceramic composite compacts with various SiC_w contents were studied with the aid of a thermogravimetric analyser. The rate of binder

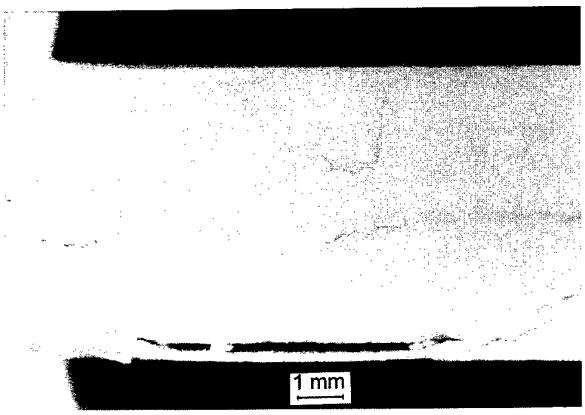

Fig. 10. Optical micrograph of the longitudinal section of IMC after binder removal using heating profile A.

removal was found to depend on a number of factors, such as the heating rate, the heating environment and the heating profile. The present investigation also confirmed that the presence of silicon carbide whiskers in the injection moulded compacts provided additional oxygen diffusion paths to enhance oxidative degradation. Experiments with various heating profiles for binder removal showed that a steady rate of weight loss over a wide temperature range was more preferable than a sudden decomposition.

ACKNOWLEDGEMENTS

This work was supported by the City University of Hong Kong Strategic Research Grant through grant number 7000185. The authors would like to thank Alcoa Chemicals, UK for their kind donation of alumina powder for this investigation. The lubricant (N34) used in this study were kindly donated by Eastman Chemical Co., Tennessee, USA.

REFERENCES

1. Edirisinghe, M.J. and Evans, J.R.G., Review: fabrication of engineering ceramics by injection moulding — I. Materials selection. *Int. J. High Tech. Ceram.*, 1986, **2**, 1–31.
2. Edirisinghe, M.J. and Evans, J.R.G., Review: fabrication of engineering ceramics by injection moulding — II. Techniques. *Int. J. High Tech. Ceram.*, 1986, **2**, 249–278.
3. Sakai, T., State of the art of injection molding of high-performance ceramics. *Advances in Polymer Technology*, **11** (1) (1991/1992) 53–67.
4. Edirisinghe, M.J., Fabrication of engineering ceramics by injection moulding. *Ceram. Bull.*, 1991, **70**, (5), 824–828.
5. Kandori, T., Kobayashi, S., Wada, S. and Kamigaito, O., SiC whisker reinforced Si_3N_4 composites. *J. Mat. Sci. Letter*, 1987, **6**, 1356–1358.
6. Stedman, S.J., Evans, J.R.G. and Woodthorpe, J., Whisker length degradation during the preparation of composite ceramic injection moulding suspensions. *J. Mat. Sci.*, 1990, **25**, 1025–1032.
7. Stedman, S.J., Evans, J.R.G. and Woodthorpe, J., Rheology of composite ceramic injection moulding suspensions. *J. Mat. Sci.*, 1990, **25**, 1833–1841.
8. Tsao, I. and Danforth, S.C., Rheological behavior of injection-moldable silicon powder–silicon carbide whisker formulations. *J. Am. Ceram. Soc.*, 1993, **76**, (12), 2977–2984.
9. Woodthorpe, J., Edirisinghe, M.J. and Evans, J.R.G., Properties of ceramic injection moulding formulations Part 3 Polymer removal. *J. Mat. Sci.*, 1989, **24**, 1038–1048.
10. Shukla, V.N. and Hill, D.C., Binder evolution from powder compacts: thermal profile for injection molded articles. *J. Am. Ceram. Soc.*, 1989, **72**, (10), 1797–1803.
11. Pinwill, I.E., Edirisinghe, M.J. and Bevis, M.J., Development of temperature-heating rate diagrams for the pyrolytic removal of binder used for powder injection moulding. *J. Mat. Sci.*, 1992, **27**, 4381–4388.
12. Edirisinghe, M.J., Binder removal from moulded ceramic bodies in different atmospheres. *J. Mat. Sci. Lett.*, 1991, **10**, 1338–1341.
13. Evans, J.R.G. and Edirisinghe, M.J., Interfacial factors affecting the incidence of defects in ceramic mouldings. *J. Mat. Sci.*, 1991, **26**, 2081–2088.
14. Wong, T.L., Li, R.K.Y. and Wu, C.M.L., Injection moulding of Al_2O_3/SiC_w composite. *J. Mat. Proc. Tech.*, 1997, **63**, (1–3), 399–404.

ELSEVIER

Composite Structures Vol. 38, No. 1–4, pp. 489–497, 1997
© 1997 Elsevier Science Ltd. All rights reserved
Printed in Great Britain
0263-8223/97/$17.00 + 0.00

PII:S0263-8223(97)00084-6

Transverse shear effects in discrete optimization of laminated compressed cylindrical shells

A. Muc

Institute of Mechanics and Machine Design, Cracow University of Technology, Warszawska 24,31-155 Kraków, Poland

This paper presents optimization problems of cylindrical shells subjected to buckling and ply failure constraints. The objective is to maximize failure load. The layers are assumed to be oriented at 0°, 90° and ±45°, so that the locations of plies in the laminate (3^N variables) are design variables. The aim of the present work is to discuss the influence of various formulations of governing equations on optimal solutions including the effects of transverse shear deformations and to present the use of different variants of genetic algorithms, i.e. different selection, mutation and crossing. A series of numerical examples illustrates the discussed problem. © 1997 Elsevier Science Ltd.

INTRODUCTION

In mechanical, aerospace and other branches of engineering composite materials are increasingly used due to their excellent weight saving and the ease of tailoring. In spite of tremendous progress in the analytical capability to analyse the behaviour of composite materials and structures there is a lack of design models which may allow efficient and, on the other hand, sufficiently accurate tailoring of their specific (anisotropic) properties to specific requirements for structural components. Therefore, the optimum design of composite structures has been a subject of research for many years. However, in order to deal with the optimization problems of laminated composite thin-walled structures in the structural design problems the following problems should initially be correctly formulated and established:

1. structural model in view of assumptions and hypotheses valid for the analysed type of governing 2-D equations;
2. optimization model in the sense of FE or other modelling of design structures;
3. optimization algorithms;

It should be emphasized that the majority of the optimization problems have been solved with the use of the classical Love–Kirchhoff (L–K) equations. On the other hand, it is well-known that the higher-ordered shell or plate theories should be employed in the analysis in view of the consistency and the correctness of theoretical results with experimental investigations. The classical theory fails to predict accurately the static and dynamic response when the structures in question are even moderately thick and/or when they exhibit high anisotropy ratio.

In their review paper, Noor and Burton [1] cited only three references [2–4] devoted to the buckling analysis of laminated cylindrical shells with the use of relationships taking into account the effects of transverse shear deformations. In general, as demonstrated, for example, by Soldatos [5] for cylindrical composite shells subjected to buckling constraints, the use of higher ordered shell theories results in a decrease of buckling loads in comparison to those obtained with the use of the L–K relations.

The goal of the present paper is two-fold:

- to present the influence of the governing 2-D shell relationships on optimal failure loads

(understood in the sense of buckling and/or first-ply-failure (FPF) loads) and optimal shell configurations (laminate topologies);
- to apply and analyse the effectiveness of a powerful solution technique, based on various versions of genetic algorithms.

The shell theory developed in this paper is based on the first order transverse shear deformation theory (FSDT), but with the use of two types of geometrical relationships referring to shallow and deep shell theories.

The optimum design of laminated cylindrical shells subjected to buckling and/or FPF constraints have been addressed by numerous investigators, but only with the L–K governing equations. They have shown that the laminate configurations have great influence on the buckling loads. Tasi *et al.* [6] have analysed the stability of composite shells composed of three layers. Hirano [7] has investigated the buckling load of angle-ply laminated shells. Uemura and Kasuya [8] have studied the coupling effects in buckling and optimization of cylinders. Onoda [9] has found that the optimal stacking sequence corresponds to the quasi-isotropic distributions of an infinite number of infinitely thin layers. Narusberg and Teters [10] have formulated and discussed various optimization problems for laminated cylinders.

GOVERNING RELATIONS

Let us consider the simply-supported cylindrical shell having a circular cross-section and loaded in the x direction by an axial compressive force P (see Fig. 1). The shell is assumed to be composed of anisotropic layers made of unidirectional plies whose material properties are identical. The total thickness of the shell is equal to t. The shell is constructed of an arbitrary number N of orthotropic layers of thickness t/N. The laminate is assumed to be symmetric, balanced and made of $0°_2$, $90°_2$, $\pm 45°$ plies, each of thickness $2t/N$. As a result only $N/4$ ply orientations are required to describe the laminate configuration. The strains in the z direction are assumed to be related to the midsurface strains and the curvature changes as follows, including the effects of transverse shear deformations

$$\varepsilon_x = \varepsilon_x^o + z\kappa_x \varepsilon_\phi = \varepsilon_\phi^o + z\kappa_\phi \varepsilon_{x\phi} = \varepsilon_{x\phi}^o + z\kappa_{x\phi}$$

$$\varepsilon_{xz} = \frac{5}{4}\varepsilon_{xz}^o\left[1-\left(\frac{z}{t/2}\right)^2\right]$$

$$\varepsilon_{\phi z} = \frac{5}{4}\varepsilon_{\phi z}^o\left[1-\left(\frac{z}{t/2}\right)^2\right] \tag{1}$$

where

$$\varepsilon_x^o = \frac{1}{R}\frac{\partial u}{\partial x}$$

$$\varepsilon_{x\phi}^o = \frac{1}{R}\left(\frac{\partial v}{\partial x}+\frac{\partial u}{\partial \phi}\right)$$

$$\varepsilon_\phi^o = \frac{1}{R}\left(\frac{\partial v}{\partial \phi}-w\right)$$

$$\varepsilon_{xz}^o = \gamma_1 + \frac{1}{R}\frac{\partial w}{\partial x}$$

$$\varepsilon_{\phi z} = \gamma_2 + \frac{1}{R}\left(\frac{\partial w}{\partial \phi}+v\right)$$

$$\kappa_x = \frac{1}{R}\frac{\partial \gamma_1}{\partial x}$$

$$\kappa_\phi = \frac{1}{R}\frac{\partial \gamma_2}{\partial \phi}$$

$$\kappa_{x\phi} = \frac{1}{R}\left(\frac{\partial \gamma_1}{\partial \phi}+\frac{\partial \gamma_2}{\partial x}\right) \tag{2}$$

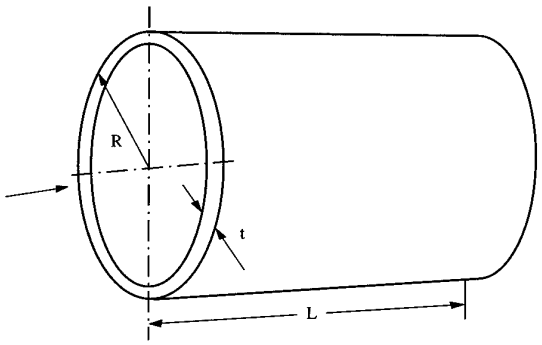

Fig. 1. Shell geometry.

Both x and ϕ are dimensionless quantities. The above kinematic relationships are supplemented by the equilibrium equations in the following form

$$\begin{aligned} N_{x,x}+N_{x\phi,\phi}=0 \quad & N_{\phi,\phi}+N_{x\phi,x}-\underline{Q}_{23} \\ =0 \quad & Q_{13,x}+Q_{23,\phi}+N_{\phi}-RPw_{xx} \\ =0 \quad & M_{x,x}+M_{x\phi,\phi}-RQ_{13} \\ =0 \quad & M_{\phi,\phi}+M_{x\phi,x}-RQ_{23}=0 \end{aligned} \tag{3}$$

where a comma after the symbols denotes differentiation with respect to x or ϕ variables. Using the classical lamination theory one can build the constitutive relationships in the appriopriate form for laminated cylinders.

In eqns (2) and (3), if we neglect the underlined terms these would be the relationships for shallow cylindrical shells — the so-called Donnel–Vlasov shallow shell theory. On the other hand, starting with the general eqns (2) and (3), the assumption of no transverse shear deformations results in the following expressions for the rotations

$$\gamma_1=-\frac{1}{R}\frac{\partial w}{\partial x}\quad \gamma_2=-\frac{1}{R}\left(\frac{\partial w}{\partial \phi}-\underline{v}\right) \tag{4}$$

Thus, eqns (2) and (3) describe four variants of the governing equations for cylindrical shells, i.e. the relationships for deep or shallow shells including (or not) the effects of transverse shear deformations. The general formulation allows us to analyse and compare their influence on optimal stacking sequences and/or on values of optimal buckling loads.

BUCKLING ANALYSIS

In this paper, the axial compressive buckling force P is estimated by the Rayleigh–Ritz method. Assuming the classical form of buckling mode for displacements u, v, w and angles of rotation γ_1, γ_2 from the eqns (2) and (3) and from the constitutive relationships we finally arrive at an eigenvalue problem defined by the vanishing of the five by five determinant

$$\det K_{rs}=0,\ r,\ s=1,\ 2,\ \ldots,\ 5 \tag{5}$$

whose elements are given by

$$\begin{aligned} K_{11}&=A_{11}\alpha^2+A_{66}n^2 \\ K_{12}&=\alpha n(A_{12}+A_{66}) \\ K_{15}&=\alpha A_{12} \\ K_{22}&=\alpha^2A_{66}+n^2A_{22}+\underline{A}_{44} \\ K_{24}&=A_{44} \\ K_{25}&=n(A_{22}+A_{44}) \\ K_{33}&=(\alpha^2D_{11}+n^2D_{66})/R^2+A_{44} \\ K_{34}&=\alpha n(D_{12}+D_{66})/R^2 \\ K_{35}&=\alpha A_{44} \\ K_{44}&=(\alpha^2D_{66}+n^2D_{22})/R^2+A_{44} \\ K_{45}&=nA_{44} \\ K_{55}&=(\alpha^2+n^2)A_{44}+A_{22}-R\alpha^2P_b \end{aligned} \tag{6}$$

The symbol P_b denotes the buckling axial load. In the symmetric matrix K_{rs}, the rest of elements equal zero. The parameter $\alpha=m\Pi R/L$, whereas m and n are wavenumbers in buckling in the x and ϕ directions, respectively. The above relationships are valid for deep cylindrical shells including transverse shear deformations. Using eqn (4) one can derive the relationships for deep cylinders described with the use of the Love–Kirchhoff hypothesis. Neglecting the underlined terms one can obtain the similar to the above relationships for the Donnell–Vlasov shallow five- (or three- L–K) parametric shell theories. It should be noted that the introduced deformation modes identically satisfy simply supported boundary conditions. However, the simply supported boundary conditions only can be satisfied rigorously if

$$A_{i6}=B_{i6}=D_{i6}=0,\ i=1,\ 2 \tag{7}$$

If these values are not equal to zero (so-called special orthotropy) overestimated approximated eigenvalues will be obtained (see e.g. Ref. [8]). It may be noticed that prebuckled shell deformations are not taken into account (a geometrically linear buckling problem). In addition, due to coupling effects arising in the buckling analysis it is necessary to equalize the A_{45} term of the stiffness matrix to zero. This results in the following equality

$$G_{13}=G_{23}=0.5G_{12} \tag{8}$$

which has been directly introduced in relationships (5) and (6).

To determine the buckling load P_b for the cylindrical shell with given dimensions and a given material system, one determines those integer values of m and n which make P_b a minimum.

FIRST-PLY-FAILURE

After a buckling load P_b has been determined, a check should be made to see that the final laminate construction is not overstressed at a load below the critical buckling load,because if that is the case the cylinder is limited to a load that will result in overstressing. Starting with the general equations (i.e. eqns (1)–(3)) reduced to the axisymmetric prebuckling deformations, assuming that there are no transverse shear deformations (i.e. eqn (4)) and that the composite laminate material is symmetric with respect to the shell midsurface, $[B] = 0$ and if there are no other coupling terms (eqn (7)), the governing equations for the lateral deflection w, and the in-plane displacement u become

$$\frac{d^4w}{dx^4} + 4\eta^4 w = P_s \frac{R^3 A_{12}}{A_{11} D_{11}}$$

$$\frac{du}{dx} = (RP_s + A_{12}w)/A_{11} \tag{9}$$

where

$$4\eta^4 = \frac{R^2(A_{22}A_{11} - A_{12}^2)}{A_{11}D_{11}} \tag{10}$$

and P_s denotes the axial load corresponding to the first-ply-failure of the shell.

Assuming the simply-supported boundary conditions and the symmetry with respect to $x = 0$, one can find that the solution of the differential eqn (9) can be written as

$$w(x) = w_p \left[1 - \frac{\cosh y \cos z + \cosh z \cos y}{\cos(\eta L) + \cosh(\eta L)} \right] \tag{11}$$

where $z = \eta(x + L/2)$, $y = \eta(x - L/2)$, $x \in [-L/2, L/2]$ and

$$w_p = P_s \frac{R^3 A_{12}}{4\eta^4 A_{11} D_{11}} \tag{12}$$

Having the explicit form of the lateral deflection w, the laminate strains ε_x, ε_ϕ can be calculated in the global coordinate system from eqns (1) and (2). Let us note that the strains are proportional to the axial load P_s. Then, using the classical transformation rules the strains for the kth ply in the local coordinate system can be calculated

$$\varepsilon_{11}^{(k)} = \varepsilon_x \cos^2 \theta_k + \varepsilon_\phi \sin^2 \theta_k$$
$$\varepsilon_{22}^{(k)} = \varepsilon_x \sin^2 \theta_k + \varepsilon_\phi \cos^2 \theta_k$$
$$\varepsilon_{12}^{(k)} = (\varepsilon_y - \varepsilon_\phi) \sin(2\theta_k) \tag{13}$$

where θ_k denotes fibre orientation of the kth ply and in the present discrete optimization problem belongs to the set: $[0°_2, 90°_2, \pm 45°]$. Comparing each of the above strains with the ultimate ones or using the relationships (9) in the arbitrary quadratic strain or strength FPF criterion (e.g. the Tsai–Wu criterion), finally, one can find (with the use of eqns (9)–(13)) the value of the P_s parameter corresponding to FPF load for the analysed cylindrical shell.

OPTIMIZATION PROBLEM

If choices can be made regarding laminate topology (i.e. the ply orientation, number of plies etc.), then an optimization can be performed to determine the construction that provides the highest failure load, i.e. P_s and/or P_b. Having all basic relations one can formulate now the optimization problem in the following form. Find

$$\max_{S_i} \min_{m,n} P_b(S_i; m, n) \tag{14}$$

subjected to the inequality constraint

$$P_b(S_i; m, n) \leq P_s(S_i; m, n) \tag{15}$$

P_s is the FPF load parameter computed using of eqn (14) and an appriopriate FPF criterion, whereas S_i constitutes a set of $3^{N/4}$ locations of plies oriented at 0° or 90° or ±45° in the laminate.

To simplify the optimization problem formulation, the eqns (14) and (15) have been replaced by the equivalent in the following form: Find

$$\max_{S_i} \min_{m,n} P_b^{m,n} - r_s(P_b^{m,n} - P_s^{m,n})^2 \tag{16}$$

The positive variable r_s controls the magnitude of the penalty term in the above objective function. It is found helpful, and respectful of reality, to allow a small tolerance in satisfaction of constraints — especially for discrete design variables. Tolerances of 0–5% have been used in this study.

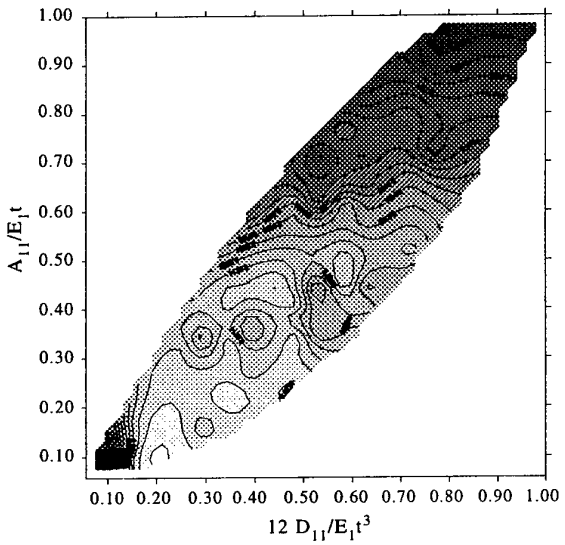

Fig. 2. Contour plot of buckling loads.

GENETIC ALGORITHMS

The existence of multiple relative or local optima is a characteristic feature of composite 2-D structures, independently on the type of design variables used in the analysis, i.e. continuous, discrete or integer (see Fig. 2). Let us notice that the contour plot shown in Fig. 2 fills only a part of the space A_{11}–D_{11} since fibres can be oriented at 0°, $\pm 45°$ and 90°. Therefore, the problem of the relative optima cannot be unique to linear programming methods. The solution of the problem by the latter methods is usually liable to depend on the initial design from which the design procedures are started. This difficulty can be alleviated by repeating the computations from different starting points and comparing the solutions until reasonable confidence is built up that the global optimum has been achieved. In the area of the optimization of 2-D thinwalled structures two approaches are introduced: (1) two-level multi-start optimization algorithms and (2) genetic (probabilistic) algorithms.

Two-level optimization algorithms are particularly directed to the analysis of continuous design variables, such as fibre orientations θ_k and layer thicknesses. At the first phase of the optimization, the layer thicknesses are kept constant and the conditional global optimal orientations are determined to maximize failure loads using a multi-start optimization method. At the second level the optimal layer orientations are kept unaltered and the conditional global optimal thicknesses are designed including also multi-start optimization methods. The obvious advantage of genetic techniques over the previously discussed algorithms is based on probabilistic search method linking both multi-start optimization algorithms, the possibility of the effective optimization analysis for disjoint or nonconvex design spaces and the existence of zero–one integer variables simplifying the computer coding. Mathematical programming methods will find the optimum in convex problems where a single global optimum exists. Genetic algorithms are local search methods that belong to the class of stochastic or random search algorithms. Although these algorithms are randomized, genetic algorithms are not a simple random walk in the space of design variables. They efficiently incorporate information from previous stages to create new search points in the design space, resulting in improved performance. Genetic algorithms use random choice as a tool to guide their search through a coding of design variables. However, it should be pointed out that the genetic algorithms do not prevent re-entry of the search into unfavourable regions in the design space. For instance, the current maximum fitness will drop back a considerable distance after reaching a new level and several generations of processing may be needed before the algorithm picks up again. The above may be stimulated, eliminated and accelerated by various factors representative of genetic algorithms. Clearly the removal of unfavourable regions is of benefit to the optimization process. However, a space condensation may be conducted rather on the basis of knowledge concerning the particular physical problem.

There are essentially three basic components necessary for the succesful implementation of a genetic algorithm. At the outset, there must be a code or scheme that allows for a bit string representation of possible solutions to the problem. In our detailed discrete optimization problem described by eqn (16) it is assumed that the fibres oriented at 0° are represented as 1, at $\pm 45°$ as 2, and at 90° as 3. The assumed sets of discrete data may possess an arbitrary number of values and, for example, the bit representing fibre orientations may be a list of 17 values, e.g. $(i-1)\times 5°$ $(i = 1, ..., 17)$. However, coding of continuous ply-angle variables involves always a rounding errors and finally it may result in finding of local not global optima.

On the other hand, for bits describing continuous ply variables the effectiveness of genetic search algorithms may be completely wrong. Next, a suitable objective function must be devised, for instance in the form given by eqn (16). The final component is the development of transformation functions, with the use of random variable generators, that mimic the biological evolution process, i.e. recombination and mutation. The above three factors may be easily adopted to the optimal design strategy for 2-D thinwalled composite structures. However, it should be emphasized that the correctness of the genetic search as well as the total number of iterations depend on various factors, such as: (1) the number of multiple relative and local optima, (2) the length of the bit string (equal to $N/4$) — for discrete optimization problems the better results can be obtained as N increases, (3) the initial population size, (4) the probability and number of crossover, (5) the probabilty of mutation, (6) the selection rule in the recombination process (the design space condensation). It is not known in advance how, for a particular optimization problem, the optimal values of the above factors can be selected or prescribed.

Due to the lack of space, we present herein some numerical results only, but in our opinion they demonstrate some general trends occurring in the optimization of 2-D laminated composite structures. In general, the numerical experiments have been designed to study how genetic information is carried by populations. Two aspects have been analyzed in details, i.e. the influence of the selection and crossover operations on the genetic search optimization process and optimization results. The selection is based on the best choice of individuals (according the assumed criterion) in an old population that can be a future parent and create a new population. Referring to Fig. 2, the selection is equivalent to the choice of the subspace in the A_{11}–D_{11} space such that it contains the global optimum — the space condensation. In the selection process individuals having good values of fitness may receive a higher weighting than bad. The question is how do we identify good values during the processing? Or on the other hand, how can we create a basis on which the genetic algorithm can learn to distinguish between good and bad? To illustrate, explain and investigate the importance of the selection operations in the genetic algorithms four selection methods have been proposed and tested herein. They have been introduced as the system of updating rules (procedures) described below.

1. The classical roulette random operation.
2. For the old population the average fitness value ($\bar{f}$) is determined and then the individuals having the fitness values greater than e.g. $0.5\bar{f}$ are selected to the new population. The rest of the new population is randomly generated among the individuals having $f \geq \bar{f}$.
3. The selection rule is the same as in the procedure 2 but each of the worst individuals (i.e. $f \leq \bar{f}$) is replaced by the best individual in the old population.
4. In the old population the worst individuals are mutated in order to obtain the better genetic material.

Variations of the average fitness values with the selection methods are shown in Fig. 3.

As may be seen, the selection methods 3 and 4 are the best. Let us show that they represent the search procedure where, in the old population, the best individuals only can offer their genetic material for new generations. It is worth noting that similar results have been obtained for different numerical examples studied herein. It is worth mentioning here that the same results have been obtained in the discrete optimization of laminated plates (Ref. [11]). Thus, it demonstrates evidently that for laminate topology optimization some general rules in the selection process may exist. As the next example, let us consider the influence of the crossover on the average of the fitness value (Fig. 4). Both mutation and crossover operations are handled variable-by-variable so the operations are taking place on comparatively

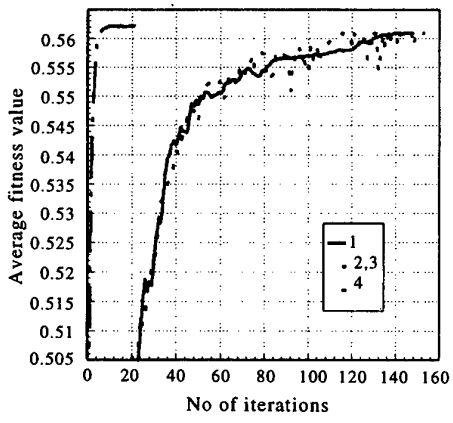

Fig. 3. Influence of selection methods.

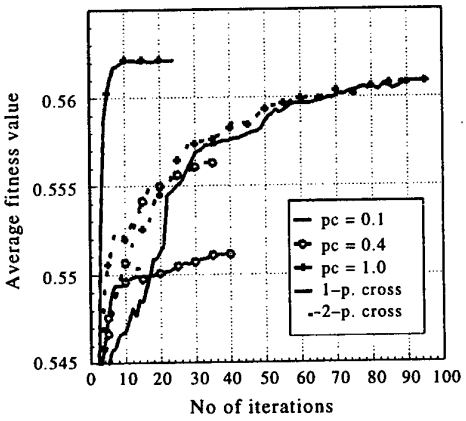

Fig. 4. Effects of crossover.

short strings. It has been reported that as the mutation probability tends to zero, the effectiveness of the optimization process increases. The identical effects have also been observed for laminated plates (Muc *et al.* [11]). Then, as it is decided whether or not the mutation can be applied to a string, a second random number decides which bit can be mutated. The numerical experiments plotted in Fig. 4 prove that the value of the crossover probability p_c and the number of the crosspoints in the string may affect the total number of iterations required for the convergence of the optimization problem. However, it does not prove how can we select the best value of p_c and the cross sites. Further work is necessary to assess this device for particular optimization problems. It is obvious that a good selection method may significantly accelerate an optimal search and allows the avoidance of the loss of convergence. In our opinion, for laminated composites there is only a few representative parameters that decide what configuration is optimal or not and they are connected directly with the form of an objective function. For instance, for compressed composite plates in Ref. [12] it has been proved that angle-ply orientations are optimal as ply orientations are continuous variables. In that case, only angle-ply orientations play a role of the representative parameter, i.e. they select and cut off a set of allowable solutions. As may be seen in Figs 3 and 4 the choice of the best individuals in populations always gives convergent solutions since they possess the representative genetic material for the optimal search. Therefore, the search for the best selection method is necessary and it should be supported by theoretical considerations of a particular optimization problem because as numerical results demonstrate, in fact, that genetic algorithms are not a completely a random process.

NUMERICAL EXAMPLES

A large number of numerical calculations for optimization with both buckling and FPF constraints have been carried out with various geometrical ratios. In general, it has been found that the optimal solutions cannot be determined uniquely. That is, there are many sets of optimal strings which give the identical values of the objective function. The optimal point is always defined and obtained, not as a function of design variables but as a function of the finite number of terms defining the stiffness matrix for a laminate. Therefore, various combinations of design variables may exist that give the identical values of the terms in the stiffness matrix. The same conclusions have been drawn from the analysis of optimization problems for laminated plates [11].

The results presented herein were obtained for a graphite–epoxy cylindrical shell having the following material properties

$$E_1 = 212.0 \text{ GPa}, E_2 = 12.72 \text{ GPa},$$

$$G_{12} = 7.42 \text{ GPa}, \nu_{12} = 1/3,$$

$$\varepsilon_1^{\max} = 0.008, \varepsilon_2^{\max} = 0.029, \varepsilon_{12}^{\max} = 0.015 \qquad (17)$$

Figures 5–7 show the variations of optimal dimensionless buckling load parameter P_b/tE_2 versus the variations of the dimensionless length parameter α. The effects in variations in

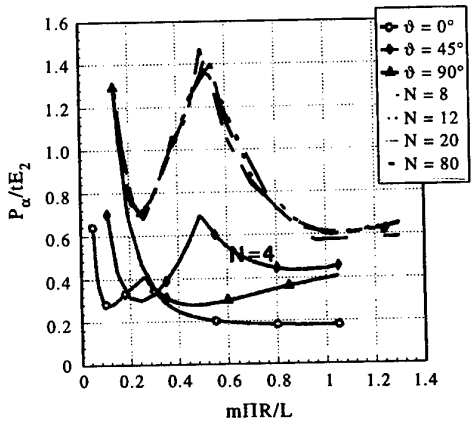

Fig. 5. Variations of optimal buckling loads with the number of layers — the Donnell–Vlasov shallow shell theory.

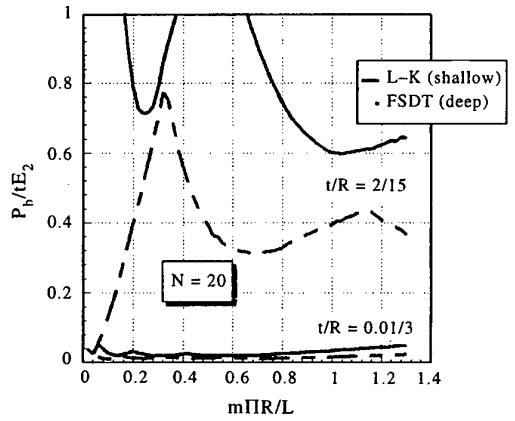

Fig. 6. Influence of the thickness ratio t/R.

number of layers in the laminate on optimal buckling loads is demonstrated in Fig. 5. As was expected, upon increasing the number of layers, the optimal buckling load increases very rapidly. However, for $N > 20$ $(N/4 = 5)$ the values of optimal buckling loads are almost insensitive to the variations of N, although the optimal string varies since the string becomes larger. Therefore, in further analysis, the length of the string has been limited to 5. On the other hand, the values of wave numbers, and in particular the value of n, increase with α. Figure 6 give an indication of the influence of the thickness ratio t/R on the values of optimal critical loads. The optimal buckling loads based on the transverse shear deformable theory are always lower than the corresponding values based on the classical (L–K) theory. Due to the relatively small value of the thickness ratio t/R, the observed discrepancies do not exceed 10% $(t/R = 0.0033)$ but become larger (even up to 220%) as the thickness ratio increases to 0.075 (Fig. 6). The

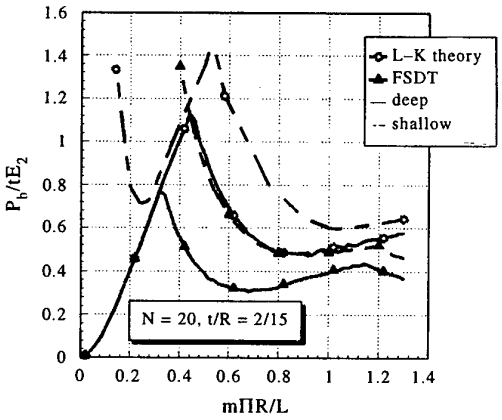

Fig. 7. Comparison of optimal buckling loads for various shell theories.

difference in values of optimal buckling loads is also a function of the α parameter and of the employed variant of the shell theory. If the parameter α tends to zero (long cylindrical shells) the difference in optimal buckling loads rapidly increases for shallow and deep formulation of the optimization and buckling problem. This simply gives an indication about the validity of the employed kinematic and constitutive relationships. It should be emphasized that the comparative review of variations of buckling loads with various parameters deals with the optimal loads. Thus, the values of P_b for the identical parameters α have been evaluated for different (optimal) laminate configurations. As may be seen in Table 1, the optimal strings are different for various formulations of the shell theories.

Figure 7 gives a comparison of optimal buckling loads for four variants of the analysed shell theories and one value of the thickness ratio t/R equal to 0.075. It appears that both transverse shear deformations and the shallowness parameters have the opposite effects on the values of optimal buckling loads. As the shallowness parameter decreases the optimal buckling load increases. Thus, investigating the optimization problems, researchers should be very careful in the choice of the appriopriate variant of the shell theory. For the analysed numerical results, especially from the point of view of the assumed material properties — eqn (17) and the low thickness ratio (less than 0.1 being the limit of validity of the classical relations for isotropic 2-D structures), ply failure has not been observed, i.e. buckling is a dominant failure mode.

CONCLUSIONS

The optimal design of laminated composite cylindrical shells is presented. The design goal is to the maximize buckling load of the axially compressed cylindrical shell. For a certain type of simply-supported boundary conditions the governing equations have been solved analytically and then used in the analysis of buckling and FPF for four variants of shell theories. The constraints are imposed on lamina failure — the governing failure equations have been given in the explicit analytical form too. A genetic algorithm is presented and applied to the optimal design. The objective function is formulated

Table 1. Comparison of optimal strings for various shell theories ($N = 20$, $t/R = 0.01/3$)

$\alpha = \frac{m\Pi R}{L}$	L–K		FSDT	
	Deep	Shallow	Deep	Shallow
0.4	11 333	11 112	11 133	13 333
0.6	12 113	11 123	11 133	11 333
0.8	11 233	12 133	11 123	11 333
1.0	11 213	11 213	11 112	11 233

for particular shell theories, i.e. the first-order transverse shear deformation theory and the classical Love–Kirchhoff theory (for both the deep and shallow variants) have been studied using a geometrically linear approach. The examples are solved to demonstrate the importance of the selection procedures in genetic algorithms and to highlight the significance of transverse shear effects in optimization problems.

The choice of the selection method seems to be one of the most important factors in genetic optimization procedures. It is shown that the selection procedures may significantly reduce the total number of iterations required in the optimal search. In our opinion a search for the best (effective) selection procedures is necessary. Now, however, not only is numerical implementation of different variants of genetic algorithms required, but also a deeper, theoretical explanation of the assumed choice.

The present study shows the effectiveness of genetic methods for optimal design of shells using both FSDT and the classical L–K theory.

It is worth emphasizing that for laminated thin-walled structures, the resulting optimal laminate topologies and failure loads are very sensitive to the applied type of 2-D shell approximations and to the thickness t/R ratio.

It has been proved that the use of classical shell theories may lead to completely wrong results in both the estimation of buckling loads and in the determination of optimal laminate configurations (strings) for orthotropic materials. For a more accurate description of the optimization problems under buckling and FPF constraints it is necessary to apply more refined shell theories based on the local (laminatewise) rather than the 3-D models as e.g. delamination problems will be taken into account.

Upon increasing the number of plies, optimal buckling pressure become insensitive to the variations of N.

ACKNOWLEDGEMENT

The support from KBN grant PB-232/T07/95/08 is gratefully acknowledged.

REFERENCES

1. Noor, A.K. and Burton, W.S., Assessment of computational models for multilayered composite shells. *Appl. Mech. Rev.*, 1990, **43**, 67–97.
2. Koszevoy, I.K., Buckling of nonhomogeneous spherical shells. *Prikladnaya Mech.*, 1982, **18**, 39–44.
3. Librescu, L., Khdeir, A.A. and Frederick, D., A shear deformable theory of laminated composite shallow shell type panels and their response analysis, I: Free vibration and buckling. *Acta Mech.*, 1989, **76**, 1–33.
4. Muc, A., Transverse shear effects in stability problems of laminated shallow shells. *Composite Structures*, 1989, **12**, 171–180.
5. Soldatos, K.P., Nonlinear analysis of transverse shear deformable composite laminated shells. *Pressure Vessel Techn.*, 1992, **114**, 105–114.
6. Tasi, J., Feldman, A. and Stang, D. A., The buckling strength of filament-wound cylinders under axial compression. *NASA-CR-266*, NASA, July 1965.
7. Hirano, Y., Buckling of angle-ply laminated circular cylindrical shells. *J. Appl. Mech.*, 1979, **46**, 233–234.
8. Uemura, M. and Kasuya, H., Coupling effects on axial compressive buckling of laminated composite cylindrical shells. *Proc. ICCM-IV*, (1982) 583–590.
9. Onoda, J., Optimal laminate configurations of cylindrical shells for axial bucking. *AIAA J.*, 1985, **23**, 1093–1098.
10. Narusberg, B. L. and Teters, G. A., *Buckling and optimization of composite shells*. Riga, Zinatne, 1988 (in Russian).
11. Muc, A. and Saj, P., Transverse shear effects in discrete optimization of laminated compressed plates under buckling and FPF constraints. *Proc. ICCM-11*, 1997.
12. Muc, A., Optimal fibre orientation for simply-supported, angle-ply under biaxial compression. *Composite Structures*, 1988, **9**, 161–172.

ELSEVIER

Composite Structures Vol. 38, No. 1–4, pp. 499–507, 1997
© 1997 Elsevier Science Ltd. All rights reserved
Printed in Great Britain
0263-8223/97/$17.00 + 0.00

PII:S0263-8223(97)00085-8

Two-dimensional modelling of solid–fluid composites

Tsutao Katayama

Department of Mechanical Engineering, Doshisha University, Tanabe-cho, Tuzuki-gun, Kyoto-fu 610-03, Japan

Hidetake Yamamoto

Faculty of Mechanical Engineering, Kobe City College of Technology, Gakuenhigashi-cho, Nishi-ku, Kobe 651-21, Japan

&

Kazuo Nishitani

Postgraduate Course, Doshisha University, Tanabe-cho, Tuzuki-gun, Kyoto-fu 610-03, Japan

The purpose of this paper is to apply biomimetic-designed composites to artificial structures. From the results of numeric modelling analysis in biomechanics, we have learned the bone structures optimized to lighten weight and understood that the solid–fluid composite structure of the cancellous bone at the joint part works to distribute the joint load perfectly. In this paper, the two-dimensional honeycomb structure filled with fluid was investigated by way of a simplified solid–fluid composite material model of the cancellous bone. Hybrid finite element analyses illustrated that the solid–fluid phase interaction is effective in dispersing compressive load. In-plane indentation tests were carried out and in-plane deformation distributions of the solid–fluid composite specimens were measured. Consequently, as for the solid–fluid composite specimens whose cells were filled up with glycerine, a good enough cell deformation mode was obtained. © 1997 Elsevier Science Ltd.

INTRODUCTION

Fibre-reinforced composites have attracted attention by way of tailored materials and have been studied. But they are used in practice as quasi-isotropic materials and their functions are not utilized effectively. However, it has been shown in many reports that biomaterials have fibre-reinforced composite structures and are optimally designed to loadings. We have studied bone structures from the viewpoint of composite materials and learnt the mechanism of optimum structures of the bone [1,2]. It was found from biomechanical results that the natural structures are perfectly optimally designed. The aim of this research was to develop biomimetic-designed composites. From the results of our biomechanics research we have considered applying the mechanical functions of the bone's composite structure to new material designs. We have recognized the solid–fluid composite structure of the cancellous bone in the bio-joints to be a material system and investigated these functions as an intelligent material; we will try to develop new materials given these functions artificially.

The purpose of this study is to learn from the cancellous bone, which has a good load dispersive and a high shock absorptive bio-structure, and to develop an artificial material prepared from those properties. The solid–fluid structure of the cancellous bone consists of the trabecular bone as a three-dimensional (3-D) open-cell structure and the marrow in the bones as a viscous fluid. But simplified modelling appears to be effective in

analysing the essential functions of the cancellous bone because 3-D analysis complicates the problem. In this paper, the two-dimensional (2-D) honeycomb structure filled with fluid is investigated by way of a simplified solid–fluid composite material model for the cancellous bone. To evaluate the load-support system under compressive loadings, a 2-D closed hexagonal cell filled with fluid is used. At first, hybrid finite element analyses were used to estimate the influence of the solid–fluid phase interaction on the compressive deformation of the material. To verify the numeric result, in-plane indentation tests were carried out and the load–indentation depth curves are obtained. And the cell's in-plane deformation distributions of the solid–fluid composite specimens were measured.

MODELLING ANALYSIS OF CANCELLOUS BONE STRUCTURE

Finite element modelling analysis of the cancellous bone in the bio-joints was investigated in order to obtain a biomimetic design of the new composites. The hexagonal unit used to replicate the solid–fluid composition of the cancellous bone is shown in Fig. 1. It is possible to express the dynamic behaviour of the solid–fluid composite systems in the hybrid finite element model with the following two assumptions [1]: the solid–fluid composition of the cancellous bone will be reproduced two-dimensionally by combining the hexagonal frame, which has a framework of two-noded beam elements rigidly jointed to each other, with the core which has six three-noded triangular elements [2]. Each hexagonal core will have a compressive modulus alone corresponding to the resistance of the bone marrow to the dynamic compressive stress and will contribute to the stress transmission of the cancellous bone independently. By assuming geometrical symmetry of the human proximal tibia to simplify the treatment, a 2-D model was applied to the right half. Figure 1(a) shows the hybrid finite element model of the tibial cancellous bone. The hybrid model consists of triangular elements for the bone marrow, beam elements for the trabecular bone and triangular elements for the cortical bone. The material properties given to the finite elements are listed in Table 1. In-plane elastic moduli of triangular elements for the bone marrow were calculated as an isotropic body. However, the Poisson ratio of an incompressive fluid is 0.5, so 0.49 was selected in order to enable the numeric analysis to be carried out. The left-hand sides of the models were fixed in the horizontal direction only, and the bases were fixed in both the vertical and horizontal directions. A large displacement

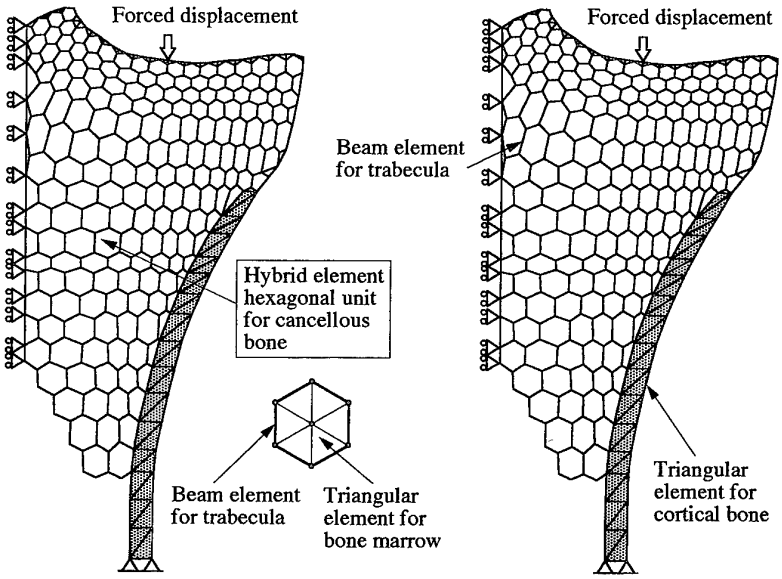

Fig. 1. Finite element model for cancellous bone of the proximal tibia. (a) Using hybrid element modelling and (b) using mono-element modelling.

Table 1. Material properties for finite element models

Material (finite element)	Young's modulus (MPa)	Shearing modulus (MPa)	Poisson's ratio
Trabecular bone (beam)	5000	–	–
Bone marrow (triangular)	1000	–	0.49
Cortical bone (triangular)	14000	3500	0.35

corresponding to the dynamic compressive loading was applied, and the incremental finite element analyses were carried out.

Figure 2 shows distributions of the maximum principal strain of the hexagonal units assuming that the cancellous bone is under compressive loading by the finite element method (FEM). Although the load is expected to be uniformly distributed on the articular surface in the ideal case, the stress propagation behaviour under one-point concentrated compressive loading was simulated in order to examine more clearly the pattern of stress dispersion under the great force assuming dynamic compressive loading. Figure 2(a) and (b) shows the results using hybrid element modelling and mono-element modelling for the cancellous bone, respectively. From Fig. 2(a), appropriate maximum principal strains were distributed sufficiently in the cancellous bone. It is expected that the applied compressive force on the articular surface is dispersed perfectly through the cancellous bone and is transmitted to the cortical bone as a uniform compressive stress. However, large maximum principal strains will be distributed near the loading point because of the considerably high compressive stresses applied locally in the analysis. To emphaisize the effect of the solid–fluid interaction, the numeric results for the case of disregarding the solid–fluid interaction are shown in Fig. 2(b). The result indicates that the bone marrow only flows in the trabecular bone framework under compressive loading and does not contribute to the stress propagation through the cancellous bone. From the figure it was found that large maximum principal strains were distributed from the loading point through a part of the cancellous bone near the cortical bone and that maximum principal strains were not distributed sufficiently in the cancellous bone. Particularly, considerable large maximum principal strains were distributed under the loading point. Therefore, comparing Fig. 2(a) with (b), if the bone mar-

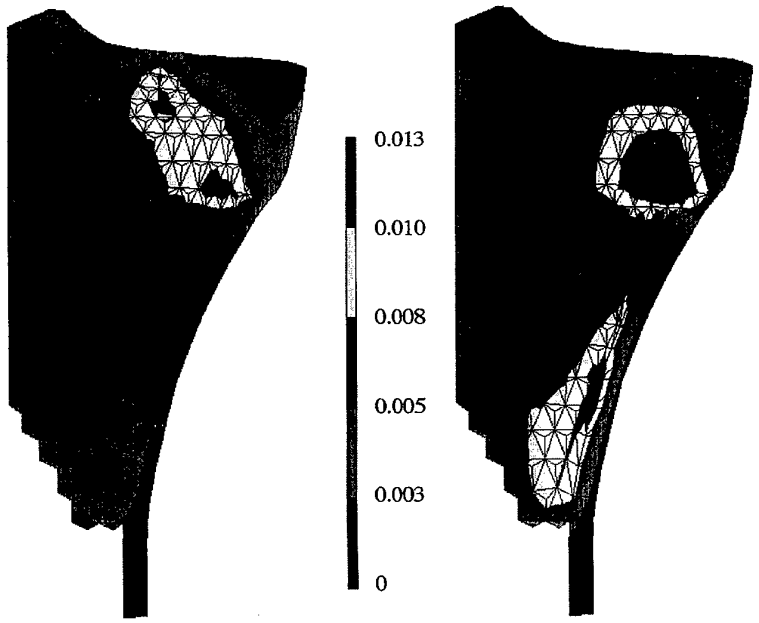

(a) Using hybrid element modelling (b) Using mono element modelling

Fig. 2. Distributions of maximum principal strain by FEM. (a) Using hybrid element modelling and (b) using mono-element modelling.

row was out of all relation to the stress propagation through the cancellous bone, 'micro-buckling' of the trabeculae would occur in the cancellous bone. Then, it is expected that the compressive loading is spent in the micro-fracture of the trabeculae and is poorly propagated to the cortical bone. The results coincident with the behaviour of the solid–fluid composite system under compressive loading were obtained from this analysis.

NUMERIC ANALYSIS OF 2-D SOLID–FLUID COMPOSITES

From the numeric results of the cancellous bone we propose solid–fluid composites for the stable support of compressive loadings. Hybrid finite element analyses were done in order to estimate the influence of the solid–fluid phase interaction on the compressive deformation of the following material models. The deformation of the specimens was regarded as a plane strain condition due to the experimental conditions. Figure 3 shows the 2-D finite element models for the solid–fluid composites (following the type A specimen) and the solid material (following the type C specimen). The hybrid hexagonal model unit for the solid–fluid composites consists of six beam elements with two rigid joints and six triangular elements with three nodes. The material properties given to the finite elements are listed in Table 2. The bulk modulus of the water under ordinary temperature and normal pressure was applied to the triangular elements. That is to say, the in-plane elastic moduli of the triangular elements were calculated as an isotropic body. However, the Poisson ratio of an incompressive fluid is 0.5, and 0.49 was selected in order to enable the numeric analysis to be carried out. Considering the symmetry of the boundary conditions, the right-hand half of the specimen was analysed. The left-hand sides of the models were fixed in the horizontal direction only, and the bases were fixed in both vertical and horizontal directions. A displacement corresponding to the experimental results was applied, and the incremental finite element analyses were carried out.

Figure 4 shows the deformation distributions of the solid–fluid composites and the solid material by FEM. As for the solid material, positive large deformations were distributed in the central part and along the diagonal line. Negative large deformations existed in the small-side part. The solid material supported the compressive load along the anisotropic axis of the honeycomb material. As for the solid–

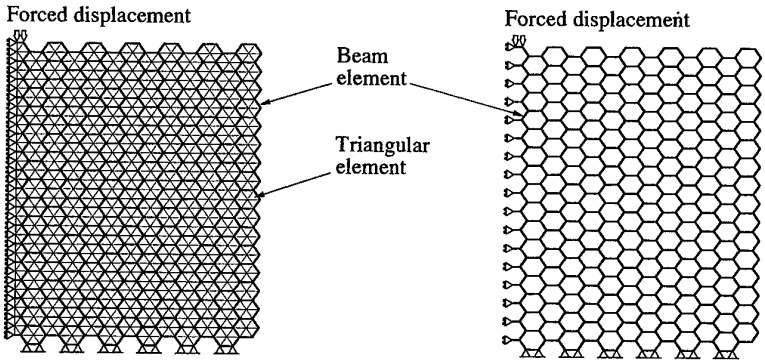

Fig. 3. Finite element models. (a) For solid–fluid composites and (b) for solid materials.

Table 2. Material properties for finite element models

Material (finite element)	Young's modulus (MPa)	Bulk modulus (MPa)	Poisson's ratio	Yield stress (MPa)
A5052H (BEAM)	7100	–	–	340
Glycerine (triangular)	132	2200	0.49	–

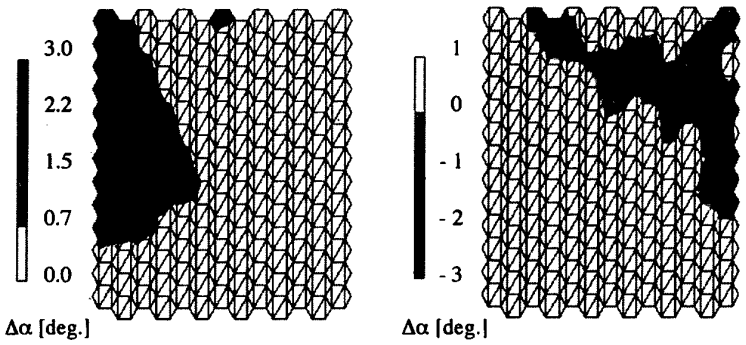

(a) For solid-fluid composites

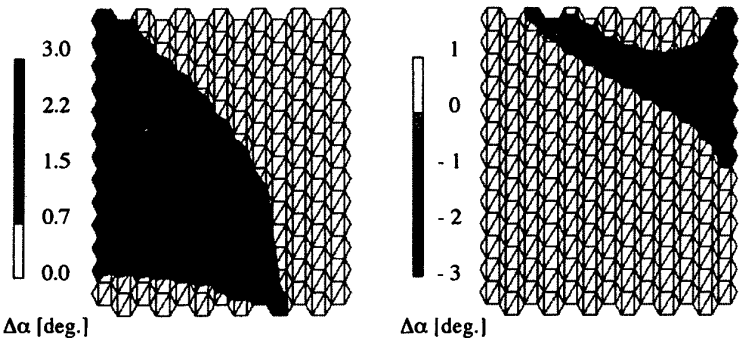

(b) For solid materials

Fig. 4. Distributions of a cell's in-plane deformation by FEM. (a) For solid–fluid composites and (b) for solid materials.

fluid composites, positive large deformations were distributed in the central part, and negative large deformations were distributed in the part along the horizontal line. The solid–fluid composites supported the compressive load in the wide part of the surface not only in the solid material but also in the fluid material. Consequently, these results illustrated that the solid–fluid phase interactions worked well on the load-support system of the solid–fluid composites.

EXPERIMENTAL SOLID–FLUID COMPOSITE MODELS

Aluminium honeycomb sheet was used for the 2-D experimental model of the solid–fluid composite because aluminium alloy is easy to assemble. The honeycomb was made of aluminium foil (A5052H) of 0.025 mm thickness and 23 mm width. The dimensions of the hexagonal cells are shown in Table 3. Honeycomb sheets were cut into pieces 85 mm high and 120 mm wide. The dimensions of the test piece are shown in Fig. 5.

Four kinds of specimens were prepared to characterize the mechanical functions of the solid–fluid composite. Theses are listed in Table 4. Both type A and type B specimens are solid–fluid composite models, and both type C and type D specimens are solid material models. Type A and type B specimens are the solid–liquid composites and the solid–air composites, respectively. The hexagonal cells of the type A specimens and type B specimens were all filled with glycerine and air, respectively, under ordinary temperature and normal pressure to observe the effect of the compressibility. Both side surfaces of type A, type B and type C

Table 3. Dimensions of hexagonal cells

Material	d (mm)	t (mm)	b (mm)	θ (degress)
A5052H	4.56	0.025	23.00	101.0

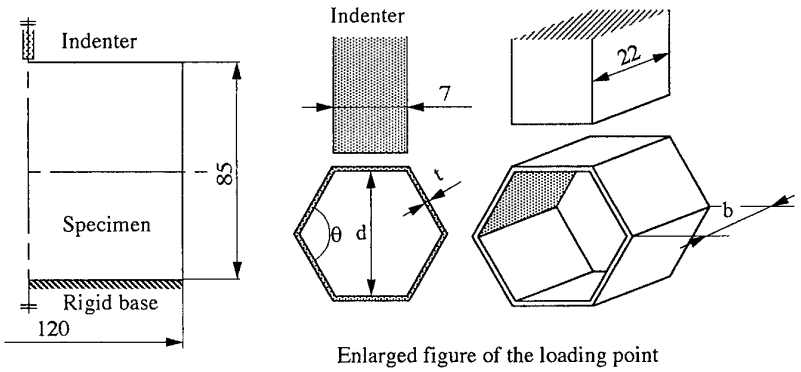

Fig. 5. Experimental conditions of the in-plane indentation test.

specimens were all sealed with polyvinyl film using an epoxy elastic adhesive. But type C specimens were made of aluminium foil with holes of about 10 μm diameter. Type C specimens were used in order to determine the influence of the film, so the deformation of the specimens is not influenced by pressure in the hexagonal cells. Type D specimens have a honeycomb structure only.

LOAD–INDENTATION DEPTH CURVES

An in-plane indentation test was proposed in order to evaluate the deformation in the specimens under compressive loading. The experimental conditions of the in-plane indentation test are shown in Fig. 5. However, honeycomb sheets are stable to out-of-plane compression, the in-plane compressive deformations are anisotropic and complex because of the geometric deformations of the hexagonal cells. However, the in-plane deformations are evaluated easier when compressing honeycomb sheets, as shown in the figure. The indenter which has a flat head was set on the load cell of the universal testing machine. The specimens were set on the base to connect the indenter with the centre cell which was stiffened with polyester resin to obtain symmetric in-plane deformation and stable deformation. Indentation tests were carried out statically using the testing machine at a cross-head speed of 5 mm/min, and the load–indentation depth curves were obtained. Figure 6 shows typical load–indentation depth curves of four types of the specimen.

The curve of the type D specimen is linear until the indentation depth reached 3 mm and shows temporary drops and rises in the load after the indentation depth went above 5 mm. The first knee point of the curve is the indentation depth of 3 mm because the initial deformation of the specimen shows simple elastic behaviour. When compressing cellular materials, the geometric rigidity decreases because of buckling. The curve becomes nonlinear over the knee point because of the buckling of the hexagonal cells. Structural condensation by the collapse of the hexagonal cells causes the load to rise. Although they have an energy absorption property, they do not suit the load-supporting material. The type C specimen shows itself to be a little more rigid than the type D specimen because both side surfaces of the type C specimen were sealed with polyvinyl film. But the type C specimen also shows linear behaviour until the indentation depth reached 3 mm and temporarily drops and rises with the load. The curve of the type C specimen is the same result as that for the type D specimen. That is to say, sealing with polyvinyl film did not change the in-plane compressive deformation pattern of the honeycomb sheet.

Table 4. List of specimens

Specimen name	Base material condition	Fluid material	Side surfaces condition
Type A specimen	Without holes	Glycerine	Film adhesion
Type B specimen	Without holes	Air	Film adhesion
Type C specimen	With holes	None	Film adhesion
Type D specimen	Without holes	None	Free

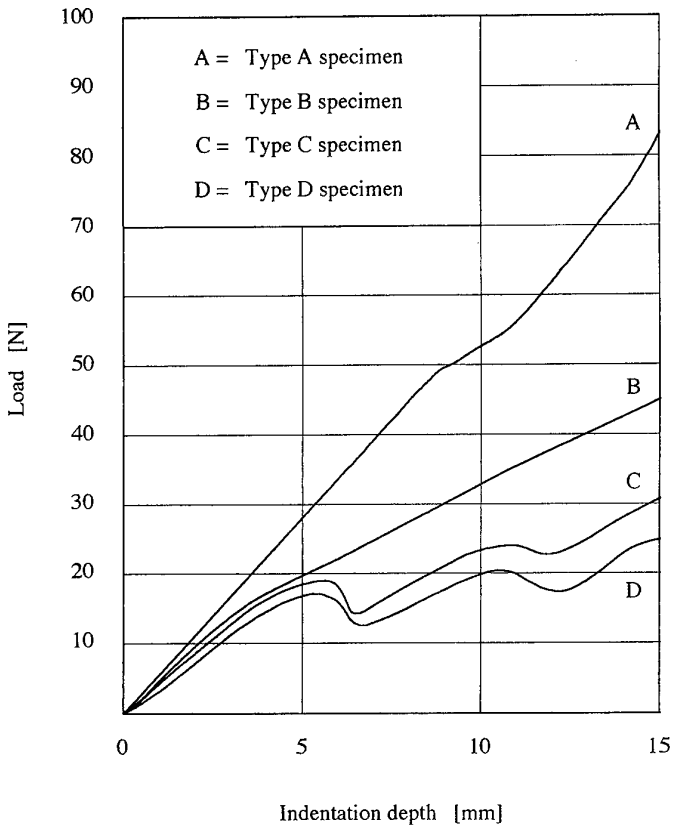

Fig. 6. Measurement of a cell's in-plane deformation.

A significant difference is seen between the curves of the type B and type C specimens. The curve of the type B specimen stayed linear until the indentation depth reached 3 mm, but did not have temporary drops and rises in load above 5 mm indentation depth. The curve had only one knee point because it was almost linear above 3 mm in the indentation depth. The initial deformation of the type B specimen was the same mechanism as with the type C specimen. It was considered that the difference between the curves of type B and type C specimens after the knee point was caused by increasing the air pressure in the hexagonal cells. When the curve is over the knee point, the geometric rigidity of the specimen decreased, and then the compressive deformations of the hexagonal cells raise the air pressure in the cells locally, which as a result, contributes to support the load. For the type A specimen the curve was linear until the indentation depth reached 8 mm. It was observed that polyvinyl film rose from the side surface of the hexagonal cells under the indenter because of the high liquid pressure of the glycerine.

IN-PLANE DEFORMATIONS OF THE CELL

The load-support system of the solid–fluid composites was examined by measuring the side surface deformation of the specimens. The side surface pictures were taken using a camera during the indentation tests. In order to minimize an error of measurement, the in–plane deformation of the specimens was carried out using the shifts of the joints between the hexagonal cells. The shifts of the joints were measured by the difference between the pictures under the indentation tests and the initial condition.

From the side surface pictures of the specimens, three in-plane deformation modes of the hexagonal cells were found around the loading point, as shown in Fig. 7. Mode I deformations came from vertical compression of the rigid cell walls and were distributed in the central part of the specimens. Mode II deformations came from the horizontal compression at the joints between the thin cell walls on both sides of the mode I deformations and mode II deformations were distributed in both sides of the specimens.

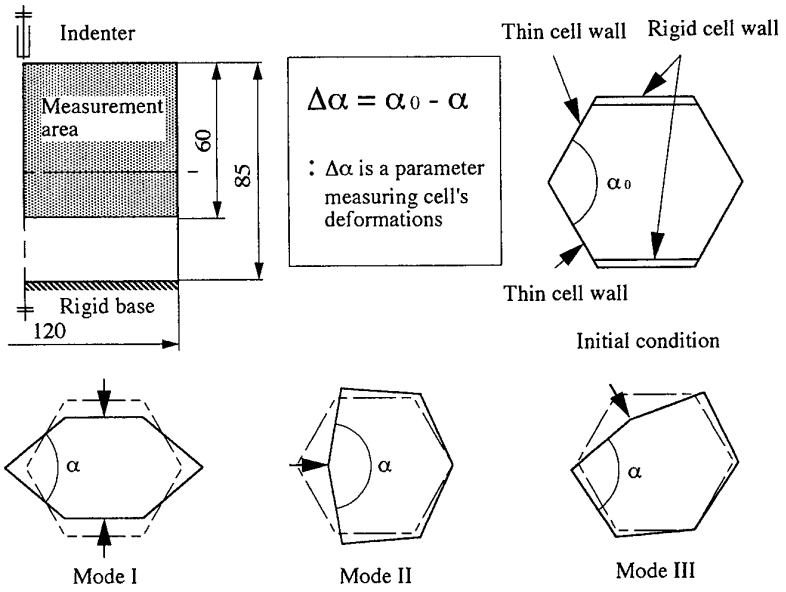

Fig. 7. Typic load–indentation depth curves.

Mode III deformations came from the diagonal compression of joints between the rigid and the thin cell walls under both mode I and mode II deformations and were distributed in the parts between the mode I and mode II deformations. The in-plane deformation distribution including these three modes can be evaluated by measuring the change of angle between the thin cell walls as a parameter. Then the type A specimen is expected to have an good load dispersion property because the sufficient liquid pressure of the glycerin in each cell acts effectively on the load transmission. Mode I and mode III deformations are distributed where the changes of the angle are positive, and mode II deformations are distributed where the changes of the angle are negative.

Figure 8 shows the in-plane deformation distributions of type A, type B and type C specimens at an indentation depth of 5.0 mm. As for the type C specimen, positive large deformations were distributed in the central part and along the diagonal line. The maximum deformations under the loading point are mode I deformations, and the large deformations in the part along the diagonal line are mode I or mode III deformations. Negative large deformations existed in the small side part. The type C specimen supports the compressive load along the anisotropic axis of the honeycomb material because only the solid material supports the load. When the hexagonal cells collapse by mode I deformation under the loading point, large buckling comes out of mode I or mode III deformations in the part along the diagonal line. As for the type A specimen, positive large deformations were distributed in the central part, and negative large deformations were distributed along the horizontal line. The positive large deformations in the central part are mode I deformations, and the negative large deformations along the horizontal line are mode II deformations. The type A specimen supports the compressive load in the wide part, because there not only solid material but also liquid material supports the load. Considering the experimental conditions large bucklings never came out of mode II deformation along the horizontal line. As for the type B specimen, the cell's in-plane deformation distribution displayed a result in between the type A and type C specimens.

CONCLUSION

From the viewpoint of the biomimetic design, the 2-D honeycomb structure filled with fluid was investigated by way of a simplified solid–fluid composite material model from a

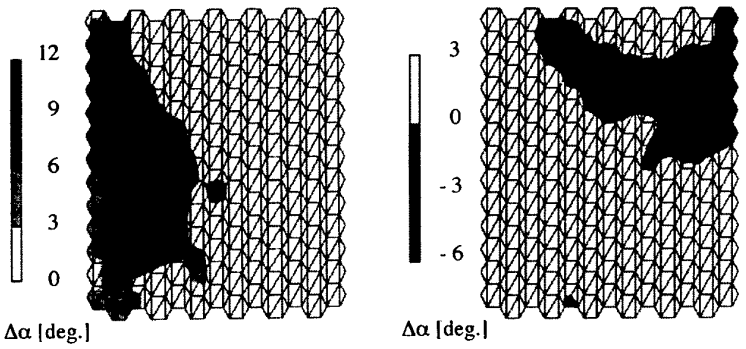

(a) Type A specimen

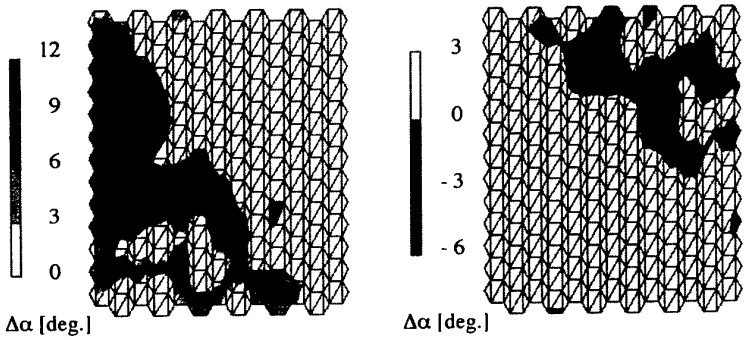

(b) Type B specimen

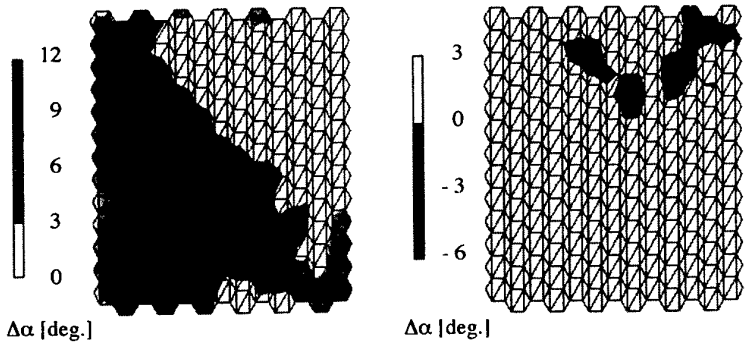

(c) Type C specimen

Fig. 8. Distributions of a cell's in-plane deformation. (a) Type A specimen, (b) type B specimen and (c) type C specimen.

cancellous bone at the joint. The results of a hybrid finite element analysis pointed out the efficiency of the solid–fluid phase interaction of the solid–fluid composites on the load dispersion. In-plane indentation tests were carried out and the load–indentation depth curve of the solid–fluid composites showed a good load support. The cell's in-plane deformation distribution of the solid–fluid composites displayed a high load dispersion property.

REFERENCES

1. Katayama, T., Yamamoto, H., Ishiyama, H., Hirasawa, Y., Inoue, N. and Watanabe, Y., A study on initial fixation of prosthesis based on biomechanical behaviour of subchondral bone. In *Proceedings of the 2nd World Congress of Biomechanics*, Amsterdam, Vol. 1, 1994, p. 106A.
2. Katayama, T., Yamamoto, H. and Inoue, N., Optimum design of artificial joints considering initial fixation of prosthesis. *Composite Struct.*, 1995, **32**, 427–433.

ELSEVIER

Composite Structures Vol. 38, No. 1–4, pp. 509–515, 1997
© 1997 Elsevier Science Ltd. All rights reserved
Printed in Great Britain
0263-8223/97/$17.00 + 0.00

PII:S0263-8223(97)00086-X

Damage growth analysis of low velocity impacted composite panels

L. Reis & M. de Freitas

Instituto Superior Técnico, Dept. Eng. Mecânica, Av. Rovisco Pais, 1096 Lisboa, Portugal

Low velocity impact loading in aircraft composite panels is a matter of concern in modern aircraft and can be caused either by maintenance accidents with tools or by in-flight impacts with debris. The consequences of impact loading in composite panels are matrix cracking, inter laminar failure and, eventually, fiber breakage for higher impact energies. Even when no visible impact damage is observed on the surface at the point of impact, matrix cracking and inter laminar failure can occur, and the carrying load of the composite laminates is considerably reduced. The greatest reduction in loading is observed in compression due to laminae buckling in the delaminated areas.

The objective of this study is to determine the limit loading capacity and the damage growth mechanisms of impacted composite laminates when subjected to compression after impact loading. For this purpose a series of impact and compression after impact tests were carried out on composite laminates made of carbon fiber reinforced epoxy resin matrix. Four stacking sequences representative of four different elastic behaviours were used. Results show that the compressive, after impact, failure stress is influenced by the stacking sequence but a relatively independent strain to failure is observed. © 1997 Elsevier Science Ltd.

INTRODUCTION

Composite panels are widely used in aeronautic and aerospace structures due to their high strength to weight ratio. The stiffness and the strength in the through-the-thickness direction of laminated composite panels is poor since no fibers are present in that direction. Impact damage may be caused by low-velocity impact or ballistic impact. Low velocity impact loading in aircraft composite panels is present either due to maintenance accidents with tools or in-flight impacts with debris. Low-velocity impact is considered potentially dangerous mainly because the damage might be left undetected. In many situations [1–3], the level of impact at which visible damage is formed is much higher than the level at which substantial loss of residual properties occurs. The low-velocity impact of CFRP laminates creates damage which may involve indentation, matrix cracking, fiber matrix debonding, delamination, inter laminar failure and, eventually, fiber breakage for higher impact energies. Even when no visible impact damage is observed at the surface (energies below Barely Visible Impact Damage, BVID), matrix cracking and interlaminar failure can occur, and the carrying load of the composite laminates is considerably reduced. Visible damage occurs if an impact is above a threshold impact energy which depends on the laminate stiffness [4,5]. The greatest reduction in after-impact loading is observed in compression due to laminae buckling in the delaminated areas. The residual laminate strength and modulus after delamination depend on the stacking sequence and the location of the delamination in the laminate. In certain cases, the lay-up of a delaminated sublaminate also influences the strength and modulus. Considerable research [6–10] has, therefore, been devoted to analyzing the impact properties and post-impact compression behaviour with a view to improving impact damage tolerance.

The objective of the present study is to determine the limit loading capacity and the damage

growth mechanisms of impacted composite laminates when subjected to compression after impact. For this purpose a series of tests were carried out on composite laminates made of carbon fiber reinforced epoxy resin matrix. Four stacking sequences representative of four different bending and compression behaviours and an instrumented falling weight impact machine were used. A discussion and some concluding remarks are presented.

MATERIALS

Composite panels were made of unidirectional prepregs of carbon fibers IM7 on an epoxy resin 977-2 from Fiberite and manufactured by Per Udsen. The nominal thickness is 0.135 mm for 60% V_f, and four stacking sequences of 24 layers were used:

lay-up B: $[45_3/0_3/-45_3/90_3]_S$
lay-up C: $[45/0/-45/90/45_2/0_2/-45_2/90_2]_S$
lay-up D: $[45_4/-45_4/0_3/90]_S$
lay-up E: $[45_3/-45_3/0_5/90]_S$

The elastic properties of the individual laminae and global properties for each panel are listed, respectively, in Tables 1 and 2, and were obtained by identification of the material properties using experimental vibration data [11]. Directions 1 and 2 are, respectively, the longitudinal and transverse direction of each laminae, and x and y are the 0° and 90° directions of the laminate, respectively. Lay-ups B and C correspond to a quasi-isotropic stacking sequence; in lay-ups D and E different global elastic properties are obtained for each direction.

Specimens with dimensions of 150 × 100 mm were cut from the panels; for each lay-up, five specimens with the 0° direction aligned with the 100 mm width (lay-up B, C, D and E) and three specimens with the 0° direction aligned with the 150 mm length (lay-up B*, C*, D* and E*) were obtained.

EXPERIMENTAL PROCEDURE AND RESULTS

Impact testing

A wide range of impact energies were chosen in order to obtain different delamination areas. An instrumented falling weight impact machine was used where the different nominal impact energies were obtained through discrete masses of 2–10 kg and a variable height up to 2 m.

The instrumentation associated with the impact machine measures the force during impact using a force transducer just above the impactor indentor. The system also provides for the measurement of the velocity at the moment of impact. The velocity during impact is calculated by integrating acceleration over time, where the acceleration is given by the force felt by the drop mass, divided by its mass. The calculated velocity is then used to derive the displacement of the impactor during impact (and consequently the deflection of the specimen) using further integration. The energy is calculated by integrating force over distance. With this measurement and calculation procedure, one not only obtains the impact energy but also the absorbed energy through the energy–time curve.

The impactor used was a hemi-spherical steel of 16 mm diameter and was clamped in a standard impact testing fixture with a window of 125 × 75 mm, as described in Airbus Industry Test Method (AITM 1.0010).

Table 1. Elastic properties of laminae

Material	E_1(GPa)	E_2(GPa)	G_{12}(GPa)	G_{13}(GPa)	G_{23}(GPa)	ν_{12}
IM7	160.0	9.0	6.9	3.8	4.3	0.20

Table 2. Elastic properties of laminates

Stacking	E_x(GPa)	E_y(GPa)	G_{xy}(GPa)	G_{xz}(GPa)	G_{yz}(GPa)	ν_{xy}
B	62.1	62.1	24.2	4.0	4.0	0.28
C	61.9	61.9	24.1	2.7	2.7	0.28
D	63.8	41.7	31.5	2.8	2.0	0.49
E	83.0	37.6	23.8	4.8	4.7	0.46

An example of two plots of an impact test for a specimen with lay-up B, unfiltered load versus integrated displacement and calculated energy versus time history are shown in Fig. 1(a) and (b), respectively.

Delamination area

A C-scan NDI ultrasonic technology with a pulse-echo and an immersion scanning method from Physical Acoustics was used, with the following C-scan data:

- Scan frequency: −5 MHz
- Scan speed (X axis): −30 mm/s
- Index axis: $-Y$ axis
- Scan interval index: −0.05 mm

There are two kinds of data processing in pulse-echo C-scanning: echo amplitude (AMP) view and time of flight (TOF) view. The latter data can be converted into a delamination depth view through the transverse sound velocity in CFRP laminates. The TOF files obtained together with an image processing software allowed the determination of the delaminated area for each specimen and energy level. An example of the images obtained by the C-scan procedure and TOF data are shown in Fig. 2(a) and (b), respectively, for after impact and after compression after impact of one of the specimens with lay-up B impacted with 12.1 J. It shows that for a quasi-isotropic stacking sequence and a low level impact energy, a small and symmetrical delaminated area is obtained.

Compression after impact

The compression after impact tests of the specimens were conducted on a universal testing machine. The tests were conducted in displacement control with a velocity of 0.5 mm/min. The testing fixture described in the Airbus testing procedure (AITM 1.0010) was used. In this fixture, and to prevent global buckling during compression, the specimens were clamped at both ends and simply supported at the side edges. In order to establish the buckling

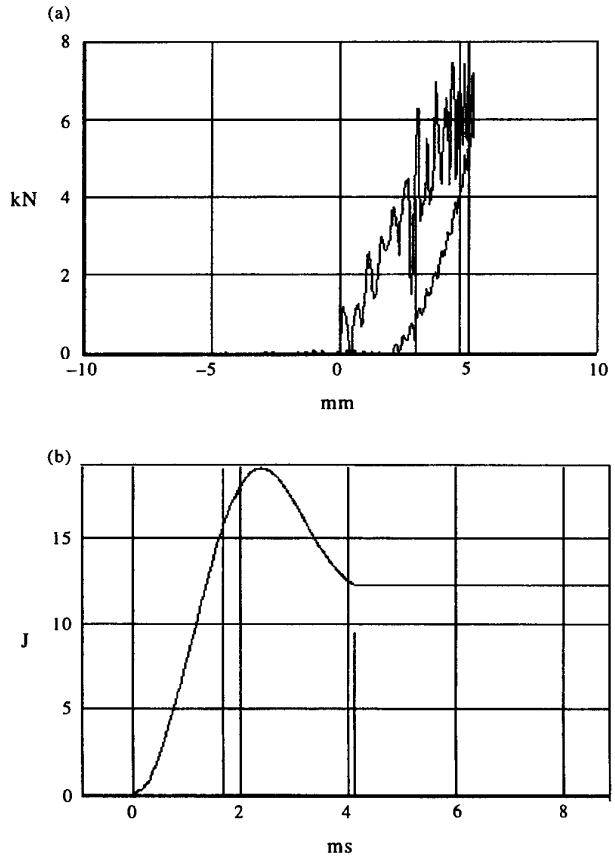

Fig. 1. (a) Force versus deflection in low velocity impact tests. (b) Impact energy versus time in low velocity impact tests.

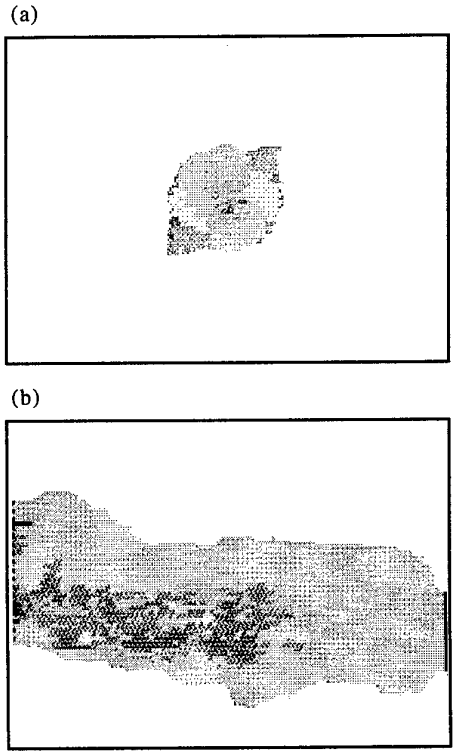

Fig. 2. C-scan views: (a) after impact; (b) compression after impact.

behaviour of the delaminated area during testing and final failure, three LVDT were attached to the specimen: one at the center of the impact zone, the second one at the opposite side and the third one on the testing fixture to monitor the vertical displacement of the specimen during the test. A schematic view of the instrumented compression after impact (CAI) testing fixture with a specimen and the three LVDT in their testing positions, is shown in Fig. 3. The different buckling behaviours were analyzed, and three types of buckling were observed, shown schematically in Fig. 4(a), (b) and (c). More than 50% of the specimens failed under the buckling behaviour shown in Fig. 4(a), meaning that the displacement of the surfaces during buckling are in the direction of the impact displacement. This is a logical behaviour due to the permanent indentation observed after impact. The buckling behaviour presented in Fig. 4(b), represents about 35% of the results, and corresponds to a variant of the previous behaviour, where the delamination buckling occurs for both sides of the lateral surfaces.

Concerning the damage growth during compression, it corresponds to a typical buckling failure where the damage growth is obtained suddenly leading to the complete failure of the specimen. As can be seen on the C-scan images of Fig. 2(a) and (b), the delamination growth is obtained in the lateral direction, perpendicular to the applied compression load. Only very small delaminations were observed in the vertical direction.

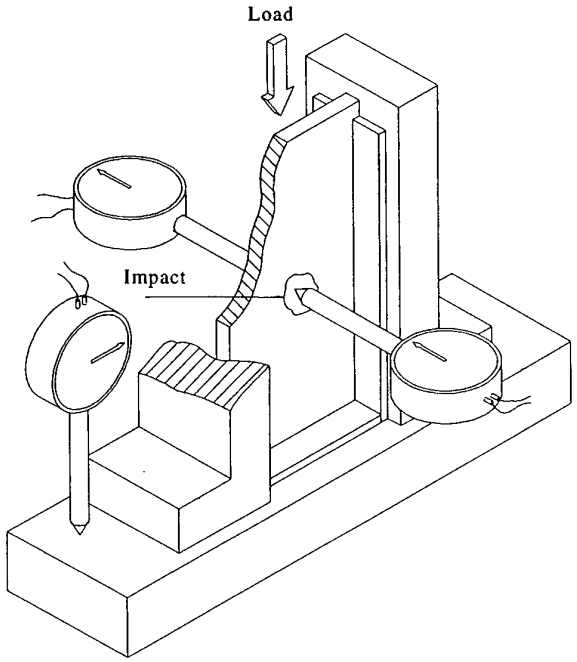

Fig. 3. Instrumented compression after impact test fixture.

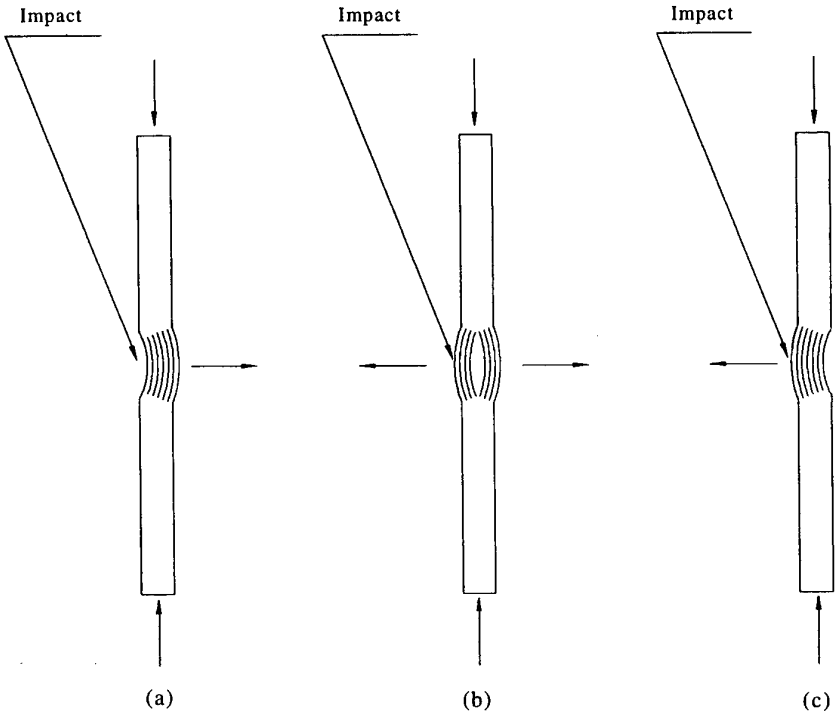

Fig. 4. Delamination buckling models.

DISCUSSION

Several specimens were tested at different impact energy levels ranging from 4 to about 80 J. These energy levels allowed increasing damaged areas in the specimens up to perforation. After impact, the delamination area of the specimens and the permanent indentation depth of the impact point were measured. The latter one is the procedure prescribed in AITM 1.0010 to establish the visibility of the surface defect. Figure 5 shows the indentation depth obtained for the range of impact energies used. Despite the scatter of the results, a direct correlation exists between the impact energy and the surface indentation depth. The AITM considers as BVID energy level (Barely Visible Impact Damage), the energy necessary to put a permanent indentation depth of 0.3 mm, and for these lay-ups we have obtained approximately 20 J of impact energy.

Concerning the delamination obtained, the shape of the delamination was identified and the delaminated areas measured. Figure 6 shows the delaminated area as a function of the absorbed energy determined as described before. Again a direct correlation exists between the two quantities, but for perforation energy levels the delaminated areas are smaller than expected. There was no practical influence of the stacking sequences on the indentation depth and delaminated areas, since the influence of the impact energy is the leading factor.

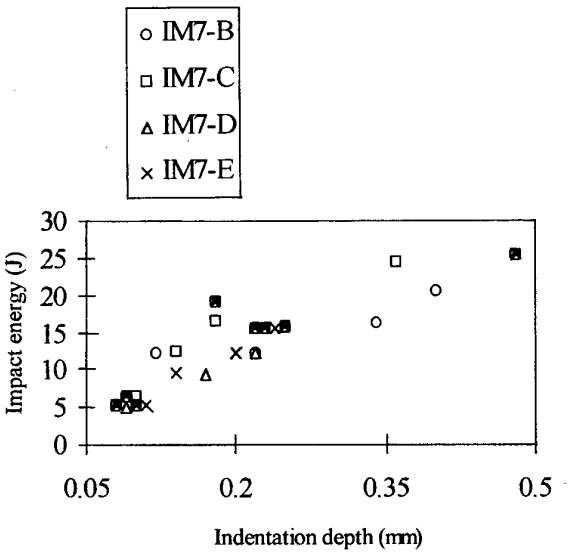

Fig. 5. Impact energy as a function of the indentation depth.

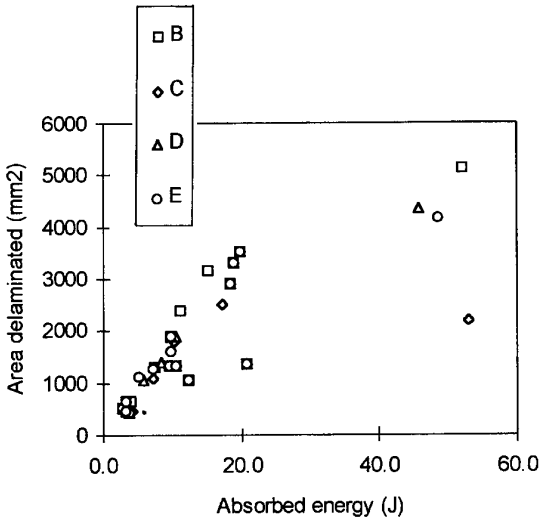

Fig. 6. Area delaminated as a function of the absorbed energy.

It has been remarked that the residual compression strength of delaminated composite laminates is highly affected due to the buckling mechanisms of the delaminated laminae. As four different stacking sequences were tested in two testing directions, the results are analyzed in two graphs. Figures 7 and 8 show the compressive residual strength as a function of the delaminated area for the B, C, D and E and B*, C*, D* and E* stacking sequences, respectively. As expected the E stacking sequence presents the smallest residual compressive strength while the E* stacking sequence presents the greatest compressive residual strength. This is due to the presence of the 0° and 90° plies, corresponding to higher elastic modulus in those directions.

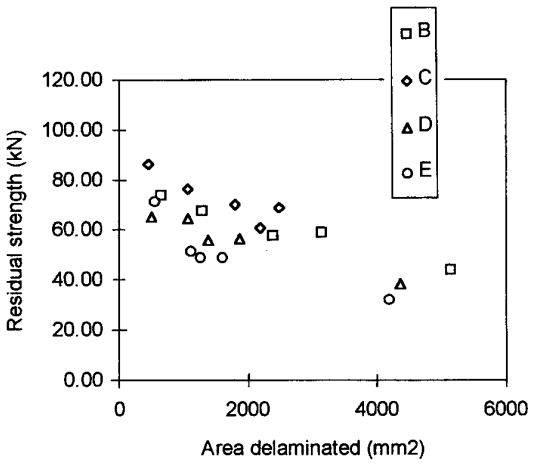

Fig. 7. Residual strength as a function of the area delaminated — specimen numbers 1–5.

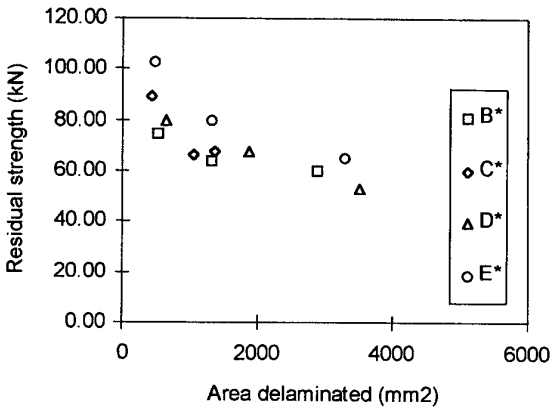

Fig. 8. Residual strength as a function of the area delaminated — specimen numbers 6–8.

For the B, C and B*, C* stacking sequences, since they represent quasi-isotropic stacking sequences, the direction of loading does not affect the compressive residual strength.

These results can be analyzed as a function of strain to failure, based on the elastic properties of each stacking sequence. The compressive residual load is then transformed in stresses and in strains and through the delaminated area related with the absorbed energy. The results presented in strains show a smaller scatter and a uniformity of the strain to failure as a function of the delaminated area and of the absorbed energy. This is shown in Fig. 9, together with a linear regression of the points. It is clear that the composite panels with different elastic moduli present similar strain to failure for the wide range of absorbed energies.

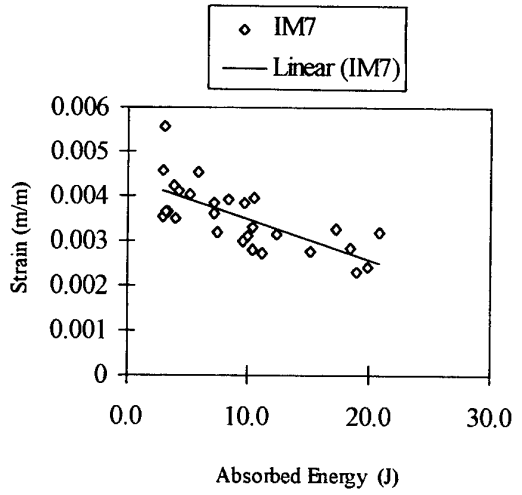

Fig. 9. Strain as a function of the absorbed energy — specimen numbers 1–8.

CONCLUSIONS

Low velocity impact and compression after impact tests of laminate composite panels were carried out and allow the following conclusions

- the delaminated area is a function of the impact energy and relatively independent of the stacking sequences used in this study
- unstable damage growth was obtained by compression after impact due to a buckling mechanism in the delaminated area
- the residual strength is influenced by the delaminated area which is a function of the impact energy
- the residual strength when considered in terms of failure load (failure stress for the same thickness) depends on the stacking sequence, but the strain to failure is not.

ACKNOWLEDGEMENTS

The authors wish to thank to Min. Defesa Nacional and OGMA, SA which have sponsored this research through the EUCLID Program, RTP 3.1, Aeronautical Applications Technology, Impact and Damage Tolerance.

REFERENCES

1. Sjoblom, P.O., Hartness, J.T. and Cordell, T.M., On low-velocity impact testing of composite materials. *J. Comp. Mater.*, 1988, **22**, 30–52.
2. Wu, H.T. and Springer, G.S., Measurements of matrix cracking and delamination caused by impact on composite plates. *J. Comp. Mater.*, 1988, **22**, 518–532.
3. Delfone, D., Poursartip, A., Coxon, B. R. and Dost, E. F., Non-penetrating impact behavior of CFRP at low and intermediate velocities. *Composites Materials: Fatigue and Fracture (Fifth Volume)*, ASTM STP 1230, ed. Martin, R. H., American Society for Testing and Materials, Philadelphia, 1995, pp. 333–350.
4. Found, M.S. and Howard, I.C., Single and multiple impact behaviour of a CFRP laminate. *Composite Structures*, 1995, **32**, 159–163.
5. Liu, S., Kutlu, Z. and Chang, F. K., Matrix cracking and delamination in laminated polymeric composites resulting from transversely concentrated loadings. *Proceedings of the Ist International Conferences on Deformation and Fracture of Composites*, pp. 30/1–30/7, Manchester, England, March 25–27, 1991.
6. Madan, R. C., Influence of low-velocity impact on composite structures. *Composites Materials: Fatigue and Fracture (Third Volume)*, ASTM STP 1110, ed. O'Brien, T. K., American Society for Testing and Materials, Philadelphia, 1991, pp. 457–475.
7. Dost, E. F., Ilcewicz, L. B. and Coxon, B. R., Effects of stacking sequence on impact damage resistance and residual strength for quasi-isotropic laminates. *Com-*

posites Materials: Fatigue and Fracture (Third Volume), ASTM STP 1110, ed. O'Brien, T. K., American Society for Testing and Materials, Philadelphia, 1991, pp. 476–500.
8. Ishikawa, T., Sugimoto, S., Matsushima, M. and Hayashi, Y., Some experimental findings in compression-after-impact (CAI) tests of CF/PEEK (APC-2) and conventional CF/EPOXY flat plates. *Composites Sci. Tech.*, 1995, **55**, 349–363.
9. Kinsey, A., Saunders, D.E.J. and Soutis, C., Post-impact compressive behaviour of low temperature curing woven CFRP laminates. *Composites*, 1995, **26**, 661–667.
10. Soutis, C. and Curtis, P.T., Prediction of the post-impact compressive strength of CFRP laminated composites. *Composite Sci. Tech.*, 1995, **56**, 677–684.
11. Araújo, A.L., Soares, C.M.M. and Freitas, M.J.M., Characterization of material parameters of composite plate specimens using optimization and experimental vibrational data. *Composites: Part B*, 1996, **27B**, 185–191.

ELSEVIER

Composite Structures Vol. 38, No. 1–4, pp. 517–524, 1997
© 1997 Published by Elsevier Science Ltd. All rights reserved
Printed in Great Britain
0263-8223/97/$17.00 + 0.00

PII:S0263-8223(97)00087-1

Application of roll forming to SMC forming

T. Katayama

Department of Mechanical Engineering, Doshisha University, Kyoto 610-03, Japan

Y. Hayakawa, M. Hakotani

Takeda Chemical Industries Ltd, Osaka 532, Japan

&

M. Shinohara

Department of Mechanical Engineering, Maizuru National College of Technology, Kyoto 625, Japan

Sheet Moulding Compound (SMC) is suitable for mass production of FRP. It is usually formed by compression moulding. Though compression moulding can make production time short, this moulding method needs a huge forming energy because of the hydrostatic stress in the mould. Roll forming needs a smaller forming energy than compression moulding, because most of the forming load works as deviatoric stress. We proposed to apply roll forming to SMC, expecting a decrease of the forming energy, a short production time and a controllability of the fibre orientation.

In this paper, we investigate the effect of the reduction, the roll velocity and the roll diameter on the forming pressure and the deformation behaviour of the materials. Considering these results, we try to construct a design system for roll forming of SMC. © 1997 Published by Elsevier Science Ltd.

INTRODUCTION

Sheet Moulding Compound (SMC) has some excellent characteristics such as a surface brilliance, formability and excellent mechanical properties, and is used in a wide range of automobile parts, housing equipment and so on. SMC is usually formed by compression moulding. This method can make production time short, but it requires large and expensive press forming machines and a huge energy for the forming because of an increasing hydrostatic stress domain generated in the mould. And with this method, it is difficult to form long products which are usually used as structural members, because of the limitation of the size of the forming machine and mould.

In the field of metal forming, roll forming is usually used to form long products. This is the process of continuous micro-reduction by driven upper and lower rollers. When this method is applied to SMC forming, there are some advantages compared with compression moulding. During roll forming, most of forming load works as the deviatoric stress, so it is possible to reduce the forming energy [1,2]. As a result, it is possible to minimize and simplify the forming machine. Moreover, because roll forming is continuous forming, it is easier to form long products than by compression moulding.

In previous studies, the influence of the reduction and the tension between roll stands has been investigated [3,4]. However, the influence of the other basic parameters such as the roll velocity and roller diameter have not yet been investigated, nor have suitable conditions for forming the products with a channel shaped cross section and a parallel flange at a short production time.

In this paper, we investigate the effects of reduction, roll velocity and the roller diameter on the forming pressure and the deformation behaviour of the materials. Considering these results, we devise a method of determining the

forming conditions and we evaluate whether this determining method is useful or not.

SMC ROLL FORMING

Concept of SMC roll forming

SMC roll forming is to gradually deform SMC with multiple roll stages and to form various cross-sectional shapes of long products. After forming, deformed materials are cured in the curing oven. Alhough the method is the same as that in metallurgical technology, the materials have heterogeneity and anisotropy. The materials have to be deformed in the lateral direction in order to control the fibre orientation, because only longitudinal spread, like metal, results in too strong an anisotropy. So, we must consider the deformation characteristics of these materials.

SMC used in this study

The contents of SMC used in this experiment are shown in Table 1. This SMC is cut into 75 × 600 mm pieces and five SMC sheets are laminated. The thickness of the laminated materials is 9 mm.

Roll forming machine

The roll forming machine shown in Fig. 1 is used in this experiment. The reduction and the roll velocity that will influence the formability are set up at each stand. The cross section of the roller is shown in Fig. 2.

Table 1. Contents of SMC

Components	Wt%	Relative density
Resin (UP, TP, etc.)	31.3	1.10
Glass fibre	28.0	2.54
$CaCO_3$ (filler)	40.7	2.70

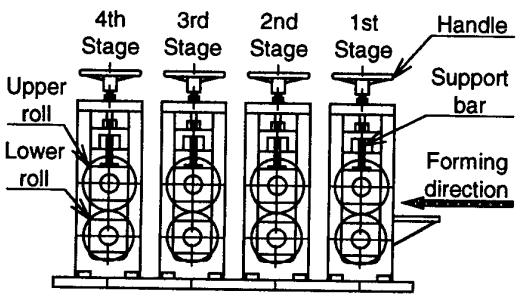

Fig. 1. Roll forming machine.

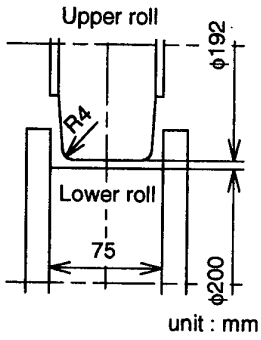

Fig. 2. Sectional view of rolls.

Forming method and measurement of experimental parameters

The product with a channel shaped cross section is formed by continuous roll forming. The product has a cross section of 75 × 20 × 4 mm (= width × flange height × web thickness, see Fig. 3). Laminated materials are inserted in the arrow direction as shown in Fig. 1 and are formed repeatedly until the web thickness becomes the target thickness. The elongation, the flange height and forming load are measured during forming.

The elongation at the web part is measured to observe the longitudinal deformation of materials during forming. To obtain the elongation, the lines in 300 mm are marked at the centre of the material's surface after laminating. The length of the marked lines are measured at each insertion into the machine. Elongation is calculated by the formula

$$E_t = \ln(e_{ln}/e_{l0}) \quad (1)$$

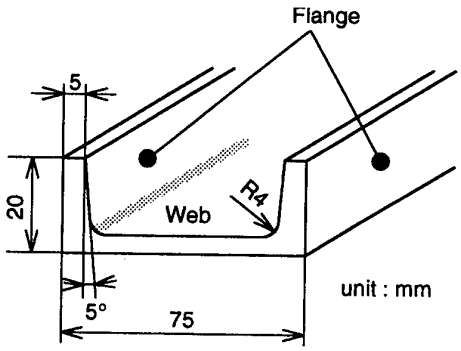

Fig. 3. Shape of final product.

where E_t is the total strain of elongation after the n-th pass, e_{ln} is the length of the marked lines after the n-th pass, and e_{l0} is the initial length of the marked line.

To observe the lateral deformation of the materials during forming, the flange height is also measured. The flange height is calculated as follows

$$F_t = \ln(f_{ln}/f_{l0}) \tag{2}$$

where F_t is the total strain of flange height after the n-th pass, f_{ln} is flange height after the n-th pass, and f_{l0} is the initial flange height (same as the thickness of laminated materials = 9 mm).

The forming load is measured by strain gauges which are attached to the support bars shown in Fig. 1.

INFLUENCE OF EACH PARAMETER ON FORMING LOAD AND DEFORMATION OF MATERIALS

In this section, we investigate the influence of each parameter such as the reduction, the roll velocity and the roller diameter on the forming load and the deformation behaviour of the material. We then try to clarify what parameter contributes to forming at lower forming loads and shorter forming times.

Forming conditions

Forming conditions are shown below.

1. Variation of reduction
   Reduction: 0.2, 0.4, 0.6 (mm)
   Roll velocity: 1.0 (m/min)
   Roll diameter: 200 (mm)
2. Variation of roll velocity
   Reduction: 0.4 (mm)
   Roll velocity: 0.5, 1.0, 1.5 (m/min)
   Roll diameter: 200 (mm)
3. Variation of roll diameter
   Reduction: 0.4 (mm)
   Roll velocity: 1.0 (m/min)
   Roll diameter: 200, 125 (mm)

In each condition, the initial thickness of the material is 9.0 mm and the final thickness of the material is 4.2 mm. The forming load, the total strain of elongation and the total strain in the flange height are measured.

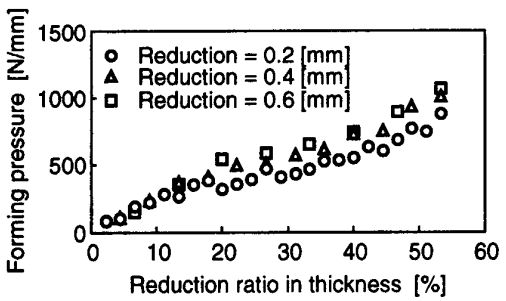

Fig. 4. Relation between forming pressure and reduction in thickness ratio.

Results

Figure 4 shows the relation between the forming pressure and the reduction in thickness ratio under the conditions of the variation of the reduction. The forming pressure, Y axis, is determined by dividing the forming load by the contact arc length between the roll and the material. The contact arc length L is calculated by eqn (3)

$$L = R\cos^{-1}\left(1 - \frac{\Delta h}{2R}\right) \tag{3}$$

where R and Δh is the roller radius and the reduction at each stage, respectively.

Under every forming condition, the contact width between the roller and the material is constant, so we can consider this value in the Y axis as forming pressure.

The value in the X axis denotes the reduction in thickness ratio, r_n, determined as follows

$$r_n = \frac{h_0 - h_n}{h_0} \times 100 \tag{4}$$

where h_0 is the initial thickness of the material and h_n is the thickness of the materials after the n-th pass.

In Fig. 4, the forming pressure slightly increases with each increment of the reduction. This seems to be caused by an increment of the deformation velocity in the thickness direction. When the reduction increases, the forming pressure does not vary much but the forming load increases because of the increment of the contact arc length. So, this increment in the forming load causes the failure of the forming.

In addition, for the other two conditions, the following results are obtained.

1. When the roll velocity increases, the materials tend to deform lateral to the rolling direction.
2. When the roller diameter increases, the material tends to deform lateral to the rolling direction.
3. When the reduction increases, the forming stages decrease and the production time becomes short.
4. When the roll velocity increases, the production time becomes short.

DETERMINATION OF SUITABLE FORMING CONDITIONS

In the previous section, we described the influence of the parameters such as the reduction, the roll velocity and the roller diameter on the forming load and the deformation behaviour of the material. In this section, based on these results, we try to construct the design system for roll forming to be suitable for forming the products with the channel shaped cross section and the parallel flange at the short production time. We evaluate this determining method by experiment.

Concept of determining the forming conditions

From the results of the previous section, the factors which contribute to the deformation in the lateral direction and the short production times were found. However, if the forming conditions are only determined by these factors, there is a possibility of failure of the forming because of the increment in the forming load. Therefore, some criterion that does not fail in forming is required in determining the forming condition.

Noticing the forming load, let the load value, F_{max}, be the load at the failure in forming. We determine the forming conditions considering this criterion. That is, the forming load which completes the next equation

$$F_{max} > F_n \ (n = 1, 2, \ldots, \text{stage number}) \tag{5}$$

where F_n is the forming load value at n-th stage.

From the results of the previous section, the forming pressure is a function of the reduction in thickness ratio, the reduction, the roll velocity and the roller diameter, i.e.

$$P_n = P_n[r_n, \Delta h_n, V_n, D_n] \tag{6}$$

where P_n, r_n, Δh_n, V_n and D_n are the forming pressure, the reduction in thickness ratio, the reduction, the roll velocity, the roller diameter at n-th stage, respectively. The forming load is calculated using the forming pressure and the contact arc length at the n-th stage by the equation

$$F_n = P_n \cdot L_n \tag{7}$$

Method of determining the forming conditions

We set up the reduction in thickness ratio, the reduction, the roll velocity, the roller diameter so as to complete eqns (5) and (7).

Considering forming pressure

In order to determine the practical forming conditions, an equation which predicts the forming pressure at any reduction, roll velocity and roller diameter is required. On the other hand, using this equation, we can set up the reduction, the roll velocity and the roller diameter at any forming pressure. Therefore, we describe the general equation deriving the forming pressure.

At first, the relational equation between the forming pressure and the reduction in thickness ratio is derived in the case that the reduction is 0.4 mm, the roll velocity is 1.0 m/min and the roller diameter is 200 mm. We consider this equation as a basic case.

The relationship between the forming pressure and the reduction in thickness ratio is derived by Fig. 4 as follows

$$P_n = P_n[r_n, 0.4, 1.0, 200] = 0.013\, r_n^3 - 1.102\, r_n^2 + 41.881\, r_n - 54.714 \tag{8}$$

In the case that the reduction, the roll velocity and the roller diameter are varied, we consider that the forming pressure is calculated as follows

$$P_n = C_1 \cdot C_2 \cdot C_3\, P_n[r_n, 0.4, 1.0, 200] \tag{9}$$

where C_1, is coefficient of reduction dependency, C_2 is the coefficient of velocity dependency and C_3 is the coefficient of diameter dependency, and these coefficients are calculated using the next equations

$$C_1 = \frac{1}{n} \sum_{k=1}^{n} \frac{P_k[r_k, \Delta h_k, 1.0, 200]}{P_k[r_k, 0.4, 1.0, 200]} \tag{10}$$

$$C_2 = \frac{1}{n}\sum_{k=1}^{n}\frac{P_k[r_k, 0.4, V_k, 200]}{P_k[r_k, 0.4, 1.0, 200]} \quad (11)$$

$$C_3 = \frac{1}{n}\sum_{k=1}^{n}\frac{P_k[r_k, 0.4, 1.0, D_k]}{P_k[r_k, 0.4, 1.0, 200]} \quad (12)$$

These coefficients are calculated at each stage and the average of the coefficients are used. Needless to say, if the reduction is 0.4 mm, $C_1 = 1$ and if the roll velocity is 1.0 m/min, $C_2 = 1$ and if the roll diameter is 200 mm, $C_3 = 1$.

From the experimental results, the relationship between C_1 and the reduction, C_2 and the roll velocity and C_3 and the roll diameter is shown in Fig. 5. C_1, C_2 and C_3 are calculated by next equations, respectively, considering n power in the consistent equation

$$C_1 = 1.2301\ \Delta h_n^{0.24} \quad (13)$$

$$C_2 = 0.5756\ e^{0.547\,V_n} \quad (14)$$

$$C_3 = 0.003\ D_n + 0.3668 \quad (15)$$

Therefore, eqn (9) is rewritten by substituting eqns (13)–(16)

$$P_n = (1.2301\ \Delta h_n^{0.24})(0.5756\ e^{0.547 V_n})(0.003\ D_n + 0.3668)(0.013\ r_n^3 - 1.102\ r_n^2 + 41.881\ r_n - 54.714) \quad (16)$$

Using this equation, we can predict the forming pressure at any reduction, roll velocity and roller diameter.

In opposition, we can set up the reduction, the roll velocity and the roller diameter which will complete eqns (5), (7) and (16) at any forming pressure.

Considering elongation in the longitudinal direction of the material

The material rolled at one stage deforms in the longitudinal direction, so the roll velocity after this stage must be faster than before. Therefore, the roll velocity after the stage is calculated as follows

$$V_{n+1} = (e^*_{ln}/e^*_{ln-1})\cdot V_n \quad (17)$$

where V_n, V_{n+1}, e^*_{ln} and e^*_{ln-1} are the roll velocity at the n-th stage and $(n+1)$th stage and the length of the marked line at the n-th stage and $(n-1)$th stage, respectively. The suffix '*' at the length of the marked line shows that the roll velocity is not 1.0 m/min and the roll diameter is not 200 mm at the stage.

e^*_{ln-1} and V_n are already known (e_{l0} and V_1 are already known), the roll velocity after the stage, V_{n+1} is determined by e^*_{ln}. So the elongation in the longitudinal direction rolled at the n-th stage must be estimated.

In the case that the roll velocity is 1.0 m/min and the roller diameter is 200 mm, the relationship between the total strain of elongation and the reduction in thickness ratio is derived from the experimental results as follows

$$\ln(e_{ln}/e_{l0}) = 0.000036\ r_n^2 + 0.005357\ r_n - 0.008956 \quad (18)$$

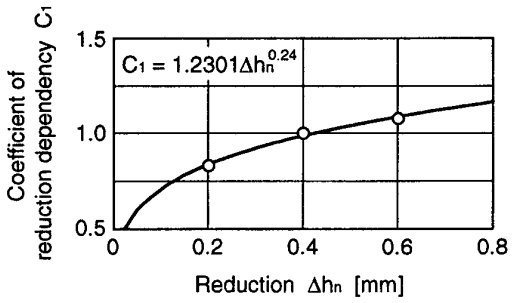

(a) Coefficient of reduction dependency

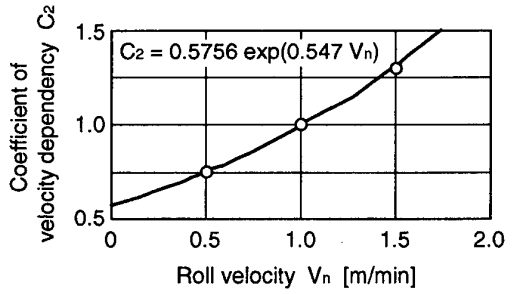

(b) Coefficient of velocity dependency

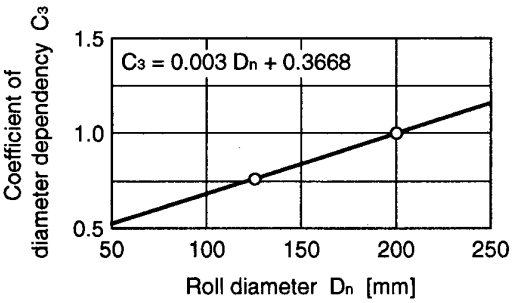

(c) Coefficient of diameter dependency

Fig. 5. Relation between coefficient and parameters for forming pressure. (a) Coefficient of reduction dependency. (b) Coefficient of velocity dependency. (c) Coefficient of diameter dependency.

In the case that the roll velocity and the roller diameter are varied, we consider that the total strain of the elongation is calculated as follows

$$C_4 C_5 \ln(e_{ln}/e_{ln-1}) = \ln(e^*_{ln}/e^*_{ln-1}) \tag{19}$$

where C_4 and C_5 are also coefficients of velocity dependency and diameter dependency, respectively, and these coefficients are calculated by the following equations

$$C_4 = \frac{1}{n} \sum_{k=1}^{n} \frac{E_{i,k}[V_k, 200]}{E_{i,k}[1.0, 200]} \tag{20}$$

$$C_5 = \frac{1}{n} \sum_{k=1}^{n} \frac{E_{i,k}[1.0, D_n]}{E_{i,k}[1.0, 200]} \tag{21}$$

From the experimental results, the relationship between C_4 and the roll velocity and C_4 and the roller diameter is shown in Fig. 6. C_4 and C_5 are calculated by the following equations, respectively

$$C_4 = -0.3313\, V_n + 1.3313 \tag{22}$$

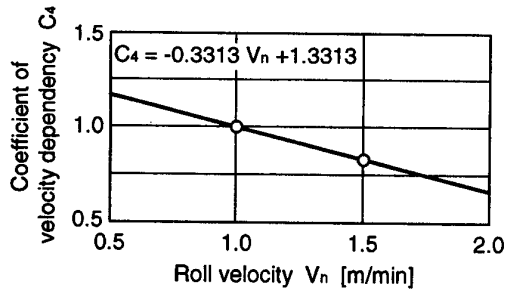

(a) Coefficient of velocity dependency

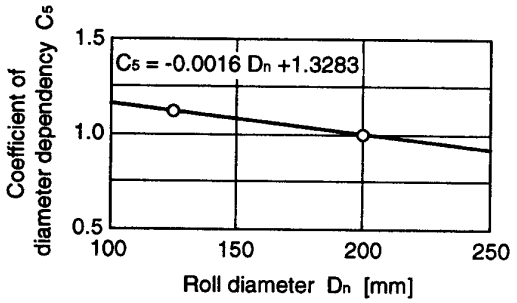

(b) Coefficient of diameter dependency

Fig. 6. Relation between coefficient and parameters for longitudinal deformation. (a) Coefficient of velocity dependency. (b) Coefficient of diameter dependency.

$$C_5 = -0.0016\, D_n + 1.3283 \tag{23}$$

Consequently, substituting the roll velocity to eqn (16), the reduction which completes eqn (5) is derived and substituting the elongation at the stage into eqns (18)–(23), the roll velocity at the next stage is obtained.

Repeating this procedure until the thickness of the material becomes 4 mm, the forming conditions (the reduction, the roll velocity and so on at each stage) is obtained.

Determining the forming conditions

We attempt to apply this design system to an example of roll forming.

First stage

When the forming is performed under the conditions that the reduction is constant, 0.6 mm, there is the possibility of failure of the forming at the latter stage of the forming. Therefore we let this forming load value (9000 N) at the latter stage of the forming be F_{max}.

At first, because the roller diameter is 200 mm and the roll velocity (V_1) is 1.0 m/min at the first stage, the reduction, the reduction in thickness ratio and the forming load at this stage are derived from eqns (5), (7) and (16)

$$\Delta h_1 = 1.85(\text{mm})\ r_1 = 20.6(\%)\ F_1 = 8765.8(\text{N})$$

Second stage

e_{l1} is derived by substituting r_1 to eqn (18) and e^*_{l1} is derived by e_{l1}. From eqn (17), the roll velocity at the second stage is derived as follows

$$V_2 = (e^*_{l1}/e^*_{l0})\ V_1 = 1.12(\text{m/min})$$

where $e^*_{l0} = e_{l0}$, $e^*_{l1} = e_{l1}$ (because $V_1 = 1.0$ m/min, $C_4 = 1$, $C_5 = 1$). From eqns (5), (7) and (16)

$$\Delta h_2 = 1.15(\text{mm})\ r_2 = 33.3(\%)\ F_2 = 8722.8(\text{N})$$

After that the forming conditions are determined by the same procedure.

Final stage

At the 6th stage

$$\Delta h_6 = 0.35(\text{mm})\ r_6 = 57.8(\%)$$

However, because the final thickness of the product is 4.0 mm, the total reduction is 5.0 mm. If Δh_6 is 0.35 mm, the final thickness of the products becomes 3.8 mm. So we adjust the

reduction so as the final thickness of the product becomes 4.0 mm

$\Delta h_6 = 0.15(\text{mm})$ $r_6 = 55.6(\%)$ $F_6 = 4238.6(\text{N})$

Figure 7 shows the determining procedure of the forming condition and Table 2 shows the forming conditions that we determined.

Estimation of this design system

Under these conditions, a roll forming test was carried out and we estimated this design system by comparing it with the conventional forming condition ($r_n = 0.4$ mm constant, $V_n = 1.0$ m/min constant).

Figure 8 shows the relationship between the forming pressure and the reduction in thickness ratio and the relationship between the forming load and the reduction in thickness ratio. In this figure, the calculated value of the forming pressure is equal to the experimental value. The experimental value and the calculated value of the forming load are the same. Moreover, the failure of the forming does not occur. So this method of determining the forming conditions seems to be correct.

Figure 9 shows the relationship between the total strain of elongation and the reduction in thickness ratio, and Fig. 10 shows the relation-

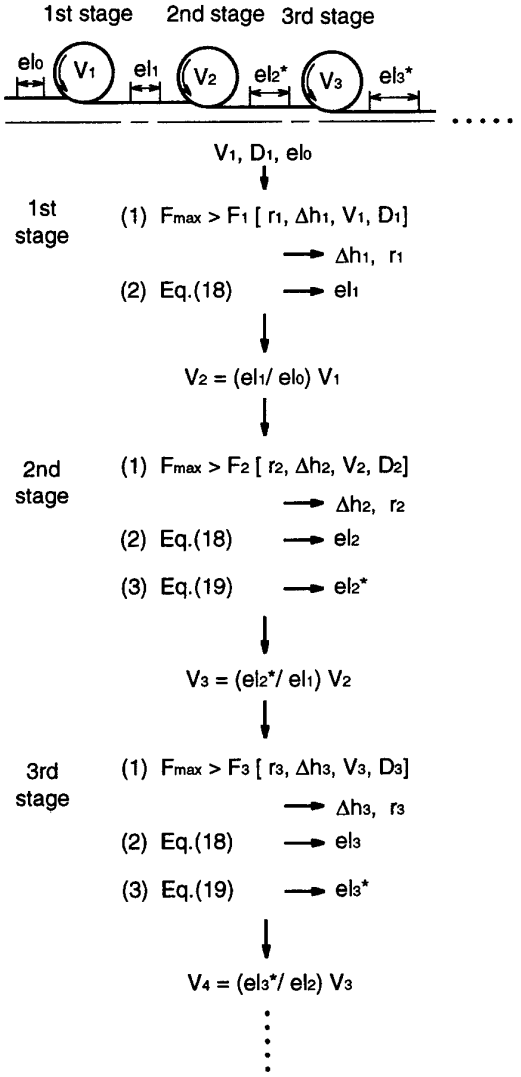

Fig. 7. The determination method of parameters.

Table 2. Forming condition

Stage	Thickness (mm)	Reduction (mm)	Roll velocity (m/min)
0	9.00	—	—
1	7.15	1.85	1.00
2	6.00	1.15	1.12
3	5.20	0.80	1.23
4	4.60	0.60	1.31
5	4.15	0.45	1.38
6	4.00	0.15	1.44

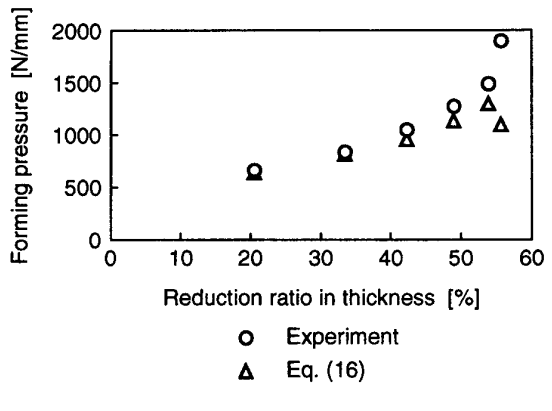

(a) Forming pressure

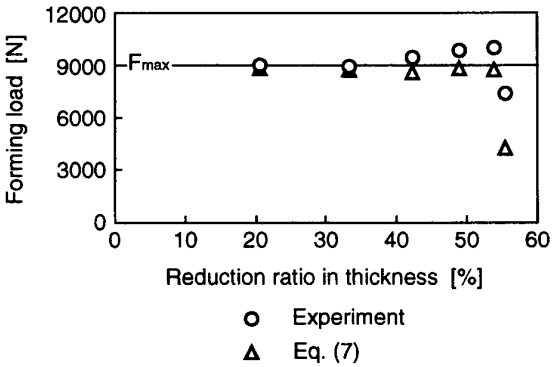

(b) Forming load

Fig. 8. Comparison between experimental value and calculated value. (a) Forming pressure. (b) Forming load.

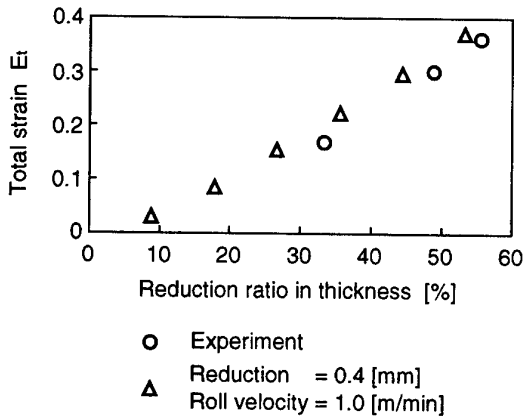

Fig. 9. Relation between elongation of the longitudinal direction and reduction in thickness ratio.

ship between the total strain in flange height and the reduction in thickness ratio. In these figures, compared with the conventional condition, the elongation is smaller and the flange height is larger. So these forming conditions contribute to the deformation in the lateral direction (the formation of the flange).

Under these conditions, the number of forming stages decreases from 12 to 6 (50% down), and the final flange height increases from 20.1 to 24.6 mm (22.6% up).

Consequently, we suggest these conditions (shown in Table 2) as the suitable conditions for forming products with a channel shaped cross section and a parallel flange in a short production time.

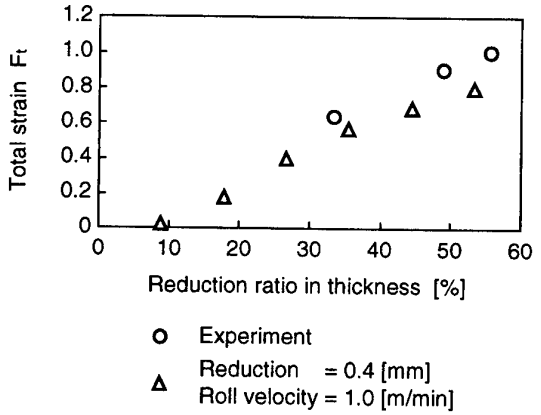

Fig. 10. Relation between flange height and reduction in thickness ratio.

CONCLUSION

In this paper, we have investigated the effects of the reduction, the roll velocity and the roller diameter on the forming pressure and the deformation behaviour of materials in order to clarify the factors which contribute to the deformation to the lateral direction and the short production time. Considering these results, we have devised a method of determining the forming conditions, the design system for forming products with a channel shaped cross section and a parallel flange in a short production time.

Consequently, the following results are obtained.

1. The factors which contribute to the deformation to the lateral direction are the increment of the roll velocity and the roller diameter.
2. The factors which contribute to short production time are the increment of the reduction and the increment of the roll velocity.
3. The determining method of the forming condition which we construct in this paper is appropriate to form products with a channel shaped cross section and a parallel flange in a short production time.

REFERENCES

1. Hirai, T., Hayakawa, Y. and Hakotani, M., *Materials and Technologies*, Woodhead Publishing, Vol. 1, 1994, p. 295.
2. Hirai, T., Roll forming of SMC considering the boundary effects caused by heterogeneous properties. *J. JSPP*, 1994, **6** (12), 922–933.
3. Katayama, T., Kurokawa, K., Hayakawa, Y. and Hakotani, M., The influence of roll velocity and reduction on formability in SMC roll forming. *Proc. of Seventh European Conference on Composite Materials*, 1996, pp. 347–352.
4. Katayama, T., Kurokawa, K., Shinohara, M., Hayakawa, Y. and Hakotani, M., Influence of filler on SMC roll forming. *Proc. of ICCM-11*, 1997 (in press).

ELSEVIER

Composite Structures Vol. 38, No. 1–4, pp. 525–530, 1997
© 1997 Elsevier Science Ltd. All rights reserved
Printed in Great Britain
0263-8223/97/$17.00 + 0.00

PII:S0263-8223(97)00088-3

Effect of cracks on thermal stress and strain of a tape automated bonded package

C. M. L. Wu, J. K. L. Lai
Department of Physics and Materials Science, City University of Hong Kong, 83 Tat Chee Avenue, Hong Kong

&

Yongli Wu
Institute of Mechanics, Chinese Academy of Science, Beijing 100080, People's Republic of China

A tape automated bonded (TAB) package is basically a composite structure. A three-dimensional finite element fracture analysis was performed to evaluate the effects of cracks in a TAB package under thermal cycling conditions. The lead–tin solder in the outer lead bond as well as the copper beam lead were taken as elasto-plastic materials. Interface cracks between the copper beam lead and the solder were included in the analysis. It was found that the prescribed cracks created new sources of stress concentrations, which are fairly mild. This result showed that the configuration of the outer lead bonds in TAB packages is generally resilient to thermal cycling, even with the presence of defects such as cracks. © 1997 Elsevier Science Ltd.

INTRODUCTION

Modern electronic assemblies consist of a few materials. For example, printed circuit boards (PCB) are usually constructed using FR-4 woven glass fibre reinforced composite plates. Because of the nature of their construction, it is appropriate to analyse these assemblies as composite structures. For example, finite element analyses have been found useful in predicting thermal and mechanical stresses in a surface-mounted component on a PCB.

Tape automated bonding (TAB) was introduced in the late 1960s, for packaging of electronic components. TAB uses a linear flex circuit beam lead pattern, in a polymer–metal cinematography format, to support, transport and perform lead interconnection to semiconductor chips. It has been considered as a viable means of reducing the cost of electronic components for the past 20 years.

The value of TAB in semiconductor fabrication has been established by its application by major international corporations. Wire-bonding assembly limits are pushed back while pad density, interconnection integrity, performance, test, and reliability are enhanced, leading to lower overall costs and a better product. TAB has been applied to the even more demanding field of very large scale integration packaging for a variety of consumer, medical, security, computer, peripheral, telecommunication, automotive and aerospace products. A comprehensive overview of TAB technology is available in ref. [1].

A TAB package is typically composed of components made up from various materials with different thermal expansion characteristics. This produces thermal stresses in the package, even under normal power cycling of the electronic equipment. On top of the thermal effects, the package is subjected to mounting constraints, resulting in externally applied stresses to the package. Repeated duty cycling can cause fatigue at joints, at interfaces between different materials, at interconnection locations or cause delimitation of the FR-4 material.

The outer leads in a TAB package are sometimes connected to PCBs or directly to liquid crystal display glass panels. The joints at the

outer leads not only function as electric conduction paths, but also act as important structural members of the whole package. Prediction of thermally induced stresses towards failure of these joints is therefore critical in assessing the reliability of the TAB package. Thermal stress analysis of multi-chip packages with a flip-chip configuration and a conduction cooling module has been carried out by Darveraux *et al.* [2]. The authors pointed out that even if a package design is optimized to be thermal-expansion matched under operating conditions, significant thermal stresses may develop during a transient. Lau *et al.* [3]. have performed a stress analysis for a TAB package with a 48-lead chip. Thermally induced stresses have been calculated and critical components more prone to fatigue failure have been identified in this paper. Jog *et al.* [4] have performed a three-dimensional (3-D) thermal stress and strain analysis of a TAB package subjected to accelerated thermal cycling. Transient temperature, stress and strain distributions have been obtained in the package see also ref [5].

It is well known that undetectable defects such as voids may exist in all electronic connections. This is no exception to TAB joints. It is therefore important to analyse the problem of TAB with built-in defects.

In this paper, a 3-D stress and strain analysis was been carried out by including an interface crack between the outer lead and solder in the TAB package. Thermal stresses and strains have been obtained.

FORMULATION

Generally the theory of uncoupled thermomechanics is used to analyse the temperature and thermal stresses in the TAB package. It means that the interaction between strain and temperature is ignored and the effects of change in dimension of the package on temperature distribution are negligible. The transient energy conservation equation governing the 3-D temperature distribution in a TAB assembly is

$$\rho C \frac{\partial T}{\partial t} = \nabla(\kappa \nabla T) + W \tag{1}$$

where ρ is the density, C is the specific heat, κ is the thermal conductivity of the material, T is the temperature and W is the heat-generation rate.

The resulting temperature distribution is employed in the following simultaneous governing equations to get the stress and the strain fields in the TAB package. The stress equilibrium is given by

$$\sigma_{ij,j} = 0 \tag{2}$$

The constitutive equation for an isotropic linear elastic solid and plastic solid including thermal strain may be written as

$$\{\sigma\} = [C_e]\{\varepsilon\} - [C_e]\{\alpha\}(T - T_0) \tag{3}$$

$$\{d\sigma\} = [C_{ep}]\{d\varepsilon\} - [C_{ep}]\{\alpha\} dT \tag{4}$$

The strain–displacement relations are

$$\varepsilon_{ij} = \frac{1}{2}(u_{i,j} + u_{j,i}) \tag{5}$$

where T_0 is the reference temperature, σ_{ij} is the components of the stress tensor, ε_{ij} is the component of the strain tensor, α is the coefficient of thermal expansion, u_i is the components of the displacement vector, $[C_e]$ is the elastic matrix and $[C_{ep}]$ is the plastic matrix.

Details on the theory of uncoupled thermomechanics can be found in refs [6] and [7].

The temperature distribution in the electronics package is calculated by solving the heat conduction equation (1) with the prescribed initial and boundary conditions. Displacements, strains and stresses everywhere inside the package are then determined by solving eqns (2)–(5) with the prescribed stress–displacement boundary conditions and with the calculated temperature distribution.

The determination of temperature distribution and stresses in TAB packaging is not an easy task. The finite element method [6,7] is one of the best candidates for obtaining numerical results for the temperature distribution and the thermal stresses in TAB package. We use a finite element code, ABAQUS [8], to calculate the temperature and stresses in the TAB package.

DESCRIPTION OF THE PROBLEM

A thin slice of a TAB package was analysed in ref. [3]. In the present investigation, a similar model as that given in ref. [3] has been made and is shown in Fig. 1. Figure 2 shows the pack-

age in the x–y plane. It can be seen from this figure that the TAB package consists of six major parts: the silicon chip, the gold bump, the polyimide ring, the copper beam lead, the lead–tin solder layer, and the FR-4 PCB. The dimensions of the various components have

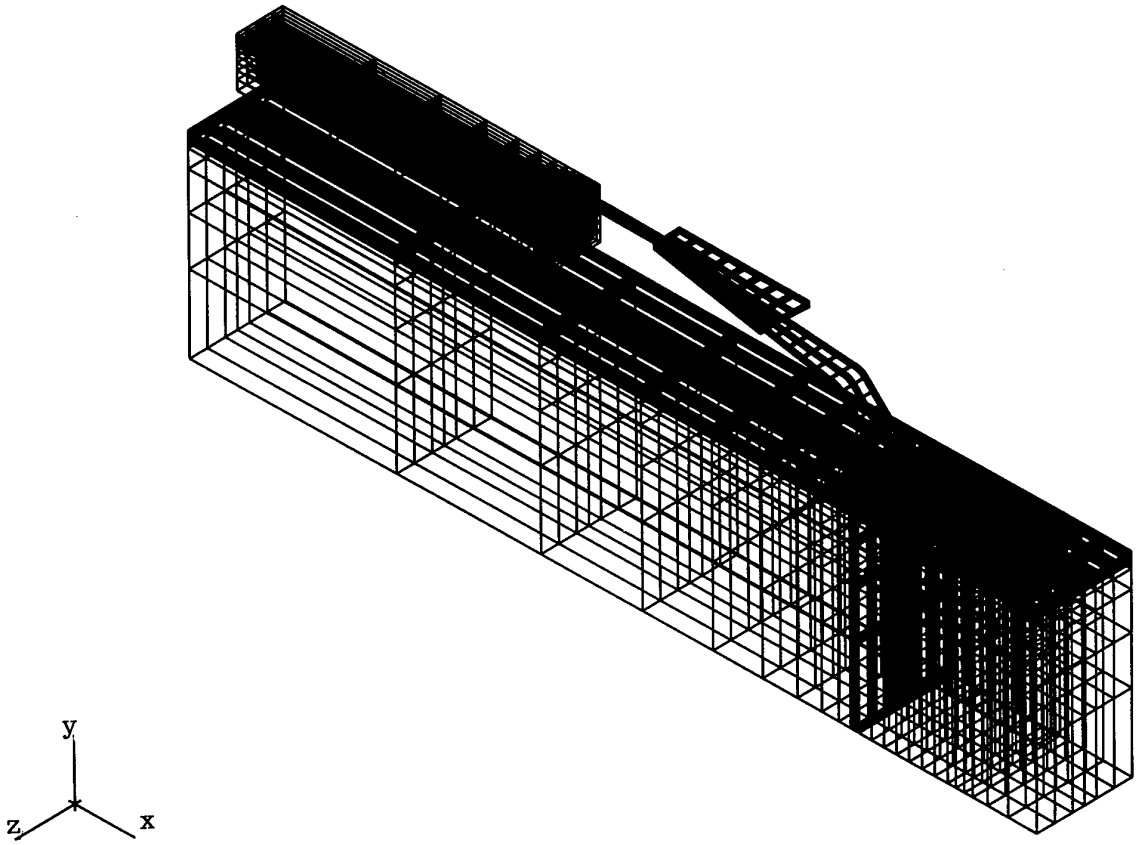

Fig. 1. A section of a TAB package.

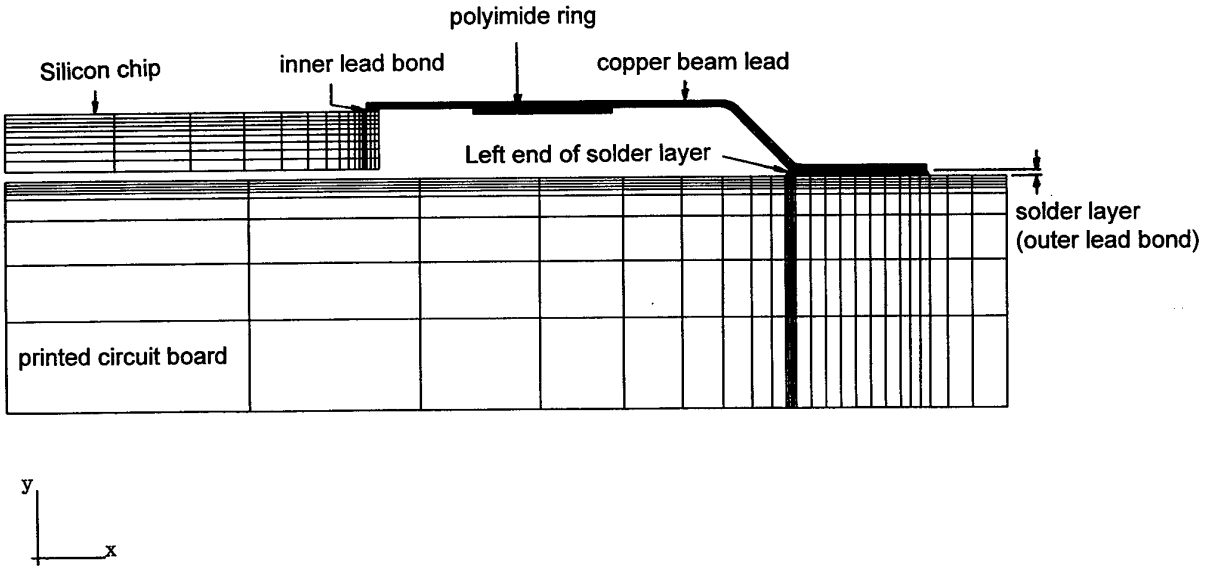

Fig. 2. The TAB package in the x–y plane.

Table 1. Material properties of the TAB package

Material	ρ (10^{-3} g/mm^3)	C (J/g K)	κ (W/mm K)	α (10^{-6}/K)	E (MPa)	ν
Pb–Sn solder	8.41	0.1498	0.04979	21.0	10,340	0.40
Copper	8.94	0.3815	0.3978	17.0	121,000	0.35
Polyimide	1.53	1.09	0.00012	20.0	4140	0.30
Gold	19.3	0.1292	0.3151	15.0	78,000	0.30
Silicon	2.33	0.7071	0.1481	2.9	131,600	0.30
FR-4	3.0	0.1	0.000262	15.0	11,000	0.28

been given in ref. [3]. The physical and mechanical properties for various materials in the TAB package are given in Table 1 [9].

For the present analysis, the silicon, the gold, polyimide and FR-4 are assumed to be linear-elastic. The copper and solder are assumed to be isotropic and under isotropic and elasto-plastic strain-hardening rule. The strain-hardening equation used to describe the elasto-plastic stress–strain behaviour is

$$\varepsilon = \frac{\sigma}{E} + \frac{\sigma - \sigma_y}{\beta E} \tag{6}$$

where σ_y is the material yield stress and β is the strain-hardening parameter. For copper, $\sigma_y = 62$ MPa, $\beta = 0.0075$. For lead–tin solder, $\sigma_y = 8.27$ MPa and $\beta = 0.1$.

To simulate the effects due to temperature cycling, it is assumed that the TAB package is subjected to temperature variation from -55 to 125°C. Residual stresses due to soldering and other manufacturing processes are not considered. That is, the package is assumed to be stress-free at the starting temperature. Defects in the OLB solder joint are included in the form of interface edge and inner cracks. The finite element model contained 2796 3-D isoparametric elements. Each element has 20 nodal points. A total of 14,641 nodes were used in the model.

RESULTS AND DISCUSSION

Three cases were analysed in this paper. In order to compare the results of the present analysis with those of previous investigators, the configuration of the present TAB package is taken as that in ref. [3]. In case 1 of the analysis, there is no interface crack in the TAB package. The finite element mesh for this case is shown in Fig. 1. It can be seen in this figure that a thin slice of the whole TAB package is modelled. In case 2, an interface edge crack between the solder and the beam lead at the OLB is included. This crack starts at the left-hand end of the solder layer shown in Fig. 2. The length of this crack is 0.031 mm. In case 3, a different interface crack between the solder and the beam lead at the OLB is included. This crack starts at a position 0.046 mm from the left-hand end of the solder layer, and has a crack length of 0.146 mm. Apart from the temperature variation from -55 to 125°C, no external forces are imposed on the package.

Figure 3 shows the 3-D deformation pattern of the package in case 1. By inspecting the deformation in close detail it was found that the chip was displaced further upwards away from the PCB, and that the beam lead together with the polyimide ring sagged down in the middle position. The deformation patterns in cases 2 and 3 were very similar to that in case 1 so they are not shown. However, by inspecting the deformation pattern at and near the crack, it was found that, as a result of thermal cycling, the cracks in both cases of crack inclusion in the model had been opened. This phenomenon is shown in Fig. 4, where the vertical displacements along the length of the OLB solder joint around the crack positions are given for all three cases. In general, the vertical displacement starts from a high value, gradually decreases along the solder length to a certain minimum value, and gradually increases again further along the solder length. In particular, the magnitude of vertical displacement is highest for case 2, followed by that in case 1, and lowest for that in case 3. The largest crack opening displacement occurred at the left-hand end of the solder layer for case 2, and has a value of 0.055 μm. For case 3, the largest crack opening displacement is 0.025 μm and occurred about half way along the crack length.

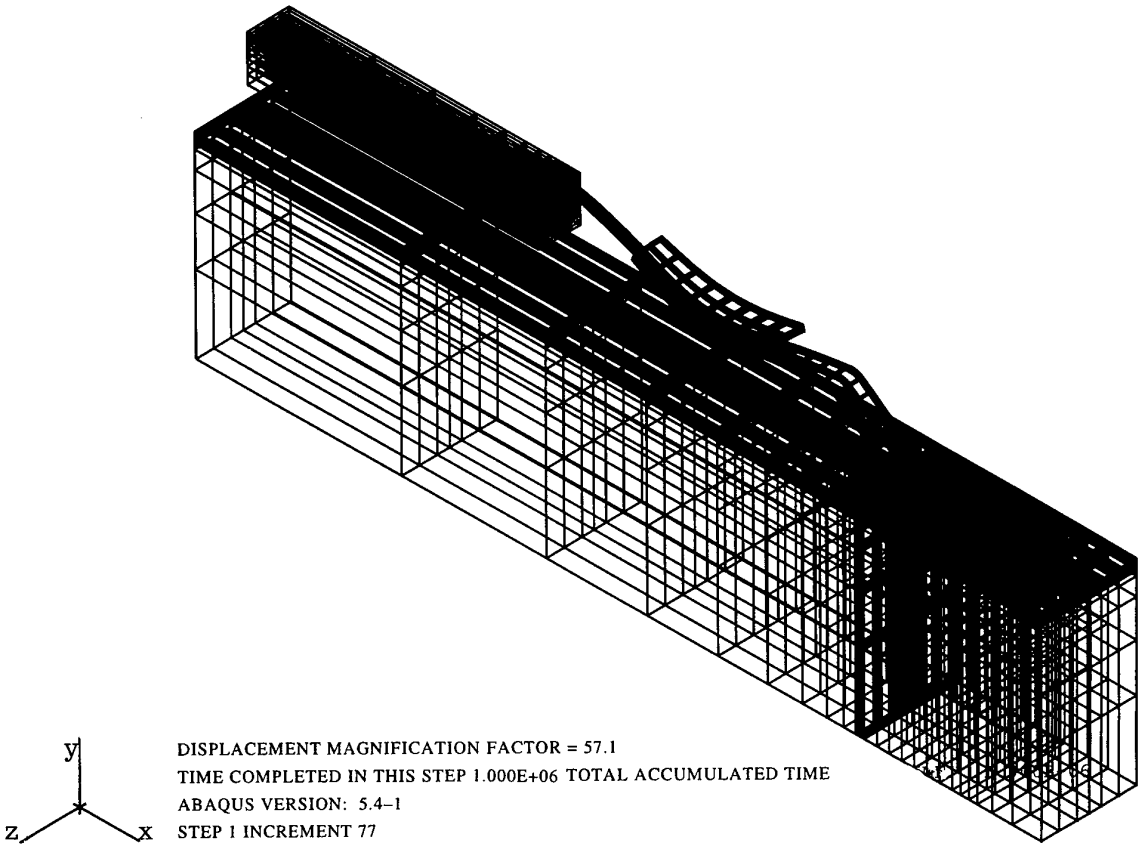

Fig. 3. Deformation of the TAB package.

Von Mises stresses in the TAB package were obtained for all cases. The stress distribution obtained in the package for case 1 is generally comparable to that in ref. [3]. It is clear that the main concern of the present investigation is at the OLB connection. Therefore von Mises stresses are only presented in this area. In particular, von Mises stress distributions are presented at the beam lead–solder interface for the beam lead and the solder. Figure 5 shows the variation of the von Mises stress for the solder at the beam lead–solder interface along the solder length. It can be seen in case 1 of the analysis, i.e. without any inclusion of cracks, the magnitude of the von Mises stress is about 11.5 MPa in the main part of the solder. Again, this is comparable to the stresses obtained in ref. [3]. There exists a small stress peak near the left-hand end of the solder. This general stress distribution pattern is altered by the inclusion of cracks. As shown in the stress distribution for case 2 in Fig. 5, the stress peak now occurs very close to the prescribed crack tip. Stress increase at both crack tips was found in case 3. Since the position of the crack nearly coincides with the position of peak stress where no crack was

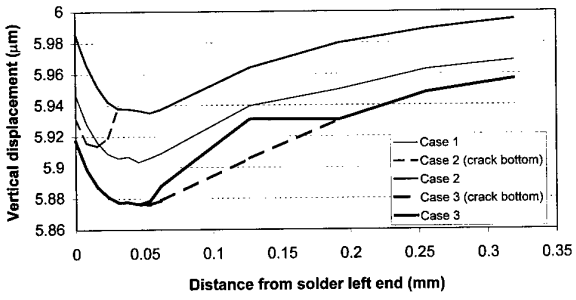

Fig. 4. Vertical displacement at the beam lead–solder interface.

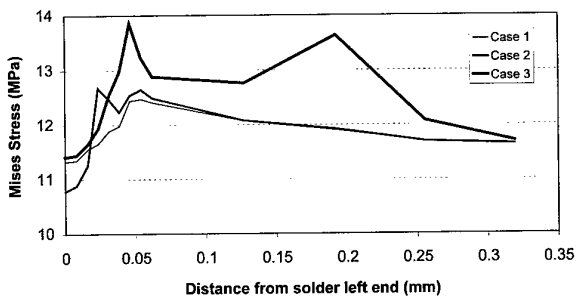

Fig. 5. Von Mises stress distribution in the solder at the beam lead–solder interface.

Fig. 6. Von Mises stress distribution in the beam lead at the beam lead–solder interface.

present, the amount of stress increase in case 3 is fairly high.

The von Mises stress distribution for the beam lead at the beam lead–solder interface along the solder length is presented in Fig. 6. The stress level is about 64 MPa for all cases and is about the same as that in ref. [3]. The variation in stress along the solder length can be observed to be very similar to that in Fig. 5.

The present analysis has demonstrated that the inclusion of cracks at the beam lead–solder interface has created sources of stress concentrations. However, when comparing the present magnitude of stress concentrations with that created in similar studies with crack inclusions for surface mount assemblies, the present magnitude is not high, and should not be a concern. It should be noted though, that the inclusion of cracks at the solder–PCB interface is expected to produce slightly higher stress concentrations than those in the present investigation.

CONCLUSIONS

The effects of cracks in a TAB package under thermal cycling condition were evaluated by a 3-D finite element fracture analysis. The lead–tin solder in the OLB as well as the copper beam lead were taken as elasto-plastic materials. Interface cracks between the copper beam lead and the solder were included in the analysis. The uncoupled thermomechanics formulation was used. The temperature distribution in the package was obtained, followed by the solution of stress and strain fields using the temperature distribution. It was found that the existence of cracks created additional, but mild, stress concentrations. This showed that the configuration of the OLB in TAB packages is generally resilient to thermal cycling conditions, even with the presence of defects such as cracks.

ACKNOWLEDGEMENTS

This work was supported by the Competitive Earmarked Research Grant of the University Grants Committee of Hong Kong Strategic through grant number 9040161.

REFERENCES

1. Lau, J. H., Erasmus, S. J. and Rice, D. W., Overview of TAB technology. In *Electronics Materials Handbook*, Vol. 1, Packaging, ASM International, 1989, pp. 274–296.
2. Darveraux, R., Turlik, I., Hwang, L.T. and Reisman, A., Thermal stress analysis of a multichip package design. *IEEE Trans Components, Hybrids, Manuf. Technol.*, 1989, **CHMT-12**, (4), 663–672.
3. Lau, J.H., Rice, D.W. and Harkings, C.G., Thermal stress analysis of TAB packages and interconnections. *IEEE Trans Components, Hybrids, Manuf. Technol.*, 1990, **CHMT-13**, (1), 182–187.
4. Jog, M.A., Cohen, I.M. and Ayyaswamy, P.S., Analysis and simulation of thermal transients and resultant stresses and strains in TAB packaging. *Trans ASME, J. Electronic Packaging*, 1993, **115**, 34–38.
5. Lau, J.H. and Harkins, C.G., Thermal-stress analysis of SOIC packages and interconnections. *IEEE Trans. Components, Hybrids, Manuf. Technol.*, 1988, **CHMT-11** (4), 380–389.
6. Lau, J. H., *Thermal Stress and Strain in Microelectronics Packaging*. Van Norstrand Reinhold, 1993.
7. Hsu, T. R., *The Finite Element Method in Thermomechanics*. Allen & Unwin, 1986.
8. *ABAQUS User's Manual*, Hibbitt, Karlsson & Sorensen Inc., Providence, RI, 1993.
9. King, J. A., *Material Handbook for Hybrid Microelectronics*. Artech House, Boston, 1988.

ELSEVIER

Composite Structures Vol. 38, No. 1–4, pp. 531–539, 1997
© 1997 Published by Elsevier Science Ltd. All rights reserved
Printed in Great Britain
0263-8223/97/$17.00 + 0.00

PII:S0263-8223(97)00089-5

Development of a composite boring bar

Shuzo Nagano, Takayuki Koizumi, Toru Fujii, Nobutaka Tsujiuchi, Hiroki Ueda & Kobe Steel

Doshisha University, Tanabe, Kyoto 610-03, Japan

A composite boring bar, whose stability against chattering is superior to not only conventional steel bars but also cemented carbide bars, has recently been developed. The main material of this composite bar is pitch-based carbon fiber reinforced plastic. Carbon fibers aligned unidirectionally in the longitudinal direction of the bars give high bending stiffness. Four types of bar having different shaped steel cores were designed by FEM analysis and produced for actual testing. A bar having a cross-shaped steel core shows the best cutting capability and stability amongst all bars designed. This bar can be used when the length (L) and diameter (D) ratio L/D is 7 or even at severe conditions while a cemented carbide bar cannot control the chatter vibration even if the L/D is less than 6. Emphasis should be placed on the fact that the cross-shaped steel core can increase the bending stiffness of the bar in both tangential and radial directions by constraining the shear deformation of the fiber layers without sacrificing the increase of resonant frequencies. © 1997 Published by Elsevier Science Ltd.

INTRODUCTION

When cutting long holes into the internal surface of machine components, chattering frequently occurs due to the low bending stiffness and low damping ability of the boring bar when the arm of the bar is long. Once the chattering occurs, the roughness of the surface of the machine components becomes unacceptable to any standard, including the dimensional accuracy, and the cutting edge is often broken. In the case of conventional steel boring bars, it becomes impractical to cut any metal components due to chattering when the ratio of bar length L to bar diameter D (L/D) is larger than 4–5 [1]. Therefore, bars made of cemented carbide are usually used when L/D is 4–6. When L/D exceeds 5–6, specially devised boring bars having anti-vibration mechanisms are sometimes required [2,3]. However, these are expensive.

Chattering during cutting occurs as self excited vibration. According to the chattering theories based on the 1-DOF vibration system, the bending stiffness and resonant frequencies of boring bars govern chattering as well as the damping ability of the bars. In order to increase the stability against chattering for boring bars, one must use materials which have a high stiffness but low density. Carbon fiber reinforced plastics (CFRP) could meet such requirements if high modulus fibers were to be used. Not only high stiffness and high resonant frequencies, but also high damping can be expected because of the polymer matrix of CFRP [4].

The objective of the present work is to develop a new boring bar using CFRP which can be used at a wide range of L/D over 6. How to design the bar and its performance are discussed and shown in this paper.

DESIGN OF CFRP BORING BAR

Chattering

Vibration during operation is classified as forced vibration and self excited vibration. Chattering of boring bars during internal cutting is due to the self excited vibrations having a regenerative feedback, generally called regenerative chattering. In practice, boring bars are designed to be stable against regenerative chattering. Figure 1 shows the regenerative

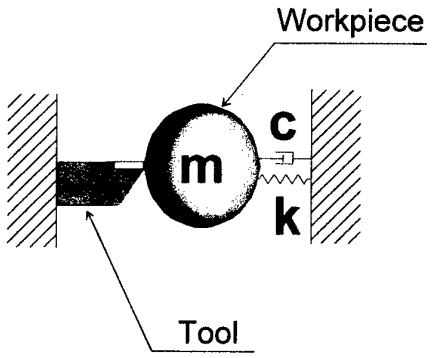

Fig. 1. Merritt's model.

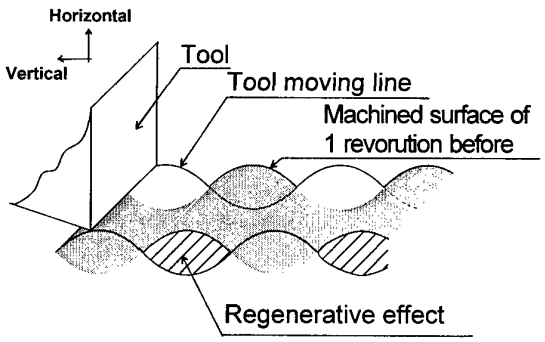

Fig. 3. Conceptional illustration of the regenerative effect.

chattering model based on the 1-DOF vibration system gived by Merritt [5]. Considering outer cutting in this model, the short tool is fixed while the workpiece is sustained by a spring and a damper. For inner hole cutting using a boring bar, a workpiece is large enough to be fixed while the bar should be represented by a mass–spring–damper combination as shown in Fig. 2. In the figure, F_1 is the cutting force acting in the tangential direction. Due to this force, the bar is bent in the vertical plane. F_H is the radial force acting in the radial direction of the hole (radial force is known as shear force in outer cutting). This force causes the bar to bend in the horizontal plane. Figure 3 illustrates how the regenerative effect due to former cutting traces occurs.

Actual cutting depth $u(t)$ at time t is defined as

$$u(t) = u_0 - y(t) + \mu y(t - T) \tag{1}$$

where u_0 is the initial cutting depth: y is the displacement of the cutting edge in the direction of the radial force: μ is all overlap ratio of the cutting edge determined by cutting edge shape, cutting depth and feed: μ governs the magnitude of the regenerative effect; T is a periodic time for the workpiece revolution. The

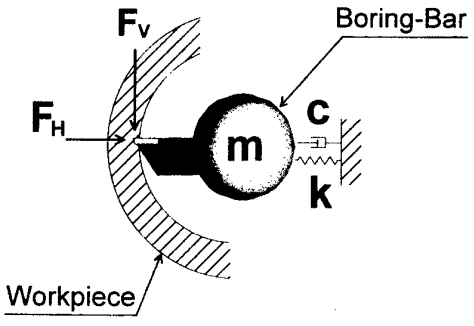

Fig. 2. Modified model.

cutting force F is a function of $u(t)$ and is given as

$$F(t) = k_c(u)t \tag{2}$$

where k_c is a cutting stiffness varying according to cutting conditions such as workpiece material, cutting speed, feed and stiffiness of the lathe. Based on the 1-DOF system shown in Fig. 2 the governing equation for a boring bar is given by

$$F(t) = m\ddot{y}(t) + c\dot{y}(t) + ky(t) \tag{3}$$

where m is an equivalent mass of the boring bar, c and k are an equivalent damping coefficient and an equivalent stiffness of the bar, respectively. By solving eqn (3) in conjunction with eqns (1) and (2), it is obvious that high equivalent stiffness and damping ability give high chattering stability to boring bars.

It is known that the frequency of chattering is almost equal to the first resonant frequency of a boring bar. From eqn (4), if the maximum acceleration of a cutting edge, a, is constant, the displacement of the cutting edge δ decreases with increasing chattering frequency f

$$|a|_{\max} = |(2\pi f)^2 \delta \sin(2\pi f t)|_{\max} \tag{4}$$

Equation (5) shows the well-known relationship between f, m and k

$$f = \frac{1}{2\pi}\sqrt{\frac{k}{m}} \tag{5}$$

So, f increases with decreasing m. Thus, lightweight bars have the advantage of stability

against chattering. In this point CFRP is one of most attractive materials for a boring bar.

Carbon fibers

The previous section reveals that high stiffness k, high damping c and small equivalent mass m give a high stability of the bar for regenerative chattering of the system. These qualities are also preferable for anti-chattering. Therefore, high stiffiness and light weight CFRP is an attractive material for boring bars. Today, graphite/epoxy composites are widely applied not only on aero or astronomic structures but also general products such as sports goods. For such applications, virtually only pan-based fibers are used. The cost of these fibers is reasonable but the Young's moduli of such fibers are not enough to give bars enough bending stiffness as compared to conventional steel bars. The Young's modulus of CFRP applied to boring bars must he higher than 200 GPa (the Young's modulus of steel). The longitudinal Young's modulus E_L of CFRP can be estimated by the law of mixtures as follows when fibers are aligned unidirectionally.

$$E_L = E_F V_F + E_m(1 - V_F) = E_F V_F \tag{6}$$

where E_F and E_m are the Young's moduli of the fibers and the matrix, respectively; V_F is a fiber volume content. Usually, E_m is much lower than E_F and V_F is higher than 50%. Therefore $E_m(1-V_F)$ in the above equation is negligible. According to eqn (6), E_F must be higher than 400 GPa which implies the same stiffness as steel bars. Pitch-based carbon fiber, whose Young's modulus is higher than 700 GPa is now commercially available. Considering the variation of material data, pitch-based carbon fibers which has a nominal Young's modulus of 700 GPa was adopted for the prototypes of CFRI boring bars. The average fiber volume content was about 55% and the observed Young's modulus of CFRP was 300–350 GPa.

Construction of boring bars

The diameter of the boring bar is to be 32 mm, considering fabrication and the standard tool size. As the cutting head, which holds a cutting tip, cannot be attached directly to the CFRP bar, a steel adapter was developed. Figure 4

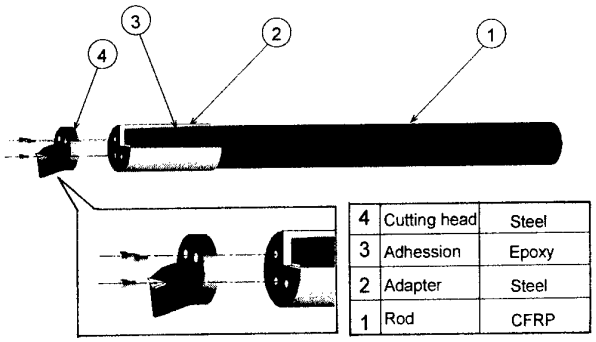

Fig. 4. Total assembly of the CFRP boring bars.

shows the schematic view of the CFRP boring bars manufactured by way of trial. The adapter whose inner hole was tapered, was bonded to the bar using an epoxy adhesive. The commercially available cutting head is fixed to this adapter using three bolts. When the CFRP boring bars are fixed to a lathe, a specially devised bar holder is used because the bars cannot be subjected to concentrated loads given by standard fastening bolts. For sufficient fixing of boring bars made from unidirectional CFRP, four types of different shapes of steel core were considered.

Type P

In the case of a Type P boring bar, a steel pipe was used as the center core of the bar (as shown in Fig. 5(a)) since lubricant is often used during the cutting operation. The outer diameter of the pipe is 15 mm while inner diameter is 8 mm. This steel pipe core is also useful to give an accurate diameter of the bar by machining after fabricating the bar in an auto clave using unidirectional prepreg.

The effect of shear deformation is appreciable when the cantilever beam bar is relatively short since the shear modulus of CFRP is over 100 times lower than the longitudinal modulus of CFRP. It is expected that this small center core cannot restrict shear deformation due to the cutting and radial forces.

Type V

In order to improve the bending stiffness, additional deformation due to shear deformation of CFRP layers should be reduced. For such a requirement, different types of steel core were

considered. Near the neutral axis of a beam, the shear stress becomes high when the beam is subjected to not only a bending moment but also a shear force. Therefore, if a material with a high shear rigidity is used as the center plate core of the composite bar, the total deflection of the bar can be reduced. Figure 5(b) shows a Type V CFRP composite boring bar with a 2 mm center plate core embedded in the vertical plane. The vertical plate is effective for the shear deformation due to cutting force.

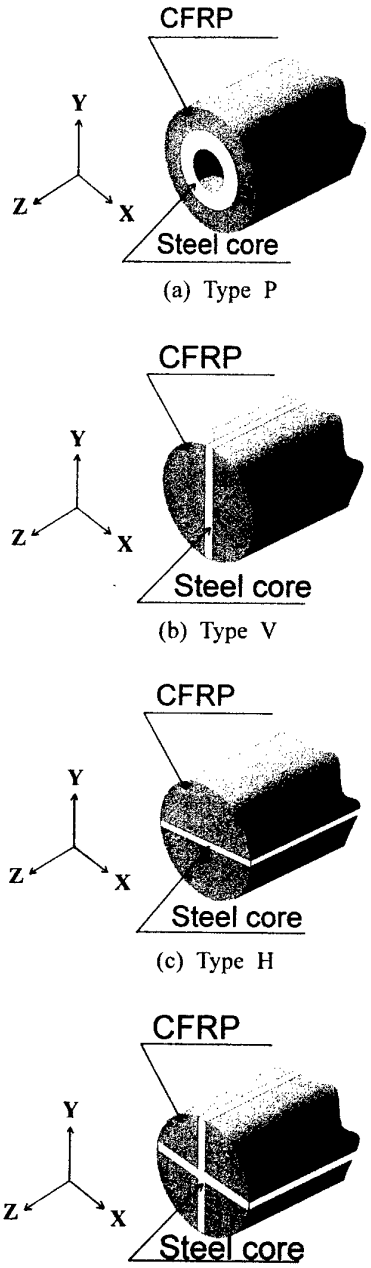

Fig. 5. Constructions of CFRP boring bars. (a) Type P. (b) Type V. (c) Type H. (d) Type C.

Type H

Type H CFRP composite boring bar has a 2 mm center plate core horizontally embedded. The horizontal plate is effective for shear deformation due to the radial force. Usually, the radial force is smaller than the cutting force. Figure 5(c) shows Type H bar. This bar is made by rotating the Type V bar on its longitudinal axis by 90°.

Type C

Type V and Type H bars can constrain only unidirectional shear deformation. However, two plates should be used in both directions as the core of a composite bar if both forces are relatively large. For such a case, a cross-shaped steel core as shown in Fig. 5(d) must be effective even if the total weight of the bar is sacrificed to some extent.

FEM ANALYSIS

The bending stiffness and the first resonant frequency of all types of CFRP boring bars were calculated by FEM analysis using SDRC 1-DEAS.

For a Type C boring bar, the stiffness is estimated when the thickness of the steel core varies. Figure 6 shows FE divisions for all boring bars. Both steel and cemented carbide boring bars are also analyzed using the same FE division of Type C. Solid elements having eight nodes were used. Each node has three degrees of translation. The material data for calculation for composite bars are given in Table 1. These values were estimated by material test. Boundary conditions of the FE model is shown in Fig. 7. The overhang of the boring bars is 224 mm and the diameter of the bars is 32 mm ($L/D = 7$). All degrees of freedom of the surface nodes contacting the internal surface of the boring bar holder are constrained, as shown by the gray area in Fig. 7.

Bending stiffness

The bending stiffness of the composite bars is calculated by concentrating a force on the node located at the free edge of the boring bar when

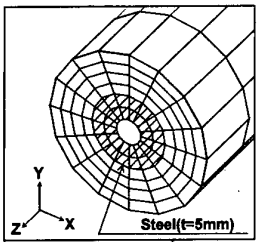

(a) Type P CFRP boring bar

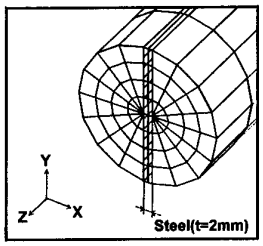

(b) Type V CFRP boring bar

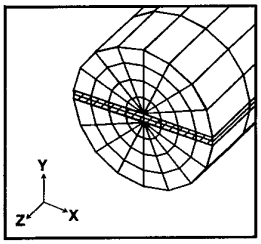

(c) Type H CFRP boring bar

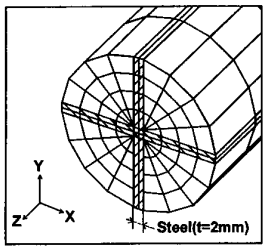

(d) Type C CFRP boring bar

Fig. 6. FE divisions of CFRP boring bars. (a) Type P CFRP boring bar. (b) Type V CFRP boring bar. (c) Type H CFRP boring bar. (d) Type C CFRP boring bar.

set-up as a cantilever beam in the vertical direction.

Figure 8 shows a comparison of bending stiffness in the direction of cutting force among

Table 1. Material properties of the CFRP used in FEM analysis

Young's modulus (GPa)	E_x	E_y	E_z
	6.85	6.85	320
Shearing modulus (GPa)	G_{xy}	G_{yz}	G_{zx}
	0.533	2.54	2.54
Poisson ratio	ν_{xy}	ν_{yz}	ν_{zx}
	0.23	0.004	0.004

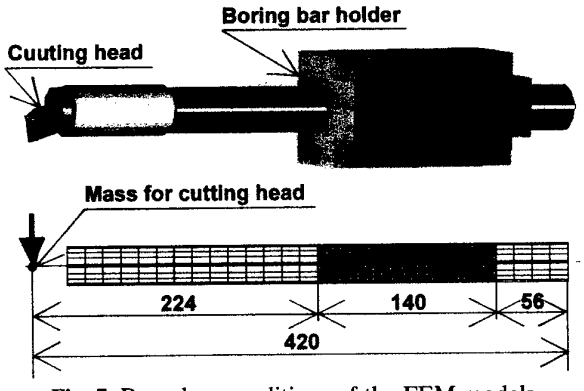

Fig. 7. Boundary conditions of the FEM models.

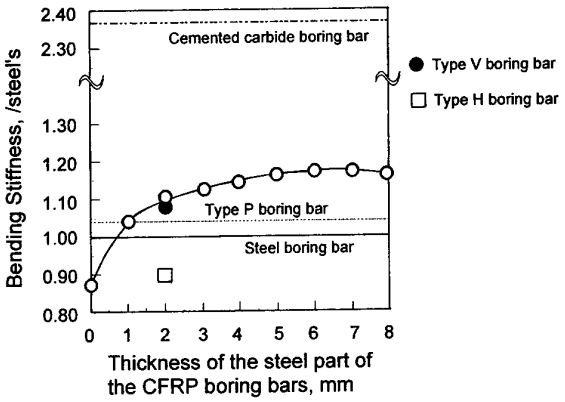

Fig. 8. Relationship between the thickness of the steel core of the CFRP boring bars and bending stiffness ($L/D = 7$).

CFRP, steel and cemented carbide bars at $L/D = 7$. The variation of bending stiffness with respect to core thickness is also given for a Type C boring bar. The ordinate is normalized by that of the steel boring bar.

If a whole bar is made of CFRP instead of steel, the tensile stiffness or bending stiffness under a pure bending moment would be 160% (320 GPa) higher than those of steel. However, the bending stiffness under both bending moment and shear force becomes 87% of that for the steel boring bar. Use of CFRP does not always increase the bending stiffness of cantilever beam bars. The reason of this low stiffness was explained in the above section. From Fig. 8, even a 1 mm thick cross-shaped steel core is effective to constrain shear deformation. Up to 6 mm, the bending stiffness of the composite bar increases with increasing thickness. Shear deformation is much constrained with increasing thickness of the steel core, but a thicker core also reduces the bending stiffness more, due to the low Young's modulus of steel. The maximum increase in bending stiffness is around 20% using CFRP. The Type H combination has a lower bending stiffness than that of the steel bar since the steel plate core does not constrain the shear deformation of CFRP layers in the Y–Z plane. For a Type P boring bar, the bending stiffness is only 4% as high as that of the steel bar. The difference in bending stiffness between a Type P bar and steel becomes less with a decrease of L/D. Finally, the bending stiffness for a Type P bar becomes lower than that of the steel bar. The Type V bar has a similar stiffness to Type C bar since the core plate vertically aligned is effective in con-

straining shear deformation of CFRP layers in the Y–Z plane. On the other hand, the cemented carbide boring bar has a bending stiffness 2.37 times higher than that of the steel boring bar. One resolution to improve the bending stiffness is to use carbon fibers with a higher Young's modulus. Although some fibers have Young's modulus higher than 1000 GPa, they are not yet commercially available.

Resonant frequency

Modal analysis of the models was also conducted to estimate the first resonant frequencies of the bars (bending mode I). In Fig. 9, a comparison of the first resonant frequency for CFRP, steel and cemented carbide bars at $L/D = 7$ is given. The variation of the first resonant frequency with respect to core thickness is also given for the Type C boring bar. The ordinate is normalized by that of the steel boring bar as well as in Fig. 9.

In contrast to bending stiffness, the resonant frequencies of CFRP boring bars are always higher than that for the steel bar. They are also comparable to the resonant frequency of the cemented carbide bar because the composite bars are one third to one quarter lighter than the steel bar. The cemented carbide bar has a higher bending stiffness but it is extremely heavy. From a viewpoint of resonant frequencies, high performance of CFRP boring bar can be expected. It is obvious that the first resonant frequency increases once with increasing in thickness and then it decreases from the Type C bar result. The maximum increase in resonant frequency is about 30% at 2 mm thickness while for bending stiffness, the maximum gain is obtained at 6–7 mm. In the present study, the thickness of all steel plate cores is 2 mm as it is expected that the resonant frequency is effective for the chattering stability.

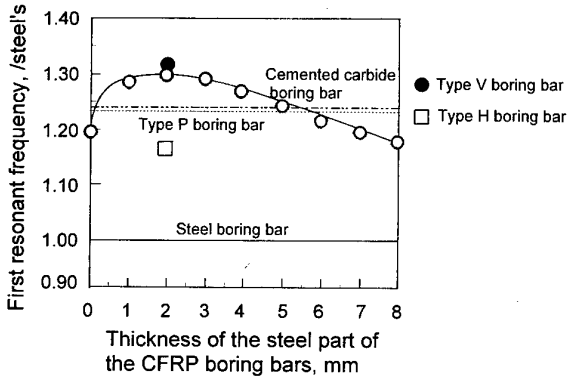

Fig. 9. Relationship between the thickness of the steel core of the CFRP boring bars and first resonant frequency ($L/D = 7$).

CUTTING EXPERIMENTS

Cutting experiments were conducted to evaluate cutting performance and stability against chattering for CFRP bars (Type P, Type V, Type C, Type H and Type C) as well as conventional steel and cemented carbide bars. The diameter of all bars is 32 mm. A conventional lathe (not a NC lathe) was used for the tests. Here, all boring bars were fixed using the specially devised bar holder to provide equal conditions of holding in the tool fixture as shown in Fig. 10. An overhang of 224 mm gives an $L/D = 7$. Thick cylindrical pipes (inner diameter: 60 mm, outer diameter: 100 mm) whose material was mild steel were used as a workpiece for the tests. Before the cutting experiment, the surface of the workpiece was smoothed to give a constant testing condition. Two tiny accelerometers were attached on the cutting head near the cutting edge to measure accelerations in the tangential and radial directions during the cutting operation. Cutting conditions are given in Table 2.

As noise occurs and chatter marks can be distinguished on the cutting surface of the workpiece when chattering occurs, it is easy to identify whether chattering has occurred or not.

RESULTS AND DISCUSSION

Cutting limits for all boring bars are plotted on a feed-cutting depth map (Fig. 11) at $L/D = 7$.

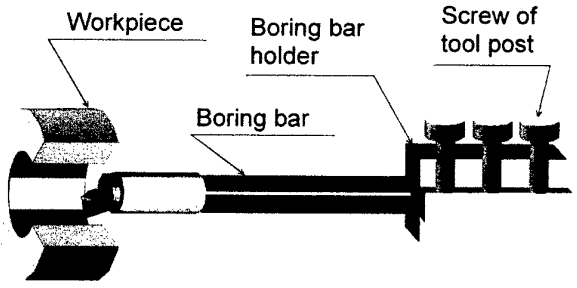

Fig. 10. System for cutting test.

Table 2. Cutting conditions in the measurement

Revolution (rpm)	Cutting depth (mm)	Feed (mm/rev)
630	0.4	0.3
		0.2
	0.2	0.3
		0.2
500	0.4	0.3
		0.2
	0.2	0.3
		0.2

As before mentioned, the steel bar was not able to cut without chattering when the L/D value was greater than 4. Even when L/D was smaller than 4, it was difficult for the steel bar to cut without chattering under several conditions. No marks in the figure mean that smooth cutting without chattering was not attained for the corresponding bars. Therefore, a mark for the steel bar cannot be found in this figure. It is found that the Type C CFRP bar has excellent performance. Although the cemented carbide sometimes attained smooth cutting at lighter conditions than those for the Type C bar, even at $L/D = 7$, it was not always stable. Once chattering occurred, it did not stop for the cemented carbide bar while the Type C CFRP bar was always stable. Good stability and cutting performance could not be obtained for both Types V and H bars. In particular, the Type V bar shows a high bending stiffness almost equal to the Type C bar and the first resonant frequency is higher than that of the Type C bar in the cutting force direction. However, the bending stiffness of the Type V bar in the radial force direction is equal to the bending stiffness of the Type H bar and it is much lower than that of the Type C bar. It is shown

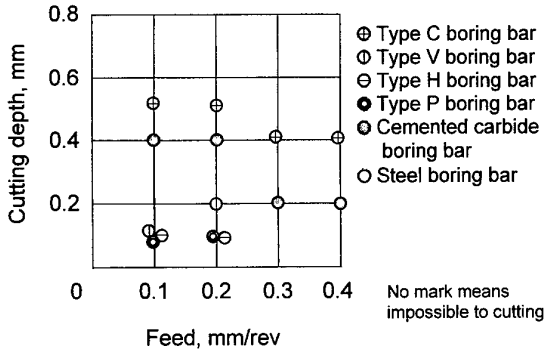

Fig. 11. Cutting limit of the boring bars.

that the bending stiffness in the radial force direction is also as important as the bending stiffness in the cutting force direction.

Figures 12 and 13 show the dynamic response for Type C CFRP and steel bars during cutting operation. Parts (a) are the acceleration–time history plots, parts (b) are the power spectra for trace (a) and parts (c) are the Lissajious plots of acceleration in X and Y directions. It must be noted that the surface of the workpiece cut by the steel boring bar was extremely rough and chattering occurred. Even for the Type C bar, oscillation occurred but the magnitude of oscillation is much smaller than that for the steel bar. The period of the main oscillation corresponds to the first resonant frequency for both cases.

Here, the maximum acceleration of Type C and steel bars are 11 and 280 G and the frequency of oscillation for the bars are 500 and 375 Hz, respectively. Maximum displacement of the cutting edge of the Type C and steel bars are calculated as 0.011 and 0.43 mm, respectively, from eqn (4). It is found that the machined surface cut by the Type C bar is acceptable for the roughness and dimensional accuracy. However, it is realized that the maximum displacement of the cutting edge of the steel bar is larger than cutting depth and the cutting edge was beating the surface of the workpiece. In this point, the advantage for chattering stability of the Type C bar is obvious.

Although the Type C bar has a high cutting ability and chattering stability as above, it has no problem entirely. From Fig. 12(b) and Fig. 13(b), the resonant frequency for the Type C bar is higher than that for the steel bar. However, an increase of the resonant frequency is not remarkable, as expected in Fig. 9. No apparent reasons could be found for this discrepancy. Holding CFRP boring bars tightly is a problem and this could be one of reasons for the above discrepancy. The method for holding the bar must be considered in the near future as well as how to attach the cutting head to the bar. Surface protection for lubricant and tips is also one of issues to be considered for practical use.

CONCLUSIONS

1. A boring bar made from unidirectional CFRP which has a high stability against chat-

tering under severe conditions at $L/D = 7$ was successfully developed.
2. The cross-shaped steel core embedded CFRP boring bar can constrain shear deformation and improves the equivalent bending stiffness of the boring bar.
3. An optimized cross-shaped steel core improves the dynamic characteristics of the total structure of the boring bar.
4. Compared with the cemented carbide boring bar, chattering can be completely suppressed, even in the range of L/D ratios greater than 7.

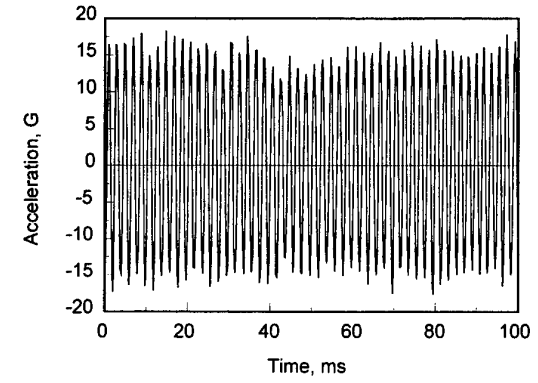

(a) Acceleration - Time history

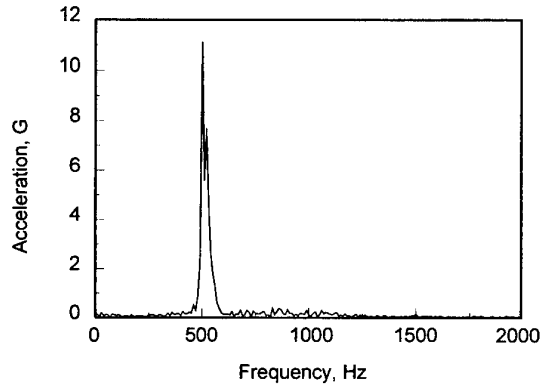

(b) Power spectrum for (a)

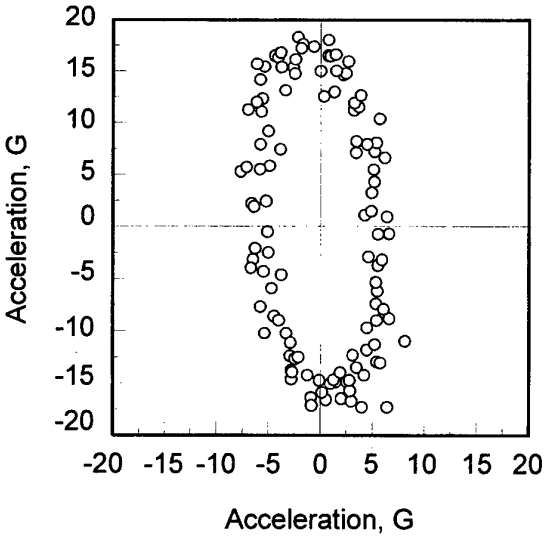

Fig. 12. Dynamic response for the Type C CFRP boring bar (630 rpm, cutting depth = 0.4 mm, feed = 0.3 mm/rev): (a) acceleration–time history, (b) power spectrum for (a), (c) Lissajious plot of acceleration in X and Y directions.

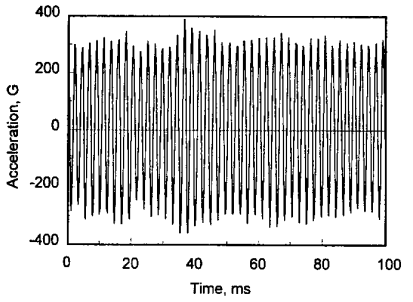

(a) Acceleration - Time history

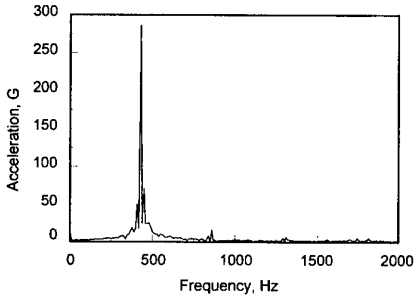

(b) Power spectrum for (a)

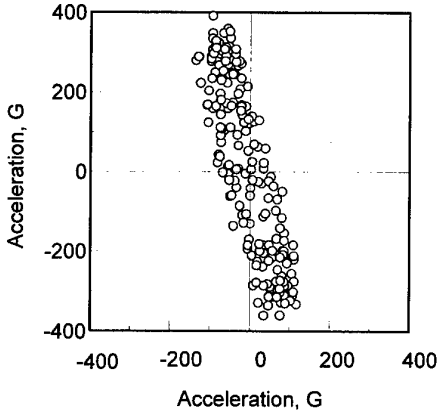

Fig. 13. Dynamic response for the steel boring bar (630 rpm, cutting depth = 0.4 mm, feed = 0.3 mm/rev): (a) acceleration–time history, (b) power spectrum for (a), (c) Lissajious plot of acceleration in X and Y directions.

REFERENCES

1. Hoshi, T., *Vibration analysis of mechanical cutting*, Kegyo Chasakai Publishing Co. Ltd, 1990.
2. Takeyama, H. *et al.*, *J. Japan Soc. precision engng*, **48**(12) (1982) 1628.
3. Kitajima, K. and Tanaka, Y., *J. Japan Soc. precision engng*, **50**(5) (1984) 860.
4. Kitajima, K. *et al.*, *J. Japan Soc. precision engng*, **53**(10) (1987) 1582.
5. Merritt, H. E. *Trans. ASME, Ser. B*, **87**(4) (1965) 27.

ELSEVIER

Composite Structures Vol. 38, No. 1–4, pp. 541–551, 1997
© 1997 Elsevier Science Ltd. All rights reserved
Printed in Great Britain
0263-8223/97/$17.00 + 0.00

PII:S0263-8223(97)00090-1

Buckling and vibration analysis of composite plate and shell structures using the PASSAS software package

D. J. Dawe

School of Civil Engineering, University of Birmingham, Edgbaston, Birmingham B15 2TT, UK

&

S. Wang

Department of Aeronautical & Automotive Engineering & Transport Studies, Loughborough University, Loughborough, Leicestershire LE11 3TU, UK

A description is given of the PASSAS finite strip software package for predicting the buckling stresses and natural frequencies of composite laminated prismatic plate and shell structures of complicated cross-section and general lamination. The basic equations underpinning the development of the properties of a transversely curved finite strip are presented in the context of first-order shear-deformation shell theory and, by reduction, in the context of thin shell theory. The B-spline finite strip method is used and this enables the specification of a wide range of end conditions. The major features of the software package are described, and these include a range of strip models, the use of multi-level substructuring techniques across the structure, including superstrips, and the use of an efficient and reliable solution procedure. Results are presented of the application of PASSAS to the solution of a small number of shell buckling and vibration problems. © 1997 Elsevier Science Ltd.

INTRODUCTION

Plate and shell structures made of fibre-reinforced composite laminated material are used frequently as major load-bearing components in a number of branches of engineering, including aeronautical and marine engineering. The structures are often prismatic, being formed of flat and/or transversely circularly curved component plates which are rigidly connected together at their longitudinal edges to form structures of arbitrary cross-sections, such as stiffened panels, box sections, etc. In the design of such structures there is often a requirement to predict accurately their buckling stresses or their natural frequencies of vibration.

The finite strip method is an efficient and very useful method for the analysis of complicated prismatic plate and shell structures, particularly for eigenvalue-type problems. The method exists in a number of variants, the most important of which at present are the semi-analytical finite strip method (or S-a FSM), which was developed first (see Cheung [1]), and the spline finite strip method (or spline FSM) introduced more recently [2]. A detailed description of the use of the two variants in predicting the buckling and post-buckling behaviour of flat plate structures has been given recently by Dawe [3] wherein many relevant publications are cited. The FSM has been developed in the context of shear-deformation theory as well as in the context of classical or thin theory [3]. Less development has been reported in the realm of the analysis of shell structures but Mohd & Dawe [4,5] have described the use of

the S-a FSM in predicting buckling stresses and frequencies of composite laminated shell structures.

The S-a FSM is often a very appropriate procedure for the analysis of prismatic structures but it does lack versatility in dealing with a range of end conditions, particularly when anisotropic materials are involved and/or when analysis is conducted in the context of thick plate or shell theory. The spline FSM can be applied much more generally, and for that reason the authors have developed the PASSAS software package [6] which incorporates the spline FSM and which is the focus of attention in this paper. The use of the spline FSM to predict the buckling stresses and frequencies of flat plates and plate structures has been described earlier by the authors [7,8]. In the present paper the scope of these studies is broadened considerably to include shell structures. The developed capability allows for arbitrary lamination of component flat or curved plates and for an analysis to be conducted within the context of first-order shear-deformation plate/shell theory or of thin theory. The new spline capability incorporates all the advanced analysis features, such as multi-level substructuring, superstrips, solution procedure, etc., which have been described by Dawe & Peshkam [9] and used later by Dawe [3], Mohd & Dawe [4,5] and Dawe & Wang [6–8].

Here, the main equations on which the properties of the shell finite strip are based are presented in the next section. The PASSAS software package is described in general terms in Section 3. A few selected applications of the package are then described in Section 4 and concluding remarks are made in Section 5.

THE BASIS OF FINITE STRIP PROPERTIES

A shear-deformation shell theory (SDST) curved plate strip which is assumed to form part of a prismatic structure is shown in Fig. 1(a). The finite strip has length A, uniform middle-surface radius of curvature R, uniform thickness h and curved breadth b at the middle surface. The local axes x, y and z are surface ones, i.e. are axial, circumferential and normal ones. The corresponding translational displacements at the middle surface are u, v and w, and the independent rotations of the middle-surface normal along the x- and y-directions are ψ_x and ψ_y, respectively. The finite strip may be subjected to the applied uniform axial (σ_x^o), circumferential (σ_y^o) and shear (τ_{xy}^o) stresses shown in Fig. 1(b), leading to buckling or it may be undergoing harmonic motion whilst vibrating in a natural mode with circular frequency p, or both these influences may be present. All displacement quantities are in fact perturbation displacement quantities representing changes that occur at the instant of buckling following the application of the applied stress system at its critical level, or representing

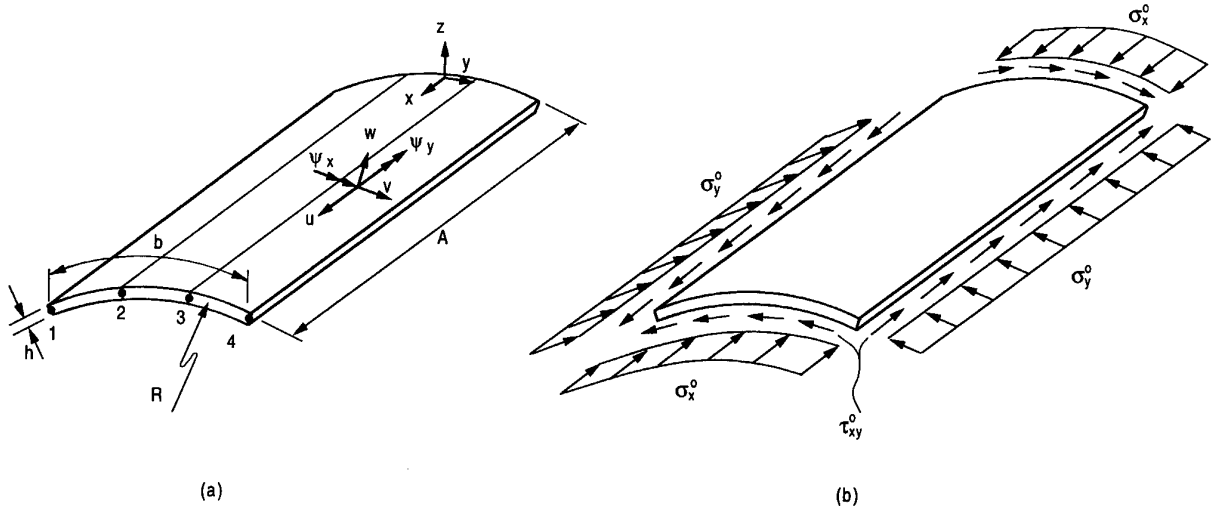

Fig. 1. A curved finite strip: (a) geometry and displacements; and (b) applied stress system.

changes that occur during vibration about a datum state which corresponds to some prescribed value of the stress system.

The linear expressions for the five significant strain components, at a general point, of the enhanced Koiter–Sanders SDST [10,11], which are used here as the basis for the strain energy expression, are

$$\varepsilon_x = \varepsilon_x^* + z\kappa_x, \quad \varepsilon_y = \varepsilon_y^* + z\kappa_y, \quad \gamma_{xy} = \gamma_{xy}^* + z\kappa_{xy} \quad \gamma_{yz} = \frac{\partial w}{\partial y} + \psi_y - \frac{v}{R}, \quad \gamma_{zx} = \frac{\partial w}{\partial x} + \psi_x \tag{1}$$

where

$$\varepsilon_x^* = \frac{\partial u}{\partial x} \quad \varepsilon_y^* = \frac{\partial v}{\partial y} + \frac{w}{R}, \quad \gamma_{xy}^* = \frac{\partial u}{\partial y} + \frac{\partial v}{\partial x}, \quad \kappa_x = \partial\psi_x/\partial x, \quad \kappa_y = \partial\psi_y/\partial y,$$

$$\kappa_{xy} = \frac{\partial \psi_y}{\partial x} + \frac{\partial \psi_x}{\partial y} + \left(\frac{1}{2R} \frac{\partial \mathrm{v}}{\partial \mathrm{x}} - \frac{\partial \mathrm{u}}{\partial \mathrm{y}} \right) \tag{2}$$

Here ε_x and ε_y are in-surface direct strains and γ_{xy} is the in-surface engineering shear strain at a general point, whilst ε_x^*, ε_y^* and γ_{xy}^* are the corresponding strains at the middle surface and κ_x, κ_y and κ_{xy} are the two direct curvatures and the twisting curvature. Also, γ_{yz} and γ_{zx} are the through-thickness shear strains.

For arbitrary lamination the constitutive equations for the laminate are

$$\begin{Bmatrix} N_x \\ N_y \\ N_{xy} \\ M_x \\ M_y \\ M_{xy} \\ Q_y \\ Q_x \end{Bmatrix} = \begin{bmatrix} A_{11} & & & & & & & \\ A_{12} & A_{22} & & & & & & \\ A_{16} & A_{26} & A_{66} & & \text{Symmetric} & & & \\ B_{11} & B_{12} & B_{16} & D_{11} & & & & \\ B_{12} & B_{22} & B_{26} & D_{12} & D_{22} & & & \\ B_{16} & B_{26} & B_{66} & D_{16} & D_{26} & D_{66} & & \\ 0 & 0 & 0 & 0 & 0 & 0 & A_{44} & \\ 0 & 0 & 0 & 0 & 0 & 0 & A_{45} & A_{55} \end{bmatrix} \begin{Bmatrix} \varepsilon_x^* \\ \varepsilon_y^* \\ \gamma_{xy}^* \\ \kappa_x \\ \kappa_y \\ \kappa_{xy} \\ \gamma_{yz} \\ \gamma_{zx} \end{Bmatrix}$$

or

$$\mathbf{F} = \mathbf{L}\mathbf{e} \tag{3}$$

Here N_x, N_y and N_{xy} are the membrane direct and shearing forces per unit length; M_x, M_y and M_{xy} are the bending and twisting moments per unit length; and Q_x and Q_y are the through-thickness shear forces per unit length. The laminate stiffness coefficients are defined as

$$(A_{ij}, B_{ij}, D_{ij}) = \int_{-h/2}^{h/2} Q_{ij}(1, z, z^2)\, \mathrm{d}z \quad (i,j = 1, 2, 6), \quad A_{ij} = k_i k_j \int_{-h/2}^{h/2} Q_{ij}\, \mathrm{d}z \quad (i,j = 4, 5) \tag{4}$$

where Q_{ij} for $i, j = 1, 2, 6$ are in-surface reduced stiffness coefficients and Q_{ij} for $i, j = 4, 5$ are through-thickness shear stiffness coefficients. The $k_i k_j$ are the prescribed shear correction factors of the first-order theory.

The strain energy of the curved finite strip can be expressed as

$$U = \frac{1}{2} \int_{-b/2}^{b/2} \int_{0}^{A} \mathbf{e}^{\mathrm{T}} \mathbf{L} \mathbf{e}\, \mathrm{d}x\, \mathrm{d}y \tag{5}$$

and is such that only first derivatives of the five fundamental displacement quantities occur in it: hence only C^0-type continuity is required for these quantities.

The potential energy of the applied stresses is

$$V_g = \frac{1}{2} h \int_{-b/2}^{b/2} \int_0^A \left(\sigma_x^o \left[\left(\frac{\partial u}{\partial x} \right)^2 + \left(\frac{\partial v}{\partial x} \right)^2 + \left(\frac{\partial w}{\partial x} \right)^2 \right] + \sigma_y^o \left[\left(\frac{\partial u}{\partial y} \right)^2 + \left(\frac{\partial v}{\partial y} + \frac{w}{R} \right)^2 \right.\right.$$

$$\left. + \left(\frac{\partial w}{\partial y} - \frac{v}{R} \right)^2 \right] + 2\tau_{xy}^o \left[\frac{\partial u}{\partial x} \frac{\partial u}{\partial y} + \frac{\partial v}{\partial x} \left(\frac{\partial v}{\partial y} + \frac{w}{R} \right) + \frac{\partial w}{\partial x} \left(\frac{\partial w}{\partial y} - \frac{v}{R} \right) \right]$$

$$+ \frac{h^2}{12} \left\{ \sigma_x^o \left[\left(\frac{\partial \psi_x}{\partial x} \right)^2 + \left(\frac{\partial \psi_y}{\partial x} \right)^2 \right] + \sigma_y^o \left[\left(\frac{\partial \psi_x}{\partial y} \right)^2 + \left(\frac{\partial \psi_y}{\partial y} \right)^2 \right] \right.$$

$$\left.\left. + 2\tau_{xy}^o \left[\frac{\partial \psi_x}{\partial x} \frac{\partial \psi_x}{\partial y} + \frac{\partial \psi_y}{\partial x} \frac{\partial \psi_y}{\partial y} \right] \right\} \right) dx\, dy \tag{6}$$

The kinetic energy of the finite strip when vibrating with circular frequency p (with the fundamental displacement quantities then regarded as amplitudes of the motion) is

$$T = \frac{1}{2} p^2 \int_{-b/2}^{b/2} \int_0^A \rho h \left[u^2 + v^2 + w^2 + \frac{h^2}{12} (\psi_x^2 + \psi_y^2) \right] dx\, dy \tag{7}$$

where ρ is the material density (which is assumed here to be uniform).

The displacement field of the finite strip is defined by expressions for the five fundamental quantities, each of which is represented as a summation of products of B-spline functions in the longitudinal x-direction and polynomial functions in the crosswise or circumferential y-direction. The field is

$$\begin{Bmatrix} u \\ v \\ w \\ \psi_y \\ \psi_x \end{Bmatrix} = \sum_{i=1}^{n+1} \begin{bmatrix} N_i & 0 & 0 & 0 & 0 \\ 0 & N_i & 0 & 0 & 0 \\ 0 & 0 & N_i & 0 & 0 \\ 0 & 0 & 0 & N_i & 0 \\ 0 & 0 & 0 & 0 & N_i \end{bmatrix} \begin{bmatrix} \bar{\theta}_k & \mathbf{0} & \mathbf{0} & \mathbf{0} & \mathbf{0} \\ \mathbf{0} & \bar{\theta}_k & \mathbf{0} & \mathbf{0} & \mathbf{0} \\ \mathbf{0} & \mathbf{0} & \bar{\theta}_k & \mathbf{0} & \mathbf{0} \\ \mathbf{0} & \mathbf{0} & \mathbf{0} & \bar{\theta}_k & \mathbf{0} \\ \mathbf{0} & \mathbf{0} & \mathbf{0} & \mathbf{0} & \bar{\theta}_{k-1} \end{bmatrix} \begin{Bmatrix} \mathbf{d}^u \\ \mathbf{d}^v \\ \mathbf{d}^w \\ \mathbf{d}^{\psi_y} \\ \mathbf{d}^{\psi_x} \end{Bmatrix} \tag{8}$$

In eqn (8) i denotes the number of a reference line (at which degrees of freedom are located) and there are $(n+1)$ reference lines for a finite strip, where n is the order of the polynomial representation of each of the fundamental quantities in the circumferential y direction. The $N_i = N_i(y)$ are standard Lagrangian shape functions which define this representation. The finite strip shown in Fig. 1(a) corresponds to $n = 3$ (i.e. cubic polynomial representation across the strip) with four reference lines, but other types of strip are available for selection. The $\mathbf{d}^u$, $\mathbf{d}^v$, $\mathbf{d}^w$, $\mathbf{d}^{\psi_y}$ and $\mathbf{d}^{\psi_x}$ are column matrices of values of generalized displacement parameters at the reference lines, relating to u, v, w, ψ_y and ψ_x, respectively.

Also in eqn (8), $\bar{\theta}_k$ and $\bar{\theta}_{k-1}$ are modified B-spline function bases of polynomial orders k and $(k-1)$. In using the spline functions the length A of a finite strip is divided into q spline sections, as shown in Fig. 2(a), which are taken to be of equal length d, with $q+1$ spline knots (labelled 0–q) within the length A and some other knots (required for the prescription of end conditions) located

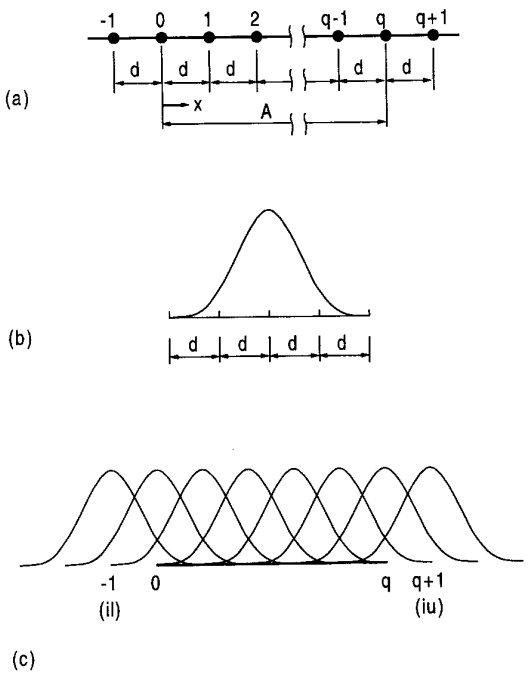

Fig. 2. Spline representation: (a) spline sections and knots; (b) local cubic spline function; and (c) a combination of local cubic spline functions.

outside of the length A. Figure 2(b) shows a local spline function and Fig. 2(c) shows the combination of local functions which contributes to the modified B-spline function basis. It is noted that Fig. 2 relates specifically to cubic spline functions, with $k = 3$. For a fuller description of spline representation the reader is referred to the related earlier studies of the authors [7,8]. It is noted that eqn (8) indicates that the so-called $B_{k,k-1}$ approach [7,8] is again used, i.e. the spline representation of ψ_x is one order lower than that of w to avoid the shear locking problem that can otherwise occur when analysing thin structures in the context of first-order SDST.

The elastic stiffness matrix **k**, geometric stiffness matrix $\mathbf{k}_g$ and consistent mass matrix **m** for the SDST curved-plate finite strip are obtained by using the displacement field of eqn (8) in the expressions for strain energy, eqn (5), for potential energy of applied stresses, eqn (6), and for kinetic energy, eqn (7), respectively. The details of this are recorded in Dawe and Wang [6–7] and are also similar to the details given in Dawe and Wang [7] for a flat finite strip.

The above description and equations relate to SDST analysis. For thin shell theory (TST) analysis the basis for the development of the properties of a finite strip can be described concisely as a simplification of the above approach. In moving from shear-deformation shell theory to thin shell theory the main simplification is associated with invoking the Kirchhoff normalcy condition, which means that the through-thickness shear strains, γ_{yz} and γ_{zx} of eqn (1) vanish. It follows, of course, that the rotations ψ_x and ψ_y are then directly related to v and w by the equations

$$\psi_x = -\frac{\partial w}{\partial x}, \quad \psi_y = \frac{v}{R} - \frac{\partial w}{\partial y} \tag{9}$$

This means that ψ_x and ψ_y are no longer independent quantities and hence u, v and w are the only fundamental quantities of TST. The basic equations of TST are obtained by substituting for ψ_x and ψ_y, given by eqn (9), in eqns (1) and (2), by reducing the set of constitutive equations in eqn (3) by removing Q_y, Q_x, γ_{yz} and γ_{zx} from consideration, by ignoring the second of equations in eqn (4), and by removing the contributions associated with ψ_x and ψ_y from the expressions for V_g and T in eqns (6) and (7). Also, the displacement field of eqn (8) is reduced in the TST analysis by removing the expressions for ψ_y and ψ_x. A further modification to this field is that in the expression for w in the TST context the shape functions $N_i(y)$ become Hermitian shape functions to reflect the fact that

there is a requirement for C^1-type continuity of w. In the TST approach only a single type of crosswise polynomial interpolation is considered (i.e. cubic interpolation for each of u, v and w). The corresponding finite strip model can still be represented by Fig. 1(a), with four reference lines. For u and v the values of the generalized displacement parameters are located at all four reference lines, as in the SDST approach, whilst for w they are located only at the two outside reference lines 1 and 4.

THE PASSAS SOFTWARE PACKAGE

The basis of PASSAS is, of course, the individual finite strip, with its properties developed as described in the previous section. However, there are numerous different finite strip models available within PASSAS and, beyond this, there are incorporated into the software package some powerful and sophisticated techniques to enable solutions to be obtained efficiently to complex problems.

In the context of SDST, the variety of curved-plate finite strip models available to the user of PASSAS arises chiefly in the specification of the strip displacement field (eqn (8)) but also in the manner in which the integrations involved in determining $\mathbf{k}$, $\mathbf{k}_g$ and $\mathbf{m}$ are evaluated in the circumferential direction. So far as the displacement field is concerned, selection can be made regarding the variation of the five fundamental quantities in both the circumferential and the longitudinal directions. In the circumferential direction the order n of Lagrangian interpolation can be chosen to be 1, 2, 3, 4 or 5, i.e. the strips are referred to as linear, quadratic, cubic, quartic or quintic strips. In the longitudinal direction, with the $B_{k,k-1}$-spline approach, values of k can be chosen to be 2, 3, 4 or 5, i.e. the choice lies between B_{21}-, B_{32}-, B_{43}- and B_{54}-spline representation. Integrations to evaluate strip properties are carried out numerically using Gauss quadrature in the circumferential and longitudinal directions. In the longitudinal direction, full integration is used with six Gauss points in each spline section. In the circumferential direction, a choice can be made between using full or reduced integration where, for a strip based on polynomial interpolation of order n, full integration corresponds to $(n+1)$ Gauss points across the strip and reduced integration to n points.

In the context of TST only a single order of circumferential polynomial interpolation is considered in PASSAS and, as intimated earlier, this order is cubic. However, there does exist choice in regard to the variation of the displacements u, v and w in the longitudinal direction. In the B_k-spline approach, k can have the values 3 or 4 or 5, i.e. the choice lies between B_3-, B_4- and B_5-spline representation. In determining strip properties, the numerical integration scheme uses four Gauss points across the strip and six Gauss points in each spline section along the strip.

Beyond the stage at which the properties of individual finite strips are established, the procedures in PASSAS which lead to the calculation of buckling stresses or natural frequencies are very much the same as described in earlier related works [5–9], and hence only a brief summary is needed here. The superstrip concept [9] is invoked, such that usually each component curved or flat plate of a structure is represented by one superstrip which is an assembly of 2^c identical individual strips (where $c = 0, 1, 2, ...$). This is done through an efficient repetitive substructuring scheme and the assembly of 2^c strips is called a superstrip of order c, or simply a SuperstripC. The superstrip has degrees of freedom located only at its outside edges and if c is chosen typically to have the value 5, say, it is a very accurate model of cross-wise structural behaviour. A prismatic structure is usually modelled as an assembly of superstrips, with rotation transformations applied as necessary to each strip edge to transform properties to a global co-ordinate system. An eccentricity transformation [9], to account for off-set connections, may also be applied if deemed to be of significance. Beyond the superstrip level, higher levels of substructuring can often be invoked when using PASSAS if the structural cross-section has a repetitive nature, and this helps further in reducing the number of effective degrees of freedom. In total the multi-level substructuring procedures can readily reduce a problem having a few hundreds of thousands of freedoms to around 100 effective freedoms. The final eigenvalue problem is non-linear and in PASSAS determination of the eigenvalues is made using an extended Sturm sequence-bisection approach. The details of this

are as given in Dawe & Wang [7] and Dawe & Peshkam [9], wherein a description is also given of the manner in which the mode shapes of buckling or vibration can be obtained.

PASSAS provides an efficient and accurate means of determining the buckling stresses under dead loading and the natural frequencies (and mode shapes) of very complicated prismatic plate and shell structures which may be made of laminated material of arbitrary lay-up and may have general end conditions. Its scope also includes the facility to deal with problems of buckling under a system of both dead and live stresses and with problems of free vibration in the presence of a dead stress system.

SELECTED APPLICATIONS

General remarks

PASSAS has been used to generate results for a considerable number and range of buckling and vibration applications involving plate and shell structures. Many such applications are described in a report [6] by the authors, whilst for plate (but not shell) structures some applications have been presented during the development stage of the software in more readily available sources [7,8]. The results of these latter applications have demonstrated clearly the accuracy and versatility of PASSAS for the solution of plate structure problems. In the present paper it is only possible to present a very limited number of applications and these are selected to be for shell structures.

In the applications described here, one specific type of strip model is employed in the context of TST and one specific type in the context of SDST. For TST analysis the B_3-spline representation is used longitudinally (and, as stated earlier, cubic crosswise polynomial interpolation is used for all TST models). For SDST analysis the B_{32}-spline representation is used longitudinally, the cubic Lagrangian interpolation is used crosswise, and full integration is used.

Vibration of thin, boron–epoxy, circular cylinders

Bert *et al.* [11,12] have presented results for the natural frequencies of thin, composite, complete circular cylinders with diaphragm ends, based on the use of Love's thin shell theory. Here, two problems considered in this earlier work are examined using PASSAS. In both problems the cylinder wall is a two-layer laminate of boron–epoxy material, with the layers of equal thickness. The material properties and geometry are defined as [11] $E_L = 213.738$ N/m^2 (31×10^6 lb/in.^{2}); $E_T = 18.615$ GN/m^2 (2.7×10^6 lb/in.^{2}); $G_{LT} = G_{TT} = 5.171$ GN/m^2 (0.75×10^6 lb/in.^{2}); $\nu_{LT} = 0.28$; $\rho = 2051.88$ kg/m^3 (192×10^{-6} lb.s^2/in.^{4}); $h = 0.508$ mm (0.02 in.); $R = 63.017$ mm (2.481 in.); $A = 800.1$ mm (31.5 in.). The two problems have also been considered by Mohd & Dawe [5] using the S-a FSM.

In the first application the cylinder wall is an unbalanced cross-ply 90°/0° laminate of two equal-thickness layers (with the outer layer being the 90° one, i.e. with fibres running circumferentially). Bert *et al.* [11,12] have presented values of natural frequencies which correspond to modes having particular numbers of half-waves in the longitudinal direction (m_o) and of full waves in the circumferential direction ($\bar{n}_o$). These values are given in Table 1 along with the SDST S-a FSM values from Mohd and Dawe [5] and the results obtained using PASSAS in the context of both SDST and TST. In the latter approach the full cylinder is modelled using one Superstrip8 (i.e. 256 finite strips) and $q = 6$. The results shown in Table 1 reveal a very close comparison of the PASSAS predictions with those of the earlier studies and also show, as expected for this thin geometry, only very small differences between the predictions based on the use of SDST and of TST.

In the second application the problem specification is changed only in that the inner layer is now orientated at 45° to the cylinder axis, giving a 90°/45° laminate. Of course, this results in significant anisotropy and the vibrational modes would be expected to be skewed. Bert *et al.* [12] have generated solutions, in the context of TST, for the natural frequencies of this cylinder based upon the assumption of helical forms of the displacement components and presented in graphical form. The lowest natural frequency, corresponding to two circumferential half-waves, is quoted as being approximately 123 Hz. Here, using the SDST spline FSM with PASSAS, the complete cylinder is again modelled with one Superstrip8 and convergence of the first six natural frequencies, with an increase in q, is examined. Results are presented in Table 2. A good manner of convergence is exhibited

Table 1. Natural frequencies of a thin, 90°/0° boron–epoxy, circular cylinder with diaphragm ends

Mode designation		Natural frequencies (Hz)			
m_o	$\bar{n}_o$	Love's theory [11]	SDST S-a FSM [5]	B-spline FSM (PASSAS)	
				SDST	TST
1	1	532	532.2	532.2	532.2
	2	235	235.4	235.4	235.4
	3	253	252.8	252.8	252.8
	4	444	443.9	443.9	444.2
	5	714	713.4	713.4	714.1
	6	1047	1046.0	1045.8	1047.4
	7	1442	1439.2	1438.9	1441.9
	8	1897	1892.7	1892.1	1897.1
2	1	1287	1286.8	1286.7	1286.7
	2	676	676.2	676.2	676.2
	3	443	442.6	442.7	442.7
	4	497	496.5	496.5	496.7
	5	728	727.1	727.0	727.7
	6	1051	1049.5	1049.4	1050.9
	7	1442	1440.0	1439.6	1442.6
	8	1897	1892.6	1892.1	1897.1

for the six frequencies and the lowest frequency forecast by PASSAS (122.7 Hz) agrees very closely with the approximate prediction of Bert *et al.* [12] (123 Hz).

Buckling and vibration of the NASA advanced structural panel

Viswanathan and Tamekuni [13] have considered the buckling of a number of stiffened plate and shell panels in their analytical study which is of the single-term 'exact' FSM type in the context of TST. One of these 'advanced structural panels' has the complicated cross-section shown in Fig. 3 and the behaviour of this panel is considered here.

In Viswanathan & Tamekuni [13] the panel shown in Fig. 3 is assumed to be made of isotropic material and to be subjected to uniform longitudinal compressive stress σ_x^o. The quoted properties are that Young's modulus $E = 71.016\ \text{GN/m}^2$ $(10.3 \times 10^6\ \text{lb/in.}^2)$ and Poisson's ratio $\nu = 0.33$. The longitudinal edges of the panel are clamped against bending. For analysis purposes the length of the panel is taken to be one half-wavelength of the buckling mode, whose shape is purely sinusoidal in the longitudinal direction for all half-wavelengths: effectively the ends of the half-wavelength are diaphragm supported. By assuming a variety of prescribed half-wavelengths the buckling of the panel is represented graphically in the form reproduced here in Fig. 4.

In applying PASSAS to this problem the analysis length is again taken to be a prescribed half-wavelength and four spline sections are used over this length. The whole cross-section is modelled using one Superstrip5 to represent each of the 22 flat or curved component plates in the context of TST. (The effect of through-thickness shear deformation is tiny here.) The PASSAS results are shown superimposed on the

Table 2. Natural frequencies predicted by PASSAS (SDST) for a thin, 90°/45° boron–epoxy, circular cylinder with diaphragm ends

q	Natural frequencies (Hz)					
	Mode 1	Mode 2	Mode 3	Mode 4	Mode 5	Mode 6
1	132.4	251.5	331.8	360.5	485.7	499.1
2	124.2	250.6	327.5	339.2	484.2	498.5
3	122.9	250.1	304.1	337.8	448.0	480.7
4	122.7	249.9	292.8	337.6	428.2	477.2
5	122.7	249.8	290.1	337.6	423.0	474.7
6	122.7	249.8	289.3	337.5	422.4	473.8
7	122.7	249.8	289.1	337.5	422.1	472.6
8	122.7	249.8	289.0	337.5	422.0	472.3

earlier results in Fig. 4. It can be seen that the two sets of results compare very closely.

We now modify this problem whilst maintaining the cross-section shown in Fig. 3, except for some changes in thickness. In doing this the aim is to show the versatility of PASSAS and to provide benchmark solutions. The length of the structure is set at 508 mm (20 in.) and the material is changed to composite laminated material. The curved component plates become balanced cross-ply laminates of 0°/90°/0°/90°/0° lay-up, with plies of equal thickness and with a total thickness of 0.762 mm (0.03 in.). The flat component plates, forming the main plate of the panel, become single-layer anisotropic plates with fibres at 45° to the longitudinal axis and with an increased thickness of 1.524 mm (0.06 in.). The material properties are taken to be as those specified earlier for boron–epoxy.

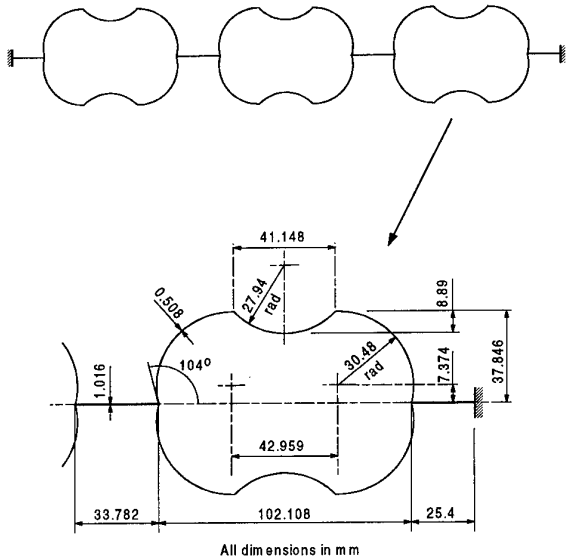

Fig. 3. Cross-section of the NASA advanced structural panel.

The buckling of this modified structure under uniform longitudinal compression has been studied using PASSAS when the ends are diaphragm supported, and calculated values of the buckling stress, $(\sigma_x^\circ)_{cr}$, are recorded in Table 3 in the form of convergence studies with increasing q, in the contexts of both TST and SDST. A good manner of convergence is evidenced.

The free vibration of the modified structure has also been considered for the situations in which first both ends are diaphragm supported, and then both ends are fully clamped. Details of the convergence with q of PASSAS results for the first six modes of vibration, in the context of SDST, are recorded in Table 4. For the diaphragm-ends case the convergence is rapid and, to four-figure accuracy, full convergence is achieved at $q = 4$. This reflects the fact that the vibrational mode shapes are simple in the longitudinal direction, with just one half-wave for each of the first six modes. For the clamped-ends case the convergence is markedly slower, probably due to the increased complexity of the mode shapes, but nevertheless convergence does occur in an orderly fashion.

CONCLUSIONS

A description has been given of the PASSAS software package for predicting the buckling stresses and natural frequencies, and mode

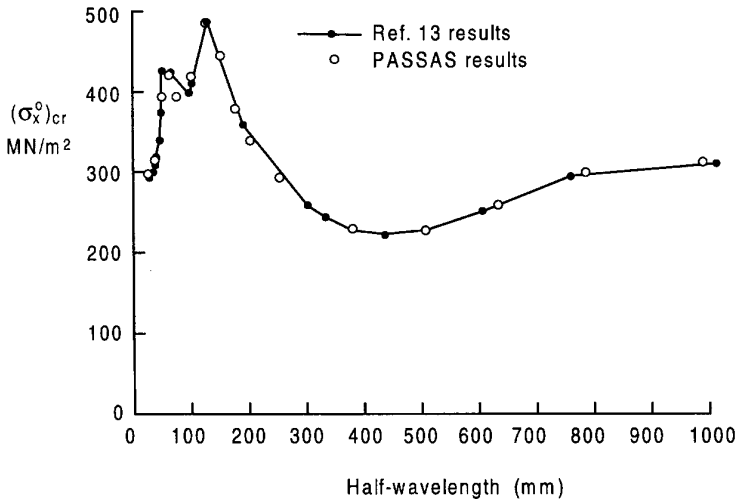

Fig. 4. Buckling results for the NASA advanced structural panel.

shapes, of prismatic plate and shell structures. The package is based on the use of the B-spline finite strip method, and strip properties can be selected to be based on the use of first-order shear-deformation theory or of classical or thin theory.

The analysis capability contained within PASSAS is rather versatile. Allowance is made for arbitrary lay-up of composite laminated component plates and for a broad specification of structure boundary conditions, and there is no restriction on the type of buckling (local, overall, coupled, etc.) that can be predicted under an applied stress system that includes shear stress. The analysis capability is also accurate and very efficient as it embodies multi-level substructuring techniques across the structure, including superstrips, in conjunction with a highly reliable solution procedure.

Table 3. Buckling stress $(\sigma_x^\circ)_{cr}$ predicted by PASSAS for the modified advanced panel with diaphragm ends

q	$(\sigma_x^\circ)_{cr}$ (MN/m^2)	
	TST	SDST
1	360.62	359.01
2	356.17	354.55
3	355.90	354.28
4	355.85	354.24
5	355.85	354.23
6	355.85	354.23
7	355.84	354.23
8	355.84	354.23

ACKNOWLEDGEMENTS

The authors are pleased to acknowledge that the work herein was supported by the Procurement Executive, Ministry of Defence, through the Defence Research Agency, Farnborough, UK.

REFERENCES

1. Cheung, Y. K., *Finite Strip Method in Structural Analysis*. Pergamon Press, Oxford, 1976.
2. Cheung, Y. K. and Fan, S. C., Static analysis of right box girder bridges by spline finite strip method. *Proc. Instn Civil Engrs*, 1983, **75**, 311–323.
3. Dawe, D. J., Finite strip buckling and postbuckling analysis. In *Buckling and Postbuckling of Composite Plates*, ed. G. J. Turvey & I. H. Marshall. Chapman & Hall, London, 1995.
4. Mohd, S. and Dawe, D. J., Finite strip vibration analysis of composite prismatic shell structures with diaphragm ends. *Comput. Struct.*, 1993, **25**, 353–362.
5. Mohd, S. and Dawe, D. J., Finite strip vibration analysis of composite prismatic shell structures with diaphragm ends. *Comput. Struct.*, 1993, **49**, 753–765.
6. Dawe, D. J. & Wang, S., Buckling and vibration of composite prismatic flat and curved plate structures using a spline finite strip approach. Final Report for

Table 4. Natural frequencies predicted by PASSAS (SDST) for the modified advanced panel with diaphragm ends and with clamped ends

End conditions	q	Values of natural frequencies (Hz) $\times 10$					
		Mode 1	Mode 2	Mode 3	Mode 4	Mode 5	Mode 6
Diaphragm	1	4144	4280	4335	4428	4531	4673
	2	4092	4219	4287	4381	4481	4631
	3	4090	4214	4285	4379	4478	4629
	4	4090	4212	4284	4378	4477	4629
	5	4090	4212	4284	4378	4477	4629
	6	4090	4212	4284	4378	4477	4629
	7	4090	4212	4284	4378	4477	4629
	8	4090	4212	4284	4378	4477	4629
Clamped	1	14,443	14,506	14,654	14,682	14,750	14,761
	2	5763	5875	5876	5932	5988	6047
	3	5615	5724	5732	5789	5847	5912
	4	5580	5691	5699	5758	5816	5883
	5	5565	5677	5685	5744	5802	5870
	6	5553	5666	5674	5733	5792	5860
	7	5545	5659	5667	5726	5785	5853
	8	5539	5652	5661	5720	5779	5847
	10	5530	5644	5653	5712	5771	5840
	12	5525	5638	5647	5707	5766	5835
	14	5521	5634	5643	5703	5762	5831
	16	5518	5631	5641	5701	5760	5829
	18	5515	5629	5638	5698	5758	5827
	20	5514	5627	5637	5697	5756	5825

Procurement Executive Ministry of Defence/Department of Trade and Industry under Agreement No.2027/209/MA, 1994.
7. Dawe, D. J. and Wang, S., Buckling of composite plates and plate structures using the spline finite strip method. *Composites Engng*., 1994, **4**, 1099–1117.
8. Dawe, D. J. and Wang, S., Spline finite strip analysis of the buckling and vibration of rectangular composite laminated plates. *Int. J. Mech. Sci.*, 1995, **37**, 645–667.
9. Dawe, D. J. and Peshkam, V., Buckling and vibration of finite-length composite plate structures with diaphragm ends, Part I: Finite strip formulation. *Comput. Meth. Appl. Mech. Engng*, 1989, **77**, 1–30.
10. Hsu, Y. S., Reddy, J. N. and Bert, C. W., Themoelasticity of circular cylindrical shells laminated of bimodulus composite materials. *J. Therm. Stresses*, 1981, **4**, 155–177.
11. Bert, C. W. and Kumar, M., Vibration of cylindrical shells of bimodulus composite materials. *J. Sound Vibr.*, 1982, **81**, 107–121.
12. Bert, C. W., Baker, J. L. and Egle, D. M., Free vibrations of multilayer anisotropic cylindrical shells. *J. Composite Mater.*, 1969, **3**, 480–499.
13. Viswanathan, A. V. & Tamekuni, M., Elastic buckling analysis for composite stiffened panels and other structures subjected to biaxial inplane loads. NASA CR-2216, 1973.

ELSEVIER

Composite Structures Vol. 38, No. 1–4, pp. 553–563, 1997
© 1997 Elsevier Science Ltd. All rights reserved
Printed in Great Britain
0263-8223/97/$17.00 + 0.00

PII:S0263-8223(97)00091-3

Use of woven CFRP for externally pressurized domes

J. Błachut & L. Dong

Department of Mechanical Engineering, The University of Liverpool, Brownlow Street, Liverpool L69 3GH, UK

Sensitivity of bifurcation buckling, first-ply failure (FPF) and last-ply failure (LPF) to the different modelling methods of woven cloth is examined numerically for a range of torispherical shells. Axisymmetric and two two-dimensional models are used for externally pressurized multi-ply domes. In the first two-dimensional model, angles between warp and weft directions on torispheres are obtained through an optical projection of an initially orthogonal woven net. In the second type of modelling, a planar/orthogonal mapping is preserved on the torispherical geometry. Bifurcation buckling seems to be insensitive to the method of modelling. Results for FPF show that differences between axisymmetric and planar models can be as high as 50%, whilst the differences for optical and planar models can reach 30%. The magnitude of LPF pressures is also sensitive to the two-dimensional modelling method adopted. Ultimate collapse loads, associated with LPFs and based on optical modelling, are up to 30% higher than those obtained for planar modelling for carbon cloth. © 1997 Elsevier Science Ltd.

INTRODUCTION

The use of carbon-fibre reinforced plastic (CFRP) for pressure hulls of underwater vehicles has been explored for a number of years. Different concepts of composite pressure hull configurations, material selection and their performance are discussed in Smith [1], Vaughan [2] and Graham *et al.* [3]. Most of the proposed pressure hull configurations would require domed closures. A number of manufacturing techniques (i.e. filament winding, vacuum bagging, autoclave, etc.) were examined in order to identify a suitable method of building a reliable pressure hull end closure [4–7]. Vacuum bagging of woven carbon pre-preg proved to be a promising way of building domed closures capable of withstanding large external pressures.

There are, however, a number of outstanding issues, both theoretical and practical, which need to be addressed. One of them is the modelling of the draping of woven material and its influence on the magnitude of buckling and collapse pressures. Various models were suggested to capture the behaviour of woven cloth when it is draped onto a curved surface (e.g. stretching, slippage, trellis effect, etc.; [8–13]). A recent literature review of existing computational models describing draping of woven fabrics on arbitrarily curved surfaces can be found in Trochu *et al.* [14].

This paper investigates the effect of local fibre distribution due to the draping of woven cloth on the bifurcation buckling, first-ply failure and last-ply failure in externally pressurized domes. Comparison is made between solely axisymmetric modelling, two-dimensional modelling using a planar distribution of fibres and two-dimensional modelling using an optical mapping of orthogonal distribution of fibres onto the torisphere. The paper is a numerical study but an experimental programme is under way and the corresponding results will be reported separately [15].

BACKGROUND INFORMATION

Hemispherical and torispherical geometries are by far the most frequently used shapes for

domed closures made of steel. The above geometries have also been investigated for composite domes where a variety of manufacturing techniques were explored. It is assumed that all composite domes will operate without an internal mandrel. A typical view of a collapsed torisphere made from 50-ply woven cloth is shown in Fig. 1.

Let us consider a torispherical shell with radius R_s for the spherical part and radius r for the knuckle segment. The short flange, of length L, is to be taken as fully clamped at the base. The wall is made from N, differently stacked, plies of woven cloth giving the total wall thickness, t (see Fig. 2). It is assumed that the wall thickness remains constant and the dome's geometry corresponds to the mid-surface of the shell. Material properties will be taken from Table 1.

Detailed information about modelling of the woven material is provided below.

MODELLING OF WOVEN CLOTH

Let us consider CFRP domes made by sequential draping of a single sheet of pre-preg woven cloth into a moulding tool. Non-axisymmetry of material properties is included in the analysis. Full two-dimensional modelling is made using doubly curved shell elements, S8R [16]. For a given ply, a local co-ordinate system, (T_1,T_2,T_3) is introduced. The fibre orientation angle, α, changes from point to point in the model. The

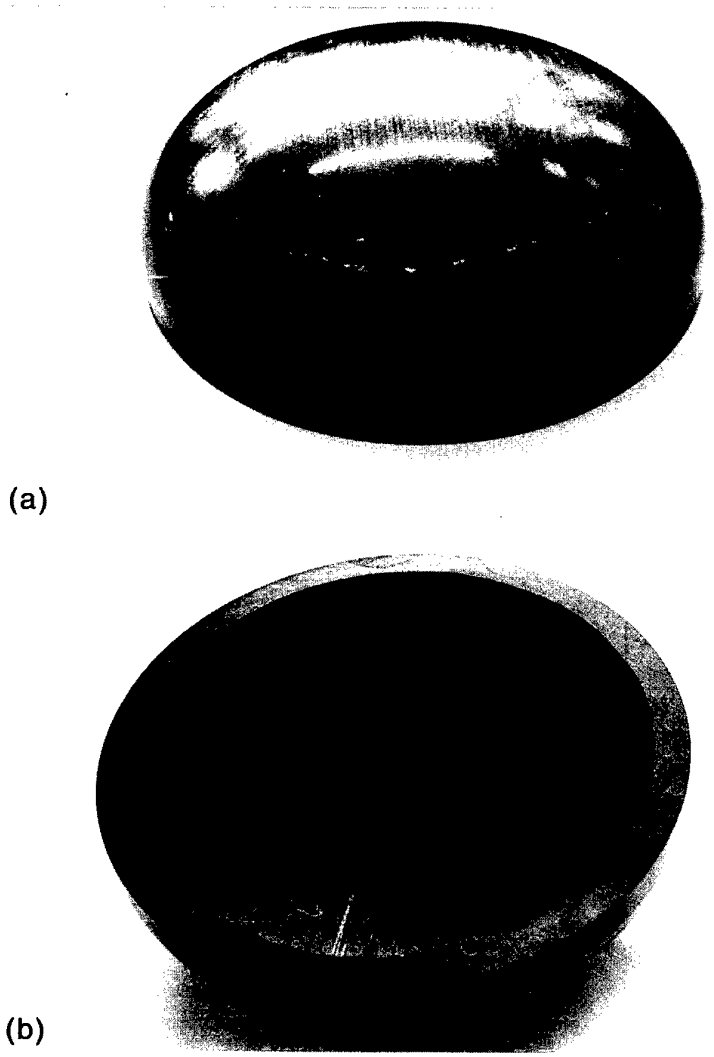

Fig. 1. A typical view of a collapsed 50-ply composite torisphere loaded by external pressure. (a) Outer surface. (b) Inner surface.

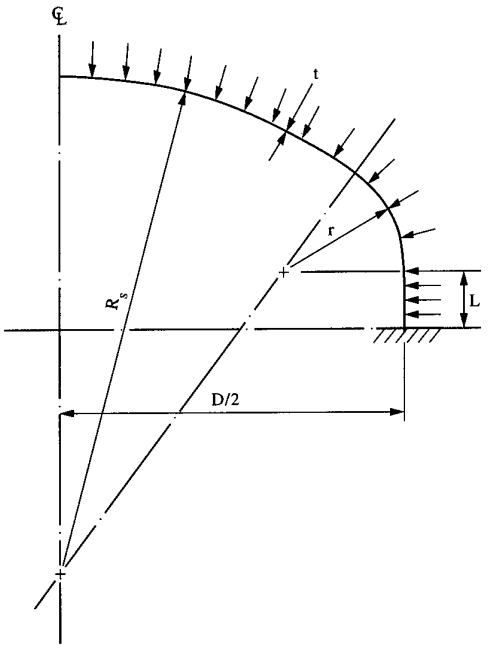

Fig. 2. Geometry of a torispherical dome.

positions of global (X,Y,Z) and local (T_1,T_2,T_3) co-ordinate systems are sketched in Fig. 3. The angle α needs to be provided for each Gauss point used in the model. This is done through the User's Subroutine ORIEN in the ABAQUS code [16]. Appendix A provides details on how the angle α is calculated. The angle α is measured between the local axis, T_1, and the fibre. This is illustrated in Fig. 3(b) and (c) for two plies, i.e. $\theta = 0°$ and $\theta = 25°$. Figure 3(b) shows a small piece of woven cloth, assumed to be locally flat, in which the weft direction coincides with the X-axis. The local (T_1,T_2) co-ordinate systems are shown in Fig. 3 at three arbitrary Gauss points, each lying on meridians $\Phi = 15°$, $\Phi = 50°$ and $\Phi = 90°$, respectively. The angle α is equal to zero for all three points shown in Fig. 3(b). However, in Fig. 3(c), the angle α varies along the arc as its length increases from the apex, through the knuckle and into the cylindrical flange. Figure 4 shows the variation of the angle α along the arc length for several meridians. It is seen that the largest variation of α occurs in the knuckle. Within the cylindrical flange the angle α equals 90° for all meridians. Once the ply is rotated, say by $\theta = 25°$ against the X-axis (see Fig. 3c), the angle α will have to be re-calculated for all Gauss points in the model.

RESULTS

Bifurcation buckling

Although the dome remains an axisymmetric component its deformation due to external pressure is not axisymmetric. Contours of normal displacements of a single-ply torisphere with a geometry given by $r/D = 0.10$, $R_s/D = 1.0$, $L/D = 0.05$, $D/t = 500$ and loaded by an external pressure $p = 0.05$ MPa are shown in Fig. 5. Four different values of θ, i.e. 0°, $\pm 45°$ and 90°, were taken to illustrate the non-axisymmetric structural response of the axisymmetric component subject to axisymmetric loading. The aim here was to check the arrangements for the distribution of α once the ply is rotated. Contours of normal displacements for a six-ply torisphere $[0°/60°/-60°]_s$ are shown in Fig. 6. The dome has the same geometry as above and it is loaded by external pressure $p = 0.05$ MPa. It is seen here that dome deforms axisymmetrically despite non-axisymmetric material properties of the draped woven material. The above dome will bifurcate into an asymmetric mode, and the buckling pressure was computed using both the ABAQUS and BOSOR-4 codes [16,17]. The latter uses purely axisymmetric modelling and it can be seen, from Table 2, that there is about 10% difference between an approximate, i.e. BOSOR-4 modelling, and a more rigorous modelling of woven cloth using an optical projection. There is also a difference between predicted wave number at bifurcation, i.e. six from BOSOR-4 and eight from ABAQUS. The eigenmode, as obtained from ABAQUS, is shown in Fig. 7. By far the simplest modelling of woven cloth would be to assume that the

Table 1. Material properties of the woven CFRP pre-preg

E_1 (GPa)	E_2 (GPa)	G_{12} (GPa)	ν_{12}	X_t (MPa)	Y_t (MPa)	X_c (MPa)	Y_c (MPa)	S (MPa)
70.0	70.0	5.0	0.1	600.0	600.0	570.0	570.0	90

orthogonal grid does not deform when draped into torispherical shape. Each element in the FE model models a planar and undistorted piece of cloth. Comparison of bifurcation pressures for a range of torispherical geometries, with the diameter to thickness ratio of 300, is shown in Fig. 8 for three types of modelling, i.e. axisymmetric (BOSOR-4), two-dimensional optical and two-dimensional planar (ABAQUS). It could be concluded that all three approaches to the modelling of woven cloth result in similar magnitudes of bifurcation buckling pressures, i.e. they seem to be insensitive to the way in which carbon fabric is modelled.

Bifurcation pressure in externally pressurized domes usually leads to the loss of structural integrity due to the lack of post-bifurcation load-carrying capacity. There are possible failure modes other than bifurcation and, in general, they depend on geometrical and material configurations. In the next two sections results are provided for failures through a brittle cracking associated with a first-ply failure and last-ply failure.

First-ply failure (FPF)

The Tsai–Wu interactive failure criterion written in stress space is adopted here [5,18]. Stresses are evaluated at the top and bottom of each ply. Several stress evaluations are usually required to obtain FPF pressures for a given material and geometrical configuration. The above-mentioned three types of modelling, i.e. axisymmetric, two-dimensional optical mapping of cloth and two-dimensional planar mapping of cloth, were used for the evaluation of FPFs. It was established numerically that for the diameter to thickness ratio of 100 the first-ply failure mechanism remains the controlling mode of failure in torispheres over a wide range of geometries. A sample of results for six-ply torispheres is shown in Fig. 9. It is seen here that the magnitude of predicted FPF pressures is significantly affected by the adopted method of cloth modelling. Predictions of FPF pressures obtained for axisymmetric and planar models differ by 25–50%. At the same time, the differences for 'optical' and 'planar' models vary from

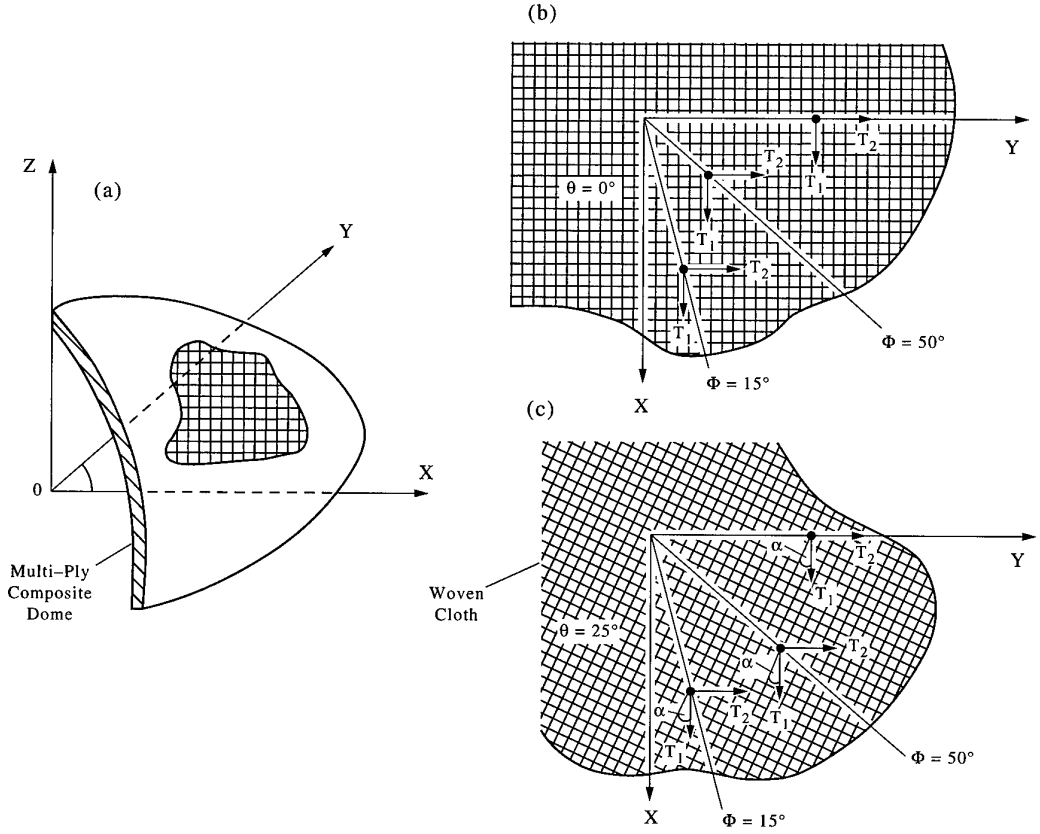

Fig. 3. (a) Multi-ply composite dome. (b) Position of local co-ordinate systems for a single-ply cover orientated at $\phi = 0°$. Also the same ply configuration stacked at $\phi = 25°$.

10 to 30%. The lowest values of FPF pressures are always obtained for planar modelling. The highest values, on the other hand, are associated with axisymmetric modelling. Similar trends have been noticed for 48-ply torispheres shown in Fig. 10.

The next section discusses the influence of fibre modelling on last-ply failure.

Last-ply failure (LPF)

The ultimate load-bearing capacity of a dome is always a desirable quantity for a designer. Some previous calculations have shown that, in externally pressurized multi-ply domes, the last-ply failure could be 5–27% larger than the corresponding FPF pressures [19]. A comparison of results obtained for 'two-dimensional optical' and 'two-dimensional planar' FE models is depicted in Fig. 11. The last-ply failure loads were obtained through successive degradation of ply properties in warp/weft directions and through sequential FE re-analyses (see Błachut and Dong [19] for more details). It is seen here that LPF pressures also depend on the adopted modelling of woven fabric. The difference between 'planar' and 'optical' LPFs varies from 10 to 30%.

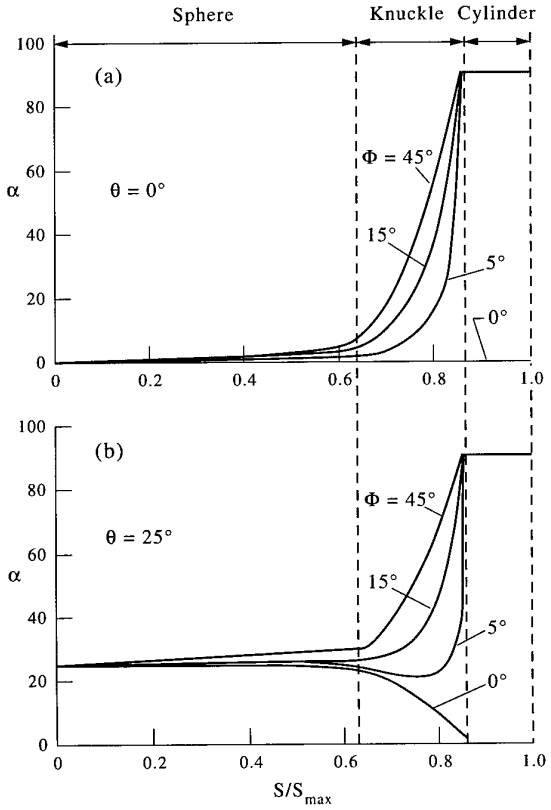

Fig. 4. Distribution of the local fibre orientation angle, α, along different meridians, i.e. $\Phi = 0°$, 5°, 15° and 45°. Two orientations are shown: (a) $\theta = 0°$ and (b) $\theta = 25°$.

CONCLUSIONS

Numerical results presented in this paper constitute a contribution to understanding of ways in which the load-bearing capacity of externally pressurized, doubly curved domed closures could be evaluated. Results show that certain mechanisms of failure, e.g. bifurcation buckling, do not seem to be sensitive to detailed modelling of composite material. Other mechanisms of failure, such as first-ply failure or last-ply failure pressures, are sensitive to the adopted FE modelling. It is therefore imperative that other methods of modelling woven fabric draped onto doubly curved surfaces are also examined in order to assess the load-bearing capacity of the shell.

REFERENCES

1. Smith, C. S., *Design of Marine Structures in Composite Materials*. Elsevier Applied Science, London, 1992.
2. Vaughan, Ch., *Mechanics of Composites Review*. WPAFB, OH, 1992.
3. Graham, D., Keron, I., Mitchell, G. and Creswell, D., DRA structural research on submarines and submersibles. *Marine Struct.*, 1994, **7**, 231–256.
4. Levy-Neto, F., The behaviour of externally-pressurised composite domes. Ph.D. thesis, University of Liverpool, 1991.
5. Błachut, J. and Galletly, G.D., Externally pressurised hemispherical fibre-reinforced plastic shells. *Proc. Instn Mech Engrs*, 1992, **206**, 179–191.
6. Błachut, J., Filament wound torispheres under external pressure. *Composite Struct.*, 1993, **26**, 47–54.
7. Błachut, J., Externally pressurised filament wound domes — scope for optimization. *Computers Struct.*, 1993, **48**, 153–160.
8. Potter, K.D., The influence of accurate stretch data for reinforcements on the production of complex structural mouldings. *Composites*, 1979, **10**, 161–173.
9. Robertson, R. E. *et al.*, Fibre rearrangements during the moulding of continuous fibre composites — flat cloth to hemisphere. *Polymer Composites*, 1981, **2**, 126–31.
10. Bergsma, O. K. & Huisman, J., Deep drawing of fabric reinforced thermoplastic In *Computer Aided Design in Composite Material Technology*, eds C. A. Brebbia, W. P. de Wilde & W. R. Blain. Springer, New York, 1988, pp. 323–34.
11. van West, B. P., Keefe, M. & Pipes, R. B., The draping of bidirectional fabric over three-dimensional surfaces. In *Proc. American Society for Composites Fourth Conference*, VPI, Technomic, PA, 1989, pp. 463–72.

12. van Der Ween, F., Algorithms for draping fabrics on doubly-curved surfaces. *Int. J. Numer. Meth. Engng*, 1991, **31**, 1415–1426.
13. Hu, J.L. and Teng, J.G., Computational fabric mechanics: present status and future trends. *Finite Elements Anal. Design*, 1996, **21**, 225–237.
14. Trochu, F., Hammami, A. and Benoit, Y., Prediction of fibre orientation and net shape definition of complex composite parts. *Composites*, 1996, **27A**, 319–328.
15. Błachut, J. & Dong, L., Analysis and collapse of thick composite torispheres, *Proc. IMechE*, 1997, submitted.
16. *ABAQUS, User's and Theory Manual*, Version 5.4. Hibbit, Karlsson & Sorensen Inc., Pawtucket, RI, 1995.
17. D. Bushnell, BOSOR-4 program for stress, buckling and vibration of complex shells of revolution. In *Structural Mechanics Software Series*, eds N. Perrone & W. Pilkey. University Press of Virginia, 1977, pp. 11–143.
18. Tsai, S. W., *Composites Design*, 4th edn. Think Composites, Dayton, OH, 1988.
19. Błachut, J. & Dong, L., Collapse of thick composite domes. *J. Marine Struct.* Submitted.

APPENDIX A

Local orientation of woven material

An end closure made from woven material is an axisymmetric component but its materials properties are not axisymmetric. Initially the rectangular woven grid distorts when a flat cloth is draped onto a doubly curved moulding tool, e.g. of torispherical shape. A model, based on an optical projection analogy, is described now in order to quantify this distortion and to evaluate the local fibre orientation in a doubly curved shell. A torispherical dome consists of two segments, i.e. spherical with radius R_s and toroidal, sometimes called knuckle, with radius r. A short cylindrical flange of length L is also included in our case. This arrangement is

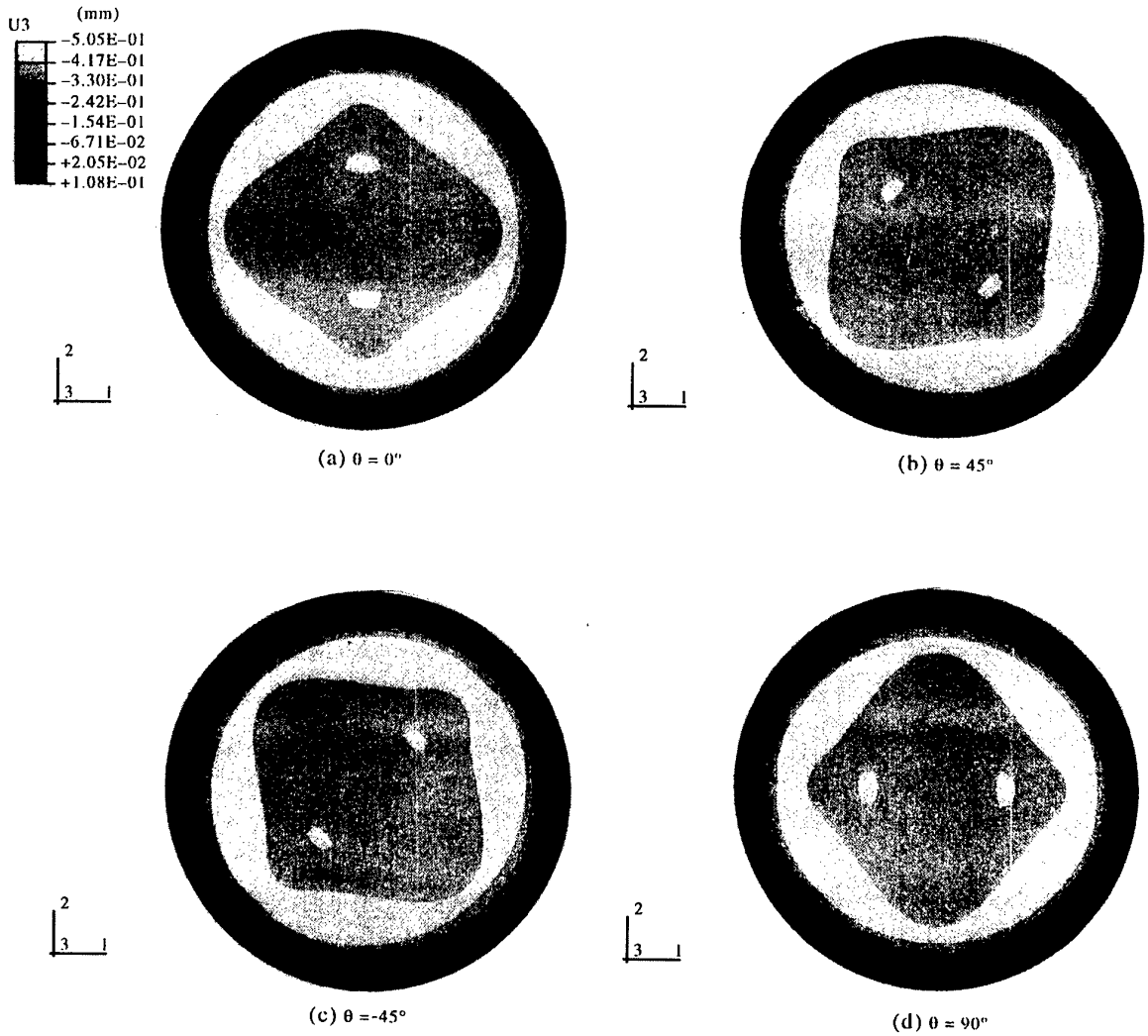

Fig. 5. Contours of normal deflections for an externally pressurized dome made from a single woven ply. Fig. 4(a)–(d) corresponds to $\theta = 0°$, $\pm 45°$ and 90°, respectively. External pressure $p = 0.05$ MPa.

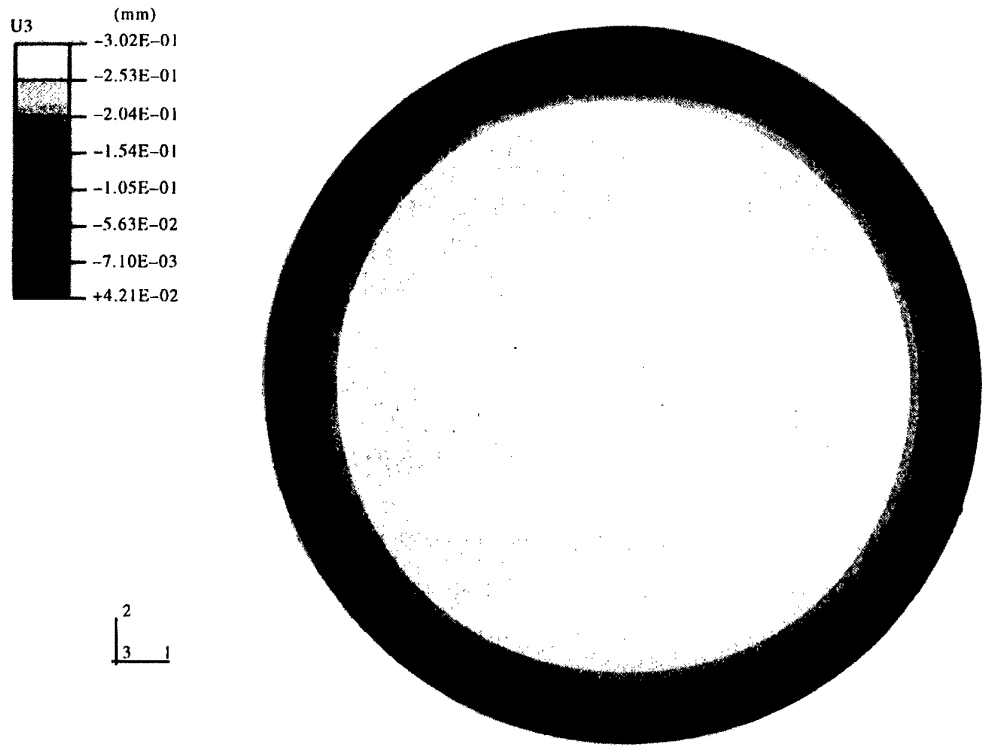

Fig. 6. Contours of normal deflections for a six-ply torisphere $[0°/60°/-60°]_s$ subjected to external pressure $p = 0.05$ MPa. Note the axisymmetric deformations.

sketched in Fig. 12, where the diameter of the torisphere is denoted by D. Equations of the spherical, knuckle and cylindrical portions can be written in the following form

$$x^2+y^2+z^2-R_s^2=0 \tag{A1}$$

$$\left(\sqrt{x^2+y^2}-\frac{D}{2}+r\right)^2+(z-z_c)^2-r^2=0 \tag{A2}$$

$$x^2+y^2-\left(\frac{D}{2}\right)^2=0 \tag{A3}$$

Let us assume that a flat woven cloth is placed horizontally above the dome. Next, the cloth is draped onto the dome in such a way that each fibre, initially represented by a straight line in the x–y plane, becomes projected by a vertical beam of light onto the shell surface. The fibre trajectory on the shell surface can be obtained as an intersection of a vertical plane with the torisphere. The vertical plane, which is perpendicular to the x–y plane, is given by

$$k(x-x_0)-(y-y_0)=0 \tag{A4}$$

where $k = \tan\theta$.

The angle θ is measured between the x-axis and the vertical plane G (see Fig. 13). Point (x_0, y_0) is an arbitrary point on the vertical plane G.

The fibre trajectory is obtained by solving the following sets of equations corresponding to

Table 2. Comparison of bifurcation and first-ply failure pressures for axisymmetric and two-dimensional modellings of woven cloth ($r/D = 0.1$, $R_s/D = 1.0$, $L/D = 0.05$ and D/t 300). Values of the failure index (FI) are also given

	p_{bif} (MPa)	p_{FPF} (MPa)	FI (at bifurcation)
BOSOR-4	0.360(6)	0.400	0.732
ABAQUS (optical)	0.325(8)	Collapse at 0.325 MPa	0.754
ABAQUS (planar)	0.345(9)	0.312	1.320

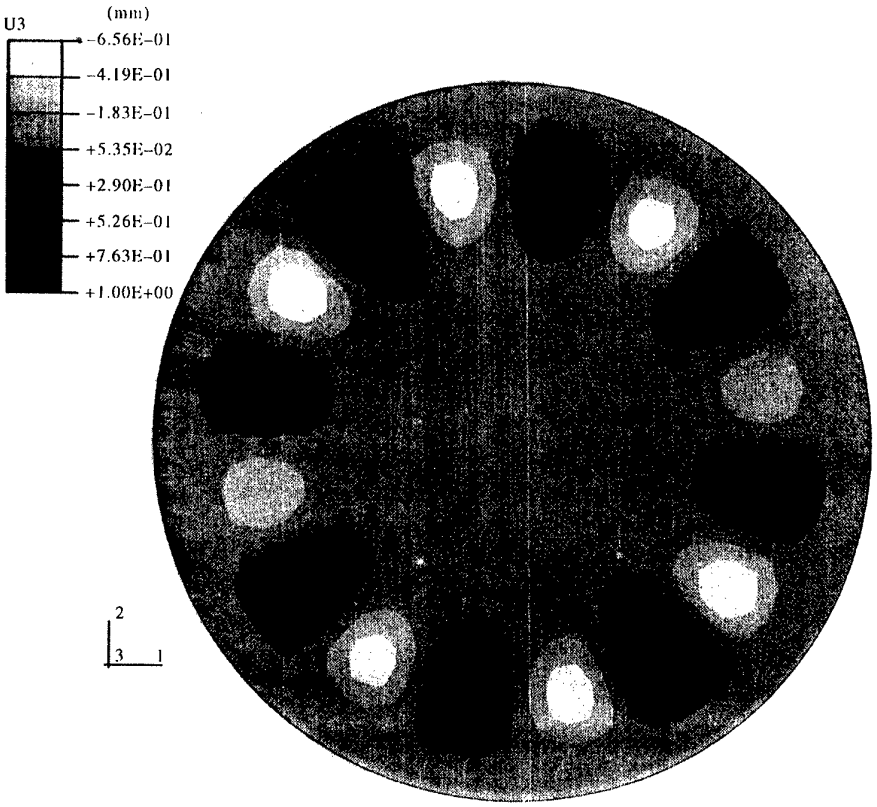

Fig. 7. A view of the torispherical shell at bifurcation buckling pressure (with eight circumferential waves).

spherical cap, knuckle and cylindrical flange, respectively

$$\text{(spherical cap)}\quad \left.\begin{aligned} F &= x^2+y^2+z^2-R_s^2=0 \\ G &= k(x-x_0)-(y-y_0)=0 \end{aligned}\right\} \tag{A5}$$

$$\text{(knuckle)}\quad \left.\begin{aligned} F &= \left(\sqrt{x^2+y^2}-\frac{D}{2}+r\right)^2 \\ &\quad +(z-z_c)^2-r^2=0 \\ G &= k(x-x_0)-(y-y_0)=0 \end{aligned}\right\} \tag{A6}$$

$$\text{(cylindrical flange)}\quad \left.\begin{aligned} F &= x^2+y^2-(D/2)^2=0 \\ G &= k(x-x_0)-(y-y_0)=0 \end{aligned}\right\} \tag{A7}$$

The corresponding direction cosines (l, m, n) of the intersection lines in the spherical and knuckle segments are as follows

$$\left.\begin{aligned} l &= \frac{z^*}{\sqrt{(1+k^2)(z^*)^2+[\beta(x+ky)]^2}} \\ m &= \frac{kz^*}{\sqrt{(1+k^2)(z^*)^2+[\beta(x+ky)]^2}} \\ n &= -\frac{\beta(x+ky)}{\sqrt{(1+k^2)(z^*)^2+[\beta(x+ky)]^2}} \end{aligned}\right\} \tag{A8}$$

where the parameters z^* and β are defined separately for the spherical and knuckle segments. For the spherical portion they are given by

$$\left.\begin{aligned} z^* &= z \\ \beta &= 1 \end{aligned}\right\} \tag{A9}$$

and for the knuckle they become

$$\left.\begin{aligned} z^* &= z-z_c \\ \beta &= \frac{\sqrt{x^2+y^2}-\dfrac{D}{2}+r}{\sqrt{x^2+y^2}} \end{aligned}\right\} \tag{A10}$$

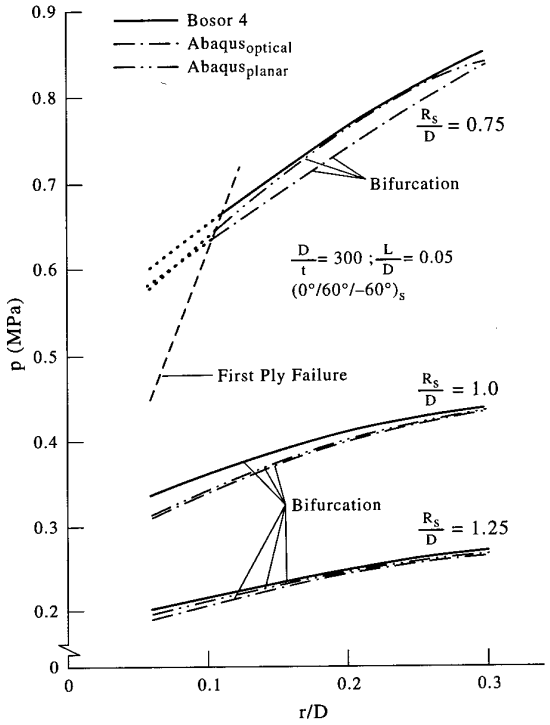

Fig. 8. Bifurcation buckling pressures obtained from BOSOR-4 axisymmetric, and two types of two-dimensional ABAQUS modelling of woven cloth. All torispheres have the same stacking sequence, i.e. $[0°/60°/-60°]_s$.

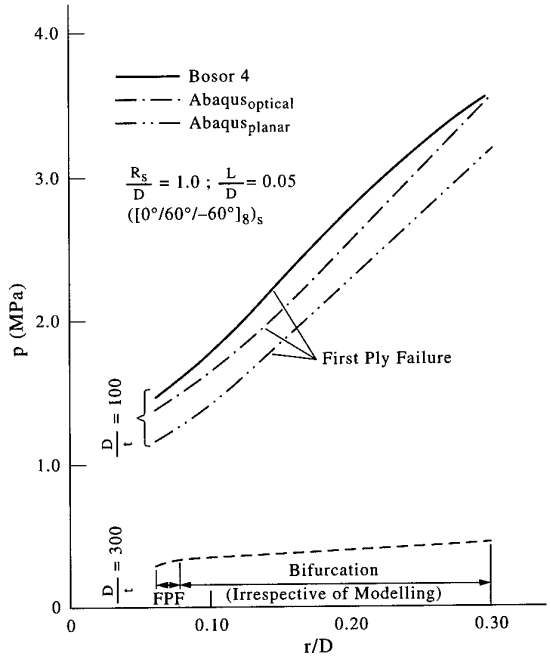

Fig. 10. Influence of cloth modelling on the bifurcation buckling pressures ($D/t = 300$) and on the FPF pressures ($D/t = 100$) in 48-ply torispheres.

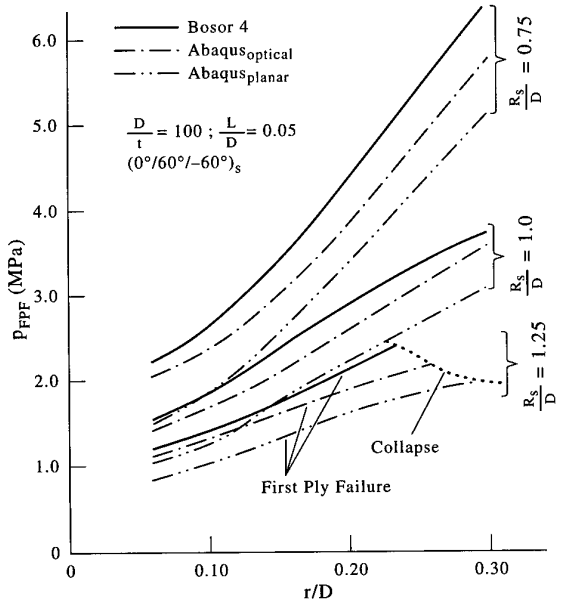

Fig. 9. Influence of cloth modelling on the first-ply failure pressures in six-ply torispheres. Note that for $R_s/D = 1.25$ domes can collapse before reaching the FPF state.

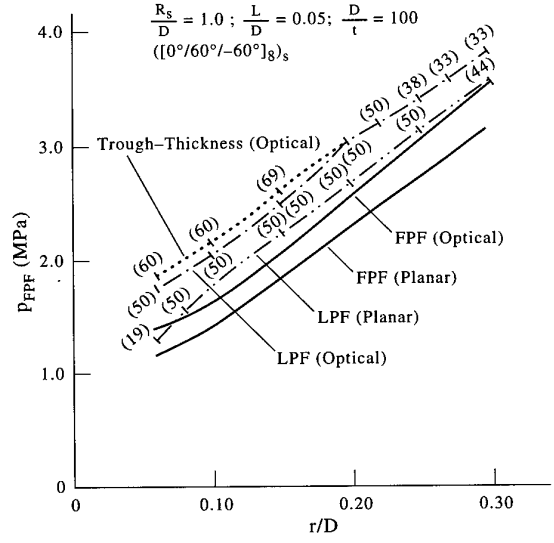

Fig. 11. Comparison of the first-ply failure and the last-ply failure pressures when two different modelling methods for the fabric are adopted. Numbers in brackets indicate the amount of damaged plies, i.e. $(n_{damaged} - n_{total})/n_{total} \times 100\%$.

The trajectory in the cylindrical part is a straight line which is parallel to the cylinder axis and in this case the direction cosines (l, m, n) are

$$\left.\begin{aligned} l &= 0 \\ m &= 0 \\ n &= -\operatorname{sign}(x+ky) \end{aligned}\right\} \tag{A11}$$

where

$$\operatorname{sign}(x) = \begin{cases} 1 \text{ for } x \geq 0 \\ -1 \text{ for } x < 0 \end{cases} \tag{A12}$$

Fibre orientation in the FE code ABAQUS is defined with respect to a local co-ordinate system (T_1, T_2, T_3). The local axis, T_3, is taken in the direction of the normal vector, $\mathbf{N}^*$, to the reference surface of undeformed shell, i.e. surface F in Fig. 13

$$\mathbf{N}^* = \frac{\partial F}{\partial x}\mathbf{i} + \frac{\partial F}{\partial y}\mathbf{j} + \frac{\partial F}{\partial z}\mathbf{k} \tag{A13}$$

The unit normal vectors N for the sphere, knuckle and cylinder are given by

$$\mathbf{N} = \frac{\mathbf{N}^*}{|\mathbf{N}^*|} = \begin{cases} \dfrac{x}{R_s}\mathbf{i} + \dfrac{y}{R_s}\mathbf{j} + \dfrac{z}{R_s} & \mathbf{k} \text{ sphere} \\ \dfrac{\beta x}{r}\mathbf{i} + \dfrac{\beta y}{r}\mathbf{j} + \dfrac{z - z_c}{r} & \mathbf{k} \text{ knuckle} \\ \dfrac{x}{\sqrt{x^2+y^2}}\mathbf{i} + \dfrac{y}{\sqrt{x^2+y^2}} & \mathbf{j} \text{ cylinder} \end{cases} \tag{A14}$$

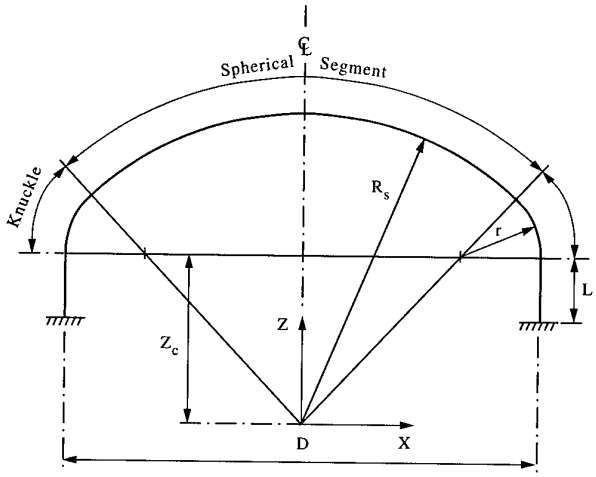

Fig. 12. Adopted notation for the torispherical dome.

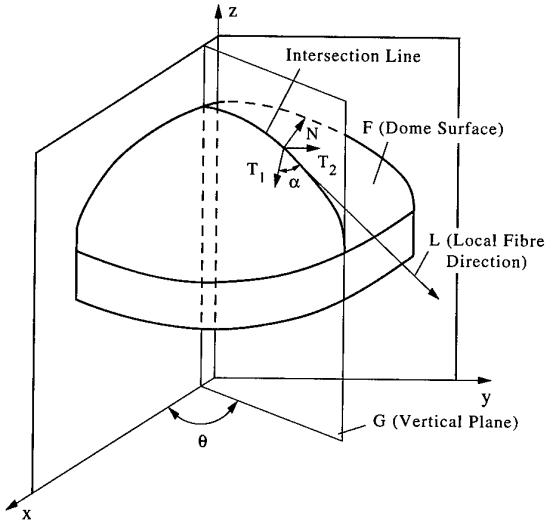

Fig. 13. Optical projection of a fibre onto a dome.

Table 3. Fibre orientation α at 32 Gauss points lying on a meridional line rotated by $\Phi = 10°$. \The ply orientation $\theta = 0°$

Segment	Gauss points	x (mm)	y (mm)	z (mm)	l	m	n	T_{12}	T_{22}	T_{32}	α (°)
Spherical	1	8.2295	1.4511	299.8836	0.9996	0	−0.0274	0	1	−0.0048	0.00573
Spherical	2	16.6191	2.9304	299.525	0.9985	0	−0.0554	0	1	−0.0098	0.02865
...	...	...	...	...	...	...	...	...	...	...	...
...	...	...	...	...	...	...	...	...	...	...	...
Spherical	18	128.5465	22.6663	270.1147	0.9030	0	−0.297	0	0.9965	−0.0836	2.057
Knuckle	19	132.5365	23.5365	268.0855	0.8771	0	−0.4804	0	0.9954	−0.0961	2.647
Knuckle	20	135.7155	23.9303	266.0093	0.8090	0	−0.5878	0	0.9919	−0.1271	4.286
...	...	...	...	...	...	0	...	...	...	...	...
...	...	...	...	...	...	...	...	...	...	...	...
Knuckle	27	147.2691	25.9675	247.092	0.1768	0	−0.9843	0	0.7135	−0.7006	43.61
Knuckle	28	147.6878	26.0414	243.2776	0.0477	0	−0.9989	0	0.2615	−0.9652	74.58
Cylindrical	29	147.7209	26.0472	240.2828	0	0	−1	0	0	−1	90.0
...	...	...	...	...	...	...	...	...	...	...	...
...	...	...	...	...	...	...	...	...	...	...	...
Cylindrical	32	147.7209	26.0472	228.4527	0	0	−1	0	0	−1	90.0

Table 4. Fibre orientation α at 32 Gauss points lying on a meridional line rotated by $\Phi = 10°$. The ply orientation $\theta = 25°$

Segment	Gauss points	x (mm)	y (mm)	z (mm)	l	m	n	T_{12}	T_{22}	T_{32}	α (°)
Spherical	1	8.2295	1.4511	299.8836	0.9060	0.4225	−0.0269	0	1	−0.0048	25.00
Spherical	2	16.6191	2.9304	299.525	0.9050	0.422	−0.0543	0	1	−0.0098	24.99
...	...	...	...	...	...	...	...	...	...	...	...
...	...	...	...	...	...	...	...	...	...	...	...
Spherical	18	128.5465	22.6663	270.1147	0.8212	0.383	−0.423	0	0.9965	−0.0836	24.64
Knuckle	19	132.5365	23.3698	268.0855	0.7984	0.3723	−0.4732	0	0.9954	−0.0961	24.59
Knuckle	20	135.7155	23.9303	266.0093	0.7381	0.3442	−0.5803	0	0.9919	−0.1271	24.53
...	...	...	...	...	...	...	...	...	...	...	...
...	...	...	...	...	...	...	...	...	...	...	...
Knuckle	27	147.2691	25.9675	247.092	0.1632	0.0761	−0.9836	0	0.7135	−0.7006	48.04
Knuckle	28	147.6878	26.0414	243.2776	0.0441	0.0206	−0.9988	0	0.2615	−0.9652	75.77
Cylindrical	29	147.7209	26.0472	240.2828	0	0	−1	0	0	−1	90.0
...	...	...	...	...	...	...	...	...	...	...	...
...	...	...	...	...	...	...	...	...	...	...	...
Cylindrical	32	147.7209	26.0472	228.4527	0	0	−1	0	0	−1	90.0

where the radii of curvature are given by eqns (A1) and (A2).

This leads to the following definitions of the local axis, T_2

$$\mathbf{T}_2 = \begin{cases} \dfrac{\mathbf{N}\times\mathbf{i}}{\sqrt{|\mathbf{N}\times\mathbf{i}|}} & \text{for } N_1 > \cos(0.1°) \\ \dfrac{\mathbf{N}\times\mathbf{k}}{\sqrt{|\mathbf{N}\times\mathbf{k}|}} & \text{for } N_1 \le \cos(0.1°) \end{cases} \tag{A15}$$

After substitutions the axis T_2 is expressed as

$$\mathbf{T}_2 = \begin{cases} \dfrac{z^*}{\sqrt{(\beta y)^2+(z^*)^2}}\mathbf{j} - \dfrac{\beta y}{\sqrt{(\beta y)^2+(z^*)^2}}\mathbf{k} & \text{sphere/knuckle for } N_1 > \cos(0.1°) \\ -\text{sign}(y)\mathbf{k} & \text{cylinder} \\ \dfrac{y}{\sqrt{x^2+y^2}}\mathbf{i} - \dfrac{x}{\sqrt{x^2+y^2}}\mathbf{j} & \text{cylinder for } N_1 \le \cos(0.1°) \end{cases} \tag{A16}$$

Finally, axis T_1 is taken as

$$\mathbf{T}_1 = \frac{\mathbf{T}_2\times\mathbf{N}}{\sqrt{|\mathbf{T}_2\times\mathbf{N}|}} \tag{A17}$$

Once the local co-ordinate system has been defined the fibre orientation α can be specified. If $\mathbf{L}$ denotes a local direction of the fibre, then the angle α between the axis $\mathbf{T}_1$ and $\mathbf{L}$ is given by

$$\cos(90° - \alpha) = \mathbf{T}_2\cdot\mathbf{L} = T_{12}l + T_{22}m + T_{32}n \tag{A18}$$

Components of the above scalar product are tabulated in Tables 3 and 4 for a torispherical geometry specified by: $r/D = 0.10$, $R_s/D = 1.0$ and $L/D = 0.05$. A meridional line rotated by $\Phi = 10°$ is taken for detailed calculations together with the stacking sequence $\theta = 0°$ (Table 3) and $\theta = 25°$ (Table 4). It is seen from the last column in Tables 3 and 4 that the largest variation of the angle α occurs in the knuckle segment.

ELSEVIER

Composite Structures Vol. 38, No. 1–4, pp. 565–571, 1997
© 1997 Elsevier Science Ltd. All rights reserved
Printed in Great Britain
0263-8223/97/$17.00 + 0.00

PII:S0263-8223(97)00092-5

Shape control of non-symmetric piezolaminated composite beams

Moshe Eisenberger & Haim Abramovich

Faculty of Civil Engineering, Technion—Israel Institute of Technology, Technion City 32000, Israel

In this paper the exact deflections of generally laminated piezoelectric composite beams are found using a new method, which includes the effect of rotary inertia and shear deformations. The effect of shear in laminated beams is more significant than in homogenous beams due to the fact that the ratio of extensional stiffness to the transverse shear stiffness is high. The exact stiffness matrix is derived, and then any set of boundary conditions, including elastic connections and assembly of members, can be solved as in the classical direct stiffness method for framed structures. In this paper several examples are given, and the posibilities for shape control are investigated. © 1997 Elsevier Science Ltd.

INTRODUCTION

The ongoing efforts to improve weight, performance, temperature stability and versatility, together with enhanced reliability of aerospace and mechanical components, led to the development of a new generation of composite structures, based of what is often called 'smart/intelligent or adaptive materials'. In recent years a considerable effort was directed to the development of these materials and structures. Yet, it is our feeling that the vast potential of smart structures still remain to be addressed. New avenues, like the development of smart composites having enhanced inherent capabilities to adapt their static and dynamic response and to sense the type, location and extent of a possible damage, are yet to be explored. To perform this task basic theoretical models, which correctly represent the electromechanical state of the structure and how to exploit the inherent conditions of the piezolaminated composite, have to be developed. It is the aim of this paper to address this issue.

A common form of a smart/intelligent structure is a thin type structure equipped with sensors and actuators. These included fibre optics, electro-rheological fluids, magneto-strictive materials, shape memory alloys and piezoelectric materials. The most common forms of the piezoelectric materials are polyvinylidene fluoride (PVDF) — a piezoelectric copolymer film — or lead zirconia titanate (PZT) — a piezoceramic-based material available at present in relatively small rectangular patches. The merit of such materials is their capability for transducing electric fields into mechanical strains, and mechanical strains into electrical charges. The piezoceramic materials can be incorporated into a laminated composite structure, either by embedding it or by mounting it onto the surface of the structure [1–5]. These 'active' laminae are used either to actuate the hosting structure by inducing strains in the non-piezoelectric, 'passive' laminae, or to sense deflections of the hosting structure by measuring the local strain fields. The active laminae, the actuators, can be continuous over the entire domain of the structure, as in the PVDF case, or discontinuous as in the case of piezoceramic (PZT) patches.

While the use of piezoelectric materials to control the response of structures has been extensively studied [1–5], the subject of controlling the shape of the composite structures has received less attention. Such works include the recent study by Donthireddy & Chandrashekhara [6] on laminated composite beams with continuous piezoelectric actuators, and the recent study by Lin *et al.* [7] on plates with

discrete piezotransduces, taking into account the thickness of the adhesive. Both studies used the finite-element method to predict the shape of the structures. Kokonis *et al.* [8] applied a first-order shear-deformation theory to derive the governing equations of a composite plate equipped with piezoelectric actuators. The solution was then obtained, using the Ritz method. Main *et al.* [9] tried to solve the question of the optimal placement and sizing of paired piezotransducers incorporated into isotropic beams and plates, while neglecting the thickness of the adhesive.

It seems that correct selection and placement of the piezoactuators into a proper hosting structure would generate enough forces to control the shape of the structure. Such a structure can be modelled as a beam made of non-symmetric laminates, which would induce coupling between the axial and lateral motions of the beam yielding new shape control capabilities, which to the best of our knowledge has not been covered in the literature.

It is the aim of the present study to apply a variant of the finite-element method, the exact element method [10], based on a first-order shear-deformation theory to control the shape of a piezolaminated composite beam. Unlike other finite-element methods, the exact element method uses the exact shape functions of the beam that are represented by a converging infinite series. Using these shape functions the solution can be obtained with any desired accuracy, yielding the exact one, without the need to divide the beam into elements and checking the convergence vs the number of elements.

First, the three coupled equations of a non-symmetric piezolaminated composite beam and its corresponding boundary conditions are derived. The shape control is performed using continuous piezoceramic layers either embedded or bonded to the surface of the structure. The displacement field is based on a first-order shear-deformation theory, which was shown by the authors to be adequate for these laminates [11]. Then, the exact element method is applied to solve the equations of motion to yield the in-plane and out-of-plane beam's deformations.

To validate the present approach the computed results were first compared with ones presented in the literature, yielding a very good match. A parametric study was then performed to investigate the influence of boundary conditions, lay-up orientation and sequence, as well as the voltages applied to the piezoceramic layers, on the change in the shapes of symmetric and non-symmetric piezolaminated composite beams with and without external mechanical loads.

DERIVATION OF DIFFERENTIAL EQUATIONS

The constitutive equations for the kth layer in the beam is

$$\sigma_k = [Q]_k \varepsilon_k - [e]_k^{\mathrm{T}} E_k \tag{1}$$

where ε is the strain, σ is the stress, E is the electric field intensity, $[Q]$ is the elastic stiffness matrix and $[e]$ is the piezoelectric coefficient matrix. In expanded form eqn (1) is written as

$$\begin{Bmatrix} \sigma_x \\ \sigma_y \\ \tau_{yz} \\ \tau_{xz} \\ \tau_{xy} \end{Bmatrix}_k = \begin{bmatrix} Q_{11} & Q_{12} & 0 & 0 & Q_{16} \\ Q_{12} & Q_{22} & 0 & 0 & Q_{26} \\ 0 & 0 & Q_{44} & Q_{45} & 0 \\ 0 & 0 & Q_{45} & Q_{55} & 0 \\ Q_{16} & Q_{26} & 0 & 0 & Q_{66} \end{bmatrix}_k$$

$$\left(\begin{Bmatrix} \varepsilon_x \\ \varepsilon_y \\ \gamma_{yz} \\ \gamma_{xz} \\ \gamma_{xy} \end{Bmatrix}_k - \begin{bmatrix} 0 & 0 & d_{31} \\ 0 & 0 & d_{31} \\ 0 & d_{15} & 0 \\ d_{15} & 0 & 0 \\ 0 & 0 & 0 \end{bmatrix}_k \begin{Bmatrix} 0 \\ 0 \\ E_3 \end{Bmatrix}_k \right) \tag{2}$$

For the beam problem $\sigma_y = \tau_{yz} = \tau_{xy} = 0$ while the strains $\varepsilon_y \neq \gamma_{yz} \neq \gamma_{xy} \neq 0$ to obtain the following reduced constitutive equations

$$\begin{Bmatrix} \sigma_x \\ \tau_{xz} \end{Bmatrix}_k = \begin{bmatrix} Q_{11} & 0 \\ 0 & Q_{55} \end{bmatrix}_k \left(\begin{Bmatrix} \varepsilon_x \\ \gamma_{xz} \end{Bmatrix}_k - \begin{bmatrix} d_{31} \\ 0 \end{bmatrix}_k E_3^K \right) \tag{3}$$

where the relations for $\bar{Q}_{ij}$ in terms of Q_{ij} are given by

$$\bar{Q}_{11} = Q_{11} + \left(\frac{Q_{16}Q_{26} - Q_{12}Q_{66}}{Q_{22}Q_{66} - Q_{26}^2} \right) Q_{12} + \left(\frac{Q_{12}Q_{26} - Q_{22}Q_{66}}{Q_{22}Q_{66} - Q_{26}^2} \right) Q_{16} \tag{4}$$

$$\bar{Q}_{55} = Q_{55} - \frac{Q_{45}^2}{Q_{44}} \tag{5}$$

The laminated beam displacement field based on a first-order shear-deformation beam theory can be expressed as

$$U = u(x) + z\phi(x) \tag{6}$$

$$W = w(x) \tag{7}$$

The strains associated with the displacements are given by (without external electric field, $E = 0$)

$$\varepsilon_x = \frac{dU}{dx} = u'(x) + z\phi'(x) \tag{8}$$

$$\gamma_{xz} = \frac{dW}{dx} + \frac{dU}{dz} = w'(x) + \phi(x) \tag{9}$$

Substituting eqns (8) and (9) into eqn (3) and integrating through the thickness yields the beam constitutive equations

$$N_x = A_{11}u' + B_{11}\phi' + E_{11} \tag{10}$$

$$Q_{xz} = A_{55}(\phi + w') \tag{11}$$

$$M_x = B_{11}u' + D_{11}\phi' + F_{11} \tag{12}$$

where

$$(A_{11}, B_{11}, D_{11}) = b \int_{-h/2}^{h/2} \bar{Q}_{11}(1, z, z^2)\, dz \tag{13}$$

$$A_{55} = kb \int_{-h/2}^{h/2} \bar{Q}_{55}\, dz \tag{14}$$

where k is the shear correction factor, b is the beam width,

$$(E_{11}, F_{11}) = b \sum_{i=1}^{m} \bar{Q}_{11}^{p} V d_{31}^{p}(1, z_i^{p}) \tag{15}$$

Note that V in eqn (9) can be DC (a constant value) or AC (time-dependent voltage $V(t)$). Also the piezoelectric induced strain is given by

$$\varepsilon_x^{p} = \sum_{i=1}^{m} \frac{V_i(d_{31})_i}{h_i} \tag{16}$$

where h_i is the thickness of the ith piezolayer. From the above relation we have the equilibrium equations as

$$\frac{d}{dx}\left[D_{11}\frac{d\phi}{dx} + B_{11}\frac{du}{dx} F_{11} \right]$$

$$-A_{55}\left(\frac{dw}{dx} + \phi \right) = n(x) \tag{17}$$

$$\frac{d}{dx}\left[A_{55}\left(\frac{dw}{dx} + \phi \right) \right] = q(x) \tag{18}$$

$$\frac{d}{dx}\left[A_{11}\frac{du}{dx} + B_{11}\frac{d\phi}{dx} + E_{11} \right] = m(x) \tag{19}$$

where $n(x)$, $q(x)$ and $m(x)$ are the distributed axial load, the distributed later load and the distributed bending moment along the beam, respectively.

If we normalize eqns (17)–(19) using the relation $\xi = x/L$, and choose for the solution the following polynomial series

$$u = \sum_{i=0}^{\infty} u_i \xi^i \tag{20}$$

$$w = \sum_{i=0}^{\infty} w_i \xi^i \tag{21}$$

$$\phi = \sum_{i=0}^{\infty} f_i \xi^i \tag{22}$$

we can write the external loads as

$$n = \sum_{i=0}^{\infty} n_i \xi^i \tag{23}$$

$$m = \sum_{i=0}^{\infty} m_i \xi^i \tag{24}$$

$$q = \sum_{i=0}^{\infty} q_i \xi^i \tag{25}$$

Substitution of these expressions and their derivatives in the differential equations yields

$$A_{11} \sum_{i=0}^{\infty} (i+1)(i+2) u_{i+2} \xi^i + B_{11} \sum_{i=0}^{\infty} (i+1)(i+2) f_{i+2} \xi^i = \sum_{i=0}^{\infty} n_i \xi^i \tag{26}$$

$$A_{55} \sum_{i=0}^{\infty} (i+1)(i+2) w_{i+2} \xi^i - A_{55} L \sum_{i=0}^{\infty} (i+1) f_{i+1} \xi^i = \sum_{i=0}^{\infty} q_i \xi^i \tag{27}$$

$$B_{11} \sum_{i=0}^{\infty} (i+1)(i+2) u_{i+2} \xi^i + D_{11} \sum_{i=0}^{\infty} (i+1)(i+2) f_{i+2} \xi^i + A_{55} L \sum_{i=0}^{\infty} (i+1) w_{i+1} \xi^i - A_{55} L^2 \sum_{i=0}^{\infty} f_i \xi^i = \sum_{i=0}^{\infty} m_i \xi^i \tag{28}$$

Equating terms with the same power of ξ in these equations, we arrive at the following recurrence formulae for u_{i+2}, w_{i+2} and f_{i+2}

$$u_{i+2}=\frac{-1}{(i+1)(i+2)A_{11}}(B_{11}L^2(i+1)(i+2)f_{i+2}-n_i) \tag{29}$$

$$w_{i+2}=\frac{-1}{(i+1)(i+2)A_{55}}(q_i-A_{55}L(i+1)f_{i+1}) \tag{30}$$

$$f_{i+2}=-\frac{(A_{55}L(i+1)w_{i+1}-A_{55}L^2f_i-m_i)}{(i+1)(i+2)D_{11}} \tag{31}$$

and we have all the u_i, w_i and f_i coefficients except for the first two, that should be found using the boundary conditions. For the stiffness matrix derivation the beam is unloaded and n_i, q_i, $m_i=0$. The terms for u_{i+2}, w_{i+2} and f_{i+2} converge to 0 as $i\to\infty$. For this case we choose as degrees of freedom in the formulation the axial displacement, the lateral deflection, and the flexural rotation at the two ends of the beam element. At $\xi=0$ we have

$$u_0=u(0) \tag{32}$$

$$w_0=w(0) \tag{33}$$

$$f_0=f(0) \tag{34}$$

so the first three terms are readily known from the boundary conditions. The terms u_1, w_1 and f_1 are found as follows: all the u_is, w_is and f_is are linearly dependent on the first two in each series, and we can write

$$u(1)=C_1u_0+C_2u_1+C_3w_0+C_4w_1+C_5f_0+C_6f_1 \tag{35}$$

$$w(1)=C_7u_0+C_8u_1+C_9w_0+C_{10}w_1+C_{11}f_0+C_{12}f_1 \tag{36}$$

$$f(1)=C_{13}u_0+C_{14}u_1+C_{15}w_0+C_{16}w_1+C_{17}f_0+C_{18}f_1 \tag{37}$$

The eighteen C coefficients are functions of the axial, shear and flexural stiffness of the element. C_1, for example, is the value of $u(1)$ calculated from eqns (20)–(22) using the recurrence formulae in eqns (29)–(31) for $u_0=1$ and $u_1=w_0=w_1=f_0=f_1=0$. For the derivation of the stiffness matrix we have to apply unit displacement or rotation at each of the six degrees of freedom of the element, one at a time and calculate all the terms in the series for u, w and ϕ using the recurrence formulae. Then the axial force, shear force and the bending moment at the two ends of the element ($\xi=0$ and $\xi=1$) will be the stiffnesses for the member.

Thus, there are six sets of geometrical boundary conditions as follows

1. $u(0)=1$; $w(0)=f(0)=u(1)=w(1)=f(1)=0$;
2. $w(0)=1$; $u(0)=f(0)=u(1)=w(1)=f(1)=0$;
3. $f(0)=1$; $u(0)=w(0)=u(1)=w(1)=f(1)=0$;
4. $u(1)=1$; $u(0)=w(0)=f(0)=w(1)=f(1)=0$;
5. $w(1)=1$; $u(0)=w(0)=f(0)=u(1)=f(1)=0$;
6. $f(1)=1$; $u(0)=w(0)=f(0)=u(1)=w(1)=0$.

Corresponding to these six sets there are six solutions ($\mathbf{U}_i$; $i=1, 6$ for $u(\xi)$, $\mathbf{W}_i$; $i=1, 6$ for $w(\xi)$ and $\mathbf{F}_i$; $i=1, 6$ for $f(\xi)$) which are found using eqns (33)–(35) and eqns (36)–(38). These are the shape functions for the laminated beam model. Then, the holding actions, i.e. stiffnesses, are

$$S(1,i)=-\frac{A_{11}}{L}\mathbf{U}_{i,1}-\frac{B_{11}}{L}\mathbf{F}_{i,1}+E_{11} \tag{38}$$

$$S(2,i)=-\frac{A_{55}}{L}[\mathbf{W}_{i,1}-\mathbf{F}_{i,0}] \tag{39}$$

$$S(3,i)=-\frac{D_{11}}{L^2}\mathbf{F}_{i,1}-\frac{B_{11}}{L^2}\mathbf{U}_{i,1}+F_{11} \tag{40}$$

$$S(4,i)=\frac{A_{11}}{L}\sum_{k=1}^{\infty}k\mathbf{U}_{i,k}+\frac{B_{11}}{L}\sum_{k=1}^{\infty}k\mathbf{F}_{i,k}-E_{11} \tag{41}$$

$$S(5,i)=\frac{A_{55}}{L}\left[\sum_{k=1}^{\infty}k\mathbf{W}_{i,k}-\sum_{k=0}^{\infty}\mathbf{F}_{i,k}\right] \tag{42}$$

$$S(6,i)=\frac{D_{11}}{L^2}\sum_{k=1}^{\infty}k\mathbf{F}_{i,k}+\frac{B_{11}}{L^2}\sum_{k=1}^{\infty}k\mathbf{U}_{i,k}-F_{11} \tag{43}$$

The equivalent end forces at the ends of the members due to the loads are found using the same procedure but the loads $n(x)$, $q(x)$ and $m(x)$ are used and all the end conditions are taken as zero. The end actions are the stiffness terms obtained using eqns (39)–(43).

RESULTS AND DISCUSSION

Based on the formulation of the problem presented in the preceding section, several beams with different boundary conditions, symmetric and non-symmetric lay-ups, applied voltages and length to thickness ratios were solved and the results are given here. The results are given both in figures and numerical tables for comparison with other researchers. Table 1 presents the mechanical properties of the materials used for the present results. The beams analysed in this paper had the following lay-ups: for the symmetric lay-up the sequence was PZT/0°/90°/90°/0°/PZT and for the non-symmetric lay-ups PZT/0°/90°/0°/90°/PZT. In Table 2 the normalized constants for the example beams are given. For all the cases presented here only one element is needed for the exact results of the analysis. The shear correction factor k was taken as 5/6 in all cases.

The first example is of a cantilever beam loaded by a distributed load q, and by an applied voltage. In Table 3 the results for the tip deflection, as a function of the slenderness ratio for the beam, for several applied voltages are given. In Fig. 1 the deflected shape of one of the cases in Table 3 is shown. It is evident that one can control the shape by applying an electric field to the PZT layers.

In the second example the results are given for a simply supported beam in Table 4 and

Table 1. Material and geometric data

Material	E_1 (N/m^2)	E_2 (N/m^2)	G_{12} (N/m^2)	ν_{12}	G_{13} (N/m^2)	G_{23} (N/m^2)	$d_{31} = d_{32}$ (m/V)	Thickness (m)
G-1195 piezoceramic	$63. \times 10^9$	$63. \times 10^9$	24.8×10^9	0.28	—	—	$-106. \times 10^{-12}$	0.0002
AS/3501 graphite–epoxy	144.8×10^9	9.65×10^9	7.1×10^9	0.30	7.1×10^9	5.92×10^9	—	0.000127

Table 2. The normalized constants for the examples

Normalized constant	PZT/0°/90°/0°/90°/PZT non-symmetric	PZT/0°/90°/90°/0°/PZT symmetric
$a_0 = \dfrac{A_{11}L^2}{D_{11}}$	$0.246755(L/t)^2$	$0.2188627(L/t)^2$
$b_0 = \dfrac{B_{11}L}{D_{11}}$	$0.0638(L/t)$	0
$c_0 = \dfrac{A_{55}L^2}{D_{11}}$	$0.012197k(L/t)^2$	$0.0108183k(L/t)^2$
$q_0 = \dfrac{qL^3}{D_{11}}$	$0.938 \times 10^{-9}(L/t)^3$	$0.832 \times 10^{-9}(L/t)^3$
$f_0 = \dfrac{F_{11}L^2}{D_{11}}$	$0.23362 \times 10^{-6}V_1(L/t)$	$0.207 \times 10^{-6}V_1(L/t)$

Table 3. Tip deflection for loaded clamped free beams with different L/t ratios for symmetric and non-symmetric lay-up beams

V	PZT/0°/90°/90°/0°/PZT			PZT/0°/90°/0°/90°/PZT	
	$L/t = 500$	$L/t = 700$	$L/t = 1000$	$L/t = 500$	$L/t = 700$
0	−0.01302307	−0.0357043	−0.10404614	−0.01492519	−0.0409237
50	−0.00940057	−0.0320818	−0.09887114	−0.01195596	−0.0373012
100	−0.00577807	−0.0284593	−0.09369614	−0.00898673	−0.0336787
200	0.00146693	−0.0212143	−0.08334614	−0.00304827	−0.0264337
300	0.00871193	−0.0139693	−0.07299614	0.00289019	−0.0191887
400	0.01600267	−0.0066588	−0.06254712	0.00887466	−0.0118779
500	0.02320193	0.0005207	−0.05229614	0.01476711	−0.0046987

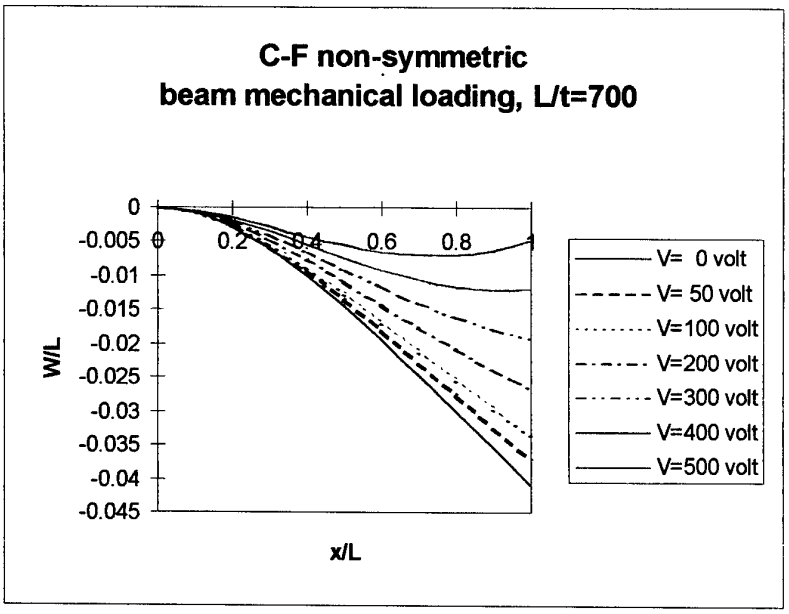

Fig. 1. Deflections of a non-symmetric cantilever beam under distributed lateral load and applied electric voltage.

Table 4. Central deflection of loaded simply supported beams with different L/t ratios for symmetric and non-symmetric lay-up beams ($L/t = 1000$)

V	PZT/0°/90°/90°/ 0°/PZT	PZT/0°/90°/0° /90°/PZT
0	−0.1084487	−0.01242993
200	−0.00566987	−0.00649143
500	0.00209263	0.00241632

Fig. 2. In Table 5 the effect of restraining both ends of the simply supported beam axially is shown.

SUMMARY

In this paper the exact shape functions for the deflection and bending slope of composite lami-

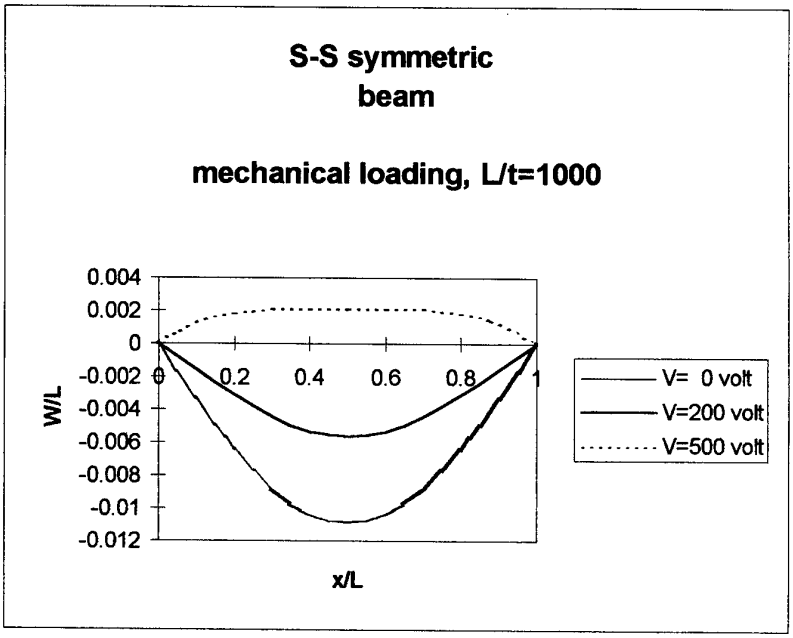

Fig. 2. Deflections of a symmetric simply supported beam under distributed lateral load and applied electric voltage.

Table 5. Central deflection of loaded simply supported beams ($L/t = 1000$) for non-symmetric lay-up and with axial restraints

V	$u(0) = u(L) = 0$	$u(0) = u'(L) = 0$
0	−0.01206120	−0.01242993
200	−0.00628658	−0.00649143
500	0.00278505	0.00241632

nated beam elements were used to derive the exact stiffness matrix for the beam. The element has only six degrees of freedom, as for the classical beam element. The advantage of the presented method is its the ability to deal with general lay-ups and geometries of the structure, and its boundary conditions, with the ease of the general finite-element method, using a minimal number of elements, but yielding exact results.

REFERENCES

1. Abramovich, H. and Livshits, A., Dynamic behavior of cross-ply laminated beams with piezoelectric layers. *Composite Struct.*, 1993, **25**, 371–379.
2. Cudney H. H., Alberts T. E. & Colvin, J. A., A classical approach to structural control with piezoelectrics. In *Proc. 33rd AIAA/ASME/ASCE/AHS/ASC Structures,Structural Dynamics, and Materials Conf.*, Dallas, TX, 1992, pp. 2118–26.
3. Clark, R. L., Flemming, M. R. and Fuller, C. R., Piezoelectric actuators for distributed vibration excitation of thin plates: A comparison between theory and experiment. *J. Vibrat. Acoust., Trans. ASME*, 1993, **115**, 332–339.
4. Akella, P., Chen, X., Cheng, W., Hughes, D. and Wen, J. T., Modeling and control of smart structures with bonded piezoelectric sensors and actuators. *Smart Mater. Struct.*, 1994, **3**, 344–353.
5. Wang, B. T. and Wang, C. C., Feasibility analysis of using piezoceramic transducers for cantilever beam modal testing. *Smart Mater. Struct.*, 1997, **6**, 106–116.
6. Donthireddy, P. and Chandrashekhara, K., Modeling and shape control of composite beams with embedded piezoelectric actuators. *Composite Struct.*, 1996, **35**, 237–244.
7. Lin, C. C., Hsu, C. Y. and Huang, H. N., Finite element analysis on deflection control of plates with piezoelectric actuators. *Composite Struct.*, 1996, **35**, 423–433.
8. Kokonis, D. B., Kollar, L. P. and Springer, G. S., Shape control of composite plates and shells with embedded actuators, I. Voltage specified. *J. Composite Mater.*, 1994, **28**, 415–458.
9. Main, J. A., Garcia, E. and Howars, D., Optimal placement and sizing of paired piezoactuators in beams and plates. *Smart Mater. Struct.*, 1994, **3**, 373–381.
10. Eisenberger, M., Abramovich, H. and Shulepov, O., Dynamic stiffness analysis of laminated beams using a first order shear deformation theory. *Composite Struct.*, 1995, **31**, 265–271.
11. Abramovich, H., Eisenberger, M. and Shulepov, O., Vibrations and buckling of cross-ply non-symmetric laminated composite beams. *AIAA J.*, 1996, **34**, 1064–1069.

ELSEVIER

Composite Structures Vol. 38, No. 1–4, pp. 573–580, 1997
© 1997 Elsevier Science Ltd. All rights reserved
Printed in Great Britain
0263-8223/97/$17.00 + 0.00

PII:S0263-8223(97)00093-7

Compressive failure of carbon–foam sandwich composites with holes and/or partial delamination

Y. W. Kwon,[a] S. H. Yoon[b] & P. J. Sistare[a]

[a]*Mechanical Engineering Department, Naval Postgraduate School, Monterey, CA 93943, USA*
[b]*Mechanical Engineering Department, Kumoh National University of Technology, Kumoh, Korea*

Compression failure of sandwich composites made of fibrous carbon–epoxy skins and foam core was investigated using an experimental study. The sandwich specimens had holes and/or partial delamination between the skin and core, and they were subjected to compressive edge loading. Different core thicknesses of sandwich specimens were considered, and hole sizes and locations were varied to examine their effects on the compression failure. The study also included compression of delaminated specimens. In order to better understand the failure mechanism, a numerical study was also conducted. Major modes of failure were core shearing, delamination and skin fracture. Depending on the given parameter, the failure mode was different. The study examined the transition of the failure mode from one kind to another depending on the variation in the parameters such as delamination and hole size and location. © 1997 Elsevier Science Ltd.

INTRODUCTION

Sandwich structures are made of strong and stiff skin materials, and light and relatively soft core materials. In particular, fiber-reinforced composite materials have been used for the skin material. Sandwich composite structures have a high strength and stiffness to density ratio, a high resistance to corrosion and an increased fatigue life. As a result, they have been used in the design and construction of various components of many civil and military structures.

Sandwich structures have complicated failure modes under compression load. Compression failure depends on the relative strength and stiffness of the skin and core materials. Some of the previous studies on sandwich composite structures are given in the References [1–9]. Pearce & Webber [1,2] studied compression failure of simply supported sandwich panels made of fibrous composite skins and a honeycomb core. Vinson [5,6] gave expressions for compressive strengths for various failure modes, and he determined the optimum skin thickness, core thickness, and cell thickness and size of a honeycomb core for compression failure. Analytical expressions for compressive strengths were developed for symmetric sandwich composites made of boron–epoxy laminated skins and a honeycomb core [3]. Somers *et al.* [10,11] examined the effect of delamination on the buckling and post-buckling behavior of sandwich beams. They derived analytical expressions to determine failure loads of partially delaminated sandwich beams for different failure modes such as dimpling, shear crimping and wrinkling failures. They found that delamination located at the core–skin interface was very critical to the failure of sandwich structures.

The objective of this study is to further understand the failure mechanisms in sandwich composite structures with initial defects such as holes and delamination, which are subjected to compressive loads. Both experimental and numerical studies were conducted for sandwich composites made of carbon–epoxy laminated skins and a foam core. Sandwich composite specimens with different core thicknesses were considered. The sandwich composites had a partial delamination and/or holes. Crack and/or

hole sizes, as well as their locations, were varied. The present study investigates how the compression failure loads and modes changed as the delamination crack and/or holes were varied.

EXPERIMENTAL PROCEDURES

This section provides detailed descriptions, illustrations and procedures of the testing carried out. The tests performed were edge-wise compression. The Instron Model 4507 tensile–compression test machine was used with a 200 kN load cell. Load and displacement data were obtained using the Instron Model 4500 data aquisition system with the Instron series IX automated materials testing software.

Testing fixtures were designed and fabricated to ensure simply supported end conditions on the loaded ends of the test specimen. The compression test specimen fixtures are shown in Fig. 1. The unloaded sides of the test specimen were unconstrained, while the loaded ends were aligned in the test fixtures with shims to ensure loading on the neutral axis. The cylindrical shafts of the test fixtures were free to rotate in the journal of the fixtures. The freedom of rotation ensured the simply supported end conditions prevailed throughout the duration of the compression test.

The specimens used throughout this study were from a symmetric sandwich composite with graphite–epoxy ($0_2°/90_2°/0_2°$) top and bottom skins and a Rohacell polymethacrylimide rigid foam inner core. All test specimens were 38.1 cm (15 in.) in length and 3.81 cm (1.5 in.) in width. The graphite–epoxy skins were nominally 0.096 cm (0.038 in.) thick. The specimen foam thickness was 0.30 cm (0.118 in.), 0.635 cm (0.25 in.) or 1.27 cm (0.5 in.). Some samples had delaminations between the skin and core. The delaminations were located on one side of the skins only at the center of the specimens. The delamination ran across the total width of the test sample, and the longitudinal length of delamination varied from 1.27 cm (0.5 in.) to 2.54 cm (1.0 in), 5.08 cm (2.0 in), 10.16 cm (4.0 in) and 15.24 cm (6.0 in). All delaminated samples had foam cores 0.635 cm (0.25 in.) thick.

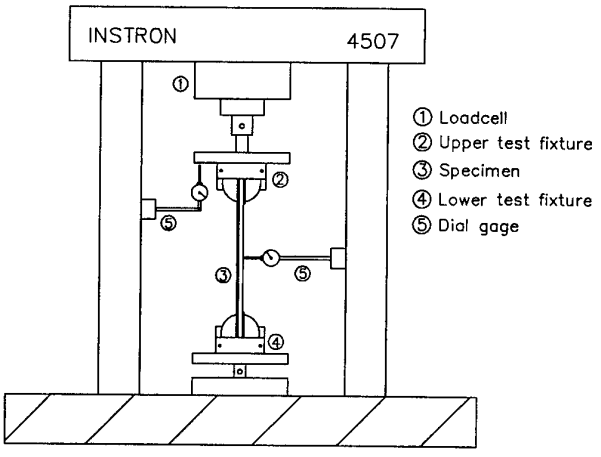

Fig. 1. Test equipment and specimen.

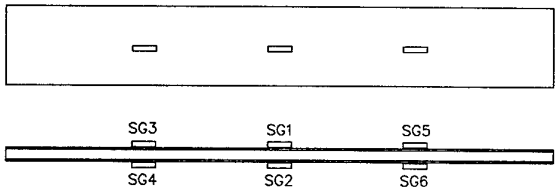

Fig. 2. Typical strain gauge locations.

The test specimens were instrumented with 1.27 cm (0.5 in.) Measurements Group, Inc. CEA-13-250UN-350 precision strain gages mounted longitudinally and back-to-back on both sides of the specimens. A typical strain gage location is shown in Fig. 2. The gages had a gage factor of 2.12. Gage outputs were connected to a Measurements Group SB-10 Switch and Balance Unit, and the strain readouts were provided by a Measurements Group P-3500 Strain Indicator. With the mounting fixtures installed on the compression test machine, the test specimen was fitted into the mounting fixtures and aligned with shims of various sizes. The center and axial deflections were measured with Sterrett dial indicators. Figure 1 illustrates the test specimen in the mounting fixtures for the typical compression test set-up.

Multiple identical compression tests were conducted on samples of the same type. The results of the multiple tests were almost identical, thereby the averge data are used for the results and discussion. Figure 3 shows four different types of samples tested: (a) specimens with no hole and no delamination; (b) specimens with delamination only; (c) specimens with holes only; and (d) specimens with both delamination and holes. A hole may be located outside the delamination zone. The detailed descriptions of these specimens are provided in the next section, where experimental results are discussed.

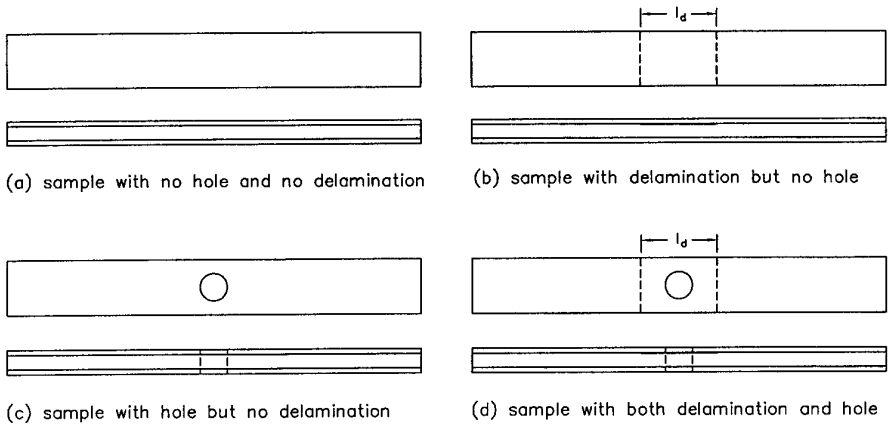

Fig. 3. Different types of specimens.

EXPERIMENTAL STUDY

Samples with no hole and no delamination

The samples consisted of the symmetric sandwich composite with each sample having either a 0.3 cm (0.118 in.), 0.635 cm (0.25 in.) or 1.27 cm (0.5 in.) foam thickness. Figure 4 shows the general trend in the compression tests exhibited by all test samples. The test specimens displayed linear compression up to the critical point for buckling. Loading continued into the buckling regime until the ultimate load in compression was obtained and the sample began to shed the load quickly. Figure 5 shows the maximum compressive (i.e. failure) load vs core thickness for the non-delaminated samples. Figure 5 shows that the compressive failure load increases almost linearly as the core thickness increases.

Upon loading, the test samples generally bent in a half-sine shape until maximum compressive loads were reached. After the maximum load, the load continuously dropped and the sample changed from a half-sine shape to an S shape. The initial failure of the specimens (i.e. reaching the maximum compressive load) was overall buckling, and the post-buckling failure was core shearing and delamination, as observed in other sandwich samples [12]. Figure 6 shows the typical S shape of the sample after core shearing. The core shear of the non-delaminated samples generally originated from points between the center and a quarter-length point on the samples.

Sample with delamination but no hole

All delaminated samples had a 0.625 cm (0.25 in.) foam thickness and a delamination length of 1.27 cm (0.5 in.), 2.54 cm (1.0 in.), 5.08 cm (2.0 in.), 10.16 cm (4.0 in.) or 15.24 cm (6.0 in.). The delamination was located between the skin and the core on only one side of the

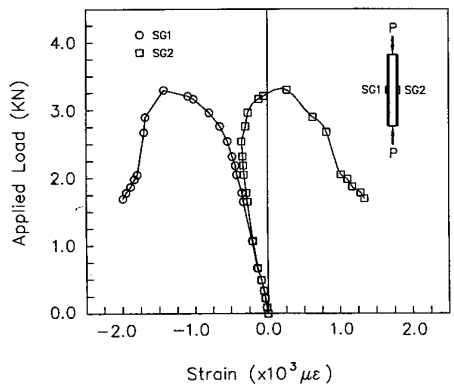

Fig. 4. Load versus strain under compressive load.

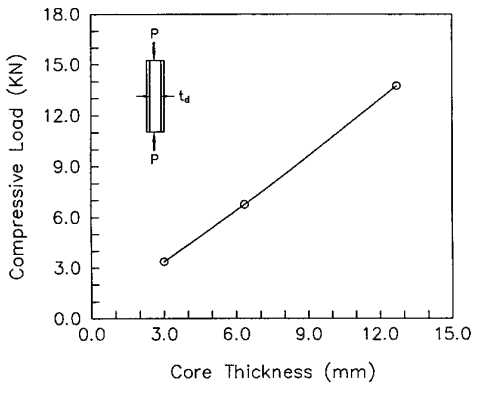

Fig. 5. Compressive failure load versus core thickness.

sandwich specimen. The delamination was also located at the center of the specimen along its length and through the width of the specimen. Figure 7 displays the maximum compressive load vs delamination length of the delaminated samples. There appears to be a threshold value of approximately 1112 N (250 lb/ft) where both the 4 and 6 in. delamination samples failed. The maximum compressive load was an almost linear function of the delamination for the 2, 1 and 0.5 in. delaminations.

The delaminated samples failed by core shearing, except for the samples with a 1.27 cm (0.5 in.) delamination. They showed no preference in bending toward or away from the side with delamination. The core shear of the delaminated samples always originated at the edge of the delamination. The samples with a

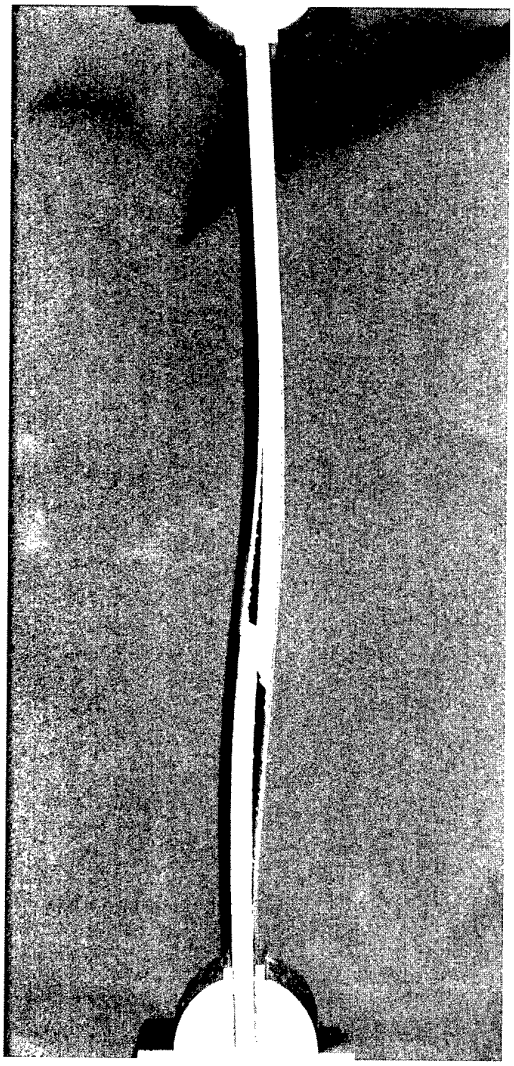

Fig. 6. Specimen with core shear failure.

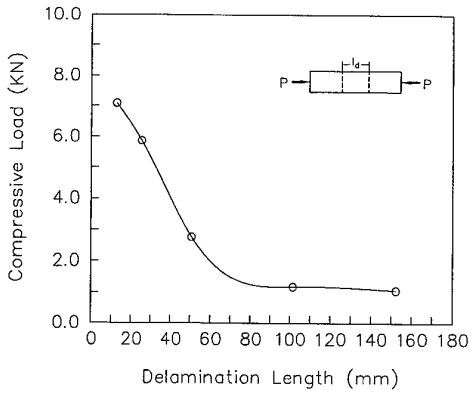

Fig. 7. Compressive failure load versus delamination size.

1.27 cm (0.5 in.) delamination failed initailly by overall buckling followed by core shearing as post-failure. The core shearing did not initiate from the delamination crack tip. Instead, it occurred at points between a quarter-length point and the near end support of the specimens. The maximum compressive force for samples with a 1.27 cm (0.5 in.) delamination was almost the same as that of the sample without delamination. The results showed that there was a threshold value for the delamination crack size under which the compressive failure load was not affected by the delamination crack. For the present samples, the threshold delamination crack size was between 1.27 cm (0.5 in.) and 2.54 cm (1.0 in.).

Samples with holes but no delamination

The first set of tests were conducted for sandwich specimens with holes at the center. Different sizes of holes were considered for the specimens with the same foam thickness. Specimens with 3 mm (0.12 in.) thick foam had two sizes of holes: 12.70 mm (0.5 in.) and 22.23 mm (0.875 in.) hole diameter. The specimen with a 12.70 mm (0.5 in.) hole initiated a core shear failure around a quarter-length point along the length of the sample. Core shearing continued into delamination between the skins and core. The failure load was 2.74 kN which was about 80% of the failure load without a hole.

Specimens without holes experienced a higher foam core shear stress around a quarter-length point along the specimen length than other locations. This is explained further in the following numerical study. The center hole introduced a stress concentration on the bending stress of the skin. However, the center hole

made the specimen more flexible compared to those without a hole. As a result, core shear stress around the quarter-point increased with the hole. However, the skin material has a much greater failure strength than the core material so that the bending stress at the hole with added stress concentration did not reach the failure strength of the skin material. Hence, failure occurred around a quarter-length point of the foam core at a lower load.

As the hole diameter was increased to 22.23 mm (0.875 in.), failure occurred at the center of the skin material. That is, bending failure occurred instead of core shear failure. Higher bending stress with a larger hole caused skin fracture next to the hole. The failure load was 2.61 kN which was lower than that for specimens with a 12.70 mm (0.5 in.) hole. The numerical study in the next section confirmed this result.

A similar observation was made for specimens with higher core thicknesses. Specimens with a 6.35 mm (0.25 in.) thick core had core shearing failure around the one-eighth point of the specimen length when a 12.70 mm (0.5 in.) diameter hole was drilled in the specimen. On the other hand, a specimen with a 19.05 mm (0.75 in.) diameter hole failed by skin fracture at the center. For specimens with 12.70 mm (0.5 in.) thick core, a center hole with a 6.35 mm (0.25 in.) diameter caused core shear failure, and a center hole with a 12.75 mm (0.5 in.) diameter resulted in skin fracture.

The experimental results showed that there was a threshold hole size for the carbon–epoxy skin–foam sandwich composite on which the failure mode varied from core shearing to skin bending fracture. Skin bending fracture occurred for a hole larger than the threshold size, while core shearing occurred for a smaller hole. As the core thickness increased with the same skin thickness, the threshold hole size decreased. A thicker core made a stiffer sample which had less bend compared to a thinner core specimen when subjected to edge compression. The stress concentration factor is larger for in-plane deformation than for bending deformation. As a result, a thicker core specimen has a greater stress concentration factor which results in skin bending failure at a smaller size of hole.

When subjected to a 12.70 mm (0.5 in.) hole at the center, the failure load increased by 124% when increasing foam thickness from 3 mm (0.12 in.) to 6.35 mm (0.5 in.). A comparison cannot be made for the sample with 12.70 mm (0.5 in.) thick foam as the sample failed by skin fracture vice core shearing. When subjected to a 19.05 mm (0.75 in.) hole at the center, the failure load increased by 96% when increasing from a foam thickness of 6.35 mm (0.25 in.) to 12.70 mm (0.5 in.). For specimens with a hole the failure load was quite linear to the core thickness, as was the case for no-hole specimens.

Because core shearing occurred around the quarter-length point of the specimen, a hole was drilled at this quarter-point to determine its effect on failure. Sandwich specimens with 12.70 mm (0.5 in.) thick foam had a 6.35 mm (0.25 in.) hole at one quarter-point, a 6.35 mm (0.25 in.) hole at both quarter-points, and a 6.35 mm (0.25 in.) hole at each quarter-point and at the center. These specimens failed by core shearing around the quarter-point at almost the same magnitude of load. That is, changing hole locations and the number of holes did not change the failure load and failure mode as long as core shearing was the failure mode.

Samples with both delamination and a hole

Four compression tests on delaminated samples were conducted to study the interaction between a hole and a delamination. All four samples had a foam thickness of 6.35 mm (0.25 in.) with a 12.70 mm (0.5 in.) hole at one quarter-point. In all cases, the delamination was on one side only and was centered length-wise.

The results showed that specimens with a delamination crack longer than the critical crack length were not affected by a hole as long as the hole size was less than the critical size, and they failed by delamination crack propagation. There was almost no change in the failure load when compared to that for the specimen with delamination only. That is, the hole did not affect the failure in these cases. On the other hand, when the delamination crack length was smaller than the critical crack length, failure was caused by bending at the hole. The failure loads with a hole were lower than those without a hole. That is, failure mode and load changed because of the hole. No core shearing failure was observed for the present specimens.

Specimens with a delamination length greater than or equal to 50.80 mm (2.0 in.) failed by

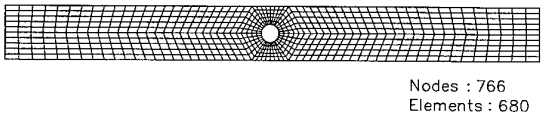

Fig. 8. Finite element mesh for a plate with a hole.

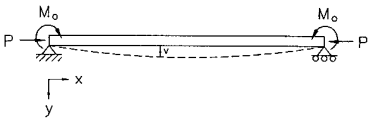

Fig. 9. Simply supported beam with end moments.

delamination crack propagation, while specimens with a delamination crack length less than or equal to 25.40 mm (1.0 in.) failed by bending failure at the hole. Therefore, the critical delamination crack length for the present specimen should be between 25.40 mm (1.0 in.) and 50.80 mm (2.0 in.).

NUMERICAL STUDY

A finite-element analysis was conducted to better understand the experimental results. The ANSYS finite-element analysis program [13] was used to conduct the numerical modeling. Five models were constructed representing the no-hole case, the center hole case, the quarter-point hole case, the case with a hole at each quarter-point and the case with a hole at each quarter-point and at the center. Figure 8 shows a typical element mesh.

A linear buckling analysis was conducted first. Four-node shell elements were used to model the specimens. For the samples with core thicknesses of 3 mm (0.12 in.) and 6.35 mm (0.25 in.), the experimental failure loads are consistently higher than the numerical linear buckling loads. The experimental failure load was 3.47 and 6.32 kN for 3 and 6 mm thick plates with no hole, respectively. The numerical failure load was 1.29 and 4.18 kN for both plates, respectively. On the other hand, the two plates with a 12.70 mm (0.5 in.) hole at the center had failure loads of 2.74 and 6.13 kN from the experiment, and 1.24 and 4.04 kN from the numerical study. This may be explained by friction in the experimental boundary fixtures. The friction caused the actual experimental boundary conditions to be other than ideal freely rotating end conditions, which caused the experimental results to be higher than the numerical results.

For the samples with a core thickness of 12.70 mm (0.5 in.), the higher compressive loads overcame the friction and the end fixtures behaved more like simply supported boundary conditions. Therefore, the numerical results agreed with the experimental results. The experiment showed that the failure loads without or with 6.35 mm holes at both quarter-points of the plate were 14.23 and 13.21 kN, while the numerical results gave 14.31 and 14.17 kN, respectively. The friction at the end support can be modeled by moments applied at the boundaries, as shown in Fig. 9. The governing equation is

$$\frac{d^2v}{dx^2} + k^2 v = -\frac{1}{EI} M_o \tag{1}$$

where

$$k = \sqrt{\frac{P}{EI}} \tag{2}$$

v is the transverse deflection of the beam, EI is the beam rigity, M_o is the end moment caused by friction and P is the compressive axial force. The solution to eqn (1) is

$$v = -\frac{M_o}{P}\frac{\cos(kL)-1}{\sin(kL)}\sin(kx) + \frac{M_o}{P}(\cos(kx)-1) \tag{3}$$

where L is the length of the beam. This solution is also given in Timoshenko & Gere [14]. The shear force V is obtained from eqns (3) and (4)

$$V = \frac{M_o k}{\cos\frac{kL}{2}}\sin\left(\frac{kL}{2} - kx\right) \tag{4}$$

Shear force V is a maximum when

$$\frac{kL}{2} - kx = \frac{\pi}{2} \tag{5}$$

Solving for x yields

$$x = \frac{L}{2}\left(1 - \sqrt{\frac{P_{cr}}{P_f}}\right) \tag{6}$$

where P_f is the failure load and P_{cr} is the Euler buckling load

$$P_{cr} = \frac{\pi^2 EI}{L^2} \tag{7}$$

The failure load was obtained from the experiment.

The sample with a core thickness of 3 mm (0.12 in.) had a failure load of 3.47 kN and a Euler buckling load of 1.29 kN. For this sample the analysis yields $x = 0.2L$. The sample with a core thickness of 6.35 mm (0.25 in.) had a failure load of 6.32 kN and a Euler buckling load of 4.18 kN. For this sample the analysis yields $x = 0.1L$. The failure locations observed from the experiment for these two samples agreed very well with the predicted failure locations.

The bending moment is

$$M = \frac{M_o}{\cos\dfrac{kL}{2}} \cos\left(kx - \frac{kL}{2}\right) \tag{8}$$

The maximum bending moment occurs at $x = L/2$, i.e. at the center of the beam. Examination of the tested samples showed that failure at the hole was due to bending while failure away from the hole was due to foam core shearing.

A stress analysis using an eight-node layered shell element was conducted to take a closer look at the stresses within the different composite layers to support the experimental findings. The analysis showed that a sample without a hole subjected to a given compressive load had a greater foam core shear stress around the quarter-point than at the center. With a hole at the center, the foam core shear stress around the quarter-point increased as the hole diameter increased. However, the carbon skin bending stress beside the hole increased at a faster rate than the foam core shear stress around the quarter-point because of the stress concentration around the hole. When the hole diameter reached a critical diameter, the bending stress at the hole became more critical in failure than the core shear stress around the quarter-point. As a result, the failure mode changed from foam core shear failure at the quarter-point to skin bending fracture at the hole. Figure 10 shows the rate of increase for both stresses with increasing hole diameter.

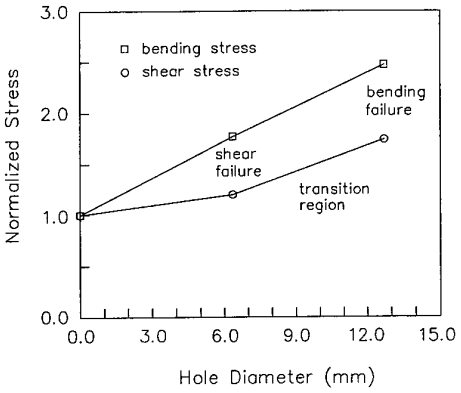

Fig. 10. Bending and shear stresses versus hole diameter.

With a 6.35 mm (0.25 in.) hole, the sample failed around the quarter-point due to foam core shear failure. With a 12.70 mm (0.5 in.) hole, the bending stress at the hole was more critical than the core shear stress at the quarter-point and the sample failed at the hole. Between these two points, the failure mode made a transition from foam core shear failure around the quarter-point to bending failure at the hole.

CONCLUSIONS

The compressive failure load was almost linearly proportional to the core thickness of samples with no delamination and no hole. For these samples, overall buckling was the initial failure (i.e. dropping from the maximum compressive load) and core shearing occurred post-failure. With a partial delamination crack between the skin and core, core shearing initiated at the crack tip with decreasing failure loads. However, a 0.5 in. delamination crack did not change the failure mode and failure load. Thus, there was a threshold value for the delamination crack size. If the crack was smaller than the threshold value there was no effect of the crack on the failure.

With a hole at the center, the foam core shear stress at the quarter-point increased as the hole diameter increased. However, the carbon skin bending stress at the hole increased at a faster rate than the foam core shear stress due to the stress concentration. When the hole diameter reached the critical diameter, the bending stress at the hole became more critical in failure than the core shear stress around the quarter-point. As a result, the failure mode

changed from foam core shear failure around the quarter-point to skin bending failure at the hole. The critical diameter decreased as the foam core thickness increased. When thick core composites were used, the critical diameter was small and failure occurred by skin fracture.

For specimens with both holes and delamination cracks, there was minimum interaction between the hole and the crack as long as the crack is large and the hole is small. That is, failure initiated at the crack tip and there was almost no change in the failure load. However, when the hole size increased and the crack size decreased, the failure was caused by skin fracture at the hole and the failure load decreased.

The experimental compression failure loads were higher than the numerical linear buckling loads for samples with core thicknesses of 3 mm (0.12 in.) and 6.35 mm (0.25 in.). This was explained by friction in the experimental boundary fixtures. The friction at the end supports was modeled by moments applied at the boundaries. The failure location was predicted and the prediction agreed well with experimental observation.

REFERENCES

1. Pearce, T. R. A. and Webber, J. P. H., Bucking of sandwich panels with laminated face plates. *Aeronaut. Qt.* 1972, **23**, 148–160.
2. Pearce, T. R. A. and Webber, J. P. H., Experimental buckling loads of sandwich panels with carbon fiber faceplates. *Aeronaut. Qt*, 1973, **24**, 295–312.
3. Suarez, J. A., Whiteside, J. B. & Hadcock, R. N., The influence of local failure modes on the compressive strength of boron/epoxy composites. In *Composite Materials: Testing and Design, Second Conf.*, ASTM STP 497. American Society of Testing Materials, 1972, pp. 237–56.
4. Vinson, J. R. & Sierakowski, R. L., *The Behavior of Structures Composed of Composite Materials*. Martinus Nijhoff, Dordrecht, 1986.
5. Vinson, J. R., Optimum design of composite honeycomb sandwich panels subjected to uniaxial compression. *AIAA J.*, 1986, **24**, 1690–1696.
6. Vinson, J. R., Comparison of optimized sandwich panels of various constructions subjected to in-plane loading. In *Proc. First Int. Conf. on Sandwich Constructions*, Stockholm, Sweden, 1989, pp. 23–49.
7. Kim, R. Y. and Crasto, A. S., A longitudinal compression test for composites using a sandwich specimens. *J. Composite Mater.*, 1992, **26** (13), 1915–1929.
8. Webber, J. P. H., Kyriakides, S. and Lee, C. T., On the wrinkling of honeycomb sandwich columns with laminated cross-ply faces. *Aeronaut. Qt.*, 1976, **27**, 264–272.
9. Yeh, W.-N. and Wu, Y. E., Enhancement of buckling characteristics for sandwich structures with fiber reinforced composite skins and core made of aluminum honeycomb and polyurethane foam. *Theor. Appl. Fract. Mech.*, 1991, **15**, 63–74.
10. Somers, M., Weller, T. and Abramovich, H., Buckling and postbuckling behavior of delaminated sandwich beams. *Composite Struct.*, 1992, **21**, 211–232.
11. Somers, M., Weller, T. and Abramovich, H., Influence of predetermined delaminations on buckling and postbuckling behavior of composite sandwich beams. *Composite Struct.*, 1991, **17**, 295–329.
12. Kwon, Y. W., Murphy, M. C. and Castelli, V., Buckling of unbalanced sandwich panels with titanium and GRP skins. *J. Pressure Vessel Technol., Trans. ASME*, 1995, **117**, 40–44.
13. DeSalvo, G. J. & Gorman, R. W., *ANSYS Engineering Analysis System User's Manual for ANSYS Revision 4.4*. Swanson Analysis System, Houston, PA, 1989.
14. Timoshenko, S. P. & Gere, J. M., *Theory of Elastic Stability*. McGraw-Hill, New York, 1961.

ELSEVIER

Composite Structures Vol. 38, No. 1–4, pp. 581–587, 1997
© 1997 Elsevier Science Ltd. All rights reserved
Printed in Great Britain
0263-8223/97/$17.00 + 0.00

PII:S0263-8223(97)00096-2

'Good vibrations', the science and application of intrinsically damped composite materials*

I. D. Grant, A. T. Lowe & S. Thomas

Structural Materials Centre, DERA, Farnborough, Hampshire GU14 6TD, UK

The work presented in this paper shows how the viscoelastic properties of an epoxy resin system can be modified to produce an intrinsically damped composite (IDC) material. Through the addition of chain extension modifiers, peak loss factors of up to 0.4 have been achieved compared to 0.005 for traditional glass reinforced epoxy (GRE) materials. Both dynamic mechanical analysis (DMA) and vibroacoustic measurement techniques were used to determine the loss factors of the IDC materials. The DMA technique was less sensitive to changes in damping due to different fibre orientations. In conclusion, potential areas of application for these novel composite materials are described. © 1997 Elsevier Science Ltd.

INTRODUCTION

One of the principal benefits offered by composite materials is the ability to tailor their mechanical properties for different applications. One area which is only recently being investigated is the ability of composite materials to provide considerable reductions in the levels of vibration and noise generated by a structure. By altering the fibre alignment it is possible to increase the vibrational loss factor of a composite material. However, this usually requires a high proportion of fibres to be orientated at $\pm 45°$ to the primary loading direction (i.e. the 0° direction), resulting in a considerable reduction in mechanical stiffness of the material in that direction. One approach to overcome this limitation is to use alternative fibres which posses, intrinsically, higher levels of damping. Investigations of this type have been carried out by Yu and Song at the US Army Natick Research Laboratories [1–3] who have studied, predominately, the damping levels achieved by using Kevlar 29 and Spectra for ballistic protection. Other workers have investigated the benefits gained through the use of interleaving in angle-ply carbon fibre epoxy laminates [4]. All these techniques show some improvements, but none of them have achieved loss factors greater than 0.05 for a composite material at frequencies above 10 Hz. Some workers [5] have speculated that the only way to achieve high loss factors would be through modifying the resin system and it is this approach which is described in this paper.

Currently, a wide range of resins are used for fibre consolidation in composite materials including polyesters, vinyl esters, phenolics and epoxies. All these resin systems exhibit viscoelastic properties, but only at high temperatures, typically in the region of 80–230°C. For a homogeneous polymer, the viscoelastic region (also known as the transition region because it corresponds to material behaviour which is neither glassy or rubbery, but somewhere in-between) occurs over a range of temperatures centred around the glass transition temperature (T_g). This region is characterised by a decrease in the real component of Young's modulus (E') in addition to an increase then decrease of both the complex component of Young's modulus (E'') and the loss factor ($\tan \delta = E''/E'$). Generally, composite materials such as GRP have a loss factor of 0.005 which is only marginally superior to that of mild steel with a value of 0.0001. In many areas of application (particularly for the aerospace industry), resin

*Reproduced with the permission of the Controller of Her Britannic Majesty's Stationery Office.

manufacturers have neglected material damping performance, tending to develop polymers with higher glass transition temperatures so that mechanical stiffness is maintained at elevated temperatures. However, in many applications, structural damping performance will be a major consideration. It is possible to develop resin systems with relatively low glass transition temperatures so that the viscoelastic region is encountered at expected operating temperatures and, consequently, higher levels of damping can be exploited. Intrinsically damped composite (IDC) materials containing 4 ply 0/90° woven XAS carbon fibre and consolidated with highly damped epoxy resin systems have shown loss factors of up to 0.4.

Obviously there is a trade off between the level of damping which is achieved and the mechanical properties, however, for many secondary structures these limitations can be overcome. Furthermore, if careful thought is given to the vibroacoustic environment a structure may experience during its life time, considerable cost savings can be made by using these composite materials in the early design phase, rather than adding additional parasitic damping whilst in service. This paper will describe the work carried out by the UK Defence Evaluation and Research Agency (DERA) in formulating these highly damped epoxy resin systems, providing information on their dynamic mechanical characteristics and typical areas of application.

COMPOSITE MATERIAL FABRICATION

The time and effort required to develop a completely new matrix system with enhanced damping properties would be immense. Consequently, the approach taken was to use proprietary resins and chain modifiers with the aim of reducing both development and eventual unit production costs.

At an early stage a decision was made to focus resources by studying only epoxy based systems, since flexibilised epoxy resins are widely used for industrial flooring and also in the electronics industry for the encapsulation of electronic devices. Chain modifiers manufactured by two independent suppliers have been investigated in combination with standard bisphenol A epoxy resins. The assessment of candidate matrix systems has been made by considering the mechanical performance and the processibility of the resin systems concurrently. Since many of the most effective flexibilising additives are highly viscous it was necessary to make some performance trade-offs to arrive at a viable practical solution. The resins investigated in this report have been designated R1816, R1818 and RF69.

Economic and environmental pressures have increased the attractiveness of using closed mould and filament winding techniques to fabricate composites. To be readily processed using these production methods, a matrix system must have a low viscosity, long pot life and only require moderate post curing. Such considerations are equally important for highly damped composites, and careful attention has been made to address these issues early in the resin development stage.

Viscosity measurements were performed on a Brookfield viscometer immediately after mixing together the matrix components. The pot life measurements are values of the useable life of a resin system when stored in a typical 2 litre laminating bucket, based on experience gained from manufacturing laminates using the various resins. In all cases the ambient temperature was 22°C. A summary of results is shown Table 1; note the comparison with a typical medium viscosity resin used for the resin transfer moulding (RTM) of components.

The RF69 system has been successfully processed using RTM and filament winding. Vosper Thornycroft Ltd (UK) have fabricated a 30 mm thick composite using RF69 and the Seeman composite resin injection moulding process (SCRIMP) with few processing difficulties. Attempts were made to RTM using the R1816, however these efforts were unsuccessful due to a combination of the high viscosity and the short pot life.

An analysis of the cure kinetics of the RF69 resin has been performed from results mea-

Table 1. Processing properties of viscoelastic resin systems at 22°C

Resin type	Viscosity (MPa s)	Pot life (h)
RF69	1100	~6
R1816	4600	~1
R1818	4600	~2.5
Derakane 411-45 (Dow)	500	0.75–3

sured on a thermal analysis (TA) 2920 differential scanning calorimeter (DSC). DSC tests were conducted from −20 to 250°C using a 10°C/min ramp rate. These measurements were then used in conjunction with a kinetics analysis package (B and D kinetics) to predict the time required to post cure the matrix at various temperatures, see Fig. 1.

It should be noted that the conditions within the DSC are not wholly representative of those found in a 2 mm thick laminate where larger amounts of resin will be reacting with less opportunity for the transfer of heat from the laminate. However, the effect of this will be to underestimate the time taken for the resin to cure. The data presented above shows that not only does the RF69 resin system have a relatively low viscosity and long pot life, but it can also be satisfactorily post cured at moderate temperatures over a short period of time.

The IDC materials used for dynamic mechanical analysis and vibroacoustic measurements have all been manufactured using hand lay-up or RTM techniques. To allow a direct comparison of results, spacers were used during hand lay-up to ensure that the panel thickness remained constant (i.e. to maintain a volume fraction of 40% fibre by weight). All laminates were cured at room temperature for 24 h followed by a post cure at 60°C for 3 days (4320 min).

DYNAMIC MECHANICAL ANALYSIS (DMA)

Dynamic mechanical analysis (DMA) provides a convenient method of testing large numbers of resin formulations and composite systems quickly and simply. Test samples were cut from hand layed-up laminates panels made from four plies of plain weave Courtaulds XAS carbon fibre and tested in three point bending using a Netzsch 242 DMA. Specimen dimensions were approximately 1.8×12.0 mm and measurements were made on a sample holder with a free bending length of 40 mm and at a frequency of 10 Hz.

Figures 2 and 3 show the results for three highly damped composite laminates measured in both 0/90° and ±45° fibre orientations. When measured at 0/90° the R1816, R1818 and RF69 exhibited a loss factor (tan δ) of approximately 0.45. However, as the temperature increased this rapidly fell to around 0.1. This represents a 1–2 order of magnitude improvement compared to traditional carbon fibre composite materials.

If the data presented in Figs 2 and 3 are then compared, as expected, the Young's modulus for the 0/90° fibre orientation is approximately four times that in the ±45° direction. However, the values for tan δ are similar in magnitude, irrespective of the fibre orientation. The peak values of tan δ appear to be actually higher for the 0/90° laminates, although for the ±45° specimens the peak is broader. These results do not comply with the analytical model previously described by the authors [6], however, there are a number of potential explanations for this.

In a composite laminate, damping occurs as a mixture of two mechanisms. One relies on damping between the fibre and resin within the laminate plies and the other on damping between the plies. Measurements made on the DMA are achieved by cyclic flexure of the composite beam samples in three point bending at constant amplitude and frequency. Damping in

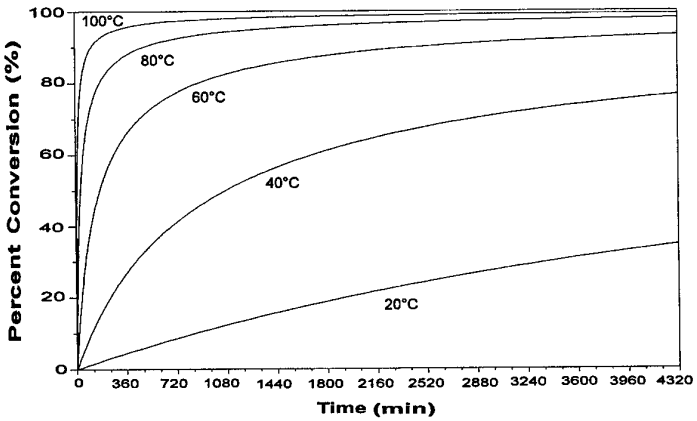

Fig. 1. DSC plot of percentage cure state vs. post cure time at different temperatures for RF69.

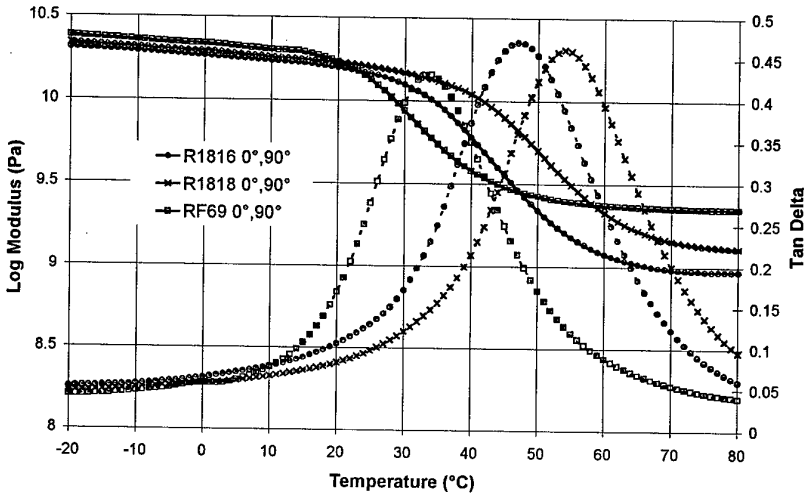

Fig. 2. DMA performance at 10 Hz of 0/90° plain weave carbon fibre, consolidated with a range of highly damped epoxy resin systems.

a flexural mode is largely due to shear effects between plies in a laminate which is analogous to constrained layer damping [7] and is dominated by inter-ply effects. Thus, the damping performance measured on the DMA is less sensitive to the properties of the individual plies than on the effect of shear in the matrix between the plies. Due to the higher stiffness of the 0/90° plies, the amount of energy that can be transferred into the matrix may be proportionally higher than for the $\pm 45°$ plies, leading to the higher value of peak tan δ.

An alternative view is given by the theoretical studies carried out by Sun and Gibson [8] on predicting the material damping of laminated polymer matrix composites. Classical lamination theory is used to show that when beams with a very small fibre length to diameter (L/d) ratio are numerically analysed there is very little difference in the value of tan δ for different fibre orientations. It is only when L/d ratios > 5000 are achieved that significant differences between fibres orientations are shown. If we make a gross simplification of the mechanisms occurring in an IDC composite material and liken the fibre tows to the individual fibres described in the work of Sun and Gibson, it is conceivable that the L/d ratio of the 40 mm long beams used by the DMA are too short to characterise the effects of fibre orientation.

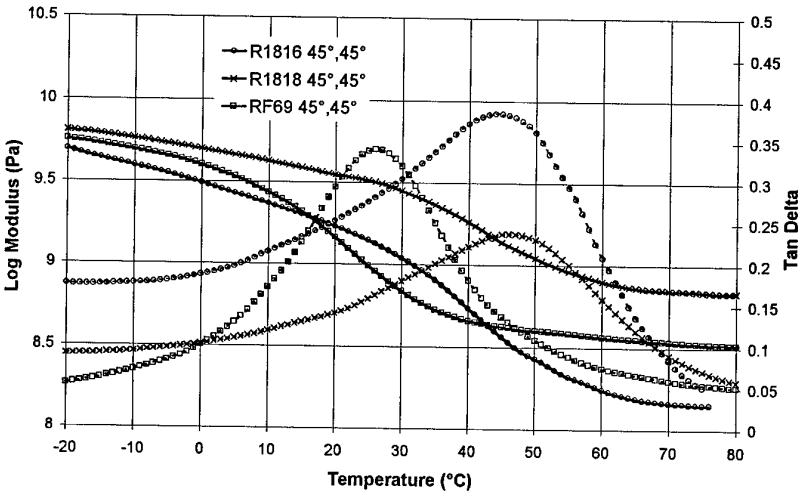

Fig. 3. DMA performance at 10 Hz of $\pm 45°$ plain weave carbon fibre, consolidated with a range of highly damped epoxy resin systems.

A further consideration when using the DMA is to remember that it does not measure the damping due to longitudinal waves. It might be expected that the longitudinal waves are dependent on the damping performance of the sum of the individual plies (i.e. shear effects within the plies) and rather less due to the shear effects between plies. If this is the case the $\pm 45°$ beam would be much more effective at damping longitudinal waves when compared with the 0/90° beam due to the higher in-plane stiffness of the 0/90° fibres. It is therefore necessary to establish the most dominant type of vibration in potential applications so that a correct value for the damping performance can be applied i.e. have multiple values for tan δ, one for flexural and the other for longitudinal vibration modes. An alternative technique for determining damping performance is given by full size beam measurements.

VIBROACOUSTIC MEASUREMENTS

To demonstrate the representative loss factors generated by this technique, the vibroacoustic performance of a plain weave E-Glass/Cycom 919 epoxy (GRE) composite material has been compared with an IDC XAS Carbon/RF69 material. The analysis was carried out using a hammer with a force gauge mounted on the head and a laser accelerometer as shown schematically in Fig. 4 below. The signals from these two transducers were then analysed and the Fourier spectrum of each calculated. The output spectrum was then divided by the input spectrum to give the transfer function. The composite beams were cut to dimensions $215 \times 37 \times 3.5$ mm, with the fibres orientated at 0/90° and $\pm 45°$.

The transfer function for a given beam sample will give the resonant frequencies of

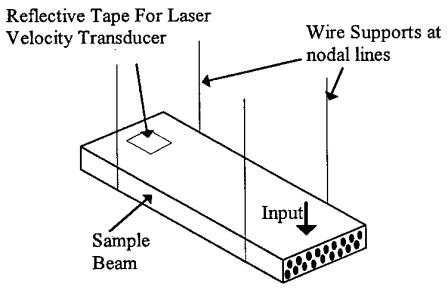

Fig. 4. Schematic diagram of vibroacoustic measurement technique.

that beam. By taking the half power points of the modes the loss factor can be calculated. With further knowledge of the beam using the following beam equation [9] it is possible to calculate the Young's modulus

$$f = \frac{\pi}{2l^2}\sqrt{\frac{EK^2}{\rho}} \tag{1}$$

Where

f = Fundamental frequency
l = Length of beam
K = Radius of gyration
E = Young's modulus
a = Beam thickness
ρ = Density

$$K = a/\sqrt{12} \tag{2}$$

To prevent any interference from the mountings and the transducers a Bruel and Kjear Laser Velocity Transducer was used and a small Dytran hammer was selected to excite the structure. The signal processing was performed using a Bruel and Kjear spectrum analyser 2035 in two channel mode. The beam samples were supported by wire loops at the nodal lines for the fundamental mode to reduce interactions between the supports and the beam. All tests were conducted in the flexural mode. The frequencies for the first four modes of each of the two resin types were taken and the loss factors calculated (see Figs 5 and 6).

As can be seen from the loss factors presented in Fig. 5, this technique gives a value of between 0.005 and 0.01 for the standard E-Glass/Cycom 919 sample. This provides confidence in this test method as these values are similar to the loss factors traditionally quoted for GRE. The Young's modulus for this material is specified by Cytec (the manufacturers) as 26 GPa and analysis via the vibroacoustic method has given a value of approximately 24 GPa. If we now examine the data for the IDC material presented in Fig. 6 we can see that the loss factors for the $\pm 45°$ and the 0/90° fibre orientations are approximately 0.2 and 0.1, respectively. These data conform to the theoretical models presented in [Refs 6 and 8] where the $\pm 45°$ fibre orientation imparts greater shear into the resin system thus introducing a higher level of viscoelastic response. However, there is some discrepancy in the measured value of Young's modulus when

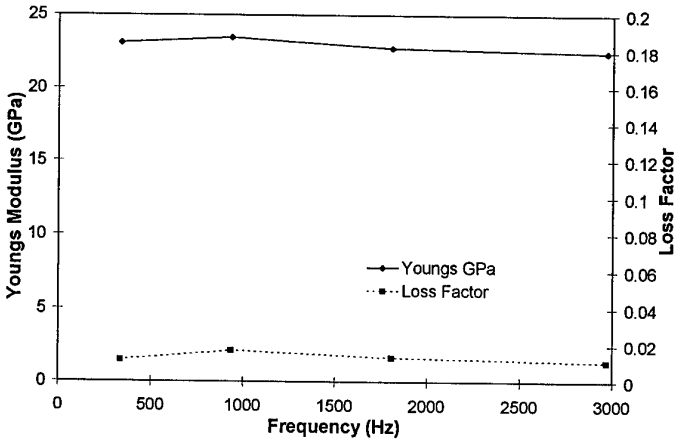

Fig. 5. Loss factor and Young's modulus for standard GRE composite material. 0°/90°.

compared with the DMA results, particularly for the 0/90° orientation (the DMA measures ~12 GPa at 10 Hz for the 0/90° and ~2 GPa for the ±45°, cf. Fig. 6). One explanation may be the inferior quality of these early hand layed up laminates compared to the test samples used for the DMA measurements which were produced by RTM. Clearly further testing is required before the definitive technique for characterising the damping properties of the IDCs (and other composites) can be specified but until then care should be taken to describe the test conditions when quoting loss factors and excitation mode.

APPLICATIONS

There are a wide range of applications for viscoelastically tuned composite materials. Many of the papers listed in the reference section show the potential benefits to be gained in ballistic impact performance but a number of other examples are given below.

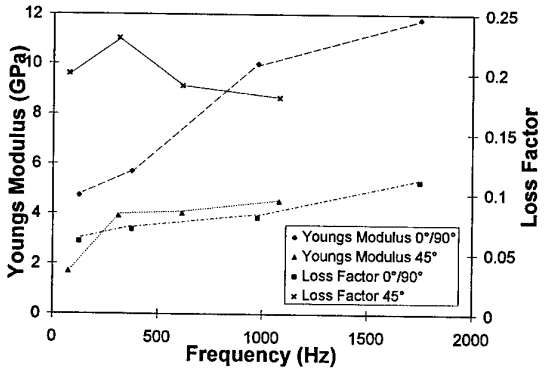

Fig. 6. Loss factor and Young's modulus for carbon fibre IDC material.

Currently many deep water oil and gas platform operators are replacing their existing sea water pipe systems with pipework manufactured from filament wound glass reinforced epoxy (GRE) composite materials. If these pipes are exposed to a continuous flow rate greater than 5 ms^{-1} then cavitation erosion can occur at bends and fittings. Work carried out by SINTEF in Holland [10] showed that under accelerated testing GRE had an erosion incubation time of 1.7 h at a flow rate of 50 m/s compared to > 30 h for a 6 Mo steel. It is known that that the erosion resistance of a composite material is resin dependant and relies on its capacity to resist the impact energy imparted by the collapsing cavitation bubbles. Consequently, if the first layers of a pipe were wound in E-glass/RF69 IDC material this could overcome the additional expense of using an internal thermoplastic liner. In addition, potential benefits could be gained in reduced noise, vibration transmission and hence fatigue damage to connected equipment due to the higher levels of structural damping. A more extreme cavitation environment is produced by composite marine propellers and IDC materials are currently being developed to provide erosion and impact protection under these conditions.

Another area associated with the oil and gas industry is the protection of drilling riser arrays from clashing damage. This problem became more significant as exploration companies began developing oil fields at depths greater than 1000 m. Initial investigations considered the use of a polyurethane coating, but these

proved to be too brittle to resist repeated impact. Consequently, a filament wound polyester fibre/R1816 is currently being evaluated.

One of the most significant areas of application for IDC materials is in the reduction of radiated noise from machinery rafts. These are used in marine applications for the siting of diesel generators, gearboxes, engines etc. Currently they are manufactured from steel or aluminium and are then isolated from the machinery and deck via rubber isolation mounts. By constructing the space frame structure from box sections filament wound at $\pm 45°$ from T300/R1816 IDC material, vibrational power transmission levels have been reduced between 10 and 20 dB across a broad frequency range.

CONCLUSIONS

A range of intrinsically damped composite (IDC) materials have been produced containing XAS/T300 carbon or E-glass fibres and consolidated with a highly modified bisphenol A epoxy resin system. Dynamic mechanical characterisation has revealed that highly damped thermoset resin systems can produce much higher loss factors than previously shown by technique such as interleaving. Due to the compromise made between Young's modulus and loss factor these materials are more suitable for use in secondary structures. Additional work is required to broaden the temperature range over which the high levels of loss are produced.

Two techniques were used to dynamically characterise the IDC materials. Generally it was found that the dynamic mechanical analysis (DMA) was less sensitive in measuring the changes in loss factor due to fibre direction than a more global vibrating beam method. Also the level of loss predicted by the DMA was higher than found on larger scale samples. Consequently great care must be taken when quoting loss factors for composite materials to ensure the test technique and mode of excitation (i.e. flexural or longitudinal) are stated.

ACKNOWLEDGEMENTS

The authors would like to acknowledge the United Kingdom Ministry of Defence for funding this project and the encouragement provided by Mrs C. Solen and Dr R. Leung.

REFERENCES

1. Yu, J. Z., Ko, F. K. and Song, J. W., The effect of fiber orientation on the dynamic mechanical behaviour of kevlar fiber reinforced composites. *Proceedings of ICCM-10*, Whistler, B.C., Canada, August 1995, Vol. VI, pp. 431–438.
2. Ko, F. K., Lei, C., Rahman, A., Shaker, M., Zavaliangos, Yu, J. Z. and Song, J. W., Viscoelastic properties of advanced polymer composites for ballistic protective applications. *Technical Report/Natick/TR-94/035*, 1993.
3. Lee, B.L., Song, J.W. and Ward, J.E., Failure of spectra polyethylene fiber-reinforced composites under ballistic impact loading. *J. Composite Materials*, 1994, **28**, (13), 1202–1226.
4. Liao, F., Su, A. and Hsu, T., Vibration damping of interleaved carbon fibre–epoxy composite beams. *J. Materials*, 1994, **28** (18), 1840–1854.
5. Benchekchou, B. and White, R. G., Fatigue of highly damped carbon fibre reinforced plastic panels at high temperature. *Proceedings of ICCM-10*, Whistler, B.C., Canada, August 1995, Vol. I, pp. 657–664.
6. House, J.R. and Grant, I.D., Viscoelastic composite materials for noise and damage tolerance. *Advanced Performance Materials*, 1996, **3**, (3/4), 295–307.
7. Beranek, L. L. and Ver, I. L., *Noise and Vibration Control Engineering*. John Wiley and Sons, 1992.
8. Sun, C.T., Wu, J.K. and Gibson, R.F., Prediction of material damping of laminated polymer matrix composites. *J. Mater. Sci.*, 1987, **22**, 1006–1012.
9. Olson, H. F., *Elements of Acoustical Engineering*, D Van Nostrand and Company, Inc.
10. Lindheim, T., Erosion performance of glass fibre reinforced plastics (GRP). *Proceedings of l'Institute Francais du Petrole Composite Materials in the Petroleum Industry Conference*, 3–4 Nov 1994, Paris.

ELSEVIER

Composite Structures Vol. 38, No. 1–4, pp. 589–597, 1997
© 1997 Elsevier Science Ltd. All rights reserved
Printed in Great Britain
0263-8223/97/$17.00 + 0.00

PII:S0263-8223(97)00097-4

Compressive behaviour of large undamaged and damaged thick laminated panels

Gang Zhou

Department of Aeronautical and Automotive Engineering and Transport Studies, Loughborough University, Loughborough, Leicestershire LE11 3TU, UK

Both intact and impact-damaged laminated panels under in-plane compressive loading are investigated with a purpose-built anti-buckling support. The readings of back-to-back strain gauges of selected locations are used to deduce panel behaviour in addition to post-mortem observation. The compression failure of intact panels is found to be close to the potted end. The failure characteristics of impact-damaged panels are dependent slightly on composite systems although they all failed in compression in the impact-damaged region with a kink shear band passing through the mid-section. E-glass/polyester panels with a greater shear angle do not seem to involve global buckling like S-glass/phenolic panels with small shear angles. The fact that the region covered by a kink shear band from impact surface to the distal surface is considerably less than the delamination area suggests that the initiation of overall failure is due to the collective result of flexural stiffness reduction compounded by the local impact damage and the associated change of fibre curvature. As a result, the residual compressive strengths are reduced significantly. Further outward propagation of the existing delamination(s) along the mid-section during loading is visible only for E-glass/polyester panels but is not significant. © 1997 Elsevier Science Ltd.

INTRODUCTION

The in-plane compressive behaviour of fibre-reinforced laminated panels has been under extensive investigation in the past two decades, due primarily to its importance as well as its complexity with particular reference to impact damage. It has been well recognised that the compressive strengths of most composite laminates are much less than the tensile strengths, and especially the compressive strengths of damaged laminates suffer reduction more significantly than the tensile and other strengths. The latter limits allowable design strain to a level of about 0.3% so that most of the weight-saving potential is yet to be fully explored, and a further increase of allowable strain up to 0.6% would offer greater commercial weight-saving benefit. Therefore, this area has an extremely important role to play in damage tolerance assessment of laminated composite structures. The complexity of compressive behaviour of laminated panels is well known due mainly to two factors. One is that three types of load introduction exist, namely end loading, surface-shear loading and the combination of the two. Although all three types of loading are used to determine intrinsic composite compressive properties, the end loading type has been dominant for the compression of large composite panels. The other is the existence of multiple failure mechanisms such as end-brooming, kink-band shear, delamination opening and global buckling, partly associated with the loading types. Different failure mechanisms give different failure stresses, indicating a complex state of stress. A really challenging additional factor is that panels in compression contain impact damage of varying severity dependent on the level of impact force or incident kinetic energy (IKE). Due to the fact that impact damage not only appears in various

forms such as matrix cracking, delamination and fibre fracture but also results in the change of local fibre curvature in the contact area, such preconditions which may act as an introduced misalignment in a subsequent compression test, often called compression-after-impact (CAI) test, could cause significant strength reduction. In particular, invisible internal delamination in an impacted panel may further propagate in compressive loading. It is really not surprising that impact damage, consisting of both material degradation and geometric change, has been found to be most detrimental to the in-plane compressive behaviour when compared to other preconditions such as voids, holes and embedded delamination [1]. Therefore, it is very important to understand the in-plane compressive behaviour of such impact-damaged as well as intact laminated panels.

In this paper, both intact and impact-damaged laminated panels under compressive loading are investigated with a purpose-built anti-buckling support. The associated damage mechanisms are closely examined with the back-to-back strain gauge readings from selected locations so that the factors controlling their initiation and propagation can be identified. Particular attention is focused on the likelihood of further propagation of impact-induced delamination under compressive loading.

DESIGN CONSIDERATIONS OF CAI TEST METHODOLOGY

The existing CAI test methods [2–5] have been designed for specific laminate systems of certain laminate thicknesses with different support strategies. While the former three methods are primarily for relatively brittle carbon fibre-reinforced laminates less than 6.4 mm thick and uses an edge clamping support strategy, the latter is mainly for glass fibre-reinforced laminates of more than 10 mm thick and uses the near-edge surface simple support strategy [5]. This technique is particularly necessary in the consideration of the fact that the present large thick impacted woven roving laminated panels not only suffer stiffness reduction, thereby reducing buckling resistance, but also show a certain amount of localised 'dishing', in addition to some inherent fibre waviness, so that they are prone to global buckling without proper support.

Unlike a material property-oriented compression test in which the gauge length and width of a specimen are often selected so as to avoid specimen instability during testing without anti-buckling support. The size of CAI test panels with reference to the delamination area has a significant influence over its compressive strength. The choice of panel dimensions for these thick laminates is completely governed by a trade-off among four factors, namely desire for large enough impact testing area to cover a delamination of unknown size associated with the maximum IKE, buckling load, uniaxial compressive strength (UCS) and load capacity of the available testing machine. This complex coupled situation stems from the fact that the CAI panel dimensions are very much constrained by the dimensions of impact specimen which are chosen in the consideration that they are large enough to well contain the greatest delamination area generated by a given maximum IKE, which in turn is unknown before an impact test is even conducted. In other words, once the dimensions of impact specimen are chosen, the maximum possible dimensions of a CAI panel is very much bounded. If impact tests carried out at the maximum IKE generate the size of delamination area reaching the periphery of testing area, it is not possible for the CAI panel to contain such a delamination area. Moreover, as the testing of unimpacted panels with identical dimensions is essential to providing reference values, a panel width thus has to be narrow enough not only for the thinnest unimpacted panel to fail in compression before buckling but also for the thickest unimpacted panel to fail at a load level which is within the load capacity of the available testing machine. It is against this background that the current CAI test methodology was developed.

COMPOSITES AND EXPERIMENTAL PROCEDURES

Panels are made of woven roving E-glass/polyester and S-glass/phenolic laminate systems both with a nominal fibre volume fraction of 60%. While the former has nominal thicknesses of 10 and 25 mm, the latter has nominal thicknesses of 14 and 19 mm. For both types of laminate systems, their interlaminar shear strengths are only one-sixteenth and one-tenth of their com-

pressive strengths, respectively, which in turn are less than their tensile strengths.

A circular plate of 500 mm diameter testing area was used for impact testing. Low-velocity and high-energy impact tests with an IKE range of 334–3000 J were carried out using an instrumented drop-weight test rig. The detailed examination of impact response, damage mechanisms and their energy-absorbing characteristics is given in Refs [6–11]. Delamination and fibre shear-out are found to be dominant damage mechanisms. Because of the nature of woven roving fabric fibre reinforcement in a single ply, the current thick laminates are more likely to yield a single delamination than that made of unidirectional prepregs, especially at relatively low to medium IKE within the present range. Obviously, at high IKE, more than one delamination could be observed, especially when IKE is sufficient enough to induce ply shear out.

Rectangular panels of 350 mm long by 250 mm wide were extracted from a 500 mm diameter impact-damaged circular plate. In order to avoid end-brooming and to enhance stability, both ends of each panel is potted using epoxy and then the potted ends are carefully machined to be parallel to each other. An anti-buckling support fixture was used to avoid the global buckling of the panel at the initial stage of loading. The central mechanism of the anti-buckling support fixture, as shown schematically in Fig. 1(a), consists of two pairs of simple movable steel plates with a cylindrical edge on the support side. These two pairs of plates are oriented such that they are normal to the surfaces of laminated panel and are parallel to the loading direction. Two support plates on the same side are 180 mm apart along the panel length and are 5 mm short of the end pots at each end to allow for panel compression. Bolts on the support fixture drive the support plates to the panel surfaces and were finger-tightened only in each test. Loading was directly introduced to both ends of the panel through a 250-ton panel tester at a constant speed of 1 mm/min. In order to predict dominant failure mechanisms, three pairs of back-to-back strain gauges were bonded to a number of selected locations as shown in Fig. 1(b) for impact-damaged panels and their data presented in terms of bending (difference of two back-to-back strain gauges) and mean (average of the two) strains against loads were used to deduce the characteristics of failure modes such as global buckling, delamination opening, global/local mechanism and kink-band shear (see Fig. 7). The linear variable displacement transducers (LVDT) were used to measure both end shortening and lateral deflection at the centre of panel. A total of either seven or nine pairs of back-to-back strain gauges were used to characterise the behaviour of undamaged panels.

TEST RESULTS AND DISCUSSION

Undamaged laminated panels

Testing of undamaged laminated panels provides not only reference compressive strength values needed in later stages for gauging an amount of strength reduction of damaged panels as mentioned earlier, but also an important physical insight into the complex panel behaviour during compressive loading. It is anticipated that examination of back-to-back

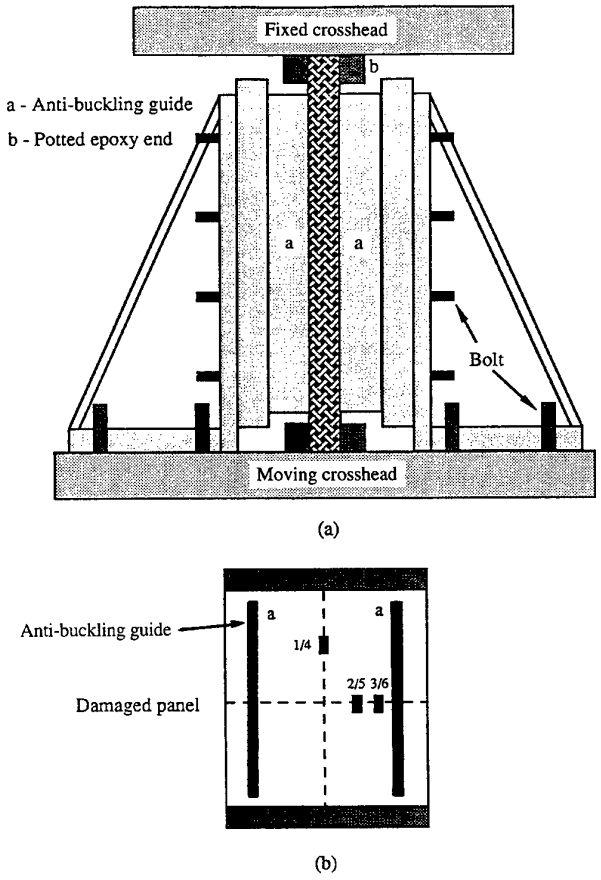

Fig. 1. (a) Experimental setup for CAI test. (b) Strain gauge locations on CAI panel.

strain gauge readings facilitates the understanding of a state of stress within a panel without the interference of impact damage.

The compressive load is applied to a laminated panel by uniformly displacing its potted ends as illustrated in Fig. 1(a). Obviously, when a panel is not damaged, the distinction between displacement and stress loadings is not necessary. The anti-buckling support plates are placed on the panel surfaces 90 mm away from the longitudinal axisymmetric axis and 5 mm short of each end pot as illustrated in Fig. 1(a) and (b). Thus, the panel is free to move both longitudinally and transversely in the panel plane. It is also free to deform in the out-of-plane direction but is constrained only along the tiny contact areas underneath the support plates which is hence analogous to a frictionless hinge. Since the support plates are gently tightened to the panel surfaces using fingers, a small out-of-plane displacement (say about 0.25 mm) underneath the support plates is not entirely impossible in practice, especially in consideration of the inherent uneven surfaces of woven fabric laminates. This implies that the anti-buckling support plates are believed not to distort the major characteristics of panel behaviour.

Figure 2(a) and (b) shows that the variation of both bending and mean strains with compressive loading from a 25 mm thick E-glass/polyester laminated panel. It can be observed that stress distribution along the panel width is reasonably uniform as the mean strains of all seven pairs of back-to-back strain gauges are virtually indistinguishable and slight bending from one end (pairs 1/8 and 2/9) seems to have occurred at the initial stage of loading, although it soon became stable until the final failure. A tiny twist at the other end is also indicated. In Fig. 3, compression failure with a kink shear band is readily observed. It was not surprising

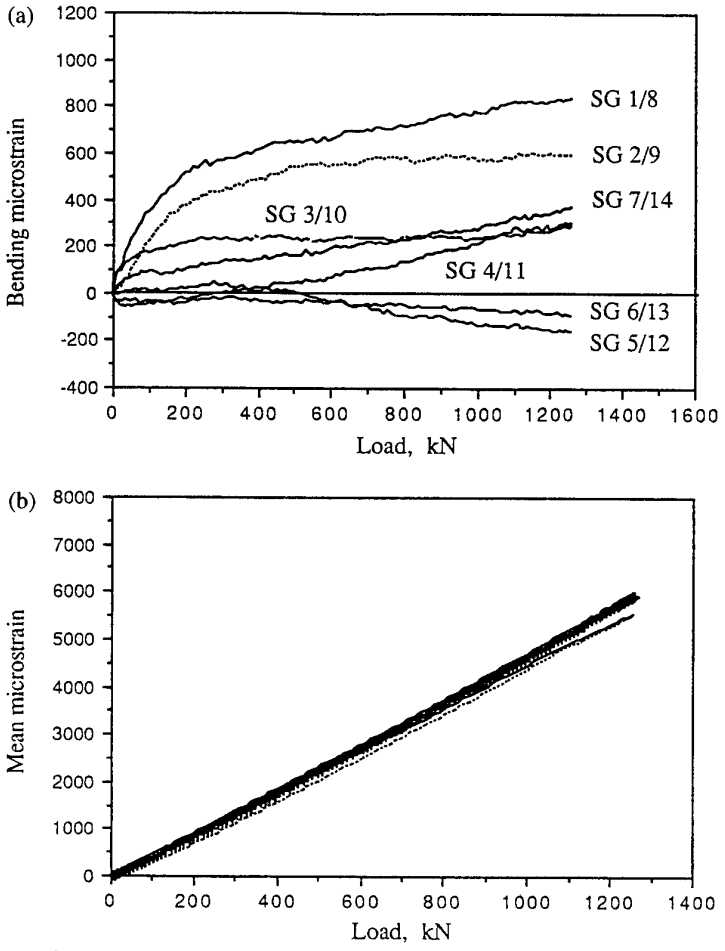

Fig. 2. (a) Load–bending strain curves and (b) load–mean strain curves of virgin panel test in 25 mm glass/polyester laminate.

that failure occurred near one of the ends where stress concentration usually develops for an undamaged laminated panel.

It is also interesting to mention that, although the axial compressive strain at failure of about 1% is identical to that measured in an intrinsic property test using an ICSTM method [12], the present compressive strength of 195 MPa is 25% lower than UCS from the latter test.

Impact-damaged laminated panels

Impact damage present in CAI panels has both local and global effects [5,13] which may be related to the failure mechanisms of CAI panels in compression. The local effect comes collectively from some of matrix cracking, fibre/matrix debonding, surface microbuckling and fibre breakage (including both shear-out and tensile fracture for some panels), all surrounding the slightly dented local impact contact area. The projected area on the distal surface through the thickness with about a 45° shearing angle provides a slightly larger area. It is expected that breaking of load-bearing fibres leads to the reduction of residual compressive strength. However, the other local damage mechanisms distributed through the thickness result in local changes in fibre curvature so that they are also likely to contribute to the initiation of local compression failure by shear with a kink band. On the contrary, the global effect from single or multiple internal delaminations spreads outside the shear-coned region. The existence of such delamination(s) divides effectively the laminate in the delaminated region into two or more sublaminates so that the flexural stiffness of these sublaminates is significantly reduced. As a result, these sublaminates with increased buckling possibility may buckle or open up, facilitating a panel failure at a load level that is considerably lower than that of an unimpacted panel. Moreover, it is of even greater concern to find out whether or not such delamination will further propagate under compressive loading, which would be an additional menace. To this end, comparing the relative magnitudes of strain readings from three pairs of back-to-back strain gauges provides us an important physical insight into such development.

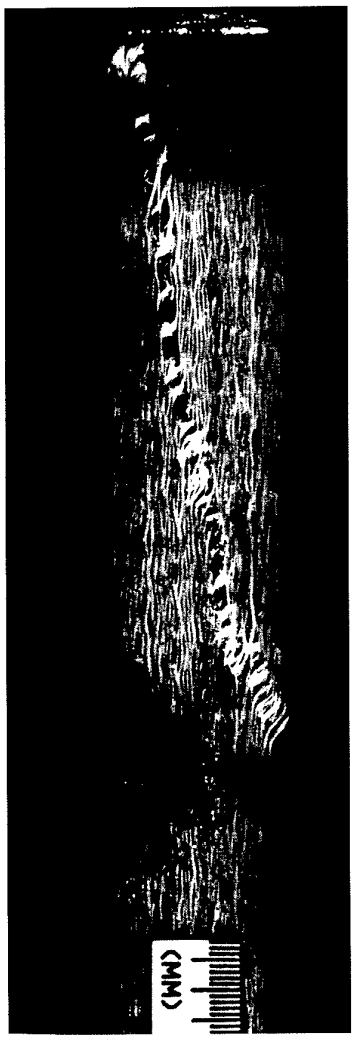

Fig. 3. Compression failure of 25 mm thick E-glass/polyester intact panel with kink shear band.

Figure 4(a) and (b) shows both load–bending strain and load–mean strain curves of three pairs of back-to-back strain gauges from a damaged 10 mm E-glass/polyester panel. Assuming a circular shape (which is almost justifiable as shown in Fig. 6(a) of Ref. [8] and in Fig. 6 of Ref. [13]), the delamination area of 8961 mm^2 is then converted to a circle of 107 mm in diameter, as shown in Fig. 4(a). When all three bending strains are either greater or smaller than three mean strains, respectively, a panel would experience either global buckling or delamination opening accordingly. Therefore, two other failure mechanisms are bounded by these two extreme cases. All four cases are illustrated in Fig. 7. Examining the strain gauge pair 1/4 indicates that global buckling did not occur until failure was approached. The fact that both bending and mean strains of the strain gauge pair 2/5 are relatively large suggests that the local buckling and delamination opening could occur simulta-

neously. Further examination of bending and mean strains of the strain gauge pair 3/6 still shows that both were taking place so that slight sideways propagation was possible. However, the permanent change of local fibre curvature and more severe local damage of the impact side makes a CAI panel completely unsymmetrical locally, thereby undoubtedly favouring a local buckling. This is confirmed by a photograph of the failed CAI panel in Fig. 6(a) showing compression failure with a kink shear band. The local delamination opening is also visible.

In Fig. 5(a) and (b), similar strain gauge responses are presented from a damaged 14 mm S-glass/phenolic panel. Judging from the developing trend of strain gauge pairs 2/5 and 3/6, local buckling and delamination opening might again have occurred simultaneously. Moreover, examining the strain gauge pair 1/4 also indicates some global buckling. The final panel failure is shown in Fig. 6(b) with a clear kink band. This, in conjunction with all three pairs of strain gauge readings, suggests that the CAI panel twisted during loading in the form of the second buckling mode.

Photographs in Fig. 6(c) and (d) show typical failed thicker CAI panels from both E-glass/polyester and S-glass/phenolic systems. The only difference here is that these thicker panels have multiple delaminations so that each sublaminate fails in compression through its own kink shear band. Therefore, adjacent kink bands may coalesce to form a major one, albeit not all the way through from one surface to the other as shown in Fig. 6(c). The other noticeable features are that the E-glass/polyester panel has a much greater shear angle formed between loading direction and the kink band than not only the undamaged E-glass/polyester panel but also the S-glass/phenolic panel, and that its kink band is more rugged than that of the latter, probably due to severe interference of the local damage. As a whole, it seems that CAI panels fail pre-

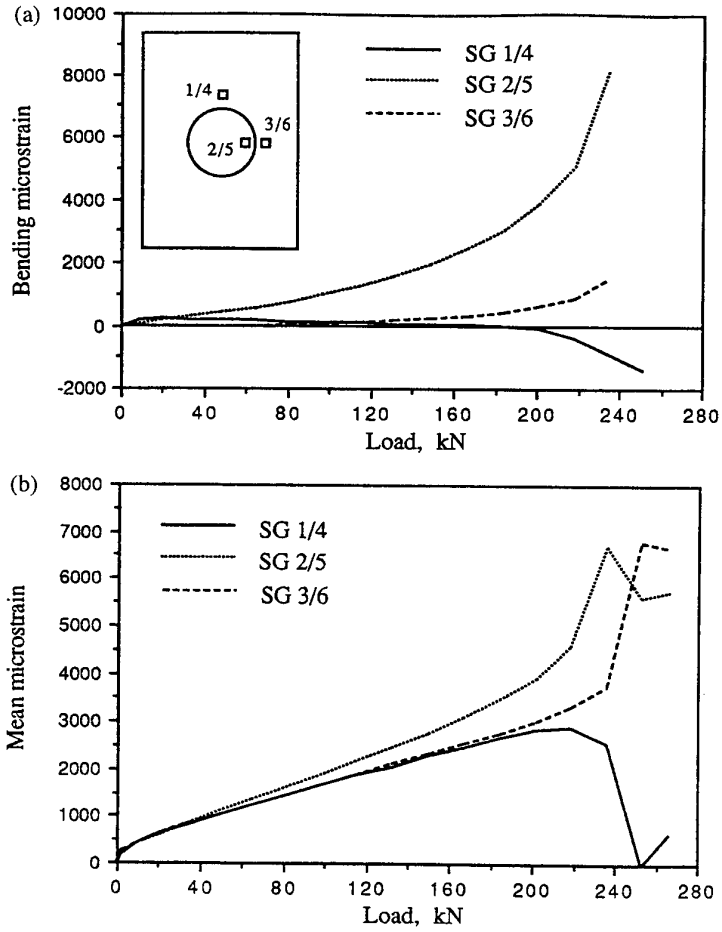

Fig. 4. (a) Load–bending strain curves and (b) load–mean strain curves of CAI test for 10 mm glass/polyester laminate.

dominantly in compression with a kink shear band developed around the mid-section.

Figure 7 summarises the qualitative variations of bending and mean strains corresponding graphically to all four failure mechanisms of CAI panels as discussed above.

CONCLUDING REMARKS

Both intact and impact-damaged laminated panels under in-plane compressive loading are investigated with a purpose-built anti-buckling support. The readings of back-to-back strain gauges of selected locations are used to deduce panel behaviour in addition to post-mortem observation. The compression failure of intact panels is found to be close to the potted end. The failure characteristics of impact-damaged panels are dependent slightly on composite systems though they all failed in compression in the impact-damaged region with a kink shear band passing through the mid-section. E-glass/polyester panels with a greater shear angle do not seem to involve global buckling like S-glass/phenolic panels with small shear angle. The fact that the region a kink shear band covers from impact surface to the distal surface is considerably less than the delamination area suggests that the initiation of overall failure is due to the collective result of flexural stiffness reduction compounded by the local impact damage and the associated change of fibre curvature. As a result, the residual compressive strengths are reduced significantly. Further outward propagation of the existing delamination(s) along the mid-section during loading is visible only for E-glass/polyester panels but is not significant.

ACKNOWLEDGEMENTS

The experimental work was carried out at the Imperial College under the supervision of Prof.

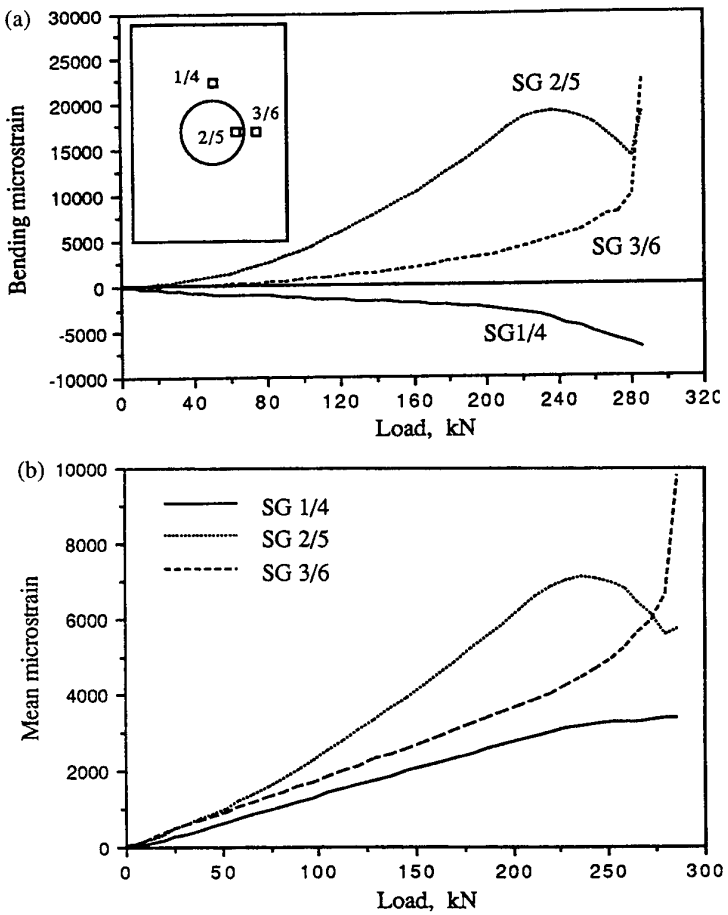

Fig. 5. (a) Load–bending strain curves and (b) load–mean strain curves of CAI test for 14 mm glass/phenolic laminate.

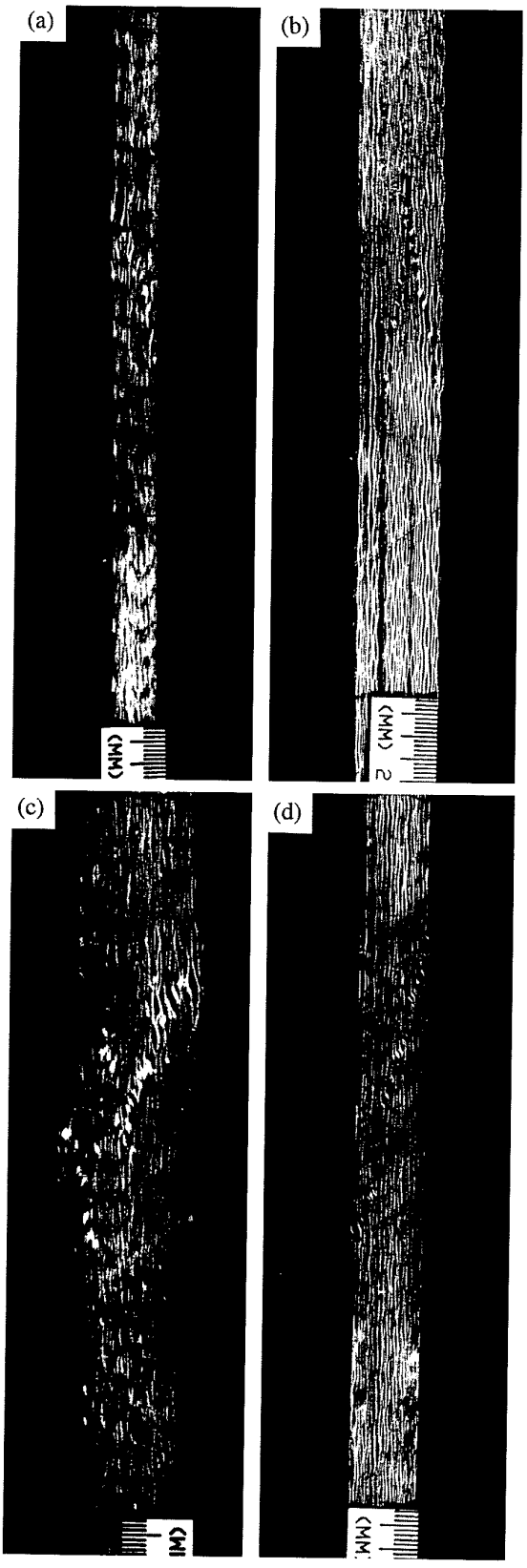

Fig. 6. Compression failure of (a,b) thin and (c,d) thick CAI panels with kink shear band from (a,c) E-glass/polyester and (b,d) S-glass/phenolic systems.

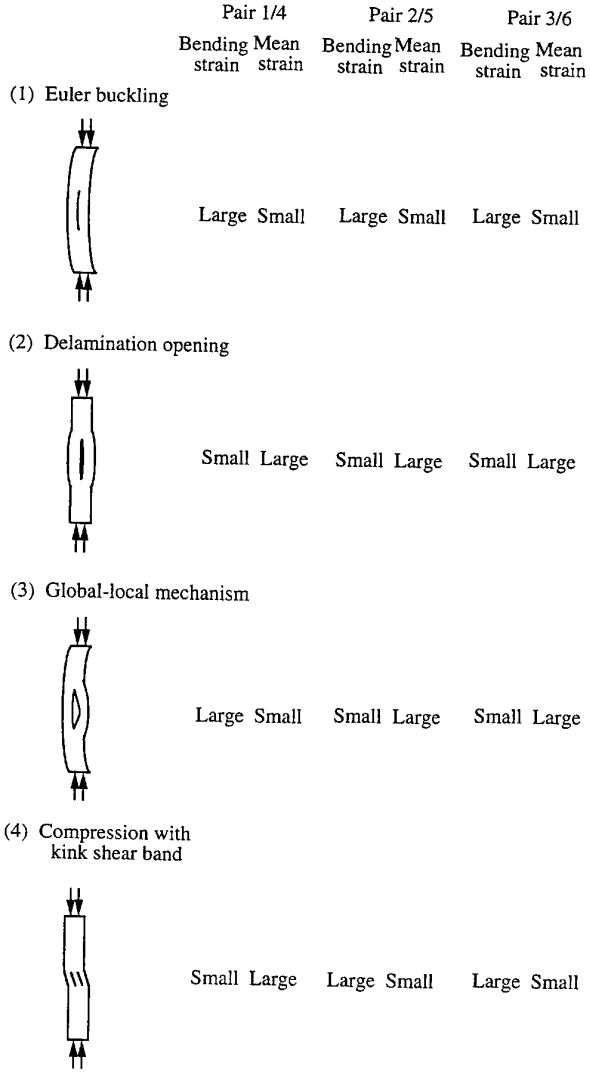

Fig. 7. Prediction of failure mechanisms of damaged laminated panels in CAI test using back-to-back strain gauges.

G. A. O. Davies with the financial and materials support from DRA UK, under contract no. 2037/377.

REFERENCES

1. Horton, R. E. and McCarty, J. E., Damage tolerance of composites. in *Engineering Materials Handbook*, Vol. 1, ASM, 1987, pp. 259–267.
2. Horton, R. E. and McCarty, J. E., Advanced composite compression tests. *Boeing Specifications Support Standard*, Boeing Aircraft, Vol. 7260, 1982.
3. Horton, R. E. and McCarty, J. E., NASA/aircraft industry standard specification for graphite fiber/toughened thermoset resin composite material. *NASA RP*, Vol. 1142, 1985.
4. Horton, R. E. and McCarty, J. E., SACMA, Recommended Method SRM 2-88, 1988.
5. Zhou, G. and Davies, G. A. O., Damage tolerance of thick glass fibre reinforced laminate structures sub-

jected to low-velocity impact. *Proc. ASME-WAM, MD*, 1994, **51**, 237–262.
6. Zhou, G. and Davies, G. A. O., Impact response of thick glass fibre reinforced polyester laminates. *Int. J. Impact Engng*, 1995, **16** (3), 357–374.
7. Zhou, G., Damage mechanisms in composite laminates impacted by a flat-ended impactor. *Composites Sci. Tech.* , 1995, **54** (3), 267–273.
8. Zhou, G., Prediction of impact damage thresholds in glass fibre reinforced laminates. *Composite Structures*, 1995, **31**, 185–193.
9. Zhou, G., Impact velocity effect on damage in laminated composites. *Proc. 7th ECCM High Performance Composites*, London, Vol. 1, 1996, pp. 117–127.
10. Zhou, G., Impact damage resistance of thick glass woven roving fibre reinforced composites-geometric effects. *Proc. Int. Conf. on Advanced Materials*, Beijing, 1996, pp. 784–789.
11. Zhou, G., Characteristics of impact energy absorption during damage development in laminated composites. *Proc. 4th Deformation and Fracture of Composites*, Manchester, 1997, pp. 55–67.
12. Zhou, G. and Davies, G. A. O., Characterisation of thick glass woven roving/polyester laminates: Part I, tension, compression and shear. *Composites*, 1995, **26** (8), 579–586.
13. Zhou, G., Effect of impact damage on residual compressive strength of GFRP laminates. *Composite Structures*, 1996, **35** (2), 171–181.

ELSEVIER

Composite Structures Vol. 38, No. 1–4, pp. 599–607, 1997
© 1997 Elsevier Science Ltd. All rights reserved
Printed in Great Britain
0263-8223/97/$17.00 + 0.00

PII:S0263-8223(97)00098-6

Size effects in thin CFRP panels subjected to impact

M. S. Found, I. C. Howard & A. P. Paran

Department of Mechanical Engineering, University of Sheffield, Mappin Street, Sheffield S1 3JD, UK

The static indentation and impact behaviour of three- and nine-ply CFRP panels circularly clamped with rings of 100 and 300 mm diameter have been evaluated. The maximum static force is similar for small and large panels for both three- and nine-ply laminates. Increasing the panel size of the three-ply laminates subjected to impact only appears to affect the threshold of perforation. For the nine-ply laminates an increase in panel size produced a reduction in delamination area and backface cracking. Interpretation of energy maps is suggested as a means of identifying when the peak impact force has occurred and the threshold of perforation. © 1997 Elsevier Science Ltd.

INTRODUCTION

The increasing use of composite materials in aerospace structures is producing a demand for more competitive designs and a reduction in manufacturing costs. Previously, full-scale components and structures have often been fabricated and tested as part of the design evaluation phase. This is both expensive and time-consuming, and alternative routes are required if composite materials are to compete with developments in advanced metallic alloys. One way forward is to undertake model simulation techniques as a means of predicting the behaviour of large components and structures. However, for composite structures subjected to varying levels of impact damage the issues are not straightforward. For example, similar structures, except for differences in size, may react quite differently when subjected to similar impact energies due to the complex interaction of the various fracture processes such as indentation, matrix cracking, delamination or fibre fractures. Therefore, initially, a more useful way forward is a combination of experimental evaluation of some of the scaling effects in order to enhance modelling methods.

The scaling effect of FRP composites subjected to impact loading has been considered by a number of workers using a dimensional analysis approach. Morton [1] showed that scaling laws may be applied to the elastic behaviour of undamaged carbon–epoxy beams. However, he identified difficulties in trying to satisfy the requirements for rate-sensitive and notch-sensitive materials. Impact tests on different sizes of carbon–epoxy plates by Qian *et al.* [2] also showed that scaling rules may be used to describe the undamaged response. In addition, they suggested that damage in terms of delamination area scales in agreement with fracture mechanics concepts. Wu and Springer [3] have identified a procedure for predicting the location and size of delaminations in carbon–epoxy plates subjected to impact using a fracture mechanics approach. Robinson and Davies [4] have shown that increasing the size of GRP specimens increases the impact energy to cause the same damage signature, and suggested that a damage energy approach may be used to predict the impact energy to produce a similar response in a different sized specimen. Davies and Zhang [5] have suggested that scaling effects in absorbing elastic energy may be removed by recognizing the different effects of damage in flexible and rigid plates. For the former, large bending strains produce tensile failure of the backface whilst a significant impactor force gives rise to matrix cracking and delamination in thicker rigid plates. Davies and

Zhang [5] showed that force maps may be used to predict initiation of delamination in terms of maximum force for a particular thickness of carbon–epoxy plates subjected to impact.

The overall aim of our programme of work on impact behaviour of FRP composites is to study the effect of static indentation, and single and repeated impacts on plain and stiffened panels, and to assess their damage tolerance. This paper reports our preliminary findings on the effect of panel size on the static indentation and impact behaviour of thin, plain CFRP panels.

EXPERIMENTAL

The material was a five-harness satin weave carbon fibre–epoxy resin supplied in prepreg sheets by Ciba-Geigy, designated 914C-713-40. The panels were laid up as three-ply (0°/90°, ±45°, 0°/90°) and nine-ply (0°/90°, ±45°, $0°/90°)_3$ laminates and autoclave moulded by Hurel-Dubois UK (Burnley, UK) to a thickness of 0.96 and 2.83 mm, respectively, at a nominal 58% fibre volume fraction. The quality of the laminates was assessed by Hurel-Dubois using the ultrasonic c-scan technique.

An instrumented dropweight impact rig, briefly described in Kumar *et al.* [6], was used for both static indentation tests and single impact tests. The test rig has recently been modified to permit the clamping of panels between two annular rings ranging from 100 to 300 mm internal diameter and also to accommodate stiffened sections [7]. Static indentation tests were performed on three- and nine-ply laminates using clamping rings of 100 and 300 mm internal diameter. Indentation was determined by measuring the difference between the upper and lower laminate surface displacements beneath the hemispherical indentor of 12 mm diameter. Electrical resistance strain gauges mounted on the indentor measured the applied load in terms of strain.

Dropweight impact tests were conducted from a height of 0.5 m for all tests, whilst the mass was varied to produce a range of incident impact energies. Impact tests were carried out on three- and nine-ply laminates up to perforation with annular clamping of 100 mm internal diameter. For the three- and nine-ply laminates clamped with 300 mm internal diameter annular rings only a few tests have been performed to date. The impact forces and displacements were obtained from data that were processed through a low-pass filter at a cut-off frequency of 3.5 kHz.

As this is a preliminary investigation into the scaling effects of thin CFRP panels, no attempt was made to undertake true scaled testing. However, for both static indentation and impact tests clamping of the laminates was to the same ring pressure for both 100 and 300 mm annular rings. In addition, the impact tests were conducted from a constant height to produce an impact velocity of the impactor of approximately 3 m/s.

Damage was assessed after the impact tests using X-radiography and microscopy techniques in order to determine the principal failure mechanisms of delaminations, backface cracking and permanent indentation of the frontface.

RESULTS

The results for static indentation of three- and nine-ply laminates when circularly clamped at 100 and 300 mm diameter are summarized in Table 1. The force to produce initiation of damage in the panels was consistent with the first small reduction in force on the force–displacement curves. In all cases the peak force was sustained over an indentor displacement of approximately 2 mm. For the 100 mm panels there was then a gradual reduction in force with increasing displacement, whilst for the 300 mm panels there was a rapid reduction in force leading to perforation of the laminates for both the three- and nine-ply laminates.

Some typical force–time responses for impact loading of undamaged panels in Fig. 1, and those for damaged panels are shown in Figs 2

Table 1. Summary of static indentation tests

Laminate	Three-ply		Nine-ply	
Panel diameter (mm)	100	300	100	300
Initial damage force (N)	400	430	2100	2150
Maximum force (N)	550	600	2700	2750

and 3. Whilst the force–time histories of the undamaged panels are of different incident impact energies, due to the greater threshold of damage initiation in the nine-ply laminate, the responses clearly identify the different behaviour of the very thin three-ply laminate. The influence of panel size is shown in Figs 2 and 3 for the three-ply and nine-ply laminates, respectively. Comparisons are made at incident kinetic energies associated with the estimated threshold of perforation, which for the 100 mm diameter panels was 2.35 and 11.4 J, respectively, for the three- and nine-ply laminates.

For the three-ply panels of 100 mm diameter the average peak impact force was 510 N and it first reached this value at an incident kinetic energy of 1.13 J. Up to the threshold of perforation of the laminate further increase in mass produced more damage and increased the impact duration and the duration of the peak force. At energies beyond the threshold of perforation the impact duration shortened and large oscillations in the accelerometer signal were observed, thought to be caused by the influence of the damaged material on the back-face on the motion of the impactor.

For the nine-ply panels of 100 mm diameter the average peak force was approximately 3500 N, which corresponds to a minimum incident kinetic energy of 5.4 J. The behaviour up

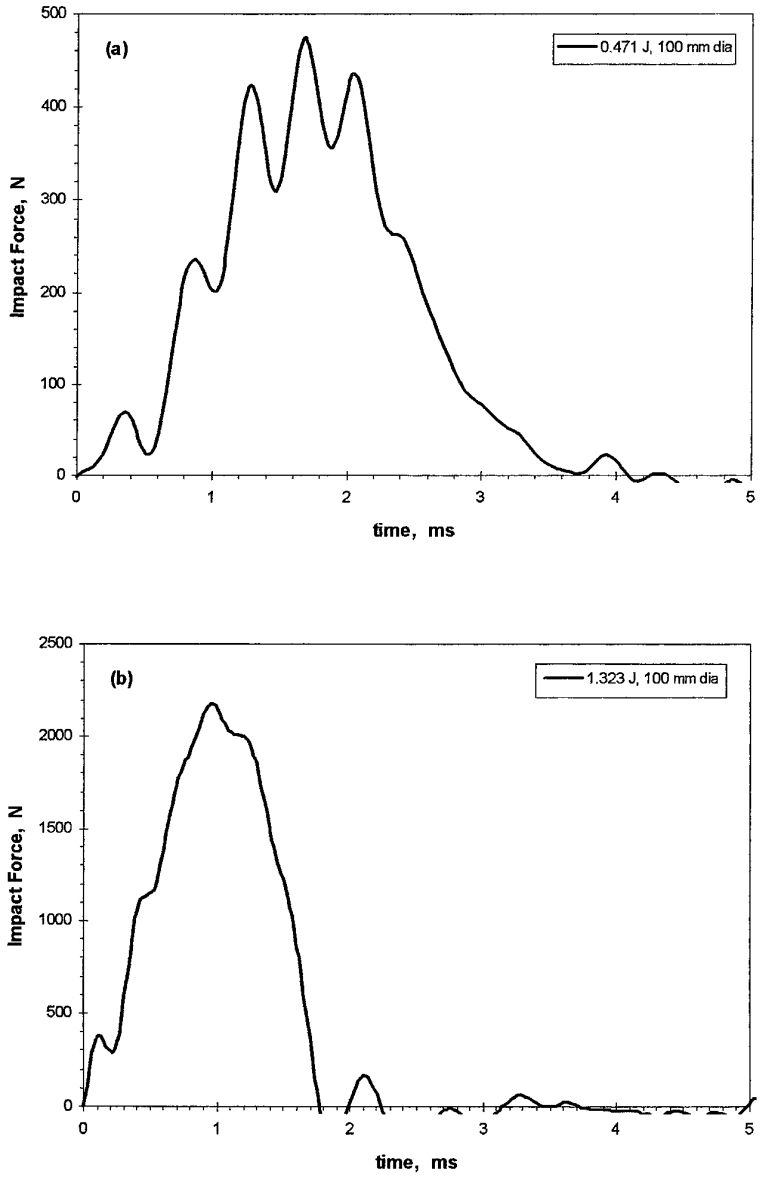

Fig. 1. Force–time histories for undamaged 100 mm diameter panels for (a) three-ply and (b) nine-ply laminates.

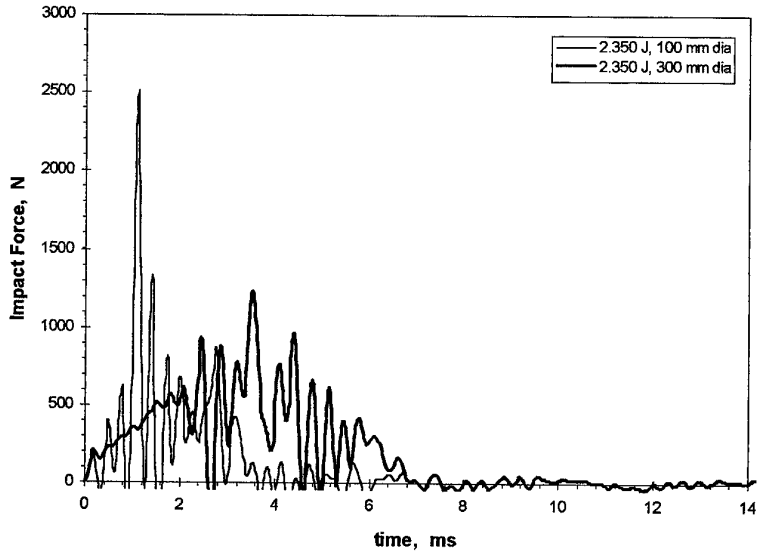

Fig. 2. Force–time histories for damaged three-ply laminates for 100 and 300 mm diameter panels.

to the threshold of perforation was similar to that for the three-ply material. However, beyond the threshold of perforation the magnitude of oscillations was far greater in the nine-ply material, thought to be due to the higher panel inertia and stiffness which together with the larger mass excites a greater dynamic effect.

Damage plots of increasing incident kinetic energy are presented in Figs 4–6 for permanent indentation of the frontface, crack length in the backface and projected delamination area, respectively. On this occasion smooth curves have been drawn through the data in order to identify trends and for ease of comparison with the limited data for the larger 300 mm diameter panels. In Fig. 4 the arrow indicates the kinetic energy at or near the threshold of perforation of the laminate. Permanent indentations greater than the laminate thickness were observed as the relative low velocity of these impacts cause extensive local damage of the backface, pushing out broken material prior to perforation of the laminate by the impactor. It is interesting to note that for the three-ply laminate the data for the 300 mm diameter panels appear to fall on

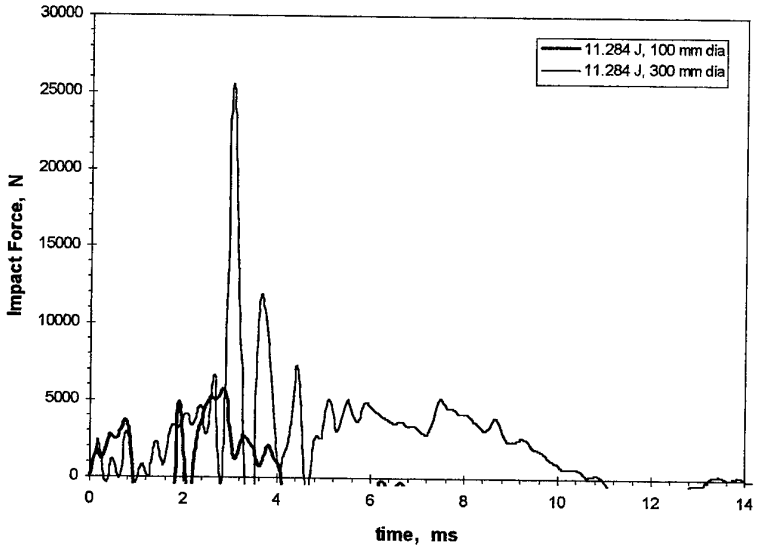

Fig. 3. Force–time histories for damaged nine-ply laminates for 100 and 300 mm diameter panels.

the same extended curve as for the 100 mm diameter panels. For the nine-ply laminates it may be fortuitous that the test at the higher impact energy for the 300 mm panel falls on the extended curve for the data for the smaller panel.

In a previous paper [7] we have reported backface cracking in terms of the largest cracks which occur in the 90° direction for this material. However, significant cracking also occurs in the 0° direction. In Fig. 5 we present the total backface crack length by summing the major crack lengths in both the 0° and 90° directions. This is justified because crack propagation in both principal directions contributes to the absorption of impact energy. Furthermore, there appears to be less scatter in the data when presented on a basis of combined crack length. The shape of the curves are significantly different for the three-ply and nine-ply laminates. As cracking of the backface is associated with tensile bending stresses there are additional membrane stresses in the thin three-ply laminate. The horizontal line indicates that the threshold of perforation has been reached such that further increases in energy produce

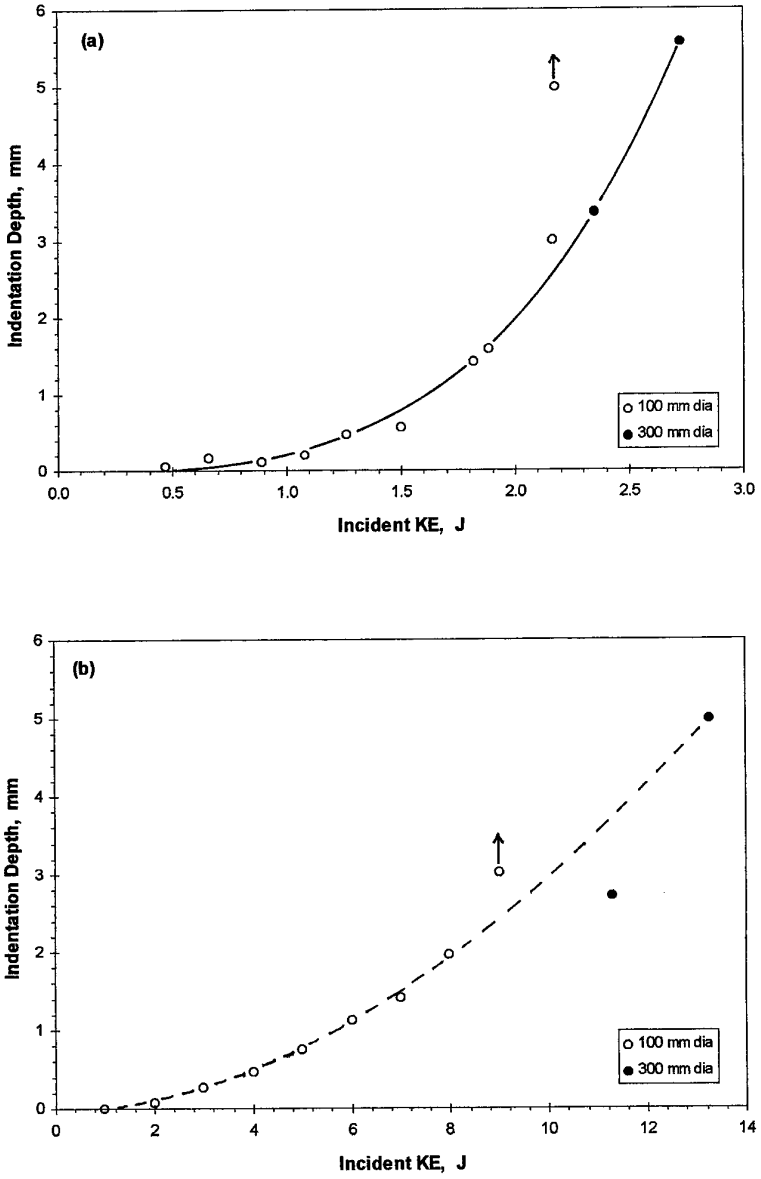

Fig. 4. Permanent indentation of the frontface for (a) three-ply and (b) nine-ply laminates.

no increase in crack propagation. The influence of increasing panel size suggests that crack length may be less than that for small panels, although the impact test at the lower energy level for the 300 mm diameter three-ply laminate appears to be similar to that for small panels.

Figure 6 suggests that in terms of delamination area there is little difference in behaviour with increasing panel size. Whilst a smooth curve fits the data up to perforation of the laminates it clearly masks the changing mechanisms suggested by the dotted line.

DISCUSSION

For the thin three-ply panels of 100 mm diameter the average peak force during impact loading was similar to the maximum force sustained during static indentation. This was expected because these panels have a relatively low inertia. However, for the thicker nine-ply panels of 100 mm diameter the average peak force was significantly higher than that observed during static indentation and, furthermore, there was considerable scatter in the data. For these panels inertia and dynamic effects are sig-

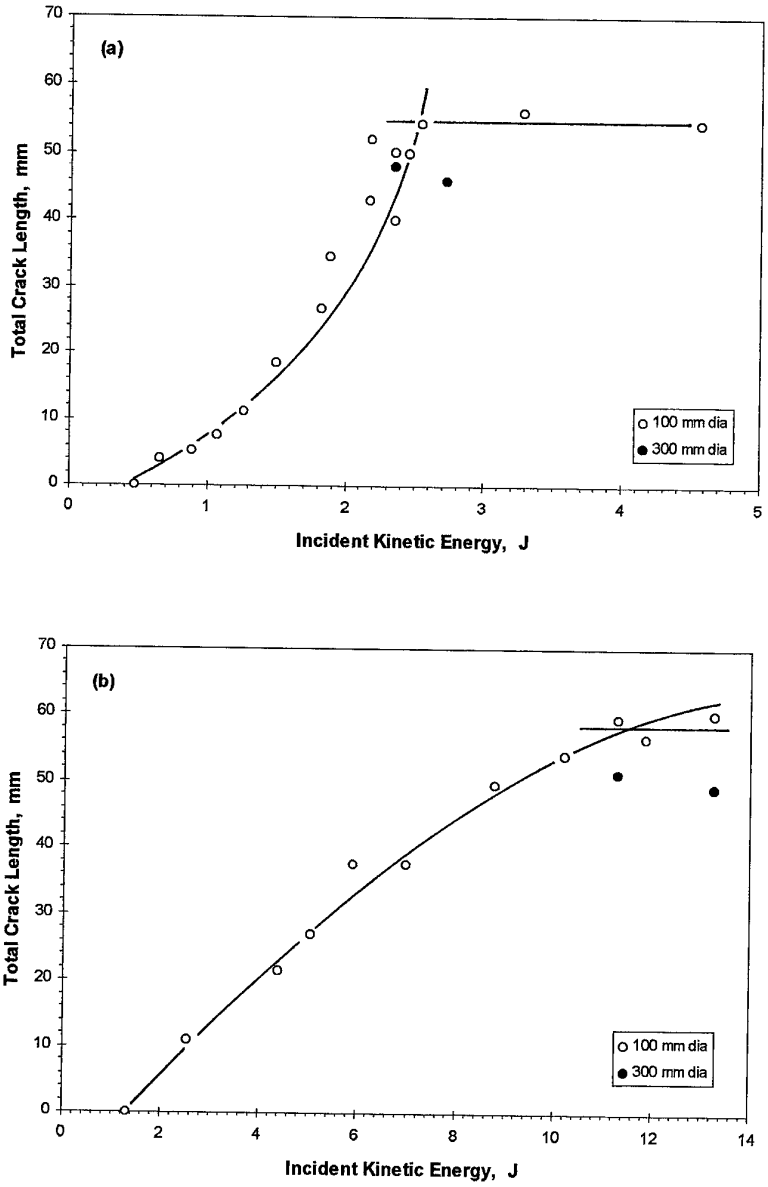

Fig. 5. Total backface crack length for (a) three-ply and (b) nine-ply laminates.

nificant and hence peak loads are much higher during impact than static loading. An increase in panel size from 100 to 300 mm diameter only gave a relatively small increase in the maximum static force of $<10\%$ for the three-ply laminate and $<3\%$ for the nine-ply laminate, i.e. within the expected scatter of test data.

Whilst Davies and Zhang [5] have shown that damage initiation during impact is best represented in terms of force, we consider that energy is perhaps a better indication of changes in damage from initiation to perforation as after limited damage the average peak force is approximately constant. Furthermore, we have found that by careful inspection of energy maps it is possible to identify the minimum energy associated with the peak impact force and to determine the energy at the threshold of perforation. Both these events appear to correspond to changes in the rate of damage growth with increasing incident kinetic energy. Taking an average value from the damage maps for 100 mm panels shown in Figs 4–6 we determined that the minimum energy at which the peak impact occurs was 1.1 J for the three-ply laminate and 4.8 J for the nine-ply laminate

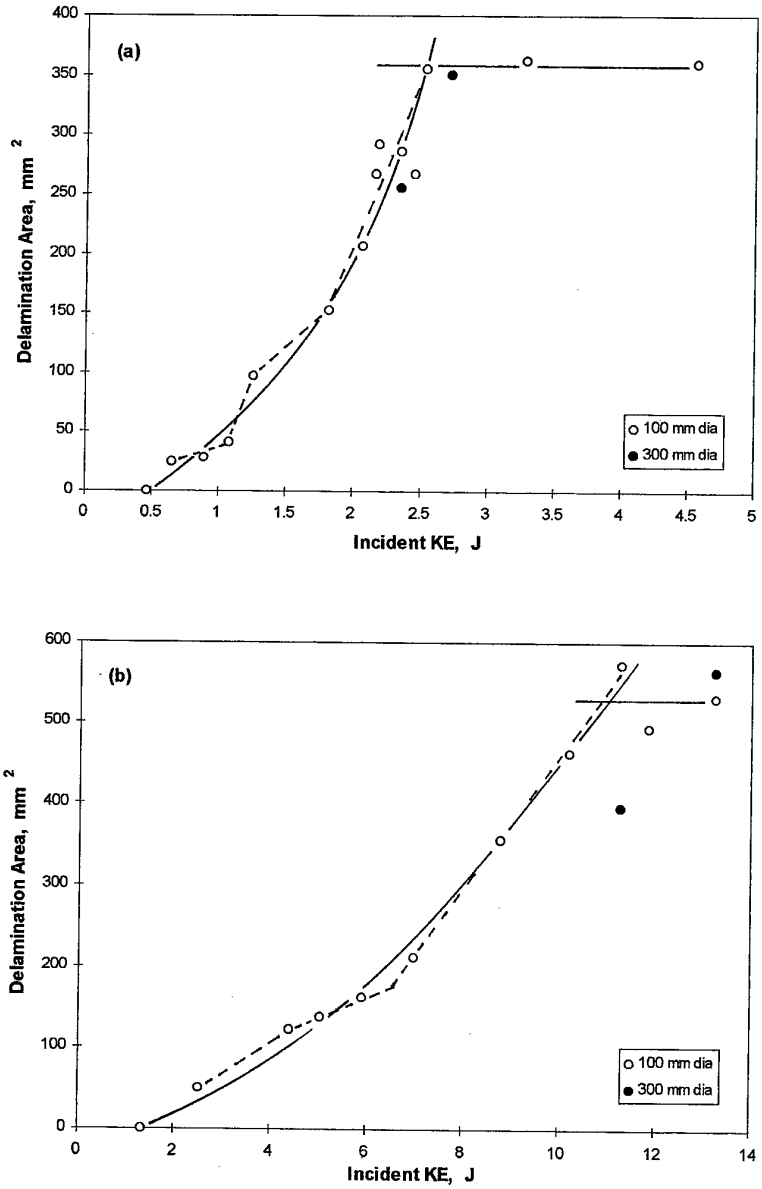

Fig. 6. Projected delamination area for (a) three-ply and (b) nine-ply laminates.

compared with values of 1.13 and 5.4 J, respectively, estimated from the plots of force vs energy. By inspecting the progress of damage in the laminates we earlier estimated the threshold of perforation to be 2.35 and 11.4 J for the three- and nine-ply laminates, respectively, for the 100 mm panels. The corresponding average values obtained from the damage maps were 2.43 and 10.5 J, however if we ignore the significantly lower value obtained from the indentation measurements for the nine-ply material we get a value of 11.3 J. For the 100 mm panels, the principal damage mechanisms initiated at a similar impact energy for the three-ply material. For the nine-ply laminates indentation was first observed at a slightly lower energy than for backface cracking or delamination.

For the limited tests on the larger 300 mm panels the results suggest that the increase in panel size does not appear to have much influence in terms of damage for the three-ply material except that the threshold of perforation will occur at higher energies. For the nine-ply laminates the increase in panel size suggests a reduction in backface crack length and delamination area at similar energies compared with the 100 mm panels. An increase in panel size produces a reduction in stiffness and hence reduced delamination would be expected. In addition, there will be increased membrane effects in the larger panels that control the backface cracking. Although tests in the larger panels were undertaken at energies to produce threshold perforation in the small panels there was no perforation observed in the larger panels.

For this preliminary investigation into scaling effects of thin CFRP panels subject to impact loading, it is only possible to draw a few tentative conclusions at this stage mainly due to the limited tests for 300 mm panels. These will be extended over a wider range of impact energies to more clearly identify the present trends. In addition, it is proposed to examine a six-ply laminate of the same material with a lay-up of $(0°/90°, 45°, 0°/90°)_2$ for which it will be possible to undertake scaled tests comparable with the nine-ply laminate using the present test rig. True scaled tests were not possible between the three- and nine-ply laminates because this would have required a significant reduction in mass applied to the three-ply laminates for which the existing carriage containing the impactor is close to its minimum mass. When these further tests have been completed we will be in a better position to modify our models and attempt to predict the behaviour of larger panels, as well as stiffened sections.

CONCLUSIONS

Whilst no specific scaling effects have been identified during this preliminary investigation we can offer the following comments. An increase in panel size from 100 to 300 mm diameter does not appear to affect the maximum static force for three- or nine-ply laminates. For the three-ply laminates, increasing the panel size has little influence on damage except that the threshold of perforation will be at a higher impact energy. For the nine-ply laminates, a reduction in delamination area and backface crack length was observed in the larger panels.

In addition we observed that combining the major cracks in the 0° and 90° directions gives a better indication of energy absorption for this material with reduced scatter. Analysis of the energy maps shows that the minimum energy at peak impact force and the threshold of perforation of the laminate can be clearly identified.

ACKNOWLEDGEMENTS

We wish to thank Hurel-Dubois UK for the supply of laminates.

REFERENCES

1. Morton, J., Scaling of impact-loaded carbon-fiber composites. *AIAA J.*, 1988, **26** (8), 989–994.
2. Qian, Y., Swanson, S. R., Nuismer, R. J. and Bucinell, R. B., An experimental study of scaling rules for impact damage in fiber composites. *J. Composite Mater.*, 1990, **24** (5), 559–570.
3. Wu, H-Y. T and Springer, G. S., Impact induced stresses, strains, and delaminations in composite plates. *J. Composite Mater.*, 1988, **22** (6), 533–560.
4. Robinson, P. and Davies, G. A. O., Impactor mass and specimen geometry effects in low velocity impact of laminated composites. *Int. J. Impact Engng*, 1992, **12**, 189–207.
5. Davies, G. A. O. and Zhang, X., Impact damage prediction in carbon composite structures. *Int. J. Impact Engng*, 1995, **16**, 149–170.
6. Kumar, M., Found, M. S. & Howard, I. C., A drop-weight instrumented impact test to compare the effect of single and multiple impacts on CFRP. In *Proc. 2nd*

Int. Seminar on Experimental Techniques and Design in Composite Materials, ed. M. S. Found. Sheffield Academic Press, 1995, pp. 84–101.

7. Found, M. S., Howard, I. C. and Paran, A. P., Impact behaviour of stiffened CFRP sections. *Composite Struct.*, 1997, in press.

ELSEVIER

Composite Structures Vol. 38, No. 1–4, pp. 609–622, 1997
© 1997 Elsevier Science Ltd. All rights reserved
Printed in Great Britain
0263-8223/97/$17.00 + 0.00

PII:S0263-8223(97)00099-8

The influence of reinforcement ring width on the buckling response of carbon fibre composite panels with circular cut-outs

J. Eiblmeier

Martec Ltd, Suite 150, 221 Chemin Freeman, Hull, Quebec J8Z 2A8, Canada

&

J. Loughlan

Department of Aerospace Technology, College of Aeronautics, Cranfield University, Cranfield, Bedfordshire MK43 OAL UK

This paper investigates the influence of cut-out diameter and the width of the circular reinforcement rings upon the buckling stability of square CFRP panels. The study undertaken at Cranfield University uses MSC/NASTRAN Finite Element Analysis (FEA) extensively for this investigation. The FEA results have been compared with results from practical tests and good agreement was found. Diagrams showing the influence of cut-out diameter and reinforcement ring width on the buckling stability of simply supported CFRP panels are presented. The results are shown for approx. 2 mm-thick $((\pm 45/0)_S)_S$ square CFRP panels with 0–50 mm wide reinforcement rings bonded around the central circular cut-outs. The panels are loaded in pure shear or in compression. The results presented can be used to find the optimum reinforcement ring width for square CFRP panels with central circular cut-outs. © 1997 Elsevier Science Ltd.

NOTATION

a: Panel length or width (square panels only) (mm)
t: Panel thickness (mm)
d: Cut-out diameter (mm)
t_R: Reinforcement ring thickness
E_L: Longitudinal material elastic modulus (N/mm^2)
E_T: Transverse material elastic modulus (N/mm^2)
E_x: Longitudinal lamina elastic modulus (N/mm^2)
E_y: Transverse lamina elastic modulus (N/mm^2)
G_{LT}: In-plane material shear modulus (N/mm^2)
G_{xy}: In-plane lamina shear modulus (N/mm^2)
υ_{LT}: Poisson's ratio of material
υ_{xy}: Poisson's ratio of lamina
L_o: Critical load under which buckling occurs in panel without a cut-out (N)
L_{cr}: Critical load under which buckling occurs in panel with a cut-out (N)
$[K_{aa}]$: Elastic stiffness matrix of structure
$[K^d_{aa}]$: Geometric (or differential) stiffness matrix of structure
$[K_n]$: Stiffness matrix of structure at non-linear load step n
ΔK: $= K_n - K_{n-1}$: Difference in stiffness matrix between nonlinear loading steps
λ_i: Eigenvalues

$\{u_a\}$: Displacement vector
Φ_{ai}: Eigenvectors

INTRODUCTION

Cut-outs are often required in structures for access, inspection or structural reasons. The stress concentration created by this disturbance in the load path and/or the requirement to increase the structural stability of these structures makes reinforcement of the cut-out often necessary. For the design of light weight structures, it is important to know the influence of the reinforcement on the structural behaviour and to know the most efficient type of reinforcement geometry.

Composite materials are increasingly used in the design of lightweight structures for their high stiffness to weight ratio. However, due to the relatively late introduction of composite materials compared to metal and the more complex behaviour under load due to the highly orthotropic material properties there is far less information available than for metal structures.

Thin composite panels with symmetrically (on both sides of the panel) reinforced cut-outs loaded in pure shear or compressive displacement behave linearly as long as the material allowables are not exceeded and the structure does not deflect out-of-plane. When buckling occurs, the loading type, panel boundary conditions and geometry of the panel and the reinforcement ring determine both the buckling behaviour and the shape and magnitude of the resulting out-of-plane deflections. If the load is further increased then the magnitude of the out-of-plane deflection increases until the material limitations are exceeded and first ply failure occurs.

This paper is intended to provide additional information about the influence of the reinforcement ring width on the buckling stability of square composite plates with central circular cut-outs loaded in uniform shear or uniaxial compressive displacement. Cut-out diameters of 0.1 and 0.25 times the length of the panel and circular reinforcement rings between 5 and 50 mm wide, have been considered in this investigation. The CFRP composite panels are manufactured from four layers of $(\pm 45/0)$ NCF fabric, resulting in approximately 2 mm thick $((\pm 45/0)_S)_S$ laminated panels. The reinforcement rings are equally manufactured from 2 mm thick $((\pm 45/0)_S)_S$ laminated panels. Following the results of previous investigations [1,2] indicating that the buckling mode is largely unaffected by the boundary panel boundary conditions, only the case of simply supported panel edges has been considered.

Finite Element analysis (NASTRAN) has been used to determine the bifurcation buckling load and the buckling shapes for the different configurations considered. Selected data points of the theoretical results were verified by comparison with data obtained from mechanical tests conducted. Reasonably good agreement between the FE analysis and the practical test results could be established.

LITERATURE REVIEW

In 1947, Levey *et al.* [3] published the first significant buckling analysis of a simply supported square metal plate with a reinforced central circular cut-out under uniaxial compressive loading. This early work is based on Timoshenko's [4] energy method for determining the buckling load of rectangular plates of constant thickness. Work by Kumai [5], Schlack [6,7] and Yoshiki *et al.* [8] followed in the 1950s and 1960s. The Rayleigh–Ritz energy method could be applied in these analyses. With the development of computers in the late 1960s it was then possible to find suitable functions which satisfy practical kinematic boundary conditions. Determination of the pre-buckling stress distribution is usually the most difficult part in using the Rayleigh–Ritz method. This is why Kawai [9] and Ritchie and Rhodes [10] used the Finite Element method to determine the pre-buckling stress distribution in an isotropic plate with a cut-out and then used the Rayleigh–Ritz method to find the buckling load. Rockey *et al.* [11] in 1967 used the Finite Element method to determine the relationship between the buckling load of a plate under shear and the reinforced or unreinforced cut-out diameter. During the early 1980s when computer power became more easily available and Finite Element systems easier to use, more knowledge about the influence of boundary conditions, cut-out size, shape, location and reinforcement type on the buckling behaviour of isotropic plates was gained. A vast number of papers have been

published over the years relating to isotropic construction.

Compared with the knowledge of cut-outs in isotropic panels, it is clear that very little is known about the structural behaviour of cut-outs in composite panels. This is partly due to the fact that composites have only been in use for approximately 20 years and have only recently been considered for serious applications.

This need has been recognized and the amount of information about cut-outs in composite plates and their influence upon the buckling stability is gradually increasing.

Martin [12] was among the first in 1972 to publish work regarding the buckling of composite plates with cut-outs loaded in uniaxial compression. An experimental investigation of the buckling behaviour and failure characteristics of compression-loaded rectangular CFRP plates with a central circular cut-out was presented in 1978 by Knauss *et al.* [13]. In his experiments the displacement loaded edges are clamped and the unloaded edges are simply supported by knife edge supports. The influence of central circular cut-outs or holes in simply supported composite plates on the buckling load is also the main topic of papers published by Marshall *et al.* [14–18] from 1984 onwards. Using the Rayleigh–Ritz method he analyzed the stability of composite plates with circular holes under uniform compressive strain or stress loading and obtained approximate analytical results up to $d/a = 0.5$ and had good agreement with experiments, as the prebuckling stress field is approximated for an infinite panel. A different but also very complex approach to solving the buckling problem of rectangular compression loaded panels with central circular cut-outs can be found in papers by Nemeth [19–22]. He used an analysis based on the Kantorovitch [23] variational method and reduced the classical two dimensional analysis for determining the plate buckling load to an equivalent one-dimensional form by approximating the plate displacements with kinematically admissible series and compared the results obtained with FE results. FE analysis has been directly used by Larsson [24] and Lee [25] to find the buckling load of orthotropic plates with circular holes. Composite panels loaded in shear with central circular cut-outs have been analyzed at first by Herman [26] using the finite element method. Klang [27] introduced for this type of problem a new analysis method based on Lekhnitskii's complex variable equations, boundary collocation and the Ritz method.

Cut-outs or holes in real structures are often reinforced with rings in order to keep the stress in the surrounding area within the material limitations or in order to enable the attachment of an access cover. These reinforcements change the stress distribution in the panel and influence the stability. For metal structures this influence on the structural behaviour of the panel has been gathered through the research carried out by many authors. However, for composite structures very little is known about this. Sullivan [28] analyzed the stress/strain concentrations around circular 1 in. cut-outs with reinforcements in a honeycomb sandwich panel. Circular holes with reinforcements in quasi isotropic composite laminates have also been investigated by Lee [29]. He performed tension and compression tests to analyze the strength and modes of failure of reinforced circular holes. However, the holes considered are very small compared to the panel size and do not represent large cut-outs.

The purpose of this research is to determine the effect of reinforcement ring width on the buckling behaviour of CFRP panels loaded in pure shear or in uniaxial compressive displacement.

As traditional mathematical analysis can only give solutions for certain boundary conditions and configurations and would nevertheless most certainly require the use of computers, it was decided to use the established and widely available MSC/NASTRAN Finite Element System for this research and verify the results with practical tests.

PLATE GEOMETRY, MATERIAL PROPERTIES, LOAD AND BOUNDARY CONDITIONS

Details of the plate geometry and the coordinate systems used are shown in Fig. 1. All test panels are cut to a size so that the free test area in the compression or shear test rig is 300 mm square for clamped or simply supported boundary conditions. The circular cut-outs are placed in the centre of the panel. The panels are balanced and symmetrically laminated from NCF (Non Crimped Fabric) CFRP ($[[\pm 45/0]_S]_S$) material, resulting in a total thick-

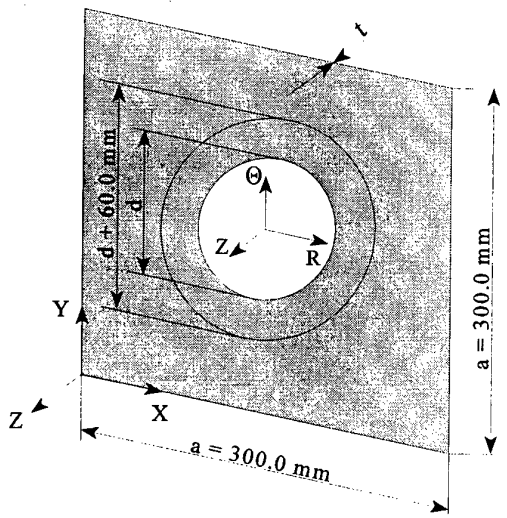

Fig. 1. Plate geometry.

ness of the panel of approx. 2 mm after curing in the autoclave. The 0° fibres and the 45° fibres are, respectively, 0.184 mm and 0.1578 mm in diameter. The material properties of NCF CFRP differ from the Ciba–Geigy Fibredux 913C-XAS pre-preg material properties due to the NCF material manufacturing method [30] The NCF and pre-preg material properties [28,31] at room temperature are listed in Table 1. The resulting properties for the panel and reinforcement ring laminate are listed in Table 2.

As the only variables are the cut-out diameter and the width of the reinforcement rings, it is possible to describe the plate geometry in terms of just two parameters. The hole-size ratio d/a (cut-out diameter d over the panel width a) and the width of the reinforcement rings. Rings manufactured from NCF CFRP were used for the reinforcement of the circular cut-outs. The lay-up used for the reinforcement rings is $[[\pm 45/0]_S]_S$, thickness: 1.998 mm.

The redux 420 adhesive which has been used to bond the reinforcement rings to one or both sides of the panel is assumed not to influence the structural behaviour of the panel. The bonding layer has been kept to a minimum thickness.

The panels were tested in pure shear and under uniform compressive edge displacement (the panel edge was kept straight under the compression loading). It has to be pointed out that uniform compressive edge stress is a different loading case, creating a different pre-buckling stress field [32] and has therefore with increasing cut-out size a different buckling response as shown in Refs [15,16].

The pre-buckling stress field depends not only on the type of loading applied, but also on the cut-out diameter, reinforcement type, and the boundary conditions at the four panel edges. The unloaded edges of the panel loaded in uniform compressive displacement are not restrained transverse in-plane. These edges therefore deform according to the poissons ratio. Under shear loading all four panel edges were kept straight and in plane.

NASTRAN BUCKLING ANALYSIS

Buckling theory presumes the existence of a bifurcation point where two infinitesimally close equilibrium configurations are possible for the same applied load (bifurcation buckling load). This is true if the structure is perfectly straight, uniform, free of end moments and lateral loads, with the applied loads perfectly centred and axial. The general form of the eigenvalue problem for buckling is in this case expressed mathematically as [33]

$$[K_{aa} - \lambda_i K^d_{aa}]\{u_a\} = 0$$

In reality imperfections exist in structures. The real structure with imperfections does not, in general, display a bifurcation point but a

Table 1. Material properties

Material	E_L [N/mm^2]	E_T [N/mm^2]	G_{LT} [N/mm^2]	υ_{LT}
NCF CFRP	135200	9000	4875	0
CFRP Pre-preg (913C-XAS)	140000	10000	5000	0

Table 2. Calculated laminate membrane engineering constants

	E_x [N/mm^2]	E_y [N/mm^2]	G_{xy} [N/mm^2]	υ_{xy}
Ring reinf.	61356	24068	23848	0
Panel	61356	24068	23848	0

limit load above which the gradient of the out of plane deflections becomes excessive. A 'Linear Buckling Analysis' ignores the effect of structural imperfections on the behaviour of the structure under load and yields a buckling load for a perfect structure which is always higher than the buckling load which is found in tests on real structures. The results obtained by NASTRAN solution sequence 105 for buckling analysis are therefore for perfect structures and give the upper limit for the buckling load on real structures. The closeness of the theoretical and practically obtained buckling loads can be an identification how 'perfect' a structure is.

A typical FE model of a panel with a cut-out has been modelled with 1000–2500 QUAD4 elements, depending on the cut-out size and whether a reinforcement ring is included. The panel with a cut-out and reinforcement ring is modelled with QUAD4 elements. QUAD4 shell elements were chosen over QUAD8 shell elements as QUAD8 shell elements are not necessarily more accurate [34] for flat plates but simply double the number of grid points and substantially increase the CPU processing time. Care had to be taken to keep the distortions of the elements within the limits suggested in the NASTRAN user manual. Element aspect ratios of up to 5 and skew up to 60° could be accepted according to information provided. However, checks were carried out on the results obtained to make sure no locking up of elements occurred. If unexpected behaviour was detected the model was re-meshed and analyzed and the results compared. Figure 2 shows a typical FE model meshed with 1840 QUAD4 elements.

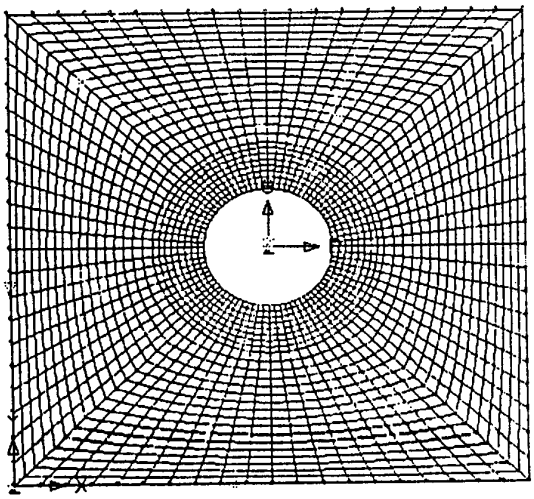

Fig. 2. Panel with cut-out meshed with QUAD4 elements.

MANUFACTURING OF TEST PANELS

As a safeguard against variations in the material properties, all the test panels were manufactured from the same batch of NCF CFRP material. Large (1250 × 950 mm) approx. 2 mm thick panels were laminated and cured in the autoclave under the same process conditions. Once cured, the NCF CFRP composite panels were sent for ultrasonic C-scan to detect possible defects in the panels which could influence test results. The panels were then cut with a NC controlled 40 000 psi water jet to the exact size required so that the free unsupported area in the test fixtures is exactly 300 × 300 mm. The water jet creates delaminations when it initially punches through the panel. To avoid this, the initial punch through was done in an area which is cut away, i.e. the centre of a the circular cut-out.

The 30 mm wide circular reinforcement rings were cut from CFRP panels, with the appropriate lay up, in the same way. The reinforcement rings were then bonded with redux 420 at room temperature to the panel. The rings had to be precisely located around the cut-out and the fibre orientation of the rings had to be lined up accurately to the fibre orientation of the surrounding panel. Strain gauges were then applied to the panels at determined locations (see Figs 3 and 4).

EXPERIMENTAL INVESTIGATION

To verify the FE results, it was considered essential to perform practical tests. However, due to costs and time required for production and testing of CFRP panels with cut-outs, only a limited number of tests could be performed to date.

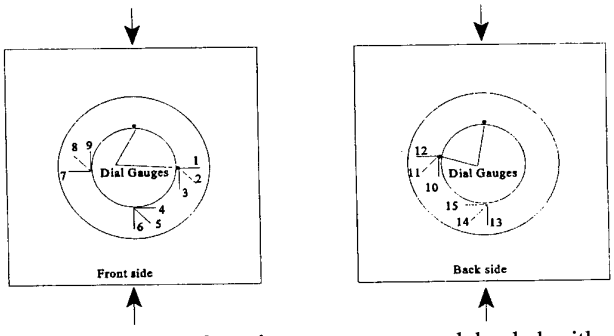

Fig. 3. Location of strain gauges on panel loaded with uniform compressive edge displacement.

Electrical resistance 3-Axis rosette strain gauges were employed to measure the strain at several locations on the panel (see Figs 4 and 5). It was only necessary to apply the strain gauges to one quarter of the panel, due to the symmetric loading and boundary conditions. This was verified by the application of strain gauges to additional locations on the panel and made it possible to analyze the strain distribution in the panel.

To detect the start of the out of plane deflections and buckling, strain gauges were attached at the same locations on the front and back side of the panel. Different strain values indicated that the panel was no longer flat and out of plane deflections were present. To find the buckling load, the 'membrane strain method' has been employed. The membrane strain values were calculated from the two opposite strain gauges and plotted versus applied load. The buckling load was estimated by locating the point where the membrane strain is maximum.

In addition to this, the out of plane deflections of the panels were measured directly with dial gauges at certain locations on the panel. This shows the magnitude and progress of the out of plane deflections with increasing load and gives an additional method to identify the start of buckling by using the 'point of inflection method'. Here the buckling load is estimated by locating the intersection point of tangents to the load deflection curve in the pre-buckled and post-buckled regions.

Also measured was the in-plane deformation of the shear or compression loaded panel edge. This measurement plotted against the applied load represents the in-plane stiffness of the panel and can also be used to illustrate the change in stiffness when buckling starts.

In the tests, the strain gauge outputs were amplified, read with a data logger and stored on

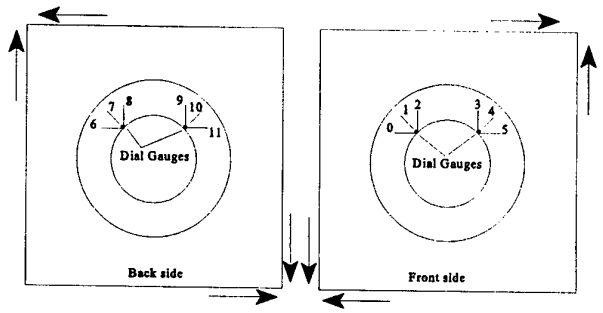

Fig. 4. Location of strain gauge on panel loaded in pure shear.

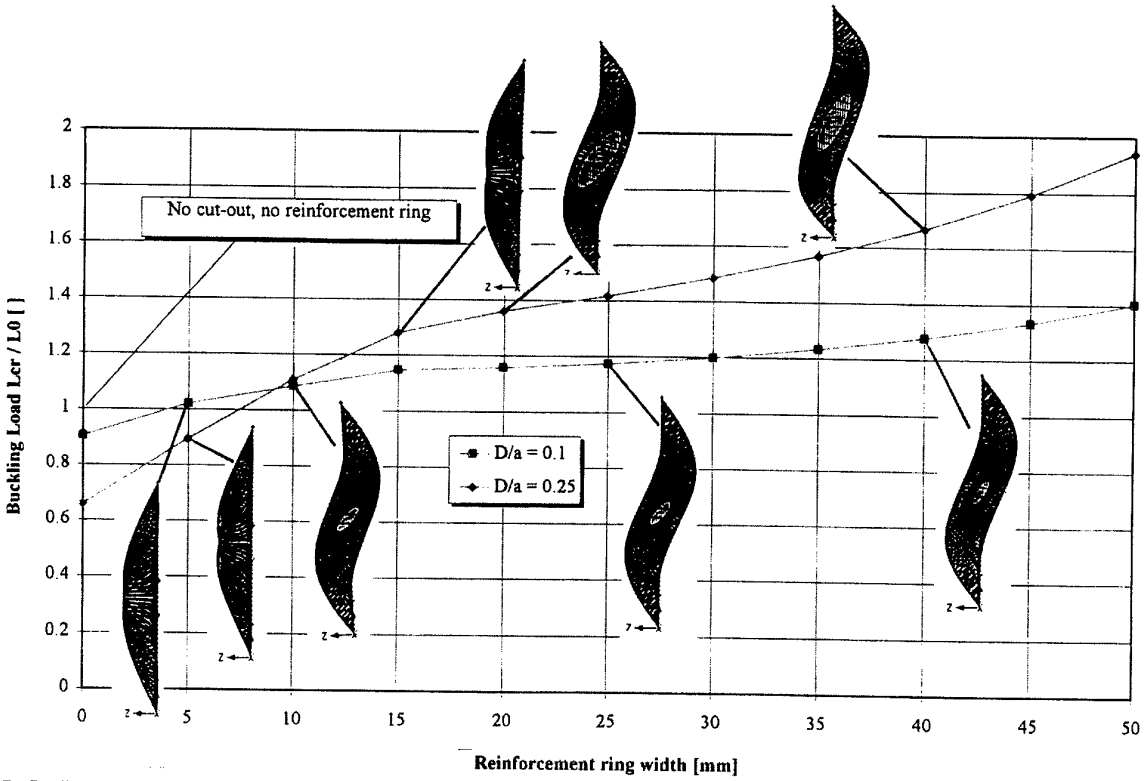

Fig. 5. L_{cr}/L_o versus width of reinforcement ring for CFRP panels loaded in shear displacement with centrally located circular cut-out and simply supported boundary conditions. Reinforcement rings applied on both sides of the panel.

a hard disk. Two tests were performed on each panel. After each test the test panel was checked to ensure that no permanent damage occurred. The dial gauge measurements were recorded manually. To accomplish this, the load was increased in steps and held constant when the dial gauge readings were taken. The measurement of the out-of-plane deflections was therefore done in a separate loading of the test panel.

INFLUENCE OF REINFORCEMENT RING WIDTH

Uniform shear displacement (square panel, central circular cut-out, simply supported B.C., uniform shear displacement, reinforcement rings on both sides, reinforcement ring material NCF $[[\pm 45/0]_s]_s$)

The MSC/NASTRAN FEA determined buckling loads presented in Fig. 5 have been normalized towards a panel without a cut-out. The buckling mode and deformed shape has been determined in the FEA for every data point presented in order to detect changes in the buckling mode. However, for clarity purposes it was not possible to illustrate in Fig. 5 the deformed shapes for every data point. The change in buckling shape with increasing reinforcement ring width is illustrated in Fig. 6 for reinforcement rings of 5–50 mm width.

For both cut-out sizes the buckling stability increases with increasing reinforcement ring width. Both curves display a convex–concave behaviour with the initial slope of the curves decreasing with increasing reinforcement ring width. Before a horizontal tangent is reached the slope starts to increase again with increasing reinforcement ring width. This change-over occurs for both curves at a reinforcement ring width of approximately 15 mm. Of interest is that the curve representing $d/a = 0.1$ indicates up to a reinforcement ring width of approximately 40 mm a higher buckling stability than the curve for $d/a = 0.25$. Due to the higher initial slope of the curve representing $d/a = 0.25$, the two curves cross over at a reinforcement ring width of approximately 40 mm. For larger reinforcement ring widths, the panel with a cut-out of $d/a = 0.25$ is more stable against buckling at the same reinforcement ring width than the panel with $d/a = 0.1$. Both curves approach a

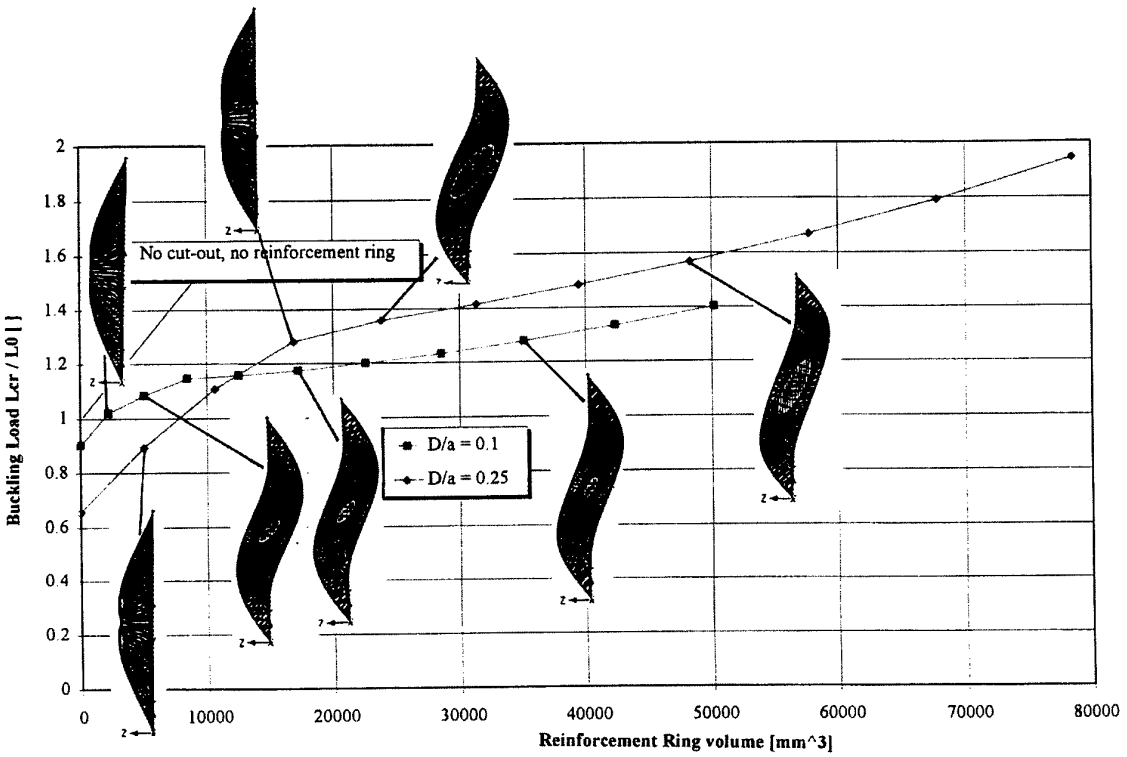

Fig. 6. Change of buckling shape with increasing reinforcement ring width. 5–10–15–20–25–30–35–40–45–50 mm reinforcement rings.

parabolic shape at large reinforcement ring widths.

The buckling shapes illustrated in Fig. 5 indicate that the buckling mode changes with increasing reinforcement ring width. At $d/a = 0.1$ the panel buckles antisymmetrically to the panel diagonal for reinforcement ring width of 10 mm or more. The reinforcement ring has sufficient stiffness to prevent the area around the cut-out from deforming and therefore the reinforcement ring deflects through the plane of the panel without being significantly deformed. For smaller reinforcement ring widths, the analysis determined a symmetrical buckling mode for a reinforcement ring width of 5 mm. In this case the panel deforms symmetrically to the panel diagonal. The area around the cut-out deforms in out-of-plane bending.

For $d/a = 0.25$ the same behaviour can generally be observed. For reinforcement ring widths of less than 20 mm the reinforcement ring is not sufficiently stiff to prevent the area around the cut-out from out-of-plane bending. The panel buckles symmetrically to the panel diagonal. If the reinforcement ring width is increased the reinforcement ring prevents deformations around the cut-out and the panel buckles antisymmetrically to the panel diagonal, with the reinforcement ring deflecting through the plane of the panel.

In order to determine the influence of the reinforcement ring volume on the buckling stability, the buckling loads, normalized towards a panel without a cut-out, are plotted in Fig. 7 versus the reinforcement ring volume. The deformed buckling shapes are illustrated for selected data points. Both curves in Fig. 7 exhibit a very similar behaviour as observed in Fig. 5.

For small reinforcement ring volumes, the panel with a cut-out of $d/a = 0.1$ is more stable against buckling than the panel with a cut-out of $d/a = 0.25$. With increasing reinforcement ring volume the difference between the two curves is decreasing and they cross over at a reinforcement ring volume of approximately 12500 mm^3. For larger reinforcement ring volumes the panel with $d/a = 0.25$ exhibits a higher buckling stability than the panel with $d/a = 0.1$. The initial slope of the curves is, up to a ring stiffener width of approximately 15 mm, decreasing with increasing ring stiffener volume. If the ring stiffener volume is increased further then the slope of the curves remains approximately constant.

From this behaviour it can be concluded that the buckling stability can be increased most efficiently by reinforcement rings with widths up to 15 mm. The results of this investigation indicate that wider reinforcement rings increase the

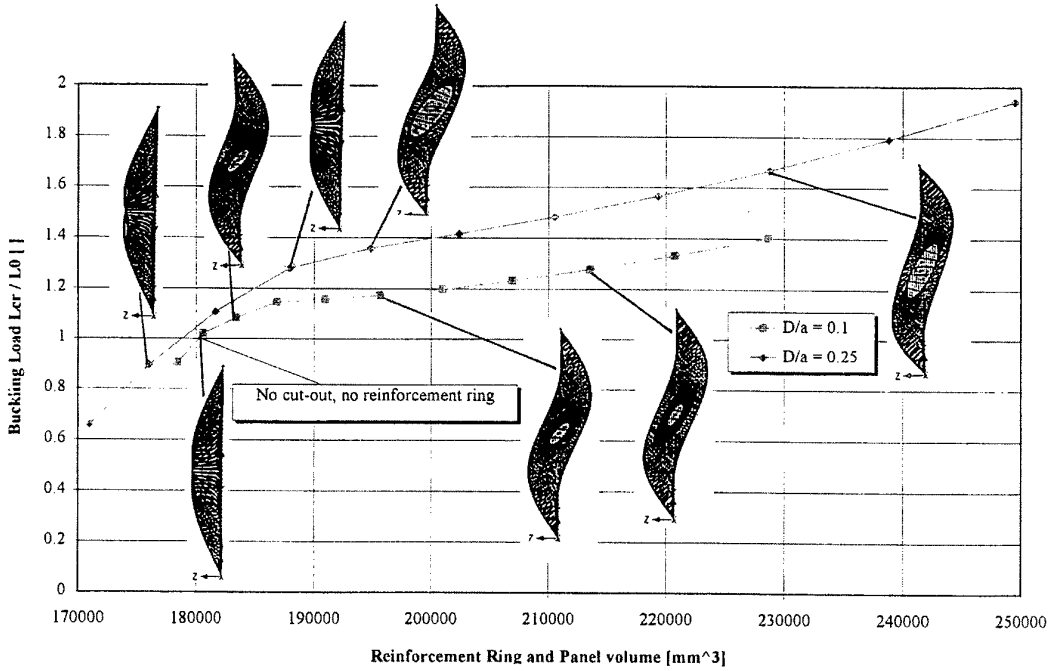

Fig. 7. L_{cr}/L_o versus volume of reinforcement ring for CFRP panels loaded in shear displacement with centrally located circular cut-out and simply supported boundary conditions. Reinforcement rings applied on both sides of the panel.

buckling stability further but less efficiently. To increase the buckling stability of a panel with $d/a = 0.1$ from $L_{cr}/L_o = 0.9$ to a value of 1.15, a reinforcement ring volume of 8476 mm^3 (15 mm width) is required whereas a further increase from $L_{cr}/L_o = 1.15$ to 1.40 requires an additional reinforcement ring volume of 41750 mm^3 (50 mm width).

In Fig. 8, the buckling loads of panels with $d/a = 0.1$ and 0.25 have been plotted versus the total volume of the panel and reinforcement ring. The buckling load of a panel without cut-out and reinforcement ring has been indicated for reference purposes.

Both curves in Fig. 8 exhibit a behaviour very similar to the behaviour observed in Figs 5 and 7. They are of convex–concave shape with the initial slope decreasing with increasing total panel and reinforcement ring volume. At higher volumes the slope is again increasing slightly. No cross-over of the curves representing $d/a = 0.1$ and $d/a = 0.25$ has been detected. The results presented in Fig. 8 indicate that the panel with $d/a = 0.25$ is, within the boundaries of this investigation, more stable against buckling than the panel with $d/a = 0.1$.

Uniform compressive displacement (square panel, central circular cut-out, simply supported B.C., uniform compressive displacement, reinforcement rings on both sides, reinforcement ring material (NCF $[[\pm 45/0]_s]_s$))

The investigation conducted for panels loaded in compressive displacement is conducted similarly to the investigation of panels loaded in uniform shear displacement. The buckling loads and buckling shapes determined for reinforcement rings with widths between 0–50 mm are plotted in Fig. 9 for $d/a = 0.1$ and $d/a = 0.25$ versus the reinforcement ring width.

The change in buckling shape with increasing reinforcement ring width is illustrated in Fig. 10 for reinforcement rings between 5–50 mm.

For both cut-out sizes the buckling load of the panel is increasing with increasing reinforcement ring width. The curves exhibit a convex–concave shape where the slope of the curves is initially decreasing with increasing reinforcement ring width but is increasing again if the reinforcement ring width is increased further. For $d/a = 0.25$ the change over from a convex to a concave curvature occurs approximately at a reinforcement ring width of 10 mm. For $d/a = 0.1$ the change over occurs approximately at a reinforcement ring width of 5 mm. If no reinforcement ring is applied, an equivalent panel width with $d/a = 0.25$ exhibits a lower buckling stability than the panel with $d/a = 0.1$. The initial slope of the curve representing $d/a = 0.25$ is higher than the slope of the curve representing $d/a = 0.1$, so that the curves cross over at a reinforcement ring width of approximately 2.5 mm. If the reinforcement ring width is increased further then the panel with $d/a = 0.25$ exhibits a increasingly higher buckling stability than the panel with $d/a = 0.1$.

The buckling modes illustrated for several points in Fig. 9 reveal that for both cut-out sizes no change in buckling mode could be detected. All the panel configurations buckle symmetrically, deflecting in the post-buckling phase to one side out-of-plane. With increasing reinforcement ring width the area around the cut-out which remains after buckling occurs

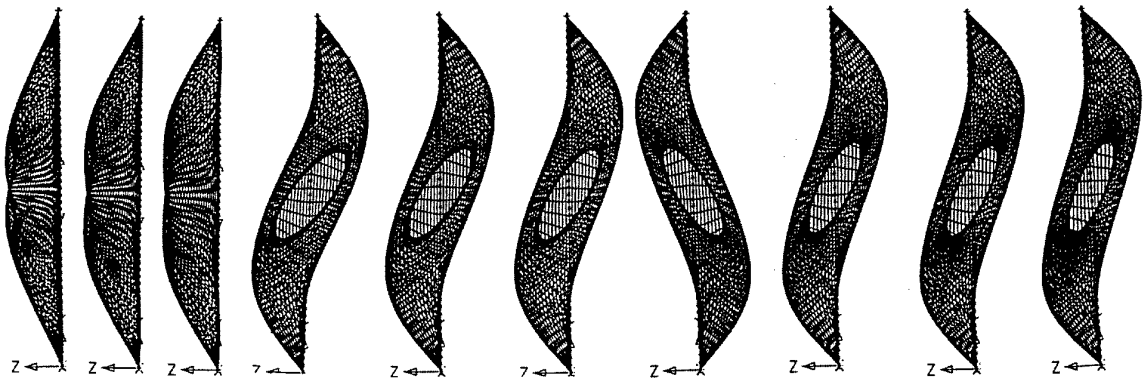

Fig. 8. L_{cr}/L_o versus total volume of panel and reinforcement ring. CFRP panels loaded in shear displacement with centrally located circular cut-out and simply supported boundary conditions. Reinforcement rings applied on both sides of the panel.

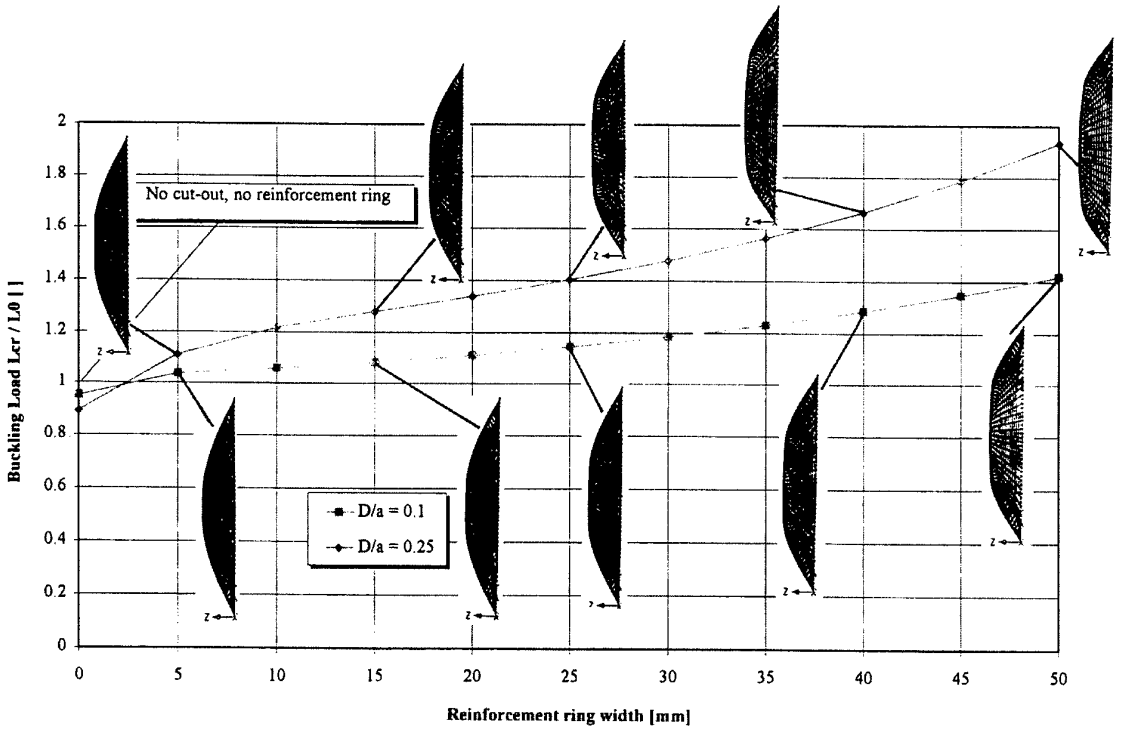

Fig. 9. L_{cr}/L_o versus width of reinforcement ring for CFRP panels loaded in uniform uniaxial compressive displacement with centrally located circular cut-out and simply supported boundary conditions. Reinforcement rings applied on both sides of the panel.

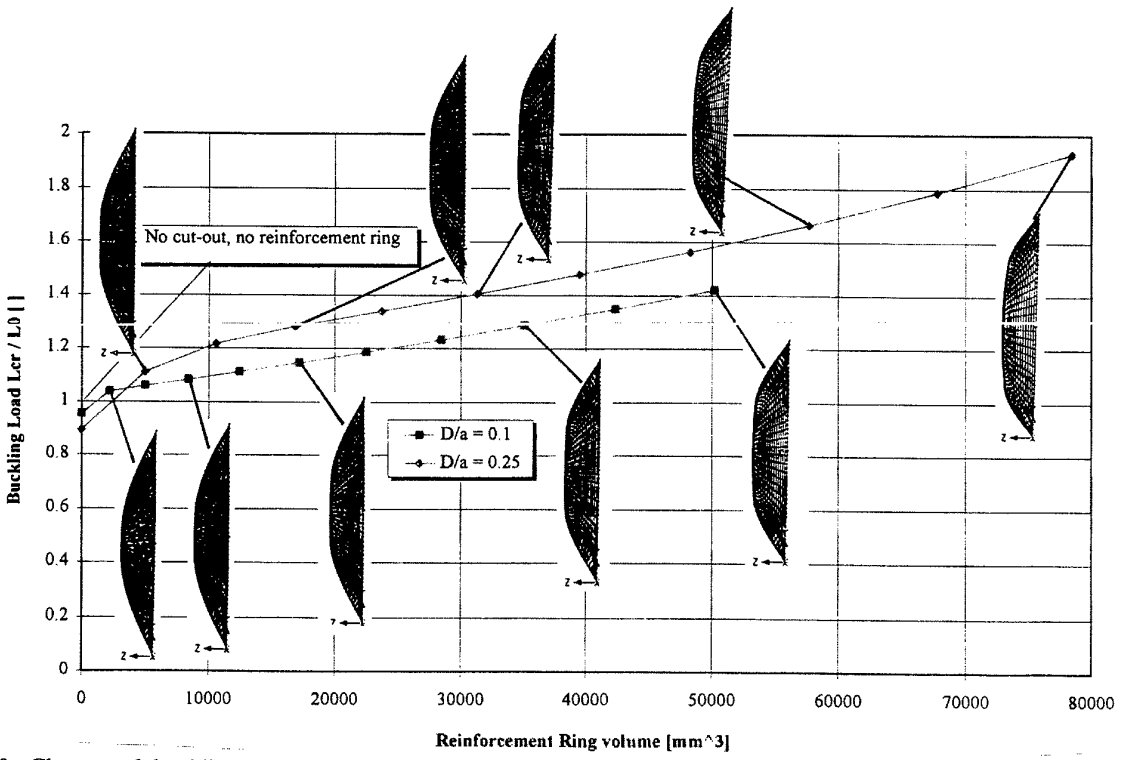

Fig. 10. Change of buckling shape with increasing reinforcement ring width. 5–10–15–20–25–30–35–40–45–50 mm reinforcement rings.

parallel to the loading direction, is increasing, indicating the stiffening effect of the reinforcement ring.

The influence of reinforcement ring volume on the buckling stability is illustrated in Fig. 11, where the buckling loads, normalized towards a panel without a cut-out, are plotted versus the reinforcement ring volume. Both curves in Fig. 11 exhibit a behaviour similar to the behaviour observed in Fig. 9. However, the curves in Fig. 11 are more linear at higher reinforcement ring volumes than the curves in Fig. 9.

The slope of the curves representing $d/a = 0.1$ and $d/a = 0.25$ are initially decreasing with increasing reinforcement ring volume. Once a reinforcement ring width of approximately 10 mm (11 000 mm^3) is reached then the slope of the curve representing $d/a = 0.25$ remains constant. For a panel with $d/a = 0.1$ the slope remains constant once a reinforcement ring width of approximately 5 mm (2000 mm^3) is reached. Both curves remain relatively linear and parallel to each other at higher reinforcement ring volumes.

The two curves cross over at a reinforcement ring volume of approximately 3400 mm^3. From then on the results indicate that the panel with $d/a = 0.25$ is more stable against buckling then a panel with $d/a = 0.1$ if the same volume of reinforcement ring material is applied around the cut-out.

From the results presented in Fig. 11 it can be concluded that reinforcement rings of small width are more efficient than wide reinforcement rings. To increase the buckling stability of a panel with $d/a = 0.25$ from $L_{cr}/L_o = 0.89$ (no reinforcement ring) to $L_{cr}/L_o = 1.22$ requires (according to Fig. 11) a reinforcement ring volume of approximately 10 700 mm^3 (10 mm wide reinforcement ring). To increase the buckling stability further to $L_{cr}/L_o = 1.56$ requires a reinforcement ring width of 35 mm (48 300 mm^3 volume).

Figure 12 illustrates the relationship between the buckling stability of a panel with a cut-out of $d/a = 0.1$ or $d/a = 0.25$ and the total volume of panel and reinforcement ring. The buckling loads have been normalized towards a panel without a cut-out.

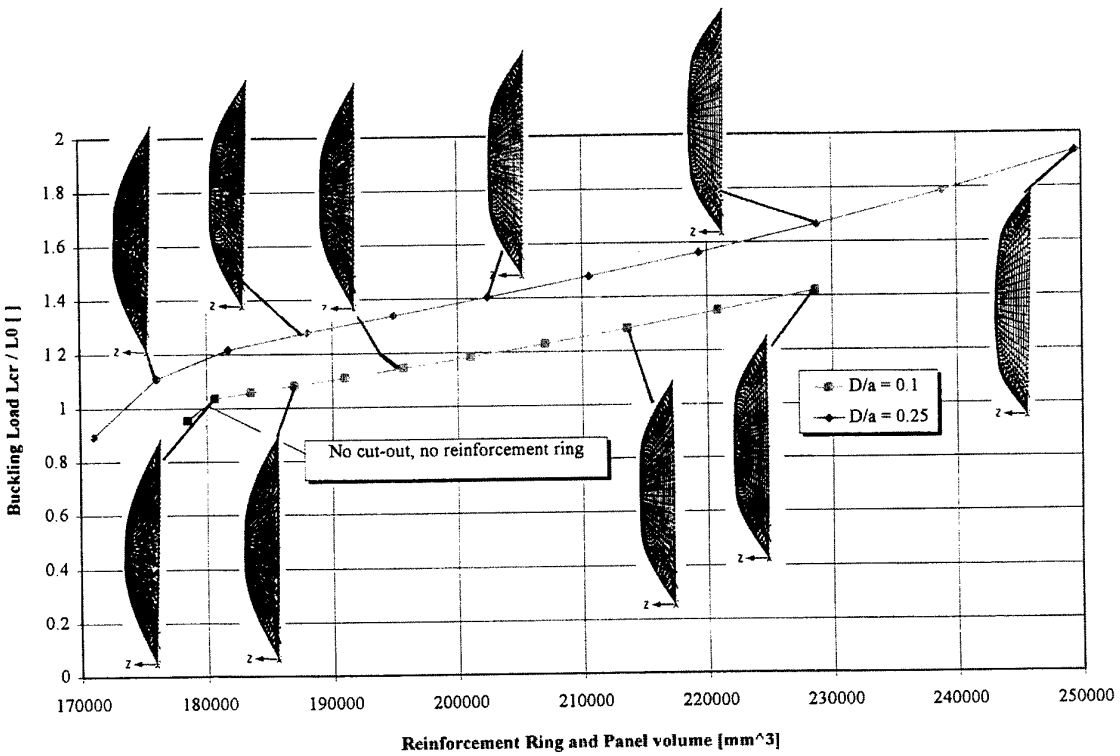

Fig. 11. L_{cr}/L_o versus volume of reinforcement ring for CFRP panels loaded in uniform uniaxial compressive displacement with centrally located circular cut-out and simply supported boundary conditions. Reinforcement rings applied on both sides of the panel.

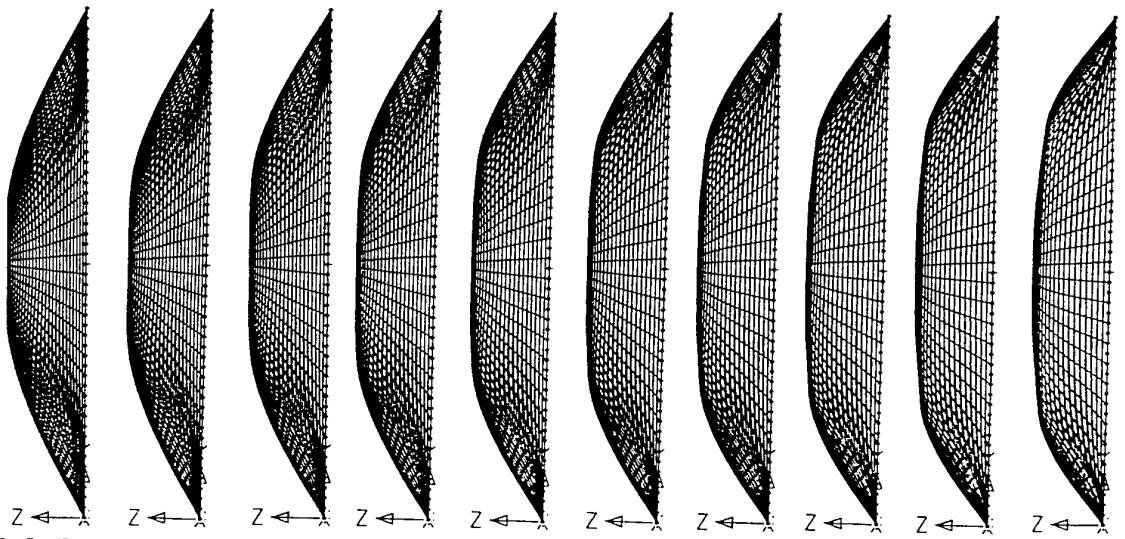

Fig. 12. L_{cr}/L_o versus total volume of panel and reinforcement ring. CFRP panels loaded uniform uniaxial compressive displacement with centrally located circular cut-out and simply supported boundary conditions. Reinforcement rings applied on both sides of the panel.

Both curves in Fig. 12 exhibit a convex–concave curvature with the initial slope decreasing with increasing panel and reinforcement ring volume. The curves develop into linear functions at higher total panel and reinforcement volumes. Over the range of volumes considered the curves are relatively parallel to each other. Figure 12 indicates that with the same total panel and reinforcement ring volume used a panel with $d/a = 0.25$ is more stable against buckling than a panel with $d/a = 0.1$, illustrating the advantage of shifting panel and reinforcement ring material to the supported panel edges away from the panel centre.

COMMENTS ON TEST RESULTS

Naturally there are differences between the idealised FE model and the real fabricated composite structure, leading to errors in determining the buckling load and structural response.

All the numerical methods which are available to predict the theoretical panel buckling loads are based on the assumption of ideal linear elastic behaviour and an abrupt growth of out of plane deflections at a discrete point. Unfortunately, real structures exhibit some degree of non-linearity around the buckling point and in the post-buckling region, and have geometric imperfections (eg. initial curvature, changes in thickness and local differences in material properties among others). Controls were in place to try to detect and avoid imperfections, but in reality the produced panels were of course not perfect. This could be seen throughout the experiments. Figure 13 gives an illustration of the practical buckling behaviour observed on a NCF CFRP panel with no cut-out. Comparing the test results of panels with

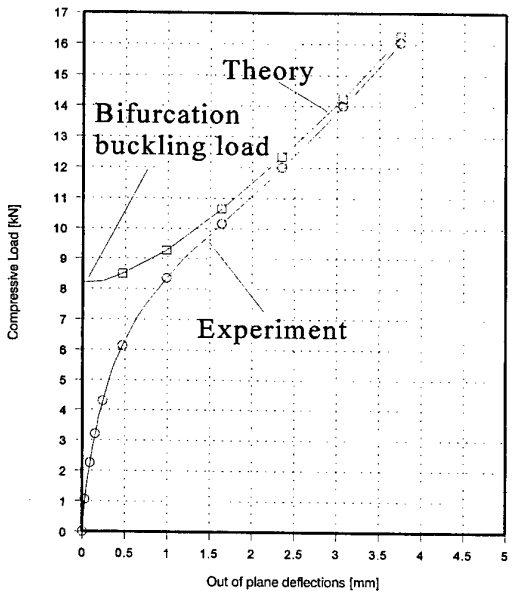

Fig. 13. Influence of imperfections on out of plane displacement.

cut-outs to panels without cut-outs (L_{cr}/L_o) eliminates the effect of imperfections to a certain degree as all the panels have been produced under the same conditions and batch of material and should therefore have similar imperfections. It also makes the results more generally applicable. The absence of a well defined bifurcation point clearly indicates that the determination of experimental buckling loads is an approximate process with varying degrees of error possible.

CONCLUSIONS

FE models for different loadings, cut-out sizes and reinforcements width have been created and analyzed to determine the influence of these parameters on the buckling load of CFRP composite panels. Practical tests have been conducted to verify these results with measured buckling loads.

It was possible to predict the influence of the different parameters on the structural behaviour of the composite panel. However, as expected the measured buckling loads were lower than the predicted values due to imperfections in the test panels which could not be accounted for in the FE model and for differences in the test apparatus. Referring the test results of panels with cut-outs to panels without cut-outs does, to a certain extent, remove the effect of imperfections and make the results in the diagrams presented more generally applicable.

The relationships presented in this paper between cut-out size, reinforcement width and buckling load, can be used by design engineers to determine the required reinforcement and to gain a better understanding of the structural behaviour of structures with reinforced cut-outs.

The buckling behaviour of panels loaded in shear is very different from the buckling behaviour of panels loaded in uniform compressive displacement and the influence of the ring reinforcement is also different for these two load cases. The following conclusions can be made:

Panels loaded in uniform shear:

1. The buckling mode of panels loaded in shear changes from symmetric to antisymmetric once the reinforcement ring exceeds a certain stiffness.
2. The reinforcement ring width and volume where the buckling mode changes from symmetric to antisymmetric increases with increasing cut-out.
3. Panels with large cut-outs yield in the area of antisymmetric buckling mode a higher buckling stability for the same reinforcement ring volume than panels with smaller cut-outs.
4. Panels with large cut-outs yield a higher buckling stability at the same panel and reinforcement ring volume than panels with smaller cut-outs.
5. In the area of antisymmetric buckling, the volume required to increase the buckling stability further (slope of the curves) is very similar for $d/a = 0.1$ and $d/a = 0.25$.

Panels loaded in uniform uniaxial compressive displacement:

1. No change in buckling mode with increasing reinforcement ring stiffness could be observed.
2. Panels with large cut-outs yields a higher buckling stability for the same reinforcement ring volume than panels with smaller cut-outs.
3. Panels with large cut-outs yield a higher buckling stability at the same panel and reinforcement ring volume than panels with smaller cut-outs.
4. The volume required to increase the buckling stability equally of $d/a = 0.1$ and $d/a = 0.25$ (slope of the curves) is very similar.

FUTURE WORK

The work presented in this paper was only a part of the PhD programme completed. Practical tests to verify the FE analysis are unfortunately quite time consuming and expensive and limited the amount of testing which could be conducted. The influence of panel aspect ratio, cut-out shape and cut-out location in the panel are useful information for the design engineer and have to be investigated. The influence of imperfections of different magnitude and forms has to be established.

ACKNOWLEDGEMENTS

The work described in this paper was undertaken as part of a PhD supported by British Aerospace. The authors wish to record their appreciation for their support and help in the manufacturing of the test panels and to the

College of Aeronautics Cranfield University for providing the test and computing facilities.

REFERENCES

1. Eiblmeier, J. and Loughlan, J., The buckling response of carbon fibre panels with reinforced cut-outs. *Composite Structures*, 1995, **32**, 97–113.
2. Eiblmeier, J., PhD Thesis, Cranfield University, College of Aeronautics, Cranfield, UK, 1996.
3. Levey, S., Wooley, R. M. and Kroll, W. D., Instability of a simply supported square plate with a reinforced circular hole in edge compression. *J. Res. Nat. Bureau Standards*, 1947, **39**, 571–577.
4. Timoshenko, S., *Theory of elastic stability*. McGraw–Hill, New York, 1936, pp. 307–326.
5. Kumai, T., Elastic stability of the square plate with a central circular hole under edge thrust. *Proceedings of the first Japan National Congress for Applied Mechanics*, 1951, pp. 81–86.
6. Schlack, J. L. Jr, Elastic stability of pierced square plates. *Exp. Mech.*, 1964, **4**, 167–172.
7. Schlack, J. L. Jr., Experimental critical Loads for perforated square plates. *Proceedings of the Society of experimental stress analysis*, Vol. 25, Pt. 1, 1968, pp. 69–74.
8. Yoshiki, M., Fujita, Y., Kawamura, A., Arai, H., Instability of plates with holes (first report). *Proceedings of the Society of Naval Architects of Japan*, Dec. 1967, pp. 137–145.
9. Kawai, T. & Ohtsubo, H., A method of solution for the complicated buckling problems of elastic plates with combined use of Rayleigh–Ritz's procedure in the Finite Element method. *Proceedings of the second Conference of Matrix Methods in Structural Mechanics*, Report AFFDL-TR-68-150, 1968, pp. 967–994.
10. Ritchie, D. & Rhodes, J., Buckling and post-buckling behaviour of plates with holes, *Aeronautical Quarterly* XXIV (1975) 281–296.
11. Rockey, K. C., Anderson, R. G., Cheung, Y. K., The behaviour of a shear web having circular holes. *Proceedings of the Swansea Symposium on thin walled structures*, 1967, p. 14.
12. Martin, J., PhD Dissertation, Case Western Reserve University, 1972.
13. Knauss, J. F., Starnes, J. H. & Henneke, E. G., The compressive failure of Graphite/Epoxy plates with circular holes. *Research Report VPI-E-78-5*, Virginia Polytechnic Institute and State University, Feb. 1978.
14. Marshall, I. H., Little, W., El Tayeby, M. M., The stability of composite panels with holes. *Reinforced Plastics Congress*, Brighton, UK, Nov. 1984.
15. Marshall, I. H., Buckling of perforated composite plate - an approximate solution. *Proceedings of the Institution of Mechanical Engineers*, C30/86, 1986.
16. Marshall, I. H., Little, W. & El Tayeby, M. M., Stability of composite panels with holes, Chapter 17. In *Mechanical Characterization of Load Bearing Fibre Composite Laminates*, eds A. H. Cardon & G. Verchery. Elsevier Applied Science Publishers, 1985, pp. 235–242.
17. Marshall, I. H., Little, W. & El Tayeby, M. M., Composite panels with circular cut-outs: Some design guidelines. *Proceedings of Reinforced Plastics Congress*, Nottingham, 1986, pp. 91–94.
18. Marshall, I. H., Little, W. & El Tayeby, M. M., Membrane stress distributions in post-buckled composite plates with circular holes. *VI International Conference on Composite Materials ICCM and ECCM*, Vol. 5, pp. 5.57–5.67.
19. Nemeth, M. P., PhD Dissertation, Virginia Polytechnic Institute and State University, May 1983.
20. Nemeth, Michael P., Stein, Manuel, Johnson, Eric, An approximate buckling analysis for rectangular orthotropic composite plates with centrally located cut-outs, NASA TP 2528, Feb. 1986.
21. Nemeth, Michael P., A buckling analysis for rectangular orthotropic plates with centrally located cut-outs, NASA TM 86263, Dec. 1984.
22. Nemeth, M. P., Buckling behaviour of compression-loaded symmetrically laminated angle-ply plates with holes. *AIAA Journal*, 1988, **26**, (3), 330–336.
23. Kantorovich, L. V., Krylov, V. I., Trans. Curtis D. Benster, *Approximate Methods of Higher Analysis*, 1964.
24. Larsson, P.-L., On the buckling of orthotropic compressed plates with circular holes. *Composite Structures*, 1987, **7**, 103–121.
25. Lee, Y. J., Lin, H. J. and Lin, C. C., A study on the buckling behaviour of an orthotropic square plate with a central circular hole. *Composite Structures*, 1989, **13**, 173–188.
26. Herman, R. J., MSc Thesis, US Naval Postgraduate School Monterey, Californian, March 1982.
27. Klang, E. C., *Shear buckling of specially orthotropic plates with centrally located cut-outs*, Semi annual Report Department of Mechanical and Aerospace Engineering; North Carolina State University, 1991.
28. Sullivan, P. D., *Analysis of a symmetric reinforcement of graphite/epoxy honeycomb sandwich panels with a circular cut-out under uniaxial compressive loading.* NTIS No.: AD-A164 490/5/HDM, Dec. 1985.
29. Lee, J. H., Strength and failure analysis of composite laminate containing a circular hole with reinforcement, AFIT/GAE/AA/87D-9, December 1987.
30. British Aerospace Cranfield Manufacturing Centre, Affordable Manufacture of Composite Aircraft Primary Structures (AMCAPS), Quarterly Technical Report, May 1994–July 1994, Appendix 3.2A, CS/94/RR/110, August 1994.
31. Ciba–Geigy Plastics, Fibredux 913 Information Sheet No. FTA 46f, July 1991.
32. Nemeth M. P., Buckling and postbuckling behaviour of laminated composite plates with a cut-out. In *Buckling and Postbuckling of Composite Plates*, eds G. J. Turvey & I. H. Marshall. Chapman and Hall, London, 1994, pp. 260–298.
33. MSC/Schwendler, NASTRAN v 67 Theoretical Manual.
34. Mac Neal Schwendler Corporation, *Practical finite element modelling and techniques using MSC/NASTRAN*, pp. 1–22, 1990.

ELSEVIER

Composite Structures Vol. 38, No. 1–4, pp. 623–630, 1997
© 1997 Elsevier Science Ltd. All rights reserved
Printed in Great Britain
0263-8223/97/$17.00 + 0.00

PII:S0263-8223(97)00100-1

Minimum cost design of hybrid composite cylinders with temperature dependent properties

Sarp Adali & Viktor E. Verijenko

Dept of Mechanical Engineering, University of Natal, Durban, 4041, South Africa

Laminated composite cylinders are optimized with the objective of minimizing the material costs by means of hybridization. They are modelled as thick cylinders working under internal and/or external pressures. The optimal designs are subject to a lower bound on the failure pressure determined by the maximum stress criteria. The cylinders are constructed such that the stress patterns match the material properties by placing the stronger material in high stress areas and the weaker material in low stress areas. The resulting structure is of hybrid construction and the cost minimization is achieved not only by using an inexpensive material but also by minimizing the amount of the expensive material used in the design. The effect of temperature change on the stresses and the material properties is included in the analysis. Numerical results are given for graphite/glass hybrid cylinders and the efficiencies of the designs are shown to be substantial by comparing the costs of hybrid and non-hybrid designs. It is also shown that neglecting the effect of temperature on the stiffness and strength parameters of the materials would lead to underdesign and premature failure. © 1997 Elsevier Science Ltd.

INTRODUCTION

An effective way of reducing the material costs of laminated structures is to match the material characteristics with the stress patterns. This idea leads to hybrid composites in which the material with superior properties is placed in high stress areas and the weaker material in low stress areas. Moreover by minimizing the amount of expensive material used in the construction, further cost savings can be achieved. The resulting structure provides a cost-effective solution for structures made of composite materials which are usually more expensive than their conventional counterparts. This idea has been previously applied to pressure vessels [1], vibrating laminates [2,3] and laminates under buckling loads [4] where it led to substantial savings in material costs.

In the present study, cost minimization of thick cylinders under internal and/or external pressures and thermal loading is studied taking the effect of temperature on the material properties into account. Hybridization and optimization are combined to design the most cost-effective laminated cylinder, choosing a combination of expensive and inexpensive composite materials for different layers. The design objective is defined as the minimization of the thickness of the expensive material used in the hybrid construction subject to the requirement that the resulting structure does not fail under the specified pressure and thermal loads.

The hybrid construction provides a design tool by which strong and weak materials are matched with high and low stress areas. The fact that high stress gradients exist in thick composite cylinders has been pointed out by Pagano [5]. More recent studies of stresses in thick composite cylinders include Refs [6] and [7]. The effect of thermal loadings on the stresses has been studied for composite tubes by Hyer *et al.* [8]. These studies show the importance of design optimization to improve the perform-

ance of thick cylinders with curvilinear anisotropy. Optimal design results for non-hybrid fibre-reinforced cylinders were given in Refs [9–11]. The use of hybridization in the design of composite cylinders with a view towards material cost minimization is the subject of the present study which includes the effect of temperature change on the material properties. It is well known that material properties as well as the structural behaviour are affected by temperature changes [12–15]. Since the optimal designs are sensitive to both elastic constants and strength parameters which can degrade under heating, taking the temperature dependence of the material into account is essential in the design process. This approach leads to realistic values for the design parameters in the presence of thermal loads [16].

The numerical results indicate that optimal use of hybridization leads to substantial savings in the material costs. Moreover a comparison of results with temperature independent and dependent material properties shows that neglecting the effect of heating on the material would lead to suboptimal designs and premature failure by producing an underdesigned structure.

BASIC EQUATIONS

Consider a multilayered thick-walled cylinder of inner radius a and outer radius b. The cylinder may be subjected to internal and external pressures as well as a temperature change denoted by p, q and ΔT, respectively. Let r and θ denote the coordinates in the radial and circumferential directions. Due to axial symmetry only radial and circumferential stresses $\sigma_{\theta k}(r)$ and $\sigma_{\theta k}(r)$ are nonzero where k indicates the layer number with $k = 1, 2, ..., K$ for a K-layered cylinder. The expressions for stresses in terms of radial and circumferential strains $\varepsilon_{rk}(r)$ and $\varepsilon_{\theta k}(r)$ are given by [17]:

$$\sigma_{rk}(r) = E_{rk}[\varepsilon_{rk} + \nu_{\theta k}\varepsilon_{\theta k} - (\alpha_{rk} + \nu_{\theta k}\alpha_{\theta k})\Delta T]V^{-1} \quad (1)$$

$$\sigma_{\theta k}(r) = E_{\theta k}[\varepsilon\theta k + \nu_{rk}\varepsilon_{rk} - (\alpha_{\theta k} + \nu_{rk}\alpha_{rk})\Delta T]V^{-1} \quad (2)$$

where $V = 1 - \nu_{rk}\nu_{\theta k}$; E_{rk} and $E_{\theta k}$ are Young's moduli in the r and θ directions; ν_{rk} and $\nu_{\theta k}$ are Poison's ratios; α_{rk} and $\alpha_{\theta k}$ are thermal expansion coefficients in the r and θ directions. Let $U_k(r)$ denote the displacement in the radial direction of a point in the kth layer. Then the strains are

$$\varepsilon_{rk} = U_k/r \quad \varepsilon_{\theta k} = \mathrm{d}U_k/\mathrm{d}r \quad (3)$$

The equation of equilibrium for the kth layer in terms of stresses in the absence of body forces is

$$\frac{\mathrm{d}(r\sigma_{rk})}{\mathrm{d}r} - \sigma_{\theta k} = 0 \quad (4)$$

By substituting eqn (3) into eqns (1) and (2), and inserting the resulting expressions into eqn (4), the differential equation for displacement is obtained as

$$r^2U''_k + rU'_k - \eta_k^2 U_k = [(\nu_{\theta k} - \eta_k^2)\alpha_{\theta k} + (1 - \nu_{rk}\eta_k^2)\alpha_{rk}]\Delta T r \quad (5)$$

where $k = 1, 2, ..., K$; $\eta_k^2 = E_{\theta k}/E_{rk} = \nu_{\theta k}/\nu_{rk}$ and a prime denotes differentiation with respect to r.

The boundary and interface conditions can be expressed as

$$\sigma_{r1}(a) = -p, \quad \sigma_{rK}(b) = -q \quad (6)$$

$$\sigma_{rk}(c_k) = \sigma_{rk+1}(c_k), \quad k = 1, 2, ..., K-1$$
$$U_{rk}(c_k) = U_{rk+1}(c_k), \quad k = 1, 2 ..., K-1 \quad (7)$$

where c_k is the interface radius between the kth and $(k+1)$-th layers.

For a K-layered cylinder, the solutions of K second order differential equations given in eqn (5) result in $2K$ integration constants. The conditions (6) and (7) provide $2+2(K-1) = 2K$ conditions to evaluate the unknown constants and provide a unique solution.

OPTIMIZATION PROBLEM

The minimum cost design refers to the problem of minimizing the material cost for a hybrid cylinder with given inner and outer radii and consisting of layers made of high-strength (expensive) and low-strength (inexpensive) composite materials. By minimizing the thickness of the high-strength layers subject to a lower bound on the failure pressure, the cost of the material used in the construction can be minimized. The inner and outer radii of the cylinder are specified as design inputs and the layer thicknesses are employed as design variables.

Let P_{ls} and P_{hs} denote the failure pressures of cylinders made of a low-strength material only and a high-strength material only. Let P_0 denote

the lower bound on the failure pressure P_f, i.e., the thickness of the high-strength layers is to be minimized subject to

$$P_f \geq P_0 \tag{8}$$

Clearly if $P_0 \leq P_{ls}$, then the minimum cost design is given by a cylinder made of low-strength material only. On the other hand, if $P_0 > P_{hs}$ then the solution does not exist for the specified high-strength material and P_0 and with the given geometric dimensions. For a hybrid cylinder to provide the minimum cost design, the inequality

$$P_{ls} < P_0 < P_{hs} \tag{9}$$

has to be satisfied.

Let t_{ls} and t_{hs} denote the thicknesses of the low-strength and high-strength layers, respectively. Then the minimum cost problem can be stated as: "Determine the minimum value of t_{hs} for a cylinder of inner radius a and outer radius b subject to internal and external pressures p and q and a temperature change ΔT such that the failure pressure P_f satisfies the inequality (8)".

Thus t_{hs} is to be minimized subject to eqn (8). with P_0 satisfying the inequality (9) for a solution given by a hybrid cylinder.

METHOD OF SOLUTION

The solution procedure involves the computation of the failure pressure using a suitable failure criterion. In the present study, the maximum stress criterion is chosen for this purpose. For the kth layer, let X_{tk} and X_{ck} denote the tensile and compressive strengths of the composite material in the fibre direction and Y_{tk} and Y_{ck} in the transverse direction. Then the requirements for non-failure can be expressed as

$$X_{ck} \leq \sigma_{\theta k}(r) \leq X_{tk}, \quad Y_{ck} \leq \sigma_{rk}(r) \leq Y_{tk} \quad \text{for } a \leq r \leq b \tag{10}$$

The failure pressure is obtained by setting

$$\sigma_{\theta k}(r) = X_{ck}, \quad \sigma_{\theta k}(r) = X_{tk} \text{ for } a \leq r \leq b \tag{11}$$

$$\sigma_{rk}(r) = Y_{ck}, \quad \sigma_{rk}(r) = Y_{tk} \text{ for } a \leq r \leq b \tag{12}$$

and computing the minimum failure pressure over r for each equation in (11) and (12). The procedure is repeated for each $k = 1, 2, \ldots, K$. Let $P_{1k}(r)$, $P_{2k}(r)$, $P_{3k}(r)$ and $P_{4k}(r)$ denote the failure pressures at r for each of the four equations in (11) and (12). Then, P_f is given by

$$P_f = \min_k \min_i \min_r |P_{ik}(r)| \tag{13}$$

where $k = 1, 2, \ldots, K$, $i = 1, 2, 3, 4$ and $c_k \leq r \leq c_{k+1}$.

In order to implement the above procedure the stresses $\sigma_{rk}(r)$ and $\sigma_{\theta k}(r)$ need to be computed. The first step in this regard is the solution of the differential eqn (5). This solution is given by

$$U_k(r) = A_k r^{\eta_k} + B_k r^{-\eta_k} + \xi_k r \tag{14}$$

where

$$\xi_k = [\Delta T/(1-\eta_k^2)][(\nu_{\theta k} - \eta_k^2)\alpha_{\theta k} + (1 - \nu_{rk}\eta_k^2)\alpha_{rk}] \tag{15}$$

and A_k and B_k are the unknown integration constants to be evaluated from the conditions (6) and (7). By substituting eqn (14) into eqn (3), the strains can be computed which are inserted into eqns (1) and (2) to obtain the stress components.

The optimization procedure involves minimizing the thickness t_{hs} of the high-strength layers subject to the constraint (8). Since $P_f = P_f(t_{hs})$, a computational algorithm can be devised such that the minimum value of t_{hs} is determined with $P_f(t_{hs}) \leq P_0$. In practice, this value corresponds to the equality $P_f(t_{hs}) = P_0$.

NUMERICAL RESULTS AND DISCUSSION

In the numerical results, the high-strength material is specified as graphite/epoxy (T300/5208) and the low-strength material as glass/epoxy (Scotchply 1002). The elastic constants and strength values for these materials are:

Graphite/epoxy: $E_\theta = 181$ GPa, $E_r = 10.3$ GPa, $\nu_\theta = 0.28$, $\alpha_\theta = 0.02 \times 10^{-6}$ K^{-1}, $\alpha_r = 22.5 \times 10^{-6}$ K^{-1}, $X_t = 1500$ MPa, $X_c = -1500$ MPa, $Y_t = 40$ MPa, $Y_c = -240$ MPa.

Glass/epoxy: $E_\theta = 38.6$ GPa, $E_r = 8.27$ GPa, $\nu_\theta = 0.26$, $\alpha_\theta = 8.6 \times 10^{-6}$ K^{-1}, $\alpha_r = 22.1 \times 10^{-6}$ K^{-1}, $X_t = 1062$ MPa, $X_c = -610$ MPa, $Y_t = 31$ MPa, $Y_c = -118$ MPa.

The temperature dependent material properties indicated by a superscript T are computed using the expressions

$$E_\theta^T = E_\theta(1 + \psi_1 \Delta T), \quad E_r^T = E_r(1 + \psi_2 \Delta T) \tag{16}$$

$$\alpha_\theta^T = \alpha_\theta(1+\beta_1\Delta T), \quad \alpha_r^T = \alpha_r(1+\beta_2\Delta T) \tag{17}$$

$$X_{t,c}^T = X_{t,c}(1+\psi_1\Delta T), \quad Y_{t,c}^T = Y_{t,c}(1+\psi_2\Delta T) \tag{18}$$

where $\psi_1 = -0.005$, $\psi_2 = -0.004$, $\beta_1 = 0.004$, $\beta_2 = 0.003$. These values are based on the graphs of the elastic constants and strength values plotted against the temperature as given in Refs [13] and [14]. The efficiencies of the optimal designs are assessed by comparing the thickness of the graphite layer in the optimal hybrid construction with the thickness of a cylinder made of graphite/epoxy only and satisfying the constraint (8). Thus, the following efficiency index I is defined

$$I = 100(t_{gr} - t_{min})/t_{gr} \tag{19}$$

where t_{gr} denotes the thickness of the all-graphite cylinder and t_{min} the thickness of the graphite layer in the optimum hybrid construction with both designs satisfying the constraint (8). It is noted that in the case of all-graphite cylinder, the inner radius is specified as a and the outer radius becomes $a+t_{gr}$, while in the hybrid construction inner and outer radii are specified as a and b, respectively. Clearly the index I indicates the percentage saving for the high-strength material which can be realized by an optimal hybrid construction as opposed to a non-hybrid construction using only the high-strength material.

Numerical results are given for three example problems involving a two-layered cylinder under internal pressure only, a two-layered cylinder under external pressure only and a three-layered cylinder under internal and external pressures.

Two-layered cylinder under internal pressure

For this case the inner layer is specified as graphite/epoxy and the outer layer as glass/epoxy. The reason for this choice is to place the stronger layer where the pressure acts. Figure 1 shows the curves of t_{min}/a and the efficiency index plotted against b/a for $\Delta T = 0$ and $\Delta T = 100$ K. The constraint on the failure pressure is specified as $P_0 = 0.5(P_{gl}+P_{gr})$ where P_{gl} and P_{gr} denote the failure pressures of the corresponding all-glass and all-graphite cylinders, respectively. It is noted that P_0 changes as b/a changes since P_{gl} and P_{gr} depend on b/a. In particular P_0 increases as b/a increases as the thicker thickness ration leads to higher failure pressures. It is observed that if the temperature dependence of material properties is neglected, t_{min} curves for $\Delta T = 0$ and $\Delta T = 100$ K become quite similar even though the efficiency indices differ. Taking the temperature dependence of the material properties into account leads to higher efficiencies. Next, the effect of the failure pressure on t_{min} and the efficiency is studied in Fig. 2 with $b/a = 1.2$. Efficiency of the designs drop as the pressure increases since the thickness of the graphite layer approaches that of an all-graphite cylinder. For the same pressure, higher temperature leads to thicker cylinders when the properties are temperature dependent, which is a physically expected result.

Two-layered cylinder under external pressure

Next, two-layered cylinders under external pressure only are studied placing the graphite/epoxy

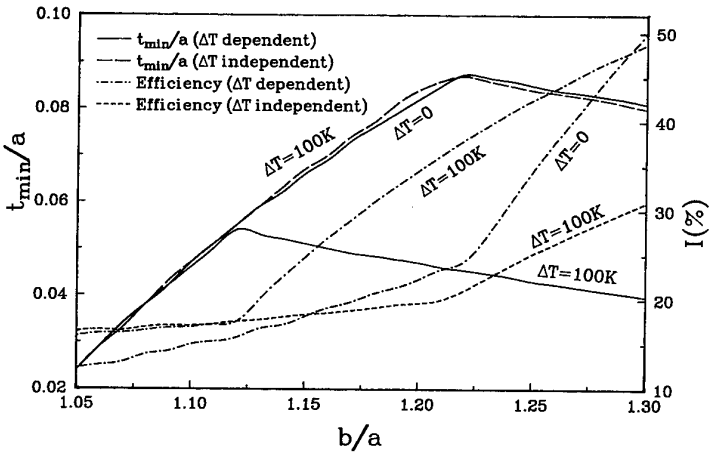

Fig. 1. Minimum thickness and efficiency vs. b/a for two-layered cylinders under internal pressure ($q = 0$).

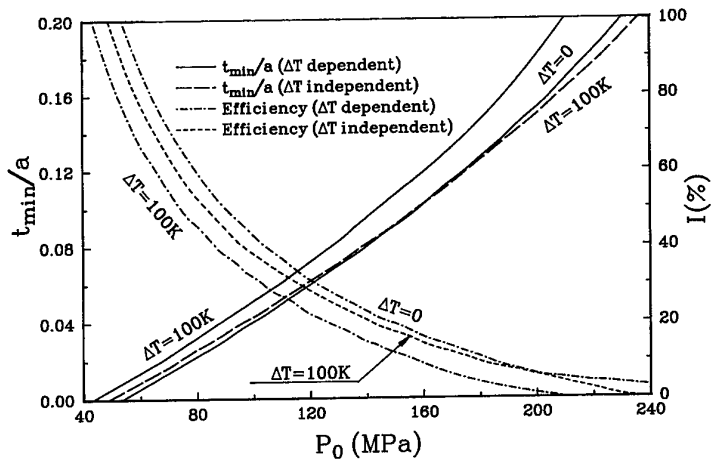

Fig. 2. Minimum thickness and efficiency vs. failure pressure with $b/a = 1.2$ and $q = 0$.

in the outer layer and the glass/epoxy in the inner layer. Again, the stronger layer is placed where the pressure acts. Figure 3 shows the curves of t_{min}/a and the efficiency plotted against b/a for $\Delta T = 0$ and $\Delta T = 100$ K with $P_0 = 0.5(P_{gl}+P_{gr})$. Comparison of Figs 1 and 3 indicate that the curves of t_{min} and the efficiency show similar trends with respect to the thickness ratio b/a for internal and external pressures. However t_{min} is not affected by temperature increase for $b/a \leq 1.12$, and t_{min} for $\Delta T = 100$ K becomes much smaller for $b/a \geq 1.12$ in the case of external pressure. The values of the failure pressures corresponding to the thicknesses given in Figs 1 and 3 are shown in Fig. 4 with respect to b/a. Even though $P_f = P_0$ increases as b/a increases, the rate of increase drops sharply for higher values of b/a. Figure 4 also shows that higher temperatures lead to thicker cylinders as expected.

Three-layered cylinder under internal and external pressures

In this case, the inner and outer layers are constructed of equal-thickness graphite/epoxy material with the middle layer constructed of glass/epoxy. t_{min} denotes the combined thickness of the graphite layers. Figure 5 shows the curves of t_{min}/a and efficiency plotted against b/a for $\Delta T = 0$ and $\Delta T = 50$ K with internal and external pressures given as $p = 150$ MPa and $q = 20$ MPa, respectively. For higher temperatures a higher thickness of the stronger material is needed, and the efficiency becomes lower. It is noted that in this case t_{min} decreases with increasing b/a because the pressures are kept constant as opposed to the situations considered in Figs 1 and 3. In Fig. 6, the internal pressure is specified as $p = 150$ MPa and the curves of minimum thickness and the efficiency

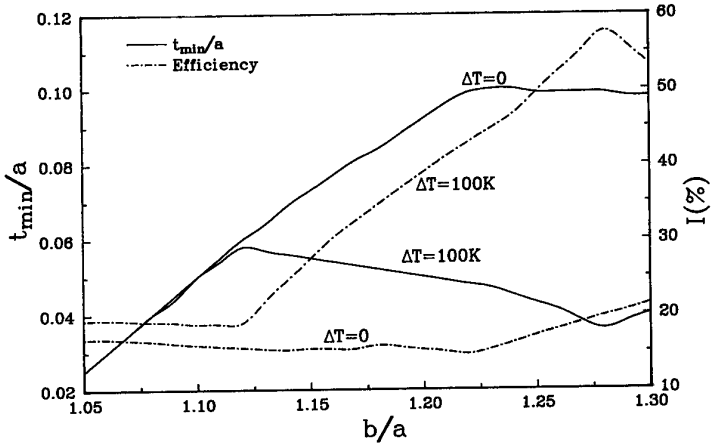

Fig. 3. Minimum thickness and efficiency vs. b/a for two-layered cylinders under external pressure ($p = 0$).

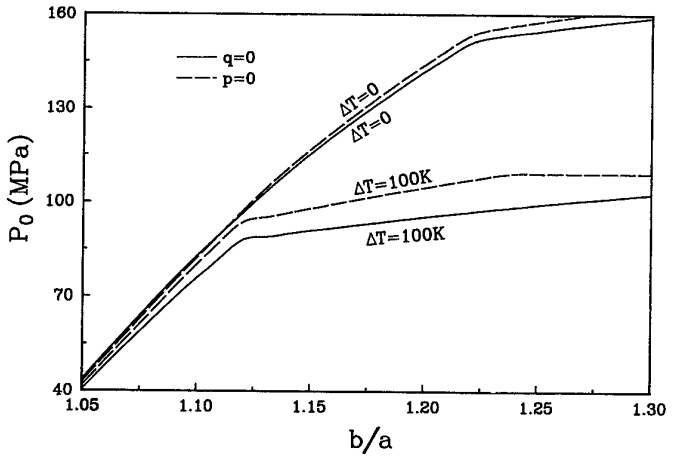

Fig. 4. Failure pressure vs. *b/a* for two-layered cylinders with temperature dependent properties.

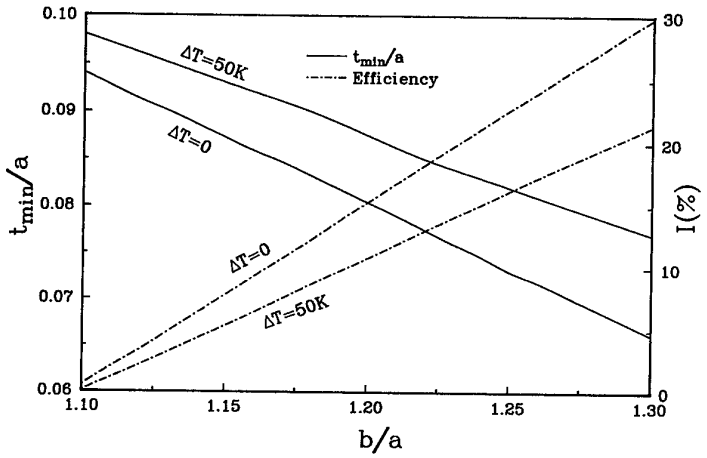

Fig. 5. Minimum thickness and efficiency vs. *b/a* for three-layered cylinders with $p = 150$ MPa, $q = 20$ MPa.

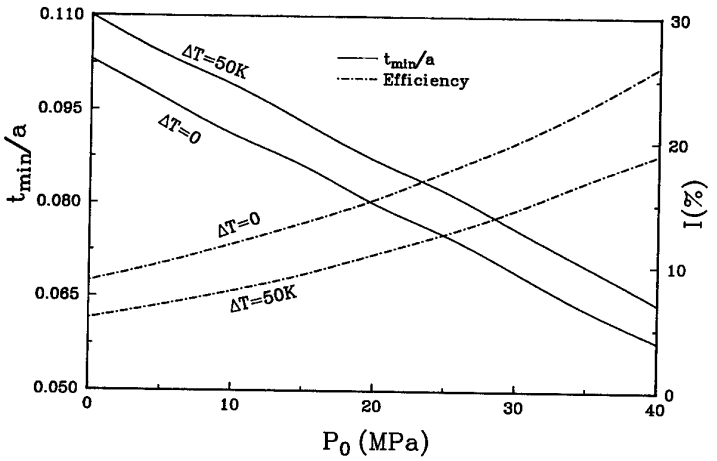

Fig. 6. Minimum thickness and efficiency vs. external failure pressure for three-layered cylinders with $b/a = 1.2$ and $p = 150$ MPa.

are plotted against the external failure pressure for a cylinder with $b/a = 1.2$. It is interesting to note that t_{min} decreases as the external pressure is increased, indicating that the stresses in the cylinder drops as external pressure counteracts against the internal pressure. For three-layered cylinders, the efficiencies are, in general, lower than those of two-layered ones working under internal or external pressure only.

CONCLUSIONS

The cost of materials used in the construction of laminated thick cylinders is minimized by means of hybridization. The hybrid cylinder is composed of layers of high- and low-strength fibre reinforced materials. The locations of these layers match the high and low stress patterns generated by internal and/or external pressures acting on the cylinder and temperature change. The cost, defined as the thickness of the high-strength layers, is minimized not only by use of the less expensive material in the lightly stressed areas, but also by using the minimum amount of the expensive material subject to the constraint that the failure pressure will be higher than a specified value. The thickness ratio b/a is specified as a problem parameter.

It is noted that a hybrid cylinder gives the optimum design if the specified failure pressure P_0 is higher than the failure pressure of the cylinder made of low-strength material only. Moreover a hybrid construction cannot be used if P_0 exceeds the failure pressure of the cylinder made of high-strength material only.

Numerical results are given for two- and three-layered cylinders using graphite/epoxy and glass/epoxy layers in the high and low stress areas. The effects of the thickness ratio b/a, the failure pressure and the temperature increase on the minimum thickness of the graphite layers and the efficiency of the designs are discussed. The efficiency is defined in comparison with the thickness of the corresponding cylinder made of the expensive material only. In the computations, temperature dependent material properties are used and comparisons are given for different temperatures. It is shown that neglecting the effect of heating on the material properties would lead to underdesign and consequently to premature failure if the cylinder works under thermal loads. It is observed that the design efficiency drops as P_f increases. However, the efficiency increases as the cylinder becomes thicker. Thus a hybrid design is more cost-effective at lower pressures and for thicker cylinders.

The cost of advanced composite materials makes up a considerable portion of the total production expenses due to the high costs of such materials as graphite, boron and kevlar. Improving the cost-effectiveness of a composite structures by means of hybridization and design optimization will increase the use of composites in engineering applications by virtue of reducing the overall costs.

REFERENCES

1. Adali, S. & Yakar, B., Minimum cost design of laminated cylinders under internal and external pressure by hybrid construction. In *Composites: Design, Manufacture and Applications, Proceedings of the Eight Int. Conf. on Composite Materials (ICCM/VII)*, Honolulu, Hawaii, 15–19 July 1991, eds S. W. Tsai and G. S. Springer, pp. 5c, 1–5c, 10.
2. Adali, S. and Duffy, K. J., Optimal hybridization of antisymmetric laminates undergoing free vibrations. *Engng Optimization*, 1991, **18** (4), 287–301.
3. Adali, S. and Duffy, K. J., Minimum cost design of vibrating laminates by hybridization. *Engng Optimization*, 1992, **19**, 255–267.
4. Adali, S. and Duffy, K. J., Optimal hybridization of symmetric, cross-ply laminates against biaxial buckling. *ASCE J. Aerospace Engng*, 1993, **6** (4), 394–406.
5. Pagano, N. J., Stress gradients in laminated composite cylinders. *J. Composite Materials*, 1971, **5**, 260–265.
6. Galmudi, D. and Dvorkin, J., Stresses in anisotropic cylinders. *Mechanics Research Communications*, 1995, **22** (2), 109–113.
7. Horgan, C. O. and Baxter, S. C., Effects of curvilinear anisotropy on radially symmetric stresses in anisotropic linearly elastic solids. *J. Elasticity*, 1996, **42**, 31–48.
8. Hyer, M. W., Cooper, D. E. and Cohen, D., Stresses and deformations in cross-ply composite tubes subjected to a uniform temperature change. *J. Thermal Stresses*, 1986, **9**, 97–117.
9. Belingardi, G., Genta, G. and Gola, M., Optimization of orthotropic multilayer cylinders and rotating discs. *L'AeroTecnica Missili E Spazio*, 1977, **56** (4), 204–209.
10. Leissa, A. W., The design of orthotropic materials for stress optimization. *Int. J. Solids and Structures*, 1978, **12**, 517–526.
11. Roy, A. K. and Tsai, S. W., Design of thick composite cylinders. *ASME J. Pressure Vessels*, 1988, **110**, 255–262.
12. Kamiya, N. and Fukui, A., Finite deflection and post-buckling behaviour of heated rectangular plates with temperature dependent properties. *Nuclear Engng Design*, 1982, **72**, 415–420.
13. Chen, J. K., Sun, C. T. and Chang, I. C., Failure analysis of a graphite/epoxy laminate subjected to combined thermal and mechanical loading. *J. Composite Materials*, 1985, **19**, 408–423.
14. Griffis, C. A., Nemes, J. A., Stonesifer, F. R. & Chang, I. C., Degradation in strength of laminated

composites subjected to intense heating and mechanical loading. In *Environmental Effects on Composite Materials,* ed. by G. S. Springer. Technomic Publishing, Lancester, Penn, Vol. 3, 1988, pp. 415–420.
15. Chen, L. W. and Chen, L. Y., Thermal buckling behaviour of laminated composite plates with temperature dependent properties. *Composite Structures*, 1989, **13**, 275–287.
16. Adali, S. & Yakar, B., Optimal design of laminated pressure vessels under internal pressure and temperature loading. In *Pressure Vessels and Components PVP-Vol. 217, Proceedings of ASME Pressure Vessels and Piping Conf.,* San Diego, California, 23–27 June 1991, ed. G. N. Brooks *et al.*, pp. 57–63.
17. Uemura, M., Iyama, H. & Fukunaga, Y., Rotational strength and optimal design of a hybrid filament wound disc. In *Composites Structures 2: Proceedings of the 2nd Int. Conf. on Composite Structures*, Paisley, Scotland, 23–27 September 1983, ed. I. H. Marshall, pp. 282–301.

ELSEVIER

Composite Structures Vol. 38, No. 1–4, pp. 631–647, 1997
© Published by 1997 Elsevier Science Ltd. All rights reserved
Printed in Great Britain
0263-8223/97/$17.00 + 0.00

PII:S0263-8223(97)00101-3

The behaviour of open and closed section carbon fibre composite beams subjected to constrained torsion

J. Loughlan & M. Ata

Structures and Materials Technology Group, College of Aeronautics, Cranfield University, Cranfield, MK43 OAL, UK

A simple engineering theoretical approach is presented in this paper which is able to predict the initial constrained torsional response of a specific class of thin-walled open-section and single-cell closed-section carbon fibre composite beams. The flat walls of the composite beams are symmetrically laminated about their own mid-planes and possess membrane orthotropy. The laminated flats are assembled in such a way that the stiffness distribution round the section is of a symmetrically disposed nature and thus the flanges of a composite box-section, for example, can have a different lay-up configuration to that of the section webs. Beams of this type are essentially uncoupled in their overall stiffnesses and thus it is possible to apply axial load or bending to the sections without inducing torsional behaviour.

The analysis procedures for such beams will, of course, be considerably less complex in nature than those associated with beams of a more general lay-up configuration. Indeed, the analysis approach adopted in this paper simply makes use of the existing theories of torsion appropriate to isotropic construction and these are then suitably modified to account for the non-isotropic nature of the composite material. The torsional and warping rigidities for use in the analysis of the composite beams are thus duly determined through the use of the appropriate equivalent engineering elastic constants of the individual thin composite walls and the concept of effective thickness is employed to account for the different stiffnesses in the walls.

In the paper some detailed attention is paid to the effects of primary and secondary warping restraint on the torsional response of open section beams and the distinct differences between sections whose behaviour is governed predominantly by primary effects and those whose response is associated solely with secondary effects are discussed. The stress systems set up in open-section and single-cell closed-section carbon fibre composite beams when subjected to torsion with variable twist are examined in the paper and in particular it is shown that although the shear flow due to primary warping restraint in open-section beams serves in part to equilibrate the applied torque, that in closed box section beams is completely self equilibrating. Comparisons are given in the paper between theory and experiment and between theory and finite element solutions and these are shown to give good agreement for the Z, angle and box section beams considered. © 1997 Published by Elsevier Science Ltd.

INTRODUCTION

Much of the research pertaining to composite structural sections, open or closed in nature, has been associated with the effects of warping restraint and of global stiffness couplings on structural response [1–8]. In the work of Mansfield & Sobey [1], the authors examine the stiffness characteristics of simple fibre composite tube profiles with particular attention being paid to the possible advantages of induced blade twist. The aeroelastic stability of a bear-

ingless composite rotor blade in the hover mode has been investigated, using a finite element formulation [2]. A beam finite element formulation incorporating the effects of warping has been developed by Lee & Kim [3]. The formulation is based on small deflection theory and is applicable to isotropic elastic materials. The finite element formulation developed by Stemple & Lee [4] is essentially an extension of the application of the approach of Ref. [3] and thus it is shown to be capable of modelling the combined bending, torsional and extensional behaviour of composite beams and through numerical tests, induced torsion and bending due to axial loading is demonstrated for selected fibre lay-up configurations.

Tests on graphite–epoxy thin-walled box-beams have been carried out by Chandra *et al.* [5] whereby the use of symmetric and antisymmetric lay-up configurations for the box-beams permit the examination of bending–torsion coupling and extension–torsion coupling respectively. The behaviour of composite I-beams with elastic couplings has been studied both theoretically and experimentally by Chandra & Chopra [6] and in this work it is shown that the local extension–twist coupling of the individual flange elements of the sections significantly influences the overall bending–torsion coupling of the I-beams. A generalised beam theory for open section laminated composite beams involving all possible coupling combinations has been derived by Zvarick & Cruse [7] using a strength of materials approach. Although generalised loading can be accommodated using their approach, it is to be noted that their theory is limited in its application to statically determinate beams and to cross-sectional geometries which are of a continuous curvilinear nature only. An asymptotically consistent theory has been proposed by Badir *et al.* [8] for composite thin-walled open section beams. Their approach yields closed-form expressions for the beam stiffness coefficients and for its stress and displacement fields and the influence of material anisotropy on the displacement field is readily identified. Their theory is shown to provide favourable agreement with the independent test data of Ref. [6] pertaining to cantilevered composite I-beams.

The torsional analysis of closed profiles which consist of one or more cells and experience variable twist, whereby the thin walls of the sections are required to resist both shear and axial components of stress, is indeed an extremely complex process to undertake. With regard to isotropic construction, mention is made here of the detailed and informative contributions made by Von Karman & Christensen [9], Fine & Williams [10], Argyris & Dunne [11], Benscoter [12] and Waldron [13].

The analytical studies of Von Karman & Christensen [9] and Fine & Williams [10], although distinctly different in their approach, use the common assumption of neglecting the effects of the warping shear strains on torsional response and it is thus considered in their work that only the St. Venant shear strain has significance.

A major contribution to the development and understanding of the complex analytical procedures necessary for dealing with the torsional–bending response of beams of arbitrary cross-section is given in the work of Argyris & Dunne [11]. The stressing of single or multi-cell tubes typical of that encountered in aircraft wing structures is dealt with by Argyris & Dunne [11] in a rational manner and their generalised theory is able, within the limitations of the closely spaced rigid rib assumption, to give exact solutions for a specific class of cylindrical tube construction.

The effect of shearing strains on beam deflections is fully accounted for in the works of Benscoter [12] and Waldron [13] and this manifests itself, in their respective analyses, through a warping shear parameter which essentially serves to give a measure of that part of the rate of twist of the beam associated with axial warping displacements. Neglecting the effects of the warping shear strains in analysis is shown, in this paper, through comparisons between the approaches of Von Karman & Christensen [9] and Benscoter [12] and with results from finite element studies, to result in significant inaccuracies in the predictions of torsional response.

The design and analysis procedures pertaining to composite box beam construction in particular, have been given consideration by a number of investigators [14–17]. The torsional stiffness of a composite box beam undergoing free torsion has been determined by Barrau & Laroze [14] using the finite difference method of analysis. The complexities associated with composite box beam construction typical of that used in aerospace applications are addressed in the works of Bicos & Springer [15] and Bauchau *et al.* [16]. In the work of Smith & Chopra

[17], the effects of cross sectional warping due to torsion and of transverse shear due to bending are appropriately accounted for in their analytical model of composite box beams and this is reflected in the good correlation of the model predictions with the experimental test data of Ref. [5].

In this paper the authors examine the torsional response of open-section and single-cell closed-section carbon fibre composite beams whereby the overall elastic couplings of the beams are eliminated through the use of constituent laminates which are symmetrically layed-up about their own mid-planes and which possess in-plane orthotropy. In particular, some specific attention is paid to the distinct differences in the response of open sections which are governed, in the main, by the effects of primary warping restraint and those whose constrained behaviour is determined solely from a consideration of secondary warping effects. Some detailed attention is also given to the quite different stress systems set up in open and closed-section carbon fibre composite beams when subjected to torsion with variable twist. The analysis procedures for composite beams with uncoupled stiffnesses will, of course, be of a less complex nature than those associated with beams of a more generalised lay-up configuration and thus the existing theories for isotropic construction can be modified in a simple manner to account for the effects of layered composite material and this approach has been employed with a considerable degree of success for such uncoupled beams. Ata [18] has examined the constrained torsional behaviour of open and closed-section carbon fibre composite beams using this approach and details of this work are reported in Refs [19,20] for open Z-section beams and with regard to single-cell closed box sections.

THEORETICAL DETAILS

The reactive response of thin-walled prismatic beams to torsional loading depends to a large extent on cross-sectional geometry and in particular on whether the section is open or closed in nature. In the case of free torsion the stresses in the thin walls of the beam will be the same at every cross-section along its length. The stresses at any section are thus closed loop shear stresses which equilibrate the applied torque. These stresses vary linearly through the thickness of the thin walls when the beam is of open cross-section in which case they are zero at the wall mid-planes and are maximum at the wall surfaces. For open section beams the closed loop shear stresses are well known as the St. Venant stresses. For closed section beams torsional equilibrium is achieved through a closed loop shear stress system in which the stresses are uniform through the thickness of the thin walls. These stresses are commonly referred to as the Bredt–Batho stresses.

When a thin-walled beam is subjected to free torsion then the cross-sections of the beam will experience a free warping distribution. In this case the longitudinal generators of the beam profile are unstrained and thus all sections of the beam will experience an identical warping distribution. For open-section beams such as Zs, channels or I-sections both primary or membrane warping and secondary or through-the-thickness bending warping are present. Primary warping is predominant for these sections and thus secondary warping is normally ignored in their analysis. Angle, T or cruciform sections, on the other hand, possess only secondary warping and this should be considered in the analysis of such beams, particularly if they are of composite construction. For closed-section beams the warping displacements to be considered are of a primary or membrane nature.

In the case of torsion associated with variable twist resulting from warping restraint there are additional distinct differences between open- and closed-section beams with regard to their reactive response. If the longitudinal warping displacements are prevented in any way then, of course, additional stress states to those already discussed for the case of free torsion will be realised.

For open-section beams subjected to constrained torsion the St. Venant stresses still exist. They are, however, now associated with a variable rate of twist and thus their magnitude changes from section to section along the beam length. For those sections whose behaviour is governed predominantly by the effects of primary warping then secondary warping is ignored in analysis and thus the equilibrium of the applied torque will now be provided by the St. Venant shear stresses and the shear stresses due to constrained primary warping. The contributions from each stress system will, of

course, depend on the location along the beam length of the cross-section being considered. The warping shear stresses will provide the more predominant contribution in the vicinity of the constrained warping location and at increasing distances away from this location the St. Venant stresses will become more and more effective.

For those sections whose constrained behaviour is governed solely by the effects of secondary warping it is found that the warping shear stresses are small compared to the St. Venant stresses and thus they are usually ignored and the applied torque is considered to be equilibrated, effectively, by the St. Venant stresses. Constrained secondary warping in sections which do not possess primary warping can cause quite high direct stresses however at the restrained location and these have to be given consideration. This is particularly true if the section is of composite construction in which case sudden failures are possible and thus it is essential to be able to predict stress levels accurately.

The response of closed box-section beams to constrained torsion is somewhat different to that of open-section beams. In this case the Bredt–Batho stresses still exist. These stresses are, of course, not a function of the section twist and thus a variable rate of twist along the beam length does not affect them. This means that, as in the case of free torsion, their magnitude remains constant and is the same at all sections along the beam length for a given applied torque. The Bredt–Batho stresses are therefore solely responsible for equilibrating the applied torque and as a result the shear stresses due to constrained warping must now be self-equilibrating in nature with respect to torque about the section shear centre as well as to transverse effects.

Composite construction

The response to applied loading of thin-walled structural sections manufactured from symmetrically laminated composite materials can be conveniently determined through the use of the appropriate engineering elastic constants of the laminated walls. The engineering constants will, of course, be prescribed differently when giving consideration to the membrane and bending modes of action respectively of the laminated walls and thus for the case of torsional loading care must be taken in the choice of constants for use in the analysis of different cross-sectional geometries.

Clearly, the membrane stiffnesses of a symmetric laminate will be unaffected by change in position of the plies in the stacking sequence but, of course, this will alter, significantly, the local through-the-thickness bending rigidities of the laminate and thus the torsional and warping rigidities of a composite structural section will be determined according to cross-sectional shape and in particular will be influenced by the lay-up configuration of the section walls. In this paper the constituent laminated walls of the beams considered are symmetrically layed-up about their own mid-planes and in addition each wall exhibits membrane orthotropy.

The equivalent engineering elastic constants of a generally orthotropic symmetric laminate are given for the membrane mode of action as follows;

$$E_x = \frac{1}{ta_{11}}, \; E_y = \frac{1}{ta_{22}}, \; G_{xy} = \frac{1}{ta_{33}}$$

$$\nu_{xy} = -\frac{a_{12}}{a_{11}}, \; \nu_{yx} = -\frac{a_{12}}{a_{22}}$$

$$m_x = -\frac{a_{13}}{a_{11}}, \; m_y = -\frac{a_{23}}{a_{22}} \qquad (1)$$

The corresponding elastic constants pertaining to the bending mode of action are then described by the following relationships;

$$E_x = \frac{12}{t^3 d_{11}}, \; E_y = \frac{12}{t^3 d_{22}}, \; G_{xy} = \frac{12}{t^3 d_{33}}$$

$$\nu_{xy} = -\frac{d_{12}}{d_{11}}, \; \nu_{yx} = -\frac{d_{12}}{d_{22}}$$

$$m_x = -\frac{d_{13}}{d_{11}}, \; m_y = -\frac{d_{23}}{d_{22}} \qquad (2)$$

In eqns (1) and (2), a_{ij} and d_{ij} are the membrane stiffness and the bending stiffness compliance coefficients, respectively, and t is the laminate thickness. The superscripts m and b refer to the membrane and bending modes of action, respectively. The constants E_x and E_y are the mutually orthogonal compression moduli of the laminate, G_{xy} is the shear modulus, ν_{xy} and

ν_{yx} are the major and minor Poisson's ratios and the constants m_x and m_y give a measure of the degree of coupling between normal and shear strains when considering membrane action of the laminate and between bending and twisting curvatures when considering laminate flexural action.

In this paper we wish to examine the torsional response of open and single-cell closed composite sections whose flat walls are especially orthotropic in the membrane mode and thus m_x and m_y are zero for this mode of action. Symmetric angle-ply and quasi-isotropic lay-up configurations, however, will be associated with local bend–twist couplings and thus m_x and m_y will not be zero in the local bending mode. The influence of local bend–twist couplings on overall section behaviour has been shown in Ref. [6] to be small and as such their effect is precluded in this paper with respect to the overall torsional response of the composite beams considered.

Open sections

The positive components of the displacement of a point in the beam section wall are shown in Fig. 1. In the global sense these are u, v and w as indicated whereas in local coordinates v_t, v_n and w are used, the tangential, normal and longitudinal or warping displacements, respectively. In Fig. 1, s is the local profile coordinate, n is the local normal coordinate measured from the mid-plane of the section walls through the wall thickness and θ is the angle of twist of the beam. The local ns coordinate system is shown in Fig. 2, which illustrates the nature of the St. Venant stresses through the wall thickness when a beam is subjected to free torsion.

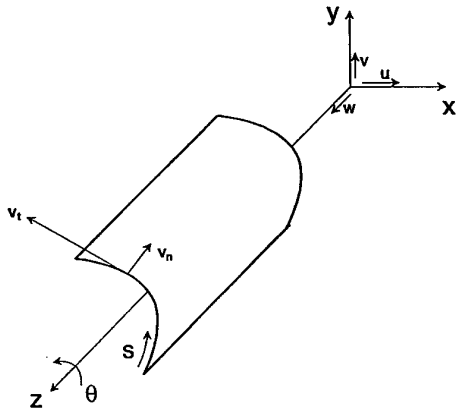

Fig. 1. Positive components of displacement of a point on the beam section.

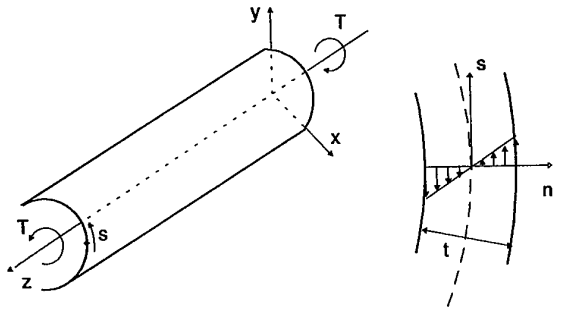

Fig. 2. Free torsion of a thin-walled beam.

The cross-sections of thin-walled open-section beams can experience two types of longitudinal warping displacement when subjected to torsional loading. These are referred to as primary and secondary warping, respectively. Primary or membrane warping is, in effect, the longitudinal displacements of the mid-plane of the cross-section and these are assumed constant across the wall thickness. Secondary or local bending warping on the other hand is the variation in longitudinal displacements across the section walls. Both types of warping are illustrated schematically in Fig. 3, with w and w^* representing the primary and secondary displacements, respectively.

Typical beam cross-sections which possess both primary and secondary warping are shown in Fig. 4(a). For such sections the effects of restrained secondary warping are usually neglected in analysis since they are generally much smaller than those associated with primary warping restraint. Not all sections possess primary warping and some typical examples of these are shown in Fig. 4(b). For these sections all of the constituent flat walls pass through the section shear centre at the single junction connecting the walls and thus primary warping does not occur and only secondary warping is pos-

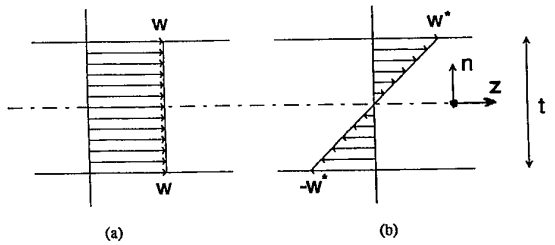

Fig. 3. Warping displacement across the wall thickness of an open-section beam: (a) primary, (b) secondary warping.

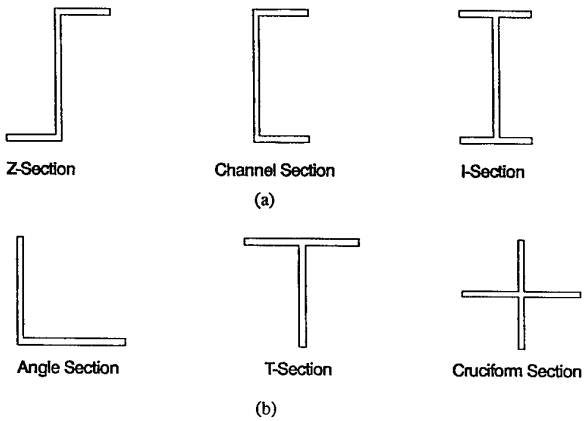

Fig. 4. Typical beam cross-sections: (a) predominant primary warping, (b) secondary warping only.

sible in this case. For sections which possess only secondary warping the effects of warping restraint can be significant and should not be ignored in analysis.

Primary warping

The constrained condition considered in the paper is that of the cantilevered beam of length L with torque T applied at the free end and the z coordinate measured along the beam from the fixed end. Giving consideration first to those open sections which possess both primary and secondary warping then secondary effects are ignored and the primary warping displacements w are described by

$$w = -\omega(s)\frac{d\theta}{dz} \tag{3}$$

where $(d\theta/dz)$ is the rate of change of the angle of twist of the beam at location z along its length and $\omega(s)$ is the sectorial coordinate of the beam cross-section. With reference to Fig. 5, the sectorial coordinate of the beam cross-section is given by

$$\omega(s) = \int_0^s P_R ds \tag{4}$$

where the integral represents twice the area A_R indicated. Clearly, P_R is the perpendicular distance from the shear centre R of the cross-section to the tangent at any point s in the mid-plane of the section as illustrated. Using eqn (4) the sectorial coordinate distribution for a Z-section beam of flange width b and web

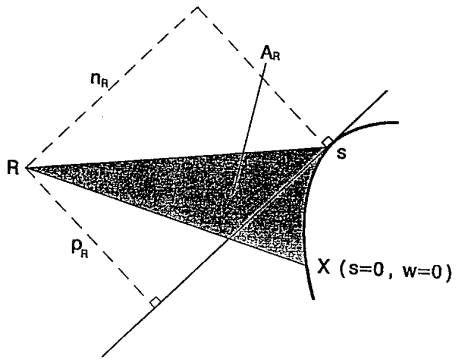

Fig. 5. Determination of the warping of an open-section beam.

height h has been determined and this is detailed in Fig. 6. For this section it is of note that the warping displacements in the web will be the same everywhere and those in the flanges will be linearly varying with zero warping points occurring in the flanges at a distance d from the flange–web junctions.

The warping shear flow in a thin-walled section resulting from constrained primary warping is written in terms of the sectorial shear function $S\omega(s)$ of the beam cross-section and this is determined as follows

$$S_\omega(s) = \int_0^s \omega(s)t ds \tag{5}$$

The sectorial shear function distribution has been determined, through the use of eqn (5), for the Z-section beam previously considered and this is illustrated in Fig. 7. It is clear that the warping shear flow around the section will be self equilibrating in the two mutually ortho-

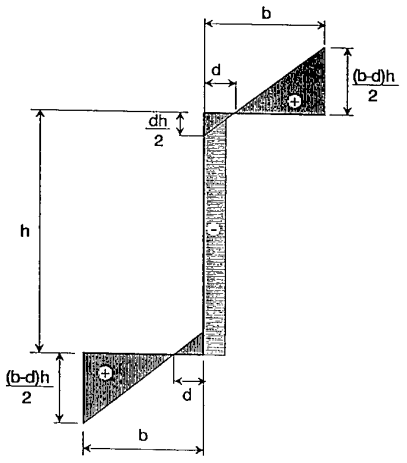

Fig. 6. Sectorial coordinate distribution for a Z-section.

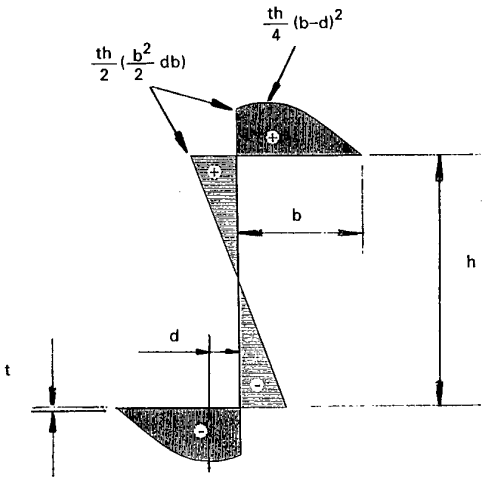

Fig. 7. Sectorial shear function distribution for a Z-section.

gonal directions perpendicular and parallel to the section web as is to be expected for the case of torsional loading. The shear flow is linearly varying in the web and is zero at the section shear centre. The maximum shear flow is noted to occur in the flanges of the section and this is at the zero warping locations at d from the flange–web junctions. It is evident that the warping shear flow distribution round the section will result in a torque about the section shear centre and this plus that associated with the St. Venant stresses then serve to equilibrate the applied torque on the beam.

The warping torque at any cross-section of a constrained thin-walled beam depends effectively on the sectorial moment of inertia Γ of the beam cross-section or, as it is often referred to, the torsion–bending constant of the beam and this is expressed as follows;

$$\Gamma = \int_{\text{section}} \omega^2(s) t \, ds \tag{6}$$

For open cross-sections which possess predominantly primary warping then the engineering elastic constants of the composite material which are of major importance are E_x in the membrane mode for the evaluation of the warping rigidity of the section and G_{xy} in the bending mode for the determination of the St. Venant torsional rigidity of the beam. This is presuming, of course, that the local x-direction of the section laminate walls is coincident with the global z-axis of the beam.

For the composite section with different lay-up configurations in its flange and web elements the St. Venant torsional rigidity term GJ is thus given as follows;

$$(GJ)_s = \frac{1}{3} \sum_{i=1}^{n} G^b_{xy_i} S_i t_i^3 = 4 \sum_{i=1}^{n} \frac{S_i}{d_{33_i}} \tag{7}$$

Also, for the section with different lay-up configurations in its component flats, we make use of the effective or average elastic compression modulus for the whole section as described by

$$E_{\text{av}} = \frac{\Sigma E^m_{xi} S_i t_i}{\Sigma S_i t_i} \tag{8}$$

The location of the zero warping points in a thin-walled composite open-section depend, not only on section geometry, but on the stiffness variation around the section resulting from the different lay-up configurations in the section walls. To account for this in analysis use is made of the concept of effective thickness and thus the zero warping points of the Z-section with different lay-ups in its flange and web elements are determined for the case of torsional loading on the basis that the axial warping stress system is self equilibrating and hence d in Fig. 6 is given by

$$d = \frac{b^2 t_{\text{eff}_1}}{h t_{\text{eff}_2} + 2b t_{\text{eff}_1}} \tag{9}$$

where t_{eff_1} and t_{eff_2} are the effective thickness of the flange and web, respectively. The effective thickness of the i-th wall of a composite open section is defined as follows

$$t_{\text{eff}_i} = \frac{E^m_{xi}}{E_{\text{av}}} t_i = \frac{1}{E_{\text{av}} a_{11_i}} \tag{10}$$

Equation (4), when used in conjunction with eqns (9) and (10) for the zero warping position d, now fully prescribes the sectorial coordinate distribution for the composite Z-section with different lay-ups in its component flats.

Equations (5) and (6) pertain essentially to isotropic construction and these are therefore appropriately modified, using the concept of effective thickness, to determine the sectorial shear function and the sectorial moment of inertia, respectively, for the composite beam.

For composite construction we may therefore write

$$S_{\omega\text{eff}}(s) = \frac{1}{E_{\text{av}}} \int_0^s \frac{\omega(s)}{a_{11_i}} \, ds \tag{11}$$

$$\Gamma_{\text{eff}} = \frac{1}{E_{\text{av}}} \int_0^s \frac{\omega^2(s)}{a_{11_i}} \, ds \tag{12}$$

For the composite section with different lay-up configurations in its flange and web elements the warping rigidity term $E\Gamma$ can now be written in the following form;

$$(E\Gamma)_s = E_{\text{av}}\Gamma_{\text{eff}} = \int_0^s \frac{\omega^2(s)}{a_{11_i}} \, ds \tag{13}$$

For the case of the cantilevered composite beam of length L with torque T applied at the free end and with the z-coordinate measured along the beam from the fixed end we are now able to prescribe the primary warping displacements w, the direct stresses σ_Γ due to constrained primary warping and the warping shear flow variation q_Γ in the following manner;

$$w = -\frac{\omega(s)T}{(GJ)_s}\left[1 - \frac{\cosh[\mu_s(L-Z)]}{\cosh(\mu_s L)}\right] \tag{14}$$

$$\sigma_\Gamma = -\frac{\omega(s)T}{\mu_s(E\Gamma)_s}\left[\frac{\sinh[\mu_s(L-Z)]}{\cosh(\mu_s L)}\right] E^m_{x_i} \tag{15}$$

$$q_\Gamma = \frac{S_{\omega_{\text{eff}}}(s)T}{(E\Gamma)_s}\left[\frac{\cosh[\mu_s(L-Z)]}{\cosh(\mu_s L)}\right] E_{\text{av}} \tag{16}$$

where

$$\mu_s^2 = \frac{(GJ)_s}{(E\Gamma)_s} \tag{17}$$

In addition to the warping stresses we have, of course, the presence of the St. Venant shear stresses which vary linearly through the wall thickness. If we consider a St. Venant shear flow q_{vi} in flat element i which is related to the maximum shear stress at the wall surfaces then this can be written as follows for the case of the cantilevered composite beam

$$q_{v_i} = \pm G^b_{xy_i}\frac{Tt_i^2}{(GJ)_s}\left[1 - \frac{\cosh[\mu_s(L-Z)]}{\cosh(\mu_s L)}\right] \tag{18}$$

The analysis approach, detailed in the previous section on 'Primary warping', accounts only for the effects of constrained primary warping and thus its application is restricted to those sections for which primary warping is predominant. The procedure outlined is able to predict the initial constrained torsional response of thin-walled open-section composite beams in a simple engineering manner and comparisons between the results determined using this approach and those obtained from finite element analysis and experiment have been found to be in good agreement.

Secondary warping

Giving consideration now to those sections which do not warp in a primary manner when subjected to torsional loading but whose warping displacements w^* vary linearly through the thickness of the section walls as shown in Fig. 3. Typical sections which possess this quality are shown in Fig. 4. The secondary warping displacements w^* through the thickness of the thin walls of the cross-section are described by

$$w^* = -\omega^*(s)\frac{d\theta}{dz} \tag{19}$$

where $w^*(s)$ is referred to as the sectorial coordinate of the beam cross-section for secondary warping.

The sectorial coordinate for secondary warping is given by

$$\omega^*(s) = \int_0^n n_R dn = n_R n \tag{20}$$

where n_R is the distance from the section shear centre R measured parallel to the tangent at any point s in the mid-plane of the cross-section as shown in Fig. 5 and n is the local through the thickness coordinate as indicated in Figs 2 and 3.

For open-section beams which exhibit only secondary warping, the shear stresses resulting from warping restraint are found to be small in comparison with the linearly varying direct stresses through the section walls and thus they are usually ignored. In this case the applied torque is therefore effectively equilibrated by the St. Venant shear stresses and the engineering elastic constants of the composite material which are of importance in analysis are thus E_x and G_{xy} both in the bending mode. Again, this presumes that the local x-axis of the section walls is coincident with the global z-axis of the beam.

The local through the thickness bending stresses in the section walls due to restrained secondary warping are, of course, largely dependent on the sectorial moment of inertia Γ^* for secondary warping and this is determined as follows

$$\Gamma^* = \frac{1}{12} \int_0^s t^3 n_R^2 \mathrm{d}s \tag{21}$$

For sections composed of flat elements and which exhibit only secondary warping, such as the angle, T and cruciform sections illustrated in Fig. 4(b), the section shear centre is at the junction connecting the individual flats and thus, in this case, $n_R = s$ and a more practical equation for Γ^* may be written as follows

$$\Gamma^* = \frac{1}{36} \sum_{i=1}^{n} S_i^3 t_i^3 \tag{22}$$

Also, for such sections with different lay-up configurations in the component flats, the torsional rigidity $(GJ)s$ of the section is as given previously by eqn (7) and the warping rigidity $(E\Gamma^*)_s$ of the section, in the secondary mode, is determined from

$$(E\Gamma^*)_s = \frac{1}{36} \sum_{i=1}^{n} Ex_i^b S_i^3 t_i^3 = \frac{1}{3} \sum_{i=1}^{n} \frac{S_i^3}{d_{11_i}} \tag{23}$$

For the composite cantilevered beam configuration with torque applied at the free end and for the beam cross-section which is associated only with secondary warping we are now able to prescribe the variations in the secondary warping displacements w^* and the direct stresses σ_Γ^* due to constrained secondary warping in the following manner

$$w^* = -\frac{\omega^*(S)T}{(GJ)s} \left[1 - \frac{\cosh\left[\mu^*(L-Z)\right]}{\cosh\left(\mu^* L\right)} \right] \tag{24}$$

$$\sigma_\Gamma^* = -\frac{\omega^*(S)T}{\mu^*(E\Gamma^*)s} \left[\frac{\sinh\left[\mu^*(L-Z)\right]}{\cosh\left(\mu^* L\right)} \right] E_{x_i}^b \tag{25}$$

where

$$\mu^{*2} = \frac{(GJ)_s}{(E\Gamma^*)_s} \tag{26}$$

The St. Venant shear flow q_{vi}^* in flat element i of the cross-section can now be determined through the use of eqn (18) by simply replacing μ_S by μ^*.

The theoretical procedure, detailed in the previous section on 'Secondary warping', is applicable only to those composite sections for which primary warping is non-existent under torsional loading. The approach is able to predict the initial constrained torsional response of such sections in a simple engineering manner and this is achieved through the use of the appropriate engineering elastic constants of the composite material defined in the bending mode of behaviour. Comparisons given in the paper with finite element results and with those obtained from experiment are shown to corroborate the simple, yet effective, theoretical approach outlined.

Single-cell closed sections

The applied torque to a closed-cell composite box is reacted through the membrane action of the section walls and thus the equivalent engineering elastic constants of the composite material which are appropriate for the analysis of such structural configurations are those defined in the membrane mode of behaviour as described by eqn (1). In the present case we wish to examine the behaviour of composite box-sections whose flat elements are specially orthotropic in the membrane mode and thus m_x and m_y are zero in this instance. The behaviour of thin-walled, closed-section composite box beams with symmetric flat walls can then be determined with some ease using the isotropic equations with suitable modifications being

made to account for the effects of the composite material. This is achieved through the use of the appropriate equivalent engineering elastic constants of eqn (1).

It is assumed that the x-direction of the section laminate walls is coincident with the global z-axis of the beam. The St. Venant torsional rigidity term GJ for the composite box section with different lay-up configurations in its flange and web elements can be written as follows

$$(GJ)_{BS} = \frac{4A^2}{\oint \frac{ds}{G_{xy}t}} = \frac{4A^2}{\oint a_{33} ds} \tag{27}$$

where A is the area enclosed by the mid-line of the box cross-section.

If we now divide by the torsion constant J of the box then an effective shear modulus for the whole section is described. This takes the form;

$$G_{\text{eff}} = \frac{\oint \frac{ds}{t}}{\oint a_{33} ds} \tag{28}$$

To account for the different stiffnesses in the composite section walls the concept of effective thickness is introduced. The effective thickness of the i-th wall is thus given in terms of the effective shear modulus for the whole section as follows

$$t_{\text{eff}_i} = \frac{G_{xy_i} t_i}{G_{\text{eff}}} \tag{29}$$

Use is made of equally spaced rigid diaphragms along the length of the composite box beams in order to prevent cross-sectional distortion and thus transverse strains. The axial normal stresses and strains in the laminated walls of the composite box are then related through, as is referred to here, the apparent elastic modulus of the composite material. This is determined, of course, in this instance, from the two-dimensional stress–strain relationships of a specially orthotropic composite material and is defined here for the laminate as

$$E_x^a = \frac{E_x}{1 - \nu_{xy}\nu_{yx}} \tag{30}$$

where E_x, ν_{xy} and ν_{yx} are given by eqn (1).

It is convenient now, using the concept of effective thickness, to define an effective apparent elastic modulus for the whole section as follows

$$E^a_{x_{\text{eff}}} = \frac{\oint E_x^a t ds}{\oint t_{\text{eff}} ds} = \frac{\Sigma E_{x_i}^a t_i S_i}{\Sigma t_{\text{eff}_i} S_i} \tag{31}$$

The effective sectorial properties and other section constants of the composite box with different lay-up configurations in its flange and web elements are now determined on the basis of the effective thickness concept. The effective sectorial coordinate distribution of the closed cell rectangular box is

$$\omega_{\text{eff}}(s) = \int_o^s \left(P_R - \frac{\psi_{\text{eff}}}{t_{\text{eff}}} \right) ds \tag{32}$$

where

$$\psi_{\text{eff}} = \frac{2A}{\oint \frac{ds}{t_{\text{eff}}}} \tag{33}$$

Equations (32) and (33) have been applied to an isotropic single-cell box with flange width b and web depth a and with a constant wall thickness t. The sectorial coordinate distribution for this is illustrated in Fig. 8. As expected the distribution is antisymmetric about the vertical and horizontal geometrical axes of symmetry of the box section resulting in zero warping of the section at these axes and maximum warping at the section corners. Clearly, such a distribution will provide an axial stress system due to warping restraint which will be self equilibrating and this, of course, is the natural response to the torsional loading of the box geometry. It is of note in Fig. 8 that for the square box, $a = b$, the warping is everywhere zero and a closed-section beam which possess this quality is commonly referred to as a *Neuber tube*.

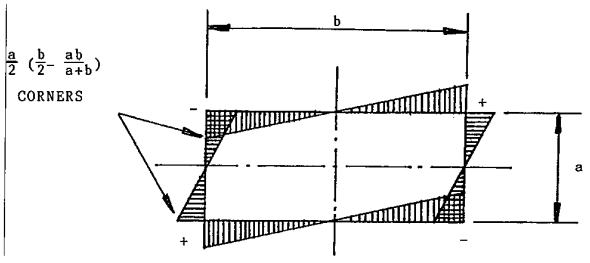

Fig. 8. Sectorial coordinate distribution for a rectangular box-section.

The effective sectorial shear function for the closed-cell composite box is determined as follows

$$S_{\omega,c_{\text{eff}}}(s) = S_{\omega,o_{\text{eff}}}(s) - \frac{1}{2A} \int_s S_{\omega,o_{\text{eff}}}(s) P_R \mathrm{d}s \quad (34)$$

where

$$S_{\omega,o_{\text{eff}}}(s) = \int_0^s \omega_{\text{eff}}(s) t \mathrm{d}s \quad (35)$$

It is to be noted in eqn (35) that the actual thickness t is used and not t_{eff}. The effective thickness, as described by eqn (29), is that determined on the basis of the torsional rigidity of the closed box-section. Since eqn (35) describes the sectorial shear function distribution for the box-section with an imaginary cut, i.e. the quasi-open section, then it is considered, in this instance, that the actual thickness is appropriate and thus the effective thickness is reflected in eqn (35) through the effective sectorial coordinate distribution $\omega_{\text{eff}}(s)$.

Equations (34) and (35) have been applied to the isotropic box considered previously in Fig. 8 and with $b = 100$ mm, $a = 50$ mm and $t = 1$ mm, the corresponding sectorial shear function distribution around the box is as indicated in Fig. 9. The distribution shown will clearly provide a shear flow system round the section due to constrained warping which will be self equilibrating in every sense and again this is the natural internal response to the torsional loading of the closed single-cell box.

For the composite box with differing lay-up configurations in its flanges and webs, the effective torsion constant, polar constant and warping shear parameter are given, respectively, as follows

$$J_{\text{eff}} = 2A\psi_{\text{eff}} \quad (36)$$

$$I_{c_{\text{eff}}} = \oint P_R^2 t_{\text{eff}} \mathrm{d}s \quad (37)$$

$$\lambda_{\text{eff}} = 1 - \frac{J_{\text{eff}}}{I_{c_{\text{eff}}}} \quad (38)$$

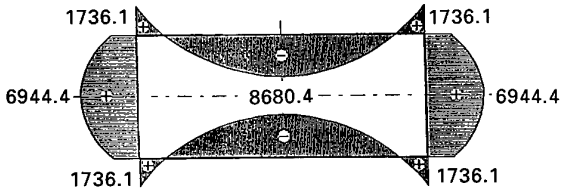

Fig. 9. Sectorial shear function distribution for rectangular box-section.

The warping rigidity of the composite box-section is now determined according to the form defined by Benscoter [12] for isotropic beams. This is

$$(E\Gamma)_{BS} = \frac{1}{\lambda_{\text{eff}}} \int_s \omega_{\text{eff}}^2(s) E_x^a t_{\text{eff}} \mathrm{d}s \quad (39)$$

The warping displacements and stresses for the cantilevered composite box beam configuration with torque T applied at the free end can now be obtained in the following form

$$w = \frac{\omega_{\text{eff}}(s)T}{(GJ)_{BS}} \left[1 - \frac{\cosh[\mu_s(L-Z)]}{\cosh(\mu_s L)} \right] \quad (40)$$

$$\sigma_\Gamma = -\frac{\omega_{\text{eff}}(s)T}{\mu_s(E\Gamma)_{BS}} \left[\frac{\sinh[\mu_s(L-Z)]}{\cosh(\mu_s L)} \right] E_{x_i}^a \quad (41)$$

$$q_\Gamma = -\frac{S_{\omega_{\text{eff}}}(s)T}{(E\Gamma)_{BS}} \left[\frac{\cosh[\mu_s(L-Z)]}{\cosh(\mu_s L)} \right] E_{x_{\text{eff}}}^a \quad (42)$$

where

$$\mu_s^2 = \frac{(GJ)_{BS}}{(E\Gamma)_{BS}} \quad (43)$$

The Bredt–Batho shear flow q_B associated with the free torsion, or St. Venant torsion, of a closed cell box is given by the familiar expression

$$q_B = \frac{T}{2A} \quad (44)$$

The total shear flow at any cross-section of the closed cell box beam subjected to restrained torsion is then given by

$$q = q_\Gamma + q_B \quad (45)$$

The analysis procedure, outlined in the previous section, is able to predict the initial constrained torsional response of a particular class of thin-walled, closed-section, composite box beams in a simple engineering manner. Essentially the composite beams are uncoupled in their overall deformations through the use of symmetrically laminated flat walls which possess membrane orthotropy. The method of approach allows different lay-up configurations in the

flange and web elements of the box-sections to be accommodated. It is considered to be simple and effective in nature and, indeed, comparisons given in the paper between the results determined using this approach and those obtained from finite element analysis and experiment are shown to be in good agreement.

SOME TYPICAL RESULTS AND DISCUSSION

All results presented in the paper are those pertaining to the cantilevered beam configuration with torque applied at the free end and with z measured along the beam axis from the fixed end. The warping shear flow distribution round a composite zed and a composite channel section beam are shown in Figs 10 and 11, respectively, in comparison with isotropic solutions corresponding to the same structural geometry. Both of these sections are those associated with predominant primary warping and thus the shear flow variations indicated in Figs 10 and 11 are those determined using the analysis procedure detailed in the section on 'Primary warping'.

The beams are 600 mm long with 50 mm wide flanges, 100 mm deep webs and have a wall thickness of 1 mm. The composite beams are considered to be manufactured from high strength carbon–epoxy preimpregnated ply

Z-beam restrained torsion
comparison of steel and composite beam
warping shear flow distribution round the section

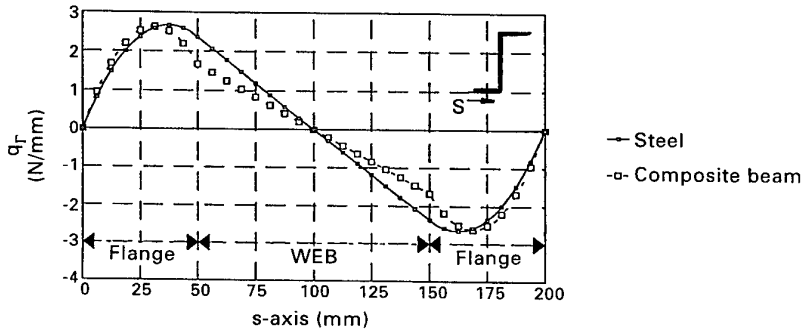

Composite beam: Flange $[0/45/-45/90]_s$ web $[45/-45)_2]_s$
At z = 120 mm, T = 10000 N mm

Fig. 10.

Channel beam restrained torsion
comparison of steel and composite beam
warping shear flow distribution round the section

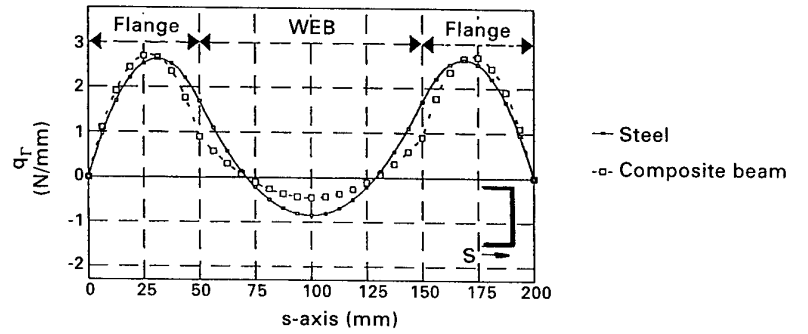

Composite beam: Flanges $[0/45/-45/90]_s$ web $[45/-45)_2]_s$
At z = 120 mm, T = 10000 N mm

Fig. 11.

sheets with a ply thickness of 0.125 mm. The lay-up configuration of the flanges of the composite beams is quasi-isotropic in nature and of the form $[0/45/-45/90]_S$ whilst an angle-ply configuration of the form $[(45/-45)_2]_S$ is employed for the webs of the beams. The appropriate engineering elastic constants of the laminated walls for use in the analysis of the composite beams have been determined using the following ply material properties: $E_1 = 140\ \text{kN/mm}^2$, $E_2 = 10\ \text{kN/mm}^2$, $G_{12} = 5\ \text{kN/mm}^2$, $\nu_{12} = 0.3$.

The isotropic results indicated in Figs 10 and 11 are those pertaining to steel construction and correspond to the material modulus of $E = 210\ \text{kN/mm}^2$ and to the Poisson's value of $\nu = 0.3$. The comparisons shown between the isotropic and composite solutions in Figs 10 and 11 are those at the cross-section which is at a distance of 120 mm from the fixed end of the beams and which correspond to an applied torque level of 10 kN mm at the free end. The warping shear flow in the composite beams is seen to be characteristically different to that of the isotropic beams whose flat walls are all of the same stiffness. The smooth transition of shear flow from flange to web with the common slope at the flange–web junctions is clearly not evident in the composite beams and this is due, of course, to the different lay-ups in the flat walls meeting at the junctions.

It is of note that the warping shear flow in the web of the Z-section beams is linear and passes through zero at the section shear centre whilst that in the web of the channel section beams is non-linear and passes through two zero locations. The shear flow variations in the webs of the Z and channel beams are, indeed, self equilibrating and thus they do not contribute to the warping torque at the cross-sections being considered. The warping torque at any cross-section is associated only with the warping shear flow variation in the flanges of the beams and in addition to the St. Venant torque serves to equilibrate the applied torque.

Comparisons are shown in Figs 12 and 13 between the theoretical and finite element solutions pertaining to the torsional response of a composite angle-section beam. Angle sections exhibit secondary warping only and thus the theoretical variations indicated are those determined using the analysis procedure outlined in the section on 'Secondary warping'. The angle beam has 50 mm flats with a 1 mm wall thickness and is 500 mm long. It is considered to be manufactured from high strength carbon–epoxy preimpregnated ply sheets with a ply thickness of 0.125 mm and has a lay-up configuration which is quasi-isotropic in nature and of the form $[0/90/45/-45]_S$. The properties of the ply sheets are the same as those mentioned previously for the composite zed and channel beams. The finite element results are based on a model which has a sufficiently refined mesh at the constrained end of the beam and which makes use of the QSL8 element, an eight noded semi-loof thin shell element, from the LUSAS finite element analysis system library.

Figure 12 shows the variations in force intensity $N^*_{\leq}$ and the St. Venant shear flow q^*_V along the length of the beam and corresponding to an applied torque of 0.2 kN mm. The curves shown are those relating to the cross-sectional location of $s = 50$ mm from the section shear centre which is just at the free edge of the component flat as indicated. N^*_Γ is the maximum through-

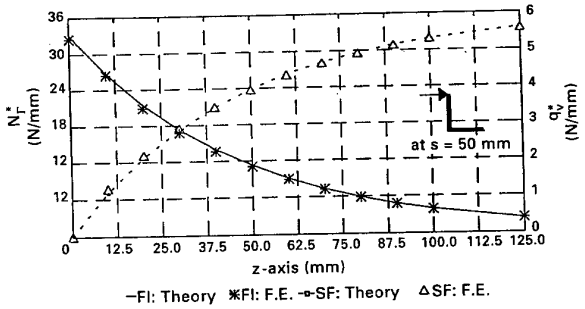

Fig. 12.

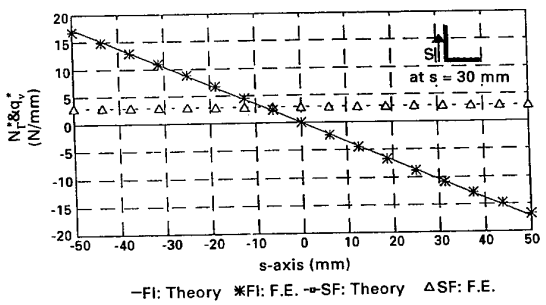

Fig. 13.

the-thickness bending stress at this location multiplied by the wall thickness, and correspondingly q_V^* relates to the maximum St. Venant shear stress. It is clear from Fig. 12 that the effects of constrained secondary warping are fairly local in nature as indicated by the fact that the St. Venant shear flow has almost reached its free torsion level of 6 N/mm within a distance of the order of one-fifth the beam length from the fixed end and it is also of note that the force intensity level has almost disappeared within this same distance.

The variations in N_Γ^* and q_V^* around the section are shown in Fig. 13 and these relate to the cross-section of the beam which is at a distance of 30 mm from the fixed end and correspond to the same applied torque level of 0.2 kN mm. The St. Venant shear flow is noted, as expected, to be the same everywhere and the force intensity distribution is seen to be zero at the section shear centre and to vary linearly to its maximum value at the free edge of the component flats. The comparisons between the theoretical and finite element solutions illustrated in Figs 12 and 13 are noted to be remarkably good and thus it would appear that the simple engineering approach detailed in the paper for determining the effects of secondary warping restraint is able to do so in a fairly accurate manner.

Comparisons are given in Figs 14 and 15 between the theoretical predictions and the experimental results associated with a composite angle-section test beam. The beam has 50 mm flats with a wall thickness of 2 mm and is 622 mm long. It is manufactured from high strength carbon–epoxy preimpregnated ply

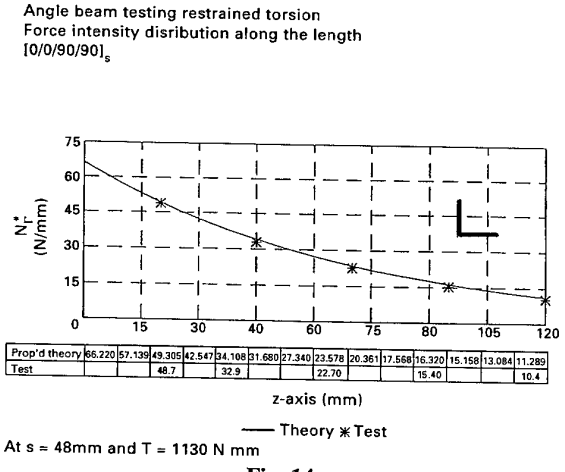

Fig. 14.

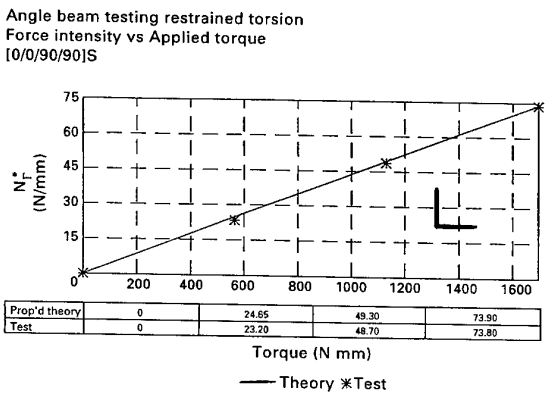

Fig. 15.

sheets with a ply thickness of 0.25 mm and with the following ply material properties: $E_1 = 140.3$ kN/mm^2, $E_2 = 11$ kN/mm^2, $G_{12} = 5.65$ kN/mm^2, $\nu_{12} = 0.34$.

The lay-up configuration of the angle-section test beam is a symmetric cross-ply of the form $[0/0/90/90]_S$ and the test results have been determined through the use of strain gauges located along the length of the beam on the wall surface at 48 mm from the section shear centre. Figure 14 shows the variation of the force intensity N_Γ^* along the length of the beam and corresponding to the applied torque level of 1.13 kN mm. Again, it is of note that the force intensity diminishes rapidly along the length of the beam from its maximum level at the constrained end and both theory and experiment are seen to illustrate the same degree of decay along the beam. Indeed, the comparison between theory and experiment is shown to be extremely close. Figure 15 shows the comparison between theory and test of the variation in force intensity N_Γ^* with applied torque at the first strain gauge location along the beam. This is at a distance of 20 mm from the fixed end of the beam and the comparison between theory and test is shown to give remarkably close agreement over the torque range considered.

Figure 16 shows the force intensity variation N_Γ along the length of a composite Z beam and at the location on the cross-section which is at 12.5 mm from the flange free edge. The cross-sectional dimensions, lay-up configuration and material properties of the carbon fibre beam are the same as those mentioned previously for the Z beam of Fig. 10. In Fig. 16 a comparison is given between the theoretical and finite element predictions for a beam of length 500 mm and corresponding to a torque level of 10 kN

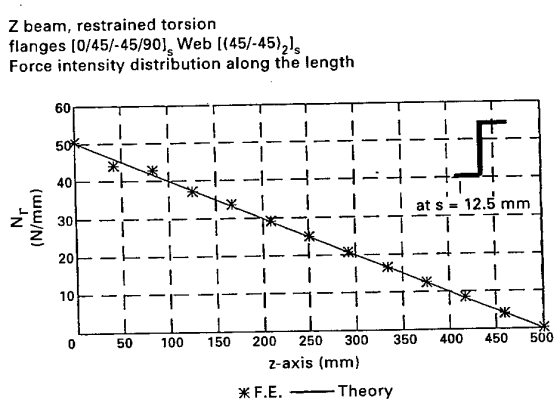

Fig. 16.

mm. Constrained primary warping is noted to have a significant influence all along the length of the beam with N_Γ reducing in a fairly gradual manner from its maximum value at the restrained end to zero at the free end of the beam. This is predicted by both the theory and finite element solutions and the comparison between the two is shown to give excellent agreement.

Details are given in Fig. 17 of the comparison between theory and experiment pertaining to a carbon composite Z test beam. The lay-up configuration in the web of the beam is $[(45/-45)_2]_S$ and that in its flanges is $[45/-45/90/0]_S$. The web depth of the beam is 100 mm, its flanges are 50 mm wide and the wall thickness of the cross-section is 2 mm. High strength carbon–epoxy preimpregnated ply sheets with a ply thickness of 0.25 mm were used in the manufacture of the beam and the ply material properties are the same as those detailed previously for the angle test beam of Fig. 15. The variation in force intensity N_Γ along the length of the beam is shown in Fig. 17 and this is in the flange at 3 mm from the flange free edge. The comparison shown between theory and experiment is for a beam of length 525 mm and relates to an applied torque level of 13.56 kN mm. The influence of constrained primary warping in open-section beams is noted again to be significant all along the beam length and this is predicted by both the theory and experimental results with the comparison between the two being exceptionally close.

The shear flow variation around the section of a single-cell composite box beam is shown in Fig. 18 which indicates the comparative predictions between theory and finite element analysis. The flanges of the beam are 100 mm wide with 50 mm deep webs and the wall thickness of the box is 1 mm. The shear flow distribution illustrated is that occurring at the cross-section which is at a distance of 39 mm from the fixed end of the beam and which corresponds to the applied torque level of 100 kN mm. The length of the beam is 600 mm and the lay-up configurations in its flanges and webs are $[0/45/-45/90]_S$ and $[(45/-45)_2]_S$, respectively.

The beam is considered to be manufactured from high strength carbon–epoxy preimpregnated ply sheets with a ply thickness of 0.125 mm and the ply material properties are those mentioned previously with reference to the Z and channel composite beams of Figs 10 and 11, respectively. The shear flow detailed in Fig. 18 is, of course, the total shear flow which is the sum of the warping and Bredt–Batho shear flows. The warping shear flow is self equilibrat-

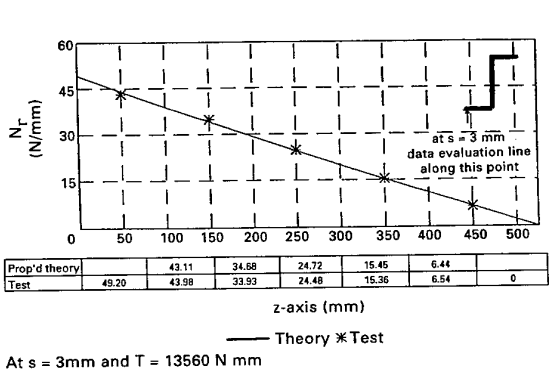

Prop'd theory		43.11	34.68	24.72	15.45	6.44	
Test	49.20	43.98	33.93	24.48	15.36	6.54	0

Fig. 17.

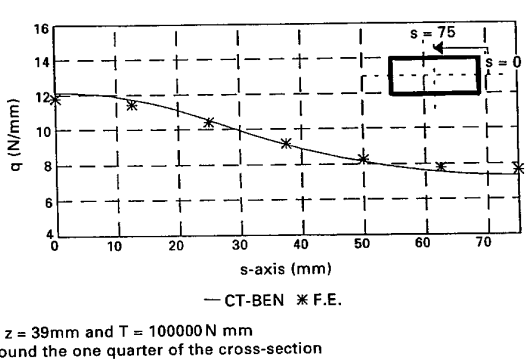

Fig. 18.

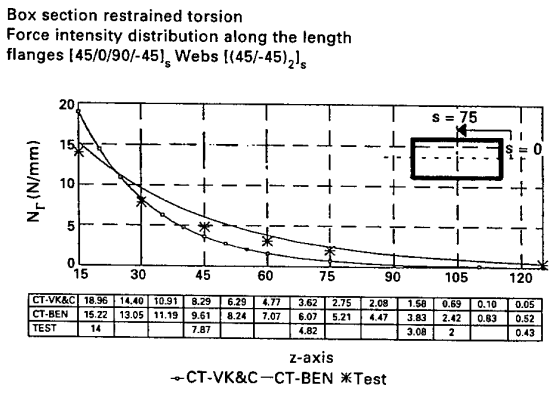

CT-VK&C	18.96	14.40	10.91	8.29	6.29	4.77	3.62	2.75	2.08	1.58	0.69	0.10	0.05
CT-BEN	15.22	13.05	11.19	9.61	8.24	7.07	6.07	5.21	4.47	3.83	2.42	0.83	0.52
TEST	14			7.87			4.82			3.08	2		0.43

Fig. 19.

ing in every sense and thus only the Bredt–Batho shear flow equilibrates the applied torque on the beam. For the beam under consideration the Bredt–Batho shear flow is noted to be $q_B = 10$ N/mm. In Fig. 18, the theoretical curve for the composite beam is based on the isotropic analysis approach of Benscoter [12] and comparison of this with the finite element predictions is shown to provide favourable agreement.

The force intensity distribution N_Γ along the length of a composite test box beam is shown in Fig. 19. The beam is manufactured from high strength carbon–epoxy preimpregnated ply sheets with a ply thickness of 0.125 mm and with the following ply material properties: $E_1 = 141.8$ kN/mm^2, $E_2 = 8.94$ kN/mm^2, $G_{12} = 5.295$ kN/mm^2, $\nu_{12} = 0.36$.

The lay-up configuration in the flanges of the box is $[45/0/90/-45]_S$ and that in the webs is $[(45/-45)_2]_S$. The flange width, web depth and wall thickness of the box section are 100 mm, 50 mm and 1 mm, respectively, and the length of the test beam is 530 mm. Two theoretical curves are shown in Fig. 19 for the composite test beam. One is based on the isotropic analysis approach proposed by Von Karman & Christensen [9] and the other is modelled on the analysis procedures for isotropic construction detailed by Benscoter [12]. The test data illustrated in Fig. 19 have been determined from strain gauges located along the length of the beam and attached to the flange at 8 mm from the flange–web junction and this has been evaluated according to the applied torque level of 180.8 kN mm.

In the work of Von Karman & Christensen [9] the warping shear strains are considered to be of a negligible magnitude in comparison with the St. Venant shear strain associated with the Bredt–Batho shear stress and thus they are ignored in their analysis. The effect of the shearing strains on torsional response is more fully accounted for in the work of Benscoter [12] however, through the use of an appropriate warping shear parameter and the comparison shown in Fig. 19 reflects the difference in the two approaches. It is of note that the experimental data tend to favour the composite theory based on the assumptions of Benscoter [12]. This is also the case with a number of other comparisons reported in Ref. [20] and thus ignoring the effects of the warping shear strain in analysis is seen, essentially, to lead to inaccurate predictions.

CONCLUSIONS

The constrained torsional response of open- and single-cell closed-section carbon fibre composite beams have been examined in this paper using simple theoretical engineering procedures. The flat walls of the composite beams are symmetrically laminated about their own mid-planes and exhibit membrane orthotropy. The torsional and warping rigidities of the composite beams, for use in the analysis procedures, have been determined through the use of the appropriate equivalent engineering elastic constants of the individual thin composite walls and for sections with different lay-up configurations in their component flats, the concept of effective thickness has been employed to account for the associated stiffness variation round the sections.

The effects of primary and secondary warping restraint on the torsional response of open section beams have been given some detailed attention in the paper and the distinct differences have been highlighted between those sections whose behaviour is governed predominantly by primary effects and those whose response is associated solely with secondary effects. For open-sections governed, essentially, by the effects of primary warping restraint, the E_x and G_{xy} properties of the laminated walls for use in the associated analysis procedure are those of the membrane and bending mode, respectively. For those sections which exhibit secondary warping only, the appropriate E_x and G_{xy} properties for use in analysis are both of the bending mode.

It is indicated in the paper that the shear flow due to primary warping restraint in open-section beams plus the St. Venant shear flow serve to equilibrate the applied torque on the beam. It is also indicated that the warping shear flow in a closed-cell box is completely self equilibrating and thus the applied torque on the box is equilibrated by the Bredt–Batho shear flow. For composite box-sections the appropriate E_x and G_{xy} properties of the laminated walls for use in the associated analysis procedure are noted to be both of the membrane mode. Comparisons are given in the paper between theory and experiment and between theory and finite element solutions for Z, angle and box-section cantilevered beams and these are shown to give extremely good agreement.

REFERENCES

1. Mansfield, E. H. and Sobey, A. J., The fibre composite helicopter blade; part 1: stiffness properties; part 2: prospects for aeroelastic tailoring. *Aeronautical Quarterly*, 1979, **XXX**, 413–499.
2. Hong, C. H. and Chopra, I., Aeroelastic stability analysis of a composite bearingless rotor blade. *J. Am. Helicopter Soc.*, 1986, **31**, 29–35.
3. Lee, S. W. and Kim, Y. H., A new approach to the finite element modelling of beams with warping effects. *Int. J. Num. Meth. Engng.*, 1987, **24**, 2327–2341.
4. Stemple, A. D. and Lee, S. W., Finite-element model for composite beams with arbitrary cross-sectional warping. *IAA Journal*, 1988, **26** (12), 1512–1520.
5. Chandra, R., Stemple, A. D. and Chopra, I., Thin-walled composite beams under bending, torsional, and extensional loads. *J. Aircraft*, 1990, **27** (7), 619–626.
6. Chandra, R. and Chopra, I., Experimental and theoretical analysis of composite I-beams with elastic couplings. *IAA J.*, 1991, **29** (12), 2197–2206.
7. Zvarick, A. G. & Cruse, T. A., Coupled elastic response of open section laminated composite beams subject to generalised beam loading. *The 33rd IAA/ASME/ASCE/AHS/ASC Structures, Structural Dynamics and Materials Conference, part 2, structures II*. Dallas, Texas, pp. 725–735, April 13–15, 1992.
8. Badir, A. M., Berdichevsky, V. L. & Armanios, E. A., Theory of composite thin-walled opened cross section beams. *34th AIAA/ASME/ASCE/AHS/ASC Structures, Structural Dynamics and Materials Conf.*, AIAA/ASME Adaptive Structures Forum, Lajolla, California, 19–22 April, 1993, pp. 2761–70.
9. Von Karman, T. and Christensen, N. B., Methods of analysis for torsion with variable twist. *J. Aeronaut. Sci.*, 1944, **11**, 110–124.
10. Fine, M. & Williams, D., *Effect of end constraint on thin-walled cylinders subject to torque*. Aeronautical Research Council, Rep. No. 2223, May 1945.
11. Argyris, J. H. & Dunne, P. C., The general theory of cylindrical and conical tubes under torsion and bending loads. *J. Royal Aeronaut. Soc.* **51** (1947) 199–269, 757–784, 884–930; **53** (1949) 461–483, 558–620.
12. Benscoter, S.U., A theory of torsion bending for multicell beams. *J. Appl. Mech.*, 1954, **20**, 25–34.
13. Waldron, P., Sectorial properties of straight thin-walled beams. *Computers and Structures*, 1986, **24** (1), 147–156.
14. Barrau, J. & Laroze, S., Torsion of a composite beam. In *Proceedings of the 2nd International Conference on Composite Structures, Composite Structures 2*, ed. I. H. Marshall. Applied Science Publishers, 1983, pp. 146–154.
15. Bicos, A. S. and Springer, G. S., Design of a composite boxbeam. *J. Comp. Mat.*, 1986, **20**, 86–109.
16. Bauchau, O. A., Coffenberry, B. S. and Rehfield, L. W., Composite box beam analysis: theory and experiments. *J. Reinforced Plastics and Composites*, 1987, **6**, 25–35.
17. Smith, E. C. & Chopra, I., Formulation and evaluation of an analytical model for composite box beams. IAA paper No: 90-0962-CP, 1990.
18. Ata, M., PhD thesis, Cranfield University, College of Aeronautics, Cranfield, Bedford, UK, November 1992.
19. Loughlan, J. and Ata, M., The restrained torsional response of open section carbon fibre composite beams. *Composite Structures*, 1995, **32**, 13–31.
20. Loughlan, J. & Ata, M., The analysis of carbon fibre composite box beams subjected to torsion with variable twist. *Computer Methods in Applied Mechanics and Engineering*, 1997.

ELSEVIER

Composite Structures Vol. 38, No. 1–4, pp. 649–660, 1997
© 1997 Elsevier Science Ltd. All rights reserved
Printed in Great Britain
0263-8223/97/$17.00 + 0.00

PII:S0263-8223(97)00102-5

Finite element analysis of bonded repairs to edge cracks in panels subjected to acoustic excitation

R. J. Callinan, S. C. Galea & S. Sanderson

Aeronautical and Maritime Research Laboratory, 506 Lorimer Street, Fishermens Bend, Victoria, 3207, Australia

The skin of an aircraft can vibrate as a result of pressure waves caused by engine and/or aerodynamic effects. In modern fighter aircraft such as the F/A-18, sound pressure levels have been recorded up to 170 dB over the surface of the skin. In the F/A-18 cracking has occurred in the lower nacelle, typically along the boundaries of the panel. These cracks often originate from a fastener line, grow along the boundary and then turn into the centre of the panel. In the case of the F/A-18, cracking was due to higher than expected pressure levels caused by an aerodynamic disturbance at the inlet lip. Attempts have been made to repair these panels with boron fibre patches, however the cracks have continued to grow. This paper aims at attempting to understand the mechanisms of cracking of the panels subjected to acoustic excitation and the influence of bonded repairs. Also, the analysis is extended to a feasibility study on the effects of enlarging the patch and increasing material damping on the stress intensity factor. © 1997 Elsevier Science Ltd.

INTRODUCTION

Acoustic fatigue is due to a very high intensity excitation as a result of pressure waves caused by engine and/or aerodynamic effects. Acoustically-induced cracking has occurred on the external surface of the lower nacelle skin on the F/A-18, illustrated in Fig. 1. In these regions overall sound pressure levels (OASPL) greater than 170 dB have been measured in flight. These high sound pressure levels appear to be a result of an aerodynamic disturbance at the inlet lip [1]. Typical cracks occur along a line of rivets or run parallel to the rivet line and may turn into the centre of the panel, as shown in the inset. Cracking generally occurs along the

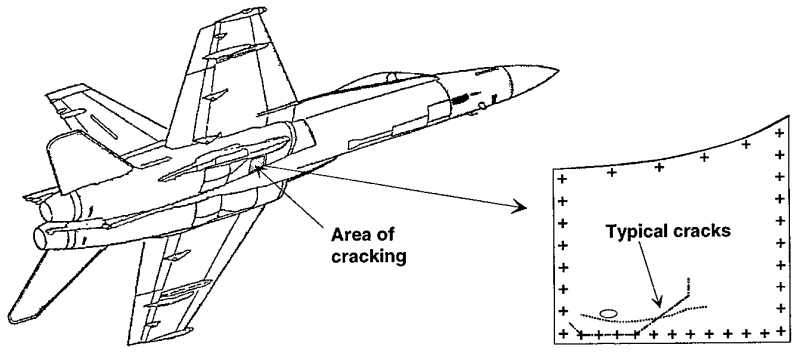

Fig. 1. Location of the cracking in the lower nacelle inlet.

longer side of the panel where the bending stresses due to out of plane vibrations are a maximum. Up to a third of the F/A-18s in the RAAF fleet are affected by these cracks.

The standard repair for such cracking is to remove and replace the panel. The standard long term fix is to incorporate additional stiffeners on the inside to stiffen the panel. This has two effects, firstly to reduce the panel's response, i.e. lower stress, for a given load, and secondly it increases the resonant frequencies of the panel to frequencies well outside the recorded excitation frequencies.

In order to reduce the cost of repairing such cracked structures, a bonded composite repair would be preferred. Such a repair was designed and implemented on an existing cracked aircraft. The benefits of such a repair are reflected in the time required to carry out the repair, typically 60 h for the mechanical repair and approximately 15–25 h for the bonded repair. While in the past boron fibre patches have been used as a cost effective means of repairing cracked aircraft structures, in this case the cracks continued to grow.

The work reported here will involve the estimation of the root mean square (RMS) response of the stress intensity factor (K) in the cracked and cracked/repaired cases as an attempt to understand the problems involved in patching cracks in such an environment. Various other patch lay-ups and geometries are also investigated.

THEORY

Random response analysis

The random response analysis capability of the NASTRAN program has been used to solve this problem [2]. This involves a solution in the frequency domain after the transfer function, $H(\omega)$, is generated. Together with the power spectral density (PSD) of the excitation, $S_I(\omega)$, the PSD of the response, $S_J(\omega)$, is determined

$$S_J(\omega) = |H(\omega)|^2 S_I(\omega) \tag{1}$$

This analysis allows the statistical properties of the system to be evaluated. Random vibrations considered here involve all frequencies at any time. After calculating the PSD, the root mean square (RMS) of the response can be determined by computing the square root of the PSD area

$$j_{\mathrm{RMS}} = \sqrt{\frac{1}{2\pi} \int_0^\infty S_j(\omega)\mathrm{d}\omega} \tag{2}$$

A similar application of finite element techniques to undertake a PSD analysis to acoustic fatigue problems has been reviewed by Climent and Casalengua [3].

Stress intensity factors

In the finite element (FE) model, the depth of the plate is modelled using a single layer of 20 noded brick elements and as such, will model bending behaviour of the skin. The skin thickness is approximately 1 mm, hence the condition of plane stress is assumed. The computation of the stress intensity factor may be determined directly from the crack tip element used around the crack tip or from displacements using a crack opening (COD) formula. The RMS crack tip stress intensity factors for modes I, II and III are derived from the standard asymptotic relations

$$K_{\mathrm{I\,RMS}} = \frac{EU_{\mathrm{RMS}}}{4}\sqrt{\frac{2\pi}{l}} \tag{3}$$

$$K_{\mathrm{II\,RMS}} = \frac{EV_{\mathrm{RMS}}}{4}\sqrt{\frac{2\pi}{l}} \tag{4}$$

$$K_{\mathrm{III\,RMS}} = GW_{\mathrm{RMS}}\sqrt{\frac{2\pi}{l}} \tag{5}$$

where E = Young's modulus, G = Shear modulus, U_{RMS} = mode I crack opening RMS displacement (ie. displacement out of the plane of the crack), V_{RMS} = mode II crack opening RMS displacement (ie. displacement in-plane, parallel to plane of crack), W_{RMS} = mode III crack opening RMS displacement (ie. displacement in-plane, transverse to plane of crack), l = length of the crack tip element.

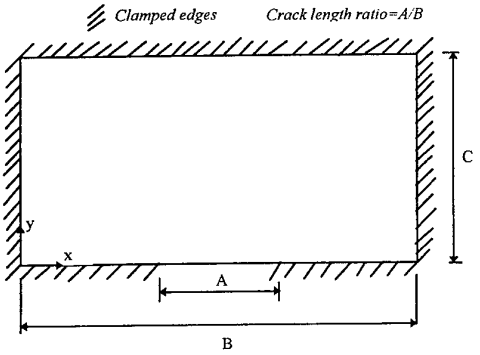

Fig. 2. Geometry of plate used for the validation of the analysis.

FEA METHODOLOGY VALIDATION

The complexity of the random response analysis and the number of assumptions made was such that validation of the analysis was necessary. Both experimental and analytical work has been carried out by Byrnes [4]. In this case the plate used is that shown in Fig. 2 and the PSD of the acoustic excitation is given in Fig. 3. Dimensions of the plate are $B = 500$ mm, $C = 166$ mm and thickness = 1.2 mm with a crack of length A. This plate was clamped along all edges except one, which was partially restrained. The unrestrained region represented a crack along one side. The length of the crack has been expressed as a ratio A/B. Material properties of the aluminium plate are given in Table 1, with the structural viscous damping ratio set to 0.055. RMS strains were measured at a point 25 mm ahead of the crack tip, the results are reproduced in Fig. 4 along with an analytical solution also developed by Byrnes [4].

The FE results are also shown in Fig. 4. Only three experimental data points were published in Ref. [4], and in each case the FE results are within 10%. However, disagreement does exist with the analytical solution for crack length to plate width ratios below 0.4 It is not clear why this difference occurs. The analytical solution is based on contributions from the first and second mode shapes only. However, the FE PSD of the response allows for many mode shapes.

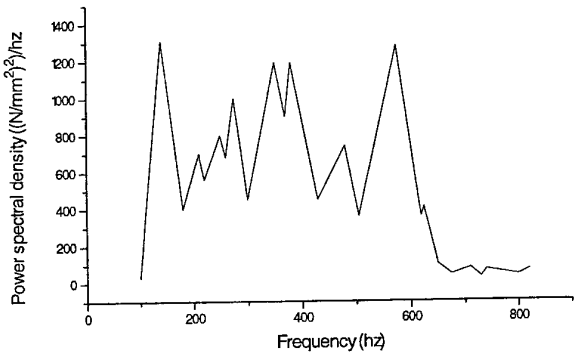

Fig. 3. Power spectral density of the pressure excitation used in [4].

FEA OF CRACKED NACELLE INLET

In order to study the cracking mechanisms of the cracked and repaired/cracked nacelle skin cases, a simplified model has been developed in which the skin is considered to be a flat rectangle. However, to take account of all shear deformations the structure has been idealised as a fully three-dimensional structure using 20 noded brick elements. The geometry of the structure is shown in Fig. 5. The mesh size of the skin structure is 75×60 elements, while the patch and skin is 40×40 elements. As shown, the unidirectional patch only extends partially across the panel. It also covers an adjacent panel as shown in the dotted outline. Sufficient elements have been used to define the minimum crack length considered. Material properties for the skin, adhesive and boron are shown in Table 1. The main reason that 20 noded bricks were used in the skin is that calculations for K can be made corresponding to a bending field. Also, the behaviour of the adhesive has been modelled as a three dimensional element, to allow for shear deformation. A structural viscous damping ratio of 0.032 has been used [1].

The boundary conditions for this model are considered to be fully clamped except for the crack region which is not restrained. The patch above the crack also remains fully constrained. Clearly, crack closure will occur at an increasing distance away from the crack tip, however the complexity in introducing such constraints has not been included in this preliminary study. The crack is initially 50 mm long with it's centre located within the patch. A number of crack lengths have been considered to simulate the crack growth. The crack is assumed to grow symmetrically until the left hand crack tip extends to the edge of the patch. At this point no more crack growth occurs due to the proximity of the panel boundary. The only growth that occurs is at the right hand crack tip. In this

Table 1. Material properties

Material	Young's modulus (MPa)	Poisson's ratio	Ratio of Young's moduli E_1/E_2	Shear modulus (MPa)	Density (Mg/mm^3)
Aluminium	71000.0	0.33	1.0	26691.0	2.77×10^{-9}
Adhesive	2273.0	0.35	1.0	842.0	1.2×10^{-9}
Boron	207000.0	0.21	10.894	4800.0	2.0×10^{-9}

study the maximum crack length considered is 196 mm.

One-third octave sound pressure measurements [1], have been made in flight using microphones located at the nacelle inlet area,

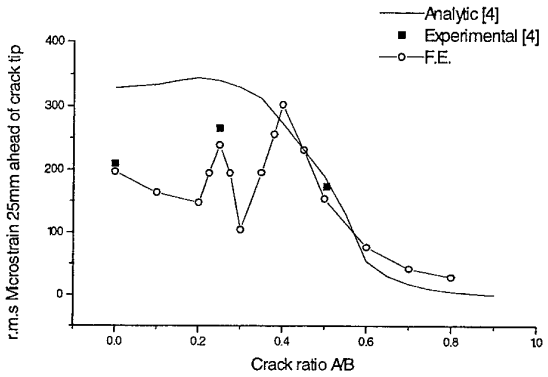

Fig. 4. Comparison of FE, experimental and analytic results.

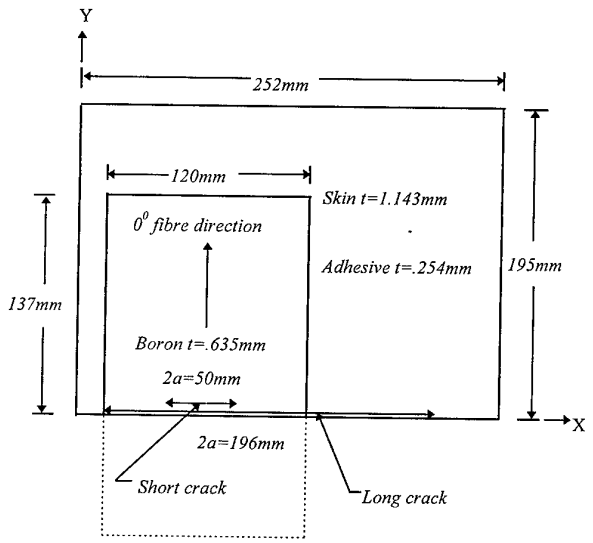

Fig. 5. Dimensions of simplified F/A-18 nacelle inlet panel, with crack and patch.

Table 2. Input power spectral density

Frequency (Hz)	Pressure spectrum level (dB)	PSD (MPa)^2/Hz
31.5	140	4.0×10^{-8}
1000	137	2.005×10^{-8}
8000	124.1	1.028×10^{-9}

and this data is shown in Fig. 6. The spectrum level, relative to the overall sound pressure level (OASPL), is derived from this data and is also shown in Fig. 6. This spectrum is now used as the excitation pressure on the FE model described above.

The relationship between the spectrum sound pressure level (SPL) and the RMS fluctuating pressure (p) is given in [3] as

$$p_{\mathrm{RMS}} = 10^{SPL/20 - 4.69897} \tag{6}$$

and the power spectral density of acoustic pressure, ie. PSD of the excitation, at any given frequency is given by

$$PSD = p_{\mathrm{RMS}}^2 = 10^{SPL/10 - 9.3979} \tag{7}$$

The curve in Fig. 6 has been approximated with the three points shown in Table 2.

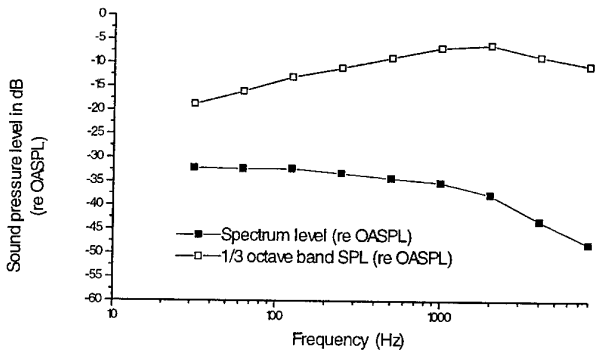

Fig. 6. Spectrum and one-third octave band levels of sound pressure over nacelle inlet.

RESULTS AND DISCUSSION

Shown in Fig. 7 are the natural frequencies versus crack length for the cracked and unrepaired panel and also the repaired panel for the first three resonant modes. In the case of the cracked unrepaired structure, increasing the crack length significantly reduces the frequencies of the panel. Also as expected, repaired panels have little variation in natural frequencies with crack length. Furthermore, the repaired panels have substantially higher natural frequencies for all modes than the unrepaired panels. The boron repair has a definite influence on the panel stiffness.

Mode shapes have been computed corresponding to a short and long crack length for the repaired panel. The first six mode shapes for a short crack length (50 mm) which is covered by the patch, are shown in Fig. 8. Clearly, the mode shapes in Fig. 8 indicate that the crack tip behaviour is dominated by the

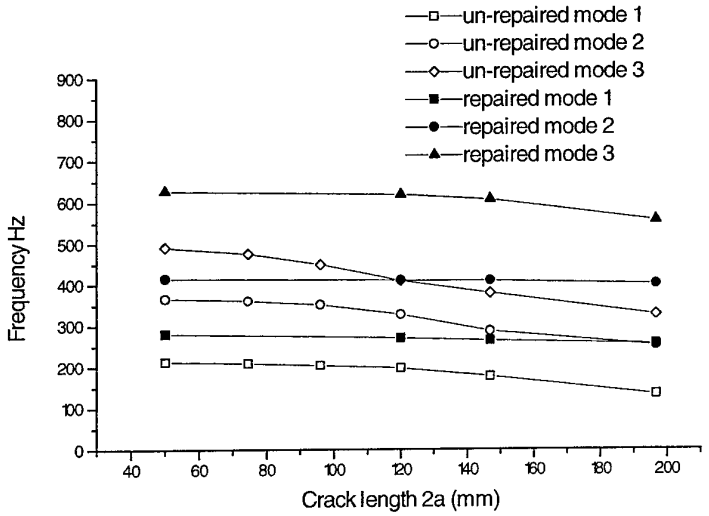

Fig. 7. Frequency versus crack length for unrepaired and repaired cases.

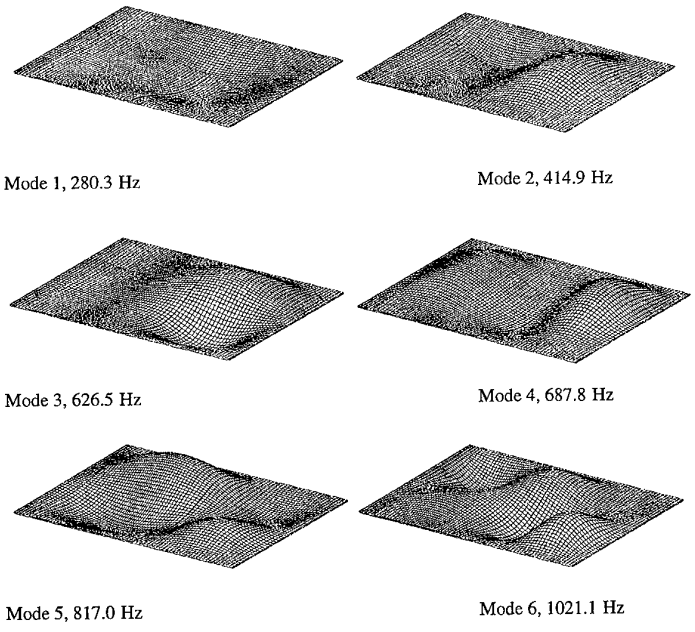

Fig. 8. Mode shapes for the repaired panel containing a short crack ($2a = 50$ mm).

mode I stress intensity factor K_I. Figure 9 shows the mode shape corresponding to a long crack (196 mm) which extends outside the patch (see Fig. 5). These mode shapes indicate that the unsupported crack tip behaviour will now receive a significant contribution from the mode III stress intensity factor K_{III}.

The modal analysis indicates that the mode I, II and III stress intensity factors will be significant. The mode I stress intensity factor K_I for the cracked unrepaired panel is shown in Fig. 10(a). As expected, the general response is an increase of K_I with crack length. The left hand crack tip is always closer to the clamped edge of the panel than the right hand crack tip, and since the bending stresses are a maximum midway along the boundary, the right hand tip gives the highest value of K_I. The values of K_I in relation to the fracture toughness, are significant and explain crack growth.

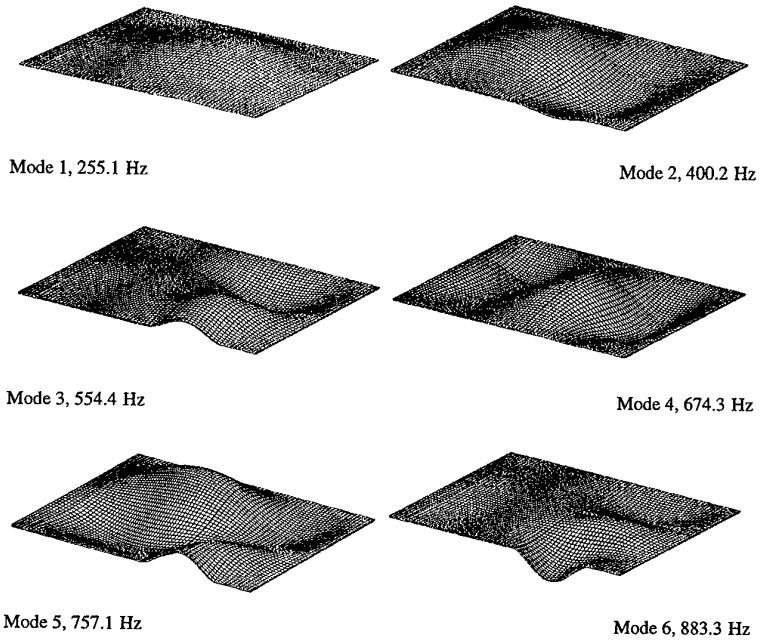

Fig. 9. Mode shapes for the repaired panel containing a long crack ($2a$ = 196 mm).

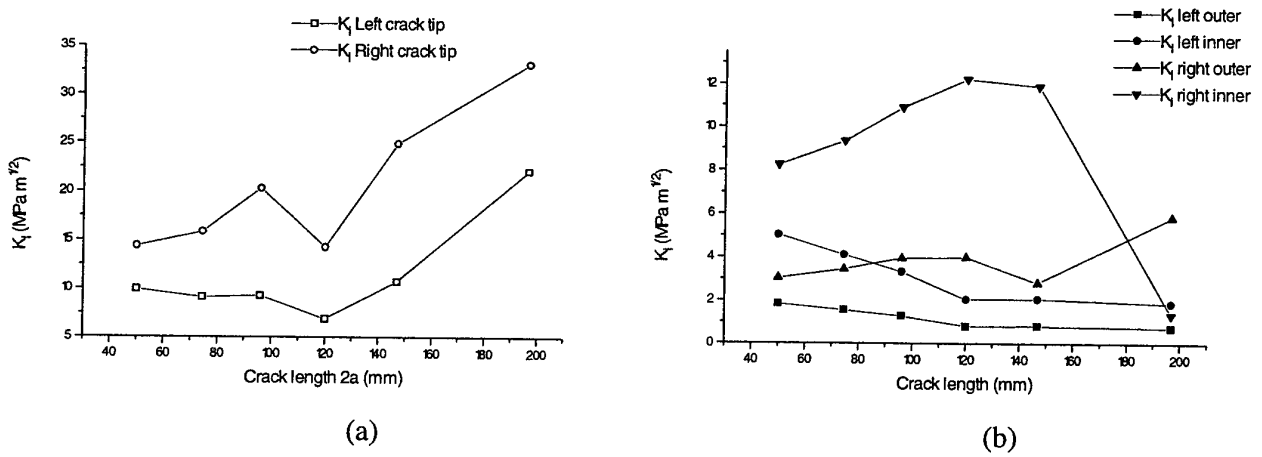

Fig. 10. (a) Stress intensity factor K_I in unrepaired panel for left and right hand crack tips. (b) Stress intensity factor K_I in repaired panel. (Note the change in scale.)

In the repaired panel the neutral axis is offset and as a result K_I is evaluated at both inner and outer surfaces of the skin; the repair being applied to the outer surface. Being a one sided repair, the repair is more effective on the outer surface which is more closely restrained [6]. These bending effects are clearly shown in Fig. 10(b). The right hand crack results in the highest values for K_I located on the inner surface. These values of K_I are significantly high before the crack grows out from under the patch and explain continued crack growth. For a normal 'static' repair in which the only significant events are manoeuvre loads and gust loads, the repair would be successful. However, in the environment of acoustic excitation at a frequency of 300 Hz the repair will not be effective.

The mode II stress intensity factor, K_{II} for the cracked unrepaired panel is shown in Fig. 11(a). Little through thickness variation of K_{11} has been found, hence values are only presented for each crack tip. Numerical values are similar to K_I and the existence of K_{II} explains the tendency of long cracks to turn into the centre of the panel. For the case of the repaired panel shown in Fig. 12(b), K_{II} has been substantially reduced.

The mode III stress intensity factor K_{III} for the cracked unrepaired panel is shown in Fig. 12(a). The values of K_{III} increase significantly with crack length for both left and right

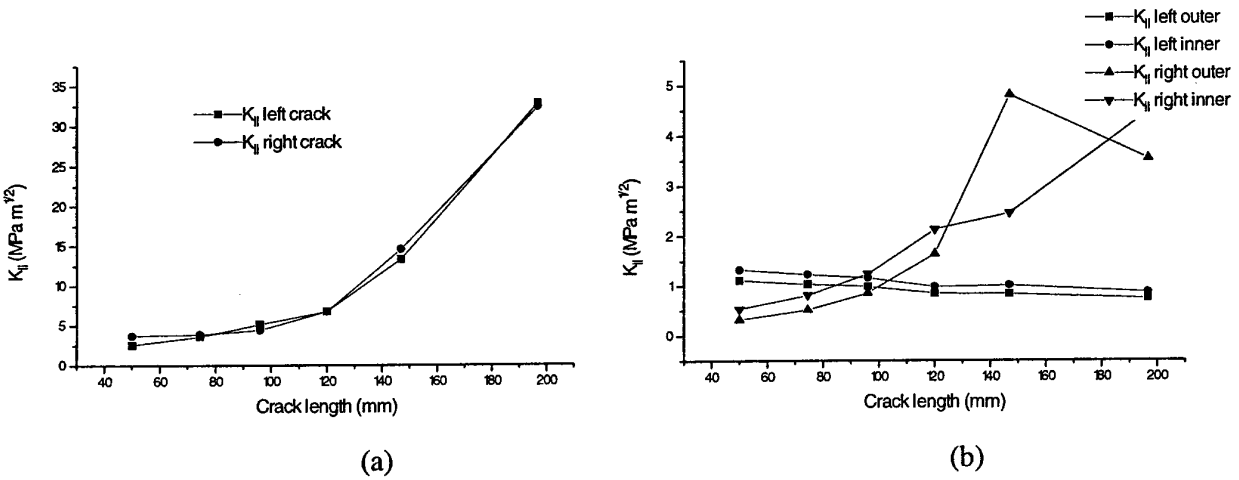

Fig. 11. (a) Stress intensity factor K_{II} for unrepaired panel. (b) Stress intensity factor K_{II} for repaired panel.

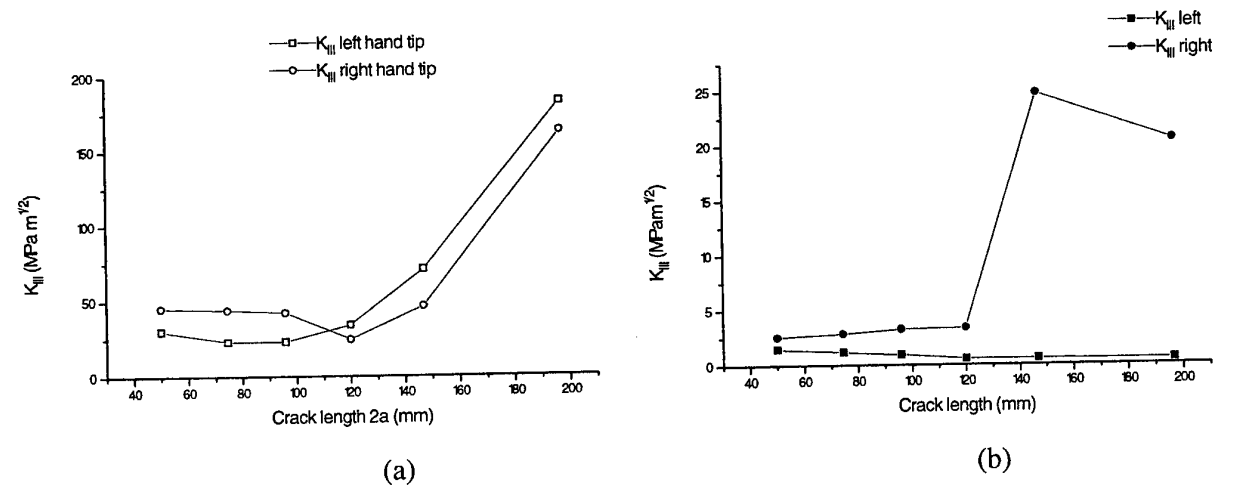

Fig. 12. (a) Stress intensity factor K_{III} for unrepaired panel. (b) Stress intensity factor K_{III} for repaired panel.

hand crack tips, and the numerical value of K_{III} is greater than K_I. Clearly K_{III} will contribute significantly to crack growth. In the case of the repaired panel, shown in Fig. 12(b), the values of K_{III} for a crack not growing outside the patch are low, but not zero. However, once the crack grows outside the patch (i.e. for crack lengths > 120 mm) K_{III} increases significantly.

For a crack length of $2a = 50$ mm, the PSD of the displacement response is proportional to the mode I stress intensity factor, and is shown in Fig. 13(a). This corresponds to some of the

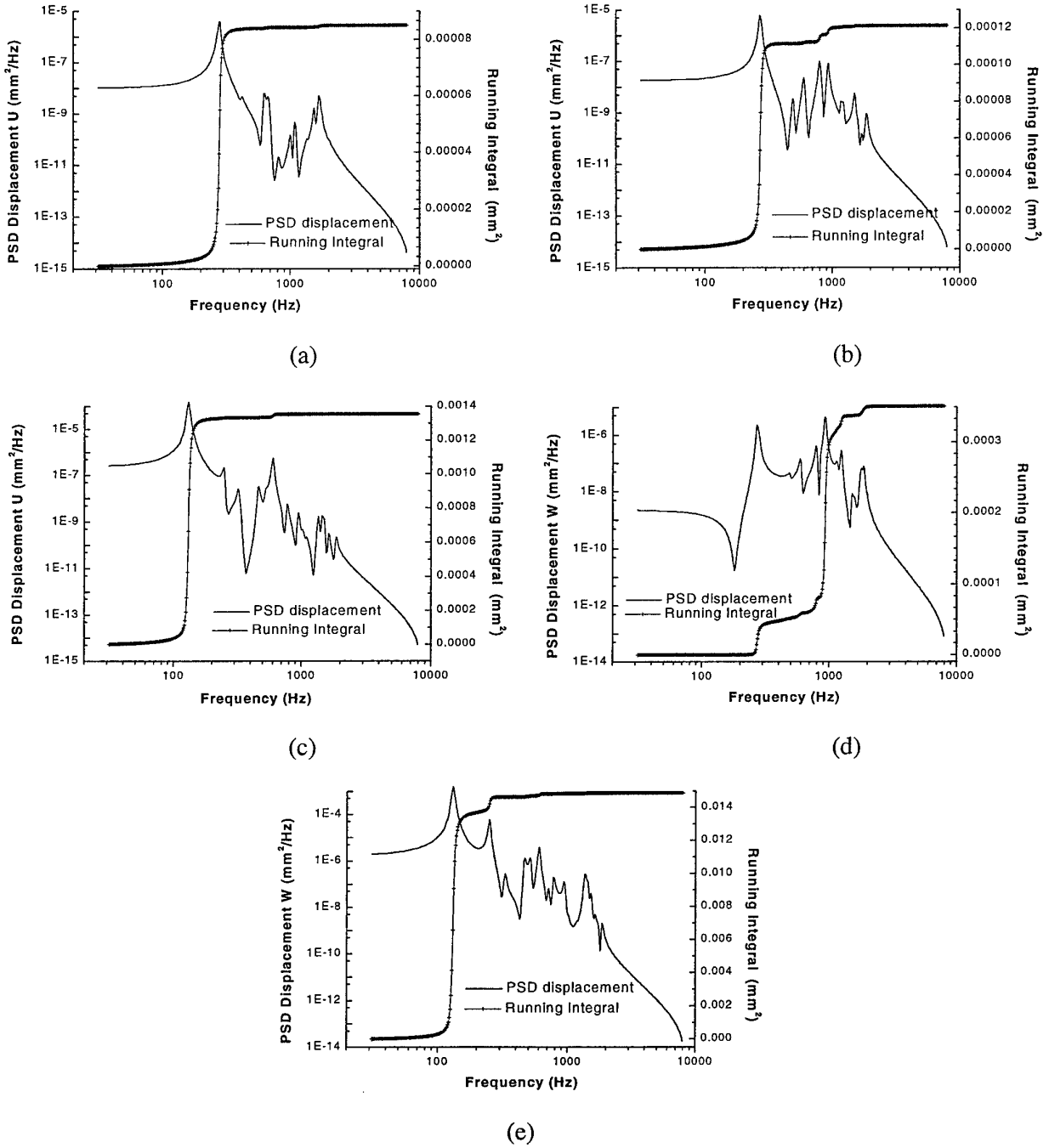

Fig. 13. PSD of displacement (αK_I) and running integral of the PSD for repaired panel of crack length (a) $2a = 50$ mm, (b) $2a = 196$ mm and (c) unrepaired panel with crack length $2a = 196$ mm. PSD of displacement (αK_{III}) and running integral of the PSD for (d) repaired panel of crack length $2a = 196$ mm and (e) unrepaired panel of crack length $2a = 196$ mm.

mode shapes shown in Fig. 8. The peak response occurs at a frequency of 280 Hz and corresponds to mode shape 1 in Fig. 8. With increasing frequency the peaks correspond sequentially to the higher modes. The contribution of the modes to the response can be determined by a running integral of the response and is shown in Fig. 13(a). These results indicate that about 98% of the response is due to mode 1.

In the case of the repaired panel containing a long crack of 196 mm the response for K_I is shown in Fig. 13(b). It is evident from the running integral that mode 1 makes the major contribution to this response followed by modes 4 and 5. However the response for K_{III} shown in Fig. 13(d), clearly shows that mode 6 makes the major contribution at a frequency of 883 Hz, followed by mode 1.

In the case of long cracks in the unrepaired panel, the response for K_I and K_{III} is shown in Fig. 13(c) and (e), respectively. In this case mode 1 makes the major contribution to these factors.

LARGE PATCH

In an attempt to improve the performance of the bonded repair, a patch covering the complete panel has been analysed. The patch contains the five unidirectional layers of boron/epoxy previously used. Again the growth of a crack is simulated, and the stress intensities have been calculated. These results are shown in Fig. 13(a), (b) and (c), and correspond to a structural viscous damping ratio of 0.032. These results show that the mode I stress intensity factor K_I shown in Fig. 14 is approximately 6 MPa (m). Although results are not shown, the mode II and III stress intensity factors are reduced to values below 2 MPa (m).

To assess the results use is made of the Paris equation, which is given by

$$\frac{da}{dN} = A(\Delta K)^n \tag{8}$$

where a is the crack length, A is a constant, N is the number of cycles, ΔK is the increment in stress intensity factor in each cycle, n is an exponent which for aluminium alloys lies between 3 and 4.

Assuming that $\Delta K_1 = K_1$ then the reduction in crack growth for the large patch is given by

$$\left(\frac{da}{dN}\right)_L = \left(\frac{da}{dN}\right)\left(\frac{K_I}{K_{ID}}\right)^n \tag{9}$$

where L denotes the large patch.

The rate of crack growth observed after application of the original patch was 2.15 mm per flight hour. Using a value of $n = 4$ the expected crack growth rate is

$$\left(\frac{da}{dN}\right)_L = 2.15x(6/12)^4$$

$$= 0.134 \text{ mm per flight hour}$$

Normally a threshold limit exists for K_I for which no crack growth occurs. Limited data is available as shown in Fig. 15. This data indicates that this design is just below the threshold value.

DAMPING

The use of constrained layer damping is well known and involves the use of a viscoelastic material sandwiched between two structural elements. The energy of the vibration is dissipated in oscillatory shear that takes place in the damping material. In terms of the current patch, the adhesive would consist of a damping material in which the properties are not adversely affected. Multi-sandwich layers may be necessary to achieve the desired result. The literature indicates that such materials exist in which the damping may be increased by four times the damping in a conventional bonded joint. To investigate this, an analysis has been carried out for these damping levels and the corresponding values for K_I are shown in Fig. 16. In comparison to Fig. 14(a), K_I is clearly reduced. Again, the likely crack growth rate is given by

$$\left(\frac{da}{dN}\right)_D = \left(\frac{da}{dN}\right)\left(\frac{K_I}{K_{ID}}\right)^n \tag{10}$$

where D denotes damping

Using the result for K_I from Fig. 16 the approximate crack growth rate is

$$\left(\frac{da}{dN}\right)_D = 2.15x(3.8/12)^4$$

$$= 0.022 \text{ mm per flight hour}$$

This predicted crack growth rate is significantly less than that for the low damped patch previously considered and gives an indication of the likely performance improvement using high damping materials in such applications. For a 6000 hour lifetime this would correspond to a crack length of 132 mm.

CONCLUSIONS

Validation of the PSD method has been achieved from both experimental data and analytical formula.

The analysis carried out has simulated and characterised the growth of the crack in the cracked and repaired panel. It has been found that after patching a significantly high mode I stress intensity factor K_I exists on the inner surface of the right hand crack tip which is likely to promote crack growth.

For a short crack length in the repaired structure, a running integral of the PSD of the displacement (α K_I), has shown that mode shape 1 contributes about 98% of the response at the crack tip. In the case of a long crack in

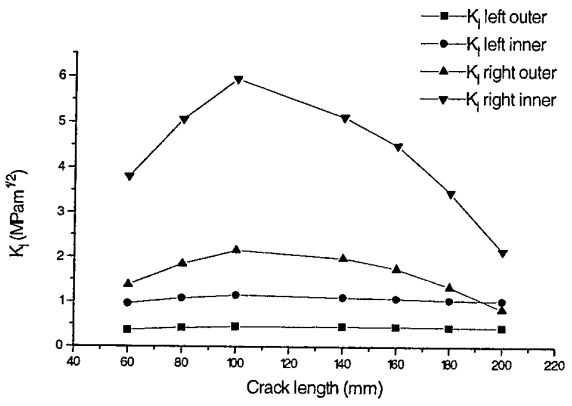

(a)

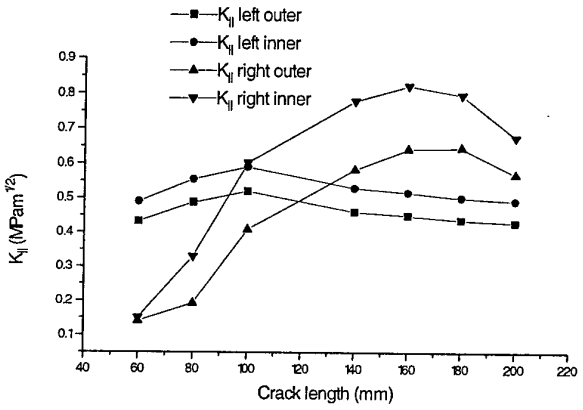

(b)

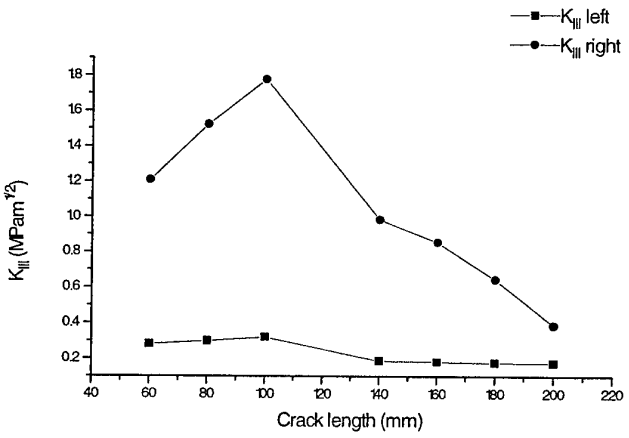

(c)

Fig. 14. (a) Stress intensity factors for (a) K_I, (b) K_{II} and (c) K_{III} for a large patch.

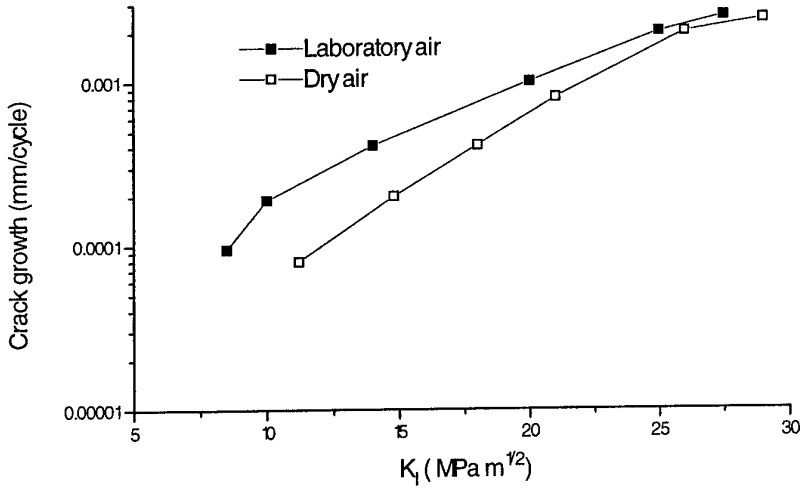

Fig. 15. Crack growth rate for 7075-T6 versus K_I, Delft University.

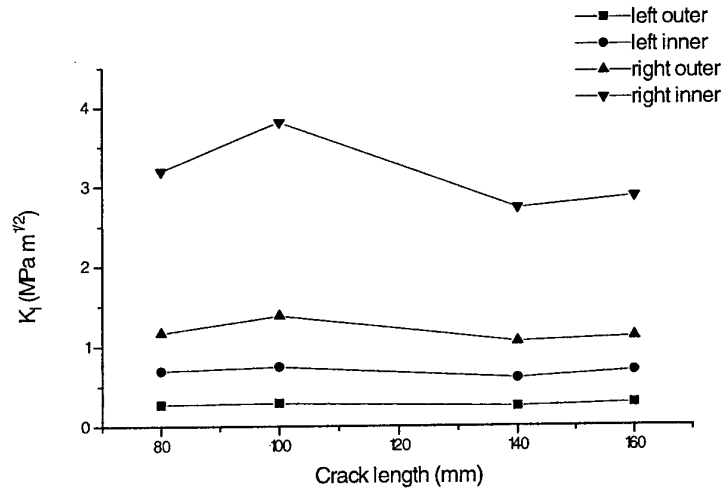

Fig. 16. Stress intensity factor K_I for large patch, with viscous damping = 0.128.

the repaired panel, the running integral showed that mode 6 provided the major contribution to the response for K_{III}. For all other cases considered mode 1 provided the major contribution to K_I and K_{III}.

For the unrepaired panel it is expected that both K_I and K_{III} will have a significant contribution to crack growth.

The use of a patch covering the complete panel is significantly more effective in reducing the stress intensity factors.

The use of damping in bonded joints may significantly lower the crack growth rate in a panel subject to acoustic excitation.

REFERENCES

1. A/B/C/D Aircraft Lower Nacelle Skin Acoustic and Strain Measurements and Sonic Fatigue Analysis. MDC 94B0044. Mar 1994.
2. Blakely MSC/NASTRAN, Basic dynamics analysis, user's guide. The MacNeal–Schwendler Corporation, Dec 1993.

3. Climent, H. and Casalengua, J., Application of a PSD technique to acoustic fatigue Stress Calculations in Complex Structures. *Symposium on 'Impact of Acoustic Loads on Aircraft Structures'*. Lillehammer, Norway, May 1994.
4. Byrne, K. P., Strains affecting the growth rate of edge cracks in acoustically excited panels. *ISVR Tech. Rep. 59*, Nov, 1972.
5. Callinan, R. J., Rose, L. R. F. and Wang, C. H., Three dimensional stress analysis of crack patching. *Proceedings of ICF9*, Sydney, April 1997.

ELSEVIER

Composite Structures Vol. 38, No. 1–4, pp. 661–666, 1997
© 1997 Elsevier Science Ltd. All rights reserved
Printed in Great Britain
0263-8223/97/$17.00 + 0.00

PII:S0263-8223(97)00103-7

Matrix crack-induced delamination in composite laminates under transverse loading

J. Wang & B. L. Karihaloo

Institute of Mechanical Engineering, Aalborg University, Pon 101, DK-9220, Aalborg East, Denmark

Fibre-reinforced multidirectional composite laminates are observed in experiments under transverse static or low-velocity impact loading to suffer considerable delamination damage. The intensity of this damage depends on the difference in the ply angles above and below the interface. In this paper a fracture mechanics model is presented for investigating the role of matrix cracks in triggering delaminations and the influence of ply angles in adjacent plies on delamination cracking. The fracture mechanics analysis shows that for a graphite fibre-reinforced composite laminate containing a transverse intraply crack, the crack-induced largest interfacial principal tensile stress is a maximum when the difference between the ply angles across the interface is 90°, and it attains a minimum when the difference is 40°. When the crack tips touch the interfaces, the minimum mode II stress singularity, which is weaker than the usual square-root type, appears when the difference between the ply angles is about 45° for one glass fibre-reinforced laminate and three graphite fibre-reinforced laminates. These results are in agreement with the experimental observation that the largest delaminations appear at the interface across which the difference between the ply angles is the largest, i.e. 90°. © 1997 Elsevier Science Ltd.

INTRODUCTION

It is widely known that under transverse static or low-velocity impact loading, matrix cracks in the laminae of a fibre-reinforced multidirectional laminate can cause delaminations between the laminae [1–6]. As the low-velocity impact-induced delaminations in laminates are the major source of the reduction in their post-impact compressive strength, the mechanisms of onset of the impact-induced delaminations has attracted the attention of many researchers in recent years [1,3,5,7,8]. There have been numerous experimental observations and finite element computations in this area. As the damage in laminates is always related to cracks (matrix and/or interfacial cracks), a strict fracture mechanics analysis is likely to provide a better physical insight into the damage mechanisms in these materials than the finite element analysis.

For fibre-reinforced multidirectional composite laminates under low-velocity impact, Chester & Clark [1] and Pavier & Clarke [5] found that the intensity of delaminations depended on the difference between the ply angles above and below the interface. Figure 1 shows the relative intensity of the observed

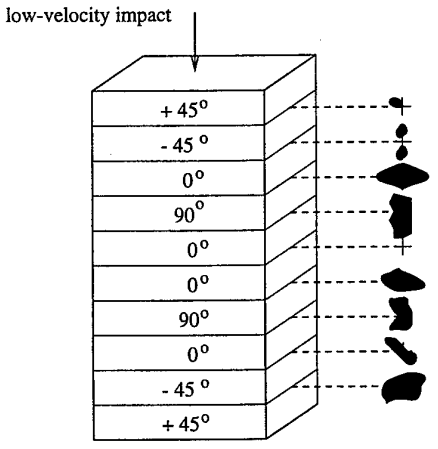

Fig. 1. A composite laminate subjected to transverse impact and the relative intensity of delaminations at the interfaces caused by the impact (after Chester & Clark [1]).

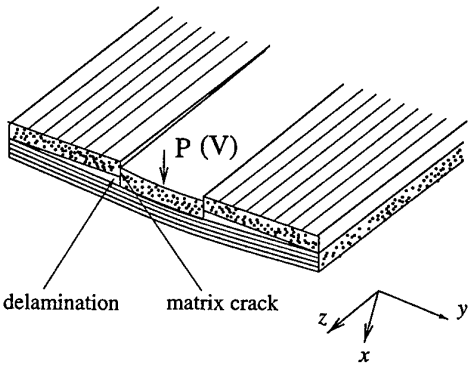

Fig. 2. A damaged composite laminate showing matrix cracks and delaminations caused by a transverse load or low-velocity impact (after Chester & Clark [1]).

delaminations in a composite laminate caused by transverse impact. It is seen that the largest delaminations appear at the interface across which the difference between the ply angles is the largest, i.e. 90°. A damage model which shows the matrix cracks and delaminations in a composite laminate under transverse impact has been presented by Chester & Clark [1], and is reproduced in Fig. 2.

In this paper an idealized fracture mechanics model is presented for investigating the role of a transverse shear crack in triggering delaminations and the influence of ply angles in adjacent plies on delamination cracking. The model consists of a cracked $[(\pm\theta)_{n_2}/(90)_{n_1}/(\mp\theta)_{n_2}]$ laminate. The inner layer is assumed to contain an intraply or interply crack, whereas the two outer layers are assumed to have no cracks [6,9]. A solution is obtained when the crack is subjected to transverse shear, i.e. mode II in fracture mechanics, for two crack configurations. First, when the crack is contained wholly within the inner layer, the crack driving-force and the *crack-induced* interfacial stresses are calculated. The fracture mechanics analysis shows that for a graphite fibre-reinforced composite laminate, when the transverse crack is an intraply crack, the *crack-induced* largest interfacial principal tensile stress is maximum when $\theta = 0°$, that is, the difference between the ply angles across the interface is 90°, and it attains a minimum when $\theta = 50°$. Secondly, when the crack tips touch the interfaces, the minimum mode II stress singularity, which is weaker than the usual square-root type, appears when θ is about 45° for one glass fibre-reinforced laminate and three graphite fibre-reinforced laminates.

FRACTURE MECHANICS MODEL

The damage model in Fig. 2 clearly shows that the delaminations are related to the transverse cracks. Clark & Saunders [10] also noted that delaminations in fibre-reinforced composite laminates under impact appear to initiate at the crossover points of matrix cracks in adjacent plies. It is noted in Fig. 2 that the matrix cracks are mainly subjected to a shear stress in the xy-plane. Only when the top layer fails at this stress state can the transverse load be transferred to the lower layer and the delaminations result. Jih & Sun [3] and Liu *et al.* [4] have classified the matrix cracks caused by a transverse load or low-velocity impact into two types: transverse shear cracks and bending cracks. The transverse shear cracks occur near the loading site due to the high transverse shear stress in this area, whereas the transverse bending cracks are mainly caused by the flexing of the laminate. It is concluded by Liu *et al.* [4] that the delaminations caused by a transverse shear crack are catastrophic in that, once formed, they propagate unstably. On the other hand, the delaminations caused by a transverse bending crack are stable. Therefore, in order to investigate the role of a transverse shear crack in triggering the delaminations, the idealized fracture mechanics model of the composite laminate shown in Fig. 3 [6,9] is used.

In the idealized fracture mechanics model of Fig. 3, the two outer layers of thickness b are assumed to be each an $(\pm\theta)_{n_2}$ angle-ply laminate. They are regarded as transversely orthotropic in the xy-plane whose principal elastic axes are parallel with the x and y axes, respectively. The elastic constants are calculated using the classical lamination theory [9]. The inner layer of thickness $2d$ is taken as a transversely isotropic material in the xy-plane. Figure 3(b) shows an intraply transverse matrix crack of length $2a$ which is in the center of the inner layer, whereas Fig. 3(c) shows an interply matrix crack whose tips touch the interfaces.

SOLUTION OF INTRAPLY CRACK

The fracture mechanics problems shown in Fig. 3(b) and (c) can be solved using the Fourier transforms and superposition procedure [6,9]. We first give the results for the intraply crack problem of Fig. 3(b). For this problem,

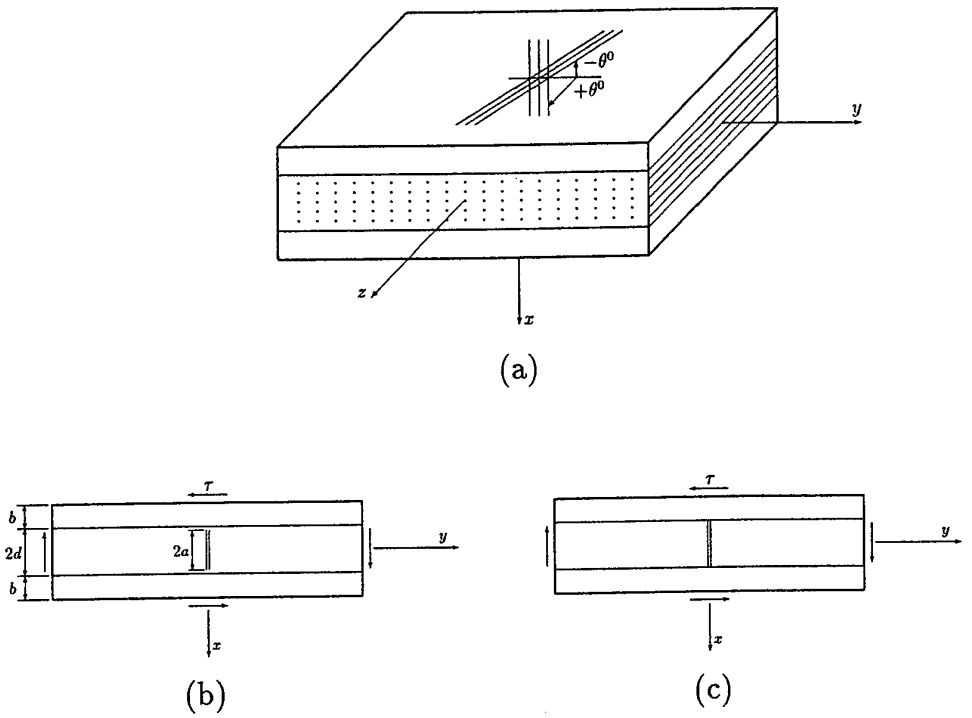

Fig. 3. A fracture mechanics model for investigating the role of a transverse matrix crack in triggering delaminations when the crack is subjected to an in-plane shear stress, mode II in fracture mechanics. (a) laminate configuration; (b) an intraply transverse matrix crack; (c) an interply transverse matrix crack.

the most relevant parameters which are related to the damage of the laminate are the mode II stress intensity factor at the crack tips and the *crack-induced* interfacial stresses. The mode II stress intensity factor at each of the tips of the crack is

$$K_{II} = F_{II}\sqrt{a}\tau \tag{1}$$

where F_{II} is determined by the configuration of the laminate.

For a typical graphite/epoxy fibre-reinforced composite material (M1 in Table 1), the variation of F_{II} is shown in Fig. 4. In the figure, $F(a/d)$ represents the value of F_{II} when the two outer layers are absent. It is seen that these layers considerably reduce the crack-driving force at the tips of the crack. From this point of view, the outer layers have the strongest constraining effect on the propagation of the crack when θ is 0°, that is, the laminate is a cross-ply one. The constraining effect decreases when θ increases from 0° to 90°.

The presence of the transverse matrix crack will inevitably cause stress concentration in the areas ahead of the crack tips. As the interfacial area is generally a weak part of the laminate, we now consider the *crack-induced* interfacial stresses. The non-dimensional (normalized by τ) *crack-induced* largest interfacial principal tensile stress σ_T, which occurs immediately ahead of the crack tips ($x = \pm d$, $y = 0$), is shown in Fig. 5.

The results show that the magnitude of σ_T is influenced by the outer ply angle θ. In contrast to the mode II intensity factor, whose magnitude is determined by F_{II}, σ_T has the maximum value when θ is 0^0. The situation worsens as the

Table 1. Material properties

Materials	Property					
	E_L (GPa)	E_T (GPa)	G_{LT} (GPa)	G_{TT} (GPa)	ν_{LT}	ν_{TT}
M1: (Gr/Ep)	138.0	11.7	4.56	4.18	0.29	0.40
M2: (Gl/Ep)	41.7	13.0	3.40	4.57	0.30	0.42
M3: (Gr/Ep)	140.1	8.36	4.31	3.20	0.253	0.297
M4: (Gr/Ep)	151.1	7.09	3.63	2.72	0.241	0.304

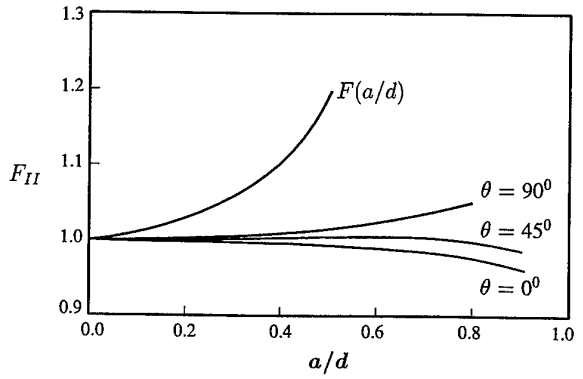

Fig. 4. Variation of F_{II} with the relative crack length a/d and the outer ply angle θ.

tips of the crack approach the interfaces, as the influence of θ becomes more prominent.

If the design objective is to minimize the crack-driving force at the tips of the crack so that the laminate is least prone to transverse cracking when subjected to a transverse load, $\theta = 0°$ should be chosen. However, if the design objective is to minimize the *crack-induced* interfacial stress so that the risk of delamination is minimized or delayed, θ should take on a non-zero value. We can deal with these conflicting design objectives by trying to find a compromise design using optimization techniques. The compromise design can be obtained by solving two optimization problems [9].

In the first optimization problem, the crack-driving force, represented by F_{II}, is minimized, whereas constraints are imposed on σ_T, $\sigma_T \leq (\underline{1}+\alpha)$, and the flexural rigidity of the laminate, $\bar{D} \geq (1-\gamma)D_0$. $\bar{D}$ is the normalized flexural rigidity of the laminate, and D_0 is its value, when $\theta = 0°$. α and γ are tolerance factors on the stress gain and stiffness loss, respectively.

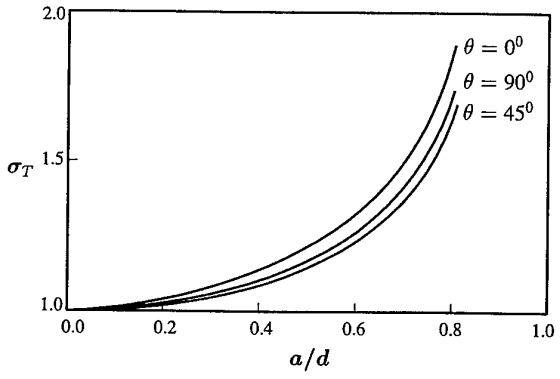

Fig. 5. Variation of the normalized *crack-induced* largest interfacial principal tensile stress with the relative crack length a/d and the outer ply angle θ.

Upper ($\bar{\theta}$, $\bar{b}$) and lower limits ($\underline{\theta}$, $\underline{b}$) are also placed on the design variables θ and b/d, respectively ($\bar{\theta} = 90°$, $\bar{b} = 4.0$; $\underline{\theta} = 0°$, $\underline{b} = 0.0$). From the solution of this optimization problem it was found that for small a/d, the active constraints were the lower limit on θ and the upper limit on b/d. The minimum of F_{II} always occurred at $\theta = 0°$. When a/d was large, the interfacial stress constraint became critical to the design. For the satisfaction of this constraint the design angle θ had to take on a non-zero value. It was found that for $\alpha = 0.5$, $\gamma = 0.15$ and $\bar{b} = 4.0$, when a/d exceeded 0.73, no optimum design was possible because of the violation of the constraint on interfacial strength. For this reason an alternative formulation of the optimization problem was considered.

In the second optimization problem, the largest interfacial tensile stress σ_T was minimized subject to the constraint that $\Phi(1)$ must not exceed 1.0 and that the flexural stiffness be adequate. The solution of this minimization problem is shown in Fig. 6. In this case, $\underline{\sigma}_T$ reaches its minimum when $\theta = 50°$ and $b/d = \bar{b}$.

SOLUTION OF INTERPLY CRACK

In this section, we show the results of the fracture mechanics solution of the crack problem shown in Fig. 3(c). In this case, the problem leads to the solution of a singular integral equation [6]. When the tips of the crack touch the interfaces, the asymptotic value of the stresses near the tips can be expressed as

$$\sigma_{ij} = \frac{K_{II}}{\sqrt{2}r^{\gamma_2}} f_{ij}(r, \theta) \tag{2}$$

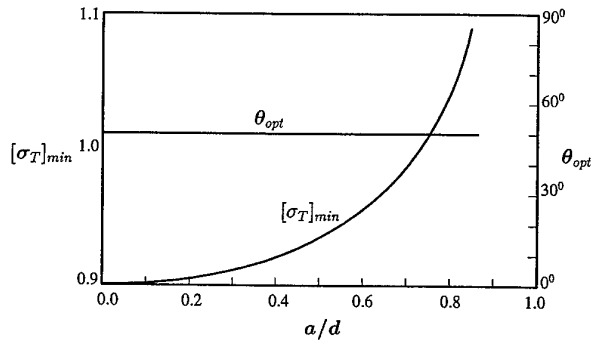

Fig. 6. Results of the optimization problem in which the normalized *crack-induced* largest interfacial principal tensile stress σ_T is minimized.

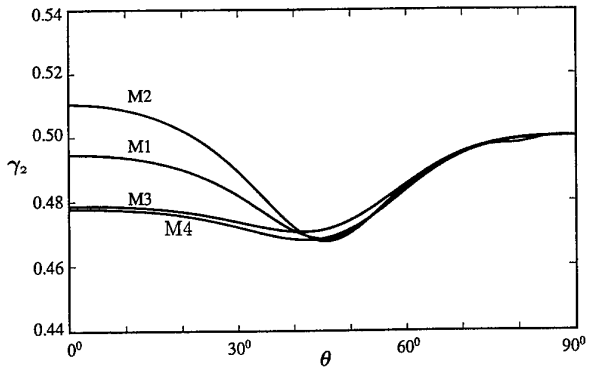

Fig. 7. Variation of the mode II stress singularity γ_2 with the outer ply angle θ for four composites. M1, M3 and M4 are graphite/epoxy composites, whereas M2 is a glass/epoxy composite.

where σ_{ij} $(i, j = 1, 2)$ are the stress components in the xy-plane. K_{II} is the mode II stress intensity factor and γ_2 is the singularity of the stress field. r is the distance away from the tips of the crack, and $f_{ij}(r, \theta)$ are the angular functions with the origin of polar coordinates at the crack tip.

The variation of the stress singularity γ_2 for the four composite materials (three graphite/epoxy composites and one glass/epoxy composite) listed in Table 1 is shown in Fig. 7. The strongest and weakest mode II singularities are given in Table 2. It is seen from Fig. 7 and Table 2 that the mode II stress singularity has its minimum value when the outer ply angle θ is about 45°, that is, the difference between the ply angles in the adjacent plies is about 45°. For the three graphite/epoxy composites the strongest singularity occurs at $\theta = 90°$, that is when the composite laminate in Fig. 3(a) degenerates into a transversely isotropic layer.

DISCUSSION AND CONCLUSIONS

For a multidirectional composite laminate under transverse static or low-velocity impact loading, the matrix cracks are obviously caused by a combination of the tensile stress perpendicular to the fibre direction and the shear stress, as shown in Fig. 2. It was shown in Ref. [11] that for quasi-isotropic laminates, the transverse shear stress near the impacted site is very high. Following this observation and the analyses by Jih & Sun [3] and Liu *et al.* [4], it is quite reasonable to assume that the occurrence of transverse cracks near the loading point is dominated by the transverse shear stress.

Table 2. Strongest and weakest mode II stress singularities

Materials	M1	M2	M3	M4
γ_{2max}	0.500	0.510	0.500	0.500
θ_{max}	90°	0°	90°	90°
γ_{2min}	0.468	0.468	0.470	0.468
θ_{min}	45°	45°	41°	42°

From the idealized fracture mechanics model presented above, the following conclusions may be drawn:

1. When the transverse crack is wholly within the inner layer (intraply transverse crack), the *crack-induced* interfacial principal tensile stress is influenced by the difference between the ply angles in the inner and outer layers. When the difference between the ply angles is 40°, the stress reaches its minimum for the graphite/epoxy composite material considered.
2. For an interply transverse crack where the crack has run through the thickness of the inner layer, the mode II stress singularity reaches its minimum for the three graphite/epoxy composites and one glass/epoxy composite when the difference between the ply angles is about 45°.

ACKNOWLEDGEMENTS

The support of the Danish Research Academy to JW through the award of a visiting postdoctoral fellowship (DANVIS) is gratefully acknowledged.

REFERENCES

1. Chester, R. J. and Clark, G., Modelling of impact damage features in graphite/epoxy laminates, in *Damage Detection in Composite Materials, ASTM STP 1128*, Masters, J. E., Ed., 1992.
2. Doxsee, L.E., Rubbrecht, P., Li, L., Verpoest, I. and Scholle, M., Delamination growth in composite plates subjected to transverse loads. *J. Comp. Mater.*, 1993, **27**, 764–781.
3. Jih, C.J. and Sun, C.T., Prediction of delamination in composite laminates subjected to low velocity impact. *J. Comp. Mater.*, 1993, **27**, 684–701.
4. Liu, S., Kutlu, Z. and Chang, F.K., Matrix cracking and delamination in laminated composite beams subjected to a transverse concentrated line load. *J. Comp. Mater.*, 1993, **27**, 436–470.
5. Pavier, M.J. and Clarke, M.P., Experimental techniques for the investigation of the effects of impact damage on carbon-fibre composites. *Composite Science and Technology*, 1995, **55**, 157–169.
6. Wang, J. and Karihaloo, B. L., Mode II and mode III stress singularities and intensities at a crack tip termi-

nating on a transversely isotropic-orthotropic bimaterial interface. *Proc. Roy. Soc.* London, Vol. A444, 1994.
7. Choi, H.Y. and Chang, F.K., A model for predicting damage in graphite/epoxy laminated composites resulting from low-velocity point impact. *J. Comp. Mater.*, 1992, **26**, 2134–2169.
8. Davies, G. A. O., Hitchings, D. and Wang, J., Prediction of threshold impact energy for onset of delamination in quasi-isotropic carbon/epoxy composite laminates under low-velocity impact. *Composite Science and Technology* (To appear) 1997.
9. Wang, J. and Karihaloo, B. L., Cracked composite laminates least prone to delamination. *Proc. Roy. Soc.*, London, Vol. A444, 1994.
10. Clark, G. and Saunders, D.S., Morphology of impact damage growth by fatigue in carbon fibre composite laminates. *Materials Forum*, 1991, **15**, 333–342.
11. Davies, G.A.O. and Zhang, X., Impact damage prediction in carbon composite structures. *Int. J. Impact Engng*, 1995, **16**, 149–170.

ELSEVIER

Composite Structures Vol. 38, No. 1–4, pp. 667–678, 1997
© 1997 Published by Elsevier Science Ltd. All rights reserved
Printed in Great Britain
0263-8223/97/$17.00 + 0.00

PII:S0263-8223(97)00104-9

Adaptive post-buckling response of carbon fibre composite plates employing SMA actuators

S. P. Thompson & J. Loughlan

Structures and Materials Technology Group, College of Aeronautics, Cranfield University, Bedford, UK

Restoration forces, associated with embedded activated pre-strained SMA wires, have successfully been employed to enhance the post-buckling behaviour of laminated plate structures while under the influence of a uniaxial load. The results of which will be presented. The manufacturing methodology of the hybrid SMA–carbon–epoxy plates is outlined. Optical micrographs illustrate the effect of embedding diametrical inclusions within a host composite. Thermal and structural finite-element analysis have been employed to predict the non-uniform temperature profile within the laminates and to provide insight to the SMA–hybrid structure adaptive response. It is shown that by utilizing the considerable control authority generated, even for a small actuator volume fraction, the out-of-plane displacement of the post-buckled laminates can be significantly reduced. Such displacement alleviation allows for the load redistribution away from the plate's unloaded edges, i.e. there is a tendency for the plate to conform to the optimal flat configuration beyond its critical buckling load. However, the stability of the adaptive response is very much dependent upon the laminate stacking sequence. It is envisaged that the range of operational performance for such an adaptive hybrid structure may be extended over conventional materials and structures. © 1997 Published by Elsevier Science Ltd.

INTRODUCTION

Enhancing the post-buckling performance of laminated plate structures utilizing adaptive control techniques, associated with the *smart structure technology*, is the subject of this paper. Such adaptive behaviour is provided for by the insertion of pre-strained nickel–titanium shape memory alloy (SMA) wire actuators into pre-fabricated laminated plate specimens, constraining the actuators sufficiently, and energizing the actuators accordingly. The ability of a structure to modify its response to an applied load, or an environmental exposure, offers significant advantages, particularly for aerospace platforms. The selection of the nickel–titanium SMA over alternative induced strain actuators, i.e. piezoceramic or electrostrictive materials, was made based on the material's high authority actuation capability, a predominant requirement when wishing to control the behaviour of structures subjected to high load levels.

Integrating SMA actuators within laminated structures has been investigated for numerous control-structure schemes including vibration suppression, acoustic control, damage containment and shape control. Investigations employing the material's unique behaviour for buckling/post-buckling control are limited.

The feasibility of using SMA actuators for actively controlling the buckling of flexible structures was first conducted by Baz *et al.* [1–3]. An external SMA helical spring has been employed to enhance the buckling characteristics of long slender beams [1]. The SMA helical spring was connected to a pneumatic power cylinder which applied a compressive loading to an elastic member. The net effect of actuation was to reduce the compressive loading on this elastic member, i.e. the actuator recov-

ery force counterbalances the applied load and prevents the beam from buckling. This work involves sensing the onset of bending, and using the SMA actuators to reduce the load on the column, thereby preventing out-of-plane deformation.

The buckling characteristics of flexible fibreglass polyester resin composite beams have been actively controlled by activating shape memory alloy wires embedded along the beam's neutral axis [2]. A closed-loop computer-controlled system was used to control the buckling of the beam, with dimensions of $637.5 \times 25.4 \times 4.5$ mm, reinforced with eight SMA wires, 0.55 mm in diameter. The results showed that the critical buckling load could be increased three times when compared to that of an uncontrolled beam.

Investigations into the lateral torsional buckling of a transversely loaded cantilevered beam, with dimensions of $406 \times 51 \times 2.5$ mm, incorporating two 0.55 mm diameter SMA wires embedded symmetrically along the beams mid-plane, have shown that the buckled beam can be brought back completely to its unbuckled configuration with appropriate SMA activation [3].

Finite-element analysis was performed to investigate the potential for active buckling control of two different stiffened panels by embedded SMA rods [4]. Changes in the predicted buckling load increased with the magnitude of the actuation level for a given structural concept. Increasing the number of actuators yielded greater predicted increases in the buckling load. The practicality of the concept relies on the development of such high authority SMA rods, whereby the necessary shape memory elongation can be generated. Energizing finer diameter SMA wires would result in lower critical buckling values, attributed to the shape memory shortening.

Preliminary results on the use of SMA fibre/strips, integrated within graphite–epoxy composite panels, demonstrate that the SMA fibres can enhance critical thermal buckling temperatures and attenuate, or even eliminate, thermal post-buckling deflections [5]. Such findings are based on the generation of in-plane tensile forces within the host laminate resulting from the elongation of the activated SMA fibre/strips. The laminate under investigation was a $[0°/\pm 45°/90°]_s$ with SMA volume fractions between 10 and 30%, initially pre-strained to 3–5%. The critical buckling temperatures are seen to increase drastically to the point where they are unrealistic as they exceed the material's maximum service temperature, although such a high SMA volume fraction may be of benefit to high-temperature matrices such as those of carbon–carbon composites. These results, as with the previous citation, rely on the shape memory elongation of the in-elastically deformed material, rather than the characteristic shortening associated with the fine diameter wires.

An analytical expression was formulated to predict the behaviour of composite laminated plates integrated with SMA fibres [6]. Accounting for the large increase in Young's modulus, when nickel–titanium transforms to its austenite phase, is shown to increase the hybrid composite plate's critical buckling value. Utilizing the recovery force generated when the SMA fibres are constrained to the host composite, the actuator may act to decrease the critical load. The analytical formulation developed, however, does not account for thermal effects.

Piezoceramic actuation has also shown improvements in the load-bearing capability of compressive loaded members [7]. SMA actuators offer the greatest potential for buckling control or post-buckling deflection alleviation as the associated recovery force is several orders of magnitude greater than the induced force of piezoceramic actuators. They also allow for direct embedding within the host laminate with minimal disruption to the local reinforcement, thus minimizing the possibility of actuator damage if located on the surface.

A numerical and experimental study of the post-buckling behaviour of laminated SMA–composite plates with arbitrary stacking sequences has been conducted. The adaptive capability is provided for by the insertion of SMA wire actuators through sleeves located within the manufactured specimens. The SMA characteristic behaviour, laminate fabrication methodology, detailed numerical analysis, testing procedure, and experimental/numerical results will be presented. From which, a conjectural assessment to the current post-buckling adaptive methodology can be drawn.

CHARACTERISTIC SHAPE MEMORY ALLOY BEHAVIOUR

Shape memory alloys, when heated, undergo a solid–solid phase transformation from their

low-temperature martensite phase to their high-temperature austenite phase [8]. When unconstrained SMA actuators are cooled below their martensitic transformation temperature and deformed, they *remember*, and return to, their original shape upon the application of the phase transition temperature. If constrained, the alloy will *attempt* to revert to its original shape resulting in the generation of a significant internal recovery force. Such a recovery force will be employed for the composite adaptive capability. Typically, strains of 6–8% can be completely recovered by heating deformed unconstrained nickel–titanium through its characteristic transition temperature. Alternatively, stresses of up to 800 MPa may be generated.

Many materials are known to exhibit the shape memory phenomena, the most common being nickel–titanium. It is this commercially available alloy that is employed for this investigation. The alloy, in the form of a 0.4 mm diameter wire, has a nominal composition of 49.8–50.0 at.% Ni and was annealed at 500°C for 1 h, thereby providing the *shape memory*.

Phase transition can occur through an increase in the ambient temperature or through resistive heating, the latter is employed for this study. Their are four important temperatures characteristic to an SMA. These are martensite finish (M_f), martensite start (M_s), austenite start (A_s) and austenite finish (A_f). Knowledge of the austenite transformation temperature is essential so that a necessary power level can be determined to induce maximum recovery force. The phase transition temperatures were determined by differential scanning calorimetry, the results of which are presented in Table 1. It is well known that the transformation temperatures are influenced by stress, σ. They vary according to the following linear relationships [9]

$$M_s = M_s(\sigma = 0) + \sigma / C_M$$

$$M_f = M_f(\sigma = 0) + \sigma / C_M$$

$$A_s = A_s(\sigma = 0) + \sigma / C_A$$

Table 1. Phase transition temperatures

Phase	Temperature (°C)
A_s	50
A_f	68
M_s	25
M_f	7

$$A_f = A_f(\sigma = 0) + \sigma / C_A \quad (1)$$

The constants C_A and C_M are material properties and are assumed to be equal. It is seen within the published literature that the values vary between 4.5 and 13.8 MPa/°C. $\sigma = 0$ denotes the stress-free temperature (Table 1).

Constraining an activated pre-strained SMA wire from returning to its memorized configuration results with the formation of a recovery stress. As stated, this stress will alter the transformation temperatures in an upward manner. If the activation temperature was equal to the stress-free austenite finish temperature, then only partial activation will result. The activation power level required to induce the full recovery stress must take into account the expected recovery stress.

To ascertain the recovery force for an individual actuator, a sample was pre-strained to 6%, clamped at either end within an Instron Universal Testing Machine, and cycled through the transformation temperature range. Clamping prevents contraction upon heating the deformed specimens. The recorded recovery force, for cycles 1, 5, 10 and 20, monitored at 10 Hz, is shown in Fig. 1. A typical operating cycle is defined as heating the actuator to reach its peak recovery force, via the input of a step DC power source, maintain the force for a short period and then allow the specimen to cool back to the ambient temperature. Cool down is achieved by removal of the DC power source.

Subjecting the actuator to the alternate heating and cooling cycles results in degradation in the recovery force. It is clearly evident that the maximum recovery force is generated during the first cycle. Subsequent cycles show a decrease in the measured recovery force. The greatest reduction occurs during the first few cycles. After 20 cycles the recovery force becomes more stable. Such behaviour being typical of nickel–titanium. The recovery force degrades due to the formation of lattice defects, such as dislocations, causing an internal stress relaxation. Such defects occur more prominently when the alloy is subjected to a complete temperature cycle, i.e. austenite→martensite [10]. The formation of defects occurs rapidly at first and then levels off. Defect formation is dependent upon the level of initial pre-strain, temperature cycle and heating rates.

If the SMA is required to show repeatable recovery force characteristics over many cycles,

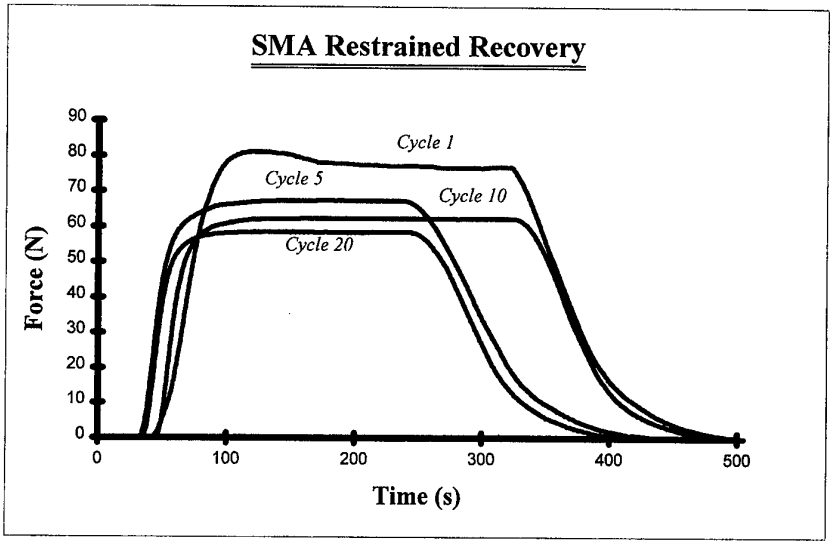

Fig. 1. SMA cyclic restrained recovery.

then they should have a low initial pre-strain. This, however, will be at the expense of the high restoration force capability. The latter can be met by increasing the volume fraction of actuators in operation.

The recovery force measurements provide an accurate means of predicting the adaptive structural behaviour. The results of Fig. 1 have been applied to a non-linear FEA. Such analysis determines the post-buckling behaviour of laminated plate structures with an improved load-bearing capability provided for by the SMA control scheme.

TEST SPECIMEN CONFIGURATION

The dimensions of the plates under investigation were 300×300 mm. The following ply stacking sequences have been considered; $[0_2°/90_2°]_s$, $[0°/\pm 45°/90°]_s$ and $[0_2°/\pm 45°]_s$. Fiberdux 913C-TS unidirectional high tensile carbon–epoxy, purchased from HEXCEL Composites, was employed for plate manufacture. Each specimen features SMA wires, pre-strained to 6% and inserted through sleeves, which run throughout the laminate at the desired location. For each specimen the SMA orientation is perpendicular to the loading direction. It is not a requirement that the SMA wires adhere to the host laminate. Restrained recovery is met through external fixtures.

Manufacture of such a laminate is as follows. The individual plies are placed accordingly. PTFE tubing, with an inner diameter of 0.46 mm and a wall thickness of 0.15 mm, containing steel wires with a diameter of 0.45 mm, are located on the neutral plane at the desired SMA positions. The embedded inclusions extrude out from the edges of the lay-up a finite distance and held taut, thus ensuring their desired alignment. The pre-preg material, featuring the embedded inclusions, are subjected to the manufacturer's recommended curing cycle. Once cured, the steel wires are withdrawn. The SMA wires are then inserted. The adaptive capability is provided for by constraining the ends of the SMA wire to an external boundary and applying the necessary temperature for phase transition.

The properties that make PTFE suitable for this application are its; (1) working temperature up to 260°C; (2) very low coefficient of friction; and (3) extremely high electrical resistance. To ensure suitable compaction during the curing process, 1.5 mm thick silicone rubber diaphragms were place between the hybrid laminate surfaces and the curing apparatus.

Optical micrographs for lay-up configurations $[0_2°/90_2°]_s$ and $[0_2°/\pm 45°]_s$ (Figs 2 and 3, respectively) show the affect the embedded inclusion has on the host laminate surface topology and the disruption it can cause to the neighbouring carbon reinforcement. Placing the inclusion parallel to the neighbouring reinforcement is clearly advantageous (Fig. 2) as such a configuration imposes minimal reinforcement disruption. However, placement of the inclusion

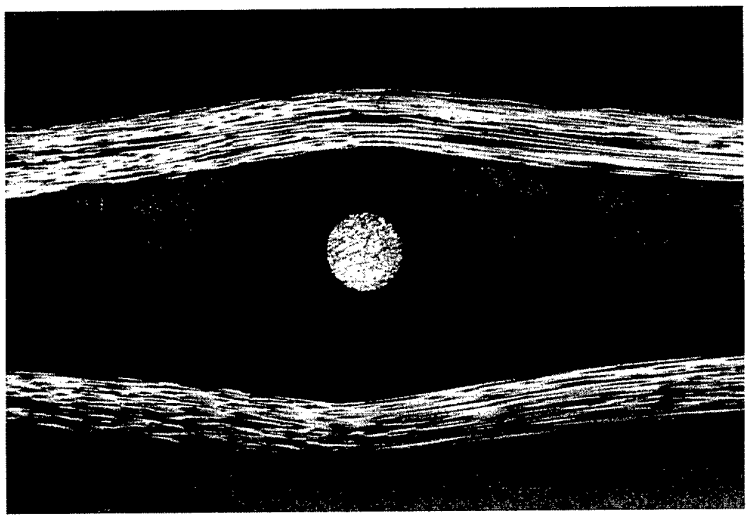

Fig. 2. $[0_2°/90_2°]_s$ optical micrograph.

at an angle to the reinforcement (Fig. 3) results in considerable reinforcement disruption and the formation of a lenticular resin-rich region extending approximately 2 mm from the inclusion interface.

Based on the research conducted regarding embedded optical fibre sensors within composite laminated constructions [11], such local ply disruption will have profound implications on the ultimate compressive load-bearing capability. This study is concerned with post-buckling deflection removal and the associated post-buckled non-uniform stress alleviation, at which the applied stresses are lower than the ultimate. Therefore, at this stage, it seems suitable to orient the embedded inclusion in a manner best suited to achieve the desired structural response.

NUMERICAL FINITE-ELEMENT ANALYSIS

Thermal, linear buckling and structural non-linear FEA was employed to predict the improved post-buckling behaviour of the SMA–carbon–epoxy laminated plate structures. The actuators are placed so as to contain a particular mode shape. The FE models were constructed using the pre- and post-processor P3/PATRAN.

SMA activation results in a non-uniform temperature profile within the laminate. Such a

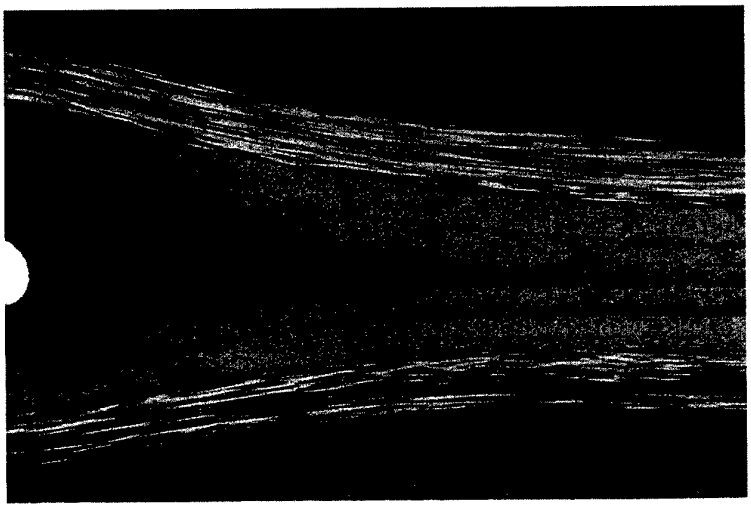

Fig. 3. $[0_2°/\pm 45_2°]_s$ optical micrograph.

temperature profile was determined by P3/THERMAL. This pre-determined temperature profile can be superimposed on the structural mesh, thus accounting for thermal stresses and temperature-dependent effects.

The FEA package MSC/NASTRAN was used to perform the buckling and geometric non-linear analysis. The linear buckling analysis, employing the Lanczos method, performs an eigensolution to predict the eigenvalues and eigenvectors, where buckling loads and their respective mode shapes can be determined. To predict the post-buckling behaviour, geometric non-linear analysis using the modified Newton–Raphson method was performed.

Thermal FEA

Activation of the SMA, through resistive heating, will subject the neighbouring laminate to a significant increase in temperature. Based on the assumption of a uniform temperature distribution in a direction parallel to the SMA wires, a two-dimensional model was used to predict the plate cross-sectional temperature profile. The SMA orientation being normal to the two-dimensional representation. The specimen's cross-sectional area was represented by 1200 thermal quadrilateral elements. The applied element material properties are listed in Table 2. The composite directional-dependent thermal conductivity is accounted for by application of $k = 15$ W/m °C in a direction parallel to the carbon reinforcement and $k = 1$ W/m°C in a direction transverse to the carbon reinforcement. A nodal heating source of 20.7 W/m was applied to the nodes at the SMA locations simulating the activation strategy. The natural convection heat transfer from the surface of the vertically inclined plate is calculated through the selection of an appropriate convection configuration available within the analysis solver. An ambient and initial specimen temperature was measured to be 25°C and applied to the model.

Table 2. Thermal properties

Property	Carbon–epoxy
ρ (kg/m^3)	1600
c_P (J/kg °C)	837
k (W/m °C)	15 (longitudinal) 1 (transverse)

Table 3. Ply properties

Property	Value
E_{11}	140×10^3 N/mm^2
E_{22}	10×10^3 N/mm^2
G_{12}	5×10^3 N/mm^2
ν_{12}	0.3
α_{11}	-0.3×10^{-6} ε/°C
α_{22}	28×10^{-6} ε/°C

Structural FEA

The laminated plates were modelled using 2304 two-dimensional shell elements (CQUAD4). Such a mesh proved sufficient in terms of analysis convergence. The carbon–epoxy lay-up was represented by the NASTRAN PCOMP and MAT8 data entries, which are based on the assumptions of classical lamination theory. Owing to the anisotropic nature of two of the laminates considered, the whole model was analysed. Individual ply material properties are shown in Table 3.

The boundary conditions applied to each edge simulate simply supported conditions with the unloaded edge supports allowing for in-plane translations. To simulate the uniform compressive edge displacement along the loaded edge, a rigid-body element (RBE2) was introduced by inserting an additional node (known as the *independent node*) at the mid-point along the top edge of the model where the compressive load is to be applied. The independent node's out-of-plane translation, along with all its rotations, are fully constrained. All the nodes along the top edge of the plate (known as *dependent nodes*) are connected to the independent node and their translations, but not rotations, are tied to that of the independent node. The dependent nodes are free to deform due to Poison's effect. In this manner, a uniform displacement is imposed along the top edge of the panel, which will not provide constraint against either shape memory adaptation or thermal expansion–contraction. This condition is identical to that enforced by the loading platen of the testing machine.

Each SMA wire was modelled with 50 CBEAM elements. The element and material properties are represented by the PBEAM and MAT1 data entries, respectively. Ten actuators where employed for lay-up configurations $[0_2°/90_2°]_s$ and $[0_2°/\pm 45°]_s$. Twelve actuators were employed for the lay-up $[0°/\pm 45°/90°]_s$. For each configuration, the actuator spacing

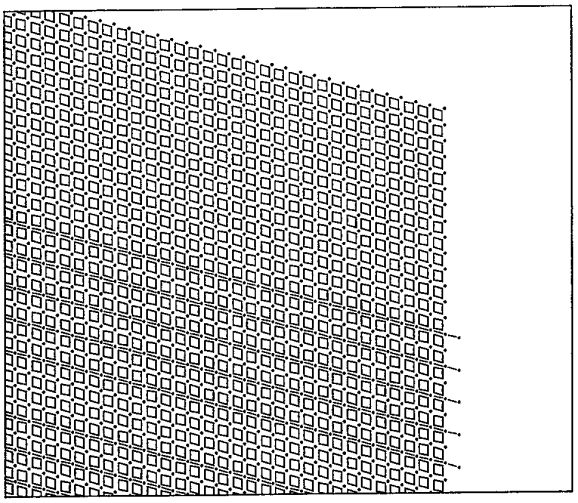

Fig. 4. Finite element representation.

was 12.5 mm, their location being in the vicinity of the crest of the buckle. Figure 4 shows a partial representation of the constructed mesh, with mesh shrink employed for illustrative purposes. It can be seen that each beam element has the same global edge length as the CQUAD4 elements. The topological nature of the beam elements is such that they are congruent with the CQUAD4 shell elements edge, and the associated nodes for each element are coincident.

RBE2 elements are applied to each coincident node set constraining the beam elements such that they translate vertically or out-of-plane in accordance with the motion of the CQUAD4 nodes. Should the beam elements wish to translate along their longitudinal direction, they are free to do so. Such constraints are identical to those within the manufactured specimens where the SMA wires have a slide fit.

Within the analysis, the adaptive capability is provided for by completely fixing one end of the line of one-dimensional elements, the other end having one degree of freedom (DOF) in the direction of the axial recovery force. At the required time of activation, a point load can be applied to the 1 DOF node placing the wire in the desired tensile stressed state. Alternatively, the adaptive capability can be provided for by completely constraining both ends of the line of one-dimensional elements and manipulating the SMA coefficient of thermal expansion such that with application of the transformation temperature, the desired tensile recovery stress will result.

Table 4. Critical buckling values

Lay-up	P_c (N)
$[0_2°/90_2°]_s$	650.0
$[0°/\pm 45°/90°]_s$	863.2
$[0_2°/\pm 45°]_s$	701.4

The results of the linear buckling analysis are presented in Table 4. The first mode shape for each panel was a single half-wave in both directions. The thickness of the laminate, away from the embedded inclusion, was measured to be 1.1–1.12 mm. An effort was made to account for the increased plate thickness in the vicinity of the embedded inclusion, on the structural response, by adding a fictitious bending stiffness to the one-dimensional elements. A clearly evident observation of Table 4 is how the lay-up orientation can effect the critical buckling value, as expected. Such buckling analysis assumes that the structure is perfect, i.e. uniform, and free from eccentric loading. In reality, geometric and material-related imperfections exist, such that when loaded in pure compression, lateral deformation is noticeable from the onset of loading.

In order to simulate the geometric non-linearity, and ensure the non-linear load path, a lateral load of 0.005 N was applied at the point of peak buckling amplitude. Such a force provides an initial maximum out-of-plane displacement of approximately 0.001 mm.

Typically, plate-like structures can support loads well beyond their buckling load. Therefore, the numerical analysis and experimental procedure involved loading the laminated structures to approximately three times the critical buckling value and then activating the optimal set of actuators. The actual applied load being 1.9 kN for lay-ups $[0_2°/90_2°]_s$ and $[0_2°/\pm 45°]_s$, and 2.5 kN for the $[0°/\pm 45°/90°]_s$ lay-up.

EXPERIMENTAL SETUP

The experimental set-up is shown in Fig. 5. Individual test specimens were located within a loading rig specifically developed for this investigation. The unloaded edges were located between knife edges and the loaded edges within flat locating grooves, 0.5 mm deep. The supports provide free transverse movement and prevent free lateral movement. The supports were initially well greased, therefore alleviating

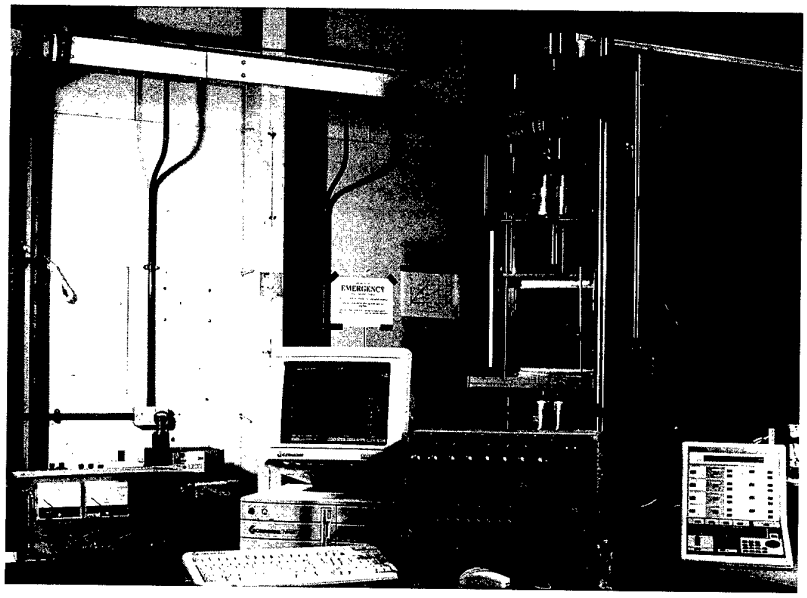

Fig. 5. Experimental setup

possible frictional effects. The pre-strained SMA wires were subjected to an initial tensioning of 1.5 N then clamped within their external fixtures. An Instron Universal Testing Machine was employed to apply the required load. The machine was configured such that it maintained load control. The out-of-plane displacement was measured using an LVDT. Applied load, LVDT displacement and temperature output were recorded using PC-based data logging software. Later in the experimental programme the recovery force of a single SMA actuator, within the test set-up, was recorded. Experimental and numerical results will now be presented.

RESULTS

Results for the on-going research programme are first presented for the $[0_2°/90_2°]_s$ lay-up (Fig. 6). For illustrative purposes, the applied load and the corresponding peak amplitude deflection are shown with respect to time. Presenting the results against time allows us to break down the out-of-plane displacement curve into five evident phases.

During *phase 1*, the applied load is ramped up to 1.9 kN. The corresponding out-of-plane displacement reaching a peak value of −2.79 mm. At this point, there is excellent

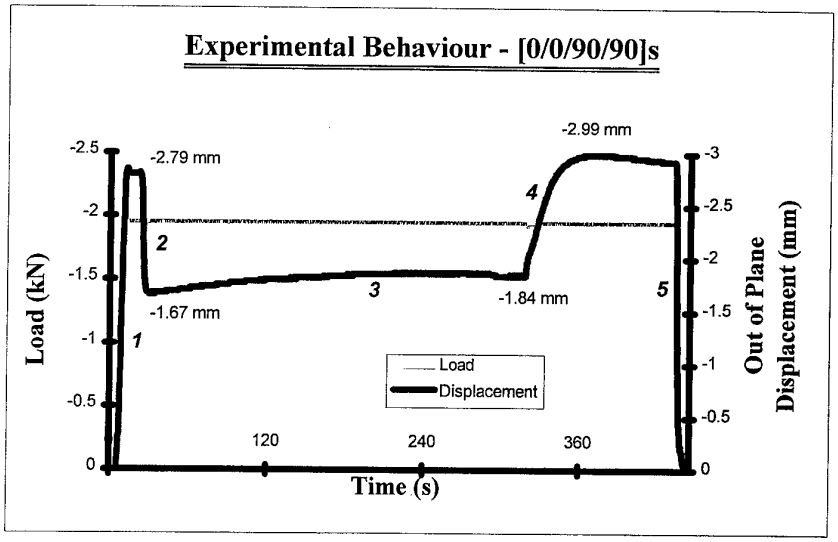

Fig. 6. $[0_2°/90_2°]_s$ post-buckling deflection behaviour.

agreement between experiment and FEA. The FEA predicting an out-of-plane displacement of −2.74 mm. The negative sign indicates the tendency of the plate to deflect away from the LVDT. Rotating the plate within its fixtures would result in positive lateral deformation, therefore ensuring loading rig influences are negligible.

Activation of the SMA actuators, connected in parallel, through application of a DC power source of approximately 140 W results in phase transition, *phase 2*. The resulting SMA restoration forces act to pull the plate back to the flat configuration. At the end of *phase 2*, the energized plate out-of-plane displacement is seen to be −1.67 mm, a reduction of 40.1% compared to the uncontrolled state. With the recovery force maintained for the duration shown, *phase 3*, the out-of-plane displacement is seen to increase to a value of −1.84 mm, this value being 34.1% lower than the uncontrolled state. The slight increase in lateral deformation is attributed to degradation in the matrix properties when exposed to the elevated temperature. At the end of *phase 3*, the plate deflection tends to its constant value as the temperature profile within the laminate approaches the steady state.

When the actuator power source is removed, the out-of-plane displacement profile is seen to increase and overshoot the initial peak displacement amplitude, *phase 4*. The overshoot is the result of the degradation in the aforementioned material properties. As the plate cools, however, the plate tends to the initial value of −2.79 mm. The test ends with the removal of the applied load, *phase 5*. As the load is removed, the lateral displacement is seen to decay to zero.

The loading–activation–deactivation–unloading behaviour was shown to exist for many cycles, all of which show repeatable behaviour. The results presented in Fig. 6 correspond to the 10th cycle.

FE results of the post-buckling alleviation, *phase 2*, predict an out-of-plane displacement of −0.3587 or −1.347 mm when restoration recovery forces of 75 or 55 N, respectively, are generated within the SMA. These forces approximate the initial cycle, and the repeatable behaviour of the transformed alloy (Fig. 1).

The out-of-plane displacement can only be reduced by 34.1%, i.e. not quite realizing the desired FEA behaviour, as a result of the following. The application of the power level to activate the SMA results in the surface temperature profile shown in Fig. 7. Experimentally recorded thermocouple readings are shown for comparison. It can be seen that the thermal FEA predicts the correct trend in thermal behaviour, however it does not account for the thermal boundary layer associated with the vertically inclined plate, the likely cause for the higher temperature readings of thermocouples 4–7. The temperature distribution through the plate thickness was such that it can be assumed to be constant.

From Fig. 7, it can clearly be seen that the temperature distribution at the outer actuator

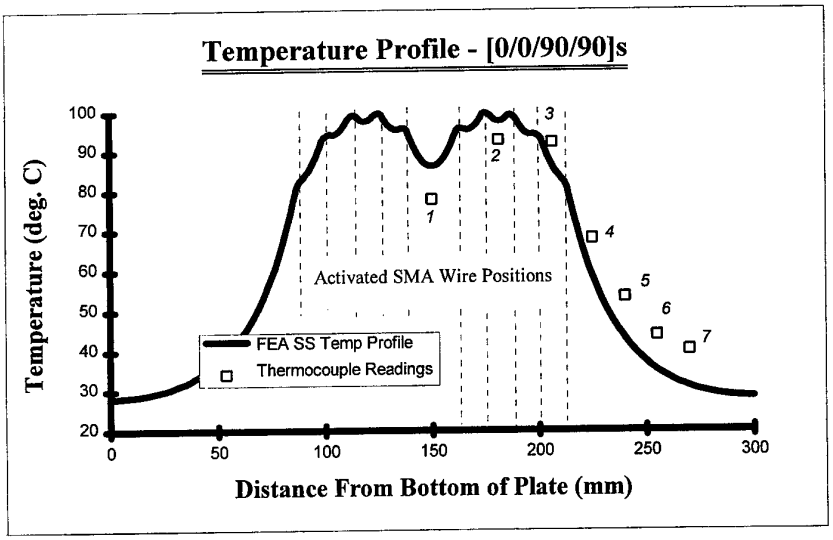

Fig. 7. Temperature profile.

locations is considerably lower than the adjacent actuator locations. The net effect of the lower temperature will be a lower restoration force. The recovery force, for one of the innermost actuators, was recorded to be 48 N. The outermost actuators are thought to be somewhat less than this. This actuator recovery force was not seen to degrade by any significant amount with successive testing. The actual power levels applied to energize the actuators fall short of the amount required for complete phase transition, therefore only partial actuation results. Nonetheless, significant control authority is evident. Increasing the power level further, enabling greater restoration forces, will subject the laminate to a temperature in excess of 100°C.

Employing a partially activated recovery force of 50 N for each SMA wire, within the FEA, results with an out-of-plane displacement of −1.504 mm. Such restoration recovery forces not only reduce the peak displacement amplitude, they also alleviate stress concentrations, typical of post-buckled configurations. Figure 8 shows the FEA longitudinal membrane stress distribution, along the plate's centre-line, when subjected to 1.9 kN with and without the adaptive control. Utilizing adaptive control, it can clearly be seen that at the plate edges the stresses are reduced from −21.98 to −10.32 N/mm^2, the negative sign indicating compression. The tendency of the adaptive plate is to redistribute the loading back towards the plate's central region to the point where a uniform stressed state exists.

The numerical analysis is currently being adapted to account for the temperature-dependent material properties. It is seen that, using data provided by the composite manufacturer, the bending stiffness about the loaded axis is reduced by 11.7% at 80°C compared to that at room temperature.

Similar results are shown in Fig. 9 for the lay-up configuration $[0°/\pm 45°/90°]_s$, with the exception that the applied load was ramped to 2.5 kN. At the end of *phase 1*, a discrepancy exists between FEA and the experimentally determined plate deformation, FEA predicting a value of −3.37 mm. Such a discrepancy is thought to be due to the inadequate representation of the increased bending stiffness associated with the increased plate thickness in the vicinity of the embedded inclusions. Work is under way to adequately account for such a surface undulation numerically and to reduce its affect experimentally.

From the experimental results (Fig. 9) an initial reduction of 33.2% in the peak lateral deformation can be realized by activation of the low-volume fraction SMA material, although this will degrade to a 28% reduction owing to temperature effects. The surface temperature profile was found to be similar to that shown in Fig. 7. FEA utilizing the 75 and 55 N recovery

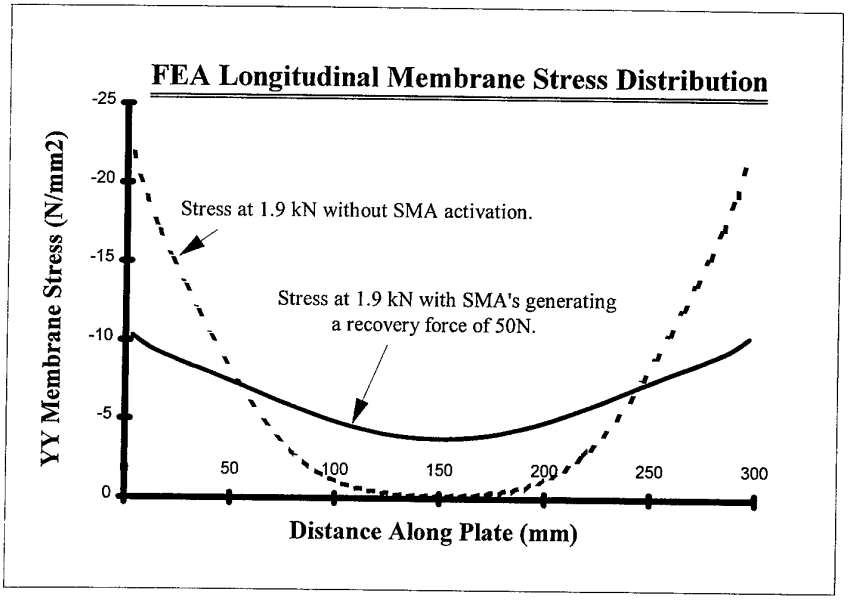

Fig. 8. Longitudinal membrane stress distribution.

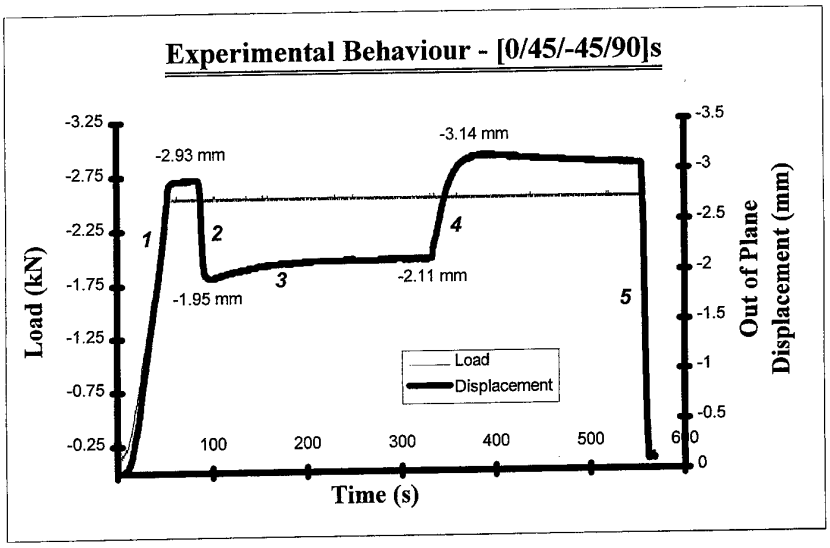

Fig. 9. $[0°/\pm 45°/90°]_s$ post-buckling deflection behaviour.

forces predict out-of-plane displacements of -1.255 and -1.976 mm, respectively, compared to the inactivated deflection of -3.37 mm. As with the previous lay-up, the magnitude of the displacement alleviation for the experiment does not quite realize the desired results of the FEA owing to SMA partial actuation.

Figure 10 shows the experimental behaviour for lay-up configuration $[0_2°/\pm 45°]_s$, loaded to 1.9 kN. The prominent features are the 49.1% reduction in post-buckled deflection, *phase 2*, and the proliferate deflection behaviour, *phases 3 and 4*, attributed to the affects of temperature on the matrix material properties. The bending stiffness about the axis parallel to the loaded axis will degrade by 26% when subjected to a temperature of 80°C. The actual maximum temperature that the plate is exposed to is approximately 100°C, resulting in further mechanical degradation. Such effects could be overcome be increasing the SMA volume fraction.

CONCLUSIONS

Activation of constrained pre-strained SMA wire actuators, located on a laminated plates neutral plane, at load levels approximately three

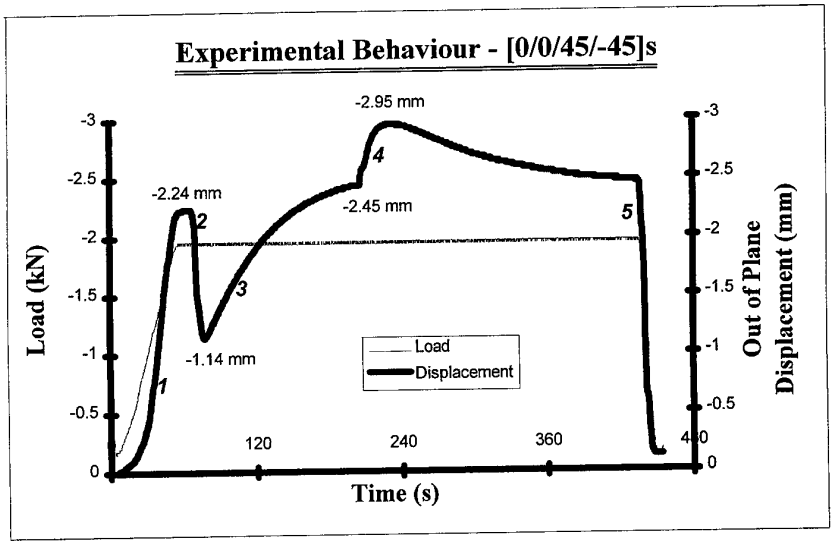

Fig. 10. $[0_2°/\pm 45°]_s$ post-buckling deflection behaviour.

times the critical buckling value results in the significant post-buckled deflection alleviation. For the laminates considered, such post-buckling deflection alleviation is achieved by incorporating relatively low-volume fractions of the SMA material. The effect of such deflection alleviation is to redistribute the applied loading so that a state of uniform axial membrane stress exists. The stability of the adapted shape is dependent upon the laminate stacking sequence. Owing to the elevated temperatures required for SMA transition, the stacking sequence chosen should be such that the temperature-dependent matrix properties are of minimal influence to the structural performance.

Modifications are currently underway to improve both the numerical analysis and the experimental procedure. The numerical analysis requires the input of suitable temperature-dependent matrix properties and an adequate representation of the material extrusion from the nominal plate surface. Improvements to the manufacturing methodology may be met by utilizing the recovery force of an increased volume fraction of finer diameter SMA wires fed through micro-tubing. The employment of micro-tubing with a wall thickness of 0.025 mm is currently being investigated. Such a wall thickness would significantly reduce the cross-sectional area of the embedded inclusion resulting in less disruption to the neighbouring ply reinforcement and plate surface topology. Studies have commenced to ascertain the recovery behaviour of an alternative nickel–titanium SMA composition. Such material having transition temperatures approximately 25°C lower than the material employed within this investigation. Should this composition exert similar recovery forces to those shown in Fig. 1, then powering the actuators to the current level will ensure full transformation and, therefore, generation of the complete recovery force.

Many *buckling critical* aerospace structural components could benefit from such adaptive capabilities, particularly when the mechanically loaded structures are exposed to an elevated temperature, i.e. next generation supersonic civil aircraft. Such an increase in the ambient temperature manifests itself in actuator phase transition and, thus, structural self-strengthening is provided for without the need for a sensory network, data processing or an electrically driven actuator input stimulus.

ACKNOWLEDGEMENTS

The authors wish to express their appreciation to Dr C. Doran, of the Defence and Evaluation Research Agency, Farnborough, UK, for providing financial and technical support, without which the research programme would not progress.

REFERENCES

1. Baz, A. & Tampe, L., Active control of buckling of flexible beams. In *Proc. ASME Design Technical Conf.*, Montreal, Canada, 1989, pp. 211–8.
2. Baz, A., Ro, J., Mutua, M. & Gilheany, J., Active buckling control of nitinol-reinforced composite beams. In *Proc. ADPA/AIAA/ASME/SPIE Conference, Active Materials and Adaptive Structures*, IOP Publishing, Alexandria, VA, 1991, pp. 167–76.
3. Baz, A. & Chen, T., Active control of the lateral buckling of nitinol reinforced composite beams. In *Active Materials and Smart Structures, SPIE Proceedings*, Vol. 2427. SPIE, 1995, pp. 30–48.
4. Thompson, D. M. and Griffin, O. H., Finite element predictions of active buckling control of stiffened panels. *J. Intell. Mater. Syst. Struct.*, 1993, **4**, 243–247.
5. Turner, T. L., Zhong, Z. W. & Mei, C., Finite element analysis of the random response supression of composite panels at elevated temperatures using shape memory alloy fibers 35th AIAA/ASME/ASCE/AMS/ASC Structures, Structural Dynamics and Materials Conference, 1994, 136–146.
6. Rogers, C. A., Liang, C. and Jia, J., Structural modification of simply-supported laminated plates using embedded shape memory alloy fibers. *Comput. Struct.*, 1991, **38**, 569–580.
7. Thompson, S. P. and Loughlan, J., The active buckling control of some composite column strips using piezoceramic actuators. *Composite Struct.*, 1995, **32**, 59–67.
8. Duerig, T. Melton, K., Stockel, D. & Wayman, C., *Engineering Aspects of Shape Memory Alloys*. Butterworth-Heinemann, 1990.
9. Lei, C. & Wu, M., Thermomechanical properties of NiTi-based SMA. In *Smart Structures and Materials*, AD Vol.24/AMD Vol.123. ASME, 1991, pp. 73–7.
10. Tadaki, T., Nakata, Y. and Shimozo, K., Thermal cycling effects in an aged Ni-rich Ti–Ni shape memory alloy. *Trans. Jap. Inst. Metals*, 1987, **28**, 883–90.
11. Udd, E., *Fibre Optic Smart Structures.* John Wiley and Sons, Chichester, 1995.

ELSEVIER

Composite Structures Vol. 38, No. 1–4, pp. 679–687, 1997
© 1997 Elsevier Science Ltd. All rights reserved
Printed in Great Britain
0263-8223/97/$17.00 + 0.00

PII:S0263-8223(97)00105-0

Numerical analysis of a sling support arrangement for GRP composite pressure vessels

D. H. Nash & W. M. Banks

Department of Mechanical Engineering, University of Strathclyde, Glasgow, G1 1XJ, UK

A flexible sling support arrangement for horizontal glass reinforced plastic pressure vessels is examined using advanced finite element methods. A mathematical model is produced employing a suitable analysis capable of representing the non-linear behaviour of a sling supported GRP vessel. This system is used to examine the phenomena occurring at the interface between the vessel and the supporting belt. Each component is initially considered some distance apart and then brought together using three-dimensional contact surfaces. External loads are thereafter applied to the combined model. Although several numerical difficulties arise due to the difference in flexibility between the vessel shell and the sling support, these are overcome and the resulting vessel strains and contact interface pressures show good agreement with experimental work. The magnitudes of the strains at the location of the saddle horn are significantly reduced. Results of a parameter study are also presented which show the effect of the sling position together with the influence of the wrap-round angle and a number of recommendations are made with respect to design. © 1997 Elsevier Science Ltd.

INTRODUCTION

Composite storage vessels can offer a distinct advantage over steel vessels, especially for the storage of hazardous liquids in the chemical process industry. Although many are aligned vertically with a skirt support, the horizontal vessel is particularly useful when there is a restriction on height and space. The most commonly used support system is the *'twin saddle arrangement'* which is similar to that of Zick [1] used for steel vessels. A second alternative is the *'longitudinal beam support'* which forms an integral part of the structure and can run the full length of the vessel. The third alternative, the *'flexible sling system'*, provides support around the lower region of the cylindrical portion of the vessel. Although each of these three systems may be used in the support of GRP vessels, evidence is still required to enable a thorough failure assessment to be carried out, and to determine those applications and situations where their use is most appropriate.

Some guidance is provided in the British Standard BS4994 [2] and also in the ASME Boiler and Pressure Vessel Code [3], Section X. However this information is only qualitative, with the exception of a reference in BS 4994 dealing with metallic pressure vessels. This indicates that in the case of a saddle support, the detailed analysis given in BS 5500 [4] may be used for GRP vessels providing caution is exercised with regard to the strain limitation. This somewhat simplistic, but safe, advice implies that it is relatively straightforward to determine the maximum strain from the analysis given in BS 5500. This treatment assumes the vessel is **isotropic** and does not address the **multi-layered anisotropic** case. In addition, the loose saddle support is recommended even though there are well known problems associated with this type of support.

Both the saddle support and beam support systems have been studied extensively and the work is thoroughly documented [5,6]. However, although some experimental studies have been carried out on the sling supported GRP vessel, there is no suitable analytical treatment as yet. This is due, in part, to the complex nature of the flexibility of the sling support and the interaction with the vessel shell. In this arrangement, a flexible sling fabricated from a strong material, say a Kevlar cloth, is used to carry the vessel rather than the vessel being supported by a more rigid steel saddle. Since the sling is highly flexible, it can change shape as the vessel deforms under load thus avoiding any rigid constraint or abrupt changes of section that occur with rigid saddles. It is this rapid change of vessel shape that introduces highly localised bending stresses into the shell. This can lead to direct failure of the composite shell or reduce the life of the vessel by accelerating failure by fatigue for cyclically loaded systems.

Recent experimental and theoretical work undertaken [6], based on thin shell theory and a Fourier series approach, has shown that the introduction of a flexible sling reduces the stresses arising at the traditional saddle horn location. Therefore, this type of support should have a potential application in GRP vessel design where displacements are larger than those found commonly in steel vessels and limiting the maximum vessel strain is often the major design criterion.

PREVIOUS WORK

Work by Tooth *et al.* [7–10], employs a shell analysis and Fourier series approach that evaluates the form of the contact interface pressure profile. This is undertaken by subdividing the contact region into a number of discrete areas around the circumference and across the saddle width. The flexibility of the support is introduced by the use of a flexibility matrix, generated by the application of unit loads on an equivalent model for the support. In the case of the saddle, this can be thought of as a tapered beam. Applying unit loads in the radial and tangential directions generates the flexibility matrix. Thereafter, the vessel shell is allowed to deform and by enforcing compatibility between the deformed surface and the imposed flexible support at the centre of the contact patch, the interface pressure can be evaluated and thereafter applied to the shell to solve for displacements and strains.

Although the method provides a reasonable agreement with the limited tests presented in the literature, there are several drawbacks associated with this method which may be of importance when applied to the sling support case. Since the form of contact pressure between the shell and the support is unknown, and may change depending on the state of loading; this may become important. In addition, it can vary during the loading sequence when a sling is used (for example, when the vessel is empty the self-weight induces one form of contact pressure profile). If the vessel is gradually filled, the contact pressure varies as the shell and slings adopt a new shape. If the filled vessel is subsequently pressurised, the shell stiffens and the sling adjusts its position. Therefore the form of contact pressure may vary and may not be uniform for all cases. The generation of a flexibility matrix for the support requires the sling to be modelled and the unit load displacement matrix to be evaluated. This is a reasonable approach for a steel saddle where the radial and tangential flexibility can be found using a beam analogy or by the use of finite elements. However, this is made somewhat more difficult when a sling is used, as the basic stiffness is very low and the sling behaves as a cloth material, therefore allowing the vessel to deform in such a manner that the problem may become non-linear. The sling is able to carry a significant load when in tension but less in bending. However the greater the tension, the stiffer the sling.

Although Erzingatzian *et al.* [11], proposed an iterative method using **finite element analysis** to determine the reaction forces at the interface of a fluid loaded, filament wound, fibre reinforced plastic pipe resting on twin rigid saddles, there are some drawbacks with his approach. This is due to the procedure of repeatedly modifying fixed boundary conditions until full contact has been achieved. Although the method shows qualitative agreement with experimental measurements, a quantitative solution is still required. In addition, the problem of introducing the more flexible support remains [12].

FINITE ELEMENT APPROACH USING GENERAL CONTACT SURFACES

A fully parametric finite element model has been developed by the present authors [12] to address the problem of the difference in component flexibility. In addition, when using this approach the contact surface interface pressures are evaluated. This system has been used to examine the phenomena occurring at the interface between the vessel and supporting belt.

Contact elements and contact stiffness

In order to represent the contact between the flexible support and the stiffer shell, the vessel and belt are modelled as discrete components and 'general surface contact elements' were introduced to represent contact and sliding between the two mating surfaces in three dimensions. The contact elements have five nodes with three degrees of freedom at each node (see Fig. 1).

Contact occurs when a contact node penetrates the target base within some tolerance. Although elastic Coulomb friction and rigid Coulomb friction are allowed, a frictionless interface was assumed between the vessel and the sling. The interface contact stiffness *KN*, is required as input to the program and can be calculated using the relationship

$$KN = c \times \mathrm{E} \times \mathrm{h}$$

where c is a factor that controls contact compatibility, usually between 0.01 and 100 [13], E is the smaller Young's modulus when considering contact between two different materials, and h is the characteristic contact length. In three dimensional (3D) configurations, h should be equal to a typical contact target length, taken here as the square root of the target surface.

In order to achieve convergence and ensure that contact occurs between the two components, one stiff and one flexible, a balance must be struck between the chosen contact stiffness value and the lower Young's modulus. A convergence study was undertaken for a two load step analysis. Firstly, the sling and shell are brought into contact by the use of a fixed displacement applied to the top of the sling denoted as LS1. The second load step is the application of gravity to the vessel (LS2). The compatibility factor, c, and the belt axial Young's modulus *EY_B* were varied and the analysis time taken to achieve convergence observed. The criteria chosen to measure the capability of the model to converge were the total number of equilibrium iterations (iter.) and the number of bisections (bis.) used by the Newton–Raphson algorithm.

From Table 1, it appears that the belt axial Young's modulus *EY_B* does not have much influence on analysis convergence. Although the third series of tests run with composite shell element SHELL91 tends to show the contrary

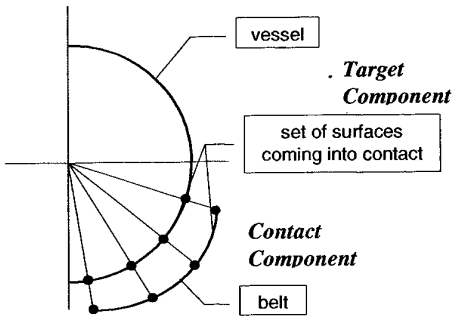

Fig. 1. Contact and target surface selection.

Table 1. Convergence test results for composite SHELL91 model

Values of *EY_B*(N/mm²)	Number of iterations and bisections											
	Values of *c**											
	0.01				0.05				0.1			
	LS 1		LS 2		LS 1		LS 2		LS 1		LS 2	
	bis.	iter	bis.	iter.	bis.	iter.	bis.	iter.	bis.	iter.	bis.	iter.
25000	0	10	1	21	0	16	12	46	–	–	–	–
20000	0	10	3	21	0	16	–	–	–	–	–	–
15000	0	10	0	16	0	19	–	–	–	–	–	–
10000	0	10	6	27	0	14	–	–	–	–	–	–
5000	0	10	1	18	0	15	–	–	–	–	–	–

*For $0.1 < c < 100$ failed to achieve convergent solutions.

revealing convergence failure for values under 25000 N/mm^2 at $c = 0.1$. Concerning the compatibility factor, evidence is that the higher the value, the longer it took to achieve convergence. From $c = 0.1$ to $c = 100$, no convergence was obtained in any of the cases. Therefore, from the convergence study, the following values of the contact parameters were selected for the purposes of carrying out a geometric parameter study.

- c = **0.01**. This value showed the best results and in addition matched with the requirement of a smooth contact between the vessel and the sling, i.e. a small value for the contact stiffness, *KN*.
- ***EY_B*** = **5000 N/mm^2**, although the results of the variation in belt axial stiffness were not significant.

GEOMETRIC PARAMETER STUDY

A fully-parametric finite element model of an orthotropic shell and flexible sling support was developed to allow a wide range of geometric parameters to be varied. As a result, a large number of parameters were involved in the model generation. In particular special attention was paid to the parameterisation of the vessel '**sling zone**' where contact occurs between the vessel and the belt and its neighbouring zone or '**study zone**', where maximum strain levels were anticipated to occur.

The data shown in Table 2 were used to define both the vessel and the belt models. For the vessel, two sets of data are provided referring to an isotropic and an orthotropic approach to the problem. Indeed, given the difficulty of obtaining a converging orthotropic model, the isotropic structure was initially employed to help understand and implement the analysis procedure. Details of the isotropic results can be found in Ref. [16]. The information obtained allowed the generation of a correct orthotropic model, which was then compared to the isotropic one. All dimensions presented are in millimetres and the reference names in parenthesis designate the parameters used in the ANSYS program (see Fig. 2.).

The wrap-round support angle was varied from 120° to 180° with an increment of 20°. One quarter of the structure was modelled due to the presence of two planes of symmetry; thus only half of the angle was necessary, varying from 60° to 90° with an increment of 10°. The vessel density was assumed to equal 2000 kg/m^3. The properties given in Table 3 correspond to those of the orthotropic test vessel.

The vessel was subjected to a three stage loading history. Since the shell and sling are modelled as discrete components a fixed distance apart, the first load step effectively closes the gap and initiates contact. A second load step introduces the gravitational acceleration vector. This is followed by the third and final load step applying the hydrostatic fluid load in ten equal increments as used in previous experimental work [14].

RESULTS AND COMPARISONS

The FE results **closely** match the experimental patterns recorded by Stafford [15]. Maximum strains were consistently found near the extremities of the supports and located in a circumferential orientation irrespective of lay-

Table 2. Main geometric parameters and their variations

Isotropic vessel	Thickness (T_V)	10.75
Orthotropic vessel	Outer layer thickness (TT_CSM)	4.01
	Middle-surface layer thickness (T_FW)	4.57
	Inner layer thickness (TB_CSM)	2.15
Belt	Belt thickness (T_B)	2.00
Vessel half-length (L)	2000	
Vessel mean radius (R)	$1016+(T_{tot}/2) = 1021.375$	
Dished end height (DEH)	393	
Belt width (W)	200 and 400	
Belt position (POS)	500, 750 and 1000	
Study zone beginning (W1)	$POS-(1.5 \times W)$	
Sling zone beginning (W2)	$POS-(0.5 \times W)$	
Sling zone end (W3)	$POS+(0.5 \times W)$	
Study zone end (W4)	$POS+(1.5 \times W)$	

up and configuration. A typical strain distribution is presented in Fig. 3 for a support angle of 180°.

With regard to **circumferential** strains at the point where the sling parts from the vessel the strain was found to be **substantially lower** than the saddle support case where the horn strain is maximum. However. the maximum outside compressive strain has moved to a new location some 10–20° before the 'horn'. This strain then reverses to a maximum tensile strain again at a distance between 10° and 20° after the belt loses contact with the vessel, which correlates with experimental results. Also, circumferential strains on the inside of the vessel were significantly lower than on the outside (see Table 5 for details of strain values). In addition, strains obtained at the vessel middle-span were also much less than those at the support. These results augur well for the sling-supported vessel. In particular. they indicate the absence of large bending strains, which are damaging at the horn of the conventional saddle-supported vessel.

The following factors are worthy of particular note.

1. The tensile strains are well below the damaging value of 2000 $\mu\varepsilon$.
2. The maximum tensile strain occurs on the outside of the vessel. This is of significance

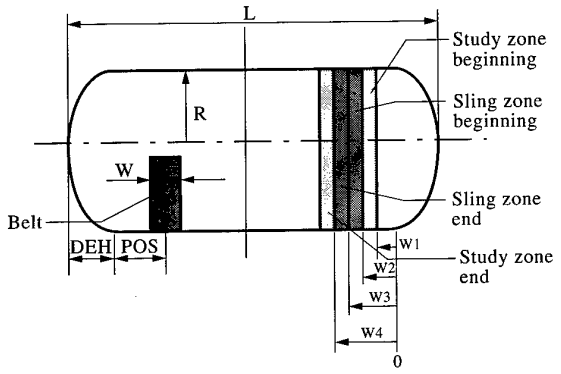

Fig. 2. Main finite element parameters.

Table 3. (a) Material properties for vessel and sling

CSM layers (outer and inner) — isotropic	
Young's modulus (E_CSM)	6160 N/mm^2
Poisson's ratios (NU_CSM)	0.32
Shear modulus (G_CSM)	2330 N/mm^2
FW layer (middle) — orthotropic	
Axial Young's modulus (EX_FW)	8270 N/mm^2
Circumferential Young's modulus (EY_FW)	38600 N/mm^2
Major Poisson's ratios (PRXY_FW)	0.26
Minor Poisson's ratios (PRYZ_FW)	0.0557
Shear modulus (GXY_V)	4140 N/mm^2
(b) The following properties correspond to those for the sling	
Circumferential Young's modulus (EX_B)	125000 N/mm^2
Axial Young's modulus (EY_B)	5000 N/mm^2
Major Poisson's ratio (PRXY_B)	0.3
Minor Poisson's ratio (PRYZ_B)	0.06

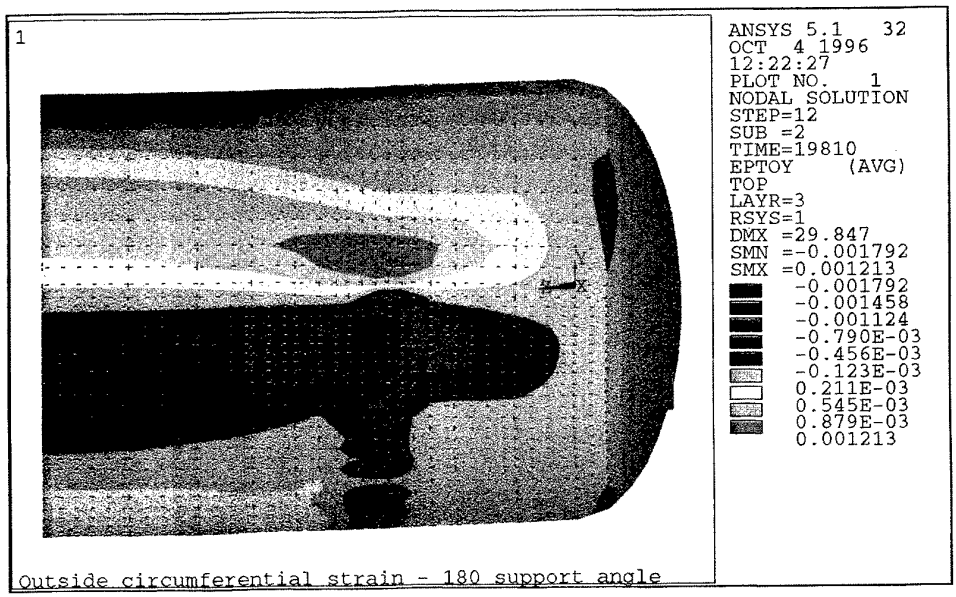

Fig. 3. Outside circumferential strain distribution for 180° sling for orthotropic vessel.

Table 5. Maximum circumferential strains for orthotropic models ($\mu\varepsilon$)

	Maximum Compressive strain		Maximum Tensile strain	
	Outer	Inner	Outer	Inner
Ref-dense	1792	924	1213	626
Ang-80	2445	929	1293	680
Ang-70	2153	944	1316	728
Ang-60	2255	1023	1432	792
Pos-1000	2009	913	1292	704
Pos-500	1907	889	1075	555
Width-400	1371	738	1032	511

*Note: Locations of these maximum vary — see text and Appendix.

when corrosive liquid is being stored. In the limit, some damage could be sustainable on the outside. The problem with strains exceeding the design limitation internally is the possibility of ingress of hazardous material into the glass fibre reinforcement thus initiating stress corrosion cracking. For the 180° support angle, the maximum inner tensile strain is 626 $\mu\varepsilon$ thus giving a fair margin of safety.

3. The compressive values are hovering near the 2000 $\mu\varepsilon$ level. However, a value slightly in excess of this should not be considered a major problem, especially when severe strain gradients are not involved. The possibility of micro-buckling has, however, always to be borne in mind.

The above results gave confidence in the method and the following parameter study was thus initiated.

PARAMETER STUDY RESULTS

Table 4 describes the variation in geometric parameters shown in Table 2, and associates a reference code which was used when undertaking the orthotropic analysis model defined earlier.

Table 4. Reference codes

	Support angle (2 × ALPHA)	Belt location (POS)	Belt width (W)	Mesh density
Ref-dense	180°			dense
Ang-80	160°	750		
Ang-70	140°		200	
Ang-60	120°			dense
Pos-1000		1000		
Pos-500	180°	500		
Width-400		750	400	

In general terms it is noted, from Table 5, that the overall data recorded for circumferential compressive strains are very close to the design limit of 2000 $\mu\varepsilon$ given by BS 4994 and even exceeded it in the 120°, 140° and 160° angle support cases. However, it should be remembered (as indicated above) that the limit is based on a tensile strain consideration. Compressive strain values are generally permitted to go a little higher. Strain plots are shown in Appendix A. These describe the variation in outside circumferential strain with varying geometric parameters and also indicate the locations for the maximum compressive and maximum tensile strain, denoted MN and MX, respectively, on the plots.

Concerning the displacements, Table 6 gives details of the displacements at the central profile and Fig. 4 presents three different views of the vessel deformed shape. The overall sagging of the vessel at its centre can easily be seen on the front view. In the bottom view, the effect of the sling can also be noted. It creates a slight inflexion on the vessel generating tensile strains. The section view reveals interesting information about the belt action on the vessel and its consequences. It clearly shows that the vessel constrained by its sling support can only expand

Table 6. Maximum displacements for orthotropic models (mm)

	Zenith displacement at central profile	Nadir displacement at central profile	Difference
Ref-dense	26.4	29.8	3.4
Ang-80	21.8	33.1	11.3
Ang-70	17.4	31.2	13.8
Ang-60	16.7	34.4	17.7
Pos-1000	30.4	33.7	3.3
Pos-500	21.6	25.0	3.4
Width-400	23.3	24.6	1.3

above the horn. This explains compressive strains where contact exists and tensile strains where the belt parts from the vessel, giving a virtually zero strain transition zone at the horn.

Considering the variation in geometric parameters, the following comments are made. With respect to support angle, the experimental data did not show significant variation in results for different support angle The FEA results however show a slight increase in the maximum strain as the support angle was reduced. Nevertheless, these strain variations remain far less than those recorded with a saddle arrangement at the same point.

Moving the sling from its initial position. i.e. 750 mm from the edge of the vessel cylindrical shell, did not result in major differences in any of the strains In general, a variation between $-100\ \mu\varepsilon$ and $+200\ \mu\varepsilon$ for the strains relative to the 750 mm location was observed; this with the same maximum displacement at the central profile. The strain difference may be due in part to the compact dimensions of the vessel under examination (length: 4 m; diameter: 2 m) which minimises bending effects on the vessel shell itself and thus the significance of the sling location. However, the results show that **the closer the belt is to the vessel ends, the lower the strains and displacements**, which is certainly due to the natural stiffness of the vessel ends.

The variation in sling width from twice the original dimension showed interesting reductions both on strain and displacement figures. In the circumferential direction, compressive strains (the larger values) were reduced by about **25%** and to a lesser extent tensile strains by around 15%. In the axial direction, a significant reduction was obtained with values 12% lower (peak value at 27%) for compressive strains and between 5 and 10% for the tensile strains. From a displacement point of view, results were again encouraging, with a reduction of 62% in maximum deflection at the central profile.

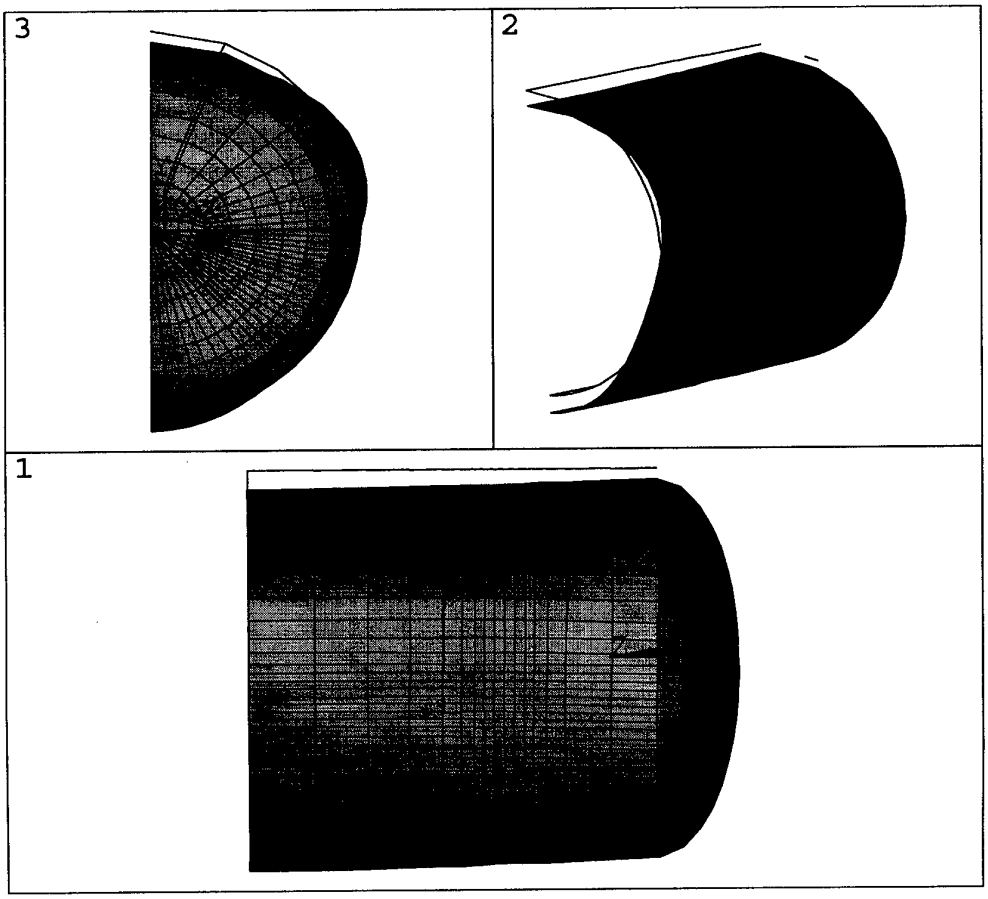

Fig. 4. Typical vessel deformed shape.

CONCLUSIONS

Comparisons between the present analysis and published experimental results [14,15] show reasonable agreement. However, the finite element models produce results consistently higher than those measured experimentally. This points towards a useful design tool. Examination of the deformed shapes of the models indicates the effectiveness of the system in offering a smooth contact interface. The model also presented an insight into the sensitivity of the system to sling stiffness and constraint condition.

The parameter study showed some behavioural similarities to the conventional saddle support. Large wrap round angles proved slightly beneficial and locating the sling near the end of the vessel ensured additional support was achieved; this resulting in lower strain levels. Increasing the width of the sling showed the greatest benefit with, in some cases, a 25% reduction resulting.

Perhaps the most significant conclusion is the lack of large bending effects, which are normally present in the case of the saddle support vessel (the most common method of support). In addition, the tensile strains are significantly lower than the compressive values. Since the tensile strains are the most damaging, this leads to promising possibilities.

While further work on more general cases is still required, the present treatment indicates potential for the sling-supported method.

REFERENCES

1. Zick, L. P. Stresses in large horizontal cylindrical vessels on two saddle supports. *Weld. Res. J. Suppl.*, **30** (1951) 435-S–45-S.
2. BS 4994, Specification for the Design and construction of vessels and tanks in reinforced plastics, British Standards Institution, London, 1987.
3. *ASME boiler and pressure vessel code*, Section X, Fiberglass-reinforced plastic pressure vessels, Appendices 1–5, Attachments and supports, 1995.
4. BS 5500, Specification for Unfired fusion welded pressure vessels, British Standards Institution, London, 1997.
5. Warrender, A. J., Wood, J., Tooth, A. S. & Banks, W. M. The support of horizontal cylindrical GRP vessels-saddles or longitudinal beams? *4th International Conference on Composite Structures*, Paisley, July 1987 (Ed. Marshall, I. H.), Analysis and design studies, Elsevier Applied Science, Vol. 1, 1987, Ch. 17, pp. 1235–1252.
6. Banks, W. M., Tooth, A. S. & Ong, L. S. The support of horizontal multi-layered GRP vessels: Saddles, slings or longitudinal beams? *8th International Conference Pressure Vessel Technology*, American Society of Engineers, Montreal, Canada, 1996, Vol. 2, pp. 315–322.
7. Duthie, G. & Tooth, A. S. The analysis of horizontal cylindrical vessels supported by saddles welded to the vessel — a comparison of theory and experiment. *3rd International Conference Pressure Vessel Technology*, American Society of Engineers, New York, USA, 1977, pp. 25–38.
8. Tooth, A.S., Duthie, G., White, G.C. and Carmichael, J., Stresses in horizontal storage vessels — a comparison of theory and experiment. *J. Strain Anal.*, 1982, **17**, 169–176.
9. Tooth, A. S. & Nash, D. H., Stress analysis and fatigue assessment of twin saddle supported pressure vessels. Pressure Vessels and Components, *ASME Conf. American Society of Mechanical Engineers*, New York, USA, 1991, pp. 41–48.
10. Tooth, A. S., Banks, W. M., Seah, C. P., & Tolson, B. A., The twin-saddle support of horizontal multi-layered GRP vessels-theoretical analysis, experimental work and a design approach. *Proc. Inst. Mech. Eng.*, I MechE, London, Vol. 208, 1994, pp. 59–74.
11. Erzingatzian, A., Hoa, S. V., & Xiao, X., Mechanical behaviour of filament wound FRP pipes on saddles supports. *8th International Conference on Pressure Vessel Technology*, American Society of Engineers, Montreal, Canada, 1996, pp. 123–123.
12. Nash, D. H., Banks, W. M., & Bernaudon, F., Finite element modelling of sling supported vessels. *Bi-Centenary Conference on Thin Walled Structures*, University of Strathclyde, Glasgow, December 1996.
13. ANSYS Structural Analysis Guide, Chapter 8, Nonlinear Structural Analysis, 1st Edition, SAS IP, 1996.
14. Guyon, B., Experimental study of the belt support of horizontal cylindrical GRP vessels. *Undergraduate Thesis*, University of Strathclyde, 1993.
15. Stafford, G., Support and local load problems associated with GRP vessels. *Undergraduate Thesis*, University of Strathclyde, 1994.
16. Bernaudon, F., The study of belt supported glass reinforced plastic pressure vessels using finite element analysis. *Undergraduate Thesis*, University of Strathclyde, 1996.

APPENDIX

The Figs 5–12 contained in this Appendix show the variation in circumferential strain (ε) on the outside surface of the vessel. Figure A1 represents the original position. Figures 6–11 show the variation in wraparound angle, sling width and sling position.

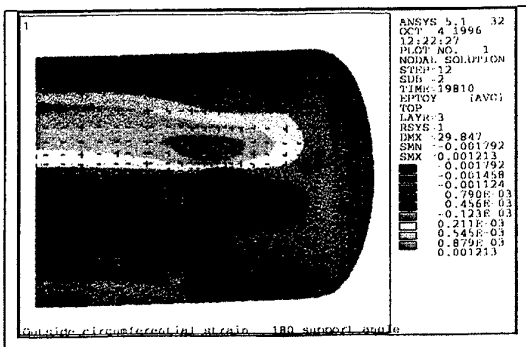

Fig. 5.

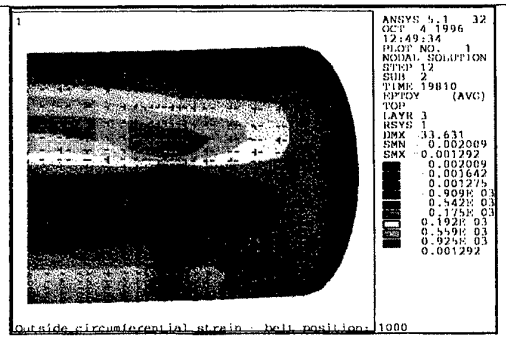

Fig. 9.

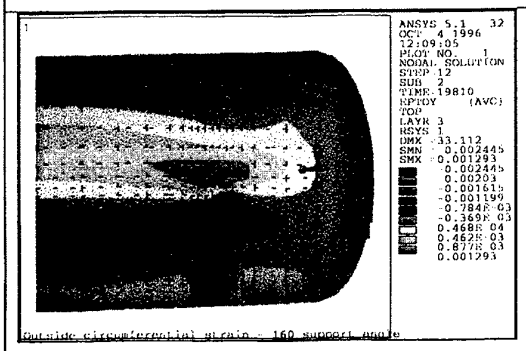

Fig. 6.

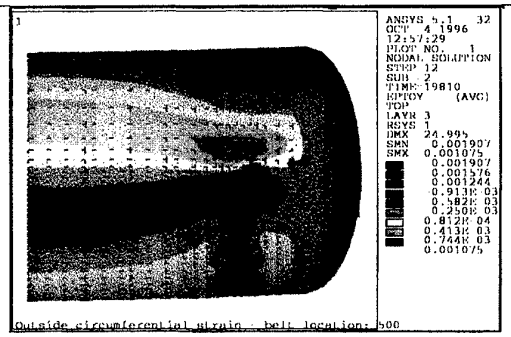

Fig. 10.

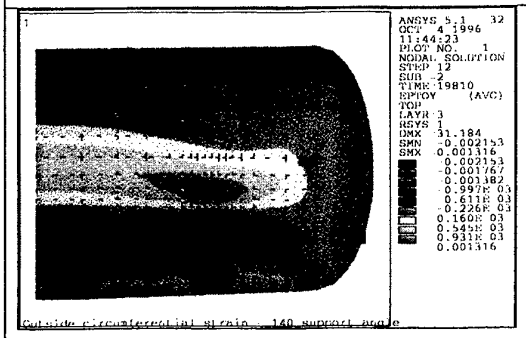

Fig. 7.

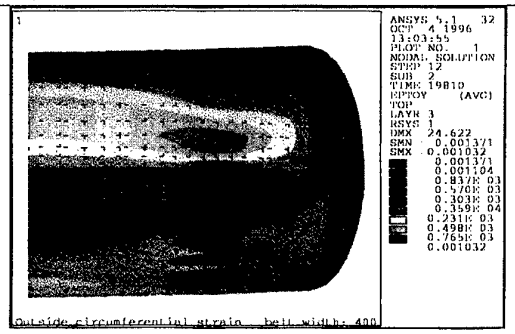

Fig. 11.

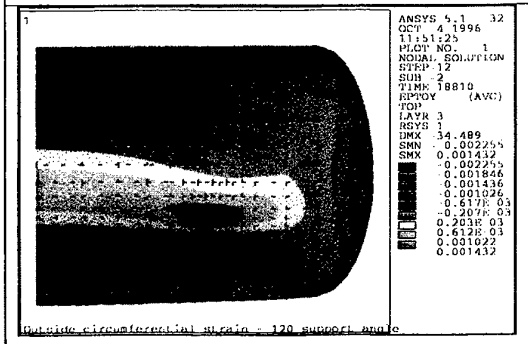

Fig. 8.

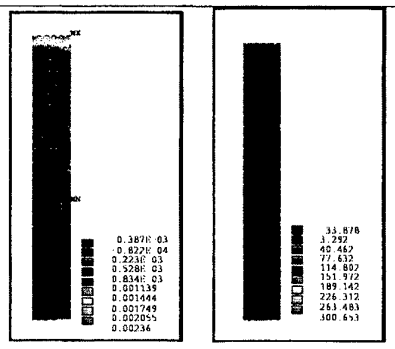

Fig. 12.

Fig. 5. 180° Sling/200 mm wide/location = 750 mm. **Fig. 6.** 160° Sling/200 mm wide/location = 750 mm. **Fig. 7.** 140° Sling/200 mm wide/location = 750 mm. **Fig. 8.** 120° Sling/200 mm wide/location = 750 mm. **Fig. 9.** 180° Sling/200 mm wide/location = 1000 mm. **Fig. 10.** 180° Sling/200 mm wide/location = 500 mm. **Fig. 11.** 180° Sling/400 mm wide/location = 750 mm. **Fig. 12.** Circumferential strain and stress in sling.

ICCI '98

The Second International Conference On Composites In Infrastructure

Short Course: January 3 - 4 1998
Conference: January 5 - 7 1998
Tucson, Arizona

Organized by

The National Science Foundation
and
The University of Arizona

The Second International Conference on Composites in Infrastructure (ICCI '98) will be held in Sheraton El Conquistador Resort in Tucson in January 1998. Following a format similar to the first conference, a short course of Design and Retrofit of Structures with Composites will be offered on Saturday and Sunday (January 3 - 4, 1998). Once again, the course will be taught by a team of experts and will cover a wide range of topics for design of new structures and repair and strengthening of existing structural elements.

The conference will begin on Monday morning and will end on Wednesday (January 5 - 7, 1998). In addition to the increased number of research investigation on composites, the last couple of years have witnessed significant growth in field application of composites. Once again, ICCI will provide a broad-based forum for discussion of many subjects related to the use of composite materials in civil engineering construction. Participants are expected to include researchers, representatives from government and regulatory agencies, practising engineers and architects, contractors, and composites manufacturers.

Further details from:

Engineering Professional Development
The University of Arizona
1224 N. Vine Avenue
Tucson, AZ 85719-4552 USA

Tel: (520) 621-3054
Fax: (520) 621-1443
Email: epd@engr.arizona.edu

Also please consult the conference website at http://engr.arizona.edu/~icci/

E C C M - 8

EUROPEAN CONFERENCE ON COMPOSITE MATERIALS
SCIENCE, TECHNOLOGIES and APPLICATIONS

3 - 6 JUNE 1998

NAPLES, ITALY

The ECCM series started in the early 1980s and conferences have so far been held in France, the United Kingdom and Germany. Organised by the Centro Materiali Compositi and the European Association for Composite Materials, ECCM-8 will take place in Naples, Italy and will consist of Symposia covering selected areas of the Science, Technology and Applications of composites:

Symposium 1:	Composites in Construction
Symposium 2:	Composites in Biomedical Applications
Symposium 3:	High Temperature and Metal Matrix Composites
Symposium 4:	Marine, Aerospace Automotive and Rail Applications
Symposium 5:	Composites: New Basic Concepts
Symposium 6:	Testing, Design, Damage, Tolerance, NDT
Symposium 7:	Cost/Reliability Ratio: Innovations in Fabrication
Symposium 8:	Fibres and Textiles

There will also be a EU workshop on Industrial and Materials Technologies (BRITE-EURAM) and a NATO workshop on Innovations on Technologies.

For further details, please contact:

ECCM-8 Conference Secretariat
DIMP-University of Naples
Piazzale V. Tecchio
80125 Naples

Tel: + 39 81 7682366/70/73
Fax: + 39 81 7614212/7682362

Email: crivisco@unina.it

The Conference also has a website at http://www.eccm98.etruria.net for continuous updating.

ANNOUNCEMENT

On 16 July 1997, during the 11th International Conference on Composite Materials (ICCM-11) in Gold Coast, Australia, an inaugural meeting was held to promote the formation of the Asian-Australasian Association for Composite Materials (AAACM). Delegates from member countries, including Australia, China, Hong Kong, India, Indonesia, Japan, Korea, Malaysia, New Zealand, Singapore, Taiwan, Vietnam were invited, and 16 representatives attended the meeting.

The formation of the AAACM was unanimously agreed and the following inaugural Executive Members were elected:

President:	Professor Y.-W. Mai, University of Sydney, Australia
Vice-President:	Professor M. Zako, University of Osaka, Japan
General Secretary:	Assoc. Professor J.-K. Kim, Hong Kong University of Science and Technology, Hong Kong

The aims of the AAACM are:

- to aid the advancement and dissemination of knowledge and technology in composite materials in general;
- to encourage and foster research and development collaborations between the composite communities of the member countries and elsewhere;
- to sponsor conferences, workshops and other scientific/technical activities among member countries.

It was also decided that the First Asian-Australasian Conference on Composite Materials (AACCM-1) would be organized by the Vice-President, Prof. M. Zako, in Osaka, Japan, in October 1998. The first Call-for-Papers announcement will be made as soon as the Organizing Committee was formed.

For further information:

Assoc. Prof. J.K. Kim, General Secretary-AAACM,
Hong Kong University of Science & Technology
Department of Mechanical Engineering, Clear Water Bay, Kowloon, Hong Kong
Phone: +852 2358 7202; Fax: +852 2358 1543; E-mail: mejkkim@usthk.ust.hk

Did you know that if you are a contributor to any Elsevier Science Book or Journal you are entitled to

30% Discount

on all our Books*?

*(except multi-volume reference works)

Contact your nearest Elsevier Science office
in order to obtain a subject catalogue

Elsevier

Pergamon

North
Holland

Excerpta
Medica

Elsevier Science, Regional Sales Office, Customer Support Department,
PO Box 211, 1000 AE Amsterdam, The Netherlands
• Telephone: +31 20-4853757 • Fax: +31 20-4853432 • E-mail: nlinfo-f@elsevier.nl

Elsevier Science, Regional Sales Office, Customer Support Department,
655 Ave of the Americas, New York, NY 10010, USA
• Telephone: +1-212-633-3730 • Fax: +1-212-633-3680 • E-mail: usinfo-f@elsevier.com

CO7A05/p12

INSTRUCTIONS TO AUTHORS

Submission of papers
Submission of a manuscript implies that it is not being considered contemporaneously for publication elsewhere. Submission of a multi-authored manuscript implies the consent of all the participating authors. All papers should be written in English. All papers will be independently refereed.

Manuscripts should be sent to the Editor, to a local member of the Editorial Board, or to the publisher.

Types of contributions
Research papers; review articles; case studies; technical notes; book reviews; reports of conferences and meetings; letters to the Editor.

Copyright
All authors must sign the 'Transfer of Copyright' agreement before an article can be published. This transfer agreement enables Elsevier Science Ltd to protect the copyrighted material for the authors, but does not relinquish the author's proprietary rights. The copyright transfer covers the exclusive rights to reproduce and distribute the article, including reprints, photographic reproductions, microform or any other reproductions of similar nature and translations, and includes the right to adapt the article for use in conjunction with computer systems and programs, including reproduction or publication in machine-readable form and incorporation in retrieval systems. Authors are responsible for obtaining from the copyright holder permission to reproduce any figures for which copyright exists.

Manuscripts
Three copies should be provided, in double-spaced typing on pages of uniform size, with a wide margin at the left. Generally, the size of the manuscript should not exceed 6000 words or about 12 printed pages. Each paper should be provided with an Abstract of about 100–150 words, reporting concisely on the purpose and results of the paper.

Wherever possible, authors should consult an issue of the journal for style and layout. The Editor reserves the right to adjust style to certain standards of uniformity.

The SI system should be used for all scientific and laboratory data; if, in certain instances, it is necessary to quote other units, these should be added in parentheses. Temperatures should be given in degrees Celsius. The unit 'billion' (10^9 in America, 10^{12} in Europe) is ambiguous and should not be used.

Tables, references and legends to illustrations should be typed on separate sheets and placed at the end of the paper. Footnotes should be avoided if they contain information which could equally well be included in the text.

Disks
For papers produced using a word-processor or TEX, please submit a disk with the **final revised version** of the manuscript. The file on disk should correspond exactly to the hard copy. The operating system and the word-processor used should be specified clearly.

Illustrations or chemical structures in electronic format may be supplied provided that the file format and the program used to produce them is clearly indicated and that a hard copy is also supplied.

More detailed guidelines and further information are available from the publisher.

References
References to published work should be numbered sequentially in order of citation and given in the text by a superscript numeral, with a reference list, in numerical order, at the end of the paper. The list should give name(s) and initial(s) of author(s) and the exact title of the paper or book. For journals there should follow the title, year of issue, volume number and initial and final page numbers of article. For books there should follow the name(s) of the editor(s) (if appropriate), the name of the publisher and the town and year of publication. Where appropriate, initial and final page numbers should also be quoted. All references in this list should be indicated at some point in the text and vice versa. Unpublished data or private communications should not appear in the reference list.

Illustrations
The *original* and two copies, which may be of a reduced size, of each illustration should be provided. Line drawings may be submitted in any medium providing that the image is black and very sharp. They should preferably all require the same degree of reduction; large diagrams, more than four times final size, are discouraged due to handling difficulties. The type area of the journal is 177 mm wide × 240 mm deep, in two columns per page, each 85 mm wide, and lettering should therefore be large enough to be legible after reduction of the illustration to fit (ideally 7pt lettering after reduction). Photographs should be submitted as contrasting black-and-white prints on glossy paper. Each illustration must be clearly numbered and the name(s) of the author(s) of the paper written on the reverse side.

Proofs
The author (or the selected author where several are involved) will receive a set of proofs for checking. No new material may be inserted in the text at the time of proof reading unless accepted by the Editors. All joint communications must indicate the name, full postal address, telephone and fax numbers, and E-mail address (if available) of the author to whom proofs should be sent.

Page charges and offprints
There will be no page charges. Twenty-five offprints of each paper will be supplied free of charge. Additional copies can be ordered at current printing prices.